Journal of Nanomaterials

Novel Micro- and Nanomaterials for Pharmaceutical Applications

Lead Guest Editor: Songwen Tan
Guest Editors: Wenjie Liu, Wenhu Zhou, Ruohui Lin, Tingting Hong, and Yuehong Wang

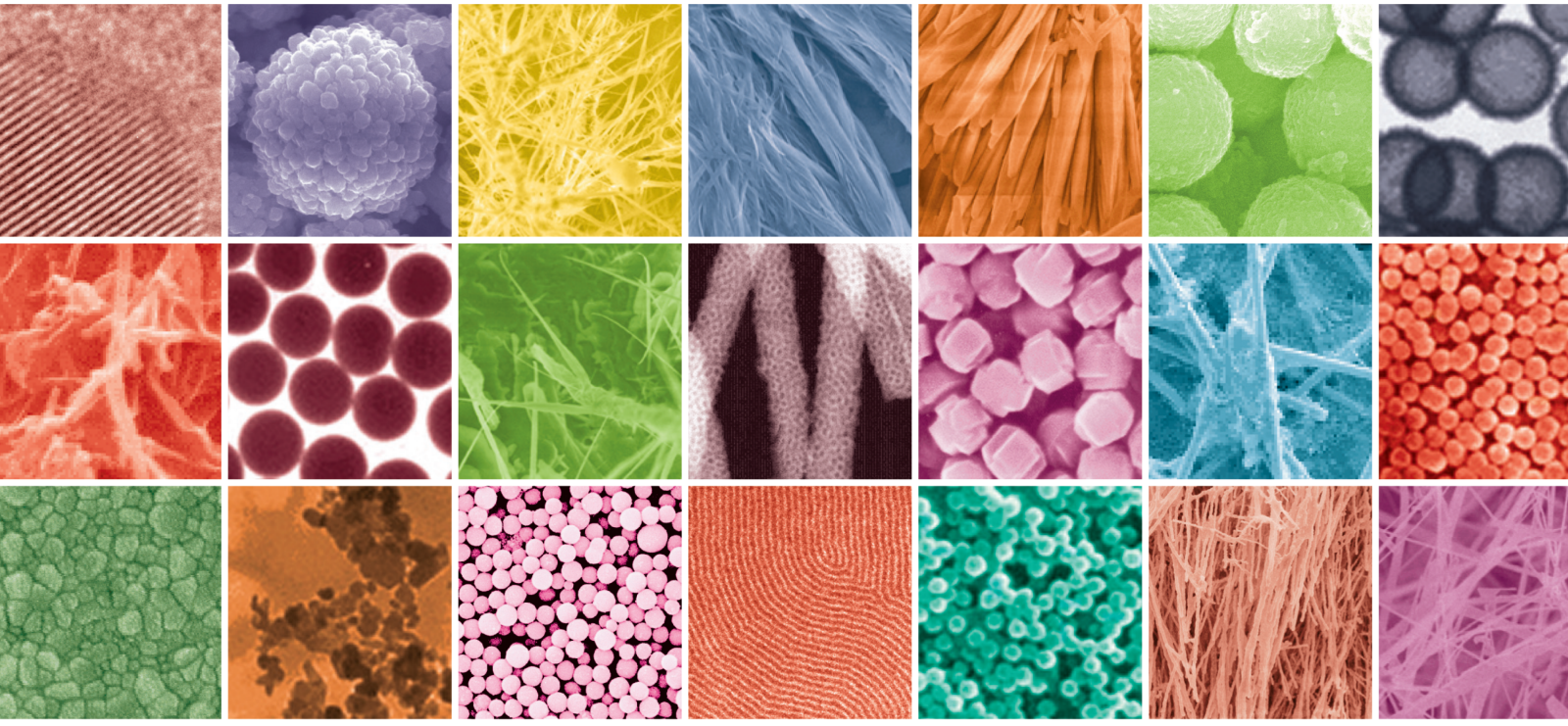

Novel Micro- and Nanomaterials for Pharmaceutical Applications

Journal of Nanomaterials

Novel Micro- and Nanomaterials for Pharmaceutical Applications

Lead Guest Editor: Songwen Tan
Guest Editors: Wenjie Liu, Wenhu Zhou, Ruohui Lin, Tingting Hong, and Yuehong Wang

Contents

Contents

Contents

Hindawi
Journal of Nanomaterials
Volume 2021, Article ID 2365353, 6 pages
https://doi.org/10.1155/2021/2365353

Research Article

Spray-Dried Quercetin-Lactose Powders for Oral Tablets with Improved Dissolution Rates and Modified Material Properties

Long Li,[1] Yuanwei Li,[1] Zhiying Wu,[1] Jinhui Chen,[2] and Jia Chen[1]

[1]*Surgical Department of Urology, Hunan Provincial People's Hospital (The First-Affiliated Hospital of Hunan Normal University), Changsha, Hunan 410005, China*
[2]*Day Surgery Ward, Hunan Provincial People's Hospital (The First-Affiliated Hospital of Hunan Normal University), Changsha, Hunan 410005, China*

Correspondence should be addressed to Jia Chen; 202070201512@hunnu.edu.cn

Received 3 July 2021; Accepted 16 July 2021; Published 20 August 2021

Academic Editor: Songwen Tan

This study is aimed at using spray drying method to codisperse it with the commonly used drug carrier lactose in different solvents and then pass it through a spray dryer to obtain different samples. The results showed that the dissolution rate and solubility of the samples obtained by dispersion in hot water and 25% ethanol were significantly higher. The water of crystallization peaks of the raw material disappeared at 105-125°C and 130-150°C (DSC). The excipient lactose had a small upward exothermic peak at 177°C and a significant heat absorption peak at 209°C before untreated (XRD). α-Lactose peaks were observed at 12.5°, 19.1°, 19.6°, and 19.9° at 2θ in both samples, and β-lactose peaks were found at 10.5° at 2θ in sample A, but not in sample B (FTIR). The complex sharp peaks of lactose at 1100 cm^{-1} and quercetin at 1700-1000 cm^{-1} became moderated (SEM). The sample obtained by spray drying has a slit-type mesoporous structure with an average pore size of about 9.3 nm.

1. Introduction

Quercetin (3,5,7-trihydroxy-2-(3,4-dihydroxyphenyl)-4Hchromen-4-one) is an important flavonoid; it is a bright citrus yellow needle-like crystal, completely insoluble in cold water but its solubility can be increased by heating, very soluble in solvents such as alcohol and lipids. It is one of the most common flavonoids in various foods and is found in a variety of fruits, vegetables, grains, and leaves, with green tea, apple, radish leaves, cranberries, apples, onions, buckwheat, and cilantro being among the more common types [1]. It is antioxidant, anti-inflammatory, antiatherosclerosis, antiobesity, antidiabetes, and other important beneficial effects on the human body [2–6]. However, because of its low solubility and absorption, its beneficial effects on the human body are very limited. In fact, preliminary pharmacokinetic studies of quercetin in humans have shown that the oral bioavailability of this compound is very low (complex metabolic reactions in the small intestine and stomach make it bioavailable, with a reported bioavailability of less than 10%). Quercetin glucoside, the natural form of this compound, has an estimated absorption range of only 3% to 17% per 100 mg of quercetin ingested in healthy individuals. The low bioavailability of quercetin is mainly due to its low absorption rate, extensive metabolism, and/or rapid elimination rate. After ingestion into the body, quercetin metabolites appear in plasma 30 minutes after ingestion but are excreted in large quantities within 24 hours [7]. This suggests that quercetin is rapidly cleared from the blood and has a short half-life. Numerous factors contribute to its practical application with significant difficulties and obstacles.

In recent years, several innovative methods for enhancing the bioavailability of insoluble quercetin have been developed [8–11]. Among them, quercetin-loaded solid lipid nanoparticles have been developed [12]. Compared with pure quercetin powder, their solubility has been improved, but they still have problems such as complicated preparation, high process requirements, and instability.

In the pharmaceutical industry, the aqueous solubility of drug candidates is a very important factor that hinders the entry of drugs into clinical applications. In general, the

bioavailability of both BCS class II and class IV drugs is constrained by the degree of dissolution and dissolution rate. Therefore, a slight improvement in the rate of dissolution can sometimes lead to a significant increase in bioavailability. According to drug theory, dosage form is a very important factor in determining the dissolution properties of a drug. For drugs absorbed from the gastrointestinal tract, amorphous drug forms are effective in increasing the solubility of compounds, thus greatly increasing the bioavailability of these drugs [13]. Unlike crystalline APIs, amorphous APIs have a more disordered structure due to the lack of long-range ordering of molecules. This disorder increases the Gibbs free energy thereby reducing the need to overcome the lattice energy during the dissolution process [14]. It has been reported that an increase in saturated solubility of amorphous drugs may promote a remarkable increase in oral bioavailability. Spray drying technique [15–17] is an important method to obtain amorphous drugs. Spray drying is also a method to well mix multiple ingredients [18].

2. Materials and Methods

2.1. Materials. The quercetin was purchased from (purity > 96 %) Sarn Chemical Technology (Shanghai) Co. Ltd. The pharmaceutical grade α-lactose monohydrate (purity ≥ 99.9%) was purchased from Jiangsu Dawning Pharmaceutical Co., Ltd., China. The anhydrous ethanol (purity ≥ 99.7%) was purchased from Shanghai Titan Technology Co. The purified water used in this experiment was made by the laboratory.

2.2. Experimental Design. In order to increase the solubility and dissolution rate of the insoluble quercetin, we used a spray drying technique in an attempt to convert quercetin and lactose crystals into an amorphous form and keep them stable over a period of time. Lactose is a normal excipient for drug loading [19]. Since quercetin is almost insoluble in cold water, its solubility can be increased by heating, very soluble in solvents such as alcohol and lipids, and in order to dissolve the API (quercetin) as much as possible to destroy its lattice structure, we dispersed the same proportion of quercetin and lactose mixture in 60°C hot water and 25% hot ethanol, respectively, and stirred them at 1000 rpm/min to dissolve and fully disperse them, respectively.

In this experiment, 200 ml of purified water and 200 ml of 25% ethanol were precisely measured and placed in a beaker and heated to 60°C. Subsequently, 0.5 g of quercetin and 9.5 g of lactose were accurately weighed and dissolved in two beakers to obtain suspension A and suspension B, respectively.

Two suspensions were dried using the identical spray drying parameters, and the spray dryer (Shanghai YC-015) was adjusted to the optimum parameters as follows: fan frequency 50.0 Hz, inlet air temperature 140°C, outlet air temperature 120°C, peristaltic pump speed 12.0 ml/min, spray pressure 0.20 MPa, and nozzle diameter 0.5 mm. Spray dry the two suspensions separately to obtain sample A and sample B.

Tablets were prepared by manually introducing powders into the biconvex-faced punch of a hydraulic press with a compression pressure of 4 MPa. A desktop tableting machine was used, and the internal diameter of the equipped tableting die was 10.0 mm (equal to the diameter of the tablets).

2.3. Characterization of Samples. Dissolution samples were obtained from RC1210G Dissolution Tester (Xinzhi, China). The extraction method was paddle method, the speed was 75 rpm/min, the temperature was 37 ± 0.2°C, and the sampling height was 500 mL. UV-Vis absorption spectra were obtained at 200~400 nm with a UV-2401 pc spectrophotometer at Shimadzu, Kyoto, Japan. The obtained sample powders were analyzed by DSC using a differential scanning calorimeter (HSC-4 DSC, Henven, China). Samples for DSC determination were prepared using a sealed aluminum pan following standard procedures. Approximately 8.0 mg of each specimen was used in the analysis. The specimen was heated from 25°C to 300°C at a rate of 5°C/min, using N_2 as the purge gas. To analyze all samples, heat flow was recorded versus temperature rise [20].

The raw materials and samples (quercetin crystals, lactose, and physical mixture and samples A and B) were studied using Fourier transform infrared spectroscopy (FTIR). The samples were compounded with dried KBr powder, pressurized into transparent flakes, and scanned for transmission sensitivity in a Nicolet 6700 FTIR spectrometer (Thermo Fisher Scientific). The FTIR spectral resolution was 1 cm^{-1}. The solid powder sample was placed on an aluminum sample peg on a carbon-band. The gold-plated samples were examined with a JSM-7200F scanning electron microscope (SEM, JEOL Ltd.). The samples were analyzed using a thermogravimetric analyzer (TGA Q5000 V3.17 Build 265). The samples were tested in an alumina pot with N_2 as equilibrium gas [21]. The temperature was set at 35°C~350°C, and the heating rate was constant at 5°C/min, under pyrolytic conditions with nitrogen flow. The crystallization characteristics of the two sample specimen powders were studied by XRD analysis. The solid samples were mounted on powder cartridges and analyzed by a Siemens D5000 diffractometer with 1.0 g of sample dispersed in the cartridge. The scan area of diffraction angle (2θ) was 5~50°, the scan rate was 1.2°/min, the scan current was 30 mA, and the scan voltage was 40 kV. N_2 adsorption experiments were performed on the powder samples separately to evaluate their relative porosity.

2.4. Results and Discussion. We analyzed the data obtained from the experimental assay. The dissolution curves of the three powders for the same conditions are shown in Figure 1, and it can be seen that the untreated quercetin crystal tablets were almost insoluble under the present experimental conditions. The dissolution rate and dissolution degree of the two powders by spray drying increased significantly compared to quercetin crystals [22]. The solubilization effect of sample B obtained by 25% ethanol dispersion was more pronounced, and the dissolution rate was also faster. This may be due to the fact that more quercetin crystals were dissolved in suspension B, causing a large amount of quercetin crystal structure to be disrupted, and more amorphous quercetin was produced during the spraying operation, causing an increase in its solubility. This was also verified in the subsequent analysis.

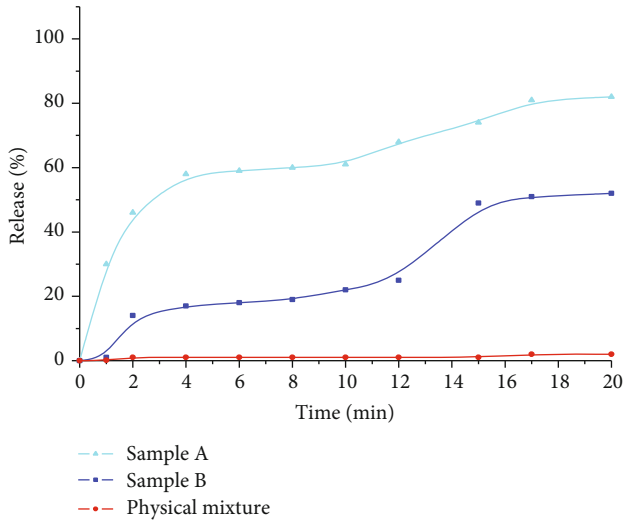

Figure 1: Release spectra of quercetin tablets in the two samples and physical mixture.

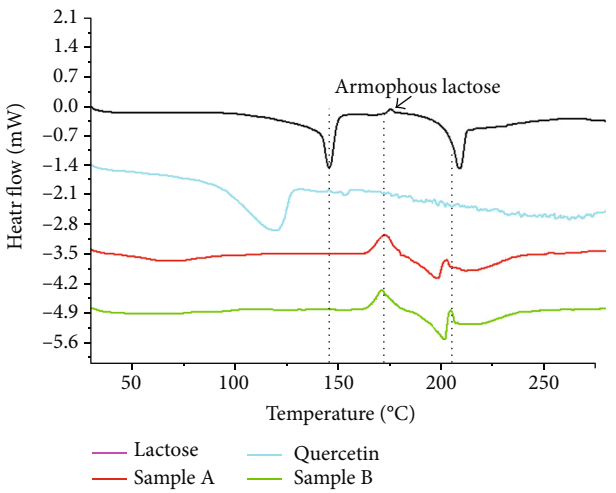

Figure 2: DSC spectrum of the raw materials and productions.

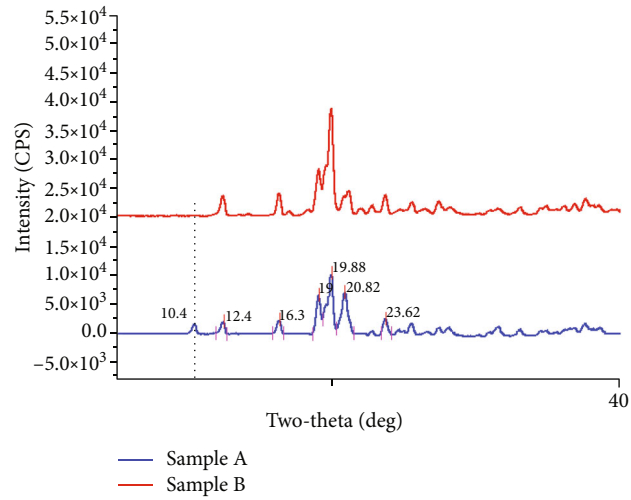

Figure 3: XRD spectrum of two samples.

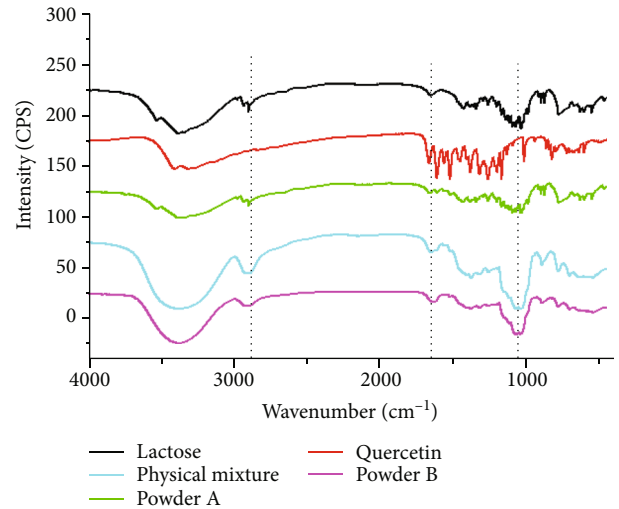

Figure 4: FTIR spectra of the raw materials and samples.

The DSC curve (Figure 2) shows that relative to the two spray-dried products. The water of crystallization peaks of the raw material disappeared at 105-125°C and 130-150°C. The excipient lactose had a small upward exothermic peak at 177°C and a significant heat absorption peak at 209°C before untreated. However, after the spray drying operation with the API, the exothermic peak widened and moved to the low temperature region, indicating the formation of amorphous structure of lactose in the product. Meanwhile, the heat-absorbing peak of lactose at 209°C disappeared, but the heat-absorbing and exothermic peaks appeared simultaneously between 198 and 205°C. By comparing the absorption curves of sample A and sample B, we found that the amorphous lactose exothermic peak of sample B shifted left relative to sample A, and the peak at 198-205°C shifted right relative to sample A. According to the analysis, it may be that more lactose but less API was dissolved in the pure water, resulting in more amorphous lactose generated and less amorphous quercetin generated. Interestingly, the disappearance of the small peak in the thermal spectrum of the quercetin API complex suggests that a homogeneous single mixture was obtained. According to the XRD spectra (Figure 3), α-lactose peaks were observed at 12.5°, 19.1°, 19.6°, and 19.9° at 2θ in both samples, and β-lactose peaks were found at 10.5° at 2θ in sample A, but not in sample B. And the peak shape of both samples was flat, and the lactose peak of sample B was slightly sharper [16]. The analysis suggested that the higher content of amorphous product was obtained in sample A, which was consistent with the results of DSC analysis. The change in peak intensity or wave number shift was studied by FTIR (Figure 4). Similarly, the complex sharp peaks of lactose at 1100 cm^{-1} and quercetin at 1700-1000 cm^{-1} became moderated. This indicates a decrease in the density and strength of hydrogen bonds, a decrease in crystalline states, and a low level of intramolecular interactions. This leads to more dispersion of vibrational energy levels and lower conformational selectivity [23, 24].

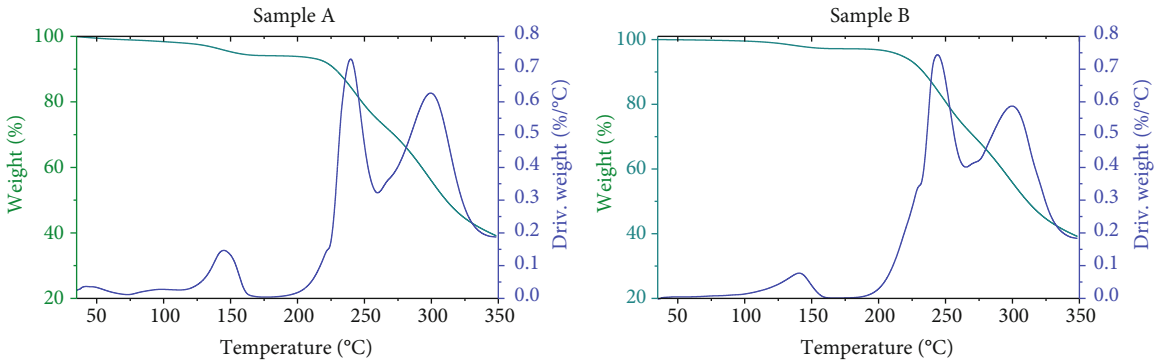

Figure 5: The TGA curve of the two samples.

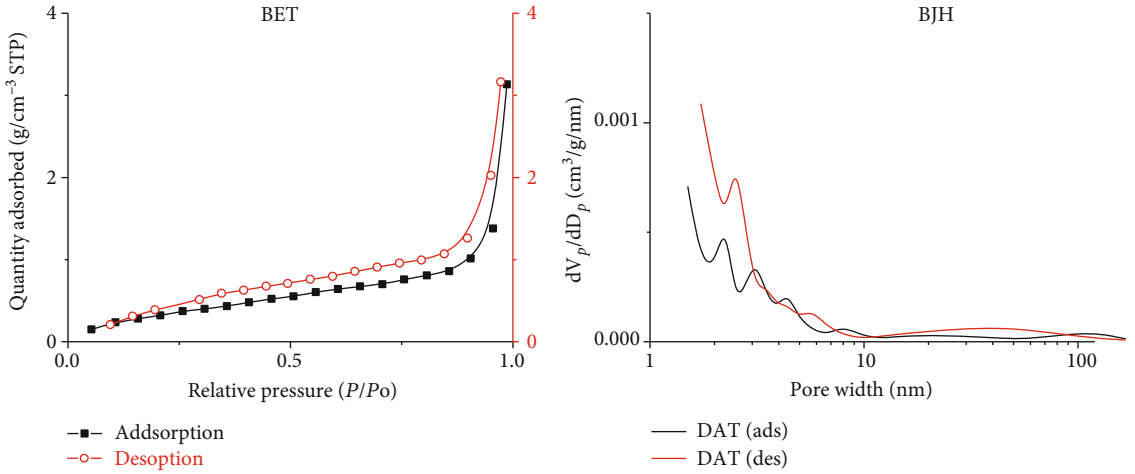

Figure 6: The N_2 adsorption and desorption curves of the sample A.

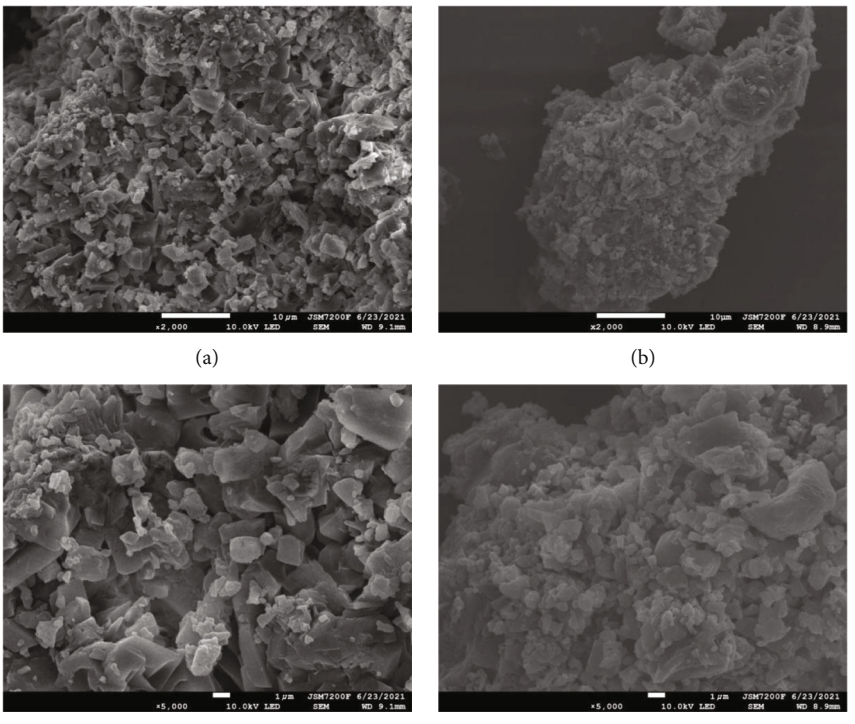

Figure 7: SEM images of the (a, b) sample A and (c, d) sample B, respectively.

According to the TGA (Figure 5) curves, the weight loss rates of the two samples were basically the same in the same temperature range and the thermal stability was the same. Except for the sample containing a small amount of water, DTG analysis samples were roughly two-step weight loss, sample A had a slightly higher weight loss rate in the first step, and the analysis might be that it contained more amorphous lactose. According to the analysis of BET and BJH (Figure 6) data, the adsorption isotherm has a hysteresis loop, and isotherm of H3 type and the adsorption and desorption branches overlap at the cavitation point, and the preliminary analysis of the sample material has slit-type pores or macropores. Combined with the SEM (Figure 7) analysis, the sample obtained by spray drying has a slit-type mesoporous structure with an average pore size of about 9.3 nm. Its porous structure can effectively promote the penetration of water, providing a guarantee for the rapid disintegration and dissolution of drugs.

3. Conclusions

In our experiments, we used pure water and 25% ethanol as the dispersion medium, followed by spray drying, respectively. The in vitro release characteristics were determined by pressing the tablets after atomization and drying. The solubility and dissolution rate of the samples obtained in both dispersion media were higher than those of the control group. In the two media, lactose and quercetin produced different dissolution characteristics such that after spray drying, both materials yielded different proportions of amorphous products. It was demonstrated that the solubility of quercetin increased after performing spray drying, and the solubilization effect was more pronounced for the sample obtained with 25% ethanol. The results showed that the dissolution rate and solubility of the samples obtained by dispersion in hot water and 25% ethanol were significantly higher. The water of crystallization peaks of the raw material disappeared at 105-125°C and 130-150°C. The excipient lactose had a small upward exothermic peak at 177°C and a significant heat absorption peak at 209°C before untreated. α-Lactose peaks were observed at 12.5°, 19.1°, 19.6°, and 19.9° at 2θ in both samples, and β-lactose peaks were found at 10.5° at 2θ in sample A, but not in sample B. The complex sharp peaks of lactose at 1100 cm^{-1} and quercetin at 1700-1000 cm^{-1} became moderated. Scanning electron microscopy images and BET data showed that the two samples obtained by spray drying contained incompletely dissolved crystals, which played a positive role in the formation of mesoporous structures, which further increased the dissolution rate. In conclusion, the spray drying technique significantly improved the solubility of quercetin and provided an idea to solve the problem of its low bioavailability.

Data Availability

The data used to support the findings of this study are included within the article.

Conflicts of Interest

The authors declare that they have no conflicts of interest.

Acknowledgments

This work was supported by the Hunan Natural Science Foundation (Grant Nos. 2020JJ4401 and 2017JJ3180) and the Scientific Research Project of Hunan Provincial Department of Education (Grant No. 20C1158).

References

[1] U. Shabbir, M. Rubab, E. B.-M. Daliri, R. Chelliah, A. Javed, and D.-H. Oh, "Curcumin, quercetin, catechins and metabolic diseases: the role of gut microbiota," *Nutrients*, vol. 13, no. 1, p. 206, 2021.

[2] H. Khan, H. Ullah, M. Aschner, W. S. Cheang, and E. K. Akkol, "Neuroprotective effects of quercetin in Alzheimer's disease," *Biomolecules*, vol. 10, no. 1, p. 59, 2020.

[3] Y. Li, J. Yao, C. Han et al., "Quercetin, inflammation and immunity," *Nutrients*, vol. 8, no. 3, p. 167, 2016.

[4] D. Xu, M.-J. Hu, Y.-Q. Wang, and Y.-L. Cui, "Antioxidant activities of quercetin and its complexes for medicinal application," *Molecules (Basel, Switzerland)*, vol. 24, no. 6, p. 1123, 2019.

[5] P. Fernández-Palanca, F. Fondevila, C. Méndez-Blanco, M. J. Tuñón, J. González-Gallego, and J. L. Mauriz, "Antitumor effects of quercetin in hepatocarcinoma in vitro and in vivo models: a systematic review," *Nutrients*, vol. 11, no. 12, p. 2875, 2019.

[6] X. Liu, Y. Zhang, L. Liu et al., "Protective and therapeutic effects of nanoliposomal quercetin on acute liver injury in rats," *BMC Pharmacology and Toxicology*, vol. 21, no. 1, p. 11, 2020.

[7] W. M. Dabeek and M. V. Marra, "Dietary quercetin and kaempferol: bioavailability and potential cardiovascular-related bioactivity in humans," *Nutrients*, vol. 11, no. 10, p. 2288, 2019.

[8] J. S. Nam, A. R. Sharma, L. T. Nguyen, C. Chakraborty, G. Sharma, and S. S. Lee, "Application of bioactive quercetin in oncotherapy: from nutrition to nanomedicine," *Molecules*, vol. 21, no. 1, article E108, 2016.

[9] Y. Zhou, G. Quan, Q. Wu et al., "Mesoporous silica nanoparticles for drug and gene delivery," *Acta Pharmaceutica Sinica B*, vol. 8, no. 2, pp. 165–177, 2018.

[10] K. T. J. Chen, M. Anantha, A. W. Y. Leung et al., "Characterization of a liposomal copper (II)-quercetin formulation suitable for parenteral use," *Drug Delivery and Translational Research*, vol. 10, no. 1, pp. 202–215, 2020.

[11] H. Y. Son, M. S. Lee, E. Chang et al., "Formulation and characterization of quercetin-loaded oil in water nanoemulsion and evaluation of hypocholesterolemic activity in rats," *Nutrients*, vol. 11, no. 2, p. 244, 2019.

[12] O. Lushchak, O. Strilbytska, A. Koliada et al., "Nanodelivery of phytobioactive compounds for treating aging-associated disorders," *GeroScience*, vol. 42, no. 1, pp. 117–139, 2020.

[13] A. Schittny, J. Huwyler, and M. Puchkov, "Mechanisms of increased bioavailability through amorphous solid dispersions: a review," *Drug Delivery*, vol. 27, no. 1, pp. 110–127, 2020.

[14] B. Wang, F. Liu, J. Xiang et al., "A critical review of spray-dried amorphous pharmaceuticals: synthesis, analysis and application," *International Journal of Pharmaceutics*, vol. 594, article ???, 2021.

[15] S. Tan, A. Ebrahimi, X. Liu, and T. Langrish, "Role of templating agents in the spray drying and postcrystallization of lactose for the production of highly porous powders," *Drying Technology*, vol. 36, no. 15, pp. 1882–1891, 2018.

[16] S. Tan, T. Jiang, A. Ebrahimi, and T. Langrish, "Effect of spray-drying temperature on the formation of flower-like lactose for griseofulvin loading," *European Journal of Pharmaceutical Sciences*, vol. 111, pp. 534–539, 2018.

[17] S. Tan, C. Zhong, and T. Langrish, "Encapsulation of caffeine in spray-dried micro-eggs for controlled release: the effect of spray-drying (cooking) temperature," *Food Hydrocolloids*, vol. 108, article ???, 2020.

[18] S. Tan, X. Chen, S. Zhai, A. Ebrahimi, T. Langrish, and Y. Chen, "Spray drying assisted synthesis of porous carbons from whey powders for capacitive energy storage," *Energy*, vol. 147, pp. 308–316, 2018.

[19] S. Tan, A. Ebrahimi, X. Liu, and T. Langrish, "Hollow flower-like lactose particles as potential drug carriers: effect of particle size and feed concentration," *Powder Technology*, vol. 320, pp. 1–6, 2017.

[20] B. Wang, H. Li, J. Xiang, J. Zheng, and J. Wang, "Fabrication of agglomerated lactose using fluidized bed for good compressibility," *Journal of Nanomaterials*, vol. 2021, Article ID 9918847, 6 pages, 2021.

[21] J. Zheng, B. Wang, J. Xiang, and Z. Yu, "Controlled Release of Curcumin from HPMC (Hydroxypropyl Methyl Cellulose) Co- Spray-Dried Materials," *Bioinorganic Chemistry and Applications*, vol. 2021, Article ID 7625585, 6 pages, 2021.

[22] M. Buchweitz, P. A. Kroon, G. T. Rich, and P. J. Wilde, "Quercetin solubilisation in bile salts: a comparison with sodium dodecyl sulphate," *Food Chemistry*, vol. 211, pp. 356–364, 2016.

[23] Z. Hajihashemi, A. Nasirpour, J. Scher, and S. Desobry, "Interactions among lactose, β-lactoglobulin and starch in co-lyophilized mixtures as determined by Fourier Transform Infrared Spectroscopy," *Journal of Food Science and Technology*, vol. 51, no. 11, pp. 3376–3382, 2014.

[24] M. A. Ottenhof, W. Mac Naughtan, and I. A. Farhat, "FTIR study of state and phase transitions of low moisture sucrose and lactose," *Carbohydrate Research*, vol. 338, no. 21, pp. 2195–2202, 2003.

Hindawi
Journal of Nanomaterials
Volume 2021, Article ID 4580949, 7 pages
https://doi.org/10.1155/2021/4580949

Research Article

Study on the Correlation among Sleep Quality, Cognitive Function, and Self-Management Ability in Hospitalized Elderly Patients with Coronary Heart Disease

Zhoumin Shen,[1] Huali Chen,[1] Yimin Cai,[1] Bifang Zhou,[1] Hongjiao Chen,[2] and Nian Xie[2]

[1]*Nursing Department, Hunan Provincial People's Hospital, Changsha, Hunan 410013, China*
[2]*Department of Nursing, Hunan Normal University School, Changsha, Hunan 410013, China*

Correspondence should be addressed to Yimin Cai; 158460107@qq.com

Received 9 July 2021; Accepted 20 July 2021; Published 3 August 2021

Academic Editor: Songwen Tan

Background. Coronary heart disease (CHD) is the leading cause of death worldwide. The incidence of cardiovascular disease is especially common in low-level and middle-income countries. With the increase in the number of patients with CHD and the complexity of treatment on patients with CHD, many hospitals are devoted to developing new models of care and management for patients with CHD. Understanding the unique characteristics of the patient's condition, including factors related to self-management, cognitive function, and sleep quality, will lead to a substantial reduction in cardiovascular disease and related mortality. *Objective*. To investigate the correlation among sleep quality, cognitive function, and self-management ability in hospitalized elderly patients with coronary heart disease (CHD). *Methods*. 120 hospitalized elderly patients with coronary heart disease (CHD) were investigated by using a self-designed general data questionnaire, Pittsburgh Sleep Quality Index (PSQI), Montreal Cognitive Function Assessment (MoCA) scale, and Coronary Heart Disease Self-management Behavior Scale (CSMS). *Results*. The Spearman analysis showed that sleep quality was positively correlated with cognitive function in hospitalized elderly CHD patients ($P < 0.05$). Sleep quality was positively correlated with self-management ability in CHD patients ($P < 0.05$). *Conclusion*. Improving the cognitive function and self-management ability of elderly patients with coronary heart disease can improve their sleep quality.

1. Introduction

Coronary heart disease (CHD) is the main cause of high morbidity and mortality, leading to immense health and economic burden globally, which concludes hypertension, atherosclerosis, cardiomyopathy, and heart failure [1]. With the aging of the population, CHD has become the most common cause of death from noncommunicable diseases, accounting for more than 40% of residents' death from disease [2, 3]. CHD is a global burden unmatched by any other noncommunicable disease. Approximately 26 million patients are diagnosed with heart failure, and over 39 billion dollars is spent annually in heart failure-related treatments [4]. Common pathological processes and risk factors include inflammation, dyslipidemia, and diabetes; meanwhile, all of these risk factors will affect the initiation and progression of CHD [5, 6]. Moreover, some other risk factors like insulin resistance, obesity, and unhealthy lifestyle such as lack of exercise, poor dietary habits, and smoking have relevance to CHD [7]. However, all the consequences of CHD cannot be fully explained by the risk factors mentioned above.

Recently, a study on the correlation among sleep quality, cognitive function, and self-management ability in hospitalized elderly patients with coronary heart disease has been increasingly favored by researchers. At present, the treatment of coronary heart disease mainly included drug therapy, percutaneous coronary intervention (PCI), lipid-lowering therapy, external counterpulsation therapy (EECP), and a comprehensive treatment containing various treatment methods [8, 9]. Although great improvement of the patients' prognosis can be achieved through treatment methods, various treatment methods and the disease itself have different

impacts on the sleep quality, cognitive function, and self-management ability of hospitalized elderly patients with coronary heart disease [10].

This study intends to explore the correlation among sleep quality, cognitive function, and self-management ability of hospitalized elderly patients with CHD, so as to provide a theoretical basis for further research in the future.

2. Object and Method

2.1. Survey Object. The objects of this study were from two tertiary first-class hospitals in Changsha city, Hunan province, from December 2017 to August 2018. In this study, a target sampling method was adopted to select 120 patients in hospitalized elderly patients with CHD.

Inclusion criteria are as follows: (1) age is ≥60 years old, (2) the patients diagnosed with ischemic heart disease in an electrocardiogram (ECG) test or had a positive result of coronary angiography, and (3) all participants voluntarily agreed to participate in this study and all provided written informed consent.

Exclusion criteria are as follows: (1) patients in critical condition, had severe cardiopulmonary insufficiency, and with abnormal liver and kidney function; (2) patients with a history of mental illness or had severe cognitive impairment; (3) patients who have language communication barriers and cannot communicate normally with others. This study has been reviewed and approved by the ethics committee of our hospital.

2.2. Survey Method. The questionnaires in this study include a self-designed general information questionnaire, Pittsburgh Sleep Quality Index (PSQI), Montreal Cognitive Function Assessment (MoCA) scale, and Coronary Heart Disease Self-Management Behavior Scale (CSMS).

2.2.1. Preparation Stage for Data Collection. In the start of the experimental design, researchers extensively studied many documents including online books and offline books, as well as the literatures related to this topic. And then, the reasonable modifications of the experimental plan were made after being reviewed by experts. Finally, the experimental plan of this study was proposed.

2.2.2. Data Collection Stage. All data were collected with the permission of relevant departments and the nursing supervisor. After patiently communicating with the research objects and obtaining their consent, the questionnaires were distributed to the objects. When all questionnaires were finished, a researcher will check the accuracy and completeness of the filled questionnaires. If there are any omissions or errors, the research objects will be asked to make a supplement for the omissions and make modification for the errors. At the same time, certain key indicators will be verified again with the research objects to ensure the authenticity of all collected data. All data were collected by the designated investigator, so as to reduce the selection bias from different investigators.

2.2.3. Data Processing and Analysis Stage. All data will be checked again, and the data that do not meet the requirement will be deleted. After that, we used the SPSS 21.0 software to statistically analyze and evaluate all collected data. Descriptive statistical analysis methods such as analysis of variance, chi-square test, and Spearman's analysis were mainly adopted in this work.

3. Result

3.1. Chi-Square Test of Sleep Status of Hospitalized Elderly with CHD. In this study, 120 questionnaires were distributed to the elderly patients with CHD. After completing the questionnaire survey, 120 valid questionnaires were received with an effective recovery rate of 100%. Among them, 66 patients are male and 54 patients are female. All patients that participated in this study are aged between 60 and 85. According to the PSQI standard, we divided the patient's sleep status into two groups, which are the normal sleep group and sleep disorder group. In the sleep quality assessment of all volunteers, the PSQI score of 7 was set as a boundary value. All volunteers were grouped according to the difference of demographic and past history of patients. The statistical significance will be assessed by comparing the differences in the incidence of patients with sleep disorder. The chi-square test of sleep status of all hospitalized elderly patients with CHD is summarized in Table 1. We found that there were 27 volunteers who had a total PSQI score over 7 in this study through data analysis of Table 1.

3.2. The Correlation among Sleep Quality, Cognitive Function, and Self-Management Ability in Patients with CHD

3.2.1. Study and Analysis of the Correlation between Sleep Quality and Cognitive Function in Patients with CHD. Poor sleep quality can predict adverse outcomes in patients with CHD [11–14]. A comprehensive understanding of the risk factors of poor sleep quality can help us take reasonable measures to reduce the risk of poor sleep quality, which may reduce the incidence and mortality of patients with CHD. Known demographic risk factors for sleep quality include age, gender, education, income, and marriage status [15–17]. The poor sleep quality is a very common issue in an older person. As so far, 50% of elderly people are suffering from severe sleep issue [18, 19]. Studies have found that the quality of sleep in the elderly has an important correlation with cognitive ability [20]. Therefore, in this study, we tried to use a statistical investigation method to study the correlation between sleep quality and cognitive ability in an elderly patient with CHD.

We performed the PSOI and MoCA normality test on all data. The results of the PSOI and MoCA normality test showed that all data collected from the total score or scores of each dimension did not obey the normal distribution. Thus, the Spearman method was used for correlation analysis. We discussed the statistical significance of the results and found that there was a negative correlation between the total score of PSOI and the total score of MoCA in Table 2. The values of negative correlation and coefficient were $P < 0.05$ and -0.112, respectively. In addition, the patients that

Table 1: Chi-square test of sleep status of hospitalized elderly with CHD.

Variable	Grouping	Normal sleep group	Sleep disorder group	Total number	Chi-square value	P value
Age	60-70	47 78.33	13 21.67	60	4.793	0.091
	70-80	39 81.25	9 18.75	48		
	≥81	8 66.67	4 33.33	12		
Gender	Male	52 78.79	14 21.21	66	3.268	0.071
	Female	42 77.78	12 22.22	54		
Living situation	Cohabitation	85 77.27	25 22.73	110	3.778	0.052
	Live alone	10 100	0 0	10		
Educational level	Uneducated	6 75	2 25	8	2.563	0.633
	Primary education	30 83.33	6 16.67	36		
	Secondary education	35 87.5	5 12.5	40		
	High school education/technical secondary education	23 85.19	4 14.81	27		
	University education	7 77.78	2 22.22	9		
Marriage	Married	86 76.79	26 23.21	112	3.007	0.222
	Divorce	2 100	0 0	2		
	Widowed	6 100	0 0	6		
Monthly earning	≤1000	18 85.71	3 14.29	21	6.312	0.097
	1000~3000	37 72.55	14 27.45	51		
	3001~5000	29 80.56	7 19.44	36		
	>5000	10 83.33	2 16.67	12		
Payment method of medical expenses	Provincial medical insurance	25 73.53	9 26.47	34	2.219	0.528
	Municipal medical insurance	37 80.43	9 19.57	46		
	New rural cooperative medical insurance	30 78.95	8 21.05	38		
	Self-pay	2 100	0 0	2		

Table 1: Continued.

Variable	Grouping	Normal sleep group	Sleep disorder group	Total number	Chi-square value	*P* value
Diagnosis report of coronary angiography	Single-vessel disease	19 70.37	8 29.63	27	15.599	≤0.001
	Double-vessel disease	19 67.86	9 32.14	28		
	Three or more vessel disease	56 86.15	9 13.85	65		
Did the patients undergo coronary stent implantation	Yes	30 71.43	12 28.57	42	1.329	0.249
	No	64 82.05	14 17.95	78		
Heart function classification	I grade	35 77.78	10 22.22	45	4.611	0.203
	II grade	40 78.43	11 21.57	51		
	III grade	14 73.68	5 26.32	19		
	IV grade	5 100	0 0	5		
Does the patient suffer from other diseases	Yes	28 77.78	8 22.22	36	2.060	0.151
	No	66 78.57	18 21.43	84		

had a higher value of total score of PSOI had poorer sleep quality from the results of Table 2.

3.2.2. Study and Analysis of the Correlation between Sleep Quality and Self-Management Ability in Patients with CHD. Many recommended therapies for CHD including revascularization by coronary artery bypass graft or percutaneous coronary intervention are significantly efficacious in reducing angina symptoms and improving prognosis. However, some complications such as heart failure, adverse cardiac events, and even death cannot be avoided [21]. Furthermore, studies have shown that the anxiety and prevalence of depression in CHD patients will also increase, which will seriously affect the health-related quality of life [22]. Therefore, it is particularly important to develop an effective intervention to support patients with CHD in an appropriate approach of management of chronic diseases. Self-management of chronic diseases is widely regarded as an effective way to support patients with chronic diseases to live the best possible quality of life [23–25]. Self-management is defined as "the individual's ability to manage the symptoms, treatment, physical and psychosocial consequences and lifestyle changes inherent in chronic diseases" [26]. Self-management not only can help patients maintain health and related function but also can help patients solve and overcome problems.

We performed the PSOI and CSMS normality test on all data. The results of the PSOI and CSMS normality test showed that all data collected from total score or scores of each dimension did not obey the normal distribution. Thus, the Spearman method was used for correlation analysis. We discussed the statistical significance of the results and found that there was a negative correlation between the total score of PSOI and the total score of CSMS in Table 3. The value of coefficient was -0.142. The patient which had a higher value of total score of PSOI had poorer sleep quality from the results of Table 3.

4. Discussion

4.1. The Status of Sleep Quality in Hospitalized Elderly Patients with CHD. Studies have showed that sleep is the basic human physiological process. A good sleep quality can help relieve fatigue and stress, improve memory, promote the recovery of the vigor, and is more favorable for disease recovery [27, 28]. There were 120 volunteers in hospitalized elderly patients with CHD that participated in this study. Among them, 26 volunteers in hospitalized elderly patients with CHD had sleep disorders from the results of PSAI test and analysis. The rate of sleep disorder was 21.67%. After analyzing and summarizing the data, we found that there were 120 hospitalized elderly CHD patients with a

Table 2: Correlation analysis between sleep quality and cognitive function in patients with CHD.

Variability	Statistics	Visual space and executive function	Name	Memory	Attention	Language	Abstract	Delayed memory	Orientation	Additional points	Cognitive total score
Dimension 1: sleep quality	r	0.060	0.009	0.033	-0.044	-0.075	0.041	0.098	-0.119	0.063	0.057
	P	0.373	0.899	0.625	0.518	0.268	0.546	0.149	0.078	0.352	0.397
Dimension 2: the time to fall asleep	r	-0.006	-0.010	-0.021	-0.007	-0.084	-0.042	0.034	-0.152*	0.081	0.009
	P	0.933	0.885	0.752	0.914	0.216	0.535	0.613	0.024	0.234	0.889
Dimension 3: bedtime	r	-0.156*	0.008	-0.076	0.024	-0.019	-0.237**	-0.024	-0.272**	0.055	-0.042
	P	0.020	0.910	0.259	0.719	0.780	≤0.001	0.727	≤0.001	0.419	0.537
Dimension 4: sleep efficiency	r	-0.003	-0.011	0.027	0.027	0.074	-0.205**	-0.149*	-0.131	-0.087	≤0.001
	P	0.962	0.875	0.686	0.686	0.273	0.002	0.027	0.052	0.200	0.998
Dimension 5: sleep disorders	r	-0.243**	-0.244**	-0.343**	-0.288**	-0.078	-0.211**	-0.298**	-0.443**	0.109	-0.349**
	P	≤0.001	≤0.001	≤0.001	≤0.001	0.251	0.002	≤0.001	≤0.001	0.108	≤0.001
Dimension 6: sleep medicine	r	-0.057	0.001	-0.117	0.036	-0.044	-0.137*	-0.072	-0.240**	-0.051	-0.065
	P	0.397	0.991	0.085	0.590	0.512	0.043	0.287	≤0.001	0.452	0.337
Dimension 7: daytime function	r	-0.227**	-0.236**	-0.211**	-0.194**	-0.180**	-0.065	-0.201**	-0.327**	0.100	-0.219**
	P	0.001	≤0.001	0.002	0.004	0.007	0.334	0.003	≤0.001	0.138	0.001
Total scores of sleep	r	-0.081	-0.082	-0.097	-0.072	-0.093	-0.165*	-0.084	-0.325**	0.074	-0.112
	P	0.232	0.225	0.153	0.291	0.167	0.014	0.216	≤0.001	0.273	0.002

Note: *$P < 0.05$, **$P < 0.01$.

total PSQI score of 5.53 ± 3.32, which was higher than that of the normal score (3.88 ± 2.52) in China [29]. Therefore, the clinical staff should be highly concerned about the sleep quality of hospitalized elderly CHD patients.

4.2. Correlation between Sleep Quality and Cognitive Function in Patients with CHD. We analyzed the statistical data of *Spearman*, and the results showed that the correlation coefficient between the sleep quality score (PSQI total score) and the MoCA total score was negative, which means the patients with higher total score of sleep quality have worse cognitive ability. In addition, the patients with higher sleep quality score have worse sleep quality. In conclusion, the CHD patients with better sleep quality have better cognitive ability. Therefore, the sleep quality of hospitalized elderly CHD patients is positively correlated with cognitive ability. The correlation between sleep dimensions and cognitive ability dimensions in this study kept consistency with the results of Kang et al.'s study. Kang et al. [30] studied the correlation between cognitive ability and sleep status of 203 elderly patients (≥60 years old) from Changsha city. They found that the Pittsburgh Sleep Quality Index (PSQI) has a negative correlation with attention, numeration ability, and language in six dimensions. Sleep maintenance disorders and daytime residual were all cardinal manifestations of sleep disorders. This may be related to less blood flow in the prefrontal cortex. In general, the prefrontal cortex is the main area that regulates cognitive activities like executive function and behavior. Sleep disorders impair cognitive ability by affecting the prefrontal cortex.

4.3. The Correlation between Sleep Quality and Self-Management Ability of Patients with CHD. We analyzed the statistical data of *Spearman*, and the results showed that the correlation coefficient between the sleep quality score (PSQI total score) and the CSMS total score was negative, which means the patients with higher total score of sleep quality have the worse self-management ability. In addition, the patients with higher sleep quality score have worse sleep quality. In conclusion, the CHD patients with poor sleep quality have poorer self-management ability. Thus, the sleep quality of hospitalized elderly CHD patients is positively correlated with self-management ability. Disease self-management refers to a healthy behavior that enhances patients' health through maintaining the patients' behavior, monitors and manages their physical and psychological symptoms, and reduces the impacts of diseases on social functions and emotions. In this study, the Pittsburgh Sleep

Table 3: Correlation analysis between sleep quality and self-management in patients with CHD.

Variability	Statistics	Dimension 1: bad management habits	Dimension 2: symptom management	Dimension 3: emotional and cognitive management	Dimension 4: emergency management	Dimension 5: disease knowledge management	Dimension 6: daily life management	Dimension 7: treatment compliance and self-management	Total scores of CSMS
Dimension 1: sleep quality	r	-0.010	0.037	-0.021	0.051	0.058	-0.103	0.068	0.024
	P	0.880	0.581	0.756	0.450	0.394	0.128	0.317	0.722
Dimension 2: the time to fall asleep	r	-0.129	-0.046	-0.074	-0.022	-0.184**	-0.205**	0.011	-0.139*
	P	0.056	0.494	0.274	0.748	0.006	0.002	0.868	0.039
Dimension 3: bedtime	r	-0.014	0.139*	-0.072	0.244**	0.083	-0.128	0.087	0.094
	P	0.840	0.039	0.288	≤0.001	0.221	0.057	0.201	0.163
Dimension 4: sleep efficiency	r	-0.120	0.126	0.067	0.345**	0.032	0.046	0.115	0.124
	P	0.076	0.062	0.325	≤0.001	0.637	0.502	0.089	0.065
Dimension 5: sleep disorders	r	0.109	0.066	-0.002	0.088	-0.013	-0.112	0.080	0.040
	P	0.106	0.333	0.972	0.191	0.853	0.098	0.240	0.553
Dimension 6: sleep medicine	r	0.033	0.115	0.139*	0.185**	0.184**	0.033	0.096	0.208**
	P	0.629	0.088	0.040	0.006	0.006	0.627	0.157	0.002
Dimension 7: daytime dysfunction	r	0.077	-0.119	-0.128	-0.128	-0.139*	-0.305**	0.032	-0.170*
	P	0.256	0.077	0.058	0.057	0.039	≤0.001	0.633	0.011
Total scores of PSOI	r	-0.050	0.060	-0.031	0.101	-0.054	-0.234**	0.123	-0.142
	P	0.458	0.378	0.652	0.134	0.424	≤0.001	0.069	0.041

Note: $^{*}P < 0.05$, $^{**}P < 0.01$.

Quality Index (PSQI) was negatively related to disease knowledge management and daily life management in two dimensions. The self-management ability of CHD patients can be improved by maintaining a good quality sleep, staying awake during the daytime, and keeping a positive attitude.

5. Conclusion

By adopting questionnaire methods and statistical analysis, we investigated the status of sleep quality, cognitive function, and self-management ability of hospitalized elderly patients with coronary heart disease and discussed the correlation relationship among them. In investigating the total PSQI score of 120 hospitalized elderly CHD patients, there was a PSQI score of 5.53 ± 3.32. The Spearman analysis showed that the sleep quality of CHD patients was positively correlated with cognitive function and self-management ability. The sleep quality of elderly patients with coronary heart disease can be improved by improving the cognitive function, as well as their self-management ability. This research work provides a theoretical basis for improving the sleep quality of hospitalized elderly patients with coronary heart disease, improving cognitive function and self-management ability, and formulating personalized nursing plans.

Data Availability

The data used to support the findings of this study are available from the corresponding author upon request.

Disclosure

The funders had no role in the design of the study; in the collection, analyses, or interpretation of data; in the writing of the manuscript; or in the decision to publish the results.

Conflicts of Interest

The authors declare no conflict of interest.

Authors' Contributions

Zhoumin Shen and Huali Chen participated in the writing of this paper. Yimin Cai guided the writing of the paper and reviewed the manuscript. Zhou participated in the design and drafting of this manuscript. All authors have read and agreed to the published version of the manuscript. Zhoumin Shen and Huali Chen contributed equally to this work and should be considered co-first authors.

Acknowledgments

This work was supported by Natural Science Foundation of Hunan Province (2018JJ2227).

References

[1] Writing Group Members, D. Mozaffarian, E. J. Benjamin et al., "Heart disease and stroke statistics-2016 update: a report from the American Heart Association," *Circulation*, vol. 133, no. 4, pp. e38–360, 2016.

[2] J. D. Schwalm, M. McKee, M. D. Huffman, and S. Yusuf, "Resource effective strategies to prevssent and treat cardiovascular disease," *Circulation*, vol. 133, no. 8, pp. 742–755, 2016.

[3] A. Liu, P. Kang, J. Liu, D. Li, and L. Zhang, "Effectiveness of comprehensive geriatric assessment in elderly patients with coronary heart disease," *Biomedical Research*, vol. 28, no. 17, 2017.

[4] G. Savarese and L. H. Lund, "Global public health burden of heart failure," *Cardiac Failure Review*, vol. 3, no. 1, p. 7, 2017.

[5] S. Zoungas, A. J. Curtis, J. J. McNeil, and A. M. Tonkin, "Treatment of dyslipidemia and cardiovascular outcomes: the journey so far–is this the end for statins?," *Clinical Pharmacology and Therapeutics*, vol. 96, no. 2, pp. 192–205, 2014.

[6] H. Haybar, M. Shokuhian, M. Bagheri, N. Davari, and N. Saki, "Involvement of circulating inflammatory factors in prognosis and risk of cardiovascular disease," *Journal of Molecular and Cellular Cardiology*, vol. 132, pp. 110–119, 2019.

[7] I. I. Abubakar, T. Tillmann, and A. Banerjee, "Global, regional, and national age-sex specific all-cause and cause-specific mortality for 240 causes of death, 1990–2013: a systematic analysis for the Global Burden of Disease Study 2013," *Lancet*, vol. 385, pp. 117–171, 2015.

[8] G. Kozdag, G. Ertas, E. Aygun et al., "Clinical effects of enhanced external counterpulsation treatment in patients with ischemic heart failure," *Anadolu Kardiyoloji Dergisi*, vol. 12, no. 3, pp. 214–221, 2012.

[9] H. Y. Ma, Z. P. Xing, R. L. Liu, S. H. Wang, and Y. L. Zhao, "Present situation and prospect of interventional therapy for coronary heart disease in China," *Austin Cardiology*, vol. 2, no. 1, p. 1010, 2017.

[10] M. Y. Ağargün, H. Kara, and O. Anlar, "Reliability and validity of Pittsburgh sleep quality ındex," *Turkish Journal of Psychiatry*, vol. 7, pp. 107–111, 1996.

[11] S. Schwartz, W. M. Anderson, S. R. Cole, J. Cornoni-Huntley, J. C. Hays, and D. Blazer, "Insomnia and heart disease: a review of epidemiologic studies," *Journal of Psychosomatic Research*, vol. 47, no. 4, pp. 313–333, 1999.

[12] D. A. Katz and C. A. McHorney, "Clinical correlates of insomnia in patients with chronic illness," *Archives of Internal Medicine*, vol. 158, no. 10, pp. 1099–1107, 1998.

[13] C. Leineweber, G. Kecklund, I. Janszky, T. Akerstedt, and K. Orth-Gomer, "Poor sleep increases the prospective risk for recurrent events in middle-aged women with coronary disease: the Stockholm Female Coronary Risk Study," *Journal of Psychosomatic Research*, vol. 54, no. 2, pp. 121–127, 2003.

[14] S. W. Schwartz, J. Cornoni-Huntley, S. R. Cole, J. C. Hays, D. G. Blazer, and D. D. Schocken, "Are sleep complaints an independent risk factor for myocardial infarction?," *Annals of Epidemiology*, vol. 8, no. 6, pp. 384–392, 1998.

[15] R. Asplund, "Sleep and cardiac diseases amongst elderly people," *Journal of Internal Medicine*, vol. 236, no. 1, pp. 65–71, 1994.

[16] N. T. Ayas, D. P. White, J. E. Manson et al., "A prospective study of sleep duration and coronary heart disease in women," *Archives of Internal Medicine*, vol. 163, no. 2, pp. 205–209, 2003.

[17] E. Jensen, O. Dehlin, B. Hagberg, G. Samuelsson, and T. Svensson, "Insomnia in an 80-year-old population: relationship to medical, psychological and social factors," *Journal of Sleep Research*, vol. 7, no. 3, pp. 183–189, 1998.

[18] V. S. Rains and T. F. Ditzler, "Sleep disorders and aging," *The New England Journal of Medicine*, vol. 326, no. 14, pp. 956-957, 1992.

[19] N. Wolkove, O. Elkholy, M. Baltzan, and M. Palayew, "Sleep and aging: 1. Sleep disorders commonly found in older people," *CMAJ*, vol. 176, no. 9, pp. 1299–1304, 2007.

[20] J. Niu, H. Han, Y. Wang, L. Wang, X. Gao, and S. Liao, "Sleep quality and cognitive decline in a community of older adults in Daqing City, China," *Sleep Medicine*, vol. 17, pp. 69–74, 2016.

[21] R. Itier and J. Roncalli, "New therapies for acute myocardial infarction: current state of research and future promise," *Future Cardiology*, vol. 14, no. 4, pp. 329–342, 2018.

[22] J. le, D. S. Dorstyn, E. Mpfou, E. Prior, and P. J. Tully, "Health-related quality of life in coronary heart disease: a systematic review and meta-analysis mapped against the International Classification of Functioning, Disability and Health," *Quality of Life Research*, vol. 27, no. 10, pp. 2491–2503, 2018.

[23] S. G. S. Gerward and D. S. D. Sahlin, "Self-care management intervention in heart failure," *Turkish Journal of Psychiatry*, vol. 21, pp. 525–525, 2019.

[24] K. Meng, G. Musekamp, M. Schuler et al., "The impact of a self-management patient education program for patients with chronic heart failure undergoing inpatient cardiac rehabilitation," *Patient Education and Counseling*, vol. 99, no. 7, pp. 1190–1197, 2016.

[25] L. P. Kimble, "A randomized clinical trial of the effect of an angina self-management intervention on health outcomes of patients with coronary heart disease," *Rehabilitation Nursing*, vol. 43, no. 5, pp. 275–284, 2018.

[26] N. H. Jonkman, M. J. Schuurmans, T. Jaarsma, L. M. Shortridge-Baggett, A. W. Hoes, and J. C. A. Trappenburg, "Self-management interventions: proposal and validation of a new operational definition," *Journal of Clinical Epidemiology*, vol. 80, pp. 34–42, 2016.

[27] A. C. Guyton and J. E. Hall, *Textbook of Medical Physiology*, WB Saunders, Philadelphia, 11th ed edition, 2006.

[28] W. F. Ganong, *Review of Medical Physiology*, Connecticut McGraw-Hill, Stamford, 23th ed edition, 2009.

[29] X. Liu, M. Tang, and L. Hu, "Reliability and validity of the Pittsburgh sleep quality index," *Chinese journal of psychiatry*, vol. 29, pp. 103–107, 1996.

[30] J. X. Kang, H. Zeng, and P. Wang, "Correlation between sleep quality and cognitive functions of the elderly in community," *Chinese General Practice*, vol. 14, pp. 439–441, 2011.

Hindawi
Journal of Nanomaterials
Volume 2021, Article ID 9260259, 5 pages
https://doi.org/10.1155/2021/9260259

Research Article

Risk Factors of Invasive Pulmonary Fungal Infections in Patients with Hepatitis B Virus Related Acute-on-Chronic Liver Failure

Xinchun He, Shigang Tang, Liang Chen, Yuqing Feng, Baining Zhu, and Caixia Yang

Department of Infectious Disease, Hunan Provincial People's Hospital (The First Affiliated Hospital of Hunan Normal University), Changsha, Hunan 410005, China

Correspondence should be addressed to Xinchun He; xinchunhe@hunnu.edu.cn

Received 9 July 2021; Accepted 19 July 2021; Published 28 July 2021

Academic Editor: Songwen Tan

To analyze the risk factors of invasive pulmonary fungal infections in patients with HBV-ACL, the clinical data and risk factors of 60 patients with HBV-ACLF complicated IPFI were analyzed retrospectively including clinical parameters, broad-spectrum antibiotics usage, neutropenia, invasive medical manipulations, serum total bilirubin, international normalized ratio (INR), and MELD scores were compared with non-IPFI. Risk factors were analyzed using mathematical tools. Candida species and Aspergillus were detected as the most prominent fungal strains (61.11% and 33.33%, respectively). The risk factors included prolong broad-spectrum antibiotic usage (OR = 4.362, $P = 0.008$), neutropenia (OR = 3.288, $P = 0.007$), invasive procedures (OR = 3.263, $P = 0.010$), serum total bilirubin (OR = 1.006, $P = 0.011$), INR (OR = 2.101, $P = 0.007$), and MELD scores (OR = 1.074, $P = 0.008$). Candida is the main IPFI strains in patients with HBV-ACLF. Broad-spectrum antibiotics usage, neutropenia, invasive manipulations, and the severity of ACLF might be risk factors for IPFI in patients with HBV-ACLF.

1. Introduction

Acute-on-chronic liver failure (ACLF) is a common medical liver disease syndrome with a high risk of short-term death and demonstrated immune dysfunction [1–3]. Damage-associated molecular patterns (DAMPs) and pathogen-associated molecular patterns (PAMPs) can lead to unbalance between systemic inflammatory response and anti-inflammatory response and are highly predisposed to develop various infections [1–4]. Frequent bacterial infections and reactivation of hepatitis B virus (HBV) infection contributed to the progression of ACLF in the Asian region. Although the introduction and the expanded access to antiviral treatment have significantly improved the outcome of patients with hepatitis B virus-related acute-on-chronic liver failure (HBV-ACLF) [3, 5–8], infections displayed a significant public health problem, contributed to increase prolonged hospitalization and additional healthcare costs, and made a deterioration in the morbidity and mortality.

Invasive pulmonary fungal infections (IPFI) play an important role in stimulating and aggravating liver failure [9, 10]. However, it remained extremely challenging to be timely and accurately diagnosed, since the onset of invasive pulmonary fungal infections (IPFI) is occult, and the early clinical manifestations such as fever, tachycardia, and cough are not specific and overlap with symptoms of bacterial infections. Furthermore, fungal conventional culture methods are poor sensitivity, requiring invasive tissue sampling. At the same time, low index of alertness for clinicians, lack of normalized diagnostic standard, and tests also attributed to the difficulty. Recent studies have revealed that (1,3)-β-D-glucan (BDG) and galactomannan (GM) in blood or respiratory samples

showed a promising diagnostic performance for IPFI. However, the interpretation in patients with HBV-ACLF is still debated.

In order to improve the recognition, diagnosis, and treatment of IPFI in patients with HBV-ACLF, the clinical data of patients with HBV-ACLF and invasive pulmonary fungal infection in our hospital were retrospectively analyzed.

2. Materials and Methods

2.1. Study Design and Patients. A total of 143 patients with HBV-ACLF from November 2013 to March 2021 were retrospectively analyzed, including 60 patients with invasive pulmonary mycosis (fungal infection group) and 83 patients without fungal infection (control group). The inclusion criteria were as follows: (1) age over 18 years; hepatitis B surface antigen-positive ≥6 months; (2) ACLF was diagnosed according to the diagnostic and treatment guidelines recommended by the Asian Pacific Association for the Study of the Liver (APASL) [1], excluding patients with any of the following conditions: (1) superinfection with hepatitis A, C, D, and E viruses; (2) malignancies, such as hepatocellular carcinoma; and (3) with one or more additional known primary or secondary causes of liver disease, other than hepatitis B. Patients with ACLF and IPFIs were assigned to the IPFI group, and patients with ACLF without IPFIs were assigned to the control group. All patients were well informed of the study, and written consent was obtained from the study subjects before enrolment. The study protocol was approved by the Ethics Committee of the Hunan Provincial People's Hospital (The First Affiliated Hospital of Hunan Normal University).

2.2. Definitions of IPFIs. Diagnoses of IPFIs [11] were based on the diagnostic criteria developed by the European Organization for Research and Treatment of Cancer and the Mycoses Study Group. The criteria were divided into host, clinical, mycological, and histopathological criteria. However, patients with ACLF often cannot tolerate lung biopsy due to coagulation dysfunction and poor basic conditions, and thus, the IPFIs in this study were probable IPFIs.

2.3. Data Collection

(1) The general condition, vital signs, number of neutrophils in peripheral blood, total bilirubin (TBIL), international normalized ratio (INR), BDG test and GM test, the type and cumulative time of antibiotics used during hospitalization, and the number of invasive operations (including abdominal puncture and/or central venous catheterization) of the HBV-ACLF patients from admission to the day of diagnosis of probable IPFIs

(2) The number of neutrophils in peripheral blood, TBIL, INR, serum creatinine, BDG test, and GM test was routinely measured in the central laboratory of our hospital

(3) The prolonged using antibiotics referred to the use of third-generation cephalosporins or carbapenems for more than 2 weeks; neutropenia in peripheral blood means that the number of neutrophils was less than 1.5×10^9/L for 10 consecutive days. The Model for End-Stage Liver Disease (MELD) scores is based on the objective parameters of serum bilirubin, serum creatinine, and the international normalized ratio of prothrombin time, and MELD scores was calculated using the following formula: MELD scores = $3.78 \times \ln$ [serum bilirubin (mg/dL)] $+ 11.2 \times \ln$ [INR] $+ 9.57 \times \ln$ [serum creatinine (mg /dL)] $+ 6.4 \times$ Etiology (etiology: biliary or alcoholic is 0; others is 1).

2.4. Statistical Analysis. ANOVA was used for analysis with the Chi-squared test. Continuous variables were described as means ± SD, and categorical variables were presented as counts (percentage). Binomial logistic regression analysis was performed. P value < 0.05 was considered statistically significant for all comparisons. Analysis was performed using the statistical software SPSS (version 23.0).

3. Results

3.1. The Clinical Data and General Information. We enrolled 60 patients (41 males and 19 females) in the IPFI group and 83 patients (65 males and 18 females) in the no-IFPI group, respectively. The baseline characteristics were comparable. The patients with IPFI had more prolonged antibiotics use [54 (90.00%) versus 51 (61.45%); $P \leq 0.001$], and invasive operation [46 (76.67%) versus 39 (46.98%); $P \leq 0.001$]; the number of patients with neutropenia, total bilirubin, INR, and MELD scores are larger for IPFI groups [41 (68.33%) versus 27 (32.53%); $P \leq 0.001$], [389.22 ± 103.41 versus 326.15 ± 102.01; $P \leq 0.001$], [3.16 ± 0.84 versus 2.67 ± 0.78; $P \leq 0.001$], and [34.87 ± 8.39 versus 30.03 ± 8.24; $P \leq 0.001$], respectively (Table 1).

3.2. Clinical Characteristics of IPFI in Patients with HBV-ACLF. Cough and fever were the most frequent clinical signs reported ($n = 53$, 88.3% and $n = 51$, 85.0%, respectively), followed by dyspnea ($n = 16$, 26.7%), hemoptysis ($n = 5$, 8.3%), and chest pain ($n = 3$, 5.0%). The positive rates of BDG and GM test were 73.3% (44/60) and 38.3% (23/60), respectively (Table 2).

3.3. Species and Constituent Ratio of IPFI in HBV-ACLF Patients. Candida species had the highest frequency 22 (61.11%) followed by Aspergillus species 12 (33.33%). Table 3 presents the fungi data for 36 infection episodes.

3.4. Analysis of Risk Factors for IPFI in Patients with HBV-ACLF. The risk factors included prolong broad-spectrum antibiotic use (OR = 4.362, $P = 0.008$), invasive procedures (OR = 3.263, $P = 0.010$), neutropenia (OR = 3.288, $P = 0.007$), serum total bilirubin (OR = 1.006, P = 0.011), INR (OR = 2.101, $P = 0.007$), and MELD scores (OR = 1.074, $P = 0.008$). The risk factors for IPFI in patients with HBV-

Table 1: Basic data for IPFI and non-IPFI with HBV-ACLF at risk for fungal infections.

Risk factors	IPFI ($n = 60$)	No IPFI ($n = 83$)	Statistical value	P value
Age	54 ± 15.56	53 ± 14.90	$\chi^2 = 0.219$	0.6401
Gender (man)	41 (68.33%)	65 (78.31%)	$\chi^2 = 1.808$	0.1788
Prolong antibiotics use	54 (90.00%)	51 (61.45%)	$\chi^2 = 14.55$	≤0.001
Invasive operation	46 (76.67%)	39 (46.99%)	$\chi^2 = 12.72$	≤0.001
Neutropenia	41 (68.33%)	27 (32.53%)	$\chi^2 = 17.90$	≤0.001
TBIL (μmol/L)	389.22 ± 103.41	326.15 ± 102.01	$F = 13.15$	≤0.001
INR	3.16 ± 0.84	2.67 ± 0.78	$F = 13.28$	≤0.001
MELD scores	34.87 ± 8.39	30.03 ± 8.24	$F = 11.85$	≤0.001

IPFI: invasive pulmonary fungal infections; TBIL: total bilirubin; INR: international normalized ratio; MELD: Model for End-Stage Liver Disease.

Table 2: Clinical signs, BDG, and GM results.

	N	%
Signs and symptoms		
Cough	53	88.3
Fever	51	85.0
Dyspnea	16	26.7
Hemoptysis	5	8.3
Chest pain	3	5.0
Investigation		
BDG test positive	44	73.3
GM test positive	23	38.3

BDG: 1,3-β-D-glucan; GM: galactomannan.

Table 3: The fungi data for 36 infection episodes.

Causative microorganism	Frequency	Constituent ratio (%)
Candida albicans	16	44.44
Aspergillus spp.	12	33.33
Candida glabrata	4	11.11
Candida krusei	2	5.56
Unclassified yeast-like fungi	2	5.56
Total	36	100

ACLF (bivariate logistic regression analysis) are described in Table 4.

Table 4: Independent risk factors for IPFI (bivariate logistic regression analysis).

	OR	95% CI	P
Prolong antibiotics use	4.362	1.458-13.050	0.008
Invasive procedures	3.263	1.317-7.949	0.010
Neutropenia	3.288	1.375-7.861	0.007
TBIL (μmol/L)	1.006	1.001-1.010	0.011
INR	2.101	1.221-3.612	0.007
MELD scores	1.074	1.019-1.133	0.008

IPFI: invasive pulmonary fungal infections; OR: odds ratio; CI: confidence interval; TBIL: total bilirubin; INR: international normalized ratio; MELD: Model for End-Stage Liver Disease.

4. Discussion

Due to immune dysfunction, ACLF patients are more susceptible to infection. One-third of ACLF patients can be detected infections, and the remaining patients approximately half would develop bacterial infections in a short time [4]. The incidence of ACLF complicated with invasive fungal infection is increasing gradually, with high mortality and poor prognosis. Verma et al. [12] reported 14.7% ACLF patients with IFI, and Lin et al. [13] reported 47.6% HBV-ACLF patients with IFI. Both of them reported that one of the commonest target sites was respiratory (approximately 34%, 25%, respectively), but their clinical manifestations were not specific and the same as bacterial pneumonia, such as cough, fever, dyspnea, hemoptysis, and chest pain. The human defense system against fungi included both the naive and acquired immune systems, including neutrophil, natural killer cells, and dendritic cells. Neutropenia typically involved in candidemia with a poor prognosis [13]. When HBV-ACLF patients were complicated with bacterial infections, it was critical to administrate antibiotics to kill them. Sometimes, frequent unreasonable and overuse antibiotics can be seen to ideally improve the outcome of ACLT patients and unfortunately lead to suppress the normal bacterial flora and fungi proliferated rapidly. These organisms can migrate across the intestinal wall to disseminate. In our study patients, it was found that the long-term use of broad-spectrum antibiotics and neutropenia was independently related to fungal infection, which was consistent with recent studies [9, 12, 14, 15].

Of the 36 confirmed IPFI cases, Candida albicans infection was the most frequent pathogens in HBV-ACLF patients, accounting for 44.44% (16/36), followed by Aspergillus 33.33% (12/36), and Candida glabrata 11.11% (4/36). These findings are also consistent with previous studies on patients with acute liver failure [12, 13, 16, 17]. And other types of severe liver diseases patients also have been reported the same spectrum of fungal infections [9, 13, 14, 18]. This may be due to the disorder of fungal flora and dysfunction of the intestinal mucosal barrier in patients with advanced

liver cirrhosis, as well as the displacement of symbiotic candida or overlapping infection with Aspergillus species.

Patients with ACLF suffered from a large number of damaged hepatocytes with a high level of jaundice and coagulation abnormalities, which led to prolonged hospital stay to be recovered and repeatedly performed all kinds of invasive procedures such as central venous catheters, artificial liver support system, and abdominal paracentesis, thus increased probability of nosocomial infection accordingly. We also showed the higher prevalence of higher undergoing invasive operations, total bilirubin, INR, and MELD scores in patients with IPFI as compared with non-IPFI. These invasive operations for developing of IPFI were similar to those previously reported [15, 19]. It is difficult to explain whether the poor liver function is the cause or result of fungal infection in the HBV-ACLF area. On the one hand, the worsening of immune paralysis and fungal ecological imbalance, coupled with the increasingly serious ACLF, is the trend of IPFI. On the other hand, the occurrence of IPFI disease triggers higher cytokine release, which leads to higher liver failure damage, and finally presents a vicious circle, which worsens the ongoing damage and immune dysfunction.

BDG is present in the cell wall of many fungi and a diagnostic value test when combined with epidemiologic risk factors, clinical manifestations, and imaging. At the same time, GM is produced by all kinds of fungal strains and becomes another mark which is routinely used in the diagnosis of invasive aspergillosis in immunosuppressed critically ill patients [20]; however, the BDG test needs further evaluation in patients with ACLF. Our study revealed that the positive rates of BDG and GM tests were 73.3% (44/60) and 38.3% (23/60), respectively. A recent meta-analysis shows that BDG has a good predictive ability in the diagnosis of IFI, with a sensitivity of 97%, a specificity of 60%, and an AUROC of 0.770 [12]. Another detection of GM in BAL samples is 56-73% sensitive and 89-94% specific for the diagnosis of invasive aspergillosis [17, 21, 22]. The above data can be used for future clinical studies, such as meta-analysis [23–25] and many other statistical tools [26, 27]. Clinical studies are suggested to be analyzed with math tools for comprehensive and scientific findings.

5. Conclusions

In conclusion, to improve the outcome in IPFI patients with HBV-ACLF, clinicians should pay more attention to this unusual and lethal condition so that it can be diagnosed early and timely, and empiric antifungal treatment should be started, until reasonable treatment can be applied. Candida species and Aspergillus were detected as the most prominent fungal strains (61.11% and 33.33%, respectively). The risk factors included prolong broad-spectrum antibiotic usage ($OR = 4.362, P = 0.008$), neutropenia ($OR = 3.288, P = 0.007$), invasive procedures ($OR = 3.263, P = 0.010$), serum total bilirubin ($OR = 1.006, P = 0.011$), INR ($OR = 2.101, P = 0.007$), and MELD scores ($OR = 1.074, P = 0.008$). Candida is the main IPFI strains in patients with HBV-ACLF. Broad-spectrum antibiotics usage, neutropenia, invasive manipulations, and the severity of ACLF might be risk factors for IPFI in patients with HBV-ACLF.

Data Availability

The data used to support the findings of this study are included within the article.

Conflicts of Interest

The authors declare that they have no conflicts of interest.

Acknowledgments

This work is supported by the Scientific Research Project of Hunan Provincial Health and Health Commission (No.:B2019054) and the Changsha Science and Technology Plan Project (No.:kq1801087).

Supplementary Materials

The medical ethics approval form. *(Supplementary Materials)*

References

[1] APASL ACLF Research Consortium (AARC) for APASL ACLF working Party, S. K. Sarin, A. Choudhury et al., "Acute-on-chronic liver failure: consensus recommendations of the Asian Pacific association for the study of the liver (APASL): an update," *Hepatology International*, vol. 13, no. 4, pp. 353–390, 2019.

[2] R. Hernaez, J. R. Kramer, Y. Liu et al., "Prevalence and short-term mortality of acute-on-chronic liver failure: a national cohort study from the USA," *Journal of Hepatology*, vol. 70, no. 4, pp. 639–647, 2019.

[3] V. Arroyo, R. Moreau, and R. Jalan, "Acute-on-chronic liver failure," *The New England Journal of Medicine*, vol. 382, no. 22, pp. 2137–2145, 2020.

[4] J. Fernández, J. Acevedo, R. Wiest et al., "Bacterial and fungal infections in acute-on-chronic liver failure: prevalence, characteristics and impact on prognosis," *Gut*, vol. 67, no. 10, pp. 1870–1880, 2018.

[5] S. L. Flamm, Y. X. Yang, S. Singh et al., "American Gastroenterological Association Institute guidelines for the diagnosis and management of acute liver failure," *Gastroenterology*, vol. 152, no. 3, pp. 644–647, 2017.

[6] European Association for the Study of the Liver Electronic address: easloffice@easloffice.eu, Clinical practice guidelines panel, J. Wendon et al., "EASL Clinical Practical Guidelines on the management of acute (fulminant) liver failure," *Journal of Hepatology*, vol. 66, no. 5, pp. 1047–1081, 2017.

[7] European Association for the Study of the Liver, "EASL Clinical Practical Guidelines on the management of acute (fulminant) liver failure," *Journal of Hepatology*, vol. 66, no. 5, pp. 1047–1081, 2017.

[8] R. Stravitz and W. M. Lee, "Acute liver failure," *Lancet*, vol. 394, no. 10201, pp. 869–881, 2019.

[9] E. A. Hassan, A. S. A. el-Rehim, S. M. Hassany, A. O. Ahmed, N. M. Elsherbiny, and M. H. Mohammed, "Fungal infection in patients with end-stage liver disease: low frequency or low

index of suspicion," *International Journal of Infectious Diseases*, vol. 23, pp. 69–74, 2014.

[10] J. S. Bajaj, R. K. Reddy, P. Tandon et al., "Prediction of fungal infection development and their impact on survival using the NACSELD cohort," *The American Journal of Gastroenterology*, vol. 113, no. 4, pp. 556–563, 2018.

[11] B. de Pauw, T. J. Walsh, J. P. Donnelly et al., "Revised definitions of invasive fungal disease from the European organization for research and treatment of cancer/invasive fungal infections cooperative group and the National Institute of Allergy and Infectious Diseases Mycoses Study Group (EORTC/MSG) consensus group," *Clinical Infectious Diseases*, vol. 46, no. 12, pp. 1813–1821, 2008.

[12] N. Verma, S. Singh, S. Taneja et al., "Invasive fungal infections amongst patients with acute-on-chronic liver failure at high risk for fungal infections," *Liver International*, vol. 39, no. 3, pp. 503–513, 2019.

[13] L. N. Lin, Y. Zhu, F. B. Che, J. L. Gu, and J. H. Chen, "Invasive fungal infections secondary to acute-on-chronic liver failure: a retrospective study," *Mycoses*, vol. 56, no. 4, pp. 429–433, 2013.

[14] T. Lahmer, A. Brandl, S. Rasch, R. M. Schmid, and W. Huber, "Fungal peritonitis: underestimated disease in critically ill patients with liver cirrhosis and spontaneous peritonitis," *PLOS ONE*, vol. 11, no. 7, article e0158389, 2016.

[15] M. Bartoletti, M. Rinaldi, Z. Pasquini et al., "Risk factors for candidaemia in hospitalized patients with liver cirrhosis: a multicentre case-control-control study," *Clinical Microbiology and Infection*, vol. 27, no. 2, pp. 276–282, 2021.

[16] J. Chen, Q. Yang, J. Huang, and L. Li, "Risk factors for invasive pulmonary aspergillosis and hospital mortality in acute-on-chronic liver failure patients: a retrospective-cohort study," *International Journal of Medical Sciences*, vol. 10, no. 12, pp. 1625–1631, 2013.

[17] J. Fernández, S. Piano, M. Bartoletti, and E. Q. Wey, "Management of bacterial and fungal infections in cirrhosis: The MDRO challenge," *Journal of Hepatology*, vol. 75, pp. S101–S117, 2021.

[18] A. Alexopoulou, L. Vasilieva, D. Agiasotelli, and S. P. Dourakis, "Fungal infections in patients with cirrhosis," *Journal of Hepatology*, vol. 63, no. 4, pp. 1043–1045, 2015.

[19] M. Bassetti, E. M. Trecarichi, E. Righi et al., "Incidence, risk factors, and predictors of outcome of candidemia. Survey in 2 Italian university hospitals," *Diagnostic Microbiology and Infectious Disease*, vol. 58, no. 3, pp. 325–331, 2007.

[20] M. A. Mennink-Kersten, J. P. Donnelly, and P. E. Verweij, "Detection of circulating galactomannan for the diagnosis and management of invasive aspergillosis," *The Lancet Infectious Diseases*, vol. 4, no. 6, pp. 349–357, 2004.

[21] T. Boch, M. Reinwald, B. Spiess et al., "Detection of invasive pulmonary aspergillosis in critically ill patients by combined use of conventional culture, galactomannan, 1-3-beta-D-glucan and Aspergillus specific nested polymerase chain reaction in a prospective pilot study," *Journal of Critical Care*, vol. 47, pp. 198–203, 2018.

[22] D. Terrero-Salcedo and M. V. Powers-Fletcher, "Updates in laboratory diagnostics for invasive fungal infections," *Journal of Clinical Microbiology*, vol. 58, no. 6, 2020.

[23] W. C. Cho, M. S. Lee, L. Lao, and G. Litscher, "Systematic review and meta-analysis in Chinese medicine," *Evidence-based Complementary and Alternative Medicine*, vol. 2014, Article ID 859309, 2 pages, 2014.

[24] N. Y. Shin, Y. J. Lim, C. H. Yang, and C. Kim, "Acupuncture for alcohol use disorder: a meta-analysis," *Evidence-based Complementary and Alternative Medicine*, vol. 2017, Article ID 7823278, 6 pages, 2017.

[25] X. He, L. Chen, H. Chen, Y. Feng, B. Zhu, and C. Yang, "Diagnostic accuracy of procalcitonin for bacterial infection in liver failure: a meta-analysis," *Bioinorganic Chemistry and Applications*, vol. 2021, Article ID 5801139, 8 pages, 2021.

[26] N. Xu, B.-B. Zhang, X.-N. Huang et al., "S100A8/A9 Molecular Complexes Promote Cancer Migration and Invasion via the p38 MAPK Pathway in Nasopharyngeal Carcinoma," *Bioinorganic Chemistry and Applications*, vol. 2021, Article ID 9913794, 11 pages, 2021.

[27] M.-Z. Yang, B.-B. Zhang, J.-C. Huang et al., "Network pharmacology reveals polyphyllin II as one hit of nano Chinese medicine monomers against nasopharyngeal carcinoma," *Bioinorganic Chemistry and Applications*, vol. 2021, Article ID 9959634, 10 pages, 2021.

Hindawi
Journal of Nanomaterials
Volume 2021, Article ID 3249816, 10 pages
https://doi.org/10.1155/2021/3249816

Research Article

Identifying a Six-Gene Signature Predicting Response to TACE in Hepatocellular Carcinoma by Bioinformatics Analysis

Xin Yao,[1] Xin Yin,[2] Wei Lu,[1] and Leitao Cao[3]

[1]*Vascular Department, Tianjin Hospital of ITCWM Nankai Hospital, China*
[2]*Traditional Chinese Medicine Department, Tianjin Hexi District Meijiang Street Community Health Service Center, China*
[3]*Vascular Surgery, Dingzhou City People's Hospital, China*

Correspondence should be addressed to Leitao Cao; caoleitao2021@sina.com

Received 9 June 2021; Revised 15 June 2021; Accepted 29 June 2021; Published 16 July 2021

Academic Editor: Songwen Tan

Background and Aim. With regard to patients with intermediate-stage, irresectable hepatocellular carcinoma (HCC), transcatheter arterial chemoembolization (TACE) is the mainstay of treatment. There is an urgent clinical requirement to identify reliable biomarkers to predict the response of HCC patients to TACE treatment. We aimed to identify a gene signature for predicting TACE response in HCC patients based on bioinformatics analysis. *Methods*. We downloaded the gene expression profile GSE104580 based on 147 tumor samples from 81 responders to TACE and 66 nonresponders from the Gene Expression Omnibus (GEO) database. Then, we randomly divided the 147 tumor samples into a training set ($n = 89$) and a validation set ($n = 58$) and screened differentially expressed genes (DEGs) in the training set. Gene Ontology (GO) term and Kyoto Encyclopedia of Genes and Genomes (KEGG) pathway enrichment analyses were performed to annotate functions of the DEGs. The DEGs were mapped into the STRING website for constructing protein-protein interaction (PPI). The predictive value of the candidate genes by receiver-operating characteristic (ROC) curves was further verified in the validation set. *Results*. We totally found 158 DEGs (92 upregulated genes and 66 downregulated genes) in the training set. The GO enrichment analysis revealed that DEGs were significantly enriched in metabolic and catabolic processes, such as drug metabolic process, fatty acid metabolic process, and small molecule catabolic process. The KEGG pathway analysis revealed that the DEGs were mainly concentrated in drug metabolism-cytochrome P450, metabolism of xenobiotics by cytochrome P450, and chemical carcinogenesis. We identified 6 candidate genes (CXCL8, AFP, CYP1A1, MMP9, CYP3A4, and SERPINC1) based on the PPI network of the DEGs, which had high predictive value in HCC response to TACE with an area under the curve (AUC) value of 0.875 and 0.897 for the training set and validation set, respectively. *Conclusion*. We identified a six-gene signature which might be biomarkers for predicting HCC response to TACE by a comprehensive bioinformatics analysis. However, the actual functions of these genes required verification.

1. Introduction

Hepatocellular carcinoma (HCC) represents a malignant tumor predominantly arising in the setting of cirrhosis and will be responsible for an estimated one million death on a global scale in 2030 [1]. As per the Global Cancer Statistics in 2018, the mortality rate of HCC is only second to lung cancer in males by gender stratification [2]. Most of HCC cases at their initial diagnosis have reached the advanced stage, which results in an unsatisfactory overall survival [3]. Transcatheter arterial chemoembolization (TACE) induces ischemia-hypoxia and local chemotherapy-induced cytotoxicity which destroys cancerous cells, which is the first-line treatment for unresectable or intermediate stage HCC [4]. However, as a palliative therapy, TACE also has several limitations. Firstly, the response rate to TACE may vary widely among HCC patients. Although TACE did offer a survival advantage over supportive treatment alone in some patients, there were still up to 60% of HCC patients who did not benefit from it in spite of multiple treatments.

Secondly, TACE has multiple side effects (AEs). A recent literature reported a total of 21,461 AEs in 15,351 patients treated with TACE [5]. Abnormal liver enzyme was the most common AE, with an incidence of 52%, followed by postembolism syndrome such as intestinal obstruction, abdominal pain, and fever, with an incidence of 47.7% [5]. In addition, fever, nausea, and fatigue were also the typical postembolization syndrome. Some serious complications including liver failure, gastroduodenal ulceration, and death may also occur [4–6]. Thirdly, TACE treatment is costly. Therefore, early identifying which patients benefit most from TACE may be of great clinical relevance and is the key goal of modern personalized medicine.

The response to TACE in HCC patients is conventionally assessed by radiologically enhanced criteria which focus on tumor size [7]. However, the use of radiologic criteria to measure response has some limitations, such as interobserver subjectivity, high interobserver variability, increased patient's radiation exposure, and misjudgment resulting from dysplastic or regenerative nodules, or perfusion abnormalities [8]. Recently, more and more researchers investigate novel biomarkers to predict patient response to TACE in HCC. For example, Mao et al. found that ASPP2 expression in cancer tissue following TACE is an independent risk factor for HCC recurrence as well as overall survival [9]. Ma et al. demonstrated serum STIP1 is a promising biomarker for outcome evaluation, therapeutic response assessment, and microvascular invasion prediction in HCC following TACE [10]. Given this, screening reliable and novel biomarkers for predicting HCC response to TACE treatment is an urgent clinical need. Due to the complicated molecular and cellular heterogeneity in HCC, we speculated that the difference in tumor gene expression may be related to the TACE response. With the development of biomedicine, high-throughput gene chip technology has begun to be popularized in the exploration of mechanism and identifying potential biomarkers.

Therefore, in this study, we downloaded and initially analyzed the GSE104580 dataset from the Gene Expression Omnibus (GEO) database to explore the DEGs associated with TACE response between TACE responders and nonresponders. We then annotated the functions of these DEGs by using the GO term enrichment analysis and Kyoto Encyclopedia of Genes and Genomes (KEGG) pathway analysis. Finally, we performed Protein-Protein Interaction (PPI) network analysis to discover candidate genes. Based on the bioinformatics analysis, novel biomarkers for predicting HCC response may be provided.

2. Methods

2.1. Microarray Data and Preprocessing. We downloaded the gene expression dataset of GSE104580 which contains microarray data from 147 tumor samples from 81 TACE responders and 66 TACE nonresponders from the GEO database and then randomly divided the 147 samples into a training set ($n = 89$) and a validation set ($n = 58$). The training set was then used to screen the DEGs associated with TACE response.

2.2. Differential Expression Analysis. We used the limma package in R software to analyze the DEGs ($|\log FC| \geq 1.2$ and the adj.p value < 0.05) associated with TACE response by comparing HCC tissues between TACE responders and nonresponders in the training set.

2.3. GO and KEGG Pathway Analysis. To explore the significantly enriched functions of the DEGs and better understand the important pathways of the DEGs participation, we used clusterProfile packages for GO and KEGG analysis. The Fisher's exact test was applied to evaluate the significance of GO and KEGG enrichments, and a q value < 0.05 indicated a statistically significant difference.

2.4. Construction of the PPI Network. The Search Tool for the Retrieval of Interacting Genes (STRING) database was applied to construct the PPI network of DEGs, and a confidence > 0.4 was set as statistically significant. Then, the Cytoscape software (version 3.6.3) was employed to visualize the obtained PPI network. Moreover, to find out the most important nodes in the PPI network, the CentiScaPe 2.2 plug-in was employed to calculate the degree, closeness, and betweenness of the network. We operationally defined genes with degree value in the top 10% as hub genes, while the betweenness value in the top 10% as bottleneck genes. The Venn diagram was then applied to screen the genes in the intersection of these two gene sets as candidate genes for predicting HCC response to TACE treatment.

2.5. Prediction and Evaluation of Predictive Biomarkers for HCC Response to TACE Treatment. To explore predictive biomarkers for HCC response to TACE treatment, we used the above hub genes as candidates to find their predictive value based on ROC curve analysis. In brief, 89 samples (TACE responders = 52, TACE nonresponders = 37) were randomly distributed as the training set, which was used to build a ROC curve. The remaining set ($n = 58$) was used as the validation set. The area under the curve (AUC) was computed to estimate the predictive accuracy of the classifier.

3. Results

3.1. Identification of DEGs between Responders to TACE and Nonresponders for HCC Patients. After differential expression analysis, we identified a total of 158 DEGs according to the thresholds of $|\log FC| \geq 1.2$ and adj.p value < 0.05, including 92 upregulated genes and 66 downregulated genes (Table 1). The volcano plot is presented in Figure 1(a). In addition, Figure 1(b) shows the heat map of expression diversity of DEGs, from which we can see that tumor samples from the TACE responders were distinguished clearly from that from the TACE nonresponders by the identified DEGs.

3.2. Integrative Bioinformatics Analysis of DEGs. Figure 2 shows the results of Go enrichment, from which we found that the DEGs were the strongest enrichment in metabolic and catabolic processes, such as drug metabolic process, fatty acid metabolic process, and small molecule catabolic process (Figure 2). In addition, the KEGG pathway analysis showed the DEGs mainly concentrated in drug metabolism-

Table 1: DEGs between HCC samples from TACE responders ($n = 52$) and nonresponders ($n = 37$) by analyzing the GSE104580 dataset.

	Upregulated DEG ($n = 92$)	Downregulated DEG ($n = 66$)
DEGs (158)	AQP1; AK021804; C7; IFIT1; RTP4; IFI27; SPARCL1; FAS; CES2; AKR7A3; ADH1C; UGT2B15; CLDN2; CYP1A2; CD5L; CYP3A4; CYP1A1; THRSP; C3P1; RDH16; LINC00844; HSD11B1; ETNPPL; NUDT6; LDHD; SLCO1B1; CFHR4; HPR; FETUB; RBP5; ADHFE1; GLYAT; GYS2; C6; CYP8B1; HAO2; FGGY; ANXA10; SRD5A2; CYP2A6; CYP2A7; CYP2C9; FLJ22763; OGDHL; GNMT; PON3; LINC01018; ACSM2A; ACSM2B; CYP4F2; DAO; UPB1; SLC6A1; APOA5; EPHX2; AGXT; HPX; HRG; PIPOX; SERPINC1; AFM; HSD17B6; SLC22A1; SLC10A1; C4BPA; F9; CYP7A1; BHMT; AASS; NR1I3; IGFBP2; CYP4A11; SPP2; CCL16; RTP3; AQP9; HGFAC; PGLYRP2; ZG16; PCK1; HPD; ADH4; ANGPTL3; ACOT12; LECT2; ADH6; ADH1A; ADH1B; ABCC6P1; KLHDC9; CYP2C18; IL32	FMO1; RP11−274H2.5; GAL3ST1; VNN2; CA9; NDRG1; SLC6A8; KISS1R; ENO2; HILPDA; SPAG4; SULT1C2; ZIC2; ASRGL1; CLGN; MAP7D2; CTHRC1; EPCAM; FOXQ1; DKK1; MMP9; COLEC12; SPINK1; CCL20; SPP1; CXCL8; HK2; MMP12; DUSP9; TRIM71; AFP; TET1; ENPP3; RFX6; KANK4; RBP2; MEP1A; XK; SLAIN1; IL13RA2; FKBP1B; STEAP2; STEAP1; FDCSP; NTS; QPCT; S100A9; S100A8; ARG2; LIN28B; POPDC3; TSPAN13; AGR2; MMP1; GCNT3; ENPP5; PKIB; CD24; MAPK13; IGF2BP3; PLBD1; C15orf48; HCAR3; BCL2A1; CA12; TREM1

cytochrome P450, metabolism of xenobiotics by cytochrome P450, and chemical carcinogenesis (Figure 3).

3.3. Construction of the PPI Network and Module Analysis. We performed PPI network to further investigate the interrelationship of the DEGs, and the results showed that the PPI network consisted of 151 nodes and 336 edges after hiding nodes which could not interact with other nodes (Figure 4). By using the CentiScape plug-in, 10 hub genes (CXCL8, CYP3A4, MMP9, UGT2B15, AFP, CYP2C9, CYP1A1, HRG, SERPINC1, and AGXT) and 8 bottleneck genes (CXCL8, AFP, CA9, CYP1A1, MMP9, CYP3A4, SERPINC1, and PCK1) were obtained. Subsequently, 6 candidate genes in the intersection of the above two gene sets were obtained by using Venn diagram analysis, including cysteine X chemokine ligand 8 (CXCL8), Alpha-fetoprotein (AFP), cytochrome P450 1A1(CYP1A1), matrix metalloproteinase-9 (MMP9), cytochrome P450 3A4 (CYP3A4), and serpin peptidase inhibitor, clade C (antithrombin), and member 1(SERPINC1). Among them, CYP1A1, CYP3A4, and SERPINC1were upregulated genes in TACE responders compared with TACE nonresponders, while CXCL8, AFP, and MMP9 were downregulated gene (Figure 5).

3.4. The Value of Candidate Genes in Predicting HCC Response to TACE Treatment. At last, we examined the predictive value of CXCL8, AFP, CYP1A1, MMP9, CYP3A4, and SERPINC1 in predicting HCC response to TACE treatment in the training set and confirmed in the validation set. The ROC curves revealed that the 6-gene signature had good performance in predicting HCC response to TACE treatment with AUC of 0.875 for the training set (Figure 6(a)) and 0.897 for the validation set (Figure 6(b)). These results suggested that the 6 differentially expressed hub genes can be used as potential biomarkers for predicting HCC response to TACE.

4. Discussion

Response to TACE treatment varies greatly among patients with HCC, and over 40% of patients do not respond to it. At present, we cannot accurately predict the efficacy of TACE because there is no effective predictor of markers. Therefore, it is urgent to determine the key genes that affect the effect of TACE treatment and actively invest in the research of multigene signatures for predicting the response of TACE treatment. In the current study, we screened out 158 significant DEGs between HCC samples from TACE responders and nonresponders. These DEGs might play decisive roles in TACE response through metabolic and catabolic processes. Also, these DEGs were significantly concentrated in pathways like drug metabolism-cytochrome P450 pathway, and chemical carcinogenesis, which may be the underlying mechanism by which the DEGs affect the TACE response. Furthermore, by constructing the PPI network, we established a six-gene signature (including CYP1A1, CYP3A4, SERPINC1, CXCL8, AFP, and MMP9) for predicting TACE response. The 6-gene signature had good performance in predicting TACE response, demonstrating that the 6-gene signature provided new insights into the biological behavior of HCC and a basis for individualized management of HCC.

The cytochrome P450 (CYP) enzyme family mainly participate in the metabolism of environmental toxicants, cancer-promoting substances, and antitumor drugs. Its function strongly correlates with the appearance and progression of tumors and the response to anticancer drugs [11, 12]. Cytochrome P450 1A1 (CYP1A1) is a subtype of the cytochrome P 450 family, which is highly expressed in human liver tissues [13, 14]. Numerous studies have confirmed the relationship between CYP1A1 gene polymorphisms and HCC risk. Moreover, it has been reported that CYP1A1 is an important regulator of the conversion of tobacco-derived polycyclic aromatic hydrocarbons (PAHs) to carcinogenic metabolites, and its polymorphism may exert an effect on raising the susceptibility to smoking-related HCC [15].

Cytochrome P450 3A4 (CYP3A4) is also a member of the CYP 450 superfamily. It is expressed mainly in human liver as well as extrahepatic tissues including lung, kidney, and intestine. The expression of CYP3A4 is induced by

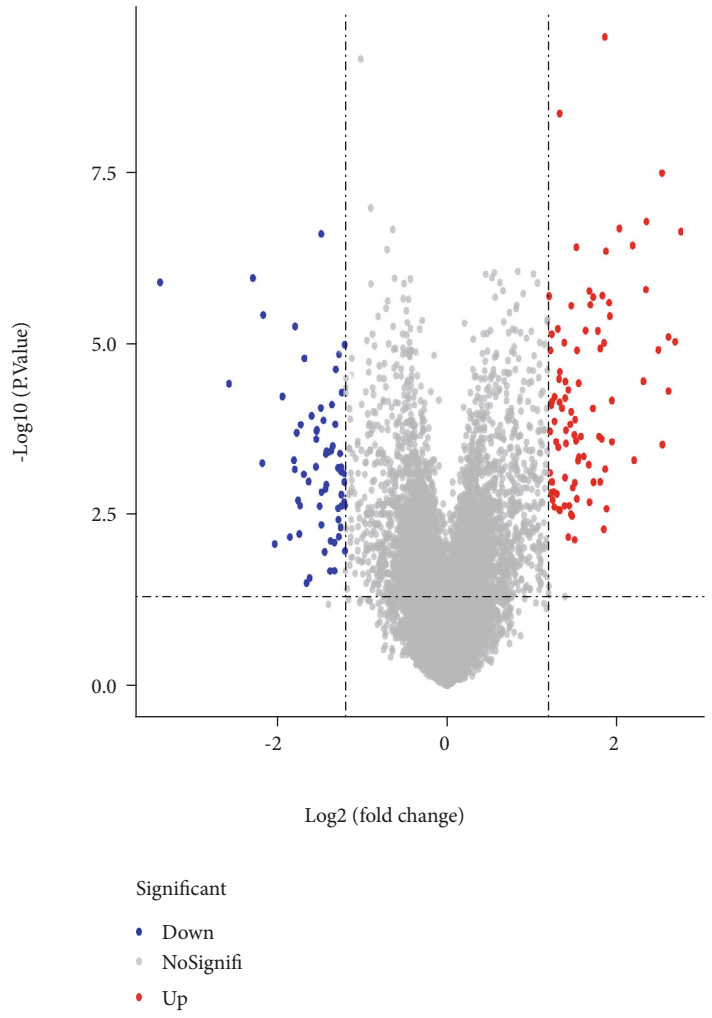

(a)

Figure 1: Continued.

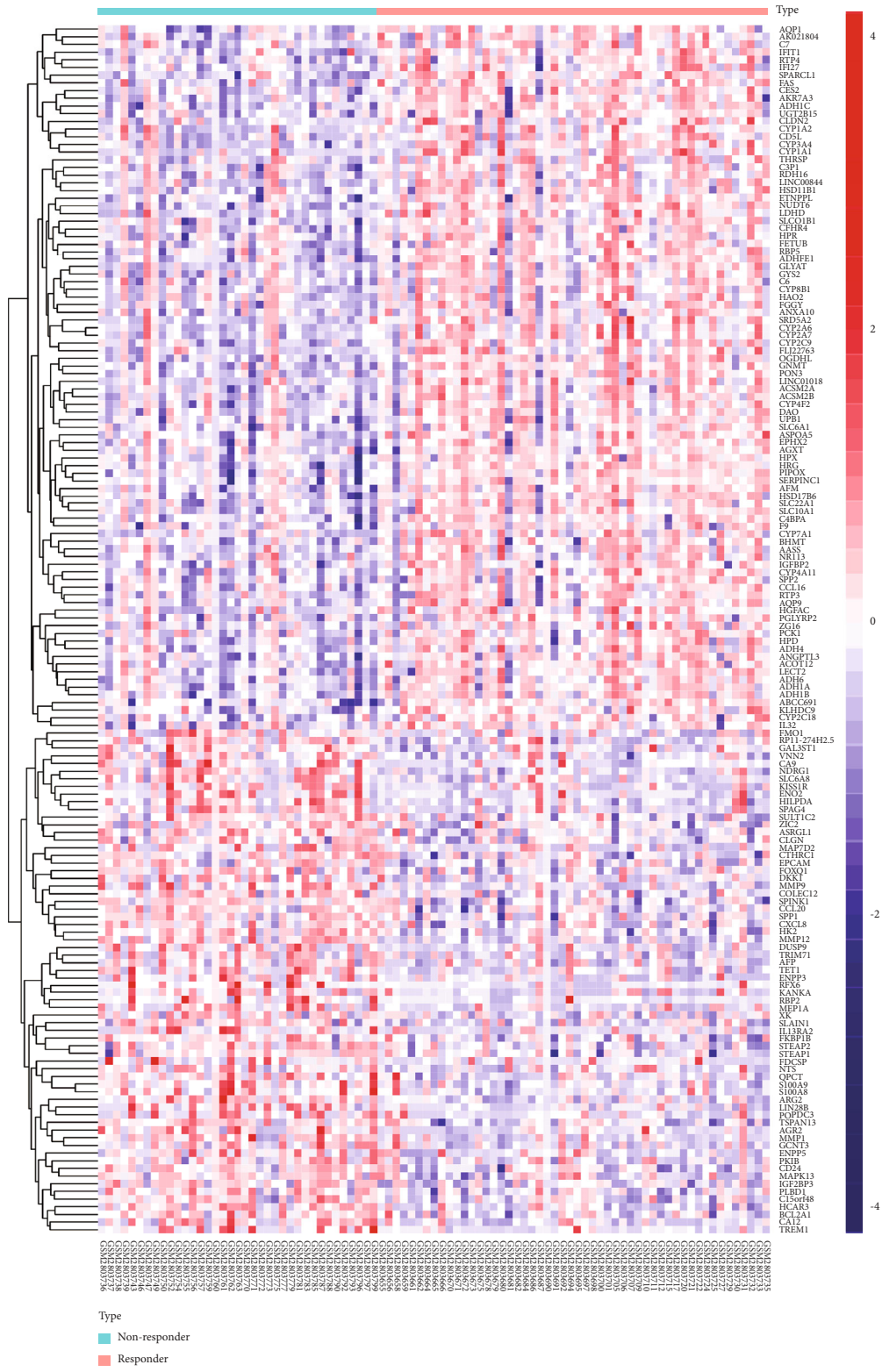

(b)

Figure 1: DEGs between HCC samples from TACE responders ($n = 52$) and nonresponders ($n = 37$) by analyzing the GSE104580 dataset. (a) The volcano plot showing DEGs between TACE responders and nonresponders, with cut-off threshold $|\log 2\,FC| \geq 1.2$ and $p < 0.05$; red dots refer to upregulated DEGs, blue dots refer to downregulated DEGs, and black dots refer to non-DEGs. (b) The heat map showing expression diversity of 158 DEGs between TACE responders and nonresponders; the color from blue to red shows the expression from low to high; white indicates no significant changes in gene expression. The red and green bars stand for HCC samples from TACE responders and nonresponders.

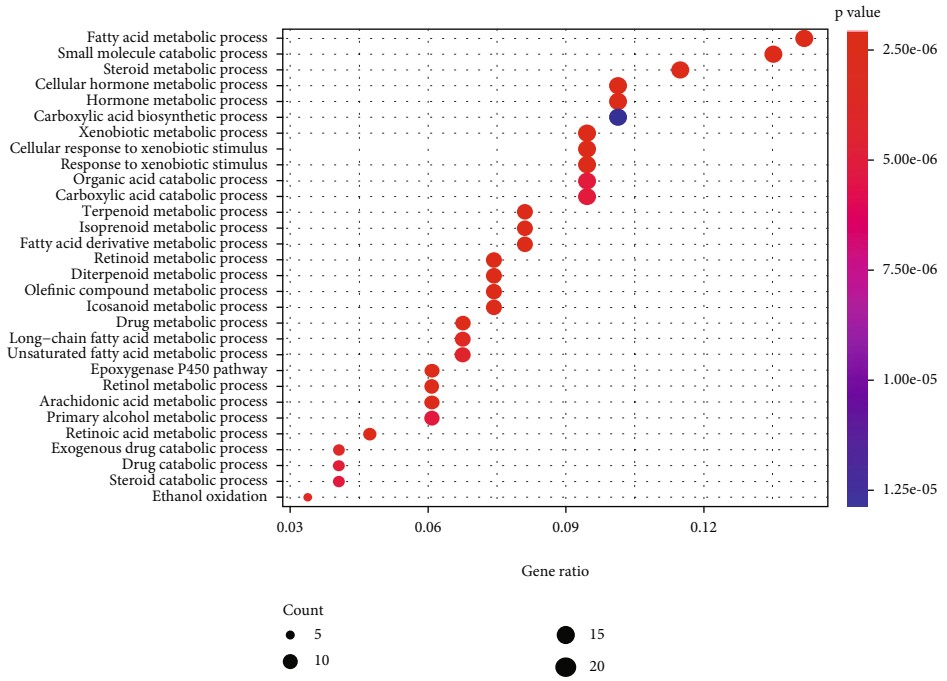

Figure 2: GO term enrichment analysis of 158 DEGs between HCC samples from TACE responders ($n = 52$) and nonresponders ($n = 37$) by analyzing the GSE104580 dataset; The DEGs were significantly enriched in metabolic and catabolic processes, such as drug metabolic process, fatty acid metabolic process, and small molecule catabolic process.

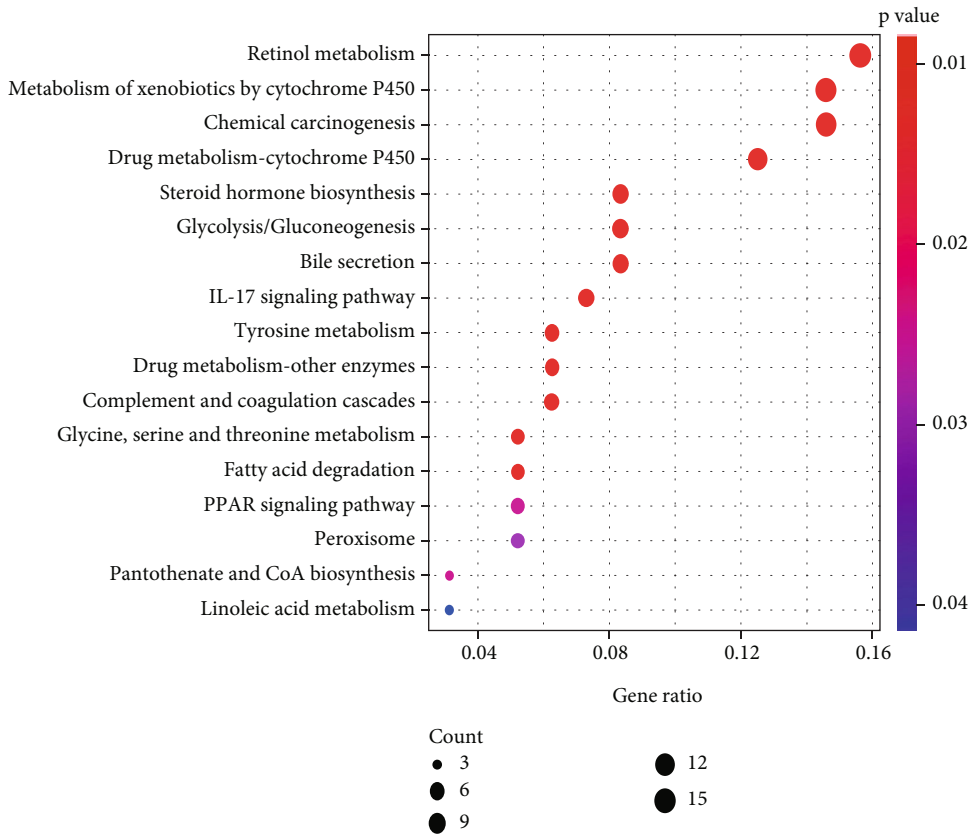

Figure 3: KEGG pathway enrichment analysis of 158 DEGs between HCC samples from TACE responders ($n = 52$) and nonresponders ($n = 37$) by analyzing the GSE104580 dataset; The DEGs were significantly enriched in drug metabolism-cytochrome P450, metabolism of xenobiotics by cytochrome P450, and chemical carcinogenesis.

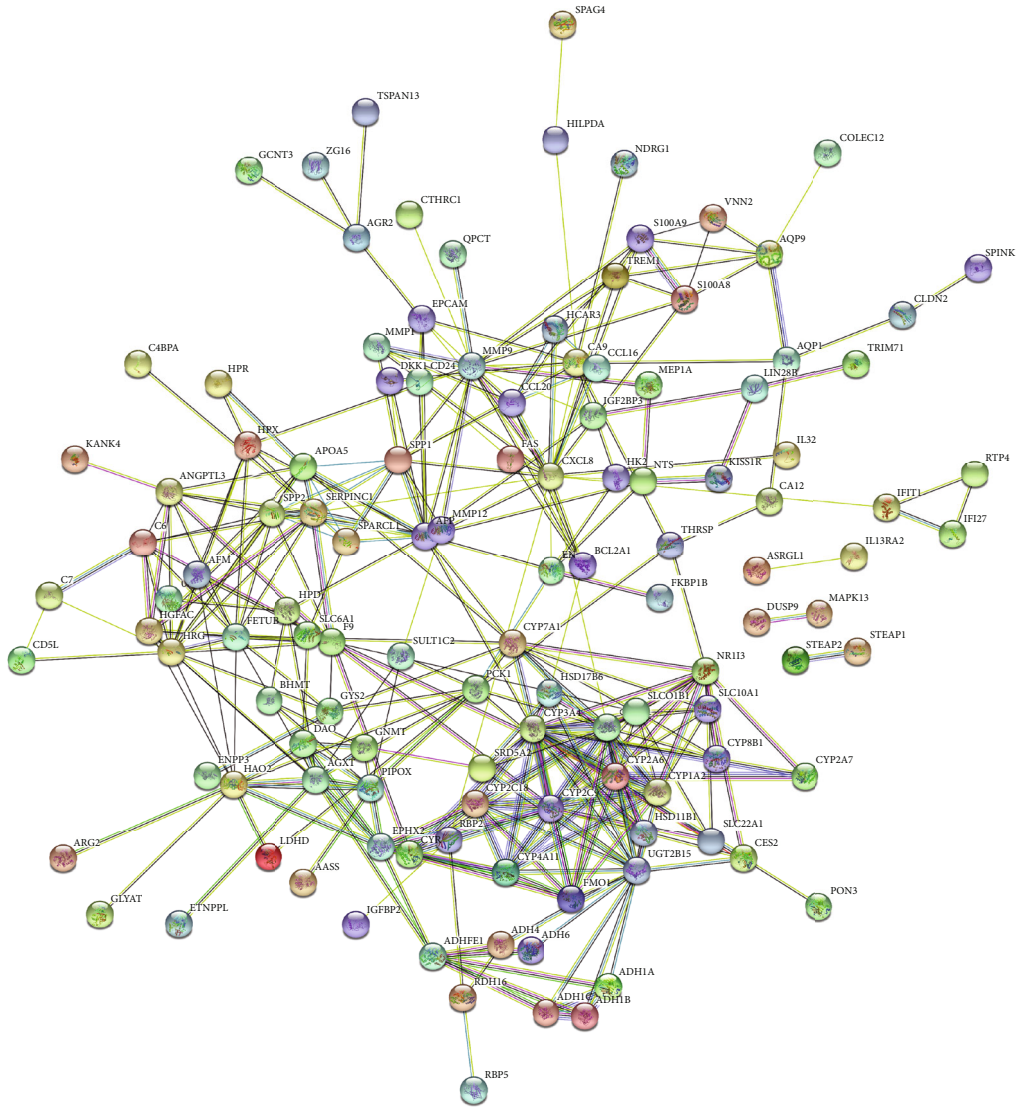

Figure 4: The PPI network of DEGs between HCC samples from TACE responders ($n = 52$) and nonresponders ($n = 37$). There were 151 nodes and 336 edges. By using the CentiScape plug-in, 10 hub genes (CXCL8, CYP3A4, MMP9, UGT2B15, AFP, CYP2C9, CYP1A1, HRG, SERPINC1, and AGXT) and 8 bottleneck genes (CXCL8, AFP, CA9, CYP1A1, MMP9, CYP3A4, SERPINC1, and PCK1) were obtained.

glucocorticoids and mainly participates in drug metabolism and lipid composition synthesis. CYP3A4 has a bidirectional function of activating some drugs and inactivating some drugs. Previous studies showed that cytochrome P450 enzymes metabolized approximately 70-80% of the drugs used in clinic, and CYP3A4 played a role in the metabolism of half of these drugs, including many cancer chemotherapeutic agents [16, 17]. Recently, several studies revealed that CYP3A4 was significantly downregulated in HCC tissues, which was associated with a poor prognosis of HCC [18, 19]. Moreover, another investigation found that CYP3A4 may be a new tumor suppressor gene, which is related to the prognosis of HCC [20].

SERPINC1 is a serine protease inhibitor. It controls the blood coagulation process of the body. Previous study found that the expression levels of SERPINC1 in the serum of HCC patients and healthy subjects were significantly different [21].

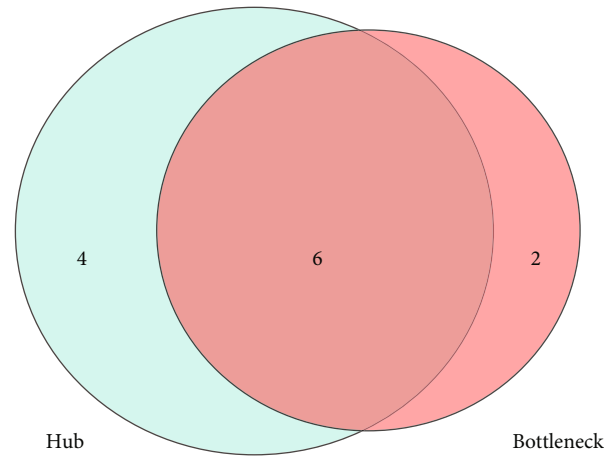

Figure 5: Venn diagram showing 6 candidate genes including CXCL8, AFP, CYP1A1, MMP9, CYP3A4, and SERPINC1.

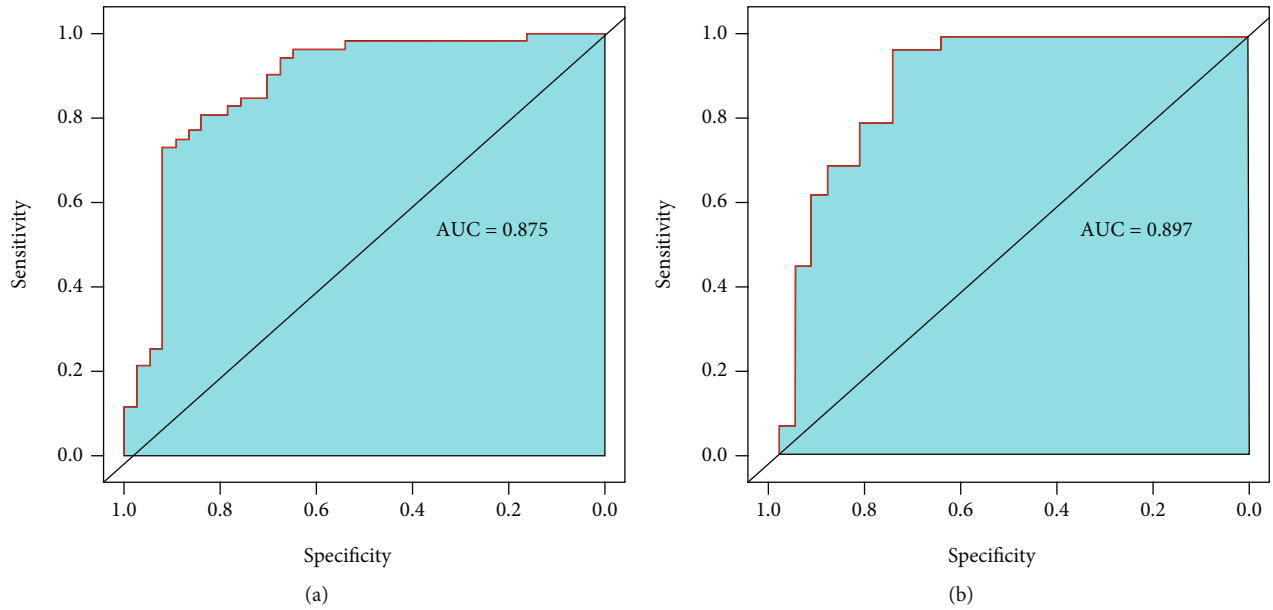

Figure 6: ROC analyses showing the value of 6 candidate genes in predicting response to TACE for HCC patients in the training set ($n = 89$) (a) and the validation set ($n = 58$) (b).

A major event in tumor growth and progression is the tumor angiogenesis. Cancer cells can secrete not only angiogenesis stimulating factors but also antiangiogenesis factors. The cleavage conformation of SERPINC1 inhibits the proliferation and migration of cancer cells through antiangiogenesis and anti-inflammatory [22, 23]. Its expression decreased in HCC [24, 25]. In the current study, upregulated expression of SERPINC1was associated with a favorable response to TACE. We therefore speculated that the high expression of SERPINC1 may contribute to the host's anticancer defense.

The chemokine CXCL8 has tumorigenic and angiogenic effects. Both inflammatory cells and tumor cells can secrete it. Studies have shown that CXCL8 played a role in the angiogenesis and metastasis of many types of tumors and is related to the poor prognosis of these tumors [26].

Specifically, CXCL8 and its receptors CXCR1 and CXCR2 may be involved in the occurrence and progression of HCC [27]. Like alpha-fetoprotein (AFP), CXCL8 also has a high predictive value in identifying HCC, and it could also independently predict the survival prognosis of patients with early HCC [28]. Interestingly, the size of HCC was positively linked to CXCL8 [27]. CXCL8 overexpressed in HCC tissues, and it may be related to the pathological staging, microvascular infiltration, and metastasis of HCC, indicating that CXCL8 may play a role in the progression and metastasis of HCC by participating in tumor proliferation and angiogenesis [29].

About 70% of HCCs secreted AFP, and it is a commonly used biomarker for diagnosing HCC in the clinic [30]. Furthermore, AFP has been confirmed to be the most common prognostic indicators of HCC in clinic. Several prognostics scores for HCC patients treated with TACE have included AFP as an important scoring factor [6, 31, 32]. Serum levels of AFP before TACE treatment and changes in AFP levels after TACE treatment were good predictors of response rate to TACE treatment and overall survival for HCC patients, respectively. The serum levels of AFP were negatively correlated with the response rate to TACE, and HCC patients with AFP level > 999,999 ng/mL would have no response to TACE. Consistent with previous studies, we found that the downregulated expression of AFP was associated with a good clinical response to TACE treatment. These results may be explained by the fact that higher levels of AFP are usually caused by late tumor stage, large tumor burden, and portal vein tumor thrombosis [6, 30].

The matrix metalloproteinase (MMP) family may degrade the extracellular matrix, destroy the normal tissue structure of cell adhesion molecules, and combine with other related enzymes to degrade the matric around the blood vessel, thereby facilitating the infiltration and metastasis of liver cancer cells. MMP 9 is a member of the MMP family and seems to exert a major effect in tumor angiogenesis through its key intervention in regulating growth plate angiogenesis and recruiting endothelial stem cells. M2 macrophages could promote the invasion and migration of HCC cells by means of changing miR-149-5p and therefore increasing the expression of MMP9 in HCC. Furthermore, the overexpression of MMP 9 in liver cancer leads to a higher TNM staging by increasing lymph node invasion and promoting metastasis, resulting in poor differentiation and an overall prognosis.

The current study still had several limitations need to be noted. Firstly, the six-gene signature lacked external validation. In future studies, external validation of the six-gene signature in more independent cohorts is necessary. Secondly, the 6 genes were obtained only by bioinformatics analysis; therefore, further experiments need to validate them and to clarify the underlying mechanism of them.

In conclusion, we identified a six-gene signature that could be used to predict the response of HCC to TACE

treatment. Hopefully, this 6-gene signature may become a favorable tool to guide the precision treatment of HCC in the future.

Data Availability

The profiles of GSE104580 can be downloaded from GEO datasets.

Conflicts of Interest

The authors declare there is no conflict of interest.

Acknowledgments

We thank the contributors of profiles GSE104580 in GEO datasets.

References

[1] A. Villanueva, "Hepatocellular carcinoma," *The New England Journal of Medicine*, vol. 380, no. 15, pp. 1450–1462, 2019.

[2] F. Bray, J. Ferlay, I. Soerjomataram, R. L. Siegel, L. A. Torre, and A. Jemal, "Global cancer statistics 2018: GLOBOCAN estimates of incidence and mortality worldwide for 36 cancers in 185 countries," *CA: a Cancer Journal for Clinicians*, vol. 68, no. 6, pp. 394–424, 2018.

[3] L. Kulik and H. B. El-Serag, "Epidemiology and management of hepatocellular carcinoma," *Gastroenterology*, vol. 156, no. 2, pp. 477–491, 2019.

[4] E. R. Garwood, N. Fidelman, S. E. Hoch, R. K. Kerlan Jr., and F. Y. Yao, "Morbidity and mortality following transarterial liver chemoembolization in patients with hepatocellular carcinoma and synthetic hepatic dysfunction," *Liver Transplantation*, vol. 19, no. 2, pp. 164–173, 2013.

[5] P. Therasse, S. G. Arbuck, E. A. Eisenhauer et al., "New guidelines to evaluate the response to treatment in solid tumors. European Organization for Research and Treatment of Cancer, National Cancer Institute of the United States, National Cancer Institute of Canada," *Journal of the National Cancer Institute*, vol. 92, no. 3, pp. 205–216, 2000.

[6] K. Memon, L. Kulik, R. J. Lewandowski et al., "Alpha-fetoprotein response correlates with EASL response and survival in solitary hepatocellular carcinoma treated with transarterial therapies: a subgroup analysis," *Journal of Hepatology*, vol. 56, no. 5, pp. 1112–1120, 2012.

[7] E. Stavropoulou, G. G. Pircalabioru, and E. Bezirtzoglou, "The role of cytochromes P450 in infection," *Frontiers in Immunology*, vol. 9, p. 89, 2018.

[8] U. M. Zanger and M. Schwab, "Cytochrome P450 enzymes in drug metabolism: regulation of gene expression, enzyme activities, and impact of genetic variation," *Pharmacology & Therapeutics*, vol. 138, no. 1, pp. 103–141, 2013.

[9] J. Mao, Z. Tan, X. Pan, and F. Meng, "ASPP2 expression predicts the prognosis of patients with hepatocellular carcinoma after transcatheter arterial chemoembolization," *Experimental and therapeutic medicine*, vol. 21, no. 4, p. 397, 2021.

[10] X. L. Ma, W. G. Tang, M. J. Yang et al., "Serum STIP1, a novel indicator for microvascular invasion, predicts outcomes and treatment response in hepatocellular carcinoma," *Frontiers in Oncology*, vol. 10, p. 511, 2020.

[11] R. A. McKinnon, P. D. Hall, L. C. Quattrochi, R. H. Tukey, and M. E. McManus, "Localization of CYP1A1 and CYP1A2 messenger RNA in normal human liver and in hepatocellular carcinoma by in situ hybridization," *Hepatology*, vol. 14, no. 5, pp. 848–856, 1991.

[12] H. Schweikl, J. A. Taylor, S. Kitareewan, P. Linko, D. Nagorney, and J. A. Goldstein, "Expression of CYP1A1 and CYP1A2 genes in human liver," *Pharmacogenetics*, vol. 3, no. 5, pp. 239–249, 1993.

[13] M. W. Yu, Y. H. Chiu, S. Y. Yang et al., "Cytochrome P450 1A1 genetic polymorphisms and risk of hepatocellular carcinoma among chronic hepatitis B carriers," *British Journal of Cancer*, vol. 80, no. 3-4, pp. 598–603, 1999.

[14] S. F. Zhou, "Drugs behave as substrates, inhibitors and inducers of human cytochrome P450 3A4," *Current Drug Metabolism*, vol. 9, no. 4, pp. 310–322, 2008.

[15] J. K. Lamba, X. Chen, L. B. Lan et al., "Increased CYP3A4 copy number in TONG/HCC cells but not in DNA from other humans," *Pharmacogenetics and Genomics*, vol. 16, no. 6, pp. 415–427, 2006.

[16] W. Jiang, L. Zhang, Q. Guo et al., "Identification of the pathogenic biomarkers for hepatocellular carcinoma based on RNA-seq analyses," *Pathology Oncology Research*, vol. 25, no. 3, pp. 1207–1213, 2019.

[17] T. Yu, X. Wang, G. Zhu et al., "The prognostic value of differentially expressed CYP3A subfamily members for hepatocellular carcinoma," *Cancer Management and Research*, vol. Volume 10, pp. 1713–1726, 2018.

[18] R. Ashida, Y. Okamura, K. Ohshima et al., "CYP3A4 gene is a novel biomarker for predicting a poor prognosis in hepatocellular carcinoma," *Cancer Genomics Proteomics*, vol. 14, no. 6, pp. 445–453, 2017.

[19] X. He, Y. Wang, W. Zhang et al., "Screening differential expression of serum proteins in AFP-negative HBV-related hepatocellular carcinoma using iTRAQ -MALDI-MS/MS," *Neoplasma*, vol. 61, no. 1, pp. 17–26, 2014.

[20] M. S. O'Reilly, S. Pirie-Shepherd, W. S. Lane, and J. Folkman, "Antiangiogenic activity of the cleaved conformation of the serpin antithrombin," *Science*, vol. 285, no. 5435, pp. 1926–1928, 1999.

[21] J. Peltier, J. P. Roperch, S. Audebert, J. P. Borg, and L. Camoin, "Quantitative proteomic analysis exploring progression of colorectal cancer: modulation of the serpin family," *Journal of Proteomics*, vol. 148, pp. 139–148, 2016.

[22] S. Y. Yoon, J. M. Kim, J. H. Oh et al., "Gene expression profiling of human HBV- and/or HCV-associated hepatocellular carcinoma cells using expressed sequence tags," *International Journal of Oncology*, vol. 29, no. 2, pp. 315–327, 2006.

[23] A. G. Wang, S. Y. Yoon, J. H. Oh et al., "Identification of intrahepatic cholangiocarcinoma related genes by comparison with normal liver tissues using expressed sequence tags," *Biochemical and Biophysical Research Communications*, vol. 345, no. 3, pp. 1022–1032, 2006.

[24] A. Brysse, M. Mestdagt, M. Polette et al., "Regulation of CXCL8/IL-8 expression by zonula occludens-1 in human breast cancer cells," *Molecular Cancer Research*, vol. 10, no. 1, pp. 121–132, 2012.

[25] X. Pan, A. C. Kaminga, S. W. Wen, and A. Liu, "Chemokines in hepatocellular carcinoma: a meta-analysis," *Carcinogenesis*, vol. 41, no. 12, pp. 1682–1694, 2020.

[26] T. H. Welling, S. Fu, S. Wan, W. Zou, and J. A. Marrero, "Elevated serum IL-8 is associated with the presence of hepatocellular carcinoma and independently predicts survival," *Cancer Investigation*, vol. 30, no. 10, pp. 689–697, 2012.

[27] F. Kubo, S. Ueno, K. Hiwatashi et al., "Interleukin 8 in human hepatocellular carcinoma correlates with cancer cell invasion of vessels but not with tumor angiogenesis," *Annals of Surgical Oncology*, vol. 12, no. 10, pp. 800–807, 2005.

[28] K. R. McIntire, C. L. Vogel, G. L. Princler, and I. R. Patel, "Serum alpha-fetoprotein as a biochemical marker for hepatocellular carcinoma," *Cancer Research*, vol. 32, no. 9, pp. 1941–1946, 1972.

[29] Y. Q. Zhang, L. J. Jiang, J. Wen et al., "Comparison of alpha-fetoprotein criteria and modified response evaluation criteria in solid tumors for the prediction of overall survival of patients with hepatocellular carcinoma after transarterial chemoembolization," *Journal of Vascular and Interventional Radiology*, vol. 29, no. 12, pp. 1654–1661, 2018.

[30] L. Liu, Y. Zhao, J. Jia et al., "The prognostic value of alpha-fetoprotein response for advanced-stage hepatocellular carcinoma treated with sorafenib combined with transarterial chemoembolization," *Scientific Reports*, vol. 6, no. 1, p. 19851, 2016.

[31] M. Tian, X. Zhang, G. Huang, W. Fan, J. Li, and Y. Zhang, "Alpha-fetoprotein assessment for hepatocellular carcinoma after transarterial chemoembolization," *Abdominal Radiology*, vol. 44, no. 10, pp. 3304–3311, 2019.

[32] P. Tangkijvanich, N. Anukulkarnkusol, P. Suwangool et al., "Clinical characteristics and prognosis of hepatocellular carcinoma: analysis based on serum alpha-fetoprotein levels," *Journal of Clinical Gastroenterology*, vol. 31, no. 4, pp. 302–308, 2000.

Hindawi
Journal of Nanomaterials
Volume 2021, Article ID 8218042, 6 pages
https://doi.org/10.1155/2021/8218042

Research Article

Thromboelastogram-Guided Transfusion Therapy Reduces Blood-Component Transfusion and Improves Coagulation Function during Orthopedic Surgery

Yan Zhang, Yue Song, Yixin Zhang, Lu Yu, and Kai Zhang

Department of Blood Transfusion, Tianjin Hospital, No. 406, Jiefang South Road, Hexi District, Tianjin 300211, China

Correspondence should be addressed to Kai Zhang; xstltwz2021@163.com

Received 18 May 2021; Revised 8 June 2021; Accepted 10 June 2021; Published 28 June 2021

Academic Editor: Songwen Tan

Massive bleeding is a serious medical complication arising from trauma, surgery, and invasive procedures. In this case, timely and effective hemostasis must be applied to patients. The aim of this study is to compare transfusion therapies guided by thromboelastogram (TEG) and conventional coagulation tests (CCTs) during orthopedic surgery, focusing on blood-component transfusion and coagulation function of patients. The patients who underwent orthopedic surgery in our hospital from May 2019 to November 2020 were retrospectively analyzed. According to different transfusion-guiding strategies, the patients were assigned into the CCT group containing 214 patients and the TEG group containing 266 patients. The TEG group used fewer volumes of blood products including red blood cell (RBC) suspension, fresh-frozen plasma, cryoprecipitate, and apheresis platelets than the CCT group ($P < 0.05$). After orthopedic surgery, the hemoglobin (Hb) and RBC counts were decreased, but the white blood cell (WBC) counts were increased in all patients receiving whether transfusion therapy guided by TEG or CCTs. Importantly, the TEG group exhibited fewer WBC counts concomitant with higher Hb and more RBC counts than the CCT group ($P < 0.05$). There was no significant difference on the platelet (PLT) counts between the two groups before and after orthopedic surgery ($P > 0.05$). Significant declines on thrombin time (TT), partial activated thromboplastin time (PATT), prothrombin time (PT), and d-dimer (D-D), along with an increase on fibrinogen (FIB) were observed in two groups after surgery. The TEG group showed reduced TT, PATT, PT, D-D, and elevated FIB compared to the CCT group ($P < 0.05$). Posttransfusion, the K value (time to reach a certain clot strength) and R value (coagulation reaction time) were decreased, the angle (α) value (clot formation rate), MA value (maximum amplitude), and CI (coagulation index) were increased in the TEG group ($P < 0.05$). When the liver function was assessed, it was found that the levels of alanine aminotransferase (ALT), aspartate aminotransferase (AST), and total serum bilirubin (TBIL) were increased significantly, and albumin (ALB) was decreased between the two groups after surgery, but the TEG group with lower levels of ALT, AST, and TBIL and a higher level of ALB than the CCT group ($P < 0.05$). With regard to the renal function, two groups had increased levels of serum creatinine (Scr) and blood urea nitrogen (BUN) with a declined uric acid (UA) level after surgery; however, the patients in the TEG group had lower levels of Scr and BUN and a higher level of UA compared to the CCT group ($P < 0.05$). In view of above data, TEG-guided transfusion therapy could reduce use of blood products, optimize blood components, and improve coagulation function for patients undergoing orthopedic surgery. TEG-guided transfusion therapy may prevent liver and renal dysfunction after orthopedic surgery.

1. Introduction

Massive blood lose is a risk for mortality and morbidity during orthopedic surgeries [1], including total hip replacement, total knee replacement [2], and spine surgery [3]. Massive bleeding is a serious and life-threatening manifestation, which can cause a variety of complications, including coagulation abnormalities, immunosuppression, infection, hypothermia, and organ damage related with massive transfusion of blood products [4, 5]. Blood transfusion involves red blood cell (RBC) suspension, fresh-frozen plasma, cryoprecipitate, and apheresis platelets, which is critical to the patients with massive

bleeding [6]. Conventional coagulation tests (CCTs), such as thrombin time (TT), partial activated thromboplastin time (PATT), prothrombin time (PT), and fibrinogen (FIB), are related to the dose and timing of transfusion [7, 8]. Shortage of blood products makes accurate judgment for time of blood transfusion and requirements of blood components urgent. However, the present massive blood transfusion protocol is fixed infusion of RBC, fresh frozen plasma (FFP), and platelets (PLTs) at a ratio of 1 : 1 : 1, likely leading to a huge waste. Thromboelastogram (TEG) has been advanced by Dr. Hartert in 1948 [9], which comprehensively analyzes the coagulation markers and represents the coagulation activity from coagulation cascade to fibrinolysis, which reflects the whole hemostasis process [10]. Studies have shown that TEG has been played a crucial role in the guidance of transfusion in cardiac surgeries for decades [11, 12]. Present researchers have attempted to establish a transfusion strategy guided by TEG during the perioperative period. However, due to variations in sample size and individual differences, different conclusions have been reported. There is limited evidence supporting its application in orthopedic surgery, and thus this study attempts to compare transfusion therapies guided by TEG and CCTs during orthopedic surgery, with a specific focus on blood-component transfusion and coagulation function of patients.

2. Methods

2.1. Patient Enrollment. From May 2019 to November 2020, patients who had undergone orthopedic surgery in our hospital were retrospectively studied and then divided into a TEG group ($n = 266$) and a CCT group ($n = 214$) in accordance with transfusion therapies guided by TEG or CCTs. All they belonged to class I-II according to the American Society of Aneshesiologists (ASA) Physical Status Classification System. Those patients were excluded due to use of anticoagulants in half a year, cognitive impairment, hematological diseases, coagulation dysfunction, hepatic and renal insufficiency, RH blood group, chronic alcoholics, pregnant women, and absence of complete clinical data. Patients in the TEG group consisted of 201 males and 66 females, aged from 13-85 years and with an average of age (48.56 ± 21) years and underwent orthopedic surgery for lumbar spinal stenosis ($n = 55$), cervical spondylosis ($n = 50$), total knee replacement ($n = 55$), fracture ($n = 100$), and lumbar disc herniation ($n = 6$). Patients in the CCT group comprised of 162 males and 52 females, aged from 13-84 years and with an average of age (48.54 ± 29) years and underwent orthopedic surgery for lumbar spinal stenosis ($n = 44$), cervical spondylosis ($n = 40$), total knee replacement ($n = 43$), fracture ($n = 80$), and lumbar disc herniation ($n = 7$). The baseline information between the two groups was not significant ($P > 0.05$).

2.2. Transfusion Therapy Guided by TEG or CCTs. The automatic coagulation analyzer SYSMEX CA 7000 (TOA Medical Electronics Co., Kobe, Japan) and the hematology analyzer (XN-3000, TOA Medical Electronics Co.) were used to examine PT (normal range [s]: 11.0-13.0), APTT (normal range [s]: 23.00-37.00), TT (normal range [s]: 12.0-19.0), and FIB (normal range [g/L]: 2.0-4.0) before and after transfusion. When the hemoglobin (Hb) was lower than 70 g/L and hematocrit (HTC) was less than 25%, RBC suspension (2 U) was transfused. If the PLT (normal range [$\times 10^9$/L]: 100-300) was lower than 50×10^9/L, apheresis platelet (10 U) was infused.

The TEG analyzer (TEG5000, Haemoscope, USA) was used to analyze R time (coagulation reaction time), K time (time to reach a certain clot strength), α value (clot formation rate), MA value (maximum amplitude), and CI (coagulation index). The normal R time ranges from 5 min to 8 min, reflecting the function of coagulation factors. Prolonged R time indicates deficiency of coagulation factors, and shortened R time indicates hypercoagulability. The normal K time ranges from 1 min to 3 min, depending on the levels of FIB, and anticoagulants could delay the K time. The α value ranges from 53° to 72°, reflecting the rate of clot formation during which FIB and PLTs are both involved. Once severe hypocoagulability occurs, clot amplitude fails to reach 20 mm, and the K time is undetectable. In this situation, the α value is more significant. A greater angle reflects faster clot formation. Prolonged K time with low angle indicates risk of hypocoagulability and blooding. Shortened K time with high angle indicates risk of hypercoagulability and clot. The normal MA value ranges from 54 mm to 72 mm, which is affected by FIB (20%) and PLT (80%), suggesting the accumulation of PLT. A smaller MA value suggests blooding, dilute blood, reduced numbers of PLTs, depletion, or deficiency of coagulation factors. A greater MA value suggests arterial and venous thrombosis and hypercoagulability. The normal CI ranges from -3 to 3 and equals $-0.6516r - 0.3772K + 0.1224\text{MA} + (-7.7922)$. CI > 3 suggests hypercoagulability, and CI < −3 suggests hypocoagulability. When the R value was more than 8 min, fresh-frozen plasma (15 mL/kg) was infused. When the MA value was less than 50 mm, the apheresis platelet (10 U) was infused. The cryoprecipitate (13 U) was infused if the angle value was more than 72°. The remaining blood products were transfused according to patients' condition and clinical experience. The usage of RBC suspension, fresh-frozen plasma, cryoprecipitate, and apheresis platelet was recorded.

2.3. Measurements of Liver and Renal Function. Fasting venous blood was collected into EDTA-contained tubes which were then centrifuged to extract the plasma. Blood sample collection was performed pretransfusion and posttransfusion. According to the instructions provided by commercial available kits, aminotransferase (ALT), aspartate aminotransferase (AST), total serum bilirubin (TBIL), albumin (ALB), serum creatinine (Scr), blood urea nitrogen (BUN), and uric acid (UA) were examined by the enzyme linked immunosorbent assay pretransfusion and posttransfusion.

2.4. Data Analysis. SPSS 20.0 software was used to process the data. The counting data was represented by percentage and analyzed by the chi-square test. The measurement data was represented by mean ± standard deviation and analyzed by

Table 1: The usage of blood products between the TEG and CCT groups.

Group	RBC suspension (U)	Fresh frozen plasma (mL)	Cryoprecipitate (U)	Apheresis platelet (10 U)	Length of hospital stay (d)
TEG ($n = 266$)	4.51 ± 0.09^{a}	254.36 ± 20.17^{a}	16.34 ± 1.25^{a}	2.04 ± 0.06^{a}	10.35 ± 2.11^{a}
CCT ($n = 214$)	6.09 ± 0.04	423.54 ± 40.28	28.64 ± 2.31	3.42 ± 0.08	11.17 ± 2.23

The letter of a suggests $P < 0.05$ compared to the CCT group.

Table 2: Blood routine tests following TEG- or CCT-guided transfusion therapy.

Group	Time	Hb (g/L)	WBC (×109/L)	PLT ($\times 10^9$/L)	RBC (×1012/L)
TEG ($n = 266$)	Preoperation	126.41 ± 12.41	8.75 ± 1.22	238.41 ± 20.33	3.97 ± 0.09
	Postoperation	106.31 ± 11.25^{ab}	10.08 ± 1.22^{ab}	149.32 ± 12.41^{a}	3.30 ± 0.06^{ab}
CCT ($n = 214$)	Preoperation	125.32 ± 12.44	8.26 ± 1.34	235.26 ± 20.12	3.98 ± 0.08
	Postoperation	76.56 ± 8.44^{a}	14.36 ± 1.15^{a}	148.26 ± 12.41^{a}	3.11 ± 0.05^{a}

The letter of a suggests $P < 0.05$ compared to the CCT group. The letter of b suggests $P < 0.05$ compared to preoperation.

Table 3: Changes of coagulation function following transfusion therapy guided by TEG or CCTs.

Group	Time	PT (s)	APTT (s)	TT (s)	FIB (g/L)	D-D (ng/mL)
TEG ($n = 266$)	Preoperation	20.31 ± 1.06	41.08 ± 4.64	26.26 ± 1.31	5.07 ± 0.05^{ab}	814.41 ± 50.33
	Postoperation	10.14 ± 1.22^{ab}	29.08 ± 3.22^{ab}	15.54 ± 1.26^{ab}	2.27 ± 0.09	760.26 ± 50.33^{a}
CCT ($n = 214$)	Preoperation	20.32 ± 1.11	41.06 ± 4.11	26.33 ± 2.17	5.09 ± 0.05^{ab}	814.26 ± 50.29
	Postoperation	13.31 ± 2.18^{a}	33.61 ± 4.33^{a}	18.64 ± 1.21^{a}	3.33 ± 0.04^{a}	783.36 ± 50.41^{a}

The letter of a suggests $P < 0.05$ compared to the CCT group. The letter of b suggests $P < 0.05$ compared to pre-operation.

the t-test. A level of $P < 0.05$ suggests a statistically significant difference.

3. Results

3.1. Reduced Blood Products by TEG-Guided Transfusion Therapy. The transfusion of RBCs and nonRBC components which involves fresh-frozen plasma, platelet, and cryoprecipitate is critical to hemostasis. The TEG group used fewer volumes of blood products including RBC suspension, fresh-frozen plasma, cryoprecipitate, and apheresis platelets than the CCT group ($P < 0.05$) ($P < 0.05$, Table 1). In addition, results showed that the TEG group had a shorter length of hospital stay than the CCT group ($P < 0.001$, Table 1).

3.2. Blood Routine Tests following TEG- or CCT-Guided Transfusion Therapy. Prior to orthopedic surgery, there was no significant difference on the value of Hb, WBC, PLT, and RBC between the TEG group and CCT group ($P > 0.05$). As listed in Table 2, after orthopedic surgery, the Hb and RBC counts were decreased, but the WBC counts were increased in all patients receiving whether transfusion therapy guided by TEG or CCTs. Importantly, the TEG group exhibited fewer WBC counts concomitant with higher Hb and more RBC counts than the CCT group ($P < 0.05$). There was no significant difference on PLT counts between the two groups before and after surgery ($P > 0.05$).

3.3. Changes of the Coagulation Function following Transfusion Therapy Guided by TEG or CCTs. There was little difference on the PT, APTT, TT, FIB, and D-D between the two groups before surgery ($P > 0.05$). Significant declines on TT, PATT, PT, and D-D, along with an increase on FIB were observed in two groups after surgery. The TEG group showed reduced TT, PATT, PT, and D-D and elevated FIB compared to the CCT group, as revealed in Table 3 ($P < 0.05$).

3.4. Changes of Coagulation Indexes on the TEG before and after Transfusion. The following TEG variables are associated with the coagulation function. The R value indicates the time to initial fibrin formation; the K value suggests the time until specific clot strength of 20 mm obtained; the MA reveals the final strength of the clot; the angle value shows rate of clot formation; the CI is obtained by the calculation of the R, K, α and MA. As shown in Table 4, the K time and R time were significantly shortened, while the values of MA, CI, and angle were increased after transfusion ($P < 0.05$).

3.5. TEG-Guided Transfusion Therapy Prevented Liver Dysfunction. There was slight difference on the levels of ALT, AST, ALB, and TBIL between the TEG and CCT groups before orthopedic surgery ($P > 0.05$). After surgery, increased levels of ALT, AST, and TBIL concomitant with a decreased level of ALB were indicated in the TEG and CCT groups. However, the TEG group showed lower levels of ALT, AST, and TBIL and a higher level of ALB compared to the CCT group ($P < 0.05$, Table 5).

Table 4: Changes of coagulation indexes on the TEG before and after transfusion.

Time	K time (min)	R time (min)	MA value (mm)	CI	Angle (°)
Before transfusion	4.54 ± 0.03	7.27 ± 0.07	47.64 ± 5.11	−2.71 ± 0.05	53.85 ± 6.22
After transfusion	3.67 ± 0.05[b]	5.96 ± 0.05[b]	57.74 ± 5.22[b]	1.46 ± 0.22[b]	62.71 ± 6.13[b]

K time: time to reach a certain clot strength; R time: coagulation reaction time; angle (α): clot formation rate; MA value: maximum amplitude; CIn: coagulation index. The letter of b suggests $P < 0.05$ compared to pretransfusion.

Table 5: Changes of liver function indexes between the TEG and CCT groups.

Group	Time	ALT (U/L)	AST (U/L)	ALB (g/mL)	TBIL (μmol/L)
TEG ($n = 266$)	Preoperation	32.27 ± 3.14	38.41 ± 3.22	33.31 ± 3.25	18.47 ± 1.26
	Postoperation	41.82 ± 4.33[b]	65.64 ± 7.14[b]	26.68 ± 2.33[b]	20.49 ± 2.33[b]
CCT ($n = 214$)	Preoperation	32.25 ± 3.11	38.21 ± 2.36	33.32 ± 3.09	18.45 ± 1.17
	Postoperation	47.21 ± 4.19[b]	72.59 ± 5.41[b]	21.21 ± 2.35[b]	23.64 ± 2.17[b]

The letter of b suggests $P < 0.05$ compared to preoperation.

Table 6: Changes of renal function indexes between the TEG and CCT groups.

Group	Time	BUN (mmol/L)	Scr (μmol/L)	UA (μmol/L)
TEG ($n = 266$)	Preoperation	6.13 ± 0.12	61.91 ± 6.41	363.25 ± 30.17
	Postoperation	7.21 ± 0.11[b]	81.95 ± 6.21[b]	314.41 ± 20.33[b]
CCT ($n = 214$)	Preoperation	6.13 ± 0.18	61.93 ± 6.22	362.19 ± 31.33
	Postoperation	7.69 ± 0.12[b]	96.58 ± 6.17[b]	297.26 ± 20.33[b]

The letter of b suggests $P < 0.05$ compared to preoperation.

3.6. TEG-Guided Transfusion Therapy Prevented Renal Dysfunction. Permanent renal dysfunction is regarded as a serious complication occurring following major surgery, possibly resulting in increased morbidity and mortality. Considering that, the renal function of patients undergoing orthopedic surgery was compared between the TEG and CCT groups. There was no significant difference on the levels of BUN, Scr, and UA between the TEG and CCT groups before surgery ($P > 0.05$). As listed in Table 6, there was an increase on the levels of BUN and Scr, with a decline on the level of UA in the two groups after surgery, but the levels of BUN and Scr were lower, and the level of UA was higher in the TEG group than those in the CCT group ($P < 0.05$).

4. Discussion

The substantial blood loss happens in the trauma, obstetrical, and surgical surgery [13]. In various clinical settings, the massive bleeding is highly related to the mortality and morbidity, especially for severe trauma patients [14]. The massive blood loss reveals the challenge to the coagulation system [3]. Blood transfusion is a relatively safe but with potential adverse reactions, which might be fatal [15]. Therefore, it is necessary to evaluate thehemostasis function and correct coagulation disorder in time, and an appropriate transfusion management should be made [16].

The TEG as a viscoelastic hemostasis assay which evaluates coagulation and fibrinolysis properties by the use of whole blood samples [17], which measures the K value, R value, the angle value, MA value, and CI, and these coagulation parameters are associated with clot factor, platelet count, FIB function, and thrombus risk [18, 19]. According to the data in this study, we found that the above parameters changed after transfusion, the K value and R value were highly decreased, and the value of MA, CI, and angle was obviously increased, which indicated the increase on clot factors and enhancement on FIB function and platelet. The PT, APTT, TT, and FIB were the basic indexes to judge whether the coagulation function is normal or not [20], and the D-D is related to the fibrinolytic activity [21]. Significant declines on TT, PATT, PT, and D-D, along with an increase on FIB were observed in two groups after surgery. The TEG group showed reduced TT, PATT, PT, D-D, and elevated FIB compared to the CCT group. The study suggested that the FIB value was higher in COVID-19 patients than that in the health group, especially for patients with thrombotic disease. The PT, APTT, D-D, and TT were related to the disease severity [22]. Some studies have shown that the TEG group reduced the consumption of blood products in the surgical surgery and severe coagulopathy [23–25], which were similar to our study, and the usage of RBC suspension, fresh-frozen plasma, cryoprecipitate and apheresis platelet in the TEG group was significantly reduced compared to the CCT group, but a study about liver transplantation indicated that the TEG group did not reduce intraoperative blood product consumption [26]. There should be more data to support above outcome since liver transplantation and orthopedic surgery belong to different types. Blood involves plasma, RBC, WBC, and PLT which represent physiological and pathological conditions of the human body [27] According to the

routine blood tests, this study revealed that there was an significant decline on the Hb and RBC and an increase on the WBC after surgery, but the WBC was lower, Hb and RBC were higher in the TEG group than those in the CCT group, and there was no obvious difference on PLT between the two groups, which suggested that the TEG group could reduce the incidence of inflammation and anemia caused by blood loss. Under the guidance of TEG, the liver function of the patients was less damaged. Our data indicated a lower growth on the ALT, AST, and TBIL and a lower decline on the ALB, representing the injury of the liver function. These findings were closer to the other COVID-19 experiments, which suggested that the severe patients were with higher growth on the ALT and AST and slight difference on TBIL between the severe patients and the mild patients [28], and 34% of patients are with lower ALB, and 6% of patients were with abnormal TBIL [29]. BUN is closely with the renal function, and the elevated BUN suggests impaired renal function [30]. Scr is widely used as a biomarker of the renal function in clinical [31], and the research found that the rise on Scr caused by drug administration might be related to the impairment on the renal function [32]. UA, excreted mostly by the kidney, might be an essential factor which relates to the acute kidney injury, chronic kidney disease, and hypertension [33]. This study indicated that there was an increase on the levels of BUN and Scr, with a decline on the level of UA in the two groups after surgery, but the levels of BUN and Scr were lower, and the level of UA was higher in the TEG group than those in the CCT group, which implied the TEG-guided transfusion therapy prevented renal dysfunction. Besides the above advantages mentioned in this paper, there are some data limitations, such as the lack of adverse reactions and mortality after blood transfusion. Further studies should be carried out to ensure its efficacy.

In summary, this study suggests that the TEG-guided transfusion strategy is superior to CCT-guided during orthopedic surgery, since TEG-guided transfusion therapy could reduce use of blood products, optimize blood components, and improve coagulation function for patients undergoing orthopedic surgery. Importantly, TEG-guided transfusion therapy may prevent liver and renal dysfunction after orthopedic surgery. However, this study was a noninterventional, observational study and did not have the capacity to allow outcome-based comparisons to determine the clinical value of TEG over CCTs or assess TEG as a predictor of bleeding or thrombosis. Therefore, further investigation with larger sample size is required.

Data Availability

The data used to support the findings of this study are included within the article.

Conflicts of Interest

The author(s) declare(s) that they have no conflicts of interest.

References

[1] Z. X. Lin and S. K. Woolf, "Safety, efficacy, and cost-effectiveness of tranexamic acid in orthopedic surgery," *Orthopedics*, vol. 39, no. 2, pp. 119–130, 2016.

[2] J. Xie, X. Feng, J. Ma et al., "Is postoperative cell salvage necessary in total hip or knee replacement? A meta-analysis of randomized controlled trials," *International Journal of Surgery*, vol. 21, pp. 135–144, 2015.

[3] J. E. Bible, M. Mirza, and M. A. Knaub, "Blood-loss management in spine surgery," *The Journal of the American Academy of Orthopaedic Surgeons*, vol. 26, no. 2, pp. 35–44, 2018.

[4] E. Guerado, A. Medina, M. I. Mata, J. M. Galvan, and M. L. Bertrand, "Protocols for massive blood transfusion: when and why, and potential complications," *European Journal of Trauma and Emergency Surgery*, vol. 42, no. 3, pp. 283–295, 2016.

[5] L. M. Carabini, C. Zeeni, N. C. Moreland et al., "Development and validation of a generalizable model for predicting major transfusion during spine fusion surgery," *Journal of Neurosurgical Anesthesiology*, vol. 26, no. 3, pp. 205–215, 2014.

[6] Z. K. McQuilten, G. Crighton, S. Brunskill et al., "Optimal dose, timing and ratio of blood products in massive transfusion: results from a systematic review," *Transfusion Medicine Reviews*, vol. 32, no. 1, pp. 6–15, 2018.

[7] F. Kong, Y. Li, and X. Liu, "Effect and clinical value of coagulation test on adverse reactions of blood transfusion in patients with major bleeding in ectopic pregnancy," *Experimental and Therapeutic Medicine*, vol. 16, no. 6, pp. 4712–4716, 2018.

[8] M. P. Sepulveda, U. A. Salgado, G. J. Barriga et al., "Usefulness of the thromboelastogram in children: correlation with habitual coagulation tests," *Revista Chilena de Pediatría*, vol. 90, no. 6, pp. 617–623, 2019.

[9] H. Hartert, "Blood clotting studies with thrombus stressography; a new investigation procedure," *Klinische Wochenschrift*, vol. 26, no. 37-38, pp. 577–583, 1948.

[10] M. Othman and H. Kaur, "Thromboelastography (TEG)," *Methods in Molecular Biology*, vol. 1646, pp. 533–543, 2017.

[11] L. Shore-Lesserson, H. E. Manspeizer, M. DePerio, S. Francis, F. Vela-Cantos, and M. A. Ergin, "Thromboelastography-guided transfusion algorithm reduces transfusions in complex cardiac surgery," *Anesthesia and Analgesia*, vol. 88, no. 2, pp. 312–319, 1999.

[12] D. Bolliger and K. A. Tanaka, "Point-of-care coagulation testing in cardiac surgery," *Seminars in Thrombosis and Hemostasis*, vol. 43, no. 4, pp. 386–396, 2017.

[13] H. P. Pham and B. H. Shaz, "Update on massive transfusion," *British Journal of Anaesthesia*, vol. 111, Suppl 1, pp. i71–i82, 2013.

[14] A. M. Abuzeid and T. O'Keeffe, "Review of massive transfusion protocols in the injured, bleeding patient," *Current Opinion in Critical Care*, vol. 25, no. 6, pp. 661–667, 2019.

[15] C. Atterbury and J. Wilkinson, "Blood transfusion," *Nursing Standard*, vol. 14, no. 34, pp. 47–52, 2000.

[16] M. Munoz, J. Stensballe, A. S. Ducloy-Bouthors et al., "Patient blood management in obstetrics: prevention and treatment of postpartum haemorrhage. A NATA consensus statement," *Blood Transfusion*, vol. 17, no. 2, pp. 112–136, 2019.

[17] N. Tekkesin, M. Tekkesin, and G. Kaso, "Thromboelastography for the monitoring of the antithrombotic effect of low-molecular-weight heparin after major orthopedic surgery,"

Anatolian Journal of Cardiology, vol. 15, no. 11, pp. 932–937, 2015.

[18] J. C. Hagedorn 2nd, J. M. Bardes, C. L. Paris, and R. W. Lindsey, "Thromboelastography for the orthopaedic surgeon," *The Journal of the American Academy of Orthopaedic Surgeons*, vol. 27, no. 14, pp. 503–508, 2019.

[19] E. Gonzalez, E. E. Moore, and H. B. Moore, "Management of trauma-induced coagulopathy with thrombelastography," *Critical Care Clinics*, vol. 33, no. 1, pp. 119–134, 2017.

[20] G. M. Zhang, W. Zhang, and G. M. Zhang, "Age-specific reference intervals for PT, aPTT, fibrinogen and thrombin time for parturient women," *Thrombosis and Haemostasis*, vol. 119, no. 6, pp. 894–898, 2019.

[21] J. I. Weitz, J. C. Fredenburgh, and J. W. Eikelboom, "A test in context: D-dimer," *Journal of the American College of Cardiology*, vol. 70, no. 19, pp. 2411–2420, 2017.

[22] X. Jin, Y. Duan, T. Bao et al., "The values of coagulation function in COVID-19 patients," *PLoS One*, vol. 15, no. 10, article e0241329, 2020.

[23] J. D. Dias, A. Sauaia, H. E. Achneck, J. Hartmann, and E. E. Moore, "Thromboelastography-guided therapy improves patient blood management and certain clinical outcomes in elective cardiac and liver surgery and emergency resuscitation: a systematic review and analysis," *Journal of Thrombosis and Haemostasis*, vol. 17, no. 6, pp. 984–994, 2019.

[24] C. F. Weber, K. Gorlinger, D. Meininger et al., "Point-of-care testing: a prospective, randomized clinical trial of efficacy in coagulopathic cardiac surgery patients," *Anesthesiology*, vol. 117, no. 3, pp. 531–547, 2012.

[25] L. De Pietri, M. Bianchini, R. Montalti et al., "Thrombelastography-guided blood product use before invasive procedures in cirrhosis with severe coagulopathy: a randomized, controlled trial," *Hepatology*, vol. 63, no. 2, pp. 566–573, 2016.

[26] R. Gaspari, L. Teofili, P. Aceto et al., "Thromboelastography does not reduce transfusion requirements in liver transplantation: a propensity score-matched study," *Journal of Clinical Anesthesia*, vol. 69, p. 110154, 2021.

[27] D. H. Kuan, C. C. Wu, W. Y. Su, and N. T. Huang, "A microfluidic device for simultaneous extraction of plasma, red blood cells, and on-chip white blood cell trapping," *Scientific Reports*, vol. 8, no. 1, p. 15345, 2018.

[28] F. Lei, Y. M. Liu, F. Zhou et al., "Longitudinal association between markers of liver injury and mortality in COVID-19 in China," *Hepatology*, vol. 72, no. 2, pp. 389–398, 2020.

[29] X. Deng, B. Liu, J. Li, J. Zhang, Y. Zhao, and K. Xu, "Blood biochemical characteristics of patients with coronavirus disease 2019 (COVID-19): a systemic review and meta-analysis," *Clinical Chemistry and Laboratory Medicine*, vol. 58, no. 8, pp. 1172–1181, 2020.

[30] M. Seki, M. Nakayama, T. Sakoh et al., "Blood urea nitrogen is independently associated with renal outcomes in Japanese patients with stage 3-5 chronic kidney disease: a prospective observational study," *BMC Nephrology*, vol. 20, no. 1, p. 115, 2019.

[31] T. D. Bjornsson, "Use of serum creatinine concentrations to determine renal function," *Clinical Pharmacokinetics*, vol. 4, no. 3, pp. 200–222, 1979.

[32] X. Chu, K. Bleasby, G. H. Chan, I. Nunes, and R. Evers, "The complexities of interpreting reversible elevated serum creatinine levels in drug development: does a correlation with inhibition of renal transporters exist?," *Drug Metabolism and Disposition*, vol. 44, no. 9, pp. 1498–1509, 2016.

[33] S. A. Fathallah-Shaykh and M. T. Cramer, "Uric acid and the kidney," *Pediatric Nephrology*, vol. 29, no. 6, pp. 999–1008, 2014.

Hindawi
Journal of Nanomaterials
Volume 2021, Article ID 9152985, 11 pages
https://doi.org/10.1155/2021/9152985

Research Article

MicroRNA-34c-5p Inhibition of NUF2 Suppresses Lung Adenocarcinoma Cell Viability and Invasion

Xiaoguang You,[1] Haiying Ren,[2] and Lijun Wen[3]

[1]*The First Affiliated Hospital of Hainan Medical University, China*
[2]*The Sixth People's Hospital of Jilin City, China*
[3]*Hainan Medical University, China*

Correspondence should be addressed to Lijun Wen; wljpd2018@163.com

Received 21 May 2021; Revised 1 June 2021; Accepted 3 June 2021; Published 21 June 2021

Academic Editor: Songwen Tan

Background. Lung cancer continues to be a burden worldwide with an estimated 2.09 million new cases of lung cancer and 1.76 million deaths in 2018. MicroRNAs (miRs) are key regulators of gene expression and show their oncogenic or antioncogenic role in human cancers including lung cancer. In this study, we test the hypothesis that miR-34c-5p functions as a candidate antioncomiR in lung adenocarcinoma by targeting NUF2. *Methods*. The expression pattern of miR-34c-5p and NUF2 was evaluated in 202 biopsy specimens from patients with lung adenocarcinoma and 176 biopsy specimens from patients with benign lung diseases. Interaction between miR-34c-5p and NUF2 was verified by the luciferase-based assay. Cell viability and invasion assays were carried out in cultured A549 cells treated with miR-34c-5p mimic, inhibitor, and siRNA against NUF2. *Results*. NUF2 was highly expressed in lung adenocarcinoma samples and related to the differentiation degree, TNM stage, and presence of lymph node metastasis (LNM). Patients with NUF2 overexpression had reduced overall survival (OS) and disease-free survival (DFS) compared to patients with underexpression. Cox multivariate analysis revealed that high expression of NUF2, advanced TNM stage, well/moderate differentiation, and existence of LNM were unfavorable prognostic factors. siRNA-mediated knockdown of NUF2 inhibits A549 cell viability and invasion. miR-34c-5p was expressed at a poor level in lung adenocarcinoma samples and related to the differentiation degree, TNM stage, and presence of LNM. miR-34c-5p underexpression contributes to reduced OS and DFS, which was demonstrated as an unfavorable prognostic factor by Cox multivariate analysis. siRNA-mediated knockdown of NUF2 could ablate miR-34c-5p inhibition-mediated effects on A549 cells. *Conclusion*. Our results prove the hypothesis that miR-34c-5p could suppress lung adenocarcinoma progression by binding to the NUF2 gene. The study is a significant step towards extending our understanding of the mode of miRNA regulation in lung adenocarcinoma.

1. Introduction

Lung cancer represents the leading cause of death among the population with malignant tumors worldwide [1]. The incidence and mortality of lung cancer in China are increasing rapidly in the past three decades, which imposes a large burden on patients and the society economy [2]. On the basis of annual projections, the National Central Cancer Registry reported that there were approximately 46.08 per 100,000 people suffering from lung cancer and 37.00 per 100,000 people dying of this disease in 2010 [2]. Lung adenocarcinoma is a frequently occurring subtype of lung cancer, originating from the smaller airways and occurring in peripheral lung tissues [3]. However, histopathology is insufficient to monitor disease progression and clinical outcome of patients with lung adenocarcinoma.

Interestingly, lung adenocarcinoma possesses different genomic alterations in contrast to other lung cancer subtypes, which suggests a wide range of molecular variations that underlie the disease [4]. Recently, approaches to lung adenocarcinoma

treatment advanced from the application of adjuvant chemotherapy to personalized treatment based on genomic alterations [5]. Recently, dysfunctions of microRNAs (miRNAs) are commonly related to lung cancer tumorigenesis by affecting their target genes, which highlights their potential in reducing drug resistance and encouraging histological subclassification techniques [6].

The miR-34 family (miR-34a, miR-34b, and miR-34c) was upregulated in lung cancer, while miR-34b/c was demonstrated to be more effective as a tumor suppressor than miR-34a [7]. Poor expression of miR-34c-5p found in the context of human cancers including colorectal cancer [8] and laryngeal squamous cell carcinoma [9] underlines its antitumor effect. NUF2 (Ndc80 kinetochore complex component) is a molecular linker between tubulin subunits and the kinetochore attachment site at kinetochore-attached microtubule ends [10]. NUF2 has been identified as an oncogene that is overexpressed in the context of several cancers, such as prostate cancer [11], pancreatic cancer [12], and colorectal cancers [13]. Increasing bioinformatics prediction shows that miR-34c-5p has a chance to interact with NUF2 3′-UTR. Therefore, we determined the expression level of miR-34c-5p and NUF2 in bronchial biopsy samples from patients with lung adenocarcinoma and benign lung diseases and correlate it with clinical features and prognosis. Furthermore, we manipulated miR-34c-5p expression in lung adenocarcinoma cell A549 and assess its effect on cell viability and invasion.

2. Materials and Methods

2.1. Gene Expression Profiles of NPC in Gene Expression Omnibus (GEO). Microarray data deposited with GEO (https://www.ncbi.nlm.nih.gov/geo/) under accession number GSE33532 between individual primary tumors and matched distant normal lung tissues were analyzed. An absolute |log 2 fold change (FC) | >0.5 plus a false discovery rate (FDR) $p < 0.05$ was used to screen as differentially expressed genes (DEGs) using the Limma package of R language between individual primary tumors and matched distant normal lung tissues.

2.2. Tissue Specimen Collection. Two hundred and two biopsy specimens were based on patients pathologically diagnosed with lung adenocarcinoma and undergoing bronchoscopy at our hospital from January 2009 to December 2015. The mean age of enrolled patients was 61.62 ± 4.34 years, and none of them received chemotherapy or radiotherapy. The tumor node metastasis (TNM) of 202 specimens was split into different stages according to the staging criteria formulated by the International Association for the Study of Lung Cancer (IASLC) [14]. The follow-up study was performed from January 2009 to December 2020, with overall survival (OS) and disease-free survival (DFS) recorded. During the same period, 176 biopsy specimens were collected from patients with benign lung diseases who visited our hospital, and there were 103 males and 73 females, with a mean age of 58.92 ± 5.23 years.

2.3. Immunohistochemistry (IHC). Tissues were fixed with 10% formaldehyde, paraffin-embedded, and cut into sections (4 μm). Sections were stained using anti-NUF2 (Santa Cruz Biotechnology, USA) and then allowed to react with goat anti-rabbit IgG (Beyotime Institute of Biotechnology, China) for 30 min. We randomly captured 5 fields of view under 200x magnification using a microscope (Nikon, Japan). Extents of staining were reflected using scores: 0 indicates no stained cells, 1 indicates 1-25% stained cells, 2 indicates 26-50% stained cells, and 3 indicates 51-100% stained cells. With regard to staining intensities, 0 reflects uncolored or not obvious stain, 1 reflects light yellow stains, 2 reflects brownish yellow stains, and 3 reflects brown stains. Final staining scores consisted of intensity and extent scores. The score was 0-1 point as negative (-), 2-3 points as weakly positive (+), and 4-6 points as positive (++). In this study, both "-" and "+" were regarded as negative and "++" as positive.

2.4. Manipulation of miR-34c-5p and NUF2 In Vitro. A549 cells were harvested in RPMI-1640 with 10% fetal bovine serum (FBS) at 37°C under 5% CO_2. Once cell confluence reached 70%-90%, the old medium was renewed with serum-free medium (1600 μL). miR-34c-5p mimic, control mimic, miR-34c-5p inhibitor, control inhibitor, siRNA targeting NUF2, and scramble siRNA (GenePharma, China) were separately delivered into A549 cells (400 μL supplemented with Lipofectamine 2000) as per the manufacturer's protocols (Invitrogen, USA). Transient transfection lasted for 48 hours.

2.5. Real-Time qPCR (RT-qPCR). Total RNA was obtained by the method of TRIzol (No. 15596026, Invitrogen, USA). The cDNA was generated using PrimeScript™ II 1st Strand cDNA Synthesis Kits (TaKaRa) for mRNA quantification. RT-qPCR was completed as instructed by the manual provided by the kit (SYBR Premix Ex Taq Kit, TaKaRa) on the real-time PCR system (Applied Biosystems, USA). The primer sequences of NUF2 were 5′-CACACCAGGAGGCATT AATGAAACT-3′ (forward) and 5′-GGAATTTCCCTCTT GCAGCACT-3′ (reverse), and the primer sequences of GAPDH were 5′-ATGGGGAAGGTGAAGGTCGG-3′ (forward) and 5′-GACGGTGCCATGGAATTTGC-3′ (reverse). The cDNA was generated using the One Step PrimeScript miRNA cDNA Synthesis Kit (TaKaRa, Japan) for miRNA quantification. The primer sequence of hsa-miR-34c-5p was 5′-AGGCAGTGTAGTTAGCTGATTGC-3′, and the primer sequence of U6 was 5′-CGCAAGGATGACACGC AAATTC-3′. The expression of miR-34c-5p was relative to U6 snRNA and NUF2 to GAPDH.

2.6. Western Blotting. After 10% SDS-PAGE followed by membrane transfer, Western blots were probed with anti-NUF2 (Santa Cruz Biotechnology) and incubation with goat anti-rabbit IgG (Beyotime Institute of Biotechnology). GAPDH was used as a loading control for normalization. Visualization for Western blots was performed by means of an enhanced chemiluminescence (ECL) method (Amersham Pharmacia, USA), and gray quantification of Western blots was analyzed using ImageJ v1.48u software.

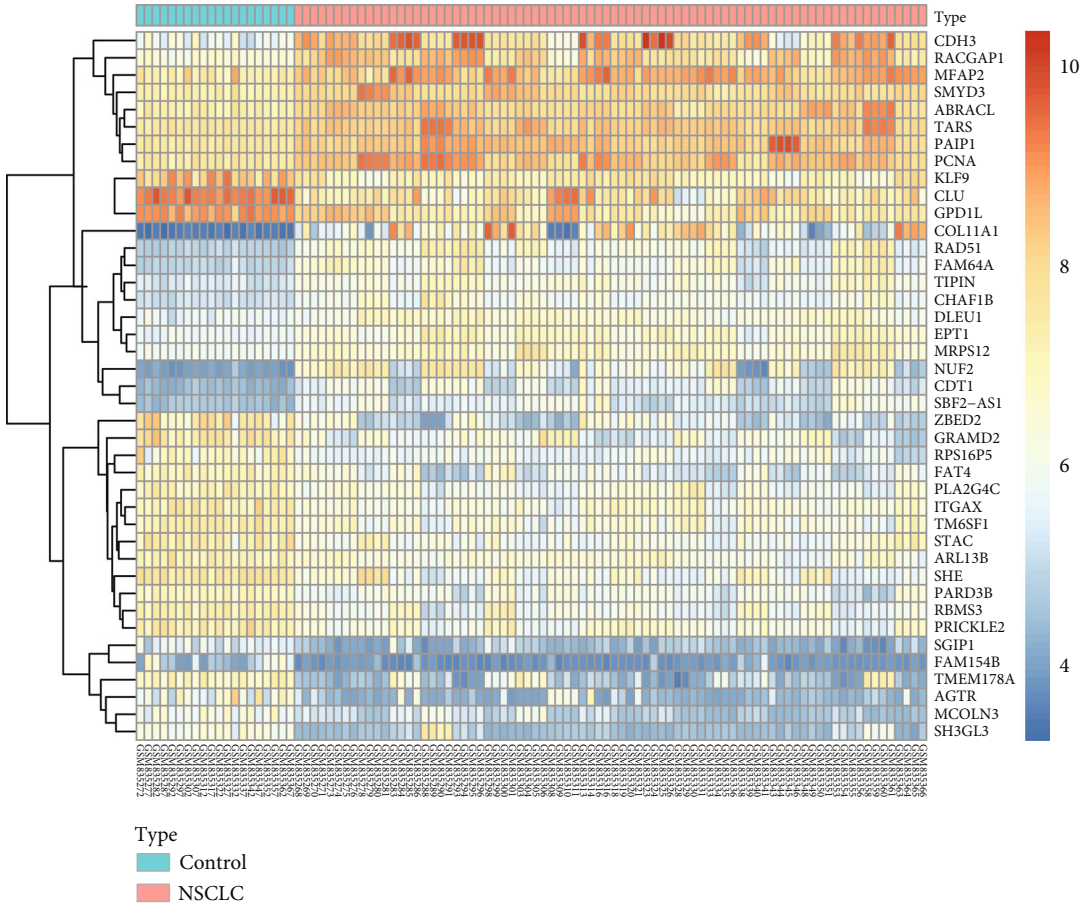

(a)

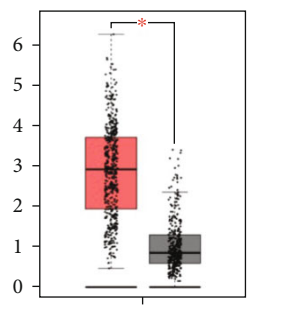

LUAD
(num(T) = 483; num(N) = 347)

(b)

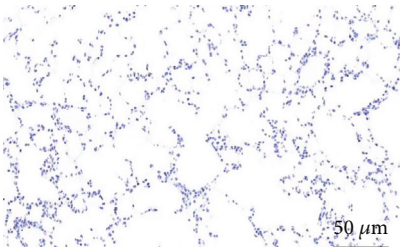

Benign lung tissues

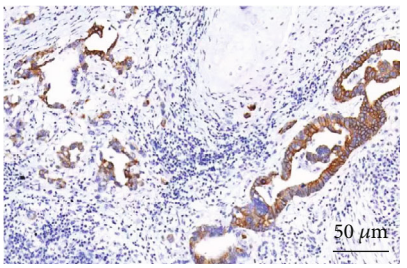

Lung adenocarcinoma tissues

(c)

Figure 1: Continued.

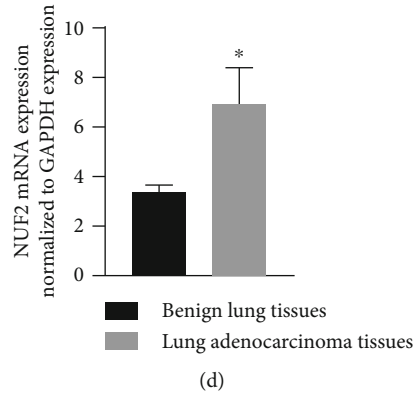

Figure 1: NUF2 is overexpressed in lung adenocarcinoma tissues. (a) DEGs between primary tumors ($n = 20$) and matched distant normal lung tissues ($n = 20$) in the GSE33532 dataset are shown in a heat map. Color scale indicates degrees of downregulation (green) and upregulation (red). (b) The expression of NUF2 in primary lung tumors ($n = 483$) and normal lung tissues ($n = 347$) in the GEPIA database. (c) Representative image of immunohistochemical staining for NUF2 in lung adenocarcinoma tissues ($n = 202$) and negative expression of NUF2 in benign lung tissues ($n = 176$); original magnification, ×200. (d) The mRNA expression of NUF2 in lung adenocarcinoma tissues ($n = 202$) and benign lung tissues ($n = 176$) determined by RT-qPCR. $^*p < 0.05$.

2.7. Luciferase Activity Assays. The wild-type NUF2 and NUF2 mutated at the putative binding sites of miR-34c-5p were independently inserted into luciferase reporter plasmids (Promega, USA), named pmirGLO-NUF2-Wt and pmirGLO-NUF2-Mut. HEK293T cells were cotransfected with reporter plasmids and either miR-34c-5p mimic or control mimic using the dual-luciferase reporter assay system (D0010, Solarbio, China).

2.8. Cell Viability and Invasion Assays. Cell viability was reflected by absorbance at different incubation with 4 h incubation of 10 μL MTT, with growth curves plotted accordingly. When performing cell invasion assays, the cells were resuspended into 3×10^5 cells per well using serum-free RPMI-1640 medium and then added to the upper chambers (BD Biosciences, USA) coated with Matrigel (BD Biosciences). Matrigel was pretreated using serum-free DMEM (1 : 10). The lower chamber was filled with DMEM with 5% FBS as for chemoattractant. Twenty-four hours later, the cells stained with 0.1% crystal violet in the lower chamber were counted in six fields with a microscope (Olympus, Tokyo, Japan).

2.9. Data Processing. All statistics were performed using SPSS Statistics 21.0. Data were displayed as the percentage or mean ± standard deviation and compared using the chi-squared test or unpaired t-test between two groups, with $p < 0.05$ regarded as a significant difference. Survival probabilities were estimated by the Kaplan-Meier method and log-rank test. Cox multivariate regression analysis was employed to identify independent risk factors for patient survival.

3. Results

3.1. Overexpression of NUF2 in Lung Adenocarcinoma Tissues. After analyzing raw data from the GSE33532 dataset, 50 DEGs between lung cancer tissue samples than their normal counterparts stood out. We depicted a heat map (Figure 1(a)) showing 50 DEGs between primary tumors and matched distant normal lung tissues from the GSE33532 dataset. The GEPIA database also showed higher expression of NUF2 in cancer samples than their normal counterparts in lung adenocarcinoma (Figure 1(b)). However, NUF2 has been

Table 1: NUF2 expression was related to differentiation, TNM stage, and the presence of LNM in lung adenocarcinoma.

Pathological index	Case	Positive rate of NUF2, n (%)	χ^2	p
Gender				
Male	113	63 (55.75)	0.363	0.717
Female	89	54 (60.67)		
Age				
<60	63	35 (55.56)	0.238	0.812
≥60	139	82 (58.99)		
Smoking history				
Yes	71	43 (60.53)	0.475	0.635
No	131	74 (56.49)		
Maximal tumor diameter				
<3 cm	143	79 (55.24)	0.612	0.541
≥3 cm	59	38 (64.41)		
TNM stage				
I+II	121	52 (42.98)	2.670	0.008
III+IV	81	65 (80.25)		
Differentiation				
Medium/well differentiation	166	84 (50.60)	2.045	0.030
Poor differentiation	36	33 (91.67)		
LNM				
Presence	60	50 (83.33)	2.360	0.018
Absence	142	67 (47.18)		

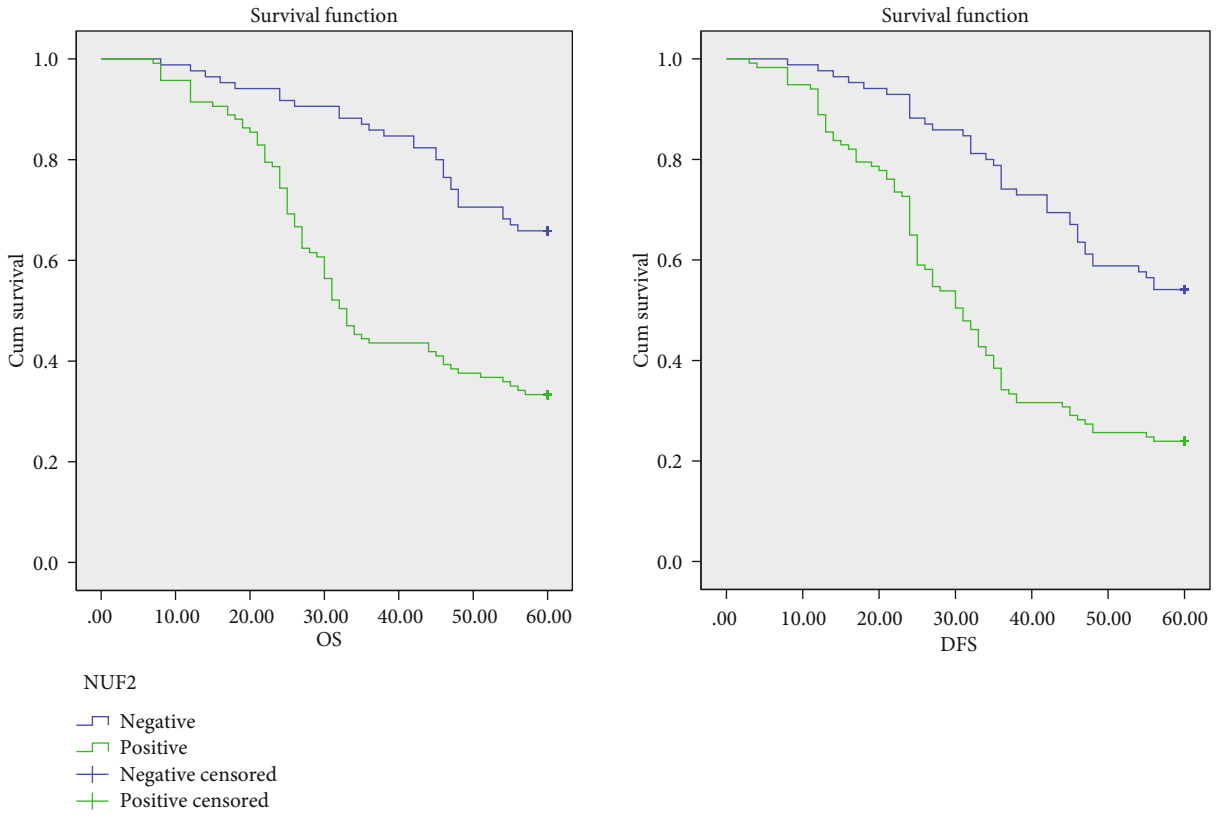

Figure 2: Kaplan-Meier curves were depicted to estimate OS and DFS of a patient with lung adenocarcinoma ($n = 202$) according to NUF2 expression. The median OS and DFS time for the positive expression group was 38.6 months and 34.2 months, respectively. The median OS and DFS time for the negative group was 52.3 months and 48.7 months, respectively.

Table 2: Multivariate survival analysis in Cox proportional hazards models for prognosis of lung adenocarcinoma.

Factors	*B*	SE	Wald	SIG.	Exp.(*B*)	95% CI for Exp.(*B*)	
						Lower	Upper
TNM	0.793	0.268	8.742	0.003	2.210	1.306	3.738
Differentiation	-0.497	0.252	3.893	0.048	0.609	0.372	0.997
LNM	0.559	0.275	4.121	0.042	1.749	1.019	3.001
High expression of NUF2	0.664	0.243	7.454	0.006	1.943	1.206	3.130

investigated rarely in lung adenocarcinoma in recent studies. In order to further confirm the expression patterns of NUF2 in lung adenocarcinoma, we collected 202 biopsy specimens from lung adenocarcinoma patients and 176 biopsy specimens from patients with benign lung diseases. Immunohistochemical staining for NUF2 was performed to estimate the positive expression of NUF2 between lung adenocarcinoma tissues and benign lung tissues. It was found that NUF2 was mainly localized in the cytoplasm as yellow-brown particles. Among 202 lung adenocarcinoma tissues, the positive rate of NUF2 reached 57.92% (117/202). Among 176 benign lung tissues, no positive staining for NUF2 was observed. The positive rate of NUF2 was notably higher in lung adenocarcinoma tissues than in benign lung tissues ($p < 0.05$, Figure 1(c)). RT-qPCR showed that lung adenocarcinoma tissues exhibited a higher mRNA expression of NUF2 than benign lung tissues ($p < 0.05$, Figure 1(d)).

3.2. Overexpression of NUF2 Contributes to Lung Adenocarcinoma Progression. Since NUF2 overexpression was observed in lung adenocarcinoma tissues, the focus of our analysis was shifted to studying the relationship between NUF2 activity and clinical variables of lung adenocarcinoma patients. We collected 202 biopsy specimens from lung adenocarcinoma patients and 176 biopsy specimens from patients with benign lung diseases, with medical records. We found that NUF2 expression was related to differentiation, TNM stage, and the existence of lymph node metastasis (LNM), as evidenced by the results that patients in stage III and stage IV, with poor differentiation, and with LNM

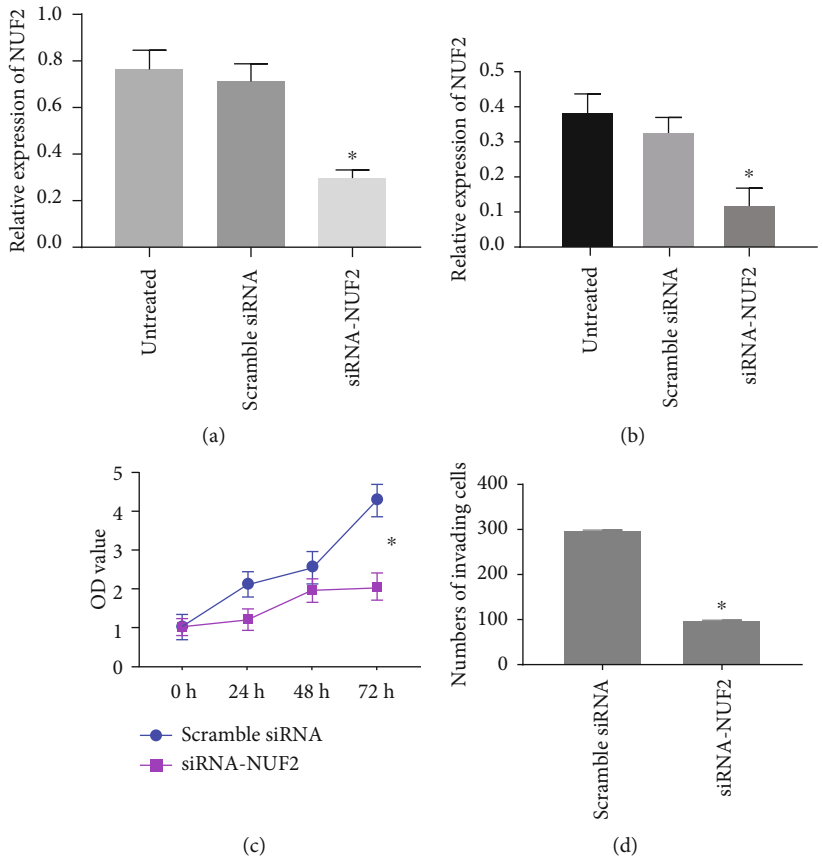

Figure 3: Knockdown of NUF2 inhibits lung adenocarcinoma A549 cell viability and invasion. (a, b) siRNA targeting NUF2 was delivered into A549 cells to specifically blunt NUF2 expression *in vitro*, with delivery of scramble siRNA as the negative control. NUF2 mRNA and protein expressions were assessed in A549 cells by the RT-qPCR and Western blot analysis. (c) Cell viability was examined by MTT assays. (d) Cell invasion was examined by Transwell assays. $^*p < 0.05$.

presented a higher positive rate of NUF2 than those in stage I and stage II, with well/moderate differentiation, and without LNM ($p < 0.05$, Table 1). Collectively, NUF2 overexpression may be associated with lung adenocarcinoma progression.

3.3. NUF2 Overexpression Predicted Poor Survival of Lung Adenocarcinoma. TCGA also showed that there was a significant difference concerning lung adenocarcinoma OS between patients with high and low expressions of NUF2 ($p = 0.0025$). The intensity and extent of NUF2 staining were evaluated, and two scores were added. Patients with – and + were classified into the negative expression group and those with ++ into the positive expression group. Patients with NUF2 overexpression had reduced OS and DFS compared to patients with underexpression ($p < 0.05$, Figure 2). Next, we included high expression of NUF2, TNM stage, differentiation, and LNM into the Cox proportional hazards model for the prognosis of lung adenocarcinoma. The results of Cox multivariate analysis revealed that (Table 2) high expression of NUF2, TNM stage, differentiation, and LNM were independent risk factors for the prognosis of lung adenocarcinoma ($p < 0.05$).

3.4. Knockdown of NUF2 Inhibits Lung Adenocarcinoma A549 Cell Viability and Invasion. We manipulated NUF2 using siRNA in A549 cells and examined the effect of NUF2 on A549 cell viability and invasion. First, the RT-qPCR analysis and Western blotting determined that siRNA designed specifically for NUF2 successfully knocked down the mRNA expression of NUF2 and diminished the protein level of NUF2 (Figures 3(a) and 3(b)). The results of MTT assays and Transwell invasion assays revealed that compared with A549 cells treated with scramble siRNA, siRNA-NUF2-treated A549 cells showed reduced cell viability and invasion ($p < 0.05$, Figures 3(c) and 3(d)).

3.5. Downregulated miR-34c-5p Was Associated with the Development and Poor Prognosis of Lung Adenocarcinoma. To further evaluate the expression pattern of miR-34c-5p in lung adenocarcinoma, we quantified miR-34c-5p in lung adenocarcinoma tissues and benign lung tissues. As shown in Table 3, patients in stage III and stage IV, with poor differentiation, and with lymph node metastasis (LNM) presented a lower expression level of miR-34c-5p than those in stage I and stage II, with well/moderate differentiation, and without LNM ($p < 0.05$). Subsequently, Kaplan-Meier curves were depicted to estimate patient OS and DFS according to miR-34c-5p expression ($p < 0.05$). The results showed that

Table 3: Association between miR-34c-5p expression and clinical variables of lung adenocarcinoma patients.

Index	The expression of miR-34c-5p	t	p
Gender			
Male	0.59 ± 0.16	0947	0.345
Female	0.57 ± 0.0.14		
Age			
<60	0.57 ± 0.21	0.959	0.588
≥60	0.59 ± 0.15		
Smoking history			
Yes	0.60 ± 0.16	0.996	0.321
No	0.57 ± 0.15		
Maximal tumor diameter			
<3 cm	0.59 ± 0.15	1.383	0.168
≥3 cm	0.56 ± 0.15		
TNM stage			
I+II	0.61 ± 0.16	3.383	0.001
III+IV	0.54 ± 0.13		
Differentiation			
Medium/well differentiation	0.64 ± 0.18	2.581	0.011
Poor differentiation	0.57 ± 0.14		
LNM			
Presence	0.54 ± 0.14	2.256	0.025
Absence	0.60 ± 0.15		

patients with low miR-34c-5p expression exhibited poor OS and DFS when compared to those with high miR-34c-5p expression (Figure 4). Next, we included low expression of miR-34c-5p, TNM stage, differentiation, and LNM into the Cox proportional hazards model for the prognosis of lung adenocarcinoma. After Cox multivariate analysis, it was revealed that miR-34c-5p underexpression, TNM stage, differentiation, and LNM were independent risk factors for lung adenocarcinoma prognosis ($p < 0.05$, Table 4).

3.6. miR-34c-5p Restrained A549 Cell Viability and Invasion by Targeting NUF2. In this part, we aim to prove the hypothesis that the anticarcinogenic effect of miR-34c-5p on lung adenocarcinoma is achieved by targeting NUF2. At first, we searched web-available databases RNA22 where miR-34c-5p sharing binding sites with NUF2 are predicted (Figure 5(a)) and starBase (http://starbase.sysu.edu.cn/) where miR-34c-5p and NUF2 are coexpressed in lung adenocarcinoma (Figure 5(b)). After dual-luciferase reporter gene assays, it was found that the pmirGLO-NUF2-WT exhibited reduced luciferase intensity upon miR-34c-5p mimic transfection ($p < 0.05$, Figure 5(c)). The qRT-PCR and Western blot analysis ($p < 0.05$, Figure 5(d)) demonstrated that NUF2 was decreased in A549 cells treated with miR-34c-3p mimic and increased in A549 cells treated with miR-34c-3p inhibitor at mRNA and protein levels. Finally, A549 cells were treated with miR-34c-3p inhibitor and siRNA-NUF2, and their viability and invasion were evaluated using MTT assays and Transwell invasion assays. When compared to A549 cells treated with NC inhibitor followed by scrambled siRNA, A549 cells treated with miR-34c-3p inhibitor followed by siRNA-NUF2 did not differ concerning cell viability and invasion ($p < 0.05$, Figures 5(e) and 5(f)), suggesting that miR-34c-3p mediated A549 cell viability and invasion by binding to NUF2.

4. Discussion

Lung adenocarcinoma, the most frequent histological subtype of non-small-cell lung cancer (NSCLC), has been indicated to be closely correlated with molecular heterogeneity [4]. Recently, the significance of miRNAs in lung cancer has been increasingly recognized regarding their therapeutic and diagnostic values [15]. In the current study, we synthesized the evidence of miR-34c-5p as a prognostic biomarker in lung adenocarcinoma and provided available evidence validating the relationship between poorly expressed miR-34c-5p and unfavorable oncologic outcomes of patients with lung adenocarcinoma. Furthermore, elevated miR-34c-5p was observed to exert inhibitory effects on lung adenocarcinoma cell viability and invasion by inhibiting NUF2.

miR-34c-5p was confirmed to be poorly expressed in lung adenocarcinoma in association with poor prognosis, setting a foundation for subsequent experiments. Importantly, miR-34c-5p has been acknowledged to be of great importance in lung-related diseases [16, 17]. Besides, miR-34c-5p has been suggested as a target for potential therapeutic strategies in cancer pain management [18]. The association between miR-34c-5p and overall survival condition of patients with lung adenocarcinoma has also been elucidated, which is largely in agreement with our finding [19]. In addition, the prognostic value of miR-34c-5p at the low expression level is consistent with its role in colon cancer according to a previous report [20]. Likewise, miR-34c-5p underexpression has been defined as an independent factor of dismal overall and DFS in patients with laryngeal squamous cell carcinoma [9]. Dysregulation of miRNAs has been identified to affect downstream targets and further function as regulators of various tumorigenic events during the progression and development of cancer [21]. When miR-34c-5p expression was forced in our study, A549 cell abilities of migration and invasion were significantly weakened. A functional study has unraveled the antiapoptotic effects of miR-34c-5p in A549 cells induced by paclitaxel in lung cancer [22]. Similarly, upregulation of miR-34c-5p has been explored to be involved in the protection mechanism of Pien Tze Huang in colorectal cancer [23]. In the context of cervical cancer, overexpressed miR-34c-5p has the ability to curtail cancer cell proliferation and migration [24], supporting our validation on the involvement of miR-34c-5p in lung adenocarcinoma.

It has been underlined that the integration of miRNAs and target genes may manifest itself as a promising approach

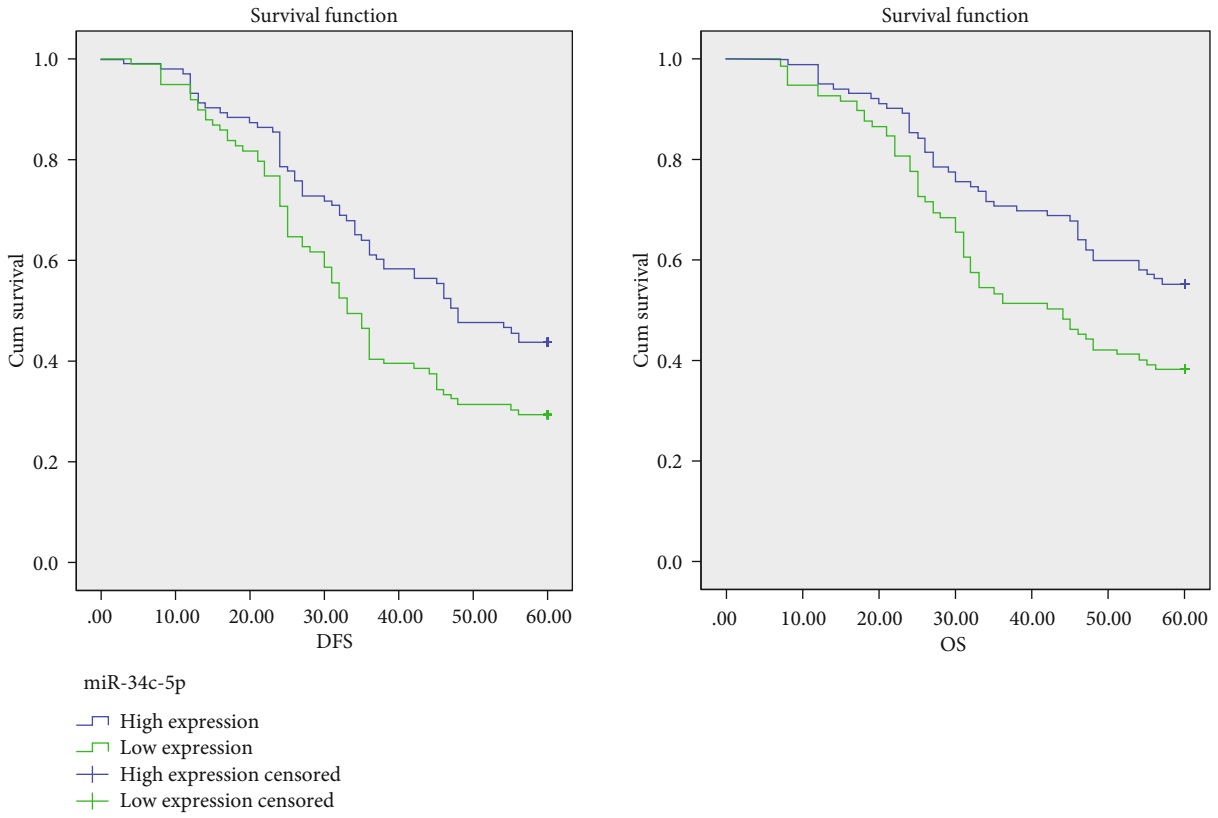

Figure 4: Kaplan-Meier curves were depicted to estimate lung adenocarcinoma patient ($n = 202$) OS and DFS according to miR-34c-5p expression. The median OS and DFS time for the low miR-34c-5p group was 44 months and 33.0 months, respectively. The median OS and DFS time for the high miR-34c-5p group was 54.0 months and 48.0 months, respectively.

Table 4: Independent risk factors for prognosis of lung adenocarcinoma.

Factors	*B*	SE	Wald	SIG.	Exp.(*B*)	95% CI for Exp.(*B*)	
						Lower	Upper
TNM	0.570	0.234	5.925	0.015	1.768	1.117	2.798
Differentiation	0.287	0.101	8.021	0.005	1.332	1.092	1.624
LNM	0.497	0.244	4.164	0.041	1.645	1.020	2.652
miR-34c-5p	0.409	0.202	3.978	0.046	1.496	1.007	2.222

for the prediction and progression of NSCLC [25]. During the investigation, it was found that miR-34c-5p could target and further regulate NUF2 in a negative manner, which was considered the underlying mechanism responsible for the antitumor potential of miR-34c-5p against lung adenocarcinoma. Similar interplay involving miR-34c-5p has been elaborated that special AT-rich sequence-binding protein 2 is a specific target of miR-34c-5p in colorectal cancer and sirtuin 6 works in tandem with miR-34c-5p in regulating colon cancer progression [8, 26]. NUF2, a key mediator of meiotic cell cycle distribution in mammalian oocytes, harbors the property to give rise to defective spindles, activated spindle assembly checkpoint, and misaligned chromosomes [27]. Notably, NUF2 has been documented to play an important part in cell senescence after irradiation, which may result in serious deadly lung injury featured with respiratory failure and pulmonary dysfunction [28]. Mounting evidences have emerged regarding NUF2-targeted therapies to combat multiple cancers, including breast cancer, hepatocellular carcinoma, and pancreatic cancer [29–31]. In lung cancer, NUF2 has also been found to be engaged by interacting with ZW10 interacting protein, a critical part of the mitotic checkpoint with prognostic value [32]. Additionally, NUF2 can be targeted by miR-3613-3p and highlighted as a potential biomarker of liver cancer [33]. Given the aforementioned data and studies, we were convinced that miR-34c-5p-dependent NUF2 inhibition conferred protection against cancerigenic behaviors of lung adenocarcinoma cells.

To sum up, our findings demonstrated that the target inhibition of miR-34c-5p on NUF2 imparted a pronounced inhibitory effect on malignant cell viability and invasion in lung adenocarcinoma, shedding light on the remarkable

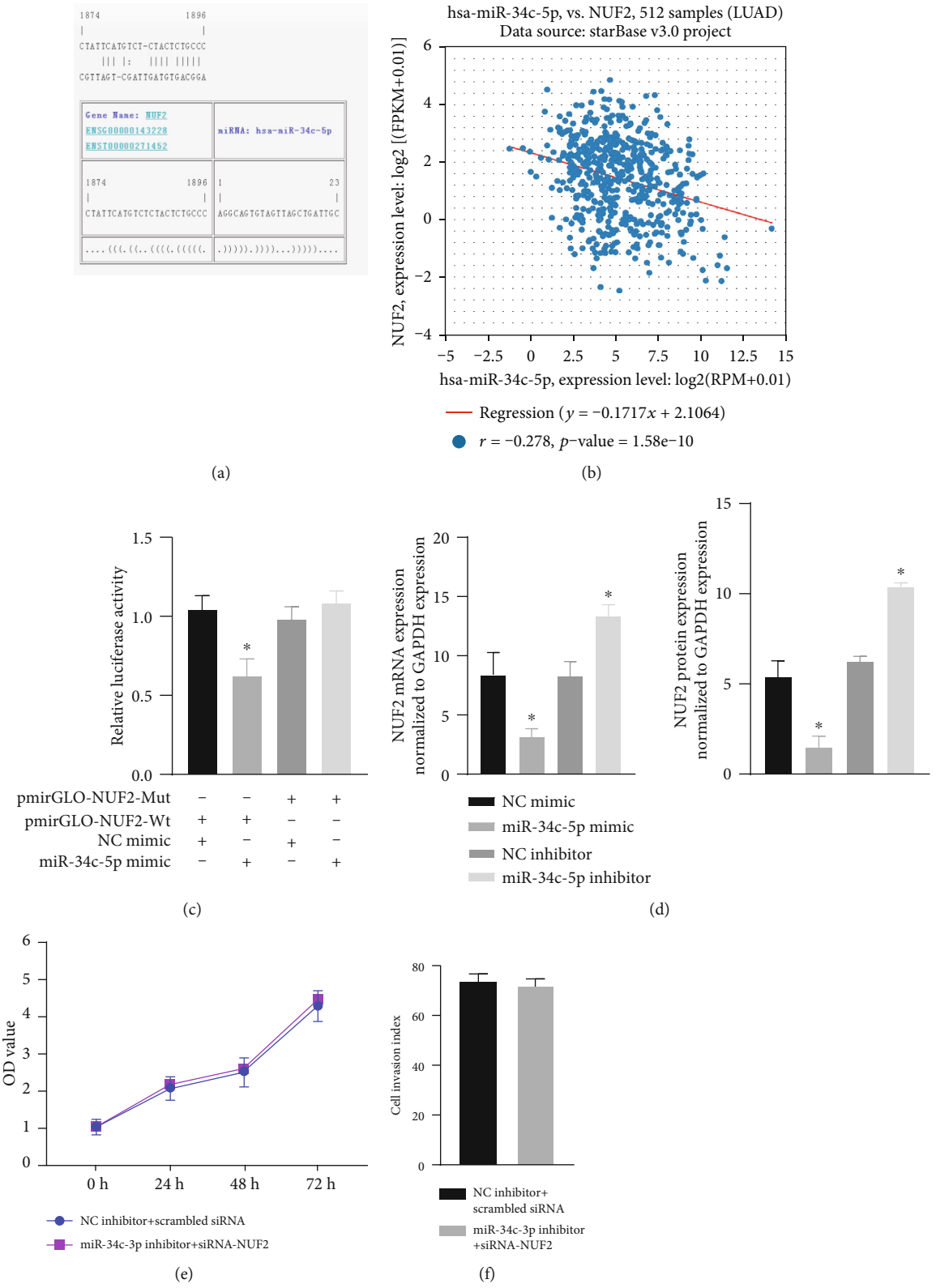

Figure 5: miR-34c-3p mediates A549 cells by binding to NUF2. (a) The binding sites of miR-34c-5p and NUF2 are predicted in the RNA22 database (https://cm.jefferson.edu/). (b) Coexpression of miR-34c-5p and NUF2 in lung adenocarcinoma in the starBase database (http://starbase.sysu.edu.cn/). (c) NUF2 as the target gene of miR-34c-3p was verified by luciferase activity assays (∗ stands for $p < 0.05$ when compared with pmirGLO-NUF2-MUT+miR-34c-5p mimic). (d) NUF2 mRNA and protein expressions in A549 cells were determined by qRT-PCR and Western blot analysis, normalized to GAPDH (∗ stands for $p < 0.05$ when compared with NC mimic or NC inhibitor). (e) Cell viability was examined by MTT assays. (f) Cell invasion was examined by Transwell assays.

potential of miR-34c-5p as a prognostic biomarker for lung adenocarcinoma. However, further investigations with regard to their functional roles *in vivo* are expected to make inroads into the implication of miRNA-mRNA in the treatment and prognosis of lung cancer. Besides, more in-depth researches as well as combined research efforts are needed to validate its applicable value in clinical practice.

Data Availability

The data used to support the findings of this study are included within the article.

Conflicts of Interest

The authors declare that they have no conflicts of interest.

Acknowledgments

The study was supported by the Finance Science and Technology Project of Hainan Province (ZDYF 2019200) and the National Natural Science Foundation (81760310).

References

[1] F. Bray, J. Ferlay, I. Soerjomataram, R. L. Siegel, L. A. Torre, and A. Jemal, "Global cancer statistics 2018: GLOBOCAN estimates of incidence and mortality worldwide for 36 cancers in 185 countries," *CA: a Cancer Journal for Clinicians*, vol. 68, no. 6, pp. 394–424, 2018.

[2] W. Chen, R. Zheng, H. Zeng, and S. Zhang, "Epidemiology of lung cancer in China," *Thoracic Cancer*, vol. 6, no. 2, pp. 209–215, 2015.

[3] P. C. Hoffman, A. M. Mauer, and E. E. Vokes, "Lung cancer," *Lancet*, vol. 355, no. 9202, pp. 479–485, 2000.

[4] S. Devarakonda, D. Morgensztern, and R. Govindan, "Genomic alterations in lung adenocarcinoma," *Lancet Oncologia*, vol. 16, no. 7, pp. e342–e351, 2015.

[5] Q. Y. Hong, G. M. Wu, G. S. Qian et al., "Prevention and management of lung cancer in China," *Cancer*, vol. 121, Suppl 17, pp. 3080–3088, 2015.

[6] M. T. Landi, Y. Zhao, M. Rotunno et al., "MicroRNA expression differentiates histology and predicts survival of lung cancer," *Clinical Cancer Research*, vol. 16, no. 2, pp. 430–441, 2010.

[7] J. S. Kim, E. J. Kim, S. Lee et al., "MiR-34a and miR-34b/c have distinct effects on the suppression of lung adenocarcinomas," *Experimental & Molecular Medicine*, vol. 51, no. 1, pp. 1–10, 2019.

[8] J. Gu, G. Wang, H. Liu, and C. Xiong, "SATB2 targeted by methylated miR-34c-5p suppresses proliferation and metastasis attenuating the epithelial-mesenchymal transition in colorectal cancer," *Cell Proliferation*, vol. 51, no. 4, article e12455, 2018.

[9] M. Re, A. Ceka, C. Rubini et al., "MicroRNA-34c-5p is related to recurrence in laryngeal squamous cell carcinoma," *Laryngoscope*, vol. 125, no. 9, pp. E306–E312, 2015.

[10] A. Nabetani, T. Koujin, C. Tsutsumi, T. Haraguchi, and Y. Hiraoka, "A conserved protein, Nuf2, is implicated in connecting the centromere to the spindle during chromosome segregation: a link between the kinetochore function and the spindle checkpoint," *Chromosoma*, vol. 110, no. 5, pp. 322–334, 2001.

[11] W. Obara, F. Sato, K. Takeda et al., "Phase I clinical trial of cell division associated 1 (CDCA1) peptide vaccination for castration resistant prostate cancer," *Cancer Science*, vol. 108, no. 7, pp. 1452–1457, 2017.

[12] P. Hu, X. Chen, J. Sun, P. Bie, and L. D. Zhang, "siRNA-mediated knockdown against NUF2 suppresses pancreatic cancer proliferation in vitro and in vivo," *Bioscience Reports*, vol. 35, no. 1, 2015.

[13] Y. Kobayashi, A. Takano, Y. Miyagi et al., "Cell division cycle-associated protein 1 overexpression is essential for the malignant potential of colorectal cancers," *International Journal of Oncology*, vol. 44, no. 1, pp. 69–77, 2014.

[14] A. Warth, T. Muley, M. Meister et al., "The novel histologic International Association for the Study of Lung Cancer/American Thoracic Society/European Respiratory Society classification system of lung adenocarcinoma is a stage-independent predictor of survival," *Journal of Clinical Oncology*, vol. 30, no. 13, pp. 1438–1446, 2012.

[15] K. Inamura, "Diagnostic and therapeutic potential of microRNAs in lung cancer," *Cancers*, vol. 9, no. 12, p. 49, 2017.

[16] H. X. Gao, Y. Su, A. L. Zhang, J. W. Xu, Q. Fu, and L. Yan, "miR-34c-5p plays a protective role in chronic obstructive pulmonary disease via targetingCCL22," *Experimental Lung Research*, vol. 45, no. 1-2, pp. 1–12, 2019.

[17] F. Akbas, E. Coskunpinar, E. Aynaci, Y. M. Oltulu, and P. Yildiz, "Analysis of serum micro-RNAs as potential biomarker in chronic obstructive pulmonary disease," *Experimental Lung Research*, vol. 38, no. 6, pp. 286–294, 2012.

[18] J. Gandla, S. K. Lomada, J. Lu, R. Kuner, and K. K. Bali, "miR-34c-5p functions as pronociceptive microRNA in cancer pain by targeting Cav2.3 containing calcium channels," *Pain*, vol. 158, no. 9, pp. 1765–1779, 2017.

[19] Y. Wang, T. Lu, Y. Wo et al., "Identification of a putative competitive endogenous RNA network for lung adenocarcinoma using TCGA datasets," *PeerJ*, vol. 7, article e6809, 2019.

[20] C. Achari, S. Winslow, Y. Ceder, and C. Larsson, "Expression of miR-34c induces G2/M cell cycle arrest in breast cancer cells," *BMC Cancer*, vol. 14, no. 1, p. 538, 2014.

[21] G. Di Leva, M. Garofalo, and C. M. Croce, "MicroRNAs in cancer," *Annual Review of Pathology*, vol. 9, no. 1, pp. 287–314, 2014.

[22] S. Catuogno, L. Cerchia, G. Romano, P. Pognonec, G. Condorelli, and V. de Franciscis, "miR-34c may protect lung cancer cells from paclitaxel-induced apoptosis," *Oncogene*, vol. 32, no. 3, pp. 341–351, 2013.

[23] Y. Wan, A. Shen, F. Qi et al., "Pien Tze Huang inhibits the proliferation of colorectal cancer cells by increasing the expression of miR-34c-5p," *Experimental and Therapeutic Medicine*, vol. 14, no. 4, pp. 3901–3907, 2017.

[24] S. Cordova-Rivas, I. Fraire-Soto, A. Mercado-Casas Torres et al., "5p and 3p strands of miR-34 family members have differential effects in cell proliferation, migration, and invasion in cervical cancer cells," *International Journal of Molecular Sciences*, vol. 20, no. 3, p. 545, 2019.

[25] L. Hu, J. Ai, H. Long et al., "Integrative microRNA and gene profiling data analysis reveals novel biomarkers and mechanisms for lung cancer," *Oncotarget*, vol. 7, no. 8, pp. 8441–8454, 2016.

[26] N. Li, D. Mao, Y. Cao, H. Li, F. Ren, and K. Li, "Downregulation of SIRT6 by miR-34c-5p is associated with poor prognosis and promotes colon cancer proliferation through inhibiting apoptosis via the JAK2/STAT3 signaling pathway," *International Journal of Oncology*, vol. 52, no. 5, pp. 1515–1527, 2018.

[27] T. Zhang, Y. Zhou, S. T. Qi et al., "Nuf2 is required for chromosome segregation during mouse oocyte meiotic maturation," *Cell Cycle*, vol. 14, no. 16, pp. 2701–2710, 2015.

[28] Y. Xing, J. Zhang, L. Lu et al., "Identification of hub genes of pneumocyte senescence induced by thoracic irradiation using weighted gene coexpression network analysis," *Molecular Medicine Reports*, vol. 13, no. 1, pp. 107–116, 2016.

[29] W. Xu, Y. Wang, Y. Wang, S. Lv, X. Xu, and X. Dong, "Screening of differentially expressed genes and identification of NUF2 as a prognostic marker in breast cancer," *International Journal of Molecular Medicine*, vol. 44, no. 2, pp. 390–404, 2019.

[30] Y. Wang, P. Y. Tan, Y. A. Handoko et al., "NUF2 is a valuable prognostic biomarker to predict early recurrence of hepatocellular carcinoma after surgical resection," *International Journal of Cancer*, vol. 145, no. 3, pp. 662–670, 2019.

[31] H. L. Fu and L. Shao, "Silencing of NUF2 inhibits proliferation of human osteosarcoma Saos-2 cells," *European Review for Medical and Pharmacological Sciences*, vol. 20, no. 6, pp. 1071–1079, 2016.

[32] W. Yuan, S. Xie, M. Wang et al., "Bioinformatic analysis of prognostic value of ZW10 interacting protein in lung cancer," *Oncotargets and Therapy*, vol. 11, pp. 1683–1695, 2018.

[33] D. Zhang, E. Liu, J. Kang, X. Yang, and H. Liu, "miR-3613-3p affects cell proliferation and cell cycle in hepatocellular carcinoma," *Oncotarget*, vol. 8, no. 54, pp. 93014–93028, 2017.

Hindawi
Journal of Nanomaterials
Volume 2021, Article ID 9977461, 7 pages
https://doi.org/10.1155/2021/9977461

Research Article

Ultrasound Parameters of Umbilical Artery Blood Flow Are Associated with Amniotic Fluid and Umbilical Artery Concentrations of Erythropoietin and Oxidative Stress Injury

Jiewen Tao, JingWang, Weiqi Jiang, Qi Meng, and Mingjuan Xu

Changhai Hospital, Second Military Medical University, China

Correspondence should be addressed to Mingjuan Xu; xumjuan1@163.com

Received 26 March 2021; Revised 29 May 2021; Accepted 1 June 2021; Published 17 June 2021

Academic Editor: Songwen Tan

Intrauterine hypoxia is the most frequent adverse intrauterine condition that occurs under a variety of circumstances including preeclampsia, placental insufficiency, high-altitude pregnancy, and any inflammatory condition during pregnancy resulting from gestational diabetes or even maternal obesity. However, early diagnosis of intrauterine hypoxia is still a challenge. In this study, we comparatively analyzed the systolic to diastolic ratio (S/D), resistant index (RI), and pulse index (PI) of the umbilical artery (UmA) and middle cerebral artery (MCA) blood flows obtained from 46 pregnant women with intrauterine hypoxia and 80 normal pregnant women at 28-31, 32-36, and 37-41 gestational weeks. Results found that the S/D, RI, and PI of UmA and MCA blood flows at 28-31, 32-36, and 37-41 gestational weeks were all increased in hypoxic fetuses than in normal fetuses ($P < 0.05$). The malondialdehyde (MDA) level was elevated but superoxide dismutase (SOD), glutathione peroxidase (GSH-Px), and catalase (CAT) activities were reduced in the UmA blood of pregnant women with intrauterine hypoxia compared with normal pregnant women ($P < 0.05$). It was found that the NADPH oxidase 2 (Nox2) and NADPH oxidase 4 (Nox4) activities were increased in the UmA blood of pregnant women with intrauterine hypoxia compared with normal pregnant women ($P < 0.05$). Results of ELISA methods showed that the expression level of survivin was lower but the expression levels of caspase-3, caspase-6, and caspase-9 were higher in the placental tissues of pregnant women with intrauterine hypoxia than those in normal pregnant women ($P < 0.05$). The concentrations of erythropoietin in the amniotic fluid and UmA blood were increased in pregnant women with intrauterine hypoxia compared with normal pregnant women ($P < 0.05$). The Spearman correlation analysis showed that the S/D, RI, and PI of UmA blood flow at 37-41 gestational weeks were positively correlated with the levels of Nox2, Nox4, and MAD and the UmA concentration of erythropoietin but negatively correlated with the activities of SOD, GSH-Px, and CAT ($P < 0.05$). In summary, the study indicates that ultrasound parameters of the UmA blood flow including S/D, RI, and PI could serve as predictors of intrauterine hypoxia.

1. Introduction

There has been an increasing death rate of children younger than 5 years occurring in the neonatal period (aged 0-28 days), which has resulted in much attention to neonatal mortality worldwide. The common causes of neonatal mortality refer to intrapartum-related factors such as hypoxic ischemic encephalopathy, preterm birth complications, infections including sepsis, meningitis, and neonatal tetanus, and other conditions including jaundice and congenital infections. Intrauterine hypoxia is the most frequent adverse intrauterine condition that occurs under a variety of circumstances including preeclampsia, placental insufficiency, high-altitude pregnancy, and any inflammatory condition during pregnancy resulting from gestational diabetes or even maternal obesity [1, 2] Accumulating evidence has showed that intrauterine hypoxia is associated with many fetal complications including low birth weight and developmental plasticity, resulting in indiscriminate damage to the developing fetus [3]. In several animal studies, intrauterine hypoxia could induce fetal growth restriction, cardiovascular dysfunction, and multiorgan morbidities of the fetus [4, 5]. Oxidative stress (OS) refers to excessive production of reactive oxygen species (ROS) and/or a decrease in antioxidant

defense, where ROS overwhelms the ability of endogenous antioxidant systems to scavenge ROS [6]. Oxidative stress has implicated in the pathogenesis of hypoxia-induced disorders during intrauterine development and postnatal life, such as coronary artery disease, heart failure, hypertension, and type II diabetes [7–9]. Understanding the impact of intrauterine hypoxia and its generation of ROS during gestation is important for understanding the consequences of both fetal and neonatal outcomes. From this point of view, the earlier the diagnosis, the higher the plasticity and the more beneficial the effects.

The umbilical cord is a nutrition exchange channel between the fetus and the mother. Evaluation of its blood flow can predict the state of fetal intrauterine hypoxia and the severity of the disease. At present, there is no gold standard for the diagnosis of fetal intrauterine hypoxia. In clinical practice, comprehensive judgment is usually made through a variety of methods, such as fetal heart rate monitoring and fetal movement count, but the accuracy is limited. Although the pathogenesis of intrauterine hypoxia remains unclear and thus management and treatment are limited, it has been reported that fetoplacental blood vessels are compromised upon intrauterine hypoxia. Doppler ultrasound can detect the hemodynamic changes of umbilical artery (UA) and middle cerebral artery (MCA) to judge the abnormal situation of fetal organs, which is the main examination method for clinical noninvasive, timely, and accurate diagnosis of fetal intrauterine hypoxia. The resistance index (RI) and pulsation index (PI) of the fetal arterial blood flow impedance were measured, the peak systolic velocity of the diastolic velocity ratio (S/D) can fully reflect the peripheral circulation impedance and blood perfusion of the supplied vessels. Severe reduction in UmA blood flow as reflected by the absent or reverse end diastolic velocity during pregnancy is related to fetal morbidity and mortality, and early delivery should be contemplated to prevent intrauterine hypoxia-induced disorders [10]. High flow resistance in the capillaries of the terminal villi contributes to a low end-diastolic velocity in the UmA and subsequent hypoxia [11]. Herein, the present study analyzed S/D, RI, and PI of UmA and MCA blood flows obtained from 46 pregnant women with intrauterine hypoxia and normal pregnant women at 28-31, 32-36, and 37-41 gestational weeks and further explored their correlations with oxidative stress.

2. Materials and Methods

2.1. Study Subjects and Baseline Demographic Variables. This retrospective study included 46 pregnant women with intrauterine hypoxia and 80 normal pregnant women who delivered their babies in our hospital from January 2019 to January 2020. The Apgar scores of newborns delivered by normal pregnant women were 8-10 one minute after birth, and those of newborns delivered by pregnant women with intrauterine hypoxia were 0-7. At the same time, the blood gas analysis of the cord blood was carried out immediately after delivery. Fetal intrauterine hypoxia was diagnosed according to the pH value of UmA blood < 7.2 and Apgar scores < 7 scores.

The pregnant women with intrauterine hypoxia had age ranging from 33 to 39 years, with an average age of 36.63 ± 5.24 years and gestational age at delivery ranging from 36 to 41 weeks, with an average gestational age of 37.90 ± 0.67 weeks. Their body mass index (BMI) was 23.40 ± 2.51 kg/m^2, gravidities were 2.30 ± 1.20 times, and abortions were 0.32 ± 0.09. The volumes of amniotic fluid, the Apgar scores of newborns one minute after birth, and the immediate pH value of UmA blood after delivery of pregnant women with intrauterine hypoxia were 28.22 ± 4.71 mm, 5.86 ± 1.18, and 7.08 ± 0.05, respectively.

The normal pregnant women had age ranging from 34 to 39 years, with an average age of 36.83 ± 4.92 years, and gestational age at delivery ranging from 37 to 40 weeks, with an average gestational age of 38.77 ± 0.74 weeks. Their BMI was $23.15 \pm 2.42\,kg/m^2$, gravidities were 2.22 ± 1.18 times, and abortions were 0.43 ± 0.20. The volumes of amniotic fluid, the Apgar scores of newborns one minute after birth, and the immediate pH value of UmA blood after delivery of the normal pregnant women were 45.93 ± 6.11 mm, 9.14 ± 0.69, and 7.30 ± 0.04, respectively.

Pregnant women complicated with malignant tumor, severe metabolic diseases, gestational diabetes mellitus and hypertension, fetal congenital malformations, and incomplete clinical data were excluded out of the study.

2.2. Ultrasound Evaluation of UmA and MCA Blood Flow. The pregnant women held their breath, and the fetus was in quiescent condition. Color Doppler Ultrasound (Voluson730, GE Company, USA) was employed to evaluate the systolic to diastolic ratio (S/D), resistant index (RI), and pulse index (PI) of UmA and MCA blood flows at 28-31, 32-36, and 37-41 gestational weeks, with the frequency set at 3.0-4.0 MHz. Each parameter was tested in triplicates to obtain the average. Ultrasound evaluation of UmA and MCA blood flows was evaluated by experienced doctors for many years.

2.3. Measurements. The UmA blood was collected immediately from after delivery and stored in 2-8°C. After centrifugation at 3500 r/min for 10 min, the upper serum was extracted. The malondialdehyde (MDA) level and superoxide dismutase (SOD), glutathione peroxidase (GSH-Px), and catalase (CAT) activities were measured in the serum by immunoradiometric assays using commercial available kits (Diagnostic Products Corp., Los Angeles, Calif., USA) according to the instructions provided by the manufacture. The activities of NADPH oxidase 2 (Nox2) and NADPH oxidase 4 (Nox4) were measured by enzyme-linked immunosorbent assay (ELISA) according to kit's instructions (R&D, Minneapolis, MN, USA). The fresh placental tissues were obtained within 30 min after delivery and then rinsed with normal saline followed by removal of calcified tissues and large vessels. The expression level of survivin protein was examined by ELISA according to kit's instructions (Abcam, Cambridge, UK) and caspase-3, caspase-6, and caspase-9 proteins according to kit's instructions (R&D, USA). The concentrations of erythropoietin in the UmA blood and amniotic fluid were measured by ELISA using a commercial available kit (R&D, USA).

Table 1: The S/D, RI, and PI of UmA and MCA blood flows in normal and hypoxic fetuses at 28-31 gestational weeks.

Group	N	UmA			MCA		
		S/D	RI	PI	S/D	RI	PI
Normal	80	2.79 ± 0.48	0.64 ± 0.07	1.01 ± 0.17	5.69 ± 1.26	0.78 ± 0.04	1.81 ± 0.19
Hypoxic	46	3.55 ± 0.44	0.71 ± 0.03	1.25 ± 0.12	3.31 ± 0.44	0.67 ± 0.04	1.28 ± 0.16
t		8.81	6.44	8.44	12.37	14.86	15.94
P		<0.001	<0.001	<0.001	<0.001	<0.001	<0.001

Note: UmA: umbilical artery; MCA: middle cerebral artery; S/D: systolic to diastolic ratio; RI: resistant index; PI: pulse index.

Table 2: The S/D, RI, and PI of UmA and MCA blood flows in normal and hypoxic fetuses at 32-36 gestational weeks.

Group	N	UmA			MCA		
		S/D	RI	PI	S/D	RI	PI
Normal	80	2.49 ± 0.38	0.61 ± 0.06	0.92 ± 0.15	5.71 ± 1.53	0.82 ± 0.05	1.77 ± 0.26
Hypoxic	46	3.71 ± 0.65	0.73 ± 0.05	1.32 ± 0.18	3.51 ± 1.25	0.70 ± 0.06	1.30 ± 0.22
t		13.31	11.46	13.38	8.29	12.04	10.32
P		<0.001	<0.001	<0.001	<0.001	<0.001	<0.001

Note: UmA: umbilical artery; MCA: middle cerebral artery; S/D: systolic to diastolic ratio; RI: resistant index; PI: pulse index.

Table 3: The S/D, RI, and PI of UmA and MCA blood flows in normal and hypoxic fetuses at 37-41 gestational weeks.

Group	N	UA			MCA		
		S/D	RI	PI	S/D	RI	PI
Normal	80	2.21 ± 0.34	0.52 ± 0.04	0.97 ± 0.17	5.17 ± 1.86	0.71 ± 0.04	1.37 ± 0.49
Hypoxic	46	3.34 ± 0.42	0.79 ± 0.06	1.31 ± 0.40	3.84 ± 1.38	0.60 ± 0.05	1.20 ± 0.25
t		16.46	30.26	6.64	4.22	13.54	2.192
P		<0.001	<0.001	<0.001	<0.001	<0.001	0.03

Note: UmA: umbilical artery; MCA: middle cerebral artery; S/D: systolic to diastolic ratio; RI: resistant index; PI: pulse index.

2.4. Statistical Analysis. SPSS 21.0 software (IBM, USA) was employed for data analysis. The measurement data were expressed as the mean ± standard deviation, and the comparison between two groups was performed by t-test. The correlation analysis was performed by Spearman's test. $P < 0.05$ was taken as statistically significant.

3. Results

3.1. Changes of Ultrasound Parameters of UmA and MCA Blood Flows in Hypoxic Fetuses. This retrospective study included 46 pregnant women with intrauterine hypoxia and 80 normal pregnant women. The two groups of pregnant women did not differ in terms of age, gestational age at delivery, BMI, gravidities, and abortion histories ($P > 0.05$); however, significant differences were found with regard to the volumes of amniotic fluid ($P = 0.010$), the Apgar scores of newborns one minute after birth ($P < 0.001$), and the immediate pH value of UmA blood after delivery ($P < 0.001$). It was observed that the S/D, RI, and PI of UmA blood flow at 28-31, 32-36, and 37-41 gestational weeks were all increased in hypoxic fetuses than in normal fetuses ($P < 0.05$). Furthermore, hypoxic fetuses exhibited higher S/D, RI, and PI of MCA blood flow than normal fetuses ($P < 0.05$). More detailed data are listed in Tables 1–3.

3.2. Serum Markers of Oxidative Stress in the UmA Blood of Pregnant Women with Intrauterine Hypoxia. Oxidative stress plays a crucial role in the pathogenesis of diseases related to hypoxia during intrauterine development and postnatal life, which is usually evaluated by expression levels of MDA, SOD, GSH-Px, and CAT. As shown in Figure 1, the MDA level was elevated but SOD, GSH-Px, and CAT activities were reduced in the UmA blood of pregnant women with intrauterine hypoxia compared with normal pregnant women ($P < 0.001$, Table 4). Furthermore, it was found that the Nox2 and Nox4 activities were increased in the UmA blood of pregnant women with intrauterine hypoxia compared with normal pregnant women ($P < 0.001$, Table 4).

3.3. Expressions of Survivin and Caspase Proteins in the Placental Tissues of Pregnant Women with Intrauterine Hypoxia. Survivin and caspase are two common apoptotic factors, both of which have been recently reported to be associated with oxidative stress. We collected placental tissues from pregnant women within 30 min after delivery. Results

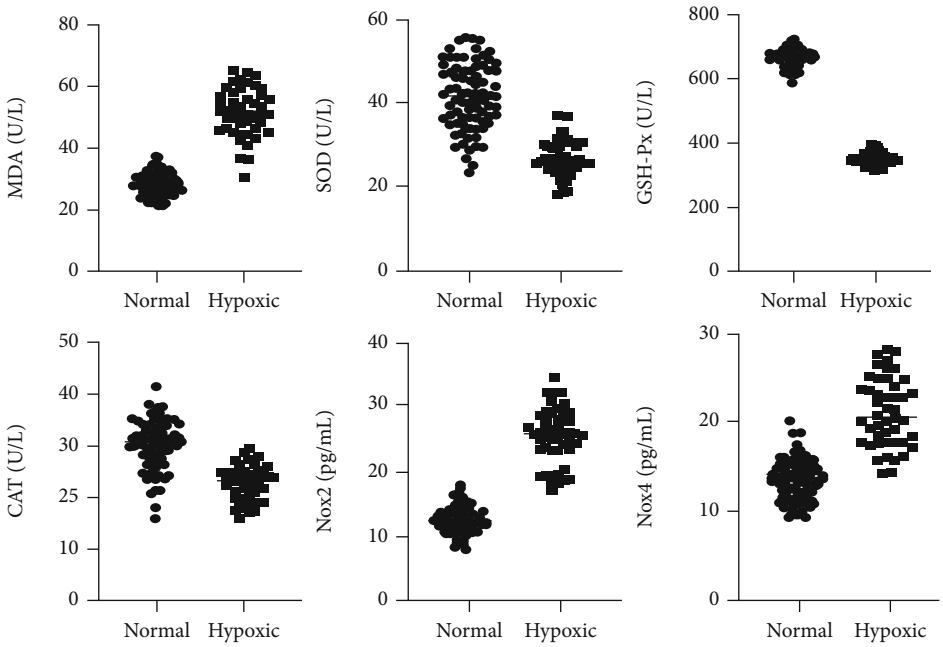

Figure 1: The levels of MDA, SOD, GSH-Px, CAT, Nox2, and Nox4 in the UmA blood between pregnant women with intrauterine hypoxia ($n = 46$) and normal pregnant women ($n = 80$).

Table 4: The levels of MDA, SOD, GSH-Px, CAT, Nox2, and Nox4 in the UmA blood between pregnant women with intrauterine hypoxia and normal pregnant women.

Marker	Normal ($n = 80$)	Hypoxic ($n = 46$)	t	P
MDA (U/L)	28.36 ± 3.58	51.49 ± 7.80	22.73	<0.001
SOD (U/L)	41.32 ± 7.84	26.70 ± 4.41	11.62	<0.001
GSH-Px (U/L)	664.76 ± 27.52	348.3 ± 20.23	68.08	<0.001
CAT (U/L)	30.24 ± 4.83	22.75 ± 3.29	9.338	<0.001
Nox2 (pg/mL)	12.51 ± 2.02	25.32 ± 4.17	23.19	<0.001
Nox4 (pg/mL)	13.61 ± 2.25	21.14 ± 3.84	13.90	<0.001

Note: MDA: malondialdehyde; SOD: superoxide dismutase; GSH-Px: glutathione peroxidase; CAT: catalase; Nox2: NADPH oxidase 2; Nox4: NADPH oxidase 4.

of ELISA methods showed that the expression level of survivin was lower but the expression levels of caspase-3, caspase-6, and caspase-9 were higher in the placental tissues of pregnant women with intrauterine hypoxia than those in normal pregnant women ($P < 0.001$, Figure 2).

3.4. Amniotic Fluid and UmA Concentrations of Erythropoietin in Intrauterine Hypoxia. In adults and fetuses, erythropoietin is a glycoprotein that regulates erythropoiesis. Its production is mainly stimulated and regulated by tissue hypoxia. Chronic intrauterine hypoxia caused by various stimuli can cause the increase of erythropoietin. It was found by ELISA methods that the concentrations of erythropoietin in the amniotic fluid and UmA blood were increased in pregnant women with intrauterine hypoxia compared with normal pregnant women ($P < 0.001$, Figure 3).

3.5. Spearman Correlation between Ultrasound Parameters of UmA Blood Flow and Oxidative Stress in Intrauterine Hypoxia. We studied the correlation between ultrasound parameters of UmA blood flow and oxidative stress in intrauterine hypoxia. It was found that the S/D, RI, and PI of UmA blood flow at 37-41 gestational weeks were positively correlated with the levels of Nox2, Nox4, and MAD and the UmA concentration of erythropoietin but negatively correlated with the activities of SOD, GSH-Px, and CAT ($P < 0.05$, Table 5).

4. Discussion

Intrauterine hypoxia can induce oxidative stress, which is not conducive to the growth and development of the fetus [12]. However, there is no effective way to prevent oxidative stress. Ultrasound parameters of UmA and MCA blood flows are important indicators for fetal physiological state and pathological injury. It was found that the S/D, RI, and PI of UmA and MCA blood flows at 28-31, 32-36, and 37-41 gestational weeks were all increased in hypoxic fetuses than in normal fetuses. The MDA, Nox2, and Nox4 levels were elevated but SOD, GSH-Px, and CAT activities were reduced in the

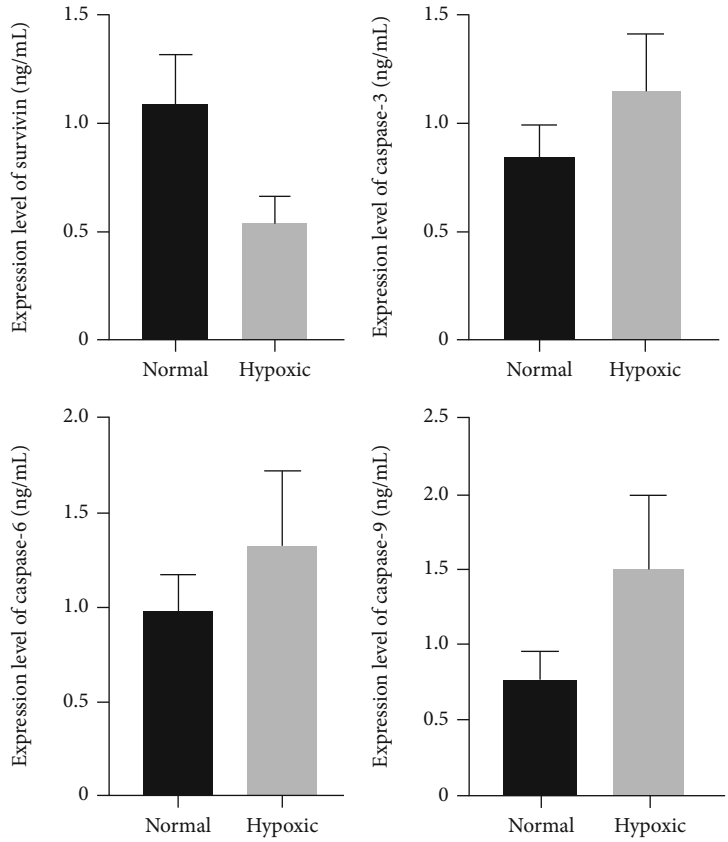

Figure 2: The expression levels of survivin, caspase-3, caspase-6, and caspase-9 in the placental tissues between pregnant women with intrauterine hypoxia ($n = 46$) and normal pregnant women ($n = 80$). Results were expressed as the mean ± standard deviation and analyzed by t-test.

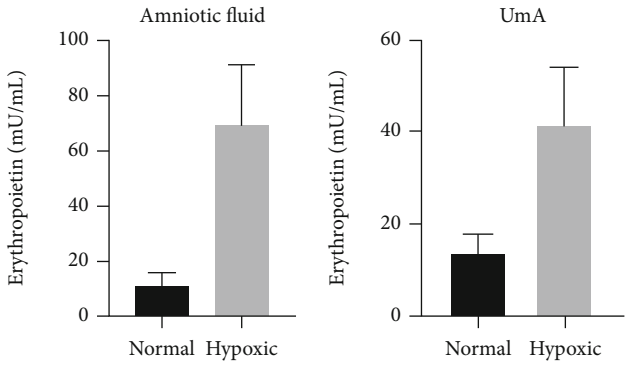

Figure 3: The concentrations of erythropoietin in the amniotic fluid and UmA blood between pregnant women with intrauterine hypoxia ($n = 46$) and normal pregnant women ($n = 80$). Results were expressed as the mean ± standard deviation and analyzed by t-test.

UmA blood of pregnant women with intrauterine hypoxia compared with normal pregnant women. The expression level of survivin was lower but the expression levels of caspase-3, caspase-6, and caspase-9 were higher in the placental tissues of pregnant women with intrauterine hypoxia than those in normal pregnant women. The concentrations of erythropoietin in the amniotic fluid and UmA blood were increased in pregnant women with intrauterine hypoxia compared with normal pregnant women. The Spearman correlation analysis showed that the S/D, RI, and PI of UmA blood flow at 37-41 gestational weeks were positively correlated with the levels of Nox2, Nox4, and MAD and the UmA concentration of erythropoietin but negatively correlated with the activities of SOD, GSH-Px, and CAT. All these findings indicate that the ultrasound parameters, S/D, RI, and PI, of UmA blood flow could reflect intrauterine hypoxia.

The UmA is the channel of material exchange between the fetus and the mother. The detection of UmA ultrasound parameters may have a reference value for prediction of fetal status [12]. Color Doppler ultrasound has the advantages of high safety, strong repeatability, and simple and convenient operation in the examination of the fetus, which can accurately predict the occurrence of fetal distress, and has high sensitivity and accuracy [13]. Gestational hypertension is a high-risk and frequently occurring disease in perinatal period. However, the pathogenesis of gestational hypertension is not completely clear at present. The main blood supply of the uterus is the uterine artery, which reflects the circulation of the uterus placenta. The monitoring of the fetal blood flow by color Doppler ultrasound in pregnant women with gestational hypertension can predict fetal oxidative stress to a certain extent [14]. Gestational diabetes mellitus can increase S/D value, which has adverse effects on fetal growth and development, suggesting that UmA blood flow parameters can be used as a reference index for fetal oxidative stress. Fetal hypoxia is the main cause of fetal distress that

Table 5: Spearman correlation between ultrasound parameters of UmA blood flow at 37-41 gestational weeks, serum markers of oxidative stress, and concentrations of UmA erythropoietin in intrauterine hypoxia.

Index	S/D		PI		RI	
	r	*P*	*r*	*P*	*r*	*P*
Nox2	0.512	<0.05	0.385	<0.05	0.441	<0.05
Nox4	0.667	<0.05	0.424	<0.05	0.475	<0.05
CAT	-0.395	<0.05	-0.411	<0.05	-0.482	<0.05
SOD	-0.221	<0.05	-0.377	<0.05	-0.398	<0.05
MDA	0.349	<0.05	0.386	<0.05	0.452	<0.05
GSH-Px	-0.429	<0.05	-0.399	<0.05	-0.469	<0.05
Erythropoietin	0.471	<0.05	0.714	<0.05	0.689	<0.05

S/D: systolic to diastolic ratio; RI: resistant index; PI: pulse index; MDA: malondialdehyde; SOD: superoxide dismutase; GSH-Px: glutathione peroxidase; CAT: catalase; Nox2: NADPH oxidase 2; Nox4: NADPH oxidase 4.

mostly occurs after labor or pregnancy [15]. If intervention measures are not taken in time, neonatal asphyxia, neonatal neurological sequela, and neonatal hypoxic encephalopathy will occur and even endanger the life and health of the fetus. UmA blood flow parameters are an important means to monitor fetal distress [16]. Fetal heart rate monitoring combined with the umbilical cord blood flow S/D ratio monitoring has high application value in clinical prediction of fetal distress, which can effectively improve the diagnostic accuracy, take effective treatment measures in time, and improve fetal prognosis [17]. Ultrasound monitoring UmA combined with fetal heart rate monitoring is helpful to diagnose fetal distress, and the uterine artery blood perfusion of hypertension pregnant women is significantly higher than that of healthy pregnant women, and the fetal UmA blood flow resistance is higher, which affects the growth and development of the fetus [18]. This study also found that the RI and pulsation index of the pregnant women with intrauterine hypoxia were significantly higher than those of the normal pregnant women, suggesting that the RI and pulsation index of fetal UmA blood flow ultrasound parameters of pregnant women are closely related to oxidative stress.

The Nox protein family, CAT, SOD, and MDA are the main members involved in oxidative stress [19]. However, the existing evidence shows that ultrasound parameters play crucial roles in the judgment of oxidative stress as reflected by weakened right ventricular systolic function of the fetus in preeclampsia. The ultrasonic characteristics of the umbilical cord blood in the context of intrauterine hypoxia are increased resistance and decreased flow [10], which is closely related to the degree of oxidative stress and apoptosis of placental cells. The ultrasonic characteristics of the umbilical cord blood flow in patients with intrauterine hypoxia during the perioperative period are significantly different from those in normal pregnancy, which can provide the basis for clinical diagnosis of fetal intrauterine hypoxia. This study also found that the levels of CAT, SOD, and GSH-Px in the UmA blood of the pregnant women with intrauterine hypoxia were significantly lower than those of the normal pregnant women, while the levels of Nox2, Nox4, and MDA were significantly higher than those of the normal pregnant women. The S/D, RI, and PI of the fetal UmA blood of pregnant women with intrauterine hypoxia were significantly positively correlated with Nox2, Nox4 and MDA levels and significantly negatively correlated with CAT, SOD, and GSH-Px activities, suggesting that ultrasound parameters of the UmA blood flow were positively correlated with oxidative stress.

Hypoxia is commonly assigned a role in the placental dysfunction characteristic of preeclampsia and intrauterine growth restriction. Preeclampsia and intrauterine growth restriction are associated with increased apoptosis of placental villous trophoblast [20]. Survivin is a member of the inhibitor of apoptosis gene family that plays a key role in apoptosis inhibition and regulation of mitosis. It was reported previously that reduced expression of survivin was related with severity of preeclampsia [21]. Survivin can bind with caspase proteins to play an antiapoptotic role. As shown in our study, the expression level of survivin was lower but the expression levels of caspase-3, caspase-6, and caspase-9 were higher in the placental tissues of pregnant women with intrauterine hypoxia than those in normal pregnant women.

Previous evidence showed that erythropoietin production is mainly stimulated and regulated by tissue hypoxia. Although the fetal kidneys are the main site of erythropoietin generation under basal conditions, recent experimental data indicate that the placenta is also an important site of erythropoietin generation in the circumstances of hypoxia [22]. Amniotic fluid erythropoietin levels have been shown to increase exponentially during fetal hypoxia in preeclamptic, diabetic, and Rh-immunized pregnancies, which are correlated inversely with cord blood pH, pO_2, and base excess, and could serve as a predictor of neonatal morbidities and neonatal intensive care unit admission [23]. In this study, it was found by ELISA methods that the concentrations of erythropoietin in the amniotic fluid and UmA blood were increased in pregnant women with intrauterine hypoxia compared with normal pregnant women. As an indicator of chronic intrauterine hypoxia, fetal erythropoietin measurements have increased our knowledge about the pathogenesis and importance of intrauterine growth restriction, abnormal fetal heart rate, and abnormal Doppler flow patterns. While the clinical application of fetal amniotic fluid erythropoietin and importance of intrauterine growth measurements in the management of high-risk pregnancies and their offspring is promising, adequately powered clinical trials are urgently warranted.

These findings obtained from the present study support the notion that ultrasound parameters of UmA blood flow including S/D, RI, and PI could serve as predictors of intrauterine hypoxia. In the future research, we will further work from the following aspects: increasing the sample size of the study and using multicenter comparative study and exploring the correlation between ultrasound parameters of UmA and MCA blood flows and blood gas.

Data Availability

The data used to support the findings of this study are included within the article.

Conflicts of Interest

All authors declare that they have no conflict of interest.

Authors' Contributions

Jiewen Tao and JingWang contributed to the work equally and should be regarded as co-first authors.

References

[1] P. Zhang, J. Ke, Y. Li et al., "Long-term exposure to high altitude hypoxia during pregnancy increases fetal heart susceptibility to ischemia/reperfusion injury and cardiac dysfunction," *International Journal of Cardiology*, vol. 274, pp. 7–15, 2019.

[2] K. L. Brain, B. J. Allison, Y. Niu et al., "Intervention against hypertension in the next generation programmed by developmental hypoxia," *Plos Biology*, vol. 17, no. 1, p. e2006552, 2019.

[3] P. J. Gonzalez-Rodriguez, F. Xiong, Y. Li, J. Zhou, and L. Zhang, "Fetal hypoxia increases vulnerability of hypoxic-ischemic brain injury in neonatal rats: role of glucocorticoid receptors," *Neurobiology of Disease*, vol. 65, pp. 172–179, 2014.

[4] C. F. Rueda-Clausen, V. W. Dolinsky, J. S. Morton, S. D. Proctor, J. R. Dyck, and S. T. Davidge, "Hypoxia-induced intrauterine growth restriction increases the susceptibility of rats to high-fat diet-induced metabolic syndrome," *Diabetes*, vol. 60, no. 2, pp. 507–516, 2011.

[5] M. Keenaghan, L. Sun, A. Wang, E. Hyodo, S. Homma, and V. S. Ten, "Intrauterine growth restriction impairs right ventricular response to hypoxia in adult male rats," *Pediatric Research*, vol. 80, no. 4, pp. 547–553, 2016.

[6] J. G. Farias, E. A. Herrera, C. Carrasco-Pozo et al., "Pharmacological models and approaches for pathophysiological conditions associated with hypoxia and oxidative stress," *Pharmacology & Therapeutics*, vol. 158, pp. 1–23, 2016.

[7] K. L. Thornburg, P. F. O'Tierney, and S. Louey, "Review: the placenta is a programming agent for cardiovascular disease," *Placenta*, vol. 31, pp. S54–S59, 2010.

[8] D. A. Giussani, E. J. Camm, Y. Niu et al., "Developmental programming of cardiovascular dysfunction by prenatal hypoxia and oxidative stress," *PLoS One*, vol. 7, no. 2, p. e31017, 2012.

[9] E. A. Herrera, B. Krause, G. Ebensperger et al., "The placental pursuit for an adequate oxidant balance between the mother and the fetus," *Frontiers in Pharmacology*, vol. 5, p. 149, 2014.

[10] A. Jurisic, Z. Jurisic, E. Lefkou, J. Pombo, and G. Girardi, "Pravastatin and-L-arginine combination improves umbilical artery blood flow and neonatal outcomes in dichorionic twin pregnancies through an nitric oxide- dependent vasorelaxant effect," *Vascular Pharmacology*, vol. 110, pp. 64–70, 2018.

[11] A. Ebrashy, O. Azmy, M. Ibrahim, M. Waly, and A. Edris, "Middle cerebral/umbilical artery resistance index ratio as sensitive parameter for fetal well-being and neonatal outcome in patients with preeclampsia: case-control study," *Croatian Medical Journal*, vol. 46, no. 5, pp. 821–825, 2005.

[12] C. F. Rueda-Clausen, J. S. Morton, G. Y. Oudit, Z. Kassiri, Y. Jiang, and S. T. Davidge, "Effects of hypoxia-induced intrauterine growth restriction on cardiac siderosis and oxidative stress," *Journal of Developmental Origins of Health and Disease*, vol. 3, no. 5, pp. 350–357, 2012.

[13] Z. Fardiazar, S. Atashkhouei, Y. Yosefzad, M. Goldust, and R. Torab, "Comparison of fetal middle cerebral arteries, umbilical and uterin artery color Doppler ultrasound with blood gas analysis in pregnancy complicated by IUGR," *Iranian journal of reproductive medicine*, vol. 11, no. 1, pp. 47–51, 2013.

[14] L. Sarno, G. M. Maruotti, G. Saccone, M. Morlando, A. Sirico, and P. Martinelli, "Maternal body mass index influences umbilical artery Doppler velocimetry in physiologic pregnancies," *Prenatal Diagnosis*, vol. 35, no. 2, pp. 125–128, 2015.

[15] S. Raicevic, D. Cubrilo, S. Arsenijevic et al., "Oxidative stress in fetal distress: potential prospects for diagnosis," *Oxidative Medicine and Cellular Longevity*, vol. 3, no. 3, p. 218, 2010.

[16] T. Avitan, A. Sanders, U. Brain, D. Rurak, T. F. Oberlander, and K. Lim, "Variations from morning to afternoon of middle cerebral and umbilical artery blood flow, and fetal heart rate variability, and fetal characteristics in the normally developing fetus," *Journal of Clinical Ultrasound*, vol. 46, no. 4, pp. 235–240, 2018.

[17] I. Aditya, V. Tat, A. Sawana, A. Mohamed, R. Tuffner, and T. Mondal, "Use of Doppler velocimetry in diagnosis and prognosis of intrauterine growth restriction (IUGR): a review," *Journal of Neonatal-Perinatal Medicine*, vol. 9, no. 2, pp. 117–126, 2016.

[18] M. Tchirikov, M. Strohner, D. Forster, and B. Huneke, "A combination of umbilical artery PI and normalized blood flow volume in the umbilical vein: venous-arterial index for the prediction of fetal outcome," *European Journal of Obstetrics, Gynecology, and Reproductive Biology*, vol. 142, no. 2, pp. 129–133, 2009.

[19] S. Perrone, E. Laschi, and G. Buonocore, "Biomarkers of oxidative stress in the fetus and in the newborn," *Free Radical Biology & Medicine*, vol. 142, pp. 23–31, 2019.

[20] C. F. Rueda-Clausen, J. L. Stanley, D. F. Thambiraj, R. Poudel, S. T. Davidge, and P. N. Baker, "Effect of prenatal hypoxia in transgenic mouse models of preeclampsia and fetal growth restriction," *Reproductive Sciences*, vol. 21, no. 4, pp. 492–502, 2014.

[21] C. F. Li, W. L. Gou, X. L. Li, S. L. Wang, T. Yang, and Q. Chen, "Reduced expression of survivin, the inhibitor of apoptosis protein correlates with severity of preeclampsia," *Placenta*, vol. 33, no. 1, pp. 47–51, 2012.

[22] K. A. Teramo and J. A. Widness, "Increased fetal plasma and amniotic fluid erythropoietin concentrations: markers of intrauterine hypoxia," *Neonatology*, vol. 95, no. 2, pp. 105–116, 2009.

[23] L. Seikku, L. Rahkonen, M. Tikkanen et al., "Amniotic fluid erythropoietin and neonatal outcome in pregnancies complicated by intrauterine growth restriction before 34 gestational weeks," *Acta Obstetricia et Gynecologica Scandinavica*, vol. 94, no. 3, pp. 288–294, 2015.

Hindawi
Journal of Nanomaterials
Volume 2021, Article ID 5452239, 13 pages
https://doi.org/10.1155/2021/5452239

Research Article

miRNA-146a and miRNA-202-3p Attenuate Inflammatory Response by Inhibiting TLR4, IRAK1, and TRAF6 Expressions in Rats following Spinal Cord Injury

Feng Sun,[1] Haiwei Zhang,[2] Jianhui Shi,[3] Tianwen Huang,[1] and Yansong Wang[4]

[1]*Department of Orthopaedic Surgery, General Hospital of General Administration of Agriculture and Reclamation, China*
[2]*Department of Imaging, General Hospital of General Administration of Agriculture and Reclamation, China*
[3]*Department of Orthopaedic Surgery, Heilongjiang Provincial Hospital, China*
[4]*Department of Spine Surgery, The First Affiliated Hospital of Harbin Medical University, China*

Correspondence should be addressed to Yansong Wang; wangyansong_2011@163.com

Received 6 April 2021; Revised 12 April 2021; Accepted 16 April 2021; Published 10 June 2021

Academic Editor: Songwen Tan

Spinal cord injury (SCI) is a catastrophic disease that induces a complex cascade of cellular reactions at the local lesion area, including secondary cell death and inflammatory reactions. Accumulating evidence has showed pro- and anti-inflammatory roles of microRNAs (miRNAs), a class of small RNAs, in SCI. The present study is aimed at investigating the effects of two miRNAs, miRNA-146a and miRNA-202-3p, on inflammatory response after SCI. Initially, we found that the expression levels of miRNA-146a and miRNA-202-3p were increased in the plasma samples of 32 SCI patients at days 3 and 7 after admission and the rat spinal cord at days 3 and 7 after SCI modeling compared with healthy controls and sham-operated rats, respectively. The expression levels of TLR4, IRAK1, and TRAF6 were declined in the rat spinal cord at days 1, 3, and 7 after SCI modeling compared with sham-operated rats. Injection of miRNA-146a mimic or miRNA-202-3p mimic decreased TLR4, IRAK1, and TRAF6 expressions in the rat spinal cord at days 1, 3, and 7 after SCI modeling, while injection of miRNA-146a antagomir or miRNA-202-3p antagomir produced opposed results. Subsequent results showed that the expression levels of tumor necrosis factor-α (TNF-α), IL-1β, IL-6, and IL-8 were upregulated in the rat serum at days 1, 3, and 7 after SCI modeling compared with sham-operated rats. Injection of miRNA-146a mimic or miRNA-202-3p mimic decreased TNF-α, IL-1β, IL-6, and IL-8 expression levels in the rat serum at days 1, 3, and 7 after SCI modeling, while injection of miRNA-146a antagomir or miRNA-202-3p antagomir yielded opposed results. The expression levels of TNF-α, IL-1β, IL-6, and IL-8 were higher in the supernatants of PC12 cells transfected with anti-miRNA-146a or anti-miRNA-202-3p than in those transfected with si-TLR4, si-IRAK1, or si-TRAF6. These findings support the notion that miRNA-146a/miRNA-202-3p exerts anti-inflammatory functions after SCI.

1. Introduction

Spinal cord injury (SCI) is a common neurodegenerative condition that remains a significant source of morbidity and cost to society [1]. Each year, more than 250,000 individuals suffer from SCI around the world, and it is estimated to be 2 to 3 million people worldwide living with functional deficits [2]. SCI may arise from traumatic causes such as high-energy mechanisms of injury and nontraumatic causes such as myelitis and spinal cord tumor [3]. Historically, clinical outcomes of patients after SCI have been frustrating. SCI typically leads to long-term or even lifelong disability, largely owing to primary and secondary white matter damage at the site of injury [4]. Therapeutic strategies for SCI involve surgical and no-surgical treatments, including early surgical decompression and fixation, utilization of vasopressor medications for mean arterial blood pressure augmentation to improve spinal cord perfusion, stem cell transplantation,

and corticosteroids [5]. However, the efficacy and timing of these adjuvant treatments remain controversial, and neuroprotective and regenerative approaches for treating SCI are still a challenge for clinical physicians.

SCI comprises a two-step process involving an initial mechanical injury followed by an inflammatory process and apoptosis [6]. Local inflammatory response in the spinal cord lesion by mechanical injury is one of the important contributors to secondary insult to neurons, glia, axons, and myelin, which is mediated by cells normally found in the central nervous system (CNS), infiltrating neutrophil and leukocytes [7]. Nevertheless, inflammatory response is required for clearance of tissue debris and promotes wound healing and tissue repair [8]. Imbalance of inflammatory response may indirectly or directly affect the prognosis of SCI.

MicroRNAs (miRNAs), a group of small RNA with length ranging from 18 to 24 nucleotides, have been underlined as gene governors by binding to their target messenger RNAs and thus mediate the process of physiology and pathology [8]. Accumulating evidence shows that numerous miRNAs are expressed in the CNS, and some of them have been confirmed to be involved in traumatic CNS injury and neurodegenerative diseases [9]. The underlying mechanisms of miRNA in CNS injuries are reviewed including inflammation, apoptosis, oxidative stress, blood-brain barrier protection, neurogenesis, and angiogenesis [10]. miRNA-146a has been reported to modulate innate immune response *via* the toll-like receptor (TLR) and inflammatory pathways in neurodegenerative diseases [11, 12]. miRNA-202-3p is located in a chromosomal fragile site in 10q26.3 and recently has been investigated in several human diseases including colorectal cancer [13], gastric cancers [14], scleroderma fibrosis [15], and lymphomagenesis [16]. However, there is currently limited information with regard to the roles of miRNA-146a/miRNA-202-3p and its mechanism of action in the context of SCI. To fill this gap, the present study determined the expressions of miRNA-146a and miRNA-202-3p in blood samples collected from patients at an indicated day of admission post-SCI and rat spinal cord lesion following weight-drop injury and the effects of two of them on inflammatory response in SCI.

2. Methods and Materials

2.1. Clinical Sample Collection. A total of 32 patients who were diagnosed with SCI by neurological examination and magnetic resonance imaging at the First Affiliated Hospital of Harbin Medical University between January 2018 and December 2019 were recruited into the study. These patients, aged from 18 to 70 years, had a hospitalization of less than 7 days, and among them, none had autoimmune diseases, neurodegenerative diseases, infectious symptoms, severe cardiovascular diseases, or malignant tumors. Additionally, 32 age-matched healthy controls (18 to 70 years) who received physical examinations at the same period were recruited as controls, and none had neurodegenerative diseases, autoimmune diseases, neurodegenerative diseases, infectious symptoms, severe cardiovascular diseases, or malignant tumors. The study was approved by the Ethics Committee of the First Affiliated Hospital of Harbin Medical University. Informed consent was obtained from each participant. Fasting peripheral venous blood (5 mL) was collected from SCI patients at their initial diagnosis and healthy controls and placed into EDTA-containing test tubes for supernatant collection after centrifugation (3000 r/min, 10 min, 4°C). The supernatants were frozen at -80°C.

2.2. Animals. A total of 54 clean Sprague-Dawley male rats, aged 6-8 weeks and weighing 240 ± 10 g, were purchased from Beijing Huafukang Bioscience Co., Inc. (license no., SCXK [Jing] 2009-0004) and housed in a humidity-controlled clean environment (40-60%) under a 12 h light/12 h dark cycle at a controlled temperature of 20-25°C in the laboratory of the First Affiliated Hospital of Harbin Medical University. These rats had free access to both food (sterilized pelleted feeds) and water. The animal experiments were approved by the Ethics Committee of the First Affiliated Hospital of Harbin Medical University and performed following the National Institutes of Health's Guidelines for Laboratory Animal Care and Use.

2.3. Establishment of the SCI Rat Model. Rats were anesthetized with 2% sodium pentobarbital (i.p. 0.25 mL/100 g). After dissection of the paraspinal muscles, a laminectomy from the lower thoracic spinal cord (T10) was performed. SCI at the T10 was induced in rats using a 10 g weight drop from a height of 50 mm [17]. Briefly, the rats were anesthetized with pentobarbital (40 mg/kg, i.p.), and then, the spine was exposed, followed by laminectomy at the T10 level. The appliance (# WH160162, Convergence Technology Co., Ltd., Shenzhen, China) (10 g) was dropped from a height of 50 mm on the exposed spinal cord. After standing for 20 seconds, the corrector was then withdrawn to produce a moderate contusion. Finally, the incision was closed in layers. The rats' hind legs began to twitch unconsciously and tails started to twist, which means the successful establishment of the SCI models. Rats in the sham group were only given a T10 laminectomy in the absence of the weight-drop injury. After surgery, all rats received erythromycin ointment for 3 consecutive days to avoid infection, and the bladders were manually voided three times daily.

2.4. Alternation of miRNA-146a and miRNA-202-3p In Vivo. SCI rats ($n = 45$) were assigned into five groups at a random manner and given tail vain injections of normal saline, miRNA-146a mimics, miRNA-146a antagomir, miRNA-202-3p mimics, and miRNA-202-3p antagomir, respectively. These plasmids were purchased from RiboBio Inc. (Guangzhou, China).

2.5. Behavioral Tests. The Basso, Beattie, and Bresnahan (BBB) locomotion rating scale [18] was employed 6^{th}, 24^{th}, and 48^{th} hours after weight-drop injury or sham operation. The BBB score evaluated hindlimb locomotor function on a scale from 0 to 21, with 0 indicating no observable movement and 21 indicating normal movement.

2.6. Histological Examination. SCI rats and sham-operated rats were sacrificed using 2% sodium pentobarbital (i.p.

0.25 mL/100 g), with 3 cm spinal cord segments containing the spinal cord lesion excised. Rat spinal cord tissues were fixed with 4% paraformaldehyde at 4°C and paraffin-embedded for hematoxylin-eosin (HE) staining. In brief, paraffin-embedded tissues were longitudinally sectioned (4 μm thick) and mounted on slides. After deparaffinization, the slides were immersed in xylene I and xylene II (each for 15 min), in 100% twice, 95%, 80%, and 70% ethanol (each for 5 min) and water (1 min) in order. Subsequently, the slides were stained with hematoxylin for 1-5 min and eosin 20 s-5 min and finally observed under the optical microscope.

2.7. RNA Extraction and Quantitative Real-Time Polymerase Chain Reaction (qRT-PCR). In order to determine plasma miRNA-146a and miRNA-202-3p expression, total RNA was extracted from human plasma samples using the kit (Life Technologies, USA) following the manuals provided by the manufacturers. The complementary DNA (cDNA) was generated using EzOmics™ One-Step qPCR Kit (BK2100, Biomics Biotechnologies Co., Ltd.) according to the manufacturer's instructions. To determine miRNA-146a and miRNA-202-3p expression in rat spinal cord tissues, total RNA was extracted from tissues using TRIzol reagents (Invitrogen, Carlsbad, CA, USA) following the manuals provided by the manufacturers. Synthesis of cDNA was performed using GoScript™ Reverse Transcriptase System (Promega, Madison, WI, USA) according to the manufacturer's instructions. The qPCR was performed using GoTaq® qPCR Master Mix (Promega) with SYBR Green (Promega) on the Applied Biosystems 7500 Real-Time PCR System (Applied Biosystems, Foster City, CA, USA). The primer information is listed in Table 1. The miR-144 level was standardized as U6 and the target mRNA level as GAPDH. Results were calculated by using the $2^{-\Delta\Delta CT}$ method.

2.8. Enzyme-Linked Immunosorbent Assay (ELISA). The expression levels of inflammatory cytokines, TNF-α, IL-1β, IL-6, and IL-8, in serum collected from SCI rats and sham-operated rats were determined using commercial ELISA kits following the manufacturer's instructions (R&D Systems, Minneapolis, MN, USA).

2.9. Cell Harvest and Transfection. The rat pheochromocytoma cell line PC12 (ATCC, USA) was maintained in DMEM (Gibco, Grand Island, NY, USA) with 10% fetal bovine serum (FBS) in a 5% CO_2 incubator with saturated humidity (95%) at 37°C. PC12 cells were seeded in 6-well plates (5×10^4 cells per mL) and then transfected with anti-miRNA-146a, anti-miRNA-202-3p, si-TLR4 (5′-GGGCUUAGAACAACUA GAATT-3′), si-IRAK1 (5′-AGCTGTCCAGGTTTCGTCA CCCAAA-3′), si-TRAF6 (5′-GCCUAAUCAUUAUGAU CUATT-3′), and si-NC (5′-UUCUCCGAACGUGUCA CGUTT-3′) (Thermo Fisher Scientific, Waltham, MA, USA) using Lipofectamine 2000 reagents (Invitrogen) following the manuals provided by the manufacturers. After 48 h transfection, lipopolysaccharide (LPS) stimulation (100 ng/mL) was performed for 4 h.

Table 1: Primer sequences used for qRT-PCR.

Target	Sequence (5′-3′)
TLR4	F: 5′-GGCAGCAGGTCGAATTGTAT-3′
	R: 5′-GCTTGTTGTTCTTCCTCTGATGT-3′
TRAF6	F: 5′-CTCAGCGCTGTGCAAACTAC-3′
	R: 5′-GATCAAGGATCGTGAGGCGT-3′
IRAK1	F: 5′-TACCTGCCCGAGGAGTACATCAA-3′
	R: 5′-TCCTCTTCCACCAGGTCTTTCAGA-3′
NF-κB	F: 5′-GATCGCCACCGGATTGAAGA-3′
	R: 5′-CTCGGGAAGGCACAGCAATA-3′
miRNA-146a	F: 5′-TGCAGGGAACCATCCACTTCG-3′
	R: 5′-CCCATGCTGGCCTTCAGTTA-3′
miRNA-202-3p	F: 5′-ATACGCGAGAGGAAGCGCA-3′
	R: 5′-AGTGCAGGGTCCGAGGTATT-3′
GAPDH	F: 5′-TGTTCCTACCCCCAATGTG-3′
	R: 5′-GTGTAGCCCAAGATGCCCT-3′
U6	F: 5′-GCTTCGGCAGCACATATACTAA-3′
	R: 5′-CGAATTTGCGTGTCATCCTT-3′

F: forward; R: reverse.

2.10. Immunoblotting Analysis. Total protein was extracted from rat spinal cord tissues and PC12 cells using RIPA lysis buffer (Solarbio, Beijing, China). The protein sample was separated using freshly prepared SDS-PAGE (Beyotime Biotechnology, Jiangsu, China), electrotransferred onto PVDF membranes (IPVH0001, Millipore, MA, USA), and probed with primary antibodies to TLR4 (ab13556), IRAK1 (ab180747), TRAF6 (ab33915), or GAPDH (ab9485, Abcam, Cambridge, UK). Immunoreactive bands were visualized with goat anti-rabbit IgG (1 : 10000, ab205718) and enhanced chemiluminescence detection reagents (Billerica, MA, USA). The blots were developed, followed by quantitative analysis using ImageJ software (National Institutes of Health, USA). The quantitative level of the protein was determined based on the gray ratio of each protein to the gray ratio of GAPDH.

2.11. Statistical Analysis. All data (mean ± standard deviation) were representative of three independent experiments (each in triplicate), and the statistical analysis was performed with SPSS 21.0 software (IBM, Armonk, NY, USA), with two-tailed $P < 0.05$ as a level of statistical significance. For statistical comparisons, unpaired Student's t-test and a one-way analysis of variance (ANOVA) with Tukey's test were performed as appropriate.

3. Results

3.1. miRNA-146a and miRNA-202-3p Were Upregulated in Patients with SCI. To study the clinical significance of miRNA-146a and miRNA-202-3p in SCI, we collected blood samples from healthy controls and SCI patients at days 1, 3, and 7 after admission to examine the plasma expression

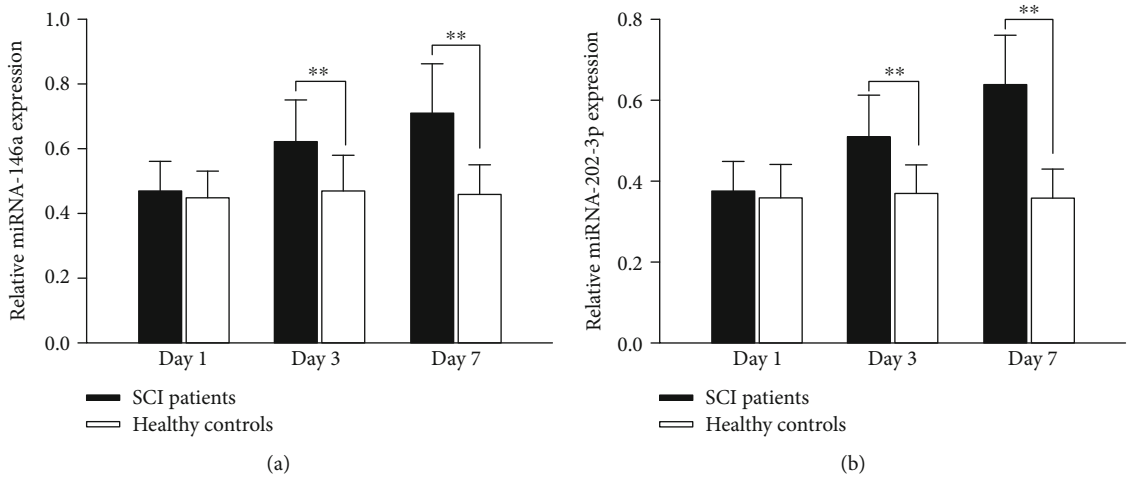

Figure 1: Relative expression levels of miRNA-146a (a) and miRNA-202-3p (b) in the plasma of SCI patients and healthy controls were determined by qRT-PCR. $^{**}P < 0.01$ by Student's t-test.

levels of miRNA-146a and miRNA-202-3p. Results of qRT-PCR showed that miRNA-146a and miRNA-202-3p expression levels did not differ between healthy controls and SCI patients at day 1 after admission ($P > 0.05$). At days 3 and 7 after admission, miRNA-146a and miRNA-202-3p were upregulated in the plasma of SCI patients, which were remarkably higher than those in the plasma of healthy controls ($P < 0.05$, Figures 1(a) and 1(b)).

3.2. Behavioral and Histological Characterization of Rats following SCI. As shown in Figure 2(a), the BBB scores of the rats at the 6^{th}, 24^{th}, and 48^{th} hours after weight-drop injury were lower than those of sham-operated rats ($P < 0.05$). Next, SCI rats and sham-operated rats were sacrificed, and spinal cord segments containing the spinal cord lesion were excised for histological examination. After fixation with paraformaldehyde, evident weight-drop injury was observed in the spinal cord segments of SCI rats (Figure 2(b)). Results of HE staining (Figure 2(c)) showed accumulation of erythrocytes, inflammatory infiltration, and hemorrhage; however, no evident inflammatory infiltration and hemorrhage were found in the spinal cord segments of sham-operated rats.

3.3. Expression of miRNA-146a and miRNA-202-3p in Rats following SCI. In order to ascertain the effects of miRNA-146a and miRNA-202-3p on SCI, SCI rats were injected with normal saline, miRNA-146a mimics, miRNA-146a antagomir, miRNA-202-3p mimics, and miRNA-202-3p antagomir, respectively. It revealed that the expression levels of miRNA-146a did not significantly differ in the spinal cord tissues among sham, SCI, miRNA-146a mimic, and miRNA-146a antagomir groups at day 1 after weight-drop injury ($P > 0.05$). The expression level of miRNA-146a was increased in rats at days 3 and 7 after weight-drop injury compared with sham-operated rats. At day 3 after weight-drop injury, injection of miRNA-146a mimics significantly increased the signal of miRNA-146a expression in SCI rats ($P < 0.05$), and injection of miRNA-146a antagomir significantly decreased miRNA-146a expression in SCI rats ($P < 0.05$, Figure 3(a)). No significant difference was found in the expression levels of miRNA-202-3p among sham, SCI, miRNA-202-3p mimic, and miRNA-202-3p antagomir groups at day 1 after weight-drop injury ($P > 0.05$). The expression level of miRNA-202-3p was increased in rats at days 3 and 7 after weight-drop injury compared with sham-operated rats. At days 3 and 7 after weight-drop injury, injection of miRNA-202-3p mimics significantly increased the signal of miRNA-202-3p in SCI rats ($P < 0.05$), and injection of miRNA-202-3p antagomir significantly decreased miRNA-202-3p expression in SCI rats ($P < 0.05$, Figure 3(b)).

3.4. The mRNA and Protein Expressions of TLR4, IRAK1, and TRAF6 in Rats following SCI. Results of qRT-PCR showed that the mRNA expressions of TLR4, IRAK1, and TRAF6 were declined in SCI rats compared with sham-operated rats at days 1, 3, and 7 after surgery ($P < 0.05$, Figure 4(a)). At days 1, 3, and 7 after weight-drop injury, injection of miRNA-146a antagomir remarkably elevated TLR4, IRAK1, and TRAF6 mRNA expressions in SCI rats ($P < 0.05$), and injection of miRNA-146a mimics yielded opposed results ($P < 0.05$, Figure 4(b)). As shown in Figure 4(c), injection of miRNA-202-3p antagomir also remarkably increased TLR4, IRAK1, and TRAF6 mRNA expressions in SCI rats ($P < 0.05$), and injection of miRNA-202-3p mimics produced opposed results ($P < 0.05$). Next, we performed immunoblotting analysis to determine protein expressions of TLR4, IRAK1, and TRAF6 in different rat groups. It was revealed that the protein expressions of TLR4, IRAK1, and TRAF6 were downregulated in SCI rats compared with sham-operated rats at day 7 after surgery ($P < 0.05$, Figure 4(d)). Injection of miRNA-146a antagomir remarkably elevated TLR4, IRAK1, and TRAF6 protein expressions in SCI rats ($P < 0.05$), and injection of miRNA-146a mimics yielded opposed results ($P < 0.05$, Figure 4(e)). Injection of miRNA-202-3p antagomir also remarkably increased TLR4, IRAK1, and TRAF6 protein expressions in SCI rats

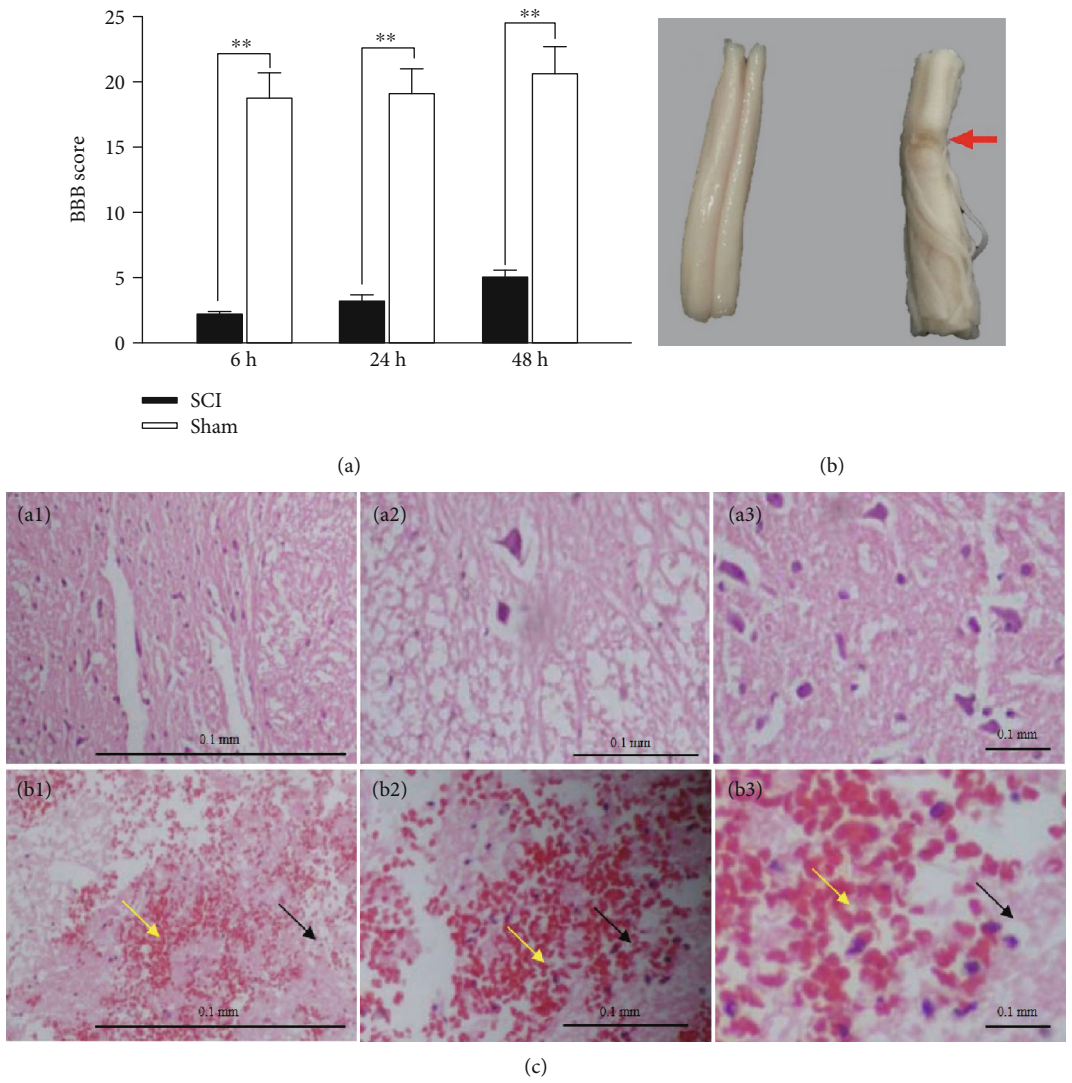

Figure 2: Behavioral and histological characterization of rats following SCI. (a) BBB scores of the rats at the 6th, 24th, and 48th hours after weight-drop injury or sham operation. $^{**}P < 0.01$ by Student's t-test. (b) Representative spinal cord segments of rats after weight-drop injury or sham operation after paraformaldehyde fixation: left, sham-operated rat; right, weight-drop-injured rats; red arrow indicates the spinal cord lesion. (c) Histological characterization of spinal cord tissues of rats after weight-drop injury or sham operation by HE staining; a1–a3 indicate sham-operated rats, and b1–b3 indicate weight-drop-injured rats; yellow arrows indicate erythrocytes, and black arrows indicate inflammatory infiltration.

($P < 0.05$), and injection of miRNA-202-3p mimics produced opposed results ($P < 0.05$, Figure 4(f)).

3.5. The Levels of Inflammatory Cytokines in Rats following SCI. Subsequently, ELISA was performed to detect the levels of inflammatory cytokines, TNF-α, IL-1β, IL-6, and IL-8, in rats after weight-drop injury or sham operation. As depicted in Figure 5(a), the levels of TNF-α, IL-1β, IL-6, and IL-8 were elevated in SCI rats compared with sham-operated rats at days 1, 3, and 7 after surgery ($P < 0.05$). Injection of miRNA-146a mimic or miRNA-202-3p mimic remarkably reduced the release of inflammatory cytokines in SCI rats at days 1, 3, and 7 after surgery ($P < 0.05$), and injection of miRNA-146a antagomir or miRNA-202-3p antagomir yielded opposed results ($P < 0.05$, Figures 5(b) and 5(c)).

3.6. miRNA-146a and miRNA-202-3p Inhibited the Release of Inflammatory Cytokines in LPS-Stimulated PC12 Cells by Regulating TLR4, IRAK1, and TRAF6. In order to confirm whether the anti-inflammatory roles of miRNA-146a and miRNA-202-3p in SCI is achieved by affecting TLR4, IRAK1, and TRAF6 expressions, PC12 cells were transfected with anti-miRNA-146a, anti-miRNA-202-3p, si-TLR4, si-IRAK1, si-TRAF6, and si-NC. As shown in Figure 6(a), the protein expressions of TLR4, IRAK1, and TRAF6 were declined in PC12 cells transfected with si-TLR4 compared with PC12 cells transfected with si-NC ($P < 0.05$). PC12 cells transfected with anti-miRNA-146a or anti-miRNA-202-3p presented higher protein expressions of TLR4, IRAK1, and TRAF6 than PC12 cells transfected with si-TLR4 ($P < 0.05$). The levels of TNF-α, IL-1β, IL-6, and IL-8 were declined in PC12 cells

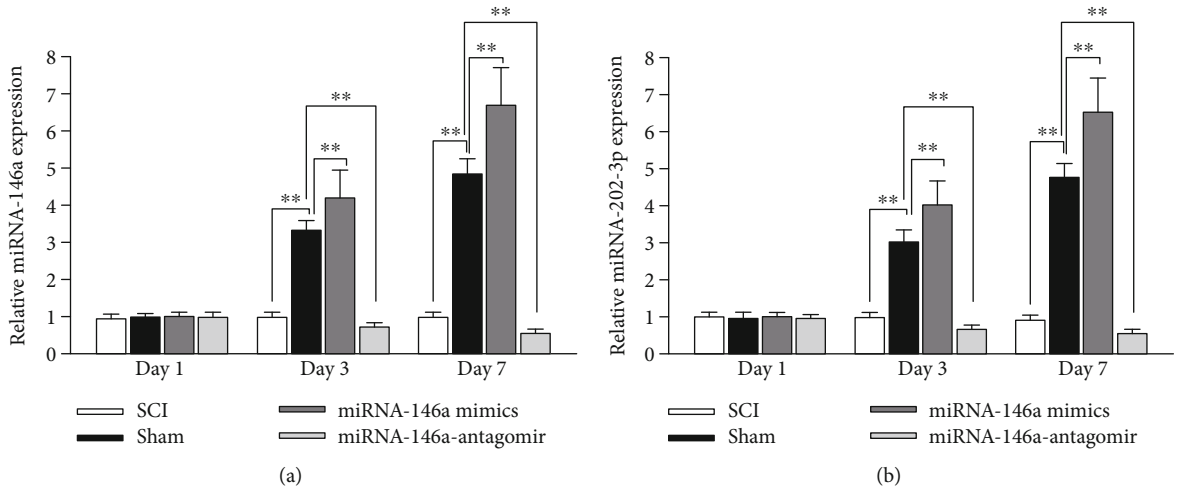

Figure 3: Expression of miRNA-146a and miRNA-202-3p in rats following SCI. (a) Expression levels of miRNA-146a in rat spinal cord tissues from sham, SCI, miRNA-146a mimic, and miRNA-146a antagomir groups at day 1 after weight-drop injury or sham operation were determined by qRT-PCR. (b) Expression levels of miRNA-202-3p in rat spinal cord tissues from sham, SCI, miRNA-202-3p mimic, and miRNA-202-3p antagomir groups at day 1 after weight-drop injury or sham operation were determined by qRT-PCR. $^{**}P < 0.01$ by Student's t-test.

transfected with si-TLR4 compared with PC12 cells transfected with si-NC ($P < 0.05$). PC12 cells transfected with anti-miRNA-146a or anti-miRNA-202-3p exhibited higher levels of inflammatory cytokines than PC12 cells transfected with si-TLR4 ($P < 0.05$, Figure 6(b)). As shown in Figure 6(c), the protein expressions of IRAK1 and TRAF6 were declined in PC12 cells transfected with si-IRAK1 compared with PC12 cells transfected with si-NC ($P < 0.05$). PC12 cells transfected with anti-miRNA-146a or anti-miRNA-202-3p presented higher protein expressions of IRAK1 and TRAF6 than PC12 cells transfected with si-IRAK1 ($P < 0.05$). The levels of TNF-α, IL-1β, IL-6, and IL-8 were declined in PC12 cells transfected with si-IRAK1 compared with PC12 cells transfected with si-NC ($P < 0.05$). PC12 cells transfected with anti-miRNA-146a or anti-miRNA-202-3p exhibited higher levels of inflammatory cytokines than PC12 cells transfected with si-IRAK1 ($P < 0.05$, Figure 6(d)). Finally, it was found that PC12 cells transfected with si-TRAF6 showed declined protein expression of TRAF6 compared with PC12 cells transfected with si-NC ($P < 0.05$). PC12 cells transfected with anti-miRNA-146a or anti-miRNA-202-3p presented higher protein expression of TRAF6 than PC12 cells transfected with si-TRAF6 ($P < 0.05$, Figure 6(e)). The levels of TNF-α, IL-1β, IL-6, and IL-8 were declined in PC12 cells transfected with si-TRAF6 compared with PC12 cells transfected with si-NC ($P < 0.05$). PC12 cells transfected with anti-miRNA-146a or anti-miRNA-202-3p exhibited higher levels of inflammatory cytokines than PC12 cells transfected with si-TRAF6 ($P < 0.05$, Figure 6(f)).

4. Discussion

Inflammatory response begins within minutes to hours following SCI and peaks approximately 1 day later, which was characterized by very early production of cytokines, chemokines, and the infiltration of neutrophils into the site of injury [19]. The resolution of inflammation is a highly controlled and coordinated process that involves the suppression of proinflammatory gene expression and inhibition of leukocyte migration and activation, followed by clearance of inflammatory cells by apoptosis and phagocytosis [20]. miRNAs have been well studied in the SCI model. For example, miR-9, miR-219, and miR-384-5p increased in the serum of mice 12 h following SCI-like surgery [21]. miR-10b, miR-100, miR-130a, miR-133a-5p, miR-133b, miR-208b, miR-365-3p, miR-378, miR-378b-3p, and miR-885-5p were changed in serum at 1 and 3 days in pig models of SCI, and these miRNAs were related to outcome measures at 12 weeks following SCI [22]. In this work, we demonstrated anti-inflammatory action of miRNA-146a and miRNA-202-3p in SCI and their mechanism of action involving three target genes, TLR4, IRAK1, and TRAF6.

Initially, we collected blood samples from healthy controls and SCI patients at days 1, 3, and 7 after admission to examine the plasma expression levels of miRNA-146a and miRNA-202-3p. It revealed that miRNA-146a and miRNA-202-3p were upregulated in the plasma of SCI patients at days 3 and 7 after admission, which was further confirmed by results from an animal SCI model after weight-drop injury. The inflammatory response post-SCI consists of two phases, early and late. The early inflammatory response may be neurotoxic in nature by releasing proinflammatory cytokines including TNF-α, IL-1β, IL-6, and IL-8 [23], which is detrimental to functional recovery. The late inflammatory response may be essential for wound repair and recovery of function [8]. miRNA-146a and miRNA-202-3p are released to regulate inflammatory response after SCI through a feedback mechanism and prevent further damage to the body, thus promoting the recovery. In a previous study reported by Tan et al. [24], they showed that miR-146a expression was declined in the SCI rat model, which is different from our results. However, their final conclusion was that miR-146a reduces inflammation in an SCI model. Similar to our results, Wei et al. determined an upregulation of

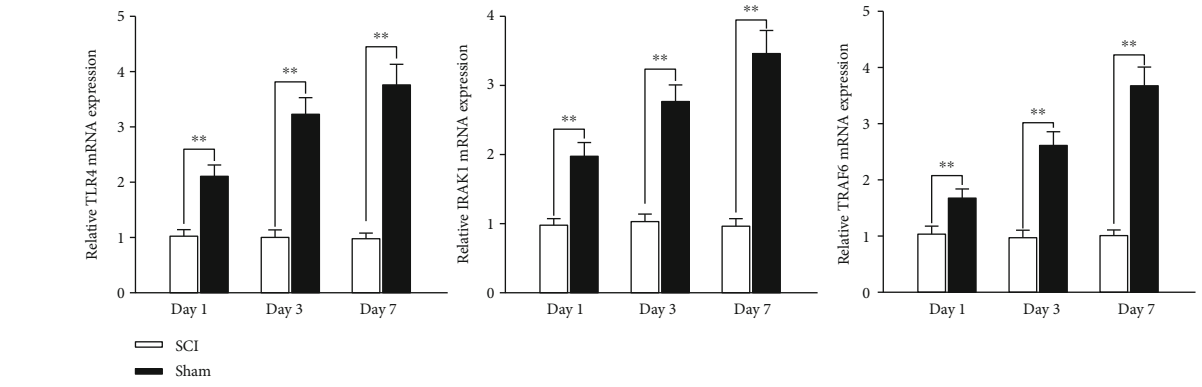

(a)

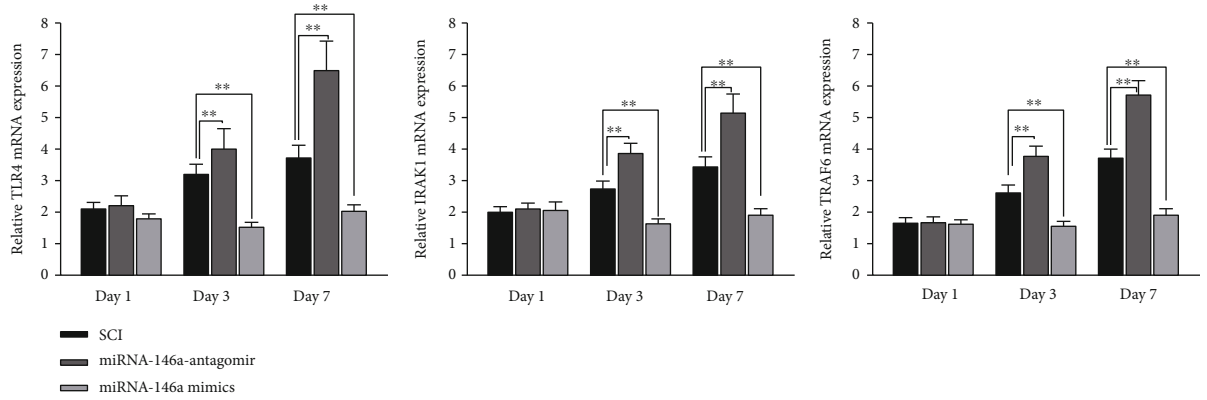

(b)

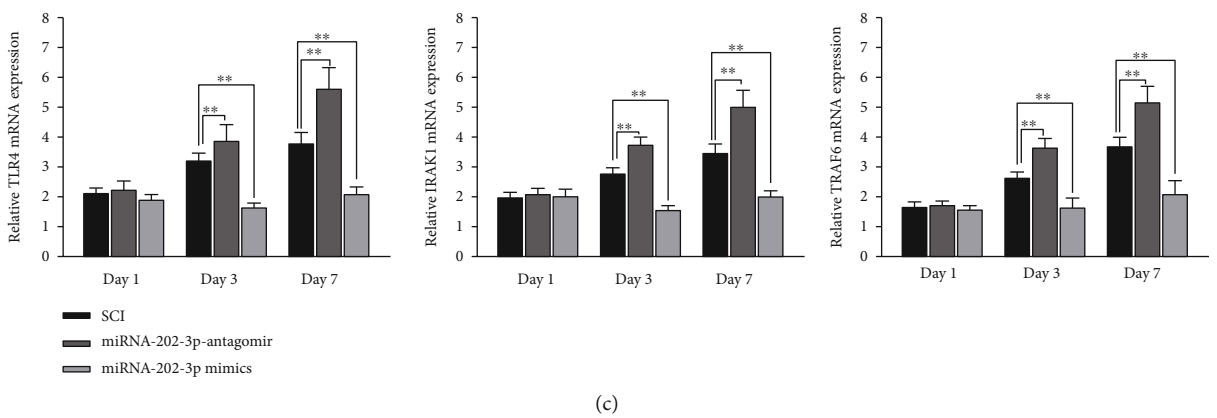

(c)

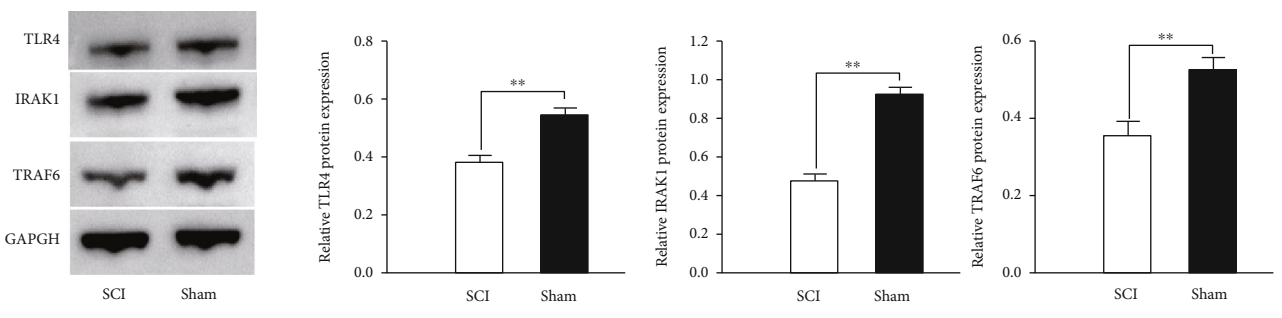

(d)

Figure 4: Continued.

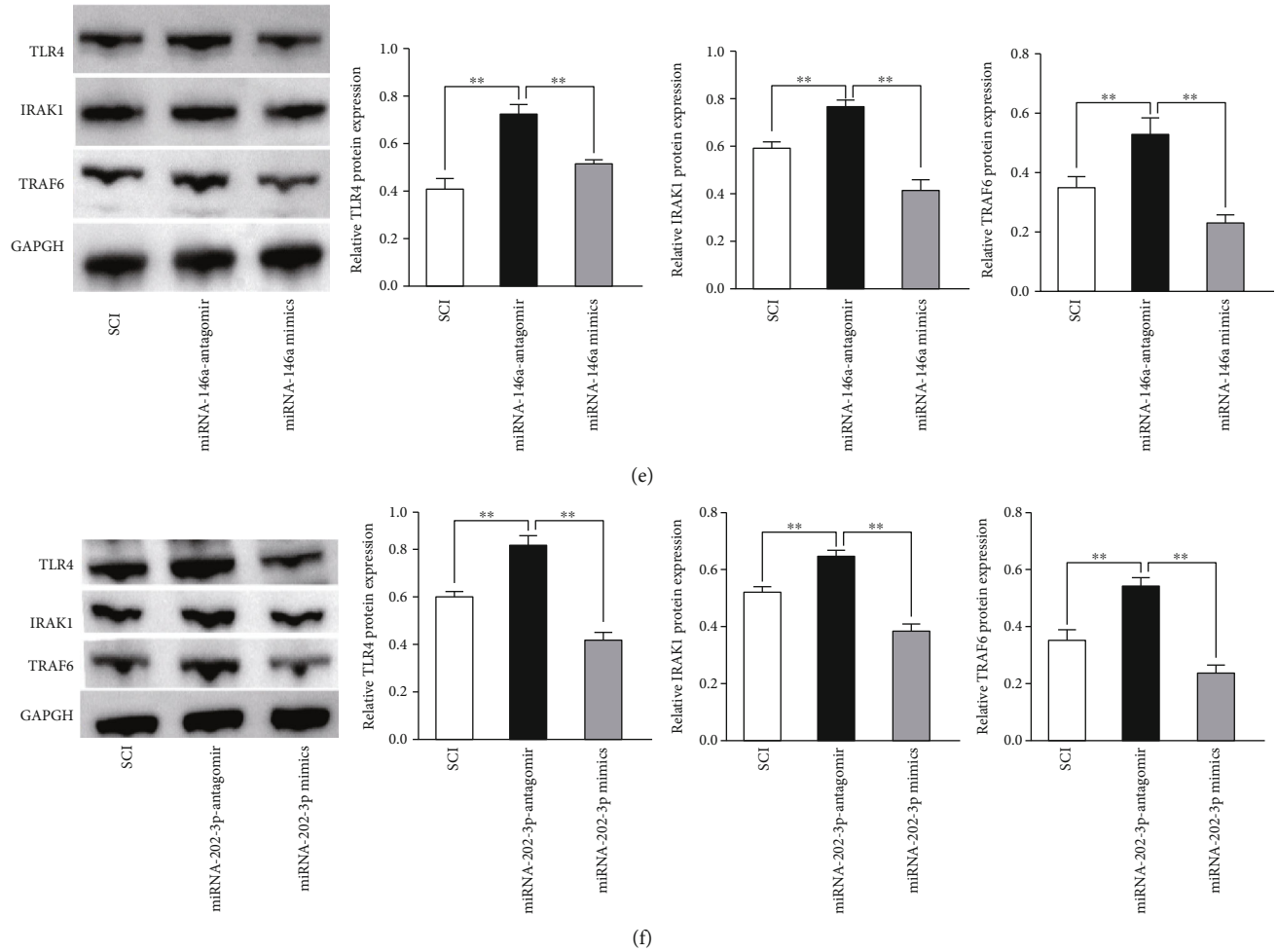

Figure 4: The mRNA and protein expressions of TLR4, IRAK1, and TRAF6 in rats following SCI. (a) qRT-PCR analysis of TLR4, IRAK1, and TRAF6 mRNA expressions in sham-operated and SCI rats at days 1, 3, and 7 after surgery. (b) qRT-PCR analysis of TLR4, IRAK1, and TRAF6 mRNA expressions among SCI, miRNA-146a mimic, and miRNA-146a antagomir groups at days 1, 3, and 7 after surgery. (c) qRT-PCR analysis of TLR4, IRAK1, and TRAF6 mRNA expressions among SCI, miRNA-202-3p mimic, and miRNA-202-3p antagomir groups at days 1, 3, and 7 after surgery. (d) Immunoblotting analysis of TLR4, IRAK1, and TRAF6 protein expressions in sham-operated and SCI rats at day 7 after surgery. (e) Immunoblotting analysis of TLR4, IRAK1, and TRAF6 protein expressions among SCI, miRNA-146a mimic, and miRNA-146a antagomir groups at day 7 after surgery. (f) Immunoblotting analysis of TLR4, IRAK1, and TRAF6 protein expressions among SCI, miRNA-202-3p mimic, and miRNA-202-3p antagomir groups at day 7 after surgery. $^{**}P < 0.01$ by Student's t-test in (a) and (d); $^{**}P < 0.01$ by one-way ANOVA with Tukey's test in other panels.

miR-146a in the animal model of SCI except on the first day after surgery [25]. No experiment based on a human sample was performed in these two previous studies. Fortunately, our study collected blood samples from healthy controls and SCI patients at days 1, 3, and 7 after admission and demonstrated upregulated miR-146a following SCI. Few previous data reported an anti-inflammatory role of miR-202-3p. Most of the studies focus on its function as a tumor suppressor in human cancer. Since inflammation plays an important role in cancerogenesis, coupled with our results, there is possibility that miR-202-3p inhibits cancer progression potentially by exerting anti-inflammatory effects.

Subsequent experiments were performed to confirm whether TLR4, IRAK1, and TRAF6 were involved in the anti-inflammatory action of miRNA-146a and miRNA-202-3p in SCI. Toll-like receptors (TLRs) provide critical signals to induce innate immune responses, and TLR4 is the receptor for lipopolysaccharide. TLR4 stimulation activates proinflammatory pathways and induces secretion of cytokines in various cell types [26]. IRAK1 and TRAF6 are known to be part of the common signaling pathway of the toll-like receptor/interleukin 1 receptor (TIR) superfamily. Several studies have reported that TLR4, IRAK1, and TRAF6 expressions were inhibited following miRNA-146a overexpression [27–29]. In our study, we found that upregulation of miRNA-146a could inhibit expressions of TLR4, IRAK1, and TRAF6 at mRNA and protein levels. Consistent with our results, Liu et al. demonstrated that miR-146 could attenuate microglial inflammatory response through TLR4/IRAK1/TRAF6-related pathways [30]. Additionally, the TLR4/IRAK1/TRAF6 axis was revealed in our work, as

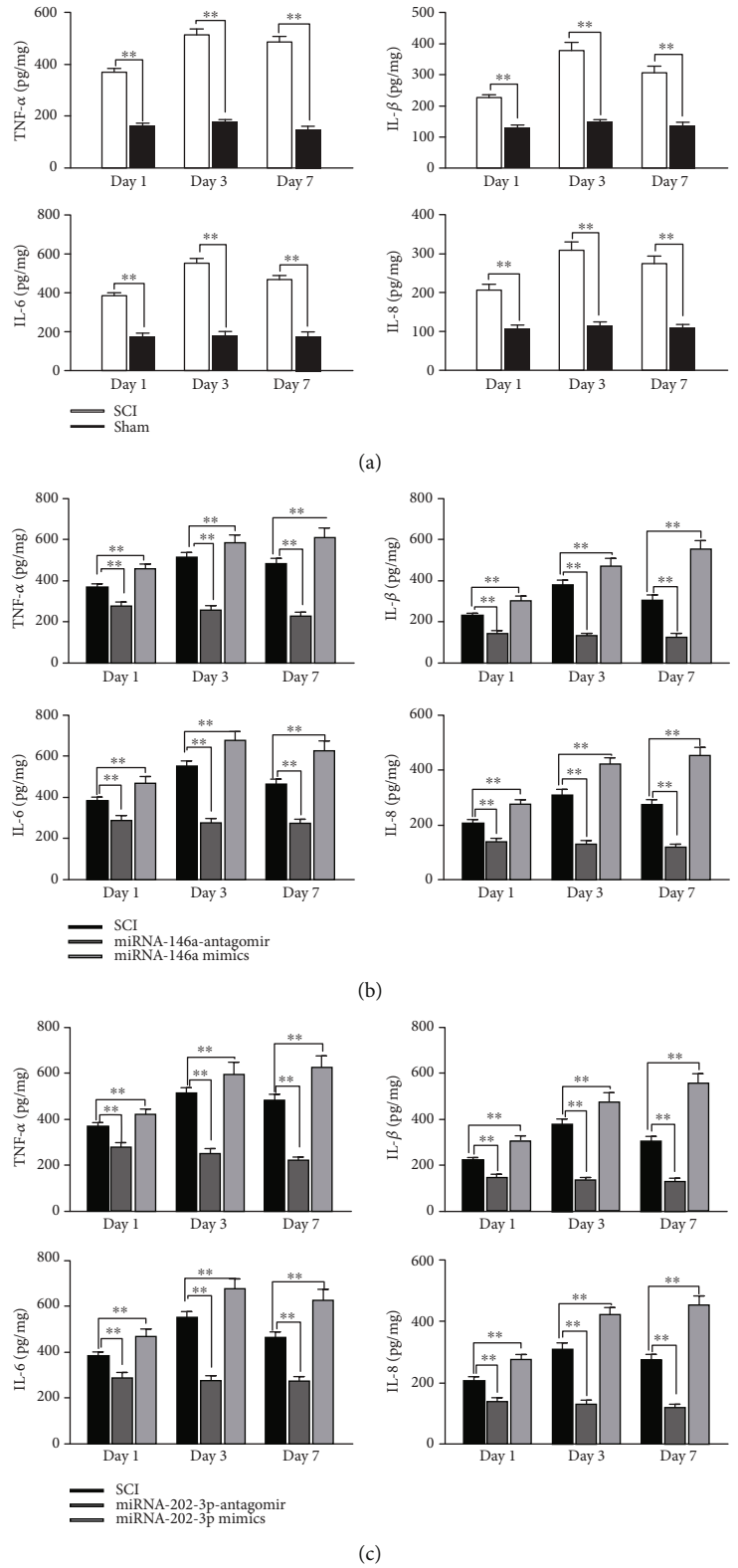

Figure 5: The levels of inflammatory cytokines in rats following SCI. (a) ELISA detection of TNF-α, IL-1β, IL-6, and IL-8 in the serum of sham-operated and SCI rats at days 1, 3, and 7 after surgery. (b) ELISA detection of TNF-α, IL-1β, IL-6, and IL-8 in rat serum among SCI, miRNA-146a mimic, and miRNA-146a antagomir groups at days 1, 3, and 7 after surgery. (c) ELISA detection of TNF-α, IL-1β, IL-6, and IL-8 in rat serum among SCI, miRNA-202-3p mimic, and miRNA-202-3p antagomir groups at days 1, 3, and 7 after surgery. $^{**}P < 0.01$ by Student's t-test in (a); $^{**}P < 0.01$ by one-way ANOVA with Tukey's test in (b) and (c).

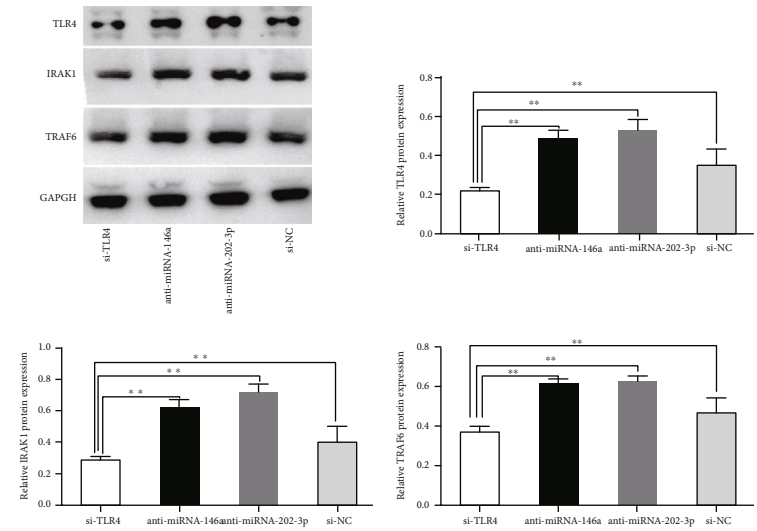

(a)

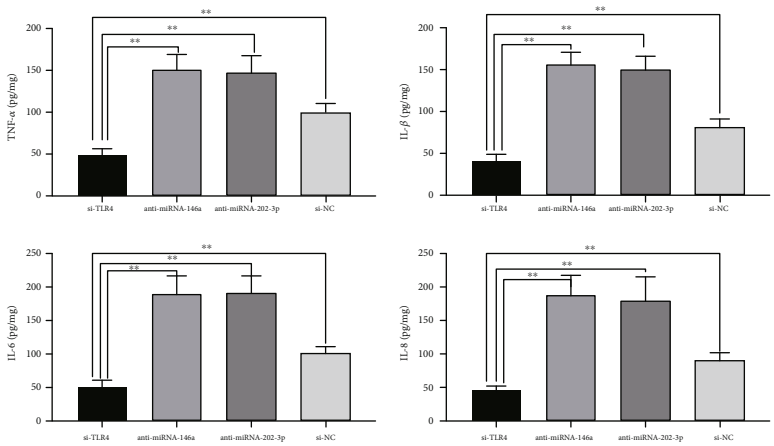

(b)

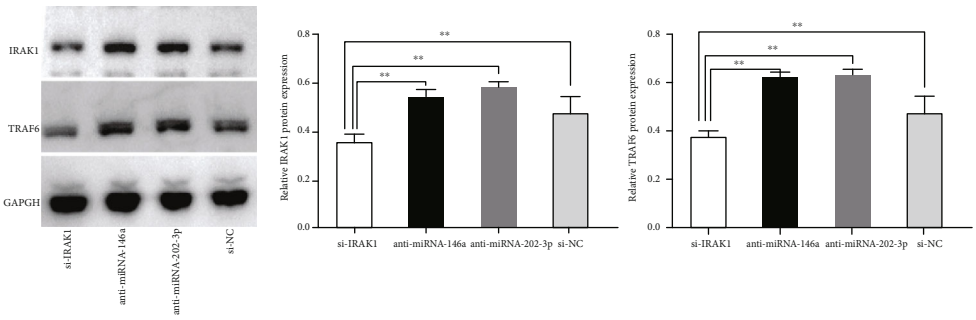

(c)

Figure 6: Continued.

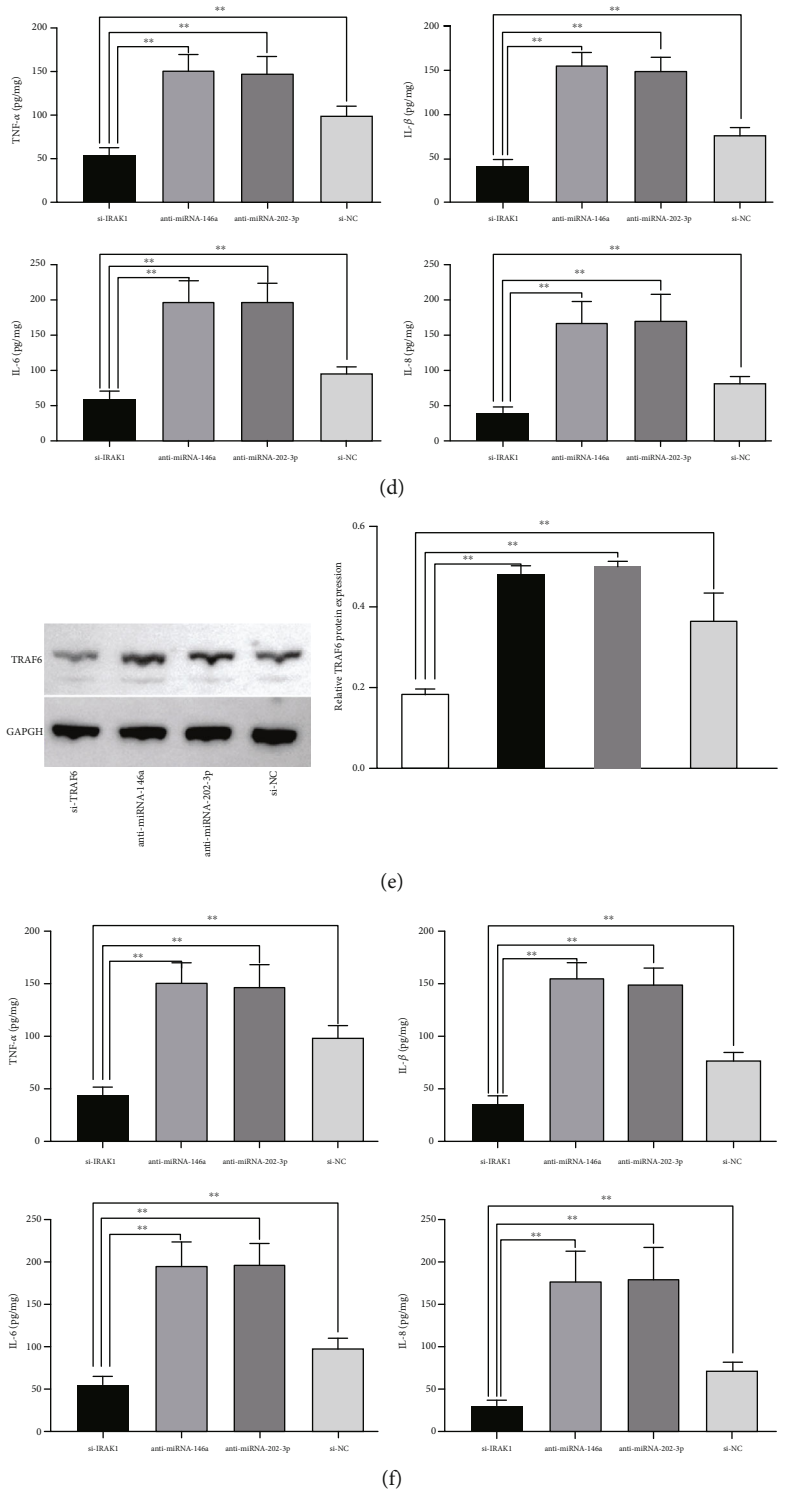

Figure 6: miRNA-146a and miRNA-202-3p inhibited the release of inflammatory cytokines in LPS-stimulated PC12 cells by regulating TLR4, IRAK1, and TRAF6. (a) Immunoblotting analysis of TLR4, IRAK1, and TRAF6 proteins in PC12 cells transfected with si-TLR4, anti-miRNA-146a, anti-miRNA-202-3p, and si-NC. (b) ELISA detection of TNF-α, IL-1β, IL-6, and IL-8 levels in PC12 cells transfected with si-TLR4, anti-miRNA-146a, anti-miRNA-202-3p, and si-NC. (c) Immunoblotting analysis of IRAK1 and TRAF6 proteins in PC12 cells transfected with si-IRAK1, anti-miRNA-146a, anti-miRNA-202-3p, and si-NC. (d) ELISA detection of TNF-α, IL-1β, IL-6, and IL-8 levels in PC12 cells transfected with si-IRAK1, anti-miRNA-146a, anti-miRNA-202-3p, and si-NC. (e) Immunoblotting analysis of TRAF6 protein in PC12 cells transfected with si-TRAF6, anti-miRNA-146a, anti-miRNA-202-3p, and si-NC. (f) ELISA detection of TNF-α, IL-1β, IL-6, and IL-8 levels in PC12 cells transfected with si-TRAF6, anti-miRNA-146a, anti-miRNA-202-3p, and si-NC. $^{**}P < 0.01$ by one-way ANOVA with Tukey's test.

evidenced by results of IRAK1 and TRAF6 inhibition after TLR4 knockdown and TRAF6 inhibition after IRAK1 knockdown, concurring with other studies [31, 32]. Similar to the anti-inflammatory action and mechanism of miRNA-146a in SCI, miRNA-202-3p was observed to ameliorate inflammation following SCI. It is the first time to report the anti-inflammatory role of miRNA-202-3p and its targeted relationship with TLR4, IRAK1, and TRAF6 in the context of SCI, required for further investigations.

In conclusion, our study provides evidence of anti-inflammatory action and mechanism of miRNA-146a and miRNA-202-3p following SCI. Once SCI occurs, miRNA-146a and miRNA-202-3p were secreted to inhibit TLR4, IRAK1, and TRAF6, three crucial parts of inflammatory pathways, protecting the body from excessive inflammation-induced secondary damage. However, our study is a preliminary study. Further *in vivo* investigations about miRNA-146a and miRNA-202-3p interaction with TLR4, IRAK1, and TRAF6 and inflammation-related signal pathways responsible for the anti-inflammatory functions of miRNA-146a and miRNA-202-3p in SCI were required.

Data Availability

The data used to support the findings of this study are included within the article.

Conflicts of Interest

All authors declare that they have no conflict of interest.

References

[1] C. S. Ahuja, S. Nori, L. Tetreault et al., "Traumatic spinal cord injury-repair and regeneration," *Neurosurgery*, vol. 80, no. 3S, pp. S9–S22, 2017.

[2] S. A. Quadri, M. Farooqui, A. Ikram et al., "Recent update on basic mechanisms of spinal cord injury," *Neurosurgical Review*, vol. 43, no. 2, pp. 425–441, 2020.

[3] M. J. Eckert and M. J. Martin, "Trauma: spinal cord injury," *The Surgical Clinics of North America*, vol. 97, no. 5, pp. 1031–1045, 2017.

[4] M. Fakhoury, "Spinal cord injury: overview of experimental approaches used to restore locomotor activity," *Reviews in the Neurosciences*, vol. 26, no. 4, pp. 397–405, 2015.

[5] M. Karsy and G. Hawryluk, "Modern medical management of spinal cord injury," *Current Neurology and Neuroscience Reports*, vol. 19, no. 9, p. 65, 2019.

[6] N. Zhang, Y. Yin, S. J. Xu, Y. P. Wu, and W. S. Chen, "Inflammation & apoptosis in spinal cord injury," *The Indian Journal of Medical Research*, vol. 135, pp. 287–296, 2012.

[7] M. B. Orr and J. C. Gensel, "Spinal cord injury scarring and inflammation: therapies targeting glial and inflammatory responses," *Neurotherapeutics*, vol. 15, no. 3, pp. 541–553, 2018.

[8] S. David, R. Lopez-Vales, and V. Wee Yong, "Harmful and beneficial effects of inflammation after spinal cord injury: potential therapeutic implications," *Handbook of Clinical Neurology*, vol. 109, pp. 485–502, 2012.

[9] T. Roitbak, "MicroRNAs and regeneration in animal models of CNS disorders," *Neurochemical Research*, vol. 45, no. 1, pp. 188–203, 2020.

[10] P. Sun, D. Z. Liu, G. C. Jickling, F. R. Sharp, and K. J. Yin, "MicroRNA-based therapeutics in central nervous system injuries," *Journal of Cerebral Blood Flow and Metabolism*, vol. 38, no. 7, pp. 1125–1148, 2018.

[11] W. J. Lukiw, Y. Zhao, and J. G. Cui, "An NF-κB-sensitive micro RNA-146a-mediated inflammatory circuit in Alzheimer disease and in stressed human brain cells∗," *The Journal of Biological Chemistry*, vol. 283, no. 46, pp. 31315–31322, 2008.

[12] A. Iyer, E. Zurolo, A. Prabowo et al., "MicroRNA-146a: a key regulator of astrocyte-mediated inflammatory response," *PLoS One*, vol. 7, no. 9, p. e44789, 2012.

[13] Q. Wang, Z. Huang, W. Guo et al., "MicroRNA-202-3p inhibits cell proliferation by targeting ADP-ribosylation factor-like 5A in human colorectal carcinoma," *Clinical Cancer Research*, vol. 20, no. 5, pp. 1146–1157, 2014.

[14] Y. Zhao, C. Li, M. Wang et al., "Decrease of miR-202-3p expression, a novel tumor suppressor, in gastric cancer," *PLoS One*, vol. 8, no. 7, p. e69756, 2013.

[15] B. Zhou, H. Zhu, H. Luo et al., "MicroRNA-202-3p regulates scleroderma fibrosis by targeting matrix metalloproteinase 1," *Biomedicine & Pharmacotherapy*, vol. 87, pp. 412–418, 2017.

[16] A. E. Hoffman, R. Liu, A. Fu, T. Zheng, F. Slack, and Y. Zhu, "Targetome profiling, pathway analysis and genetic association study implicate miR-202 in lymphomagenesis," *Cancer Epidemiology, Biomarkers & Prevention*, vol. 22, no. 3, pp. 327–336, 2013.

[17] H. Li, C. Wang, T. He et al., "Mitochondrial transfer from bone marrow mesenchymal stem cells to motor neurons in spinal cord injury rats via gap junction," *Theranostics*, vol. 9, no. 7, pp. 2017–2035, 2019.

[18] D. M. Basso, M. S. Beattie, and J. C. Bresnahan, "A sensitive and reliable locomotor rating scale for open field testing in rats," *Journal of Neurotrauma*, vol. 12, no. 1, pp. 1–21, 1995.

[19] M. B. Leal-Filho, "Spinal cord injury: from inflammation to glial scar," *Surgical Neurology International*, vol. 2, no. 1, p. 112, 2011.

[20] M. G. Fehlings and G. W. Hawryluk, "Scarring after spinal cord injury," *Journal of Neurosurgery: Spine*, vol. 13, no. 2, pp. 165–167, 2010.

[21] S. Hachisuka, N. Kamei, S. Ujigo, S. Miyaki, Y. Yasunaga, and M. Ochi, "Circulating microRNAs as biomarkers for evaluating the severity of acute spinal cord injury," *Spinal Cord*, vol. 52, no. 8, pp. 596–600, 2014.

[22] S. Tigchelaar, F. Streijger, S. Sinha et al., "Serum microRNAs reflect injury severity in a large animal model of thoracic spinal cord injury," *Scientific Reports*, vol. 7, no. 1, p. 1376, 2017.

[23] A. T. Stammers, J. Liu, and B. K. Kwon, "Expression of inflammatory cytokines following acute spinal cord injury in a rodent model," *Journal of Neuroscience Research*, vol. 90, no. 4, pp. 782–790, 2012.

[24] Y. Tan, L. Yu, C. Zhang, K. Chen, J. Lu, and L. Tan, "miRNA-146a attenuates inflammation in an in vitro spinal cord injury model via inhibition of TLR4 signaling," *Experimental and Therapeutic Medicine*, vol. 16, no. 4, pp. 3703–3709, 2018.

[25] J. Wei, J. Wang, Y. Zhou, S. Yan, K. Li, and H. Lin, "MicroRNA-146a contributes to SCI recovery via regulating TRAF6

and IRAK1 expression," *BioMed Research International*, vol. 2016, Article ID 4013487, 8 pages, 2016.

[26] Y. C. Lu, W. C. Yeh, and P. S. Ohashi, "LPS/TLR4 signal transduction pathway," *Cytokine*, vol. 42, no. 2, pp. 145–151, 2008.

[27] J. Wang, Z. Cui, L. Liu et al., "miR-146a mimic attenuates murine allergic rhinitis by downregulating TLR4/TRAF6/NF-κB pathway," *Immunotherapy*, vol. 11, no. 13, pp. 1095–1105, 2019.

[28] Y. Li, W. Li, J. Lin, C. Lv, and G. Qiao, "miR-146a enhances the sensitivity of breast cancer cells to paclitaxel by downregulating IRAK1," *Cancer Biotherapy & Radiopharmaceuticals*, 2020.

[29] X. He, Y. Zheng, S. Liu et al., "miR-146a protects small intestine against ischemia/reperfusion injury by down-regulating TLR4/TRAF6/NF-κB pathway," *Journal of Cellular Physiology*, vol. 233, no. 3, pp. 2476–2488, 2018.

[30] G. J. Liu, Q. R. Zhang, X. Gao et al., "miR-146a ameliorates hemoglobin-induced microglial inflammatory response via TLR4/IRAK1/TRAF6 associated pathways," *Frontiers in Neuroscience*, vol. 14, p. 311, 2020.

[31] H. Li, Y. Wang, X. Hu, B. Ma, and H. Zhang, "Thymosin beta 4 attenuates oxidative stress-induced injury of spinal cord-derived neural stem/progenitor cells through the TLR4/MyD88 pathway," *Gene*, vol. 707, pp. 136–142, 2019.

[32] L. Q. Wang and H. J. Zhou, "lncRNA MALAT1 promotes high glucose-induced inflammatory response of microglial cells via provoking MyD88/IRAK1/TRAF6 signaling," *Scientific Reports*, vol. 8, no. 1, p. 8346, 2018.

Hindawi
Journal of Nanomaterials
Volume 2021, Article ID 9934998, 8 pages
https://doi.org/10.1155/2021/9934998

Research Article

A Novel Machine Learning-Based Systolic Blood Pressure Predicting Model

Jiao Zheng[1] **and Zhengyu Yu**[2]

[1]*Drug Clinical Trial Institution Department, Hunan Provincial People's Hospital (The First Affiliated Hospital of Hunan Normal University), Changsha, Hunan 410000, China*
[2]*Faculty of Engineering and IT, University of Technology, Sydney, Sydney, NSW 2007, Australia*

Correspondence should be addressed to Zhengyu Yu; zhengyu.yu@uts.edu.au

Received 26 March 2021; Accepted 22 May 2021; Published 8 June 2021

Academic Editor: Hassan Karimi-Maleh

Blood pressure (BP) is a vital biomedical feature for diagnosing hypertension and cardiovascular diseases. Traditionally, it is measured by cuff-based equipment, e.g., sphygmomanometer; the measurement is discontinued and uncomfortable. A cuff-less method based on different signals, electrocardiogram (ECG) and photoplethysmography (PPG), is proposed recently. However, this method is costly and inconvenient due to the collections of multisensors. In this paper, a novel machine learning-based systolic blood pressure (SBP) predicting model is proposed. The model was evaluated by clinical and lifestyle features (gender, marital status, smoking status, age, weight, etc.). Different machine learning algorithms and different percentage of training, validation, and testing were evaluated to optimize the model accuracy. Results were validated to increase the accuracy and robustness of the model. The performance of our model met both the level of grade A (British Hypertension Society (BHS) standard) and the American National Standard from the Association for the Advancement of Medical Instrumentation (AAMI) for SBP estimation.

1. Introduction

Currently, hypertension or high blood pressure (BP) is one of the riskiest factors that affect cerebrovascular (CVDs) and cardiovascular diseases and causes around 31% of death in the world [1]. World Health Organization (WHO) reported 9.4 million death from hypertension in the world health statistics in 2014 [2]. After diabetes, hypertension is known as the second dangerous factor of cardiovascular disease [3]. Because many people unrealize the effect of hypertension and do not control it, it is also named silent killer. BP is one of the essential periodic features providing valuable medical information to diagnostic cardiovascular diseases. Diastolic blood pressure (DBP) is the lower bound of the BP. Systolic blood pressure (SBP) is the upper bound of the BP. The average BP is called mean arterial pressure (MAP) in a cardiac cycle [4]. Hypertension occurs and affects the internal body organs when the SBP is higher than 140 mmHg or the DSP is higher than 90 mmHg [5]. The typical value of MAP should stay between 70 mmHg and 110 mmHg [6]. Hypertension patients test BP occasionally. Incorrect measurements are recorded with high possibility due to the BP varies by eating habits, tobacco, stress, etc. Therefore, to achieve an accurate diagnosis, continuous BP monitoring is essential. Besides, the continuous BP record improves the prescriptions of appropriate medicine and treatment by doctors.

The most common and accurate BP measurement methods are cuff-based or invasive [7]. However, the equipment is limited to the health care centre and hospitals. The most common devices used for BP measurement are based on auscultatory and oscillometric methods, which determine the values of SBP and DBP with no risk and pain. However, the measurements from those devices are cuff-based and discontinuous. It is inconvenient to cuff inflation and deflation repeat for the patients. The development of cuff-less BP measurement has been proposed in the last decades [8]. The method based on pulse wave velocity (PWV) and pulse

transit time (PPT) has been introduced to estimate the cuffless continuous BP [9]. Also, continuous wave radar (CWR), bioimpedance (BImp), and electrocardiogram (ECG) sensor are processed in BP estimation [10]. The most common estimation method is based on photoplethysmography (PPG) [7]. The pulse arrival time (PAT) can be calculated by PPG signal and ECG signal. Several challenges were applied in these methods, such as implantation of arterial wave propagation models, signal calibration, and various parameters from difference signals [11]. Recently, machine learning-based measurement methods are developed to reduce the calibration processes by using the signals of PPG and ECG [12]. BP is measured by a series of parameter of features extracted from the signals of PPG and ECG by machine learning. A single PPG signal-based measurement method is also proposed due to its simplicity. This approach can generate estimated BP continuously [13]. This paper presents a novel machine learning-based SBP predicted method by several features and SBP values.

2. Materials and Methods

A novel modelling method is proposed to predict the estimation of SBP in this paper. The proposed method is designed by the extraction of clinical measurement and lifestyle variables with machine learning techniques. Figure 1 illustrates the workflow of the SBP predicted method, which is summarised below.

(1) *Extract Data from Datasets*. In this method, only 250 samples with low BP were implemented.

(2) *Extract Features*. There were 501 features, including one target feature, SBP, 17 clinical features, and 483 genetic markers. This method initially covered 13 features. However, to increase the performance accuracy, part of the features was unselected when the model was evaluated.

(3) *Algorithm Comparison*. Machine learning methods, such as linear regression (LR), support vector machine (SVM), decision tree regression (DTR), Gaussian process regression (GPR), and artificial neural network (ANN), had been computed to address the best approach for the model. The result indicated that ANN was the best accurate method.

(4) In ANN, three different stages were designed to optimize the performance of the network

  (a) Three training algorithms, the Levenberg-Marquardt Algorithm (LMA), the Bayesian Regularization Algorithm (BRA), and the Scaled Conjugate Gradient Algorithm (SCGA), had been selected in the network

  (b) Various percentage of training, validation, and testing had been compared

  (c) The different numbers of hidden neurons had been adjusted

(5) When the model was evaluated, kept the training algorithm, percentage of training, validation, and testing, and the number of hidden neurons. In order to validate the results by different features, the step of feature extraction was operated again by unselecting one of the features for each testing and validation. The results indicated that all 12 features were suitable for the model

(6) After the final model was evaluated, the result was predictable with minimized errors

2.1. Datasets. The datasets we used in our research work are from Dr. Raymond Lam, GlaxoSmithKline, which includes eighteen feature variables and 500 subjects [14]. In this research, 250 subjects indicated as high blood pressure (hypertension) are higher than 140 mmHg, and 250 subjects are lower than 140 mmHg. Eighteen feature variables contain one response feature (SBP) and seventeen features (clinical covariates). Due to some variables of features were ambiguous classified and calculated, our research selected thirteen variables for training, testing, and estimating.

2.2. Systolic Blood Pressure. SBP represents BP value which is exerting against the walls of the artery when the heart is beating. SBP is an essential value for the BP measurement, and it is an important feature to detect hypertension [4].

2.3. Gender. In the datasets, the variable of gender is in binary. M denotes male, and F denotes female. The differences in gender indicate the difference in the regulation of BP [15]. A study of ambulatory BP monitoring for 24 hours has been presented recently [16]. The results have addressed that men have more possibility to have cardiovascular disease than age-matched women [17]. The BP in men is higher than the BP in women [18].

2.4. Marital Status. Marital status is one of the variables from the datasets. Y denotes married, and N denotes not married. According to the previous research, it is shown that never-married people have more risks of hypertension than married people in men. However, never-married women are associated with less risk of hypertension than married women [19].

2.5. Smoking Status. In the smoking status, Y denotes smoker, and N denotes nonsmoker. Research study indicates that the artery walls become sticky when the inhaled cigarette chemicals are absorbed into the bloodstream. The number of fatty plaques sticks to the artery walls, called atherosclerosis leading to cardiovascular disease. When the artery walls become narrower and narrower, the blood travels through the arteries difficultly [20].

2.6. Age. Age plays a vital role in relation with BP [21–23]. When the age increases, the blood vessels become stiffer, which can lead to a rise in BP as well as an increase in the risk of hypertension. People aged 50 or higher are the most prevalent hypertensions group, especially in isolated systolic hypertension. Due to the change of artery structure

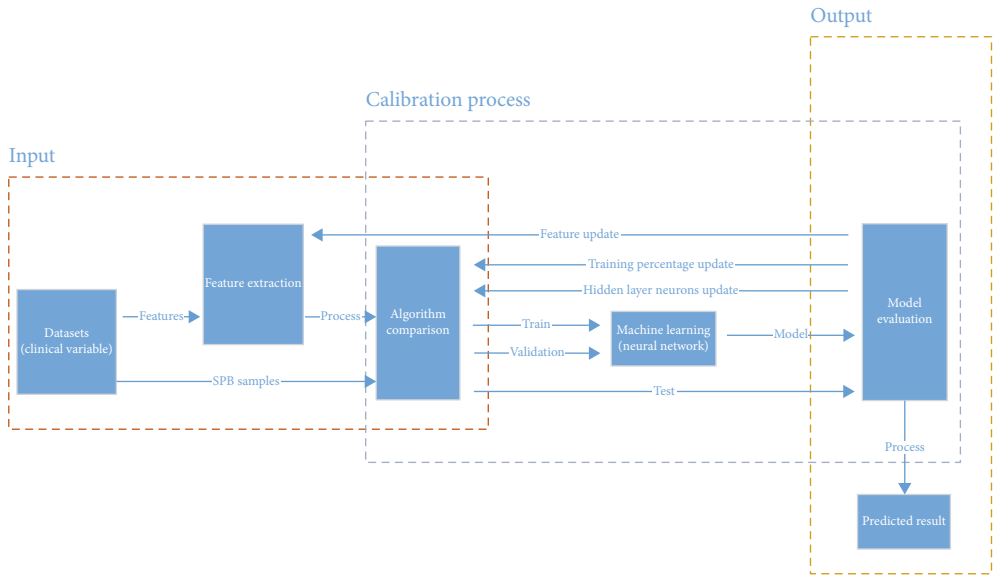

Figure 1: Workflow diagram for SBP predicted model.

associated with age increases, e.g., artery stiffness, the BP increases cardiovascular risk [24, 25].

2.7. Weight/Overweight. Weight is a continuous variable in the dataset; the unit is pound. The BP rises following by the bodyweight increase. Overweight will increase the possibility to develop hypertension [26]. In the datasets, three categories are classified. 1 denotes normal, 2 denotes overweight, and 3 denotes obese.

2.8. Height. A study proposed an inverse linear relationship between SBP and height. Lower SBP was associated with greater height [27]. In the datasets, height is a continuous variable with the unit (inches).

2.9. Body Mass Index (BMI). BMI is a measurement index indicating whether the body is obese or overweight [28]. The categories have been classified as follows:

(1) *Underweight*. Less than 20

(2) *Normal Weight*. 20-25

(3) *Overweight*. 26-30

(4) *Obese*. 30-above

It is calculated by weight and height.

$$\frac{\text{Weight}}{\text{Height}^2} * 703. \quad (1)$$

2.10. Exercise Level. According to the research, exercise accelerates the heart pump. The faster the heart pumps, the higher SBP rises. During the exercise, the expected level of SBP is between 160 mmHg and 220 mmHg [29]. In this paper, the exercise level has been divided into three. 1, 2, and 3 denote low, medium, and high, respectively.

Table 1: Machine learning algorithms.

Algorithm	MAE (mmHg)
Linear regression (LR)	13.18
Support vector machine (SVM)	13.13
Decision tree regression (DTR)	14.82
Gaussian process regression (GPR)	12.92
Artificial neural network (ANN)	10.78

2.11. Alcohol Consumption. A recent clinical study has suggested that alcohol consumption can raise BP rapidly [30]. A single drink of alcohol affects an acute BP rise for 2 hours [31]. Moreover, a sustained BP rise can be caused by alcohol consumption for a few days. Long-time alcohol consumption links to risk factors, such as cardiovascular disease and high blood pressure [32]. In datasets, the alcohol consumption level is defined by 1, 2, and 3, which denote low, medium, and high, respectively.

2.12. Stress Level. The body generates a surge of hormones when they are in stressful situations. This action causes the heart to pump faster, and the blood vessels become narrow, which leads to spike in BP temporarily. The research finds that reducing stress can lower body BP [33]. We also have three levels of stress in datasets: 1 denotes low, 2 denotes medium, and 3 denotes high.

2.13. Salt (NaCl) Intake Level. High sodium or salt intake can contribute to high BP and speed up the risk of cardiovascular disease [34]. WHO reports that 5 grams or less salt intake for adults helps decrease BP and the risk of heart disease [35]. However, most people take 9-12 grams daily on average [36, 37]. This amount of salt consumption is twice the recommended maximum level. The member states of WHO agree to reduce world population's salt consumption by 30% before 2025, which prevents 2.5 million deaths caused by high sodium consumption [38].

Table 2: Artificial neural network training algorithm.

Training algorithm	MAE (mmHg)	STD (mmHg)
LMA	11.13	13.77
BRA	6.28	10.51
SCGA	9.51	12.32

Table 3: Different percentage of data training, validation, and testing.

Percentage of data training, validation, and testing	MAE (mmHg)	STD (mmHg)
70% training, 15% validation, 15% testing	6.28	10.51
80% training, 10% validation, 10% testing	5.85	8.78
90% training, 5% validation, 5% testing	5.16	7.66

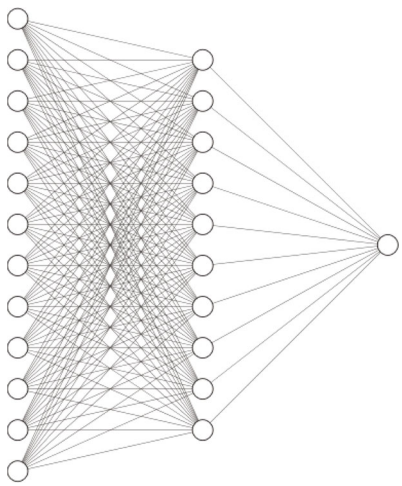

Figure 2: The structure of an artificial neural network.

From the datasets, due to several variables of features are ambiguous, only 13 variables with 250 nonhypertension samples had been selected in the model. In order to predict the most accurate estimated SBP, an algorithm comparison had been designed. Algorithms such as LR, SVM, GPR, and ANN had been processed to generate the most optimized result. The outcomes from the algorithms had been recorded in Table 1.

After computing five machine learning methods, as the Table 1 shown, the ANN method had the best performance; the mean average error (MAE) was about 10.78 mmHg, which was lower than other methods. Therefore, the ANN was the primary method for our research to predict the SBP.

2.14. Training Algorithm

2.14.1. Levenberg-Marquardt. The LMA provides the solution to minimize the nonlinear least-squares problem [39].

Table 4: Different numbers of hidden neurons.

Number of hidden neurons	MAE (mmHg)	STD (mmHg)
4 hidden neurons	10.05	12.61
5 hidden neurons	9.99	12.71
6 hidden neurons	9.87	12.55
7 hidden neurons	7.44	9.65
10 hidden neurons	5.16	7.66
11 hidden neurons	4.97	7.63
15 hidden neurons	3.03	6.11
16 hidden neurons	6.86	9.06
20 hidden neurons	9.11	12.06

Table 5: 12 different features.

ID	Feature
1	Gender
2	Marital status
3	Smoking status
4	Age
5	Weight
6	Overweight
7	Height
8	Body mass index (BMI)
9	Exercise level
10	Alcohol consumption
11	Stress level
12	Salt (NaCl) intake level

It is one of the most popular algorithms for optimization [40]. In several kinds of problems, LMA generates better results than gradient descent and other conjugate gradient techniques [41]. It is a blended method of Gauss-Newton and vanilla gradient descent iteration [42]. If the solution is far from the true result, the algorithm acts like a gradient descent method: slow, ensures the converge. If the current solution is close to the true result, it acts like a Gauss-Newton method [43].

2.14.2. Bayesian Regularization. Bayesian regularization has also been named Bayesian regularized artificial neural networks (BRANNs), which is more reliable than the classical ANN backpropagation nets, with no need for prolix cross-validation. It is a machine learning algorithm that converts a nonlinear regression into a ridge regression [44].

2.14.3. Scaled Conjugate Gradient. As a supervised learning algorithm for feedforward neural network, SCG is one of the conjugate gradient algorithms. The operation of SCG is smoother and faster than the standard backpropagation nets. The training algorithm from SCG has benchmarked performance against the classical BP algorithm. BP utilizes the optimization theory of gradient descent with the selected variable from the user. The offline trained network uses a fixed variable, whereas the SCG algorithm uses these variables as the

Table 6: Cumulative error percentage with excluded feature.

Feature Excluded	1	2	3	4	5	6	7	8	9	10	11	12
Error (mmHg)												
<5	38%	57%	26%	32%	40%	44%	41%	31%	29%	29%	51%	40%
<10	68%	85%	58%	58%	72%	72%	70%	60%	58%	62%	80%	68%
<15	89%	95%	78%	78%	89%	88%	88%	78%	78%	79%	93%	86%

Table 7: Comparison of performance on different error stages.

		Error < 5 mmHg	Error < 10 mmHg	Error < 15 mmHg
Results		67%	89%	97%
BHS	Grade A	60%	85%	95%
	Grade B	50%	75%	90%
	Grade C	40%	65%	85%

second-order approximation. Less learning iterations occur to accelerate the learning process.

The ANN method in this paper had been separated into three different training methods, LMA, BRA, and the SCGA. We initially set the number of hidden neurons as 10, 80% data for training, 10% data for validation, and 10% data for testing to address the best training algorithm. The results had been illustrated in Table 2:

From Table 2, the results indicated that the BRA training method was the most accurate method.

In the next step, we adjusted the percentage of the training data and compared the result in Table 3.

According to Table 3, the most accurate result was generated by 90%, 5%, and 5% for training, validation, and testing, respectively.

Figure 2 presents the structure of ANN, the input layer contained 12 features, and the output layer contained 1 feature which was SBP. The training performance was evaluated by changing the number of hidden neurons on the hidden layer. In our model, as displayed in Figure 2, only one hidden layer applied. Initially, the hidden neurons had been set up as 10, and the different numbers of hidden neurons had been trained to determine the most accurate network structure.

As Table 4 presented, the best accurate model was with 15 hidden neurons. Therefore, the ANN applied the BRA training method with 90% training, 5% validating, and 5% testing, with 15 hidden neurons generated the most accurate results.

3. Results and Discussion

In Results and Discussion, as mentioned, several features were ambiguous. It is possible to generate more errors in the system. Several tests had been completed to compare the performance in order to avoid these ambiguous features. We validated that all the features used in the model were suitable to generate the result. The result validation process is presented as follows.

In Table 5, the above 12 features had been trained, validated, and tested in the ANN with the target feature, SBP. To validate the results, we unselected one of the features for each training. For instance, in the first training, the feature ID 1, gender, was excluded in the 12 features; therefore, only 11 features were operated in the first training. For each training, different error levels (from 5 mmHg to 30 mmHg) had been recorded in Table 6.

From Tables 6, 12 different features had been unselected one by one. The higher the error percentage was, the higher the accuracy was. When we unselected feature ID 3, smoking status, the results (26%, 58%, and 78%) were lower than any other results in the table, which meant the values of feature ID 3 were more significant than other values of features. However, if we unselected feature ID 2, marital status, the results (57%, 85%, and 95%) were higher than any other results in the table. Therefore, the values of feature ID 2 were less vital than any other values of features in the table. From Table 7, the error percentage after training 12 features were 67%, 89%, and 97% for error less than 5 mmHg, 10 mmHg, and 15 mmHg, respectively, whose accuracy was higher than any others in Table 6. Therefore, it is unnecessarily to unselect any feature in the training process, and all the 12 features should be trained.

Figure 3 presents the error histogram with 20 bins; the orange line indicates zero error, the blue bar represents training errors, and the test errors are red. The figure illustrated that the most significant number of errors are near the orange line, zero error; the number of errors decreased when the error became larger.

The results from Table 7 illustrated that our prediction model had 67%, 89%, and 97% accuracy when an error was less than 5 mmHg, 10 mmHg, and 15 mmHg, respectively. Comparing to the British Hypertension Society (BHS) standard [45], the performance of our model met the level of grade A (BHS standard) for SBP estimation.

Moreover, Table 8 illustrated the American National Standard from the Association for the Advancement of Medical Instrumentation (AAMI). According to the standard, the

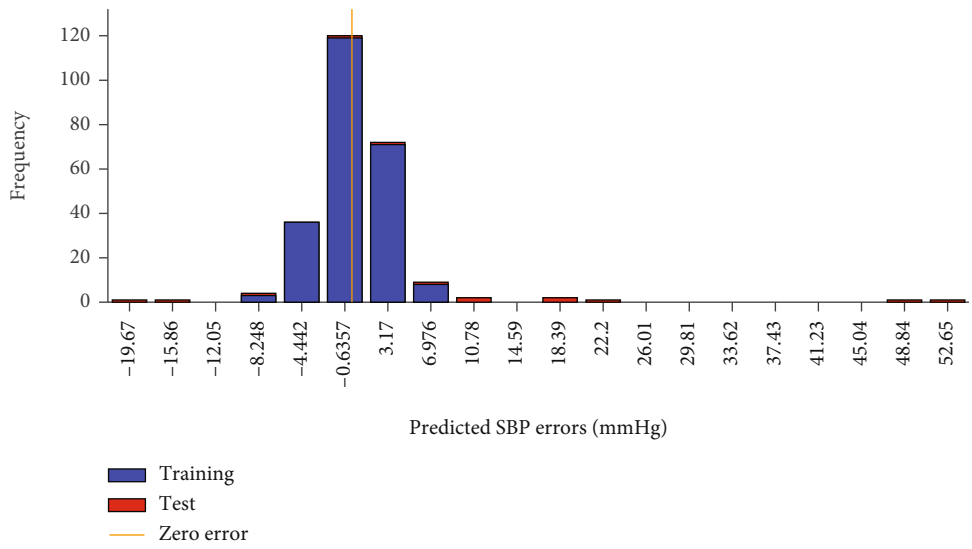

Figure 3: Error histogram of predicted SBP errors.

Table 8: Comparison of performance on results.

	MAE (mmHg)	STD (mmHg)
Results	3.03	6.11
Advancement of Medical Instrumentation (AAMI)	5.00	8.00

BP estimation method for noninvasive should less than 5 mmHg and 8 mmHg for MAE and STD. Our results were 3.03 mmHg (MAE) and 6.11 mmHg (STD), which met the AAMI standard [46].

4. Conclusions

In this paper, we proposed a novel model based on machine learning algorithm to predict SBP. The model included three stages, which were input, calibration process, and output.

In the first stage, datasets associated with clinical and lifestyle features were selected and extracted. Values of 13 features, including SPB values, had been selected as training data. Five machine learning algorithms, such as LR, SVM, DTR, GPR, and ANN, had been compared in this stage. The result indicated that ANN had the best accuracy.

The calibration process was the second stage. Three different training algorithms, LMA, BRA, and SCGA, had been trained in ANN. After comparing with the value of MAE and STD, BRA was addressed as the best training algorithms. In the next step, the comparison of different percentage of data training, validation, and testing had been completed. The most accurate result was generated by 90%, 5%, and 5% for training, validation, and testing, respectively. The next step was to adjust the structure of ANN; we assumed that the ANN included one hidden layer, which initially contained 10 hidden neurons. Several different hidden neurons were applied to discover that the ANN generated the most accurate results in the condition of 15 hidden neurons.

In the third stage, the model was evaluated by amending inputted data of features. To validate the results, values of feature with significant uncertainties were unselected in the model. The accumulated error percentage of the evaluated model meets grade A in BHS standard and AAMI standard in estimating SBP. Therefore, our proposed predicted model was accurate and reliable. Nevertheless, the model would be optimized further if the data of the features were more robust.

Data Availability

The data used are from R. Lam, "Blood Pressure." These are available at http://www.math.yorku.ca/Who/Faculty/Ng/ssc2003/BPMain.htm (accessed March 03, 2021).

Conflicts of Interest

The authors declare that there is no conflict of interest regarding the publication of this paper.

References

[1] D. Mozaffarian, E. J. Benjamin, A. S. Go et al., "Heart disease and stroke statistics—2015 update: a report from the American Heart Association," *Circulation*, vol. 131, no. 4, pp. e29–e322, 2015.

[2] W. H. Organization, *World Health Statistics 2015*, World Health Organization, 2015.

[3] C. Höcht, "Blood pressure variability: prognostic value and therapeutic implications," *ISRN Hypertension*, vol. 2013, Article ID 398485, 16 pages, 2013.

[4] W. Chen, T. Kobayashi, S. Ichikawa, Y. Takeuchi, and T. Togawa, "Continuous estimation of systolic blood pressure using the pulse arrival time and intermittent calibration," *Medical and Biological Engineering and Computing*, vol. 38, no. 5, pp. 569–574, 2000.

[5] M. Korsager Larsen and V. V. Matchkov, "Hypertension and physical exercise: the role of oxidative stress," *Medicina*, vol. 52, no. 1, pp. 19–27, 2016.

[6] C. J. Rodriguez, K. Swett, S. K. Agarwal et al., "Systolic blood pressure levels among adults with hypertension and incident cardiovascular events: the atherosclerosis risk in communities study," *JAMA Internal Medicine*, vol. 174, no. 8, pp. 1252–1261, 2014.

[7] H. Gesche, D. Grosskurth, G. Küchler, and A. Patzak, "Continuous blood pressure measurement by using the pulse transit time: comparison to a cuff-based method," *European Journal of Applied Physiology*, vol. 112, no. 1, pp. 309–315, 2012.

[8] R. Wang, W. Jia, Z.-H. Mao, R. J. Sclabassi, and M. Sun, "Cuff-free blood pressure estimation using pulse transit time and heart rate," in *2014 12th International Conference on Signal Processing (ICSP)*, pp. 115–118, Hangzhou, China, October 2014.

[9] X. Ding, B. P. Yan, Y. T. Zhang, J. Liu, N. Zhao, and H. K. Tsang, "Pulse transit time based continuous cuffless blood pressure estimation: a new extension and a comprehensive evaluation," *Scientific Reports*, vol. 7, no. 1, p. 11554, 2017.

[10] D. Buxi, J. M. Redout, and M. R. Yuce, "Blood pressure estimation using pulse transit time from bioimpedance and continuous wave radar," *IEEE Transactions on Biomedical Engineering*, vol. 64, no. 4, pp. 917–927, 2016.

[11] E. R. J. Seitsonen, I. K. J. Korhonen, M. J. van Gils et al., "EEG spectral entropy, heart rate, photoplethysmography and motor responses to skin incision during sevoflurane anaesthesia," *Acta Anaesthesiologica Scandinavica*, vol. 49, no. 3, pp. 284–292, 2005.

[12] B. McCarthy, C. J. Vaughan, B. O'Flynn, A. Mathewson, and C. Ó Mathúna, "An examination of calibration intervals required for accurately tracking blood pressure using pulse transit time algorithms," *Journal of Human Hypertension*, vol. 27, no. 12, pp. 744–750, 2013.

[13] F. Miao, N. Fu, Y. T. Zhang et al., "A novel continuous blood pressure estimation approach based on data mining techniques," *IEEE Journal of Biomedical and Health Informatics*, vol. 21, no. 6, pp. 1730–1740, 2017.

[14] R. Lam, "Blood Pressure," March 2021, http://www.math.yorku.ca/Who/Faculty/Ng/ssc2003/BPMain.htm.

[15] J. F. Reckelhoff, "Gender differences in the regulation of blood pressure," *Hypertension*, vol. 37, no. 5, pp. 1199–1208, 2001.

[16] N. Wiinberg, A. Høegholm, H. R. Christensen et al., "24-h ambulatory blood pressure in 352 normal Danish subjects, related to age and gender," *American Journal of Hypertension*, vol. 8, no. 10, pp. 978–986, 1995.

[17] S. Khoury, S. A. Yavows, T. K. O'Brien, and J. R. Sowers, "Ambulatory blood pressure monitoring in a nonacademic setting: effects of age and sex," *American Journal of Hypertension*, vol. 5, no. 9, pp. 616–623, 1992.

[18] V. L. Burt, P. Whelton, E. J. Roccella et al., "Prevalence of hypertension in the US adult population: results from the Third National Health and Nutrition Examination Survey, 1988-1991," *Hypertension*, vol. 25, no. 3, pp. 305–313, 1995.

[19] J. Holt-Lunstad, W. Birmingham, and B. Q. Jones, "Is there something unique about marriage? The relative impact of marital status, relationship quality, and network social support on ambulatory blood pressure and mental health," *Annals of Behavioral Medicine*, vol. 35, no. 2, pp. 239–244, 2008.

[20] P. Primatesta, E. Falaschetti, S. Gupta, M. G. Marmot, and N. R. Poulter, "Association between smoking and blood pressure: evidence from the health survey for England," *Hypertension*, vol. 37, no. 2, pp. 187–193, 2001.

[21] E. Pinto, "Blood pressure and ageing," *Postgraduate Medical Journal*, vol. 83, no. 976, pp. 109–114, 2007.

[22] S. Franklin, "Ageing and hypertension: the assessment of blood pressure indices in predicting coronary heart disease," *Journal of hypertension. Supplement: official Journal of the International Society of Hypertension*, vol. 17, no. 5, pp. S29–S36, 1999.

[23] S. I. Chaudhry, H. M. Krumholz, and J. M. Foody, "Systolic hypertension in older persons," *JAMA*, vol. 292, no. 9, pp. 1074–1080, 2004.

[24] S. S. Franklin, M. J. Jacobs, N. D. Wong, G. J. L'Italien, and P. Lapuerta, "Predominance of isolated systolic hypertension among middle-aged and elderly US hypertensives: analysis based on National Health and Nutrition Examination Survey (NHANES) III," *Hypertension*, vol. 37, no. 3, pp. 869–874, 2001.

[25] A. M. Borzecki, A. T. Wong, E. C. Hickey, A. S. Ash, and D. R. Berlowitz, "Hypertension control: how well are we doing?," *Archives of Internal Medicine*, vol. 163, no. 22, pp. 2705–2711, 2003.

[26] R. Stamler, J. Stamler, W. F. Riedlinger, G. Algera, and R. H. Roberts, "Weight and blood pressure: findings in hypertension screening of 1 million Americans," *JAMA*, vol. 240, no. 15, pp. 1607–1610, 1978.

[27] B. Rosner, R. J. Prineas, J. M. H. Loggie, and S. R. Daniels, "Blood pressure nomograms for children and adolescents, by height, sex, and age, in the United States," *The Journal of Pediatrics*, vol. 123, no. 6, pp. 871–886, 1993.

[28] W. Drøyvold, K. Midthjell, T. I. L. Nilsen, and J. Holmen, "Change in body mass index and its impact on blood pressure: a prospective population study," *International Journal of Obesity*, vol. 29, no. 6, pp. 650–655, 2005.

[29] T. G. Pickering, G. A. Harshfield, H. D. Kleinert, S. Blank, and J. H. Laragh, "Blood pressure during normal daily activities, sleep, and exercise: comparison of values in normal and hypertensive subjects," *JAMA*, vol. 247, no. 7, pp. 992–996, 1982.

[30] M. G. Marmot, P. Elliott, M. J. Shipley et al., "Alcohol and blood pressure: the INTERSALT study," *BMJ*, vol. 308, no. 6939, pp. 1263–1267, 1994.

[31] A. L. Klatsky, G. D. Friedman, A. B. Siegelaub, and M. J. Gérard, "Alcohol consumption and blood pressure: Kaiser-Permanente multiphasic health examination data," *New England Journal of Medicine*, vol. 296, no. 21, pp. 1194–1200, 1977.

[32] P. D. Arkwright, L. J. Beilin, I. Rouse, B. K. Armstrong, and R. Vandongen, "Effects of alcohol use and other aspects of lifestyle on blood pressure levels and prevalence of hypertension in a working population," *Circulation*, vol. 66, no. 1, pp. 60–66, 1982.

[33] T. L. Lindquist, L. J. Beilin, and M. W. Knuiman, "Influence of lifestyle, coping, and job stress on blood pressure in men and women," *Hypertension*, vol. 29, no. 1, pp. 1–7, 1997.

[34] H. Karppanen and E. Mervaala, "Sodium intake and hypertension," *Progress in Cardiovascular Diseases*, vol. 49, no. 2, pp. 59–75, 2006.

[35] W. H. Organization, *Guideline: Sodium Intake for Adults and Children*, World Health Organization, 2012.

[36] M. H. Weinberger, "Salt sensitivity of blood pressure in humans," *Hypertension*, vol. 27, no. 3, pp. 481–490, 1996.

[37] P. Strazzullo, L. D'Elia, N. B. Kandala, and F. P. Cappuccio, "Salt intake, stroke, and cardiovascular disease: meta-analysis of prospective studies," *BMJ*, vol. 339, p. b4567, 2009.

[38] W. H. Organization, *Reducing salt intake in populations: report of a WHO forum and technical meeting, 5-7 October 2006, Paris, France*.

[39] K. Levenberg, "A method for the solution of certain non-linear problems in least squares," *Quarterly of Applied Mathematics*, vol. 2, no. 2, pp. 164–168, 1944.

[40] C. T. Kelley, *Iterative Methods for Optimization*, SIAM, 1999.

[41] K. Madsen, H. B. Nielsen, and O. Tingleff, *Methods for Non-linear Least Squares Problems*, 2004.

[42] J. Nocedal and S. Wright, *Numerical Optimization*, Springer Science & Business Media, 2006.

[43] W. H. Press, H. William, S. A. Teukolsky, A. Saul, W. T. Vetterling, and B. P. Flannery, *Numerical Recipes 3rd Edition: The Art of Scientific Computing*, Cambridge university press, 2007.

[44] F. Burden and D. Winkler, "Bayesian regularization of neural networks," *Artificial neural networks*, pp. 23–42, 2008.

[45] E. O'brien, B. Waeber, G. Parati, J. Staessen, and M. G. Myers, "Blood pressure measuring devices: recommendations of the European Society of Hypertension," *BMJ*, vol. 322, no. 7285, pp. 531–536, 2001.

[46] A. f. t. A. o. M. Instrumentation, "American national standards for electronic or automated sphygmomanometers," 1987, ANSI/AAMI SP 10-1987.

Hindawi
Journal of Nanomaterials
Volume 2021, Article ID 2289275, 8 pages
https://doi.org/10.1155/2021/2289275

Research Article

Right Anterior Minithoracotomy Is an Alternative, Less Invasive Approach to Median Sternotomy during Aortic Valve Replacement for Patients with Low Left Ventricular Ejection Fraction

Zheng Qu, Bin You, and Ping Li

Department of Cardiac Surgery, Beijing Anzhen Hospital, Capital Medical University, China

Correspondence should be addressed to Bin You; 8272011@163.com

Received 7 May 2021; Accepted 17 May 2021; Published 7 June 2021

Academic Editor: Songwen Tan

The concept of minimally invasive cardiac surgery has been put forward for more than decades and continued to develop. Recently, minimally invasive aortic valve surgery is established as a safe and effective treatment for various aortic valvular heart diseases and ascending aorta disorders. This study is aimed at analyzing the safety and effectiveness of aortic valve replacement (AVR) through right anterior minithoracotomy for the treatment of patients with low left ventricular ejection fraction (LVEF). Retrospective analyses of 43 cases with low LVEF undergoing AVR through median sternotomy and 43 cases with low LVEF undergoing AVR through right anterior minithoracotomy were performed. Extracorporeal circulation time and aortic cross-clamping time were longer in patients undergoing AVR through right anterior minithoracotomy than those in patients undergoing AVR through median sternotomy ($P < 0.05$). Patients undergoing AVR through right anterior minithoracotomy exhibited declines in the cardiac surgery intensive care unit (CSICU) stay, duration of mechanical ventilation, and the length of hospital stay than those undergoing AVR through median sternotomy ($P < 0.05$). The volumes of 24 h chest drainage were reduced in patients undergoing AVR through right anterior minithoracotomy compared with those undergoing AVR through median sternotomy ($P < 0.05$). The incidence rates of blood transfusion within 24 h and postoperative atrial fibrillation were lower in patients undergoing AVR through right anterior minithoracotomy than those in patients undergoing AVR through median sternotomy ($P < 0.05$). As for cardiac function, patients with right anterior minithoracotomy had decreased left ventricular end diastolic diameter (LVEDD) but increased LVEF and left ventricular fractional shortening (LVFS) when compared to median sternotomy ($P < 0.05$). With regard to inflammatory response, the serum levels of interleukin-6 (IL-6), interleukin-8 (IL-8), and tumor necrosis factor-α (TNF-α) in patients with right anterior minithoracotomy were much lower than those in median sternotomy ($P < 0.05$). All these results indicate that right anterior minithoracotomy is an alternative, less invasive approach to median sternotomy during AVR for patients with low LVEF.

1. Introduction

Aortic valve disease, as the most common form of valvular heart disease, includes aortic stenosis and regurgitation [1–3]. Aortic stenosis refers to the abnormal structure of the aortic valve, which limits the blood flow to the body and ultimately overburdens left ventricular contraction function [4–6]. Aortic regurgitation represents a diastolic reversal of blood flow from the aorta to the left ventricle, which can be caused by the primary disease of aortic valve or the abnormal tissue and structure around the aortic valve [7–9]. The incidence of aortic stenosis is age-dependent and thus is expected to increase due to demographic aging of the global population [10]. It is well recognized that severe aortic stenosis is followed by a poor prognosis if left untreated. The symptoms of aortic stenosis are associated with increased mortality [11]. Aortic valve replacement (AVR) through a median sternotomy incision has been the gold standard treatment as a safe, long-term, and effective treatment for aortic valve disease for decades since the 1950s [12–14]. In fact,

more and more surgeons aimed to reduce surgical infection and improve clinical and cosmetic results by changing the chest incision approach in the treatment of aortic valve disease [15]. Over the years, with the increasing application of minimally invasive and new techniques, aortic valve surgery has been significantly improved [16]. Minimally invasive aortic valve replacement (MIAVR) is defined as a smaller chest incision rather than median sternotomy, and the two main techniques of MIAVR are ministernotomy and right anterior minithoracotomy [17]. The main information available focused on the ministernotomy approaches; only a few studies evaluated the right anterior minithoracotomy approach for aortic valve disease, which revealed some advantages in terms of low incidence of atrial fibrillation and less blood transfusion and duration of mechanical ventilation [18–21]. Left ventricular ejection fraction (LVEF) refers to the ratio of stroke volume to end diastolic volume, which is an essential measurement of cardiac function [22, 23]. Reduced LVEF may be associated with worse patient outcomes, while the optimal threshold for "normal" LVEF is uncertain. Usually, LVEF more than 55% is regarded to be "normal" by guidelines [24]. According to the 2016 European Society of Cardiology Heart Failure guidelines, heart failure was newly defined with LVEF ranging from 40 to 49% [25–27]. This study retrospectively analyzed 43 cases with low LVEF undergoing AVR through median sternotomy and 43 cases with low LVEF undergoing AVR through right anterior minithoracotomy, in a bid to find an alternative, less invasive approach to median sternotomy during AVR for patients with low LVEF.

2. Materials and Methods

2.1. Subject Assignments. A total of 86 patients diagnosed with aortic valve disease with low LVEF were retrospectively studied in our hospital from September 2019 to September 2020, among which 43 cases underwent AVR through median sternotomy and 43 cases underwent AVR through right anterior minithoracotomy. Patients undergoing AVR through median sternotomy consisted of 25 males and 18 females, aged ranging from 22 to 68 years and with an average age of 47.17 ± 12.27 years. Patients undergoing AVR through right anterior minithoracotomy comprised of 26 males and 17 females, aged ranging from 22 to 76 years and with an average age of 48.48 ± 12.14 years. More detailed baseline variables of included patients, such as smoking, alcohol consumption, body mass index, heart rate at admission, disease duration, NYHA classification, and type of aortic valve disease, complication with diabetes, and complication with hypertension between the two groups are listed in Table 1.

2.2. Eligibility Criteria. Patients who were included in this study should meet the following criteria: (a) the diagnosis of aortic valve diseases confirmed by clinical manifestations, physical examination, electrocardiogram, cardiac color Doppler ultrasound, and chest X-ray, (b) LVEF < 50%, (c) tolerance to surgery and no contraindication to surgery, (d) signed informed consent, and (e) requirement of coronary angiography for patients over 50 years old and with angina pectoris symptoms before operation to exclude the influence of coronary heart disease. Patients were excluded for the following reasons: (a) serious mental diseases or cognitive impairment; (b) liver and kidney dysfunction, malignant tumors, malignant arrhythmia, and blood diseases; (c) other organic heart diseases; (d) sternum, spine malformation, and pericardial adhesions; (e) a history of cardiac surgery or thoracotomy; (f) pulmonary hypertension, severe atrioventricular block, acute infection, and requirement for emergency surgery; (g) poor pulmonary function; and (h) pregnancy and lactation.

2.3. Surgery Protocols. All patients underwent routine chest computed tomography (CT) scan to determine the location of the ascending aorta before operation. Minimally invasive AVR through right anterior minithoracotomy was performed if more than 50% of the ascending aorta was located on the right side of the sternum with the main pulmonary artery as transection, the distance between the ascending aorta and chest was less than 12 cm, there was no serious calcification in the aortic valve and aortic wall, and the aortic valve diameter was no less than 20 mm. In addition, severe obesity and thoracic deformity may lead to the difficulty of visual field exposure in minimally invasive surgery, and a cardiothoracic ratio < 0.7 should be considered.

Surgery protocols for patients undergoing AVR through right anterior minithoracotomy were as follows: after general anesthesia and tracheal cannula, the patients were maintained in the supine position, with the right chest back raised, followed by a scan of ultrasound probe through the esophagus and equipment with defibrillation electrodes on the body surface with the sternum and rib marked. After a transverse incision (6-8 cm) in the third intercostal space at the right sternum, the right internal mammary artery can be ligated and separated for exposure requirement, and the pericardium was cut and suspended for about 3 cm in front of the phrenic nerve to locate the aorta with increasing exposure by cutting the 3^{rd} or 4^{th} costal cartilage at the right edge of the sternum. The patients were injected with heparin into the vein, with separation of the femoral artery and vein, and the femoral artery was inserted with blood-supply catheter and the femoral vein was inserted with drainage catheter aimed at building an extracorporeal circulation system. The ascending aorta was occluded with blocking forceps, and the aorta was obliquely cut on the aortic valve annulus to infuse cardioplegia through the left and right coronary arteries, respectively. The diseased aortic valve should be cut off when detected, the artificial valve should be replaced according to the size of the diseased valve, and the aortic incision was sutured if there was no abnormality. The left ventricular gas should be exhausted, and the blocking forceps at the ascending aorta was removed to observe the heartbeat, making use of a defibrillator to return the normal heartbeat if necessary. The extracorporeal circulation instruments were withdrawn when everything runs normal, and temporary pacing leads were sutured into the epicardium in case of arrhythmia, and a catheter was placed into the right ribs as a drainage tube to exhaust gas or collect effusion from the chest; the chest tissue was sutured after lung tissue restored its function.

Table 1: Baseline variables of included patients.

Variable	Median sternotomy	Right anterior minithoracotomy	P
Age (years, mean ± SD)	47.17 ± 12.27	48.48 ± 12.14	0.62
Gender/male (%)	25 (58.1%)	26 (60.5%)	0.83
Smoking (%)	16 (37.2%)	17 (39.5%)	0.83
Alcohol consumption (%)	9 (20.9%)	11 (25.6%)	0.61
Body mass index (kg/m^{-2}, mean ± SD)	24.57 ± 4.12	24.81 ± 4.07	0.79
Heart rate at admission (time (min), mean ± SD)	87.76 ± 18.49	88.26 ± 18.78	0.90
Disease duration (years, mean ± SD)	8.11 ± 1.71	8.02 ± 1.65	0.80
NYHA classification (%)			0.93
Class I	4 (9.3%)	5 (11.6%)	
Class II	16 (37.2%)	14 (32.6%)	
Class III	15 (34.9%)	17 (39.5%)	
Class IV	8 (18.6%)	7 (16.3%)	
Type of aortic valve disease (%)			0.91
Aortic stenosis	8 (18.6%)	7 (16.3%)	
Aortic insufficiency	21 (48.8%)	23 (53.5%)	
Both	14 (32.6%)	13 (30.2%)	
Diabetes (%)	9 (20.9%)	8 (18.6%)	0.79
Hypertension (%)	10 (23.3%)	9 (20.9%)	0.79

There were 43 cases undergoing AVR through median sternotomy and 43 cases undergoing AVR through right anterior minithoracotomy.

Surgery protocols for patients undergoing AVR through median sternotomy were as follows: after general anesthesia and tracheal cannula, the patients were maintained in the supine position, with the sternum split completely under the extracorporeal circulation system. Next, the patients underwent left ventricular venting, aorta occlusion, aortotomy, and perfusion of cardioprotective solution through left and right coronary arteries. The remaining operation procedures were similar as right anterior minithoracotomy.

After treatment, all patients were moved to the cardiac surgical intensive care unit (CSICU) equipped with a ventilator until they were conscious and breathed spontaneously with stable vital signs. Protamine and heparin were given routinely to improve myocardial edema and to stabilize circulation, and warfarin anticoagulation was performed in case of chest drainage less than 100 ml in 6 hours after operation. The patients were transferred to the general ward for further treatment, and electrocardiogram, echocardiography, and anteroposterior and lateral chest X-ray were reviewed before discharge.

2.4. Efficacy Criteria and Endpoints. The efficacy was determined according to the following criteria: the aortic valve returning to normal and the cardiac function recovering to above grade II were regarded as excellent, the aortic valve restoring partially and cardiac function returning to grade I were regarded as good, and no any positive changes on the aortic valve and the cardiac function were regarded as poor. Total cure rate = (excellent + good)/total patients. Before operation and 1 month after operation, the LVEF, left ventricular end diastolic dimension (LVEDD), and left ventricular fractional shortening (LVFS) were detected, respectively, 3 times by multifunctional color echocardiography (Philips, Netherlands). Fasting venous blood (at least fasting 8 hours) (5 ml) was collected before and 3 h after operation. The serum samples were detected by an enzyme-linked immunosorbent assay (ELISA) kit (RapidBio, USA), in order to determine the levels of interleukin-6 (IL-6), interleukin-8 (IL-8), and tumor necrosis factor-α (TNF-α).

2.5. Statistical Analysis. All data were processed by SPSS 25.0 software and were consistent with the normal distribution. The measurement data were described as mean ± standard deviation and analyzed by the t-test. The counting data were defined as a ratio or percentage and analyzed by the chi-squared test. A level of $P < 0.05$ was considered statistically significant.

3. Result

3.1. Efficacy Comparison between AVR through Right Anterior Minithoracotomy and Median Sternotomy. The total curative rate was 88.37% for patients with low LVEF undergoing AVR through right anterior minithoracotomy, including 16 cases (37.21%) defined as excellent, 22 cases (51.16%) defined as good, and 5 cases (11.63%) defined as poor. The total curative rate of patients undergoing AVR through median sternotomy was 86.05%, involving 14 cases (32.56%) defined as excellent, 23 cases (53.49%) defined as good, and 6 cases (13.95%) defined as poor. There was no significant difference in the total curative rate between the two groups ($\chi^2 = 1.167$, $P = 0.093$, Figure 1).

3.2. AVR through Right Anterior Minithoracotomy Improved Intraoperative Indicators. There was no significant difference in surgery time between patients with low

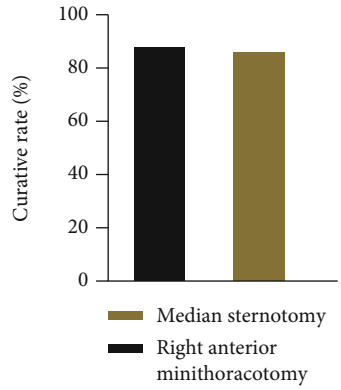

Figure 1: The total curative rate between patients with low LVEF undergoing AVR through right anterior minithoracotomy and patients undergoing AVR through median sternotomy.

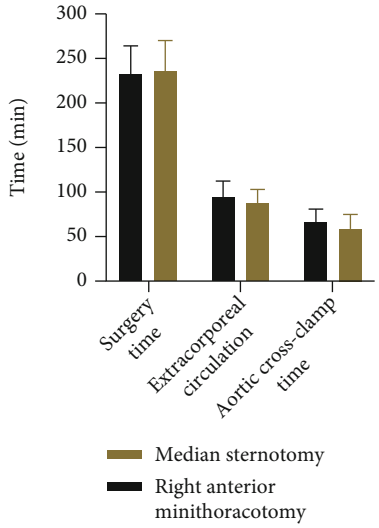

Figure 2: The time of surgery, extracorporeal circulation, and aortic cross-clamping between patients with low LVEF undergoing AVR through right anterior minithoracotomy and patients undergoing AVR through median sternotomy.

LVEF undergoing AVR through right anterior minithoracotomy and patients undergoing AVR through median sternotomy (233.45 ± 30.94 min vs. 236.77 ± 33.96 min, $P > 0.05$). The durations of extracorporeal circulation (95.78 ± 16.23 min vs. 87.67 ± 15.93 min) and aortic cross-clamping (66.79 ± 15.92 min vs. 58.98 ± 15.61 min) in patients undergoing AVR through right anterior minithoracotomy were longer than those in patients undergoing AVR through median sternotomy, respectively ($P < 0.05$, Figure 2).

3.3. AVR through Right Anterior Minithoracotomy Reduced Hospital Stay and Incidence of Postoperative Atrial Fibrillation. For patients undergoing AVR through right anterior minithoracotomy, the length of CSICU stay, the duration of mechanical ventilation, the length of hospital stay, and the volume of chest drainage within 24 h were 1.78 ± 0.28 d, 15.44 ± 5.74 h, 8.68 ± 2.74 d, and 159.85 ± 25.99 ml, respectively. For patients undergoing AVR through

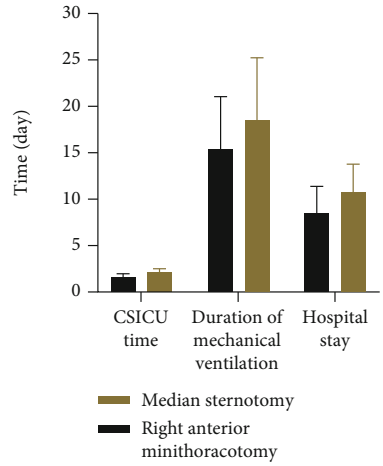

Figure 3: The CSICU stay, hospital stay, and duration of mechanical ventilation between patients with low LVEF undergoing AVR through right anterior minithoracotomy and patients undergoing AVR through median sternotomy.

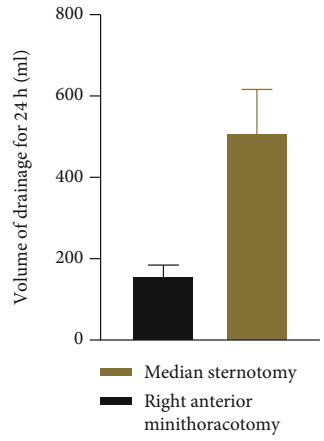

Figure 4: The volume of chest drainage within 24 hours between patients with low LVEF undergoing AVR through right anterior minithoracotomy and patients undergoing AVR through median sternotomy.

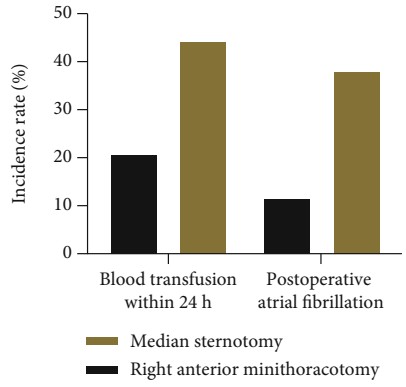

Figure 5: The incidence rates of blood transfusion within 24 h and postoperative atrial fibrillation between patients with low LVEF undergoing AVR through right anterior minithoracotomy and patients undergoing AVR through median sternotomy.

Table 2: Cardiac function between patients with low LVEF undergoing AVR through right anterior minithoracotomy and patients undergoing AVR through median sternotomy.

Group	Case	Time	LVEDD (mm)	LVFS (%)	LVEF (%)
Median sternotomy	43	Before operation	65.66 ± 10.12	26.86 ± 4.23	29.64 ± 5.52
		After operation	53.79 ± 9.63	30.37 ± 4.48	51.37 ± 6.12
Right anterior minithoracotomy	43	Before operation	64.56 ± 8.29	26.92 ± 4.76	29.15 ± 5.04
		After operation	49.02 ± 7.61	37.89 ± 6.68	59.81 ± 7.32
t/P (median sternotomy)			5.632/0.013	6.146/0.001	7.042/0.001
t/P (right anterior minithoracotomy)			14.510/0.001	7.510/0.001	8.050/0.001
t/P (group comparison after treatment)			7.154/0.001	4.972/0.017	6.134/0.001

LVEF: left ventricular ejection fraction; LVEDD: left ventricular end diastolic dimension; LVFS: left ventricular fractional shortening.

Table 3: The levels of inflammatory factors in patients with low LVEF undergoing AVR through right anterior minithoracotomy and patients undergoing AVR through median sternotomy.

Group	Case	Time	IL-6 (pg/ml)	IL-8 (pg/ml)	TNF-α (pg/ml)
Median sternotomy	43	Before operation	99.61 ± 11.35	0.38 ± 0.12	11.84 ± 10.33
		After operation	145.62 ± 29.52	0.80 ± 0.17	25.34 ± 15.94
Right anterior minithoracotomy	43	Before operation	99.38.56 ± 12.05	0.37 ± 0.13	11.82 ± 10.26
		After operation	131.41 ± 27.53	0.67 ± 0.12	21.31 ± 12.18
t/P (median sternotomy)			21.473/0.001	5.384/0.001	10.476/0.001
t/P (right anterior minithoracotomy)			35.296/0.001	4.215/0.017	6.942/0.001
t/P (group comparison after treatment)			14.152/0.001	3.981/0.033	5.172/0.011

IL-6: interleukin-6; IL-8: interleukin-8; TNF-α: tumor necrosis factor-α.

median sternotomy, the length of CSICU stay, the duration of mechanical ventilation, the length of hospital stay, and the volume of chest drainage within 24 h were 2.14 ± 0.57 d, 18.53 ± 6.72 h, 10.78 ± 2.95 d, and 508.97 ± 102.37 ml, respectively. As shown in Figure 3, patients undergoing AVR through right anterior minithoracotomy exhibited declines in the CSICU stay, duration of mechanical ventilation, and the length of hospital stay than those undergoing AVR through median sternotomy ($P < 0.05$). The volumes of 24 h chest drainage were reduced in patients through right anterior minithoracotomy compared with those through median sternotomy ($P < 0.05$, Figure 4). Among patients undergoing AVR through right anterior minithoracotomy, 9 cases (20.93%) required blood transfusion within 24 h, 1 died (2.33%) within 30 d after treatment, 6 cases (13.95%) had ventricular arrhythmia, 2 cases (4.65%) had low cardiac output syndrome, 2 cases (4.65%) had infection, 2 cases (4.65%) had renal failure, 1 case had pleural effusion (2.33%), 2 cases had pneumothorax (4.65%), and 4 cases (9.30%) had atrial fibrillation. Among patients undergoing AVR through median sternotomy, 19 cases (44.19%) required for blood transfusion within 24 h, 2 deaths (4.65%) within 30 d after surgery, 7 cases (16.29%) with ventricular arrhythmia, 3 cases (6.98%) with low cardiac output syndrome, 2 cases (4.65%) with infection, 3 cases (6.98%) with renal failure, 1 case with pleural effusion (2.33%), 3 cases with pneumothorax (6.98%), and 13 cases (30.23%) with atrial fibrillation were observed. The incidence rates of blood transfusion within 24 h and postoperative atrial fibrillation were lower in patients undergoing AVR through right anterior minithoracotomy than those in patients undergoing AVR through median sternotomy ($P < 0.05$, Figure 5). In terms of death within 30 d after surgery, incidence rates of ventricular arrhythmia, low cardiac output syndrome, infection, renal failure, pleural effusion, and pneumothorax, no remarkable difference was found between these two groups of patients ($P > 0.05$).

3.4. AVR through Right Anterior Minithoracotomy Improved Cardiac Function. After AVR through right anterior minithoracotomy or median sternotomy, patients with low LVEF showed declined LVEDD concomitant with elevated LVFS and LVEF ($P < 0.05$). Lower LVEDD with higher LVFS and LVEF was revealed in patients undergoing AVR through right anterior minithoracotomy than those through median sternotomy ($P < 0.05$, Table 2).

3.5. AVR through Right Anterior Minithoracotomy Attenuated Inflammatory Response. To compare the effects of AVR through right anterior minithoracotomy and median sternotomy on inflammatory response of patients with low LVEF, the serum levels of IL-6, IL-8, and TNF-α were determined by ELISA methods before and after surgery. No matter AVR through right anterior minithoracotomy or median sternotomy could reduce the serum levels of IL-6, IL-8, and TNF-α in patients with low LVEF. As listed in Table 3, the serum levels of IL-6, IL-8, and TNF-α were lower in patients

undergoing AVR through right anterior minithoracotomy than those through median sternotomy ($P < 0.05$).

4. Discussion

Aortic valve stenosis and aortic valve regurgitation are the main clinical manifestations of aortic valve diseases, which are very common in valvular heart diseases [28, 29]. Aortic stenosis is the most common valvular heart disease that is associated with aging in developed countries [30–32]. The European system for cardiac operative risk evaluation (EuroSCORE) reports that preoperative low LVEF is a risk factor for heart surgery. According to previous results, patients with aortic valve disease and low LVEF had a poor prognosis after conservative drug therapy, and the 3-year mortality rate is still relatively high [33]. For decades, conventional AVR has been considered the first recommendation for the treatment of aortic valve diseases, especially for severe or symptomatic aortic stenosis [34, 35]. The first AVR was reported in 1962 by Harken et al. [36]. AVR for patients with low LVEF is still challenging, and the prognosis is still controversial. With the development of surgical techniques, a new approach MIAVR was first proposed by Cosgrove and Sabik in 1996. It was reported as an effective treatment with lower costs and less surgical trauma [37, 38]. Several studies have shown that MIAVR achieved much better outcomes compared with conventional AVR [39, 40].

In this study, we analyzed the safety and effectiveness of AVR through right anterior minithoracotomy for treating patients with LVEF. We found that extracorporeal circulation time and aortic cross-clamping time were longer in patients undergoing AVR through right anterior minithoracotomy than those in patients undergoing AVR through median sternotomy. The difference may be explained by limited exposure to the operation field and requirement for high-quality surgical skills. However, the surgery time for patients undergoing AVR through right anterior minithoracotomy or median sternotomy was similar, which may be explained by reduced time of chest closure and blood stopping. These findings were similar to other studies. For instance, Ariyaratnam et al. demonstrated that MIAVR has similar hospital outcomes compared to conventional AVR, and it is quicker and does not confer any significant increase in complications or length of hospital stay [41]. Although there was a slight difference in surgery time between the two groups in our analysis, it is determined by a variety of factors, such as severity of condition on patients, the skill of surgeons, and accident occurrence during operation. According to the data in this study, patients undergoing AVR through right anterior minithoracotomy exhibited declines in the CSICU stay, duration of mechanical ventilation, and the length of hospital stay than those undergoing AVR through median sternotomy. The volumes of 24 h chest drainage were reduced in patients undergoing AVR through right anterior minithoracotomy compared with those undergoing AVR through median sternotomy. The incidence rates of blood transfusion within 24 h and postoperative atrial fibrillation were lower in patients undergoing AVR through right anterior minithoracotomy than those in patients undergoing AVR through median sternotomy. There were more other studies indicating some advantages on the above aspects [17, 21, 42, 43]. Some researches indirectly demonstrated that MIAVR restored the myocardium function of the left ventricles to a certain degree [44–46]. Lower LVEDD with higher LVFS and LVEF was revealed in patients undergoing AVR through right anterior minithoracotomy than those through median sternotomy. The pathobiology of degenerative aortic valve stenosis is complex and involves immunological and inflammatory responses, including oxidized lipids, various cytokines, and biomineralization [47]. In addition, inflammation has received much attention in shaping the biomarker network of aortic valve stenosis [48]. We also found that the serum levels of IL-6, IL-8, and TNF-α were lower in patients undergoing AVR through right anterior minithoracotomy than those through median sternotomy, which suggested that MIAVR made less injury and reduced inflammatory response in patients.

In summary, our study indicates that right anterior minithoracotomy is an alternative, less invasive approach to median sternotomy during AVR for patients with low LVEF, since patients undergoing AVR through right anterior minithoracotomy showed reduced hospital stay and lower incidence of postoperative atrial fibrillation, with decreased pain, limited skin incision, and maintained cardiac function. Considering that this investigation is a retrospective study, further studies including patients with data about sudden cardiac death after a one-year follow-up are required to evaluate the long-term efficacy and safety of AVR through right anterior minithoracotomy for treating patients with low LVEF. Nevertheless, power analysis to ensure sample size was warranted in further prospective studies.

Data Availability

The data used to support the findings of this study are included within the article.

Conflicts of Interest

The authors declare that they have no conflicts of interest.

References

[1] B. Iung and A. Vahanian, "Epidemiology of valvular heart disease in the adult," *Nature Reviews Cardiology*, vol. 8, no. 3, pp. 162–172, 2011.

[2] V. T. Nkomo, J. M. Gardin, T. N. Skelton, J. S. Gottdiener, C. G. Scott, and M. Enriquez-Sarano, "Burden of valvular heart diseases: a population-based study," *Lancet*, vol. 368, no. 9540, pp. 1005–1011, 2006.

[3] B. A. Carabello and W. J. Paulus, "Aortic stenosis," *Lancet*, vol. 373, no. 9667, pp. 956–966, 2009.

[4] P. Urban, M. Rabajdova, I. Spakova et al., "Molecular recognition of aortic valve stenosis and regurgitation," *European review for medical and pharmacological sciences*, vol. 23, no. 24, pp. 10996–11003, 2019.

[5] A. Rassa and F. Zahr, "Hypertension and aortic stenosis: a review," *Current hypertension reviews*, vol. 14, no. 1, pp. 6–14, 2018.

[6] M. Zakkar, A. J. Bryan, and G. D. Angelini, "Aortic stenosis: diagnosis and management," *BMJ*, vol. 355, article i5425, 2016.

[7] O. A. Akinseye, A. Pathak, and U. N. Ibebuogu, "Aortic valve regurgitation: a comprehensive review," *Current problems in cardiology*, vol. 43, no. 8, pp. 315–334, 2018.

[8] M. R. Starling, M. M. Kirsh, D. G. Montgomery, and M. D. Gross, "Mechanisms for left ventricular systolic dysfunction in aortic regurgitation: importance for predicting the functional response to aortic valve replacement," *Journal of the American College of Cardiology*, vol. 17, no. 4, pp. 887–897, 1991.

[9] N. Flint, N. C. Wunderlich, H. Shmueli, S. Ben-Zekry, R. J. Siegel, and R. Beigel, "Aortic regurgitation," *Current Cardiology Reports*, vol. 21, no. 7, p. 65, 2019.

[10] J. J. Thaden, T. Y. Nkomo, and M. Enriquez-Sarano, "The global burden of aortic stenosis," *Progress in Cardiovascular Diseases*, vol. 56, no. 6, pp. 565–571, 2014.

[11] G. Wagner, S. Steiner, G. Gartlehner et al., "Comparison of transcatheter aortic valve implantation with other approaches to treat aortic valve stenosis: a systematic review and meta-analysis," *Systematic reviews*, vol. 8, no. 1, p. 44, 2019.

[12] W. S. Edwards and L. Smith, "Aortic valve replacement with a subcoronary ball valve," *Surgical forum*, vol. 9, pp. 309–313, 1958.

[13] S. Siregar, F. de Heer, R. H. Groenwold et al., "Trends and outcomes of valve surgery: 16-year results of Netherlands Cardiac Surgery National Database," *European Journal of Cardio-Thoracic Surgery*, vol. 46, no. 3, pp. 386–397, 2014.

[14] M. Di Eusanio, D. Fortuna, R. De Palma et al., "Aortic valve replacement: results and predictors of mortality from a contemporary series of 2256 patients," *The Journal of thoracic and cardiovascular surgery*, vol. 141, no. 4, pp. 940–947, 2011.

[15] M. Di Eusanio, W. Vessella, R. Carozza et al., "Ultra fast-track minimally invasive aortic valve replacement: going beyond reduced incisions," *European Journal of Cardio-Thoracic Surgery*, vol. 53, suppl_2, pp. ii14–ii18, 2018.

[16] T. C. Nguyen, M. D. Terwelp, V. H. Thourani et al., "Clinical trends in surgical, minimally invasive and transcatheter aortic valve replacementdagger," *European Journal of Cardio-Thoracic Surgery*, vol. 51, no. 6, pp. 1086–1092, 2017.

[17] M. Jahangiri, A. Hussain, and E. Akowuah, "Minimally invasive surgical aortic valve replacement," *Heart*, vol. 105, Suppl 2, pp. s10–s15, 2019.

[18] M. Glauber, M. Ferrarini, and A. Miceli, "Minimally invasive aortic valve surgery: state of the art and future directions," *Annals of cardiothoracic surgery*, vol. 4, no. 1, pp. 26–32, 2015.

[19] R. K. Ghanta, D. J. Lapar, J. A. Kern et al., "Minimally invasive aortic valve replacement provides equivalent outcomes at reduced cost compared with conventional aortic valve replacement: a real-world multi-institutional analysis," *The Journal of thoracic and cardiovascular surgery*, vol. 149, no. 4, pp. 1060–1065, 2015.

[20] R. Q. Attia, G. L. Hickey, S. W. Grant et al., "Minimally invasive versus conventional aortic valve replacement: a propensity-matched study from the UK national data," *Innovations*, vol. 11, no. 1, pp. 15–23, 2016.

[21] M. Seitz, J. Goldblatt, E. Paul, T. Marcus, M. Larobina, and C. H. Yap, "Minimally invasive aortic valve replacement via right infra-axillary mini-thoracotomy: propensity matched initial experience," *Heart, Lung and Circulation*, vol. 28, no. 2, pp. 320–326, 2019.

[22] A. Kosaraju, A. Goyal, Y. Grigorova, and A. N. Makaryus, "Left ventricular ejection fraction," in *StatPearls*, Treasure Island (FL), 2021.

[23] N. N. Aljaber, Z. A. Mattash, S. A. Alshoabi, and F. H. Alhazmi, "The prevalence of left ventricular thrombus among patients with low ejection fraction by trans-thoracic echocardiography," *Pakistan Journal of Medical Sciences*, vol. 36, no. 4, pp. 673–677, 2020.

[24] J. Yeboah, C. J. Rodriguez, W. Qureshi et al., "Prognosis of low normal left ventricular ejection fraction in an asymptomatic population-based adult cohort: the multiethnic study of atherosclerosis," *Journal of Cardiac Failure*, vol. 22, no. 10, pp. 763–768, 2016.

[25] L. H. Lund, "Heart failure with mid-range ejection fraction: lessons from CHARM," *Cardiac failure review*, vol. 4, no. 2, pp. 70–72, 2018.

[26] C. S. Lam and S. D. Solomon, "The middle child in heart failure: heart failure with mid-range ejection fraction (40-50%)," *European Journal of heart failure*, vol. 16, no. 10, pp. 1049–1055, 2014.

[27] P. Ponikowski, A. A. Voors, S. D. Anker et al., "2016 ESC guidelines for the diagnosis and treatment of acute and chronic heart failure: the Task Force for the diagnosis and treatment of acute and chronic heart failure of the European Society of Cardiology (ESC) developed with the special contribution of the Heart Failure Association (HFA) of the ESC," *The European Heart Journal*, vol. 37, no. 27, pp. 2129–2200, 2016.

[28] P. G. Supino, J. S. Borer, J. Preibisz, and A. Bornstein, "The epidemiology of valvular heart disease: a growing public health problem," *Heart failure clinics*, vol. 2, no. 4, pp. 379–393, 2006.

[29] K. Maganti, V. H. Rigolin, M. E. Sarano, and R. O. Bonow, "Valvular heart disease: diagnosis and management," *Mayo Clinic Proceedings*, vol. 85, no. 5, pp. 483–500, 2010.

[30] M. Van Hemelrijck, M. Taramasso, C. De Carlo et al., "Recent advances in understanding and managing aortic stenosis," *F1000Research*, vol. 7, p. 58, 2018.

[31] B. R. Lindman, M. A. Clavel, P. Mathieu et al., "Calcific aortic stenosis," *Nature reviews Disease primers*, vol. 2, article 16006, 2016.

[32] J. G. Schnitzler, L. Ali, A. G. Groenen, Y. Kaiser, and J. Kroon, "Lipoprotein(a) as orchestrator of calcific aortic valve stenosis," *Biomolecules*, vol. 9, no. 12, p. 760, 2019.

[33] R. A. Spampinato, R. Bochen, F. Sieg et al., "Multi-biomarker mortality prediction in patients with aortic stenosis undergoing valve replacement," *Journal of Cardiology*, vol. 76, no. 2, pp. 154–162, 2020.

[34] S. Arora, J. A. Misenheimer, and R. Ramaraj, "Transcatheter aortic valve replacement: comprehensive review and present status," *Texas Heart Institute Journal*, vol. 44, no. 1, pp. 29–38, 2017.

[35] R. Bilkhu, M. A. Borger, N. P. Briffa, and M. Jahangiri, "Sutureless aortic valve prostheses," *Heart*, vol. 105, Suppl 2, pp. s16–s20, 2019.

[36] D. E. Harken, W. J. Taylor, A. A. Lefemine et al., "Aortic valve replacement with a gaged ball valve," *American Journal of Cardiology*, vol. 9, no. 2, pp. 292–299, 1962.

[37] D. M. Cosgrove 3rd and J. F. Sabik, "Minimally invasive approach for aortic valve operations," *The Annals of thoracic surgery*, vol. 62, no. 2, pp. 596-597, 1996.

[38] L. H. Cohn, D. H. Adams, G. S. Couper et al., "Minimally invasive cardiac valve surgery improves patient satisfaction while

reducing costs of cardiac valve replacement and repair," *Annals of surgery*, vol. 226, no. 4, pp. 421–426, 1997.

[39] J. Lamelas, A. Sarria, O. Santana, A. M. Pineda, and G. A. Lamas, "Outcomes of minimally invasive valve surgery versus median sternotomy in patients age 75 years or greater," *The annals of thoracic surgery*, vol. 91, no. 1, pp. 79–84, 2011.

[40] M. Glauber, A. Miceli, D. Gilmanov et al., "Right anterior minithoracotomy versus conventional aortic valve replacement: a propensity score matched study," *The Journal of thoracic and cardiovascular surgery*, vol. 145, no. 5, pp. 1222–1226, 2013.

[41] P. Ariyaratnam, M. Loubani, and S. C. Griffin, "Minimally invasive aortic valve replacement: comparison of long-term outcomes," *Asian Cardiovascular and Thoracic Annals*, vol. 23, no. 7, pp. 814–821, 2015.

[42] D. Gilmanov, S. Bevilacqua, M. Murzi et al., "Minimally invasive and conventional aortic valve replacement: a propensity score analysis," *The Annals of thoracic surgery*, vol. 96, no. 3, pp. 837–843, 2013.

[43] A. Harky, A. Al-Adhami, J. S. K. Chan, C. H. M. Wong, and M. Bashir, "Minimally invasive versus conventional aortic root replacement - a systematic review and meta-analysis," *Heart, Lung and Circulation*, vol. 28, no. 12, pp. 1841–1851, 2019.

[44] M. Asami, T. Pilgrim, J. Lanz et al., "Prognostic relevance of left ventricular myocardial performance after transcatheter aortic valve replacement," *Circulation: Cardiovascular Interventions*, vol. 12, no. 1, article e006612, 2019.

[45] A. E. Duncan, S. Sarwar, B. Kateby Kashy et al., "Early left and right ventricular response to aortic valve replacement," *Anesthesia and analgesia*, vol. 124, no. 2, pp. 406–418, 2017.

[46] D. Han, B. Tamarappoo, E. Klein et al., "Computed tomography angiography-derived extracellular volume fraction predicts early recovery of left ventricular systolic function after transcatheter aortic valve replacement," *European Heart Journal-Cardiovascular Imaging*, vol. 22, no. 2, pp. 179–185, 2021.

[47] K. I. Cho, I. Sakuma, I. S. Sohn, and S. H. Jo, "Inflammatory and metabolic mechanisms underlying the calcific aortic valve disease," *Atherosclerosis*, vol. 277, pp. 60–65, 2018.

[48] G. G. Schiattarella and C. Perrino, "Inflammation in aortic stenosis: shaping the biomarkers network," *International Journal of Cardiology*, vol. 274, pp. 279-280, 2019.

Hindawi
Journal of Nanomaterials
Volume 2021, Article ID 9985899, 7 pages
https://doi.org/10.1155/2021/9985899

Research Article

Risk Factors Associated with the Incidence of Ventricular Arrhythmias Complicating Acute Myocardial Infarction and Prognosis Analysis

Guibin Li, Shengxin Liu, Jiali Jin, Kejun Ding, and Caizhen Qian

Department of Cardiology, Zhuji People's Hospital, China

Correspondence should be addressed to Caizhen Qian; wsygr1988@163.com

Received 10 March 2021; Accepted 11 May 2021; Published 1 June 2021

Academic Editor: Songwen Tan

Ventricular arrhythmias (VTA) usually occur following acute myocardial infarction (AMI). However, risk factors for VTA attack after AMI have been not well-recognized. The purpose of the study is to identify risk factors associated with the incidence of VTA complicating AMI. A total of 200 patients with AMI who were admitted to our hospital from February 2018 to February 2020 were retrospectively analyzed. These 200 patients were classified into a non-VTA group ($n = 140$) and a VTA group ($n = 60$) based on the occurrence of VTA within 24 after AMI. Patients in the VTA group were older than those in the non-VTA group. The VTA group had more numbers of WBCs and neutrophils than the non-VTA group. The level of serum potassium was lower, but the levels of cTnT and CK-MB were higher in the VTA group than in the non-VTA group. The VTA group presented an increase in proportions of anterior MI, TpTe, and proportions of Killip classification ≥ class II but a decline in LVEF when comparable to the non-VTA group. The two groups were not significantly different concerning other variables including sex, tobacco use, alcohol consumption, diabetes mellitus, hypertension, heart rate, Scr, SUA, BUN, PTL counts, TC, TG, HDL-C, LDL-C, D-dimer, BNP, LVS, LVP, and LVEDd. The levels of hsCRP, endothelin-1, and TNF-α were remarkably higher in the VTA group than in the non-VTA group ($P < 0.001$). Multivariate logistic regression analysis was performed, with clinical variables including age, WBCs, neutrophils, serum potassium, cTnT, CK-MB, hsCRP, endothelin-1, TNF-α, anterior MI, TpTe, proportions of Killip classification ≥ class II, and LVEF as an independent variable and with the occurrence of VTA as a dependent variable. It was revealed that serum potassium, cTnT, CK-MB, hsCRP, endothelin-1, TpTe, proportions of Killip classification ≥ class II, and LVEF were independent risk factors of VTA complicating AMI. Compared with the non-VTA group, the incidence rate of simple left heart failure, total heart failure, stroke, and dyslipidemia in the VTA group was significantly higher than those in the non-VTA group ($P < 0.05$). It was found that the proportion of all-cause deaths within one year outside the hospital was higher in the VAT group than in the non-VAT group ($P < 0.05$). Collectively, the study demonstrates serum potassium, cTnT, CK-MB, hsCRP, endothelin-1, TpTe, proportions of Killip classification ≥ class II, and LVEF were independent risk factors of VTA complicating AMI.

1. Background

Acute myocardial infarction (AMI) is myocardial necrosis caused by acute and persistent ischemia and hypoxia of coronary arteries [1]. AMI is accompanied by increased serum myocardial enzyme activity and progressive changes in an electrocardiogram, which can be complicated by arrhythmia, shock, or heart failure, and can often be life-threatening [2]. Sudden cardiac death results from sustained ventricular arrhythmia (VTA) and ventricular fibrillation complicating AMI in approximately 20-50% of cases [3]. VTA is a serious sequela of ventricular remodeling after MI. It is often replaced by weak fibrous tissue scars and necrotic myocardium in the infarct area. The diseased ventricular wall abducts and bulges, causing the myocardium in the necrotic area to lose its contractile function, and the local ventricular muscle compliance decreases and abnormal movement occurs, forming a left ventricular aneurysm. Owing to the high incidence of coronary artery disease, the number of sudden cardiac deaths each year in the general population is

estimated at 250/million, with rates remaining stable during the past decade [4]. Deaths of AMI patients are often sudden, which is closely related to VTA attack, especially the cardiogenicity caused by malignant VTA with hemodynamic disorders [5]. In recent years, the treatment and prediction of VTA have been continuously developed, and many new technologies have been continuously applied in this field.

The incidence and mortality of VTA are high in the early stage of AMI. Therefore, it has become the focus of clinical research to find an effective predictor of VTA and to carry out risk stratification. Henkel et al. reported that the incidence of malignant VTA in patients with acute myocardial infarction was 1.9%-10.2%, and the risk of death was 6 times higher than that in patients without VTA after AMI [6]. Sanjuan et al. reported that the incidence of VTA in the early stage of AMI was 20.0%, and its mortality was 3.3 times of that in the non-VTA patients [7]. The main mechanisms underlying VA attack during the acute stage of AMI are electrolyte and autonomic imbalance concomitant with declined pH leading to increased tissue excitability, enhanced automaticity, and finally in electrical instability [8]. According to the available data, predictors independently associated with ventricular tachycardia and ventricular fibrillation are continuously characterized, such as atrial fibrillation, cardiogenic shock, baseline heart rhythm more than 70 beats/min, chronic kidney disease, family history of sudden cardiac death, left main stenosis, low serum potassium concentration, and ST resolution less than 70% [9]. Of note, there are still significant challenges in risk stratification for VTA.

2. Materials and Methods

2.1. Patient Population. A total of 213 patients with AMI who were admitted to the Department of Cardiology of our hospital from February 2018 to February 2020 were initially selected into this retrospective study. Each patient had coronary angiography, and subsequent PCI was performed without any delay. The culprit vessels of MI involve the left main coronary artery, left anterior descending coronary artery, left circumflex coronary artery, and right coronary artery, classifying as anterior wall involvement and nonanterior wall involvement. After surgery, antiplatelet therapy was performed. Finally, the study encompassed 200 participants with informed content per patient and with the approval of the Ethics Committee of our hospital, as we excluded 13 patients considering the following exclusion criteria: history of cardiopulmonary resuscitation, infectious diseases, or myocarditis symptoms; severe skeletal muscle injury or trauma; previous history of AMI; AMI diagnosed in other hospitals and transferred into our hospital for further treatment; MI lasted more than 24 hours; history of PCI and coronary artery bypass grafting; history of rheumatic disease and nephropathy; and oral administration of antiarrhythmic drugs within 2 weeks. These 200 patients were classified into a non-VTA group and a VTA group based on the occurrence of VTA within 24 after AMI.

2.2. The Diagnosis of AMI. The diagnosis of AMI was made in accordance with a consensus document of The Joint European Society of Cardiology/American College of Cardiology Committee for the redefinition of myocardial infarction [10, 11]: significant elevations of sensitive and specific biomarkers, such as cardiac troponin T (cTnT) and creatine kinase-myocardial band isoenzyme (CK-MB); ischemic symptoms, such as chest pain lasting at least 20 min; ST segment elevation in two or more limb or precordial leads.

2.3. Detection of VTA. All these patients were monitored by the standard 12-lead 24-hour electrocardiogram (EGG) at admission to the hospital, and the electrocardiographic T wave and Q wave (QT) intervals were measured by the authors without the knowledge of any outcome values. The diagnostic criteria considered for VTA were as follows: ventricular tachycardia, defined as three or more consecutive ventricular complexes at a rate of greater than 120 beats/min; premature ventricular contractions (PVCs) including frequent (>5 isolated unifocal beats/min), bigeminy (alternate sinus and ventricular beats), multifocal (multifocal beats in the same hour of recording), couplets (two consecutive ventricular beats, R-on-T according to $\text{R-R}'/\text{R-T} < 0.85$), and overall frequency (total number of PVCs in the recording divided by the number of analyzable hours and expressed as the number per hour).

2.4. Data Collection and Outcome Measures. Outcome analysis was performed on the following indicators: sex, age, tobacco use, alcohol consumption, diabetes mellitus, hypertension, heart rate, white blood cells (WBCs), neutrophils, glycosylated hemoglobin (HbA1C), blood glucose, serum potassium, serum creatinine (Scr), serum uric acid (SUA), blood urea nitrogen (BUN), platelet (PTL) count, total cholesterol (TC), triglycerides (TG), high-density lipoprotein cholesterol (HDL-C), low-density lipoprotein cholesterol (LDL-C), blood-D-dimer, B-type natriuretic peptide (BNP), cTnT, CK-MB, high-sensitivity C-reactive protein (hsCRP), endothelin-1, TNF-α, anterior or nonanterior MI, the interval from the peak to the end of the T wave (TpTe), Killip classification of cardiac function at admission, ventricular septal thickness (LVS), left ventricular posterior wall thickness (LVP), left ventricular end-diastolic diameter (LVEDd), and left ventricular ejection fraction (LVEF).

2.5. Laboratory Analysis. Blood samples were drawn from each patient at admission into the hospital and collected into tubes supplemented with ethylenediaminetetraacetic acid. The levels of HbA1C, GLA, blood glucose, serum potassium, Scr, SUA, BUN, TC, TG, LDL-C, and HDL-C were measured by an automatic biochemistry analyzer (Hitachi 7150, Hitachi Ltd., Tokyo, Japan). Peripheral blood platelets were counted by an automated hematology analyzer (Hemato-Flow, Beckman Coulter, USA). D-Dimer was evaluated by an immunoturbidimetric assay using the Advanced D-Dimer assay (Dade-Behring, Deerfield, IL, USA) and CRP using BeckmannAssay360 (Beckman, Bera, CA, USA). Plasma B-type natriuretic peptide (BNP) levels were ascertained using a high-sensitivity immunoradiometric assay (Shionogi, Osaka, Japan). The concentration of cTnT was examined by immunoassay (Elecsys 1020, Boehringer

Table 1: Significant difference concerning clinical variables between AMI patients with or without VTA occurrence.

Variable	VTA group ($n = 60$)	Non-VTA group ($n = 140$)	χ^2/t	P
Age (years)	68.95 ± 10.68	57.64 ± 10.36	5.67	<0.001
WBCs ($\times 10^9$ cells/L)	15.73 ± 2.68	11.84 ± 3.49	7.71	<0.001
Neutrophils ($\times 10^9$ cells/L)	13.53 ± 1.12	9.45 ± 2.89	10.59	<0.001
Potassium (mmol/L)	3.50 ± 0.33	4.10 ± 0.33	10.28	<0.001
cTnT (ng/mL)	6.38 ± 3.88	4.79 ± 2.99	3.14	0.002
CK-MB (U/L)	204.69 ± 90.23	178.54 ± 8.62	3.40	<0.001
Anterior MI (n (%))	40 (66.7%)	71 (50.7%)	2.08	0.037
TpTe (ms)	140.52 ± 28.32	123.88 ± 32.87	3.41	<0.001
Killip class II (n (%))	13 (21.7%)	14 (10.0%)	2.21	0.027
LVEF (%)	55.26 ± 13.25	58.96 ± 10.35	2.12	0.035

$P < 0.05$ means significant difference.

Mannheim Diagnostics, Germany), and the activity of CK-MB was examined by the immune inhibition method (Synchron CX9, Beckman Coulter, USA). TNF-α was measured by the enzyme-linked immunosorbent assay (ELISA) kit (Biosource, Camarillo, CA) and endothelin-1 by the ELISA kit (Enzo Life Sciences, Switzerland).

2.6. Killip Classification of Cardiac Function. Killip classification was performed for clinical estimate of cardiac function [11]. Class I is defined no observation of heart failure with an elevation in pulmonary capillary wedge pressure. Class II is defined as mild and moderate heart failure with rales, S3 gallop and pulmonary venous hypertension, pulmonary congestion, and wet rales in the lower half of the lung fields. Class III is defined as severe heart failure with evident pulmonary edema with rales throughout the lung fields. Class IV is defined as cardiogenic shock with a sign of hypotension (systolic blood pressure < 90 mmHg) and evidence of peripheral vasoconstriction such as oliguria, cyanosis, and diaphoresis.

2.7. Statistical Methods. SPSS22.0 software was employed to perform data management and analysis. Continuous variables are expressed as mean ± standard deviation and compared by the t test. Categorical variables are expressed as proportions and analyzed using the chi-square test or Fisher's exact probability method. Univariate and multivariate logistic regression analyses were used to determine the independent risk factors of AMI patients with VTA occurrence. $P < 0.05$ is considered as statistically significant.

3. Result

3.1. Baseline Characteristics. Totally, 200 patients with AMI were finally included into the study; we further split patients into two groups: VTA group ($n = 60$) and non-VTA group ($n = 140$). The detailed data regarding comparison of clinical and laboratory characteristics among patients with and without VTA are shown in Tables 1 and 2. As shown in Table 1, patients in the VTA group exhibited remarkable difference from those in the non-VTA group in terms of age, WBCs, neutrophils, serum potassium, cTnT, CK-MB, anterior MI, TpTe, proportions of Killip classification ≥ class II, and LVEF ($P < 0.05$). Patients in the VTA group were older than those in the non-VTA group. The VTA group had more numbers of WBCs and neutrophils than the non-VTA group. The level of serum potassium was lower, but the levels of cTnT and CK-MB were higher in the VTA group than in the non-VTA group. The VTA group presented an increase in proportions of anterior MI, TpTe, and proportions of Killip classification ≥ class II but a decline in LVEF when comparable to the non-VTA group. As shown in Table 2, the two groups were not significantly different concerning other variables including sex, tobacco use, alcohol consumption, diabetes mellitus, hypertension, heart rate, Scr, SUA, BUN, PTL counts, TC, TG, HDL-C, LDL-C, D-dimer, BNP, LVS, LVP, and LVEDd.

3.2. Levels of hsCRP, Endothelin-1, and TNF-α Were Associated with VTA Attack. It has been reported that hsCRP may serve as a predictor of short-term and long-term mortality after acute coronary syndromes. Endothelin-1 is an important vasoconstricting substance, and its rapid elevation in plasma is related to the onset of AMI. TNF-α has been well-studied for its deleterious cardiovascular effects. Thereupon, we were wondering the relationship between hsCRP, endothelin-1, TNF-α, and VTA attack. As we detected, the levels of hsCRP, endothelin-1, and TNF-α were remarkably higher in the VTA group than in the non-VTA group ($P < 0.001$, Figure 1).

3.3. Independent Risk Factors of VTA Complicating AMI. In order to find out independent risk factors of VTA complicating AMI, multivariate logistic regression analysis was performed, with clinical variables including age, WBCs, neutrophils, serum potassium, cTnT, CK-MB, hsCRP, endothelin-1, TNF-α, anterior MI, TpTe, proportions of Killip classification ≥ class II, and LVEF as an independent variable and with the occurrence of VTA as a dependent variable. It was revealed that serum potassium, cTnT, CK-MB, hsCRP, endothelin-1, TpTe, proportions of Killip classification ≥ class II, and LVEF were independent risk factors of VTA complicating AMI (Table 3).

Table 2: Comparison of baseline variables between AMI patients with or without VTA occurrence.

Variable	VTA group ($n = 60$)	Non-VTA group ($n = 140$)	χ^2/t	P
Sex/male	45 (75.00%)	100 (71.45%)	0.518	0.604
Tobacco use (n (%))	33 (55%)	85 (60.7%)	1.26	0.09
Alcohol consumption (n (%))	15 (25%)	26 (18.5%)	1.87	0.16
Hypertension (n (%))	35 (58.3%)	78 (55.7%)	1.54	0.19
Diabetes mellitus (n (%))	13 (21.7%)	40 (28.5%)	0.57	0.26
Heart rate (time/min)	80.69 ± 13.64	80.34 ± 14.67	0.38	0.64
HbA1C (%)	6.47 ± 1.54	6.28 ± 2.88	0.482	0.630
Blood glucose (mmol/L)	8.77 ± 3.29	8.98 ± 4.99	0.299	0.765
Scr (μmol/L)	81.15 ± 28.24	83.09 ± 37.43	0.360	0.719
SUA (mmol/L)	372.97 ± 28.72	381.63 ± 37.48	0.247	0.805
BUN (mmol/L)	6.87 ± 2.59	7.11 ± 2.57	0.604	0.547
PTL ($\times 10^9$ cells/L)	268.41 ± 109.78	250.20 ± 144.22	0.875	0.383
TC (mmol/L)	4.69 ± 1.44	4.40 ± 1.24	1.443	0.151
TG (mmol/L)	1.75 ± 0.68	1.79 ± 0.67	0.385	0.701
HDL-C (mmol/L)	1.32 ± 0.43	1.37 ± 0.65	0.546	0.585
LDL-C (mmol/L)	2.79 ± 0.67	2.71 ± 0.54	0.891	0.374
D-dimer (μg/mL)	1.55 ± 0.40	1.39 ± 0.83	1.423	0.156
BNP (pg/mL)	183.78 ± 89.54	179.55 ± 65.29	0.373	0.710
LVS (mm)	9.50 ± 0.75	9.68 ± 0.53	1.931	0.055
LVP (mm)	9.53 ± 0.65	9.71 ± 0.82	1.509	0.133
LVEDd (mm)	52.33 ± 9.53	51.68 ± 6.29	0.569	0.570

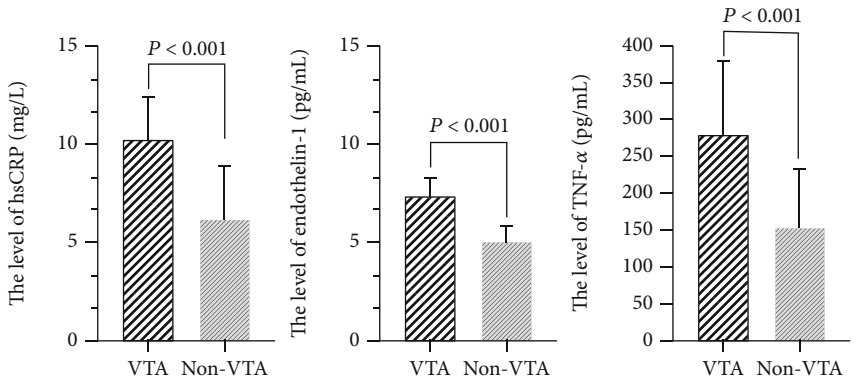

Figure 1: The levels of hsCRP, endothelin-1, and TNF-α between the AMI patients with or without VTA attack.

Table 3: Multivariate logistic regression analysis for independent risk factors of VTA complicating AMI.

Independent variable	OR (95% CI)	P
Serum potassium	3.012 (1.356-4.578)	<0.001
cTnT	2.434 (1.410-3.766)	0.004
CK-MB	1.968 (1.211-3.112)	0.009
hsCRP	1.593 (1.120-2.491)	0.019
Endothelin-1	2.742 (1.714-4.157)	0.027
TpTe	7.224 (2.613-17.97)	<0.001
Killip classification ≥ class II	1.874 (1.033-3.174)	0.034

3.4. Association between Hospitalization Complications and VTA Occurrence. Among the selected patients, compared with the non-VTA group, the incidence rate of simple left heart failure, total heart failure, stroke, and dyslipidemia in the VTA group was significantly higher than those in the non-VTA group ($P < 0.05$). In terms of other complications between the two groups, including atrial fibrillation, ventricular fibrillation, cardiac arrest, pulmonary hypertension, hypotension, cardiogenic shock, left ventricular mural thrombus, lung infection, renal impairment, anemia, hypoproteinemia, and syncope, no statistical difference was exhibited ($P > 0.05$, Table 4).

Table 4: Association between hospitalization complications and VTA occurrence.

Complications	VTA group ($n = 60$)	Non-VTA group ($n = 140$)	χ^2	P
Atrial fibrillation	5 (8.3%)	11 (7.83%)	0.114	0.909
Ventricular fibrillation	4 (6.6%)	7 (11.7%)	0.473	0.636
Cardiac arrest	2 (3.3%)	3 (2.14%)	0.494	0.621
Pulmonary hypertension	2 (3.3%)	5 (3.5%)	0.084	0.933
Simple left heart failure	20 (33%)	15 (10.7%)	3.858	<0.001
Total heart failure	11 (18.3%)	2 (1.4%)	4.444	<0.001
Hypotension	2 (3.3%)	3 (2.1%)	0.494	0.621
Cardiogenic shock	3 (5%)	6 (4.2%)	0.223	0.823
Left ventricular mural thrombus	3 (5%)	2 (1.4%)	1.482	0.138
Stroke	20 (33%)	4 (2.8%)	6.078	<0.001
Lung infection	13 (21.6%)	16 (11.4%)	1.884	0.595
Renal impairment	8 (13.3%)	16 (11.4%)	1.210	0.090
Anemia	4 (6.7%)	3 (2.1%)	1.595	0.110
Hypoproteinemia	3 (5%)	2 (1.4%)	1.482	0.138
Dyslipidemia	15 (25%)	16 (11.4%)	2.430	0.015
Syncope	1 (1.7%)	0 (0%)	1.531	0.126

Table 5: Association between the short-term and long-term of all-cause death and VTA attack.

Death	VTA group ($n = 60$)	Non-VTA group ($n = 140$)	χ^2	P
All-cause deaths in the hospital	2 (3.3%)	1 (0%)	1.396	0.163
All-cause deaths within 1 year outside the hospital	8 (13.3%)	1 (0.7%)	3.945	<0.001

3.5. Association between the Short-Term and Long-Term of All-Cause Death and VTA Attack. Patients were followed up one year by clinic or using telephone conducted by trained nurses or doctors who were blinded to the information of patients until all-cause death occurred or through to the last day of the follow-up. All-cause death was defined as death mainly due to AMI, stroke, congestive heart failure, and malignant arrhythmia. There were 2 (3.3%) cases of all-cause deaths in the hospital in the VTA group and 1 case in the non-VTA group. There were 8 (13.3%) cases of all-cause deaths in the hospital in the VTA group and only 1 case in the non-VTA group. It was found that the proportion of all-cause deaths within one year outside the hospital was higher in the VAT group than in the non-VAT group, and the difference was statistically significant ($P < 0.05$). There was no significant difference in the proportion of all-cause deaths in the hospital between the two groups ($P > 0.05$, Table 5). These data suggested that VTA attack following AMI was associated with the long-term of mortality.

4. Discussion

In clinical work, VTA is one of the most common complications of acute MI, which significantly increases the mortality rate. Potential risk factors related to the occurrence of VTA have been confirmed recently, including low LVEF, heart function, NYHA grade ≥ 3, male, persistent electrical asynchrony, and increased transmural repolarization dispersion [12–14]. Among them, the most abundant evidence is recognized as the strongest predictor of LVEF, which is also the strongest predictor of sudden cardiac death [15]. Ventricular premature beats are the most common arrhythmia in clinical practice, often appearing in normal people or patients with structural heart disease. The pathogenesis of ventricular premature beats mainly involves changes in sympathetic nerve tension that cause abnormalities in cardiomyocyte autonomy, microreentry loops, and triggering activities. Another finding of this study is that frequent ventricular premature beats are one of the risk predictors of VTA in VTA patients. A meta-analysis pointed out that frequent ventricular premature beats can increase the risk of adverse events in patients with nonstructural heart disease [16]. For structural heart disease, especially after MI, frequent ventricular premature beats are significantly associated with increased mortality [17]. Another finding of this study is that frequent ventricular premature beats are one of the risk predictors of VTA patients. VTA patients themselves are complicated with severe myocardial ischemia and involve cardiac structure and electrocardiographic remodeling. The heart foundation is poor, and the ventricular transmural negative dispersion increases. Premature ventricular beats, especially R on T ventricular premature beats, are prone to occur. There is a difference in electrical conductance between the scar edge and the surrounding viable myocardium. Premature ventricular beats originating around the scar can easily trigger scar reentrant VTA. Frequent ventricular premature beats increase the chance of VTA to a certain extent. Traditional

experience believes that inferior MI is mostly caused by occlusion of the right coronary artery and left circumflex artery, and the branches of the arteries supplying the sinoatrial node and atrioventricular node mostly originate from the right coronary artery, so inferior MI is easily complicated by slowness arrhythmia, including sick sinus syndrome, I-III degree atrioventricular block [18]. Left anterior descending artery occlusion and extensive anterior wall MI are themselves two strong predictors of VTA and further combined with inferior MI, suggesting a large infarct size and severe vascular disease [19]. Myocardial electrical remodeling is more significant with neural remodeling, and its neurohumoral effect activation, increased sympathetic nerve tension, and cardiac electrical homeostasis imbalances, and other related factors that cause malignant VTA, have been further aggravated, which has promoted the formation of ECG reentry loops and ventricular in patients with VTA.

Our results revealed that serum potassium, cTnT, CK-MB, hsCRP, endothelin-1, TpTe, proportions of Killip classification ≥ class II, and LVEF were independent risk factors of VTA complicating AMI. Colombo et al. reported that short- and long-term mortality and the occurrence of VTA in patients with AMI were negatively linked with serum potassium concentration [20]. cTnT has been suggested as a new, more specific marker of myocardial cellular damage compared with CK-MB. The secretion of CK-MB seems to be affected by the duration of resuscitation and the presence of cardiogenic shock, which has to be considered when analyzing serum CK-MB levels after cardiopulmonary resuscitation. The elevation of cTnT appears to be only associated with AMI, but not with the duration of chest compressions, or with the number of defibrillations administered. Given that, it is necessary to detect cTnT and CK-MB post-AMI. In a study performed by Anderson et al., they found that hsCRP was increased in AMI patients (4.69 mg/L) compared with controls (2.69 mg/L) [21]. Although our results failed to found a relationship between BNP and the occurrence of VTA, Blangy et al. demonstrated an increased serum BNP and an increased hsCRP were associated with a higher incidence of ventricular tachycardia [22]. The plasmatic levels of endothelin-1 and related peptides produced during the synthesis of endothelin-1 from its precursor molecule preproendothelin-1 were considered as potential risk markers for cardiovascular events. The associations of endothelin-1 with aging, blood pressure, lung function, and chronic kidney disease have been reported, as their association between endothelin-1 levels and evidence of cardiac remodeling, including increased left atrial diameter and left ventricular mass [23]. Novo et al. also supported the role of endothelin-1 in cardiovascular diseases, as its plasmatic levels affected the cardiovascular and cerebrovascular risk profile [24].

In this study, we also compared the hospitalization complications between the two groups. Among the selected patients, compared with the non-VTA group, the incidence of simple left heart failure, total heart failure, stroke, and dyslipidemia in the VTA group was significantly higher than those in the non-VTA group. In terms of other complications between the two groups, including atrial fibrillation, ventricular fibrillation, cardiac arrest, pulmonary hypertension, hypotension, cardiogenic shock, left ventricular mural thrombus, lung infection, renal impairment, anemia, hypoproteinemia, and syncope, no statistical difference was exhibited. Patients were followed up for one year. We found the proportion of all-cause deaths within 1 year was higher in the VAT group than in the Non-VAT group, and the difference was statistically significant. There was no significant difference in the proportion of all-cause deaths in the hospital between the two groups.

Altogether, the study demonstrates serum potassium, cTnT, CK-MB, hsCRP, endothelin-1, TpTe, proportions of Killip classification ≥ class II, and LVEF were independent risk factors of VTA complicating AMI.

Data Availability

The data used to support the findings of this study are included within the article.

Conflicts of Interest

The authors declare that they have no conflicts of interest.

References

[1] G. Arora and V. Bittner, "Chest pain characteristics and gender in the early diagnosis of acute myocardial infarction," *Current Cardiology Reports*, vol. 17, no. 2, p. 5, 2015.

[2] G. W. Reed, J. E. Rossi, and C. P. Cannon, "Acute myocardial infarction," *Lancet*, vol. 389, no. 10065, pp. 197–210, 2017.

[3] A. H. Bui and J. W. Waks, "Risk stratification of sudden cardiac death after acute myocardial infarction," *The Journal of Innovations in Cardiac Rhythm Management*, vol. 9, no. 2, pp. 3035–3049, 2018.

[4] T. M. Kolettis, "Coronary artery disease and ventricular tachyarrhythmia: pathophysiology and treatment," *Current Opinion in Pharmacology*, vol. 13, no. 2, pp. 210–217, 2013.

[5] V. P. Kuriachan, G. L. Sumner, and L. B. Mitchell, "Sudden cardiac death," *Current Problems in Cardiology*, vol. 40, no. 4, pp. 133–200, 2015.

[6] D. M. Henkel, B. J. Witt, B. J. Gersh et al., "Ventricular arrhythmias after acute myocardial infarction: a 20-year community study," *American Heart Journal*, vol. 151, no. 4, pp. 806–812, 2006.

[7] R. Sanjuan, M. L. Blasco, H. Martinez-Maicas et al., "Acute myocardial infarction: high risk ventricular tachyarrhythmias and admission glucose level in patients with and without diabetes mellitus," *Current Diabetes Reviews*, vol. 7, no. 2, pp. 126–134, 2011.

[8] J. P. Piccini, J. S. Berger, and D. L. Brown, "Early sustained ventricular arrhythmias complicating acute myocardial infarction*," *The American Journal of Medicine*, vol. 121, no. 9, pp. 797–804, 2008.

[9] T. S. Podolecki, R. K. Lenarczyk, J. P. Kowalczyk et al., "Risk stratification for complex ventricular arrhythmia complicating ST-segment elevation myocardial infarction," *Coronary Artery Disease*, vol. 29, no. 8, pp. 681–686, 2018.

[10] J. S. Alpert, K. Thygesen, E. Antman, and J. P. Bassand, "Myocardial infarction redefined–a consensus document of The Joint European Society of Cardiology/American College of Cardiology committee for the redefinition of myocardial infarction," *Journal of the American College of Cardiology*, vol. 36, no. 3, pp. 959–969, 2000.

[11] K. Thygesen, J. S. Alpert, A. S. Jaffe et al., "Fourth universal definition of myocardial infarction (2018)," *Global Heart*, vol. 13, no. 4, pp. 305–338, 2018.

[12] E. E. Brodie, D. Allan, D. N. Brooks, J. McCulloch, and W. S. Foulds, "Flash and pattern reversal visual evoked responses in normal and demented elderly," *Cortex*, vol. 28, no. 2, pp. 289–293, 1992.

[13] C. M. Tompkins, V. Kutyifa, A. Arshad et al., "Sex differences in device therapies for ventricular arrhythmias or death in the multicenter automatic defibrillator implantation trial with cardiac resynchronization therapy (MADIT-CRT) trial," *Journal of Cardiovascular Electrophysiology*, vol. 26, no. 8, pp. 862–871, 2015.

[14] M. Hayashi, W. Shimizu, and C. M. Albert, "The spectrum of epidemiology underlying sudden cardiac death," *Circulation Research*, vol. 116, no. 12, pp. 1887–1906, 2015.

[15] P. A. Pellikka, A. Arruda-Olson, F. A. Chaudhry et al., "Guidelines for performance, interpretation, and application of stress echocardiography in ischemic heart disease: from the American Society of Echocardiography," *Journal of the American Society of Echocardiography*, vol. 33, no. 1, pp. 1–41.e8, 2020.

[16] V. Lee, H. Hemingway, R. Harb, T. Crake, and P. Lambiase, "The prognostic significance of premature ventricular complexes in adults without clinically apparent heart disease: a meta-analysis and systematic review," *Heart*, vol. 98, no. 17, pp. 1290–1298, 2012.

[17] J. T. Bigger Jr., J. L. Fleiss, R. Kleiger, J. P. Miller, and L. M. Rolnitzky, "The relationships among ventricular arrhythmias, left ventricular dysfunction, and mortality in the 2 years after myocardial infarction," *Circulation*, vol. 69, no. 2, pp. 250–258, 1984.

[18] S. Rasoul, M. J. de Boer, H. Suryapranata et al., "Circumflex artery-related acute myocardial infarction: limited ECG abnormalities but poor outcome," *Netherlands Heart Journal*, vol. 15, no. 9, pp. 286–290, 2007.

[19] H. Tikz, Y. Balbay, R. Atak, T. Terzi, Y. Gençl, and E. K. Utüuk, "The effect of thrombolytic therapy on left ventricular aneurysm formation in acute myocardial infarction: relationship to successful reperfusion and vessel patency," *Clinical Cardiology*, vol. 24, no. 10, pp. 656–662, 2001.

[20] M. G. Colombo, I. Kirchberger, U. Amann, L. Dinser, and C. Meisinger, "Association of serum potassium concentration with mortality and ventricular arrhythmias in patients with acute myocardial infarction: a systematic review and meta-analysis," *European Journal of Preventive Cardiology*, vol. 25, no. 6, pp. 576–595, 2018.

[21] D. R. Anderson, J. T. Poterucha, T. R. Mikuls et al., "IL-6 and its receptors in coronary artery disease and acute myocardial infarction," *Cytokine*, vol. 62, no. 3, pp. 395–400, 2013.

[22] H. Blangy, N. Sadoul, B. Dousset et al., "Serum BNP, hs-C-reactive protein, procollagen to assess the risk of ventricular tachycardia in ICD recipients after myocardial infarction," *Europace*, vol. 9, no. 9, pp. 724–729, 2007.

[23] M. Jankowich and G. Choudhary, "Endothelin-1 levels and cardiovascular events," *Trends in Cardiovascular Medicine*, vol. 30, no. 1, pp. 1–8, 2020.

[24] G. Novo, A. Sansone, M. Rizzo, F. P. Guarneri, C. Pernice, and S. Novo, "High plasma levels of endothelin-1 enhance the predictive value of preclinical atherosclerosis for future cerebrovascular and cardiovascular events: a 20-year prospective study," *Journal of Cardiovascular Medicine (Hagerstown, Md.)*, vol. 15, no. 9, pp. 696–701, 2014.

Hindawi
Journal of Nanomaterials
Volume 2021, Article ID 9967676, 8 pages
https://doi.org/10.1155/2021/9967676

Research Article

Psychoeducational Intervention Benefits the Quality of Life of Patients with Active Systemic Lupus Erythematosus

Hongyan Xu, Qiao Teng, Yan Zeng, Chunping Tian, Bowen Yang, and Xiaoling Yao

Hunan Provincial People's Hospital, The First Affiliated Hospital of Hunan Normal University, China

Correspondence should be addressed to Xiaoling Yao; mlohdae@163.com

Received 25 March 2021; Accepted 20 May 2021; Published 26 May 2021

Academic Editor: Songwen Tan

Objectives. Systemic lupus erythematosus (SLE) is a complex and relapsing autoimmune disease and worsens the quality of life (QOL) of patients by affecting their physical and psychological status. The effectiveness of psychoeducational interventions on patients with active SLE was investigated. *Methods*. Eight-five patients with active SLE were randomly assigned to an observation group or a control group; patients in the observation group received psychoeducational interventions. The following variables were evaluated within a week after admission, 3 and 6 months after psychoeducational intervention: the World Health Organization Quality of Life Instrument- (WHOQOL-) BREF scores, the Medical Outcomes Study Short Form 36 (SF-36) scores, the Beck Depression Inventory, and Spielberger's State-Trait Anxiety Inventory (STAI). *Results*. We found that scores of all four domains of the WHOQOL-BREF scale were remarkably increased 3 months after psychoeducational intervention in the intervention group and significantly higher than the control group ($P < 0.05$); 6 months after psychoeducational intervention, psychological and social domain scores of the WHOQOL-BREF scale were remarkably higher in the intervention group than those in the control group, while other scores of three domains were not. PF, RP, BP, GH, RE, and MH scores of the SF-36 scale were remarkably increased 3 months after psychoeducational intervention in the intervention group rather than VT and SF, while all scores of subscales were notably higher in the intervention group than those in the control group ($P < 0.05$). Six months after psychoeducational intervention, PF, RP, BP, GH, and RE scores of the SF-36 scale were remarkably higher in the intervention group than those in the control group, while VT, SF, and MH scores were not. Three months after psychoeducational intervention, the levels of depression and anxiety of SLE patients were reduced and significantly lower than those in the control group ($P < 0.05$). Six months after psychoeducational intervention, the level of depression was still reduced, while the level of anxiety was not. Compared with the control group, the levels of depression and anxiety of SLE patients were remarkably declined in the observation group 6 months after psychoeducational intervention ($P < 0.05$). *Conclusion*. These data suggest psychoeducational interventions can significantly improve and maintain the QOL of patients with active SLE.

1. Background

Systemic lupus erythematosus (SLE) is a chronic, progressive, recurrent autoimmune disease involving multiple systems throughout the body, characterized by the loss of self-tolerance and formation of nuclear autoantigens and immune complexes [1]. SLE has heterogeneous presentation with a strong female predilection and is involved in more than one organ, including the skin, kidneys, joints, and nervous system [2]. Due to the multitude of presentations, manifestations, and serological abnormalities at onset for patients with SLE, the disease is a long-term fight and challenging. It is challenging to reach a correct and prompt diagnosis, let alone initiation of the appropriate therapy [3]. Therapeutic approaches predominantly involve immunomodulation and immunosuppression and are targeted to the specific organ manifestation to achieve low disease activity [4]. Although many treatment advances and improved diagnostics, SLE leads to substantial morbidity and premature mortality, especially in pregnancy [5]. Current management strategies, although helpful, are limited by high failure rates and toxicity, mainly focusing on attenuation of the patients' symptoms and improvement of quality of life (QOL) [6]. Both the disease itself and the side effects caused by the long-term use

of hormones and immunosuppressive drugs have severely affected the QOL of patients [7]. At the same time, the repeated attacks of the disease and the long-term use of hormones and other drugs often cause great mental stress to patients, and most patients have different negative emotional reactions. Once the QOL significantly reduced and further affected the development and outcome of the disease [8]. Several randomized controlled trials have confirmed that stress-reduction program or psychoeducational intervention could improve the outcome and QOL of SLE patients [9, 10].

Recent evidence has shown that an interdisciplinary multidimensional approach encompassing psychological factors, emotion regulation strategies, and education on illness is more effective in improving quality of life, both in the short- and long-term, than usual treatments alone [11]. Psychoeducational interventions pay more attention to the influence of patients' psychological changes on the prognosis of the disease in addition to the conventional nursing care in the past [12]. Individualized psychological intervention programs are developed based on different psychological problems of patients. The specific measures are as follows: (1) negative psychological intervention measures: SLE patients usually have a lot of negative emotions after the diagnosis of the disease, which adversely affects the treatment process and recovery process of the patient, which we call negative psychological problems. The focus of our intervention for this kind of psychological problems is respect and encouragement, encourage the patients' relatives and friends to give patients full respect and love, and enhance the patient's sense of identity; (2) positive psychological intervention measures: some patients have good psychological quality, so they have a certain degree of confidence in overcoming the disease and hope that they will be respected and valued by others. We call this a positive psychological problem. For this kind of personalized psychological needs, we must fully understand the reasonable aspects and try our best to solve them; and for those that are difficult to satisfy, we must also do a good job of explaining and communicating, so as not to make patients feel frustrated, and do our best to create a comfortable and satisfying psychological environment for patients. The application of psychoeducational intervention in clinical nursing work is ultimately to improve the prognosis of patients and improve the QOL of patients. Therefore, a corresponding quantitative standard of QOL is needed to evaluate whether the intervention measures are reasonable. The present study is aimed at investigating effectiveness of psychoeducational interventions to improve the outcome and QOL of patients with active SLE by analyzing the following variables within a week after admission, 3 and 6 months after psychoeducational intervention: the World Health Organization Quality of Life Instrument- (WHO-QOL-) BREF scores, the Medical Outcomes Study Short Form 36 (SF-36) scores, the Beck Depression Inventory, and Spielberger's State-Trait Anxiety Inventory (STAI).

2. Materials and Methods

2.1. Subject Design and Entry Criteria. Patients who met the diagnostic criteria issued by the American College of Rheumatology for SLE [13], had active disease (score ≥ 6 at screening on the Safety of Oestrogens in Lupus Erythematosus National Assessment SLE Disease Activity Index (SELENA-SLEDAI)) [14], and aged over 15 years were eligible for study subjects. The diagnostic criteria are detailed as follows: cheek erythema: fixed erythema, flat or elevated, erythema on the two zygomatic protrusions; discoid erythema: a flaky erythema that rises from the skin adheres to keratin desquamation and hair follicle plugs: atrophic scars can occur in old lesions; photosensitivity: it has a clear reaction to sunlight, causing a rash, which is known from the medical history or observed by the doctor; oral ulcers: oral or nasopharyngeal ulcers observed by a doctor are generally painless; arthritis: nonerosive arthritis, involving two or more peripheral joints, with tenderness, swelling, or fluid accumulation; serositis: pleurisy or pericarditis; kidney disease: urine protein > 0.59/24 h or +++, or cast (red blood cell, hemoglobin, granular, or mixed cast); neuropathy: epileptic seizures or psychosis, except for drugs or known metabolic disorders; hematological diseases: hemolytic anemia or leukopenia, or lymphopenia, or thrombocytopenia; immunological abnormality: anti-dsDNh antibody is positive, or anti-Sm antibody is positive, or antiphospholipid antibody is positive (including anticardiophosinolipid antibody, or lupus anticoagulant, or one of the three false positive syphilis serum tests lasting at least 6 months; antinuclear antibodies: antinuclear antibodies are abnormal at any time and when no drugs are used to induce "drug-induced lupus." Among these items, those who meet four or more items can diagnose SLE after excluding infections, tumors, and other connective tissue diseases. Exclusion criteria: illiteracy; severe active lupus nephritis or central nervous system (CNS) lupus; transferred to the intensive care unit (ICU) due to disease exacerbation; complicated with other autoimmune rheumatic disorders; primary diabetes, primary kidney disease, and malignant tumors; pregnant or lactating women; mental disorders; failing to complete the questionnaire due to various reasons. There were 89 hospitalized with SLE from January 2018 to January 2020 in our hospital. Considering that 2 cases were transferred to ICU due to worsening condition and 2 cases were withdrawn voluntarily, 85 patients who underwent all screening procedures and met the entry criteria were finally enrolled in the study. All patients were required to fill the WHOQOL-BREF questionnaire survey (Chinese version), the SF-36 questionnaire, the Beck Depression Inventory, and Spielberger's STAI, within a week after admission. Afterward, 85 SLE patients were randomly assigned to an intervention group with 42 cases and a control group with 43 cases. Both groups were given the same treatment protocols for SLE, health education, and nontargeted psychological comfort, while the patients in the intervention group received psychoeducational interventions according to questionnaire surveys they filled. Three and six months after psychoeducational interventions began, two groups of patients were required to fill these four questionnaires.

2.2. The WHOQOL-BREF Scale. The WHOQOL-BREF questionnaire survey (Chinese version) [15] is a cross-cultural instrument developed for use across patient groups in many

countries and contains 24 questions in 4 fields covering physical (7 items), psychological (6 items), social (3 items), and environment (8 items) domains. It uses a Likert-type five-point scale to grade the patient's response to the WHOQOL-BREF items. The scale gives continuous scores ranging from 4 to 20 for each domain. A higher score signifies better QOL. Keeping in view that the WHOQOL-BREF questionnaire survey is best measured by the patient himself/herself and not his or her physician or nurse. A higher score indicates a favorable condition. A higher domain score reflects a better QOL on the corresponding domain.

2.3. The MOS SF-36 Scale. The SF-36 scale is a self-administered instrument that has two major domains involving physical health and mental health [16]. It contains 36 questions that are divided over 8 subscales: physical function (PF, the ability to carry out physical activities); physical role (RP, measure of the interference of physical health in work or other daily activities); bodily pain (BP); general health (GH, a health assessment carried out by the subject); vitality (VT, the feeling of enthusiasm and energy the patient presents); social function (SF, the ability to carry out normal social activities without interference from physical or emotional problems); emotional role (RE, the interference of emotional problems at work and in other daily activities); and mental health (MH, the feeling of peace, happiness, and calm expressed by the patient). The SF-36 has been used extensively in health outcome studies in SLE patients and has excellent reliability (the subscales have internal reliability of 0.85 or better) and validity.

2.4. Psychological Parameters. We employed two instruments, the Beck Depression Inventory and Spielberger's State-Trait Anxiety Inventory (STAI), to measure psychological parameters of SLE. The Beck Depression Inventory [17] is a self-administered questionnaire consisting of 21 items that assess the cognitive components of depression rather than the behavioral and somatic ones. This is not a diagnostic instrument, but it does give an indication of the depth of depression in patients with any diagnosis. The scores on this instrument can be classified into the following categories: no depression, slight depression, moderate depression, and severe depression. Spielberger's State-Trait Anxiety Inventory (STAI) [18], created by Spielberger, Gorsuch, and Lushene, encompasses two separate self-evaluation scales that measure 2 independent concepts of anxiety, i.e., state and trait.

2.5. Psychoeducational Interventions. Intervention content: (a) disease knowledge: basic understanding of the clinical manifestations, outcome and treatment protocols of the disease, and the importance of self-care; confidence reconstruction about marriage and childbirth for unmarried patients by delivering scientific explanations; (b) emotion and feeling: being encouraged in depressed mood after the disease was attenuated or cured by exampling some cases with good treatment effect and stable disease; receiving easy and pleasant communication from peers about their feelings and thoughts; for those being concerned about treatment costs and family burden caused by SLE since there has a long-term psychological process of fighting, nurses should patiently tell them that as long as they received systemic treatment to maintain the stability of the disease, the occurrence of complications can be reduced, and the reduction of medication and treatment will relatively means lower treatment costs. Once the disease is stable, they can make money to reduce the economy burden. At the same time, it is necessary to tell the family members about the patient's concerns, to ensure family member support in all aspects; (c) behavioral intervention: frequent examination of the patient's compliance to treatment and clear notification about the importance of accurate dosage and timing of medication; some patients, in order to reduce the side effects of hormones, often secretly reduce the dosage of medication by themselves, which is very unfavorable to the control of the active period of the disease; nurses must ensure that the patient takes the medication in time every day; patients should tell the medical staff about their discomfort at any time without any hesitation, and the medical staff will deal with the symptoms and signs immediately to avoid the aggravation of the disease and reduce the occurrence of complications; foster good habits to establish health life style; strike a proper balance between work and rest; do everything in one's power; positive about life and grateful for family and friend help; (d) discharge instructions: accurate medication, regulator return visit, self-protection, caution for having a cold; fertility guidance for women with childbearing age; comfortable communication with patients about their mental state, recognition of the disease, approval of treatment, adaptation to the environment, influence on interpersonal communication, attitude towards family members and friends, future plans, etc. For those who had poor acceptance and showed no evident effect, the intervention will be repeated many times. After the patients were discharged from hospital, the nurse should keep in touch with them, make regular telephone follow-up visits, understand the psychological status of the patients, carry out timely psychological intervention, and obtain regular feedback. For special cases such as severe depression and suicidal tendency, professional psychotherapists should be invited to give special help.

2.6. Statistical Processing. The data was processed by SPSS 21.0 statistical software. The measurement data is expressed by mean ± standard deviation, and the t test is performed. The count data is expressed by cases (percentage), and the chi-square test is performed. $P < 0.05$, the difference was statistically significant.

3. Results

3.1. Description of Participant Demographics. A total of 85 hospitalized with SLE from January 2018 to January 2020 were eligible for study enrollment and randomly assigned to a study group with 42 cases and a control group with 43 cases. Participant demographics are listed in Table 1. There were no significant differences with regard to age, sex, SLEDAI scores, level of education, manual or nonmanual

Table 1: Participant demographics, by group.

Demographics	Intervention group ($n = 42$)	Control group ($n = 43$)	P
Age (years)	37.58 ± 5.28	35.76 ± 4.87	0.10
Female (%)	100	95.35	0.16
SLEDAI score	9.62 ± 3.75	10.14 ± 3.81	0.53
Level of education (years)	9.59 ± 2.64	9.88 ± 2.71	0.62
Occupation			0.64
Nonmanual worker	28	30	
Manual workers	14	13	
Married (%)	73.81	76.74	0.75
Disease duration (years)	6.09 ± 1.52	5.76 ± 1.14	0.26
Treatment with corticosteroids (%)	45	47	0.91
Treatment with immunosuppressants (%)	34	30	0.76
Hospital stay (days)	18.47 ± 6.11	16.59 ± 4.63	0.11

NS: not significant.

workers, marriage, disease duration, treatment with corticosteroids and immunosuppressants, and hospital stay between the intervention group and the control group ($P > 0.05$), and the two groups were comparable.

3.2. Psychoeducational Interventions Increased the WHOQOL-BREF Scores of Patients with Active SLE. In order to demonstrate whether psychoeducational interventions improve the QOL of patients with active SLE, each patient was required to fill the WHOQOL-BREF questionnaire survey within a week after admission, 3 and 6 months after psychoeducational intervention. The WHOQOL-BREF scale contains 4 fields covering physical, psychological, social, and environment domains and gives continuous scores ranging from 4 to 20 for each domain. A higher score signifies better QOL. As shown in Table 2(a), no significant difference was detected in physical, psychological, social, and environment domain scores of the WHOQOL-BREF scale between the intervention group and the control group within a week after admission ($P > 0.05$); it was found that scores of all four domains of the WHOQOL-BREF scale were remarkably increased 3 months after psychoeducational intervention in the intervention group (physical domain: 13.13 ± 2.79 vs. 16.34 ± 3.87, $P < 0.001$; psychological domain: 12.95 ± 3.04 vs. 16.12 ± 4.03, $P < 0.001$; social domain: 15.08 ± 3.53 vs. 18.02 ± 4.79, $P = 0.002$; environment domain: 13.82 ± 1.94 vs. 17.86 ± 4.12, $P < 0.001$) and significantly higher than the control group (Table 2(b), $P < 0.05$); 6 months after psychoeducational intervention, psychological and social domain scores of the WHOQOL-BREF scale were remarkably higher in the intervention group than those in the control group, while other scores of three domains were not (Table 2(b), $P < 0.05$). Results revealed that psychoeducational interventions improved the QOL of patients with active SLE.

3.3. Psychoeducational Interventions Increased the SF-36 Scores of Patients with Active SLE. The SF-36 scale was also used to reflect the QOL of patients with active SLE. Each patient was required to fill the SF-36 questionnaire survey within a week after admission, 3 and 6 months after psychoeducational intervention. There was no evident difference in terms of PF, RP, BP, GH, VT, SF, RE, and MH scores of the SF-36 scale between the intervention group and the control group within a week after admission (Table 3(a), $P > 0.05$). PF, RP, BP, GH, RE, and MH scores of the SF-36 scale were remarkably increased 3 months after psychoeducational intervention in the intervention group (PF: 76.34 ± 20.12 vs. 87.46 ± 14.87, $P = 0.005$; RP: 32.53 ± 28.29 vs. 56.46 ± 35.48, $P = 0.001$; BP: 55.75 ± 17.63 vs. 69.14 ± 16.96, $P < 0.001$; GH: 40.59 ± 15.63 vs. 48.92 ± 14.57, $P = 0.013$; RE: 46.27 ± 37.40 vs. 67.73 ± 35.34, $P = 0.008$; MH: 55.42 ± 12.58 vs. 70.68 ± 21.75, $P < 0.001$) rather than VT (46.84 ± 9.76 vs. 53.48 ± 20.43, $P = 0.061$) and SF (53.76 ± 22.01 vs. 62.91 ± 29.13, $P = 0.108$), while all scores of subscales were notably higher in the intervention group than those in the control group (Table 3(b), $P < 0.05$). Six months after psychoeducational intervention, PF, RP, BP, GH, and RE scores of the SF-36 scale were remarkably higher in the intervention group than those in the control group, while VT, SF, and MH scores were not (Table 3(b), $P < 0.05$). These data suggested that psychoeducational interventions improved the QOL of patients with active SLE.

3.4. Psychoeducational Interventions Attenuated the Depression and Anxiety of Patients with Active SLE. SLE is a relapsing autoimmune disease, and SLE patients are required to fight this disease for a long time. SLE patients must keep themselves from depression and anxiety. To study the effects of psychoeducational interventions on the depression and anxiety of patients with active SLE, we employed two instruments, the Beck Depression Inventory and the STAI, to measure psychological parameters of SLE patients. The observation and control groups exhibited no significant difference in the levels of depression and anxiety before psychoeducational intervention ($P > 0.05$). Three months after psychoeducational intervention, the levels of depression and anxiety of SLE patients were reduced (15.2 ± 10.37 vs. 7.56 ± 5.11, $P < 0.001$; 65.68 ± 28.36 vs. 45.00 ± 28.75, $P = 0.001$) and significantly lower than those in the control group (Table 4, $P < 0.05$). Six months after psychoeducational

Table 2

(a) The WHOQOL-BREF scores of patients with active SLE between the intervention group and the control group within a week after admission

WHOQOL scale	Within a week at admission		P
	Intervention group ($n = 42$)	Control group ($n = 43$)	
Physical	13.13 ± 2.79	13.55 ± 3.36	0.53
Psychological	12.95 ± 3.04	13.17 ± 3.44	0.76
Social	15.08 ± 3.53	14.69 ± 3.78	0.62
Environmental	13.82 ± 1.94	14.25 ± 2.31	0.36

(b) The WHOQOL-BREF scores of patients with active SLE between the intervention group and the control group, 3 and 6 months after psychoeducational intervention

WHOQOL scale	Three months after intervention		P	Six months after intervention		P
	Intervention group ($n = 42$)	Control group ($n = 43$)		Intervention group ($n = 42$)	Control group ($n = 43$)	
Physical	16.34 ± 3.87	13.45 ± 2.73	<0.001	14.88 ± 3.24	14.12 ± 3.65	0.31
Psychological	16.12 ± 4.03	12.89 ± 2.69	<0.001	15.25 ± 3.98	12.56 ± 3.33	0.001
Social	18.02 ± 4.79	13.94 ± 3.61	<0.001	16.87 ± 4.57	15.03 ± 3.48	0.04
Environmental	17.86 ± 4.12	15.01 ± 3.52	<0.001	15.69 ± 4.07	14.66 ± 2.85	0.18

Table 3

(a) The SF-36 scores of patients with active SLE between the intervention group and the control group within a week after admission

SF-36 scale	Within a week at admission		P
	Intervention group ($n = 42$)	Control group ($n = 43$)	
PF	76.34 ± 20.12	77.43 ± 19.13	0.80
RP	32.53 ± 28.29	33.45 ± 26.78	0.88
BP	55.75 ± 17.63	53.69 ± 21.57	0.63
GH	40.59 ± 15.63	39.63 ± 15.36	0.78
VT	46.84 ± 9.76	47.49 ± 15.14	0.82
SF	53.76 ± 22.01	52.85 ± 18.73	0.84
RE	46.27 ± 37.40	45.27 ± 41.15	0.91
MH	55.42 ± 12.58	57.94 ± 16.32	0.43

(b) The WHOQOL-BREF scores of patients with active SLE between the intervention group and the control group, 3 and 6 months after psychoeducational intervention

SF-36 scale	Three months after intervention		P	Six months after intervention		P
	Intervention group ($n = 42$)	Control group ($n = 43$)		Intervention group ($n = 42$)	Control group ($n = 43$)	
PF	87.46 ± 14.87	78.21 ± 17.53	0.01	84.95 ± 15.23	76.04 ± 16.37	0.01
RP	56.46 ± 35.48	38.89 ± 27.13	0.01	52.55 ± 29.09	35.54 ± 23.17	0.004
BP	69.14 ± 16.96	51.99 ± 18.16	<0.001	65.25 ± 20.72	54.11 ± 27.15	0.04
GH	48.92 ± 14.57	38.42 ± 16.09	0.002	50.32 ± 15.15	37.77 ± 17.54	<0.001
VT	53.48 ± 20.43	45.72 ± 14.15	0.04	49.58 ± 20.18	46.66 ± 17.39	0.48
SF	62.91 ± 29.13	50.74 ± 20.20	0.03	55.38 ± 24.04	53.59 ± 25.16	0.74
RE	67.73 ± 35.34	52.02 ± 33.95	0.04	65.91 ± 32.39	51.55 ± 29.53	0.04
MH	70.68 ± 21.75	60.44 ± 20.26	0.03	58.73 ± 19.03	61.24 ± 25.80	0.80

Table 4: The depression (Beck Depression Inventory) and anxiety (STAI) of patients with active SLE between the intervention group and the control group within a week after admission, 3 and 6 months after psychoeducational intervention.

	Within a week at admission			Three months after intervention			Six months after intervention		
	Intervention group ($n = 42$)	Control group ($n = 43$)	P	Intervention group ($n = 42$)	Control group ($n = 43$)	P	Intervention group ($n = 42$)	Control group ($n = 43$)	P
Depression (Beck Depression Inventory)	15.20 ± 10.37	16.53 ± 11.19	0.57	7.56 ± 5.11	17.23 ± 13.21	<0.001	10.12 ± 8.42	17.55 ± 13.78	0.004
Anxiety (Spielberger's STAI)	65.68 ± 28.36	68.81 ± 25.36	0.59	45.00 ± 28.75	69.46 ± 26.38	<0.001	54.99 ± 27.41	68.31 ± 30.94	0.04

Table 5: Comparison of the incidence of clinical complications between the intervention group and the control group, 3 and 6 months after psychoeducational intervention.

Complications	Three months after intervention		P	Six months after intervention		P
	Intervention group ($n = 42$)	Control group ($n = 43$)		Intervention group ($n = 42$)	Control group ($n = 43$)	
Allergy	1	2	0.57	4	7	0.38
Infection	0	1	0.32	1	2	0.57
Kidney injury	0	0	0	1	3	0.32
Total complications	1	3	0.32	5	12	0.07

intervention, the level of depression was still reduced (15.2 ± 10.37 vs. 10.12 ± 8.42, $P = 0.016$), while the level of anxiety was not (65.68 ± 28.36 vs. 54.99 ± 27.41, $P = 0.083$). Compared with the control group, the levels of depression and anxiety of SLE patients were remarkably declined in the observation group, 6 months after psychoeducational intervention (Table 4, $P < 0.05$). These data suggested that psychoeducational interventions were beneficial for the mental health of patients with active SLE.

3.5. Clinical Complications. We performed statistics on the number of SLE patients with clinical complications such as allergies, infections, and kidney injury between the intervention group and the control group, 3 and 6 months after psychoeducational intervention. It was revealed that there was no significant difference with regard to the incidence of allergies, infections, and kidney injury and the incidence of total complications between the intervention group and the control group, 3 and 6 months after psychoeducational intervention (Table 5, $P > 0.05$).

4. Discussion

SLE is an autoimmune disease, which can affect multiple systems and multiple organs of the body, undergoes repeated changes, and has unusually complex clinical manifestations. The effectiveness of psychoeducational interventions on the QOL of patients with active SLE was explored. A total of 85 patients with active SLE were included in this study and grouped into the observation group and the control group. Four scales were used to reflect the QOL and mental status of patients after psychoeducational interventions. The nursing measures are as follows: (1) skin care: instruct patients to keep their skin clean and dry, add moisture and nutrients in time, reduce skin pressure, and avoid chemical irritation; (2) care for edema: if patients develop edema of the lower extremities, they should control their intake into the water and sodium content, keep the lower limbs elevated, and avoid electrolyte disturbance and dehydration; (3) recurrence prevention measures: patients with SLE may have fever, hair loss, and joint pain in the early stages of recurrence. Patients should avoid influenza during treatment, and female patients should avoid unplanned births. In addition, nurses create a good treatment environment, protect patients from external interference, and reduce disease recurrence. (4) Psychoeducational intervention: after the onset of the patient's illness, his social role changes, and he cannot adapt to it for a while. There will be tension, anxiety, pessimism, and other negative psychology. At this time, the nursing staff should comfort, encourage the patient, and guide the patient's family to care for and enlighten the patient. Let patients regain their confidence and adapt to the new environment.

We found that scores of all four domains of the WHOQOL-BREF scale were remarkably increased 3 months after psychoeducational intervention in the intervention group and significantly higher than the control group; 6 months after psychoeducational intervention, psychological and social domain scores of the WHOQOL-BREF scale were remarkably higher in the intervention group than those in the control group, while other scores of three domains were not. PF, RP, BP, GH, RE, and MH scores of the SF-36 scale were remarkably increased 3 months after psychoeducational intervention in the intervention group rather than VT and SF, while all scores of subscales were notably higher in the intervention group than those in the control group. Six months after psychoeducational intervention, PF, RP, BP,

GH, and RE scores of the SF-36 scale were remarkably higher in the intervention group than those in the control group, while VT, SF, and MH scores were not. Three months after psychoeducational intervention, the levels of depression and anxiety of SLE patients were reduced and significantly lower than those in the control group. Six months after psychoeducational intervention, the level of depression was still reduced, while the level of anxiety was not. Compared with the control group, the levels of depression and anxiety of SLE patients were remarkably declined in the observation group, 6 months after psychoeducational intervention. All these findings revealed that psychoeducational intervention could effectively improve the QOL of patients with active SLE.

Nursing staff should pay attention to the changes in the patient's mood, thinking, speech, and behavior, understand the impact of various factors on the patient's psychological activities, pay attention to understanding the patient's physical, psychological, and social information through communication, and find out the patient's psychological health problems, so as to formulate corresponding psychological support and treatment measures, such as use of listening assurance techniques, comfort and enlightenment, care and sympathy, explanation, advice and guidance, encouragement, and extreme language applications [19]. Nurses must patiently explain to patients the occurrence and development process of the disease, the purpose and significance of various examinations and treatments, as well as the rapid development of medicine, immunology, pharmacy, and molecular biology, and the improvement of diagnosis and treatment technology, and the prognosis has been greatly improved. A happy mood plays a positive role in promoting the improvement of the disease, which is very important for stable treatment. It has been reported that mental stress or stress can cause immune system disorders through the neuroendocrine system and promote or aggravate SLE. Psychological supports and programs are effective in dealing with patients suffering from SLE and high levels of daily stress as it significantly reduces the incidence of psychological disorders associated with SLE and improves and maintains the QOL of patient, despite there being no significant reduction in the disease activity index [20].

The improvements found in the QOL of SLE patient and reduced levels of depression and anxiety suggest that psychoeducational interventions could cope with the disease easier and change patients' mental health. Furthermore, the impact of therapy on QOL and psychosocial aspects may have implications for longer-term health behaviors and health outcomes. These preliminary results should be verified in further studies. If the findings are confirmed, then this could signal a new, more effective approach to dealing with SLE, given that a comprehensive, overall view of these patients is necessary when treating the clinical and psychological aspects of the disease.

Data Availability

The data used to support the findings of this study are included within the article.

Conflicts of Interest

The authors declare that they have no conflicts of interest.

Funding

This work was supported by the project Nos. 2018JJ6017 and 2017SK50503.

References

[1] L. Durcan, T. O'Dwyer, and M. Petri, "Management strategies and future directions for systemic lupus erythematosus in adults," *The Lancet*, vol. 393, no. 10188, pp. 2332–2343, 2019.

[2] G. Fortuna and M. T. Brennan, "Systemic lupus erythematosus: epidemiology, pathophysiology, manifestations, and management," *Dental Clinics of North America*, vol. 57, no. 4, pp. 631–655, 2013.

[3] G. D. Sebastiani, I. Prevete, A. Iuliano, and G. Minisola, "The importance of an early diagnosis in systemic lupus erythematosus," *The Israel Medical Association Journal*, vol. 18, no. 3-4, pp. 212–215, 2016.

[4] A. Fava and M. Petri, "Systemic lupus erythematosus: diagnosis and clinical management," *Journal of Autoimmunity*, vol. 96, pp. 1–13, 2019.

[5] A. Lateef and M. Petri, "Systemic lupus erythematosus and pregnancy," *Rheumatic Diseases Clinics of North America*, vol. 43, no. 2, pp. 215–226, 2017.

[6] M. Gatto, M. Zen, L. Iaccarino, and A. Doria, "New therapeutic strategies in systemic lupus erythematosus management," *Nature Reviews Rheumatology*, vol. 15, no. 1, pp. 30–48, 2019.

[7] J. D. Correa, L. G. A. Branco, D. C. Calderaro et al., "Impact of systemic lupus erythematosus on oral health-related quality of life," *Lupus*, vol. 27, no. 2, pp. 283–289, 2018.

[8] R. P. Goswami, R. Chatterjee, P. Ghosh, G. Sircar, and A. Ghosh, "Quality of life among female patients with systemic lupus erythematosus in remission," *Rheumatology International*, vol. 39, no. 8, pp. 1351–1358, 2019.

[9] C. M. Greco, T. E. Rudy, and S. Manzi, "Effects of a stress-reduction program on psychological function, pain, and physical function of systemic lupus erythematosus patients: a randomized controlled trial," *Arthritis and Rheumatism*, vol. 51, no. 4, pp. 625–634, 2004.

[10] E. W. Karlson, M. H. Liang, H. Eaton et al., "A randomized clinical trial of a psychoeducational intervention to improve outcomes in systemic lupus erythematosus," *Arthritis and Rheumatism*, vol. 50, no. 6, pp. 1832–1841, 2004.

[11] C. Conversano, A. Poli, R. Ciacchini, P. Hitchcott, L. Bazzichi, and A. Gemignani, "A psychoeducational intervention is a treatment for fibromyalgia syndrome," *Clinical and Experimental Rheumatology*, vol. 37, Supplement 116, 1, pp. 98–104, 2019.

[12] L. T. Nguyen, K. Alexander, and P. Yates, "Psychoeducational intervention for symptom management of fatigue, pain, and sleep disturbance cluster among cancer patients: a pilot quasi-experimental study," *Journal of Pain and Symptom Management*, vol. 55, no. 6, pp. 1459–1472, 2018.

[13] M. C. Hochberg, "Updating the American College of Rheumatology revised criteria for the classification of systemic lupus erythematosus," *Arthritis & Rheumatism*, vol. 40, no. 9, p. 1725, 1997.

[14] M. Petri, M. Y. Kim, K. C. Kalunian et al., "Combined oral contraceptives in women with systemic lupus erythematosus," *The New England Journal of Medicine*, vol. 353, no. 24, pp. 2550–2558, 2005.

[15] The Whoqol Group, "The World Health Organization Quality of Life Assessment (WHOQOL): development and general psychometric properties," *Social Science & Medicine*, vol. 46, no. 12, pp. 1569–1585, 1998.

[16] J. E. Ware Jr. and C. D. Sherbourne, "The MOS 36-item short-form health survey (SF-36). I. Conceptual framework and item selection," *Medical Care*, vol. 30, no. 6, pp. 473–483, 1992.

[17] X. Wang, Y. Wang, and T. Xin, "The psychometric properties of the Chinese version of the Beck Depression Inventory-II with middle school teachers," *Frontiers in Psychology*, vol. 11, p. 548965, 2020.

[18] K. Gerreth, J. Chlapowska, K. Lewicka-Panczak, R. Sniatala, M. Ekkert, and M. Borysewicz-Lewicka, "Self-evaluation of anxiety in dental students," *BioMed Research International*, vol. 2019, Article ID 6436750, 6 pages, 2019.

[19] G. S. Alarcon, G. McGwin Jr., A. Uribe et al., "Systemic lupus erythematosus in a multiethnic lupus cohort (LUMINA). XVII. Predictors of self-reported health-related quality of life early in the disease course," *Arthritis and Rheumatism*, vol. 51, no. 3, pp. 465–474, 2004.

[20] N. Navarrete-Navarrete, M. I. Peralta-Ramirez, J. M. Sabio-Sanchez et al., "Efficacy of cognitive behavioural therapy for the treatment of chronic stress in patients with lupus erythematosus: a randomized controlled trial," *Psychotherapy and Psychosomatics*, vol. 79, no. 2, pp. 107–115, 2010.

Hindawi
Journal of Nanomaterials
Volume 2021, Article ID 9993172, 6 pages
https://doi.org/10.1155/2021/9993172

Research Article

Investigation on the Status Quo of Self-Health Management of Patients with Bipolar Disorder and Analysis of Influencing Factors

Shan Cai, Lin Zhou, Xiao Yang, Chenyu Ma, Liuliu Xu, and Ruilian Qian

The Affiliated Brain Hospital of Nanjing Medical University, China

Correspondence should be addressed to Liuliu Xu; caishan@njmu.edu.cn and Ruilian Qian; 2209188046@qq.com

Received 10 March 2021; Revised 18 March 2021; Accepted 24 March 2021; Published 24 May 2021

Academic Editor: Songwen Tan

In this study, we aim to explore the status quo of self-health management of patients with bipolar disorder and influencing factors. A total of 80 patients with bipolar disorder were included and assigned into the observation group and the control group, with 40 cases per group. The patients in the control group were given general health education, and those in the observation group were given personalized education combined with peer support. It was found that there was no significant difference in gender, age, educational degree, marital status, and living state between the observation group and the control group ($P > 0.05$). There are significant differences with regard to self-management between the two groups. The observation group showed stronger self-care ability, health education level, self-protection ability, and emotional control ability than the control group ($P < 0.05$). Before the intervention, no significant difference in Hamilton Depression Rating Scale (HAMD) scores was observed between the observation group and the control group ($P > 0.05$). After the intervention, the HAMD scores were lower in the observation group than in the control group ($P < 0.05$), suggesting an alleviation in manic and depressive episodes in the observation group. It was also revealed that the observation group exhibited lower Functioning Assessment Short Test (FAST) scores in all aspects than the control group, suggesting personalized education combined with peer support could significantly improve the quality of life of patients with bipolar disorder. Self-health management ability of the patients was regarded as the dependent variable and healthy education level, health literacy, and objective support as the independent variables, and the regression model was performed. The results show that information acquisition ability, communication and interaction ability, objective social support, subjective social support, and utilization of social support can all affect the self-health management ability of patients. Personalized education combined with peer support can effectively alleviate the condition of patients with bipolar disorder, improve the degree of overall functional impairment, enhance the patient's self-management ability, and promote their recovery. It is worthy of promotion and application. In conclusion, information acquisition ability, communication and interaction ability, objective social support, subjective social support, and utilization of social support can all affect the self-health management ability of patients.

1. Background

Bipolar disorder refers to a mood disorder that has both manic and depressive episodes [1]. The clinical manifestations are repeated alternating manic episodes and depressive episodes or a mixed episode of both [2]. Bipolar disorder is a complicated mental disorder caused by a multifactor genesis with both biological-genetic and psychosocial factors [3]. The disorder was characterized by limited treatment, high recurrence rate, and suicide rate [4, 5]. Because bipolar disorder can damage the cognitive function and social function of patients, it will not only affect the patient's own quality of life but also bring a heavy burden to their family and society [6, 7]. The Hamilton Depression Rating Scale (HAMD) is a clinician-rated instrument that is considered standard scales for evaluating depressive symptoms worldwide [8]. The Functioning Assessment Short Test (FAST) is a brief instrument designed to assess the main functioning problems experienced by psychiatric patients, particularly bipolar patients, which consists of 24 items that assess impairment or disability in six specific areas of functioning: autonomy, occupational functioning, cognitive functioning, financial issues, interpersonal relationships, and leisure time [9].

Studies have found that personalized education combined with peer support can improve the patient's condition and enhance their overall functions and self-management capabilities [10, 11], but this conclusion remains to be verified. Self-health management refers to the whole process of analyzing, predicting, and preventing one's own health information and risk factors. The management method is to monitor your own health information at any time with the help of health scales, health assessment software, or health information systems [12]. It is an entry point to maximize the effect of health management for patients with bipolar disorder, which can help patients establish correct health management beliefs, improve health literacy, and prompt the elderly to take responsibility for their health. This study intends to use health education or personalized education combined with peer support to observe differences in patients' self-health management capabilities and their influencing factors.

2. Materials and Methods

2.1. Clinical Data. Eighty patients with bipolar disorder who were admitted to the hospital from January 2019 to January 2020 were selected and divided into the observation group and the control group according to different nursing methods. The control group and the observation group each had 40 cases. This study was completed under the supervision and approval of the peer support service supervision group. Inclusion criteria are as follows: (1) initial diagnosis of bipolar disorder according to the 10^{th} edition of the International Classification of Diseases for bipolar disorder (PMID: 32447353), (2) with a junior high school education or above and ability to receive personalized education and peer support, (3) ability to answer the questionnaire survey, and (4) an informed consent available from patients or family members. Exclusion criteria are as follows: (1) those with other serious mental illnesses, (2) those with severe physical illnesses, (3) those with mental disorders caused by alcohol and drugs, and (4) those with hearing impairments or language disorders that are difficult to communicate effectively.

2.2. Method. The control group used general health education, and the observation group used personalized education combined with peer support.

2.2.1. Personalized Education. Formulation of education plan: evaluate the patient's personal situation and formulate a personalized education plan based on the patient's condition, personality, education level, family situation, and living environment.

Health education: it is possible to explain the causes of bipolar disorder, treatment plan, usage and dosage of drugs, and adverse reactions to patients and their families through oral education, health manuals, and health knowledge lectures and what needs attention in life. It emphasizes the importance of taking medication as prescribed and guides them to develop a regular and healthy lifestyle. At the same time, they teach family members how to deal with the patient's illness so that they can effectively deal with the patient's condition.

Psychological education: the psychology of bipolar disorder is relatively fragile. Therefore, when communicating with patients, you should show enthusiasm and respect and listen patiently to what the patients say so that they can express their emotions, find out the crux of the problem, and provide them with psychological guidance, such as guiding them to express anger and vent their emotions and improve their ability to cope with conflicts, so as to be able to handle interpersonal relationships and improve self-protection.

2.2.2. Peer Support. Recruitment of counselors. We first extended the peer support service to various clinical departments, which aroused a great response. Many patients actively signed up and asked to participate in the peer support service. Finally, according to the abovementioned conditions required for service development, after evaluation, we selected qualified peer counselors from some active participants.

Implementation method. The implementation of peer support is divided into separate activities in closed wards and open wards, and the activities of each phase are attended by two counselors and two supervisors. We have developed a flow of activities. Before the start of the activity, we will make full preparations. We will work out the theme with the counselor in the previous week, prepare the materials needed for the activity, meet with the counselor and supervisor of related activities, discuss the process of the activity and possible emergencies, and get ready. Go through the process 40 minutes before the start of the event to ensure that the event goes smoothly. The process of the activity is that the two counselors first introduce themselves and then the counselors explain the theme, significance, and precautions of the activity, emphasize the principle of confidentiality, read the counselor's declaration together, and the recovered people introduce themselves and know each other. Warm-up activity: the counselor shared the meaning of the warm-up activity at a turning point and transferred to the theme activity. After the activity, everyone's sharing session. Finally, the counselor summarized and sang our garden song and thanked everyone for their participation and support to the service activities with the supervisor. Another of our counselors will record the entire activity and finally leave the image data.

2.3. Observation Indicators. HAMD score. The YMRS scale and the HAMD scale were used to evaluate the patients' manic and depressive episodes. The higher the score, the more serious the condition. The HAMD scores before and after the intervention were compared between the two groups.

FAST score. The FAST scale was used to evaluate the patients' overall functional impairment from the aspects of autonomous life, occupational function, interpersonal relationship, leisure, etc., and the FAST scores of the two groups after intervention were compared.

Self-management level. The self-care ability, health education level, self-protection ability, emotional control ability, and other self-management levels after intervention were compared between the two groups.

Table 1: Comparison of general information of the two groups of patients.

	Control group ($n = 40$)	Observation group ($n = 40$)	X^2	P value
Gender (male/female)	18/22	19/21	0.68	0.25
Age	35.68 ± 5.76	35.76 ± 5.89	1.36	0.69
Marital status				
Unmarried	12	13		
Married	25	23	2.65	0.16
Divorced	2	2		
Death of a spouse	1	2		
Level of education				
Junior high school and below	7	6	1.67	0.23
High school and technical secondary school	18	17		
College degree or above	15	17		
Living state				
Living alone	16	18	1.65	0.38
Not living alone	24	22		

2.4. Statistical Analysis. The SPSS 22.0 software was used to process the count data, the c2 test was performed using n (%), and the measurement data was performed using the t-test, which was represented by mean ± standard deviation. The difference was statistically significant at $P < 0.05$.

3. Results

3.1. Comparison of General Information of Patients with Bipolar Disorder. There were 80 patients with bipolar disorder included in the study, and they were split into the observation and control groups. It was found that there was no significant difference in gender, age, educational degree, marital status, and living state between the two groups of patients ($P > 0.05$); see Table 1 for details.

3.2. Comparison of Self-Management Levels before and after Intervention between the Two Groups. Through comparison, it is found that there are significant differences in self-management levels between the two groups of patients after intervention. After intervention, the self-management level of patients in the observation group, such as self-care ability, health education level, self-protection ability, and emotional control ability, was stronger than that of the control group. The difference was statistically significant ($P < 0.05$); see Table 2 for details.

3.3. Comparison of HAMD Scores before and after Intervention between the Two Groups. After comparing the HAMD scores before and after the intervention of the two groups, it was found that there was no statistical difference in the scores before the intervention ($P > 0.05$), while the HAMD scores of the observation group after the intervention were lower than those of the control group, and the improvement of manic and depressive episodes in the observation group was strong. In the control group, the difference was statistically significant ($P < 0.05$); see Table 3 for details.

3.4. Comparison of FAST Scores between the Two Groups of Patients after Intervention. By observing the patient's autonomous life, occupational function, interpersonal relationship, leisure, and other aspects, the overall functional impairment of the patient was evaluated, and the FAST score was performed. The results showed that the scores of the observation group were lower than those of the control group in all aspects, suggesting that the observation group has a good treatment effect; see Table 4 for details.

3.5. Multifactor Analysis of Patients' Self-Health Management Ability. We use the patient's self-health management ability as the dependent variable and the statistically significant data in the single factor analysis as the independent variable and perform multiple stepwise regression analysis. Health education level, health literacy, objective support, etc. enter the regression model. The results show that information acquisition ability, communication and interaction ability, objective social support, subjective social support, and utilization of social support can all affect the self-health management ability of patients; see Table 5 for details.

4. Discussion

Bipolar disorder is a common clinically severe mental disorder. In the intermittent period, patients completely deal with the normal state, but in the onset period, patients may experience emotional instability, inattention, irritability, substance abuse, and suicidal ideation. Due to the high recurrence rate of the disease, drug treatment and psychotherapy are indefinitely needed to reduce the risk of recurrence [13]. However, some patients lack sufficient knowledge of the disease, which results in pessimistic and desperate psychology. In addition, some patients lack understanding of the degree of harm of the disease, which leads to a decline in self-management ability after discharge from the hospital and a decrease in medication compliance. Standard health education is only conducted through oral education by nursing staff [14]. Although it can meet the basic needs of patients during treatment in the hospital, it cannot take into account the personal situation of each patient. As a result, patients

Table 2: Comparison of self-management levels between the two groups of patients after intervention.

Group	Self-care ability	Health education level	Self-protection ability	Emotional control
Control group ($n = 40$)	61.23 ± 5.69	69.65 ± 3.39	62.38 ± 7.59	58.67 ± 3.85
Observation group ($n = 40$)	84.68 ± 6.85	89.62 ± 5.87	87.65 ± 6.58	76.58 ± 4.52
T value	16.35	14.68	13.65	16.59
P value	≤0.001	≤0.001	≤0.001	≤0.001

Table 3: Comparison of HAMD scores between the two groups before and after intervention.

Group	Before the intervention	After the intervention
Control group	23.65 ± 3.59	15.67 ± 2.15
Observation group	23.69 ± 2.89	9.78 ± 1.59
T value	0.15	10.36
P value	0.64	≤0.001

and their families do not fully understand the content of health education, which is not conducive to disease. Therefore, it is necessary to strengthen the health education of patients in order to enhance the patients' awareness of the disease and improve the patients' self-management ability and disease control effect.

This study implemented personalized education and peer support for patients with bipolar disorder and achieved ideal results. In this study, the HAMD scores of the observation group and the control group after intervention were lower than those before the intervention, and the improvement of manic episodes and depressive episodes in the observation group was better than that of the control group. Personalized education combined with peer support for patients with bipolar disorder can alleviate the symptoms of patients and help improve the prognosis of patients. Individualized education can formulate targeted education programs to fit each patient's cognition and understanding ability so that patients and their families can better master the content of health education. It not only can improve the patients' self-care awareness and the family's ability to respond to the patient's condition but also enable patients to master the methods of emotional control and catharsis at the onset of disease, improve the patients' unhealthy psychology through psychological education, enhance the enthusiasm of patients, and enable them to actively participate in treatment and nursing [15, 16]. However, the use of personalized education alone has limited impact on health education and self-management after discharge from the hospital [17]. Peer support means that people who have faced, encountered, and overcome misfortunes and disasters can provide useful support, encouragement, and hope and even become mentors and friends for those facing the same situation [18]. Peers are organized with each other through interaction between group members to guide and help each other. Group members have no hierarchy among each other, can listen to each other, discuss problems, share patient knowledge and experience that many medical staff do not have, and increase their sense of social role. Since group members are all patients with bipolar disorder, they are more likely to resonate and communicate more naturally [19].

In addition, peer support has the following advantages for patients with bipolar disorder: for patients, it can improve curative effect and reduce relapse and can improve the social support, social function, quality of life, and service satisfaction of patients with severe mental illness; for peers, the social role of "service providers" greatly enhances their sense of self-efficacy, making them feel fulfillment and their own value, thereby enhancing self-confidence and self-esteem. Patients with mental illness often pay more attention to themselves. Less caring about others, peer work has helped them achieve a leap in their roles. Peer service allows recovered patients to experience the connotation of work and is also a transition for them to engage in other jobs in the future. It is beneficial to its continuous recovery; for medical workers, companions can act as a bridge between medical workers and patients, explain the doctor's advice to the patient, convey the patient's intentions and ideas to the doctor, and enhance the doctor-patient relationship. Mutual understanding between the two can improve patient compliance and improve curative effect. As far as the general public is concerned, there has been discrimination against patients with mental illness for a long time, and the public's awareness of mental illness is very low. The survey in some areas in 2005 showed that it was only 30%-40%. Peer support allows recovered patients to provide services to others, participate in the work of popularizing mental illness knowledge, and affirm that they can support themselves from the perspective of social roles and are people who contribute and are valuable to society. This enables the public to wait for them equally, understand that mental illness can be cured clinically, and strengthen the public's awareness of severe mental illness, thereby eliminating the fear of patients with mental illness, diminishing discrimination, and reducing the stigma of patients with mental illness. Conversely, social acceptance of patients with mental illness can also have a positive impact on their recovery, which is more conducive to the return of patients with mental illness to society. In this study, the scores of all FAST dimensions such as autonomous life, occupational function, interpersonal relationship, and leisure in the observation group were lower than those in the control group. In addition, choose patients with stable illness, high education, strong communication skills, and cheerful personality as the team leader so that they can lead by example, set an example for the team members, and supervise and help the team members, which will help improve the team members' self-management ability. In this study, the

Table 4: Comparison of FAST scores between the two groups of patients after intervention.

Group	Independent life	Professional ability	Interpersonal relationships	Leisure
Control group	1.89 ± 0.35	7.85 ± 0.95	8.65 ± 1.29	1.98 ± 0.43
Observation group	1.35 ± 0.58	5.86 ± 0.86	6.28 ± 1.16	1.46 ± 0.37
T value	5.89	10.36	14.68	8.79
P value	0.010	≤0.001	0.020	≤0.001

Table 5: The correlation between patients' self-health management ability, health literacy, and social support.

Project	R	P
Information acquisition ability	0.36	0.001
Communication and interaction ability	0.29	0.001
Objective social support	0.28	≤0.001
Subjective social support	0.34	0.010
Utilization of social support	0.18	0.010

observation group's self-care ability, health education level, self-protection ability, emotional control ability, and other self-management levels after intervention were better than those of the control group. It can be seen from this that the use of personalized education combined with peer support in patients with bipolar disorder can help improve the patient's self-management ability and facilitate the early recovery of patients. In this study, personalized education combined with peer support can effectively alleviate the condition of patients with bipolar disorder, improve the degree of overall functional impairment, enhance the patient's self-management ability, and promote their recovery. It is worthy of popularization and application.

In this study, by comparing the general information of the two groups of patients, it was found that there was no significant difference in gender, age, and educational level between the two groups of patients. Through comparison, it is found that there are significant differences in self-management levels between the two groups of patients after intervention. After the intervention, the self-management level of patients in the observation group, such as self-care ability, health education level, self-protection ability, and emotional control ability, was stronger than that of the control group, and the difference was statistically significant. After comparing the HAMD scores before and after the intervention of the two groups, it was found that there was no statistical difference in the scores before the intervention, while the HAMD scores of the observation group after the intervention were lower than those of the control group, and the improvement of manic and depressive episodes in the observation group was strong than that in the control group. The FAST score was carried out to evaluate the overall functional impairment of the patient by observing the patient's autonomous life, occupational function, interpersonal relationship, leisure, and other aspects. The results showed that the scores of the observation group were lower than those of the control group in all aspects, suggesting that the observation group has a good treatment effect. We use the patient's self-health management ability as the dependent variable and the statistically significant data in the single factor analysis as the independent variable and perform multiple stepwise regression analysis. Education level, health literacy, objective support, etc. enter the regression model. The results showed that information acquisition ability, communication and interaction ability, objective social support, subjective social support, and utilization of social support can all affect the self-health management ability of patients.

In summary, personalized education combined with peer support can effectively alleviate the condition of patients with mental disorders, improve the degree of overall functional impairment, enhance the patient's self-management ability, and promote their recovery. It is worthy of promotion and application. In addition, information acquisition ability, communication and interaction ability, objective social support, subjective social support, and utilization of social support can all affect the self-health management ability of patients.

Data Availability

The data used to support the findings of this study are included within the article.

Conflicts of Interest

The authors declare that they have no conflicts of interest.

Acknowledgments

The study was supported by the Study on Education in the Fourth Clinical Medical College of Nanjing Medical University in 2019 (SLYB2019-01).

References

[1] L. Tondo, G. H. Vazquez, and R. J. Baldessarini, "Depression and mania in bipolar disorder," *Current Neuropharmacology*, vol. 15, no. 3, pp. 353–358, 2017.

[2] J. K. Muller and F. M. Leweke, "Bipolar disorder: clinical overview," *Medizinische Monatsschrift für Pharmazeuten*, vol. 39, no. 9, pp. 363–369, 2016.

[3] N. Freund and G. Juckel, "Bipolar disorder: its etiology and how to model in rodents," *Methods in Molecular Biology*, vol. 2011, pp. 61–77, 2019.

[4] E. M. Camacho, D. Ntais, S. Jones et al., "Cost-effectiveness of structured group psychoeducation versus unstructured group support for bipolar disorder: results from a multi-centre

pragmatic randomised controlled trial," *Journal of Affective Disorders*, vol. 211, pp. 27–36, 2017.

[5] J. N. Miller and D. W. Black, "Bipolar disorder and suicide: a review," *Current Psychiatry Reports*, vol. 22, no. 2, p. 6, 2020.

[6] B. Sole, E. Jimenez, C. Torrent et al., "Cognitive impairment in bipolar disorder: treatment and prevention strategies," *The International Journal of Neuropsychopharmacology*, vol. 20, no. 8, pp. 670–680, 2017.

[7] C. D. M. Bonnin, M. Reinares, A. Martinez-Aran et al., "Improving functioning, quality of life, and well-being in patients with bipolar disorder," *The International Journal of Neuropsychopharmacology*, vol. 22, no. 8, pp. 467–477, 2019.

[8] A. M. Carneiro, F. Fernandes, and R. A. Moreno, "Hamilton depression rating scale and Montgomery-Asberg depression rating scale in depressed and bipolar I patients: psychometric properties in a Brazilian sample," *Health and Quality of Life Outcomes*, vol. 13, no. 1, p. 42, 2015.

[9] A. R. Rosa, J. Sánchez-Moreno, A. Martínez-Aran et al., "Validity and reliability of the functioning assessment short test (FAST) in bipolar disorder," *Clinical Practice and Epidemiology in Mental Health*, vol. 3, no. 1, p. 5, 2007.

[10] F. Lobban, N. Akers, D. Appelbe et al., "A web-based, peer-supported self-management intervention to reduce distress in relatives of people with psychosis or bipolar disorder: the REACT RCT," *Health Technology Assessment*, vol. 24, no. 32, pp. 1–142, 2020.

[11] J. A. Cook, M. E. Copeland, J. A. Jonikas et al., "Results of a randomized controlled trial of mental illness self-management using wellness recovery action planning," *Schizophrenia Bulletin*, vol. 38, no. 4, pp. 881–891, 2012.

[12] C. A. Janney, M. S. Bauer, and A. M. Kilbourne, "Self-management and bipolar disorder–a clinician's guide to the literature 2011-2014," *Current Psychiatry Reports*, vol. 16, no. 9, p. 485, 2014.

[13] J. R. Geddes and D. J. Miklowitz, "Treatment of bipolar disorder," *Lancet*, vol. 381, no. 9878, pp. 1672–1682, 2013.

[14] D. A. Perlick, C. Jackson, S. Grier et al., "Randomized trial comparing caregiver-only family-focused treatment to standard health education on the 6-month outcome of bipolar disorder," *Bipolar Disorders*, vol. 20, no. 7, pp. 622–633, 2018.

[15] M. P. DelBello, "Treating bipolar disorder in pediatric patients and educating patients and parents," *The Journal of Clinical Psychiatry*, vol. 80, no. 1, 2019.

[16] F. Rouillon, I. Gasquet, R. P. Garay, and S. Lancrenon, "Impact of an educational program on the management of bipolar disorder in primary care," *Bipolar Disorders*, vol. 13, no. 3, pp. 318–322, 2011.

[17] F. Gumus, S. Buzlu, and S. Cakir, "Effectiveness of individual psychoeducation on recurrence in bipolar disorder; a controlled study," *Archives of Psychiatric Nursing*, vol. 29, no. 3, pp. 174–179, 2015.

[18] J. F. Kelly, L. Hoffman, C. Vilsaint, R. Weiss, A. Nierenberg, and B. Hoeppner, "Peer support for mood disorder: characteristics and benefits from attending the Depression and Bipolar Support Alliance mutual-help organization," *Journal of Affective Disorders*, vol. 255, pp. 127–135, 2019.

[19] B. Puschner, J. Repper, C. Mahlke et al., "Using peer support in developing empowering mental health services (UPSIDES): background, rationale and methodology," *Annals of Global Health*, vol. 85, no. 1, 2019.

Hindawi
Journal of Nanomaterials
Volume 2021, Article ID 6453888, 10 pages
https://doi.org/10.1155/2021/6453888

Research Article

Computed Tomography Imaging Agent Based on Gold Nanoparticles for Internal Iliac Artery Embolization after Endovascular Abdominal Aortic Repair and CCN3 Protection Mechanism

Siying Pei,[1] Yao Sun,[2] Dongxu Fan,[2] Shuhua Deng,[3] Haoran Mei,[2] and Hanrui Wang[2]

[1]*College of Basic Medicine, Jiamusi University, China*
[2]*Department of Vascular Surgery, The First Affiliated Hospital of Jiamusi University, China*
[3]*Nursing Department, Jiamusi Central Hospital, China*

Correspondence should be addressed to Hanrui Wang; whr496196111@163.com

Received 9 April 2021; Revised 12 April 2021; Accepted 16 April 2021; Published 20 May 2021

Academic Editor: Songwen Tan

Abdominal aortic aneurysm is more stressful and has more complications in many diseases. During treatment and repair, arteriosclerosis, abdominal congestion deposition, and abdominal swelling cannot be eliminated. In this paper, we used the seed growth method to obtain gold nanoparticles (AuNPs) with good morphology and dispersion. The AuNPs of larger aspect ratio synthesized in this experiment moved their longitudinal plasmon resonance absorption peak to the near-infrared region, which provided suitable materials for subsequent experiments and laid the foundation for the photothermal therapy of tumors. Experiments show that near-infrared rays can penetrate into deep tissues to overcome the shortcomings that visible light cannot penetrate abdominal aorta well. AuNPs absorb near-infrared rays, thereby generating heat energy to achieve the purpose of treating tumors. In addition, AuNPs also have fluorescent properties, combined with other forms of imaging methods, to achieve the purpose of multimodal imaging, and improve the diagnostic accuracy of studying the protection mechanism of the nephroblastoma overexpressed (NOV or CCN3) gene.

1. Introduction

Abdominal aortic aneurysm (AAA) is defined as a permanent local expansion of the abdominal aorta exceeding 3.0 cm or a diameter exceeding 1.5 times the normal diameter [1], which is a common clinical disease in vascular surgery. According to the survey, 3.9%-7.2% of men and 1.0%-1.3% of women over the age of 50 in the United States may suffer from AAA [2]. The incidence rate increases rapidly with age. 12.5% of men over the age of 50 and 5.2% from 74 to 84 years of women are diagnosed with AAA, and more than 10,000 people die from AAA every year, and the mortality rate of ruptured AAA patients is as high as 90% [3]. The mechanism of AAA is not yet clear. Various factors such as genetic susceptibility, atherosclerosis, and various protease abnormalities may cause it to occur. Various causes will eventually cause degeneration of the middle layer of the aorta, resulting in local permanent blood vessels. The natural course of AAA is closely related to the diameter of the tumor, mainly manifested by the gradual increase of the tumor and the formation of arterial wall thrombosis due to hemodynamic disturbances. The rate of increase in the diameter of the AAA is related to the diameter of the tumor [4]. When the diameter of the AAA tumor is less than 4 cm, the annual diameter increases by about 1-4 mm. When the diameter of the tumor is greater than 5 cm, the diameter increase rate will exceed 5 mm/year. At this time, the tumor rupture rate will reach 20%. If the tumor diameter is greater than 6 cm, the tumor diameter increase rate will further increase to 7-8 mm/year, and the final tumor rupture rate will be as high 40%. Therefore, it is generally considered that tumors larger than 5 cm and women with smaller abdominal aorta

diameters larger than 4.5 cm require surgical treatment. When the size of the tumor grows too fast (>5 mm/half a year) or when the tumor causes pain, it should be timely surgical treatment [5].

Malignant tumors are major diseases that endanger human health. According to the National Cause of Death Survey, the annual mortality rate of malignant tumors in my country is about 10000. Clinical studies have shown that early diagnosis and early treatment are the most effective ways to reduce cancer mortality. Therefore, it is an urgent problem to be solved in the field of biomedicine to strive for new methods of early specific diagnosis of cancer [6]. There are many clinical diagnostic methods for tumors, and imaging is the most widely used clinical examination method. The principle is to differentiate the normal tissue from the diseased tissue according to the different attenuations of rays by different tissues on the image [7]. At present, we commonly used clinical contrast agents including ionic and nonionic, mainly small molecule compounds based on iodine, such as iohexol [8]. However, these small molecule iodine contrast agents have many shortcomings, so the imaging time is short. Lacking of targeting and specificity, it is often accompanied by side effects, with certain renal toxicity. Therefore, the development of multifunctional, high-sensitivity, and high-specificity contrast agents is an effective measure to improve the accuracy of early diagnosis of tumors, and it is also the current development trend of nanomedicine and imaging diagnostics. In recent years, the research on gold nanomaterials has made great progress. People has not only prepared nanoparticles of different sizes but also controlled their morphology and prepared many different shapes of gold nanomaterials. Gold nanoparticles (AuNPs) have unique optical properties. Good biocompatibility and the high atomic number and electron density make it a new potential contrast agent that has attracted wide attention from researchers. The small size of nanoparticles can make the diameter smaller than that of capillaries and thus can enter more tissues [9]. Moreover, due to the enhanced permeability of capillaries in cancerous tissues, nanoparticles can accumulate more in cancerous tissues through leakage, so as to better visualize tumor sites. Because of nonmetal atoms, iodine has good radiation attenuation intensity. Therefore, the contrast agents currently used in the clinic are mainly small molecular compounds based on iodine (such as iohexol). But due to the short imaging time of this small molecular compound, it lacks specificity, and it has certain toxic and side effects on the kidney. Figure 1 shows the schematic process of Au-assisted CT mapping used in abdominal aortic aneurysm. In recent years, experimental studies have shown that the contrast agent based on AuNPs has good contrast effect and can reduce the toxic and side effects of traditional contrast agents [10]. Compared with iodine, gold has a higher atom ordinal number and radiation absorption coefficient. The contrast ratio of gold per unit mass is better than that of iodine, and the modified AuNPs have a longer imaging time and better imaging effect before and after entering the organism [11]. Therefore, using AuNPs for imaging, it is possible to achieve better imaging results at lower radiation doses. With proper functional modification, the targeting and long circulation of gold nanoprobes can be achieved, which can be precise. It shows the tumor morphology, location, and size, with high sensitivity, which can improve the ability of tumor identification and diagnosis. The earliest experiments have confirmed that AuNPs can be used as linear contrast agents [12]. They will be coated with biological phase. Spherical AuNPs (dispersed in buffer) of the capacitive stabilizer were injected into the veins of mice with subcutaneously implanted breast cancer, and then, radiographic imaging was performed using a mammary gland camera. After injection of the gold nanoparticle contrast agent, it could not pass [13]. The blood vessels seen by the rays appear, and even the blood vessels of only the diameter can be seen, and the tumor site can be clearly distinguished [14]. By comparing the contrast effect of the same mass concentration of the iodine contrast agent, it is found that the AuNPs used as contrast agents exhibit a better contrast than iodine contrast. The AuNPs coated with Ryukyu were used for in vivo imaging experiments. It is proved that the coated contrast agent takes longer to develop than the iodine contrast agent [15].

Currently, AuNPs of various shapes, such as gold nanospheres, gold nanowires, gold nanorods, gold nanocages, and gold nanoshells, have been successfully prepared [16]. There are many methods for synthesizing AuNPs, but the "seed" growth method is currently the most widely used synthesis method and is also the method of synthesizing AuNPs in this experiment [17]. The basic principle of the seed growth method is to add a certain amount of gold nanoparticle seed crystals to the reaction solution. By controlling the concentration of the gold seed and the ratio of the growth solution, the directional growth of the gold seed becomes a gold nanorod with a certain aspect ratio. In this experiment, we used the seed growth method to obtain AuNPs with good morphology, and the dispersion of the AuNPs was good. The AuNPs of larger aspect ratio synthesized in this experiment moved their longitudinal plasmon resonance absorption peak to the near-infrared region, which provided suitable materials for subsequent experiments and laid the foundation for photothermal therapy of tumors. In addition, under the same intensity of X-ray irradiation, gold nanoions showed a significant effective analysis intensity and resolution compared to blank samples. Experiments show that near-infrared rays can penetrate into deep tissues to overcome the shortcomings that visible light cannot penetrate the abdominal aorta well. AuNPs absorb near-infrared rays, thereby generating heat energy to achieve the purpose of treating tumors. In addition, AuNPs also have fluorescent properties, combined with other forms of imaging methods, to achieve the purpose of multimodal imaging, and improve the diagnostic accuracy of studying the protection mechanism of CCN3.

2. Materials and Methods

Here, we reviewed the inpatients with surgical diagnosis of AAA from December 2012 to December 2019. Based on medical history, surgical records, and CT image data of preoperative and postoperative review, imaging data and surgery

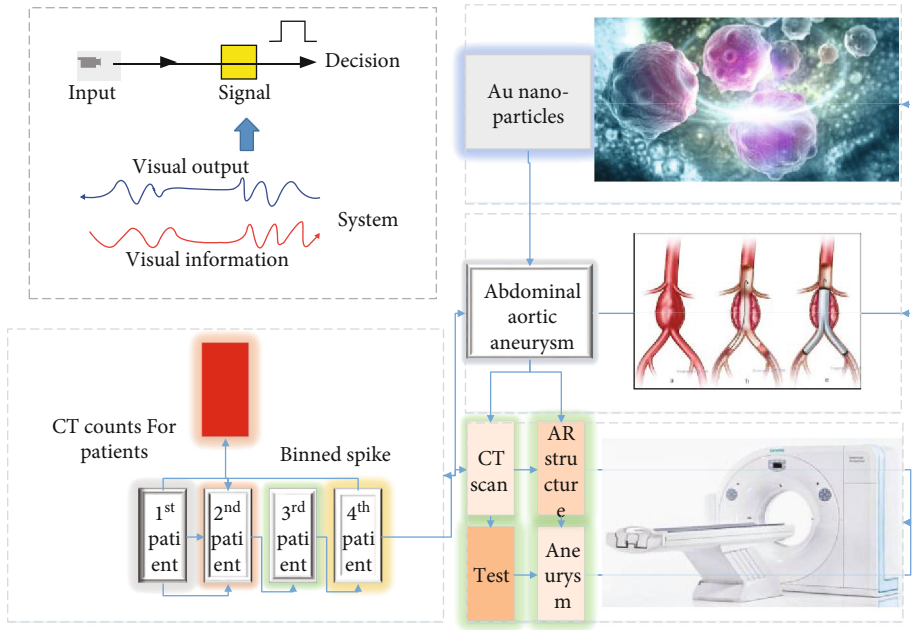

Figure 1: The schematic diagram of Au-assisted CT mapping used in abdominal aortic aneurysm.

showed 32 patients with bilateral internal iliac intact, without stenosis and occlusion. According to the different treatments of intraoperative IIA, they were divided into three groups, namely, the bilateral IIA embolism group, unilateral IIA embolism group, and retained bilateral IIA group. Among them, there were 11 patients in the bilateral IIA embolization group, 9 males and 2 females, aged 66-80 years old, with an average of (73 ± 5) years old. 9 patients were in the unilateral IIA embolization group, 6 males and 3 females, aged 69-89 years old, with an average of (76 ± 6) year. 12 patients were in the bilateral IIA group, all male, aged 34-84 years old, with an average of (62 ± 15) year.The patient was placed in a supine position and routinely sterilized and draped. 32 patients were treated with 2% lidocaine (10 mL/g, Zizhu Pharmaceutical Co., Ltd.). After local anaesthesia, a sharp knife was used to take about 5 mm at the strongest point of bilateral inguinal femoral artery pulsation. The schematic process of patients verified by CT scan can be seen in Figure 2. After skin incision, the bilateral femoral artery was punctured by modified Seldinger's technique [18], and the 6F vascular sheath group (Termo, Japan) was placed. After the same local anaesthesia, the left brachial artery was punctured and the 5F vascular sheath was inserted. The pig tail catheter was inserted into the abdomen. The upper segment of the aorta was monitored by angiography at any time. The black loach guide wire and the 5F gold-labeled pig tail catheter (COOK, USA) were fed through the femoral artery sheath to the level above the bilateral renal artery, and the AAA and peripheral vascular morphologies were observed by angiography. If the patients need to embolize IIA, we insert the Cobra catheter through the vascular sheath and select it to the corresponding IIA, then select the corresponding coil according to the size of the main artery of the IIA (COOK MWCE, United States). After the catheter is inserted into the IIA trunk, embolization is satisfactory. The gold-marked pig tail catheter scale is used as the measurement benchmark to proofread the digital subtraction angiography (DSA) machine (Siemens Artis Zeego, Germany) Leonardo postprocessing workstation measurement tool. After measuring the basic data of AAA, we combine the operation with the mappings. Before the commodity trading advisors (CTA) measurement data, we select the appropriate size stent graft (Medtronic Endurant stent graft system, United States). The femoral artery was sent into the main body stent, and under DSA fluoroscopy, and the main body stent was released at a suitable position in the tumor neck and half released until the contralateral iliac branch was completely released from the tumor cavity. After inserting the guide wire catheter into the aortic iliac branch cavity through the contralateral vascular sheath, the iliac branch stent graft is connected to the external iliac artery, and then, the main body stent is completely released to the common iliac artery or the iliac branch stent is connected to the iliac arteries. After withdrawing the main stent and bilateral femoral artery sheaths, the puncture point was closed with a vascular suture device, and finally, the pig tail catheter indwelling through the brachial artery sheath was subjected to the final angiography. The position of the stent has been clarified, and there is no endoleak. For cases where bilateral IIA is preserved, the process of embolizing IIA is omitted during the operation, and the bilateral iliac branch stent is connected to extend the common iliac artery, retaining the IIA opening.

AuNPs were synthesized in an aqueous solution as follows: first, the gold salt solution is decomposed in an appropriate solution. Second, the gold salt solution is reduced in a certain reducing agent. Finally, the stabilizer synthesis of stable AuNPs was observed. At present, the most popular method for preparing AuNPs is to reduce haucl4 with citrate in the aqueous solution under heating. For this method, by changing the concentration of gold and the concentration

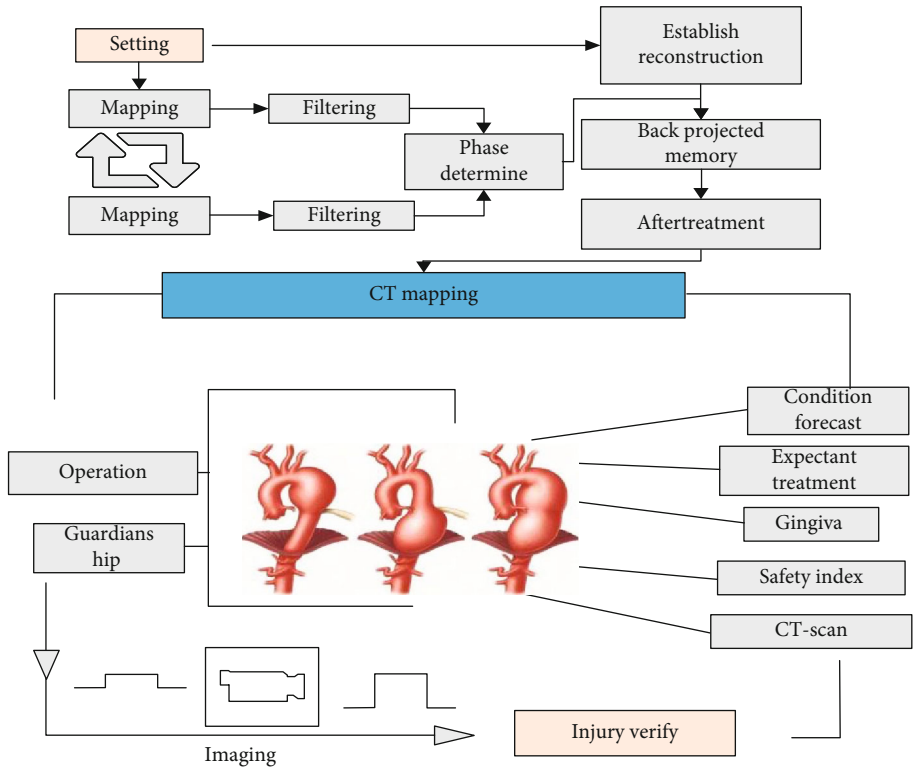

Figure 2: The schematic process of patients verifies by CT scan.

of citrate, a large number of AuNPs with an average particle size (21.8 ± 4.5) nm can be prepared.

3. Results

3.1. Endoluminal Repair of Abdominal Aortic Aneurysm Embolizes Internal Iliac Artery Circulation. The unilateral internal iliac embolism group is slightly older than the bilateral internal iliac embolism group, and the retention of the bilateral internal iliac group is relatively young. The AAA classification composition ratio between the three groups is large, and the bilateral internal iliac embolism group is type IIC [19]. Mainly, while the unilateral internal iliac embolism group is mainly type IIB, and the number of cases of AAA type IIA and type IIB of the bilateral internal iliac group is about the same. The maximum tumor diameter of AAA between the three groups is not much different. The pelvic ischemic complications only appeared in the bilateral internal iliac embolism group in this study 20]. The 4 cases of pelvic ischemic complications were mainly gluteal muscle ischemia, and all patients complained of a little soreness on the buttocks on the first day after surgery. When walking, the aggravation of gluteal muscle avascular necrosis and intestinal ischemia was absent. One week after the operation, the four patients had basically relieved the symptoms of gluteal muscle ischemia before discharge and complained of no obvious hip pain and discomfort after walking for about 500 meters. Two cases of type II endoleak caused by reflux after internal iliac artery embolization were found in the double-stage IIA embolization group after CT review. Currently, two cases of type II endoleak are under follow-up. The patient has no complaints, and the CT review image is not seen. Type II endoleaks increase and do not require intervention. The secondary intervention occurred in the bilateral IIA occlusion group. Here, we use Au nanoparticles to enhance the ion diffusion. And Figure 3 shows the functions of the Au nanoparticles in the ion passage and drug effect. When a blood vessel is severely narrowed or occluded, the potential anastomotic vessels present in the surrounding tissue of the blood vessel will supply open blood flow to the ischemic area, manifesting as the surrounding branch vessels to the anastomotic vessels gradually thicken and the blood flow gradually increases. The function of the original ischemic area is restored and free from necrosis. This pathophysiological change is called collateral circulation, which is an endogenous bypass vascular network that exists in most tissues. It is open during occlusion and ischemic injury. The collateral circulation can be an arterial-arterial connection or a connection of new microcirculation small vessels, which most intuitively represents the increase in the diameter of these collateral circulation blood vessels.

The establishment of collateral circulation also occurred after ethylene vinyl acetate (EVAR) embolization IIA. In order to clarify this result, pelvic blood vessels were involved in this process after embolization IIA. This study selected theoretically the most complete pelvic ischemia bilateral IIA embolism group and pelvic ischemia. The comparatively lighter unilateral IIA embolization group preoperative and postoperative CTA images were used as a comparison, and the changes in the diameter of the pelvic vessels before and after the operation in this group of patients were measured. At the same time, the pelvic vessels before and after the

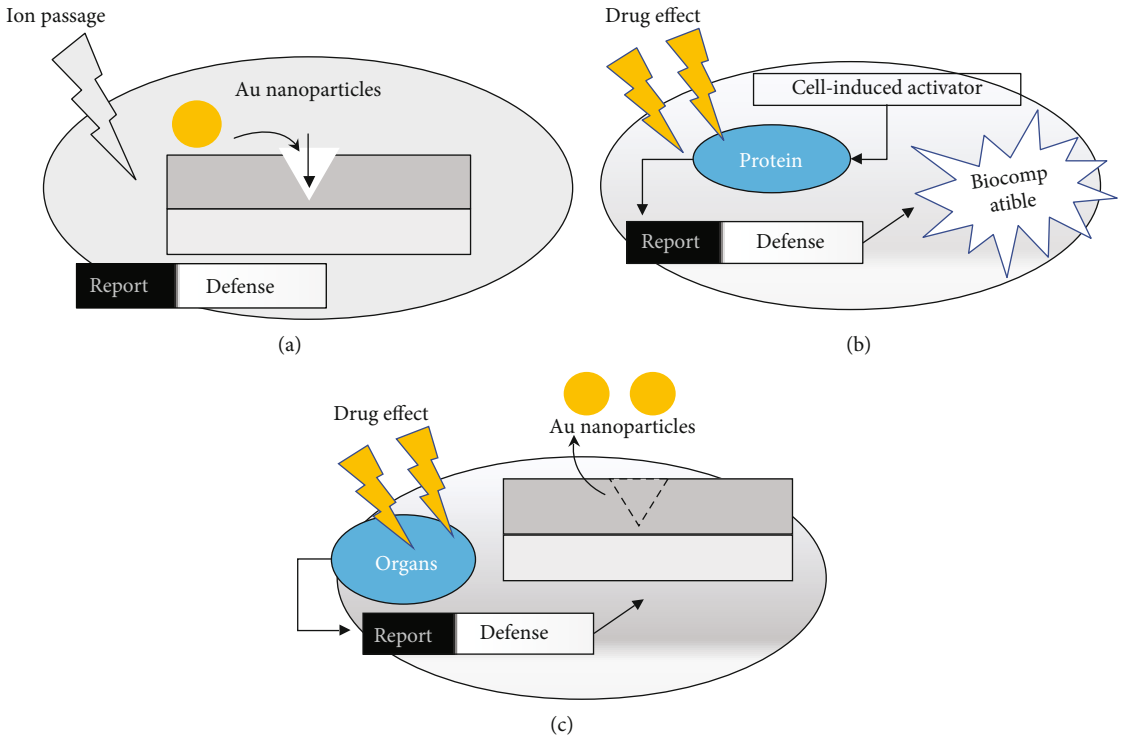

Figure 3: The functions of the Au nanoparticles in the ion passage and drug effect.

operation in the bilateral IIA group were retained as a comparison reference. It takes time to establish the collateral circulation, which depends on various factors such as the patient's age, vascular conditions, circulation status, and exercise status. In this study, 4 patients in the bilateral IIA embolism group developed pelvic ischemic symptoms and dilated blood vessels. The symptoms can be significantly alleviated, and the patients complained of basically relieved symptoms within 1 week after surgery and then were approved for discharge and continued to take oral cilostazol and beraprost sodium to improve circulation and prevent symptom recurrence. We considered that the relief of pelvic ischemic symptoms in these 4 patients is related to the eventual establishment of collateral circulation and considered transient gluteal muscle ischemia, so these 4 patients were included in this study. It is reported that observation of collateral circulation arterial models in the dogs' and pigs' hearts, rabbit hind limbs, mouse hind limbs, and other collateral circulation arteries is generally well established after 3 weeks to 5 weeks after operation, so this study selected patients from 3 months to 6 months after surgery. The CT images of the postoperative review were used as observation objects to obtain good observation of collaterals and control the influence of time variables on collateral circulation.

In this study, first, the two attending physicians carefully reviewed the postoperative CT images of patients in the bilateral IIA embolization group and the unilateral IIA embolization group and recorded the blood vessels that participated in the blood supply to the pelvic organs and muscle groups after surgery as shown in Figure 4. The observable blood vessels were the inferior mesenteric artery, inferior abdominal wall artery, deep circumflex iliac artery, superficial iliac artery,

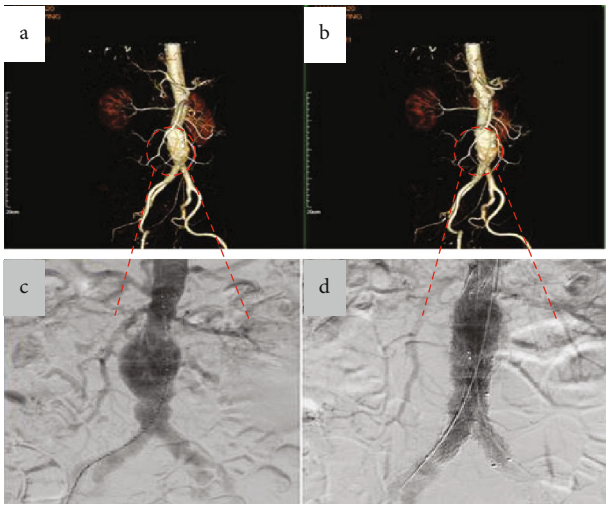

Figure 4: The CT mapping of the patients in the bilateral IIA embolization group and the unilateral IIA embolization group. The letters a and c indicate the bilateral IIA embolization group and the letters b and d indicate the unilateral IIA embolization group.

external pudendal artery, medial femoral artery, ascending branch of lateral femoral artery, and median sacral artery. From the baseline information in this group of AAA patients, it can be seen that most AAA patients have risk factors associated with hypertension, heart disease, smoking history, etc., and there is a high possibility of vascular sclerosis and occlusion. The vascular wall sclerosis of AAA patients is often very serious, so the abovementioned blood vessels may slowly occlude in the process of vascular wall sclerosis as the age

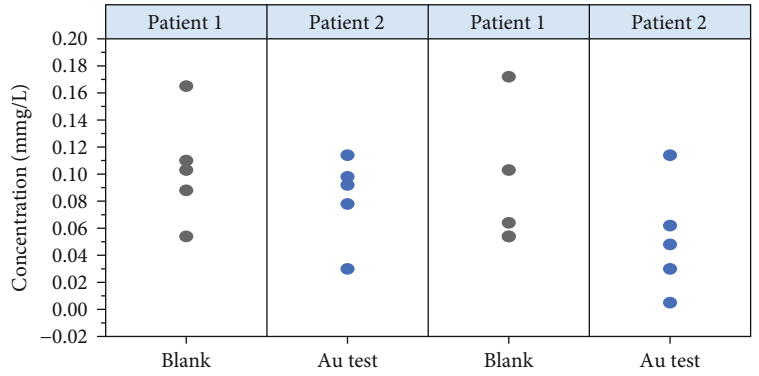

Figure 5: The concentration of AuNPs in the patients.

and time of the patient increase. If EVAR is used to embolize and close IIA, the muscles and organs of the pelvic area need to rely on the abovementioned blood vessels to maintain blood supply. It can be seen from the CTA images of this group of patients that only 2 were detected in the unilateral sacral median artery embolization group and bilateral embolism group after embolization of IIA in this group of patients. While in the two groups for the subabdominal artery and inferior mesenteric artery, the detection rate is 100% in both. The detection rate, the medial circumflex femoral artery, and the ascending branch of the lateral circumflex femoral artery are more than 80% in both groups. The detection concentration of the external pudendal artery and superficial circumflex iliac artery are mostly hovering between 0.02 mmg/L and 0.20 mmg/L. Only lateral pudendal arteries were detected in the Au test group (Figure 5).

In this study, the diameter of the abovementioned arteries in the group was significantly thicker than before the operation, and P was less than 0.05. When comparing the differences in blood vessels before and after the IA group on both sides, the diameter of the corresponding blood vessels after the operation, except under the abdominal wall, was almost equal to the diameter of the blood vessels before the operation. Outside the artery, the P value is greater than 0.05 and the average diameter of the blood vessels before and after the pancreas makes no significant difference in this group and has no apparent clinical significance. This means that the two-sided IIV embryo group is better than the two-sided IIA group. The ascending branches of the lateral rotary artery are significantly thicker than the corresponding blood vessels, preoperative CTA. Further, embryos of the bilateral IIA group and the retention of the bilateral IIV, in the bilateral IIA group after the mean metabolism of the CTA blood vessels at the pose, the lower abdominal standard, deep intestinal martyrdom, the internal femoral artery, and the ascending branches of the external femoral artery were significantly thicker than the bilateral IIA group obtained. Statistically speaking, the P value was below 0.05. The lower mesentery, surface, and vulgarity series were statistically insignificant between the two groups, and the P value was greater than 0.05. The branch of the internal intestinal martyrdom is mainly divided into branches of the walls and branches of the internal organs. The branches of the wall nourish the pelvis and external muscle groups such as closed muscle arteries,

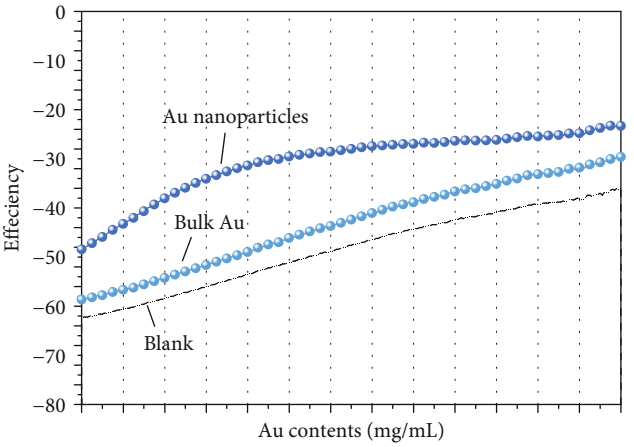

Figure 6: The effects of different states of AuNPs and blank tests.

upper enteral arteries, lower enterus arteries, enteric tendon arteries, and lateral sacral arteries. Nutrients for pelvic and outer genital gluteus muscle, including the upper bladder artery, lower bladder artery, lower rectal artery, and inner pubic region, are mainly supplied by upper and lower buttock arteries. The upper entrance is divided into deep branches and flat branches, and flat branches reach from the back of the main hall to the main hall and provide the main hall as shown in Figure 6, Au bulk runs deep through the middle gluten muscle and is delivered to the middle gluten muscle, and au nanoparticles are delivered mainly to the lower part of the main hall and the back of the thigh bone. The lower buttocks and distal parts are also first derived from the outer femoral artery. The perforated artery is supported by the ascending branch, and the closed artery is divided into the front and back branches. The front branch corresponds to the inner branch, and the femoral artery and the rear branch correspond to the imperial artery. Shameful branches of the pubis are anastomy. Reticular bowel martyrdom is mainly divided into the intestinal muscle branches, intestinal branches, abdominal wall branches, mainly intestinal muscles, intestinal bones, abdominal blood supply, and deep branches of upper hip, and fourth tendon arteries.

Side valve vessels that have anaesthetic branches and are directly connected to the upper and royal arteries, or are

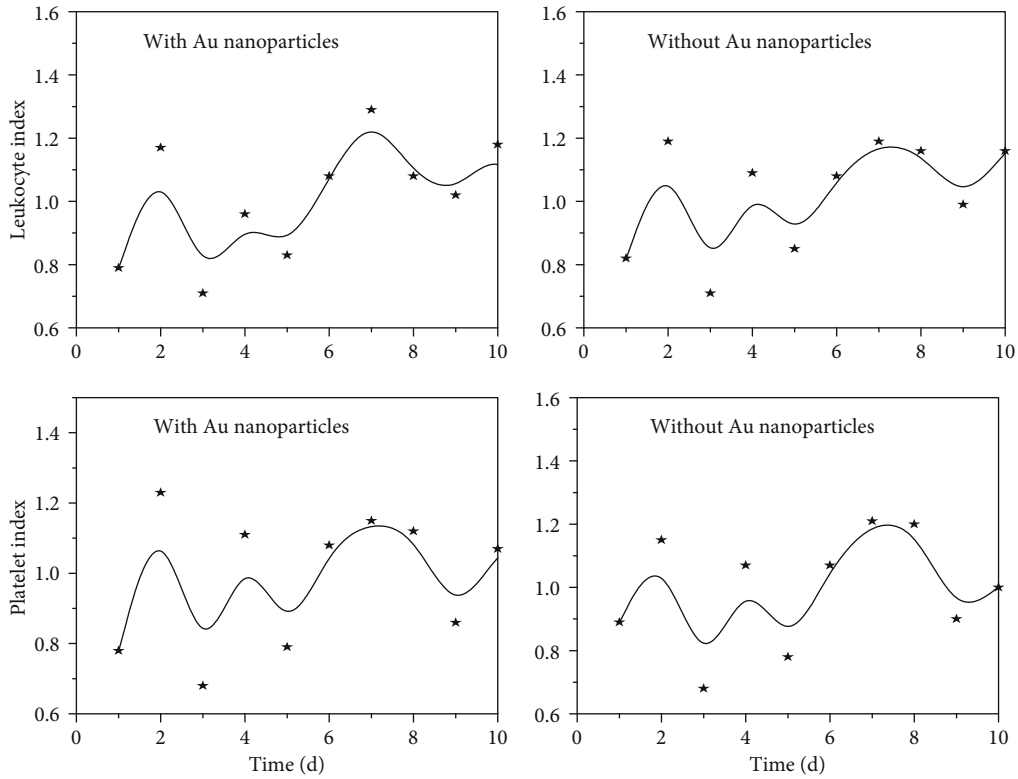

Figure 7: The platelet index and leukocyte index of CCN3 in the presence and absence of AuNPs.

delivered directly to parts of the buttocks, the upper branches of the outer femoral artery, the deep intestinal artery, and the anastomy are transferred to the lower intestines: the abdominal parameter. The supply of distal muscles is an important guarantee for the blood supply of the buttock muscle after the internal enteric artery embolism by EVAR. In summary, the IIA on both sides of the EVAR embryo, the lower abdominal artery, the deep intestinal martyrdom, the inner thigh artery, and the lateral thigh artery may be lateral circulatory vessels of the buttock muscle, preventing cervical muscle ischemia after surgery. This has an important remuneration function. In order to determine the unavoidable EVAR of Embolia IIA, the lower abdominal artery, the deep intestinal artery, the inner thigh artery, and the lateral rotational femoral artery after the preoperative CTA are preoperative. The opening is narrow and small, and the ascending branches of the lower building charterie, the deep intestinal artery, the inner thigh artery, and the outer thigh artery can be completely supplemented to predict the possibility of postoperative cervical ischemia. The blood supply of the bladder is abundant and includes mainly bladder branches of the upper, middle, and lower bladder arteries, vassals and uterine arteries, vaginal arteries, closed arteries, and royal arteries. The blood supply of the prostate is also relatively plentiful, especially twice. In the internal sham artery, lower rectal artery, and lower bladder artery branch, prostate artery from the lower bladder artery is the most important. From the blood supply of the uterus and its accessories comes above all: bilateral uterine arteries and their branches, and abdominal aorta are shared directly. The blood supply of the perineum and the penis is mainly obtained from the bilateral internal sham artery and its branches. An S-shaped colon is obtained mainly from the Si-shaped double-percussion artery submersion. It forms a high anastomy in the descending branches of the left double artery and a low anastomy in the rectal artery. The blood supply of the rectum includes the lower mesentery artery, the subcutaneous artery from the branches of the middle colon, the inner enteric artery, and the lower rectal artery of the inner chambers. There is a lot of anastomy between these three blood vessels. It can be seen that the blood source of the pelvic organ is relatively complex. The anaesthesia between them is the anastomy of the pelvic ganglia and is basically the anastomy of the visceral branches IIA and a lack of potential communication between the vascular branches and the vascular branches of the intestinal tract. If the internal intestinal martyrdom is embolism or blocked, the blood supply of the internal branch of intestinal martyrdom is mainly redistributed to the branches of the internal intestinal system and the lower mesenteric artery of the inverse blood flow of the lateral accompanying vessels of the external enteric artery and the femoral artery. Arteries and other blood vessels are connected to branches of the internal intestinal system and can reach a wide range of the pelvis. Organs can receive a blood supply. This may be the reason why there are relatively few ischemic complications associated with the embolism of the internal intestinal organs.

3.2. CCN3 Protection Mechanism. The study found that the abdominal aortic aneurysm tissue has four main characteristics: immune cells invade the blood camp wall, increased

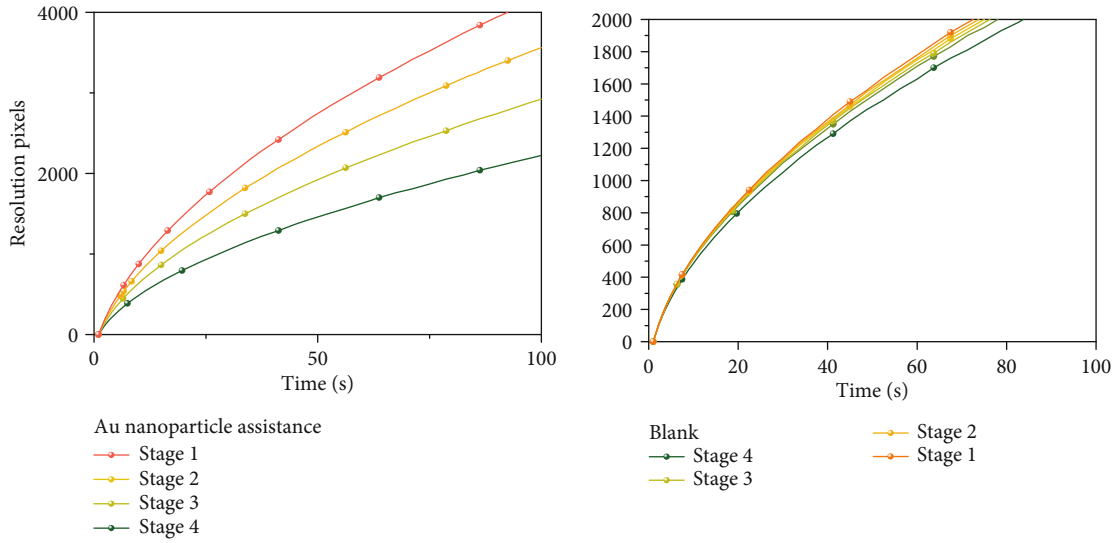

Figure 8: The resolution pixels in different stages.

matrix proteinase activity, destruction of elastin and collagen in the middle and outer layers of the blood vessel, and remodeling of the blood vessel matrix. From the perspective of a pathogenic mechanism, abdominal aortic aneurysm is the result of the interaction of vascular smooth muscle cell apoptosis, enzymatic abnormalities, and inflammation. It is currently known that multiple risk factors are associated with abdominal aortic aneurysms. Family history is positively correlated with the occurrence of abdominal aortic aneurysms. Plasma levels and blood glucose levels are negatively correlated with abdominal aortic aneurysms-6. In view of the serious consequences of the rupture of abdominal aortic aneurysms and the complexity of the etiology, it is particularly important to further study its pathogenesis. CCN3 protein is an extracellular matrix signal-related protein, which has the function of signal regulation and transmission, and belongs to the CCN protein family. This protein family has six structurally similar members, of which CCN3 is also known as N0V. In recent years, studies have found that CCN3 has a wide range of physiological functions and is involved in regulating blood stem cell hyperplasia 7, hepatocyte fibrosis, tumor angiogenesis, bone regeneration, fibrosis, fibrosis, cancer, and other physiological and pathological processes. CCN3 has four protein binding sites, which can combine different ligands to exert different signal regulation effects. Previously, our experimental group found that CCN3, as an extracellular signaling protein, can regulate endothelial cell inflammation and inhibit inflammation factors. Expressed in vascular diseases, inflammation of endothelial cells is an important part of disease occurrence, such as arteritis, atherosclerosis, and deep vein thrombosis. In our early experiments, we fed with a high-fat diet. We later found that atherosclerosis was significantly increased (unpublished). Based on the vascular inflammation regulation of CCN3, we speculate that CCN3 may be involved in regulating the pathogenesis of abdominal aortic aneurysms.

We tested human and mouse abdominal aorta with and without Au nanoparticles. The expression of CCN3 in the platelet index and leukocyte index was changed, and it was found that the expression of CCN3 was reduced as shown in Figure 7. Using the CCN3 gene knockout mouse abdominal aortic aneurysm model, it was found that the lack of CCN3 has the effect of promoting the development of abdominal aortic aneurysm. After analysis, it was found that ERK1/2 was derived from the blood vessels. The abnormal activation of the extracellular lunar, extracellular signal-regulated kinase 1/2, and the signaling pathway are induced by CCN3-deficient mice. After blocking the ERK1 signaling pathway by genes and drugs, W and drugs blocked the production of ROS and successfully inhibited the occurrence of abdominal aortic aneurysms in CCN3 mice. Based on the above results, we conclude that CNN3 exerts its ability to inhibit vascular inflammation by regulating the generation of the ERK signaling pathway and ROS role. In the study of the mechanism of aneurysms, the excessive activation of the Angl-ATIR and classic and nonclassical TGF-B signaling pathways leads to abnormal activation of vascular inflammation signaling pathways and enhanced inflammation. As shown in Figure 8, when inflammation-related signaling pathways are activated in stages 1 and 2, the resolution pixels of cells such as fibroblasts and smooth muscle cells secrete a ratio of 6 using Au NPs compared to the blank group. CCN3 protein has a wide range of physiological functions, involved in regulating cell proliferation, hepatocyte differentiation, and tumor blood vessels. We revealed that CCN3 regulates vascular endothelial inflammation by inhibiting NF-κB signaling pathway plays a protective role in inflammation. In view of the important role of endothelial cells in the regulation of vascular function, we speculate that CCN3 has a regulatory role in vascular inflammatory diseases such as abdominal aortic aneurysms.

4. Discussion

Reviewing the CTA pelvic vascularity of 4 patients with gluteal muscle ischemia after embolizing bilateral IIA in this

study, the 4 patients had severe calcification of abdominal aorta and iliac arteries, aged 73-80 years, with an average of (77 ± 3) years. In the bilateral internal iliac artery embolization group, it is relatively older, although there were preoperative and inferior abdominal wall arteries, deep iliac arteries, medial femoral artery, and ascending branch of lateral femoral artery. The superficial iliac artery is basically present. The corresponding blood vessels also thickened at 3 months after surgery. Comparing with other patients without gluteal muscle claudication in the bilateral internal iliac embolism group, no significant difference was found in CTA images before and after surgery. But according to literature reports, age is a predictor of claudication of gluteal muscles and the 4 patients having a higher age have more vascular plaques. And the other 2 patients have a history of diabetes, hypertension, and chronic renal insufficiency. It is also a factor we fully consider before deciding whether to embolize the internal iliac artery before surgery. For AAA patients with unilateral embolization IIA, one side IIA is preserved during EVAR to ensure blood supply to one pelvic organ and muscle group, and there is an extensive collateral circulation communication between the two sides of IIA, which makes pelvic ischemia complicated. The incidence of morbidity was significantly reduced. In this study, the unilateral IIA embolization group had no pelvic ischemic complications and had a lower incidence of endoleaks than the bilateral IIA embolization group. Further analysis of thin layer CT data in combination with VR vascular reconstruction technology makes it possible to find communication patterns between the pelvic and pelvic regions and muscle groups according to embolis IIA (e.g., the main stem of the lower mesenteric artery) by EVAR surgery. In a group of patients having 100%, the mesentery artery and the superior mesentery artery side subcommunication was observed. The arch of the artery, which mainly has an important communication branch between the upper mesentery artery and the lower mesentery artery, is an important communication branch. In general, the limbic arterial arch is relatively thin. The Rioran artery arch is relatively thick and frequent. The presence of these two important branches opens the lower mesentery artery when the opening is blocked and avoids the occurrence of intestinal ischemia. The closure stop geometry has a wide range of anaesthetic branches in the pool, and after the literature, there is the possibility of an anaesthetic branch with the medial femoral artery, the lower abdominal standard, and the flat branches of the opposite IIA. This group of patients is particularly patients with bilateral intraeal osteoedema. Abdominal abnormalities, medial rotational femoral arteries, vulcanic arteries, and closed arteries are associated with the IIA vulva artery branches, where lower abdominal and medial rotation femoral arteries are more common. In addition, the deep retheral artery is transferred through the anastotic branch on the surface of the lithium orbit to the upper enterus, and the upper branch of the outer rotational femoral artery is transferred through the lower hip branch to the branch of the imperial artery. The use of the IIA branch on the emboli side facilitates communication and promotes the connection of the secondary monitoring circulation and the construction of the above-mentioned vessel networks. Therefore, if the IA embolism is unavoidable in EVAR, you must select the IA progenitor embolism to minimise the effect of IIV on distal blood vessels, containing no branches of IGE. This is the same as IIA stem embolism. Compared to peripheral asthma embolism, the risk of pelvic ischemia is lower. In combination with the lateral collateral pathway connecting to the enteric artery embolism mentioned above, the preoperative CTA assesses the complete presence of the lower abdominal standard, the medial femoral artery, the deep intestinal artery, and the outer femoral artery. Since the stem contains no branches, the lower abdominal standard, the medial rotary artery, the deep ileum artery, and the lateral rotational femoral artery to the side branches of the IIA branch are relatively safe insurgery, which is not affected by embryoorism.

Accurate and controllable observation and analysis of intra-abdominal internal arterial circulation have become the focus and difficulty of treating abdominal aortic aneurysms. Among them, nanogold ions have strong absorption of X-rays at low dimensions and have local plasma resonance effect in the near ultraviolet band, which can significantly enhance the CT image signal. In this paper, we used the seed growth method to obtain AuNPs with good morphology and good dispersion of gold nanogold. The AuNPs of larger aspect ratio synthesized in this experiment moved their longitudinal plasmon resonance absorption peak to the near-infrared region, which provided suitable materials for subsequent experiments and laid the foundation for photothermal therapy of tumors. In addition, under the same intensity of X-ray irradiation, gold nanoions showed significant effective analysis intensity and resolution compared to blank samples. Experiments show that near-infrared rays can penetrate into deep tissues to overcome the shortcomings that visible light cannot penetrate the abdominal aorta well. AuNPs absorb near-infrared rays, thereby generating heat energy to achieve the purpose of treating tumors. In addition, AuNPs also have fluorescent properties, combined with other forms of imaging methods, to achieve the purpose of multimodal imaging, and improve the diagnostic accuracy of studying the protection mechanism of CCN3.

Data Availability

The data used to support the findings of this study are included within the article.

Ethical Approval

All data, models, and code generated or used during the study appear in the submittal complying With Ethics of Experimentation Statement. The study follows the principles of the Declaration of Helsinki.

Conflicts of Interest

The authors declare that they have no conflicts of interest.

Authors' Contributions

Siying Pei and Yao Sun contributed equally to this work and should be considered as coauthor.

Acknowledgments

The authors acknowledge the Funding of Mechanism of Notch signaling pathway on angiogenesis in diabetic rats (Grant: 2018-KYYWF-0967).

References

[1] N. Sakalihasan, R. Limet, and O. D. Defawe, "Abdominal aortic aneurysm," *Lancet*, vol. 365, no. 9470, pp. 1577–1589, 2005.

[2] E. Lindvall, J. Davis, A. Martirosian, G. Garcia, and L. Husak, "Bilateral internal iliac artery embolization results in an unacceptably high rate of complications in patients requiring pelvic/acetabular surgery," *Journal of Orthopaedic Trauma*, vol. 32, no. 9, pp. 445–451, 2018.

[3] H. Shan, A. Padole, F. Homayounieh et al., "Competitive performance of a modularized deep neural network compared to commercial algorithms for low-dose CT image reconstruction," *Nature Machine Intelligence*, vol. 1, no. 6, pp. 269–276, 2019.

[4] D. I. Tsilimigras, F. Sigala, G. Karaolanis et al., "Cytokines as biomarkers of inflammatory response after open versus endovascular repair of abdominal aortic aneurysms: a systematic review," *Acta Pharmacologica Sinica*, vol. 39, no. 7, pp. 1164–1175, 2018.

[5] G. Dovell, C. A. Rogers, R. Armstrong, R. A. Harris, R. J. Hinchliffe, and R. Mouton, "The effect of mode of anaesthesia on outcomes after elective endovascular repair of abdominal aortic aneurysm," *European Journal of Vascular and Endovascular Surgery*, vol. 59, no. 5, pp. 729–738, 2018.

[6] G. Giordano, D. Meo, and M. S. Lio, "Internal iliac artery aneurysm embolization with direct percutaneous puncture and thrombin injection," *Radiology Case Reports*, vol. 15, no. 3, pp. 210–213, 2020.

[7] Q. Yang, P. Yan, Y. Zhang et al., "Low-dose CT image denoising using a generative adversarial network with Wasserstein distance and perceptual loss," *IEEE Transactions on Medical Imaging*, vol. 37, no. 6, pp. 1348–1357, 2020.

[8] P. Kjellin, H. Pärsson, and H. I. V. Lindgren, "Onyx embolization for occlusion of the proximal internal iliac artery during EVAR in patients with unsuitable landing zones in the common iliac artery," *Cardiovascular and Interventional Radiology*, vol. 42, no. 7, pp. 956–961, 2019.

[9] F. A. Lederle, T. C. Kyriakides, K. T. Stroupe et al., "Open versus endovascular repair of abdominal aortic aneurysm," *The New England Journal of Medicine*, vol. 380, no. 22, pp. 2126–2135, 2019.

[10] V. T. le, V.-C. Nguyen, X.-T. Cao et al., "Highly effective degradation of nitrophenols by biometal nanoparticles synthesized using Caulis spatholobi extract," *Journal of Nanomaterials*, vol. 2021, Article ID 6696995, 11 pages, 2021.

[11] J. Beik, M. Jafariyan, A. Montazerabadi et al., "The benefits of folic acid-modified gold nanoparticles in CT-based molecular imaging:radiation dose reduction and image contrast enhancement," *Artificial Cells Nanomedicine and Biotechnology*, vol. 46, no. 8, pp. 1993–2001, 2017.

[12] V. T. Huong, N. T. T. Phuong, N. T. Tai et al., "Gold nanoparticles modified a multimode clad-free fiber for ultrasensitive detection of bovine serum albumin," *Journal of Nanomaterials*, vol. 2021, Article ID 5530709, 6 pages, 2021.

[13] T. F. X. O'Donnell, L. T. Boitano, S. E. Deery et al., "Open versus fenestrated endovascular repair of complex abdominal aortic aneurysms," *Annals of Surgery*, vol. 271, no. 5, pp. 969–977, 2020.

[14] R. A. Stokmans, P. P. H. L. Broos, M. R. H. M.v. Sambeek, J. A. W. Teijink, and P. W. M. Cuypers, "Overstenting the hypogastric artery during endovascular aneurysm repair with and without prior coil embolization: a comparative analysis from the ENGAGE Registry," *Journal of Vascular Surgery*, vol. 67, no. 1, pp. 134–141, 2018.

[15] G. Courtois, M. E. Makrygiannis, R. Hachemi et al., "Positron emission tomography/computed tomography predicts and detects complications after endovascular repair of abdominal aortic aneurysms," *Journal of Endovascular Therapy*, vol. 26, no. 4, pp. 520–528, 2019.

[16] A. Pandey, S. Khadka, and Y. Wan, "Hydroxyethyl starch-based functionalization of gold nanorods: a possible alternative to polyethylene glycol as a surface modifier," *Journal of Nanomaterials*, vol. 2021, Article ID 5555448, 11 pages, 2021.

[17] X. Zheng, S. Ravishankar, Y. Long, and J. A. Fessler, "Pwls-Ultra: an efficient clustering and learning-based approach for low-dose 3d CT image reconstruction," *IEEE Transactions on Medical Imaging*, vol. 37, no. 6, pp. 1498–1510, 2018.

[18] Y. Han, D. Wu, A. Sun et al., "Selective embolization of the internal iliac arteries for the treatment of severe hemorrhagic cystitis following hematopoietic SCT," *Bone Marrow Transplantation*, vol. 41, no. 10, pp. 881–886, 2008.

[19] P. Kulig, K. Lewandowski, B. Banaś, P. Piekorz, A. Kostka, and M. Zaniewski, "Short-term outcomes of endovascular repair of abdominal aortic aneurysm, including ruptured cases," *Videosurgery and Other Miniinvasive Techniques*, vol. 13, no. 2, pp. 243–249, 2018.

[20] M. Ripepi, G. Varetto, L. Gibello, M. A. Ruffino, P. Fonio, and P. Rispoli, "Successful percutaneous transgluteal embolization of a complex arteriovenous malformation feeding a hypogastric artery aneurysm," *Journal of Vascular Surgery Cases and Innovative Techniques*, vol. 4, no. 1, pp. 45–49, 2018.

Hindawi
Journal of Nanomaterials
Volume 2021, Article ID 9973539, 8 pages
https://doi.org/10.1155/2021/9973539

Research Article

Treatment of Yunnan Baiyao plus Kangfuxin Solution Reduces Inflammatory Response and Prevents Patients with Nasopharyngeal Carcinoma against Radiation-Induced Oral Mucositis

Xiuyu Tang, Jiahui Sun, Jie Deng, and Bin Shi

The State Key Laboratory Breeding Base of Basic Science of Stomatology (Hubei-MOST) and Key Laboratory for Oral Biomedical Ministry of Education, School and Hospital of Stomatology, Wuhan University, Wuhan, China

Correspondence should be addressed to Bin Shi; shibin_dentist@whu.edu.cn

Received 25 March 2021; Accepted 27 April 2021; Published 17 May 2021

Academic Editor: Songwen Tan

Oral mucositis refers to secondary mucosal damage, which usually occurs during cancer treatment. Generally, patients with head and neck cancers receiving radiotherapy will develop mucositis. Oral mucositis usually begins with mucosal inflammation and is characterized by erythema and confluent ulcers. The purpose of the study is to explore the therapeutic effects of Yunnan Baiyao combined with Kangfuxin solution on radiation-induced oral mucositis and the influence on production of inflammatory factors in patients with nasopharyngeal carcinoma (NPC) after radiotherapy. Clinical variables of 90 NPC patients were retrospectively analyzed. All patients underwent combined treatment (normal saline and inhalation of dexamethasone, gentamicin, and vitamin B_{12}) 1st after radiotherapy, among which 45 patients received additional treatment of Yunnan Baiyao plus Kangfuxin solution and assigned as the study group. We found that additional treatment of Yunnan Baiyao plus Kangfuxin solution remarkably attenuated pain and dry mouth and reduced the degree of mucosal hyperaemia, edema, and ulceration in NPC patients undergoing radiotherapy ($P < 0.05$). It was also found that additional treatment of Yunnan Baiyao plus Kangfuxin solution notably inhibited the release of inflammatory factors and cancer-related markers, as evidenced by lower serum levels of C-reactive protein (CRP), tumor necrosis factor-α (TNF-α), interleukin-1 (IL-1), matrix metalloproteinase-9 (MMP-9), serum hypoxia-inducible factor-1 α (HIF-1α), and vascular endothelial growth factor (VEGF) detected in the study group than the control group ($P < 0.05$). Additionally, the numbers of CD^{+3} and CD^{+4} subpopulations of T lymphocytes and the ratio of CD^{+4}/CD^{+8} in the study group were significantly higher than those in the control group ($P < 0.05$), and the number of CD^{+8} subpopulations in the study group was significantly lower than those in the control group ($P < 0.05$). In conclusion, these results indicated that additional treatment of Yunnan Baiyao plus Kangfuxin solution reduces inflammatory response and prevents patients with NPC against radiation-induced oral mucositis.

1. Introduction

Nasopharyngeal carcinoma (NPC) is a common head and neck cancer in Southeast Asia and South China, which has distinct ethnic and regional distribution characteristics [1]. At present, most patients are diagnosed with local advanced or late stage, about 90% of cases are diagnosed as lymph node metastasis, and about 5-10% of patients have distant metastasis [2]. NPC has unique clinical biological profiles such as associated Epstein-Barr virus infection and high radiosensitivity. Radiotherapy has long been recognized as the mainstay for the treatment of NPC [3]. Although intensity-modulated radiotherapy combined with radiotherapy can control primary NPC, local recurrence and distant metastasis are still the main obstacles to the success of NPC treatment [4]. Additionally, radiation can not only kill malignant tumor cells but also damage normal cells in radiation field and its surrounding area. Oral mucosa is stratified squamous epithelium with rapid renewal and high radiosensitivity. Oral mucositis is a common adverse reaction of NPC after

radiotherapy [5]. Radiotherapy-induced oral mucositis are characterized by dry mouth, taste dysfunction, oral mucosal congestion, edema, erosion, and ulcer, which seriously affect the patient's eating function, eventually lead to malnutrition and electrolyte disorder [6]. Currently, there are effective mucoprotective strategies for the management of oral mucositis. Severe mucositis can not only affect a patients' quality of life but also result in requirements for narcotic analgesics, total parenteral nutrition, interruption of cancer therapy, prolong hospitalization, and increases of the risk of local and systemic infection [7]. Accumulating evidence has suggested that the pathogenesis of oral mucositis is associated with a cascade of inflammatory events, which chronologically consist of five continuous overlapping phases: initiation, upregulation of inflammation, signaling and amplification, ulceration, and finally, wound healing [8, 9]. Oral mucositis caused by radiotherapy and chemotherapy is easy to diagnose but difficult to cure, and in recent years, a variety of medicines have been applied to the prevention and treatment of oral mucositis, but medicines with definite clinical recommended efficacy need to be developed or discovered [10]. Yunnan Baiyao (YNBY), as traditional Chinese medicine, has been attached great importance for hundreds of years, which has significant clinical efficacy in the aspects of hemostasis, improving blood circulation and dispersing blood stasis and anti-inflammation [11, 12]. Kangfuxin solution was extracted from cockroaches, which was defined as Chinese herbal medicine, and studies have indicated that Kangfuxin solution can maintain normal cell function by inhibiting the opening of calcium-dependent potassium channels caused by radiation injury, so as to reduce the pain and discomfort of patients after radiotherapy and chemotherapy [13]. The present study investigates preventive and therapeutic effects of Yunnan Baiyao combined with Kangfuxin solution on radiation-induced oral mucositis and the influence on serum levels of inflammatory factors in patients with NPC after radiotherapy.

2. Material and Method

2.1. Patient Selection and Distribution. A total of 90 patients with NPC treated with initial radiotherapy in our hospital were retrospectively analyzed form January 2013 to December 2016. They were divided into study group and control group with 45 cases, respectively, and there were 26 males and 19 females in study group who diagnosed pathologically as squamous cell carcinoma, the age ranged from 34 to 67 years old, with an average age of 48.7 ± 11.0)years. The Karnofsky Performance Scale (KPS) score was 65.9 ± 4.0 before radiotherapy, and the prescribed radiation dose was 72.0 ± 2.0 Gy. There were 23 males and 23 females in the control group which diagnosed pathologically as squamous cell carcinoma, the age ranged from 37 to 69 years old, with an average age of 49.4 ± 10.5 years. The KPS score was 66.3 ± 4.5 before radiotherapy, and the prescribed radiation dose was 72.0 ± 2.0 Gy. There was no significant difference in age, gender, pathological type, KPS score, and radiation dose between the two groups ($P > 0.05$). The eligible study subjects should meet the following inclusion criteria: (a) diagnosed with NPC by pathological examination; (b) aged from 18 to 69 years old; (c) initially diagnosed as NPC and pathologically defined as squamous cell carcinoma; (d) be treated with 30 times of radiotherapy with 70-74 Gy radiation dose each time; (e) the KPS score > 70 before radiotherapy; (f) occurrence of grade I oral mucosal during radiotherapy; (g) the hemoglobin ≥ 100 g/L, platelet $\geq 75 \times 10^9$/L, white blood cell count $\geq 3.0 \times 10^9$/L, absolute neutrophil count $\geq 1.5 \times 10^9$/L; (h) informed consent was signed. The patients were consistent with any of the below criteria should be excluded: (a) grade II or more oral mucosal reaction occurred during radiotherapy; (b) medical history of radiotherapy to the face and neck; (c) radiotherapy and chemotherapy history of other tumors; (d) complicated by other oral diseases before radiotherapy; (e) immune deficiency; (f) allergic reaction to the drugs in this study; (g) negative treatment compliance; (h) special populations during pregnancy and lactation. Figure 1 shows the screening process of eligible study subjects. The study was approved by the Medical Ethics Committee of our hospital.

2.2. Treatment Procedures. All patients were fixed under the simulator and treated with intensity-modulated radiotherapy (IMRT) with Siemens high-energy linear accelerator. The radiation dose ranged from 60 Gy to 70 Gy, and the single dose was 2 Gy with 5 days a week. At the first day of radiotherapy, local application of physiological saline combined with dexamethasone, gentamicin, and vitamin B_{12} was used to the control group: dexamethasone 5 mg, gentamicin 160,000 u, and vitamin B 12 mg were added into 100 mL of physiological saline as atomization inhalation for 15minutes each time and twice a day, while Yunnan Baiyao (Yunnan Baiyao Group Co., Ltd., National Medicine Permission Number: Z53020798, specification: 4 g) as oral administration and Kangfuxin solution (Inner Mongolia Dual Fufangtai Pharmaceutical Co., Ltd, National Medicine Permission Number: Z15020805, specification: 30 mL × 4) for gargling and local application of physiological saline combined with dexamethasone, gentamicin, and vitamin B_{12} for atomization inhalation were applied to the study group. The atomization method was the same as that of the control group, Kangfuxin solution 10 mL was used to gargle for 2 minutes to make it fully contact with the surface of oral mucosa after cleaning the oral cavity in the morning and evening, and food and water should not be eaten after gargling within 1 hour. Yunnan Baiyao powder was orally administrated, with 0.5 g once and 3 times a day. Fish and bean products were forbidden during medication. The treatment started from the beginning of radiotherapy to the 7 days after the radiotherapy. There were no adverse reactions in the course of medication in the study group and the control group.

2.3. Classification of Radiation-Induced Oral Mucositis. The classification of radiation-induced oral mucositis was made based on radiation therapy oncology group (RTOG) [14], which was detailed in Table 1. In addition, patient outcome was also analyzed by scoring symptoms including pain, mucosal hyperaemia and edema, mucosal ulceration, and

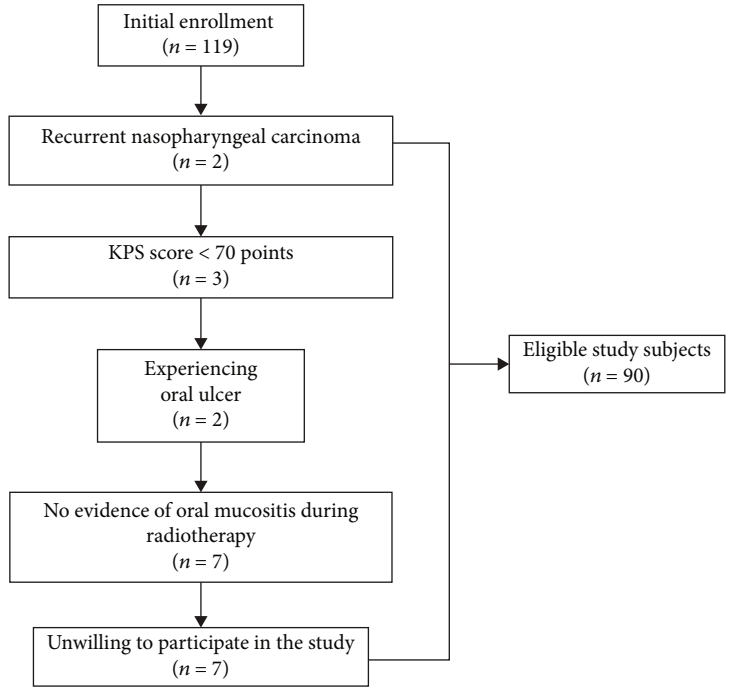

Figure 1: The screening process of eligible study subjects. Finally, 90 eligible patients with nasopharyngeal carcinoma meet predefined inclusion and exclusion criteria and were recruited into the present study.

Table 1: Classification of radiation-induced oral mucositis.

Grade	Symptom	Treatment
0	No evidence of oral mucositis	No requirement
1	Feeling slight pain but no need of painkillers, with evidence of mild hyperaemia of oral mucosa	No requirement
2	Feeling moderate pain, visible spotted mucositis, detectable inflammatory substances in the secretion	Administration of painkiller
3	Presence of flaky oral mucositis, accounting for 50% of the radiation area, with pain need to be relieved by anesthetic drugs	Administration of anesthetic drugs
4	Mucosal ulceration, bleeding, and erosions occurring in the inflammatory areas, accounting for more than 50% of radiation area	Treatment discontinued or changing patterns of nutrition

dry mouth. The total score, respectively, was 0-6 points for each symptom. The lower the score was, the better the efficacy was.

2.4. Serum Extraction. Two tubes of fasting venous blood (5 mL) were collected from each patient, and blood collection was performed twice before and after treatment. The blood samples were refrigerated under 4°C for 45 minutes and centrifuged with 3500 r/min for 15 min. The serum was extracted from testing tube, which was immediately stored in a low-temperature refrigerator (MDF-U5412, SANYO, Japan) at -80°C.

2.5. Reagents and Cytokine Determination. Cytokine detection in the serum was achieved by commercial kits (RapidBio, West Hills, CA, USA; C-reactive protein (CRP), tumor necrosis factor-α (TNF-α), interleukin-1 (IL-1), matrix metalloproteinase-9 (MMP-9), hypoxia-inducible factor-1 α (HIF-1α), and vascular endothelial growth factor (VEGF)). Serum cytokine measurement was performed using an enzyme-linked immunosorbent assay (ELISA) method as specified by the kit manufactures at test and reference wavelengths of 450 and 550 nm, respectively. The results were expressed in mg/L, μg/L, or ng/L and relative to standard curves obtained from titrations of the corresponding recombinant factors provided the kit manufactures. The manufacturers guarantee the specificity of each individual kit.

2.6. Flow Cytometric Analysis of T Cell Subpopulation. Venous blood (2 mL) was extracted into EDTA anticoagulant tube and centrifuged with lymphocyte separation solution (2 mL) at the speed of 1500 r/min for 10 minutes so as to collect the layer containing lymphocyte, which was rinsed with 2 mL phosphate-buffered solution (PBS), and centrifuged twice at the same speed and time to discard the supernatant. The final cell suspension was divided into two test tubes with 5 mL volumes, respectively, and have them made with the concentration of $1 \times 106\,mL^{-1}$. Four test tubes were added with lymphocyte cell suspension 500 μL, respectively, the monoclonal antibody (McAb) of mouse anti-human CD^{+3},

Table 2: The scores of symptoms of oral mucositis including pain, mucosal hyperaemia and edema, mucosal ulceration, and dry mouth.

Group	Case	Time	Pain	Mucosal hyperaemia and edema	Mucosal ulceration	Dry mouth
Control group	45	Before treatment	4.20 ± 1.11	4.37 ± 1.24	3.97 ± 0.88	3.73 ± 0.81
		After treatment	2.29 ± 0.67	2.01 ± 0.67	1.74 ± 0.39	1.65 ± 0.32
t			4.127	5.169	3.594	3.419
P			0.033	0.012	0.017	0.022
Study group	45	Before treatment	4.16 ± 1.09	4.33 ± 1.22	3.95 ± 0.85	3.71 ± 0.79
		After treatment	1.41 ± 0.36[a]	1.08 ± 0.42$^{\triangle}$	0.94 ± 0.21$^{\triangle}$	0.91 ± 0.15$^{\triangle}$
t			5.394	5.713	4.837	5.284
P			0.01	0.001	0.013	0.001

The results were expressed as mean ± standard deviation and analyzed by the t-test. $^{\triangle}$ indicates $P < 0.05$ compared with the control group.

Table 3: The classification of radiation-induced oral mucositis was evaluated in the control and observation group after treatment.

Group	Case	Grade 0	Grade 1	Grade 2	Grade 3	Grade 4
Control group	45	1 (2.22%)	14 (31.11%)	21 (46.67%)	7 (15.56%)	2 (4.44%)
Study group	45	4 (8.89%)	18 (40.00%)	21 (46.67%)	2 (4.44%)	0
χ^2				2.203		
P				0.028		

The results were described by ratio or percentage and analyzed by the chi-square test.

CD^{+4}, and CD^{+8} (120 μL), all conjugated with fluorescin isothiocyanate (FITC) and analyzed by flow cytometry (FAC Scan, BD Pharmingen, U.S), and McAb of mouse anti-human IgG in positive control (120 μL), which was examined by BIO450 enzyme-labelled instrument, and kept the solution away from light for 30 minutes. Centrifugation was performed again at the speed of 2000 R/min maintaining 15 minutes and rinsed with 2 mL PBS, and the above two procedures were performed one more time to get the supernatant but discarded it; finally, PBS 500 μL was added into the solution. All data were analyzed by CellQuest Plot software.

2.7. Statistical Analysis. All data were processed by the SPSS 23.0 software. The measurement data were defined as mean ± standard deviation and analyzed by the t-test. The counting data were described by ratio or percentage and analyzed by the chi-square test. A level of $P < 0.05$ was considered statistically significance.

3. Result

3.1. Yunnan Baiyao plus Kangfuxin Solution Relieved the Symptoms of Irradiation-Induced Oral Mucositis. We first scored 90 NPC patients about their symptoms of oral mucositis including pain, mucosal hyperaemia and edema, mucosal ulceration, and dry mouth after radiotherapy. Each symptom was scored from 0 to 6 points. The lower the score was, the better the efficacy was. As shown in Table 2, although the scores of symptoms were all decreased after normal saline and inhalation of dexamethasone, gentamicin, and vitamin B_{12} with or without additional treatment of Yunnan Baiyao plus Kangfuxin solution ($P < 0.05$), this decrease was greater for patients with additional treatment of Yunnan Baiyao plus Kangfuxin solution. The study group exhibited few points than the control group after treatment ($P < 0.05$). These data suggested that additional treatment of Yunnan Baiyao plus Kangfuxin solution relieved the symptoms of irradiation-induced oral mucositis in NPC patients after radiotherapy.

3.2. Yunnan Baiyao plus Kangfuxin Solution Attenuated the Disease Severity of Irradiation-Induced Oral Mucositis. Subsequently, the classification of radiation-induced oral mucositis was evaluated in the control and observation groups after normal saline and inhalation of dexamethasone, gentamicin, and vitamin B_{12} with or without additional treatment of Yunnan Baiyao plus Kangfuxin solution. The control group had 1 case with no evidence of oral mucositis, 14 cases of grade 1, 21 cases of grade 2, 7 cases of grade 3, and 2 cases of grade 4. The study group had 4 cases with no evidence of oral mucositis, 18 cases of grade 1, 21 cases of grade 2, 2 cases of grade 3, and 0 case of grade 4. It was revealed that the control group and the study group were significantly different with regard to occurrence of radiation-induced oral mucositis according to classifications ($P < 0.05$, Table 3).

3.3. Yunnan Baiyao plus Kangfuxin Solution Reduced Inflammatory Response in Irradiation-Induced Oral Mucositis. Early inflammation is a major factor of mucosal reactions to radiotherapy. Radiation-induced oral mucositis is associated with continuing presence of systemic inflammation. Given that, the release of inflammatory factors was examined by ELISA detection of serum CRP, TNF-α, IL-1, and MMP-9 before and after normal saline and inhalation of dexamethasone, gentamicin, and vitamin B_{12} with or

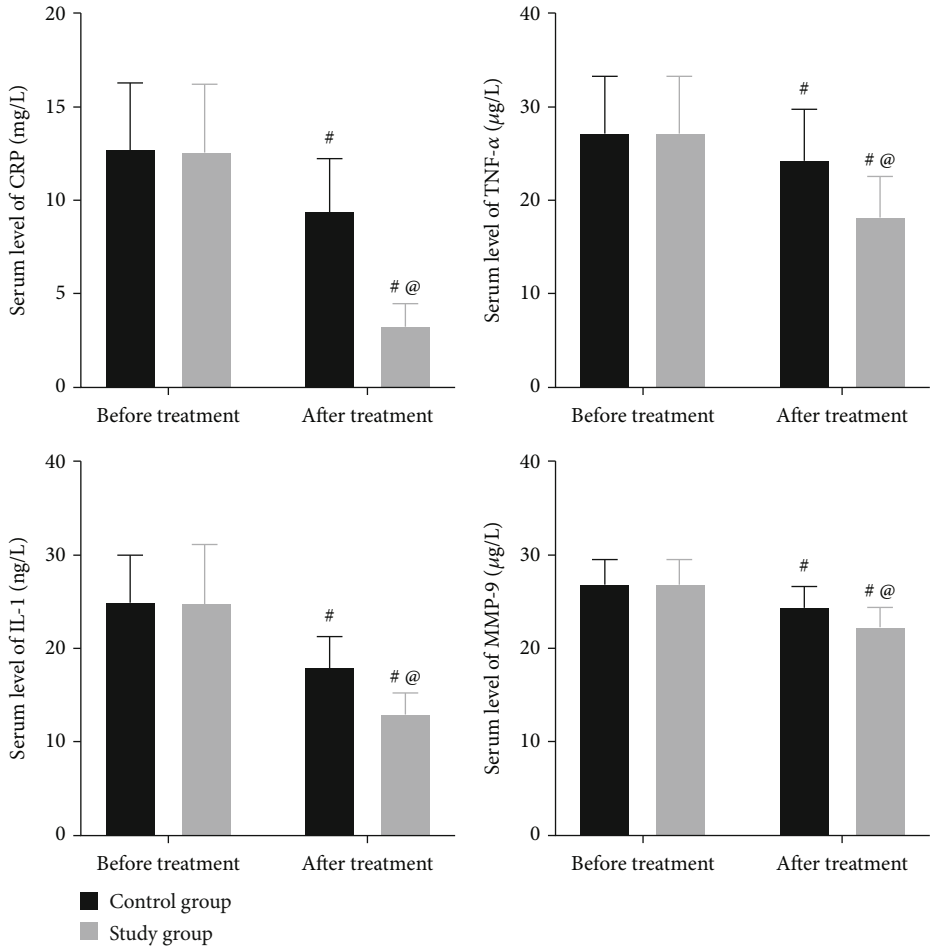

Figure 2: ELISA detection of serum levels of CRP, TNF-α, IL-1, and MMP-9 in the control and study groups before and after treatment. The results were expressed as were defined as mean ± standard deviation and analyzed by the t-test. # indicates $P < 0.05$ compared with before treatment, and @ indicates $P < 0.05$ compared with the control group.

without additional treatment of Yunnan Baiyao plus Kangfuxin solution. Although the serum levels of CRP, TNF-α, IL-1, and MMP-9 were all remarkably declined after normal saline and inhalation of dexamethasone, gentamicin, and vitamin B_{12} with or without additional treatment of Yunnan Baiyao plus Kangfuxin solution ($P < 0.05$), the study group exhibited declined serum levels of CRP, TNF-α, IL-1, and MMP-9 than the control group after treatment ($P < 0.05$, Figure 2). These results indicated that additional treatment of Yunnan Baiyao plus Kangfuxin solution reduced inflammatory response in NPC patients with irradiation-induced oral mucositis.

3.4. Yunnan Baiyao plus Kangfuxin Solution Reduced HIF-1α and VEGF Expressions in Irradiation-Induced Oral Mucositis. HIF-1α is a transcription factor induced by hypoxia or inflammation and plays a pivotal role in physiological and pathological processes. Results of ELISA showed that the serum level of HIF-1α in the two groups were significantly lower after treatment than those before treatment ($P < 0.05$), and the change was more significant in the study group than those in the control group ($P < 0.05$, Figure 3). VEGF is a potent angiogenic cytokine implicated in tumour vasculogenesis. Previous evidence showed that VEGF was upregulated after ulceration. Our ELISA results revealed that the serum level of VEGF in the two groups were significantly lower after treatment than those before treatment ($P < 0.05$). The study group had a declined VEGF level when comparable to the control group ($P < 0.05$, Figure 3).

3.5. Yunnan Baiyao plus Kangfuxin Solution Sustained T Lymphocytes. Increasing evidence points that oral mucositis may be related with autoimmune dysregulation that is characterized by reduced T cells. The numbers of CD^{+3}, CD^{+4} T cells and the ratio of CD^{+4}/CD^{+8} were increased significantly, and the numbers of CD^{+8} were declined significantly after treatment than those before treatment ($P < 0.05$); these changes were more obvious in the study group compared with the control group ($P < 0.05$, Table 4).

4. Discussion

The management of oral mucositis mainly depends on local medication. Bacterial infection is often secondary to oral mucositis, which further reduces the tolerance of local normal tissues to radiation. Therefore, gentamicin is generally

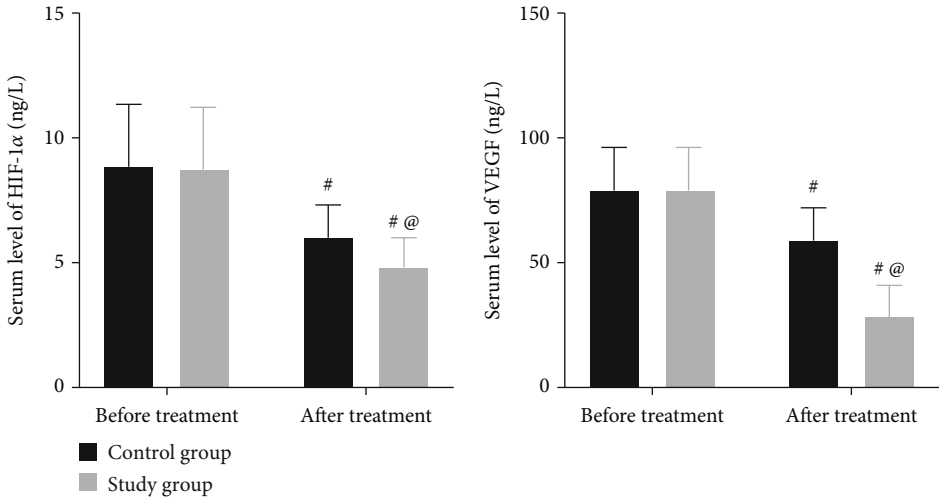

Figure 3: ELISA detection of serum levels of HIF-1α and VEGF in the control and study group before and after treatment. The results were expressed as were defined as mean ± standard deviation and analyzed by the t-test. # indicates $P < 0.05$ compared with before treatment, and @ indicates $P < 0.05$ compared with the control group.

Table 4: The numbers of CD^{+3}, CD^{+4}, and CD^{+8} subpopulations of T cells and the ratio of CD^{+4}/CD^{+8} in the control and study group before and after treatment.

Group	Case	Time	CD^{+4} (%)	CD^{+8} (%)	CD^{+3} (%)	CD^{+4}/CD^{+8}
Control group	45	Before treatment	36.56 ± 10.52	29.14 ± 3.05	54.33 ± 12.85	0.82 ± 0.36
		After treatment	40.29 ± 10.43	32.37 ± 4.48	69.94 ± 12.57	1.31 ± 0.49
t			6.149	7.134	8.529	3.475
P			0.001	0.001	0.001	0.021
Study group	45	Before treatment	36.46 ± 10.03	29.12 ± 3.06	53.91 ± 12.87	0.84 ± 0.34
		After treatment	48.14 ± 11.04[a]	37.19 ± 6.10△	80.65 ± 10.99△	1.73 ± 0.65△
t			7.021	10.102	24.395	4.839
P			0.001	0.001	0.001	0.016

The results were expressed as mean ± standard deviation and analyzed by the t-test. △ indicates $P < 0.05$ compared with the control group.

used in clinical antibacterial treatment for oral mucositis [15]. Dexamethasone can reduce the response of tissue to inflammatory factors and help to control inflammation in oral mucositis [16]. Vitamin B_{12} can promote the regeneration of epithelial cells, maintain the function of epithelial cells, and accelerate the healing of oral ulcer [17]. The patients in the control group were given an inhalation (15 min once, twice for one day) of 16 F.U gentamicin, 5 mg dexamethasone, and 2 mg vitamin B_{12}.

Yunnan Baiyao is a traditional Chinese herbal medicine that has been used to treat wounds for over 100 years. It is called "holy medicine" for traumatology. It is good at promoting blood circulation to stop bleeding, dispersing blood stasis, and detumescence. It has the pharmacological effects of hemostasis, bacteriostasis, and removing blood stasis. It can promote the synthesis of collagen, promote the growth of epidermal cells, and improve the local microcirculation, which is conducive to the rapid repair of damaged mucosa [18].

Kangfuxin liquid is a drug extracted from the dried body of Fusarium falcatum, with effective components polyols and peptides [19]. It can promote fibroblasts to synthesize a large amount of collagen, which is conducive to the growth of epidermal cells in injured tissues, accelerate the proliferation of granulation tissue, induce the proliferation of mucosal capillary vessels, improve local blood supply, and facilitate the rapid repair of wounds [20, 21]. Kangfuxin liquid contains mucosamine that can enhance the immune function and promote wound healing [22]. In this study, Yunnan Baiyao combined with Kangfuxin liquid was used in the prevention and treatment of oral mucositis after radiotherapy, and satisfactory results were achieved. The degree of oral mucositis of patients was milder, and the incidence of severe injury above grade 3 was significantly lower than that of patients who were treated with local application of normal saline combined with dexamethasone, gentamicin, and vitamin B_{12} by aerosol inhalation. In addition, the safety of Yunnan Baiyao and Kangfuxin Liquid was good, and there was no special discomfort during the treatment.

The inflammation was induced in oral mucositis of patients. The level of CRP was increased in cancer patients after radiotherapy [23]. TNF-α is a cytokine secreted by the

monocyte macrophage system, which has a variety of biological activities and participates in the occurrence and development of inflammatory diseases such as infection, trauma, autoimmune diseases, and malignant tumors [24]. IL-1, a member of the interleukin family, is produced by activated monocyte macrophages. It can stimulate T lymphocyte activation, synthesize CRP, and cause fever and cachexia [25]. TGF-β1 is a member of the transforming growth factor family, which can transform the phenotype of normal fibroblasts [26]. MMP-9 is a member of matrix metalloproteinase family, which can degrade or remodel extracellular matrix and release TGF-β1 [27]. In this study, we found that the levels of CRP, TNF-α, IL-1, TGF-β1, and MMP-9 in NPC patients with radiotherapy were significantly higher than those before radiotherapy. The results suggest that radiation injury can stimulate the body to produce inflammatory response, activate monocyte macrophages, and increase the levels of inflammatory factors. However, the levels of CRP, TNF-α, IL-1, TGF-β1, and MMP-9 in patients with adjuvant therapy of Yunnan Baiyao and Kangfuxin liquid were significantly reduced, suggesting that Yunnan Baiyao and Kangfuxin liquid can alleviate radiation-induced oral mucositis, which may be related to the fact that the glucosamine components in Kangfuxin liquid can regulate the synthesis of inflammatory substances such as interleukin, interferon, and leukotriene.

In summary, Yunnan Baiyao combined with Kangfuxin liquid effectively prevents radiotherapy-induced oral mucositis and reduces the release of inflammatory factors, compared with normal saline combined with dexamethasone, gentamicin, and vitamin B_{12}. Yunnan Baiyao combined with Kangfuxin liquid improves the quality of life in patients, and this approach is effective, user-friendly, safe, and appropriate for clinical application. Nevertheless, large-scale populations should be recruited to strengthen the validation of our results.

Data Availability

The data used to support the findings of this study are included within the article.

Conflicts of Interest

All authors declare that they have no conflict of interest.

Authors' Contributions

Xiuyu Tang and Jiahui Sun contributed equally to this work and regarded as co-first authors.

References

[1] Y. P. Chen, A. T. C. Chan, Q. T. Le, P. Blanchard, Y. Sun, and J. Ma, "Nasopharyngeal carcinoma," *Lancet*, vol. 394, no. 10192, pp. 64–80, 2019.

[2] R. Guo, Y. P. Mao, L. L. Tang, L. Chen, Y. Sun, and J. Ma, "The evolution of nasopharyngeal carcinoma staging," *The British Journal of Radiology*, vol. 92, no. 1102, p. 20190244, 2019.

[3] X. S. Sun, X. Y. Li, Q. Y. Chen, L. Q. Tang, and H. Q. Mai, "Future of Radiotherapy in Nasopharyngeal Carcinoma," *The British Journal of Radiology*, vol. 92, no. 1102, p. 20190209, 2019.

[4] A. W. M. Lee, W. T. Ng, J. Y. W. Chan et al., "Management of locally recurrent nasopharyngeal carcinoma," *Cancer Treatment Reviews*, vol. 79, p. 101890, 2019.

[5] P. J. Li, K. X. Li, T. Jin et al., "Predictive model and precaution for oral mucositis during chemo-radiotherapy in nasopharyngeal carcinoma patients," *Frontiers in Oncology*, vol. 10, p. 596822, 2020.

[6] X. X. Zhu, X. J. Yang, Y. L. Chao et al., "The potential effect of oral microbiota in the prediction of mucositis during radiotherapy for nasopharyngeal carcinoma," *eBioMedicine*, vol. 18, pp. 23–31, 2017.

[7] M. Agulnik and J. B. Epstein, "Nasopharyngeal carcinoma: current management, future directions and dental implications," *Oral Oncology*, vol. 44, no. 7, pp. 617–627, 2008.

[8] R. V. Lalla, D. P. Saunders, and D. E. Peterson, "Chemotherapy or radiation-induced oral mucositis," *Dental Clinics of North America*, vol. 58, no. 2, pp. 341–349, 2014.

[9] M. Kishimoto, M. Akashi, K. Tsuji et al., "Intensity and duration of neutropenia relates to the development of oral mucositis but not odontogenic infection during chemotherapy for hematological malignancy," *PLOS ONE*, vol. 12, no. 7, p. e0182021, 2017.

[10] W. Parulekar, R. Mackenzie, G. Bjarnason, and R. C. Jordan, "Scoring oral mucositis," *Oral Oncology*, vol. 34, no. 1, pp. 63–71, 1998.

[11] J. L. Ren, H. Dong, Y. Han et al., "Network pharmacology combined with metabolomics approach to investigate the protective role and detoxification mechanism of _Yunnan Baiyao_ formulation," *Phytomedicine*, vol. 77, p. 153266, 2020.

[12] X. Ren, Y. Zhu, L. Xie, M. Zhang, L. Gao, and H. He, "Yunnan Baiyao diminishes lipopolysaccharide-induced inflammation in osteoclasts," *Journal of Food Biochemistry*, vol. 44, no. 6, p. e13182, 2020.

[13] Y. Luo, M. Feng, Z. Fan et al., "Effect ofKangfuxinSolution on Chemo/Radiotherapy-Induced Mucositis in Nasopharyngeal Carcinoma Patients: A Multicenter, Prospective Randomized Phase III Clinical Study," *Evidence-Based Complementary and Alternative Medicine*, vol. 2016, Article ID 8692343, 7 pages, 2016.

[14] J. Bardy, A. Molassiotis, W. D. Ryder et al., "A double-blind, placebo-controlled, randomised trial of active manuka honey and standard oral care for radiation-induced oral mucositis," *The British Journal of Oral & Maxillofacial Surgery*, vol. 50, no. 3, pp. 221–226, 2012.

[15] D. P. Saunders, On behalf of the Mucositis Study Group of the Multinational Association of Supportive Care in Cancer/International Society of Oral Oncology (MASCC/ISOO), T. Rouleau et al., "Systematic review of antimicrobials, mucosal coating agents, anesthetics, and analgesics for the management of oral mucositis in cancer patients and clinical practice guidelines," *Support Care Cancer*, vol. 28, no. 5, pp. 2473–2484, 2020.

[16] P. Molina Prats, F. Gomez Garcia, F. Martinez Diaz, R. Amaral Mendes, and P. Lopez-Jornet, "The therapeutic effects of apigenin and dexamethasone on 5-fluorouracil-induced oral mucositis - a pilot study using a Syrian hamster model," *Journal of Oral Pathology & Medicine*, vol. 46, no. 2, pp. 142–147, 2017.

[17] G. Liang, W. Du, Q. Ke, B. Huang, and J. Yang, "The effects of recombinant human granulocyte colony-stimulating factor mouthwash on radiotherapy-induced oral mucositis in locally advanced nasopharyngeal carcinoma patients," *Advances in Clinical and Experimental Medicine*, vol. 26, no. 3, pp. 409–413, 2017.

[18] S. C. Lenaghan, L. Xia, and M. Zhang, "Identification of nanofibers in the Chinese herbal medicine: Yunnan Baiyao," *Journal of Biomedical Nanotechnology*, vol. 5, no. 5, pp. 472–476, 2009.

[19] K. S. Qu, Y. Li, Y. Liang et al., "KangFuXin Liquid in the Treatment of Diabetic Foot Ulcer: A Systematic Review and Meta-Analysis," *Evidence-Based Complementary and Alternative Medicine*, vol. 2019, Article ID 3678714, 10 pages, 2019.

[20] J. B. Zou, X. F. Zhang, Y. J. Shi et al., "Therapeutic Efficacy of Kangfuxin Liquid Combined with PPIs in Gastric Ulcer," *Evidence-Based Complementary and Alternative Medicine*, vol. 2019, Article ID 1324969, 13 pages, 2019.

[21] X. J. Ma and G. Y. Huang, "Current status of screening, diagnosis, and treatment of neonatal congenital heart disease in China," *World Journal of Pediatrics*, vol. 14, no. 4, pp. 313-314, 2018.

[22] H. Yao, S. Wei, Y. Xiang et al., "Kangfuxin Oral Liquid Attenuates Bleomycin-Induced Pulmonary Fibrosis via the TGF-β1/Smad Pathway," *Evidence-Based Complementary and Alternative Medicine*, vol. 2019, Article ID 5124026, 14 pages, 2019.

[23] E. M. Thurner, S. Krenn-Pilko, U. Langsenlehner et al., "The elevated C-reactive protein level is associated with poor prognosis in prostate cancer patients treated with radiotherapy," *European Journal of Cancer*, vol. 51, no. 5, pp. 610–619, 2015.

[24] J. R. Bradley, "TNF-mediated inflammatory disease," *The Journal of Pathology*, vol. 214, no. 2, pp. 149–160, 2008.

[25] C. A. Dinarello, "Interleukin-1 in the pathogenesis and treatment of inflammatory diseases," *Blood*, vol. 117, no. 14, pp. 3720–3732, 2011.

[26] K. K. Kim, D. Sheppard, and H. A. Chapman, "TGF-β1 Signaling and Tissue Fibrosis," *Cold Spring Harbor Perspectives in Biology*, vol. 10, no. 4, p. a022293, 2018.

[27] H. Huang, "Matrix Metalloproteinase-9 (MMP-9) as a Cancer Biomarker and MMP-9 Biosensors: Recent Advances," *Sensors*, vol. 18, no. 10, p. 3249, 2018.

Hindawi
Journal of Nanomaterials
Volume 2021, Article ID 9946224, 7 pages
https://doi.org/10.1155/2021/9946224

Research Article

Oral Administration of Mifepristone Combined with Ultrasound-Guided Radiofrequency Ablation in Treating Patients with Uterine Fibroids: Efficacy, Safety, and Alternations of Inflammatory Cytokines, Adhesion Molecules, and Growth Factors

Aiqin Hou, Zhen Yan, Yuanyuan Zhang, and Jing Hou

Affiliated Hospital of Yan'an University, China

Correspondence should be addressed to Jing Hou; hgfytu2233@163.com

Received 25 March 2021; Revised 8 April 2021; Accepted 12 April 2021; Published 17 May 2021

Academic Editor: Songwen Tan

Uterine fibroids are one of the most common and yet understudied diseases in women mainly during their reproductive years. The study analyzed the efficacy and safety of oral administration of mifepristone combined with ultrasound-guided radiofrequency ablation in treating patients with uterine fibroids, as well as changes of inflammatory cytokines including procalcitonin (PCT), high-sensitivity C-reactive protein (hs-CRP), and tumor necrosis factor-alpha (TNF-α), adhesion molecules including monocyte chemotactic protein 1 (MCP-1) and soluble intercellular adhesion molecule 1 (sICAM-1), and growth factors including vascular endothelial growth factor (VEGF), epidermal growth factor (EGF), basic fibroblast growth factor (bFGF), transforming growth factor-β (TGF-β), and TGF-β receptor. A total of 130 patients who were admitted into our hospital for uterine fibroids from December 2016 to June 2018 were included, among which 65 women were given ultrasound-guided radiofrequency ablation alone (control group) and the remaining women were given oral administration of mifepristone combined with ultrasound-guided radiofrequency ablation (experimental group). Reduced volumes of uterus and fibroids were observed in both two groups after treatment ($P < 0.05$). It was found that the experimental group exhibited higher total effective rate and smaller volumes of uterus and fibroids than the control group ($P < 0.05$). Following treatment, the levels of MCP-1, sICAM-1, VEGF, EGF, bFGF, TGF-β, TGF-β receptor, PCT, hs-CRP, and TNF-α in the serum in the two groups were declined ($P < 0.05$), while this decline was more significantly in the experimental group than the control group ($P < 0.05$). Besides, there was no significant difference in the incidence rate of adverse reactions between the two groups ($\chi^2 = 0.781$, $P > 0.05$). These results collectively indicate the high efficacy and safety of oral administration of mifepristone combined with ultrasound-guided radiofrequency ablation in treating patients with uterine fibroids, as this combination therapy could inhibit the expressions of inflammatory cytokines, adhesion molecules, and growth factors.

1. Introduction

Uterine fibroids are commonly seen in benign uterine tumors in fertile females, also defined as fibroids or myomas [1, 2]. It influences on extensive population and the estimated prevalence may range from 80 to 90% by the age of 50 years [3]. Some research found that it occurs more often among older female and African descent that is likely to be caused by the effect of both genetic and environmental factors [4]. Although many females with fibroids are symptom-free, nearly 30% of them reveal some symptoms based on different location and size, involving back pain, pelvic pain and pressure, urinary frequency and urgency, anemia, constipation, abnormal uterine bleeding, and infertility [5, 6]. The current available approach for uterine fibroids is mainly surgical interventions, but the strategy of treatment is decided by a variety of factors, including patient's age, delivery time, desire to remain fertility or rejection of radical therapy such as

hysterectomy, also associating with fibroid's location, size and quantity, and the severity of symptoms [7, 8]. More proof demonstrates that the economic impact of surgical interventions is huge, and new effective treatments for uterine fibroids are necessity, especially for a female who wants to retain their fertility [9].

Medication combined with nonsurgical therapy may be an actionable alternative for uterine fibroid, and over the last decade, the application of selective progesterone receptor modulators called as antiprogestins have been prevailing [10]. Mifepristone, one kind of progesterone receptors inhibitors, was the first effective compound in the use of long-term treatment of fibroids, since fibroid growth decided by the sexual steroids, and more study indicated that mifepristone can produce unique endometrial changes and decrease the growth of uterine fibroids through a variety of ways [10–12]. Except for medication interruption, ultrasound-guided radiofrequency ablation (RFA) was performed in a minimally invasive manner, which is widely accepted as a reliable and effective treatment. It can induce coagulation necrosis by entering uterine fibroids through laparoscopy, vagina, or cervix [13].

Cell adhesion molecules (CAMs) possess a family of molecules that mediate the contact and binding between cells or between cells and extracellular matrix. Adhesion molecules play crucial roles in cell recognition, cell activation and signal transduction, cell proliferation and differentiation, and cell motility. They are also engaged in various biological processes, such as immune response, inflammation, coagulation, tumor metastasis, and wound healing [14, 15]. Growth factors are secreted by many cell types that could regulate cellular growth, proliferation, and differentiation. Uterine cellular events such as proliferation and differentiation are regulated by activation of growth factors acting by paracrine or autocrine mechanisms [16]. Interestingly, the presence of inflammatory cells in uterine fibroids may result in excessive extracellular matrix (ECM) production and tissue remodeling, eventually leading to leiomyoma growth [17]. Therefore, in this study, the changes of serum inflammatory cytokines including inflammatory cytokines including procalcitonin (PCT), high-sensitivity C-reactive protein (hs-CRP), and tumor necrosis factor-alpha (TNF-α); adhesion molecules including monocyte chemotactic protein 1 (MCP-1) and soluble intercellular adhesion molecule 1 (sICAM-1); and growth factors including vascular endothelial growth factor (VEGF), epidermal growth factor (EGF), basic fibroblast growth factor (bFGF), transforming growth factor-β (TGF-β), and TGF-β receptor will be analyzed by mifepristone combined with ultrasound-guided radiofrequency ablation, in order to provide more reliable data for clinical management for uterine fibroid.

2. Materials and Methods

2.1. Patient Enrollment. In this study, we recruited 130 patients who were diagnosed with uterine fibroids in our hospital from December 2016 to June 2018. All patients could provide complete clinical data. Eligible study subjects should meet the following inclusion criteria: presence of symptoms, such as anemia, abdominal pain, and menorrhagia; diagnosed as submucosal uterine fibroids in accordance with the International Federation of Gynecology and Obstetrics (FIGO) classification I-II [18]; clear presentation of size and location of fibroids through transabdominal ultrasound, with a safe access path; without undergoing high-intensity focused ultrasound (HIFU) or surgical resection before ultrasound guided radiofrequency ablation; and signing an informed consent approved by the Ethics Committee of our hospital. Patients were excluded from the study if they were complicated by other malignant tumors, severe liver and kidney dysfunction, severe metabolic system diseases, and severe neurological diseases, without complete clinical data, during menstruation, pregnancy or lactation, with acute pelvic inflammatory disease, allergic to drugs mentioned in this study, and had taken hormone drugs in recent two months.

2.2. Patient Information. Among 130 patients with uterine fibroids, there were 75 cases presenting abdominal pain, 53 presenting secondary anemia, 103 cases presenting menorrhagia, 18 cases presenting difficult defecation, 32 cases presenting frequent urination, and 53 cases presenting other symptoms. These 130 patients were divided into the control group ($n = 65$) and the experimental group ($n = 65$) according to the treatment method. The patients in the control group were aged ranging from 29 to 35 years, with an average of age (32.3 ± 3.6) years, and the disease duration was 1 to 4 years with an average of disease duration (2.4 ± 1.3) years. The control group had an average of fibroid diameter (3.32 ± 0.98) cm, with 23 cases of single fibroid and 42 cases of multiple fibroids. The patients in the experimental group were aged ranging from 29 to 34 years, with an average of age (32.4 ± 3.8) years, and the disease duration was 1 to 4 years with an average of disease duration (2.4 ± 1.5) years. The experimental group had an average of fibroid diameter (3.19 ± 1.08) cm, with 26 cases of single fibroid and 39 cases of multiple fibroids. There were 40 cases with birth history and 8 cases with a history of induced abortion in the control group and 34 cases with birth history and 12 cases with a history of induced abortion. There was no statistical difference in age, disease duration, diameter of fibroids, single or multiple fibroids, birth history, and history of induced abortion between the two groups ($P > 0.05$).

2.3. Treatment. Ultrasound-guided radiofrequency ablation was performed. The patients were treated with routine vaginal and cervical disinfection at first, and the curettage was performed after the fibroid was detected by the intraluminal probe and abdominal probe. If the diameter of the myoma was less than 3 cm, the self-coagulation knife was directly placed into the center of the myoma. If the diameter of the myoma is more than 3 cm, the self-coagulation knife was penetrated into from one side to the other side. With the guide of ultrasound, self-coagulation knife radiofrequency with a power of 30 + 3 W was leaded into lesions longitudinally and withdrawn when reaching full electrical resistance in tissue, keeping the process for many times until all lesions were coagulated and necrotic. The patients were given hemostatics or antibiotics to prevent bleeding and infection after

operation. The average operation time was (27.43 ± 5.98) min, and the average blood loss was (14.2 ± 4.8) ml. The patients in the experimental group continued to receive oral administration of mifepristone (10 mg/time, once a day for 3 months).

2.4. Collection and Processing of Human Blood Sample. Blood samples were collected from all patients before treatment and 3 months after treatment, respectively, and two test tubes of samples were collected at one time for enzyme-linked immunosorbent assay (ELISA) of adhesion molecules, growth factors, and inflammatory factors. The collection processes were as followed: elbow venous blood (5 ml) was collected from each patient after fasting for at least 8 hours and then stored in refrigerator at 4°C for 45 minutes. The blood sample was centrifuged for 15 min at 3500 r/min in a centrifuge with 10 cm radius to get the supernatant as serum. The serum was immediately stored at -80°C.

2.5. Experimental Instruments. Experimental instruments used in this study were as follows: automatic multifunction microplate reader (Fluostar Omega, Bio-Gene Technology Co., Ltd. China), Panasonic refrigerator (MDF-U5412, SANYO Electric Co., Ltd. Japan), spectrophotometer (OD-1000+, Shanghai Gene Sci Medical Technology Co., Ltd., China), automatic biochemical analyzer (AU64, Olympus Corporation. J.P.), and ELISA kits (Sigma-Aldrich. USA).

2.6. ELISA. The blank control, sample, and standard wells were set. At first, 50 μl serum sample was put into the standard holes; 40 μl of the PH9 buffer with 0.05 mol/L concentration and 10 μl serum samples were added into sample holes successively, then mixing them gently. The reaction holes covered by microplate sealers placed at 37°C for 30 minutes, then pouring off the sample liquid completely and cleaning the holes 3 times with butter diluted by distilled water, 3 minutes each time. With the exception of blank holes, 50 μl of ELISA reagent was added into the other holes; then, A and B color reagent with 50 μl was poured into the three kinds of holes successively and gently mix the liquid in each hole. Adding 50 μl of reaction termination solution to each hole until color yellow appears, and the blank holes were used as the zero reference value within 15 minutes, the absorbance (OD value) in each hole was measured with a spectrophotometer with 450 nm wavelength, and the concentrations of VEGF, EGF, bFGF, TGF β, MCP-1, sICAM-1, PCT, hs CRP, and TNF-α in the sample were calculated by using the standard curve.

2.7. Efficacy Evaluation. Clinical response of patients with uterine fibroids to ultrasound-guided radiofrequency ablation alone or combined with oral administration of mifepristone was evaluated. Complete response was defined when all symptoms and signs of the patients disappeared, and uterine fibroids have found to be disappeared in B-ultrasound examination of uterine appendages. Excellent response was defined when the symptoms and signs of the patients basically disappeared or significantly reduced, and the volume reduction rate of uterine fibroids was more than 50% indicated in B-ultrasound examination of uterine appendages. Good response was defined when the patient's symptoms and signs have been alleviated, and the volume of uterine fibroids reduced by 25%-50% showed in B-ultrasound examination of uterine appendages. No response was defined when there was no any improvement in symptoms, and B-ultrasound examination of uterine appendages described that the volume of uterine fibroids decreased less than 25% or increased. Total response rate = 100.00% − rate of case with no response.

2.8. Calculation of Volumes of Uterine and Fibroids. The volumes of uterus and fibroids were calculated following the formula: $V = \pi abc/6$, where abc indicate the length, width, and thickness of uterus and fibroids, respectively.

2.9. Data Analysis. All data were processed by the SPSS 20.0 software. The measurement data were defined as mean ± standard deviation and analyzed by the t-test. The counting data were described by ratio or percentage and analyzed by the chi-square test. A level of $P < 0.05$ was considered statistically significant.

3. Result

3.1. Oral Administration of Mifepristone Combined with Ultrasound-Guided Radiofrequency Ablation Showed Favorable Patient Outcome. There were 29 cases showing complete response, 22 cases showing excellent response, 12 cases showing good response, and 2 cases showing no response in the experimental group. There were 19 cases showing complete response, 25 cases showing excellent response, 7 cases showing good response, and 14 cases showing no response in the control group. The total response rate in the experimental group was higher than that in control group ($\chi^2 = 7.195$, $P < 0.05$, Table 1). Next, the volumes of uterus and fibroids were measured and calculated. It was found that patients with uterine fibroids exhibited reduced volumes of uterus and fibroids following either ultrasound guided radiofrequency ablation or oral administration of mifepristone combined with ultrasound guided radiofrequency ablation ($P < 0.05$). At the same time, the volumes of uterus and fibroids were smaller in the experimental group than those in the control group ($P < 0.05$, Table 2).

3.2. Oral Administration of Mifepristone Combined with Ultrasound-Guided Radiofrequency Ablation Notably Reduced the Secretion of Adhesion Molecules. Adhesion molecules represent a group of cell-surface molecules and are likely to be of central importance in mediating cell-extracellular matrix and specific cell-cell interactions within both neoplastic and inflammatory sites. MCP-1 and sICAM-1 expressions were associated with the pathogenesis of endometriosis from previous evidence. We are interested in a hypothesis that MCP-1 and sICAM-1 expressions are altered in patients with uterine fibroids undergoing oral administration of mifepristone combined with ultrasound-guided radiofrequency ablation. We found that the serum levels of MCP-1 and sICAM-1 in patients with uterine fibroids were significantly decreased following either ultrasound-guided radiofrequency ablation or oral administration of mifepristone combined with

Table 1: Clinical response of patients with uterine fibroids to ultrasound-guided radiofrequency ablation alone or combined with oral administration of mifepristone.

Group	Complete response [n (%)]	Excellent response [n (%)]	Good response [n (%)]	No response [n (%)]	Total response rate	χ	P
Experimental group	29 (44.62%)	22 (33.85%)	12 (18.46%)	2 (3.08%)	96.92%	7.195	<0.05
Control group	19 (29.23%)	25 (38.46%)	7 (10.77%)	14 (21.54%)	78.46%		

Table 2: The volumes of uterus and fibroids of patients with uterine fibroids following ultrasound-guided radiofrequency ablation alone or combined with oral administration of mifepristone.

Group	N	Before or after treatment	The volume of uterus (cm^3)	The volumes of fibroids (cm^3)
Control group	65	Before	244.43 ± 25.65	77.70 ± 7.33
		After	188.34 ± 19.44	55.32 ± 8.60
t			14.658	26.443
P			0.001	0.001
Experimental group	65	Before	245.32 ± 30.22	78.16 ± 8.54
		After	160.54 ± 10.55*	41.54 ± 5.87*
t			32.443	38.667
P			0.001	0.001

Compared to the control group, *$P < 0.05$.

ultrasound-guided radiofrequency ablation ($P < 0.05$). Besides, the serum levels of MCP-1 and sICAM-1 were declined in the experimental group compared with the control group ($P < 0.05$, Table 3).

3.3. Oral Administration of Mifepristone Combined with Ultrasound-Guided Radiofrequency Ablation Remarkably Reduced the Release of Growth Factors. Growth factors, relatively small and stable, secreted, or membrane-bound polypeptide ligands, have been implicated in proliferation, differentiation, angiogenesis, survival, inflammation, and tissue repair, or fibrosis through the activation of signal transduction pathways by binding to their receptors on the surface of target cells. Numerous differentially expressed growth factors have been identified in leiomyoma and myometrial cells. Given the roles of growth factors in the pathogenesis of uterine fibroids, we are wondering the effects of oral administration of mifepristone combined with ultrasound-guided radiofrequency ablation on the release of growth factors in patients with uterine fibroids. Results revealed that the serum levels of VEGF, EGF, bFGF, TGF-β, and TGF-β receptor in patients with uterine fibroids were significantly decreased following either ultrasound-guided radiofrequency ablation or oral administration of mifepristone combined with ultrasound-guided radiofrequency ablation ($P < 0.05$). Besides, the serum levels of VEGF, EGF, bFGF, TGF-β, and TGF-β receptor were declined in the experimental group compared with the control group ($P < 0.05$, Table 4).

3.4. Oral Administration of Mifepristone Combined with Ultrasound-Guided Radiofrequency Ablation Significantly Inhibited Inflammatory Cytokine Production. Inflammatory imbalance has been demonstrated to contribute to leiomyoma development and growth, which would provide an avenue for the development of preventative treatments. In this part, we attempted to examine inflammatory response in patients with uterine fibroids after oral administration of mifepristone combined with ultrasound-guided radiofrequency ablation. After treatment, the serum levels of PCT, hs-CRP, and TNF-α were declined in the experimental and control group ($P < 0.05$), and the experimental group exhibited lower serum levels of PCT, hs-CRP, and TNF-α than the control group ($P < 0.05$, Table 5).

3.5. The Incidence of Adverse Reactions. There were 2 cases with nausea, 2 cases with mild dizziness, and 1 case with vaginal discharge in the control group, with a 7.69% incidence rate of adverse reactions. There were 3 cases of nausea, 2 cases of mild dizziness, and 1 case with vaginal discharge in the experimental group, with a 9.23% incidence rate of adverse reactions. There was no significant difference in the incidence of adverse reactions between the two groups ($\chi^2 = 0.781$, $P > 0.05$).

4. Discussion

The management of fibroids has been multidisciplinary in the past years. Different therapeutic approaches are now available for women with uterine fibroids, among which medical therapy may be less invasive [19]. Medical therapy is an option for women with symptomatic uterine fibroids who consider fertility preservation or expect a less aggressive operation after shrinkage of the uterine volume [20]. The underlying mechanism of most medical therapies is based on the inhibition of myoma growth. Recently, the US-guided RF ablation is reported as a relatively safe and

Table 3: The serum levels of MCP-1 and sICAM-1 in patients with uterine fibroids following ultrasound-guided radiofrequency ablation alone or combined with oral administration of mifepristone.

Group	N	Before or after treatment	MCP-1 (μg/L)	sICAM-1 (μg/L)
Control group	65	Before	33.29 ± 3.11	458.77 ± 29.12
		After	25.48 ± 6.22	404.32 ± 19.17
t			15.487	21.909
P			0.001	0.001
Experimental group	65	Before	34.14 ± 6.55	459.32 ± 17.12
		After	19.78 ± 4.08$^{\#}$	366.56 ± 12.54$^{\#}$
t			19.221	33.762
P			0.001	0.001

Compared to the control group, $^{\#}P < 0.05$; MCP-1: monocyte chemotactic protein 1; sICAM-1: soluble intercellular adhesion molecule 1.

Table 4: The serum levels of TGF-β, TGF-β receptor, VEGF, EGF, and bFGF in patients with uterine fibroids following ultrasound-guided radiofrequency ablation alone or combined with oral administration of mifepristone.

Group	N	Before or after treatment	TGF-β (μg/L)	TGF-β receptor (μg/L)	VEGF (ng/L)	EGF (ng/L)	bFGF (ng/L)
Control group	65	Before	45.67 ± 8.12	25.32 ± 4.66	105.38 ± 35.11	12.54 ± 3.42	103.84 ± 21.74
		After	39.40 ± 7.77	20.67 ± 3.12	89.24 ± 20.26	9.08 ± 2.17	81.95 ± 13.82
t			8.324	6.521	14.183	6.196	16.412
P			0.001	0.001	0.001	0.001	0.001
Experimental group	65	Before	46.14 ± 8.45	26.91 ± 6.33	106.54 ± 34.97	12.87 ± 4.15	104.67 ± 19.83
		After	30.33 ± 9.56$^{\&}$	15.73 ± 5.38$^{\&}$	71.54 ± 12.93$^{\&}$	5.01 ± 0.87$^{\&}$	52.71 ± 13.26$^{\&}$
t			21.435	11.548	37.548	7.955	14.084
P			0.001	0.001	0.001	0.001	0.001

Compared to the control group, $^{\&}P < 0.05$; TGF-β: transforming growth factor β; VEGF: vascular endothelial growth factor; EGF: epidermal growth factor; bFGF: basic fibroblast growth factor.

Table 5: The serum levels of PCT, hs-CRP, and TNF-α in patients with uterine fibroids following ultrasound-guided radiofrequency ablation alone or combined with oral administration of mifepristone.

Group	N	Before or after treatment	PCT (pg/ml)	hs-CRP (pg/ml)	TNF-α (pg/ml)
Control group	65	Before	135.21 ± 57.44	221.02 ± 48.15	324.96 ± 38.75
		After	92.13 ± 16.77	182.59 ± 41.87	254.42 ± 47.36
t			37.952	27.841	33.149
P			0.001	0.001	0.001
Experimental group	65	Before	134.84 ± 56.81	222.43 ± 49.01	327.15 ± 39.74
		After	56.34 ± 17.33$^{\$}$	103.46 ± 33.67$^{\$}$	201.26 ± 31.28$^{\$}$
t			45.529	47.586	44.437
P			0.001	0.001	0.001

Compared to the control group, $^{\&}P < 0.05$; PCT: procalcitonin; hs-CRP: high-sensitivity C-reactive protein; TNF-α: tumor necrosis factor-α.

effective procedure for uterine fibroids with various localizations and sizes [21]. In this study, we explored the clinical efficacy of medical therapy (mifepristone) combined with the US-guided RF ablation in treating women with uterine fibroids and the effects of his combined approach on serum levels of MCP-1, sICAM-1, and TGF-β of patients.

In 2008, Esteve et al. [22] performed a randomized controlled trial by randomly assigning 100 women to receive oral mifepristone 5 mg or 10 mg daily for 3 months and found 5 mg doses of mifepristone reduced leiomyoma and uterine volumes similar to 10 mg doses. In 2009, Engman et al. [23] randomized 30 women with uterine fibroids to receive either 50 mg mifepristone or placebo every other day during 3 months prior to surgery and evaluated uterine blood flow and leiomyoma volume once a month until surgery. It was revealed mifepristone may offer an effective treatment option for women with uterine fibroids with uterovaginal bleeding. As shown in our study, compared with women with uterine fibroids receiving the US-guided RF ablation alone, women with uterine fibroids receiving the US-guided RF ablation

and administration of 10 mg mifepristone once a day for 3 months had fewer volumes of uterus and fibroids.

Another important finding of the study is that the US-guided RF ablation and administration of 10 mg mifepristone more significantly reduced serum levels of MCP-1, sICAM-1, and TGF-β than ablative technology alone. Higher production of MCP-1 is associated with augmented inflammatory reaction in endometrium, which might be detrimental to reproductive outcome in women with uterine fibroids [24]. CAMs have been implicated in leukocyte-endothelial interactions, including ICAM-1, vascular cell adhesion molecule-1 (VCAM-1), and E-selectin all of which are regulated by sex steroids, while CAM expression in the uterine and ovarian appears to be associated with certain disease states in women of reproductive age [25]. The normal cyclic variation in peripheral sICAM-1 and sVCAM-1 levels may reflect uterine and/or ovarian tissue remodeling events, and sICAM-1 levels could be utilized as biological markers of endometriosis [26–28]. Numerous differentially expressed growth factors have been identified in leiomyoma and myometrial cells. Mu et al. [29] and Plewka et al. [30] both demonstrated high expression of VEGF that can probably cause malignant transformation and more extensive growth of leiomyoma. EGF stimulates DNA synthesis and polyploidization in leiomyomal smooth muscle cells and participates in the pathogenesis of human uterine fibroids [31]. Previous evidence showed that the regulation of bFGF in leiomyomas and in myometrium is affected by sex steroid hormones [32]. TGF-β is a polypeptide that consists of three isoforms, TGF-β1, TGF-β2, and TGF-β3. At present, TGF-β is considered to be one of the key factors in the pathophysiology of uterine fibroids [33]. TGF-β expression was increased as the growth of uterine fibroids in women bearing childbearing age, which shows considerable potential as a therapeutic target for uterine fibroids [34]. Chronic inflammation is regarded as one of the challenges for the treatment of human diseases [35]. Inflammatory imbalance has been demonstrated to contribute to leiomyoma development and growth, which would provide an avenue for the development of preventative treatments. As reported in the study performed by Sevostyanova et al. [36], activation of adaptive immunity, angiogenic factors, and inflammatory cell reactions was observed in patients with uterine fibroids with reproductive failure, that is why detection of CRP, IFN-γ, and TNF-α in serum is necessary to perform in pregravid preparation of women, including in vitro fertilization program. Considering the implication of inflammatory cytokines, adhesion molecules, and growth factors in the development of uterine fibroids, their repression caused by the US-guided RF ablation and administration of 10 mg mifepristone further demonstrated the clinical efficacy of mifepristone combined with the US-guided RF ablation in treating women with uterine fibroids.

In summary, our data support the higher clinical efficacy of mifepristone combined with the US-guided RF ablation than the US-guided RF ablation alone. Nevertheless, these results are preliminary, as the number of patients was restricted and the actual follow-up time was limited. In the future, we will extend sample size power and perform multicenter study, so as to provide more evidence for clinical promotion of mifepristone combined with the US-guided RF ablation.

Data Availability

The data used to support the findings of this study are included within the article.

Conflicts of Interest

The authors declare that they have no conflict of interest.

Authors' Contributions

Aiqin Hou and Zhen Yan contributed equally to this work.

Acknowledgments

The study is supported by Yan'an University Cultivation Fund Project (2018ZD-02), Basic research program of Natural Science in Shaanxi Province (2019JQ-986), and Yan'an science and Technology Bureau [(2020)64].

References

[1] M. Gupta, N. Jamwal, S. Sabharwal, and S. Sobti, "A prospective interventional study to evaluate the effects of medical therapy (Mifepristone 25 mg) on the management of uterine fibroids," *Journal of Family Medicine and Primary Care*, vol. 9, no. 7, pp. 3230–3235, 2020.

[2] A. S. Boosz, P. Reimer, M. Matzko, T. Romer, and A. Muller, "The conservative and interventional treatment of fibroids," *Deutsches Ärzteblatt International*, vol. 111, no. 51-52, pp. 877–883, 2014.

[3] M. Grube, F. Neis, S. Y. Brucker et al., "Uterine fibroids - current trends and strategies," *Surgical Technology International*, vol. 34, pp. 257–263, 2019.

[4] M. S. De La Cruz and E. M. Buchanan, "Uterine fibroids: diagnosis and treatment," *American Family Physician*, vol. 95, no. 2, pp. 100–107, 2017.

[5] E. Giuliani, S. As-Sanie, and E. E. Marsh, "Epidemiology and management of uterine fibroids," *International Journal of Gynaecology and Obstetrics*, vol. 149, no. 1, pp. 3–9, 2020.

[6] W. H. Parker, "Etiology, symptomatology, and diagnosis of uterine myomas," *Fertility and Sterility*, vol. 87, no. 4, pp. 725–736, 2007.

[7] F. Faustino, M. Martinho, J. Reis, and F. Aguas, "Update on medical treatment of uterine fibroids," *European Journal of Obstetrics, Gynecology, and Reproductive Biology*, vol. 216, pp. 61–68, 2017.

[8] J. Donnez and M. M. Dolmans, "Uterine fibroid management: from the present to the future," *Human Reproduction Update*, vol. 22, no. 6, pp. 665–686, 2016.

[9] J. Donnez, P. Arriagada, O. Donnez, and M. M. Dolmans, "Emerging treatment options for uterine fibroids," *Expert Opinion on Emerging Drugs*, vol. 23, no. 1, pp. 17–23, 2018.

[10] M. Farris, C. Bastianelli, E. Rosato, I. Brosens, and G. Benagiano, "Uterine fibroids: an update on current and emerging medical treatment options," *Therapeutics and Clinical Risk Management*, vol. Volume 15, pp. 157–178, 2019.

[11] S. Mukherjee and S. Chakraborty, "A study evaluating the effect of mifepristone (RU-486) for the treatment of leiomyomata uteri," *Nigerian Medical Journal*, vol. 52, no. 3, pp. 150–152, 2011.

[12] C. Malartic, O. Morel, G. Akerman, L. Tulpin, P. Desfeux, and E. Barranger, "La mifépristone dans la prise en charge des fibromes utérins," *Gynécologie, Obstétrique & Fertilité*, vol. 36, no. 6, pp. 668–674, 2008.

[13] L. D. Bradley, R. P. Pasic, and L. E. Miller, "Clinical performance of radiofrequency ablation for treatment of uterine fibroids: systematic review and meta-analysis of prospective studies," *Journal of Laparoendoscopic & Advanced Surgical Techniques. Part A*, vol. 29, no. 12, pp. 1507–1517, 2019.

[14] A. Makker, M. M. Goel, D. Nigam et al., "Endometrial expression of homeobox genes and cell adhesion molecules in infertile women with intramural fibroids during window of implantation," *Reproductive Sciences*, vol. 24, no. 3, pp. 435–444, 2017.

[15] M. S. Islam, A. Ciavattini, F. Petraglia, M. Castellucci, and P. Ciarmela, "Extracellular matrix in uterine leiomyoma pathogenesis: a potential target for future therapeutics," *Human Reproduction Update*, vol. 24, no. 1, pp. 59–85, 2018.

[16] P. Ciarmela, M. S. Islam, F. M. Reis et al., "Growth factors and myometrium: biological effects in uterine fibroid and possible clinical implications," *Human Reproduction Update*, vol. 17, no. 6, pp. 772–790, 2011.

[17] O. Protic, P. Toti, M. S. Islam et al., "Possible involvement of inflammatory/reparative processes in the development of uterine fibroids," *Cell and Tissue Research*, vol. 364, no. 2, pp. 415–427, 2016.

[18] C. Perrine, M. Levaillant Jean, and F. Hervé, "Surgical techniques and outcome in the management of submucous fibroids," *Current Opinion in Obstetrics & Gynecology*, vol. 25, pp. 332–338, 2013.

[19] S. K. Laughlin-Tommaso, "Non-surgical management of myomas," *Journal of Minimally Invasive Gynecology*, vol. 25, no. 2, pp. 229–236, 2018.

[20] M. H. Cheng, H. T. Chao, and P. H. Wang, "Medical treatment for uterine myomas," *Taiwanese Journal of Obstetrics & Gynecology*, vol. 47, no. 1, pp. 18–23, 2008.

[21] G. Yuce, A. Tayarer, H. L. Keskin, B. Genc, and M. Canyigit, "Ultrasound guided percutaneous radiofrequency thermal ablation of symptomatic uterine fibroids - results from a single center and 52 weeks of follow up," *Ginekologia Polska*, vol. 91, no. 8, pp. 447–452, 2020.

[22] J. L. Carbonell Esteve, R. Acosta, B. Heredia, Y. Pérez, M. C. Y. Castañeda, and A. V. Hernández, "Mifepristone for the treatment of uterine leiomyomas: a randomized controlled trial," *Obstetrics and Gynecology*, vol. 112, no. 5, pp. 1029–1036, 2008.

[23] M. Engman, S. Granberg, A. R. Williams, C. X. Meng, P. G. Lalitkumar, and K. Gemzell-Danielsson, "Mifepristone for treatment of uterine leiomyoma. A prospective randomized placebo controlled trial," *Human Reproduction*, vol. 24, no. 8, pp. 1870–1879, 2009.

[24] S. Miura, K. N. Khan, M. Kitajima et al., "Differential infiltration of macrophages and prostaglandin production by different uterine leiomyomas," *Human Reproduction*, vol. 21, no. 10, pp. 2545–2554, 2006.

[25] M. Ueda, Y. Yamashita, M. Takehara et al., "Gene expression of adhesion molecules and matrix metalloproteinases in endometriosis," *Gynecological Endocrinology*, vol. 16, no. 5, pp. 391–402, 2002.

[26] L. Kuessel, R. Wenzl, K. Proestling et al., "Soluble VCAM-1/soluble ICAM-1 ratio is a promising biomarker for diagnosing endometriosis," *Human Reproduction*, vol. 32, no. 4, pp. 1–10, 2017.

[27] N. Bonello and R. J. Norman, "Soluble adhesion molecules in serum throughout the menstrual cycle," *Human Reproduction*, vol. 17, no. 9, pp. 2272–2278, 2002.

[28] M. H. Wu, B. C. Yang, Y. C. Lee, P. L. Wu, and C. C. Hsu, "The differential expression of intercellular adhesion molecule-1 (ICAM-1) and regulation by interferon-gamma during the pathogenesis of endometriosis," *American Journal of Reproductive Immunology*, vol. 51, no. 5, pp. 373–380, 2004.

[29] Y. Mu, J. He, R. Yan, X. Hu, H. Liu, and Z. Hao, "IGF-1 and VEGF can be used as prognostic indicators for patients with uterine fibroids treated with uterine artery embolization," *Experimental and Therapeutic Medicine*, vol. 11, no. 2, pp. 645–649, 2016.

[30] D. Plewka, M. Morek, E. Bogunia, J. Waloszek, and A. Plewka, "Expression of VEGF isoforms and their receptors in uterine myomas," *Ginekologia Polska*, vol. 87, no. 3, pp. 166–177, 2016.

[31] Y. Y. Ren, H. Yin, R. J. Tian et al., "Different effects of epidermal growth factor on smooth muscle cells derived from human myometrium and from leiomyoma," *Fertility and Sterility*, vol. 96, no. 4, pp. 1015–1020.e1, 2011.

[32] X. Wu, A. Blanck, M. Olovsson, B. Möller, and B. Lindblom, "Expression of basic fibroblast growth factor (bFGF), FGF receptor 1 and FGF receptor 2 in uterine leiomyomas and myometrium during the menstrual cycle, after menopause and GnRHa treatment," *Acta Obstetricia et Gynecologica Scandinavica*, vol. 80, no. 6, pp. 497–504, 2001.

[33] M. Ciebiera, M. Wlodarczyk, M. Wrzosek et al., "Role of transforming growth factor β in uterine fibroid biology," *International Journal of Molecular Sciences*, vol. 18, no. 11, p. 2435, 2017.

[34] T. Shen, H. Shi, Q. Xu, Q. Song, Y. Xu, and Y. Huang, "Effects of TGF-β on uterine fibroids of women of childbearing age and uterine artery embolization," *Minimally Invasive Therapy & Allied Technologies*, vol. 26, no. 5, pp. 292–299, 2017.

[35] K. M. le, N. Trinh, V. D. Nguyen et al., "Investigating the Anti-Inflammatory Activity of Curcumin-Loaded Silica- Containing Redox Nanoparticles," *Journal of Nanomaterials*, vol. 2021, Article ID 6655375, 11 pages, 2021.

[36] O. Sevostyanova, T. Lisovskaya, G. Chistyakova et al., "Proinflammatory mediators and reproductive failure in women with uterine fibroids," *Gynecological Endocrinology*, vol. 36, no. -sup1, pp. 33–35, 2020.

Hindawi
Journal of Nanomaterials
Volume 2021, Article ID 9955488, 7 pages
https://doi.org/10.1155/2021/9955488

Research Article

Propofol Combined with Fentanyl Is Superior to Propofol Alone in Sedation Protocols for Painless Gastrointestinal Endoscopy

Jie Chang[1] **and Chun Yang**[2]

[1]*Department of Anesthesiology, The Second Hospital of Jiaxing, China*
[2]*Department of Anesthesiology, The Affiliated Hospital of Jiaxing University, China*

Correspondence should be addressed to Chun Yang; mail17816519327@163.com

Received 10 March 2021; Revised 26 April 2021; Accepted 29 April 2021; Published 17 May 2021

Academic Editor: Songwen Tan

Sufficient propofol or fentanyl doses necessary to prevent the response to skin incision do not necessarily reduce hemodynamic responses during surgery. The purpose of this study was to characterize the pharmacodynamic interaction between propofol and fentanyl with respect to the sedative effects and safety during painless gastrointestinal endoscopy. From October 2018 to October 2020, 200 patients undergoing painless gastrointestinal endoscopy in our department's outpatient or inpatient clinic were selected and randomly divided into a control group and an observation group, 100 patients per group. Prior to surgery, the patients in the two groups were required to be connected to an electrocardiogram monitor and then were instructed to lie on the left side and receive continuous oxygen infusion of 2-3 L/min with a nasal cannula. The control group was injected with propofol injection (100 mg/min). The observation group was given fentanyl intravenous injection at a dose of 0.1 μg/kg followed by propofol injection (100 mg/min). Painless gastrointestinal endoscopy was performed after the patients entered a sleep state and the eyelash reaction disappeared. Outcome analysis was performed on preoperative and intraoperative hemodynamic indicators, including heart rate, blood oxygen saturation, dose of propofol, time for endoscopy, recovery time, hospitalization after recovery, Montreal Cognitive Assessment (MoCA) score, and Mini-Mental State Examination (MMSE) score. The incidence rate of adverse reactions in the observation group was 6%, which was notably lower than that of the control group (18%). The total response rate of the observation group was 98%, which was significantly higher than that of the control group (90%) ($P < 0.05$). The intraoperative heart rate and blood oxygen saturation of the observation group were higher than those of the control group ($P < 0.0$ss). The patients receiving sedation with propofol plus fentanyl had fewer doses of propofol and shorter recovery time than those receiving propofol alone ($P < 0.05$). It was also revealed that the patients receiving sedation with propofol plus fentanyl exhibited more MoCA and MMSE scores than those receiving propofol alone 30 min after sedation during painless gastrointestinal endoscopy. Taken together, sedation with propofol combined with fentanyl was more effective and safer than that with propofol alone in painless gastrointestinal endoscopy, which can ensure a wake-up state, stable breathing cycle, and better gastrointestinal painless procedure.

1. Background

Gastrointestinal endoscopy plays an important role in the discovery of digestive tract diseases, especially early cancer, and has been gradually included in the scope of routine physical examination [1]. The endoscopy is performed to identify potentially premalignant lesions in the gastrointestinal tract, sample or resect the area of interest, await histologic results, and then plan a treatment and/or surveillance strategy [2]. Detection of subtle lesions and decision about whether they are clinically significant depend on the skills and experience of endoscopists. For patients undergoing gastrointestinal endoscopy, most of them still need to rely on the effect of anesthesia to achieve a stable examination, so as to reduce the patient's fear of the examination and make comfortable medical treatment more extensive and safer [3]. The

anesthesia requirements and technical level of painless gastrointestinal endoscopy are also constantly updated and improved [4]. However, because gastrointestinal endoscopy is an intrusive operation, patients often experience various degrees of stress, fear, nausea, increased blood pressure, and pulse speed when undergoing the examination [5]. Some patients even refuse the examination because of fear, leading to delays in diagnosis and treatment.

Endoscopic diagnosis and treatment are safe, minimally invasive, and effective diagnosis and treatment methods commonly used in gastroenterology clinics. It is currently a rapidly developing, mature technology and widely used clinical medical technology. However, in the process of endoscopic diagnosis and treatment, patients usually have varying degrees of tension, fear, anxiety, nausea, bloating, abdominal pain, and other discomforts, which often affect the examination. In recent years, painless endoscopy is a good aid to gastrointestinal endoscopy through the application of anesthetics [6]. It has the characteristics of being painless and more humane, low missed diagnosis rate, and no serious complications. It is currently widely used in clinical practice. However, propofol for injection, which is routinely used in painless gastrointestinal endoscopy, has no analgesic effect. When encountering strong painful stimuli, patients still respond and affect operation [7].

How to obtain a better anesthesia effect, shorten the awakening time, and improve the comfort of patient examinations requires continuous exploration and research. Painless gastrointestinal endoscopy is a common clinical method to diagnose and treat digestive system diseases, which can minimize the suffering of patients [8]. Therefore, it is favored by patients and physicians. In the process of painless gastrointestinal endoscopy, it is often necessary to use propofol for anesthesia. It has a good anesthesia and sedative effect, and it has fast onset and can make the patient wake up quickly, but it will also affect the patient's respiratory system and heart. The blood vessels have a certain inhibitory effect, and no better analgesic effect can be achieved. In this study, we recruited 200 patients undergoing painless gastrointestinal endoscopy to characterize the pharmacodynamic interaction between propofol and fentanyl with respect to the sedative effects and safety during painless gastrointestinal endoscopy.

2. Materials and Methods

2.1. Ethical Statement. The MoCA and MMSE scales were performed with the approval of the Ethics Committee of the Affiliated Hospital of Jiaxing University.

2.2. Inclusion and Exclusion Criteria. The study subjects in this study should meet the following inclusion and exclusion criteria. Inclusion criteria were as follows: (1) requirement for gastrointestinal endoscopy; (2) I-II grades according to the American Society of Anesthesiologists (ASA) Classification System which was developed to offer clinicians a simple categorization of a patient's physiological status that can be helpful in predicting operative risk [9]; (3) education level reaching primary school or above; (4) age ranging from 18 to 70 years old; and (5) providing informed content. Exclusion criteria were as follows: (1) those with contraindications to endoscopy; (2) those allergic to the medication used in this observation; (3) those with severe obstructive pulmonary disease and severe snoring; (4) those with cognitive impairments or neurological disorders; and (5) those with severe heart, liver, and kidney dysfunction.

2.3. Participants. From October 2018 to October 2020, 200 patients who underwent painless gastrointestinal endoscopy in our department's outpatient or inpatient clinic were selected as study subjects who meet the inclusion and exclusion criteria. These 200 patients were randomly arranged into the control group and observation group, 100 per group. The control group consisted of 48 males and 52 females, aged 22 to 70 years old, with an average age of 42.46 ± 5.63 years and an average weight of 66.5 ± 8.2 kg. The patients in the control group underwent painless gastrointestinal endoscopy for the following reasons: chronic inflammation of the digestive tract ($n = 30$), physical examination ($n = 27$), esophageal reflux ($n = 12$), gastric polyps ($n = 9$), intestinal polyps ($n = 10$), constipation ($n = 9$), and lower abdominal pain ($n = 3$); gastroscopy was performed in 54 cases and colonoscopy in 46 cases. The observation group consisted of 45 males and 55 females, aged 22 to 71 years old, with an average age of 46.22 ± 5.19 years and an average weight of 68.3 ± 7.5 kg. The patients in the observation group underwent painless gastrointestinal endoscopy for the following reasons: physical examination ($n = 28$), chronic inflammation of the digestive tract ($n = 26$), gastric polyps ($n = 12$), gastric ulcer ($n = 12$), intestinal polyps ($n = 12$), constipation ($n = 6$), and lower abdominal pain ($n = 4$); gastroscopy was performed in 56 cases and colonoscopy in 44 cases. The two groups exhibited no significant differences in sex, age, weight, and disease ($P > 0.05$), and they were comparable.

2.4. Sedation Protocols. Eight hours before painless gastrointestinal endoscopy, the patients in the two groups were required to abstain from food and drink, be given an indwelling needle, have the venous channel open by intravenous infusion of normal saline, and be connected to the ECG monitor to observe and record the patient's blood pressure, heart rate, and oxygen saturation After confirming that they are within the normal range, the patient is instructed to lie on the left side and given continuous oxygen infusion of 2-3 L/min with a nasal cannula. The control group was injected slowly with propofol injection (Guangdong Jiabo Pharmaceutical Co., Ltd., National Medicine Zhunzi H20051842), and the injection speed was 100 mg/min; the observation group was given fentanyl intravenously at a dose of 0.1 μg/kg and then injected with propofol, and the injection speed is 100 mg/min. Painless gastrointestinal endoscopy can be performed after the patient enters a sleep state and the eyelash reaction disappears. Both groups used our Olympus 260 series electronic gastrointestinal endoscopy for inspection operations. Gastroscopy can usually be done with a single dose. Propofol can be added to colonoscopy according to the situation. During the examination, blood pressure, heart rate, oxygen saturation, and patient response are closely

monitored, and the dosage of propofol and the patients's wake-up time after anesthesia are recorded. Those with abnormal blood pressure and heart rate can be treated symptomatically. Record the patient's blood pressure, heart rate, and blood oxygen saturation before and after the examination.

2.5. Evaluation of Patient Outcomes. The sedative effects of anesthetic drugs were evaluated as follows: 80-100 points indicate excellent response (namely, the patient has no adverse reactions and the painless gastrointestinal surgery is successfully finished); 80-100 points indicate good response (namely, the patient experiences mild adverse reactions and the painless gastrointestinal surgery is basically finished); and less than 60 points indicate poor response (namely, the patient experiences serious adverse reactions and the painless gastrointestinal surgery is difficult to finish). Total response rate = (excellent + good response)/total number of cases × 100%. Adverse reactions following painless gastrointestinal surgery include intraoperative respiratory depression, vomiting, and dizziness. The hemodynamic parameters of painless gastrointestinal surgery include heart rate and blood oxygen saturation.

2.6. Mini-Mental State Examination (MMSE) Scale. In clinical and research settings, the MMSE is the most widely used instrument for the screening of cognitive impairment worldwide, which correlates well with more time-consuming Intelligence Quotient (IQ) tests, but it will not easily pick up cognitive problems caused by focal brain lesions. Scale items involve orientation (What is the time, date, day, month, and year? What is the name of this ward, hospital, district, town, and country?), registration (name three objects only once; repeat the objects until the patient can repeat them accurately), attention and calculation (ask the patient to subtract 7 from 100 and then 7 from the result four more times), recall (ask the patient to repeat the names of the three objects learnt in the registration test), and language (each of two simple objects named; an accurate repetition of the phrase; give a 3-stage command; write "Close your eyes" on a blank piece of paper and ask the patient to follow the written command; ask the patient to write a sentence. Score 1 point if the sentence is sensible and contains a noun and a verb; draw a pair of intersecting pentagons with each side approximately 1 inch long). Total maximum scores are 30 points. A score of 17 or less for illiteracy, 20 or less for primary school, and 24 or less for senior high school and above will pick up about 90% of patients with cognitive impairments, with about 10% false positives. If the postoperative score is 2 points lower than the preoperative score, it is considered that the cognitive function of patients was decreased.

2.7. Montreal Cognitive Assessment (MoCA) Scale. The MoCA is a 30-point scale containing the following subitems: visuospatial/executive functions, naming, memory, attention, language-sentence repetition, and language-verbal fluency.

Visuospatial/executive functions: shapes were changed from circle to triangle, and Roman alphabets were replaced in the trail making test part B as there was no substitute for Roman alphabets in Chinese. The number of steps required for the completion of the task was retained.

Naming: the picture of a rhinoceros was replaced with an elephant to reflect local familiarity.

Memory: the word "velvet" was replaced with "silk" and "daisy" was replaced with "rose" to reflect local familiarity.

Attention: Arabic numerals were used instead of Roman alphabets for the reasons given above; the numbers and positions of responses were retained

Language-sentence repetition: the name used in the Chinese version was changed to a more common Chinese name to reflect local familiarity.

Language-verbal fluency: phonemic letter fluency was replaced by animal fluency as there is no letter-equivalent linguistic unit in Chinese.

A score of 26 or more indicates normal cognitive function.

2.8. Statistical Methods. The data was processed by using SPSS 21.0 statistical software. The measurement data is expressed as mean ± standard deviation, and the t-test is performed. The count data is expressed as cases (percentage), and the chi-square test is performed. The difference was statistically significant ($P < 0.05$).

3. Results

3.1. Sedation with Propofol plus Fentanyl Inhibited the Incidence of Intraoperative Respiratory Depression during Painless Gastrointestinal Endoscopy. The incidence of adverse reactions was analyzed in sedation protocols of propofol with or without fentanyl for painless gastrointestinal endoscopy. The patients experienced adverse reactions including intraoperative respiratory depression, vomiting, and dizziness. There were 5 cases of intraoperative respiratory depression, 5 cases of vomiting, and 5 cases of dizziness in the observation group. The control group had 13 cases of intraoperative respiratory depression, 6 cases of vomiting, and 6 cases of dizziness. The two groups showed significant difference in the incidence of intraoperative respiratory depression (Figure 1, $P = 0.0485$). However, no significant difference was detected in the total incidence of adverse reactions ($P = 0.077$).

3.2. Propofol plus Fentanyl Conferred Better Sedative Effects than Propofol Alone for Painless Gastrointestinal Endoscopy. In order to compare the sedative effects of protocols of propofol with or without fentanyl during painless gastrointestinal endoscopy, each patient was evaluated as having excellent response, good response, and poor response. The observation group had 88 patients with excellent response, 10 with good response, and 2 with poor response. The control group had 80 patients with excellent response, 10 with good response, and 10 with poor response. The total response rate of the observation group was 98%, which was significantly higher than that of the control group (90%) ($Z = 2.382$, $P < 0.05$, Table 1).

3.3. Sedation with Propofol plus Fentanyl Maintained Hemodynamic Status during Painless Gastrointestinal

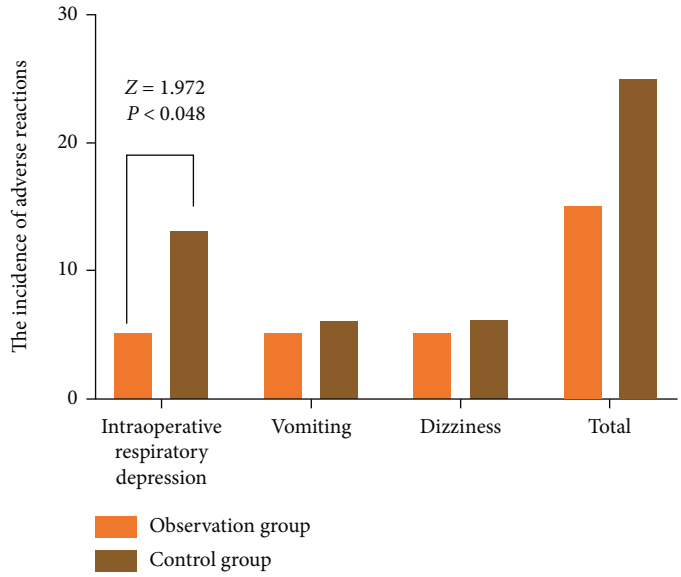

Figure 1: The incidence of adverse reactions after painless gastrointestinal endoscopy in the observation and control groups.

Table 1: Sedative effects of propofol plus fentanyl or propofol alone during painless gastrointestinal endoscopy.

	Excellent response	Good response	Poor response	Total response rate
Observation group ($n = 100$)	88	10	2	98
Control group ($n = 100$)	80	10	10	90
Z		—	—	2.382
P		—	—	0.017

Endoscopy. Subsequent analysis was performed to examine the influence of protocols of propofol with or without fentanyl on the hemodynamic status of the patients undergoing painless gastrointestinal endoscopy. The heart rate and blood oxygen saturation were evaluated to reflect patient hemodynamic status. There was no significant difference in the heart rate and blood oxygen saturation between the two groups before painless gastrointestinal endoscopy. During the gastrointestinal endoscopy, the heart rate and blood oxygen saturation in the observation group were higher than those in the control group ($P < 0.05$, Table 2).

3.4. Sedation with Propofol plus Fentanyl Promoted Patient Recovery after Painless Gastrointestinal Endoscopy. Each patient was evaluated for dose of propofol, time for endoscopy, recovery time, and hospitalization after recovery after painless gastrointestinal endoscopy. As shown in Table 3, the patients receiving sedation with propofol plus fentanyl had fewer doses of propofol and shorter recovery time than those receiving propofol alone ($P < 0.05$), indicating that sedation with propofol plus fentanyl promoted patient recovery after painless gastrointestinal endoscopy. However, no remarkable difference was found with regard to time for endoscopy and hospitalization after recovery ($P > 0.05$).

3.5. MoCA and MMSE Scores of Patients Receiving Sedation with Propofol plus Fentanyl or Propofol Alone during Painless Gastrointestinal Endoscopy. The potential for individuals to develop cognitive impairment as a consequence of major surgery with anesthesia has been increasingly recognized. We used MoCA and MMSE scales to reflect the cognitive function of patients receiving sedation with propofol plus fentanyl or propofol alone before and 30 min and 60 min after sedation during painless gastrointestinal endoscopy. The MoCA and MMSE scores between the observation group and the control group before and 60 min after gastrointestinal endoscopy were not statistically different ($P > 0.05$). The patients receiving sedation with propofol plus fentanyl exhibited more MoCA and MMSE scores than those receiving propofol alone 30 min after sedation during painless gastrointestinal endoscopy ($P < 0.05$, Figure 2).

4. Discussion

Gastrointestinal diseases are one of the more common diseases in clinical medicine. With the continuous progress and development of social economy and culture, people's material lifestyles are changing day by day, and the incidence of gastrointestinal diseases has increased significantly. At present, the main treatment of gastrointestinal diseases in clinical medicine is painless gastrointestinal endoscopy [10]. Through gastrointestinal endoscopy, the patient's specific gastrointestinal disease can be clarified and the patient can be treated. Propofol is the commonly used anesthetic before painless gastrointestinal surgery [11]. Due to many factors, its anesthesia effect is not very obvious, and it is easy

Table 2: Preoperative and intraoperative heart rate and blood oxygen saturation of patients receiving sedation with propofol plus fentanyl or propofol alone during painless gastrointestinal endoscopy.

	Heart rate (times/min)		Blood oxygen saturation (%)	
	Preoperative	Intraoperative	Preoperative	Intraoperative
Observation group ($n = 100$)	72.36 ± 1.31	67.98 ± 1.22	98.65 ± 1.75	96.12 ± 1.26
Control group ($n = 100$)	72.56 ± 1.37	63.26 ± 1.25	98.36 ± 1.69	94.26 ± 1.36
t	1.055	27.023	1.192	10.031
P	0.293	0.0001	0.235	0.0001

Table 3: Dose of propofol, time for endoscopy, recovery time, and hospitalization after recovery of patients receiving sedation with propofol plus fentanyl or propofol alone during painless gastrointestinal endoscopy.

Group	Dose of propofol (mg)	Time for endoscopy (min)	Recovery time (min)	Hospitalization after recovery (min)
Observation group ($n = 100$)	114.89 ± 7.34	15.01 ± 6.47	5.67 ± 1.48	20.97 ± 5.32
Control group ($n = 100$)	129.47 ± 8.14	16.22 ± 7.18	7.73 ± 1.56	22.17 ± 7.49
t	13.300	1.252	9.580	1.306
P	<0.0001	0.212	<0.0001	0.193

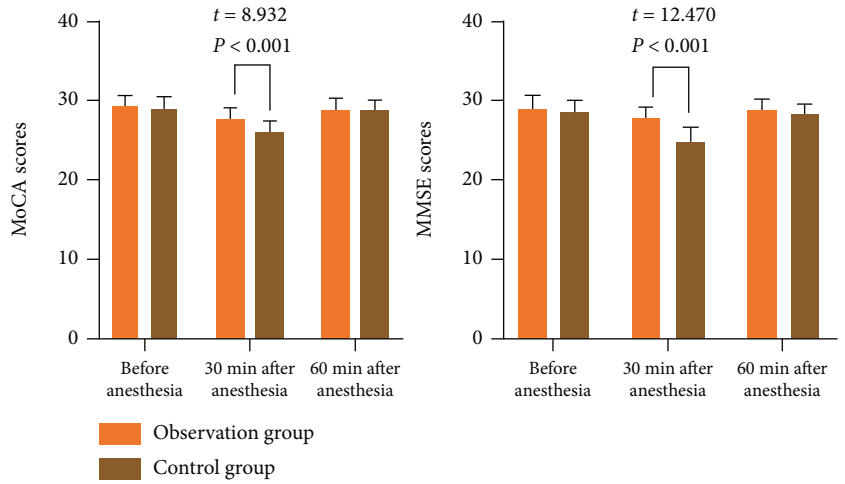

Figure 2: MoCA and MMSE scores of patients receiving sedation with propofol plus fentanyl or propofol alone during painless gastrointestinal endoscopy.

to cause adverse reactions in patients [12]. Many scholars in the medical field believe that propofol combined with low-dose fentanyl can not only have a good anesthesia effect but also reduce the incidence of adverse reactions in patients [13]. Therefore, in order to clarify the effect of the combination of propofol and fentanyl on painless gastrointestinal surgery, this study launched a study on the application of propofol and fentanyl. The results of this study showed that the two groups showed significant difference in the incidence of intraoperative respiratory depression. However, no significant difference was detected in total incidence of adverse reactions. In terms of response rate and preoperative and intraoperative heart rate and blood oxygen saturation and intraoperative hemodynamic comparison, the observation group was better than the control group. The reason is that the propofol drug in the control group is an anesthesia-inducing drug, and its chemical name is diisopropylphenol. By activating the GABA receptor-chloride ion complex, it can inhibit the central nervous system and finally achieve sedation and hypnosis [14]. Based on the propofol drug, the observation group implemented fentanyl citrate. This drug is an analgesic with a molecular structure similar to morphine. It is combined with propofol as an anesthetic. Fentanyl is a synthetically powerful horse mouth analgesic. It is mainly absorbed through the gastrointestinal tract and fully binds to the human body proteins. It not only has a small impact on the cardiovascular function of patients but also can achieve analgesia [15]. The dosage of propofol combined with fentanyl was significantly reduced, and the patient's consciousness recovered faster after the operation was

extubated, and the eye opening time was shorter. However, with propofol alone, the dosage is large, the breathing is easily inhibited, the recovery of consciousness after extubation after the operation is slow, and the recovery from opening eyes is slow. It can be seen that the effect of propofol combined with small dose of fentanyl is better [16].

Although gastrointestinal endoscopy does not take a long time, it can also cause a certain degree of pain to the patient during the examination. Therefore, anesthesia is usually required. The ideal anesthesia state is to ensure the stability of the patient's hemodynamic changes during the detection process; at the same time, it can be quickly induced by anesthesia, and the patient can be quickly awakened after the operation [17]. At present, propofol is usually used in gastrointestinal endoscopy. Although it has good anesthesia and sedation, it can induce anesthesia quickly and can make the patient wake up quickly after surgery, but it also affects patients. The respiratory system and cardiovascular system have inhibitory effects [18], as shown by our results. Fentanyl is a synthetic opioid receptor agonist [19]. Compared with propofol, it has a shorter induction time for anesthesia and does not have much impact on the cardiovascular system. Remifentanil is an opioid receptor agonist with a short half-life and will not affect liver and kidney function. The results of this study confirm that the application of a small amount of remifentanil combined with a small dose of propofol in a painless gastrointestinal endoscopy can achieve a very ideal anesthesia effect and can ensure that the patient is in a wakeful state and is stable. The breathing cycle of the painless gastrointestinal endoscopy is significantly improved, and its anesthesia effect is far superior to that of the conventional dose of fentanyl combined with propofol anesthesia.

In this study, the two groups showed significant difference in the incidence of intraoperative respiratory depression. However, no significant difference was detected in the total incidence of adverse reactions. The total response rate of the observation group was 98%, which was significantly higher than that of the control group (90%), and the difference was statistically significant. There was no significant difference in heart rate, blood oxygen saturation, and hemodynamics between the two groups before operation. The intraoperative heart rate and blood oxygen saturation of the observation group were higher than those of the control group, and the difference was statistically significant. The MoCA and MMSE scores of the two groups before and after anesthesia were not statistically different. The MoCA and MMSE scores of the observation group were higher than those of the control group at 30 minutes after anesthesia, and there was a statistical difference.

In summary, propofol plus fentanyl in painless gastrointestinal endoscopy can achieve a very ideal sedative effect, ensure that the patient is in a wakeful state, and ensure the patient's breathing cycle is stable, so that the safety of gastrointestinal endoscopy has been significantly improved. Propofol combined with low-dose fentanyl is safer, can reduce the incidence of adverse reactions in patients, and has certain clinical application value. Nevertheless, different doses of fentanyl combined with propofol in sedation protocols for painless gastrointestinal endoscopy will be explored in further study.

Data Availability

The data used to support the findings of this study are included within the article.

Conflicts of Interest

The authors declare that they have no conflicts of interest.

References

[1] P. Valdastri, M. Simi, and R. J. Webster 3rd, "Advanced technologies for gastrointestinal endoscopy," *Annual Review of Biomedical Engineering*, vol. 14, no. 1, pp. 397–429, 2012.

[2] A. M. Thaker and V. R. Muthusamy, "Advanced imaging techniques in gastrointestinal endoscopy," *Journal of Laparoendoscopic & Advanced Surgical Techniques Part A*, vol. 27, no. 3, pp. 234–241, 2017.

[3] A. S. o. P. Committee, D. S. Early, J. R. Lightdale et al., "Guidelines for sedation and anesthesia in GI endoscopy," *Gastrointestinal Endoscopy*, vol. 87, no. 2, pp. 327–337, 2018.

[4] C. J. Rees, S. Koo, and K. W. Oppong, "Future directions in therapeutic gastrointestinal endoscopy," *The Lancet Gastroenterology & Hepatology*, vol. 3, no. 10, pp. 663-664, 2018.

[5] M. R. Borgaonkar, L. Hookey, R. Hollingworth et al., "Indicators of safety compromise in gastrointestinal endoscopy," *Canadian Journal of Gastroenterology*, vol. 26, no. 2, pp. 71–78, 2012.

[6] O. S. Lin, "Sedation for routine gastrointestinal endoscopic procedures: a review on efficacy, safety, efficiency, cost and satisfaction," *Intestinal Research*, vol. 15, no. 4, pp. 456–466, 2017.

[7] T. Nishizawa and H. Suzuki, "Propofol for gastrointestinal endoscopy," *United European Gastroenterology Journal*, vol. 6, no. 6, pp. 801–805, 2018.

[8] L. Zhang, Y. Bao, and D. Shi, "Comparing the pain of propofol via different combinations of fentanyl, sufentanil or remifentanil in gastrointestinal endoscopy," *Acta Cirúrgica Brasileira*, vol. 29, no. 10, pp. 675–680, 2014.

[9] D. J. Doyle, A. Goyal, P. Bansal, and E. H. Garmon, *American Society of Anesthesiologists Classification*, StatPearls, Treasure Island, FL, USA, 2021.

[10] J. J. McGoran, M. E. McAlindon, P. G. Iyer et al., "Miniature gastrointestinal endoscopy: now and the future," *World Journal of Gastroenterology*, vol. 25, no. 30, pp. 4051–4060, 2019.

[11] D. Stogiannou, A. Protopapas, A. Protopapas, and K. Tziomalos, "Is propofol the optimal sedative in gastrointestinal endoscopy?," *Acta Gastroenterologica Belgica*, vol. 81, no. 4, pp. 520–524, 2018.

[12] R. Zhang, Q. Lu, and Y. Wu, "The comparison of midazolam and propofol in gastrointestinal endoscopy: a systematic review and meta-analysis," *Surgical Laparoscopy, Endoscopy & Percutaneous Techniques*, vol. 28, no. 3, pp. 153–158, 2018.

[13] A. Amini, A. Arhami Dolatabadi, H. Kariman et al., "Low-dose fentanyl, propofol, midazolam, ketamine and lidocaine combination vs. regular dose propofol and fentanyl combination for deep sedation induction; a randomized clinical trial," *Emergency*, vol. 6, no. 1, article e57, 2018.

[14] M. Hara, Y. Kai, and Y. Ikemoto, "Propofol activates GABAA receptor-chloride ionophore complex in dissociated hippocampal pyramidal neurons of the rat," *Anesthesiology*, vol. 79, no. 4, pp. 781–788, 1993.

[15] F. Zhang, J. Tong, W. Qing, Z. Hu, J. Hu, and Q. Liao, "MDR1 genotypes and haplotypes are closely associated with postoperative fentanyl consumption in patients undergoing radical gastrectomy," *Journal of Nanomaterials*, vol. 2021, Article ID 5587399, 8 pages, 2021.

[16] H. S. Bakhamees, A. Mercan, and Y. M. El-Halafawy, "Combination effect of low dose fentanyl and propofol on emergence agitation in children following sevoflurane anesthesia," *Saudi Medical Journal*, vol. 30, no. 4, pp. 500–503, 2009.

[17] H. Hosseinzadeh, S. E. Golzari, E. Torabi, and M. Dehdilani, "Hemodynamic changes following anesthesia induction and LMA insertion with propofol, etomidate, and propofol + etomidate," *Journal of Cardiovascular and Thoracic Research*, vol. 5, no. 3, pp. 109–112, 2013.

[18] J. E. Mandel, G. R. Lichtenstein, D. C. Metz, G. G. Ginsberg, and M. L. Kochman, "A prospective, randomized, comparative trial evaluating respiratory depression during patient-controlled versus anesthesiologist-administered propofol-remifentanil sedation for elective colonoscopy," *Gastrointestinal Endoscopy*, vol. 72, no. 1, pp. 112–117, 2010.

[19] D. Lu, L. Jiang, C. Dai, K. Yan, and J. Gao, "Fentanyl exerts an antitumor effect on papillary thyroid cancer by regulating the miR-204/KLF5 axis," *Journal of Nanomaterials*, vol. 2021, Article ID 5563901, 8 pages, 2021.

Hindawi
Journal of Nanomaterials
Volume 2021, Article ID 9962950, 7 pages
https://doi.org/10.1155/2021/9962950

Research Article

Diagnosis of Neonatal Congenital Heart Disease: A Combination of Heart Murmur, SpO2 Abnormality, Tachypnea, and Extracardiac Malformations

Kai Chen,[1] Jiao Wang,[2] Huihui Zhou,[1] and Xiang Huang[1]

[1]*Department of Pediatrics, Ningbo Yinzhou No. 2 Hospital, Zhejiang, China*
[2]*Department of Pediatric Medicine, The First Affiliated Hospital of Jiamusi University, Jiamusi, China*

Correspondence should be addressed to Xiang Huang; woai527@zju.edu.cn

Received 9 March 2021; Revised 9 April 2021; Accepted 10 April 2021; Published 15 May 2021

Academic Editor: Songwen Tan

Congenital heart disease (CHD) is one of the commonest congenital malformations that are mostly asymptomatic at birth, which challenges the diagnosis of neonatal CHD. An early accurate prenatal diagnosis will give parents a choice, as well as the opportunity to plan the delivery and improve the postnatal outcome. The purpose of the study is to evaluate the value of heart murmurs, SpO2 abnormalities, tachypnea, and extracardiac malformations in screening neonatal CHD. All 4500 newborns in the obstetrics department of our hospital from January 2019 to January 2020 are selected as study subjects. Newborns were grouped according with the presence of heart murmurs, tachypnea, transdermal SpO2 < 95%, and extracardiac malformations alone or in combination (≥3). Patients with murmur, tachypnea, and abnormal SpO2 were assigned into group A, those with murmur, tachypnea, and extracardiac malformations into group B, those with murmurs, SpO2, and extracardiac malformations into group C, those with SpO2, tachypnea, and extracardiac malformations into group D, and those with all four into group E. The color echocardiography identified 65 children with CHD (1.4%) among the included 4,500 newborns. When murmur, tachypnea, abnormal SpO2, and extracardiac malformation were independently used to diagnose CHD, the sensitivity ranged from 30.68% to 51.26%, with specificity ranging from 47.36% to 82.65% and Youden's index (YI) ranging from 0.13 to 0.36. When murmur, tachypnea, abnormal SpO2, extracardiac malformation were together used to diagnose CHD, 91.23% sensitivity, 95.26 specificity, and 0.91 YI were observed. In conclusion, a combination of four indicators, murmur, tachypnea, abnormal SpO2, and extracardiac malformation yielded good performance in diagnosing neonatal CHD.

1. Backgrounds

Congenital heart disease (CHD) is a congenital malformation caused by the abnormal development of the heart and large blood vessels during the fetal period, which seriously endangers the lives and quality of life of children [1]. In China, the total prevalence of CHD at birth increases continuously over the past 40 years. Significant differences in sex, geographical regions, ethnicity, income levels, and monitoring models were witnessed [2, 3]. Despite advances in prenatal and newborn screening, it may present undiagnosed to the emergency department. CHD has variable signs and symptoms or is often nonspecific, which makes recognition and treatment challenging [4]. The concept of CHD is extensive, and some children with mild CHD do not need intervention and can heal naturally, but some severe children do not receive timely intervention and can be life threatening within a few days after birth [5]. So far, the great progress in the field of the diagnosis and treatment of CHD has been achieved. Noninvasive imaging diagnostic techniques, including echocardiography, magnetic resonance imaging and multislice spiral CT, has been developed, leading to more and more accurate diagnosis of CHD in the neonatal period [6]. Children with CHD, especially severe CHD, should be cured as soon as possible to restore their normal hemodynamics and provide the most basic guarantee for the development of important organs in children.

1.1. Theoretical Basis for Early Radical Cure

1.1.1. Benefit to the Lungs. The growth of the lungs in the first year after birth includes the development of new alveoli and pulmonary blood vessels, which reduces the pressure and flow of the pulmonary circulation to normal, so that the pulmonary vascular system will recover in the first year after birth. It can transform and develop normally.

1.1.2. Benefit to the Brain. The most serious sequela of children with critically ill CHD are hypoxic-ischemic brain damage and structural defects [7]. Studies have confirmed that children with bruising heart disease have up to 30% of the risk of brain hypoplasia during the fetal period [8]. The newborn's brain weighs about 350 grams, which is about a quarter of that of an adult. The human brain grows rapidly in the first year after birth. Therefore, the early cure of cardiovascular disease and the restoration of normal hemodynamic perfusion can contribute to the development and growth of the brain.

1.1.3. Provide Protection: Reduce the Risk of Death. The risk of the first-stage surgery in the neonatal period is significantly less than the risk of not being able to perform the first-stage surgery in the later period. The risk of the initial palliative surgery plus the second-stage radical surgery is much higher.

1.1.4. Benefit to the Family. Children with CHD are a huge family pressure. Parents always live in a place of great fear. Early radical treatment can enable parents to treat their children and live normally.

1.1.5. Good for Society. Early surgery can improve the quality of life of children, and the resources and costs required for staged surgery will greatly increase. Research data at home and abroad shows that for some complicated CHD, as well as early cases of severe cyanosis and cardiac insufficiency, if the diagnosis can be obtained in the neonatal period, it can provide more adequate opportunities and conditions for early intervention and give the necessary drug intervention and interventional therapy, or early surgical correction can significantly improve the prognosis of children and avoid death.

Recently, CHD screening has received an increasing attention. Some researchers focus on identification of molecular biomarkers for heart diseases [9, 10]. CHD presents distinct symptoms owing to conditions of different types of heart defects, including rapid heartbeat, shortness of breath, excessive sweating, fatigue, poor feeding, chest pain, blue tinge to the skin (cyanosis), and clubbed fingernails [11]. CHD develops shortly after birth and the symptoms do not develop until early childhood or teenage years. However, some complications may develop during adulthood such as the infections of the respiratory tract and lungs, heart infection, endocarditis, pulmonary hypertension, high blood pressure, and the heart failing to pump enough blood finally leading to a heart failure [12]. Therefore, early diagnosis of CHD and effective intervention can effectively increase the survival rate of births, improve the physical fitness of the people, and reduce the burden on families and society. Herein, we explore the values of heart murmurs, SpO2 abnormalities, tachypnea, and extracardiac malformations in the screening of neonatal CHD, in order to find a reliable and easy-to-promote screening method for neonatal CHD.

2. Materials and Methods

2.1. Study Subjects. All 4,500 newborns born in the Obstetrics Department of our hospital from January 2019 to January 2020 are initially enrolled into this retrospective study. Among these newborns, the male to female ratio is about 1.07 : 1, for 2326 and 2174 cases, respectively. The preterm to term newborn ratio is about 1.94 : 1, for 2970 and 1530 cases, respectively. The average gestational age at birth was 39.21 ± 1.23 weeks, and the average birth weight was 3236 ± 324 g. Newborns meeting the following inclusion criteria were included as eligible subjects: born in the Obstetrics Department of our hospital, regardless of gender; no death before discharge; birth weight of more than 1000 g or the gestational age of more than 28 weeks; the age ranging from 0.5 to 12 months; and an informed consent obtained from the guardian. Newborns were excluded from the study if they had been diagnosed with CHD before birth, their guardians were unwilling for newborn receiving the color Doppler echocardiography, and they were required for oxygen treatment. The study was approved by the Ethics Committee of our hospital.

2.2. Subject Grouping. Newborns with heart murmurs, tachypnea, transdermal SpO2 < 95%, or differences between upper and lower extremities > 3% were classified as positive screening cases. Positive screening cases were arranged into the following groups: murmur group, tachypnea group, abnormal SpO2 group, and extracardiac malformation group. Additionally, mixed groups where newborns with 3 or 4 positive indicators were set as follows: murmur, tachypnea, and abnormal SpO2 are in group A; murmur, tachypnea, and extracardiac malformations are in group B; murmurs, abnormal SpO2, extracardiac malformations are in group C; SpO2, tachypnea, and extracardiac malformations are in group D; all four items are in group E.

2.3. Echocardiography Examinations. Cardiac sonographers performed echocardiography examinations to confirm the diagnosis of CHD among these 4,500 newborns. Newborns was lying from a supine to lateral position and their long axis of the left ventricle, apical four chamber, short axis of great artery, and suprasternal fossa were screened by echocardiography (iE33, Philips Healthcare, Hamburg, Germany).

2.4. Examinations of Heart Murmur, Tachypnea, Abnormal SpO2, and Extracardiac Malformations. All 4,500 newborns were screened by trained and qualified pediatricians and child health doctor to evaluate the presence of heart murmur, tachypnea, abnormal SpO2, and extracardiac malformations. The child health doctor was responsible for transcutaneous oxygen saturation measurement, and the pediatrician was responsible for cardiac auscultation to ensure that the results of transcutaneous oxygen saturation measurement

are accurate. Newborns with grade II at cardiac auscultation was considered positive for heart murmur [13]. Respiratory status was also assessed at cardiac auscultation and newborns with breathing frequency > 60 times/min, deep breathing, and irregular rhythm were considered positive for tachypnea [14]. Measurement of transcutaneous SpO2 was performed on the transcutaneous oxygen saturation tester (RAD-5, Masimo Corp., Irvine, CA, USA). During the test, the child should be in a quiet state and the value of transcutaneous oxygen saturation should be stable for more than 3 s before recording the value to ensure the accuracy of the data. A right hand or any foot less than 95% was considered as positive for abnormal SpO2 [15]. Each newborn will undergo color echocardiography within 3–7 days after birth to screen for extracardiac malformations [16]. Extracardiac malformations included central nervous system malformation, urinary system malformation, digestive system malformation, maxillofacial abnormality, visceral inversion, fetal edema, limb abnormality, respiratory system malformation, and abdominal wall abnormality. The color echocardiographic results will be the gold standard for CHD diagnosis, except for mild valve regurgitation.

2.5. Statistical Analysis. All data were processed by the SPSS 23.0 software. The counting data were described by ratio or percentage and analyzed by the chi-square test. The area under the receiver operating characteristic (ROC) curve (AUC) was used to evaluate the diagnostic value. A level of $P < 0.05$ was considered statistically significant.

Table 1: Types of 65 cases of CHD.

Type	Number (%)
Ventricular septal defect	18 (27.7%)
Atrial septal defect (diameter > 5 mm)	12 (18.5%)
Patent ductus arteriosus	8 (12.3%)
Pulmonary valve stenosis	8 (12.3%)
Atrioventricular septal defect	4 (6.2%)
Tricuspid atresia with ventricular septal defect	4 (6.2%)
Right ventricular double outlet	2 (3.1%)
Aortic stenosis	2 (3.1%)
Coarctation of the aorta	2 (3.1%)
Complete ectopic pulmonary venous drainage	3 (4.6%)
Mitral valve atresia	1 (1.5%)

Table 2: The month old of included newborns and positive rates for heart murmur, tachypnea, abnormal SpO2, and/or extracardiac malformations.

Age (month)	Total number	Positive number	Detection rate (%)
0–3	1980	42	2.1
4–6	1640	17	1.0
7–12	880	6	0.7
Total	4500	65	1.4

3. Results

3.1. CHD Detection Was Associated with Newborns' Month Old. Among 4,500 newborns, 517 newborns were positive for heart murmur, tachypnea, abnormal SpO2, and/or extracardiac malformations. The positive rate was 11.5%. Among 517 newborns, there were 275 female newborns and 242 male newborns. Female newborns (275/2,174) showed a higher positive rate than male newborns (242/2,326). The difference was statistically significant ($\chi^2 = 5.176$, $P = 0.018$). Preterm newborns (398/2,970) showed a higher positive rate than term newborns (119/1,530). The difference was statistically significant ($\chi^2 = 25.349$, $P < 0.001$). These 517 newborns were screened by color echocardiography, and 65 newborns were identified with CHD (Table 1), mainly including 18 cases with ventricular septal defects, 12 cases with atrial septal defects, 8 cases with patent ductus arteriosus, and 8 cases with pulmonary valve stenosis. The incidence rate of CHD was 1.4%. Next, age-stratified analysis was performed to evaluate the association between detection rates of CHD and newborns' month old. As shown in Table 2, the incidence of CHD was correlated with newborns' month old ($\chi^2 = 4.982$, $P = 0.023$). Among 65 cases of CHD, there were 55 preterm newborns and 10 term newborns.

3.2. Diagnostic Performance of Heart Murmur, Tachypnea, Abnormal SpO2, or Extracardiac Malformations for CHD. Heart murmur, tachypnea, abnormal SpO2, or extracardiac malformations were separately used to diagnose CHD. As shown in Table 3, the sensitivity ranged from 30.68% to 51.26% and the specificity ranged from 47.36% to 82.65% and Youden's index ranged from 0.13 to 0.36. The AUC when heart murmur, tachypnea, abnormal SpO2, or extracardiac malformations were separately used to diagnose CHD ranged from 0.315 to 0.684, and the average AUC was 0.492 (Figure 1).

3.3. Diagnostic Performance of Heart Murmur, Tachypnea, Abnormal SpO2, and Extracardiac Malformations in Combination for CHD. Newborns positive for heart murmur, tachypnea, and abnormal SpO2 are classified into group A. Newborns positive for murmur, tachypnea, and extracardiac malformations are classified into group B. Newborns positive for murmurs, abnormal SpO2, and extracardiac malformations are classified into group C. Newborns positive for SpO2, tachypnea, and extracardiac malformations are classified into group D. Newborns positive for four indicators are classified into group E. Heart murmur, tachypnea, abnormal SpO2, and extracardiac malformations in combination were used to diagnose CHD. As shown in Table 4 and Figure 2, the AUC (95% CI) of group A was 0.685 (0.514–0.759), with the sensitivity of 55.6% and the specificity of 89.65%; the AUC (95% CI) of group B was 0.714 (0.621–0.802), with the sensitivity of 81.6% and the specificity of 91.23%; the AUC (95% CI) of group C was 0.701 (0.638–0.798), with the sensitivity of 78.69% and the specificity of 89.65%; the AUC (95% CI) of group D was 0.723 (6.435–0.814), with

Table 3: Diagnostic performance of heart murmur, tachypnea, abnormal SpO2, or extracardiac malformations alone for CHD.

Index	Murmur group	Tachypnea group	Abnormal SpO2 group	Extracardiac malformation group
Sensitivity (%)	40.32	31.25	51.26	30.68
Specificity (%)	47.36	78.98	82.65	54.23
Youden's index	0.21	0.15	0.36	0.13

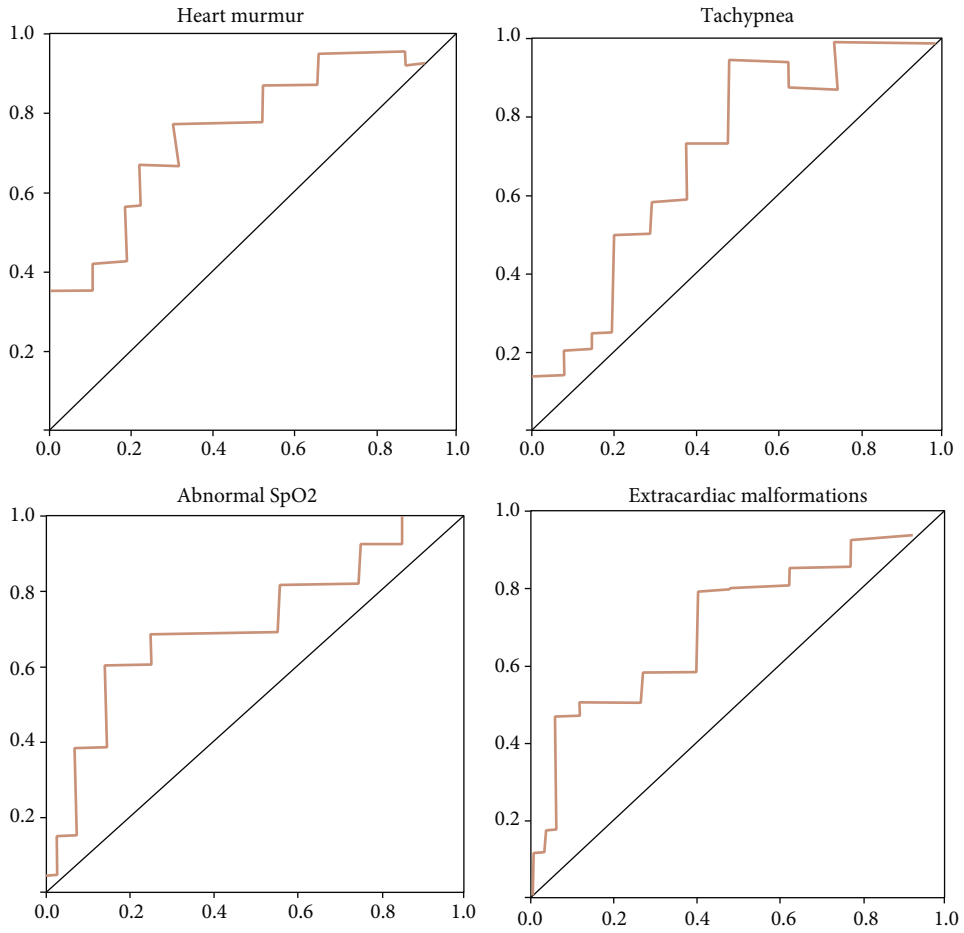

Figure 1: The AUC when heart murmur, tachypnea, abnormal SpO2, or extracardiac malformations were separately used to diagnose CHD.

Table 4: Diagnostic performance of heart murmur, tachypnea, abnormal SpO2, and extracardiac malformations in combination for CHD.

Index	A group	B group	C group	D group	E group
Sensitivity (%)	71.6	55.6	62.39	68.65	91.23
Specificity (%)	89.65	91.23	89.65	94.68	95.26
Youden's index	0.57	0.71	0.75	0.65	0.91

the sensitivity of 68.65% and the specificity of 94.68%; the AUC (95% CI) of group E was 0.912 (0.841–0.987), with the sensitivity of 91.23% and the specificity of 95.26%. These results indicated that heart murmur, tachypnea, abnormal SpO2, and extracardiac malformations in combination yield a best diagnostic performance for CHD.

3.4. Follow-Up Data. Due to the particularity of childhood diseases in growth and development, some cases with mild CHD can heal naturally during the growth and development process. Follow-up was performed on 65 confirmed cases of cardiac color Doppler ultrasound after 3 months (Table 5). Among them, there were 18 patients with ventricular septal defect in the neonatal period. A total of 4 cases were perimembranous ventricular septal defects with a defect diameter < 5 mm, and they self-healed after 3 months, with a self-healing rate of 22.2%; of the 12 cases of atrial septal defect, 3 cases of atrial septal defect did not detect the shunt bundle again, indicating that septal defect healed spontaneously, with a self-healing rate of 25.0%; 8 patients with patent ductus arteriosus were detected, of which 3 were self-healing with a cure rate of 37.5%, and the self-healing rate of other types of patients was 22.2%.

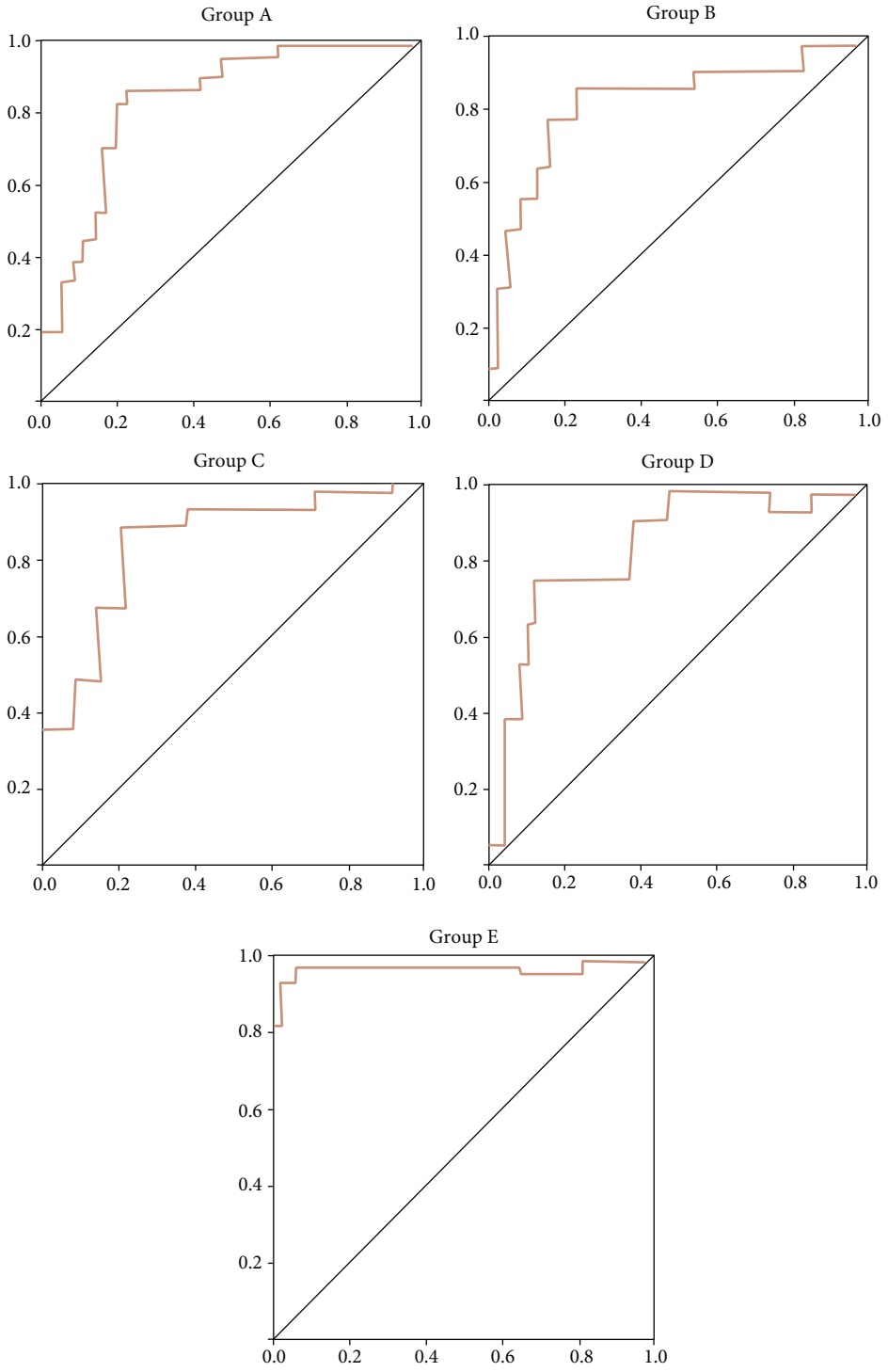

Figure 2: The AUC when heart murmur, tachypnea, abnormal SpO2, and extracardiac malformations were used in combination to diagnose CHD. Newborns positive for heart murmur, tachypnea, and abnormal SpO2 are classified into group A. Newborns positive for murmur, tachypnea, and extracardiac malformations are classified into group B. Newborns positive for murmurs, abnormal SpO2, and extracardiac malformations are classified into group C. Newborns positive for SpO2, tachypnea, and extracardiac malformations are classified into group D. Newborns positive for four indicators are classified into group E.

4. Discussion

CHD is a cardiovascular malformation caused by the abnormal development of the heart and blood vessels in the fetus. It is the most common heart disease in children. Foreign literature reports that the incidence of CHD is 9/1,000, most of which are mild or moderate CHD, do not require treatment, or only need post infant treatment [17]; among them, about 1/4 of children have CHD and need to be treated in infants. During the period, surgery or catheter intervention is

Table 5: Follow-up data after 3 months.

CHD classification	Neonatal period	After 3 months	Self-healing rate
Ventricular septal defect	18	14	22.2%
Atrial septal defect	12	9	25.0%
Patent ductus arteriosus	8	5	37.5%
Others	27	21	22.2%

required as soon as possible, most of which need to be treated in the neonatal period [1]. The incidence of congenital heart disease among newborns in my country in recent years is 7‰–8‰, and about 140,000 new children are newly diagnosed each year, accounting for the first birth defect in recent years. Among them, 60% die within one year of age and only 20% are actually treated. CHD is one of the important causes of neonatal death. Therefore, early screening of neonatal CCHD and early intervention and treatment can significantly reduce the occurrence of serious adverse consequences.

According to past experience, the diagnosis of critically ill congenital heart disease is mainly completed by prenatal ultrasound diagnosis and postnatal newborn physical examination, which makes up to 30% of infants not diagnosed with critically ill congenital heart disease before discharge from the hospital [18]. When these children return to the hospital with serious consequences of heart failure and shock, severe brain damage may occur during the period and some children may become disabled. At present, more and more institutions use transcutaneous oxygen saturation meters to screen for congenital heart disease. The United States will directly advocate that newborns receive pulse oximeters for early screening for CCHD, which will provide mature, noninvasive, and painless pulses. The oximeter screening is included in the routine monitoring of newborns to increase the detection rate of CCHD [19]. Murmur is an important sign of CHD and the main reason for CHD visits. Gum is more common in newborns, but it is mainly caused by accelerated blood flow and patent ductus arteriosus. Tachypnea in newborns can be manifested as rapid breathing rate, rhythm, strength, depth, and imbalance between inhalation and exhalation. SpO2 is an important indicator of oxygen metabolism in the body. Normal neonates SpO2 < 95% or difference between upper and lower limbs > 3% indicates hypoxia or abnormal blood shunting in the body, and cardiovascular disease should be watched out for. If the SpO2 drop alone is more obvious, you should be wary of it being more critical CHD [20].

The test results showed that 4,500 newborns were screened by color echocardiography to identify 65 children with CHD and the preliminary statistics of the incidence of CHD were 1.4%. When murmur, tachypnea, abnormal SpO2, and extracardiac malformation were independently used to diagnose CHD, the sensitivity ranged from 30.68% to 51.26%, with specificity ranging from 47.36% to 82.65% and Youden's index (YI) ranging from 0.13 to 0.36. Compared with the individual screening index, the related evaluation of the mixed group is relatively ideal, with a sensitivity of 89.36 and a specificity of 90.36%. When murmur, tachypnea, abnormal SpO2, extracardiac malformation were together used to diagnose CHD, 91.23% sensitivity, 95.26 specificity, and 0.91 YI were observed, suggesting that the use of the four mixed indicators for screening has better curative effects and is worthy of clinical promotion.

Due to the particularity of childhood diseases in growth and development, some mild congenital heart diseases can heal naturally during the growth and development process. Follow-up on confirmed cases of cardiac color Doppler ultrasound after 3 months was done. Among them, there were 18 patients with ventricular septal defect in the neonatal period and 4 patients healed themselves after 3 months, with a self-healing rate of 22.2%; of the 18 patients with atrial septal defect, 3 cases of atrial septal defect did not detect the shunt again, indicating that atrial septal defect healed spontaneously, with a self-healing rate of 25.0%; 8 patients with patent ductus arteriosus were detected, of which 3 were self-healing with a cure rate of 37.5% and the self-healing rate of other types of patients was 22.2%.

The above data show that the combined screening of 4 indicators including murmur, SpO2 abnormality, tachypnea, and extracardiac malformations has better results and is worthy of clinical promotion.

Data Availability

The data used to support the findings of this study are included within the article.

Conflicts of Interest

All authors declare that they have no conflict of interest.

Authors' Contributions

Kai Chen and Jiao Wang contributed equally to this work.

References

[1] R. Sun, M. Liu, L. Lu, Y. Zheng, and P. Zhang, "Congenital heart disease: causes, diagnosis, symptoms, and treatments," *Cell Biochemistry and Biophysics*, vol. 72, no. 3, pp. 857–860, 2015.

[2] L. Zhao, L. Chen, T. Yang et al., "Birth prevalence of congenital heart disease in China, 1980-2019: a systematic review and meta-analysis of 617 studies," *European Journal of Epidemiology*, vol. 35, no. 7, pp. 631–642, 2020.

[3] S. Han, C. Y. Wei, Z. L. Hou et al., "Prevalence of congenital heart disease amongst schoolchildren in Southwest China," *Indian Pediatrics*, vol. 57, no. 2, pp. 138–141, 2020.

[4] P. Judge and G. Meckler Mshs, "Congenital heart disease in pediatric patients: recognizing the undiagnosed and managing complications in the emergency department," *Pediatric Emergency Medicine Practice*, vol. 13, no. 5, pp. 1–28, 2016.

[5] E. Garne, M. S. Olsen, S. P. Johnsen et al., "How do we define congenital heart defects for scientific studies?," *Congenital Heart Disease*, vol. 7, no. 1, pp. 46–49, 2012.

[6] X. J. Ma and G. Y. Huang, "Current status of screening, diagnosis, and treatment of neonatal congenital heart disease in China," *World Journal of Pediatrics*, vol. 14, no. 4, pp. 313-314, 2018.

[7] P. S. McQuillen, A. J. Barkovich, S. E. Hamrick et al., "Temporal and anatomic risk profile of brain injury with neonatal repair of congenital heart defects," *Stroke*, vol. 38, no. 2, pp. 736–741, 2007.

[8] T. A. Glauser, L. B. Rorke, P. M. Weinberg, and R. R. Clancy, "Congenital brain anomalies associated with the hypoplastic left heart syndrome," *Pediatrics*, vol. 85, no. 6, pp. 984–990, 1990.

[9] W. Liu, J. Q. Cai, M. J. Tang, and Q. J. Yang, "Bioinformatics-Based Identification of lncRNA-miRNA-mRNA Network in Dilated Cardiomyopathy and Drug Prediction," *Journal of Nanomaterials*, vol. 2021, Article ID 5566316, 10 pages, 2021.

[10] W. Liu, J. Ye, J. Q. Cai, M. F. Xie, M. J. Tang, and Q. J. Yang, "Immune-Related Genes: Potential Regulators and Drug Therapeutic Targets in Hypertrophic Cardiomyopathy," *Journal of Nanomaterials*, vol. 2021, Article ID 5528347, 14 pages, 2021.

[11] C. H. Meller, S. Grinenco, H. Aiello et al., "Congenital heart disease, prenatal diagnosis and management," *Archivos Argentinos de Pediatría*, vol. 118, no. 2, pp. e149–e161, 2020.

[12] E. M. Leusveld, R. M. Kauling, L. W. Geenen, and J. W. Roos-Hesselink, "Heart failure in congenital heart disease: management options and clinical challenges," *Expert Review of Cardiovascular Therapy*, vol. 18, no. 8, pp. 503–516, 2020.

[13] J. Bodegard, P. T. Skretteberg, K. Gjesdal et al., "Low-grade systolic murmurs in healthy middle-aged individuals: innocent or clinically significant? A 35-year follow-up study of 2014 Norwegian men," *Journal of Internal Medicine*, vol. 271, no. 6, pp. 581–588, 2012.

[14] C. L. Hermansen and A. Mahajan, "Newborn respiratory distress," *American Family Physician*, vol. 92, no. 11, pp. 994–1002, 2015.

[15] N. Naqvi, V. L. Doughty, L. Starling et al., "Hypoxic challenge testing (fitness to fly) in children with complex congenital heart disease," *Heart*, vol. 104, no. 16, pp. 1333–1338, 2018.

[16] R. C. Rosa, R. F. Rosa, P. R. Zen, and G. A. Paskulin, "Congenital heart defects and extracardiac malformations," *Revista Paulista de Pediatria*, vol. 31, no. 2, pp. 243–251, 2013.

[17] J. Marek, V. Tomek, J. Skovranek, V. Povysilova, and M. Samanek, "Prenatal ultrasound screening of congenital heart disease in an unselected national population: a 21-year experience," *Heart*, vol. 97, no. 2, pp. 124–130, 2011.

[18] J. I. Hoffman, "Confirming the value of pulse oximetry screening for diagnosing critical congenital heart disease," *Evidence-Based Medicine*, vol. 18, no. 3, p. e26, 2013.

[19] E. Goldmuntz, "The epidemiology and genetics of congenital heart disease," *Clinics in Perinatology*, vol. 28, no. 1, pp. 1–10, 2001.

[20] A. K. Ewer, A. T. Furmston, L. J. Middleton et al., "Pulse oximetry as a screening test for congenital heart defects in newborn infants: a test accuracy study with evaluation of acceptability and cost-effectiveness," *Health Technology Assessment*, vol. 16, no. 2, pp. 1–184, 2012.

Hindawi
Journal of Nanomaterials
Volume 2021, Article ID 9995954, 8 pages
https://doi.org/10.1155/2021/9995954

Research Article

Additional Treatment with Low-Molecular-Weight Heparin Provides a Better Patient Outcome for Neonatal Pulmonary Hemorrhage with Unfractionated Heparin Treatment

Youmin Zheng,[1] Lingling Chen,[1] Lingzi Zhang,[1] and Yongxia Liu[2]

[1]*Taizhou Hospital of Zhejiang Province, China*
[2]*Department of Blood Transfusion, Yanan University Affiliated Hospital, No. 43 North Street, Baota District, Yanan City, Shanxi Province 716000, China*

Correspondence should be addressed to Yongxia Liu; liuyongxia9303@163.com

Received 26 March 2021; Accepted 24 April 2021; Published 11 May 2021

Academic Editor: Songwen Tan

Pulmonary hemorrhage occurring in preterm newborns is a catastrophic event and is significantly associated with neonatal deaths. Low-weight-molecular heparin is a medical agent usually used as anticoagulants during pregnancy and has the advantages of good absorption, long half-life, and high bioavailability. This study evaluated the pulmonary function and coagulation function in neonates with pulmonary hemorrhage following intravenous drip of low-molecular-weight heparin and the effects of low-molecular-weight heparin on serum prealbumin and retinol-binding protein levels. A total of 96 neonates with pulmonary hemorrhage were included as study subjects and arranged into the control group and the observation group, 48 per group, based on intravenous drip of unfractionated heparin with or without low-molecular-weight heparin. The neonates receiving intravenous drip of unfractionated heparin and low-molecular-weight heparin exhibited elevated partial pressure of oxygen (PaO_2) concomitant with declined partial pressure of carbon ($PaCO_2$) compared to those receiving unfractionated heparin treatment alone. With regard to pulmonary function, neonates receiving combined treatment of unfractionated heparin and low-molecular-weight heparin displayed increased forced expiratory volume in the first second (FEV1), FEV1/forced expiratory vital capacity (FVC), and peak expiratory flow (PEF) ($P < 0.05$) when comparable to neonates receiving unfractionated heparin treatment alone. As for coagulation function, neonates with pulmonary hemorrhage had decreased activated partial thromboplastin time (APTT), prothrombin time (PT), thromboplastin time (TT), and fibrinogen (FIB) after treatment. Expectedly, these decreases were more significantly in neonates undergoing unfractionated heparin coupled with low-molecular-weight heparin ($P < 0.05$). The control group was given unfractionated heparin, and the observation group was given unfractionated heparin coupled with low-molecular-weight heparin. In addition to pulmonary function and coagulation function, it was also observed that neonates undergoing unfractionated heparin coupled with low-molecular-weight heparin exhibited higher serum levels of serum prealbumin and retinol-binding protein than those treated with unfractionated heparin alone. Finally, higher recovery rate and lower incidence rate of complications, such as pulmonary infection, intracranial hemorrhage, and respiratory distress, were found in the observation group than the control group ($P < 0.05$). In conclusion, additional treatment with low-molecular-weight heparin could provide a better patient outcome for neonatal pulmonary hemorrhage with unfractionated heparin treatment, as it could notably improve pulmonary function and coagulation function and reduce the incidence of complications.

1. Introduction

Pulmonary hemorrhage represent a life-threatening event that shows an approximate incidence of 0.1% in all infants, while the incidence rate reaches to 5%-11% in newborns who are preterm or suffer intrauterine growth restriction [1]. Preterm infants usually experience pulmonary hemorrhage within 72 hours after birth, leading to significant morbidity and mortality and long-term neurological sequelae [2]. The occurrence of neonatal pulmonary hemorrhage is

attributed to several factors including low body weight, premature delivery, intrauterine growth restriction, coagulation dysfunction, infection, the administration of exogenous surfactant, intubation in delivery room, and previous use of blood components [3–5]. Interestingly, the phenomenon that pulmonary hemorrhage follows a neurological insult has been termed as neurogenic pulmonary hemorrhagic edema, indicating the relationship between pulmonary hemorrhage and neonatal neurological disease [6]. The histologic characteristics of the lung in the context of pulmonary hemorrhage remain to be characterized, and it seems that pulmonary maldevelopment such as pulmonary hypoplasia and presence of intra-acinar arterioles may contribute to pulmonary hemorrhage. So far, mechanical ventilation, medication, and circulatory management have been performed treating neonatal pulmonary hemorrhage [7–9], but the mortality rate of the children is still high.

Heparin is a polysaccharide activator of antithrombin by producing protease interaction exosites for blood clotting proteinases, thus promoting the inactivation of thrombin. Nonfractionated heparin has a mixture of polysaccharides with molecular weight from 3,000 to 30,000 Daltons [10, 11]. The administration of heparin has been reported to reduce the risk of developing intraventricular hemorrhage and parenchymal venous infarct which is a condition complicating intraventricular hemorrhage [12]. Low-weight-molecular heparin is a medical agents usually used as anticoagulants during pregnancy and has the advantages of good absorption, long half-life, high bioavailability, and low incidence of adverse reactions [13, 14]. The purpose of this study is to analyze the effect of low-molecular-weight heparin on pulmonary function and coagulation function of newborn with pulmonary hemorrhage and additional influence on expressions of serum prealbumin and retinol-binding protein, so as to provide reference for clinical treatment.

2. Material and Method

2.1. Inclusion and Exclusion Criteria. This retrospective study received the approval of Ethics Committee of our hospital, and the informed consent was obtained from each guardian. Eligible newborns with pulmonary hemorrhage should meet the following inclusion criteria: (a) in accordance with the "diagnosis and treatment of neonatal pulmonary hemorrhage" issued by Chinese Medical Association; 9b) the platelet level was less than 80×10^9/L; (c) the mother of neonate the did not use drugs related to fibrinolysis and coagulation during prenatal and delivery; (d) all the guardians of the neonate implemented informed consent. The newborns with pulmonary hemorrhage who died within 24 hours after admission or whose family members gave up treatment, complicated by congenital heart disease and abnormal liver and kidney function, congenital genetic diseases, hyperbilirubinemia, severe intrauterine infection, coagulation dysfunction, or immune function diseases, and stayed in coma after resuscitation treatment with low Apgar score (PMID: 3183690) (no less than 3) should be excluded.

2.2. Eligible Study Subjects. A number of 96 neonates with pulmonary hemorrhage in our hospital from December 2016 to December 2018 were analyzed and divided into the observation group with 48 cases and the control group with 48 cases according to different treatments. The control group involved 28 males and 20 females, with age ranging from 1 to 21 days, an average of 7.59 ± 0.51 days, weighing from 2011 to 4510 g, an average of 3520 ± 720 g; with Apgar scores ranging from 5 to 10 points, an average of 7.04 ± 1.35 points; with onset time ranging from 30 minutes to 24 days after birth, an average of 11.28 ± 3.54 days. There were 25 premature infants, 13 full-term infants, and 10 late born infants among them. There were 30 males and 18 females in observation group involving 24 cases of premature infants, 13 cases of full-term infants, and 11 cases of late birth, with aging from 1 to 24 days, an average age of 7.39 ± 0.48 days, weighing from 2046 to 4571 g, an average weight of 3582 ± 697 g; with Apgar scores from 5 to 10 points, an average of 7.10 ± 1.29 points; with onset time ranging from 40 minutes to 22 days after birth, an average of onset time 11.15 ± 3.45 days. The two groups were comparable ($P > 0.05$).

2.3. Management Protocols. All newborns with pulmonary hemorrhage were given regular treatments including anti-shock measures, anti-infection, better fluid, and electrolyte balance. Afterwards, they underwent orotracheal intubation by using the ventilator (Stephanie, Germany) with inspired oxygen (FiO2) 0.6-1.0, mean airway pressure (MAP) 0.78-1.18 kPa, inspiratory time (Ti) 33%, respiration rate (RR) 8-12 Hz, and amplitude 3-5 (oscillating pressure 1.96-4.90). Parameters were changed according to the blood gas value, and the pH value of blood gas, partial pressure of oxygen (PaO_2), partial pressure of carbon ($PaCO_2$) were, respectively, maintained at 7.4-7.5, 60-80 mmHg, and 35-55 mmHg. When fraction of inspired oxygen (FiO_2) was no more than 40%, and mean airway pressure (MAP) was no more than 0.78 kPa, it can be transferred to synchronized intermittent mandatory ventilation (SIMV), and continuous positive airway pressure (CPAP) was given after ventilator removed. The control group was treated with unfractionated heparin (6 μg/kg, body weight, No. 21071115, Hainan Changshi Medicine Co., Ltd., China) injected into vein once every 6 hours, and the drug was withdrew after the activated partial thromboplastin time (APTT), prothrombin time (PT), fibrinogen (FIB), and thrombin time (TT) recovered, respectively, to 25-37 s, 11-14 s, 2-4 g/L, and 12-16 s. As for the observation group, on the basis of the treatment in the control group, were additionally treated with low-molecular-weight heparin (40 μg/kg, body weight, No. 21060805, Jilin Huakang Pharmaceutical Co., Ltd., China) dripped into vein twice a day for preventive treatment, and the withdrawal criteria were consistent with that of the control group.

2.4. Outcomes. The value of PaO_2 and $PaCO_2$ were, respectively, recorded before, 6 h, and 24 h after treatment. The changes of the first second forced expiratory volume (FEV1), FEV1/forced vital capacity (FVC), and peak expiratory flow (PEF) were analyzed by pulmonary function tester

(CHESTAT-8800, Japan). Blood sample (2 mL) was collected from each fasting patient before and after treatment and placed in tube with the presence of 0.109 mol sodium citrate with ratio 1 : 9. APTT, PT, TT, and FIB were measured by automatic blood coagulation analyzer (CA15000, SYSMEX, Japan). The levels of prealbumin and retinol-binding protein before and after treatment were detected by automatic biochemical analyzer (MODULE P800, Roche, Switzerland) using corresponding kits (Sichuan Maccura Biotechnology Co., Ltd., China).

2.5. Recovery Criteria of Pulmonary Hemorrhage. The blood gas value and ventilator parameters returned to normal, and there was no blood aspirated from trachea. Bilateral pulmonary rales disappeared or significantly reduced, and clinical symptoms disappeared or significantly improved.

2.6. Statistical Methods. SPSS21.0 statistical software was used for data analysis. The counting data were expressed as percentage (%) and detected by chi-square test; the measurement data were described as mean ± standard deviation and analyzed by t test and one-way and two-way analysis of variance (ANOVA). With $\alpha = 0.05$ as the test level, the P value of less than 0.05 indicates that the difference was statistically significant.

3. Results

3.1. Additional Treatment with Low-Molecular-Weight Heparin Maintained Arterial Partial Pressures of Neonates with Pulmonary Hemorrhage. $PaCO_2$ and PaO_2 are an essential component of patient care. We first examined $PaCO_2$ and PaO_2 of each patient in the observation and control group before, 6 h, and 24 h after treatment. It was found that the PaO_2 was notably increased, and $PaCO_2$ was descended in both groups after intravenous drip of unfractionated heparin and low-molecular-weight heparin ($P < 0.05$). The newborns with pulmonary hemorrhage undergoing unfractionated heparin coupled with low-molecular-weight heparin exhibited elevated PaO_2 concomitant with declined $PaCO_2$ compared with those receiving unfractionated heparin treatment alone at indicated time points (6 h and 24 h after treatment) ($P < 0.05$). Additionally, the elevation of PaO_2 and the reduction of $PaCO_2$ were greater in the observation group when comparable to the control group ($P < 0.05$, Table 1 and Figure 1).

3.2. Additional Treatment with Low-Molecular-Weight Heparin Restored Pulmonary Function of Neonates with Pulmonary Hemorrhage. Pulmonary function testing is usually performed to diagnose many categories of pulmonary disease. We next evaluated the FEV1, FEV1/FVC, and PEF to reflect the pulmonary function of neonates with pulmonary hemorrhage. No remarkable difference was observed between the observation and control group before treatment ($P > 0.05$). After unfractionated heparin treatment with or without additional low-molecular-weight heparin treatment, FEV1, FEV1/FVC, and PEF were all increased in the two groups ($P < 0.05$). The newborns with pulmonary hemorrhage undergoing unfractionated heparin coupled with low-molecular-weight heparin exhibited elevated FEV1, FEV1/FVC, and PEF when comparable to those receiving unfractionated heparin treatment alone ($P < 0.05$, Table 2).

3.3. Additional Treatment with Low-Molecular-Weight Heparin Improved Coagulation Function of Neonates with Pulmonary Hemorrhage. Pulmonary hemorrhage is a coagulation disorder. In this part, the anticoagulation effects of unfractionated heparin treatment with or without additional low-molecular-weight heparin treatment on pulmonary hemorrhage were evaluated. As shown in Table 3, before treatment, the observation and control groups were comparable as no significance existed in coagulation parameters ($P > 0.05$). After unfractionated heparin treatment with or without additional low-molecular-weight heparin treatment, APTT, PT, TT and FIB were all remarkably reduced in the two groups ($P < 0.05$). These reductions were more significant in the newborns with pulmonary hemorrhage undergoing unfractionated heparin coupled with low-molecular-weight heparin than those receiving unfractionated heparin treatment alone ($P < 0.05$).

3.4. Additional Treatment with Low-Molecular-Weight Heparin Increased Prealbumin and Retinol-Binding Protein Levels in Neonates with Pulmonary Hemorrhage. Prealbumin and retinol-binding protein belong to hepatic secretory proteins that are markers of visceral protein stores and used as indicators of nutritional status. The serum levels of prealbumin and retinol-binding protein showed little difference between the two groups before unfractionated heparin treatment with or without additional low-molecular-weight heparin treatment ($P > 0.05$). After treatment, there were significant increases in the serum levels of prealbumin and retinol-binding protein in the two groups ($P < 0.05$). The newborns with pulmonary hemorrhage undergoing unfractionated heparin coupled with low-molecular-weight heparin exhibited elevated serum levels of prealbumin and retinol-binding protein compared with those receiving unfractionated heparin treatment alone ($P < 0.05$, Figure 2).

3.5. Efficacy and Safety of Additional Treatment with Low-Molecular-Weight Heparin for Neonates with Pulmonary Hemorrhage. Finally, we calculated the recovery rate and incidence rate of complications, such as pulmonary infection, intracranial hemorrhage, and respiratory distress to evaluate the efficacy and safety of additional treatment with low-molecular-weight heparin for neonates with pulmonary hemorrhage. There were 35 cured neonates out of 48 cases in the control group with 72.92% cure rate and involved 3 cases of pulmonary infection, 2 cases of intracranial hemorrhage, 1 case of respiratory distress out of 48 cases with 12.50% complication rate; there were 44 cured neonates out of 48 cases in the observation group with 91.67% cure rate and contained 1 case of pulmonary infection and 1 case of intracranial hemorrhage out of 48 cases with 4.17% complication rate, suggesting that the cure rate and complication rate improved significantly in the observation group compared with the control group ($P < 0.05$, Figure 3).

Table 1: The $PaCO_2$ and PaO_2 of each patient in the observation and control group before, 6 h, and 24 h after unfractionated heparin treatment with or without additional low-molecular-weight heparin treatment.

Group	Time	PaO2 (mmHg)	PaCO2 (mmHg)
Control group ($n = 48$)	Before treatment	50.62 ± 5.01	59.39 ± 4.74
	6 h after treatment	56.46 ± 6.16	50.16 ± 5.24
	24 h after treatment	72.41 ± 4.56	42.51 ± 3.11
F		31.410	16.120
P		0.001	0.001
Observation group ($n = 48$)	Before treatment	50.171 ± 5.89	59.31 ± 4.77
	6 h after treatment	62.72 ± 4.51	42.29 ± 4.26
	24 h after treatment	84.28 ± 3.71	37.01 ± 2.75
F		57.740	32.630
P		0.001	0.001

PaO2: partial pressure of oxygen; PaCO2: artery partial pressure of carbon.

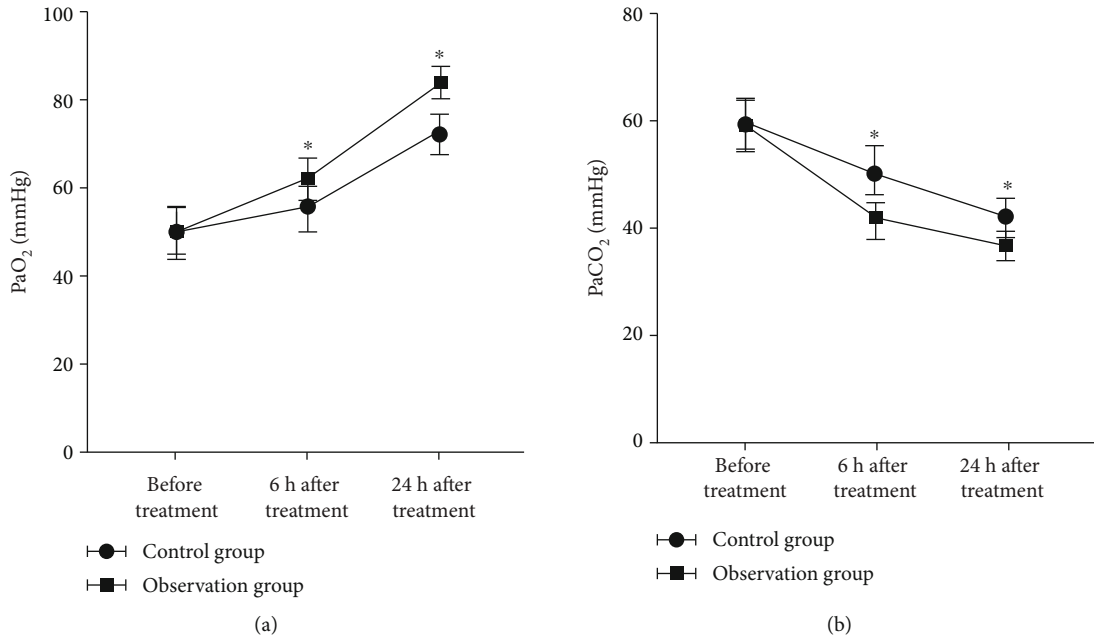

Figure 1: Alternations of $PaCO_2$ and PaO_2 of neonates with pulmonary hemorrhage before, 6 h, and 24 h after intravenous drip of unfractionated heparin with or without low-molecular-weight heparin treatment. * indicates $P < 0.05$ compared with the control group at indicated time points after treatment.

4. Discussion

Heparin is an anticoagulant for the prevention and treatment of venous thrombosis [15]. Low-molecular-weight heparin prepared from heparin has different pharmacokinetic and pharmacodynamics characteristics from unfractionated heparin, and it can reduce capillary permeability, improve local edema, and promote smooth muscle contraction and local hemostasis [16]. At the same time, low-molecular-weight heparin can significantly improve the vasoconstriction and oxygen supply in neonate [17].

The alveolar elastic fibrous tissue and bronchial wall fiber development of neonate are dysplasia, and alveolar surfactant is less, prone to alveolar and bronchial occlusion, which leading to hypoxia and microvascular damage [18]. Neonates with lung dysplasia have more blood vessels with less alveolar tissue, easy to cause bleeding phenomenon [19]. The increase of capillary pressure in alveolar wall caused by many factors leads to pulmonary hemorrhagic disease. Pulmonary hemorrhage is an important cause of perinatal death and complications [20]. Low-molecular-weight heparin plays a positive role in improving lung function of patients with lung disease.

Table 2: The FEV1, FEV1/FVC, and PEF of each patient in the observation and control group before and after unfractionated heparin treatment with or without additional low-molecular-weight heparin treatment.

Group	Time	FEV1 (L)	FEV1/FVC (%)	PEF (L/s)
Control group ($n = 48$)	Before treatment	1.31 ± 0.36	49.6 ± 7.44	5.90 ± 0.96
	After treatment	2.58 ± 0.48	58.6 ± 8.65	7.11 ± 1.21
t		2.586	5.172	3.857
P		0.012	0.007	0.014
Observation group ($n = 48$)	Before treatment	1.30 ± 0.41	49.2 ± 6.48	5.84 ± 0.78
	After treatment	3.15 ± 0.52*	66.9 ± 7.44*	8.85 ± 1.33*
t		3.125	8.635	5.173
P		0.021	0.001	0.001

The symbol of * indicates $P < 0.05$ compared with the control group; FEV1: the first second forced expiratory volume; FVC: forced vital capacity; PEF: peak expiratory flow.

Table 3: The changes of coagulation parameters function of each patient in the observation and control group before and after unfractionated heparin treatment with or without additional low-molecular-weight heparin treatment.

Group	Time	APTT (s)	PT (s)	TT (s)	FIB (g/L)
Control group ($n = 48$)	Before treatment	82.3 ± 8.52	19.3 ± 2.69	20.8 ± 2.76	5.24 ± 0.83
	After treatment	66.6 ± 7.25	14.1 ± 2.85	15.6 ± 2.63	3.31 ± 0.79
t		10.176	6.175	5.746	3.963
P		0.001	0.001	0.004	0.024
Observation group ($n = 48$)	Before treatment	83.0 ± 9.77	19.6 ± 3.10	21.3 ± 3.05	5.14 ± 0.79
	After treatment	50.5 ± 8.35*	10.2 ± 1.24*	12.3 ± 1.25*	2.57 ± 0.76*
t		21.084	8.173	6.712	4.183
P		0.001	0.001	0.001	0.016

The symbol of * indicates $P < 0.05$ compared with the control group; APTT: activated partial thromboplastin time; PT: prothrombin time; TT: thrombin time; FIB: fibrinogen.

Nasal continuous positive airway pressure (NCPAP) combined with low-molecular-weight heparin in the treatment of severe pneumonia has a good effect, which is helpful to improve the lung function and blood oxygen level of patients [21]. Low-molecular-weight heparin combined with acetylcysteine in the treatment of IIPs can improve the lung function of patients more effectively than single drug treatment. On the basis of conventional treatment, low-molecular-weight heparin combined with acetylcysteine in the treatment of IIPs can improve lung function more effectively than single drug treatment. On the basis of conventional treatment, the use of low-dose low-molecular-weight heparin calcium in the treatment of chronic obstructive pulmonary disease can significantly improve the total effective rate and blood gas index. The effect of rivaroxaban in the treatment of elderly patients with acute exacerbation of chronic obstructive pulmonary disease (AECOPD) is better than that of low-molecular-weight heparin calcium injection, which may be related to the age of patients. In the future research, we will analyze the patients with different ages separately to provide reference for more reasonable clinical treatment. On the basis of conventional treatment, increasing the use of low-molecular-weight heparin can improve the treatment effect of acute exacerbation of chronic obstructive pulmonary disease, and low-molecular-weight heparin combined with budesonide in the treatment of severe pneumonia in children can help to improve tidal breathing pulmonary function and accelerate the disappearance of symptoms and signs. This study also found that FEV1, FEV1/FVC, and peak expiratory flow of the two groups were significantly increased after treatment, suggesting that low-molecular-weight heparin can significantly improve pulmonary function and coagulation function in neonate with pulmonary hemorrhage. In the future study, we will further analyze the changes of blood gas indexes of the two groups after treatment, so as to provide reference for more reasonable clinical treatment.

Organ system development of neonate is not perfect, and they are prone to get infection, shock, even disseminated intravascular coagulation, and organ failure which cause death. Incomplete development of neonatal coagulation mechanism is the main cause of neonatal pulmonary hemorrhage death. At the same time, due to the physiological protection of the newborn, the coagulation function of the newborn is maintained in a low activity state. Therefore, improving coagulation dysfunction and hemostasis is an important idea for clinical treatment. APTT, PT, TT, and FIB are sensitive indicators of coagulation system [22]. Low-molecular-weight heparin can play a role in the

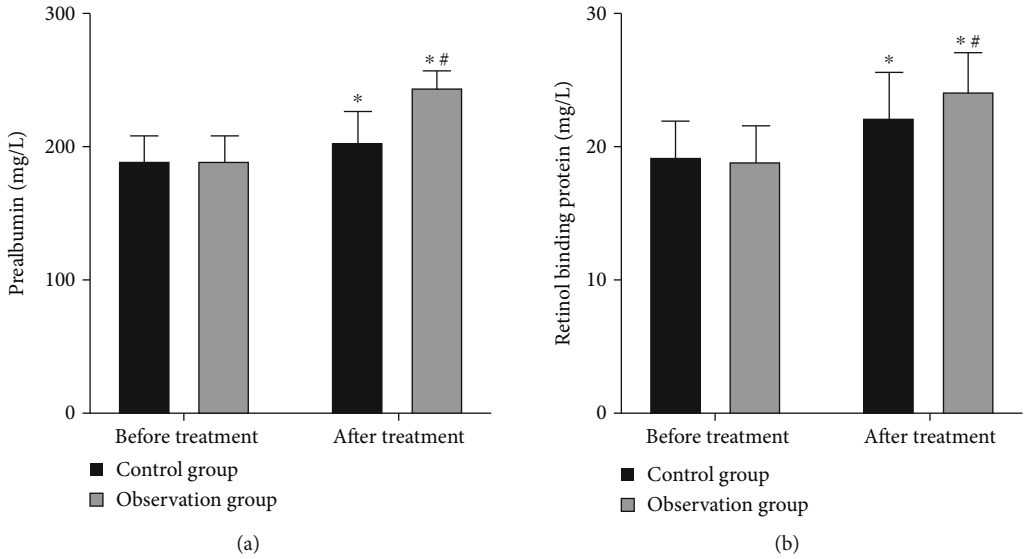

Figure 2: The serum levels of prealbumin and retinol-binding protein in neonates with pulmonary hemorrhage before and after intravenous drip of unfractionated heparin with or without low-molecular-weight heparin treatment. * indicates $P < 0.05$ after treatment. # indicates $P < 0.05$ compared with the control group.

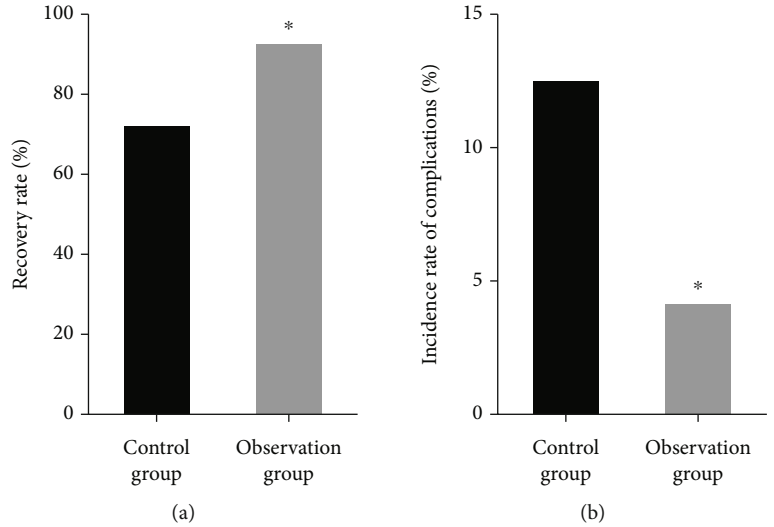

Figure 3: The recovery rate and incidence rate of complications after intravenous drip of unfractionated heparin with or without low-molecular-weight heparin treatment. * indicates $P < 0.05$ compared with the control group.

treatment of venous thrombosis by regulating the abnormal levels of the above factors. Low-molecular-weight heparin combined with prednisone can effectively improve the renal function of children with nephrotic syndrome, but has no obvious adverse effect on blood coagulation. Fasudil hydrochloride combined with low-molecular-weight heparin calcium can affect APTT, PT, TT, and FIB concentrations, improve blood hypercoagulability in patients with ischemic stroke, and improve the clinical therapeutic effect of ischemic stroke. This study also found that the pulmonary function indexes of the two groups were significantly improved after treatment, and the coagulation function indexes such as activated partial thromboplastin time, prothrombin time, and the level of coagulogenic enzyme phase were significantly decreased, suggesting that the clinical effect of low-molecular-weight heparin and the improvement of pulmonary function in patients with neonatal pulmonary hemorrhage are related to the abnormal coagulation function indexes.

Prealbumin is a thyroxine and retinol-binding protein synthesized by hepatocytes, which belongs to the category of carrier protein [23]. Liver is also an important place for the synthesis of coagulation factors [24], and abnormal or damaged liver function can lead to abnormal expression of coagulation factors and prealbumin. There was significant difference in plasma prealbumin between patients with AECOPD and healthy controls before and after treatment [25]. The detection of plasma prealbumin is helpful to reflect the nutritional status of COPD patients [26]. The decrease of prealbumin in patients with COPD reflects the severity of

COPD to a certain extent, which can be an important reference index for clinicians to judge the prognosis of COPD. Retinol-binding protein is also a sensitive indicator of nutritional status. In a study reported by Delgado et al., an increased level of retinol-binding protein was found after parenteral support of critically ill infants during short period of intensive care [27].

In conclusion, additional treatment with low-molecular-weight heparin could provide a better patient outcome for neonatal pulmonary hemorrhage with unfractionated heparin treatment, as it could notably improve pulmonary function and coagulation function and reduced the incidence of complications. There were many factors influencing newborns, and the number of study subjects included in this study is limited; we will further increase the sample size and observation indicators in future studies and use multicenter comparative study to provide reference for more reasonable clinical treatment.

Data Availability

The data used to support the findings of this study are included within the article.

Conflicts of Interest

The authors declare that they have no conflicts of interest.

References

[1] I. Agarwal and L. M. Ernst, "Perinatal pulmonary hemorrhage: a retrospective autopsy case series," *Pediatric and Developmental Pathology*, vol. 23, no. 4, pp. 267–273, 2020.

[2] M. Lee, K. Wu, A. Yu et al., "Pulmonary hemorrhage in neonatal respiratory distress syndrome: radiographic evolution, course, complications and long-term clinical outcomes," *Journal of Neonatal-Perinatal Medicine*, vol. 12, no. 2, pp. 161–171, 2019.

[3] A. Aziz and A. Ohlsson, "Surfactant for pulmonary haemorrhage in neonates," *Cochrane Database of Systematic Reviews*, vol. 2, article CD005254, 2020.

[4] C. H. Ferreira, F. Carmona, and F. E. Martinez, "Prevalencia, fatores de risco e prognostico associados a hemorragia pulmonar em recem-nascidos," *Jornal de Pediatria*, vol. 90, no. 3, pp. 316–322, 2014.

[5] R. Orbach, D. Mandel, R. Lubetzky et al., "Pulmonary hemorrhage due to Coxsackievirus B infection–a call to raise suspicion of this important complication as an end-stage of enterovirus sepsis in preterm twin neonates," *Journal of Clinical Virology*, vol. 82, pp. 41–45, 2016.

[6] A. Lodha, P. S. Shah, and J. Hellmann, "Pulmonary haemorrhage associated with neonatal neurological disease," *Heart, Lung & Circulation*, vol. 18, no. 1, pp. 45–48, 2009.

[7] Y. Shi, S. Tang, H. Li, J. Zhao, and F. Pan, "New treatment of neonatal pulmonary hemorrhage with hemocoagulase in addition to mechanical ventilation," *Biology of the Neonate*, vol. 88, no. 2, pp. 118–121, 2005.

[8] V. Vobruba, T. Grus, F. Mlejnsky, J. Belohlavek, J. Hridel, and L. Lambert, "Management of severe pulmonary hemorrhage in a neonate on veno-arterial ECMO by the temporary clamping of the endotracheal tube - a case report," *Perfusion*, vol. 33, no. 1, pp. 77–80, 2018.

[9] B. H. Su, H. Y. Lin, F. K. Huang, M. L. Tsai, and Y. T. Huang, "Circulatory management focusing on preventing intraventricular hemorrhage and pulmonary hemorrhage in preterm infants," *Pediatrics and Neonatology*, vol. 57, no. 6, pp. 453–462, 2016.

[10] X. Huang, A. R. Rezaie, G. J. Broze Jr., and S. T. Olson, "Heparin is a major activator of the anticoagulant serpin, protein Z-dependent protease inhibitor∗," *The Journal of Biological Chemistry*, vol. 286, no. 11, pp. 8740–8751, 2011.

[11] G. Izaguirre, S. Aguila, L. Qi et al., "Conformational activation of antithrombin by heparin involves an altered exosite interaction with protease∗," *The Journal of Biological Chemistry*, vol. 289, no. 49, pp. 34049–34064, 2014.

[12] M. Bruschettini, O. Romantsik, S. Zappettini, R. Banzi, L. A. Ramenghi, and M. G. Calevo, "Heparin for the prevention of intraventricular haemorrhage in preterm infants," *Cochrane Database of Systematic Reviews*, vol. 5, article CD011718, 2016.

[13] H. Resic, N. Kukavica, V. Sahovic, and F. Masnic, "Different effects of low weight molecular heparin and unfractioned heparin on lipid profile and coagulation at haemodialysis patients," *Bosnian Journal of Basic Medical Sciences*, vol. 10, no. 1, pp. 56–S62, 2010.

[14] F. E. Canpolat, D. Orhan, S. Yigit, G. Kale, M. Yurdakok, and G. Tekinalp, "The effects of antenatal anticoagulants (low-molecular-weight heparin and aspirin) on neonatal pulmonary vasculature in rabbits," *Pediatric and Developmental Pathology*, vol. 13, no. 2, pp. 107–111, 2010.

[15] C. S. Ong, J. A. Marcum, K. J. Zehr, and D. E. Cameron, "A century of heparin," *The Annals of Thoracic Surgery*, vol. 108, no. 3, pp. 955–958, 2019.

[16] G. Camporese and E. Bernardi, "Low-molecular-weight heparin for thromboprophylaxis," *Current Opinion in Pulmonary Medicine*, vol. 15, no. 5, pp. 443–454, 2009.

[17] M. A. Rodger, J. C. Gris, J. I. P. de Vries et al., "Low-molecular-weight heparin and recurrent placenta-mediated pregnancy complications: a meta-analysis of individual patient data from randomised controlled trials," *Lancet*, vol. 388, no. 10060, pp. 2629–2641, 2016.

[18] C. D. Baker and S. H. Abman, "Impaired pulmonary vascular development in bronchopulmonary dysplasia," *Neonatology*, vol. 107, no. 4, pp. 344–351, 2015.

[19] C. Li, X. Li, C. Deng, and C. Guo, "Circulating fibrocytes are increased in neonates with bronchopulmonary dysplasia," *PLoS One*, vol. 11, no. 6, article e0157181, 2016.

[20] S. Godfrey, "Pulmonary hemorrhage/hemoptysis in children," *Pediatric Pulmonology*, vol. 37, no. 6, pp. 476–484, 2004.

[21] A. M. De Klerk and R. K. De Klerk, "Nasal continuous positive airway pressure and outcomes of preterm infants," *Journal of Paediatrics and Child Health*, vol. 37, no. 2, pp. 161–167, 2001.

[22] M. Milos, D. C. Herak, and R. Zadro, "Discrepancies between APTT results determined with different evaluation modes on automated coagulation analyzers," *International Journal of Laboratory Hematology*, vol. 32, no. 1p2, pp. 33–39, 2010.

[23] Y. Zhang, M. Zhang, X. Yang, and H. Wang, "Significance of retinol binding protein and prealbumin in neonatal nutritional evaluation," *Pakistan Journal of Pharmaceutical Sciences*, vol. 31, no. 4, pp. 1613–1616, 2018.

[24] H. Stefan and B. Joris, "Measurement of Blood Coagulation Factor Synthesis in Cultures of Human Hepatocytes," *Methods in Molecular Biology*, vol. 1250, pp. 309–316, 2015.

[25] S. Arora, K. Madan, A. Mohan, M. Kalaivani, and R. Guleria, "Serum inflammatory markers and nutritional status in patients with stable chronic obstructive pulmonary disease," *Lung India*, vol. 36, no. 5, pp. 393–398, 2019.

[26] A. Mohan, S. Arora, A. Uniyal et al., "Evaluation of plasma leptin, tumor necrosis factor-α, and prealbumin as prognostic biomarkers during clinical recovery from acute exacerbations of chronic obstructive pulmonary disease," *Lung India*, vol. 34, no. 1, pp. 3–8, 2017.

[27] A. F. Delgado, H. M. Kimura, A. L. Cardoso, D. Uehara, and F. R. Carrazza, "Nutritional follow-up of critically ill infants receiving short term parenteral nutrition," *Revista do Hospital das Clinicas; Faculdade de Medicina da Universidade de Sao Paulo*, vol. 55, no. 1, pp. 3–8, 2000.

Hindawi
Journal of Nanomaterials
Volume 2021, Article ID 9942260, 7 pages
https://doi.org/10.1155/2021/9942260

Research Article

High Expressions of Notch and Survivin in Elderly Patients with Glioma Contribute to an Unfavorable Prognosis

Yuguo Liao, Kangsheng Zhou, Haikun Li, and Lin Yang

Neurosurgery Department, Huidong People's Hospital, China

Correspondence should be addressed to Yuguo Liao; liaoyuguo1892368@126.com

Received 26 March 2021; Accepted 26 April 2021; Published 11 May 2021

Academic Editor: Songwen Tan

Gliomas account for 24% of all primary brain and central nervous system tumors. To date, elderly patients constitute 10-25% of patients with a diagnosis of glioblastoma multiforme, but limited attention has been put on their optimal treatment, largely due to a very poor expected survival (only 4-6 months). Unraveling the molecular mechanism of gliomas provides an opportunity to develop novel biomarkers and therapeutic targets. In this study, we collected fasting blood samples from elderly patients diagnosed with glioma and who received treatment in our hospital between May 2016 and May 2019 and determined the expression levels of Notch and Survivin proteins in different clinical stages and their relationship with patient survival. A total of 68 healthy volunteers in this hospital during the same period served as healthy controls. Compared with the healthy controls, the expressions of Notch 1, Notch 2, Notch 3, and Survivin protein in the serum of elderly glioma patients were remarkably increased ($P < 0.05$), but the expression of caspase-3 protein declined ($P < 0.05$). As the clinical stage of the patient advanced, the expressions of Notch 1, Notch 2, Notch 3, and Survivin increased, and this increase was statistically significant ($P < 0.05$). It was observed that high expressions of serum Notch 1, Notch 2, Notch 3, and Survivin were associated with poor overall survival of elderly patients with glioma. We used γ-secretase inhibitor MRK-003 and specific ligand Jagged1 to alter the Notch pathway in U251 cells. It was revealed that MRK-003 incubation effectively suppressed the mRNA expression of Survivin in U251 cells, but Jagged1 stimulation significantly promoted the mRNA expression of Survivin in U251 cells. Results of MTT and transwell migration assays revealed reduced U251 cell viability and migration following MRK-003 treatment and enhanced cell viability and migration following Jagged1 stimulation. In conclusion, the finding obtained from these results supports that Notch and Survivin proteins contribute to the development of glioma in elderly patients and could serve as prognostic factors.

1. Introduction

Gliomas represent the most common primary brain and central nervous system tumors worldwide and occur almost exclusively in the following four lobes of the brain: frontal (23.6%), temporal (17.4%), parietal (10.6%), and occipital (2.8%), leading to significant morbidity and mortality in adults, especially elderly people [1, 2]. To date, elderly patients already account for 10-25% of all patients with a diagnosis of glioblastoma multiforme, but limited attention has been put on their optimal treatment, largely due to a very poor expected survival ranging only from 4 to 6 months [3]. In this context, the increasing aging of the population will contribute to at least twofold increase in the number of glioma diagnoses in elderly patients in the following two decades [4, 5]. Because of the inability to tolerate the treatment, elderly patients with gliomas have far less chance to undergo resection and receive adjuvant therapies than their younger counterparts and typically only receive palliative care [6]. Therefore, the management of gliomas in elderly patients has received much attention and becomes an important and challenging topic in neurooncology.

Unraveling the molecular mechanism of gliomas provides an opportunity to develop novel biomarkers and therapeutic targets. Notch is a crucial evolutionary conserved pathway that engages in the modulation of central cellular processes during embryonic and postnatal development, and it encodes for four paralogs, Notch 1-4 [7]. The Notch pathway inhibits neuronal differentiation in the central nervous system through maintenance of neural stem cells and

commitment of neural progenitor cells into the glial lineage. Notch is therefore often implicated in the development of brain tumors, as tumor cells share various characteristics with neural stem and progenitor cells [8]. Survivin is known as a member of the inhibitor of apoptosis family and is nearly undetectable in most normal tissues in adults. It is highly expressed in almost all human malignancies [9]. Recent studies focus on nanoparticles based on Survivin-targeting treatments as brain cancer therapies [8]. Caspase-3 is a member of cysteinyl aspartate-specific proteases that are highly conserved in multicellular organisms and function as a key regulatory molecule in neurogenesis and synaptic activity [10]. In this study, we collected fasting blood samples from elderly patients diagnosed with glioma and who received treatment in our hospital between May 2016 and May 2019 and determined the expression levels of Notch and Survivin proteins in different clinical stages and their relationship with patient survival.

2. Materials and Methods

2.1. Patient Information. The study recruited elderly patients with glioma according to predefined inclusion and exclusion criteria. Inclusion criteria are age ≥ 60 years, initial diagnosis of glioma according to the 2007 WHO classification of tumor of the central nervous system [11], and patients' or their family members' signed informed content. Exclusion criteria are patients with other malignant tumors; patients with severe metabolic system diseases such as diabetes; patients with immune system diseases; patients with severe heart, kidney, and lung dysfunction; and patients with severe cognitive dysfunction. Finally, a total of 100 elderly patients with glioma diagnosed and treated in our hospital from May 2016 to May 2019 were recruited into the study. Among these 100 patients, 65 were males and 35 were females, aged 62-77 years old, with an average of 66.6 ± 8.6 years; there were 29 patients in clinical phase I, 21 patients in clinical phase II, 30 patients in clinical phase III, and 20 patients in clinical phase IV. The 68 healthy persons undergoing physical examination in this hospital during the same period were selected as the control group. There was no statistical difference in the average age and gender ratio between the two groups ($P > 0.05$). A 6-year follow-up was performed on each patient. The study protocol was approved by the Ethics Committee of our hospital.

2.2. Blood Sample Collection and Enzyme-Linked Immunosorbent Assay (ELISA). Fasting venous blood from each elderly patient was sampled and centrifuged at low speed to separate the upper serum for testing. The serum levels of Notch 1, Notch 2, Notch 3, Survivin, and caspase-3 were measured by ELISA methods using commercial available kits (Santa Cruz Company, Elabscience Company, and Omega Company) following the instructions provided by the manufacturers.

2.3. Classification of High, Medium, and Low Expressions. Elderly patients with high, medium, and low serum expressions of Notch 1, Notch 2, Notch 3, Survivin, and caspase-3 were classified according to the following threshold values: Notch 1 (low expression: ratio to β-actin < 0.45, medium expression: $0.45 \leq$ ratio to β-actin ≤ 0.50, and high expression: ratio to β-actin > 0.50), Notch 2 (low expression: ratio to β-actin < 0.40, medium expression: $0.40 \leq$ ratio to β-actin ≤ 0.55, and high expression: ratio to β-actin > 0.55), Notch 3 (low expression: ratio to β-actin < 0.45, medium expression: $0.45 \leq$ ratio to β-actin ≤ 0.55, and high expression: ratio to β-actin > 0.55), and Survivin (low expression: ratio to β-actin < 0.35, medium expression: $0.35 \leq$ ratio to β-actin ≤ 0.40, and high expression: ratio to β-actin > 0.40). Besides, the serum levels of caspase-3 in patients with different stages were detected.

2.4. Cell Culture. Human glioma cell line U251 (Shanghai North Connaught Biotechnology Co., Ltd., China) was maintained in DMEM with 10% fetal bovine serum (FBS, Gibco, USA), 100 μg/mL streptomycin, and 100 IU/mL penicillin in a humidified environment in the presence of 5% CO_2. U251 cells were seeded into the 6-well plate and allowed to settle overnight. Afterwards, the cultured cells were treated with 10 μM γ-secretase inhibitor (GSI) MRK-003 for 48 h to block the Notch signaling pathway [12].

2.5. Soluble Jagged1 Ligand Immobilization. The recombinant rat Jagged1-Fc fusion chimera (R&D Systems, Minneapolis, MN) was dissolved in phosphate-buffered saline and immobilized in flat-bottom 96-well plates for 20 hours at 4°C at 10 μg/mL (100 μL/well). Human IgG-Fc (R&D Systems) was used and served as the control for Jagged1. U251 cells were seeded into the plates coated with Jagged1 or IgG-Fc at 10^5 cells/well.

2.6. Survivin Promoter Luciferase Assay. U251 cells were cotransfected with reporter plasmids for Survivin promoter (pLuc-surP-596, Invitrogen, USA) and pN3-N1ICD using Lipofectamine 2000 (Invitrogen) as per the manufacturer's manual. Dual-luciferase assays were performed using GeneCopoeia's dual-luciferase assay kit (D0010, Beijing Solarbio Science & Technology Co., Ltd., Beijing, China) on a GloMax 20/20 Luminometer (Promega, USA) using pRL-TK (Renilla luciferase) as the loading control.

2.7. Quantitative Real-Time Polymerase Chain Reaction (qRT-PCR). Total RNA was extracted from U251 cells using the TRIzol reagent. The extracted RNA was then reverse transcribed into cDNA using the PrimeScript RT kit (Takara, Japan). qRT-PCR was performed as per the instructions of the SYBR® Premix Ex Taq™ II Kit (Takara) in an ABI 7300 thermal cycler (Applied Biosystems, Foster City, CA, USA). The relative mRNA level of Survivin to β-actin was calculated by relative quantification ($2^{-\Delta\Delta CT}$ method). The primer sequences for Survivin are forward: 5′-CTTTCTCAAGG ACCACCG-3′ and reverse: 5′-CACGACGACCATTGTC ACC-3′. The primer sequences for β-actin are 5′-CTCCAT CCTGGCCTCGCTGT-3′ and reverse: 5′-GCTGTCACC TTCACCGTTCC-3′.

Table 1: Expression levels of Notch proteins in elderly patients with glioma at different clinical stages.

Group no.			Notch 1/β-actin	Notch 2/β-actin	Notch 3/β-actin
1	Healthy control ($n = 68$)		0.33 ± 0.07	0.29 ± 0.04	0.31 ± 0.05
2	Elderly glioma ($n = 100$)		0.46 ± 0.09	0.40 ± 0.09	0.45 ± 0.10
3		Stage I ($n = 29$)	0.39 ± 0.08	0.32 ± 0.04	0.36 ± 0.05
4		Stage II ($n = 21$)	0.42 ± 0.06	0.37 ± 0.08	0.41 ± 0.09
5		Stage III ($n = 30$)	0.49 ± 0.11	0.45 ± 0.08	0.50 ± 0.13
6		Stage IV ($n = 20$)	0.57 ± 0.12	0.51 ± 0.12	0.61 ± 0.13
Statistical comparison	t1-2		2.369	3.754	2.584
	P1-2		0.025	0.033	0.025
	F3-6		45.15	34.87	36.94
	P3-6		0.017	0.029	0.014

2.8. MTT Assay. Following a 48 h period of cell treatment, U251 cell viability was determined using the MTT assay. In brief, U251 cells (5×10^3 cells/well) were plated into the 96-well plate, and the plate was added with 10 μL of MTT solution (R&D Systems, USA), followed by 4 h of further incubation. The absorbance at 450 nm wavelength (OD450) was measured at indicated time points (24^{th} and 48^{th}) using a plate reader (Thermo Scientific, Watertown, USA).

2.9. Transwell Migration Assay. U251 cell migration was assessed using a transwell (8 μm pore size), and 5×10^4 cells were plated into each well of the upper chamber uncoated with the membrane. The lower chamber was added with the medium containing 10% FBS. After cells were incubated for 24 hours, those that migrated from the upper chamber into the lower chamber were fixed with methanol and stained with 0.1% crystal violet dye. A microscopic view was captured under an inverted microscope.

2.10. Statistical Analysis. Data statistics were completed using SPSS 21.0 statistical software (IBM Corp., Armonk, NY, USA). The measurement data were expressed by the mean $\pm$ standard deviation. The t-test was used to compare the two groups. One-way analysis of variance was used for multiple-group comparisons. If the overall comparison was different, the F test was used for pairwise comparison. The possibility of a difference less than 0.05 was held to be statistically significant.

3. Results

3.1. Expression Levels of Notch Proteins in Elderly Patients with Glioma according to Different Clinical Stages. First, we collected blood samples from 100 elderly patients with glioma and performed ELISA methods to examine expression levels of Notch 1, Notch 2, and Notch 3. Results showed that compared with healthy controls, the expression levels of Notch 1, Notch 2, and Notch 3 in elderly patients with glioma were evidently increased ($P < 0.05$, Table 1). Next, we classified 100 elderly patients with glioma based on their clinical stage. It was revealed that the expression levels of Notch 1, Notch 2, and Notch 3 were associated with the clinical stage of glioma ($P < 0.05$, Table 1), suggesting that high expression of Notch proteins may contribute to the progression of glioma.

3.2. Expression Levels of Survivin and Caspase-3 Proteins in Elderly Patients with Glioma according to Different Clinical Stages. Subsequently, we examined expression levels of Survivin and caspase-3 in blood samples from 100 elderly patients with glioma by ELISA methods. Results of ELISA revealed that elderly patients with glioma presented an elevated expression level of Survivin concomitant with a declined expression level of caspase-3 compared with healthy controls ($P < 0.05$, Table 2). In addition, higher Survivin expression levels and lower caspase-3 expression levels reflected the advanced clinical stage of glioma ($P < 0.05$, Table 2), indicating that Survivin and caspase-3 proteins may be associated with the progression of glioma.

3.3. High Expressions of Notch and Survivin Proteins Were Associated with Poor Overall Survival of Elderly Glioma. The overall survivals of elderly patients with high expression levels of Notch 1, Notch 2, Notch 3, and Survivin were shorter than those with medium expressions ($P < 0.05$). Elderly patients with medium expression levels of Notch 1, Notch 2, Notch 3, and Survivin were longer than those with low expressions ($P < 0.05$). The Kaplan-Meier curve was plotted to depict the overall survival of elderly patients with glioma. As shown in Figure 1, expression levels of Notch 1, Notch 2, Notch 3, and Survivin were correlated with the prognosis of elderly patients with glioma. As expression levels of Notch and Survivin proteins increased, the patient's prognosis became worse.

3.4. Alternation of Notch Pathway Affected Survivin Expression in Glioma Cells. Previous evidence demonstrated the relationship between Notch activation and Survivin expression in human cancers. Considering these given facts, we asked if Notch mediates Survivin in glioma. To test this hypothesis, we used γ-secretase inhibitor MRK-003, which blocks the activation of Notch receptors by inhibiting γ-secretase activity, to examine the effect of Notch inhibition on Survivin expression in U251 cells. Results of qRT-PCR

Table 2: Expression levels of Notch proteins in elderly patients with glioma at different clinical stages.

Group no.			Survivin/β-actin	Caspase-3/β-actin
1	Healthy control ($n = 68$)		0.30 ± 0.05	0.50 ± 0.12
2	Elderly glioma ($n = 100$)		0.40 ± 0.07	0.42 ± 0.08
3		Stage I ($n = 29$)	0.34 ± 0.05	0.55 ± 0.11
4		Stage II ($n = 21$)	0.38 ± 0.09	0.49 ± 0.10
5		Stage III ($n = 30$)	0.41 ± 0.10	0.40 ± 0.08
6		Stage IV ($n = 20$)	0.48 ± 0.11	0.36 ± 0.07
Statistical comparison	t1-2		2.551	3.174
	P1-2		0.036	0.022
	F3-6		49.21	36.47
	P3-6		0.014	0.021

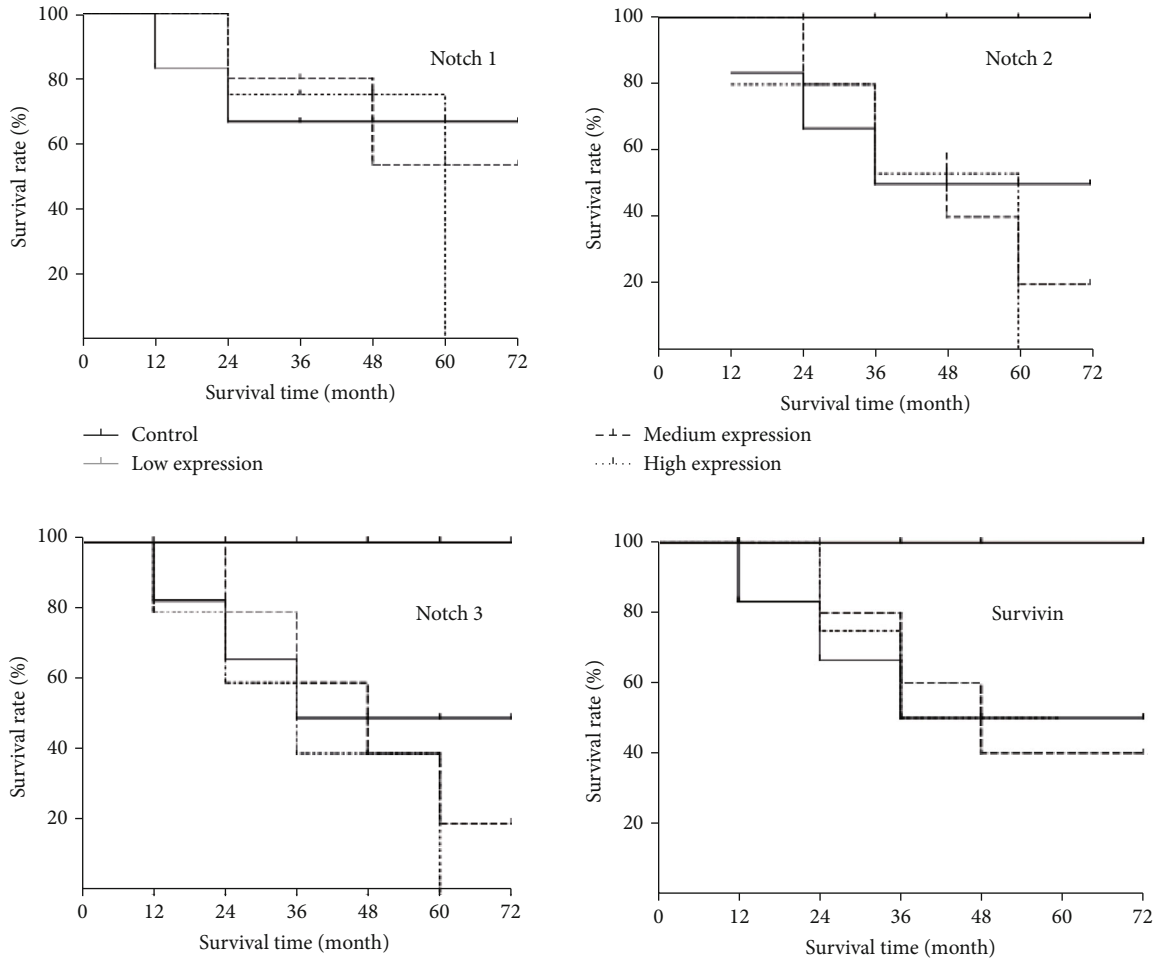

Figure 1: The Kaplan-Meier curve was plotted to depict the overall survival of elderly patients with glioma according to high, medium, and low expression levels of Notch 1, Notch 2, Notch 3, and Survivin.

displayed that the incubation of cells with MRK-003 effectively suppressed the mRNA expression of Survivin in U251 cells (Figure 2(a)). Next, we are also wondering the effect of Notch activation on Survivin expression in U251 cells. Since the Notch pathway is activated upon specific ligands like Jagged1 binding to the related transmembrane receptors, U251 cells were cultured for 48 h on immobilized Jagged1 ligand and then analyzed for Survivin expression. As expected, an increased mRNA expression of Survivin was detected in U251 cells treated with Jagged1 compared with those treated with IgG-Fc (Figure 2(b)). Notably, the delivery of pN3-N1ICD in combination with the Survivin

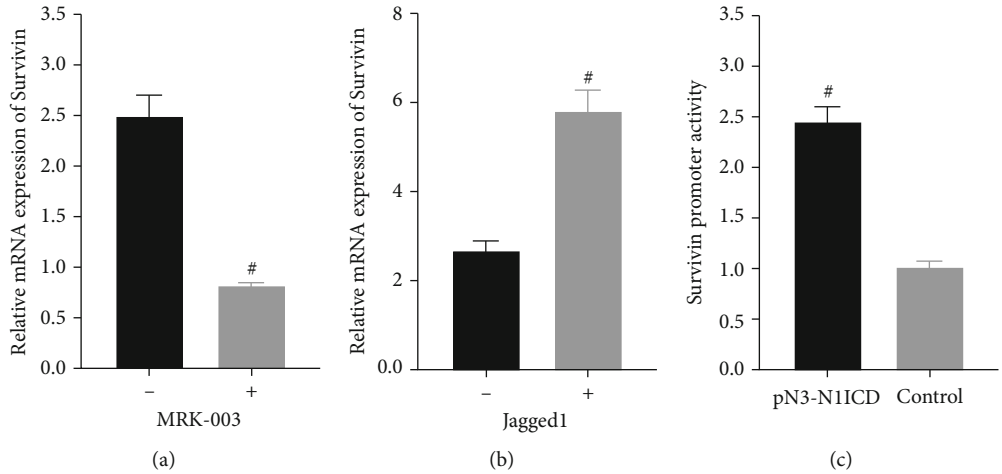

Figure 2: Alternation of the Notch pathway affects Survivin expression in glioma cells. The mRNA expression of Survivin was determined by qRT-PCR in the cultured U251 cells treated with 10 μM γ-secretase inhibitor (GSI) MRK-003 for 48 h to block the Notch signaling pathway (a) and stimulated with 10 μg/mL Jagged1 to activate the Notch signaling pathway (b). (c) The delivery of pN3-N1ICD in combination with Survivin promoter into U251 cells yielded a 2.4-fold increase in Survivin promoter activity. # indicates $P < 0.05$ compared with the corresponding control.

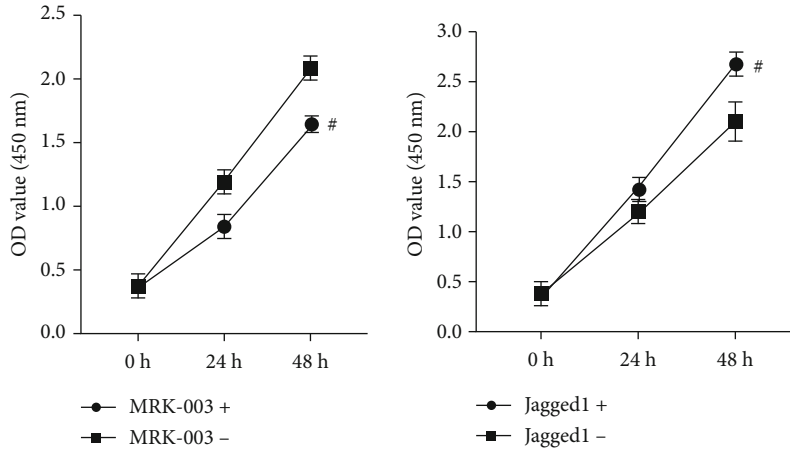

Figure 3: Alternation of the Notch pathway affects glioma cell viability. Reduced cell viability was detected by MTT assays in the cultured U251 cells treated with 10 μM γ-secretase inhibitor (GSI) MRK-003 for 48 h, and increased cell viability was detected in the cultured U251 cells stimulated with 10 μg/mL Jagged1 to activate the Notch signaling pathway. # indicates $P < 0.05$ compared with the corresponding control.

promoter into U251 cells yielded a 2.4-fold increase in Survivin promoter activity (Figure 2(c)). These findings indicated that Notch activation was associated with Survivin overexpression in glioma.

3.5. Alternation of Notch Pathway Affected Glioma Cell Viability and Migration. Next, we set out to ascertain the effects of the Notch pathway on U251 cell viability and migration. Results of MTT assays revealed reduced U251 cell viability following MRK-003 treatment and enhanced cell viability following Jagged1 stimulation (Figure 3). Results of transwell migration assays demonstrated fewer U251 cells migrating from the upper chamber into the lower one upon MRK-003 treatment and more U251 cells migrating from the upper chamber into the lower one upon Jagged1 stimulation (Figure 4). These findings indicated that activation of the Notch pathway may contribute to the development of glioma.

4. Discussion

Gliomas are the most common malignant tumors in clinical practice, common in the elderly population. Glioma patients are usually in the middle and advanced stages when they are clinically diagnosed, and the prognosis is poor. Analyzing the related biological macromolecules of the onset and clinical stage of glioma and exploring the relationship between it and the prognosis of patients are of great value to clinical diagnosis and treatment, as well as the improvement of the prognosis of patients. As revealed by the analysis on the

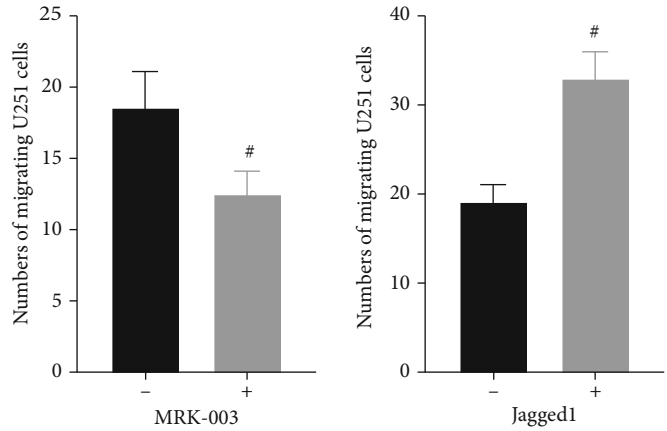

Figure 4: Alternation of the Notch pathway affects glioma cell migration. Transwell assays detected fewer U251 cells migrating from the upper chamber into the lower one upon MRK-003 treatment and more U251 cells migrating from the upper chamber into the lower one upon Jagged1 stimulation. # indicates $P < 0.05$ compared with the corresponding control.

clinical value of high expression of Notch and Survivin proteins in elderly patients with glioma and its relationship with the prognosis of patients, compared with healthy controls, the expression of Notch 1, Notch 2, Notch 3, and Survivin proteins in the elderly glioma group significantly increased while the expression of caspase-3 significantly decreased. Besides, with the increase in the clinical stages of patients, the abovementioned protein changes became more apparent, with significant differences between the clinical stages. Therefore, the expression of Notch and Survivin in elderly patients with glioma is closely related to the clinical stage and prognosis of patients.

The abnormal expression of Notch protein is closely related to the pathogenesis of various malignant tumors [13, 14] and is a potential target of drug therapy [15]. In the investigation of the inhibitory effect of Notch 1 blocker on tumor growth of the osteosarcoma mouse model and related molecular mechanisms, it was discovered that Notch 1 blocker can inhibit the tumor growth of the osteosarcoma mouse model. The molecular mechanisms involved in this process include reducing the production of proproliferation molecules and proinvasion molecules and increasing the production of proapoptosis and invasion-inhibiting molecules [16]. The analysis of the effect of RNAi interference with the expression of Notch 1 gene in melanoma cells on the immune mechanism of mouse tumors also confirmed that siNotch 1 can inhibit the Notch pathway of melanoma cells and then reduce its secretion of TGF-β; as a result, its inhibitory effect on lymphocytes is reduced, the infiltration of gp100 antigen-specific $CD8^+$ T cells in tumor tissues is increased, the secretion of IFN-γ is promoted, the proportion of Treg cells is lowered, and the body's antitumor immune function is enhanced [17]. Previous studies have also proposed that in renal clear cell carcinoma cell lines, overactivated Notch 1 can promote cancer by regulating the PTEN/PI3K/AKT signaling pathway; this provides a new treatment strategy for the treatment of renal clear cell carcinoma [18]. In our study, compared with the control group, the expression of Notch 1, Notch 2, and Notch 3 proteins in the elderly glioma group significantly increased; with the increase in the clinical stages of patients, the abovementioned protein changes became more apparent, with significant differences between the clinical stages. This indicates that the expression of Notch in elderly patients with glioma is closely related to the clinical stage and prognosis of the patients.

Survivin is a member of the inhibitor of apoptosis protein family. It is expressed in a cell cycle-dependent manner during mitosis. It is located in distinct parts of the mitotic apparatus and plays an essential role in cell division and inhibition of apoptosis. Survivin is expressed in most human cancers, but not in normal adult tissues [19, 20]. Inhibition of Survivin has been well-studied as a cancer therapeutic. For example, Carrasco and his team found specific inhibition of Survivin expression by LY2181308-sensitized tumor cells to chemotherapeutic-induced apoptosis. Most importantly, they found that LY2181308 yielded antitumor activity in an *in vivo* human xenograft tumor model, and this model was sensitized to gemcitabine, paclitaxel, and docetaxel [21]. With the increase of age, the mechanism of neurogenesis decrease is still unclear, but it has been reported that it involves the changes of the microenvironment of neural progenitor cells. Astrocytes regulate the cycle of neural progenitor cells by acting on the expression level of Survivin, a known mitotic regulator. Among the cell cycle genes found in the elderly neural progenitor cells, Survivin is the only one that can restore the proliferation of the elderly brain neural progenitor cells. Miranda et al. provide a mechanism for the gradual loss of neurogenesis in the brain in relation to aging and reveal that targeted silencing of Survivin expression directly or through Wnt signaling could stimulate adult neurogenesis [22]. Survivin exhibits its antiapoptotic function in part by inhibiting caspase-3 activity [23]. The results in our study also demonstrate that compared with the healthy control, the expression of Survivin protein in the elderly glioma group was significantly increased while the expression of caspase-3 significantly was reduced; with the increase in the clinical stages of patients, the abovementioned protein changes became more apparent, with significant differences between the clinical stages. It suggests that Survivin and Survivin-dependent caspase-3 proteins are also closely

related to the clinical stage and prognosis of elderly patients with glioma.

In summary, the present study showed that Notch and Survivin proteins were overexpressed in elderly glioma and their upregulation may contribute to the development of glioma in elderly patients and could serve as prognostic factors. We also demonstrate that activation of the Notch pathway mediates upregulation of Survivin expression and leads to glioma cell viability and migration. Finally, these data might be helpful in identifying the molecular mechanism involved in the elevated level of Survivin in glioma cells, and targeting these factors might be an important implication in the development of new therapeutic strategies aimed at blocking Notch activation in glioma cells.

Data Availability

The data used to support the findings of this study are included within the article.

Conflicts of Interest

The authors declare that they have no conflicts of interest.

References

[1] R. Chen, M. Smith-Cohn, A. L. Cohen, and H. Colman, "Glioma subclassifications and their clinical significance," *Neurotherapeutics*, vol. 14, no. 2, pp. 284–297, 2017.

[2] Q. T. Ostrom, H. Gittleman, L. Stetson, S. M. Virk, and J. S. Barnholtz-Sloan, "Epidemiology of gliomas," *Cancer Treatment and Research*, vol. 163, pp. 1–14, 2015.

[3] F. Laigle-Donadey and J. Y. Delattre, "Glioma in the elderly," *Current Opinion in Oncology*, vol. 18, no. 6, pp. 644–647, 2006.

[4] G. Minniti, G. Lombardi, and S. Paolini, "Glioblastoma in elderly patients: current management and future perspectives," *Cancers (Basel)*, vol. 11, no. 3, p. 336, 2019.

[5] N. Laperriere, M. Weller, R. Stupp et al., "Optimal management of elderly patients with glioblastoma," *Cancer Treatment Reviews*, vol. 39, no. 4, pp. 350–357, 2013.

[6] J. Gallego Perez-Larraya and J. Y. Delattre, "Management of elderly patients with gliomas," *The Oncologist*, vol. 19, no. 12, pp. 1258–1267, 2014.

[7] G. Monticone and L. Miele, "Notch pathway: a journey from notching phenotypes to cancer immunotherapy," *Advances in Experimental Medicine and Biology*, vol. 1287, pp. 201–222, 2021.

[8] M. Teodorczyk and M. H. H. Schmidt, "Notching on cancer's door: notch signaling in brain tumors," *Frontiers in Oncology*, vol. 4, p. 341, 2014.

[9] F. Shojaei, F. Yazdani-Nafchi, M. Banitalebi-Dehkordi, M. Chehelgerdi, and M. Khorramian-Ghahfarokhi, "Trace of survivin in cancer," *European Journal of Cancer Prevention*, vol. 28, no. 4, pp. 365–372, 2019.

[10] M. D'Amelio, V. Cavallucci, and F. Cecconi, "Neuronal caspase-3 signaling: not only cell death," *Cell Death and Differentiation*, vol. 17, no. 7, pp. 1104–1114, 2010.

[11] D. N. Louis, H. Ohgaki, O. D. Wiestler et al., "The 2007 WHO classification of tumours of the central nervous system," *Acta Neuropathologica*, vol. 114, no. 2, pp. 97–109, 2007.

[12] H. D. Lewis, M. Leveridge, P. R. Strack et al., "Apoptosis in T cell acute lymphoblastic leukemia cells after cell cycle arrest induced by pharmacological inhibition of notch signaling," *Chemistry & Biology*, vol. 14, no. 2, pp. 209–219, 2007.

[13] J. Guo, P. Li, X. Liu, and Y. Li, "NOTCH signaling pathway and non-coding RNAs in cancer," *Pathology - Research and Practice*, vol. 215, no. 11, p. 152620, 2019.

[14] Y. Li, J. Ma, X. Qian et al., "Regulation of EMT by Notch signaling pathway in tumor progression," *Current Cancer Drug Targets*, vol. 13, no. 9, pp. 957–962, 2013.

[15] L. Wang, F. Jin, A. Qin et al., "Targeting Notch1 signaling pathway positively affects the sensitivity of osteosarcoma to cisplatin by regulating the expression and/or activity of caspase family," *Molecular Cancer*, vol. 13, no. 1, p. 139, 2014.

[16] P. Liu, Y. Man, Y. Wang, and Y. Bao, "Mechanism of BMP9 promotes growth of osteosarcoma mediated by the Notch signaling pathway," *Oncology Letters*, vol. 11, no. 2, pp. 1367–1370, 2016.

[17] Z. Yang, Y. Qi, N. Lai et al., "Notch1 signaling in melanoma cells promoted tumor-induced immunosuppression via upregulation of TGF-β1," *Journal of Experimental & Clinical Cancer Research*, vol. 37, no. 1, p. 1, 2018.

[18] S. Liu, X. Ma, Q. Ai et al., "NOTCH1 functions as an oncogene by regulating the PTEN/PI3K/AKT pathway in clear cell renal cell carcinoma," *Urologic Oncology*, vol. 31, no. 6, pp. 938–948, 2013.

[19] J. Zhou, X. Guo, W. Chen, L. Wang, and Y. Jin, "Targeting survivin sensitizes cervical cancer cells to radiation treatment," *Bioengineered*, vol. 11, no. 1, pp. 130–140, 2020.

[20] D. C. Altieri, "Targeting survivin in cancer," *Cancer Letters*, vol. 332, no. 2, pp. 225–228, 2013.

[21] R. A. Carrasco, N. B. Stamm, E. Marcusson, G. Sandusky, P. Iversen, and B. K. R. Patel, "Antisense inhibition of survivin expression as a cancer therapeutic," *Molecular Cancer Therapeutics*, vol. 10, no. 2, pp. 221–232, 2011.

[22] C. J. Miranda, L. Braun, Y. Jiang et al., "Aging brain microenvironment decreases hippocampal neurogenesis through Wnt-mediated survivin signaling," *Aging Cell*, vol. 11, no. 3, pp. 542–552, 2012.

[23] A. Lebelt, R. Rutkowski, W. Och et al., "Survivin, caspase-3 and MIB-1 expression in astrocytic tumors of various grades," *Advances in Medical Sciences*, vol. 61, no. 2, pp. 237–243, 2016.

Hindawi
Journal of Nanomaterials
Volume 2021, Article ID 8298994, 9 pages
https://doi.org/10.1155/2021/8298994

Research Article

Endoleak Detection after Endovascular Aortic Aneurysm Repair Using Ultrasound Based on Nanoscale Bubble Contrast Agents and Their Effects on Vascular Smooth Muscle Cell Proliferation and Migration

Siying Pei,[1] Yao Feng,[2] Shuqing Fang,[3] Song Jin,[4] Dongxu Fan,[4] Fanxu Song,[5] and Hanrui Wang[4]

[1]*College of Basic Medicine, Jiamusi University, China*
[2]*The First Affiliated Hospital of Jiamusi University, China*
[3]*Department of Nephrology, Jiamusi Central Hospital, China*
[4]*Department of Vascular Surgery, The First Affiliated Hospital of Jiamusi University, China*
[5]*The Third Affiliated Hospital of Jiamusi University, China*

Correspondence should be addressed to Hanrui Wang; whr496196111@163.com

Received 8 April 2021; Accepted 25 April 2021; Published 11 May 2021

Academic Editor: Songwen Tan

Abdominal aortic aneurysm (AAA) is the most common vascular disease that causes disability and death. Its morbidity is relatively subtle, and the mortality rate is high. Clinically, endovascular aortic aneurysm repair (EVAR) has gradually become the primary treatment of AAA due to its unique advantages such as low trauma and low incidence of short-term complications. However, the outcome of EVAR is greatly compromised by the possible occurrence of endoleaks. Contrast-enhanced ultrasound (CEUS) is a promising alternative technique to detect endoleaks following EVAR due to lack of exposure to ionizing radiation. Traditional ultrasound contrast agents with an overlarge size (microscale) leading to reluctant accumulation in target organs and instability trigger the requirement of nanoscale contrast agents that enter tumor tissues through the enhanced permeability and retention effect. In this study, we used ultrasound based on nanoscale bubble contrast agents to evaluate endoleak detection after endovascular aortic aneurysm repair and analyzed the effects of nanoscale bubble contrast agents on vascular smooth muscle cell (VSMC) proliferation and migration. Among 52 AAA patients a month following EVAR, there were 16 cases of endoleaks after EVAR detected by nanobubble contrast-enhanced ultrasound, including 6 cases of type I endoleak (1 case of type Ia endoleak and 5 cases of type Ib endoleak), 7 cases of type II endoleak, and 3 cases of type III endoleak; there were 12 cases of endoleak after EVAR detected by computed tomography angiography (CTA), including 6 cases of type I endoleak (1 case of type Ia and 5 cases of type Ib), 5 cases of type II endoleak, and 1 case of type III endoleak. Six months after EVAR, 3 cases of type III endoleak were detected by both nanobubble contrast-enhanced ultrasound and CTA. Vascular smooth muscle cells (VSMCs) used for *in vitro* experiments were subjected to ultrasound irradiation and platelet-derived growth factor (PDGF) treatment with or without the addition of nanobubble contrast agents. After high-intensity and long-term irradiation (0.75 W/cm^2 and 1 W/cm^2 irradiation for 120 s and 150 s, respectively) by ultrasound with or without the addition of nanobubble contrast agents, PDGF-induced VSMC migration was inhibited ($P < 0.01$). Low-intensity and short-term ultrasound irradiation did not differ PDGF-induced VSMC migration ($P > 0.05$), but 0.5 W/cm^2 and 90 s ultrasound irradiation could significantly inhibit PDGF-induced VSMC migration without the addition of nanobubble contrast agents ($P < 0.05$). When VSMCs were irradiated at 1, 0.75, 0.5, and 0.35 W/cm^2 for 30 s to 150 s, ultrasound irradiation with or without the addition of nanobubble contrast agents remarkably reduced PDGF-induced VSMC proliferation, as evidenced by reduced OD values ($P < 0.05$). In conclusion, ultrasound based on nanoscale bubble contrast agents is an effective alternative detection method for the occurrence of AAA patients who are not suitable for CTA.

1. Introduction

Abdominal aortic aneurysm (AAA) is a disease with a serious increase in morbidity year by year. The main risk is rupture, and the total mortality of ruptured tumor is 80% to 90% [1]. Endovascular aortic aneurysm repair (EVAR) has become the main method for clinical treatment of diseases such as abdominal aortic aneurysm and abdominal aortic dissection [2]. Compared with open surgery, perioperative morbidity, mortality, and average length of stay of EVAR patients have obvious advantages [3]. However, with the passage of time, due to factors such as the reintervention rate of EVAR and the need for lifelong monitoring, the advantages of EVAR are becoming increasingly unclear. One of the factors that seriously affect the reintervention rate is the occurrence of endoleaks. At the same time, the presence of an endoleak increases the risk of tumor growth and rupture after EVAR [4]. Therefore, in the intracavitary treatment of EVAR, it is very important for the prognosis of patients to find the endoleak and solve the endoleak accordingly [5].

Contrast-enhanced ultrasound (CEUS) has been used more and more in the follow-up of EVAR in recent years. It is a new type of noninvasive imaging technology. It is based on conventional ultrasound examination and is injected by intravenous ultrasound [6]. Agents are used to enhance the human body's blood flow scattering signal, thereby merging the resolution, sensitivity, and specificity of a high ultrasound diagnosis. The ultrasound contrast agent can be kept in the blood pool of the human body for a certain period, thereby enhancing the visualization effect of blood vessels and real-time observation of blood flow perfusion in the lesion area. With the development of nanotechnology and molecular biology, nanotype contrast agents, due to their outstanding characteristics of small molecules and strong penetrating power, will strongly promote the expansion of ultrasound molecular imaging to the extravascular field.

This study is based on the advantages of noninvasive, nonradiative, easy to operate, and good repeatability of nanobubble contrast agents, which can actively gather in the tumor tissue, enhance tumor tissue visualization, improve the sensitivity and accuracy of tumor detection, and achieve extravascular detection of lesions and ultrasound molecular imaging, compared with the examination results of ultrasound nanobubbles in endoleaks after intraluminal repair of patients with AAAs, showing that the ultrasonic imaging of nanobubbles that detected complications after intraluminal repair of AAAs has a good positive rate, and further analysis of the effects of nanobubble ultrasound contrast agents in the proliferation and migration of vascular smooth muscle cells can provide a reliable diagnosis basis for the clinic and has extremely high clinical application value.

2. Materials and Methods

2.1. Nanobubble Contrast Agents. The preparation of nanobubbles is mainly to prepare the mixed contrast agent of microbubbles and nanobubbles by the film hydration method and then separate the pure nanobubbles by centrifugation, static, or filter methods or to add surfactants in the production process; in addition to increasing the operation process, it will also increase the potential possibility of sample pollution and reduce the production of nanobubbles, and by adjusting the dosage and preparation conditions of the liposome, we can make a suitable liposome film, which can directly prepare pure nanobubbles, and test the indicators of nanobubbles [7]. Figure 1 shows the preparation of nanovesicles and their state in blood vessels.

AAA is divided into a true one and a pseudo one according to the composition structure of the aneurysm [8]. True AAA is the permanent limited expansion of the abdominal aorta, the blood vessel wall is intact, the blood is still in the vascular lumen, and the wall of the true AAA has a three-layer structure of arterial walls. Pseudo-AAA can be regarded as an injury to the wall of the arterial tube, causing blood to flow from the lumen of the artery to the outside, and a tumor-like structure is formed by wrapping the external tissue [9]. The wall of the pseudo-AAA is compressed by the surrounding organization structure. In clinical work, the most common causes are atherosclerosis and degenerative changes. These two causes may exist at the same time, or they may exist separately [10, 11].

As shown in Figure 2, when the diameter of a solid tumor grows to about 2 mm, angiogenic factors are released to induce angiogenesis, the micro vessels formed by the tumor tissue are irregularly shaped and swollen, the endothelial cells are loosely arranged, and a gap of 380-780 nm can be formed between the endothelial cells [12]. The return of the lymphatic system is missing [13]. These vascular characteristics promote the high permeability and retention effect of lipid particles in the tumor tissue, which is what we call the EPR effect [14, 15]. It is generally believed that ultrasound contrast agents with a diameter of less than 7 nm can pass through the gap of the inner wall of the tumor blood vessel and enter the surrounding tumor tissue.

2.2. Contrast Process of Nanobubble Agent. The process of imaging tumor tissue with a nanobubble ultrasound contrast agent is shown in Figure 3. Compared with other types of nanoscale ultrasound contrast agents, the core of the nanobubble ultrasound contrast agent is a gas, which has a stronger backscattering ability in the ultrasonic sound field, and due to the compressibility of the gas, the nanobubbles will have a diameter. It has a nonlinear acoustic characteristic, so that it can better develop the target tissue, and it can use the nanobubble-sensitive ultrasound contrast imaging technology with its nonlinear acoustic characteristic [16, 17]. In addition, the nanobubble ultrasound contrast agent has the unique characteristics of many surface-active centers, high surface reactivity, long half-life in vivo, strong adsorption capacity, and not being degraded by various enzymes in the body and cells. Research applications in imaging and therapeutics have broad prospects [18].

Studies have shown that when different examination methods are used for patients with AAAs, different degrees of atherosclerosis and calcification can be seen on the walls of AAAs, indicating that there is also atherosclerosis in patients with AAAs and degenerative changes [19, 20]. Animal experiments have confirmed that long-term feeding of

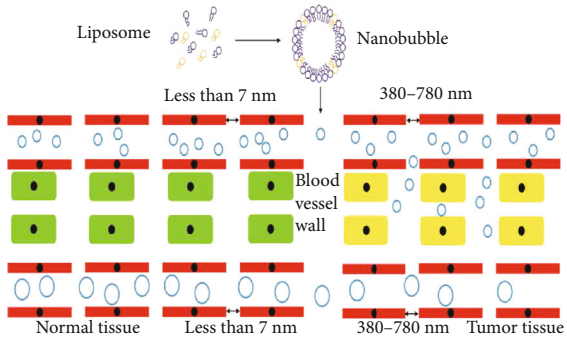

FIGURE 1: Preparation of nanobubbles and their states in blood vessels.

an arteriosclerosis diet to primates can easily form aneurysms, proving that atherosclerosis plays an important role in the formation of AAAs [21]. Some scholars believe that degenerative changes have a greater effect, because in AAA specimens, metalloproteinases are overexpressed, which is an elastase, which can degrade elastic fibers in the arterial wall, resulting in compliance of the arterial wall and the decrease in the formation of aneurysms; in addition, increased metalloproteinase inhibitors and low expression of antiproteolytic enzymes also indirectly confirm the role of degenerative degeneration in the formation of AAAs [19, 22].

2.3. Patients. From June 2018 to June 2019, a total of 52 patients, including 39 males and 13 females, aged 56-85 years, and with an average age of 68.5 ± 6.72 years, were diagnosed with AAA and underwent EVAR in our hospital. The abdominal aorta had various degrees of atherosclerosis and multiple spot block formations. All patients underwent computed tomography angiography (CTA) and ultrasound examination at the first month and the sixth month after surgery to determine whether there was an endoleak. If there was an endoleak, the location and the type of the endoleak were determined by CTA and nanobubble ultrasound contrast examination.

2.4. Inclusion Criteria. Using the Chinese vascular surgery guidelines, the local expansion of the artery is more than 50% of the outer diameter of the normal artery. AAA is generally defined as the outer diameter of the abdominal aorta that exceeds 3 cm. This numerical standard is calculated based on the average value of the normal population, but there are also studies that show that the outer diameter of the abdominal aorta is positively correlated with age, sex, body surface area, etc.; the normal outer diameter of the abdominal aorta will vary greatly according to gender, age, and body surface area, so the outer diameter of the abdominal aorta that exceeds 3 cm which is defined as an active abdominal aneurysm is not very rigorous; so in clinical work, AAA usually refers to the outer diameter of the artery that exceeds 50% of the outer diameter of the adjacent normal artery. In this study, the outer diameter of the AAA was measured and compared with the outer diameter of the neighboring normal artery, when more than 50% were included in the study.

2.5. Ultrasound Contrast Examination. The patient was fasted and placed in a supine position. Firstly, the position, size, range, and thrombus of the AAA were observed by two-dimensional grayscale ultrasound and whether there was any change compared with that before surgery. Secondly, the position and presence of the stent graft were observed, the blood flow in the stent graft was observed by color Doppler technology, the abnormal blood flow in and around the stent graft was monitored in real time, and finally, the spectrum Doppler technology was used to analyze the hemodynamic of the abnormal site to determine whether there is an endoleak; if an abnormal blood flow signal appears in the external tumor cavity of the stent graft, it is judged as positive for an endoleak [23, 24]. For patients with endoleaks, rough classification is based on the location of the endoleak and related blood flow. The classification of an endoleak was defined as previously reported by White et al. [25]. The surgical society agrees that when the data is collated, it will be classified according to the more stringent and standardized ultrasound-typing guidelines. Each patient is examined by two senior physicians or deputy chief physicians, and the analysis results are summarized and analyzed. For the two doctors who have different examination results, the chief physician conducts a third examination combined with the first two physicians checking the results and gives the final diagnosis.

2.6. Cell Treatment. Human aortic VSMCs (Shanghai Cell Bank, Chinese Academy of Sciences, Shanghai, China) was maintained in DMEM with 10% fetal bovine serum (FBS, Gibco, USA), 100 μg/ml streptomycin, and 100 IU/ml penicillin in a humidified environment in the presence of 5% CO_2. VSMCs used for *in vitro* experiments were subjected to ultrasound irradiation and platelet-derived growth factor (PDGF) treatment with or without addition of nanobubble contrast agents. In brief, VSMCs were placed onto a 6-well culture plate and serum-starved for 48 h. The culture plate was placed in a 37°C water bath, and 10 ng/ml PDGF (Gibco, USA) was added to the culture solution [26]. Following 24 h of culture, ultrasound irradiation was performed. The ultrasound probe was fixed at a distance of 3 mm from the bottom of the culture plate, with a frequency of 1 MHz and indicated irradiation times (0 s, 30 s, 60 s, 90 s, 120 s, and 150 s) under the intensity of 0.35 W/cm^2, 0.5 W/cm^2, 0.75 W/cm^2, and 1.0 W/cm^2. As for addition of nanobubble contrast agents, the culture medium with the addition of PDGF addition was added again with 1 μl/m nanobubble contrast agents and incubated for 24 h, followed by parallel ultrasonic irradiation.

2.7. MTT Assay. VSMC proliferation was determined using an MTT assay. In brief, 24 h after ultrasonic irradiation, VSMCs (2×10^3 cells/well) were plated into 96-well plates. The optical density (OD) of each well was measured at 450 nm using a plate reader (Thermo Scientific, Watertown, USA).

2.8. Transwell Migration Assay. VSMC migration was assessed using a transwell (8 μm pore size), and 24 h after ultrasonic irradiation, 5×10^4 cells were plated into each well of the upper chamber uncoated with the membrane. The lower chamber was added with the medium containing 10%

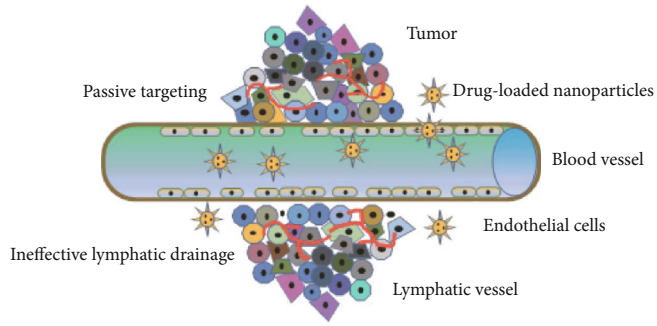

Figure 2: Drug-loaded nanoparticles diffuse to the tumor site through the enhanced permeability and retention effect.

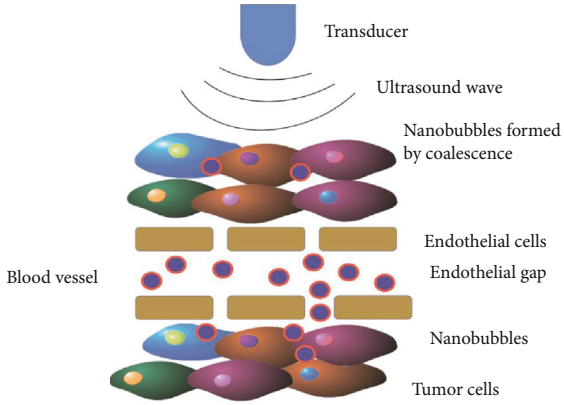

Figure 3: The contrast process of tumor tissues by ultrasound using nanobubble contrast agents.

FBS. After cells were incubated for 24 hours, those that migrated from the upper chamber into the lower chamber were fixed with methanol and stained with 0.1% crystal violet dye. A microscopic view was captured under an IX71 inverted microscope (OLYMPUS, Olympus Corporation, Tokyo, Japan).

2.9. Statistical Methods. SPSS 26.0 international standard statistical software was used for statistical data analysis, the variable was evaluated as positive for endoleak, and the positive rate of endoleak detected by the two inspection methods was calculated. The McNemar test was used to compare the detection frequency of the two inspection parties. When $P < 0.05$, the difference was statistically significant. By calculating the k value and comparing the consistency of ultrasound, according to the Landis and Koch guidelines, the k value represents different consistency in different intervals. When the k value is 0.21-0.40, it means that the consistency is poor; when the k value is 0.41-0.60, it means moderate consistency; when the k value is 0.61-0.80, it means better consistency; and when the k value is 0.81-1.0, it means excellent consistency.

3. Results

3.1. Endoleak Detection a Month and Six Months after EVAR Using Nanobubble Contrast-Enhanced Ultrasound. Among 52 AAA patients, there were 16 cases of endoleak after EVAR detected by nanobubble contrast-enhanced ultrasound, including 6 cases of type I endoleak (1 case of type Ia endoleak and 5 cases of type Ib endoleak), 7 cases of type II endoleak, and 3 cases of type III endoleak. The detection rate was 30.76%. There were 12 cases of endoleak after EVAR was detected by CTA, including 6 cases of type I endoleak (1 case of type Ia and 5 cases of type Ib), 5 cases of type II endoleak, and 1 case of type III endoleak. The detection rate was 23.08%. A total of 11 cases of endoleak were detected by both nanobubble contrast-enhanced ultrasound and CTA, and the classification of the endoleak was the same. However, 1 case of type Ib endoleak, 3 cases of type II endoleak, and 1 case of type III endoleak were detected by nanobubble contrast-enhanced ultrasound, which were not evident by CTA (Table 1). As for the classification of the endoleak, 11.5% were type I endoleak (1.9% of type Ia endoleak and 9.6% of type Ib endoleak), 13.46% of type II endoleak, and 5.77% of type III endoleak were detected by nanobubble contrast-enhanced ultrasound. The CTA detected 26.92% of the patients with endoleak of which type I endoleak accounted for 13.46% including 3.84% type Ia and 9.6% type Ib endoleak, type II endoleak accounted for 9.6%, and type III endoleak accounted for 3.84% (Table 2). Six months after EVAR, there were 3 cases of type III endoleak that were detected by both nanobubble contrast-enhanced ultrasound and CTA (Table 3). The CTA examination results are the same as the ultrasound examination results.

Table 1: Endoleak detection a month after EVAR using nanobubble contrast-enhanced ultrasound.

Nanobubble contrast-enhanced ultrasound	CTA		Total
	Positive	Negative	
Positive	11	5	16
Negative	3	33	36
Total	14	38	52

3.2. Effect of Nanobubble Contrast Agents on PDGF-Induced VSMC Migration. After high-intensity and long-term irradiation (0.75 W/cm^2 and 1 W/cm^2 irradiation for 120 s and 150 s, respectively) by ultrasound with or without the addition of nanobubble contrast agents, PDGF-induced VSMC migration was inhibited ($P < 0.01$). Low-intensity and short-term ultrasound irradiation did not differ PDGF-induced VSMC migration ($P > 0.05$), but 0.5 W/cm^2 and 90 s ultrasound irradiation could significantly inhibit

Table 2: Endoleak detection according to classifications a month after EVAR using nanobubble contrast-enhanced ultrasound.

Result	Type I		Type II	Type III	Type IV	Total
	Ia	Ib				
Nanobubble contrast-enhanced ultrasound	1.9%	9.6%	13.46%	5.77%	0	30.76%
CTA	3.84%	9.6%	9.6%	3.84%	0	26.92%

Table 3: Endoleak detection according to classifications six months after EVAR using nanobubble contrast-enhanced ultrasound.

Time	Type I		Type II		Type III	
	Ultrasound	CTA	Ultrasound	CTA	Ultrasound	CTA
One month	6	6	7	5	3	1
Six months	0	0	3	3	0	0

PDGF-induced VSMC migration without the addition of nanobubble contrast agents ($P < 0.05$). All in all, the inhibition of PDGF-induced VSMC migration was the greatest for 1 W/cm^2 ultrasound irradiation for 150 s in the presence of nanobubble contrast agents ($P < 0.01$, Figures 4 and 5). Figure 6 presents the numbers of migrating VSMC by ultrasound irradiation at 1, 0.75, 0.5, and 0.35 W/cm^2 for 30 s to 150 s with or without the addition of nanobubble contrast agents.

3.3. Effect of Nanobubble Contrast Agents on PDGF-Induced VSMC Proliferation. When VSMCs were irradiated at 1, 0.75, 0.5, and 0.35 W/cm^2 for 30 s to 150 s, ultrasound irradiation with or without the addition of nanobubble contrast agents remarkably reduced PDGF-induced VSMC proliferation, as evidenced by reduced OD values ($P < 0.05$, Tables 4–7). When VSMCs were irradiated at 1 W/cm^2 for 90 s and 150 s, nanobubble contrast agents remarkably enhanced PDGF-induced VSMC proliferation ($P < 0.05$). When VSMCs were irradiated at 1 W/cm^2 for 30 s, 60 s, and 120 s, nanobubble contrast agents remarkably reduced PDGF-induced VSMC proliferation ($P < 0.01$). When VSMCs were irradiated at 0.75 W/cm^2, 60 s of ultrasound irradiation led to the smallest inhibitory effect on PDGF-induced VSMC proliferation ($P < 0.05$), and 90 s of ultrasound irradiation with the addition of nanobubble contrast agents led to the smallest inhibitory effect on PDGF-induced VSMC proliferation ($P < 0.05$).

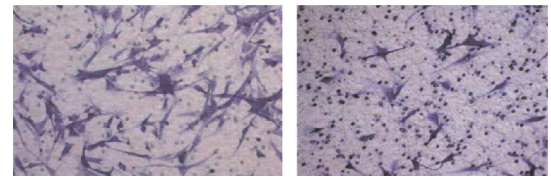

Figure 4: Representative views of VSMCs migrating from the uncoated upper chamber into the lower one before and after ultrasound irradiation.

4. Discussion

In this study, among 52 cases of AAA, 39 were male and 13 were female and the average age was 68.1 ± 6.68 years. In the examination of whether there is an endoleak after endovascular repair of AAA, ultrasound also found that the 52 patients had different degrees of atherosclerosis and multiple plaque formations; most of the plaques were mixed echo and strong echo plaques; strong echo plaques and mixed echo plaques showed that the abdominal aorta had different degrees of degeneration, which was the same as the previous research results. In this study, 42 patients with AAA underwent intracavitary repair. There was no significant difference in the detection rate of the endoleak after intracavitary repair of AAA between the two methods. The k value of the two inspection methods ($k = 0.703$) is calculated, and it is found that the two inspection methods are highly consistent, the classification of the endoleak is generally based on the location of the extravasation of the contrast agent, but there is lack of information such as the direction of internal blood flow [27, 28]. Different doctors may have different classifications of endoleaks. However, with the help of color Doppler technology, ultrasound can provide more blood flow information, and the classification of endoleaks is based on the relationship between blood flow signal, stent graft, and peripheral blood vessels, and especially for the type II endoleak, it can be traced back according to the branch pipe of the backflow. Although most type II endoleaks do not need to be treated, they still need to be treated when the blood perfusion volume is large and the AAA gradually becomes large. At this time, the artery traced by ultrasound will provide reliable reference for the treatment of coil embolism in the clinical bed. But ultrasound is easy to be interfered by tissue movement to produce false images. Currently, it is necessary for patients to hold their breath. In addition, ultrasound is not satisfied with deep and low velocity blood flow and depends on the technology and experience of the examiner. Although ultrasound has the above limitations, they do not affect that it becomes a reliable method for the follow-up of endoleaks after endovascular repair of AAA.

In the study, we found that the frequency of VSMCs was 1 MHz; the sound intensity was 0.35 W/cm^2, 0.50 W/cm^2, 0.75 W/cm^2, and 1 W/cm^2; and the time was 20 s, 30 s, 60 s, 90 s, 120 s, and 150 s, after continuous ultrasound irradiation, whether or not micro irradiation was combined. In this study, the number of vascular smooth muscle cell migration increased significantly. It can cause significant migration of

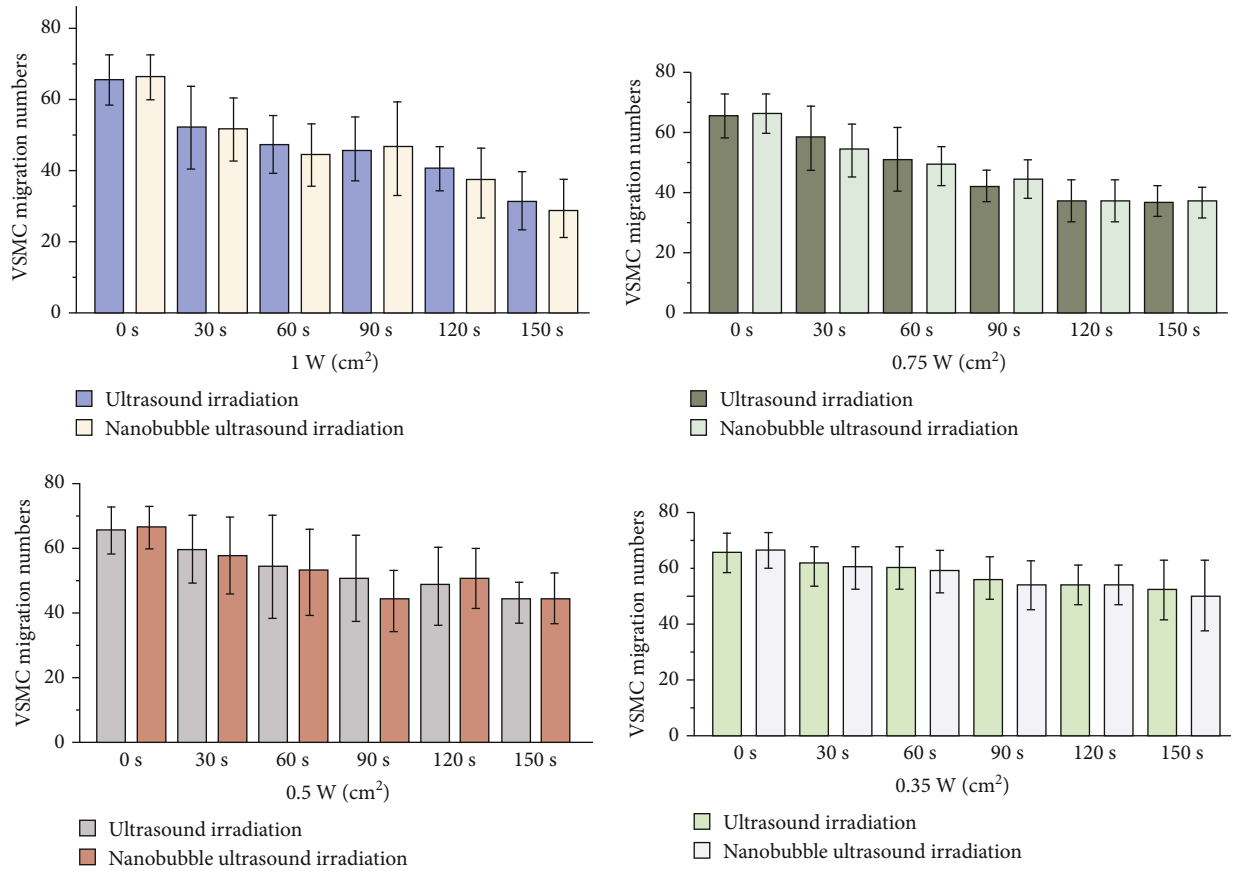

Figure 5: The numbers of PDGF-induced VSMCs under the ultrasound irradiation of 1, 0.75, 0.5, and 0.35 W/cm^2 for 30 s to 150 s with or without the addition of nanobubble contrast agents.

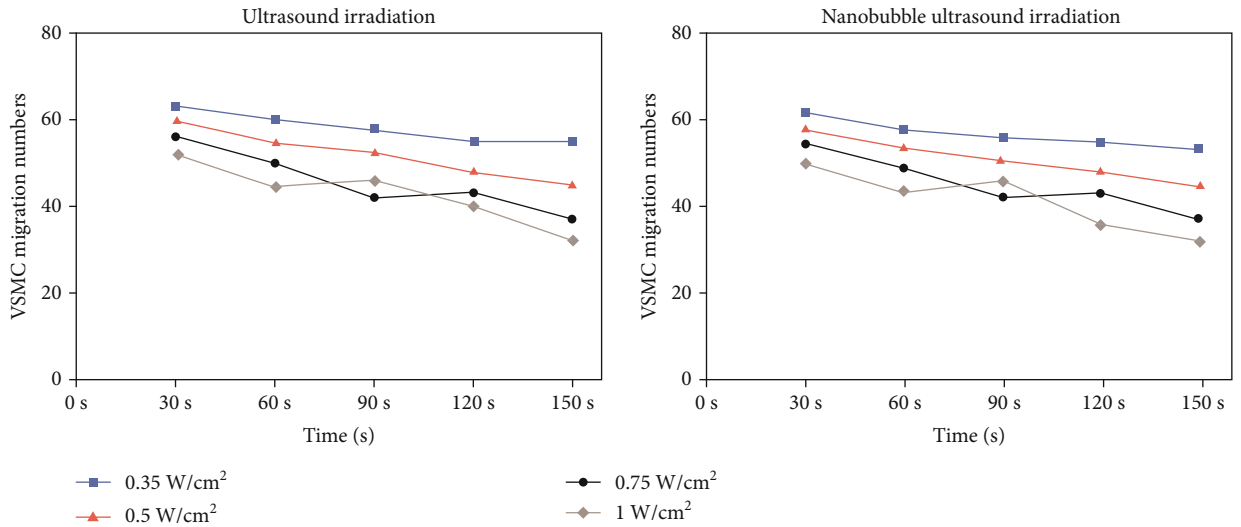

Figure 6: The numbers of migrating VSMC by ultrasound irradiation at 1, 0.75, 0.5, and 0.35 W/cm^2 for 30 s to 150 s with or without addition of nanobubble contrast agents.

VSMCs. Whether or not nanobubble contrast agents were added, PDGF-induced VSMC migration was significantly reduced after high-intensity and long-term ultrasound irradiation, which proves that ultrasound irradiation with a certain intensity and irradiation time or ultrasound irradiation based on nanobubble contrast agents can inhibit the migration of VSMCs in a certain dose.

The biological behavior of VSMCs, such as proliferation and migration, is a dynamic process, which is regulated by many factors including the signal transduction pathway,

Table 4: The OD value of VSMCs under the ultrasound irradiation of 1 W/cm^2 with or without the addition of nanobubble contrast agents.

Time (s)	0	30	60	90	120	150
Ultrasound irradiation group	0.886 ± 0.004	0.697 ± 0.005	0.686 ± 0.006	0.662 ± 0.005	0.687 ± 0.015	0.645 ± 0.006
Nanobubble ultrasound irradiation group	0.886 ± 0.004	0.685 ± 0.010	0.663 ± 0.003	0.697 ± 0.008	0.665 ± 0.005	0.673 ± 0.010

Table 5: The OD value of VSMCs under the ultrasound irradiation of 0.75 W/cm^2 with or without the addition of nanobubble contrast agents.

Time (s)	0	30	60	90	120	150
Ultrasound irradiation group	0.776 ± 0.004	0.674 ± 0.007	0.692 ± 0.008	0.670 ± 0.006	0.660 ± 0.007	0.663 ± 0.007
Nanobubble ultrasound irradiation group	0.776 ± 0.004	0.678 ± 0.006	0.674 ± 0.003	0.682 ± 0.004	0.662 ± 0.009	0.667 ± 0.005

Table 6: The OD value of VSMCs under the ultrasound irradiation of 0.5 W/cm^2 with or without the addition of nanobubble contrast agents.

Time (s)	0	30	60	90	120	150
Ultrasound irradiation group	0.775 ± 0.006	0.692 ± 0.003	0.684 ± 0.006	0.678 ± 0.006	0.686 ± 0.008	0.678 ± 0.006
Nanobubble ultrasound irradiation group	0.775 ± 0.006	0.686 ± 0.002	0.682 ± 0.005	0.683 ± 0.007	0.682 ± 0.005	0.675 ± 0.004

Table 7: The OD value of VSMCs under the ultrasound irradiation of 0.35 W/cm^2 with or without the addition of nanobubble contrast agents.

Time (s)	0	30	60	90	120	150
Ultrasound irradiation group	0.769 ± 0.006	0.682 ± 0.004	0.688 ± 0.007	0.681 ± 0.007	0.678 ± 0.007	0.683 ± 0.005
Nanobubble ultrasound irradiation group	0.769 ± 0.006	0.695 ± 0.003	0.686 ± 0.008	0.692 ± 0.005	0.685 ± 0.006	0.692 ± 0.007

cytokines, growth factors, vasoactive substances, and extracellular matrix. In this study, the number of VSMC migration increased significantly after the stimulation of PDGF, which indicated that the dose of PDGF in this study could cause VSMC proliferation and migration significantly [29]. Whether an ultrasound contrast agent is added or not, the proliferation and migration of VSMCs are significantly reduced, which prove that ultrasound with a certain intensity and irradiation time can inhibit the proliferation and migration of VSMCs at a certain dose. More importantly, we found that the number of VSMCs in the process of proliferation and migration was gradually reduced with the extension of irradiation time, reaching the lowest point when the sound intensity reached 1 W/cm^2 and the time reached 150 s. First, under the premise of not causing irreversible damage to cells, 1 W/cm^2 and 150 s are the most obvious conditions for the inhibition of vascular smooth muscle cell migration. Second, such results are caused by the limited sound intensity and time point we selected [30]. If we choose a higher or lower sound intensity and a longer or shorter time, we may find more obvious inhibition, and this is also the limitation of our research. Further research can be carried out through experiments in the future. Similarly, there is a similar situation about the value of VSMCs after ultrasonic treatment with certain intensity and irradiation time. At the same time, in the comparison between the irradiation group and the combination group, we found that the migration number of VSMCs in the irradiation group was lower than that in the ultrasound irradiation group at the same time and sound intensity. We think that this is because the ultrasound contrast agent, as a kind of artificial cavitation nucleus, increased the concentration of the cavitation nucleus in the body and reduced the ultrasound cavitation; the threshold value enhances the cavitation effect and reduces the threshold value of ultrasonic energy needed to produce the cavitation effect [31, 32]. For the proliferation of VSMCs, in the comparison between the irradiation group and the irradiation group, under the same time and sound intensity, the value of VSMCs in the irradiation group was higher than that in the ultrasound irradiation group, which may be due to the fact that the density of ultrasound nanovesicles as an artificial cavitation nucleus was not enough to reduce the ultrasound cavitation threshold, which can enhance the cavitation effect but cannot reduce the threshold value of the ultrasound energy needed to produce cavitation effect, so the effect of migration inhibition is not as good as that of the microbubble contrast agent.

In this paper, we studied the enhancement of the acoustic intensity and the sensitivity of the detection of the endoleak caused by the nanobubble ultrasound contrast agent. The nanobubble ultrasound contrast agent can scan the blood flow inside the stent graft and the aneurysm cavity from multiple angles and in real time. It is also more sensitive to the capture of some low-speed blood flow signals. The detection effect of the nanobubble ultrasound contrast agent on the endoleak is higher than that of the conventional ultrasound

effect of CTA and is the same. In the occult endoleak, the detection effect of the endoleak is even higher than that of CTA, and the cost of contrast-enhanced ultrasound is lower, there is no radiation, and the contrast-enhanced ultrasound is metabolized by the lung. Therefore, a more effective examination method is provided for the patients who are not suitable for CTA visit. Due to the lack of large sample data accumulation and analysis, it is believed that through the continuous accumulation and research, nanobubble ultrasound has a broader application prospect in the follow-up of AAA after intracavitary repair.

Data Availability

The data used to support the findings of this study are included within the article.

Ethical Approval

All data, models, and code generated or used during the study appear in the submittal complying with the Ethics of Experimentation Statement. The study follows the principles of the Declaration of Helsinki.

Disclosure

Siying Pei and Yao Feng should be considered as co-first authors.

Conflicts of Interest

No potential conflict of interest was reported by the authors.

Authors' Contributions

Siying Pei and Yao Feng contributed equally to this work.

Acknowledgments

Scientific research business fee project of Heilongjiang Provincial Education Department (Grant: 2016-KYYWF-0586, 2018-KYYWF-0967).

References

[1] N. Sakalihasan, R. Limet, and O. D. Defawe, "Abdominal aortic aneurysm," *Lancet*, vol. 365, no. 9470, pp. 1577–1589, 2005.

[2] A. Calero and K. A. Illig, "Overview of aortic aneurysm management in the endovascular era," *Seminars in Vascular Surgery*, vol. 29, no. 1-2, pp. 3–17, 2016.

[3] A. Patel, R. Edwards, and S. Chandramana, "Surveillance of patient's post-endovascular abdominal aortic aneurysm repair (EVAR), a web-based survey of practice in the UK," *Clinical Radiology*, vol. 68, no. 6, pp. 580–587, 2016.

[4] A. A. Contador, D. E. D. Siqueira, O. B. Jacobsen et al., "Duplex ultrasound, and computed tomography angiography in the follow-up of endovascular abdominal aortic aneurysm repair: a comparative study," *Radiologic Brasilia*, vol. 49, no. 4, pp. 229–233, 2016.

[5] M. Serac, I. Marfanoid, A. Tombic, S. Sarac, and M. Bezmarević, "Endovascular repair of ruptured abdominal aortic aneurysm," *Vojnosanitetski Pregel*, vol. 71, no. 1, pp. 78–82, 2016.

[6] D. A. Vessel, I. S. Shacking, K. V. Bacalao et al., "On the problem of internal optical loss and current leakage in laser heterostructures based on AlGaInAs/InP solid solutions," *Semiconductors*, vol. 50, no. 9, pp. 1225–1230, 2016.

[7] J. DuPont, A. McCurley, and S. Bende, "Mechanism of aging-associated hypertension: role of smooth muscle cell mineralocorticoid receptor regulation of vascular L-type calcium channels," *Journal of Beijing Polytechnic University*, vol. 31, no. 31, pp. 399–404, 2016.

[8] C. E. Wells, N. D. Pugh, and J. P. Woodcock, "Abdominal aortic aneurysm detection by common femoral artery Doppler ultrasound waveform analysis," *Journal of Medical Engineering & Technology*, vol. 35, no. 1, pp. 34–39, 2016.

[9] M. Serac, I. Marfanoid, A. Tombic, S. Sarac, and M. Bezmarević, "Endovascular repair of ruptured abdominal aortic aneurysm," *Vojnosanitetski Pregled*, vol. 71, no. 1, pp. 78–82, 2014.

[10] X. L. Li, Q. F. Deng, X. Zhang et al., "The design and implementation of decompression sickness bubble detection system based on dynamic ultrasound images," *Journal of Medical Imaging and Health Informatics*, vol. 8, no. 5, pp. 900–906, 2016.

[11] S. Fukuda, H. Watanabe, K. Isaura et al., "Multicentre investigations of the prevalence of abdominal aortic aneurysm in elderly Japanese patients with hypertension," *Circulation Journal*, vol. 79, no. 3, pp. 524–529, 2016.

[12] M. Mell, T. Garg, and L. C. Baker, "Under-utilization of routine ultrasound surveillance after endovascular aortic aneurysm repair," *Annals of Vascular Surgery*, vol. 34, no. 6, pp. 24-25, 2017.

[13] M. Kuribayashi, "Vascular calcification pathological mechanism and clinical application: role of vascular smooth muscle cells in vascular calcification," *Clinical Calcium*, vol. 25, no. 5, pp. 661–669, 2016.

[14] T. L. Chen, H. J. Mao, and C. Chen, "The role and mechanism of alpha-klotho in the calcification of rat aortic vascular smooth muscle cells," *BioMed Research International*, vol. 16, no. 7, 197 pages, 2016.

[15] X. D. Chang, B. H. Zhang, L. H. Li, and Z. C. Feng, "T3 inhibits the calcification of vascular smooth muscle cells and the potential mechanism," *American Journal of Translational Research*, vol. 8, no. 11, pp. 4694–4704, 2016.

[16] Y. R. Jiang, J. Yang, X. W. Liu, Y. Li, and Q. T. Zeng, "Effects and related mechanism of quercetin on thrombin-induced proliferation and migration of rat vascular smooth muscle cells," *Chinese Journal of Cardiovascular Diseases*, vol. 44, no. 8, pp. 696–699, 2016.

[17] Y. Wang, H. X. Zhou, and L. Wang, "Changes of calcium mobilization and calcium-sensitization mechanism in vascular smooth muscle cells in hypertension," *Chinese Pharmacological Bulletin*, vol. 30, no. 2, pp. 287–291, 2016.

[18] J. A. Leopold, "Vascular calcification: mechanisms of vascular smooth muscle cell calcification," *Trends in Cardiovascular Medicine*, vol. 25, no. 4, pp. 267–274, 2016.

[19] Y. H. Kim, J. H. Han, E. J. Yun et al., "Inhibitory effect of a novel naphthoquinone derivative on proliferation of vascular smooth muscle cells through suppression of platelet-derived growth factor receptor β tyrosine kinase," *European Journal of Pharmacology*, vol. 733, pp. 81–89, 2014.

[20] B. Tang, X. S. Dong, Z. Wei, H. Q. Qiao, H. C. J. B. Liu, and X. Y. Sun, "Enhanced autophagy by enviroximes contributes to the antiaesthetic mechanisms in vascular smooth muscle cells," *Journal of Vascular Research*, vol. 51, no. 4, pp. 259–268, 2016.

[21] F. Malgorzata and C. M. Shanahan, "ER stress regulates alkaline phosphatase gene expression in vascular smooth muscle cells via an ATF4-dependent mechanism," *Bic Research Notes*, vol. 11, no. 1, pp. 483–485, 2016.

[22] H. D. Liu, W. Xiong, Q. Y. Liu et al., "Role of CMKLR1 on mouse vascular smooth muscle cells proliferation and related mechanism," *Chinese Journal of Cardiovascular Diseases*, vol. 44, no. 7, pp. 605–609, 2016.

[23] M. F. Shih, K. H. Pan, and J. Y. Cherng, "Possible mechanisms of di(2-ethylhexyl) phthalate-induced MMP-2 and MMP-9 expression in A7r5 rat vascular smooth muscle cells," *International Journal of Molecular Sciences*, vol. 16, no. 12, pp. 28800–28811, 2016.

[24] R. Sudor, F. Sato, T. Akech, and H. Wachi, "7-Ketocholesterol-induced lysosomal dysfunction exacerbates vascular smooth muscle cell calcification via oxidative stress," *Genes to Cells*, vol. 20, no. 12, pp. 982–991, 2016.

[25] G. H. White, J. May, R. C. Waugh, X. Chaufour, and W. Yu, "Type III and type IV endoleak: toward a complete definition of blood flow in the sac after endoluminal AAA repair," *The European Journal of Vascular and Endovascular Surgery*, vol. 5, no. 4, pp. 305–309, 1998.

[26] I. C. Lo, T. M. Lin, L. H. Chou et al., "Ets-1 mediates platelet-derived growth factor-BB-induced thrombomodulin expression in human vascular smooth muscle cells," *Cardiovascular Research*, vol. 81, no. 4, pp. 771–779, 2009.

[27] U. A. Kaysi, M. Basra, G. K. Ozlem et al., "Long-acting progestin-only contraceptives impair endometrial vasculature by inhibiting uterine vascular smooth muscle cell survival," *Proceedings of the National Academy of Sciences of the United States of America*, vol. 112, no. 16, pp. 5153–5158, 2016.

[28] A. Frismantiene, M. Philippova, P. Erne, and T. J. Resink, "Smooth muscle cell-driven vascular diseases and molecular mechanisms of VSMC plasticity," *Cellular Signalling*, vol. 52, pp. 48–64, 2016.

[29] D. M. Liu, W. Cui, B. Liu et al., "Atorvastatin protects vascular smooth muscle cells from TGF-β1-stimulated calcification by inducing autophagy via suppression of the β-catenin pathway," *Cellular Physiology and Biochemistry*, vol. 33, no. 1, pp. 129–132, 2016.

[30] J. B. Koenig and I. Z. Jaffe, "Direct role for smooth muscle cell mineralocorticoid receptors in vascular remodelling: novel mechanisms and clinical implications," *Current Hypertension Reports*, vol. 16, no. 5, pp. 427–425, 2016.

[31] A. M. Thompson, K. A. Martin, and E. M. Rzucidlo, "Resveratrol induces vascular smooth muscle cell differentiation through stimulation of SirT1 and AMPK," *PLoS One*, vol. 9, no. 1, pp. 495–498, 2016.

[32] H. M. Liu, X. M. Li, F. Qin, and K. X. Huang, "Selenium suppresses oxidative-stress-enhanced vascular smooth muscle cell calcification by inhibiting the activation of the PI3K/AKT and ERK signalling pathways and endoplasmic reticulum stress," *Journal of Biological Inorganic Chemistry*, vol. 19, no. 3, pp. 375–388, 2016.

Hindawi
Journal of Nanomaterials
Volume 2021, Article ID 9918847, 6 pages
https://doi.org/10.1155/2021/9918847

Research Article

Fabrication of Agglomerated Lactose Using Fluidized Bed for Good Compressibility

Bo Wang,[1] Huijie Li,[1] Jia Xiang,[1] Jiao Zheng,[2] and Junyan Wang[3]

[1]*Xiangya School of Pharmaceutical Sciences, Central South University, Changsha, Hunan 410000, China*
[2]*Drug Clinical Trial Institution Department, Hunan Provincial People's Hospital (The First Affiliated Hospital of Hunan Normal University), Changsha, Hunan 410000, China*
[3]*Faculty of Engineering, Monash University, Melbourne 3800, Australia*

Correspondence should be addressed to Jiao Zheng; zhengjiao51@163.com and Junyan Wang; junyan.wang@monash.edu

Received 6 March 2021; Revised 12 March 2021; Accepted 10 April 2021; Published 6 May 2021

Academic Editor: Tingting Hong

In this work, a fluidized bed agglomeration process was used to produce agglomerated lactose with good compressibility. In the fluidized bed agglomeration, large lactose crystals were used as the core materials, fine-milled lactose particles were bound to the surface of large lactose cores, and lactose solution was used as the binder. A suspension of lactose solution is sprayed onto the fluidized lactose particles, forming liquid bridges among the large and small lactose particles to form agglomerated lactose. Good hardness of 75-88 N was achieved for the agglomerated lactose. The particle size and bulk density can be controlled. The effects of agglomeration parameters, including solution concentration and temperature, atomizing pressure, peristalsis speed, and material temperature, were investigated for the agglomeration result and the characteristics of the agglomerated lactose. The result also shows that high solution temperature and high solution concentration can improve fluidized bed agglomeration efficiency.

1. Introduction

Excipients are inactive substances formulated with the active pharmaceutical ingredient (API) of a medication. Many excipients, like lactose, starch, and microcrystalline cellulose, contribute to the property, stability, safety, and many other aspects of drug manufacturing and have been widely used in the pharmaceutical industry [1]. Different kinds of excipients are frequently used together to achieve multiple properties for a medication; meanwhile, the ones that can improve the quality of pharmaceutical preparations or the production efficiency have attracted more and more attention [1, 2]. For instance, there have been several types of lactose excipient [3, 4], which have typical values of fluidity, viscosity, compressibility, particle size and particle size distribution, enteric disintegration performance, and so on. These values have great influence on the physical and chemical properties of pharmaceutical preparations, such as disintegration and dissolution and bioequivalence *in vivo* and *in vitro*. In practice, solid dosage forms require different types of excipients to be added to the API in order to obtain the desired physicochemical properties, such as flowability, compressibility, disintegration, solubility, and stability [4–8], for the medication. The excipients are mixed and granulated with the APIs using different equipment to ensure their mixing uniformity. The typical mixing and granulation techniques in the pharmaceutical industry include direct mixing, dry and wet granulation, spray drying, and freeze drying [9].

Agglomeration is the technique that binds small particles to create large aggregates. It is also presented as granulation in a macro sense, where pharmaceutical ingredients are frequently granulated with some excipients to create visible round particles for production of tablets and capsules [5, 6]. Through agglomeration/granulation technology, the APIs and excipients can be evenly mixed with a suitable particle size distribution and provide good material uniformity, fluidity, and compressibility for the subsequent preparation process, such as the tableting process [7]. A good agglomeration/granulation also contributes to the stability in transportation and storage, provides desired disintegration and

dissolution, and ensures that the drug has the expected dissolution curve and AUC (area under the curve) *in vivo*, ensuring good absorption of the drug for a better therapeutic effect.

At present, typical agglomeration/granulation includes the formation of solid bridges, adhesion, sintering, chemical reaction, crystallization, and colloidal particle deposition [8, 9], among which dry granulation and wet granulation are the two main methods in practice [2, 10]. The dry granulation methods generally bind the fine particles by compression force, for those materials with good compressibility, namely, high molecular interactions. The wet granulation methods use a solvent (i.e., water), solution, or suspension as the binder to provide bridging forces required for the fine powders to form large particles. In this work, a fluidized bed agglomeration process was used to produce the agglomerated lactose. A suspension of lactose solution is sprayed onto the fluidized lactose particles, forming liquid bridges among the large and small lactose particles to form agglomerated lactose. The effects of agglomeration parameters, including solution concentration and temperature, atomizing pressure, peristalsis speed, and material temperature, were investigated for the agglomeration.

2. Materials and Methods

2.1. Preparation of Lactose Suspension. The pharmaceutical-grade α-lactose monohydrate (>99.9%) was purchased from Jiangsu Dawning Pharmaceutical Co., Ltd., China. Four groups of lactose solution were prepared with lactose concentrations of 5%, 15%, 25%, and 40% (w/w) using the α-lactose monohydrate. The lactose solutions were added with 10% (w/w) fine-milled lactose of 300 mesh (Jiangsu Dawning Pharmaceutical) for efficient granulation [11] to obtain lactose suspension samples as the agglomeration binder. Adding lactose into the solution to prepare suspension is to increase wet particles in the fluidized bed, increasing effective collision between particles, accelerating particle adhesion, and increasing agglomeration rate.

2.2. Agglomeration. The schematic diagram of the fluidized bed granulator and the agglomeration parameters is shown in Figure 1. In a typical agglomeration, 120 g milled lactose of 120 mesh and 100 g fine-milled lactose of 300 mesh were mixed and added into a fluidized bed granulator (Shenzhen Xinyite Technology Co., Ltd, China). The fluidized bed granulator was preheated for 30 minutes. 150 mL lactose suspension was gradually sprayed onto the fluidized lactose mixture in the granulator at a controlled spraying speed. 5 min of the subdry process was performed to ensure a stable temperature of the materials in the fluidized bed. An additional volume of 150 mL of lactose suspension was sprayed subsequently in order to investigate the effect of the binder. The agglomeration stopped after 600 mL lactose suspension was sprayed in total. The concentration, temperature, peristaltic speed, and atomizing pressure were investigated for the lactose agglomeration.

2.3. Product Characteristics. The calculation of the D_{50} value is generally used as a representative parameter of the particle

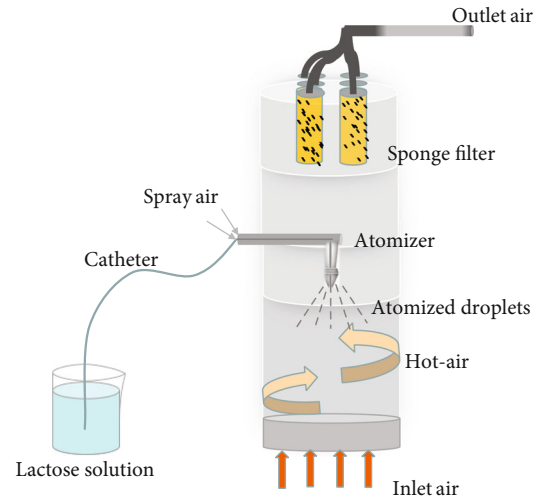

Granulation condition

Parameter	*Setting*
Spray rate (*ml*/*m in*)	10
Spray pressure (*MPa*)	0.2
Inlet temperature (°C)	80
Material temperature (°C)	30~40
Spray/*Sub-dry duration* (*mVin*)	15/5

Figure 1: Schematic diagram of the fluidized bed granulator and the agglomeration parameters.

size in a fluidized bed granulation process. The particle size distribution (D_{50} values) was determined by a laser scattering particle size distribution analyzer LA-960 (Horiba, Japan). The agglomeration rate constant (K) is defined as a function of D_{50}, calculated by linear regression, using the following equation:

$$D_{50,t} = K \cdot t + D_{50,t=0}, \quad (1)$$

where $D_{50,t}$ is the average particle size of the particles at time t, $D_{50,t=0}$ is the average particle size of the raw material before agglomeration, and t is the agglomeration time.

The bulk density was determined for the agglomerated lactose samples. The samples were gently and uniformly filled into the cylinder to 50 cm^2. The weight of the filled powder was measured. The bulk density ρ was determined with $\rho = M/V$ (mass over volume). The tablet hardness was measured to evaluate the compressibility of the agglomerated lactose. Typically, 0.25 g agglomerated lactose was compressed with a diameter of 8 mm on a single-punch tablet press under a compression pressure of 10 MPa. The tablet hardness was measured in a hardness tester (Tianjin Jingtuo, China) three times to obtain the average value.

DSC analysis was performed using a differential scanning calorimeter (HSC-4 DSC, Henven, China) for the agglomerated lactose. The sample for DSC measurement was prepared following standard procedures using a sealed aluminum pan. About 5 mg of sample was used in the analysis. The sample

Table 1: The particle characteristics of the agglomerated lactose fabricated with different lactose concentrations and sprayed volume of lactose suspension.

Lactose concentration (w/w)	Sprayed volume (mL)	D_{50} (μm)	K (μm/min)	Bulk density (g/mL)	Tablet hardness (N)
5%	150	60.00	0.62	0.4708	75.21
	300	66.91		0.4948	76.55
	450	78.43		0.5032	78.22
	600	87.56		0.5229	78.76
15%	150	64.11	0.70	0.4823	76.23
	300	69.83		0.5022	77.22
	450	84.22		0.5243	78.43
	600	92.55		0.5492	80.21
25%	150	72.32	1.98	0.4874	78.34
	300	107.59		0.5121	80.54
	450	130.89		0.5317	81.28
	600	169.28		0.5618	83.45
40%	150	79.21	2.16	0.4924	85.21
	300	118.32		0.5282	87.31
	450	140.76		0.5508	87.92
	600	179.44		0.6022	88.34

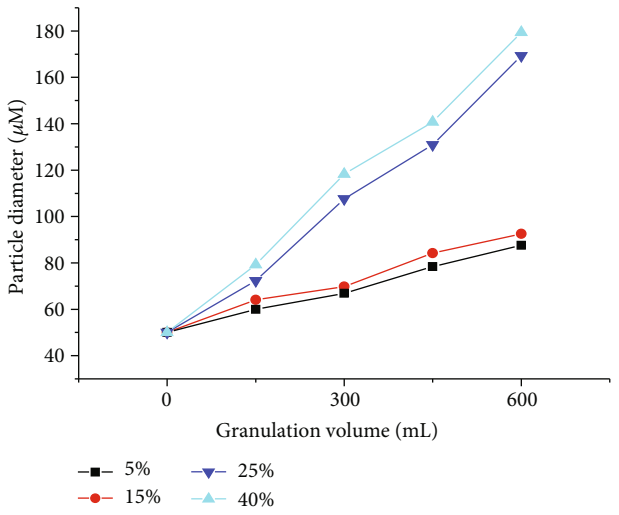

Figure 2: The change in particle size D_{50} as functions of lactose concentration and spraying volume of the lactose suspension.

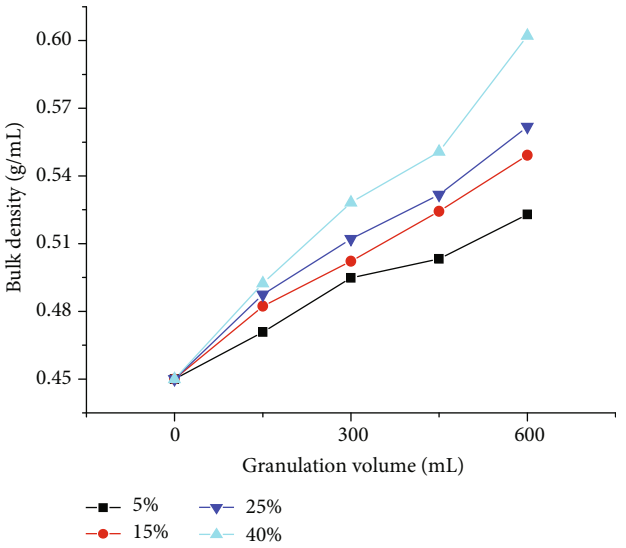

Figure 3: The change in bulk density of agglomerated lactose as functions of lactose concentration and spraying volume of the lactose suspension.

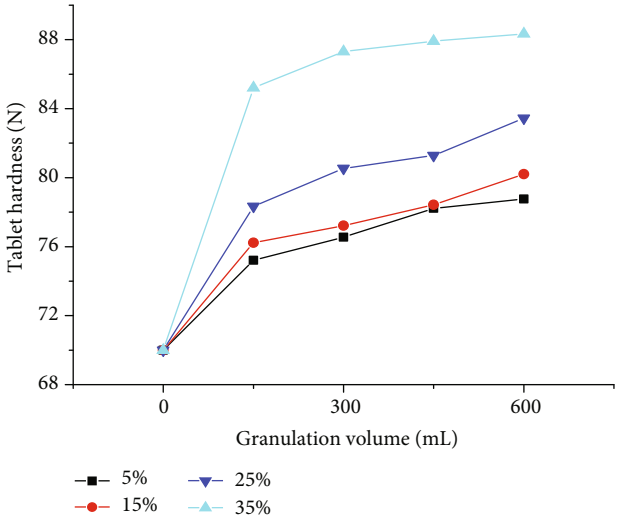

Figure 4: The change in tablet hardness as functions of lactose concentration and spraying volume of the lactose suspension.

was heated from room temperature of 25°C to 300°C using a ramp rate of 5°C/min, with N_2 as the purge gas. Heat flow as a function of increasing temperature was recorded for the analysis of each sample. Fourier transform infrared (FTIR) spectroscopy was used to investigate the agglomerated lactose and the raw material (α-lactose monohydrate). The specimen was mixed with KBr powder, tableted, and scanned for transmission sensitivity in a Nicolet 6700 FTIR spectrometer (Thermo Fisher Scientific). The FTIR spectra used a resolution of 1 cm^{-1} with 64 scans. The agglomerated lactose sample manufactured with the 40% lactose suspension was placed on carbon tape on an aluminum sample spike. The gold-plated particles were observed by a JSM-7200F scanning electron microscope (SEM, JEOL Ltd.). XRD analysis was used to investigate the crystalline characteristics of the agglomerated lactose. Solid samples were loaded on powder holders and analyzed using a Siemens D5000 diffractometer. During the XRD detection, the samples were scanned from 5° to 40° with a scanning rate of 0.02°/s, a scanning current of 30 mA, and a scanning voltage of 40 kV.

3. Results and Discussion

Due to its relatively mild process and stable raw material properties, the loss of material weight for the production is

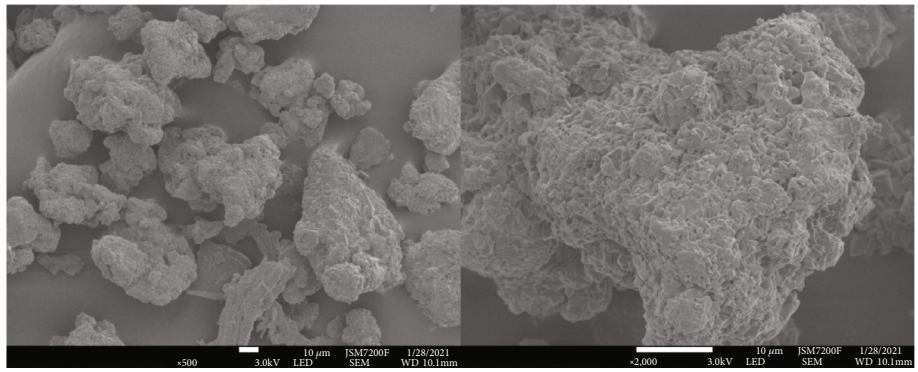

(a)

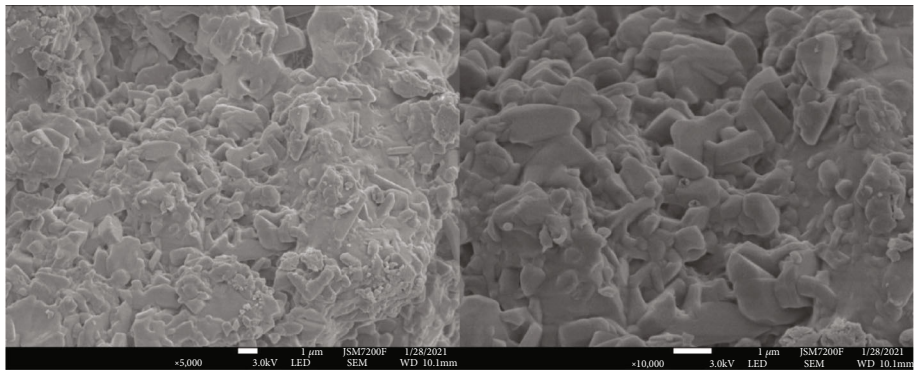

(b)

Figure 5: SEM images of the agglomerated lactose manufactured with the 40% lactose suspension showing fine-milled lactose on the particle surface. Scale bars: 10 μm (a), 1 μm (b).

less than 5%. The yield of the agglomeration process is over 95%, where some loss was induced by the air blowing in the fluidized bed equipment. Table 1 shows the measured particle size D_{50}, agglomeration rate constant K, bulk density, and tablet hardness. The result suggests that the particle size of agglomerated lactose largely increases with the lactose concentration (w/w) and the sprayed volume of binder solution (Figure 2), as more lactose has been added to the agglomeration system. High lactose weight concentration (w/w) and the sprayed volume of binder solution also contribute to the viscosity and binding efficiency for a high agglomeration rate constant. The bulk density and tablet hardness increase with the lactose concentration and the sprayed volume, since the ratio of large lactose of 300 mesh (which has relatively lower bulk density and compressibility) decreases.

In the agglomeration process, wet particles form liquid bridges when they coalesce. In the subsequent drying step, the solid bridges that hold the particles together form large particles from the liquid bridges. When the solution has a lactose concentration of 25%, the agglomeration rate constant K is relatively high compared to other binders. As reported by Fujiwara et al. [12], 10% PVP solution has a K value of 2.17, 10% HPMC has a K value of 1.16, and 8% HPC solution has a K value of 1.71. With the lactose solution and suspension as the binder, the bulk density and compressibility of lactose powder increase as functions of the agglomeration

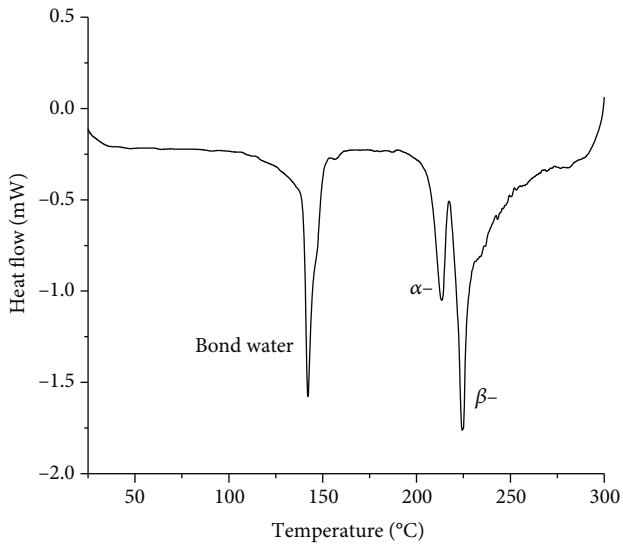

Figure 6: DSC spectrum of the agglomerated lactose.

parameters. As shown in Figure 3, when the particle size of lactose increases with the granulation time, its bulk density will gradually increase with the increase of the particles. For the same reason, high lactose concentration also increases the agglomeration rate.

Generally, small particles show poor flowability but good compressibility [13]. The result, however, shows that both

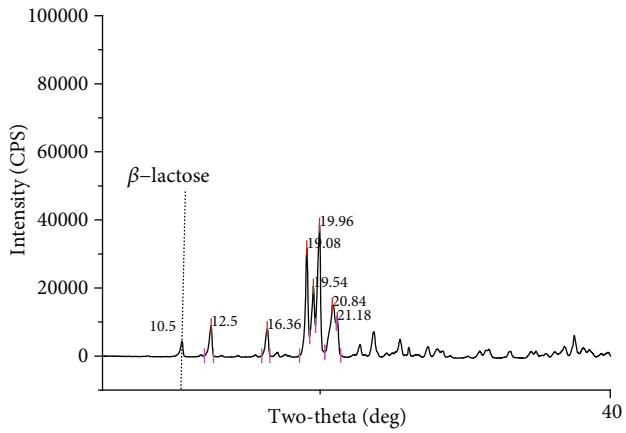

Figure 7: XRD spectrum of the agglomerated lactose.

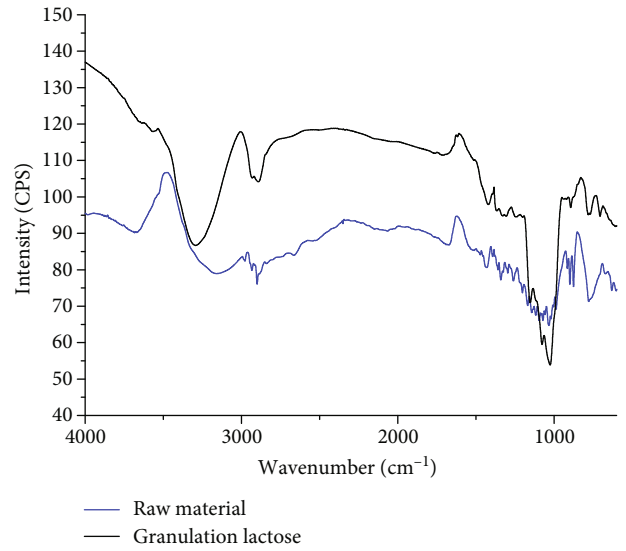

Figure 8: FTIR spectra of the agglomerated lactose and lactose monohydrate (raw material).

the tablet hardness and the particle size of the agglomerated lactose increase at the same time (Figure 4) for the following possible reason. At a spray pressure of 20 MPa, atomized droplets were smaller than the size of lactose particles, where the agglomerated lactose particles were loose and were composed of fine-milled lactose linked through solid bridges formed after drying. The aggregation of fine particles was confirmed by SEM (Figure 5). The SEM shows that the surface of particles is porous and the structure is fluffy. When the particle size increases, more fine particles are aggregated resulting in increases in the compressibility (due to the number of fine particles) and the flowability (due to the size of the aggregates). The particles would have good flowability and good compressibility when the size is over 140 μm [14]. Besides, the temperature of the solution, the temperature of the material in the fluidized bed chamber and the spraying speed of lactose suspension play important roles in the agglomeration process, improving the granulation speed and efficiency. High temperatures and low spraying speeds of lactose suspension induce fast drying rates of the fluidized lactose, affecting the binding and formation of solid bridges among the fine lactose particles.

The DSC curve (Figure 6) shows that the agglomerated lactose is lactose monohydrate, where the dehydration peak is shown at 145°C. β-Lactose peak is shown alongside α-lactose peak, indicating that the process transfers α-lactose to β-lactose [15, 16]. According to the XRD spectrum (Figure 7), α-lactose peaks are observed at 2θ of 12.5°, 19.1°, 19.6°, and 19.9°. β-Lactose peaks are at 2θ of 10.5° and 20.8°, indicating that a small amount of β-lactose was produced [17, 18]. The FTIR spectra confirmed that the materials are lactose monohydrate [19] with a peak of -OH of water at 3600 cm^{-1} (Figure 8).

4. Conclusions

This work used a fluidized bed agglomeration process to produce the agglomerated lactose with good compressibility. In the fluidized bed agglomeration, large lactose crystals were used as the core materials, fine-milled lactose particles were bound to the surface of large lactose cores, and lactose solution was used as the binder. The fine-milled lactose of 300 mesh contributed to the compressibility of the agglomerated lactose. Good harness of the tablets around 75-88 N was achieved when 0.25 g agglomerated lactose was compressed with a diameter of 8 mm on a single-punch tablet press under a compression pressure of 10 MPa. The particle size and bulk density can be controlled. Instrumental analysis indicated the production of β-lactose.

Data Availability

All data used to support the findings of this study are included within the article.

Conflicts of Interest

The authors declare that there is no conflict of interest regarding the publication of this paper.

Acknowledgments

This work was supported by the 131 Talent Engineering Fund (2020-32), Scientific Research Project of Hunan Provincial Department of Education (20C1156), Scientific Research Project of Hunan Provincial Health Commission (202115011227), and Clinical Pharmacy Project of Medical Research Fund of Hunan Medical Association (HMA202001008).

References

[1] J. B. M. Fernandes, M. T. Celestino, M. I. B. Tavares et al., "The development and characterization of propranolol tablets using tapioca starch as excipient," *Anais da Academia Brasileira de Ciências*, vol. 91, no. 1, article e20180094, 2019.

[2] N. Garg, P. Pandey, D. Kaushik, and H. Dureja, "Development of novel multifunction directly compressible co-processed excipient by melt granulation technique," *International Journal of Pharmaceutical Investigation*, vol. 5, no. 4, pp. 266–274, 2015.

[3] S. Lute, R. Dhenge, and A. Salman, "Twin screw granulation: effects of properties of primary powders," *Pharmaceutics*, vol. 10, no. 2, p. 68, 2018.

[4] S. Tan, A. Ebrahimi, and T. Langrish, "Template-directed flower-like lactose with micro-meso-macroporous structure," *Materials & Design*, vol. 117, pp. 178–184, 2017.

[5] T. Ito, K. Okada, K. H. Leong et al., "A time-domain nmr study of the state of water in wet granules with different fillers and its contribution to the wet granulation process and to the characteristics of granules," *Chemical and Pharmaceutical Bulletin*, vol. 67, no. 3, pp. 271–276, 2019.

[6] N. Hirai, T. Takatani-Nakase, and K. Takahashi, "Application of near-infrared spectrometry to evaluate the mechanism of wet granulation using a high-speed mixer with porous calcium silicate and sugar alcohols," *Chemical and Pharmaceutical Bulletin*, vol. 66, no. 11, pp. 1027–1034, 2018.

[7] S. Shanmugam, "Granulation techniques and technologies: recent progresses," *BioImpacts*, vol. 5, no. 1, pp. 55–63, 2015.

[8] L. Cai, L. Farber, D. Zhang, F. Li, and J. Farabaugh, "A new methodology for high drug loading wet granulation formulation development," *International Journal of Pharmaceutics*, vol. 441, no. 1-2, pp. 790–800, 2013.

[9] S. M. Iveson, J. D. Litster, K. Hapgood, and B. J. Ennis, "Nucleation, growth and breakage phenomena in agitated wet granulation processes: a review," *Powder Technology*, vol. 117, no. 1-2, pp. 3–39, 2001.

[10] O. A. Adeleye, M. N. Femi-Oyewo, and M. A. Odeniyi, "The effect of processing variables on the mechanical and release properties of tramadol matrix tablets incorporating Cissus populnea gum as controlled release excipient," *Polymers in Medicine*, vol. 44, no. 4, pp. 209–220, 2014.

[11] S. A. L. de Koster, K. Pitt, J. D. Litster, and R. M. Smith, "High-shear granulation: an investigation into the granule consolidation and layering mechanism," *Powder Technology*, vol. 355, pp. 514–525, 2019.

[12] M. Fujiwara, M. Dohi, T. Otsuka, K. Yamashita, and K. Sako, "Influence of binder droplet dimension on granulation rate during fluidized bed granulation," *Chemical and Pharmaceutical Bulletin*, vol. 61, no. 3, pp. 320–325, 2013.

[13] Y. Kudo, M. Yasuda, and S. Matsusaka, "Effect of particle size distribution on flowability of granulated lactose," *Advanced Powder Technology*, vol. 31, no. 1, pp. 121–127, 2020.

[14] Y. Özalp, M. M. Onayo, and N. Jiwa, "Evaluation of lactose-based direct tableting agents' compressibility behavior using a Compaction Simulator," *Turkish Journal of Pharmaceutical Sciences*, vol. 17, no. 4, pp. 367–371, 2020.

[15] S. Tan, A. Ebrahimi, and T. Langrish, "Preparation of core-shell microspheres of lactose with flower-like morphology and tailored porosity," *Powder Technology*, vol. 325, pp. 309–315, 2018.

[16] S. Tan, A. Ebrahimi, X. Liu, and T. Langrish, "Hollow flower-like lactose particles as potential drug carriers: effect of particle size and feed concentration," *Powder Technology*, vol. 320, pp. 1–6, 2017.

[17] A. S. Barham and B. K. Hodnett, "In situ X-ray diffraction study of the crystallization of spray-dried lactose," *Crystal Growth & Design*, vol. 5, no. 5, pp. 1965–1970, 2005.

[18] S. Tan, T. Jiang, A. Ebrahimi, and T. Langrish, "Effect of spray-drying temperature on the formation of flower-like lactose for griseofulvin loading," *European Journal of Pharmaceutical Sciences*, vol. 111, pp. 534–539, 2018.

[19] S. Tan, A. Ebrahimi, X. Liu, and T. Langrish, "Role of templating agents in the spray drying and postcrystallization of lactose for the production of highly porous powders," *Drying Technology*, vol. 36, no. 15, pp. 1882–1891, 2018.

Hindawi
Journal of Nanomaterials
Volume 2021, Article ID 9997180, 6 pages
https://doi.org/10.1155/2021/9997180

Review Article

New Insight on Pathophysiology, Diagnosis, and Treatment of Odontogenic Maxillary Sinusitis

Jianhua Zhu,[1] Wei Lin,[2] Wenwen Yuan,[3] and Lili Chen[4]

[1]*Graduate School of Zhejiang University, China*
[2]*Department of Otorhinolaryngology, Litongde Hospital, China*
[3]*Department of Stomatology, Litongde Hospital, China*
[4]*Department of Stomatology, The Second Affiliated Hospital of Zhejiang University, Zhejiang, China*

Correspondence should be addressed to Lili Chen; y216180119@zju.edu.cn

Received 11 March 2021; Revised 19 March 2021; Accepted 19 March 2021; Published 6 May 2021

Academic Editor: Songwen Tan

Odontogenic maxillary sinusitis is often ignored by otolaryngologists, dentists, and imageological diagnosis doctors. Traditional treatments are often frustrating for refractory maxillary sinusitis and odontogenic maxillary sinusitis. In the last few years, new progress has been made in the diagnosis, pathophysiology, and treatment of odontogenic maxillary sinusitis. Periodontitis, polyposis, and iatrogenesis are regarded as causes of odontogenic maxillary sinusitis. Dental implant dislocation into the maxillary sinus and augmentation are the main cause of iatrogenesis compared to root canal full material. The symptoms are too similar to distinguish odontogenic maxillary sinusitis from chronic rhinosinusitis. Computed tomography is the gold standard for diagnosis, while it is difficult to rule out odontogenic maxillary sinusitis by conventional panoramic radiographs. Cone-beam computed tomography (CBCT) is currently the most broadly used to make diagnosis and differential diagnosis for maxillary sinus disease. The imaging diagnosis, clinical diagnosis, and pathological diagnosis are often not completely in accordance. Most researchers believe that odontogenic maxillary sinus infection results from the spread of apical pathogenic microbial infections: either through the local vascular system, lymphatic system, or the Haval system of the alveolar bone itself. DNA and RNA sequencing of mucosal tissues of maxillary sinus disease confirmed that the mechanisms of odontogenic maxillary sinusitis and nonodontogenic maxillary sinusitis are different. Microbial RNA sequencing of the maxillary sinus also verifies this conclusion. Clinical serum testing of chemical factors has not been widely exploited. It is unknown whether the thickening of the maxillary sinus membrane is the result of pathogen infection or inflammatory mediators. Many doctors have recommended a consensus on multidisciplinary cooperation management, but a global consensus has not yet been reached. Diagnosis methods for odontogenic maxillary sinus disease are diversified. Tissue DNA and RNA sequencing, chemical factor determination, and microbiological DNA and RNA sequencing have appeared, and the misdiagnosis rate has gradually decreased. The pathophysiology of odontogenic maxillary sinusitis and chronic rhinosinusitis is different. The molecular mechanism of the thickening of the Schneider membrane in odontogenic sinus is unknown.

1. Background

The first professor to propose the concept of odontogenic maxillary sinus was William H. Bauer in 1943 [1]. Over the past decades, the concept has evolved, and odontogenic maxillary sinus has become a well-recognized condition in both the dental and otolaryngology communities [2]. Periodontitis, apical periodontitis, and root canal therapy superfilling materials such as silver amalgam and dental tissue are the main motivation of odontogenic maxillary sinus infection [3, 4]. Since the development of dental implant surgery, many documents have pointed out that iatrogenic factors such as implants and maxillary sinus lifting materials have been accounting for more and more causation [5–9]. Odontogenic maxillary sinusitis has not been documented in the ear, nose, and throat (ENT) practice guidelines in 2012, 2017, and earlier. The "European Position Paper on Rhinosinusitis and Nasal Polyps 2020" mentions the diagnosis of

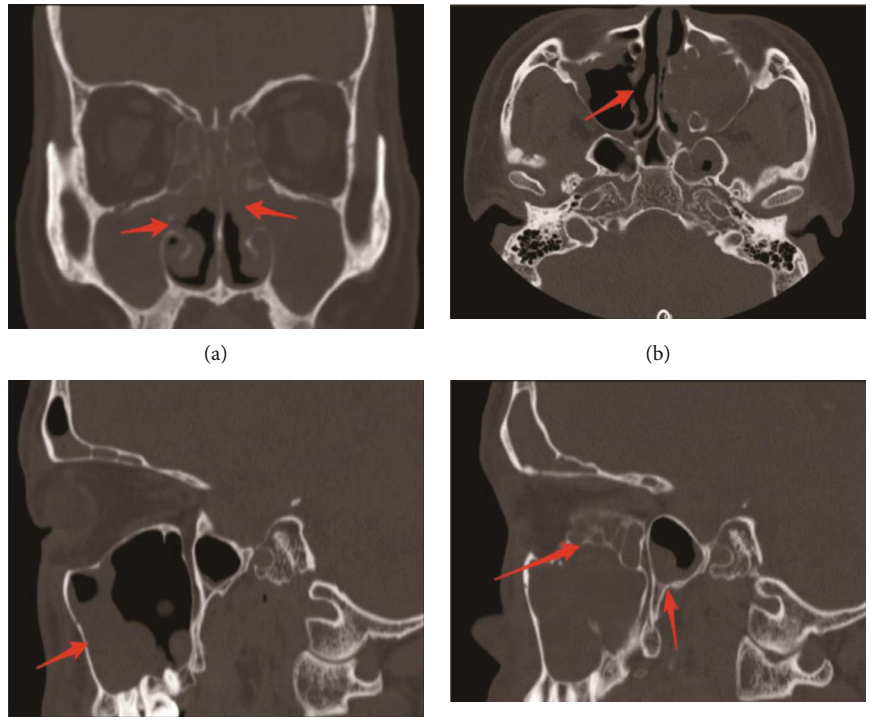

(a) (b) (c) (d)

Figure 1: Individual with chronic maxillary sinusitis. (a) Bilateral chronic maxillary sinusitis. The arrows show that the lesions scatter over the adjacent tissues finally to the other side of the sinus. (b) The transverse image of the infected area. The arrow shows the infected area. (c) The cross-sectional view of the maxillary sinus on the right. The arrow shows that the lesion spreads to other parts of the maxillary sinuses. (d) The sagittal position of the left maxillary sinus. The arrows show that the lesion spreads to adjacent tissues and finally spreads to other maxillary sinuses.

odontogenic maxillary sinusitis in the classification of rhinosinusitis [10, 11]. Due to the different population bases of various literature statistics, the proportion of odontogenic maxillary sinusitis diagnosis is inconsistent, about 10%-40% [12–14].

2. Diagnosis

It is inaccurate to diagnose with maxillary sinusitis depending on panoramic film alone. Computed tomography (CT) and cone-beam computed tomography (CBCT) are regarded as better options for diagnosing maxillary sinus disease which have been proven in our daily practice [15, 16]. CBCT is currently the most commonly used method to diagnose maxillary sinusitis. However, it is not enough to diagnose maxillary sinusitis according to imaging data alone [16]. It is reported that the pathological examination results are not always in accordance with the CBCT presentation before operation [16–18]. Early differential diagnosis of maxillary sinusitis, sinus mucosa thickening, sinus cyst, maxillary sinus endometrial papillary inverted fold, and sinus mucosal bleeding is not easy [19, 20]. Emphasis with the identification between imaging diagnosis, clinical diagnosis, or pathological diagnosis is important [16]. Dobros and Zarzecka tried to establish a diagnostic model of odontogenic maxillary sinusitis based on symptoms [4].

With the development of science, new diagnostic methods have emerged. More and more literatures which emphasize diagnosis and differential diagnosis utilizing maxillary-related cytokines and chemical factors have gradually increased [21]. Interferon-α; interferon-γ; proinflammatory cytokines including brain-derived neurotrophic factor (BDNF), tumor necrosis factor-alpha (TNF-α), and IL-3; viral-associated chemokines including IP-10 (CXCL10), I-TAC (CXCL11), MCP-3 (CCL7), and MIG (CXCL9); microbial peptides, Toll-like receptors; picric acid receptors; neopterin levels; α-defensins; and prostaglandin D2 all have been selected for laboratory detection for chronic maxillary sinusitis. However, whether it can be used for the differential diagnosis of odontogenic maxillary sinusitis from maxillary sinus needs further study [22–28], whereas cytokines and chemokines are currently detected in local tissues, and detection in serum is relatively rare. Rapoport et al. tried to compare microbial DNA probes with a conventional microbial culture to find the pathogenic microbial as well as chemosensitivity and found that DNA probes are more accurate and reliable than traditional methods [29]. However, the detection efficiency is limited and needs further expansion.

3. Pathophysiology

The pathological characteristics of odontogenic maxillary sinusitis and chronic sinusitis are different [18, 30]. It is

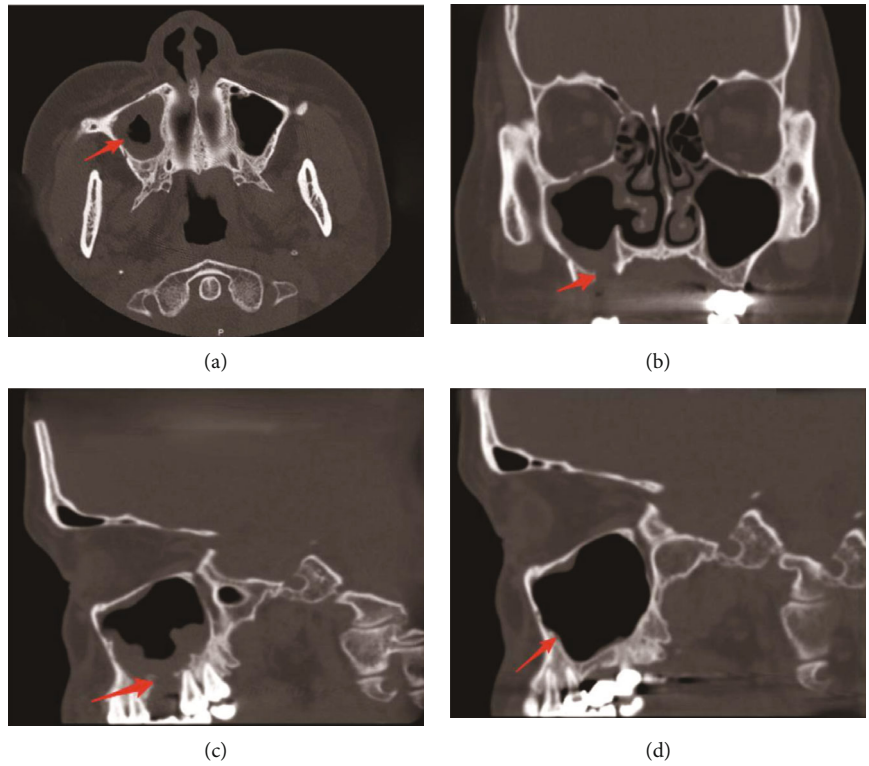

Figure 2: Individual with right maxillary sinusitis. (a) The transverse image of the infected area. The arrow shows that the lesions lie in the right maxillary sinus. The left sinus is normal. (b) Comparison sagittal image of left maxillary sinus in the same patient. The arrow shows communication between the oral and the maxillary sinus. (c) The coronal image of the infected area. The patient suffered from odontogenic maxillary sinusitis and had been tooth extracted through the traditional Caldwell-Luc approach. After recurrence, FESS surgery and local mucosal flap transposition were performed transorally. (d) Comparison sagittal image of right maxillary sinus in the same patient.

viewed that the pathophysiology of rhinogenic sinusitis has various reasons leading to the inflammation of the sinus ostium complex, which spreads to the tissues around the ostium, and finally to other maxillary sinus locations, blocking the ability of maxillary sinus mucosal clearance. The cascade of inflammation will lead to damage by the infiltrating cells, causing edema, fluid extravasation, mucus production, engorgement, and sinus obstruction in the process (such as Figures 1(a)–1(d)). The origin of odontogenic maxillary sinusitis is the pathogenic teeth; from the teeth, it diffuses to the maxillary sinus floor, then from the maxillary sinus floor, it spreads to the maxillary sinus ostium and finally to the tissues around the maxillary sinus ostium and other accessory sinuses. The microorganisms even scatter over the orbital and brain [20, 28, 31–35]. The odontogenic maxillary sinusitis can be used as an important basis for distinguishing odontogenic maxillary sinusitis from nonodontogenic maxillary sinusitis (such as Figures 2(a)–2(d)).

In terms of anatomy, it is believed that the veins, arterial connections, and lymphatic system are the main way which make lesion bacteria diffuse from the periodontal to the maxillary sinus. The Haval system in the alveolar bone also acts as an important approach for evaluating the spread of infection [36]. Studies have verified this theory through autopsy, angiography, and radiographic scintigraphy [37, 38]. There are various reasons for the thickening of the maxillary sinus mucosa. Some authors use CBCT analysis to infer that the thickening of the maxillary sinus mucosa is closely related to periodontal conditions and root apex conditions. The Schneider membranes of many patients have gradually recovered after root canal treatment [39, 40]. It is unclear whether the thickening of the maxillary sinus mucosa and early maxillary sinus inflammation is the result of inflammatory mediators or the scatter of microorganisms to the maxillary sinus [39, 40]. Further research and confirmation in the future are essential.

Maxillary sinusitis is the dysfunction of the host mucosal epithelium under environmental pressure to initiate an inflammatory response. The inflammatory response cascade amplifies the process along corresponding inflammatory mediators. But the complete molecular mechanism is currently unclear [35, 41]. Interestingly, inflammatory mediators are different in various countries, even in different regions of the same country because of different susceptible microorganisms [22, 42]. The inflammatory mediators are different between odontogenic maxillary sinusitis and nonodontogenic maxillary sinusitis. The pathways involved in inflammation are also various [22, 36, 38, 43–45]. In terms of the microorganism, the identification of microbial DNA or RNA sequencing, the detection of virulence genes, and the determination of drug resistance genes are

supplementary methods for routine culture negative results in clinical work. Microbiological gene sequencing showed that microbial communities were constant compared to normal maxillary sinus and chronic maxillary, but the species changed [46, 47]. The microbial dominant bacteria between the odontogenic maxillary sinusitis and the chronic maxillary sinusitis are different by the microbial gene sequencing. For chronic sinus disease, anaerobic bacteria, streptococcus, Pseudomonas aeruginosa, or predominate fungi are dominated. Refractory maxillary results from microbial membrane colonization, which has yet to be confirmed by further experiments [48]. The research on proteomics and metabolomics is mainly focused on chronic maxillary, while there are limited data. Limited literature on the differential diagnosis of odontogenic maxillary has been documented [23, 45]. Microbial DNA or RNA detection, proteomics testing, and metabolomics identification are the current and future development directions for the diagnosis and differential diagnosis of microbial infections.

4. Treatment

Elimination of infection source in odontogenic maxillary sinusitis is important for preventing symptom persistence. Antibiotics play a part in treating odontogenic maxillary sinusitis whenever combined with other appropriate treatments. Clindamycin and clavulanate potassium can overcome drug resistance during the treatment of chronic and odontogenic maxillary sinusitis. When maxillary sinus inflammation scatters to adjacent organs, the length of antibiotics is reported for 3 weeks to 3 months, or even longer [49]. Previous evidence showed that 50% of all odontogenic sinusitis pathogens were resistant to clindamycin, making this a poor choice for antibiotic therapy [50]. Craig et al. proposed functional endoscopic sinus surgery (FESS) as the first choice for maxillary sinus treatment prior to endodontic treatment [51]. Tsuzuki et al. proposed that extraction is the prior choice instead of FESS and dental implant [52]. Yoo et al. believe that dental endodontic treatment and medicine are given priority, and FESS is required according to the treatment results [53]. Akiyama et al. proposed that the apical surgery was performed simultaneously with FESS to achieve better results [54]. Aukstakalnis et al. provide grading odontogenic maxillary sinusitis, which is of positive significance for the selection of treatment options and cooperation among multiple departments [55]. Endodontic history and the lesions of odontogenic maxillary sinusitis are candidates for FESS [56]. Craig et al. completed a survey of experts related to odontogenic maxillary sinusitis governance in the United States and achieved consensus on the management of sinus disease. Among them, the participating dentists are relatively scarce, and the numbers of experts participating in the survey are also relatively few [57]. Some researchers proposed that dental surgery should be performed first to eliminate the source of infection, followed by sinus surgery to relieve symptoms and prevent recurrence of sinusitis [56]. The consensus needs further supplementation and improvement.

5. Conclusion

Odontogenic maxillary sinusitis, as a category of chronic maxillary sinus disease, is receiving more and more attention from otolaryngology and maxillofacial surgeons. Dentists and radiologists are gradually joining the management. With gradual comprehension of pathophysiology and microbiology of odontogenic maxillary sinusitis and the improvement of clinical treatment effects, more and more doctors from different countries have accepted the consensus on the management of the disease. Nevertheless, a global management consensus has not yet been signed in, and subsequent studies based on clinical evidence are warrant.

Data Availability

The data used to support the findings of this study are included within the article.

Conflicts of Interest

All authors declare that they have no conflict of interest.

References

[1] W. H. Bauer, "Maxillary sinusitis of dental origin," *American Journal of Orthodontics & Oral Surgery*, vol. 29, no. 3, pp. B133–B151, 1943.

[2] H. A. Newsome and D. M. Poetker, "Odontogenic sinusitis: current concepts in diagnosis and treatment," *Immunology and Allergy Clinics of North America*, vol. 40, no. 2, pp. 361–369, 2020.

[3] M. N. Chapman, R. N. Nadgir, A. S. Akman et al., "Periapical lucency around the tooth: radiologic evaluation and differential diagnosis," *Radiographics*, vol. 33, no. 1, pp. E15–E32, 2013.

[4] K. Dobros and J. Zarzecka, "Challenges in diagnosing odontogenic lesions in maxillary sinuses," *Otolaryngologia Polska*, vol. 74, no. 3, pp. 12–16, 2019.

[5] M. Chiapasco, G. Felisati, A. Maccari, R. Borloni, F. Gatti, and F. Di Leo, "The management of complications following displacement of oral implants in the paranasal sinuses: a multicenter clinical report and proposed treatment protocols," *International Journal of Oral and Maxillofacial Surgery*, vol. 38, no. 12, pp. 1273–1278, 2009.

[6] J. R. Lechien, R. Lamartine Monteiro, S. Kampouridis, R. Javadian, and M. Horoi, "Unilateral chronic maxillary rhinosinusitis after bone maxillary graft for dental implant placement: a case report," *Clinical Case Reports*, vol. 8, no. 9, pp. 1827–1830, 2020.

[7] Y. Manor, Y. Anavi, R. Gershonovitch, A. Lorean, and E. Mijiritsky, "Complications and management of implants migrated into the maxillary sinus," *The International Journal of Periodontics & Restorative Dentistry*, vol. 38, no. 6, pp. e112–e118, 2018.

[8] P. Galindo-Moreno, M. Padial-Molina, G. Avila, H. F. Rios, P. Hernandez-Cortes, and H. L. Wang, "Complications associated with implant migration into the maxillary sinus cavity," *Clinical Oral Implants Research*, vol. 23, no. 10, pp. 1152–1160, 2012.

[9] A. Safadi, O. J. Ungar, I. Oz, I. Koren, A. Abergel, and S. Kleinman, "Endoscopic sinus surgery for dental implant displacement into the maxillary sinus–a retrospective clinical study," *International Journal of Oral and Maxillofacial Surgery*, vol. 49, no. 7, pp. 966–972, 2020.

[10] W. J. Fokkens, V. J. Lund, C. Hopkins et al., "European position paper on rhinosinusitis and nasal polyps 2020," *Rhinology*, vol. 58, Suppl S29, 2020.

[11] W. J. Fokkens, "EPOS2020: a major step forward," *Rhinology*, vol. 58, no. 1, p. 1, 2020.

[12] S. Cartwright and C. Hopkins, "Odontogenic sinusitis an underappreciated diagnosis: our experience," *Clinical Otolaryngology*, vol. 41, no. 3, pp. 284-285, 2016.

[13] Z. Turfe, A. Ahmad, E. I. Peterson, and J. R. Craig, "Odontogenic sinusitis is a common cause of unilateral sinus disease with maxillary sinus opacification," *International Forum of Allergy & Rhinology*, vol. 9, no. 12, pp. 1515–1520, 2019.

[14] A. Wuokko-Landen, K. Blomgren, A. Suomalainen, and H. Valimaa, "Odontogenic causes complicating the chronic rhinosinusitis diagnosis," *Clinical Oral Investigations*, vol. 25, no. 3, pp. 947–955, 2021.

[15] A. D. Miller, "Respiratory muscle control during vomiting," *Canadian Journal of Physiology and Pharmacology*, vol. 68, no. 2, pp. 237–241, 1990.

[16] Z. Huang, H. Xu, N. Xiao et al., "Predictive significance of radiographic density of sinus opacity and bone thickness in unilateral maxillary sinus mycetoma," *ORL: Journal for Otorhinolaryngology and Its Related Specialties*, vol. 81, no. 2-3, pp. 111–120, 2019.

[17] I. Oreski, T. Greguric, P. Gulin, N. Prica Oreski, D. Brajdic, and D. Vagic, "Differences in self-reported symptoms in patients with chronic odontogenic and non-odontogenic rhinosinusitis," *American Journal of Otolaryngology*, vol. 41, no. 2, p. 102388, 2020.

[18] A. Raman, P. Papagiannopoulos, H. N. Kuhar, P. Gattuso, P. S. Batra, and B. A. Tajudeen, "Histopathologic features of chronic sinusitis precipitated by odontogenic infection," *American Journal of Rhinology & Allergy*, vol. 33, no. 2, pp. 113–120, 2019.

[19] H. Wang, Z. Tan, M. You, and W. J. Liu, "Imaging classification diagnosis and maxillary sinus floor augmentation of maxillary sinus cystic lesions," *Hua Xi Kou Qiang Yi Xue Za Zhi*, vol. 37, no. 5, pp. 457–462, 2019.

[20] M. Sakir and S. Ercalik Yalcinkaya, "Associations between periapical health of maxillary molars and mucosal thickening of maxillary sinuses in cone-beam computed tomographic images: a retrospective study," *Journal of Endodontia*, vol. 46, no. 3, pp. 397–403, 2020.

[21] K. Scheckenbach and M. Wagenmann, "Cytokine patterns and endotypes in acute and chronic rhinosinusitis," *Current Allergy and Asthma Reports*, vol. 16, no. 1, p. 3, 2016.

[22] X. Wang, N. Zhang, M. Bo et al., "Diversity of TH cytokine profiles in patients with chronic rhinosinusitis: a multicenter study in Europe, Asia, and Oceania," *The Journal of Allergy and Clinical Immunology*, vol. 138, no. 5, pp. 1344–1353, 2016.

[23] S. M. Daines, Y. Wang, and R. R. Orlandi, "Periostin and osteopontin are overexpressed in chronically inflamed sinuses," *International Forum of Allergy & Rhinology*, vol. 1, no. 2, pp. 101–105, 2011.

[24] Y. Sun, B. Zhou, C. Wang et al., "Biofilm formation and toll-like receptor 2, toll-like receptor 4, and NF-kappaB expression in sinus tissues of patients with chronic rhinosinusitis," *American Journal of Rhinology & Allergy*, vol. 26, no. 2, pp. 104–109, 2012.

[25] M. Tizzano, B. D. Gulbransen, A. Vandenbeuch et al., "Nasal chemosensory cells use bitter taste signaling to detect irritants and bacterial signals," *Proceedings of the National Academy of Sciences of the United States of America*, vol. 107, no. 7, pp. 3210–3215, 2010.

[26] R. J. Lee, G. Xiong, J. M. Kofonow et al., "T2R38 taste receptor polymorphisms underlie susceptibility to upper respiratory infection," *The Journal of Clinical Investigation*, vol. 122, no. 11, pp. 4145–4159, 2012.

[27] X. Feng, M. K. Ramsden, J. Negri et al., "Eosinophil production of prostaglandin D_2 in patients with aspirin-exacerbated respiratory disease," *Journal of Allergy and Clinical Immunology*, vol. 138, no. 4, pp. 1089–1097.e3, 2016.

[28] T. G. Stead, A. Retana, J. Houck, B. C. Sleigh, and L. Ganti, "Preseptal and postseptal orbital cellulitis of odontogenic origin," *Cureus*, vol. 11, no. 7, 2019.

[29] S. K. Rapoport, A. J. Smith, M. Bergman, K. A. Scriven, I. Brook, and S. K. Mikula, "Determining the utility of standard hospital microbiology testing: comparing standard microbiology cultures with DNA sequence analysis in patients with chronic sinusitis," *World Journal of Otorhinolaryngology - Head and Neck Surgery*, vol. 5, no. 2, pp. 82–87, 2019.

[30] N. R. London Jr., I. Lina, and M. Ramanathan Jr., "Aeroallergens, air pollutants, and chronic rhinitis and rhinosinusitis," *World Journal of Otorhinolaryngology - Head and Neck Surgery*, vol. 4, no. 3, pp. 209–215, 2018.

[31] A. M. Saibene, G. C. Pipolo, P. Lozza et al., "Redefining boundaries in odontogenic sinusitis: a retrospective evaluation of extramaxillary involvement in 315 patients," *International Forum of Allergy & Rhinology*, vol. 4, no. 12, pp. 1020–1023, 2014.

[32] K. V. Arunkumar, "Orbital infection threatening blindness due to carious primary molars: an interesting case report," *Journal of Maxillofacial and Oral Surgery*, vol. 15, no. 1, pp. 72–75, 2016.

[33] A. Safadi, S. Kleinman, I. Oz et al., "Questioning the justification of frontal sinusotomy for odontogenic sinusitis," *Journal of Oral and Maxillofacial Surgery*, vol. 78, no. 5, pp. 762–770, 2020.

[34] A. Laulajainen-Hongisto, L. Lempinen, E. Farkkila et al., "Intracranial abscesses over the last four decades; changes in aetiology, diagnostics, treatment and outcome," *Infectious Diseases*, vol. 48, no. 4, pp. 310–316, 2015.

[35] M. Boruk, C. Railwah, A. Lora et al., "Elevated S100A9 expression in chronic rhinosinusitis coincides with elevated MMP production and proliferation in vitro," *Scientific Reports*, vol. 10, no. 1, p. 16350, 2020.

[36] I. G. Pereira, P. Vaz, R. F. Almeida, A. C. Braga, and A. Felino, "IRAK4 gene polymorphism and odontogenic maxillary sinusitis," *Clinical Oral Investigations*, vol. 19, no. 8, pp. 1815–1824, 2015.

[37] C. Glaser, M. Pruckmayer, A. Staudenherz, M. Rasse, S. Lang, and T. Leitha, "Utility of technetium-99m-sestamibi to assess osseous tumor spread," *Journal of Nuclear Medicine*, vol. 37, no. 9, pp. 1526–1528, 1996.

[38] A. A. Haider, M. J. Marino, W. C. Yao, M. J. Citardi, and A. U. Luong, "The potential of high-throughput DNA sequencing of the paranasal sinus microbiome in diagnosing odontogenic

sinusitis," *Otolaryngology and Head and Neck Surgery*, vol. 161, no. 6, pp. 1043–1047, 2019.

[39] U. Aksoy and K. Orhan, "Association between odontogenic conditions and maxillary sinus mucosal thickening: a retrospective CBCT study," *Clinical Oral Investigations*, vol. 23, no. 1, pp. 123–131, 2019.

[40] T. Van Den Munckhof, S. Patel, G. Koller, E. Berkhout, F. Mannocci, and F. Foschi, "Schneiderian membrane thickness variation following endodontic procedures: a retrospective cone beam computed tomography study," *BMC Oral Health*, vol. 20, no. 1, p. 133, 2020.

[41] Y. J. Tsai, C. Y. Hao, C. L. Chen, P. H. Wu, and W. B. Wu, "Expression of long pentraxin 3 in human nasal mucosa fibroblasts, tissues, and secretions of chronic rhinosinusitis without nasal polyps," *Journal of Molecular Medicine (Berlin, Germany)*, vol. 98, no. 5, pp. 673–689, 2020.

[42] D. K. Kim, K. M. Eun, M. K. Kim et al., "Comparison between signature cytokines of nasal tissues in subtypes of chronic rhinosinusitis," *Allergy, Asthma & Immunology Research*, vol. 11, no. 2, pp. 201–211, 2019.

[43] T. Van Zele, S. Claeys, P. Gevaert et al., "Differentiation of chronic sinus diseases by measurement of inflammatory mediators," *Allergy*, vol. 61, no. 11, pp. 1280–1289, 2006.

[44] V. K. Anand, A. Kacker, A. F. Orjuela, C. Huang, C. Manarey, and J. Xiang, "Inflammatory pathway gene expression in chronic rhinosinusitis," *American Journal of Rhinology*, vol. 20, no. 4, pp. 471–476, 2018.

[45] C. Jardeleza, D. Jones, L. Baker et al., "Gene expression differences in nitric oxide and reactive oxygen species regulation point to an altered innate immune response in chronic rhinosinusitis," *International Forum of Allergy & Rhinology*, vol. 3, no. 3, pp. 193–198, 2013.

[46] V. R. Ramakrishnan, L. J. Hauser, L. M. Feazel, D. Ir, C. E. Robertson, and D. N. Frank, "Sinus microbiota varies among chronic rhinosinusitis phenotypes and predicts surgical outcome," *Journal of Allergy and Clinical Immunology*, vol. 136, no. 2, pp. 334–342.e1, 2015.

[47] V. R. Ramakrishnan, L. M. Feazel, L. J. Abrass, and D. N. Frank, "Prevalence and abundance of Staphylococcus aureus in the middle meatus of patients with chronic rhinosinusitis, nasal polyps, and asthma," *International Forum of Allergy & Rhinology*, vol. 3, no. 4, pp. 267–271, 2013.

[48] J. H. Fastenberg, W. D. Hsueh, A. Mustafa, N. A. Akbar, and W. M. Abuzeid, "Biofilms in chronic rhinosinusitis: pathophysiology and therapeutic strategies," *World Journal of Otorhinolaryngology - Head and Neck Surgery*, vol. 2, no. 4, pp. 219–229, 2016.

[49] B. P. Erickson and W. W. Lee, "Orbital cellulitis and subperiosteal abscess: a 5-year outcomes analysis," *Orbit*, vol. 34, no. 3, pp. 115–120, 2015.

[50] S. Puglisi, S. Privitera, L. Maiolino et al., "Bacteriological findings and antimicrobial resistance in odontogenic and non-odontogenic chronic maxillary sinusitis," *Journal of Medical Microbiology*, vol. 60, no. 9, pp. 1353–1359, 2011.

[51] J. R. Craig, C. I. McHugh, Z. H. Griggs, and E. I. Peterson, "Optimal timing of endoscopic sinus surgery for odontogenic sinusitis," *Laryngoscope*, vol. 129, no. 9, pp. 1976–1983, 2019.

[52] K. Tsuzuki, K. Kuroda, K. Hashimoto et al., "Odontogenic chronic rhinosinusitis patients undergoing tooth extraction: oral surgeon and otolaryngologist viewpoints and appropriate management," *The Journal of Laryngology and Otology*, vol. 134, no. 3, pp. 241–246, 2020.

[53] B. J. Yoo, S. M. Jung, H. N. Lee, H. G. Kim, J. H. Chung, and J. H. Jeong, "Treatment strategy for odontogenic sinusitis," *American Journal of Rhinology & Allergy*, vol. 35, no. 2, pp. 206–212, 2021.

[54] K. Akiyama, Y. Nakai, Y. Samukawa, M. Miyake, and H. Hoshikawa, "Assessment of simultaneous surgery for odontogenic sinusitis," *The Journal of Craniofacial Surgery*, vol. 30, no. 1, pp. 239–243, 2019.

[55] R. Aukstakalnis, R. Simonaviciute, and R. Simuntis, "Treatment options for odontogenic maxillary sinusitis: a review," *Stomatologija*, vol. 20, no. 1, pp. 22–26, 2018.

[56] J. L. Mattos, B. J. Ferguson, and S. Lee, "Predictive factors in patients undergoing endoscopic sinus surgery for odontogenic sinusitis," *International Forum of Allergy & Rhinology*, vol. 6, no. 7, pp. 697–700, 2016.

[57] J. R. Craig, R. W. Tataryn, T. L. Aghaloo et al., "Management of odontogenic sinusitis: multidisciplinary consensus statement," *International Forum of Allergy & Rhinology*, vol. 10, no. 7, pp. 901–912, 2020.

Hindawi
Journal of Nanomaterials
Volume 2021, Article ID 9928051, 5 pages
https://doi.org/10.1155/2021/9928051

Research Article

Serum Hormone Levels, T Lymphocyte Subsets, and Achievement of Pregnancies in Patients with Premature Ovarian Insufficiency following Administration of Ethinylestradiol/Drospirenone

Jiewen Tao, Jing Wang, Weiqi Jiang, Qi Meng, and Mingjuan Xu

Changhai Hospital, Second Military Medical University, Shanghai, China

Correspondence should be addressed to Mingjuan Xu; xumjuan1@163.com

Received 25 March 2021; Revised 7 April 2021; Accepted 16 April 2021; Published 5 May 2021

Academic Editor: Songwen Tan

Primary ovarian insufficiency (POI) is closely associated with ovarian hormone deficiency, amenorrhea, menopause, and infertility in women. Hormone replacement therapy remains the mainstay of treatment and management of POI. A combined oral contraceptive (Yasmin) containing 0.02 mg ethinylestradiol and 3 mg drospirenone has been shown to be a well-tolerated and effective combination that provides high contraceptive reliability and good cycle control. Herein, we aim to examine clinical efficacy of ethinylestradiol/drospirenone in treating patients with POI and its effects on serum hormone levels, body mass, lipid metabolism, and T lymphocyte subsets. Retrospective analysis of clinical records and follow-up data from 80 patients with POI was performed. The control group contained 40 patients with POI receiving oral administration of 0.035 mg ethinylestradiol and 2 mg cyproterone acetate once a day for consecutive 21 days with drug withdrawal of 7 days in 3 months. The observation group contained 40 patients with POI receiving oral administration of 0.02 mg ethinylestradiol and 3 mg drospirenone once a day for consecutive 28 days in 3 months. There was no significant difference on serum levels of follicle stimulating hormone (FSH), luteinizing hormone (LH), and testosterone (T), concentrations of high- and low-density lipoprotein cholesterol (HDL-C and LDL-C), and triglycerides (TG), body mass, the numbers of CD^{+3}, CD^{+4}, CD^{+8} T cells, and ratio of CD^{+4}/CD^{+8} between the control and observation group ($P > 0.05$) before treatment. After treatment, serum levels of FSH, LH, and T, concentrations of LDL-C, and TG, body mass, and CD^{+8} T cells were reduced but the concentration of HDL-C, CD^{+3}, and CD^{+4} T cells and ratio of CD^{+4}/CD^{+8} were increased in both two groups ($P < 0.05$); these changes were more significant in the observation group compared with the control group ($P < 0.05$). Besides, the total response rate of the observation group was 90.00%, which is higher than that of the control group, 77.50% ($P < 0.05$). The pregnancy rate of the observation group was 45.00%, which is higher than that of the control group, 30.00% ($P < 0.05$). Taken together, these results suggest that the combined oral contraceptive (Yasmin) containing 0.02 mg ethinylestradiol and 3 mg drospirenone restores hormone levels, improves body mass and lipid metabolism, and sustains autoimmune function for patients with POI, suggesting ethinylestradiol/drospirenone treatment is effective in treating POI.

1. Introduction

Premature ovarian insufficiency (POI) refers to ovarian dysfunction or premature menopause which is defined as cessation of menstruation before the age of 40 [1]. Clinically, POI is associated with raised follicle-stimulating hormone, raised gonadotropins, and oestrogen deficiency. The disorder usually leads to infertility, menopausal symptoms, decreased bone density, psychological distress such as depression and anxiety [2, 3], and even increased risks of cardiovascular and neurological diseases [4]. According to recent evidence, the etiology for POI has been attributed to genetic defects, iatrogenic factors involving radiotherapy, chemotherapy, and surgery, and autoimmune; however, the majority of cases remain unexplained [5]. In recent years, stem cell therapy has attracted extensive attention in the field of regenerative

medicine, and it has been used in the treatment of reproductive system diseases, but there is no data to confirm whether the treatment can improve the therapeutic effect [6]. Many health complications correlated with POI are directly associated with ovarian hormone deficiency, mainly estrogen deficiency, and some reports reveal that appropriate physiologic estrogen and progestin replacement relieve menopausal symptoms, although trial data from Women's Health Initiative (WHI), which is a study of natural menopause women, indicated that multiple increased health risks related to use of estrogen/progestin therapy (EPT), but the results of the study to evaluate the HRT safety in natural postmenopausal female cannot be simply applied to female with POI. As for now, hormone replacement therapy (HRT) is the most efficient treatment for female with POI [2, 7, 8]. There are many drug delivery routes, doses, and types of oestrogen and progestin preparations for the treatment of female with POI [8]. In this study, clinical efficacy of ethinylestradiol/drospirenone in treating patients with POI and its effects on serum hormone levels, body mass, lipid metabolism, and T lymphocyte subsets.

2. Materials and Methods

2.1. Study Subjects. A total of 80 patients diagnosed with POI with complete clinical data, and follow-up data were retrospectively analyzed, and they were arranged into the control group with 40 cases and the observation group with 40 cases according to different treatment methods. The control group was treated with ethinylestradiol and cyproterone acetate, with age ranging from 30 to 40 years (34.21 ± 2.43 years). The observation group was treated with drospirenone ethinylestradiol tablets (II), with age ranging from 31 to 39 years (34.12 ± 3.36 years). Eligible study subjects should meet the following inclusion criteria: (a) menstrual cycle was changed for more than seven days, and the number of changes was more than two times; (b) follicle stimulating hormone (FSH) > 25 U/l; (c) anti-Müllerian hormone (AMH) < 1 ng/ml; (d) the informed content was obtained from included patients or their family members. POI patients complicated by immunological diseases such as systemic erythema and idiopathic thrombocytopenic purpura, with surgical histories involving ovariectomy, salpingectomy, uterine artery embolization, and oophorocystectomy, genital tract malformations, medical history of hormone drugs within 3 months, serious cardiac, liver, and kidney dysfunction, mental or cognitive disabilities, poor compliance to treatment protocols, and withdrawal from the study were excluded from this study. A one-year follow-up was performed to evaluate achievements of pregnancies. The study protocol was approved by the Ethics Committee of our hospital.

2.2. Treatment Protocols. The control group contained 40 patients with POI receiving oral administration of ethinylestradiol and cyproterone tablets (Zhejiang Xianju Pharmaceutical Co., Ltd., National Medicine Permission Number: H20065479, specifications: 0.035 mg ethinylestradiol and 2 mg cyproterone acetate) once a day for consecutive 21 days with drug withdrawal of 7 days in 3 months. The observation group contained 40 patients with POI receiving oral administration of drospirenone ethinylestradiol tablets (II) (Bayer Weimar GmbH und Co. Ltd., Registration Number: H20140972, specification: 0.02 mg ethinylestradiol and 3 mg drospirenone) once a day for consecutive 28 days in 3 months.

2.3. Blood Sample Collection. Two tubes of fasting blood were collected from each patient, and blood collection was performed twice a day before and after treatment. In brief, 5 ml of venous blood was extracted from each patient fasting for at least 8 hours by vacuum blood sampling needle each time and stored in a refrigerator under 4°C for 45 minutes. The agglutinated blood was centrifuged in a centrifuge with 3500 r/min for 15 minutes. The serum extracted from testing tube, which was immediately stored in a low-temperature refrigerator (MDF-U5412, SANYO, Japan) at -80°C.

2.4. Hormonal and Biochemical Measurements. Serum levels of testosterone (T), luteinizing hormone (LH), and FSH were measured by chemiluminescence immunoassay using commercial available kits (Shanghai Westang Bio-Tech Co., Ltd., China). Serum levels of triglycerides (TG) were determined by oxidase method, HDL-cholesterol (HDL) by synthetic polymer/detergent HDL-C assay (SPD method), and LDL-cholesterol (LDL) by surfactant LDL-C assay (SUR method) using commercial available kits (Shenzhen Jvfeng Co., Ltd., China). CD^{+3}, CD^{+4}, and CD^{+8} T cells were sorted out by XL-type flow cytometer (Beckman Coulter, USA) using commercial available kits (Sangon, Shanghai, China), and the ratio of CD^{+4}/CD^{+8} was calculated.

2.5. Body Mass Measures. The patient stands upright on the floor of the height meter, with the heel close together, the tip toe of the foot is 60 degrees, the arms naturally droop, and the eyes are looking at the front horizontally, getting the data with cm measurement unit; the patient naturally stands on the weight pound, getting the stable data with 0.1 kg accurate unit, and body mass index (BMI) formula = body mass/height^2, comparison on the pregnancy rate in the two groups during the follow-up period of 12 months.

2.6. Assessment of Clinical Response. Normal menstrual cycles and hormone levels [9] were defined as excellent response. Relative improvement in menstrual cycles and hormone levels were defined as good response. No improvement in clinical symptoms was defined as no response. Total response rate = (excellent + good) response/40 × 100%.

2.7. Statistical Analysis. All data were processed by the SPSS 23.0 software. The measurement data were defined as mean ± standard deviation and analyzed by the t-test. The counting data were described by ratio or percentage and analyzed by the chi-square test. A level of $P < 0.05$ was considered statistically significance.

3. Results

3.1. Ethinylestradiol/Drospirenone Treatment Significantly Restored Serum Hormone Levels of POI Patients. The serum

Table 1: Comparison of serum hormone levels before treatment and after treatment in the two groups.

Group	Case	Time	LH (mlU/ml)	FSH (mIU/ml)	T (g/dl)
Control group	40	Before treatment	10.56 ± 2.15	26.42 ± 5.24	75.21 ± 6.47
		After treatment	8.87 ± 2.25	19.25 ± 2.41	71.35 ± 4.32
t			4.127	8.169	6.594
P			0.033	0.001	0.001
Observation group	40	Before treatment	10.49 ± 1.84	26.33 ± 5.62	74.38 ± 6.21
		After treatment	6.13 ± 1.35[a]	15.73 ± 2.22[a]	50.54 ± 4.47[a]
t			8.065	15.468	21.837
P			0.001	0.001	0.001

The letter of a indicates $P < 0.05$ compared with the control group; t test was performed for statistical comparison; FSH: follicle growth hormone; LH: luteinizing hormone; T: testosterone.

Table 2: Comparison of body mass and lipid metabolism before treatment and after treatment in the two groups.

Group	Case	Time	HDL-C (mmoL/l)	LDL-C (mmoL/l)	TG (mmoL/l)	Body mass (kg/m^2)
Control group	40	Before treatment	1.56 ± 0.65	4.12 ± 1.24	1.95 ± 0.33	30.36 ± 3.52
		After treatment	2.01 ± 0.41	3.11 ± 0.56	1.35 ± 0.12	26.82 ± 3.29
t			3.941	4.528	5.719	10.227
P			0.037	0.029	0.014	0.001
Observation group	40	Before treatment	1.55 ± 0.64	3.23 ± 1.22	1.98 ± 0.31	32.31 ± 3.36
		After treatment	2.53 ± 0.24[a]	2.33 ± 0.45[a]	1.01 ± 0.16[a]	22.34 ± 3.32[a]
t			5.067	4.314	5.296	17.534
P			0.003	0.012	0.001	0.001

The letter of a indicates $P < 0.05$ compared with the control group; t test was performed for statistical comparison; HDL-C: high density lipid-cholesterol; LDL-C: low density lipid-cholesterol; TG: triglycerides.

levels of LH, FSH, and T in the observation group were not remarkably different from those in the control group before treatment ($P > 0.05$). The serum levels of LH, FSH, and T were reduced after treatment in both two groups. The serum levels of LH, FSH, and T in the observation group were lower than those in the control group ($P < 0.05$, Table 1), suggesting that ethinylestradiol/drospirenone treatment significantly restored serum hormone levels of POI patients.

3.2. Ethinylestradiol/Drospirenone Treatment Significantly Improved Body Mass and Lipid Metabolism in POI Patients. POI is associated with the occurrence of osteoporosis, abnormal lipid metabolism, and cardiovascular disease in women. In this part, we compared the effects of ethinylestradiol and ethinylestradiol/drospirenone treatment on body mass and lipid metabolism in POI patients. Before treatment, there was slightly difference in body mass and lipid metabolism in the two groups ($P > 0.05$). After treatment, body mass and lipid metabolism in the two groups were improved ($P < 0.05$). It was revealed that the improvement in the observation group was greater than that in the control group ($P < 0.05$, Table 2).

3.3. Ethinylestradiol/Drospirenone Treatment Significantly Increased T-Lymphocyte Subpopulations. Previous evidence showed that POI may result from autoimmune dysregulation characterized by reduced T cells. The numbers of CD^{+3} and CD^{+4} T cells and the ratio of CD^{+4}/CD^{+8} were increased in the two groups but the number of CD^{+8} T cells was declined after treatment ($P < 0.05$). The observation group had more CD^{+3} and CD^{+4} T cells, higher ratio of CD^{+4}/CD^{+8}, and fewer CD^{+8} T cells than the control group ($t = 4.169$, $P = 0.018$; $t = 3.475$, $P = 0.023$; $t = 3.846$, $P = 0.0.017$; $t = 4.218$, $P = 0.012$, Table 3). These data showed that ethinylestradiol/drospirenone treatment could sustain autoimmune function in POI patients.

3.4. Ethinylestradiol/Drospirenone Treatment Remarkably Improved Clinical Response of POI Patients. The total response rate in the observation group was 90.00%, including 24 cases (60.00%) defined as excellent response, 12 cases (30.00%) defined as good response, and 4 cases (10.00%) defined as no response. The total response rate in the control groups was 77.50%, including 20 cases (50.00%) defined as excellent response, 11 cases (27.50%) defined as good response, and 9 cases (22.50%) defined as no response. The total response rate in the observation groups was higher than that in control group ($\chi^2 = 6.284$, $P < 0.05$, Figure 1).

3.5. Ethinylestradiol/Drospirenone Treatment Yielded Better Achievement of Pregnancies for POI Patients. After 1-year follow-up, there were 18 pregnant women out of 40 cases in the observation group, and the pregnancy rate was 45.00%. There were 12 pregnant women out of 40 cases in the control

Table 3: Comparison of T cell subpopulations before treatment and after treatment in the two groups.

Group	Case	Time	CD^{+4} (%)	CD^{+8} (%)	CD^{+3} (%)	CD^{+4}/CD^{+8}
Control group	40	Before treatment	36.56 ± 10.52	40.14 ± 11.05	54.33 ± 12.85	0.82 ± 0.36
		After treatment	40.29 ± 10.43	35.37 ± 10.48	59.94 ± 12.57	1.21 ± 0.39
t			7.143	8.017	6.247	6.475
P			0.001	0.001	0.001	0.001
Observation group	40	Before treatment	36.46 ± 10.03	40.12 ± 11.06	53.91 ± 12.87	0.84 ± 0.34
		After treatment	48.14 ± 11.04[a]	30.19 ± 10.10[a]	64.65 ± 10.99[a]	1.63 ± 0.35[a]
t			10.542	19.102	21.719	6.839
P			0.001	0.001	0.001	0.001

The letter of a indicates $P < 0.05$ compared with the control group; t test was performed for statistical comparison.

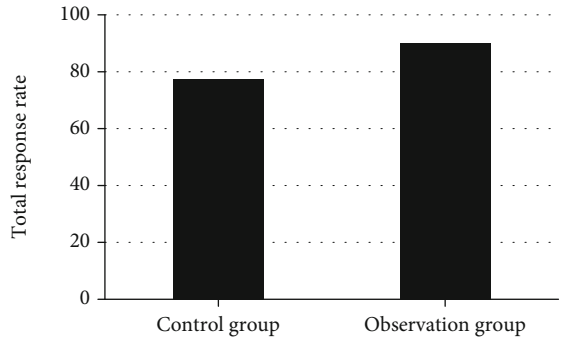

Figure 1: The total response rate in the observation and control group. Chi-square test was performed for statistical comparison.

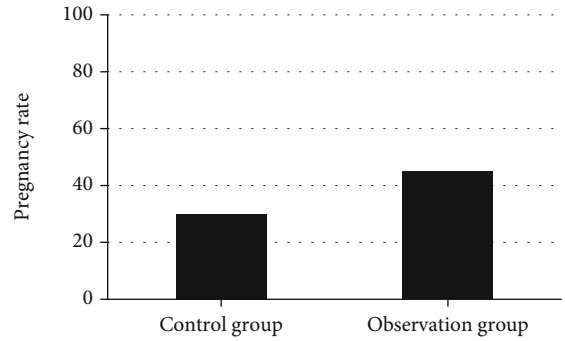

Figure 2: The pregnancy rate in the observation and control group. Chi-square test was performed for statistical comparison.

group, and the pregnancy rate was 30.00%. The pregnancy rate was higher in the observation group than that in the control group ($\chi^2 = 3.425$, $P < 0.05$, Figure 2).

4. Discussion

Women with POI experience sustained sex steroid deficiency for longer periods compared with women who experienced normal menopause. Management for POI includes hormonal replacement therapy up to at least age 50, counseling and emotional support, and calcium and vitamin supplements [10, 11]. Evidence suggests that pregnancies might occur in women with primary ovarian insufficiency when high FSH concentrations are declined by ethinyloestradiol or gonadotrophin-releasing hormone analogues, followed by ovulation induction using low dose gonadotrophins [12]. However, there are no published prospective trials supporting the hypothesis that reduction of FSH concentrations allows development of follicles. Recently, a novel hormonal approach to optimize fertility for POI patients has been reported [13]. Estrogen-progestogen therapy combined with dehydroepiandrosterone and melatonin could optimize fertility and result in successful pregnancy in POI patients. However, management of POI is still a challenging issue for clinicians, and women with POI have a higher risk of infertility. In this study, we retrospectively analyzed 80 POI patients among which 40 received oral administration of ethinyloestradiol and 40 received oral administration of ethinylestradiol/drospirenone. Results revealed that ethinylestradiol/drospirenone can reduce levels of serum FSH, LH, and T and improve clinical efficiency, body mass, and lipid metabolism.

POI patients were characterized by elevated serum FSH, LH, and T levels [2, 14, 15]. It was found that patients with oral administration of ethinylestradiol/drospirenone exhibited lower serum FSH, LH, and T levels than those with oral administration of ethinylestradiol alone. A previous randomized controlled trial showed the combined oral contraceptive Yasmin (drospirenone 3 mg plus ethinylestradiol 30 microg [DRSP 3 mg/EE 30 microg]) is a well-tolerated and effective combination that provides high contraceptive reliability and good cycle control [16]. Another randomized, open-label, controlled, multicentre trial performed in healthy Chinese women found that ethinylestradiol plus drospirenone showed a more favorable effect on weight and premenstrual symptoms than ethinylestradiol plus desogestrel [17]. Another finding of our study showed that ethinylestradiol plus drospirenone improved body mass and lipid metabolism of POI patients more significantly than ethinylestradiol alone. In a randomized study conducted by Gaspard et al. [18], they made a conclusion that the combined low-dose oral administration of Yasmin displayed a favorable lipid profile with increased total HDL cholesterol. Yasmin may be regarded as responsible for the stable LDL cholesterol levels due to its antiandrogenic or missing androgenic activity. Anttila et al. performed a pooled analysis and found a 24/4 regimen of drospirenone 3 mg/ethinylestradiol 20 μg is

associated with a bleeding profile and cycle control [19]. It is believed that ethinylestradiol plus drospirenone (Yasmin) could effectively inhibit androgen levels in the oarium, leading to the decrement in plasma free testosterone level and free androgen index. Previous evidence showed that POI may result from autoimmune dysregulation characterized by reduced T cells [20]. POI appears to be a complex disease entity with multiple underlying etiopathogenic contributions including the possibility of several distinctly different autoimmune mechanisms [21]. Another finding of our study is elevated T-lymphocyte subpopulations in POI patients following ethinylestradiol/drospirenone treatment, suggesting that ethinylestradiol/drospirenone treatment could sustain autoimmune function in POI patients.

In conclusion, ethinylestradiol plus drospirenone (Yasmin) could significantly restore hormone levels, improve body mass and lipid metabolism, sustain autoimmune function, and increase clinical curative effects, and it merits further promotion in clinic. However, sample size is relatively small, which is a limitation for the present study. Further investigation should be warrant in large sample size.

Data Availability

The data used to support the findings of this study are included within the article.

Conflicts of Interest

The authors declare that they have no conflicts of interest.

Authors' Contributions

Jiewen Tao and JingWang contributed to the work equally and should be regarded as co-first authors.

References

[1] J. S. Laven, "Primary ovarian insufficiency," *Seminars in Reproductive Medicine*, vol. 34, no. 4, pp. 230–234, 2016.

[2] S. D. Sullivan, P. M. Sarrel, and L. M. Nelson, "Hormone replacement therapy in young women with primary ovarian insufficiency and early menopause," *Fertility and Sterility*, vol. 106, no. 7, pp. 1588–1599, 2016.

[3] A. Podfigurna-Stopa, A. Czyzyk, M. Grymowicz et al., "Premature ovarian insufficiency: the context of long-term effects," *Journal of Endocrinological Investigation*, vol. 39, no. 9, pp. 983–990, 2016.

[4] S. Tsiligiannis, N. Panay, and J. C. Stevenson, "Premature ovarian insufficiency and long-term health consequences," *Current Vascular Pharmacology*, vol. 17, no. 6, pp. 604–609, 2019.

[5] M. De Vos, P. Devroey, and B. C. Fauser, "Primary ovarian insufficiency," *Lancet*, vol. 376, no. 9744, pp. 911–921, 2010.

[6] J. Na and G. J. Kim, "Recent trends in stem cell therapy for premature ovarian insufficiency and its therapeutic potential: a review," *Journal of ovarian research*, vol. 13, no. 1, p. 74, 2020.

[7] L. Webber, R. A. Anderson, M. Davies, F. Janse, and N. Vermeulen, "HRT for women with premature ovarian insufficiency: a comprehensive review," *Human reproduction open*, vol. 2017, no. 2, article hox007, 2017.

[8] P. Machura, M. Grymowicz, E. Rudnicka et al., "Premature ovarian insufficiency - hormone replacement therapy and management of long-term consequences," *Przeglad menopauzalny= Menopause review*, vol. 17, no. 3, pp. 135–138, 2018.

[9] L. A. Cole, D. G. Ladner, and F. W. Byrn, "The normal variabilities of the menstrual cycle," *Fertility and Sterility*, vol. 91, no. 2, pp. 522–527, 2009.

[10] A. J. Fenton, "Premature ovarian insufficiency: pathogenesis and management," *Journal of mid-life health*, vol. 6, no. 4, pp. 147–153, 2015.

[11] S. Luisi, C. Orlandini, C. Regini, A. Pizzo, F. Vellucci, and F. Petraglia, "Premature ovarian insufficiency: from pathogenesis to clinical management," *Journal of Endocrinological Investigation*, vol. 38, no. 6, pp. 597–603, 2015.

[12] J. H. Check, "Mild ovarian stimulation," *Journal of Assisted Reproduction and Genetics*, vol. 24, no. 12, pp. 621–627, 2007.

[13] S. Dragojevic Dikic, M. Vasiljevic, A. Jovanovic et al., "Premature ovarian insufficiency - novel hormonal approaches in optimizing fertility," *Gynecological Endocrinology*, vol. 36, no. 2, pp. 162–165, 2020.

[14] S. Sahmay, T. A. Usta, T. Erel, N. Atakul, and B. Aydogan, "Elevated LH levels draw a stronger distinction than AMH in premature ovarian insufficiency," *Climacteric*, vol. 17, no. 2, pp. 197–203, 2014.

[15] S. N. Kalantaridou, K. A. Calis, V. H. Vanderhoof et al., "Testosterone deficiency in young women with 46,XX spontaneous premature ovarian failure," *Fertility and Sterility*, vol. 86, no. 5, pp. 1475–1482, 2006.

[16] S. Kelly, E. Davies, S. Fearns et al., "Effects of oral contraceptives containing ethinylestradiol with either drospirenone or levonorgestrel on various parameters associated with well-being in healthy women: a randomized, single-blind, parallel-group, multicentre study," *Clinical Drug Investigation*, vol. 30, no. 5, pp. 325–336, 2010.

[17] F. Guang-Sheng, B. Mei-Lu, C. Li-Nan et al., "Efficacy and safety of the combined oral contraceptive ethinylestradiol/-drospirenone (Yasmin) in healthy Chinese women: a randomized, open-label, controlled, multicentre trial," *Clinical Drug Investigation*, vol. 30, no. 6, pp. 387–396, 2010.

[18] U. Gaspard, J. Endrikat, J. P. Desager, C. Buicu, C. Gerlinger, and R. Heithecker, "A randomized study on the influence of oral contraceptives containing ethinylestradiol combined with drospirenone or desogestrel on lipid and lipoprotein metabolism over a period of 13 cycles," *Contraception*, vol. 69, no. 4, pp. 271–278, 2004.

[19] L. Anttila, W. Neunteufel, F. Petraglia, J. Marr, and M. Kunz, "Cycle control and bleeding pattern of a 24/4 regimen of drospirenone 3 mg/ethinylestradiol 20 mug compared with a 21/7 regimen of desogestrel 150 mug/ethinylestradiol 20 mug: a pooled analysis," *Clinical Drug Investigation*, vol. 31, no. 8, pp. 519–525, 2011.

[20] A. La Marca, A. Brozzetti, G. Sighinolfi, S. Marzotti, A. Volpe, and A. Falorni, "Primary ovarian insufficiency: autoimmune causes," *Current Opinion in Obstetrics & Gynecology*, vol. 22, no. 4, pp. 277–282, 2010.

[21] V. K. Tuohyand and C. Z. Altuntas, "Autoimmunity and premature ovarian failure," *Current Opinion in Obstetrics & Gynecology*, vol. 19, pp. 366–369, 2007.

Hindawi
Journal of Nanomaterials
Volume 2021, Article ID 9920481, 5 pages
https://doi.org/10.1155/2021/9920481

Research Article

Values of Magnetic Resonance Imaging and Computed Tomography in the Diagnosis of Patients with Syndromes of Subacromial Impingement

Xingfang Jiang,[1,2] Zhiyan Guo,[2] Linlin Hu,[2] Pan Liu,[3] Leiming Xu,[1] and Jiangfeng Pan[2]

[1]*The Second Affiliated Hospital of Zhejiang University, China*
[2]*Affiliated Jinhua Hospital, Zhejiang University, China*
[3]*Beijing Friendship Hospital, Capital Medical University, China*

Correspondence should be addressed to Leiming Xu; zmjidf@163.com and Jiangfeng Pan; panjiangfeng967@163.com

Received 26 March 2021; Revised 2 April 2021; Accepted 5 April 2021; Published 30 April 2021

Academic Editor: Songwen Tan

Subacromial impingement syndrome (SIS) is defined as pressurization and impingement between the acromion, the bursa under the acromion, and the rotator cuff during the abduction and elevation of the shoulder joint, resulting in pain and a functional disturbance of elevation. It is the most common disorder of the shoulder, accounting for 44-65% of all complaints of shoulder pain during a physician's office visit. The study was performed with the aim of valuing the magnetic resonance imaging (MRI) and computed tomography (CT) in diagnosing patients with SIS. A total of 68 patients with SIS were selected as study subjects and subjected to MRI and CT examinations. The diagnostic accuracy and sensitivity of MRI and CT were, respectively, 97.06 and 70.59% ($P < 0.05$); the detection rates of SIS grade I, grade II, and grade III by MRI were 91.67%, 96.77%, and 100%, respectively, which were significantly higher than 50%, 80.65%, and 68% by CT, respectively ($P < 0.05$). MRI and CT detection indicated that there was no significant difference in extensive rotator cuff tear, acromion stenosis, and normal acromion detected by MRI and CT ($P > 0.05$). In conclusion, the diagnostic accuracy, sensitivity, and detection rate of acromion of MRI were higher compared with those of CT examination, and MRI is more suitable in the clinical diagnosis of SIS.

1. Introduction

Subacromial impingement syndrome (SIS), as a result of the compression of suprahumeral structures, is a frequent cause of chronic anterior shoulder pain concomitant with limited range of motion, accounting for 50-70% of main complaints of shoulder pain in primary health care [1, 2]. SIS is characterized by a series of pathological changes, ranging from subacromial bursitis to rotator cuff tendinitis and full-thickness rotator cuff tear [3]. According to Roy et al. [4], SISs can be broadly classified into external or internal types. External impingement is caused by abnormal contact between the humeral head and extra-articular structures, thus resulting in subacromial or subcoracoid impingement. Internal impingement usually affects overhead-throwing athletes [5] and involves the structures located between the humeral head and the glenoid, which is separated into posterosuperior and anterosuperior subtypes. SIS encompasses a spectrum of subacromial pathologies, including rotator cuff tears, rotator cuff tendinosis, calcific tendinitis, tendonitis, and bursitis of the shoulder [6]. Results vary as different clinical tests, and imaging is helpful in evaluating the signs of SIS [7]. Magnetic resonance imaging (MRI) is an excellent noninvasive tool for the diagnosis of the pathologies of the shoulder [1, 8]. This imaging method has been reported to effectively demonstrate the soft tissue lesions upon SIS [9]. Computed tomography (CT) arthrography is a cost-effective, useful method used for the preoperative assessment of various shoulder pathologies, such as full-thickness rotator cuff tears [10] In this study, the MRI and CT technologies were performed to diagnose SIS, and the clinical pathological results were taken as the gold standard to analyze the diagnostic value of the MRI and CT technologies in diagnosing SIS, with focus on acromion morphology and A-H distance, in a bid to

seek a scientific and effective way for the early diagnosis of SIS and to improve function recovery of patients.

2. Material and Methods

2.1. Eligibility of Study Subjects. In total, our study enrolled 68 patients who were diagnosed with SIS and received treatment in our hospital from July 2017 to September 2019. There were 35 males and 33 females, with age ranging from 25 to 70 years and with an average age of 47.56 ± 4.21 years, including 38 right shoulders with SIS and 30 left shoulders with SIS. Inclusion criteria were as follows: (a) diagnostic criteria of SIS, (b) the age is more than 25 years old, and (c) all signed the informed consent issued by the Ethics Committee of our hospital. Exclusion criteria were as follows: (a) patients with severe organic diseases of the cardiac, liver, and kidney; (b) patients with mental disorders; (c) patients with imaging contraindications; (d) patients complicated with severe cardiovascular and cerebrovascular diseases; and (e) patients with allergy to lidocaine.

2.2. Diagnosis of SIS. Diagnosis of SIS was performed as previously reported [11]. SIS is diagnosed if the patients have the following three or more symptoms: (a) a tenderness over the anterior margin of the acromion. (b) Neer impingement test shows a positive sign; the patient remains in a sitting position, while the examiner stands by the side of the patient's body with his scapula in one hand, passively elevating the affected arm from the ventral direction to cause impingement between the greater tuberosity and the acromion; a positive sign was described as pain from 60 to 120 abduction. (c) The pain of the shoulder joint in active activity is significantly stronger than that in passive activity. (d) Pain is felt upon shoulder abduction. (e) There are osteophytes on the acromion.

2.3. MRI and CT Examinations. All patients were examined by MRI and CT. A 1.5-Tesla Espree MRI scanner (Siemens, Erlangen, Germany) was used to examine the patient who was kept in the supine position, with lateral shoulder joint as the neutral position. A turbo spin-echo (TSE) sequence and a 3 cm diameter loop coil were applied, with parameters as below: parameters of T_2WI FS in the routine scanning axial position were set as TE 80 and TR 5400; T_1WI in the oblique coronal position was TE 20 and TR 500; PDWI was TE 30 and TR 4400; T_2WI was TE 100 and TR 4000. The parameters of T_2WI FS in the oblique position were TE 30 and TR 4400 with 3 mm thickness and 0.3 mm layer distance, FOV is $160 \times 160 \times 80$, and the matrix is 250×250. For CT examination, a 64-slice spiral CT (Philips, USA) was used, with scanning parameters set as follows: 120 kV tube voltage, 250 mAs tube current, 1 mm collimation, 5 mm scanning thickness, and 60 cm FOV were performed from the subscapular angle to the coracoid process. The images were uploaded to the ADW4.2 image processing workstation for processing, and the images were analyzed by three senior doctors.

2.4. Bigliani Classification and Acromion Humeral (A-H) Distance. Bigliani classification [12] was performed to type the acromion morphology of these SIS patients. Flat acromion was defined as type I, curved acromion as type II, and hooked acromion as type III. Besides, the A-H distance was measured by MRI and CT [13]. A-H distance less than 0.5 cm was defined as an extensive rotator cuff tear, 0.5-1.0 cm as an acromion stenosis, and 1.0-1.5 cm as a normal acromion.

Table 1: More SIS patients were diagnosed by MRI than CT.

Examination method	Accuracy	Sensitivity	Specificity
MRI	97.06	97.06	100.00
CT	70.59	70.59	100.00

MRI: magnetic resonance imaging; CT: computed tomography.

2.5. Statistics. SPSS 20.0 software (IBM Corp., Armonk, NY) was used to process the data, and a chi-square test was performed for statistical analysis. $P < 0.05$ was considered to be statistically significance at a level of 5% (two-tailed).

3. Results

3.1. More SIS Patients Were Diagnosed by MRI than CT. In this study, a total of 68 patients were diagnosed as SIS by pathology. MRI examination confirmed 66 patients with SIS, 2 cases were missed, and none was misdiagnosed. CT examination confirmed 48 patients with SIS, 17 cases were missed, and 3 cases were misdiagnosed. These results suggested that MRI exhibited a better diagnostic performance for SIS than CT. As shown in Table 1, the diagnostic accuracy of MRI was 97.06% which was significantly higher than the 70.59% of CT ($\chi^2 = 17.569$, $P < 0.05$). The sensitivity of MRI was 97.06% which was significantly higher than the 70.59% of CT ($P < 0.05$).

3.2. MRI and CT Presentations. All 66 patients presented abnormal signal intensity on MRI and morphology in the supraspinatus tendon (Figures 1(a) and 1(b)), among which 22 patients (33%) with normal supraspinatus tendon and patchy hyperintense T2WI signal, 26 patients (40%) with increased or decreased thickness in supraspinatus tendon with abnormal and mingle signal, 13 patients (20%) with calcified tendinitis of supraspinatus muscle and nodule low T1WI and T2WI signals and high-density shadow in DR at 1-2 cm away from the greater tuberosity of the humerus, and 5 patients (7%) with full-thickness tears of the supraspinatus tendon, involving continuous hypointense signal interruption on oblique coronal T2WI, intermediate signal intensity on T1WI, and hyperintense signal intensity on T2WI. The patients mainly presented supraspinatus tendon injury on MRI, including 63 patients with thickened subacromial bursa with effusion, 41 patients with effusion in the shoulder joint, and 36 cases with glenoid labrum tear (Figures 1(c) and 1(d)). Results of CT examination showed 21 patients with hyperosteogeny in the acromion and acromioclavicular joint (Figure 1(e)), 28 cases with subacromial distance stenosis, 18 cases with the greater tuberosity of the humerus sclerosis, and 16 cases with calcification in the long head tendon and supraspinatus tendon of the musculus biceps brachii.

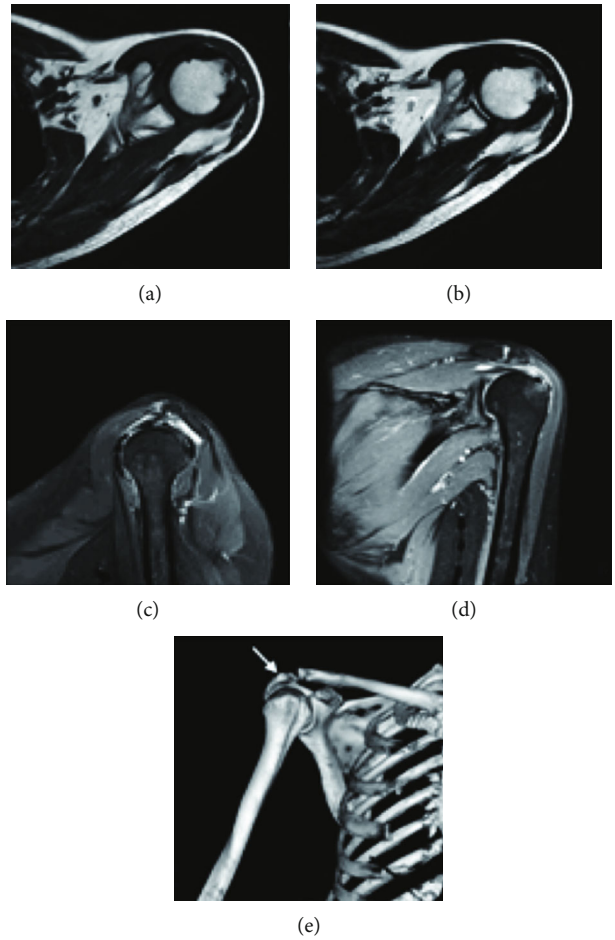

Figure 1: MRI and CT images of patients with SIS. T1WI (a) and T2WI (b) examined by MRI, which indicated the swelling condition of the supraspinatus tendon and uneven signal; oblique (c) and coronal (d) positions detected by MRI—partial tear of the supraspinatus tendon is shown in (c) and subacromial bursitis is seen in (d); (e) the CT three-dimensional reconstruction image of hook grade acromion, and hyperosteogeny occurred in the acromion margin.

3.3. Detection Rates of Acromion Morphology by MRI and CT. After pathological examination, there were 8 cases of grade I, 22 cases of grade II, and 38 cases of grade III. As shown in Table 2, the detection rates of grade I, grade II, and grade III by MRI were 91.67%, 96.77%, and 100%, respectively, which were significantly higher than 50.00%, 80.65%, and 68.00% by CT, respectively ($P < 0.05$).

3.4. Detection of A-H Distance by MRI and CT. Measurement of the A-H distance could be used to assess the impact of rehabilitation or surgical interventions for rotator cuff tendinopathy. The A-H distance less than 0.5 cm was defined as an extensive rotator cuff tear, 0.5-1.0 cm as an acromion stenosis, and 1.0-1.5 cm as a normal acromion. MRI and CT detection indicated that there was no significant difference in extensive rotator cuff tear, acromion stenosis, and normal acromion detected by MRI and CT ($P < 0.05$, Table 3).

Table 2: Detection rates of acromion morphology by MRI and CT.

Examination method	Grade I ($n = 12$)	Grade II ($n = 31$)	Grade III ($n = 25$)
MRI	11 (91.67)	30 (96.77)	25 (100)
CT	6 (50.00)	25 (80.65)	17 (68.00)
χ^2	5.042	4.026	9.524
P	0.025	0.045	0.002

MRI: magnetic resonance imaging; CT: computed tomography.

Table 3: Detection of A-H distance (cm) by MRI and CT.

	A-H distance < 0.5	A-H distance between 0.5 and 1.0	A-H distance between 1.0 and 1.5
MRI	10 (15.15)	19 (28.79)	37 (56.06)
CT	8 (16.67)	15 (31.25)	25 (52.08)

MRI: magnetic resonance imaging; CT: computed tomography.

4. Discussion

SIS represents a spectrum of pathology ranging from subacromial bursitis to rotator cuff tendinopathy and full-thickness

rotator cuff tears. When the shoulder is abducted or lifted, repeated friction and impingement between the humerus and the acromion tissue leads to rotator cuff tear, tissue damage under the acromion, and functional degeneration. Shoulder function impairment and pain are the main clinical symptoms of SIS [3]. The diagnosis of SIS is based on the physical examination or history of patients. However, in clinical treatment, doctors should analyze the pathology degree of disease, A-H distance, and shoulder peak shape before appropriate treatments.

The pathological changes of SIS mainly include three stages [14]. In the first stage, hemorrhage and edema appeared in the acromion bursa and rotator cuff; in the second stage, obvious tendinitis and rotator cuff fibrosis appeared with thickening and partial cuff tearing; and in the third stage, full thickness tendon tears, bony changes, and tendon ruptures were observed [14]. In the clinic, MR multiplanar imaging is routinely used for the diagnosis of rotator cuff diseases. The main scanning planes are axial, oblique coronal, and oblique sagittal. Axial MRI can clearly show the shoulder joint capsule, the long head of the biceps femoris tendon, and the glenoid labrum of the shoulder; oblique coronal MRI clearly represents the rotator cuff and its muscle groups, acromion bursa, which is more sensitive to supraspinatus tendon injury and its surrounding bursa and fat layer lesion distribution; oblique sagittal MRI indicates the rotator cuff structure in the same layer and the tissue structure in the subacromial channel, which improve the diagnosis accuracy of rotator cuff injury and show the morphology of acromion perfectly. The normal supraspinatus tendon is oval or flat with a smooth edge and 1.0-1.2 cm thickness, and it connects to supraspinatus muscle at the 12 o'clock direction of the humeral head moving forward outside, gradually getting thinner and ending above the greater tubercle of the humerus. MRI shows a slightly hyperintense signal on T1WI and a hypointense signal on T2WI. The muscle tendon attachment is wide with a heterogeneous signal. In the early stage of the rotator cuff injury, enhanced strip signals of PDWI and T1WI in the tendon were observed by MRI. The tendons were notably thickened, with an unclear outline. In the middle stage of the rotator cuff injury, the patients with high signal intensity both on T1WI and T2WI were observed by MRI [15]. The direct signs of MRI are divided into two types: continued and interrupted tendons, retraction of the broken end, and increased signal intensity are diagnosed as a complete tear; increased signal intensity, morphological change, and rough edge are diagnosed as an incomplete tear. In this study, MRI and CT technologies were applied in the diagnosis of SIS. It was found that the diagnostic accuracy and sensitivity of MRI for SIS were significantly higher than that of CT, suggesting that MRI has a better diagnostic value. MRI potentially offers improved soft tissue contrast and spatial resolution, providing increased image detail, and it can clearly display bone joint and lesion tissue, with high resolution, multiple sequences, directions, and parameters [16]. MRI can evaluate the extent and configuration of rotator cuff abnormalities, document abnormalities of the cuff muscles and adjacent structures, and suggest mechanical imbalance within the cuff [17]. MRI can also provide information about RCT including tear dimensions, tear depth or thickness, tendon retraction, and tear shape that is required for optimal treatment planning and prognostic accuracy [18]. In this study, the detection rates of type I, type II, and type III after MRI examination were 91.67%, 96.77%, and 100%, respectively, which were significantly higher than those after examination (50.00%, 80.65%, and 68.00%, respectively), suggesting that MRI has a higher detection rate than CT in examining acromion morphology. MRI and CT examinations found that the normal subacromial distance of SIS patients was significantly higher than that of narrow acromial and extensive rotator cuff tears, but the detection rate of the normal subacromial distance of MRI was slightly higher than that of CT examination. MRI may show the degree of rotator cuff injury of SIS patients more clearly, but it is not clear when used to scan the acromial osteophyte and acromial shape. In the study reported by Rour and Jongsoon [19], MRI results revealed that patients with grade III SIS were more likely to have rotator cuff injury and outlet stenosis. The rotator cuff injury is mainly caused by the mechanical compression of the acromion to the rotator cuff in SIS. It can be seen that there is a close relevance between subacromial space stenosis and rotator cuff injury. The narrower the subacromial space stenosis is, the more prone to injury. Akyol et al. [20] reported that there was positive relevance among the incidence of acromion osteophyma, lesion extent, and patient's age. However, we could not perform age-stratified analysis due to the small sample size. In the future, we will recruit more SIS patients for age-stratified analysis to strength the diagnostic value of MRI for SIS.

In conclusion, MRI has higher diagnostic value than CT in SIS, exhibiting better detection rate in the diagnosis of the acromion shape and A-H distance. MRI can provide more comprehensive evidence for the clinical diagnosis and treatment of SIS.

Data Availability

The data used to support the findings of this study are included within the article.

Conflicts of Interest

The authors declare that they have no conflicts of interest.

References

[1] A. R. Shire, T. A. B. Staehr, J. B. Overby, M. Bastholm Dahl, J. Sandell Jacobsen, and D. Hoyrup Christiansen, "Specific or general exercise strategy for subacromial impingement syndrome-does it matter? A systematic literature review and meta analysis," *BMC musculoskeletal disorders*, vol. 18, no. 1, p. 158, 2017.

[2] C. Mitchell, A. Adebajo, E. Hay, and A. Carr, "Shoulder pain: diagnosis and management in primary care," *BMJ*, vol. 331, no. 7525, pp. 1124–1128, 2005.

[3] A. K. Harrison and E. L. Flatow, "Subacromial impingement syndrome," *The Journal of the American Academy of Orthopaedic Surgeons*, vol. 19, no. 11, pp. 701–708, 2011.

[4] E. A. Roy, I. Cheyne, G. T. Andrews, and B. B. Forster, "Beyond the cuff: MR imaging of labroligamentous injuries in the athletic shoulder," *Radiology*, vol. 278, no. 2, pp. 316–332, 2016.

[5] D. J. Lin, T. T. Wong, and J. K. Kazam, "Shoulder injuries in the overhead-throwing athlete: epidemiology, mechanisms of injury, and imaging findings," *Radiology*, vol. 286, no. 2, pp. 370–387, 2018.

[6] L. Gebremariam, E. M. Hay, R. van der Sande, W. D. Rinkel, B. W. Koes, and B. M. Huisstede, "Subacromial impingement syndrome–effectiveness of physiotherapy and manual therapy," *British Journal of Sports Medicine*, vol. 48, no. 16, pp. 1202–1208, 2014.

[7] L. Pesquer, S. Borghol, P. Meyer, M. Ropars, B. Dallaudiere, and P. Abadie, "Multimodality imaging of subacromial impingement syndrome," *Skeletal Radiology*, vol. 47, no. 7, pp. 923–937, 2018.

[8] S. Shinagawa, K. Okamura, Y. Yonemoto et al., "Shoulder tenderness was associated with the inflammatory changes on magnetic resonance imaging in patients with rheumatoid arthritis," *Scientific reports*, vol. 9, no. 1, article 19599, 2019.

[9] D. Norenberg, M. Armbruster, Y. N. Bender et al., "Diagnostic performance of susceptibility-weighted magnetic resonance imaging for the assessment of sub-coracoacromial spurs causing subacromial impingement syndrome," *European Radiology*, vol. 27, no. 3, pp. 1286–1294, 2017.

[10] J. H. Oh, J. Y. Kim, J. A. Choi, and W. S. Kim, "Effectiveness of multidetector computed tomography arthrography for the diagnosis of shoulder pathology: comparison with magnetic resonance imaging with arthroscopic correlation," *Journal of Shoulder and Elbow Surgery*, vol. 19, no. 1, pp. 14–20, 2010.

[11] R. Diercks, C. Bron, O. Dorrestijn et al., "Guideline for diagnosis and treatment of subacromial pain syndrome," *Acta Orthopaedica*, vol. 85, no. 3, pp. 314–322, 2014.

[12] O. Le Reun, J. Lebhar, F. Mateos, J. L. Voisin, H. Thomazeau, and M. Ropars, "Anatomical and morphological study of the subcoracoacromial canal," *Orthopaedics & Traumatology, Surgery & Research*, vol. 102, no. 8, pp. S295–S299, 2016.

[13] K. M. McCreesh, "Acromiohumeral distance measurement in rotator cuff tendinopathy: is there a reliable, clinically applicable method? A systematic review," *British Journal of Sports Medicine*, vol. 49, no. 5, pp. 298–305, 2015.

[14] L. A. Michener, P. W. McClure, and A. R. Karduna, "Anatomical and biomechanical mechanisms of subacromial impingement syndrome," *Clinical Biomechanics (Bristol, Avon)*, vol. 18, no. 5, pp. 369–379, 2003.

[15] C. Sasiponganan, R. Dessouky, O. Ashikyan et al., "Subacromial impingement anatomy and its association with rotator cuff pathology in women: radiograph and MRI correlation, a retrospective evaluation," *Skeletal Radiology*, vol. 48, no. 5, pp. 781–790, 2019.

[16] M. Freygant, E. Dziurzynska-Bialek, W. Guz et al., "Magnetic resonance imaging of rotator cuff tears in shoulder impingement syndrome," *Polish Journal of Radiology*, vol. 79, pp. 391–397, 2014.

[17] J. T. Aoyama, P. Maier, S. Servaes et al., "MR imaging of the shoulder in youth baseball players: anatomy, pathophysiology, and treatment," *Clinical Imaging*, vol. 57, pp. 99–109, 2019.

[18] Y. Morag, J. A. Jacobson, B. Miller, M. De Maeseneer, G. Girish, and D. Jamadar, "MR imaging of rotator cuff injury: what the clinician needs to know," *Radiographics*, vol. 26, no. 4, pp. 1045–1065, 2006.

[19] L. D. Rour and K. L. Jongsoon, "Internal- and external-rotation peak toque in little league baseball players with subacromial impingement syndrome: improved by closed kinetic chain shoulder training," *Journal of Sport Rehabilitation*, vol. 25, pp. 263–265, 2016.

[20] Y. Akyol, Y. Ulus, D. Durmus, B. Tander, and Y. Bek, "Shoulder muscle strength in patients with subacromial impingement syndrome: its relationship with duration of quality of life and emotional status," *Ftr Turkiye Fiziksel Tip Ve Rehabilitasyon Dergisi*, vol. 59, no. 3, pp. 176–181, 2013.

Hindawi
Journal of Nanomaterials
Volume 2021, Article ID 9918812, 6 pages
https://doi.org/10.1155/2021/9918812

Research Article

Magnetic Resonance Imaging Classifications of Rotator Cuff Tear Are Associated with Different Shoulder Outcome Scores

Xingzhen Hu, Xiaoxing Wang, Weisi Mao, Lingling Ying, and Zongzhang Huang

Ningbo Yinzhou No. 2 Hospital, Ningbo City, 315000 Zhejiang Province, China

Correspondence should be addressed to Zongzhang Huang; hzongzhang@163.com

Received 24 March 2021; Revised 13 April 2021; Accepted 16 April 2021; Published 28 April 2021

Academic Editor: Songwen Tan

Objective. Rotator cuff tear (RCT) accounts for 50% of shoulder injuries, leading to chronic pain and disability in the upper extremity. The study is conducted to investigate the association between resonance imaging (MRI) classifications of patients with RCT and different shoulder outcome scores. *Methods*. From September 2018 to October 2019, 112 patients underwent shoulder MRI at our institution and selected as eligible study subjects according to inclusion and exclusion criteria. Among these 112 patients, 69 cases had confirmed history of shoulder trauma and 43 cases were due to chronic shoulder joint pain. The shoulder function of patients was evaluated by University of California Los Angeles Shoulder (UCLA) score, Constant-Murley score, Shoulder Pain and Disability Index (SPADI), and simple shoulder test (SST). *Results*. Among the 112 patients, there were 34 cases, 58 cases, and 20 cases with MRI classifications at grades I, II, and III, respectively. There was no significant difference in the injured tendons in patients with different MRI classifications ($P > 0.05$). The injury at the supraspinatus was more common. The scores of UCLA, Constant-Murley, and SST in patients with MRI grading at grade I were significantly higher than those at grades II and III ($P < 0.05$), which were significantly higher in patients at grade II than those at grade III ($P < 0.05$). SPADI score in patients with MRI grading at grade I was significantly lower than that at grades II and III ($P < 0.05$), while there was no significant difference in SPADI score between patients at grades II and III ($P > 0.05$). MRI classifications were negatively correlated with scores of UCLA, Constant-Murley, and SST ($P > 0.05$). There was no significant correlation between MRI grade and SPADI scores ($P > 0.05$). *Conclusion*. The supraspinatus tendon injury is more common in patients with RCT. MRI classifications were negatively correlated with scores of UCLA, Constant-Murley, and SST.

1. Introduction

Rotator cuff tear (RCT) accounts for 50% of shoulder injuries, leading to chronic pain and disability in the upper extremity [1]. The prevalence of RCT increases with advanced age, and more than 50% individuals in their 80s suffer from RCT [2]. The initial treatment for most RCT cases is conservative, with physical therapy, analgesics, and possibly corticosteroid or plasma-rich protein injections. There are a wide variety of surgical options, such as rotator cuff repair, superior capsule reconstruction, subacromial decompression, as well as reverse shoulder arthroplasty [3, 4]. However, reinjury rates of RCT range from 11% to 94% after surgical intervention [5]. Failed rotator cuff repair may be attributed to some nonmodifiable and modifiable patient factors, such as age, tendon quality, rotator cuff tear characteristics, acute or chronic rotator cuff tear, bone quality, tobacco use, and medications, and surgical variables, such as the technique, timing, tension on the repair, the biomechanical construct, and fixation, as well as the postoperative rehabilitation strategy [6].

Many surgeons rely on magnetic resonance imaging (MRI) to assist in decision-making and presurgical planning for patients with RCT [7]. MRI provides more comprehensive evaluation of the glenohumeral joint, including more accurate evaluation of articular cartilage and labroligamentous structures, factors that dictate conservative treatment, guide surgical management, and help set patient expectations [8]. However, MRI interpretation following rotator cuff repair can be challenging and requires familiarity with

different types of RCT, their surgical treatments, normal postoperative MRI appearance, and complications [9]. In this study, we evaluated the severity of RCT according to MRI and analyzed the association between MRI evaluations and different shoulder outcome scores including University of California Los Angeles (UCLA) shoulder score, Constant-Murley scale, Shoulder Pain and Dysfunction Index (SPADI), and simplified shoulder functional testing (SST), in a bid to provide reference for diagnosis and management of RCT.

2. Materials and Methods

2.1. Study Design and Subjects. From September 2018 to October 2019, 112 patients underwent shoulder MRI at our institution and selected as eligible study subjects according to inclusion and exclusion criteria. Among these 112 patients, 69 cases had confirmed history of shoulder trauma and 43 cases were due to chronic shoulder joint pain. The disease duration ranged from 2 days to 2 years, with an average disease duration of 1.3 ± 0.6 years. There were 41 left shoulders with RCT and 71 right shoulders with RCT. This retrospective study received the approval of the Ethics Committee of our hospital, and the informed consent was obtained from each subject. The inclusion criteria were as follows: (a) meeting the diagnostic criteria of RCT [10]; (b) with complete MR images; and (c) informed of study design and objective. The exclusion criteria were as follows: (a) previous treatment for shoulder joint injury; (b) history of osteoarthritis, ligament fracture, and other bone and joint diseases; (c) complicated with hypertension and diabetes mellitus; and (d) cognitive and communication impairment. All patients complained different degrees of shoulder pain. Most of the patients have intermittent shoulder pain at the beginning, and the symptoms were aggravated after work and sleeping on the side at night. At the same time, the patients had difficulties in forward elevation, abduction, internal rotation, and extension, with local tenderness instead of high skin temperature. The pain arc sign was positive; namely, the pain increased upon elevation and adduction in the range of 60-120°. Neer impingement test shows a positive sign; namely, the big tubercle of the humerus and acromial impact showed pain. Among 112 cases, 16 cases underwent arthroscopic shoulder surgery and 96 received medication and physical therapy. There were 63 males and 49 females, aged ranging from 20 to 70 years and with an average age of 50.27 ± 8.69 years.

2.2. MRI Protocols. MRI examination was performed on patient shoulders by using a MR scanner (Siemens MAGNETOM Avanto1.5 T), with GP-FLEX pliable coil. Patients were scanned in the neutral position. The parameters were set as follows: field of view (FOV) was $24\,\text{cm} \times 24\,\text{cm}$; scanning thickness and gap were 4 mm and 1 mm, respectively; and matrix was 256×256 or 512×512. Regular scanning sequence was applied, including fast spin echo (TSE) T2-weighted imaging (T2WI) (where the repetitive time (TR)/echo time (TE) was 4000/78 ms), short-term inversion recovery sequence (STIR) (among them, TR/TE was 4000/28 ms), and spin echo (SE) T1-weighted imaging (T1WI) (where TR/TE was 450/13 ms). The horizontal axis, oblique coronal, and oblique sagittal were chosen.

2.3. MR Image Analysis. Each MR study was reviewed by three radiologists experienced in musculoskeletal MR imaging. The examiners were blinded to the patient's name, clinical history, and arthrographic surgical results. A consensus was reached in each case as to whether the patient had a rotator cuff tear, an intact tendon with tendinitis, or a normal cuff. The rotator cuff tendons were assessed and classified into four grades according to previous report [11]. Grade 0 was defined as a tendon that was normal in signal intensity and morphology. Grade I was defined as a tendon with increased signal intensity but normal morphology. Grade II was defined as a tendon with both abnormal signal intensity and morphology. Abnormal morphology was defined as obvious tendon thinning or irregularity. A grade III tendon was defined as one with a definite large area of discontinuity in the normal signal void of the tendon. The area of discontinuity typically showed increased signal intensity on T2WI. A-H distance was measured by MRI as previously reported [12]. A-H distance less than 0.5 cm was defined as an extensive rotator cuff tear, 0.5-1.0 cm as acromion stenosis, and 1.0-1.5 cm as normal acromion. Fatty infiltration of the rotator cuff muscles was graded according to the Goutallier classification with sagittal proton density images [13, 14]. Based on this classification system, grade 0 represents no fat, grade I represents trace fatty streaks, grade II represents less than 50% fat, grade III represents 50% fat, and grade IV represents more than 50% fat. The global fatty degeneration index (GFDI) of each patient was calculated and classified into <1, 1-1.5, and >1.5 [15].

2.4. Assessment of Shoulder Function by Different Shoulder Outcome Scores. In this study, the UCLA shoulder score, Constant-Murley scale, SPADI, and SST were performed to evaluate the shoulder function of 112 patients. The UCLA scale was classified into three levels, including 34-35 scores indicating excellent shoulder outcome, 29-33 scores indicating good shoulder outcome, and <29 scores indicating poor shoulder outcome [16]. The Constant-Murley scores are involved with three items, shoulder range of motion (ROM), pain, and activity, with a total score of 75 [17]. The higher scores are indicative of better shoulder function. The SPADI scale encompasses 5 pain and 8 functional issues, with scores ranging from 0 to 100 scores [18]. The higher scores are indicative of poorer shoulder function. The SST scale involves pain symptoms and impacts on rest, life, and work, including 12 issues and with scores ranging from 0 to 12 scores [19]. The higher scores are indicative of better shoulder function.

2.5. Data Processing. SPSS 20.0 software (IBM Corp, Armonk, NY) was used to process the data. The counting data was described by "*n* and (%)" and tested by the chi-square test; the measurement data were described by (mean ± standard deviation), the comparison between two groups was tested by *t*-test, and comparison over two groups

were tested by F test; Pearson coefficient was applied for correlation analysis. The level of significant difference represented as P value < 0.05.

3. Results

3.1. MRI Classification. There were 34 cases defined as grade I. A T1WI coronal oblique image demonstrates increased signal intensity in the distal supraspinatus tendon, with no evidence of thinning irregularity or discontinuity, while a normal subdeltoid fat plane was visible (Figure 1). There were 58 cases defined as grade II. A T1WI coronal oblique image demonstrates diffuse increased signal intensity in the supraspinatus tendon, and it was irregular in appearance and thinned. A T2WI coronal oblique image demonstrates high signal intensity consistent with fluid in the subacromial-subdeltoid bursa (Figure 2). There were 20 cases defined as grade III. A T1WI coronal oblique image demonstrates complete disruption of the supraspinatus tendon, and the tendon has retracted to the level of the acromioclavicular joint with irregular and frayed edges. The subacromial-subdeltoid fat plane is lost. It was observed considerable atrophy of the supraspinatus muscle and degenerative changes in the acromioclavicular joint. A T2WI coronal oblique image at the level of the acromioclavicular joint demonstrates the disruption of the supraspinatus tendon as it is outlined by high-signal-intensity fluid. A large amount of fluid is visible in the subacromial and subdeltoid burse. Increased signal intensity of T2WI was noted in the proximal retracted tendon edges (Figure 3). MRI classifications of 112 patients were listed in Table 1.

3.2. Association between MRI Classifications and Injured Tendons. MRI classifications of 112 patients were subclassified according to the injured tendons of muscles (supraspinatus, infraspinatus, subscapularis, and teres minor ones). There were 97 cases with abnormal morphology of supraspinatus tendons and high signal intensity, including 29 grade I, 51 grade II, and 17 grade III. There were 6 cases with abnormal morphology of subscapularis tendons and high signal intensity, including 2 grade I, 3 grade II, and 1 grade III. There were 2 cases with abnormal morphology of teres minor tendons and high signal intensity, including 1 grade I and 1 grade II. There were 7 cases with abnormal morphology of infraspinatus tendons and high signal intensity, including 2 grade I, 3 grade II, and 2 grade III. As shown in Table 2, MRI classifications were not significantly correlated with injured tendons among 112 patients with RCTs.

3.3. Association between MRI Classifications and Different Shoulder Outcome Scores. The UCLA, Constant-Murley, and SST scores of patients defined as MRI grade I were significantly higher than those of grades II and III ($P < 0.05$), and those of grade II were significantly higher than those of grade III ($P < 0.05$). The SPADI scores of MRI grade I were significantly lower than those of grade II and grade III ($P < 0.05$), and there was no significant difference between grade II and grade III ($P > 0.05$). Results are revealed in Table 3. The results of Pearson correlation analysis (Table 4) showed

Figure 1: MRI grade 1 (pointed by the downward arrow in the figure): the supraspinatus tendon was continuous, and the T2WI hyperintense signal shadow (revealed as a strip) was found near the attachment end of the humerus, and the boundary was still clear; MRI grade 2 (pointed by the upward arrow in the figure): the subscapularis tendon was revealed continuous, and the shape near the attachment of the humerus was distorted and irregular, and T2WI hyperintense signal shadow (revealed as a patch) was found.

Figure 2: MRI grade 2 (the arrow pointed in the figure): the supraspinatus tendon was continuous, but the boundary was irregular, T2WI hyperintense signal shadow (revealed as strips) was found, and long T2WI fluidity signal shadow was found in the axillary fossa, joint cavity, and deep deltoid fascia.

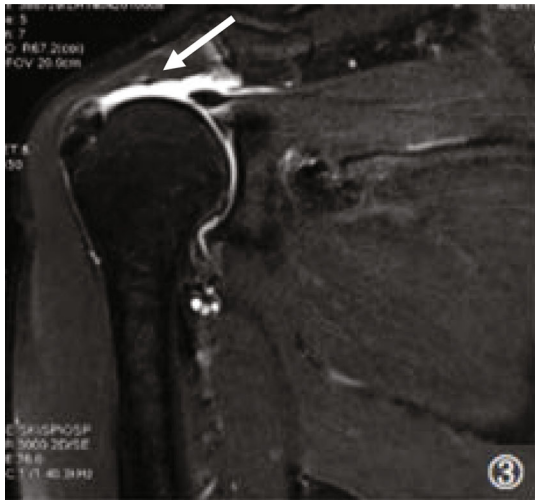

Figure 3: MRI grade 3 (the arrow pointed in the figure): the attachment end of the greater tuberosity of the humerus in the supraspinatus tendon indicated emptiness and was filled with liquid signal shadow. It was found that the continuity of the tendon was interrupted and the broken ends were retracted. Effusion in the deltoid bursa below the acromion was found.

Table 1: MRI classifications.

MRI grade	Case	Percentage (%)
Grade 1	34	30.36
Grade 2	58	51.79
Grade 3	20	17.86

MRI: magnetic resonance imaging.

that MRI grades were negatively correlated with the UCLA, Constant-Murley, and SST scores ($P < 0.05$). There was no significant correlation between MRI grade and SPADI scores ($P > 0.05$).

3.4. Association between A-H Distance, Fatty Infiltration of the Rotator Cuff Muscles, and Different Shoulder Outcome Scores. After MRI examination, among 112 patients with RCTs, there were 19 with A-H distance < 0.5 cm, 32 with A-H distance between 0.5 and 1.0, and 61 with A-H distance between 1.0 and 1.5. No significant difference was observed among patients with A-H distance < 0.5 cm, between 0.5 and 1.0, and between 1.0 and 1.5 ($P > 0.05$). Among 112 patients with RCTs, there were 86 with GFDI < 1, 11 with GFDI from 1 to 1.5, and 15 with GFDI > 1.5. No significant difference was observed among patients with GFDI < 1, GFDI from 1 to 1.5, and GFDI > 1.5 ($P > 0.05$).

4. Discussion

Treatment selection and prognosis evaluation largely depend on the dimensions and extent of RCT, tear morphologic features, involvement of the subscapularis and infraspinatus tendons or of contiguous structures, the condition of the involved tendon, and presence of muscle atrophy [20, 21]. MRI can evaluate the extent and configuration of rotator cuff abnormalities, document abnormalities of the cuff muscles and adjacent structures, and suggest mechanical imbalance within the cuff [22]. In addition to that, MRI can provide information about RCT including tear dimensions, tear depth or thickness, tendon retraction, and tear shape that is required for optimal treatment planning and prognostic accuracy [23]. In this study, we evaluated the severity of RCT according to MRI and then analyzed the association between MRI evaluations and shoulder function scored by UCLA, Constant-Murley, SPADI, and SST scores.

From previous studies, researchers mainly focused on analysis of the correlation between different shoulder outcome scores in patients with RCTs. For example, Assuncao et al. [24] found that the UCLA and American Shoulder and Elbow Surgeons (ASES) scores showed a very high correlation ($r = 0.91$). Allom et al. [25] found a correlation between the Constant-Murley and Oxford scales for open procedures ($r = 0.77$) and for arthroscopic procedures ($r = 0.89$). Cunningham et al. [26] found the correlation between the ASES and Single Assessment Numerical Evaluation scales for primary arthroscopic repair ($r = 0.75$). Gilbart and Gerber [27] found a correlation of 0.80 between the Constant-Murley and Subjective Shoulder Value scales. Romeo et al. [28] compared the results of the UCLA, Constant-Murley, and SST scales applied in patients who underwent open surgery. Skutek et al. [29] found a correlation between the ASES and Constant-Murley scales ($r = 0.87$), the UCLA scale and the Constant-Murley ($r = 0.66$), the Constant-Murley and SST scales ($r = 0.76$), and the Constant-Murley and SST scales ($r = 0.70$) in a study of patients undergoing open repair. However, few literatures reported the correlations between MRI results and different shoulder outcome scores in patients with RCTs. In this study, we evaluated a significant negative correlation between MRI results and the UCLA scores in RCT patients with RCT, indicating that the lower MRI grades and the higher UCLA score correspond to better shoulder function. However, the correlation coefficient is not high ($r = -0.358$), suggesting that UCLA score is not effective in judging the degree of RCT, concurring with other study [30]. The reasons may include the following three points: (a) general classification of patients' functional activities makes it easy to produce errors; (b) assessment of muscle strength and range of motion only through the measurement of shoulder flexion activity generally involving the biceps brachii, deltoid anterior bundle, pectoralis major, and other muscle groups is less representative of the overall shoulder activity; (c) only two items including satisfaction and dissatisfaction make it difficult to reflect the actual condition. In this study, there was a significant negative correlation between the SSR score, Constant-Murley score, and the MRI grades, indicating the higher the SSR and Constant-Murley scores were, the better shoulder function was presented. The Constant-Murley score is composed of shoulder range of motion, pain symptoms, and functional activities, while the evaluation of shoulder range of motion and functional activities is comprehensive and specific, involving internal rotation, external rotation, flexion, and abduction activities [31]. Although the classification of pain score is relatively simple and there are individual differences

Table 2: MRI classifications and injured tendons (n (%)).

MRI grade	n	Supraspinatus	Subscapularis	Teres minor	Infraspinatus
Grade 1	34	29 (85.29)	2 (5.88)	1 (2.94)	2 (5.88)
Grade 2	58	51 (87.93)	3 (5.17)	1 (1.72)	3 (5.17)
Grade 3	20	17 (85.00)	1 (5.00)	0 (0.00)	2 (10.00)
x^2			1.228		
P			0.976		

MRI: magnetic resonance imaging.

Table 3: MRI classifications and different shoulder outcome scores (mean ± standard deviation).

MRI classification	n	UCLA	Constant-Murley	SPADI	SST
Grade I	34	$33.05 \pm 5.28^{*\#}$	$68.23 \pm 10.25^{*\#}$	$60.38 \pm 10.35^{*\#}$	$10.15 \pm 1.67^{*\#}$
Grade II	58	$30.16 \pm 5.02^{*}$	$60.14 \pm 8.37^{*}$	69.37 ± 11.84	$8.06 \pm 1.35^{*}$
Grade III	20	25.27 ± 4.13	51.49 ± 7.68	72.54 ± 12.06	5.24 ± 0.96
F		15.497	23.047	9.249	78.048
P		<0.001	<0.001	<0.001	<0.001

MRI: magnetic resonance imaging; UCLA: University of California Los Angeles; SPADI: Shoulder Pain and Disability Index; SST: simple shoulder test.

Table 4: Correlation analysis between MRI classifications with scores of UCLA, Constant-Murley, SPADI, and SST.

Shoulder outcome scores	MRI classification	
	r	P
UCLA	-0.358	<0.001
Constant-Murley	-0.487	<0.001
SPADI	0.038	0.476
SST	-0.702	<0.001

MRI: magnetic resonance imaging; UCLA: University of California Los Angeles; SPADI: Shoulder Pain and Disability Index; SST: simple shoulder test.

in subjective evaluation of patients, the Constant-Murley score can accurately determine the degree of RCT to a large extent due to the small proportion of the pain score. The SST score mainly involves the influence of pain symptoms and diseases on the rest state, life, and work of patients. The evaluation is simple and easy to operate. The range of motion and muscle strength of human shoulder joint in different directions can be effectively considered by using 12 different life problems, which can comprehensively evaluate the joint function of patients with shoulder injury [32]. It was previously reported that the SPADI score exhibited low credibility due to repeated test [33]. As shown in our results, there was no significant correlation between MRI grades and the SPADI score, which was consistent with the above study. It revealed that the SPADI score is insufficient in evaluating shoulder function of patients with RCT.

In conclusion, our results show a negative correlation between UCLA, Constant-Murley, and SST scores. Poorer MRI grades are indicative of higher scores of UCLA, Constant-Murley, and SST. However, the was no significant correlation between SPADI and MRI grades, which provide reference for decision-making for evaluating shoulder function using different scores in patients with RCTs.

Data Availability

The data used to support the findings of this study are included within the article.

Conflicts of Interest

The authors declare that they have no conflicts of interest.

References

[1] D. Gigliotti, M. C. Xu, M. J. Davidson, P. B. Macdonald, J. R. S. Leiter, and J. E. Anderson, "Fibrosis, low vascularity, and fewer slow fibers after rotator-cuff injury," *Muscle & Nerve*, vol. 55, no. 5, pp. 715–726, 2017.

[2] R. Z. Tashjian, "Epidemiology, natural history, and indications for treatment of rotator cuff tears," *Clinics in Sports Medicine*, vol. 31, no. 4, pp. 589–604, 2012.

[3] J. Micallef, J. Pandya, and A. K. Low, "Management of rotator cuff tears in the elderly population," *Maturitas*, vol. 123, pp. 9–14, 2019.

[4] J. D. Osborne, A. L. Gowda, B. Wiater, and J. M. Wiater, "Rotator cuff rehabilitation: current theories and practice," *The Physician and Sportsmedicine*, vol. 44, no. 1, pp. 85–92, 2016.

[5] B. T. N. le, X. L. Wu, P. H. Lam, and G. A. Murrell, "Factors predicting rotator cuff retears: an analysis of 1000 consecutive rotator cuff repairs," *The American Journal of Sports Medicine*, vol. 42, no. 5, pp. 1134–1142, 2014.

[6] B. T. Elhassan, R. M. Cox, D. R. Shukla et al., "Management of failed rotator cuff repair in young patients," *The Journal of the American Academy of Orthopaedic Surgeons*, vol. 25, no. 11, pp. e261–e271, 2017.

[7] M. J. Tuite, "Magnetic resonance imaging of rotator cuff disease and external impingement," *Magnetic Resonance Imaging Clinics of North America*, vol. 20, no. 2, pp. 187–200, 2012.

[8] J. S. Roy, C. Braen, J. Leblond et al., "Diagnostic accuracy of ultrasonography, MRI and MR arthrography in the characterisation of rotator cuff disorders: a systematic review and meta-analysis," *British Journal of Sports Medicine*, vol. 49, no. 20, pp. 1316–1328, 2015.

[9] E. McCrum, "MR imaging of the rotator cuff," *Magnetic Resonance Imaging Clinics of North America*, vol. 28, no. 2, pp. 165–179, 2020.

[10] J. B. Cowan, A. Bedi, J. E. Carpenter, C. B. Robbins, J. J. Gagnier, and B. S. Miller, "Evaluation of American Academy of Orthopaedic Surgeons Appropriate Use Criteria for the management of full-thickness rotator cuff tears," *Journal of Shoulder and Elbow Surgery*, vol. 25, no. 7, pp. 1100–1106, 2016.

[11] M. B. Zlatkin, J. P. Iannotti, M. C. Roberts et al., "Rotator cuff tears: diagnostic performance of MR imaging," *Radiology*, vol. 172, no. 1, pp. 223–229, 1989.

[12] K. M. McCreesh, J. M. Crotty, and J. S. Lewis, "Acromiohumeral distance measurement in rotator cuff tendinopathy: is there a reliable, clinically applicable method? A systematic review," *British Journal of Sports Medicine*, vol. 49, no. 5, pp. 298–305, 2015.

[13] D. Goutallier, J. M. Postel, J. Bernageau, L. Lavau, and M. C. Voisin, "Fatty muscle degeneration in cuff ruptures. Pre- and postoperative evaluation by CT scan," *Clinical Orthopaedics and Related Research*, vol. 304, pp. 78–83, 1994.

[14] B. Fuchs, D. Weishaupt, M. Zanetti, J. Hodler, and C. Gerber, "Fatty degeneration of the muscles of the rotator cuff: assessment by computed tomography versus magnetic resonance imaging," *Journal of Shoulder and Elbow Surgery*, vol. 8, no. 6, pp. 599–605, 1999.

[15] N. S. Cho and Y. G. Rhee, "The factors affecting the clinical outcome and integrity of arthroscopically repaired rotator cuff tears of the shoulder," *Clinics in Orthopedic Surgery*, vol. 1, no. 2, pp. 96–104, 2009.

[16] J. Lin, "Platelet-rich plasma injection in the treatment of frozen shoulder: a randomized controlled trial with 6-month follow-up," *International Journal of Clinical Pharmacology and Therapeutics*, vol. 56, no. 8, pp. 366–371, 2018.

[17] E. A. Malavolta, J. H. Assuncao, M. E. C. Gracitelli, P. A. A. Simoes, D. K. Shido, and A. A. Ferreira Neto, "Correlation between the UCLA and Constant-Murley scores in rotator cuff repairs and proximal humeral fractures osteosynthesis," *Revista Brasileira de Ortopedia*, vol. 53, no. 4, pp. 441–447, 2018.

[18] S. Vrouva, C. Batistaki, E. Koutsioumpa, D. Kostopoulos, E. Stamoulis, and G. Kostopanagiotou, "The Greek version of Shoussslder Pain and Disability Index (SPADI): translation, cultural adaptation, and validation in patients with rotator cuff tear," *Journal of Orthopaedics and Traumatology*, vol. 17, no. 4, pp. 315–326, 2016.

[19] M. L. Koehorst, E. van Trijffel, and R. Lindeboom, "Evaluative measurement properties of the patient-specific functional scale for primary shoulder complaints in physical therapy practice," *The Journal of Orthopaedic and Sports Physical Therapy*, vol. 44, no. 8, pp. 595–603, 2014.

[20] C. A. Kwong, Y. Ono, M. J. Carroll et al., "Full-thickness rotator cuff tears: what is the rate of tear progression? A systematic review," *Arthroscopy*, vol. 35, no. 1, pp. 228–234, 2019.

[21] D. I. Dabija, J. S. Pennings, K. R. Archer et al., "Which is the best outcome measure for rotator cuff tears?," *Clinical Orthopaedics and Related Research*, vol. 477, no. 8, pp. 1869–1878, 2019.

[22] J. T. Aoyama, P. Maier, S. Servaes et al., "MR imaging of the shoulder in youth baseball players: anatomy, pathophysiology, and treatment," *Clinical Imaging*, vol. 57, pp. 99–109, 2019.

[23] Y. Morag, J. A. Jacobson, B. Miller, M. De Maeseneer, G. Girish, and D. Jamadar, "MR imaging of rotator cuff injury: what the clinician needs to know," *Radiographics*, vol. 26, no. 4, pp. 1045–1065, 2006.

[24] J. H. Assuncao, E. A. Malavolta, M. E. C. Gracitelli, D. Y. Hiraga, F. R. da Silva, and A. A. Ferreira Neto, "Clinical outcomes of arthroscopic rotator cuff repair: correlation between the University of California, Los Angeles (UCLA) and American Shoulder and Elbow Surgeons (ASES) scores," *Journal of Shoulder and Elbow Surgery*, vol. 26, no. 7, pp. 1137–1142, 2017.

[25] R. Allom, T. Colegate-Stone, M. Gee, M. Ismail, and J. Sinha, "Outcome analysis of surgery for disorders of the rotator cuff: a comparison of subjective and objective scoring tools," *The Journal of Bone and Joint Surgery. British volume*, vol. 91, no. 3, pp. 367–373, 2009.

[26] G. Cunningham, A. Ladermann, P. J. Denard, O. Kherad, and S. S. Burkhart, "Correlation between American Shoulder and Elbow Surgeons and single assessment numerical evaluation score after rotator cuff or SLAP repair," *Arthroscopy*, vol. 31, no. 9, pp. 1688–1692, 2015.

[27] M. K. Gilbart and C. Gerber, "Comparison of the subjective shoulder value and the Constant score," *Journal of Shoulder and Elbow Surgery*, vol. 16, no. 6, pp. 717–721, 2007.

[28] A. A. Romeo, A. Mazzocca, D. W. Hang, S. Shott, and B. R. Bach, "Shoulder scoring scales for the evaluation of rotator cuff repair," *Clinical Orthopaedics and Related Research*, vol. 427, pp. 107–114, 2004.

[29] M. Skutek, R. W. Fremerey, J. Zeichen, and U. Bosch, "Outcome analysis following open rotator cuff repair. Early effectiveness validated using four different shoulder assessment scales," *Archives of Orthopaedic and Trauma Surgery*, vol. 120, no. 7-8, pp. 432–436, 2000.

[30] A. Kirkley, S. Griffin, and K. Dainty, "Scoring systems for the functional assessment of the shoulder," *Arthroscopy*, vol. 19, no. 10, pp. 1109–1120, 2003.

[31] K. Vrotsou, M. Avila, M. Machon et al., "Constant-Murley score: systematic review and standardized evaluation in different shoulder pathologies," *Quality of Life Research*, vol. 27, no. 9, pp. 2217–2226, 2018.

[32] J. S. Roy, J. C. Macdermid, K. J. Faber, D. S. Drosdowech, and G. S. Athwal, "The simple shoulder test is responsive in assessing change following shoulder arthroplasty," *The Journal of Orthopaedic and Sports Physical Therapy*, vol. 40, no. 7, pp. 413–421, 2010.

[33] J. D. Breckenridge and J. H. McAuley, "Shoulder Pain and Disability Index (SPADI)," *Journal of Physiotherapy*, vol. 57, no. 3, p. 197, 2011.

Hindawi
Journal of Nanomaterials
Volume 2021, Article ID 9999484, 16 pages
https://doi.org/10.1155/2021/9999484

Research Article

COX-2 Regulates the Proliferation and Apoptosis of Activated Hepatic Stellate Cells through CDC27

Yang Hu,[1,2,3,4] Nian Fu,[4] Li Xian Chen,[4] Jian Hua Xiao,[1,2,3] and Xue Feng Yang[4]

[1]*Institute of Pathogenic Biology, Hengyang Medical College, University of South China, Hunan, China*
[2]*Hunan Provincial Key Laboratory for Special Pathogens Prevention and Control, University of South China, Hengyang, 421001 Hunan, China*
[3]*Hunan Province Cooperative Innovation Center for Molecular Target New Drug Study, University of South China, Hengyang, 421001 Hunan, China*
[4]*Department of Gastroenterology, The Affiliated Nanhua Hospital, Hengyang Medical College, University of South China, 336 Dongfeng South Road, Hengyang, 421002 Hunan Province, China*

Correspondence should be addressed to Jian Hua Xiao; jhxiao223@163.com and Xue Feng Yang; yxf9988@126.com

Received 15 March 2021; Revised 20 March 2021; Accepted 1 April 2021; Published 28 April 2021

Academic Editor: Songwen Tan

Cyclooxygenase-2 (COX-2) is an important rate-limiting enzyme in the synthesis of prostaglandins (PGs), which can be upregulated by various stimuli. COX-2 has been shown to be involved in the occurrence and development of hepatic fibrosis by regulating the proliferation and apoptosis of hepatic stellate cells (HSCs) in previous studies. The aims of the study are to study the mechanism of how COX-2 regulates the proliferation and apoptosis of HSCs and to provide new targets for the prevention and treatment of hepatic fibrosis. A short hairpin RNA targeting COX-2 was constructed, and the changes in proliferation and apoptosis of liver tissue cells and HSCs were observed, respectively. COX-2-shRNA-1 significantly suppressed the proliferation of HSCs in vivo. Moreover, knockdown of COX-2 significantly suppressed cell proliferation and accelerated cell cycle arrest and apoptosis in vitro. Among those differential genes related to cell proliferation and apoptosis, CDC27 and Sh3kbp1 were upregulated, but Plcd4 was suppressed. Mechanistically, the influence of COX-2 on HSCs partly depends on upregulating CDC27. Our results demonstrated that COX-2 regulates the proliferation and apoptosis of activated hepatic stellate cells through the CDC27 pathway. This study contributes to our understanding of the effect of COX-2 for the treatment of hepatic fibrosis.

1. Introduction

Hepatic fibrosis, a common pathophysiological process in many chronic liver diseases, is manifested by the excessive and abnormal deposition of extracellular matrix components in the liver. It is the necessary stage for the development of chronic liver disease to cirrhosis. It is now believed that liver fibrosis may be reversed to normal, while cirrhosis is not. However, there is no effective method for the treatment of liver fibrosis.

Cyclooxygenase-2 (COX-2) is an important rate-limiting enzyme in the synthesis of prostaglandin (PGs). COX-2 is hardly expressed in normal tissues, but can be upregulated when stimulated by various factors. Extensive research has shown that COX-2 participates in some pathological processes, such as cell malignant transformation, inflammatory response, and catalyzing the biosynthesis of arachidonic acid (AA) to affect disease processes. Research in the area of hepatic fibrosis showed that COX-2 is an important molecule that affects the development of it. Celecoxib, a COX-2 inhibitor, suppresses the hepatic fibrosis induced by bile duct ligation (BDL) and thioacetamide (TAA) [1]. Other researchers used CCL4 to replicate the model of hepatic fibrosis and found that COX-2 knockout mice had less necrosis, degeneration, and connective tissue hyperplasia than the wild-type mice [2]. These mice also had lower expression of α-smooth muscle actin (α-SMA) in the liver tissue and less serum hyaluronic acid (HA), collagen IV (IV-C), and collagen III (PC III). Short hairpin RNA was used to silence COX-2 in nonalcoholic fatty liver disease (NAFLD) rats, and the liver tissue steatosis, inflammatory degree, and hepatic fibrosis were significantly reduced in COX-2 silencing rats [3].

Table 1: The sequences and products of amplified gene primer.

Gene	Primer	Sequences	Length (bp)
COX-2	Forward Reverse	ATCTAGTCTGGAGTGGGAGG AATGAGTACCGCAAACGCTT	420
α-SMA	Forward Reverse	TGTGCTGGACTCTGGAGATG GATCACCTGCCCATCAGG	292
Serpinb2	Forward Reverse	GTAGATGTGAACGAGGAGG GTATGGTGCGGGTAATGT	142
Cdc27	Forward Reverse	ACTGGCGACCTGTTACTA CTGGCTTCTCACCTATTT	359
Sh3kbp1	Forward Reverse	AGAAATGGACAGCAGGAC TTGTTTGATGACAGGAGC	271
Dusp1	Forward Reverse	TTGTTTGATGACAGGAGC TGGAGACAGGGAAGTTGAAGA	171
Dusp6	Forward Reverse	CACGGTGACAGTGGCTTAC AGACATTCTGGTTGGAGG	215
TP53	Forward Reverse	GGAGTGCAAAGAGAGCACTG CTCATTCAGCTCTCGGAACA	134
Cxcl10	Forward Reverse	TTCCTGCAAGTCTATCCTG TGTTCTTCTTCATTGTGGC	170
Plcd4	Forward Reverse	TTTTGGCAACATTAGCAC GACAACCAGGGCAGATAG	438
GAPDH	Forward Reverse	TATCGGACGCCTGGTTAC GCATCAAAGGTGGAAGAAT	852

CDC27 is a core subunit of anaphase-promoting complex/cyclosome (APC/C). APC/C is a type of E3 ligase complex that regulates chromosome segregation and mitotic exit [4]. APC/C reportedly participates in the TGF-β signaling pathway, and TGF-β activates CDC27, which promoted liver fibrosis via the TGF-β pathway in both HSC and hepatocyte [5]. Recent evidence suggests that COX-2 may be involved in the development of hepatic fibrosis by regulating the proliferation and apoptosis of hepatic stellate cells (HSCs). SC-236, a selective COX-2 inhibitor, had an antihepatic fibrosis effect and significantly promoted the apoptosis and growth inhibition of isolated cultured HSCs [6]. Celecoxib, another COX-2 inhibitor, has been reported to suppress the formation of hepatic fibrosis in rats by inhibiting the proliferation of platelet-derived growth factor- (PDGF-) induced HSCs and promoting the apoptosis of these HSCs [1].

However, the mechanism of how COX-2 regulates the proliferation and apoptosis of HSCs remains unclear. Therefore, this study silenced the expression of COX-2 in hepatocytes and hepatic stellate cells in liver fibrosis rats by using short hairpin RNA. Then the changes of proliferation and apoptosis of HSCs and related gene expression profiles after COX-2 silencing were observed. Based on our experimental results, we found that COX-2 regulated the proliferation and apoptosis of activated hepatic stellate cells through the CDC27 pathway.

2. Materials and Methods

2.1. Animal Model. 48 male SD rats (Nanjing Junke Bioengineering Co., Ltd.) were randomly divided into four groups by body weight: control group (control), liver fibrosis model group (model), null plasmid control group (sh-NC), and COX-2-shRNA-1 group (COX-2-shRNA-1). Except for the control group, the other 3 groups were fed a high-fat diet for 12 weeks after a week of adaptive feeding. Rats in the COX-2-shRNA-1 group and the sh-NC groups were injected with adenovirus plasmids and adenovirus no-load physique grains (PBS dilution) through the caudal vein from the beginning of the high-fat diet, respectively. The dose and time of injection were 1×10^9 pfu/each and once weekly. Rats in the control group and the model group were given an equal volume of PBS through the caudal vein. After 12 weeks of rearing, the rats were sacrificed by caesarean section to take 0.5~1.5 g of the left lateral lobe of the rat liver and immediately put it into ice-cold William E medium filled with a mixed gas of 95% oxygen and 5% CO for subsequent experiments. This experiment had been approved by the Animal Management Committee of our hospital.

2.2. Reverse Transcription-PCR. Reverse transcription-PCR (RT-PCR) was used to detect the mRNA expression of COX-2, α-SMA, CDC27, Sh3kbp1, Serpinb2, cxcl10, Dusp6, Dusp1, TP53, and Phlcd4. Total RNA from each liver sample and HSCs was extracted by Trizol reagent (Generay Biotech, China), and cDNA was synthesized by using Revert Aid First Strand cDNA synthesis Kit (Ferramentas, Germany), according to the manufacturer's instructions. PCR was performed under the manufacturer's manual. Band intensity was measured by a densitometer and was normalized for comparison. RT-PCR was performed on target gene using specific primers (Table 1). GAPDH was selected as the internal reference gene. The expression level of gene was analyzed using the equation $2^{-\Delta\Delta CT}$ method, where $\Delta\Delta CT = \Delta CT_{\text{experimental group}} - \Delta CT_{\text{control group}}$; $\Delta CT_{\text{experimental group}} = CT_{\text{target gene,experimental group}} -$

$CT_{\text{internal reference gene,experimental group}}$; $\Delta CT_{\text{control group}} = CT_{\text{target gene,control group}} - CT_{\text{internal reference gene,control group}}$; and $2^{-\Delta\Delta CT}$ represents the multiple expression of gene in the experimental group relative to the control group.

2.3. Immunohistochemistry. Liver tissues were fixed in 4% formaldehyde solution for 3 to 5 days. Then, tissues were removed from the fixative solution and trimmed to an appropriate shape and thickness. Tissues were dehydrated, transparented, and embedded in wax, then dewaxed with xylene and rehydrated with gradient alcohol. Three of the most important steps were blocking and inactivating endogenous peroxidase and performing antigen retrieval. Primary antibodies anti COX-2 and α-SMA were used and incubated overnight in a refrigerator at 4°C (PBS buffer solution instead of primary antibody as a negative control). The samples were transferred to room temperature and equilibrated for 30 minutes and rinsed with PBS for 3×5 minutes before adding a secondary antibody. The secondary antibody was incubated at 37°C for 15 minutes and rinsed with PBS for 3×5 minutes. DAB staining was used.

2.4. Culture of HSC Cell Lines. HSC cell lines (HSC-T6) were obtained from the American Type Culture Collection (ATCC) and were cultured at 37°C with 5% CO_2 in a cell incubator. Cells were cultured in DMEM medium (Gibco, USA) supplemented with 10% fetal bovine serum (FBS) plus 1% 100 μg/ml penicillin/streptomycin. Cells were seeded in 6-well plates and grown to reach 70% confluence before transfection. For transfecting cells, cells were transfected with different plasmids using FuGENE HD Transfection reagent (Roche, Switzerland) following the manual instruction. Then, transfected cells were harvested for molecular assays.

2.5. Cell Transfection. shRNA targeting COX-2 (COX-2-shRNA) or CDC27 (sh-CDC27) were synthesized by Win Run Biotechnology Co, Ltd. (Changsha, China). The applied shRNA sequences for COX-2 were as follows: COX-shRNA-1, 5′-CCTCGTCCAGATGCTATCTTT-3′; COX-shRNA-2, 5′-AGTTCCAGTATCAGAACCGCATTGCCTCT-3′; and COX-shRNA-3, 5′-GACACCTTCAACATTGAAGACCAG GAGTA-3′. The applied shRNA sequences targeting CDC27 were 5′-CCGGGCCTATAACAGTGACTTGATTC TCGAGAATCAAGTCACTGTTATAGGCTTTTTTG-3′. According to the manufacturer's protocol, HSC-T6 cells (5×10^5) were seeded in 6-well plates, incubated for 24 h, and then 200 ng/ml specific shRNA or negative control (NC) was transfected into the cells by using Lipofectamine®2000 (Invitrogen; USA). Effects of the shRNA were evaluated by western blotting and RT-PCR. A fluorescence microscope was used to observe the expression of green fluorescent protein in cells to evaluate the fluorescence density.

2.6. MTT Assay. Cells were treated for 24 h, 48 h, and 72 h. Then, 5 mg/ml MTT solution (in PBS) was added into the basal medium at 1 : 10 ratio. After 4-hour incubation, the remaining MTT solution was removed, and cells were solubilized with dimethyl sulfoxide. Optical density (OD) values were measured at the wavelength of 490 nm to reflect cell viability: cell proliferation rate = (experimental group OD − control group OD)/(NC group OD − control group OD).

2.7. Flow Cytometry Assay. HSC-T6 cells were harvested after 48 h posttransfection. The culture medium was then changed into serum-free Hank's balanced salt solution. Then, cells were rinsed in pre-cold PBS. Fluorescein isothiocyanate-(FITC-) conjugated Annexin V and propidium iodine (PI) staining buffer were sequentially added. Cell apoptosis was then measured on a flow cytometry (BD, USA).

2.8. Cell Cycle Assay. Cell cycle of HSC-T6 cells was monitored by flow cytometry. After 48 h posttransfection, all groups of HSC-T6 cells were digested by trypsin and were washed in precold PBS. Cells were fixed by 70% cold ethanol overnight and were resuspended in 100 μg/ml RNase A in PBS for 30 min incubation at 37°C. Cell nuclei were stained by 50 μg/ml PI for 30 min. Cell cycle was then measured on flow cytometry using fluorescent-assisted cell sorting (FACS).

2.9. DNA Microarray Assay and Data Analysis. Microarray-based oligonucleotide hybridization approach was used to quantify expression levels of target gene [4]. In brief, total RNA was obtained as mentioned above. Then, the obtained sample RNA was labeled by fluorescence and turned into DNA. The labeled DNA was dissolved in 80 μl hybridization solution ($3 \times$ SSC, 0.2% SDS, $5 \times$ Denhart's, and 25% formamide) and hybridized at 42°C overnight. After the hybridization is completed, it was first washed in a liquid containing 0.2% SDS and $2 \times$ SSC at 42°C for 5 min and then washed in a $0.2 \times$ SSC medium for 5 minutes in room temperature. After the slide is dried, it can be used for scanning. LuxScan 3.0 software (CapitalBio Corp., China) was used firstly to transform images into digital signals. Linear correction across chips was performed based on global mean values of cy5 and cy3 signals for normalization of means. All data from this experiment can be divided into three groups: (1) all data include the whole signal data set containing those with or without differential expressions, and ratio values were defined after Lowess normalization. (2) Checked genes include those genes with effective signals after assay. (3) Differentially expressed genes were screened out and annotated by pathway and GO database for functional assay and statistical analysis using Capital Bio software.

2.10. Western Blotting. Western blotting was used to quantify the expression of COX-2 and CDC27. In brief, rat hepatic tissues or cultured HSCs were lysed in RIPA buffer and proteins were quantified by BCA kit. About 20~40ug protein samples were loaded onto SDS-PAGE gel for electrophoresis separation and were transferred to PVDF membrane. After blocking, the membrane was incubated with primary antibody including rabbit anti-COX-2 (#12282, CST, USA), rabbit anti-CDC27 (#9499, CST, USA), and rabbit anti-β-actin (#4970, CST, USA) overnight. On the next day, HRP-conjugated secondary antibody was added for room temperature incubation for 2 h. The membrane was then developed by ECL substrate, and images were captured by a computerized system.

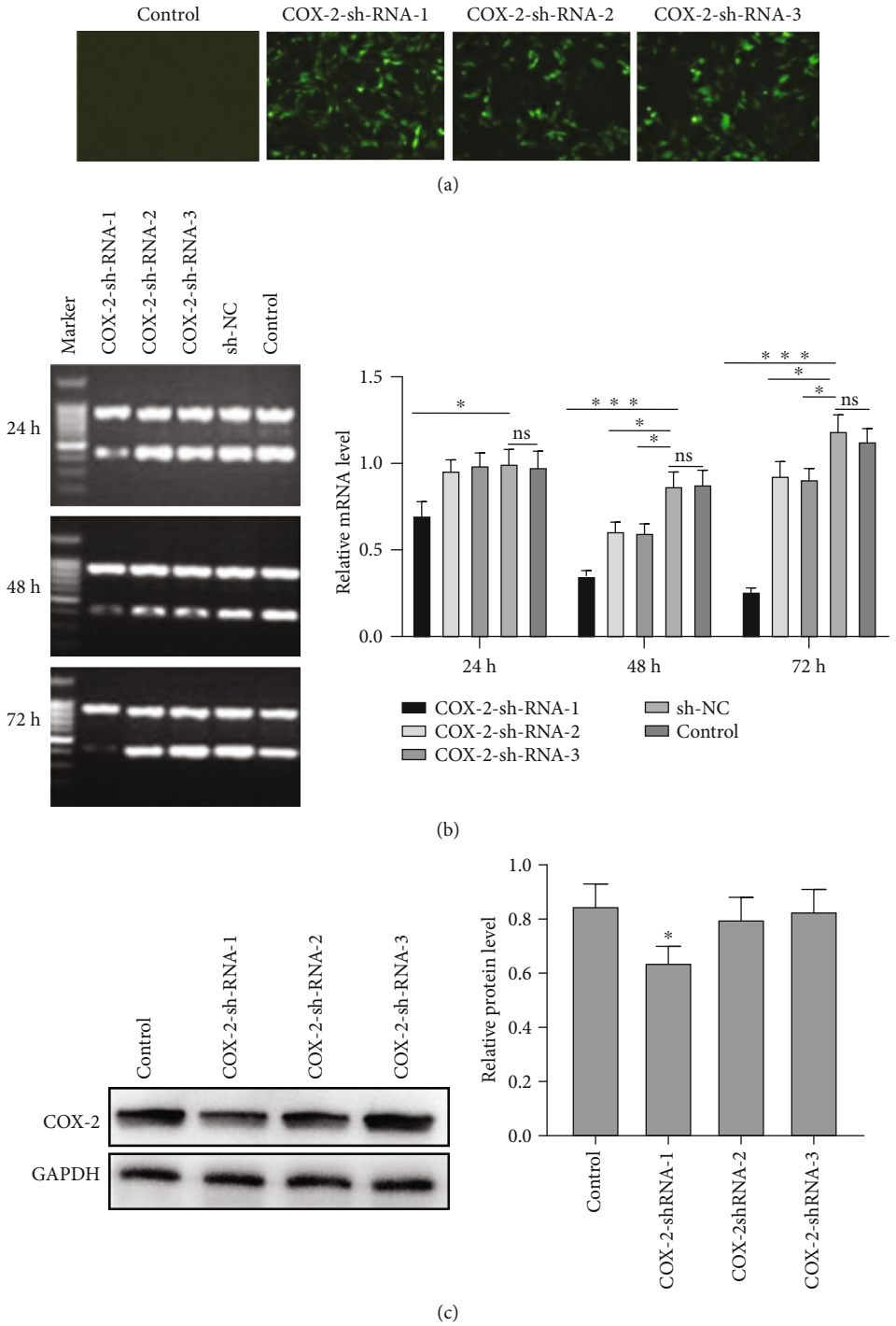

Figure 1: COX-2 expression in each group after knocking down COX-2. (a) Green fluorescent protein expression was observed by a fluorescent microscope after transfection with COX-2-shRNA-1, COX-2-shRNA-2, and COX-2-shRNA-3 (magnification 100x). (b) RT-PCR was used to measure the efficiency of shRNA-mediated gene knockdown in 24, 48, and 72 hours. (c) The protein levels of COX-2 were significantly inhibited by COX-2-shRNA-1. $^{*}p < 0.05$; $^{***}p < 0.001$; and ns: no significant difference, compared with the sh-NC group and control group.

2.11. Statistics. All data were presented as the mean ± standard deviation (SD). The differences between two groups were analyzed using unpaired Student's *t*-test. One-way ANOVA was used for multiple groups. A statistical significance was defined when $p < 0.05$. All statistical analyses was performed using SPSS18.0 software.

3. Results

3.1. COX-2 Expression in Each Group after Knocking Down COX-2. To evaluate the transfection efficiency of COX-2-shRNA, the fluorescence density of cells exceeded 70-85%, as observed by the fluorescent microscope (Figure 1(a)). No

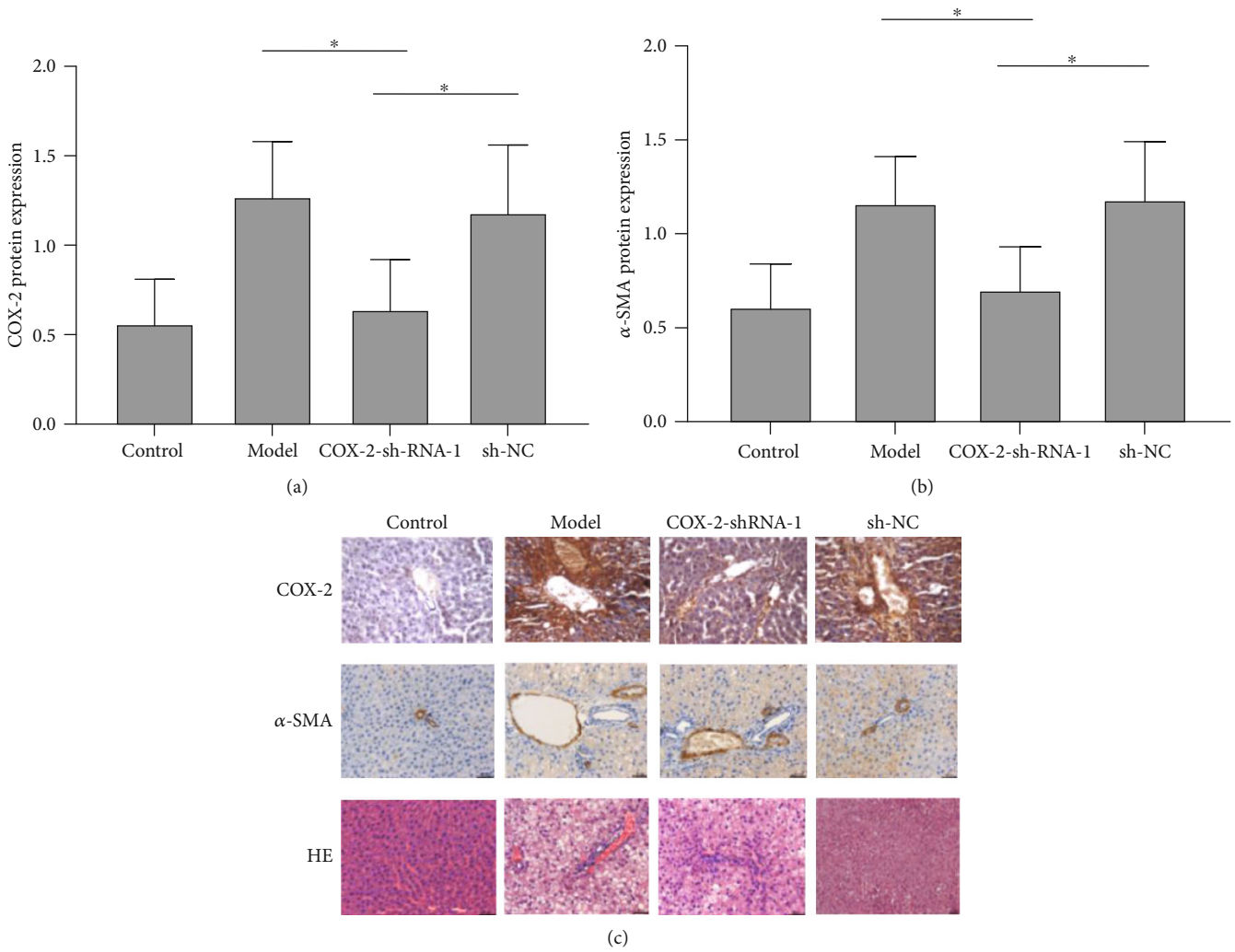

Figure 2: (a) Western blotting for the protein expression of COX-2 after shRNA injection in hepatic tissues. (b) Western blotting for the protein expression of α-SMA after shRNA injection in hepatic tissues. (c) Detection the expression of COX-2 and α-SMA by immunohistochemistry in the liver tissue in rats (magnification 200x). $^{*}p < 0.05$, compared with the sh-NC group and COX-2-shRNA-1 group.

fluorescent signal was observed in the control group, indicating a successful cell transfection. All the three-specific shRNA of COX-2 downregulate the COX-2 expression after transfection of 48 hours and 72 hours, and the most significant effect was caused by COX-2-shRNA-1 ($p < 0.001$, Figure 1(b)). After transfection of 24 hours, COX-2 mRNA decreased in the COX-2-shRNA-1-transfected group ($p < 0.05$). Further analysis of the results showed that a remarkably decreased COX-2 protein expression in the COX-2-shRNA-1-transfected group at 48 h ($p < 0.05$) while the other two groups showed no major difference (Figure 1(c)). What emerges from the results reported here is that the construction of shRNA targeting COX-2 is successful and can be used for further experiments.

3.2. Knockdown of COX-2 Suppresses Proliferation of HSCs in Liver Tissue of Rats with Hepatic Fibrosis. To investigate the effect of COX-2 on proliferation and apoptosis of HSCs in the liver tissue of rats with hepatic fibrosis, we firstly generated a rat model in which COX-2 nanomedicine-shRNA-1 was injected. As the first evidence to support COX-2 nanomedicine for liver fibrosis, western blotting showed that the expression level of COX-2 nanomedicine in liver fibrosis model rats was significantly increased, and it can be effectively inhibited by transfection with COX-2 nanomedicine-shRNA-1 ($p < 0.05$, Figure 2(a)). As the indicator of HSC proliferation, the expression patterns of α-SMA showed similarity with COX-2 nanomedicine, as shown by the elevated expression in the model group and the downregulated expression in the COX-2 nanomedicine-shRNA-1 group ($p < 0.05$, Figure 2(b)). Detection of COX-2 nanomedicine and α-SMA in liver tissues by immunohistochemistry indicated that the expression trends of COX-2 nanomedicine and α-SMA were consistent with the results of western blotting (Figure 2(c)). Taken together, these results suggest that knockdown of COX-2 nanomedicine suppresses proliferation of HSCs in the liver tissue of rats with hepatic fibrosis.

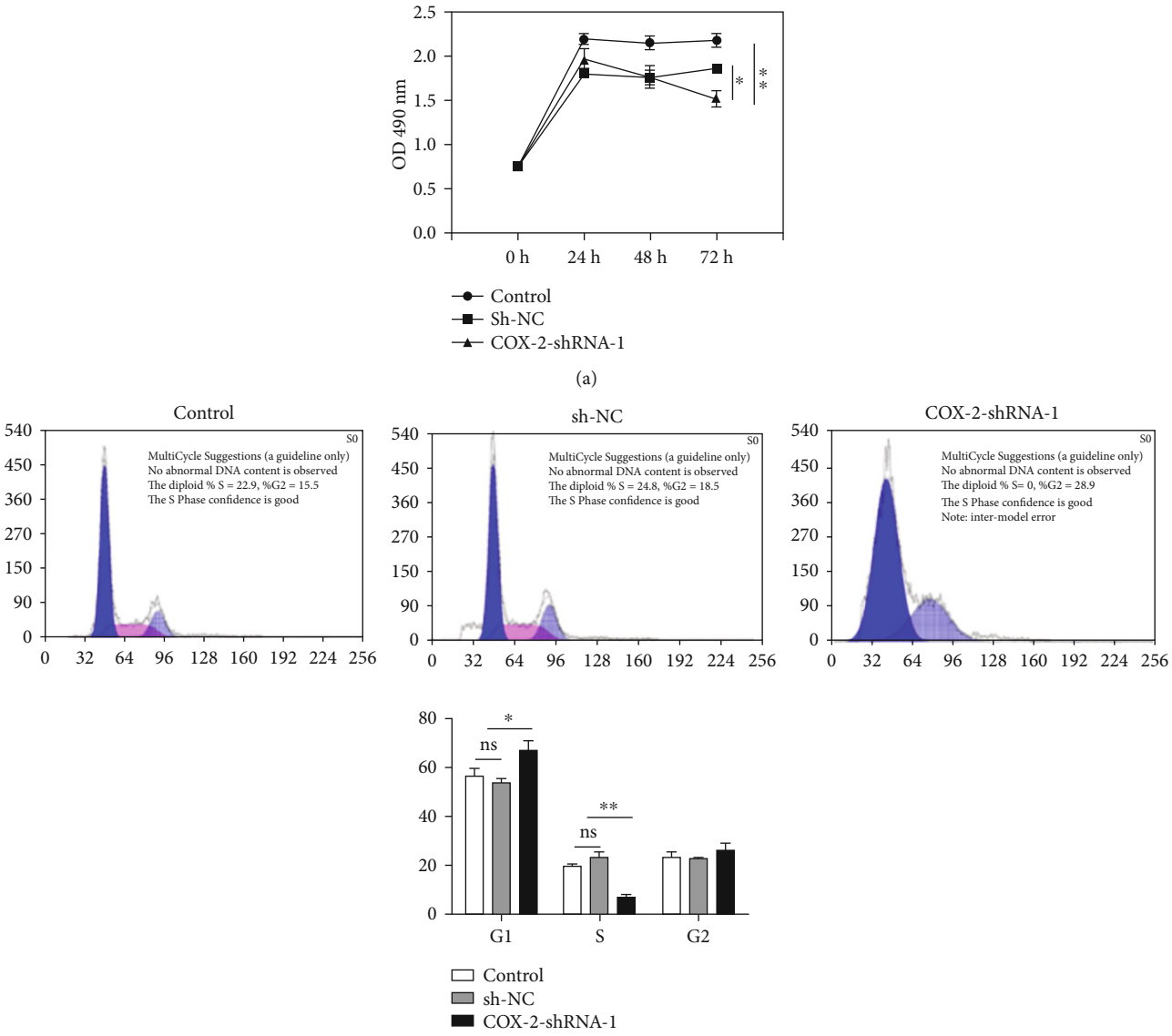

Figure 3: Continued.

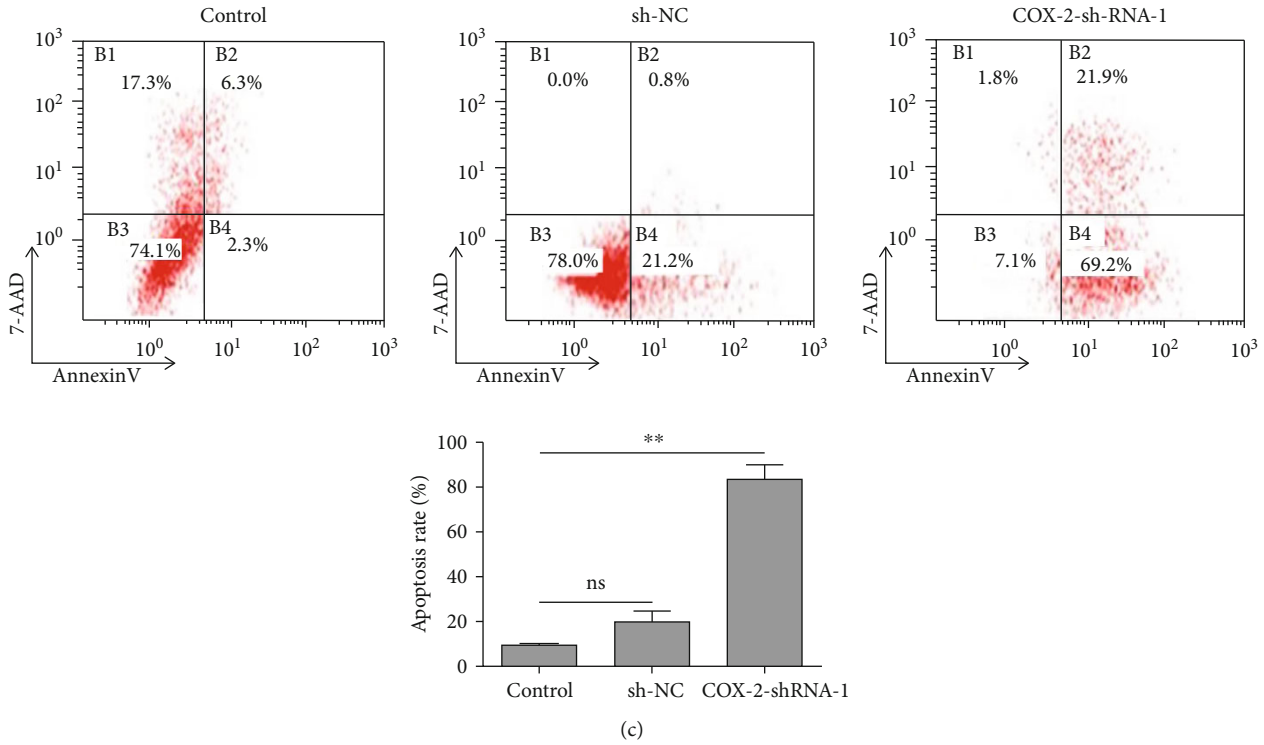

Figure 3: Knockdown of COX-2 suppressed stellate cell proliferation and induced cell apoptosis. (a) MTT assay for relative cell proliferation rate of HSCs after COX-2 knockdown. (b) Cell cycle analysis for cultured HSCs after COX-2 knockdown. (c) Flow cytometry approach for measuring changes in apoptotic rate after COX-2 knockdown. $^{*}p < 0.05$; $^{**}p < 0.01$; and ns: no significant difference, compared with the sh-NC group.

3.3. Cox-2-shRNA-1 Suppressed Proliferation and Induced Apoptosis of HSCs In Vitro. Next, we investigated the effect of COX-2 knockdown on hepatic cell proliferation and apoptosis in vitro. Cell proliferation was remarkably inhibited after transfection at 72 h as demonstrated by the MTT assay ($p < 0.05$, Figure 3(a)). Further analysis of the cell cycle revealed that knockdown of COX-2 increased the percentage of cells arresting at G1 phase (Figure 3(b)). Moreover, cell apoptotic rate in the COX-2-shRNA-1 group was found significantly higher by FACS ($p < 0.01$, Figure 3(c)). Overall, these results suggest that knockdown of COX-2 effectively suppressed hepatic stellate cell proliferation and accelerating their apoptosis.

3.4. Changes in Expression of Dynamic Genes of Hepatic Stellate Cells after Knockdown of COX-2. To further investigate the mechanism of COX-2 in regulating proliferation and apoptosis of hepatic stellate cells, gene chip assay was used to compare differential between the untreated and treated cells. Gene chip results showed that 37 genes were upregulated and 8 genes were downregulated after shRNA transfection with 48 hours (Table 2). Analysis of cells after 72 hours transfection showed that 50 genes in HSCs showed increased, while 46 genes showed decreased (Table 3). We also performed GO annotation on those differentially expressed genes, among which three proliferation-associated genes were upregulated (Il6, Csf2, and Atf3) at 48 h, but without any downregulated gene. At 72 h, three proliferation genes (CDC27, TP53, and Cxcl10) were unregulated and three genes (DUsp1, Serpinb2, and Plcd4) were downregulated. For all 8 genes associated with cell apoptosis, we found four of them (Il1b, Il6, Ccl2, and Phlda3) were upregulated at 48 h and without any gene down-regulated. At 72 h, Tp53 was upregulated while Sh3kbp1, Pea15, and Plcd4 were suppressed (Tables 1–3). Those genes with significant changes were further validated by RT-PCR. As the results demonstrated that COX-2-shRNA-1 elevated CDC27, but decreased the Plcd4 gene transcripts. However, opposite trends were observed as Sh3kbp1 was upregulated, plus DUsp1 upregulated, in sharp contrast with DNA chip assay (Figures 4(a) and 4(b)). No significant change was found in other candidate genes (Figure 4(c)). In summary, COX-2-shRNA-1 modulated the cell proliferation and apoptosis related to the change in the expression of CDC27 and Plcd4.

3.5. COX-2-shRNA-1 Regulated the Proliferation and Apoptosis of HSCs through Regulating CDC27. CDC27 has been demonstrated in modulating cell proliferation [7] and apoptosis of tumor cells [8]. Therefore, we speculate that COX-2 may affect cell proliferation and apoptosis by affecting CDC27. Our conjecture was confirmed by the results that knockdown of COX-2 significantly elevated the protein level of CDC27, and this can be attenuated by knockdown of CDC27 (Figure 5(a)). The role of CDC27 on hepatic stellate cell proliferation was further investigated. Compared with the COX-2-shRNA-1 group, increased cell proliferation in the COX-2-shRNA-1+ sh-CDC27 group indicated the

Table 2: Differential gene expression profiles between COX-2-shRNA-1 and sh-NC at 48 hours posttransfection.

	Oligo_id	Name	Ratio	Description
1	Rn30002068	Ppef2	7.8223	Protein phosphatase
2	Rn30009092	—	3.1274	Immunoresponsive gene 1
3	R001746_01	Cxcl10	2.4468	Small inducible cytokine B10 precursor
4	Rn30015483	Gbp4	2.4271	Similar to guanylate nucleotide-binding protein 4
5	Rn30001057	Oasl1	2.4164	2′-5′-Oligoadenylate synthetase-like 1
6	Rn30004185	—	2.3045	Antisense RNA overlapping MCH protein.
7	Rn30021148	Ifit3	2.2743	Tetratricopeptide repeat 3
8	Rn30015485	Gbp4	2.2279	Similar to guanylate nucleotide-binding protein 4
9	Rn30001055	Oasl1	2.2037	2′-5′-Oligoadenylate synthetase-like 1
10	Rn30020145	—	2.1558	
11	R000595_01	Cx3cl1	2.0349	Chemokine (C-X3-C motif) ligand 1
12	Rn30020616	Cxcl11	1.9534	Chemokine (C-X-C motif) ligand 11
13	R001188_01	Il1b	1.9086	Interleukin-1 beta precursor (IL-1 beta).
14	Rn30005625	Mdm2	1.8729	Similar to mdm2 gene product
15	Rn30024865	isg12(b)	1.8722	Putative ISG12(B) protein.
16	Rn30016690	Isg20	1.8707	Interferon-stimulated protein (predicted)
17	Rn30021722	Apol9a	1.8058	
18	Rn30005624	Mdm2	1.767	Similar to mdm2 gene product
19	R003548_01	Kcnt1	1.7082	Potassium channel subfamily T member 1
20	Rn30015487	Gbp5	1.6855	Similar to guanylate-binding protein 5
21	R003549_01	Csf2	1.6817	Colony-stimulating factor
22	R001026_01	Atf3	1.665	Cyclic AMP-dependent transcription factor ATF-3
23	Rn30004011	Scin	1.6441	Scinderin
24	R001191_01	Il6	1.6382	Interleukin-6
25	Rn30015486	Gbp5	1.6332	Similar to guanylate-binding protein 5
26	Rn30008444	Ifi27l	1.6328	Putative ISG12(a) protein
27	Rn30008951	Elovl4	1.6118	Similar to Elovl4
28	Rn30016019	Irf7	1.5875	Interferon regulatory factor 7
29	R002891_01	Cyp2d4v1	1.573	Cytochrome P450 2D18
30	Rn30001796	Mx2	1.5626	Interferon-induced GTP-binding protein Mx3.
31	R000644_01	Ccl2	1.5596	Chemokine (C-C motif) ligand 2
32	Rn30023693	—	1.5285	—
33	Rn30026248	—	1.528	Macrophage inflammatory protein 2-beta precursor
34	Rn30016526	Ccdc37	1.5222	Similar to C230069K22Rik protein
35	Rn30012826	Aadac	1.5185	Arylacetamide deacetylase
36	Rn30001056	Oasl2	1.5141	2′-5′-Oligoadenylate synthetase-like 2
37	Rn30008269	Phlda3	1.502	Pleckstrin homology-like domain family A member 3
38	R003539_01	Mapk8ip1	0.6656	C-Jun-amino-terminal kinase-interacting protein 1
39	Rn30026086	—	0.6545	Ankyrin repeat domain 11
40	Rn30018744	Ptov1	0.6483	Prostate tumor overexpressed gene 1
41	Rn30003851	Sh3kbp1	0.6376	SH3-domain kinase binding protein 1
42	Rn30001871	—	0.6282	Steroid-sensitive protein 1
43	R002280_01	Thra_v2	0.6144	Thyroid hormone receptor alpha
44	R002312_01	Pla2g2a	0.512	Phospholipase A2, membrane-associated precursor
45	Rn30001610		0.4945	Leucine-rich repeats and calponin homology (CH) domain containing 3

Table 3: Differential gene expression profiles between COX-2-shRNA-1 and sh-NC at 72 hours posttransfection.

	Oligo_id	Name	Ratio	Description
1	Rn30022454	—	6.1452	Tripartite motif-containing 65
2	Rn30006362	Purb	3.4474	
3	R001746_01	Cxcl10	2.8634	Small inducible cytokine B10 precursor
4	Rn30020145	—	2.652	
5	Rn30001057	Oasl1	2.6028	2′-5′-Oligoadenylate synthetase-like 1
6	Rn30005291	Cdc27	2.4796	Cell division cycle 27 homolog
7	Rn30006471	—	2.3552	PFTAIRE protein kinase 1
8	Rn30015483	Gbp4	2.3519	Similar to guanylate nucleotide-binding protein 4
9	Rn30021673	—	2.3392	¨C
10	R000595_01	Cx3cl1	2.3344	Fractalkine precursor
11	Rn30001055	Oasl1	2.3048	2′-5′-Oligoadenylate synthetase-like 1
12	Rn30002812	Enah	2.2328	Enabled homolog
13	Rn30018127	—	2.2025	Diaphanous homolog 1
14	Rn30024865	isg12(b)	2.2007	Putative ISG12(B) protein
15	Rn30025470	—	2.1365	RNA-binding motif protein 27
16	Rn30025880	—	2.0773	Topoisomerase (DNA) II beta-binding protein
17	Rn30021148	Ifit3	2.0594	Human interferon-inducible proteins
18	Rn30002530	Rfc1	2.035	VIP-receptor-gene repressor protein
19	Rn30006955	—	1.9683	Peptidyl-prolyl *cis-trans* isomerase G
20	Rn30024339	Gbf1	1.9515	Golgi-specific brefeldin A-resistance factor 1
21	Rn30015485	Gbp4	1.9459	Similar to guanylate nucleotide-binding protein 4
22	Rn30009903	Trp53	1.8363	Cellular tumor antigen p53
23	Rn30010375	—		
24	Rn30006914	Loxl3	1.7087	Similar to lysyl oxidase-like 3
25	Rn30018257	Hsp90ab1	1.7047	Heat shock protein HSP 90-beta (HSP 84).
26	Rn30016830	Chd4	1.6964	Mi-2 autoantigen
27	Rn30021722	Apol9a	1.6932	¨C
28	Rn30015487	Gbp5	1.6803	Similar to guanylate-binding protein 5
29	Rn30009073	—	1.6721	¨C
30	Rn30008992	—	1.6509	WAS protein family, member 2
31	Rn30017948	Psmb10	1.6478	Proteasome subunit, beta type 10
32	Rn30005283	—	1.644	Rap1 interacting factor 1 homolog (yeast)
33	Rn30019336	Pogz	1.6139	Pogo transposable element with ZNF domain
34	Rn30023995	NIPBL	1.6115	PREDICTED: similar to delangin
35	Rn30021836	Olr1214	1.5675	Olfactory receptor Olr1214
36	R003169_01	Acsl6	1.5651	Long-chain-fatty-acid–CoA ligase 6
37	R004194_01	Zfp709	1.565	Zinc finger protein 14
38	Rn30004337	RGD1565597	1.5561	Similar to RIKEN cDNA 2210421G13
39	Rn30007454	—	1.5487	Complement receptor 2
40	Rn30003220	—	1.545	13-day embryo male testis cDNA
41	Rn30015924	Trub1	1.5415	TruB pseudouridine (psi) synthase homolog 1
42	Rn30019481	Gabpb2	1.5354	Transcription factor GABP beta 2-1 chain
43	Rn30009011	RGD1305500	1.5248	DNA segment, Chr 19, ERATO Doi 737
44	Rn30015486	Gbp5	1.5204	Guanylate-binding protein 5
45	Rn30015488	—	1.5197	Guanylate nucleotide-binding protein 2
46	R002891_01	Cyp2d4v1	1.5187	Cytochrome P450 2D18
47	Rn30016434	—	1.5155	RGD1310888-predicted protein

Table 3: Continued.

	Oligo_id	Name	Ratio	Description
48	Rn30001002	—	1.5108	
49	R001164_01	—	1.5085	Granzyme M precursor
50	Rn30023011	—	1.5073	
51	Rn30000745	Hspa1b	0.6661	Heat shock 70 kDa protein 1A/1B
52	Rn30010844	—	0.6653	
53	R002646_01	—	0.665	
54	Rn30013433	Med31	0.6623	RNA polymerase II transcription subunit 31
55	Rn30003203	Dynlt3	0.6605	T-complex-associated testis-expressed 1-like
56	Rn30022044	—	0.6596	—
57	Rn30003825	Nt5c1b	0.6581	Retinol dehydrogenase 14
58	Rn30025065	P4ha2	0.6576	Procollagen-proline, 2-oxoglutarate-4-dioxygenase, alpha II polypeptide
59	Rn30000745	Hspa1b	0.6555	Heat shock 70 kDa protein 1A/1B
60	Rn30019963	—	0.6548	—
61	Rn30005770	Ero1l	0.6482	ERO1-like protein alpha precursor
62	Rn30024141	—	0.6465	¨C
63	Rn30019903	Rassf1	0.6464	Ras association domain family 1 isoform 2
64	Rn30003533	Dusp1	0.6461	Dual specificity protein phosphatase 1
65	Rn30020658	RGD1563649	0.6446	Similar to ORF4
66	Rn30006166	Pea15a	0.6435	Phosphoprotein enriched in astrocytes 15
67	Rn30012217	Arg1	0.6427	Arginase-1 (EC 3.5.3.1)
68	Rn30023334	—	0.6392	
69	Rn30023867	Rnase1l2	0.6379	
70	Rn30002222	Pgk1	0.6341	Phosphoglycerate kinase 1
71	R002211_01	Aldoc	0.6301	Fructose-bisphosphate aldolase C
72	Rn30002683	RGD1560553	0.6288	PREDICTED: similar to hypoxia-induced gene 1
73	Rn30018943	—	0.6233	DNA-3-methyladenine glycosylase
74	Rn30006243	—	0.619	
75	Rn30025357	—	0.6154	
76	Rn30000745	Hspa1b	0.6086	Heat shock 70 kDa protein 1A/1B
77	Rn30003851	Sh3kbp1	0.6013	SH3-domain kinase binding protein 1
78	Rn30000745	Hspa1b	0.5944	Heat shock 70 kDa protein 1A/1B
79	Rn30005084	LOC499742	0.5851	LRRGT00150.
80	Rn30000745	Hspa1b	0.5848	Heat shock 70 kDa protein 1A/1B
81	Rn30015841	Bnip3	0.581	BCL2/adenovirus E1B-interacting protein 3
82	Rn30014271	RGD1559815	0.5793	Da1-12
83	Rn30000745	Hspa1b	0.5732	Heat shock 70 kDa protein 1A/1B
84	Rn30000745	Hspa1b	0.5731	Heat shock 70 kDa protein 1A/1B
85	Rn30000745	Hspa1b	0.5706	Heat shock 70 kDa protein 1A/1B
86	Rn30000745	Hspa1b	0.5699	Heat shock 70 kDa protein 1A/1B
87	Rn30026196	Hist1h4m	0.5511	Histone H4.
89	Rn30000745	Hspa1b	0.545	Heat shock 70 kDa protein 1A/1B
90	Rn30024135	LOC499698	0.5425	C-reactive protein precursor.
91	Rn30000745	Hspa1b	0.5364	Heat shock 70 kDa protein 1A/1B
92	Rn30015672	Car9	0.51	Similar to carbonic anhydrase 9
93	Rn30004468	Upp1	0.4769	Uridine phosphorylase 1
94	Rn30014956	Plcd4	0.4744	Phospholipase C, delta 4
95	R001854_01	Ccl20	0.4709	Small inducible cytokine A20 precursor
96	Rn30022206	Dusp6	0.4411	Dual specificity protein phosphatase 6

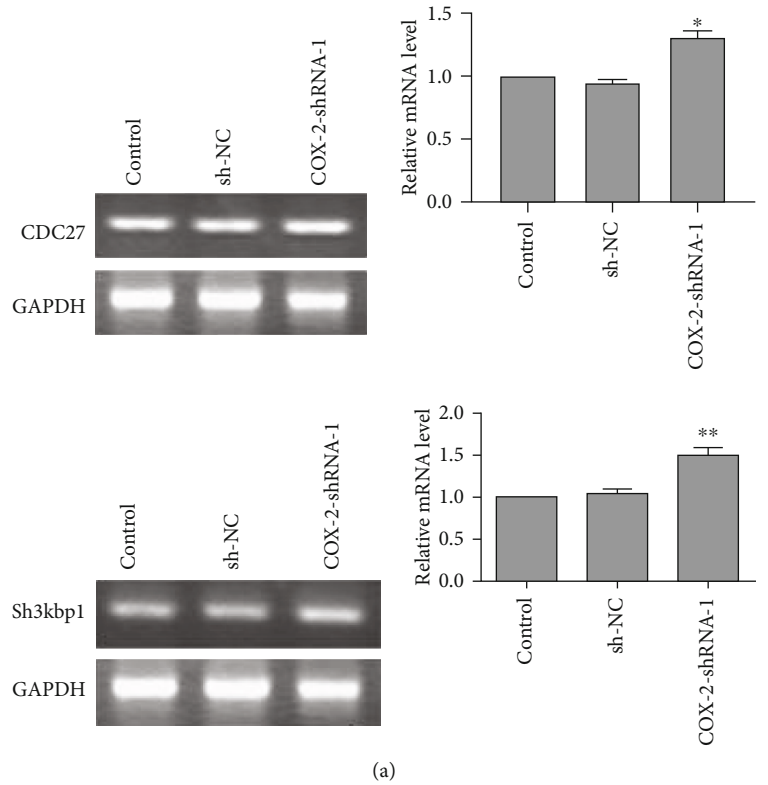

(a)

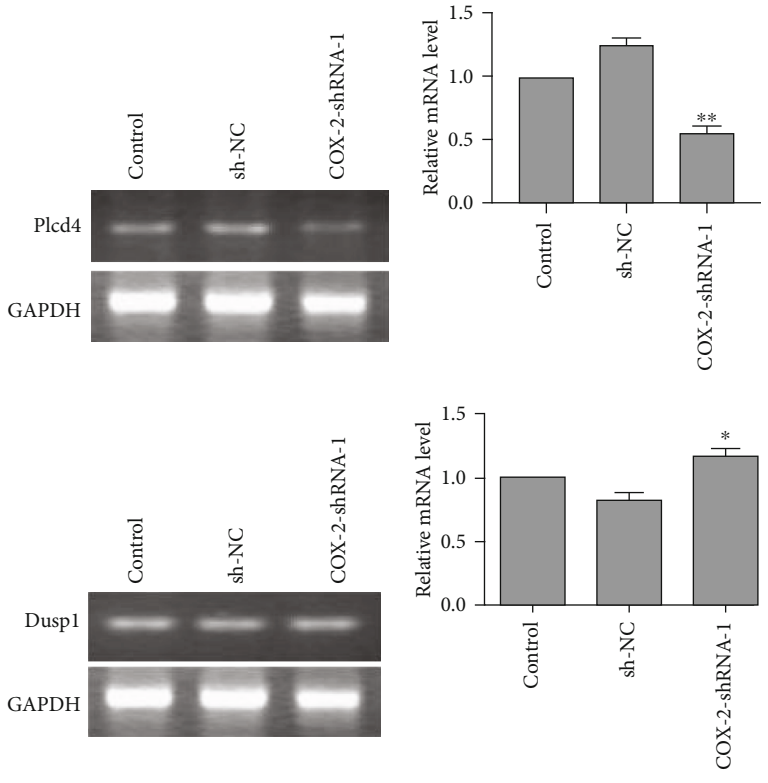

(b)

Figure 4: Continued.

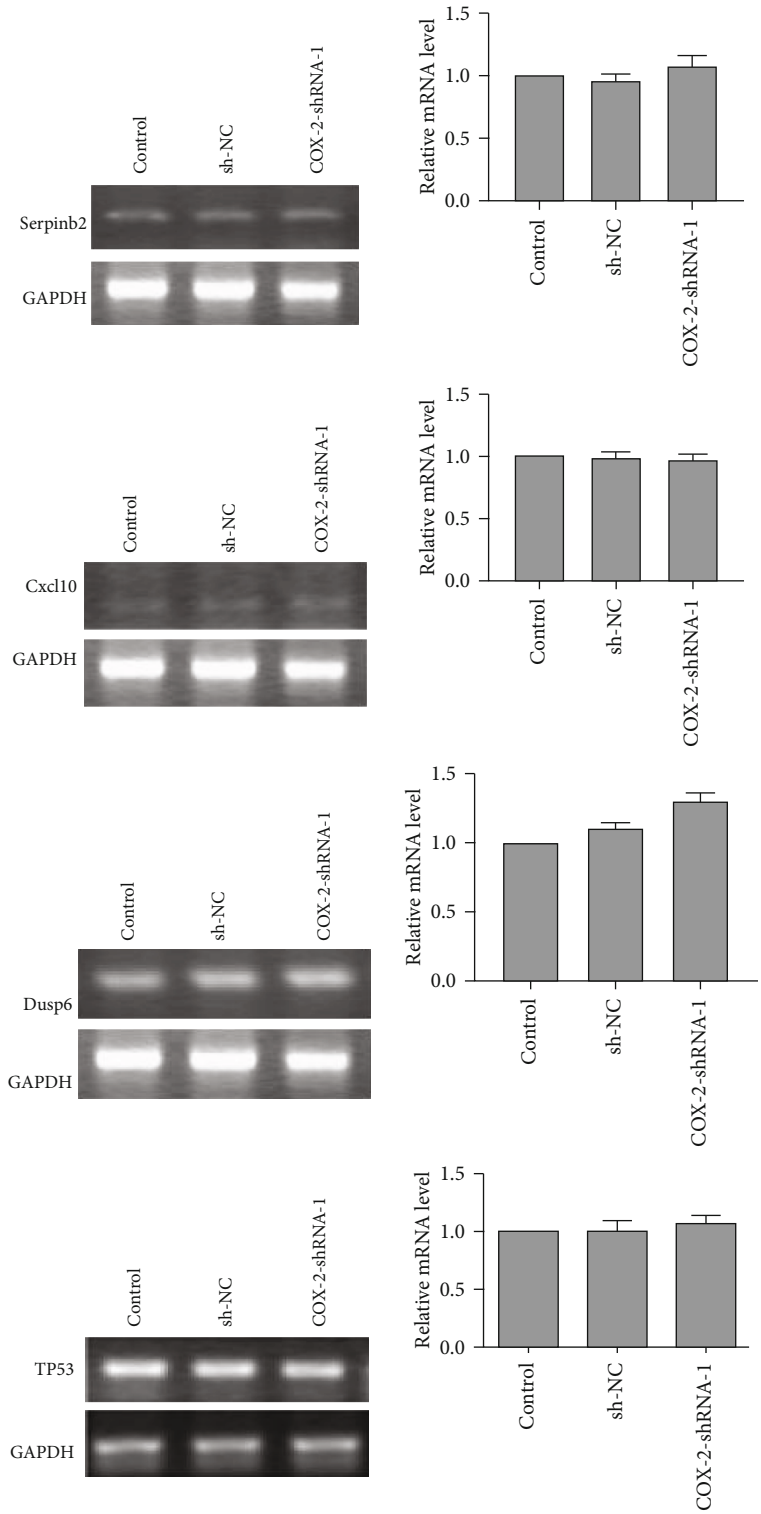

(c)

Figure 4: Differential gene expression profiles in COX-2 knockdown cells. (a) Expression of CDC27 and Sh3kbp1 were detected by RT-PCR in cells. (b) Expression of Phlcd4 and Dusp1 was detected by RT-PCR. (c) The expressions of Serpinb2, cxcl10, Dusp6, and TP53 genes were measured by RT-PCR. $^{*}p < 0.05$ and $^{**}p < 0.01$, compared with the sh-NC group.

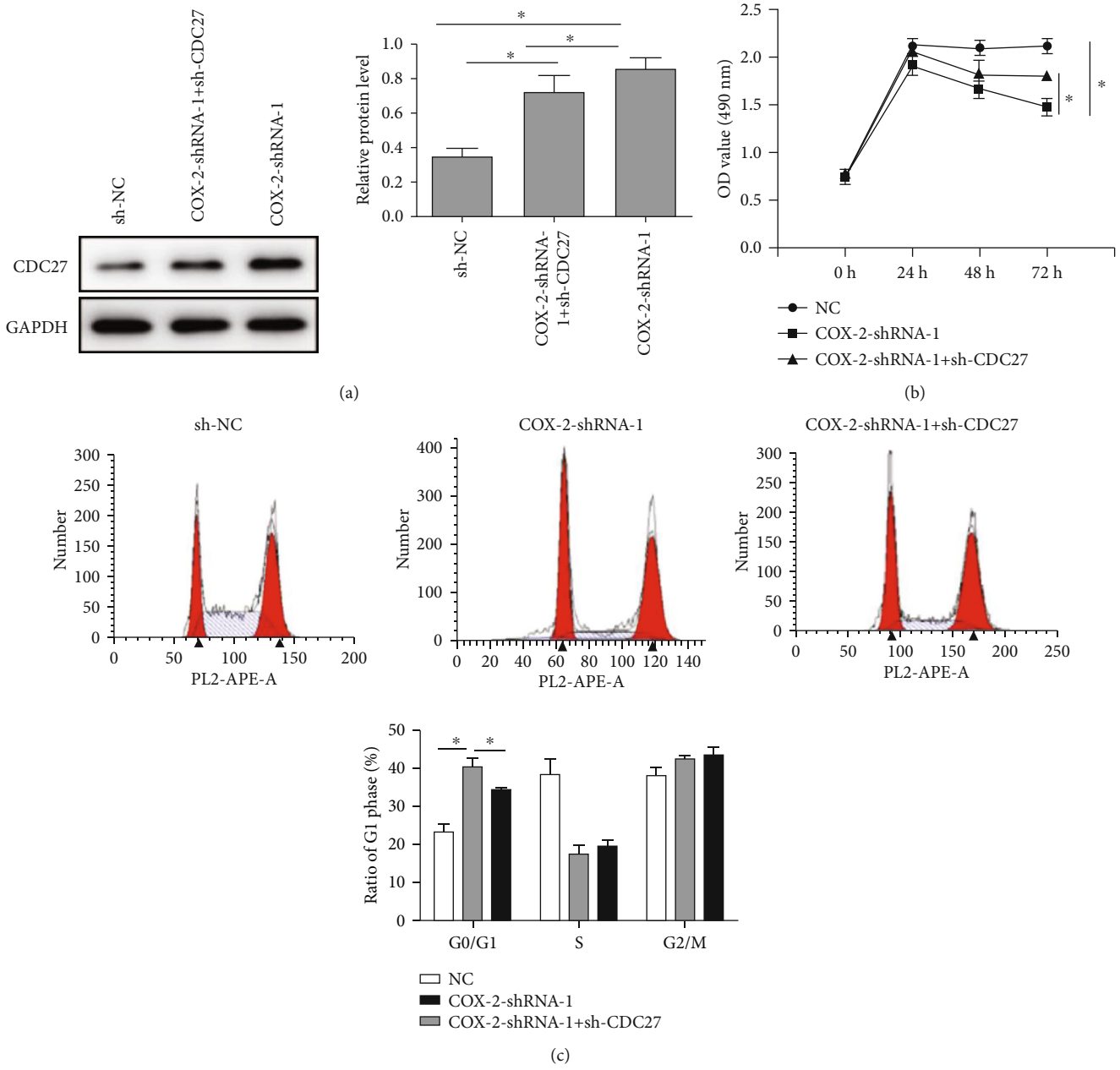

Figure 5: Continued.

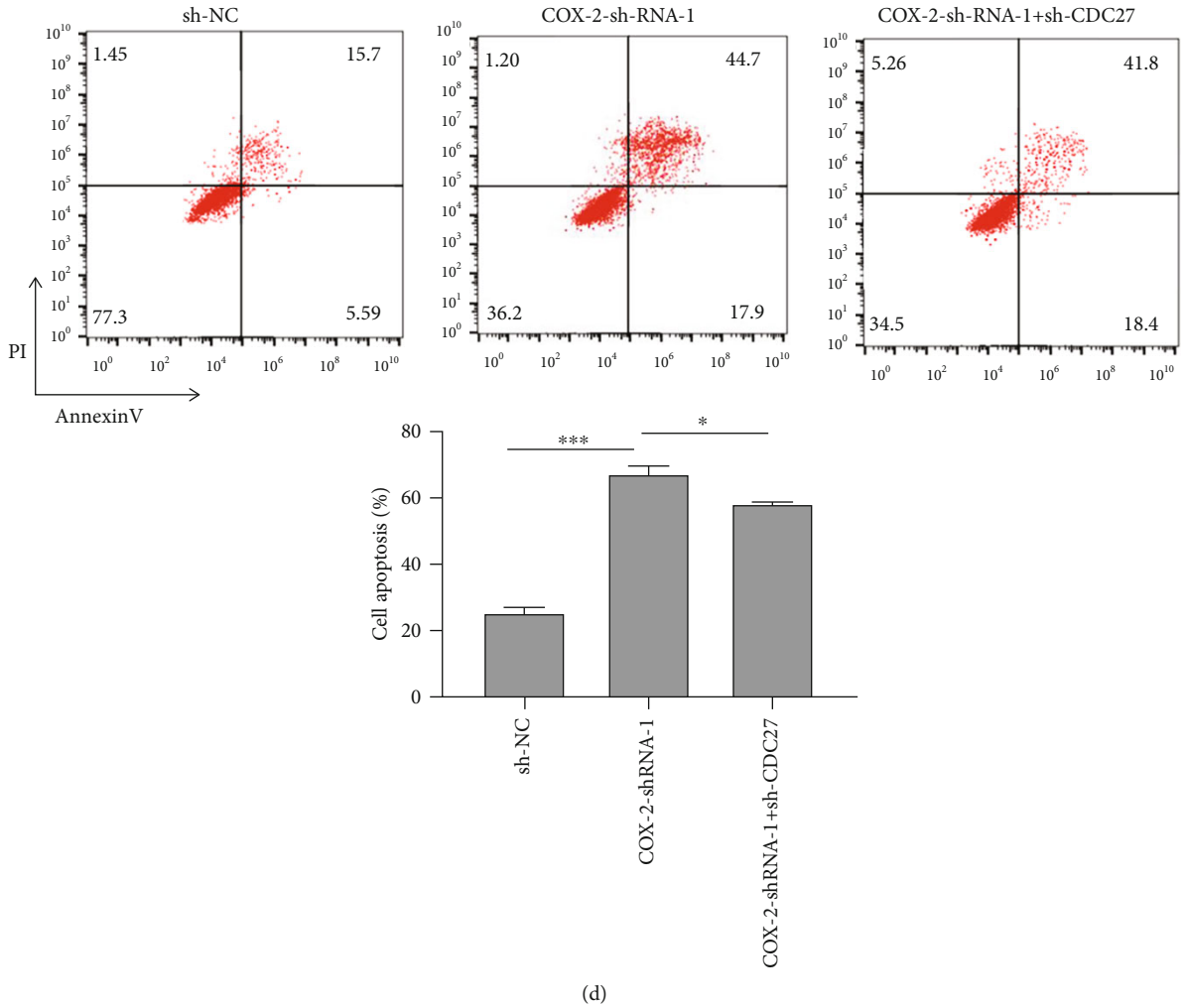

Figure 5: Effects of shRNA-mediated COX-2 knockdown on HSCs related with the changed expression of CDC27. (a) Western blotting for CDC27 protein expression in all groups. (b) Cell proliferation was detected in cotransfection of COX-2 and CDC27 shRNA cells, COX-2-shRNA-1 cells, and sh-NC cells. (c) HSC-T6 cells were transfected with COX-2-shRNA-1, or sh-NC, or cotransfected with COX-2-shRNA-1 and sh-CDC27. Cell cycle analysis was examined by flow cytometry. (d) Apoptosis of HSC-T6 cells transfected with COX-2-shRNA and CDC27-shRNA, COX-2 nanomedicine-shRNA-1, and sh-NC was examined by flow cytometry. $^{*}p < 0.05$ and $^{***}p < 0.001$, compared with the sh-NC group and COX-2-shRNA-1 group.

proproliferation effect of CDC27 (Figure 5(b)). In the previous results, knockdown of COX-2 induced more cells to arrest in G0/G1 phase, but on this basis, knockdown of CDC27 showed a weakened effect (Figure 5(c)). Cotransfection of CDC27-shRNA and COX-2-shRNA-1 decreased the cell apoptotic rate when compared with the COX-2-shRNA-1 group, suggesting that knockdown of CDC27 attenuated the proapoptotic effect of COX-2-shRNA-1 in HSCs (Figure 5(d)). What emerges from the results reported in the above is that COX-2 knockdown suppressed proliferation and accelerated apoptosis via activating CDC27 expression in HSCs.

4. Discussion

The primary effector cell in hepatic fibrosis is the HSCs [9]. HSCs are activated and transformed from quiescent to activated when the liver is damaged by mechanical stimulation or the inflammation. Activated HSCs have a strong ability to synthesize extracellular matrix, then leading to the formation of liver fibrosis or cirrhosis. Therefore, inhibiting the proliferation of HSCs and promoting its apoptosis have become the main strategy to treat liver fibrosis [10].

Previous studies have shown that COX-2 may be involved in the development of hepatic fibrosis by regulating the proliferation and apoptosis of HSCs [4]. SC-236 was used to prevent the occurrence of carbon tetrachloride-induced hepatic fibrosis in rats, which is mainly related to its regulation on the apoptosis and proliferation of HSCs [4]. However, the side effect of COX-2 inhibitors such as cardiovascular events or gastrointestinal bleeding limits its wide application [11]. Therefore, the nucleotide-based inhibitor for gene expression has been raised as a novel treatment approach. RNA interference (RNAi), a phenomenon of posttranscriptional gene silencing (PTGS),

provides new insights for treating liver fibrosis [12]. Previous experiments showed that COX-2-shRNA-1 can effectively treat experimental liver fibrosis [3].

In this study, we found that knockdown of COX-2 effectively suppressed the proliferation of HSCs in the liver of rats with hepatic fibrosis, which has been proved by the decrease in α-SMA and the number of α-SMA immune-positive cells. More clearly, knockdown of COX-2 suppressed proliferation and facilitated apoptosis of HSCs. Our results were consistent with most literature reports [1, 6]. We argue that the regulation of COX-2 on HSC cell behavior might be the primary mechanism of it in hepatic fibrosis pathogenesis.

For the further evidences of COX-2 in regulating hepatic fibrosis, we employed mRNA microarray assay to examine the expression of a series of proliferative and apoptotic relative genes. Knockdown of COX-2 in HSCs leads to some cell proliferation genes to change; some of them upregulated, such as Il6, Csf2, Atf3, Cdc27, Tp53, and Cxcl10; and some of them downregulated including Dusp1, Serpinb2, and Plcd4. As for the apoptotic related genes, upregulation of Il1b, Il6, Ccl2, Phlda3, and Tp53 and downregulation of Sh3kbp1, Peal5, and Plcd4 genes were demonstrated. Sh3kbp1 gene may regulate various cell behaviors [13], and Plcd4 gene expression was associated with breast cancer cell proliferation [14]; CXCL10 induced cell proliferation and apoptosis [15, 16]. After silencing the COX-2 gene in HSCs, the expression of CDC27 is enhanced, which is the only gene with consistent results in DNA chips and RT-PCR. CDC27 was previously reported to facilitate proliferation [7]. It has potent protein binding affinity [8, 17] and participates in various biological processes including ubiquitination mediated proteolysis [18], cell cycle regulation [19], cell division [20], and transformation at metaphase of mitosis [21, 22]. In this study, we found that CDC27 knockdown could accelerate HSC proliferation and inhibit cell apoptosis, indicating that RNAi silencing of COX-2 could modulate HSCs growth, inhibit cell proliferation, and induce cell apoptosis via CDC27 upregulation. Moreover, CDC27 has been postulated to be one major target for induced cell apoptosis and cell cycle arrest in cancer cells [23]. The expression of COX-2 and CDC27 has been associated during immune response regarding macrophage proliferation [24]. This study, on the other hand, revealed the regulation of CDC27 gene expression by COX-2 knockdown, suggesting that CDC27 exerted its role at the downstream of COX-2. Our data thus provide the first-hand information on how COX-2 regulates HSC proliferation, cell cycle, and cell apoptosis by regulating CDC27 gene expression, revealing an unknown pathway of HSC behavior. However, the detailed molecular mechanism for COX-2 regulation on CDC27 gene expression is still unclear yet and thus requires further mechanistic studies to fulfill the weakness of the current study.

In summary, the current study described the regulation of HSC proliferation and apoptosis by COX-2/CDC27 axis and found that such regulatory pathway played important roles in mediating severity of hepatic fibrosis. Our overall findings provide a promising treatment target for early intervention of liver fibrosis.

Data Availability

The datasets used and/or analyzed during the current study are available from the corresponding author on reasonable request.

Ethical Approval

All animal procedures were approved by the Institutional Animal Care and Use Committee of University of South China (2011002A), Hengyang, China.

Conflicts of Interest

The authors declare no conflict of interest, financial, or otherwise.

Authors' Contributions

Yang Hu designed the experiments. Yang Hu, Li Xian Chen, and Nian Fu performed the experiments and analyzed the date. Yang Hu wrote the manuscript. Jian Hua Xiao and Xue Feng Yang have modified the language expression of the article. All authors have read and approved the manuscript.

Acknowledgments

This study was funded by the Scientific Research Project of Hunan Provincial Health and Family Planning Commission (No. A2017015), the Hunan Provincial Union Fund for Natural Science and Cities (No. 2016JJ5010), the financial support from the Program for Hunan Provincial Science and Technology Department (No. 2018DK51707), and the National Natural Science Foundation of China (No. 81373465).

References

[1] Y. H. Paik, J. K. Kim, J. I. Lee et al., "Celecoxib induces hepatic stellate cell apoptosis through inhibition of Akt activation and suppresses hepatic fibrosis in rats," *Gut*, vol. 58, no. 11, pp. 1517–1527, 2009.

[2] H. Hu, X. Jing, X. Zou, and J. Wu, "Role of cyclooxygenase 2 and its inhibitor valdecoxib in liver fibrosis," *Zhonghua Yi Xue Za Zhi*, vol. 94, no. 10, pp. 784–787, 2014.

[3] X. Ni, H. W. Liao, W. S. Ou et al., "Construction of COX-2 short hairpin RNA expression vector and its inhibitory effect on hepatic fibrosis," *Biotechnology & Biotechnological Equipment*, vol. 32, no. 3, pp. 1–10, 2018.

[4] L. Chang, Z. Zhang, J. Yang, S. H. McLaughlin, and D. Barford, "Atomic structure of the APC/C and its mechanism of protein ubiquitination," *Nature*, vol. 522, no. 7557, pp. 450–454, 2015.

[5] J. Zhu, Z. Luo, Y. Pan et al., "H19/miR-148a/USP4 axis facilitates liver fibrosis by enhancing TGF-β signaling in both hepatic stellate cells and hepatocytes," *Journal of Cellular Physiology*, vol. 234, no. 6, pp. 9698–9710, 2019.

[6] A. Planagumà, J. Clària, R. Miquel et al., "The selective cyclooxygenase-2 inhibitor SC-236 reduces liver fibrosis by mechanisms involving non-parenchymal cell apoptosis and PPARgamma activation," *The FASEB Journal*, vol. 19, no. 9, pp. 1120–1122, 2008.

[7] L. Qiu, J. Wu, C. Pan et al., "Downregulation of CDC27 inhibits the proliferation of colorectal cancer cells via the accumulation

of p21Cip1/Waf1," *Cell death & disease*, vol. 7, no. 1, p. e2074, 2016.

[8] V. P. Bermudez, S. A. MacNeill, I. Tappin, and J. Hurwitz, "The influence of the Cdc27 subunit on the properties of the Schizosaccharomyces pombe DNA polymerase delta," *Journal of Biological Chemistry*, vol. 277, no. 39, pp. 36853–36862, 2002.

[9] S. Karvar, E. A. Ansa-Addo, J. Suda et al., "Moesin, an ERM family member, regulates hepatic fibrosis," *Hepatology*, vol. 72, no. 3, pp. 1073–1084, 2019.

[10] S. Bi, F. Chu, M. Wang et al., "Ligustrazine-oleanolic acid glycine derivative, G-TOA, selectively inhibited the proliferation and induced apoptosis of activated HSC-T6 cells," *Molecules*, vol. 21, no. 11, p. 1599, 2016.

[11] C. C. Szeto, K. Sugano, J. G. Wang et al., "Non-steroidal anti-inflammatory drug (NSAID) therapy in patients with hypertension, cardiovascular, renal or gastrointestinal comorbidities: joint APAGE/APLAR/APSDE/APSH/APSN/PoA recommendations," *Gut*, vol. 69, no. 4, pp. 617–629, 2020.

[12] J. M. Bangen, L. Hammerich, R. Sonntag et al., "Targeting CCl4 -induced liver fibrosis by RNA interference-mediated inhibition of cyclin E1 in mice," *Hepatology*, vol. 66, no. 4, pp. 1242–1257, 2017.

[13] R. Dejournett, R. Kobayashi, S. H. Pan et al., "Phosphorylation of the proline-rich domain of Xp95 modulates Xp95 interaction with partner proteins," *The Biochemical Journal*, vol. 401, no. 2, pp. 521–531, 2007.

[14] D. W. Leung, C. Tompkins, J. Brewer et al., "Phospholipase C delta-4 overexpression upregulates ErbB1/2 expression, Erk signaling pathway, and proliferation in MCF-7 cells," *Molecular cancer*, vol. 3, no. 1, p. 15, 2004.

[15] Q. Jiang, F. Wang, L. L. Shi et al., "C-X-C motif chemokine ligand 10 produced by mouse Sertoli cells in response to mumps virus infection induces male germ cell apoptosis," *Cell death & disease*, vol. 8, no. 10, p. e3146, 2017.

[16] M. Wornle, H. Schmid, M. Merkle, and B. Banas, "Effects of chemokines on proliferation and apoptosis of human mesangial cells," *BMC Nephrology*, vol. 5, no. 1, 2004.

[17] A. Schreiber, F. Stengel, Z. Zhang et al., "Structural basis for the subunit assembly of the anaphase-promoting complex," *Nature*, vol. 470, no. 7333, pp. 227–232, 2011.

[18] L. A. MacFarlane and P. R. Murphy, "Regulation of FGF-2 by an endogenous antisense RNA: effects on cell adhesion and cell-cycle progression," *Molecular Carcinogenesis*, vol. 49, no. 12, pp. 1031–1044, 2010.

[19] J. M. Pérez-Pérez, O. Serralbo, M. Vanstraelen et al., "Specialization of CDC27 function in theArabidopsis thalianaanaphase-promoting complex (APC/C)," *The Plant Journal*, vol. 53, no. 1, pp. 78–89, 2008.

[20] D. Li, G. Morley, M. Whitaker, and J. Y. Huang, "Recruitment of Cdc20 to the kinetochore requires BubR1 but not Mad2 in Drosophila melanogaster," *Molecular and Cellular Biology*, vol. 30, no. 13, pp. 3384–3395, 2010.

[21] L. Zhang, T. Fujita, G. Wu, X. Xiao, and Y. Wan, "Phosphorylation of the anaphase-promoting complex/Cdc27 is involved in TGF-beta signaling," *The Journal of Biological Chemistry*, vol. 286, no. 12, pp. 10041–10050, 2011.

[22] T. Fujita, M. W. Epperly, H. Zou, J. S. Greenberger, and Y. Wan, "Regulation of the anaphase-promoting complex-separase cascade by transforming growth factor-beta modulates mitotic progression in bone marrow stromal cells," *Molecular Biology of the Cell*, vol. 19, no. 12, pp. 5446–5455, 2008.

[23] S. J. Lee and S. A. Langhans, "Anaphase-promoting complex/-cyclosome protein Cdc27 is a target for curcumin-induced cell cycle arrest and apoptosis," *BMC Cancer*, vol. 12, no. 1, 2012.

[24] W. C. Lim and V. T. Chow, "Gene expression profiles of U937 human macrophages exposed to *Chlamydophila pneumoniae* and/or low density lipoprotein in five study models using differential display and real-time RT-PCR," *Biochimie*, vol. 88, no. 3-4, pp. 367–377, 2006.

Hindawi
Journal of Nanomaterials
Volume 2021, Article ID 9956962, 10 pages
https://doi.org/10.1155/2021/9956962

Research Article

Evaluation of a Modified Flow-Through Method for Predictive Dissolution and In Vitro/In Vivo Correlations of Immediate Release and Extended Release Formulations

Hanxi Yi,[1] Fan Liu,[2] Guoqing Zhang,[1] and Zeneng Cheng[1]

[1]*Division of Biopharmaceutics and Pharmacokinetics, Xiangya School of Pharmaceutical Sciences, Central South University, China*
[2]*Neurology Department, The First Affiliated Xiangya Hospital, Central South University, China*

Correspondence should be addressed to Zeneng Cheng; chengzn@csu.edu.cn

Received 7 March 2021; Revised 22 March 2021; Accepted 30 March 2021; Published 28 April 2021

Academic Editor: Tingting Hong

The present study evaluated the ability of a modified flow-through method for predicting in vivo performance of immediate release (IR) and extended release (ER) formulations. In vitro dissolution of two model drugs, paracetamol IR tablets and felodipine ER tablets, was investigated under tuned conditions using the modified flow-through method and compared with the compendial quality control (QC) basket method. The in vivo absorption properties of paracetamol IR tablets and felodipine ER tablets were investigated in healthy volunteers. In vitro-in vivo correlation (IVIVC) analysis was performed based on the obtained in vitro and in vivo data. Our results demonstrated that the compendial QC method was not able to reflect in vivo actual absorption, while satisfactory discriminatory power and comparable in vitro dissolution/in vivo absorption were achieved for both paracetamol IR tablets and felodipine ER tablets by the modified flow-through method. This study indicated that the modified flow-through method is a potential tool to reflect in vivo performance of the IR and ER formulations.

1. Introduction

Over the past three decades, dissolution testing methodology has been introduced in many pharmacopeias, and it is widely recognized that comparison of percent in vitro dissolution and in vivo absorption can provide useful information [1, 2]. Usually, in vitro dissolution tests are operated in vessel-based systems, commonly known as the basket and paddle apparatuses to demonstrate suitable dissolution curves of the drugs. In vitro dissolution tests can act a valuable role in formulation development and can be helpful for in vivo product characterization. One of the goals of in vitro dissolution studies is to estimate the in vivo characteristics of the formulations [3–6].

In the biopharmaceutics research area, one of persisting challenges is relating percent in vitro drug dissolved with in vivo performance [7–9]. The value of compendial dissolution methods, acted as quality control (QC) tool for forecasting the drug's in vivo performance, can be significantly increased when an in vitro-in vivo correlation (IVIVC) is achieved [10]. The term IVIVC was defined by the Food and Drug Administration (FDA) as "a predictive mathematical model describing the relationship between an in vitro property of a dosage form and an in vivo response" [11]. Lack of a correlation between in vivo behavior and in vitro dissolution data may cause undesirable management of the important production parameters based on dissolution test and limit biopharmaceutical explanation of in vitro testing data [12–14].

Both the basket and paddle approaches, acted as highly prevalent methods for common drug formulations, are conducted in closed situation (finite sink), thus cannot reflect the actual circumstances of in vivo gastrointestinal system [15, 16]. Concerning the in vivo condition, the drug dissolution manner was mainly occurred in the site that free drugs close to or adhering to the mucosal surface. Consequently, the diffusional process to the absorption site is often fast that is resulting an infinite sink, and the free drugs are immediately entered into the body circulatory system after the dissolution. Therefore, the possibility of achieving successful

IVIVCs in this aspect is enhanced when the in vitro dissolution tests closely approach the gastrointestinal infinite sink environment [17]. For current stationary testing systems, the necessity for keeping an infinite sink requires employing a large dissolution medium volume and high agitation speed. However, Levy et al. [18] have reported that the agitation speed should be maintained relatively low in most cases for building good IVIVCs. Also, the dissolution tests often demand to operate at low agitation for detecting slight variations between products. Unfortunately, relatively low agitation with high medium volume testing conditions causes unsatisfied homogeneity, and the withdrawn sample would not reflect the actual entire dissolved system. Therefore, an intrinsic disagreement remains in static apparatuses between the necessities for large medium volumes with low agitation speeds and homogeneity [17].

In the past, limited success has been achieved in the field of IVIVC with passionate investigation efforts [19–22]. One explanation for this restricted achievement was due to the poor in vivo predictivity of the traditional in vitro dissolution methods. For example, the basket and paddle methods, two of the universally recommended dissolution systems, cannot offer gastrointestinal tract hydrodynamics mechanism, which is an important characteristic for the in vivo circumstances. The flow-through method, defined as the FDA official USP 4 apparatus, can provide a continuous flow of fresh dissolution medium, thus providing a perfect sink environment [23–25]. This dissolution approach offers a testing condition much closer to that of the gastrointestinal tract, and it was suggested as a potential tool for establishing IVIVC [26].

To further mimic the in vivo conditions, we modified the flow-through apparatus with open-loop configuration by positioning the flow-through cell on a shaker, which simulates mechanical destructive forces due to intestinal motility. The paracetamol immediate release (IR) tablets and felodipine extended release (ER) tablets were selected as the model drugs, and they were classified as "class I" drug and "class II" drug, respectively, based on biopharmaceutics classification system [27–29]. In the present study, the in vitro dissolution characteristics between the generic and innovator products of the model drugs were investigated and compared using modified flow-through method and compendial method, respectively. In vitro dissolution data were correlated with in vivo absorption profiles obtained from healthy volunteers. A level A IVIVC analysis and profile comparisons were applied to assess the predictive performance of the modified flow-through method.

2. Materials and Methods

2.1. Materials. Standards of paracetamol and felodipine were purchased from National Institutes for Food and Drug Control (Beijing, China). Hydrochloric acid (analytical grade) was obtained from Sinopharm Chemical Reagent Co., Ltd., and polysorbate 80 (analytical grade) was purchased from Tianjin Fengchuan Chemical Reagent Science and Technology Co., Ltd.

2.2. Formulations. Five different products of 500 mg paracetamol IR tablets obtained from commercial sources within their shelf life period were studied: Ouhuatai® (test 1), Guangzhou Ouhua Pharmaceutical Co., Ltd., China; Jinshi® (test 2), Jinshi General Pharmaceutical Factory, China; Haoyisheng® (test 3), Sichuan Good Doctor-Panxi Pharmaceutical Co, Ltd., China; Nanjixue® (test 4), Guangdong Medi-world Pharmaceutical Co., Ltd., China; Panadol®, Sino-American Tianjin SmithKline and French Lab., Ltd., China, which was used as the reference product (innovator). Four different products of 5 mg felodipine ER tablets obtained/provided from commercial sources within their shelf life period were studied: HINYE® (test 1), provided by Hunan HINYE pharmaceuticals Co. Ltd., China; Lifeon® (test 2), Hefei Lifeon Pharmaceutical Co. Ltd., China; Yitexin® (test 3), Nanjing EASEHEAL Pharmaceutical Co. Ltd., China; Plendil®, AstraZeneca Pharmaceutical Co., Ltd., which was used as the reference product (innovator).

2.3. Quantitative Analysis of Paracetamol and Felodipine. The amounts of paracetamol dissolved in the samples were analyzed by a microvolume UV-vis spectrophotometer (Quawell, San Jose, CA, USA) using 1 mm path absorbance for spectroscopic measurements, and the samples were analyzed at $\lambda = 244$ nm. The dissolved felodipine levels in the samples were analyzed using a validated reversed phase HPLC system. An Agilent TC-C18 column (4.6 mm × 150 mm, 5 μm, Walbdbrom, Germany) was employed, and the mobile phase consisted of water: methanol (10 : 90, v/v). The flow rate was 1.0 mL/min, and the injection volume was 20 μL. The detection wavelength was set at 362 nm.

Paracetamol concentrations in plasma were determined by HPLC with UV detection. The mobile phase was acetonitrile-water in a ratio of 20 : 80 (v/v). The flow rate was 1.0 mL/min, and the column temperature was 30°C.The injection volume was 20 μL, and chromatograms were recorded at 244 nm. The levels of felodipine in the plasma samples were quantified using an Agilent 6460 triple quadrupole LC-MS/MS system (Agilent, Waldbronn, Germany) equipped with an electrospray ionization source (ESI). The mobile phase consisted of acetonitrile-7 mM ammonium acetate solution (including 0.05% formic acid) in a ratio of 63 : 37 (v/v) at a flow rate of 0.28 mL/min. The injection volume was 10 μL, and the column temperature was maintained at 40°C. The mass spectrometer was operated in positive ion mode using multiple reactions monitoring (MRM). The precursor-product ion transition monitored was m/z 384.1 → 338.0. The other optimized MS/MS parameters were as follows: fragmentor voltage 150 V, collision energy 2 eV, source temperature 350°C, drying gas (N_2) flow 4 L/min, nebulizer pressure 137.9 kPa, and capillary voltage 4 kV.

2.4. Dissolution Testing

2.4.1. Quality Control (QC) Method. The compendial QC method (Chinese Pharmacopoeia) using the basket for paracetamol IR tablet consisted of 900 mL hydrochloric acid water solution (pH 1.2) as a dissolution medium at 37 ± 0.5°C, and the basket rotation speed was 100 rpm.

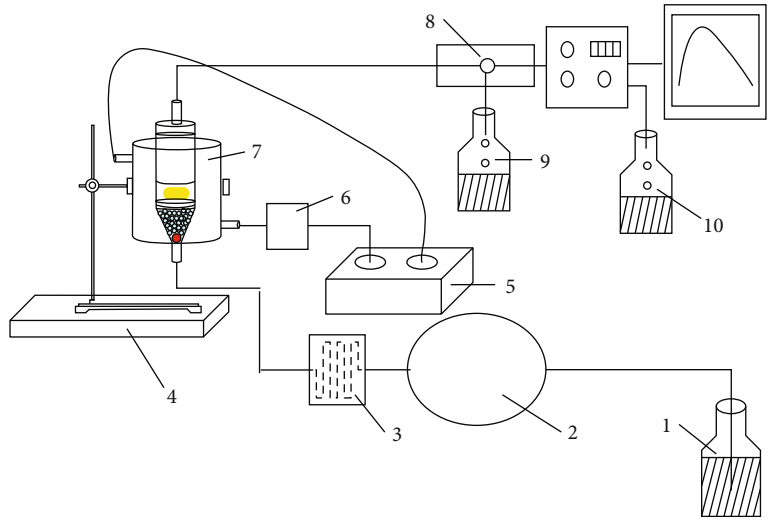

Figure 1: Schematic diagram of the flow-through dissolution apparatus. 1: dissolution media bottle; 2: high-precision liquid inlet pump; 3: heat exchange heater; 4: shaker; 5: thermostatic water bath; 6: peristaltic pump; 7: flow-through cell; 8: three-way valve; 9: waste collection bottle; 10: waste collection bottle.

Experiments were conducted in twelve replicates. Sample aliquots were withdrawn at 5, 10, 15, 20, 25, 30, 45, and 60 min and replaced with an equal volume of fresh medium to maintain a constant total volume. The samples were filtered through a 0.45 μm filter and then analyzed spectrophotometrically at 244 nm.

The compendial QC method (USP 35) using the basket for felodipine ER tablet consisted of 500 mL 1% (w/v) polysorbate 80 as a dissolution medium at 37 ± 0.5°C, and the basket rotation speed was 100 rpm. Experiments were conducted in twelve replicates. Sample aliquots were withdrawn at 1, 2, 3, 4, 5, 6, 7, and 8 h and replaced with an equal volume of fresh medium to maintain a constant total volume. The samples were filtered through a 0.45 μm filter and then analyzed by HPLC.

2.4.2. Modified Flow-Through Method. The modified flow-through apparatus is based on the principle of the USP apparatus 4. As presented in Figure 1, the modified assembly consists of a reservoir, a pump for the dissolution medium, a flow-through cell (diameters: 22.6 mm) positioned on a shaker, and a water bath. One glass bead of 5 mm diameter was positioned in the apex of the flow-through cell, the lower conical part of the cell was filled with glass beads of 1-mm diameter, and a glass microfiber filter (GF/D Whatman) was placed on the top of the cell. The temperature of the flow cell unit was maintained at 37.0 ± 0.5°C.

Experiments for paracetamol IR tablets and felodipine ER tablets were conducted in twelve replicates in an open system. The dissolution media were warmed up to 37.0 ± 0.5°C. The dissolution medium, prepared according to compendial method, was pH 1.2 hydrochloric acid water solution for paracetamol and 1% (w/v) polysorbate 80 for felodipine. The agitational speed of the shaker was 100 rpm, and the optimized flow rate of the media was set as 14 and 4 mL/min for paracetamol IR tablets and felodipine ER tablets, respectively. For each interval, samples were collected in clean tubes at the following times: 2, 4, 6, 8, 10, 15, 20, 25, 30, 35, 40, 45, 50, 55, and 60 min for paracetamol and every 0.5 h up to 8 h for felodipine.

2.5. Comparative Bioavailability Studies. Paracetamol IR tablets bioavailability study: this study was an open, single-dose, randomized study with a cross-over design carried out in accordance with the guidelines of the Declaration of Helsinki. Twelve healthy male volunteers participated in the study (aged 19-26 years, weight 52-70 kg). Each subject was assigned randomly and administered each of the three products (dose: 500 mg; products: test 1, test 3, and reference) according to a complete crossover Latin square design (3×3) with a washout period of 3 days. Blood samples (3 mL) were collected at the following time points: 0 (predose), 10, 20, 30, 40, 50, 60 min, 1, 1.25, 1.5, 2, 3, 4, 6, 8, and 10 h after drug intake.

Felodipine ER tablets bioavailability study: in an open-labeled, randomized, two-way crossover design, 20 male healthy volunteers (aged 22-30 years, weight 55-76 kg) were randomly divided into two groups to receive the felodipine reference tablet followed by the test 1 tablet (dose: 10 mg), or vice versa, with 7-day washout period between doses. The venous blood samples were collected at 0.5, 1.0, 1.5, 2.0, 3.0, 4.0, 5.0, 6.0, 8.0, 10.0, 12.0, 16.0, 24.0, 36.0, and 48.0 h after dosing.

2.6. Modeling of Drug Release/Absorption Kinetics. To characterize paracetamol IR tablet and felodipine ER tablet release/absorption kinetics, a model-dependent approach using zero-order, first-order, and Weibull mathematical equations was applied. The mathematical model that best expressed the dissolution/absorption profile of paracetamol IR tablets and felodipine ER tablets was selected based on the coefficient of determination (R^2) and model selection criteria (MSC). The modeling was performed using the DDSolver software (a menu-driven add-in program in Microsoft Excel) [30, 31].

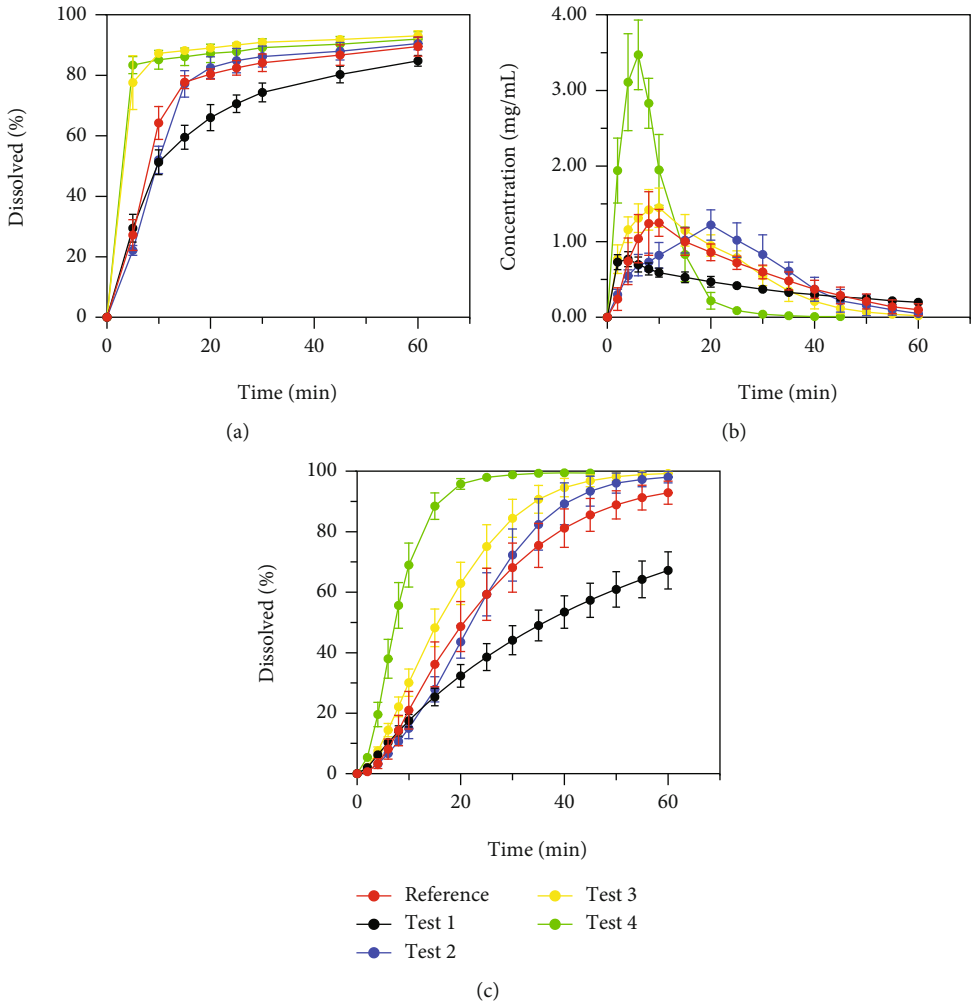

FIGURE 2: Dissolution profile comparison of paracetamol IR tablets using QC method and modified flow-through method. (a) The cumulative dissolution profiles using QC method (basket); (b) the differential dissolution profiles using modified flow-through method; (c) the cumulative dissolution profiles integrated from differential dissolution profiles. All data are the mean ± SD, $n = 12$.

2.7. Similarity of In Vitro Dissolution Profiles. In vitro dissolution profile sameness was assessed using the model-independent approach—the similarity factor (f_2, Equation (1)) [10, 11].

$$f_2 = 50 \cdot \log \left\{ \left[1 + \frac{1}{n} \sum_{t=1}^{n} (R_t - T_t)^2 \right]^{-0.5} \times 100 \right\}, \quad (1)$$

where n is the number of time points and R_t and T_t are the dissolution value of the reference and test formulations at time t, respectively. The f_2 is basically a measurement of the similarity in the percent drug dissolved between the two curves. An f_2 value greater than 50 (50-100) demonstrates similarity of the curves.

2.8. In Vitro-In Vivo Correlations. The average plasma concentration versus time curve of paracetamol IR tablets/felodipine ER tablets was transformed into the percent dose absorbed versus time using Wagner-Nelson or Loo-Riegelman method based on their determined compartmental models [32–35]. The Wagner-Nelson method is suitable for one-compartment model, and the Loo-Riegelman method fits for the two-compartment model.

Level A IVIVCs for paracetamol IR tablets/felodipine ER tablets were evaluated by plotting the mean percent drug dissolved (F_{dis}) from modified flow-through method/QC method versus the mean percent drug absorbed (F_{abs}), respectively. Linear regression analysis was used to evaluate the correlations. The F_{abs} versus F_{dis} curve comparisons of paracetamol IR tablets and felodipine ER tablets were also examined using the estimated release/absorption kinetics parameters.

3. Results and Discussion

3.1. Dissolution Testing

3.1.1. QC Method. Figure 2(a) and Figure 3(a) show the dissolution profiles of paracetamol IR tablets and felodipine ER tablets using the QC method, respectively. For paracetamol IR tablets, the test 2 product showed dissolution

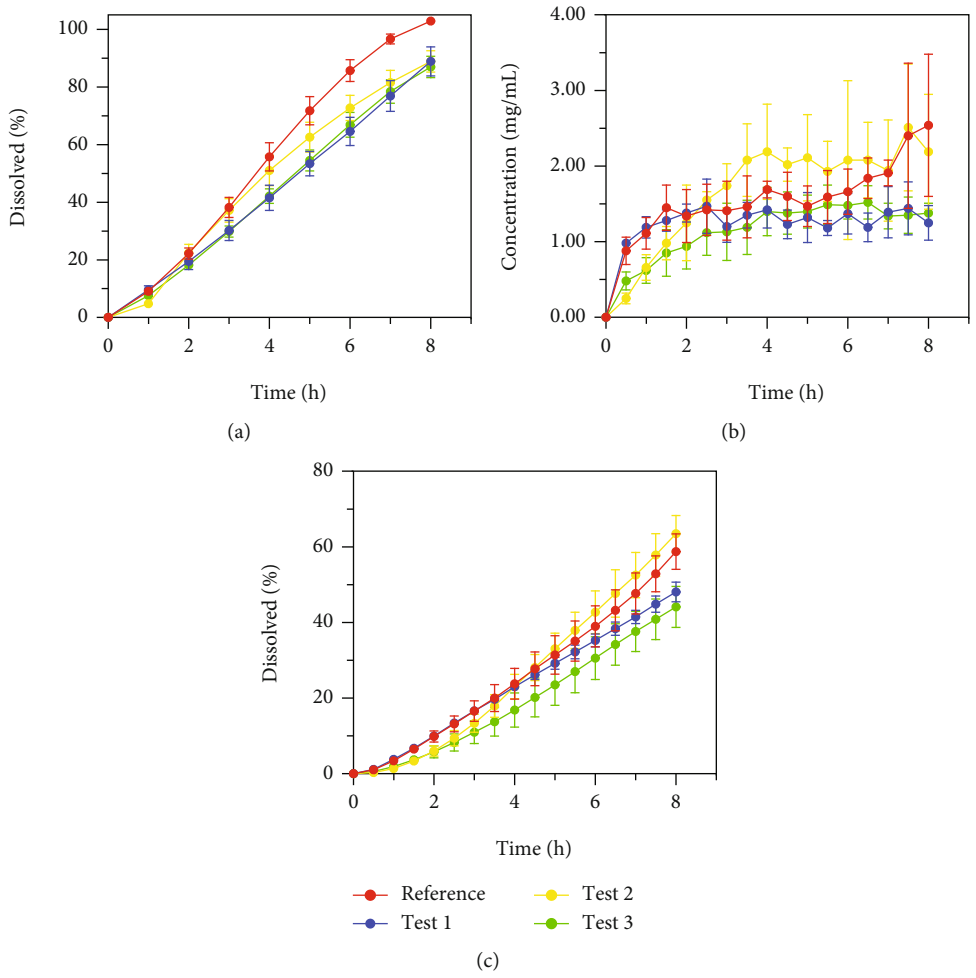

Figure 3: Dissolution profiles comparison of felodipine ER tablets using QC method and modified flow-through method. (a) The cumulative dissolution profiles using QC method (basket); (b) the differential dissolution profiles using modified flow-through method; (c) the cumulative dissolution profiles integrated from differential dissolution profiles. All data are the mean ± SD, $n = 12$.

similarity with the reference product ($f_2 = 65.06$), while there were no similarities for test 1, test 3, and test 4 products compared with the reference formulation ($f_2 = 47.33$, 34.29, and 33.11, respectively). Test 3 and test 4 products dissolved fastest (approximately 85% of the labeled drug dissolved in 10 min), the reference and test 2 products dissolved about 85% in 30 min, and test 1 dissolved slowest (only 75% of the labeled drug dissolved in 30 min). More than 85% drug released was observed in all products within 60 min. For felodipine ER tablets, test 2 product had f_2 similarity with the reference product ($f_2 = 53.05$), while there are no similarities for test 1 and test 3 products compared with the reference ($f_2 = 42.66$ and 43.61, respectively). More than 85% drug was released in 8 h for all felodipine products.

3.1.2. Modified Flow-Through Method. The differential dissolution profiles of paracetamol IR tablets and felodipine ER tablets using the modified flow-through method are shown in Figure 2(b) and Figure 3(b), respectively. The corresponding cumulative dissolution profiles were integrated from differential dissolution profiles, which are shown in Figure 2(c) and Figure 3(c), respectively. As demonstrated in Figure 2(b), the differential dissolution profiles of paracetamol test 1 and test 4 products exhibited significant differences compared with that of reference product, and test 3 product had similar profile with the reference. For example, the peak concentration ($C_{\text{max dissolution}}$) of test 1 is much lower than the reference, while the $C_{\text{max dissolution}}$ of test 4 is approximately 2.8-fold higher than the reference. These differences in generic and reference products resulted in corresponding discrepancies in cumulative dissolution profiles (shown in Figure 2(c)). The f_2 value (62.80) obtained from test 2 and reference comparison was similar with that of QC method (65.06), while the f_2 values for test 1, test 3, and test 4 (36.58, 47.05, and 20.96, respectively) showed large differences compared with the QC method (47.33, 34.29, and 33.11, respectively). The dissolution profiles obtained from modified flow-through method are more smoothly and discriminative compared with the QC basket method, which might be suitable to detect small product deviations. For felodipine ER tablets, although the differential dissolution profiles of generic products exhibited significant differences compared with that of reference

Table 1: Mathematical models and release/absorption kinetics parameters comparisons for paracetamol IR tablets and felodipine ER tablets.

Formulations		Dissolution/deconvolution methods	Dissolution models	Model parameters	R^2	MSC
Paracetamol IR tablets						
In vitro dissolved	Reference	QC method	$F = 100 * \{1 - \text{Exp}[-((t/\text{Td})\text{^}\beta)]\}$	Td = 12.164 β = 0.802	0.8678	1.52
		Modified flow-through method		Td = 27.661 β = 1.412	0.9976	5.79
	Test 1	QC method		Td = 19.019 β = 0.639	0.9756	3.21
		Modified flow-through method		Td = 52.734 β = 0.991	0.999	6.61
	Test 2	QC method		Td = 13.241 β = 1.090	0.9129	1.94
		Modified flow-through method		Td = 26.470 β = 1.891	0.9997	7.85
	Test 3	QC method		Td = 0.656 β = 0.230	0.9083	1.89
		Modified flow-through method		Td = 19.956 β = 1.524	0.9999	8.62
	Test 4	QC method		Td = 0.064 β = 0.129	0.9579	2.67
		Modified flow-through method		Td = 9.255 β = 1.717	0.9986	6.24
In vivo absorbed	Reference	Wagner-Nelson method		Td = 22.254 β = 2.303	0.9986	5.75
	Test 1	Wagner-Nelson method		Td = 20.629 β = 1.588	0.9959	4.69
	Test 2	Wagner-Nelson method		Td = 19.318 β = 1.297	0.9374	1.97
Felodipine ER tablets						
In vitro dissolved	Reference	QC method	$F = k0 * t$	$k0$ = 13.547	0.9857	3.99
		Modified flow-through method		$k0$ = 6.608	0.9729	3.48
	Test 1	QC method		$k0$ = 10.829	0.996	5.28
		Modified flow-through method		$k0$ = 5.860	0.9939	4.98
	Test 2	QC method		$k0$ = 11.747	0.9809	3.71
		Modified flow-through method		$k0$ = 6.987	0.9307	2.54
	Test 3	QC method		$k0$ = 10.887	0.9929	4.69
		Modified flow-through method		$k0$ = 5.011	0.9526	2.92
In vivo absorbed	Reference	Loo-Riegelman method		$k0$ = 7.046	0.9814	3.7
	Test 1	Loo-Riegelman method		$k0$ = 7.765	0.9914	4.48

F is the fraction (%) of drug released at time t; Td is the mean dissolution time, when 63.2% of the drug in the dosage form has been released; β is the shape parameter; $k0$ is the zero-order release constant.

product, their corresponding cumulative dissolution profiles were similar (shown in Figure 3(c)), with the f_2 values 68.64, 73.10, and 55.30 for test 1, test 2, and test 3 compared with reference, respectively. These f_2 values showed a large difference compared with the corresponding values (42.66, 53.05, and 43.61, respectively) obtained from QC method. The total amounts of drug released were much lower than that of QC method; only no more than 60% drug released was observed in all products within 8 h.

3.2. Evaluation of Release/Absorption Kinetics. The model parameters, determination coefficient (R^2), and MSC were determined for all formulations and presented in Table 1. According to the R^2 and MSC, the dissolution/absorption profiles of paracetamol IR tablets were best described by the Weibull model, and acceptable fitting results were also achieved by first-order model. For felodipine ER tablets, the in vitro drug release/in vivo absorption profiles were best explained by the zero-order model.

3.3. IVIVC Analysis and Profile Comparisons

3.3.1. Deconvolution of In Vivo Data. According to the minimum Akaike's information criterion (AIC) estimation of the compartment models using Phoenix WinNonlin 6.1 software, the concentration-time profile of paracetamol IR tablets was best described by one-compartment model, and the in vivo profile characteristics of felodipine ER tablets was best described by two-compartment model. Therefore, the Wagner-Nelson method was employed for deconvolution of paracetamol IR tablets in vivo data, and the Loo-Riegelman method was applied to felodipine ER tablets. Figures 4(a)–4(c) show the F_{abs} profiles of paracetamol reference, test 1, and test 3 products, respectively, obtained by the Wagner-Nelson method, and Figures 5(a) and 5(b) present the F_{abs} curves of felodipine reference and test 1 formulations, respectively, based on the Loo-Riegelman method.

3.3.2. Profile Comparisons. As demonstrated in Figures 4 and 5, the F_{dis} profiles of both paracetamol IR tablets and

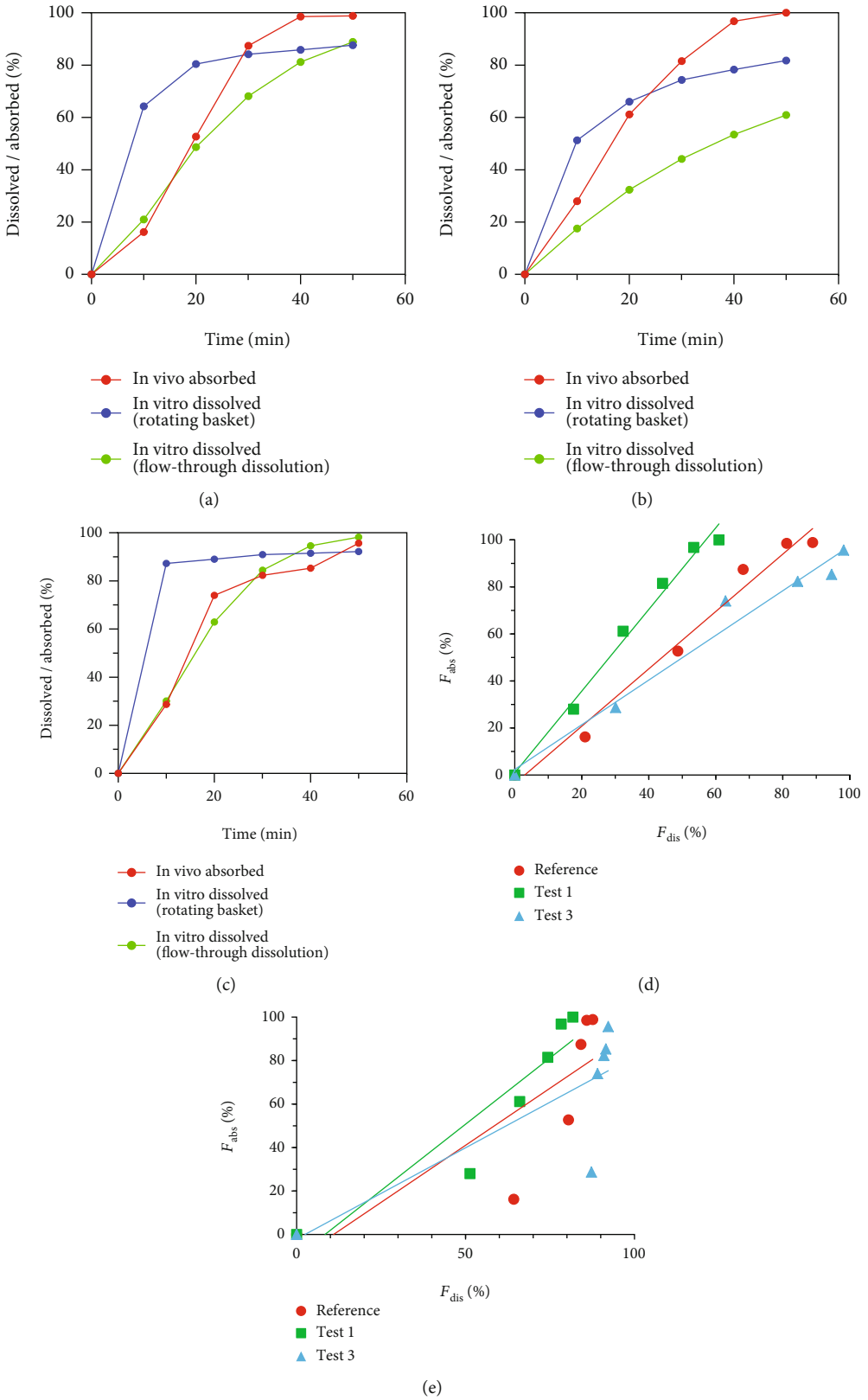

Figure 4: Profile comparison and IVIVC analysis of the in vitro percent drug dissolved (F_{dis}) versus the in vivo percent drug absorbed (F_{abs}) of paracetamol IR tablets. (a) In vitro dissolved and in vivo absorbed profiles for paracetamol reference tablet; (b) in vitro dissolved and in vivo absorbed profiles for paracetamol test 1 tablet; (c) in vitro dissolved and in vivo absorbed profiles for paracetamol test 3 tablet; linear regression plots of mean F_{abs} versus mean F_{dis} obtained from modified flow-through method (d) and QC method (e). All in vitro ($n = 12$) and in vivo ($n = 4$) data are the mean ± SD.

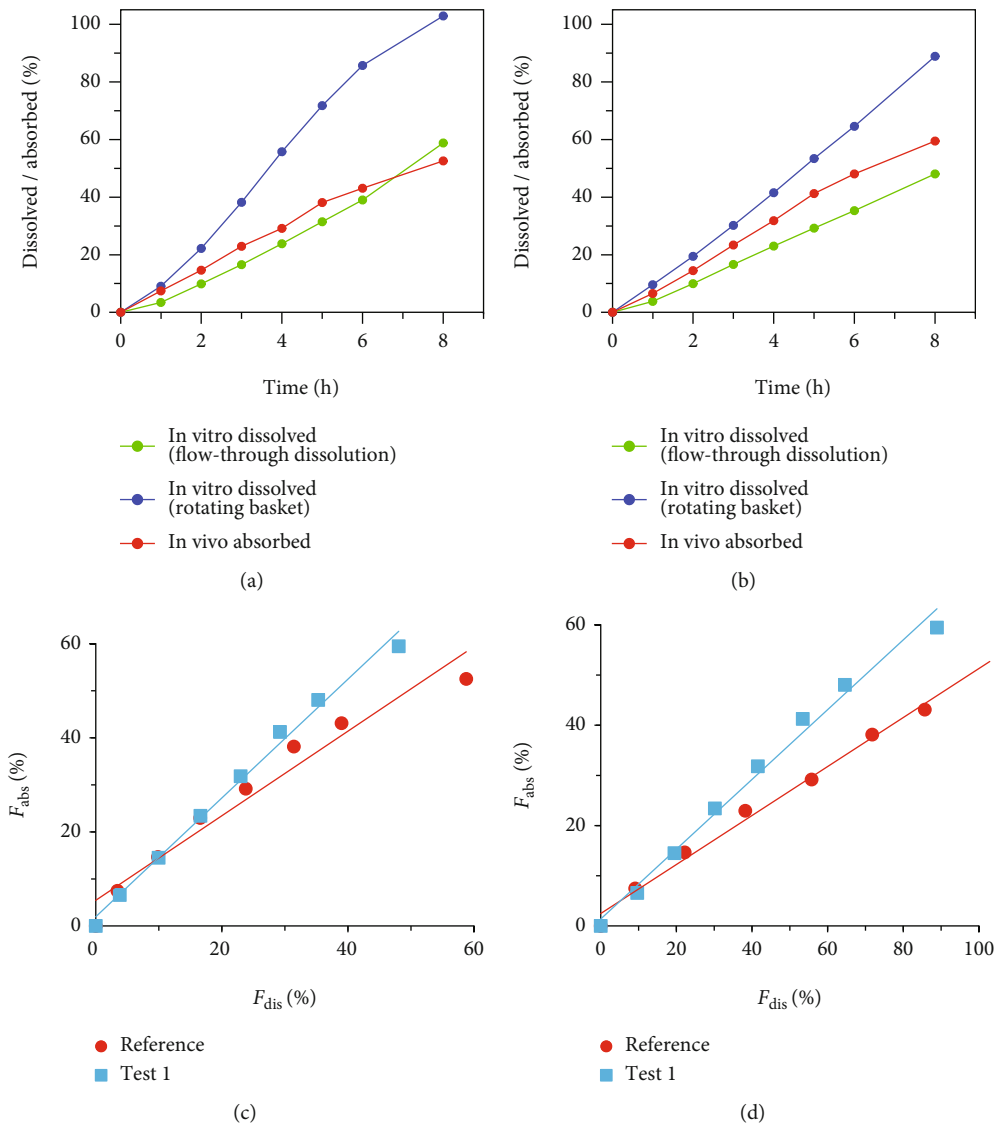

Figure 5: Profiles comparison and IVIVC analysis of the in vitro percent drug dissolved (F_{dis}) versus the in vivo percent drug absorbed (F_{abs}) of felodipine ER tablets. (a) In vitro dissolved and in vivo absorbed profiles for felodipine reference tablet; (b) in vitro dissolved and in vivo absorbed profiles for felodipine test 1 tablet; linear regression plots of mean F_{abs} versus mean F_{dis} obtained from modified flow-through method (c) and QC method (d). All in vitro ($n = 12$) and in vivo ($n = 10$) data are the mean ± SD.

felodipine ER tablets from the QC methods were steeper than the corresponding in vivo F_{abs} profiles, while the F_{dis} profiles obtained from modified flow-through method were similar or slightly lower than the F_{abs} profiles. Figures 4(a)–4(c) show that the dissolution profiles of paracetamol IR tablets obtained from the QC method displayed a high dissolution at initial times and a lower dissolution rate after 30 min than the in vivo absorption profiles. In contrast, smooth dissolution profiles were obtained by the modified flow-through method. The dissolution profile of paracetamol reference product obtained by the modified flow-through method was similar with the absorption profile at initial time (20 min), afterward the dissolution rate was lower than the absorption rate. The dissolution profile of paracetamol test 1 was completely lower than the absorption profile during the whole period of time, while in vitro profile of paracetamol test 3 nearly overlapped with the in vivo absorption profile. Figures 5(a) and 5(b) show that the dissolution rate of felodipine reference and test 1 products using QC method was significantly larger than the absorption rate, while the in vitro rate was comparable with in vivo rate in terms of modified flow-through method.

3.3.3. In Vitro-In Vivo Correlation. Figures 4(d) and 4(e) and Figures 5(c) and 5(d) demonstrate the level A IVIVC plots of paracetamol IR tablets and felodipine ER tablets, respectively. For paracetamol IR tablets, the QC method did not show correlations, while linear regression analysis of F_{abs} versus F_{dis} resulted in a significant correlation ($R^2 > 0.98$) for the three formulations in terms of the modified flow-through method. The in vitro dissolution of reference and test 3 from modified flow-through method were close to the in vivo absorption, as

indicated by the estimated regression slopes (1.2199 and 0.9450 for reference and test 3, respectively), and the in vitro dissolution of test 1 ran behind of its in vivo absorption (the regression slope = 1.7359). For felodipine ER tablets, both the QC and modified flow-through methods yield essentially linear correlations ($R^2 > 0.96$). The in vitro release of felodipine reference and test 1 ran ahead of in vivo absorption using QC method (regression slopes of 0.4883 and 0.6953 for felodipine reference and test 1), and the in vitro release using modified flow-through method was close to the in vivo absorption (regression slopes of 0.8990 and 1.2526 for felodipine reference and test 1). The IVIVC analysis indicate that the modified flow-through method could reasonably reflect the in vivo absorption of paracetamol IR tablets and felodipine ER tablets.

4. Conclusion

The modified flow-through method can provide the differential dissolution profiles of the formulations and is able to discriminate the subtle instantaneous release differences between the generic products and innovator. The discriminatory power of modified flow-through method is superior to the QC compendial method and achieve good correlations with the in vivo absorption data. Our study demonstrated that the modified flow-through method is a potential powerful tool for predicting the in vivo performance of formulations.

Data Availability

The data used to support the findings of this study are included within the article.

Conflicts of Interest

The authors declare that there is no conflict of interest regarding the publication of this article.

Acknowledgments

This work was supported by the National Natural Science Foundation of China (project number: 82073940).

References

[1] G. Zhang, M. Sun, S. Jiang et al., "Investigating a modified apparatus to discriminate the dissolution capacity _in vitro_ and establish an IVIVC of mycophenolate mofetil tablets in the fed state," *Journal of Pharmaceutical Sciences*, vol. 110, no. 3, pp. 1240–1247, 2021.

[2] G. F. Gao, M. Ashtikar, R. Kojima et al., "Predicting drug release and degradation kinetics of long-acting microsphere formulations of tacrolimus for subcutaneous injection," *Journal of Controlled Release*, vol. 329, pp. 372–384, 2021.

[3] E. Sjögren, B. Abrahamsson, P. Augustijns et al., "_In vivo_ methods for drug absorption - Comparative physiologies, model selection, correlations with _in vitro_ methods (IVIVC), and applications for formulation/API/excipient characterization including food effects," *European Journal of Pharmaceutical Sciences*, vol. 57, pp. 99–151, 2014.

[4] V. H. Sunesen, B. L. Pedersen, H. G. Kristensen, and A. Müllertz, "In vivo in vitro correlations for a poorly soluble drug, danazol, using the flow-through dissolution method with biorelevant dissolution media," *European Journal of Pharmaceutical Sciences*, vol. 24, no. 4, pp. 305–313, 2005.

[5] V. R. S. Uppoor, "Regulatory perspectives on in vitro (dissolution)/in vivo (bioavailability) correlations," *Journal of Controlled Release*, vol. 72, no. 1-3, pp. 127–132, 2001.

[6] B. Sánchez-Dengra, I. González-García, M. González-Álvarez, I. González-Álvarez, and M. Bermejo, "Two-step _in vitro_ - _in vivo_ correlations: deconvolution and convolution methods, which one gives the best predictability? Comparison with one-step approach," *European Journal of Pharmaceutics and Biopharmaceutics*, vol. 158, pp. 185–197, 2021.

[7] P. Jain, R. S. Pawar, R. S. Pandey et al., "In-vitro in-vivo correlation (IVIVC) in nanomedicine: is protein corona the missing link?," *Biotechnology Advances*, vol. 35, no. 7, pp. 889–904, 2017.

[8] J. V. Andhariya, J. Shen, S. Choi, Y. Wang, Y. Zou, and D. J. Burgess, "Development of _in vitro-in vivo_ correlation of parenteral naltrexone loaded polymeric microspheres," *Journal of Controlled Release*, vol. 255, pp. 27–35, 2017.

[9] M. A. Nguyen, T. Flanagan, M. Brewster et al., "A survey on IVIVC/IVIVR development in the pharmaceutical industry - past experience and current perspectives," *European Journal of Pharmaceutical Sciences*, vol. 102, pp. 1–13, 2017.

[10] FDA CDER, *Guidance for industry: dissolution testing of immediate-release solid oral dosage forms*, Food and Drug Administration, Center for Drug Evaluation and Research (CDER), 1997.

[11] FDA, *Guidance for industry: extended release oral dosage forms: development, evaluation, and application of in vitro/in vivo correlations*, Food and Drug Administration, Rockville, MD, 1997.

[12] R. C. Rossi, C. L. Dias, L. Bajerski, A. M. Bergold, and P. E. Fröehlich, "Development and validation of discriminating method of dissolution for fosamprenavir tablets based on in vivo data," *Journal of Pharmaceutical and Biomedical Analysis*, vol. 54, no. 3, pp. 439–444, 2011.

[13] M. G. Davanço, D. R. Campos, and P. D. O. Carvalho, "_In vitro_ - _in vivo_ correlation in the development of oral drug formulation: a screenshot of the last two decades," *International Journal of Pharmaceutics*, vol. 580, article 119210, 2020.

[14] S. Suarez-Sharp, M. Li, J. Duan, H. Shah, and P. Seo, "Regulatory experience with in vivo in vitro correlations (IVIVC) in new drug applications," *The AAPS Journal*, vol. 18, no. 6, pp. 1379–1390, 2016.

[15] S. Gite, M. Chogale, and V. Patravale, "Development and validation of a discriminating dissolution method for atorvastatin delayed-release nanoparticles using a flow-through cell: a comparative study using USP apparatus 4 and 1," *Dissolution Technologies*, vol. 23, no. 2, pp. 14–20, 2016.

[16] Y. Saibi, H. Sato, and H. Tachiki, "Developing in vitro–in vivo correlation of risperidone immediate release tablet," *AAPS PharmSciTech*, vol. 13, no. 3, pp. 890–895, 2012.

[17] J. E. Tingstad and S. Riegelman, "Dissolution rate studies I: design and evaluation of a continuous flow apparatus," *Journal of Pharmaceutical Sciences*, vol. 59, no. 5, pp. 692–696, 1970.

[18] G. Levy, J. R. Leonards, and J. A. Procknal, "Interpretation of _in vitro_ dissolution data relative to the gastrointestinal absorption characteristics of drugs in tablets," *Journal of Pharmaceutical Sciences*, vol. 56, no. 10, pp. 1365–1367, 1967.

[19] M. F. Mohamed, S. Trueman, A. A. Othman, J. Han, T. R. Ju, and P. Marroum, "Development of in vitro–in vivo correlation for upadacitinib extended-release tablet formulation," *The AAPS Journal*, vol. 21, no. 6, p. 108, 2019.

[20] A. al Durdunji, H. S. AlKhatib, and M. al-Ghazawi, "Development of a biphasic dissolution test for Deferasirox dispersible tablets and its application in establishing an in vitro-in vivo correlation," *European Journal of Pharmaceutics and Biopharmaceutics*, vol. 102, pp. 9–18, 2016.

[21] T. H. Kim, S. Shin, S. W. Jeong, J. B. Lee, and B. S. Shin, "Physiologically relevant in vitro-in vivo correlation (IVIVC) approach for sildenafil with site-dependent dissolution," *Pharmaceutics.*, vol. 11, no. 6, p. 251, 2019.

[22] C. Mircioiu, V. Anuta, I. Mircioiu, A. Nicolescu, and N. Fotaki, "In vitro-in vivo correlations based on in vitro dissolution of parent drug diltiazem and pharmacokinetics of its metabolite," *Pharmaceutics.*, vol. 11, no. 7, p. 344, 2019.

[23] M. Nicklasson, A. Orbe, J. Lindberg et al., "A collaborative study of the in vitro dissolution of phenacetin crystals comparing the flow through method with the USP paddle method," *International Journal of Pharmaceutics*, vol. 69, no. 3, pp. 255–264, 1991.

[24] M. Nicklasson, B. Wennergren, J. Lindberg et al., "A collaborative in vitro dissolution study using the flow-through method," *International Journal of Pharmaceutics*, vol. 37, no. 3, pp. 195–202, 1987.

[25] B. Wennergren, J. Lindberg, M. Nicklasson et al., "A collaborative in vitro dissolution study: comparing the flow-through method with the USP paddle method using USP prednisone calibrator tablets," *International Journal of Pharmaceutics*, vol. 53, no. 1, pp. 35–41, 1989.

[26] S. Jiang, G. Zhang, L. Wang, Y. Zeng, W. Liu, and Z. Cheng, "Development of a two-compartment system in vitro dissolution test and correlation with in vivo pharmacokinetic studies for celecoxib," *AAPS PharmSciTech*, vol. 21, no. 2, 2020.

[27] R. Löbenberg and G. L. Amidonb, "Modern bioavailability, bioequivalence and biopharmaceutics classification system. New scientific approaches to international regulatory standards," *European Journal of Pharmaceutics and Biopharmaceutics*, vol. 50, no. 1, pp. 3–12, 2000.

[28] Z. Zhou, C. Dunn, I. Khadra, C. G. Wilson, and G. W. Halbert, "Influence of physiological gastrointestinal surfactant ratio on the equilibrium solubility of BCS class II drugs investigated using a four component mixture design," *Molecular Pharmaceutics*, vol. 14, no. 12, pp. 4132–4144, 2017.

[29] N. Katori, N. Aoyagi, and T. Terao, "Estimation of agitation intensity in the GI tract in humans and dogs based on in vitro/in vivo correlation," *Pharmaceutical Research*, vol. 12, no. 2, pp. 237–243, 1995.

[30] Y. Zhang, M. Huo, J. Zhou et al., "DDSolver: an add-in program for modeling and comparison of drug dissolution profiles," *The AAPS Journal*, vol. 12, no. 3, pp. 263–271, 2010.

[31] J. Zuo, Y. Gao, N. Bou-Chacra, and R. Löbenberg, "Evaluation of the DDSolver software applications," *BioMed Research International*, vol. 2014, 9 pages, 2014.

[32] X. Hu, J. Zhang, X. Tang et al., "An accelerated release method of risperidone loaded PLGA microspheres with good IVIVC," *Current Drug Delivery*, vol. 15, no. 1, pp. 87–96, 2018.

[33] R. Praveen, P. R. Prasad Verma, J. Venkatesan, D. H. Yoon, S. K. Kim, and S. K. Singh, "_In vitro_ and _in vivo_ evaluation of gastro-retentive carvedilol loaded chitosan beads using Gastroplus ™," *International Journal of Biological Macromolecules*, vol. 102, pp. 642–650, 2017.

[34] A. Simon, M. I. Amaro, A. M. Healy, L. M. Cabral, and V. P. de Sousa, "Comparative evaluation of rivastigmine permeation from a transdermal system in the Franz cell using synthetic membranes and pig ear skin with _in vivo-in vitro_ correlation," *International Journal of Pharmaceutics*, vol. 512, no. 1, pp. 234–241, 2016.

[35] T. D. S. Honório, E. C. Pinto, H. V. A. Rocha et al., "In vitro–in vivo correlation of efavirenz tablets using GastroPlus®," *AAPS PharmSciTech*, vol. 14, no. 3, pp. 1244–1254, 2013.

Hindawi
Journal of Nanomaterials
Volume 2021, Article ID 5164100, 10 pages
https://doi.org/10.1155/2021/5164100

Review Article

Mechanism, Clinical Significance, and Treatment Strategy of Warburg Effect in Hepatocellular Carcinoma

Hui Chen,[1] Qing Wu,[2] Liu Peng,[1] Ting Cao,[1] Man-Ling Deng,[1] Yi-Wen Liu,[1] Jia Huang,[1] Yang Hu,[1] Nian Fu,[1] Ke-Bing Zhou,[1] Mei-Ling Yang,[3] and Xue-Feng Yang[1]

[1]*Department of Gastroenterology, The Affiliated Nanhua Hospital, Hengyang Medical College, University of South China, Hengyang, 421002 Hunan Province, China*
[2]*Department of General Practice, The Affiliated Nanhua Hospital, Hengyang Medical College, University of South China, Hengyang, 421002 Hunan Province, China*
[3]*Department of Oncology, The Affiliated Nanhua Hospital, Hengyang Medical College, University of South China, Hengyang, 421002 Hunan Province, China*

Correspondence should be addressed to Mei-Ling Yang; 1376343078@qq.com and Xue-Feng Yang; yxf009988@sina.com

Received 8 April 2021; Revised 12 April 2021; Accepted 15 April 2021; Published 28 April 2021

Academic Editor: Songwen Tan

Hepatocellular carcinoma (HCC) is a primary malignancy of the liver and the third leading cause of cancer death worldwide. The incidence of HCC accounts for more than 90% of primary HCC. Like most solid malignancies, the occurrence and development of HCC are closely related to the Warburg effect. The Warburg effect of HCC is mainly manifested as increased glucose uptake by HCC cells, increased glycolysis, restricted mitochondrial oxidative phosphorylation, increased pentose phosphate pathway in HCC cells, and increased glutamine decomposition. As the contribution of glycolysis to the total ATP of tumor cells generally does not exceed 50% to 60%, oxidative phosphorylation (OXPHOS) still makes a considerable contribution to the ATP of tumor cells. In some cases, there will be an anti-Warburg effect. HCC Warburg effect is closely related to HCC cell proliferation, apoptosis, immune escape, migration and invasion, chemotherapy resistance, and treatment failure. The mechanism of the Warburg effect in HCC is complex, involving the expression of stimulating the key glycolysis enzymes by hypoxia-inducible factor-1(HIF-1), the activation of oncogenes and the inactivation of tumor suppressor genes, the continuous activation of related signaling pathways, the participation of noncoding RNA, and the rate of metabolism gene mutation of enzyme. This article synthetically discusses the characteristics of glucose metabolism in HCC cells, the mechanism of Warburg effect, clinical significance, and corresponding treatment strategies and provides new perspectives for the prevention and treatment of HCC.

1. Preface

For most normal cells, glucose metabolism with glucose as a substrate is the main energy metabolism method. One of the main characteristics that distinguish tumor cells from normal cells is that tumor cells mainly use glycolysis of glucose to produce lactic acid for metabolic energy production, while oxidative phosphorylation (OXPHOS) is in a relatively inhibited state, this is the Warburg effect of tumor cells (Figure 1) [1]. Tumor cells can evade the normal apoptosis program through the Warburg effect and enhance the proliferation and migration ability, which is a key factor in the pathogenesis of tumors. The Warburg effect can not only occur in the hypoxic tumor microenvironment but can also occur under aerobic conditions, so it is also called "aerobic glycolysis" [2]. It is that tumor cells use a series of molecular mechanisms to weaken aerobic respiration under aerobic conditions, carry out efficient glycolysis, and then obtain a large amount of adenosine triphosphate (ATP) and create a microenvironment suitable for tumor cells to survive proliferation advantage. In addition, the Warburg effect suppresses the monitoring and lethality of T lymphocytes through local hypoxia, creating tumor immune escape. By inhibiting the pathways related to the Warburg effect, some antitumor drugs such as glucose and dichloroacetic acid can more effectively inhibit the proliferation advantage and immune escape

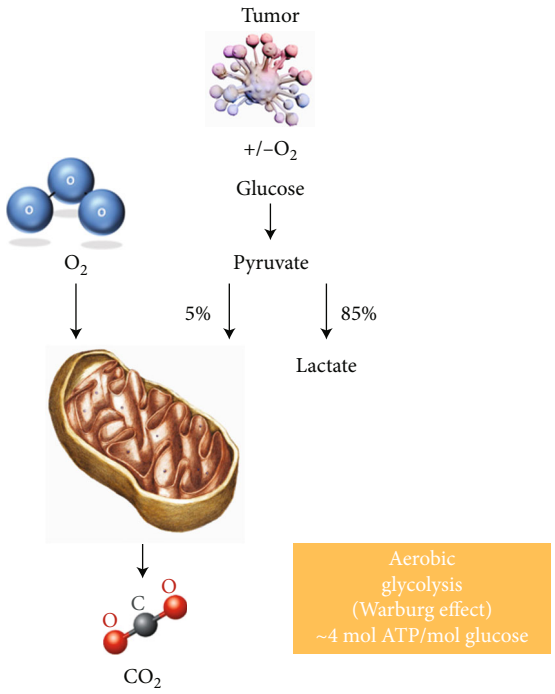

Figure 1: Tumor Warburg effect.

of tumor cells brought about by the Warburg effect, thereby inhibiting tumor cell growth and promoting tumor cell death. Further studies have found that the contribution of glycolysis to the total ATP of tumor cells generally does not exceed 50%~60% [3]; therefore, OXPHOS still makes a considerable contribution to the ATP of tumor cells. In some cases, there will be an anti-Warburg effect [4]. Hepatocellular carcinoma (HCC) is the main histological subtype of liver cancer, accounting for 90% of primary liver cancer, and is the third most common cause of cancer-related mortality worldwide [5]. Like most solid malignancies, Warburg effect plays an important role in the pathogenesis of HCC [1, 6]. This article synthetically discusses the characteristics of glucose metabolism in HCC cells, the mechanism of Warburg effect, clinical significance, and corresponding treatment strategies and provides new perspectives for the prevention of HCC and the development of targeted drugs.

2. HCC Warburg Effect

2.1. Increased Glucose Uptake of HCC Cells. After glucose is absorbed into the blood from the digestive tract, it needs to enter the cells for metabolism in the body. This process relies on glucose transporter (GLUT). On March 30, 2020, Boyi Gan's research group at MD Anderson Cancer Center in the United States and his collaborators published a paper in Nature Cell Biology, stating that they found that cystine ingested by the cystine transporter SLC7A11 was reduced to cysteine in the cell. The acid needs to consume a large amount of reduced nicotinamide adenine dinucleotide phosphate (NADPH). Intracellular NADPH is mainly derived from the bypass of glucose metabolism—the pentose phosphate pathway, so it is highly dependent on the supply of glucose. In the absence of glucose, the high expression of SLC7A11 in cancer cells will lead to the significant accumulation of cystine and other disulfides in the cell, the breakdown of the redox system, and the rapid cell death. It suggests that for patients with cancer cells, the lack of glucose will have a more adverse effect on the body. 14 human GLUTs (GLUT1-14) have been found, and they play a role in different tissues and cells; most of which are expressed in liver tissues [7, 8]. Compared with nontumor tissues, the expression of GLUT-1 in HCC was significantly increased [8, 9], suggesting that HCC cells have increased glucose uptake. Amann et al. [9] found that the expression level of GLUT1mRNA in HCC tissues and cell lines was significantly increased. Inhibiting the expression of GLUT1 in HCC cell lines can reduce glucose uptake and lactate secretion.

2.2. Enhanced Glycolysis of HCC Cells. Under normal circumstances, most cells in the human body mainly rely on the tricarboxylic acid (TCA) cycle and OXPHOS to be fully oxidize to supply cell energy under aerobic conditions; in the case of hypoxia, it mainly relies on glycolysis production capacity to supply cell energy. The productivity of glycolysis is higher than that of OXPHOS, allowing cancer cells to gain a competitive advantage. In addition to energy production, glycolysis also provides many precursor substances, which can maintain the tumor microenvironment and the stability of HIF. A few cells with extremely metabolically active, such as nerve cells and white blood cells, often use glycolysis to provide part of their energy even if they are not hypoxic. Individual cells, such as mature red blood cells, are completely dependent on glycolysis due to lack of mitochondria. Like most tumor cells, HCC cells mainly rely on glycolysis to supply cell energy, whether aerobic or anaerobic. This is the so-called Warburg Phenomenon, also known as "aerobic glycolysis," which is manifested in the increased expression and enhanced activity of the rate-limiting enzyme of glycolysis. For example, the of hexokinase (HK) increases, 6-phosphofructokinase-1 (G6P) increases, pyruvate kinase (PK) increases and activity enhance, and the metabolite lactic acid increases [1, 2, 10, 11].

2.3. Limited Mitochondrial Oxidative Phosphorylation. The aerobic oxidation of glucose is roughly divided into three stages. The first stage: glucose is decomposed into pyruvate in the cytoplasm through glycolysis. The second stage: pyruvate enters the mitochondria, oxidative decarboxylation produces acetyl CoA. This process is catalyzed by the pyruvate dehydrogenase complex. The third stage: acetyl CoA TCA cycle and OXPHOS in the mitochondria. It is generally believed that TCA is mainly regulated by isocitrate dehydrogenase (IDH) and α-ketoglutarte dehydrogenase complex. The TCA is the final metabolic pathway of the three major nutrients of sugar, fat, and amino acids. The oxidation of glucose, fat, and amino acids in the body eventually produces acetyl CoA, which then enters TCA for decomposition. TCA itself does not produce ATP, only OXPHOS reaction to generate ATP to provide $NADH^{+}H^{+}$ and FADH2. OXPHOS is coupled with ADP phosphorylation to generate ATP during the electron transport process of the respiratory

chain. As early as 1996, Capuano et al. discovered mitochondria isolated from biopsies of human hepatocellular carcinoma exhibit a decreased rate of respiratory ATP synthesis and a decreased ATPase activity [12].

2.4. Enhancing the Pentose Phosphate Pathway of HCC Cells. The pentose phosphate pathway (PPP) is another way of oxidative decomposition of glucose besides glycolysis and TCA cycle. PPP is also called the hexose monophosphate shunt. It is a pathway through which glucose-6-phosphate is metabolized to produce NADPH and ribose-5-phosphate. Glucose-6-phosphate dehydrogenase (glucose-6-phosphate dehydrogenase, G6PD) is the rate-limiting enzyme of the oxidative arm of the PPP, and its expression is significantly increased in HCC tissues. The data obtained by Kowalik MA and others from patients undergoing HCC resection or liver biopsy showed that compared with their adjacent tissues, G6PD was significantly upregulated in most HCC tissues [13]. PPP includes two stages: oxidation and nonoxidation. In the oxidation stage, glucose-6-phosphate is converted to ribulose-5-phosphate and CO2, and two molecules of NADPH are generated; in the nonoxidation stage, ribulose-5-phosphoric acid is isomerized to ribose-5-phosphate or converted into two intermediate metabolites in glycolysis, fructose-6-phosphate and glyceraldehyde-3-phosphate. For tumor cells, the most important effect of PPP is produce NADPH, maintain redox homeostasis, prevent oxidative damage, and protect tumor cells.

2.5. Enhanced Decomposition of Glutamine. Glycolysis is dominant in most tumor energy metabolism, but some tumor cells still use OXPHOS as the main energy production pathway, or a mixed energy production pathway of glycolysis and OXPHOS [14]. Due to the Warburg effect, tumor cells obtain biosynthetic precursors and NADPH through the TCA cycle. The demand for biosynthetic precursors and NADPH has increased dramatically. In order to meet the needs, tumor cells often rely on the decomposition of glutamine to maintain the TCA cycle and provide biosynthetic precursors and NADPH [15, 16]. It was discovered a long time ago that in the human HCC cell line HepG2 cells, when glutamine is sufficient, the promoter of its transporter ASCT2 is activated, which increases the expression of ASCT2 [17].

3. HCC Glucose Metabolism Reverse Warburg Effect

Some tumors have two-compartment tumor metabolism or metabolic coupling. In the biphasic model of tumor metabolism, tumor cells induce the surrounding stromal fibroblasts to produce the Warburg effect, which makes the fibroblasts differentiate into myofibroblasts. Through aerobic glycolysis, the myofibroblasts produce a large amount of energy metabolism such as lactic acid and pyruvate. However, when glucose is metabolized to lactic acid, only 2 ATP is produced per glucose molecule, and after a glucose molecule is completely oxidized, oxidative phosphorylation can produce up to 36 ATP. However, tumor cells preferentially ferment glucose even when oxygen is sufficient. This is because no matter how much stimulation, the aerobic glycolysis cells have a high ratio of ATP/ADP and NADH/NAD+. In addition, even small changes in the ATP/ADP ratio can affect its growth. Cells with insufficient ATP usually undergo apoptosis. When the ability of normal proliferating cells to produce ATP from glucose metabolism is impaired, they will undergo cell cycle arrest and reactivate catabolism. At the same time, there are signaling pathways to sense energy status. The product is then transported to tumor cells, enters the tumor cell mitochondria, provides fuel for the TCA cycle, and generates a large amount of ATP through oxidative phosphorylation, which promotes tumor cell proliferation and resists apoptosis [18, 19]. Whether HCC cells provide fuel for the TCA cycle through two-compartment tumor metabolism has not been reported in the literature.

3.1. Mechanism of Warburg Effect in HCC

3.1.1. The Role of Hypoxia-Inducible Factor-1 (HIF-1)

(1) HIF1 Upregulates the Expression of GLUT1 in HCC Cells. Due to the rapid growth of tumor cells, the formation of new blood vessels is relatively lagging, and most of the new blood vessels are malformed and cannot adequately supply nutrients and oxygen. Therefore, there is hypoxia or hypoxia in most tumor tissues. Hypoxia-induced HIF1 can upregulate the expression of GLUT1 on the surface of HCC cells and increase glucose uptake [20]. Inhibiting the expression of hypoxia-inducible factor 1 alpha, the expression of GLUT1 in HCC cells was significantly reduced, and the uptake of glucose was reduced [21].

(2) HIF1 Stimulates the Expression of Glycolytic Rate-Limiting Enzymes. Zhuonan et al. found that while the expression of HIF-1 in liver tissue increased in low temperature environment, the levels of HK-2 and pyruvate dehydrogenase kinase (PDK-1) increased [22]. Golinska et al. investigated the consequences of HIF-1 deficiency in mice, using the well-established Hepa-1 wild-type (WT) and HIF-1β-deficient (c4) model, found that HIF-1β-deficient Hepa-1 c4 tumours grew significantly more slowly than WT tumours, and (as expected) showed significantly lower expression of many glycolytic enzymes [23]. Mathupala et al. found the hepatoma cells transfected type II hexokinase gene promoter to hypoxic conditions activate the type II hexokinase promoter almost 3-fold, a value that approaches 7-fold in the presence of glucose [10].

(3) HIF1 Stimulates the Expression of Pyruvate Dehydrogenase Kinase 1. Increased expression of HIF-1 can be found in almost all HCC tissues [24]. HIF-1 is particularly crucial for shifting the metabolic program of cancer cells from oxidative phosphorylation to glycolysis [25]. HIF-1 can stimulate the expression of PDK1; PDK1 can phosphorylate the pyruvate dehydrogenase complex, inactivate the latter and then prevent acetone acid enters the TCA cycle [26].

(4) HIF1 Stimulates the Expression of a Less Active Complex I Subunit. Hypoxia results in an inefficient transfer of electrons

Table 1: The effects and targets of hypoxia-inducible factor-1 (HIF-1) on glucose metabolism of HCC cells.

Metabolism type	Target	Effects	Reference
Glucose uptake	GLUT1	Upregulated expression, enhanced activity	[21, 22]
Aerobic glycolysis	6-phosphofructokinase-1	Upregulated expression	[23]
	Hexokinase	Upregulated expression	[23–25]
	Pyruvate kinase	Upregulated expression	[25]
	Pyruvate dehydrogenase complex	Upregulate the expression of pyruvate dehydrogenase kinase 1	[27]
Tricarboxylic acid cycle and oxidative phosphorylation	Isocitrate dehydrogenase, IDH		
	α-Ketoglutarte dehydrogenase complex		
	Complex I-IV	Upregulate NDUFA4L2 expression	[28]
	ATP synthase		
Pentose phosphate pathway	Glucose-6-phosphate dehydrogenase, G6PD		
Glutamine metabolism	ASCT2		
	Glutaminase		

during oxidative phosphorylation leading to increased oxidative stress. NDUFA4L2 is a less active subunit of complex I in the oxidative phosphorylation electron transport chain, and it is also a direct transcriptional target of HIF [27]. Lai et al. found that HIF inhibitor, digoxin, profoundly inhibited growth of tumors that expressed high level of NDUFA4L2 in orthotopic model [27].

In summary, HIF-1 plays an important role in the metabolic reprogramming of HCC. The effect of HIF-1 on the glucose metabolism of HCC cells and its targets are shown in Table 1.

3.1.2. Activation of Oncogenes and Inactivation of Tumor Suppressor Genes

(1) Upregulation of GLUT1 Expression in HCC Cells. In HCC cells, the activated protooncogenes mainly include c-myc and K-Ras. The mutations of the protooncogenes c-myc and K-Ras can upregulate the expression of glucose transporters on the surface of HCC cells, thereby increasing glucose uptake. Glypican-3 enhances the glycolysis of HCC cells by upregulating the glycolysis genes of GLUT1, HK2, and LDH-A [28, 29]. This may be one of the reasons for the enhanced glycolysis in HCC cells.

(2) Stimulating the Expression of Glycolytic Rate-Limiting Enzymes. C-myc and K-Ras gene mutations can not only upregulate the expression of GLUT1 in HCC cells but also stimulate the expression of glycolytic rate-limiting enzymes, such as HK, G6P, and PK, thereby increasing the level of glycolysis [28, 29]. p53 is a major tumor suppressor gene; wild-type p53 can suppress tumour development by multiple pathways, mutation of TP53, and the resultant inactivation of p53 allow evasion of tumour cell death and rapid tumour progression [30]. p53 in half mutations occur in human cancers (in half of all human cancers) [31], but the wild-type p53 (WTp53) is often retained in HCC and suppressing pyruvate-driven oxidative phosphorylation by inducing PUMA [30]. The role of p53 in tumors is conflicting, and further research is needed.

(3) Mitochondrial Dysfunction in HCC Cells. K-Ras gene mutation can cause mitochondrial dysfunction in HCC cells, which in turn weakens the level of oxidative phosphorylation of glucose metabolism, forcing HCC cells to change their energy metabolism from oxidative phosphorylation to aerobic sugars. Fermentation is the main thing [28, 29].

3.1.3. Continuous Activation of Related Signal Pathways

(1) Promote Glycolysis of Tumor Cells. Take the PI3K/AKT/mTOR signaling pathway as an example. Their continuous activation can promote glycolysis of tumor cells. In the pathway, AKT is a serine/threonine kinase whose expression is significantly enhanced in HCC tissues [32], which can induce the expression of HK II and the activation and phosphorylation of sphosphofructokinase-2 (PFK2) to enhance glycolysis of HCC cells [32]. Combretastatin A4 phosphate (CA4P) can also reduce HIF-1α through PI3K/AKT/mTOR signaling pathway and synergistically inhibit HCC [33]. Akt can also use mTOR-mediated expression of glycolytic enzymes through the activation of HIF-1α, NFκB, and c-Myc [34].

3.1.4. Noncoding RNA Is Involved in Regulation

(1) Noncoding RNA Regulates GLUT1 to Participate in Glucose Uptake of Hepatoma Cells. LINC01638 lncRNA [35], lncRNA HOTAIR [36], miR-181a-5p [37], and MiR-505 [38] increase the uptake of glucose by cancer cells by upregulating the expression of GLUT1 on the surface of HCC cells and promote the proliferation of hepatocellular carcinoma cells; lncRNA SLC2A1-AS1 [39], miR-342-3p [40], miR-455-5p [41], and miR-328-3p [42] can reduce the expression of GLUT1 on the surface of HCC cells. Inhibiting the uptake of glucose by cancer cells inhibits the proliferation of hepatocellular carcinoma cells.

Table 2: The effects and targets of noncoding RNA on glucose metabolism of HCC cells.

Metabolism type	Target	Effects	Noncoding RNAs
Glucose uptake	GLUT1	Up	LINC01638 lncRNA [34] lncRNA HOTAIR [35] miR-181a-5p [36] MiR-505 [37]
		Down	lncRNA SLC2A1-AS1 [38] miR-342-3p [39] miR-455-5p [40] miR-328-3p [41]
Aerobic glycolysis	6-Phosphofructokinase-1	Up	
		Down	
	Hexokinase	Up	miR-181a-5p [36]
	Pyruvate kinase	Up	miR-4417 [43] circMAT2B [44]
		Down	LncRNA WPDC2p [45] miR-199a [46] miR-491-5p [47] miR-122 [48]
	LDH	Up	miR-181a-5p [36]
		Down	
Tricarboxylic acid cycle and oxidative phosphorylation	Pyruvate dehydrogenase complex	Up	
		Down	
	Isocitrate dehydrogenase, IDH	Up	
		Down	
	α-Ketoglutarte dehydrogenase complex	Up	
		Down	
	Complex I-IV	Up	lncRNA MALAT1 [49]
	ATP synthase	Down	
Pentose phosphate pathway	Glucose-6-phosphate dehydrogenase,G6PD	Up	
		Down	
Glutamine metabolism	ASCT2	Up	
		Down	
	Glutaminase	Up	

(2) Noncoding RNA Is Involved in Glycolysis of HCC. Various noncoding RNAs (ncRNAs) including microRNAs (miRNAs), long noncoding (lncRNAs), and circular RNAs (circRNAs) have recently been proved to play potential roles in glycolysis in hepatocellular carcinoma [43]. For example, miR-4417 [44] and circMAT2B [45] can activate PKM2 expression, thereby promoting glycolysis in HCC, while LncRNA WPDC2p [46], miR-199a [47], MiR-491-5p [48], and miR-122 [49] can inhibit the expression of PKM2.

(3) Noncoding RNA Is Involved in TCA and OXPHOS. The mitochondria of HCC cells contain a large amount of lncRNA metastasis-associated lung adenocarcinoma transcript 1 (MLAT1). MALAT1 knockdown induced alterations in the CpG methylation of mtDNA, and in mitochondrial transcriptomes, at the same time, HCC cells have changes in mitochondrial structure, low oxidative phosphorylation (oxphos), and decreased ATP production [50].

In short, noncoding RNA can affect HCC metabolism through multiple pathways, and its effects on HCC cell carbohydrate metabolism and targets are shown in Table 2.

3.1.5. Mutations in Rate-Limiting Enzyme Genes. According to reports, some specific types of HCC IDH1 may show a higher mutation rate. For example, Jung et al. detected 48 cases of HCC (including 20 cases of clear cell type and 13 cases of pseudoglandular pattern) IDH1, with a mutation rate of 10.4%; all of which were clear cell type HCC [51]. IDH is one of the rate-limiting enzymes of the TCA cycle, responsible for the oxidative decarboxylation of isocitrate into α-ketoglutarate and $NADH^+H^+$. IDH mutation changes the active site of the enzyme and endows the enzyme with new catalytic activity, using α-ketoglutar-ate (α-KG) to produce high levels of R-2-hydrox-yglutarate (R-2-HG); the molecular structure of 2-HG and α-KG is very similar [52], and it is speculated that 2-HG may participate in OXPHOS by inhibiting α-KG through competition.

3.1.6. Glycolysis Inhibits Oxidative Glycolysis. Domenis et al. reported that the well-differentiated HCC cell line HepG2 OXPHOS system is rarely damaged [53]. If glycolysis is inhibited, such as silencing the expression of hexokinase-2 in HCC cells, the flow of glucose to pyruvate and lactic acid is inhibited, but the flow of tricarboxylic acid is maintained [54]. As we all know, the metabolic fate of pyruvate produced by glycolysis is determined by the route of NADPH+H+. When aerobic NADPH+H+ enters the mitochondria for oxidation, pyruvate undergoes aerobic oxidation without producing lactic acid. NADPH+H+ cannot be oxidized under hypoxia; pyruvic acid acts as a hydrogen acceptor to generate lactic acid. In most cases, HCC cells are in a hypoxic microenvironment, NADPH+H+ cannot be oxidized, pyruvate produced by glycolysis can only be used as a hydrogen acceptor to produce lactic acid, and oxidative phosphorylation is restricted.

3.1.7. Mitochondria Are Damaged. The "Warburg effect" illustrates that tumor cells tend to choose aerobic glycolysis over OXPHOS, as does HCC cells. In the past, as represented by Warburg, it was believed that tumor cells mainly used aerobic glycolysis for energy because mitochondria were damaged, and oxidative phosphorylation dysfunction occurred [1]. It is now believed that the reprogramming of tumor cell metabolic pathways is not caused by simple mitochondrial dysfunction [55].

4. The Clinical Significance of Warburg Effect of HCC Glucose Metabolism

4.1. The Clinical Significance of the Warburg Effect of HCC Glucose Metabolism

4.1.1. Warburg Effect Promotes the Proliferation of HCC Cells. The Warburg effect is a metabolic hallmark of cancer. Tumor cells rapidly adjust their energy source to glycolysis in order to efficiently proliferate in a hypoxic environment [56]. The main physiological significance of glycolysis. It is to provide energy quickly. The ATP production rate of glycolysis may be 100 times faster than that of OXPHOS [57]. The production rate of ATP produced by glycolysis increases, giving cancer cells a selective growth advantage. Inhibition of the expression of key enzymes of glycolysis and tumor cell proliferation is inhibited. For example, when HK2 expression is silenced, glucose flux to pyruvate and lactate of HCC cells is inhibited, and the proliferation and death of HCC cells increase at the same time [58].

4.1.2. Warburg Effect Inhibits Apoptosis of HCC Cells. Pyruvate dehydrogenase E1α subunit (PDHA1) is one of the main factors for metabolic switch from OXPHOS to aerobic glycolysis and has been suggested to be closely associated with tumorigenesis [59]. Upregulated PDHA1 gene expression in HCC cell line SMMC-7721 and HepG2 can inhibit Warburg effect and enhanced mitochondria-mediated apoptosis pathway [59].

4.1.3. Warburg Effect Promotes Tumor Cell Metastasis. Aerobic glycolysis can produce a large amount of lactic acid and creat an acidic microenvironment, which is conducive to tumor cell invasion and metastasis [43]. Todisco et al. [17] found that increased G6PD expression is related to HCC metastasis and poor prognosis, while decreased g6pd expression inhibits the proliferation, migration, and invasion of HCC cell lines.

4.1.4. Warburg Effect Ultimately Leads to Tumor Immune Escape. The enhanced of tumor aerobic glycolysis is accompanied by the production and extracellular transport of a large amount of glycolysis end product in tumor cells, which leads to lactic acid in the tumor microenvironment accumulation and acidic microenvironment. The high lactate titer and acidic microenvironment outside the cell can directly hinder the extracellular transport of CTL and NK cells, thereby directly affecting the proliferation and cytokine secretion of CTL and NK cells, resulting in impaired killing function [60]. On the other hand, the acid degradation of IFN-γ weakens the differentiation of initial T cells into tumor suppressor type 1 helper T cells (Th1) and promotes them to differentiate into type 2 helper T cells (Th2) [61] and promote the proliferation of myeloid-derived suppressor cells (MDSC) in the tumor, and ultimately lead to the immune escape of the tumor through a variety of mechanisms.

4.2. The Clinical Significance of the Reverse Warburg Effect of HCC Glucose Metabolism

4.2.1. Promote Tumor Cell Proliferation and Resist Apoptosis. Martinez-Outschoorn et al. [62] found that some tumors have a two-compartment tumor metabolism, which is called the reverse Warburg effect or metabolic coupling. In the biphasic model of tumor metabolism, epithelial tumor cells induce the surrounding stromal fibroblasts to produce the Warburg effect, which makes the fibroblasts differentiate into myofibroblasts, and the myofibroblasts produce large amounts of energy such as lactic acid and pyruvate through aerobic glycolysis. The metabolites are then transported to epithelial tumor cells, enter the tumor cell mitochondria, provide fuel for the TCA cycle, and generate large amounts of ATP through OXPHOS to promote tumor cell proliferation and resist apoptosis [63, 64].

4.2.2. It May Be the Cause of Chemotherapy Resistance and Treatment Failure. The biphasic metabolism of tumor may be the cause of chemotherapy resistance and treatment failure, and it may also explain the contradictory phenomenon of high mitochondrial respiration and low glycolysis rate in some tumor cells [65]. This pattern indicates that there is a host-parasite relationship between tumor cells and surrounding fibroblasts or metabolic coupling [7]. The metabolic coupling includes two levels: (i) the metabolic coupling of fibroblasts and tumor cells and (ii) the coupling of aerobic glycolysis and OXPHOS in tumor cells.

5. Treatment Strategies for HCC Based on Positive and Negative Warburg Effect

5.1. Before Treatment with Energy Metabolism Drugs, It Is Necessary to Evaluate the Metabolic Characteristics of HCC Patients. Due to the difference in cell origin and

differentiation of tumors, not all tumor cells exhibit glycolysis, and the contribution of glycolysis to the total ATP of tumor cells ranges from 1% to 64% [66]. HCC is a highly heterogeneous cancer, both at the molecular and histological level [67]. According to the WHO classification standards, it is divided into highly differentiated, moderately differentiated, and poorly differentiated HCC. Poorly differentiated, undifferentiated, and fast-growing tumors are generally glycolysis-based, and OXPHOS is inhibited. For example, the undifferentiated HCC cell line JHH-6XPHOS system is significantly damaged, and its metabolism is mainly glycolysis [68].

5.2. According to the Patient's Metabolic Characteristics, Select the Appropriate Treatment Drug. HCC cells, like most tumors, have different cellular energy metabolism, but in general, they are still dominated by glycolytic phenotypes and rely on the consumption of glutamine. Studies have found that even if the tumor tissue is rich in oxygen, its glycolysis is still in the production capacity, but oxidative phosphorylation is relatively inhibited [6]. The specific strategy is as follows.

5.2.1. Reduce Glucose Transport into Cells. The GLUT1 gene is a key rate-limiting factor encoding glucose transport to cancer cells. Shang et al. [69] found that using siRNA to inhibit the expression of GLUT1, HCC cells are reducing glucose. At the same time of uptake and secretion of lactic acid, the growth and migration potential of HCC cells is weakened [69].

5.2.2. Inhibition of Glycolysis. Hexokinase is the first rate-limiting enzyme in the glycolysis pathway. Hexokinase catalyzes the phosphorylation of glucose into glucose 6-phosphate. Glucose 6-phosphate can be used for glycolysis or pentose phosphate pathway. DeWaal et al. reported that silencing HK2 expression, HCC cell glucose flux to pyruvate and lactate is inhibited, while HCC cell proliferation decreased and death increased, knockout HK2 in mice can reduce proliferation and the incidence of tumors induced by diethylnitrosamine (DEN) [11].

5.2.3. Inhibition of Decomposition of Glutamine. Glutamine is the amide of glutamic acid. L-glutamine is the amino acid encoded in protein synthesis. It is a nonessential amino acid in mammals and can be converted from glucose in the body. Lee et al. reported that mitochondrial dependence on glutamine can drive the chemotherapy resistance of HCC stem cells [70]. The high level of glutamine in the blood provides a ready source of carbon and nitrogen to support the biosynthesis, energy metabolism, and cell homeostasis of cancer cells and promote tumor growth. Glutamine is transported into the cell by the transporter SLC1A5 (the solute carrier family 1 neutral amino acid transporter member 5) in the cell. Under nutrient-deficient conditions, cancer cells can obtain glutamine by breaking down macromolecules. Excessive activation of the oncogene RAS can promote pinocytosis. Cancer cells remove extracellular proteins and degrade them into amino acids including glutamine to provide nutrients for cancer cells.

5.2.4. Inhibition of the Pentose Phosphate Pathway. The pentose phosphate pathway is a branch of glycolysis and a bypass pathway of glucose metabolism, producing NADPH and pentose. NADPH is a hydrogen donor for various anabolism in the body, and pentose is a nucleoside and is necessary for rapid cell proliferation. The same study reported that G6PD silencing significantly inhibited HepG2 cell line invasion [71]. In vivo studies reinforced the relevance of G6PD in HCC progression, as G6PD suppression inhibited tumor growth in Huh7 orthotopic tumor and mouse xenograft models [72].

5.2.5. Promote Oxidative Phosphorylation. Pyruvate dehydrogenase E1α subunit (PDHA1) is one of the main factors for the metabolic switch from OXPHOS to aerobic glycolysis and has been suggested to be closely associated with tumorigenesis. Sun etc. observed that the PDHA1 protein was reduced in HCC specimens by immunohistochemistry and Western blot, which was significantly associated with poor overall survival [73]. At the same time, mitochondrial OXPHOS was enhanced accompanied with higher ATP. Sun et al. also found that apoptosis was promoted, and intrinsic pathway proteins were increased in PDHA1-overexpressing cells.

5.3. Combination Medication. Due to the high metabolic adaptability of tumor cells, when any metabolic pathway encounters obstacles, tumor cells will automatically switch or activate other pathways to avoid stress damage. Therefore, tumor metabolic regulation therapy should jointly block or regulate multiple metabolisms. The biphasic metabolism of tumors may be the cause of chemotherapy resistance and treatment failure [74]. For HCC chemotherapy resistance and treatment failure, multisite and multipath combination medication should be considered.

6. Summary

HCC is a primary liver cancer with high mortality, and its pathogenesis is related to the Warburg effect. The Warburg effect of HCC is mainly manifested in the increased glucose uptake of HCC cells, increased glycolysis, restricted mitochondrial oxidative phosphorylation, increased pentose phosphate pathway in HCC cells, and increased glutamine decomposition. In some cases, there will be a reverse Warburg effect. HCC Warburg effect and reverse Warburg effect are closely related to HCC cell proliferation, apoptosis, immune escape, migration and invasion, chemotherapy resistance, and treatment failure. Therefore, subsequent in-depth discussions on the Warburg effect mechanism of liver cancer cells and the corresponding clinical significance can provide a new way for the prevention of liver cancer and the development of targeted drugs.

Data Availability

The datasets used and/or analyzed during the current study are available from the corresponding author on reasonable request.

Conflicts of Interest

The authors declare no conflict of interest, financial or otherwise.

Authors' Contributions

Hui Chen and Qing Wu equally contributed to this work. Hui Chen, Qing Wu, Liu Peng, Ting Cao, Man-Ling Deng, Yi-Wen Liu, Jia Huang, Yang Hu, Nian Fu, Ke-Bing Zhou, Mei Ling Yang, and Xue-Feng Yang all contributed to the literature review and the writing of this manuscript. Hui Chen and Qing Wu are all co-first authors.

Acknowledgments

This work was supported by the Scientific Research Project of Hunan Provincial Health and Family Planning Commission (No. A2017015); the Natural Science Foundation of Hunan Province, China, (No. 2016JJ5010); and the National Natural Science Foundation of China (No. 81373465).

References

[1] O. Warburg, "On the origin of cancer cells," *Science*, vol. 123, no. 3191, pp. 309–314, 1956.

[2] X. L. Zu and M. Guppy, "Cancer metabolism: facts, fantasy, and fiction," *Biochemical and Biophysical Research Communications*, vol. 313, no. 3, pp. 459–465, 2004.

[3] W. H. Koppenol, P. L. Bounds, and C. V. Dang, "Otto Warburg's contributions to current concepts of cancer metabolism," *Nature Reviews. Cancer*, vol. 11, no. 5, pp. 325–337, 2011.

[4] M. Lee and J. H. Yoon, "Metabolic interplay between glycolysis and mitochondrial oxidation: the reverse Warburg effect and its therapeutic implication," *World Journal of Biological Chemistry*, vol. 6, no. 3, pp. 148–161, 2015.

[5] F. Bray, J. Ferlay, I. Soerjomataram, R. L. Siegel, L. A. Torre, and A. Jemal, "Global cancer statistics 2018: GLOBOCAN estimates of incidence and mortality worldwide for 36 cancers in 185 countries," *CA: a Cancer Journal for Clinicians*, vol. 68, no. 6, pp. 394–424, 2018.

[6] J. Feng, J. Li, L. Wu et al., "Emerging roles and the regulation of aerobic glycolysis in hepatocellular carcinoma," *Journal of Experimental & Clinical Cancer Research*, vol. 39, no. 1, p. 126, 2020.

[7] S. Karim, D. H. Adams, and P. F. Lalor, "Hepatic expression and cellular distribution of the glucose transporter family," *World journal of gastroenterology*, vol. 18, no. 46, pp. 6771–6781, 2012.

[8] T. Aboushousha, S. Mamdouh, H. Hamdy et al., "Immunohistochemical and biochemical expression patterns of TTF-1, RAGE, GLUT-1 and SOX2 in HCV-associated hepatocellular carcinomas," *Asian Pacific Journal of Cancer Prevention*, vol. 19, no. 1, pp. 219–227, 2018.

[9] T. Amann, U. Maegdefrau, A. Hartmann et al., "_GLUT1_ Expression Is Increased in Hepatocellular Carcinoma and Promotes Tumorigenesis," *The American Journal of Pathology*, vol. 174, no. 4, pp. 1544–1552, 2009.

[10] S. P. Mathupala, A. Rempel, and P. L. Pedersen, "Glucose Catabolism in Cancer Cells:," *The Journal of Biological Chemistry*, vol. 276, no. 46, pp. 43407–43412, 2001.

[11] W. Gao, J. Sun, F. Wang et al., "Deoxyelephantopin suppresses hepatic stellate cells activation associated with inhibition of aerobic glycolysis via hedgehog pathway," *Biochemical and Biophysical Research Communications*, vol. 516, no. 4, pp. 1222–1228, 2019.

[12] F. Capuano, D. Varone, N. D'Eri et al., "Oxidative phosphorylation and F(O)F(1) ATP synthase activity of human hepatocellular carcinoma," *Biochemistry and Molecular Biology International*, vol. 38, no. 5, pp. 1013–1022, 1996.

[13] M. A. Kowalik, A. Columbano, and A. Perra, "Emerging role of the pentose phosphate pathway in hepatocellular carcinoma," *Frontiers in oncology*, vol. 7, p. 87, 2017.

[14] D. Chandra and K. K. Singh, "Genetic insights into OXPHOS defect and its role in cancer," *Biochimica Biophysica Acta (BBA)-Bioenergetics*, vol. 1807, no. 6, pp. 620–625, 2011.

[15] M. H. Gao, P. Monian, N. Quadri, R. Ramasamy, and X. Jiang, "Glutaminolysis and transferrin regulate ferroptosis," *Molecular Cell*, vol. 59, no. 2, pp. 298–308, 2015.

[16] V. H. Villar, F. Merhi, M. Djavaheri-Mergny, and R. V. Durán, "Glutaminolysis and autophagy in cancer," *Autophagy*, vol. 11, no. 8, pp. 1198–1208, 2015.

[17] C. I. Bungard and J. D. McGivan, "Glutamine availability up-regulates expression of the amino acid transporter protein ASCT2 in HepG2 cells and stimulates the ASCT2 promoter," *The Biochemical Journal*, vol. 382, no. 1, pp. 27–32, 2004.

[18] S. Todisco, P. Convertini, V. Iacobazzi, and V. Infantino, "TCA cycle rewiring as emerging metabolic signature of hepatocellular carcinoma," *Cancers (Basel)*, vol. 12, no. 1, p. 68, 2019.

[19] M. A. C. Déry, M. D. Michaud, and D. E. Richard, "Hypoxia-inducible factor 1: regulation by hypoxic and non-hypoxic activators," *The International Journal of Biochemistry & Cell Biology*, vol. 37, no. 3, pp. 535–540, 2005.

[20] X. Hongping, C. Jianxiang, G. Hengjun et al., "Hypoxia-inducible factors in physiology and medicine," *Cell*, vol. 148, no. 3, pp. 399–408, 2012.

[21] T. Mizuno, M. Nagao, Y. Yamada et al., "Small interfering RNA expression vector targeting hypoxia-inducible factor 1 alpha inhibits tumor growth in hepatobiliary and pancreatic cancers," *Cancer Gene Therapy*, vol. 13, no. 2, pp. 131–140, 2006.

[22] Z. Zhuonan, G. Sen, J. Zhipeng et al., "Hypoxia preconditioning induced HIF-1α promotes glucose metabolism and protects mitochondria in liver I/R injury," *Clinics and Research in Hepatology and Gastroenterology*, vol. 39, no. 5, pp. 610–619, 2015.

[23] M. Golinska, H. Troy, Y. L. Chung et al., "Adaptation to HIF-1 deficiency by upregulation of the AMP/ATP ratio and phosphofructokinase activation in hepatomas," *BMC cancer*, vol. 11, no. 1, p. 198, 2011.

[24] G. William and J. Kaelin, "The von Hippel-Lindau protein, HIF hydroxylation, and oxygen sensing," *Biochemical and Biophysical Research Communications*, vol. 338, no. 1, pp. 627–638, 2005.

[25] C. C. L. Wong, A. K. L. Kai, and I. O. L. Ng, "The impact of hypoxia in hepatocellular carcinoma metastasis," *Frontiers in Medicine*, vol. 8, no. 1, pp. 33–41, 2014.

[26] C. Haan, G. Walbrecq, I. Kozar, I. Behrmann, and A. D. Zimmer, "Phosphorylation of the pyruvate dehydrogenase complex precedes HIF-1-mediated effects and pyruvate dehydrogenase kinase 1 upregulation during the first hours of hypoxic treatment in hepatocellular carcinoma cells," *Hypoxia (Auckl)*, vol. 4, pp. 135–145, 2016.

[27] R. K. Lai, I. M. Xu, D. K. Chiu et al., "NDUFA4L2 fine-tunes oxidative stress in hepatocellular carcinoma," *Clinical Cancer Research*, vol. 22, no. 12, pp. 3105–3117, 2016.

[28] R. Liu, Y. Li, L. Tian et al., "Gankyrin drives metabolic reprogramming to promote tumorigenesis, metastasis and drug resistance through activating β-catenin/c-Myc signaling in human hepatocellular carcinoma," *Cancer Letters*, vol. 443, pp. 34–46, 2019.

[29] J. H. Kim, H. Y. Kim, Y. K. Lee et al., "Involvement of mitophagy in oncogenic K-Ras-induced transformation: overcoming a cellular energy deficit from glucose deficiency," *Autophagy*, vol. 7, no. 10, pp. 1187–1198, 2011.

[30] J. Kim, L. Yu, W. Chen et al., "Wild-type p53 promotes cancer metabolic switch by inducing PUMA-dependent suppression of oxidative phosphorylation," *Cancer Cell*, vol. 35, no. 2, pp. 191–203.e8, 2019.

[31] V. J. N. Bykov, S. E. Eriksson, J. Bianchi, and K. G. Wiman, "Targeting mutant p53 for efficient cancer therapy," *Nature Reviews. Cancer*, vol. 18, no. 2, pp. 89–102, 2018.

[32] P. H. C. Diniz, S. D. C. Silva, P. V. T. Vidigal et al., "Expression of MAPK and PI3K/AKT/mTOR proteins according to the chronic liver disease etiology in hepatocellular carcinoma," *Journal of Oncology*, vol. 2020, Article ID 4609360, 9 pages, 2020.

[33] X. Yang, M. Gao, M. Miao et al., "Combining combretastatin A4 phosphate with ginsenoside Rd synergistically inhibited hepatocellular carcinoma by reducing HIF-1α via PI3K/AKT/mTOR signalling pathway," *The Journal of Pharmacy and Pharmacology*, vol. 73, no. 2, pp. 263–271, 2021.

[34] L. Yu, X. Chen, L. Wang, and S. Chen, "The sweet trap in tumors: aerobic glycolysis and potential targets for therapy," *Oncotarget*, vol. 7, no. 25, pp. 38908–38926, 2016.

[35] X. Chen, L. Wang, and H. Wang, "LINC01638 lncRNA promotes cancer cell proliferation in hepatocellular carcinoma by increasing cancer cell glucose uptake," *Oncology Letters*, vol. 18, no. 4, pp. 3811–3816, 2019.

[36] S. Wei, Q. Fan, L. Yang et al., "Promotion of glycolysis by HOTAIR through GLUT1 upregulation via mTOR signaling," *Oncology Reports*, vol. 38, no. 3, pp. 1902–1908, 2017.

[37] X. Zhuang, Y. Chen, Z. Wu et al., "Mitochondrial miR-181a-5p promotes glucose metabolism reprogramming in liver cancer by regulating the electron transport chain," *Carcinogenesis*, vol. 41, no. 7, pp. 972–983, 2020.

[38] L. Ren, Y. Yao, Y. Wang, and S. Wang, "MiR-505 suppressed the growth of hepatocellular carcinoma cells via targeting IGF-1R," *Bioscience reports*, vol. 39, no. 7, 2019.

[39] R. Shang, M. Wang, B. Dai et al., "Long noncoding RNASLC2A1-AS1regulates aerobic glycolysis and progression in hepatocellular carcinoma via inhibiting the STAT3/-FOXM1/GLUT1 pathway," *Molecular Oncology*, vol. 14, no. 6, pp. 1381–1396, 2020.

[40] W. Liu, L. Kang, J. Han et al., "miR-342-3p suppresses hepatocellular carcinoma proliferation through inhibition of IGF-1R-mediated Warburg effect," *Oncotargets and Therapy*, vol. 11, pp. 1643–1653, 2018.

[41] Y. Hu, Z. Yang, D. Bao, J. S. Ni, and J. Lou, "miR-455-5p suppresses hepatocellular carcinoma cell growth and invasion via IGF-1R/AKT/GLUT1 pathway by targeting IGF-1R," *Pathology-Research and Practice*, vol. 215, no. 12, article 152674, 2019.

[42] W. Yi, M. J. Tu, Z. Liu et al., "Bioengineered miR-328-3p modulates GLUT1-mediated glucose uptake and metabolism to exert synergistic antiproliferative effects with chemotherapeutics," *Acta Pharmaceutica Sinica B*, vol. 10, no. 1, pp. 159–170, 2020.

[43] Y. Lai, H. Huang, M. Abudoureyimu et al., "Non-coding RNAs: emerging regulators of glucose metabolism in hepatocellular carcinoma," *American Journal of Cancer Research*, vol. 10, no. 12, pp. 4066–4084, 2020.

[44] L. Song, W. Zhang, Z. Chang et al., "miR-4417 targets tripartite motif-containing 35 (TRIM35) and regulates pyruvate kinase muscle 2 (PKM2) phosphorylation to promote proliferation and suppress apoptosis in hepatocellular carcinoma cells," *Medical Science Monitor*, vol. 23, article 900296, pp. 1741–1750, 2017.

[45] Q. Li, X. Pan, D. Zhu, Z. Deng, R. Jiang, and X. Wang, "Circular RNA MAT2B promotes glycolysis and malignancy of hepatocellular carcinoma through the miR-338-3p/PKM2 Axis under hypoxic stress," *Hepatology*, vol. 70, no. 4, pp. 1298–1316, 2019.

[46] Y. F. Guan, Q. L. Huang, Y. L. Ai et al., "Nur77-activated lncRNA WFDC21P attenuates hepatocarcinogenesis via modulating glycolysis," *Oncogene*, vol. 39, no. 11, pp. 2408–2423, 2020.

[47] L. F. Zhang, J. T. Lou, M. H. Lu et al., "Suppression of miR-199a maturation by HuR is crucial for hypoxia-induced glycolytic switch in hepatocellular carcinoma," *The EMBO journal*, vol. 34, no. 21, pp. 2671–2685, 2015.

[48] Q. Xu, C. Dou, X. Liu et al., "Oviductus ranae protein hydrolysate (ORPH) inhibits the growth, metastasis and glycolysis of HCC by targeting miR-491-5p/PKM2 axis," *Biomedicine & Pharmacotherapy*, vol. 107, pp. 1692–1704, 2018.

[49] A. M. Liu, Z. Xu, F. H. Shek et al., "miR-122 targets pyruvate kinase M2 and affects metabolism of hepatocellular carcinoma," *PLoS One*, vol. 9, no. 1, article e86872, 2014.

[50] Y. Zhao, L. Zhou, H. Li et al., "Nuclear-Encoded lncRNA *MALAT1* Epigenetically Controls Metabolic Reprogramming in HCC Cells through the Mitophagy Pathway," *Molecular Therapy-Nucleic Acids*, vol. 23, pp. 264–276, 2021.

[51] J. H. Lee, D. H. Shin, W. Y. Park et al., "IDH1 R132C mutation is detected in clear cell hepatocellular carcinoma by pyrosequencing," *World journal of surgical oncology*, vol. 15, no. 1, p. 82, 2017.

[52] S. Chang, S. Yim, and H. Park, "The cancer driver genes *IDH1/2, JARID1C/ KDM5C, and UTX/ KDM6A*: crosstalk between histone demethylation and hypoxic reprogramming in cancer metabolism," *Experimental & Molecular Medicine*, vol. 51, no. 6, pp. 1–17, 2019.

[53] R. Domenis, M. Comelli, E. Bisetto, and I. Mavelli, "Mitochondrial bioenergetic profile and responses to metabolic inhibition in human hepatocarcinoma cell lines with distinct differentiation characteristics," *Journal of Bioenergetics and Biomembranes*, vol. 43, no. 5, article 9380, pp. 493–505, 2011.

[54] D. DeWaal, V. Nogueira, A. R. Terry et al., "Hexokinase-2 depletion inhibits glycolysis and induces oxidative phosphorylation in hepatocellular carcinoma and sensitizes to metformin," *Nature communications*, vol. 9, no. 1, p. 446, 2018.

[55] A. S. Tan, J. W. Baty, L. F. Dong et al., "Mitochondrial genome acquisition restores respiratory function and tumorigenic potential of cancer cells without mitochondrial DNA," *Cell Metabolism*, vol. 21, no. 1, pp. 81–94, 2015.

[56] F. Jin, Y. Wang, Y. Zhu et al., "The miR-125a/HK2 axis regulates cancer cell energy metabolism reprogramming in hepatocellular carcinoma," *Scientific Reports*, vol. 7, no. 1, p. 3089, 2017.

[57] J. W. Locasale and L. C. Cantley, "Altered metabolism in cancer," *BMC biology*, vol. 8, no. 1, 2010.

[58] C. Dou, H. Mo, T. Chen et al., "ZMYND8 promotes the growth and metastasis of hepatocellular carcinoma by promoting HK2-mediated glycolysis," *Pathology - Research and Practice*, vol. 219, article id 153345, 2021.

[59] X. Huang, G. Gan, X. Wang, T. Xu, and W. Xie, "The HGF-MET axis coordinates liver cancer metabolism and autophagy for chemotherapeutic resistance," *Autophagy*, vol. 15, no. 7, pp. 1258–1279, 2019.

[60] M. Yang, J. Li, P. Gu, and X. Fan, "The application of nanoparticles in cancer immunotherapy: Targeting tumor microenvironment," *Bioactive materials*, vol. 6, no. 7, pp. 1973–1987, 2020.

[61] A. Brand, K. Singer, G. E. Koehl et al., "LDHA-associated lactic acid production blunts tumor immunosurveillance by T and NK cells," *Cell Metabolism*, vol. 24, no. 5, pp. 657–671, 2016.

[62] U. E. Martinez-Outschoorn, Z. Lin, C. Trimmer et al., "Cancer cells metabolically "fertilize" the tumor microenvironment with hydrogen peroxide, driving the Warburg effect," *Cell Cycle*, vol. 10, no. 15, pp. 2504–2520, 2011.

[63] X. Y. Hu and L. B. Ivashkiv, "Cross-regulation of signaling pathways by interferon-γ: implications for immune responses and autoimmune diseases," *Immunity*, vol. 31, no. 4, pp. 539–550, 2009.

[64] L. J. Reitzer, B. M. Wice, and D. Kennell, "Evidence that glutamine, not sugar, is the major energy source for cultured HeLa cells.," *The Journal of Biological Chemistry*, vol. 254, no. 8, pp. 2669–2676, 1979.

[65] X. S. Chen, L. Y. Li, Y. D. Guan, J. M. Yang, and Y. Cheng, "Anticancer strategies based on the metabolic profile of tumor cells: therapeutic targeting of the Warburg effect," *Acta Pharmacologica Sinica*, vol. 37, no. 8, pp. 1013–1019, 2016.

[66] Y. Sugiyama, T. Shudo, S. Hosokawa, A. Watanabe, M. Nakano, and A. Kakizuka, "Emodin, as a mitochondrial uncoupler, induces strong decreases in adenosine triphosphate (ATP) levels and proliferation of B16F10 cells, owing to their poor glycolytic reserve," *Genes Cells*, vol. 24, no. 8, pp. 569–584, 2019.

[67] J. Calderaro, M. Ziol, V. Paradis, and J. Zucman-Rossi, "Molecular and histological correlations in liver cancer," *Journal of Hepatology*, vol. 71, no. 3, pp. 616–630, 2019.

[68] Z. F. Karagonlar, S. Akbari, M. Karabicici et al., "A Novel Function for KLF4 in Modulating the De-differentiation of EpCAM-/CD133- nonStem Cells into EpCAM+/CD133+ Liver Cancer Stem Cells in HCC Cell Line HuH7," *Cells*, vol. 9, no. 5, p. 1198, 2020.

[69] R. Shang, M. Wang, B. Dai et al., "Long noncoding RNA SLC2A1-AS1 regulates aerobic glycolysis and progression in hepatocellular carcinoma via inhibiting the STAT3/FOXM1/-GLUT1 pathway," *Molecular Oncology*, vol. 14, no. 6, pp. 1381–1396, 2020.

[70] A. C. K. Lee, P. M. Lau, Y. W. Kwan, and S. K. Kong, "Mitochondrial fuel dependence on glutamine drives chemoresistance in the cancer stem cells of hepatocellular carcinoma," *International Journal of Molecular Sciences*, vol. 22, no. 7, p. 3315, 2021.

[71] H. Hu, X. Ding, Y. Yang et al., "Changes in glucose-6-phosphate dehydrogenase expression results in altered behavior of HBV-associated liver cancer cells," *American Journal of Physiology. Gastrointestinal and Liver Physiology*, vol. 307, no. 6, pp. G611–G622, 2014.

[72] M. C. Herzig, J. A. Zavadil, K. Street et al., "DNA Alkylating Agent Protects Against Spontaneous Hepatocellular Carcinoma Regardless of O6-Methylguanine-DNA Methyltransferase Status," *Cancer Prevention Research*, vol. 9, no. 3, pp. 245–252, 2016.

[73] J. Sun, J. Li, Z. Guo et al., "Overexpression of pyruvate dehydrogenase E1α subunit inhibits Warburg effect and induces cell apoptosis through mitochondria-mediated pathway in hepatocellular carcinoma," *Oncology Research*, vol. 27, no. 4, pp. 407–414, 2019.

[74] E. Dapat, S. Jacinto, and T. Efferth, "Substrate specificity of Aglaia loheri active isolate towards P-glycoprotein in multidrug-resistant cancer cells," *Natural Product Communications*, vol. 11, no. 11, pp. 1683–1688, 2016.

Hindawi
Journal of Nanomaterials
Volume 2021, Article ID 9956466, 7 pages
https://doi.org/10.1155/2021/9956466

Research Article

Preparation of Gelatin/Polycaprolactone Electrospun Fibers Loaded with Cis-Platinum and Their Potential Application for the Treatment of Prostate Cancer

Yang Jin,[1] Peng Sun,[2] Tong Wu,[3] Jin Wang,[4] Xiaoyu Huang,[5] Shishuai Zuo,[2] Zilian Cui,[2,5] Ji Chen,[2] Lianjun Li,[2] Ning Suo,[2] Xunbo Jin,[2,5] and Dong Zhang[2,5]

[1]*Department of Anesthesiology, Shandong Provincial Hospital, Cheeloo College of Medicine, Shandong University, Jinan, Shandong 250021, China*
[2]*Department of Urology, Shandong Provincial Hospital Affiliated to Shandong First Medical University, Jinan, Shandong 250021, China*
[3]*Department of Chemotherapy, Shandong Second Provincial General Hospital, Shandong Provincial ENT Hospital, Jinan, Shandong 250021, China*
[4]*Department of Urology, The First Affiliated Hospital of Shandong First Medical University, Jinan, Shandong 250021, China*
[5]*Department of Urology, Shandong Provincial Hospital, Cheeloo College of Medicine, Shandong University, Jinan, Shandong 250021, China*

Correspondence should be addressed to Dong Zhang; zd_sdu@163.com

Received 9 March 2021; Revised 31 March 2021; Accepted 7 April 2021; Published 22 April 2021

Academic Editor: Songwen Tan

Although the development of nanomaterials for cancer therapy has received much attention in recent years, prostate cancer still remains one of the most troubling cancers in males. In this work, biomimetic polycaprolactone (PCL)/gelatin (GT)/cis-platinum (CDDP) (PG@CDDP) fibrous films were developed *via* electrospinning technology. The microstructure and chemical properties of PG@CDDP fibers are investigated. It is found that the microscopic morphology and diameter of PG@CDDP fibers are changed compared to those of the PG fibers. The Fourier transform-infrared spectroscopy and wide-angle X-ray diffraction demonstrate that CDDP is successfully incorporated into the fibers. The human prostate cancer cells *in vitro* to electrospun films (PG and PG@CDDP) were evaluated based on initial cell response and cell viability. The density, elongation, and viability of adhered cancer cells significantly reduce with an increased concentration of CDDP in PG fibers. Thus, the developed PG@CDDP fiber matrix has great potential as candidate scaffolds for the treatment of prostate cancer.

1. Introduction

Cancer has been the main cause of human death for centuries due to the uncontrolled proliferation of cancer cells as well as tumor metastasis [1–3]. Particularly, prostate cancer is a common malignant tumor in males and has been regarded as a global issue in developing and underdeveloped countries [4, 5]. Generally, prostate cancer can be described as adenocarcinoma, but it can develop into other histopathological types, e.g., small-cell and neuroendocrine carcinoma [4, 6]. Traditional chemotherapy (e.g., the combination of docetaxel (Taxotere) and prednisone) and radiotherapy are still the most commonly used strategy in clinical cancer treatment [7, 8]. However, both strategies had some limitations, such as serious side effects, limited therapeutic efficacy, multidrug resistance, and poor efficacy for metastatic tumors [8–11].

Recently, micro-/nanomaterials have gained increasing attention for the treatment of cancer owing to enhanced therapeutic efficiency and relatively mild systemic side effect [8, 11, 12]. In particular, micro-/nanofibers as a bioscaffold have been designed as promising carriers for delivering anticancer drugs because of a high loading capacity and high encapsulation efficiency [13–15]. While numerous micro-/nanofabrication strategies, e.g., phase separation, synthetic

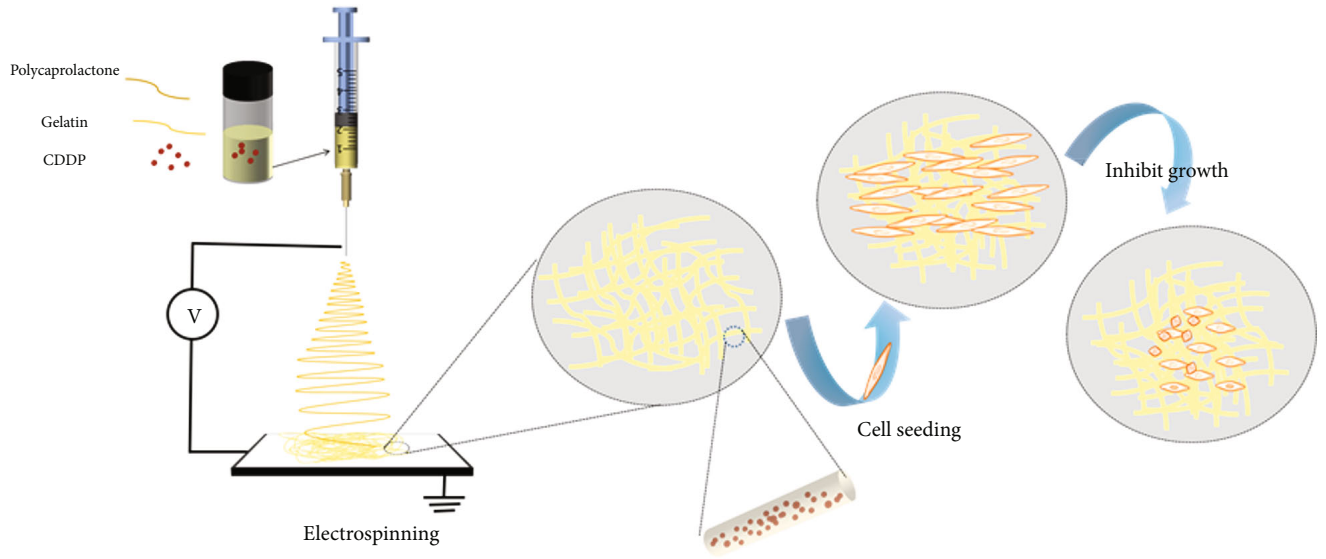

Figure 1: Schematic diagram of the preparation of PG@CDDP fibers and their interaction with prostate cancer cells.

molding, self-assembly, and drawing, have provided useful tools to prepare ultrafine fiber, in the past decade, electrospinning has received more interest in developing ultrafine polymer fibers for drug delivery applications owing to their extracellular matrix- (ECM-) like structure, excellent biological properties, high mechanical strength, porous mesh with remarkable interconnectivity, high specific surface area, and aspect ratio [16–19]. Electrospun fibrous films can be conveniently implanted into the location of the tumor for the controlled release of chemotherapeutics and ultimately achieve the purpose of curing cancer [20, 21].

Gelatin/polycaprolactone fibers are selected in this study as an anticancer drug delivery system because both polymers possess excellent biocompatible, tunable biodegradable, and nontoxic degradation products [16, 22, 23]. It does not require surgical removal after the completion of drug release. Anticancer drug (cis-platinum) has been widely used as a chemotherapy medication to treat many cancers [24, 25]. In the present work, biodegradable polycaprolactone (PCL)/gelatin (GT)/cis-platinum (CDDP) (PG@CDDP) fibrous films were fabricated *via* electrospinning technology. The morphology and chemical properties of PG@CDDP fibers were investigated by scanning electron microscopy (SEM) and Fourier transform infrared (FTIR) and X-ray diffraction (XRD) spectroscopy. The human prostate cancer cells (T24) *in vitro* that interacted with electrospun fiber films were tested.

2. Experimental Section

2.1. Materials. Cis-platinum (CDDP) was purchased from Macklin (Shanghai, China). Polycaprolactone (PCL) was bought from Aladdin (Shanghai, China). Gelatin (GT) and trifluoroethanol (TFE) were obtained from Sigma-Aldrich (USA). All reagents were of analytical grade and used without further purification. Deionized (DI) water in all experiments was used.

2.2. Preparation of GT/PCL Solutions. Solutions of PCL/GT (PG) were obtained by mixing 10% (*w*/*v*) PCL/TFE and 10% (*w*/*v*) GT/TFE at the mass ratio of 1 : 1 and under stirring for 24 h. To make miscible and transparent PG/TFE solutions, 10 μL acetic acid was added to the PG solutions according to previous studies [23]. Next, a certain amount of CDDP (i.e., 0.05 g and 0.1 g) was introduced into PG solutions to prepare 10 mL PG@0.5%CDDP and PG@1%CDDP solutions, respectively.

2.3. Electrospinning. Briefly, solutions of PG@CDDP in a 5 mL syringe were delivered at a feeding rate of 1.0 mL/h by a syringe pump (Langer, Baoding, China). A high-voltage power supply (Dongwen, Tianjin, China) of 12.5 kV was used between a blunt metal needle tip and a collector, separated at a distance of 14 cm. All the electrospinning processes were performed on a perpendicular electrospinning strategy at room temperature (21–23°C) with an ambient humidity of 45–50%.

2.4. Scanning Electron Microscopy (SEM). The morphology of PG composite fibers was observed using SEM (VEGA3, TESCAN, Czech). Before imaging, samples were sputter-coated with gold to increase conductivity. The average diameter of PG composite fibers was analyzed by detecting at least 50 fiber segments using ImageJ.

2.5. Fourier Transform Infrared (FTIR) Spectroscopy. A Nicolet iN10 FTIR spectrometer (Thermo Fisher Scientific, Waltham, MA, USA) was applied to detect the FTIR spectra of PG composite fibers over the range of 500–4000 cm^{-1} at a scanning resolution of 2 cm^{-1} during 32 scans.

2.6. X-Ray Diffraction (XRD) Spectroscopy. XRD spectroscopy was carried out to detect the crystal structures of PG composite fibers. The materials were measured between 5 and 80° (2θ) at a scanning rate of 1.0° (2θ) per minute

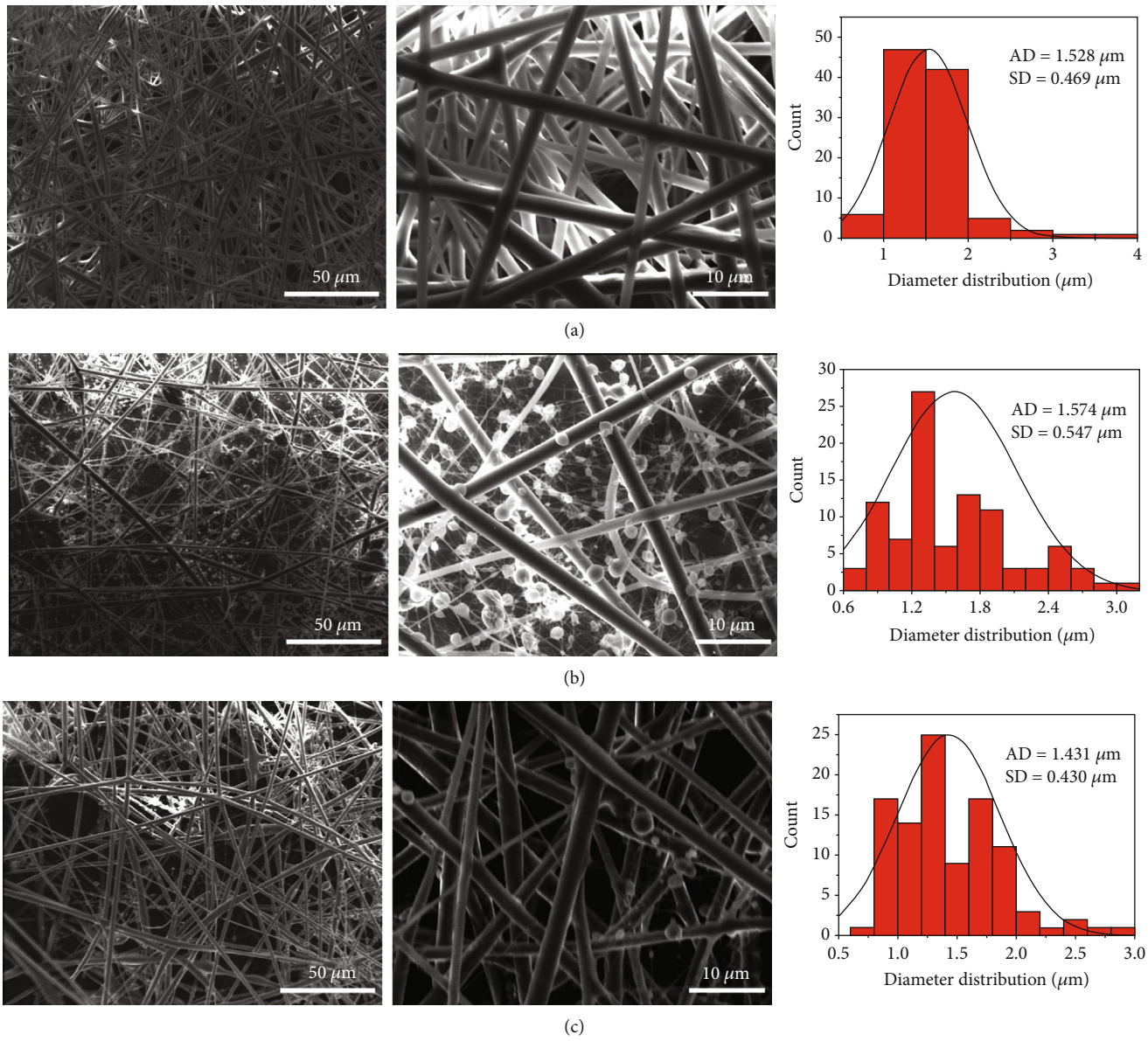

Figure 2: SEM images and fiber diameter distribution of the electrospun fibers of (a) PG, (b) PG@0.5%CDDP, and (c) PG@1%CDDP.

operating with voltage 40 kV and current 30 mA equipped by Cu Kα radiation.

2.7. In Vitro Drug Release. 40 mg of PG@0.5%CDDP or PG@1.5%CDDP nanofibers was added in 3 mL of normal saline (0.9%NaCl) and incubated at 37°C in a shaker. At predetermined time intervals, 1 mL aliquots of solution were removed for the measurement and replaced with 1 mL fresh buffer solution. Aliquots of solution were detected using a High-Performance Liquid Chromatography (HPLC) system (Shimadzu, Kyoto, Japan).

2.8. Cell Assays

2.8.1. Cell Culture. Human prostate cancer cells (T24) were purchased from Biyuntian Biological Technology Co., Ltd. (Shanghai, China). Cells were cultured and expanded in RPMI-1640 supplemented with 10% FBS (Biological Industries, Israel) at 37°C with 5% CO_2 in the air. The cells were harvested at 80–90% confluency from culture flasks by trypsin at 37°C for further subcultures.

2.8.2. Fluorescence Staining. Cancer cells were seeded in 24-well plates at a density of 5.0×10^4 cells/well for 1 d. The cells were fixed with 4% paraformaldehyde for 15 min, rinsed three times with PBS, and then permeabilized with 0.1% X-100 for 6 min. The fixed cells were washed twice with PBS and blocked with 5% bovine serum albumin (BSA) in PBS for 40 min. The cell cytoskeleton and nuclei were labeled with TRITC-phalloidin and 4′,6-diamidino-2-phenylindole (DAPI) for 20 min. Cell images were obtained using a fluorescent microscope. The elongation factor of the cell was analyzed as the major axis/minor axis of the cells. By definition, the roundness is equal to 1 for a completely round cell.

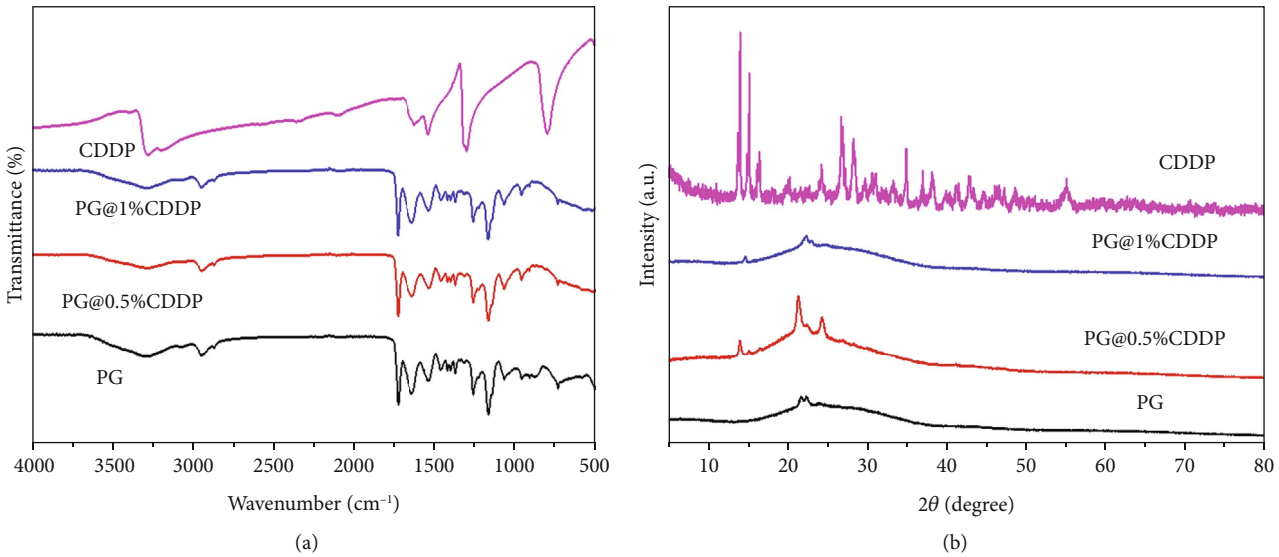

Figure 3: (a) FTIR spectra and (b) XRD patterns of CDDP, PG, PG@0.5%CDDP, and PG@1%CDDP fibers.

2.8.3. Cell Viability. Cancer cells were seeded in 24-well plates at a density of 3.0×10^3 cells/well for 1, 3, and 5 d. Next, the medium was exchanged with a fresh medium containing 10% Cell Counting Kit-8 (Absin Bioscience Inc., China) and incubated for 2 h. The optical density (OD) values of the medium were measured at 450 nm using a microplate reader.

2.9. Statistical Analysis. All values were shown as mean ± standard deviation (SD). Statistical analysis was performed using Origin 9. One-way analysis of variance (ANOVA) with Tukey's test was used to identify differences between groups. A value of $p < 0.05$ was considered to be statistically significant.

3. Results and Discussion

3.1. Preparation and Characterization of Composite Fibers. The preparation process of PG@CDDP fibers and their interaction with prostate cancer cells are illustrated in Figure 1. The electrospun GT/PCL couple is one of the most intensively investigated natural-synthetic hybrid fiber systems owing to its excellent electrospinnability, ECM-like structure, favorable biological properties, sufficient mechanical strength, and capability for drug loading.

The morphology of nanofibers plays a critical role in their (bio)physicochemical properties, such as mechanical strength, biodegradation, and cell responses [26–29]. The morphology of composite fibers was observed by SEM (Figure 2). As shown in Figure 2(a), the prepared fibers were highly uniform and smooth with an averaged diameter of 1.528 ± 0.469 nm. When 0.5% CDDP was added into the PG system, there was no significant difference in the fiber diameter between PG@0.5%CDDP fibers and PG fibers (Figure 2(b)). However, the microstructure of PG@0.5%CDDP fibers greatly changed compared to that of the PG fibers. And small particles among the fibers were found in the PG@0.5%CDDP system, probably due to the formation of phase separation after the addition of CDDP. With an increased amount of CDDP, the diameter of PG@1%CDDP fibers slightly reduced as compared to those of the PG and PG@0.5%CDDP fibers. Small particles among the PG@1%CDDP fibers significantly decreased compared to those among the PG@0.5%CDDP system. Taken together, these results indicate that the microstructure of PG fibers was dependent on the introduction of CDDP.

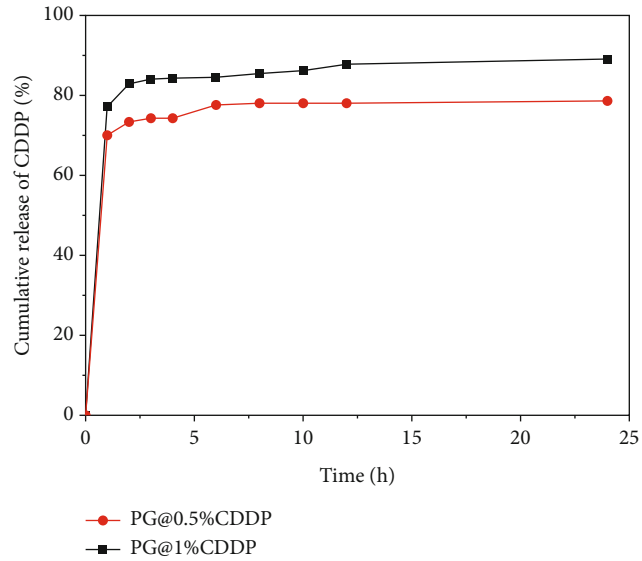

Figure 4: *In vitro* release of CDDP from PG@0.5%CDDP and PG@1%CDDP fibers.

The chemical groups of PG-based composite fibers were analyzed by FT-IR. Figure 2(a) shows the FT-IR spectra of CDDP, PG fibers, PG@0.5%CDDP fibers, and PG@1%CDDP fibers. In the CDDP group, the typical band at 3200–3283 cm^{-1} belonged to the asymmetric and symmetric tensile vibrations of N–H; the typical band at 1300–1618 cm^{-1} was assigned to the symmetric and asymmetric bending vibrations of H–N–H; the peak at 800 cm^{-1} corresponded to the tensile vibration signal of N–Pt [30].

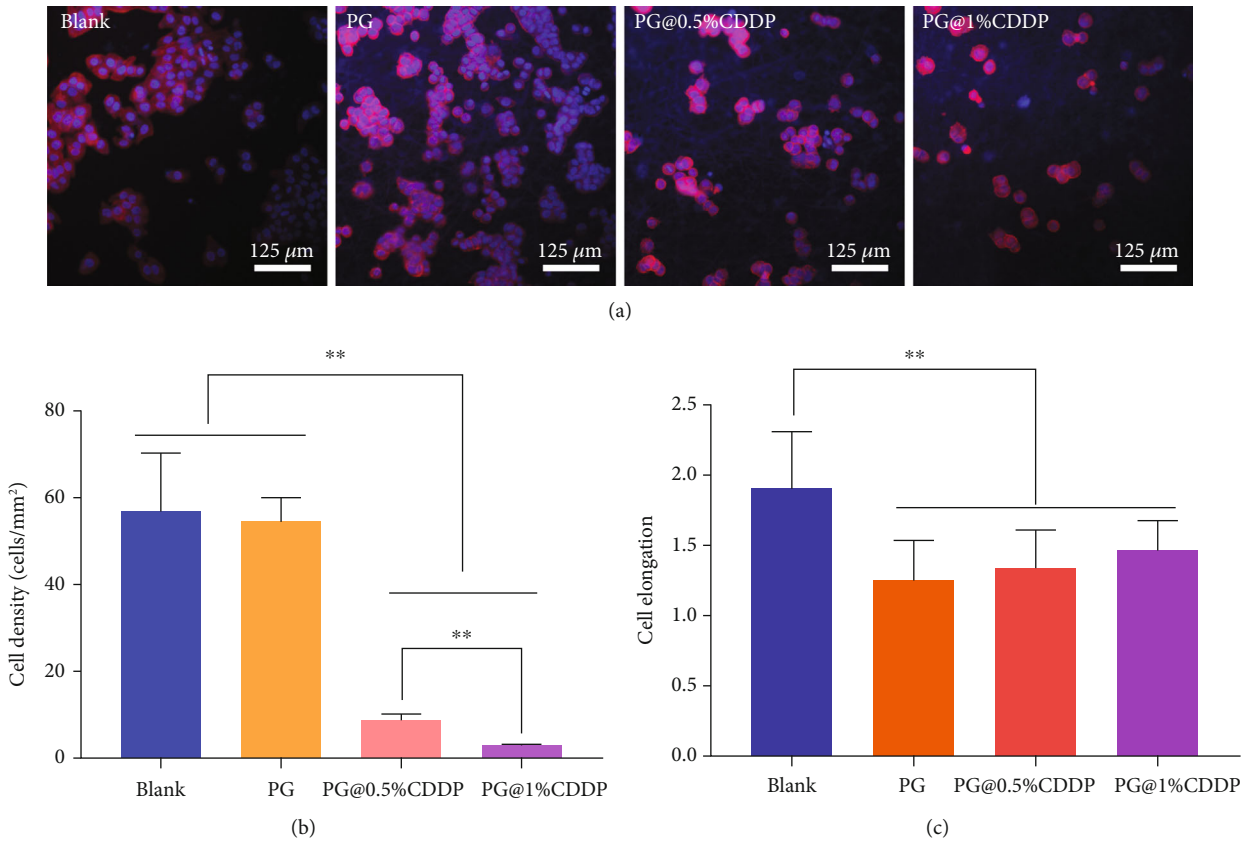

FIGURE 5: (a) Fluorescent images of blank, PG, PG@0.5%CDDP, and PG@1%CDDP fibers after 1 d of cell culture. (b) Cell density and (c) cell elongation on blank, PG, PG@0.5%CDDP, and PG@1%CDDP fibers.

In the PG group, the typical bands for peptide bonds from GT were found [31], e.g., amide-A band at 3200–3500 cm^{-1} corresponding to N–H stretching vibrations, the amide II band corresponding to 1534 cm^{-1}, and the amide III band corresponding to 1239 cm^{-1}; the typical bands from PCL were found, e.g., the peak at 1700 cm^{-1} corresponding to C=O asymmetric, the peak at 2920 cm^{-1} corresponding to C–H asymmetric, and the peak at 2840 cm^{-1} corresponding to C–H symmetric [32]. The spectra of PG@0.5%CDDP and PG@1%CDDP fibers include all of the characteristic peaks of PG. Particularly, the peak at 800 cm^{-1} in PG@0.5%CDDP and PG@1%CDDP fibers was detected, indicating that CDDP was successfully loaded into PG fibers.

The XRD patterns of CDDP and PG-based fibers are shown in Figure 3(b). The CDDP had obvious crystallization peaks between 10 and 20° [33]. The PG group possessed characteristic diffraction peaks between 20 and 25° [22, 23]. When PG was loaded with different concentrations of CDDP, the PG@0.5%CDDP and PG@1%CDDP fibers showed the characteristic diffraction peak of CDDP at 10–20°, and the typical diffraction peak of PG appeared between 20 and 25°, also suggesting that CDDP was successfully loaded into PG fibers.

An initial burst release of PG@0.5%CDDP fibers was detected within the first 1 h (70% of the drug was released), followed by a sustained release profile (Figure 4). Similarly, there was an initial burst found in release in the PG@1%CDDP fibers (77% of the drug was released). A sustained release in PG@1%CDDP fibers was observed with increasing the time from 0 to 12 h.

3.2. Anticancer Behavior of PG-Based Composite Fibers. Cancer cell adhesion is the initial response to the microenvironment, which precedes other cellular behaviors, e.g., spreading, migration, and proliferation [34, 35]. The composite fibers were tested *in vitro* for their anticancer behaviors against human prostate cancer cells. Initial cell response on all samples after 1 d was measured with a fluorescence staining of the actin cytoskeleton and nucleus. It was found that the PG fibrous films containing CDDP greatly affected the attachment and morphology of cancer cells (Figure 5(a)). With an increased amount of CDDP from 0 to 1%, the number of adhered cells gradually decreased and the expression of the actin cytoskeleton (red) reduced.

To better understand the effect of PG@CDDP fibers on the initial behavior of cancer cells, cell density, elongation, and area per cell were quantified by the analysis of the positively stained cells. Figure 5(b) displays that the density of cancer cells significantly decreased with increasing the concentration of CDDP in PG fibers, indicating that the released CDDP from PG fibers greatly inhibited the attachment of cancer cells. Cell elongation is an essential morphological feature for the interaction between cells and biomaterials by mediating the cytoskeleton actin and stimulating the cell nucleus, affecting cell migration, viability, and proliferation [36, 37]. Figure 5(c) shows that the cell elongation of PG-

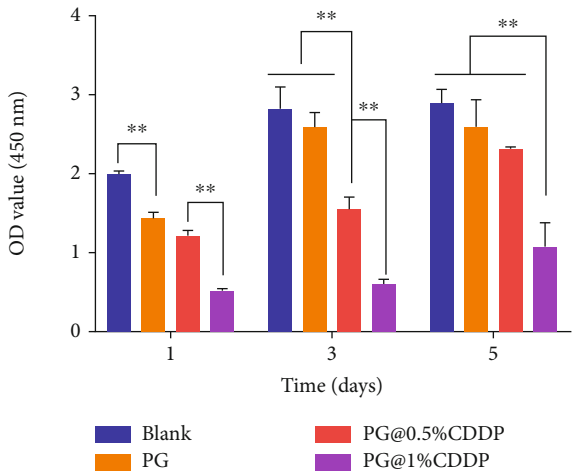

Figure 6: The viability of cancer cells on blank, PG, PG@0.5%CDDP, and PG@1%CDDP fibers after 1, 3, and 5 d of cell culture.

based fibers was significantly reduced compared to that of the blank, which suggests that PG-based fibers could suppress the migration of cancer cells.

The CCK-8 viability assay was performed after 1, 3, and 5 d of incubation. As shown in Figure 6, after 1 d of incubation, the OD value decreased with an increased concentration of CDDP in PG fibers, indicating that the addition of CDDP in PG fibers had a negative effect on the viability of cancer cells. After 3 and 5 d of incubation, the viability of cancer cells displayed a similar trend with that of 1 d of incubation. Taken together, the designed and prepared PG@CDDP fibers significantly inhibited cell attachment and viability, having great potential for the treatment of prostate cancer.

4. Conclusions

In summary, a PG@CDDP fibrous matrix was successfully fabricated using the electrospinning strategy. CDDP was introduced into the PG fibers based on the measurements of FT-IR spectroscopy and XRD. Small particles were found in PG@CDDP fibers compared to the PG fibers due to the addition of CDDP. The diameter of PG@1%CDDP fibers slightly reduced compared to those of the PG and PG@0.5%CDDP fibers. An initial burst release of PG@1%CDDP fibers within the first 1 h was found, followed by a sustained release profile from 0 to 12 h. The density, elongation, and viability of adhered cancer cells significantly decreased with increasing the concentration of CDDP in PG fibers. Therefore, the prepared PG@CDDP fiber matrix shows great potential for the treatment of prostate cancer.

Data Availability

The data used to support the findings of this study are available from the corresponding author upon request.

Conflicts of Interest

The authors declare no competing financial interest.

Acknowledgments

The authors are very grateful for the financial support by Key Research and Development Plan of Shandong Province (No. 2018GSF118127), the National Natural Science Foundation of China (Nos. 81602226, 81202016), Shandong Provincial Natural Science Foundation (Nos. ZR2015HQ002, ZR2020QH069), Shandong Province Medical and Health Science Technology Development Project (No. 2019WS464), and China Postdoctoral Science Foundation (Nos. 2016M590638, 2016M590641).

References

[1] V. Shanmugam, S. Selvakumar, and C.-S. Yeh, "Near-infrared light-responsive nanomaterials in cancer therapeutics," *Chemical Society Reviews*, vol. 43, no. 17, pp. 6254–6287, 2014.

[2] C. Wang, J. Yang, C. Dong, and S. Shi, "Glucose oxidase-related cancer therapies," *Advanced Therapeutics*, vol. 3, article 2000110, 2020.

[3] J.-J. Wang, K.-F. Lei, and F. Han, "Tumor microenvironment: recent advances in various cancer treatments," *European Review for Medical and Pharmacological Sciences*, vol. 22, no. 12, pp. 3855–3864, 2018.

[4] H. Barabadi, K. Damavandi Kamali, F. Jazayeri Shoushtari et al., "Emerging theranostic silver and gold nanomaterials to combat prostate cancer: a systematic review," *Journal of Cluster Science*, vol. 30, no. 6, pp. 1375–1382, 2019.

[5] M. Barani, F. Sabir, A. Rahdar, R. Arshad, and G. Z. Kyzas, "Nanotreatment and nanodiagnosis of prostate cancer: recent updates," *Nanomaterials*, vol. 10, no. 9, p. 1696, 2020.

[6] J. E. McNeal, "Origin and development of carcinoma in the prostate," *Cancer*, vol. 23, no. 1, pp. 24–34, 1969.

[7] P. McGale, C. Taylor, C. Correa et al., "Effect of radiotherapy after mastectomy and axillary surgery on 10-year recurrence and 20-year breast cancer mortality: meta-analysis of individual patient data for 8135 women in 22 randomised trials," *The Lancet*, vol. 383, 2014.

[8] S. Gai, G. Yang, P. Yang et al., "Recent advances in functional nanomaterials for light-triggered cancer therapy," *Nano Today*, vol. 19, pp. 146–187, 2018.

[9] S. Mura, J. Nicolas, and P. Couvreur, "Stimuli-responsive nanocarriers for drug delivery," *Nature Materials*, vol. 12, no. 11, pp. 991–1003, 2013.

[10] E. Blanco, H. Shen, and M. Ferrari, "Principles of nanoparticle design for overcoming biological barriers to drug delivery," *Nature Biotechnology*, vol. 33, no. 9, pp. 941–951, 2015.

[11] J. Shi, P. W. Kantoff, R. Wooster, and O. C. Farokhzad, "Cancer nanomedicine: progress, challenges and opportunities," *Nature Reviews. Cancer*, vol. 17, no. 1, pp. 20–37, 2017.

[12] W. Qiao, B. Wang, Y. Wang, L. Yang, Y. Zhang, and P. Shao, "Cancer therapy based on nanomaterials and nanocarrier systems," *Journal of Nanomaterials*, vol. 2010, Article ID 796303, 2010.

[13] T. Okuda, K. Tominaga, and S. Kidoaki, "Time-programmed dual release formulation by multilayered drug-loaded nanofiber meshes," *Journal of Controlled Release*, vol. 143, no. 2, pp. 258–264, 2010.

[14] X. Xu, X. Chen, P. Ma, X. Wang, and X. Jing, "The release behavior of doxorubicin hydrochloride from medicated fibers prepared by emulsion-electrospinning," *European Journal of*

Pharmaceutics and Biopharmaceutics, vol. 70, no. 1, pp. 165–170, 2008.

[15] X. Hu, S. Liu, G. Zhou, Y. Huang, Z. Xie, and X. Jing, "Electrospinning of polymeric nanofibers for drug delivery applications," *Journal of Controlled Release*, vol. 185, pp. 12–21, 2014.

[16] J. Xue, M. He, H. Liu et al., "Drug loaded homogeneous electrospun PCL/gelatin hybrid nanofiber structures for anti-infective tissue regeneration membranes," *Biomaterials*, vol. 35, no. 34, pp. 9395–9405, 2014.

[17] R. Qi, R. Guo, F. Zheng, H. Liu, J. Yu, and X. Shi, "Controlled release and antibacterial activity of antibiotic-loaded electrospun halloysite/poly(lactic-co-glycolic acid) composite nanofibers," *Colloids Surfaces B Biointerfaces*, vol. 110, pp. 148–155, 2013.

[18] B. Song, C. Wu, and J. Chang, "Dual drug release from electrospun poly(lactic-co-glycolic acid)/mesoporous silica nanoparticles composite mats with distinct release profiles," *Acta Biomaterialia*, vol. 8, no. 5, pp. 1901–1907, 2012.

[19] X.-Z. Sun, G. R. Williams, X.-X. Hou, and L.-M. Zhu, "Electrospun curcumin-loaded fibers with potential biomedical applications," *Carbohydrate Polymers*, vol. 94, no. 1, pp. 147–153, 2013.

[20] G. Xia, H. Zhang, R. Cheng et al., "Localized controlled delivery of gemcitabine via microsol electrospun fibers to prevent pancreatic cancer recurrence," *Advanced Healthcare Materials*, vol. 7, no. 18, p. 1800593, 2018.

[21] S. Chen, S. K. Boda, S. K. Batra, X. Li, and J. Xie, "Emerging roles of electrospun nanofibers in cancer research," *Advanced Healthcare Materials*, vol. 7, no. 6, p. 1701024, 2018.

[22] Q. Zhou, H. Zhang, Y. Zhou et al., "Alkali-mediated miscibility of gelatin/polycaprolactone for electrospinning homogeneous composite nanofibers for tissue scaffolding," *Macromolecular Bioscience*, vol. 17, pp. 1–10, 2017.

[23] B. Feng, H. Tu, H. Yuan, H. Peng, and Y. Zhang, "Acetic-acid-mediated miscibility toward electrospinning homogeneous composite nanofibers of GT/PCL," *Biomacromolecules*, vol. 13, no. 12, pp. 3917–3925, 2012.

[24] W. Shen, X. Chen, J. Luan, D. Wang, L. Yu, and J. Ding, "Sustained codelivery of cisplatin and paclitaxel via an injectable prodrug hydrogel for ovarian cancer treatment," *ACS Applied Materials & Interfaces*, vol. 9, no. 46, pp. 40031–40046, 2017.

[25] A. Sherif, L. Holmberg, E. Rintala et al., "Neoadjuvant cisplatinum based combination chemotherapy in patients with invasive bladder cancer: a combined analysis of two Nordic studies," *European Urology*, vol. 45, no. 3, pp. 297–303, 2004.

[26] G. Yang, X. Li, Y. He, J. Ma, G. Ni, and S. Zhou, "From nano to micro to macro: electrospun hierarchically structured polymeric fibers for biomedical applications," *Progress in Polymer Science*, vol. 81, pp. 80–113, 2018.

[27] H. Chen, X. Huang, M. Zhang et al., "Tailoring surface nanoroughness of electrospun scaffolds for skeletal tissue engineering," *Acta Biomaterialia*, vol. 59, pp. 82–93, 2017.

[28] Q. Zhou, J. Xie, M. Bao et al., "Engineering aligned electrospun PLLA microfibers with nano-porous surface nanotopography for modulating the responses of vascular smooth muscle cells," *Journal of Materials Chemistry B*, vol. 3, no. 21, pp. 4439–4450, 2015.

[29] Q. Zhang, Y. Ji, W. Zheng et al., "Electrospun nanofibers containing strontium for bone tissue engineering," *Journal of Nanomaterials*, vol. 2020, Article ID 1257646, 2020.

[30] E. Ortiz-Islas, M. E. Manríquez-Ramírez, A. Sosa-Muñoz et al., "Preparation and characterisation of silica-based nanoparticles for cisplatin release on cancer brain cells," *IET Nanobiotechnology*, vol. 14, no. 3, pp. 191–197, 2020.

[31] I. Rajzer, E. Menaszek, R. Kwiatkowski, J. A. Planell, and O. Castano, "Electrospun gelatin/poly(ε-caprolactone) fibrous scaffold modified with calcium phosphate for bone tissue engineering," *Materials Science & Engineering. C, Materials for Biological Applications*, vol. 44, pp. 183–190, 2014.

[32] A. Khalf and S. Madihally, "Modeling the permeability of multiaxial electrospun poly(ε-caprolactone)-gelatin hybrid fibers for controlled doxycycline release," *Materials Science & Engineering. C, Materials for Biological Applications*, vol. 76, pp. 161–170, 2017.

[33] U. Aggarwal, A. K. Goyal, and G. Rath, "Development and characterization of the cisplatin loaded nanofibers for the treatment of cervical cancer," *Materials Science & Engineering. C, Materials for Biological Applications*, vol. 75, pp. 125–132, 2017.

[34] U. Cavallaro and G. Christofori, "Cell adhesion and signalling by cadherins and Ig-CAMs in cancer," *Nature Reviews. Cancer*, vol. 4, no. 2, pp. 118–132, 2004.

[35] G. Jacquemet, H. Hamidi, and J. Ivaska, "Filopodia in cell adhesion, 3D migration and cancer cell invasion," *Current Opinion in Cell Biology*, vol. 36, pp. 23–31, 2015.

[36] Q. Zhou, J. Chen, Y. Luan et al., "Unidirectional rotating molecular motors dynamically interact with adsorbed proteins to direct the fate of mesenchymal stem cells," *Science advances*, vol. 6, article eaay2756, 2020.

[37] Y. Jia, W. Yang, K. Zhang et al., "Nanofiber arrangement regulates peripheral nerve regeneration through differential modulation of macrophage phenotypes," *Acta Biomaterialia*, vol. 83, pp. 291–301, 2019.

Hindawi
Journal of Nanomaterials
Volume 2021, Article ID 9997806, 7 pages
https://doi.org/10.1155/2021/9997806

Research Article

miR-598 Represses Cell Migration and Invasion of Non-Small-Cell Lung Cancer by Inhibiting MSI2

Junbin Guo, Tairan Liu, Meiyun Su, and Qingxian Yan

Department of Hematology and Oncology, The First People's Hospital of Wen Ling, China

Correspondence should be addressed to Qingxian Yan; gjb24242021@163.com

Received 5 March 2021; Revised 15 March 2021; Accepted 30 March 2021; Published 19 April 2021

Academic Editor: Songwen Tan

Non-small-cell lung cancer (NSCLC) is one of the most frequent solid tumors and regarded as a significant threat to individual health around the world. MicroRNAs (miRs) are recognized as critical governors of gene expression during carcinogenesis, while their clinical significance and mechanism in NSCLC occurrence and development are required for further investigation. In this report, we characterized the functional role of miR-598 and its regulation mechanism in NSCLC. The expression level of miR-598 in NSCLC tissues and cell lines was detected by qRT-PCR. A549 cells were transiently transfected with miR-598 mimics or miR-598 inhibitors. Scratch assay and Transwell assay were used to detect cell transfection, migration, and invasion. Possible binding sites of miR-598 in MSI2 mRNA were predicted by bioinformatics and validated by dual-luciferase reporter gene system. The ability of migration and invasion was examined on cells transfected with MSI2 alone or cotransfected A549 cells with miR-598. The expression of miR-598 in NSCLC tissues was significantly lower than that in adjacent tissues, and the expression of miR-598 in NSCLC cell lines (A549, H1650, and H1299) was also significantly lower than that of normal lung epithelial cell line BEAS-2B. A549 cells were significantly inhibited in migration and invasion after transfection with miR-598 mimics, while miR-598 inhibitors were significantly enhanced in migration and invasion. MSI2 was a direct target gene of miR-598. MSI2 can promote the migration and invasion of A549 cells, but the ability to promote cell migration and invasion was reversed when miR-598 was introduced. In conclusion, miR-598 inhibits the migration and invasion of NSCLC by downregulating the target gene MSI2.

1. Introduction

Lung cancer is a common malignant tumor of the respiratory system, and the incidence and mortality rates of lung cancer have significantly increased in recent years in China [1]. Due to diversity in lifestyles and socioeconomic development, lung cancer presents geographic and gender differences in China [2]. Non-small-cell lung cancer (NSCLC) is the most common type of lung cancer, accounting for about 80% to 85% [3]. In the recent three decades, the 5-year survival of patients with lung cancer remains only 19% with minimal improvement [4]. Although the design of nanoparticle-based carriers for targeted drug delivery has shown promise in treating human cancers [5, 6], therapeutic strategies of NSCLC are still needed to be further explored. Thus, it is imperative and meaningful to explore the underlying molecular mechanisms and identify novel prognostic biomarkers and potential therapeutic targets for lung cancer [7].

As an endogenous class of noncoding small-molecule RNAs with a length of 18 to 22 nucleotides, miRNAs specifically bind to the 3′UTR end of the target gene mRNA molecules, thereby regulating the expression of the target gene and participating in proliferation, migration, invasion, apoptosis, and epithelial-mesenchymal transition of a variety of tumor cells [8]. An in-depth study of miRNA-related molecular mechanisms is of great significance for the diagnosis and treatment of NSCLC [9]. Studies have shown that miR-598 is significantly suppressed in colorectal cancer [10], gastric cancer [11], osteosarcoma [12], retinoblastoma [13], and ovarian cancer [14], suggesting that miRNA-598 may be a potential tumor suppressor miRNA. In recent years, miRNA-598 has been

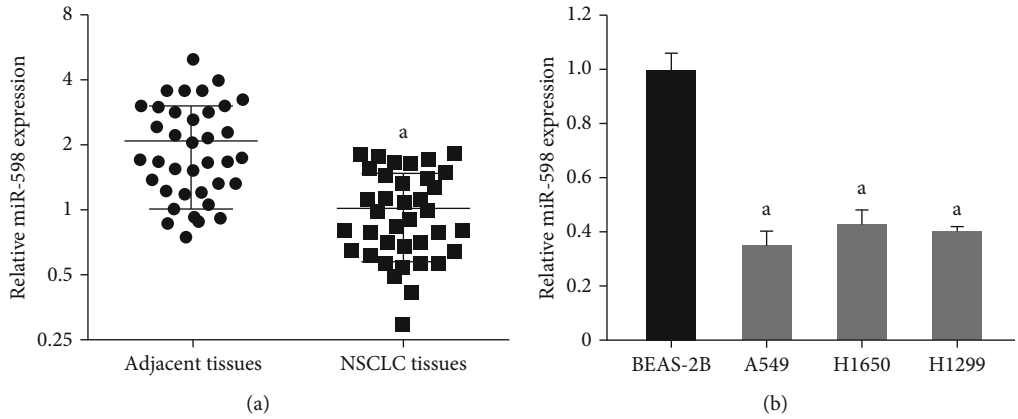

Figure 1: Expressions of miR-598 in NSCLC tissues and cell lines. (a) Relative expression levels of miR-598 in NSCLC tissues ($n = 37$) and corresponding adjacent tissues ($n = 37$) were determined by qRT-PCR. (b). Relative expression levels of miR-598 in the three NSCLC cell lines and normal lung epithelial cell line BEAS-2B were determined by qRT-PCR. a indicates $P < 0.01$ compared with corresponding adjacent tissues and BEAS-2B, respectively.

widely studied in inhibiting tumor cell growth, migration, and invasion, but its role in the occurrence and development of NSCLC is unclear. Musashi 2 (MSI2) protein is a member of the Musashi protein family. MSI2 is not only an important molecular marker of stem cells and early progenitor cells but also closely related to the prognosis and metastasis of various tumors [15]. MSI2 is highly expressed in the context of pancreatic cancer [16], liver cancer [17], and glioma [18], and its expression level is closely related to the invasion and metastasis of tumor cells.

This study investigated the expression of miR-598 in non-small-cell lung cancer tissues and the effect of miRNA-598 targeting MSI2 NSCLC cell migration and invasion in order to provide new theoretical basis for the diagnosis and treatment of NSCLC.

2. Materials and Methods

2.1. Sample Collection. Thirty-seven cases of primary NSCLC tissues resected by thoracic surgery from August 2017 to March 2019 in the First People's Hospital of Wen Ling were collected. At the same time, normal lung tissues from the above cases (distance from the lesion > 5 cm and pathologically confirmed no tumor cell infiltration) were set as a control. Of the 37 patients, 18 were males and 19 were females, with an average age of 56.7 ± 8.9 years. Among them, 23 were having squamous cell carcinomas and 14 were having adenocarcinomas. All patients were not treated with chemotherapy and radiation before surgery. After the specimens were cut, they were quickly frozen in liquid nitrogen and then transferred to a -80°C refrigerator for storage. Patients in this study have signed an informed consent, and this study was approved by the hospital medical ethics committee.

2.2. Cell Culture. Human lung cancer cell lines A549, H1650, and H1299 and human normal lung epithelial cells BEAS-2B were purchased from the Cell Resource Center of Shanghai Institutes for Biological Sciences, Chinese Academy of Sciences. All cells were routinely cultured in RPMI-1640 medium (including 10% fetal calf serum + 100 U/mL penicillin + 100 μg/mL streptomycin), placed in a 37°C, 5% CO_2 saturated humidity incubator.

2.3. qRT-PCR Experiment. The total RNA of tissues and cells was extracted by a Trizol method. TaqMan MicroRNA Reverse Transcription kit was used for reverse transcription reaction. The reaction conditions were 16°C for 30 min, 42°C for 30 min, and 85°C for 5 min. TaqMan MicroRNA Assay Real-time PCR kit was used for quantitative amplification reaction; the reaction conditions were 95°C for 5 min, 95°C for 15 s, 62°C for 30 s, and a total of 40 cycles. The reaction uses U6 as an internal reference, and the sequence of the primers is as follows: miR-598 is 5′-AGCTACGTCATCGT TGTCATC-3′; U6 is 5′-CTCGCTTCGGCAGCACA-3′. Three replicates were made for each test index, and the expression level of miR-598 was relatively quantified by the 2-$\Delta\Delta$Ct method.

2.4. Cell Transfection. When A549 cells grow to about 80%, Lipofectamine 2000 reagents (Invitrogen, Carlsbad, CA, USA) were used to transfect miRNA control (miR-NC), miR-598 mimics, and miR-598 inhibitors (GenePharma, Shanghai, China) into A549 cells. The fresh medium was changed after 8 h, and cells were collected for subsequent experiments after 48 h.

2.5. Scratch Healing Assay. A549 cells were seeded into a 6-well plate. After the cells were covered with the bottom of the well, a "1"-shaped scratch was made on the bottom of the culture plate with a 10 μL sterile pipette tip. Under the inverted microscope, observe the migration of cells in the scratches after 36 h and take pictures. Measure the width of the scratch at three locations along the edge of the scratch at an equal interval, and take the average value (scratch healing rate (%) = (0 h scratch width − 36 h scratch width)/0 h scratch width × 100%).

2.6. Transwell Invasion Assay. Transwell experiments were performed using an 8 μm polycarbonate filter culture

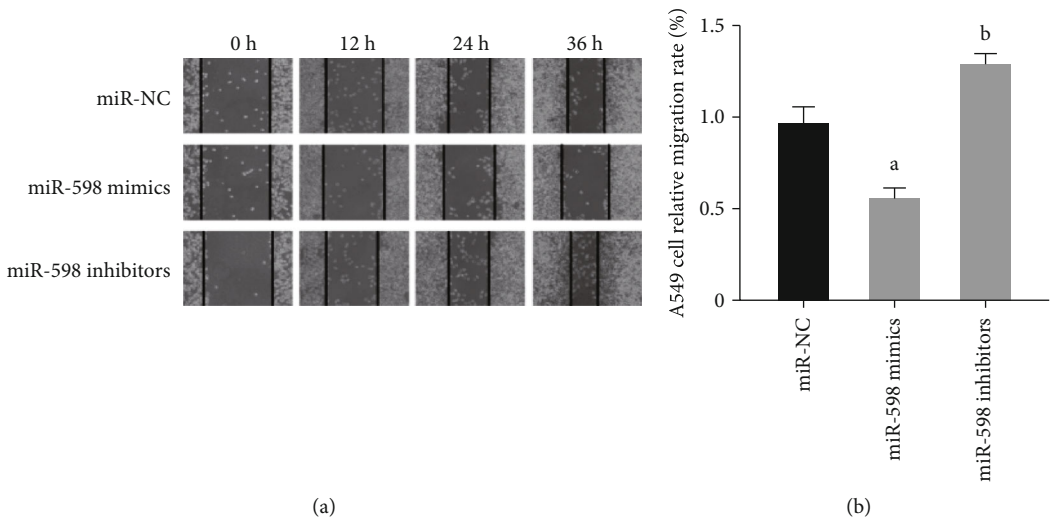

Figure 2: An inhibitory effect of miR-598 on migration of A549 cells: (a) representative image of the scratch healing from 0 to 36 h after miR-598 mimic or inhibitor transfection, examined by scratch test; (b) A549 cell migration rate after 36 h transfection of miR-598 mimic or inhibitor transfection. a indicates $P < 0.01$, and b indicates $P < 0.05$ compared with miR-NC, respectively.

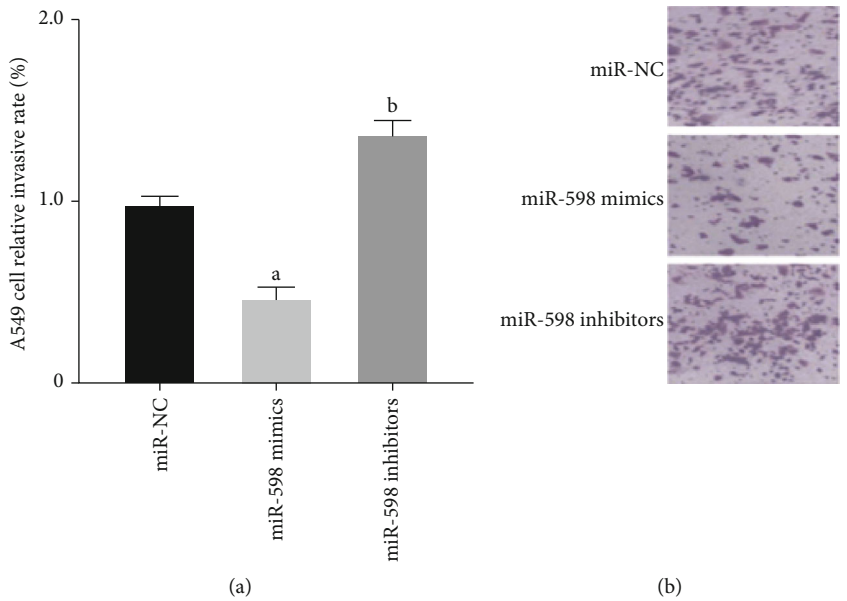

Figure 3: An inhibitory effect of miR-598 on invasion of A549 cells: (a) A549 cell invasion rate after 36 h transfection of miR-598 mimic or inhibitor transfection; (b) representative image of cells invading from the upper Transwell chambers to the lower chamber. a indicates $P < 0.01$, and b indicates $P < 0.05$ compared with miR-NC, respectively.

chamber preplated with Matrigel. A549 cells in the logarithmic growth phase were made into 1×10^5 cell suspension at a density of 1 mL/mL, and 200 μL of the cell suspension was inoculated into the upper chamber of the Transwell chamber. 500 μL of RPMI-1640 culture medium containing 10% fetal bovine serum (Gibco, Grand Island, NY, USA) was added to the lower chamber, and three replicates were set in each group. After 36 hours of incubation at 37°C and 5% CO_2, gently wipe away the Matrigel and the upper nonmembrane cells with a cotton swab, fix the cells with 4% paraformaldehyde for 10 minutes, and stain with 0.1% crystal violet for 10 minutes. The number of cells in 5 fields of view was counted randomly under a 100x microscope, and the average was taken as the number of cells passing through each chamber.

2.7. Double-Luciferase Reporter Gene Detection. 293FT cells (ATCC, USA) were seeded into a 24-well plate (1.5×105 /well), and when the cells grew to about 80%, the plasmid miR − NC + pGL3 − MSI2 − wt, miR − 598 mimics + pGL3 − MSI2 − wt, miR − NC + pGL3 − MSI2 − mut, and miR − 598 mimics + pGL3 − MSI2 − mut were cotransfected into 293FT cells, and fresh DMEM medium was replaced after 6 h. 48 hours after transfection, the cells in each group were

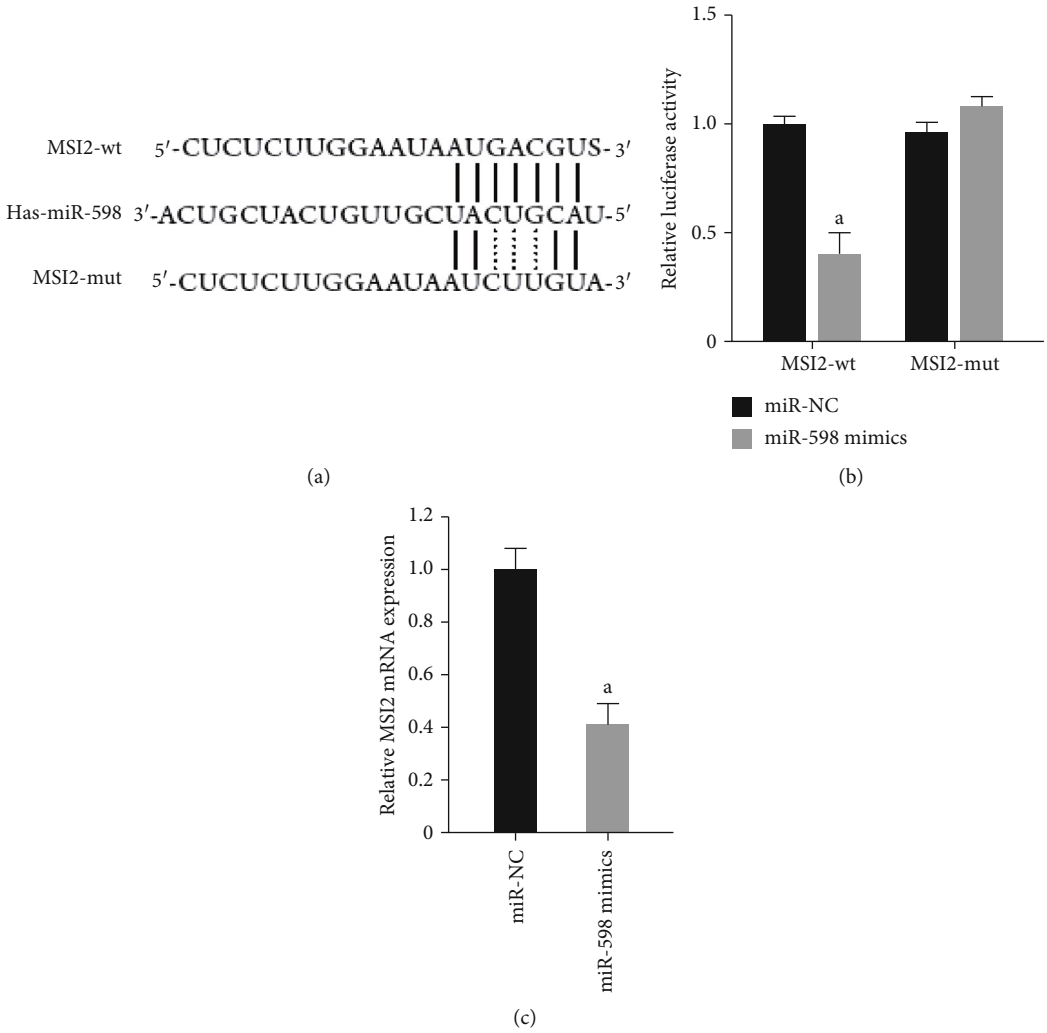

Figure 4: MSI2 is the target gene of miR-598: (a) sequence alignment of miR-598 and its conserved target site in RTKN-3′-UTR, predicted in the ENCORI database (http://starbase.sysu.edu.cn/); (b) relative luciferase activity in 293FT cells cotransfected with pGL3-MSI2-wt or pGL3-MSI2-mut reporter plasmids containing miR-598 potential binding sites or control plasmids; (c) the MSI2 mRNA expression level in A549 cells upon miR-598 mimic transfection. a indicates $P < 0.01$ compared with miR-NC.

lysed, and the fluorescence intensity of the cells in each group was expressed by the ratio of firefly luciferase activity to Renilla luciferase activity according to the instructions of the dual-luciferase reporter assay system.

2.8. Western Blotting. Cells were lysed on ice for 30 min with RIPA lysate, and protein concentration was quantified by bicinchoninic acid (BCA) assay. 12% sodium dodecyl sulfate-polyacrylamide gel electrophoresis (SDS-PAGE) was used for gel electrophoresis separation, and the protein loading amount of each lane was 20 μg. Concentrated gel was electrophoresed at 60 V for 1 h, and separated gel was electrophoresed at 100 V for 2 h. The membrane was transferred by conventional wet transfer method for 90 min, blocked with 5% bovine serum albumin (BSA) in Tris-buffered saline Tween (TBST) buffer for 1 h, and added with primary antibody to MSI2 (ab76148, Abcam, Cambridge, UK) or β-actin at 4°C for overnight incubation. After two times, the corresponding secondary antibody was added and incubated at room temperature for 2 h, and the membrane was washed 3 times with TBST. The ECL light-emitting kit was illuminated and developed and analyzed after fixing.

2.9. Statistical Processing. All experiments were repeated three times, and the experimental data were expressed as mean ± standard deviation. SPSS 20 software was used for statistical analysis. One-way analysis of variance was used for data comparison between multiple groups, and q test was used for pairwise comparison. $P < 0.05$ was considered statistically significant.

3. Results

3.1. miR-598 Was Downregulated in NSCLC Tissues and Cell Lines. To study expression pattern of miR-598 in the context of lung cancer, the expression of miR-598 in 37 cases of lung cancer and adjacent tissues was detected by qRT-PCR. The results showed that compared with normal tissues, the

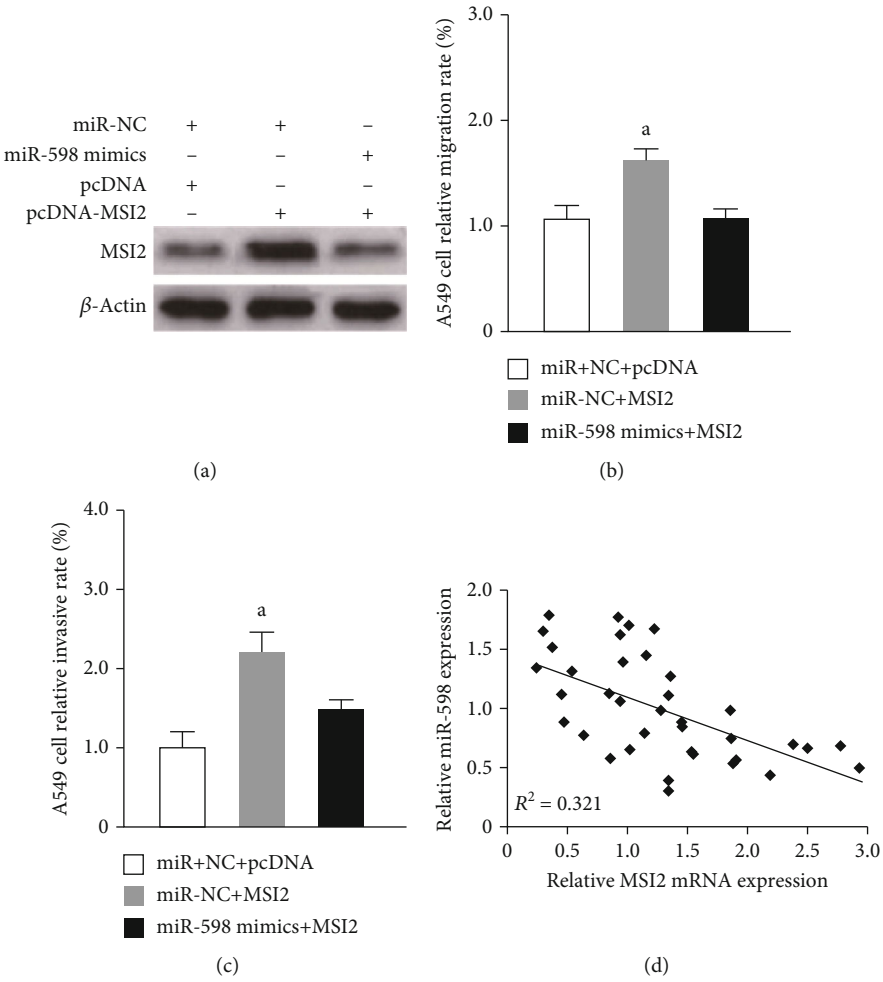

Figure 5: miR-598 represses NSCLC cell migration and invasion by regulating MSI2: (a) Western blots of MSI2 protein in A549 cells transfected with miR-598 mimic and MSI2 expression vector; (b) migration of A549 cells examined by Transwell test after with transfection with miR-598 mimic and MSI2 expression vector; (c) invasion of A549 cells examined by Transwell test after transfection with miR-598 mimic and MSI2 expression vector; (d) expression of miR-598 was negatively correlated with the expression of MSI2 in NSCLC tissues. a indicates $P < 0.01$ compared with A549 cells transfected with MSI2 expression vector.

expression of miR-598 in lung cancer tissues was significantly downregulated ($P < 0.001$, Figure 1(a)). In lung cancer cell line compared to human normal lung skin cells BEAS-2B, the expression of miR-598 in A549, H1650, and H1299 was also downregulated ($P < 0.001$, Figure 1(b)).

3.2. miR-598 Inhibited NSCLC Cell Migration. The results of scratch test showed that compared with the negative control group, the migration ability of A549 cells in the miR-598 mimic group was significantly inhibited ($P < 0.01$), while the miR-598 inhibitor group had enhanced migration ability ($P < 0.01$, Figures 2(a) and 2(b)).

3.3. miR-598 Inhibited NSCLC Cell Invasion. Transwell invasion assays showed that compared with the negative control group, the invasion ability of A549 cells in the miR-598 mimic group was significantly reduced ($P < 0.01$), while the invasion ability of the miR-598 inhibitor group was enhanced ($P < 0.05$, Figures 3(a) and 3(b)).

3.4. MSI2 Was a Target Gene of miR-598. Bioinformatics prediction in the ENCORI database (http://starbase.sysu.edu.cn/) showed that miR-598 and the 3′UTR of the oncogene MSI2 have multiple base binding sites, which may be a good target gene for miR-598 (Figure 4(a)). Subsequently, the dual-luciferase reporter gene system was used to detect the correlation of MSI2 and miR-598. The MSI2 gene wild-type (MSI2-wt) and MSI2-mutant (MSI2-mut) luciferase reporter vectors were constructed and cotransfected in 293FT cells with miR-598 mimics.

The results showed that miR-598 mimics significantly inhibited MSI2 wild-type luciferase activity ($P < 0.01$) without affecting MSI2-mutant luciferase activity (Figure 4(b)). Subsequently, the MSI2 mRNA expression level in A549 cells overexpressing miR-598 mimics was detected, and the expression level was significantly reduced ($P < 0.01$, Figure 4(c)).

3.5. miR-598 Inhibited NSCLC Cell Migration and Invasion by Regulating MSI2. In order to prove that miR-598 inhibited

the migration and invasion of lung cancer cells by regulating MSI2, we transfected the MSI2 gene alone or cotransfected with miR-598 mimics in A549 cells and found that the level of MSI2 protein increased after transfection alone. Protein levels returned to normal after cotransfection with miR-598 mimics (Figure 5(a)). The subsequent scratch test results showed that MSI2 could significantly enhance the migration ability of A549 cells, but when miR-598 mimics were introduced, the cell migration ability was significantly reversed (Figure 5(b)). Transwell invasion experiment results showed that MSI2 can significantly enhance the invasion ability of A549 cells, but the cell invasion ability was also significantly reversed when miR-598 was introduced (Figure 5(c)). At last, we performed Spearman correlation analysis and found that the expression of miR-598 was negatively correlated with the expression of MSI2 in NSCLC tissues (Figure 5(d)).

4. Discussion

Current research suggested that miRNAs were closely related to the occurrence and development of diseases such as differentiation, proliferation, invasion, and apoptosis of lung cancer cells [19]. miRNAs can downregulate the activity of oncogenes to inhibit tumorigenesis and cancer development [20]. Therefore, finding and studying miRNA molecules closely related to the occurrence and development of lung cancer are of great significance for exploring the initiation mechanism of lung cancer, preventing the occurrence of lung cancer metastasis, and selecting appropriate targets for intervention and treatment.

miR-598 has been well-studied as a tumor suppressor in several human cancers. For example, miR-598 was reported previously to inhibit epithelial mesenchymal transition through targeted regulation of the JAG1 gene, thereby effectively inhibiting colorectal cancer cell migration and invasion [10]. However, another study claimed that miR-598 functioned as an oncomiR that its overexpression promoted colorectal cancer cell proliferation and cell cycle progression [21]. The controversial role of miR-598 merits further investigation in human cancers. In our study, we upregulated or inhibited the expression of miR-598 in A549 cells through miR-598 mimics and miR-598 inhibitors and verified that miR-598 may play a role in suppressing the migration and invasion of tumor cells in lung cancer cells through scratch and Transwell experiments. Concurring with our results, Yang and his team found that miR-598 suppressed the EMT process to suppress the invasion and migration in NSCLC [22]. Tong et al. demonstrated that ectopic expression of miR-598 reduced NSCLC cell proliferation and invasion *in vitro* [23]. Differently, our double-luciferase experiments verified that MSl2 was the downstream target gene, responsible for the inhibitory role of miR-598 in migration and metastasis of lung cancer cells.

MSI2 protein is a member of the Musashi protein family. Although accumulating evidence showed a role for the MSI2 paralogue MSI1 as oncogenic in some cancer types [24, 25], MSI2 has attracted much less attention. However, MSI2 has been shown to be oncogenic in a mouse model of colon cancer [26]. Besides, myofibroblast-specific MSI2 knockout inhibits hepatocellular carcinoma progression in a mouse model [27]. Elevated MSI2 expression is associated with poor survival in leukemia [28], and MSI2 knockdown or genetic deletion reduced engraftment and caused a defect in hematopoietic stem cell maintenance in vivo as a result of decreased proliferation [29]. In addition, in our experiments, increasing the expression level of MSl2 significantly enhanced the migration and invasion of lung cancer cells. Consistent with our results, MSI2 is an important regulator of the occurrence and metastasis of NSCLC, which may be closely related to the activation of the TGF-β signaling pathway as a result of MSI2 upregulation [30]. In the study reported by Cheng et al., they supported that an increased expression of MSI2 could promote lung cancer cell proliferation and invasion [31]. Although we do not know whether MSI2 regulates the migration and invasion of lung cancer cells and whether it is related to the above signaling pathways, the reason for the migration and invasion of non-small-cell lung cancer is still explained from a new direction through this experiment, and it provides a new target for cancer treatment.

In conclusion, our study provides evidence that miR-598 represses cell migration and invasion in NSCLC through targeted inhibition of MSI2. However, we must acknowledge there are limitations or further investigations in the present study. First, miR-598 acting as oncomiR should be validated in a mouse model of NSCLC. Second, *in vitro* data should be strengthened in more than a single NSCLC cell line.

Data Availability

The data used to support the findings of this study are included within the article.

Conflicts of Interest

All authors declare that they have no conflict of interest.

References

[1] M. Cao and W. Chen, "Epidemiology of lung cancer in China," *Thoracic Cancer*, vol. 10, no. 1, pp. 3–7, 2019.

[2] X. Lin, M. S. Bloom, Z. Du, and Y. Hao, "Trends in disability-adjusted life years of lung cancer among women from 2004 to 2030 in Guangzhou, China: A population-based study," *Cancer Epidemiology*, vol. 63, article 101586, 2019.

[3] R. S. Herbst, D. Morgensztern, and C. Boshoff, "The biology and management of non-small cell lung cancer," *Nature*, vol. 553, no. 7689, pp. 446–454, 2018.

[4] F. Sun, L. Li, P. Yan et al., "Causative role of PDLIM2 epigenetic repression in lung cancer and therapeutic resistance," *Nature Communications*, vol. 10, no. 1, p. 5324, 2019.

[5] X. Yu, I. Trase, M. Ren, K. Duval, X. Guo, and Z. Chen, "Design of nanoparticle-based carriers for targeted drug delivery," *Journal of Nanomaterials*, vol. 2016, 15 pages, 2016.

[6] C. D. Fahrenholtz, J. Swanner, M. Ramirez-Perez, and R. N. Singh, "Heterogeneous responses of ovarian cancer cells to silver nanoparticles as a single agent and in combination with cisplatin," *Journal of Nanomaterials*, vol. 2017, 11 pages, 2017.

[7] F. Oberndorfer and L. Mullauer, "Molecular pathology of lung cancer: current status and perspectives," *Current Opinion in Oncology*, vol. 30, no. 2, pp. 69–76, 2018.

[8] G. Di Leva, M. Garofalo, and C. M. Croce, "MicroRNAs in cancer," *Annual Review of Pathology*, vol. 9, no. 1, pp. 287–314, 2014.

[9] K. L. Wu, Y. M. Tsai, C. T. Lien, P. L. Kuo, and A. J. Hung, "The roles of microRNA in lung cancer," *International Journal of Molecular Sciences*, vol. 20, no. 7, p. 1611, 2019.

[10] J. Chen, H. Zhang, Y. Chen et al., "miR-598 inhibits metastasis in colorectal cancer by suppressing JAG1/Notch2 pathway stimulating EMT," *Experimental Cell Research*, vol. 352, no. 1, pp. 104–112, 2017.

[11] N. Liu, H. Yang, and H. Wang, "miR-598 acts as a tumor suppressor in human gastric cancer by targeting IGF-1R," *Oncotargets and Therapy*, vol. Volume 11, pp. 2911–2923, 2018.

[12] K. Liu, X. Sun, Y. Zhang, L. Liu, and Q. Yuan, "MiR-598: a tumor suppressor with biomarker significance in osteosarcoma," *Life Sciences*, vol. 188, pp. 141–148, 2017.

[13] F. Liu, Q. Zhang, and Y. Liang, "MicroRNA-598 acts as an inhibitor in retinoblastoma through targeting E2F1 and regulating AKT pathway," *Journal of Cellular Biochemistry*, vol. 121, no. 3, pp. 2294–2302, 2020.

[14] F. Xing, S. Wang, and J. Zhou, "The expression of microRNA-598 inhibits ovarian cancer cell proliferation and metastasis by targeting URI," *Molecular Therapy - Oncolytics*, vol. 12, pp. 9–15, 2019.

[15] K. J. Hope and G. Sauvageau, "Roles for MSI2 and PROX1 in hematopoietic stem cell activity," *Current Opinion in Hematology*, vol. 18, no. 4, pp. 203–207, 2011.

[16] W. Sheng, M. Dong, C. Chen, Y. Li, Q. Liu, and Q. Dong, "Musashi2 promotes the development and progression of pancreatic cancer by down-regulating Numb protein," *Oncotarget*, vol. 8, no. 9, pp. 14359–14373, 2017.

[17] M. H. Wang, S. Y. Qin, S. G. Zhang et al., "Musashi-2 promotes hepatitis Bvirus related hepatocellular carcinoma progression via the Wnt/β-catenin pathway," *American Journal of Cancer Research*, vol. 5, no. 3, pp. 1089–1100, 2015.

[18] J. L. Cox, P. J. Wilder, J. M. Gilmore, E. L. Wuebben, M. P. Washburn, and A. Rizzino, "The SOX2-interactome in brain cancer cells identifies the requirement of MSI2 and USP9X for the growth of brain tumor cells," *PLoS One*, vol. 8, no. 5, article e62857, 2013.

[19] Z. S. Hashemi, S. Khalili, M. Forouzandeh Moghadam, and E. Sadroddiny, "Lung cancer and miRNAs: a possible remedy for anti-metastatic, therapeutic and diagnostic applications," *Expert Review of Respiratory Medicine*, vol. 11, no. 2, pp. 147–157, 2017.

[20] A. A. Svoronos, D. M. Engelman, and F. J. Slack, "OncomiR or tumor suppressor? The duplicity of microRNAs in cancer," *Cancer Research*, vol. 76, no. 13, pp. 3666–3670, 2016.

[21] K. P. Li, Y. P. Fang, J. Q. Liao et al., "Upregulation of miR-598 promotes cell proliferation and cell cycle progression in human colorectal carcinoma by suppressing INPP5E expression," *Molecular Medicine Reports*, vol. 17, no. 2, pp. 2991–2997, 2018.

[22] F. Yang, K. Wei, Z. Qin et al., "MiR-598 suppresses invasion and migration by negative regulation of Derlin-1 and epithelial-mesenchymal transition in non-small cell lung cancer," *Cellular Physiology and Biochemistry*, vol. 47, no. 1, pp. 245–256, 2018.

[23] X. Tong, P. Su, H. Yang et al., "MicroRNA-598 inhibits the proliferation and invasion of non-small cell lung cancer cells by directly targeting ZEB2," *Experimental and Therapeutic Medicine*, vol. 16, no. 6, pp. 5417–5423, 2018.

[24] C. F. Wang, H. C. Zhang, X. M. Feng, X. M. Song, and Y. N. Wu, "Knockdown of MSI1 inhibits the proliferation of human oral squamous cell carcinoma by inactivating STAT3 signaling," *International Journal of Molecular Medicine*, vol. 44, no. 1, pp. 115–124, 2019.

[25] P. Gong, Y. Wang, Y. Gao et al., "Msi1 promotes tumor progression by epithelial-to-mesenchymal transition in cervical cancer," *Human Pathology*, vol. 65, pp. 53–61, 2017.

[26] S. Wang, N. Li, M. Yousefi et al., "Transformation of the intestinal epithelium by the MSI2 RNA-binding protein," *Nature Communications*, vol. 6, no. 1, article 6517, 2015.

[27] C. Qu, L. He, N. Yao et al., "Myofibroblast-specific Msi2 knockout inhibits hepatocellular carcinoma progression in a mouse model," *Hepatology*, 2021.

[28] R. J. Byers, T. Currie, E. Tholouli, S. J. Rodig, and J. L. Kutok, "MSI2 protein expression predicts unfavorable outcome in acute myeloid leukemia," *Blood*, vol. 118, no. 10, pp. 2857–2867, 2011.

[29] M. G. Kharas, C. J. Lengner, F. Al-Shahrour et al., "Musashi-2 regulates normal hematopoiesis and promotes aggressive myeloid leukemia," *Nature Medicine*, vol. 16, no. 8, pp. 903–908, 2010.

[30] A. E. Kudinov, A. Deneka, A. S. Nikonova et al., "Musashi-2 (MSI2) supports TGF-β signaling and inhibits claudins to promote non-small cell lung cancer (NSCLC) metastasis," *Proceedings of the National Academy of Sciences*, vol. 113, no. 25, pp. 6955–6960, 2016.

[31] T. Cheng, Z. Zhang, Y. Cheng et al., "ETV4 promotes proliferation and invasion of lung adenocarcinoma by transcriptionally upregulating MSI2," *Biochemical and Biophysical Research Communications*, vol. 516, no. 1, pp. 278–284, 2019.

Hindawi
Journal of Nanomaterials
Volume 2021, Article ID 5587399, 8 pages
https://doi.org/10.1155/2021/5587399

Research Article

MDR1 Genotypes and Haplotypes Are Closely Associated with Postoperative Fentanyl Consumption in Patients Undergoing Radical Gastrectomy

Fan Zhang,[1] **Jianbin Tong**,[1] **Wenxiang Qing**,[1] **Zhonghua Hu**,[1] **Jie Hu**,[2] **and Qin Liao**[1]

[1]*Department of Anesthesiology, The Third Xiangya Hospital, Central South University, Changsha, China*
[2]*Department of Anesthesiology, Xiangya Hospital, Central South University, Changsha, China*

Correspondence should be addressed to Jie Hu; hujie0126@163.com and Qin Liao; xy3yyliaoqin@sina.com

Received 23 February 2021; Revised 20 March 2021; Accepted 23 March 2021; Published 2 April 2021

Academic Editor: Tingting Hong

Fentanyl is a powerful opioid analgesic, and its analgesic effect is greatly different among individuals. This study was aimed at exploring the effects of multidrug resistance gene-1 (*MDR1*) genetic variation on postoperative fentanyl consumption. A total of 135 patients, who planned to undergo radical gastrectomy with general anesthesia, were studied. The subjects received patient-controlled analgesia (PCA) by intravenous fentanyl within 48 hours after operation and maintained a numerical rating scale (NRS) score ≤ 3. The consumption and side effects of fentanyl were recorded within 24 hours and 48 hours after the operation. Single nucleotide polymorphisms (SNPs) of all patients with *MDR1* 1236C>T, 2677G>T/A, and 3435C>T were screened by polymerase chain reaction-restriction fragment length polymorphism (PCR-RFLP) or DNA sequence analysis after PCR. There was no difference in postoperative fentanyl consumption among patients having 2677G>T/A and 3435C>T polymorphisms (all $P > 0.05$). *MDR1* 1236C>T polymorphisms and haplotypes combined by three SNPs, however, significantly affected postoperative fentanyl consumption (all $P < 0.05$). Moreover, 1236TT genotype carriers consumed more fentanyl during 24 hours ($P = 0.038$) and 48 hours ($P = 0.003$) postoperatively. The *MDR1* TTT haplotype carriers needed more fentanyl compared with the CGC haplotype carriers during the first 48 hours after surgery ($P = 0.017$). Nausea, vomiting, and dizziness were not found to have significant differences among the above three SNPs and their haplotypes ($P > 0.05$). *MDR1* 1236C>T polymorphism and haplotypes were factors contributing to the individual variability in postoperative fentanyl consumption.

1. Introduction

Fentanyl is a widely used narcotic analgesic, but its analgesic efficacy has a large interindividual variation among patients [1, 2]. The analgesic effect of fentanyl is affected by many factors, and the gene polymorphism is one of the main factor [3–5]. Gene polymorphism plays an important role in the pharmacokinetics and pharmacodynamics of fentanyl [5]. Drug metabolizing enzymes and targets of fentanyl are both likely affected by gene polymorphisms, which in turn affect the analgesic effect of fentanyl [6, 7]. The genes contributing to drug transporters of fentanyl, however, remain largely unexplored.

P-Glycoprotein (P-gp) which is the product of the *MDR1* gene, acts as a transmembrane efflux pump in the blood-brain barrier, liver, kidney, and intestine [8]. The expression and function of P-gp are regulated by *MDR1* gene SNPs, including exon 1236C>T, 2677G>T/A, and 3435C>T SNPs [9–11]. 1236C>T and 3435C>T are synonymous mutations. They may affect the P-gp function by altering protein folding [9]. In contrast, 2677G>T/A is a nonsynonymous mutation due to the substitution of amino acid alanine with serine or threonine [9]. *MDR1* mRNA expression in heart tissue is significantly elevated in 2677AT or TT genotype carriers [10], and the homozygous T allele of 3435C>T reduces P-gp expression in the upper gastrointestinal tract [11]. On the

other hand, these three SNPs are in strong linkage disequilibrium and form haplotypes. Haplotypes containing mutant alleles have been shown to exhibit large structural modifications that result in conformational changes in the binding site and subsequent reductions in P-gp activity [12, 13].

Fentanyl is one of the substrates of P-gp [14–16]. Human and animal studies have shown that P-gp affects the absorption, distribution, excretion, and clinical effects of fentanyl [14–16]. Several authors have identified that *MDR1* 1236C>T and 3435C>T SNPs have significant effects on postoperative fentanyl consumption [7, 17]. However, other studies cannot identify such associations [18] or obtain the opposite results [19]. Overall, the effects of three *MDR1* SNPs on fentanyl efficacy are not definite. It may be the result of considering only one of the three SNPs. Since SNPs are in incomplete linkage disequilibrium, it may be necessary to consider the SNP combination to accurately assess the role of common polymorphisms in the efficacy of fentanyl. No studies, so far, have analyzed whether haplotypes of *MDR1* 1236C>T, 2677G>T/A, and 3435C>T led to variability in the dosage of fentanyl among patients. Hence, in this study, we evaluated whether genetic polymorphisms of 1236C>T, 2677G>T/A, and 3435C>T and their haplotypes affect postoperative fentanyl requirements for analgesia.

2. Materials and Methods

2.1. Ethical Statements. The research plan was reviewed and approved by the institutional ethics committee of the Third Xiangya Hospital. Each patient received information about the aim of the study and provided written informed consent. Moreover, participants were assured that the participation is completely voluntary and personal information is not disclosed to third parties.

2.2. Patient Selection. Since the liver and intestines affect the metabolism and absorption of fentanyl, we chose patients who were scheduled for radical gastrectomy by general anesthesia in the present study. Exclusion criteria were as follows: patient refusal; ASA classification more than III; patients with severe liver injury, renal impairment, diabetes mellitus, cardiovascular disease, psychiatric disorders, chronic pain, and pregnancy or lactation; patients taking drugs that are substrates of P-gp; long-term use of analgesic; allergy to fentanyl; or drug abuse.

2.3. Anesthesia and Postoperative Analgesia. General anesthesia was induced with 0.05 mg/kg midazolam, 0.2 mg/kg etomidate, 0.12 mg/kg vecuronium, and 4-6 μg/kg fentanyl. Anesthesia was maintained by 1%-2% sevoflurane inhalation, continuous infusion of propofol (4-12 mg·kg^{-1}·h^{-1}), and intermittent intravenous bolus of 0.05 mg/kg vecuronium. During surgery, intravenous infusion of fentanyl was started before skin incision, appended 2 μg/kg each time intraoperatively, and administration stopped once the surgeons opened the abdominal cavity. The total dose of fentanyl was less than 12 μg/kg, and the residual effect on postoperative fentanyl dose was avoided. After surgery, all patients were administered 8 mg ondansetron to prevent postoperative nausea and vomiting. Then, patients were extubated and observed in the postanesthesia care unit (PACU) for 2 hours. The antagonist of muscle relaxation was not used. The NRS score was recorded after extubation. Patients were considered to have inadequate pain control if NRS > 3, and fentanyl (20 μg per time) was intravenously given until NRS ≤ 3. Patients then received patient-controlled intravenous analgesia(PCIA) with fentanyl during the first 48 hours after surgery. In the analgesic pump, 30 μg/kg fentanyl was filled in normal saline, with a total volume of 240 mL. The pump was programmed to administer a 1.5 mL/h background dose, 20 μg bolus of fentanyl solution, and 5-minute lockout time. Postoperative pain was controlled with NRS ≤ 3 at rest. All enrolled patients used no opioid receptor antagonists and other analgesic drugs except for fentanyl after operation.

Table 1: Prime sequences of *MDR1* 1236C>T, 2677G>T/A, and 3435C>T.

Primer	Sequence
MDR1 1236C>T	F: 5′-TTCACTTCAGTTACCCATC-3′
	R: 5′-CATAGAGCCTCTGCATCA-3′
MDR1 2677G>T/A	F: 5′-GTCTGGACAAGCACTGAAAGA-3′
	R: 5′-GTGGGGAGGAAGGAAGAACA-3′
MDR1 3435C>T	F: 5′-GATCTGTGAACTCTTGTTTTCA-3′
	R: 5′-GAAGAGAGACTTACATTAGGC-3′

2.4. Genotyping. Genomic DNA from peripheral blood leukocytes was extracted using E.Z.N.A.™ SQ Blood DNA Kit (D5032-02). The primer design software Oligo 6 designed primers (Table 1). 1236C>T and 3435C>T were genotyped by the PCR-RFLP method (Figures 1(a) and 1(b)), and *MDR1* 2677G>T/A was screened by DNA sequencing (Figure 1(c)). The restriction enzyme BsuRI (Lot: 00143447, Thermo Scientific) was used to distinguish the T allele from the C allele of 1236C>T, and the restriction enzyme MboI (Lot: 00098836, Fermentas) was employed to distinguish the T allele from the C allele of 3435C>T.

2.5. Data Collection. During the first 24 hours and 48 hours, patients' age, gender, BMI, length of incision, duration of surgery, and postoperative fentanyl consumption were collected. The NRS was recorded at 4 hours, 8 hours, 12 hours, 24 hours, and 48 hours after the operation. The incidence of side effects, including nausea, vomiting, respiratory depression, and lethargy, was recorded in the first 48 hours.

2.6. Statistical Analysis. The sample size of this research was calculated based on the frequency of *MDR1* genotypes. According to the allele frequency of *MDR1* gene SNPs (1236C>T, 2677G>T/A, and 3435C>T) and their haplotypes previously reported in Chinese [7, 20], it was required that the sample size of 108 patients showed an absolute difference of 20% in the difference of fentanyl dose (power = 80%, α = 0.05). As a result of clinical experience and preliminary experiment, absolute difference of 20% was chosen as a minimum detectable difference. PASS 11 software (NCSS, Kaysville, UT) was used to calculate statistical power samples.

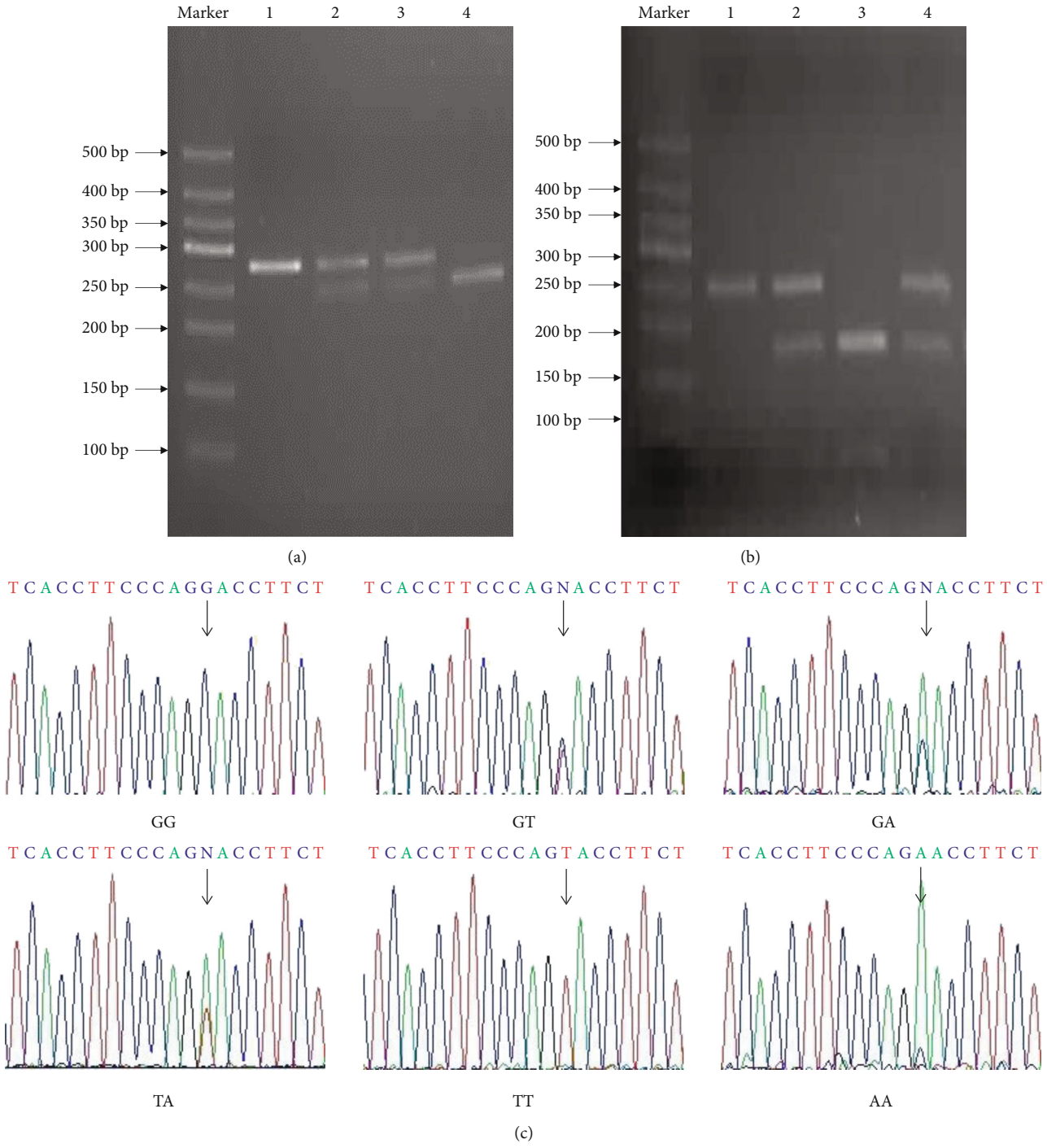

Figure 1: Genotyping of *MDR1* SNPs. (a) 1236C>T products after enzymatic degradation. Lane 1: TT, mutant homozygote; lanes 2 and 3: CT, mutant heterozygote; lane 4: CC, wild type. (b) 3435C>T products after enzymatic degradation. Lane 1: TT, mutant homozygote; lanes 2 and 4: CT, mutant heterozygote; lane 3: CC, wild type. (c) 2677G>T/A sequencing typing. GG, GT, GA, TA, TT, AA.

Clinical research and genotyping were blinded to the clinical outcome of patients. Data were analyzed using SPSS 19.0. $P < 0.05$ was statistically significant. All continuous variables were checked for normal distribution, and data were presented as means ± standard deviation or medians and range. Comparison of postoperative fentanyl consumption was performed using Kruskal-Wallis H test. Allele and genotype frequencies were estimated by gene counting. The deviation from the Hardy-Weinberg equilibrium was evaluated by chi-square tests.

3. Results

3.1. General Patient Information. In this study, 147 patients were recruited, and 12 of them were excluded because of patient quitting ($n = 5$), unavailability of blood samples

Table 2: Demographics and clinical characteristics of 1236C>T and 3435C>T.

Factors	1236C>T			*P* value	3435C>T			*P* value
	CC	CT	TT		CC	CT	TT	
Cases	27	66	42		53	62	20	
Age (year)	52.8 ± 13.9	53.7 ± 12.8	51.2 ± 13.5	0.770	52.0 ± 13.5	54.2 ± 12.6	50.1 ± 14.3	0.607
Gender (male/female)	18/9	38/28	28/14	0.553	35/18	40/22	12/8	0.891
Height (cm)	161.4 ± 7.1	161.9 ± 6.9	163.9 ± 6.9	0.422	161.9 ± 6.8	162.5 ± 7.3	163.4 ± 6.2	0.807
Weight (kg)	53.1 ± 7.9	54.2 ± 8.8	58.4 ± 11.6	0.146	54.1 ± 7.7	56.2 ± 11.0	55.6 ± 10.6	0.680
Surgery time (min)	226.9 ± 104.1	188.6 ± 51.6	203.1 ± 65.0	0.172	196.7 ± 67.9	205.2 ± 71.6	197.3 ± 71.0	0.868
Length of incision (cm)	19.2 ± 3.8	19.9 ± 3.7	19.8 ± 2.9	0.774	18.7 ± 3.0	20.6 ± 3.8	19.8 ± 3.1	0.089
NRS score 24 h postoperatively	2.1 ± 0.3	2.1 ± 0.3	2.2 ± 0.2	0.814	2.1 ± 0.2	2.1 ± 0.3	2.2 ± 0.3	0.218
NRS score 48 h postoperatively	2.0 ± 0.2	2.0 ± 0.2	2.1 ± 0.3	0.337	2.0 ± 0.3	2.0 ± 0.2	2.1 ± 0.3	0.133

1236C>T: CC: wild type; CT: mutant heterozygote; TT: mutant homozygote. 3435C>T: CC: wild type; CT: mutant heterozygote; TT: mutant homozygote. NRS: numerical rating scale..

Table 3: Demographics and clinical characteristics of 2677G>T/A.

Factors	2677G>T/A						*P* value
	GG	GT	GA	TA	TT	AA	
Cases	33	37	20	13	25	7	
Age (year)	53.8 ± 13.7	54.5 ± 12.4	57.2 ± 9.4	48.6 ± 13.0	50.7 ± 14.3	39.5 ± 13.6	0.209
Gender (M/F)	24/9	23/14	12/8	7/6	17/8	2/5	0.334
Height (cm)	162.4 ± 6.9	162.2 ± 7.8	162.0 ± 6.6	160.9 ± 6.0	165.3 ± 6.8	157.2 ± 2.2	0.378
Weight (kg)	52.2 ± 8.8	55.8 ± 8.7	57.2 ± 7.5	53.7 ± 10.2	59.5 ± 13.3	49.8 ± 3.1	0.235
Surgery time (min)	191.2 ± 66.4	204.1 ± 65.6	197.0 ± 95.1	213.4 ± 51.7	196.7 ± 64.3	230.0 ± 95.1	0.920
Length of incision (cm)	18.4 ± 2.8	19.3 ± 2.8	20.9 ± 4.4	21.4 ± 4.6	20.0 ± 2.9	18.3 ± 1.9	0.150
NRS score 24 h postoperatively	2.1 ± 0.2	2.0 ± 0.3	1.9 ± 0.2	1.9 ± 0.3	2.1 ± 0.3	2.2 ± 0.2	0.246
NRS score 48 h postoperatively	2.1 ± 0.3	2.0 ± 0.2	2.0 ± 0.1	1.9 ± 0.2	2.1 ± 0.2	2.2 ± 0.3	0.371

2677G>T/A: GG: wild type; GT, GA, and TA: mutant heterozygote; TT and AA: mutant homozygote. NRS: numerical rating scale..

($n = 2$), analgesic pump failure ($n = 2$), and other conditions ($n = 3$). Finally, this study included 135 patients, all of whom were of Chinese Han ethnicity. Tables 2 and 3 show the demographics and clinical data of the patients. There was no significant difference in demographic and clinical data among different *MDR1* genotypes and haplotypes (all $P > 0.05$).

3.2. Genotypes and Allele Frequency of MDR1 SNPs. Of 135 patients, 27 cases were 1236CC genotype, 66 cases were 1236CT, and 42 cases were 1236TT. The mutation frequency of allele T was 55.6%. 2677G>T/A polymorphism developed six genotypes: GG, GT, GA, TA, TT, and AA. Among the 135 patients, 33 cases were carriers of the GG genotype, 37 cases were carriers of the GT genotype, 20 cases were carriers of the GA genotype, 13 cases were carriers of the TA genotype, 25 cases were carriers of the TT genotype, and seven cases were carriers of the AA genotype, and the mutation frequency of the allele T and allele A was 37.0% and 17.4%, respectively. There were 53 carriers of the 3435CC genotype, 62 carriers of the CT genotype, and 20 carriers of the TT genotype, and the mutation frequency of allele T was 37.8%. The allelic frequencies of 1236C>T, 2677G>T/A, and 3435C>T conformed to the Hardy-Weinberg equilibrium ($P > 0.05$).

3.3. Linkage Disequilibrium and Haplotype Analysis. Haploview software used the existing genotype data to calculate linkage disequilibrium statistics and infer the population haplotype model. Haploview software showed that there was strong linkage disequilibrium of *MDR1* 1236C>T, 2677G>T/A, and 3435C>T. Four haplotypes (TTT, CGC, CAC, and TGC) which were constructed by three *MDR1* SNPs represented 90.7% of all haplotypes observed in this study.

3.4. Correlation between the Three SNPs of MDR1 Gene and Their Haplotypes and Postoperative Fentanyl Consumption. In this study, there was no statistically significant difference in postoperative fentanyl consumption in 2677G>T/A and 3435C>T at 24 hours and 48 hours after surgery ($P > 0.05$). However, there was a significant difference in postoperative fentanyl consumption among the polymorphisms of 1236C>T. Specifically, the 1236TT genotype carriers needed more fentanyl for postoperative analgesia within the first 24 hours and 48 hours after surgery ($P = 0.038$ and $P = 0.003$, respectively) (Table 4). Among the haplotypes of the *MDR1*

Table 4: Postoperative fentanyl consumption in different genotypes during the first 24 hours and 48 hours postoperatively.

MDR1 SNPs	Cases	Frequency (%)	Fentanyl dose for 24 hours (μg/kg)	*P* value	Fentanyl dose for 48 hours (μg/kg)	*P* value
1236C>T	135	100				
CC	27	20.0	7.4 (6.6-10.1)		14.8 (13.1-17.2)	
CT	66	48.9	8.9 (7.0-11.6)	0.038[a]	19.1 (15.6-24.7)	0.003[b]
TT	42	31.1	10.1 (7.7-15.3)		22.2 (17.6-26.4)	
2677G>T/A						
GG	33	24.5	8.7 (7.4-10.5)		18.2 (14.7-21.1)	
GT	37	27.4	8.3 (6.6-13.5)		16.8 (14.1-25.4)	
GA	20	14.8	8.4 (6.9-11.5)	0.864	16.3 (13.5-21.7)	0.128
TA	13	9.6	11.0 (7.5-15.1)		22.0 (18.8-28.3)	
TT	25	18.5	9.8 (7.6-15.0)		23.8 (17.9-26.2)	
AA	7	5.2	8.4 (6.3-19.1)		14.9 (13.7-29.9)	
3435C>T						
CC	53	39.3	8.3 (6.9-10.5)		18.0 (14.0-22.8)	
CT	62	45.9	9.0 (7.0-13.7)	0.575	19.6 (14.8-25.1)	0.176
TT	20	14.8	9.9 (7.6-15.0)		24.0 (18.7-26.2)	

1236C>T: CC: wild type; CT: mutant heterozygote; TT: mutant homozygote. 2677G>T/A: GG: wild type; GT, GA, and TA: mutant heterozygote; TT and AA: mutant homozygote. 3435C>T: CC: wild type; CT: mutant heterozygote; TT: mutant homozygote. [a,b]1236TT genotype carriers received more fentanyl than 1236CC genotype carriers at 24 hours and 48 hours postoperatively.

Table 5: Postoperative fentanyl consumption in different *MDR1* haplotypes at the first 24 hours and 48 hours postoperatively.

Haplotypes	Frequency (%)	Fentanyl dose for 24 hours (μg/kg)	*P* value	Fentanyl dose for 48 hours (μg/kg)	*P* value
TTT	32.2	10.0 (7.4-15.0)		21.7 (17.2-26.2)	
CGC	23.3	8.3 (6.7-10.0)		16.7 (14.0-20.1)	
CAC	17.8	7.8 (6.8-11.9)	0.247	17.1 (13.8-23.6)	0.017[c]
TGC	17.4	10.1 (7.5-13.7)		19.8 (15.1-25.5)	
Other	9.3	8.7 (7.2-11.9)		19.4 (14.6-21.3)	

[c]The haplotype TTT required more fentanyl than the CGC haplotype at 48 hours postoperatively.

gene, the TTT haplotype consumed more fentanyl than the CGC haplotype within the first 48 hours after surgery ($P = 0.017$) (Table 5).

3.5. Correlation between Side Effects and the Three MDR1 SNPs and Their Haplotypes. The main side effects of fentanyl were nausea, vomiting, and dizziness at postoperative 48 hours. There was no significant difference in nausea, vomiting, and dizziness within 48 hours postoperatively among 1236C>T, 2677G>T/A, 3435C>T, and their haplotypes ($P > 0.05$) (Table 6). None of the patients experienced respiratory depression or other serious side effects.

4. Discussion

In this study, we found that *MDR1* 1236C>T SNP and the *MDR1* gene haplotypes constructed from 1236C>T, 2677G>T/A, and 3435C>T were predictive of individual variations in postoperative fentanyl consumption. Moreover, 1236TT carriers and *MDR1* TTT haplotype carriers needed more postoperative fentanyl in patients undergoing radical gastrectomy.

The *MDR1* 1236C>T mutation is more commonly detected in Chinese Han. In our study, the frequency of the 1236T variant was 55.6%, and Xiao et al. [20] report that the frequency of the 1236T variant is 67.8% in Chinese Han. The *MDR1* 1236C>T mutation may induce a change in the substrate binding site and reduce the P-gp activity [9, 21]. Zhang et al. [7] has found that patients with the TT genotype of 1236C>T consume significantly more fentanyl than those with the CC and CT genotypes within 24 hours and 48 hours after lower segment caesarean section surgery, and we got the same results within 24 hours and 48 hours after radical gastrectomy. Elkiweri et al. [22] have indicated that fentanyl concentration in the rat's brain is decreased in the presence of the P-gp inhibitor verapamil. P-gp is a transmembrane efflux pump from inside the cell [8]. These results could not be explained by P-gp distributed in the blood-brain barrier but by P-gp in the liver. The decrease of P-gp activity in hepatocytes of the TT genotype groups means that fentanyl is accumulated in the liver and metabolized by hepatic microsomal enzymes, resulting in increased consumption of fentanyl [7].

In addition, we also found that there was no significant difference in postoperative fentanyl consumption among the 2677G>T/A and 3435C>T genotypes, which was consistent with Kim et al.'s study [18]. In another study [21], 2677G>T/A and 3435C>T are not associated with fentanyl's pharmacokinetics and pharmacodynamics. The above

Table 6: Incidence of nausea, vomiting, and dizziness of 1236C>T, 2677G>T/A, and 3435C>T genotypes and haplotypes.

MDR1	Nausea		*P* value	Vomiting		*P* value	Dizziness		*P* value
	Yes	No		Yes	No		Yes	No	
1236C>T									
CC	6 (22.2%)	21 (77.8%)		7 (25.9%)	20 (74.1%)		7 (25.9%)	20 (74.1%)	
CT	23 (34.8%)	43 (65.2%)	0.214	10 (15.2%)	56 (84.8%)	0.455	17 (25.8%)	49 (74.2%)	0.825
TT	18 (42.9%)	24 (57.1%)		7 (16.7%)	35 (83.3%)		13 (31.0%)	29 (69.0%)	
2677G>T/A									
GG	10 (30.3%)	23 (69.7%)		5 (15.2%)	28 (84.8%)		7 (21.2%)	26 (78.8%)	
GT	13 (35.1%)	24 (64.9%)		7 (18.9%)	30 (81.1%)		10 (27.0%)	27 (73.0%)	
GA	8 (40.0%)	12 (60.0%)	0.449	5 (25.0%)	15 (75.0%)	0.789	7 (35.0%)	13 (65.0%)	0.446
TA	2 (15.4%)	11 (84.6%)		1 (7.7%)	12 (92.3%)		2 (15.4%)	11 (84.6%)	
TT	12 (48.0%)	13 (52.0%)		4 (16.0%)	21 (84.0%)		10 (40.0%)	15 (60.0%)	
AA	2 (28.6%)	5 (71.4%)		2 (28.6%)	5 (71.4%)		1 (14.3%)	6 (85.7%)	
3435C>T									
CC	20 (37.7%)	33 (62.3%)		11 (20.8%)	42 (79.2%)		11 (20.8%)	42 (79.2%)	
CT	17 (27.4%)	45 (72.6%)	0.155	10 (16.1%)	52 (83.9%)	0.763	18 (29.0%)	44 (71.0%)	0.240
TT	10 (50.0%)	10 (50.0%)		3 (15.0%)	17 (85.0%)		8 (40.0%)	12 (60.0%)	
Haplotypes									
TTT	42.5%	57.5%		16.1%	83.9%		34.5%	65.5%	
CGC	30.2%	69.8%		15.9%	84.1%		31.7%	68.3%	
CAC	29.2%	70.8%	0.128	27.1%	72.9%	0.302	18.8%	81.2%	0.178
TGC	42.6%	57.4%		19.1%	80.9%		19.1%	80.9%	
Other	20.0%	80.0%		8.0%	92.0%		32.0%	68.0%	

researches demonstrate that *MDR1* 2677G>T/A and 3435C>T mutations do not affect the analgesic effect of fentanyl.

MDR1 1236C>T, 2677G>T/A, and 3435C>T constructed four main haplotypes. In this study, the proportions of TTT, CGC, CAC, and TGC haplotypes were 32.2%, 23.3%, 17.8%, and 17.4%, respectively, which were consistent with previous studies [23]. These data showed that the TTT haplotype was the predominant genotype of Chinese Han populations. No studies have analyzed whether *MDR1* haplotypes contribute to the individual variability in postoperative fentanyl consumption. We found that the *MDR1* gene haplotypes constructed from the SNPs, 1236C>T, 2677G>T/A, and 3435C>T, could predict the individual variability in postoperative fentanyl consumption. TTT haplotype carriers needed more fentanyl within the first 48 hours after surgery, while CGC haplotype carriers needed less fentanyl. It has been reported that the efflux ability of P-gp in cells transfected with *MDR1* CGC is higher than that in cells overexpressing the *MDR1* TTT variant haplotype [12]. Thus, our results could also be explained by the transport activity of P-gp in hepatocytes, which were decreased in the TTT haplotype and increased in the CGC haplotype, leading to differences in fentanyl metabolism. Overall, using the commonly detected haplotypes (1236C>T, 2677G>T/A, and 3435C>T) could be more efficient compared to just studying only one polymorphism. Our study provided preliminary evidence that the *MDR1* haplotype could influence fentanyl response.

Postoperative nausea, vomiting, and dizziness are common side effects of fentanyl. Our data showed that the frequency of nausea, vomiting, and dizziness was 34.8%, 17.8%, and 27.4%, respectively. No significant differences in the aforementioned side effects were found among 1236C>T, 2677G>T/A, 3435C>T, and their haplotypes within 24 hours and 48 hours postoperatively. Severe side effects, such as respiratory depression, were not detected in this study.

There were some limitations in our study. First, the 2677G>T/A allele G could mutate to allele A or T, and the frequency of the allele A variant was low. We only observed seven AA carriers in this study, while limited sample sizes might affect the objectivity of this research to a certain extent. Second, whether the *MDR1* 1236C>T SNP and haplotypes affect the efflux ability of P-gp-mediated fentanyl in hepatocytes is only speculation and needs further verification. However, our findings provided preliminary evidence that the *MDR1* 1236C>T polymorphism and haplotypes composed of 1236C>T, 2677G>T/A, and 3435C>T greatly contributed to the individual variability in postoperative analgesia with fentanyl. As far as we know, this is the first study to explore the effect of *MDR1* gene haplotypes on fentanyl analgesia. It is possible to improve the perioperative pain management by preoperative *MDR1* genotyping.

5. Conclusion

The *MDR1* gene 1236C>T polymorphism and haplotypes composed of 1236C>T, 2677G>T/A, and 3435C>T greatly contributed to the individual variability of postoperative fentanyl consumption in patients undergoing radical gastrectomy.

Data Availability

The data used to support the findings of this study may be released upon application to the Department of Anesthesiology, Third Xiangya Hospital, Central South University, which can be contacted at xy3irb@163.com.

Conflicts of Interest

The authors declare that they have no conflicts of interest.

Authors' Contributions

Fan Zhang performed the conceptualization; Fan Zhang, Jie Hu, and Qin Liao performed the data curation; Fan Zhang and Jie Hu performed the formal analysis; Fan Zhang and Wenxiang Qing performed the investigation; Jianbin Tong, Zhonghua Hu, and Qin Liao performed the methodology; Fan Zhang and Jie Hu gathered the resources; Fan Zhang wrote the original draft; Jianbin Tong, Jie Hu, and Qin Liao wrote, reviewed, and edited the manuscript.

Acknowledgments

We would like to express our heartfelt gratitude to the study participants for their valuable contributions.

References

[1] K. Ikeda, S. Ide, W. Han, M. Hayashida, G. R. Uhl, and I. Sora, "How individual sensitivity to opiates can be predicted by gene analyses," *Trends in Pharmacological Sciences*, vol. 26, no. 6, pp. 311–317, 2005.

[2] T. Naito and J. Kawakami, "Interindividual variation of pharmacokinetic disposition of and clinical responses to opioid analgesics in cancer pain patients," *Yakugaku Zasshi*, vol. 135, no. 5, pp. 709–715, 2015.

[3] E. Lucenteforte, L. Vagnoli, A. Pugi et al., "A systematic review of the risk factors for clinical response to opioids for all-age patients with cancer-related pain and presentation of the paediatric STOP pain study," *BMC Cancer*, vol. 18, no. 1, 2018.

[4] E. J. M. Kuip, W. H. Oldenmenger, M. F. Thijs—Visser et al., "Effects of smoking and body mass index on the exposure of fentanyl in patients with cancer," *PLoS One*, vol. 13, no. 6, article e0198289, 2018.

[5] G. S. Gerhard, S. Kaniper, and B. Paynton, "Fentanyl overdoses and pharmacogenetics," *Pharmacogenetics and Genomics*, vol. 30, no. 1, pp. 5–8, 2020.

[6] Q. Yan, Y. Su, L. Gao et al., "Impact of CYP3A4 * 1G polymorphism on fentanyl analgesia assessed by analgesia nociception index in Chinese patients undergoing hysteroscopy," *Chinese Medical Journal*, vol. 131, no. 22, pp. 2693–2698, 2018.

[7] J. Zhang, L. Zhang, X. Zhao, S. Shen, X. Luo, and Y. Zhang, "Association between MDR_1/CYP3A4/$OPRM_1$ gene polymorphisms and the post-caesarean fentanyl analgesic effect on Chinese women," *Gene*, vol. 661, pp. 78–84, 2018.

[8] F. J. Sharom, "The P-glycoprotein multidrug transporter," *Essays in Biochemistry*, vol. 50, no. 1, pp. 161–178, 2011.

[9] C. H. Hsin, M. S. Stoffel, M. Gazzaz et al., "Combinations of common SNPs of the transporter gene ABCB1 influence apparent bioavailability, but not renal elimination of oral digoxin," *Scientific Reports*, vol. 10, no. 1, 2020.

[10] K. Meissner, G. Jedlitschky, H. Meyer zu Schwabedissen et al., "Modulation of multidrug resistance P-glycoprotein 1 (ABCB1) expression in human heart by hereditary polymorphisms," *Pharmacogenetics*, vol. 14, no. 6, pp. 381–385, 2004.

[11] M. Omar, A. Crowe, R. Parsons, H. Ee, C. Y. Tay, and J. Hughes, "P-glycoprotein expression in Helicobacter pylori-positive patients: the influence of MDR1 C3435T polymorphism," *Journal of Digestive Diseases*, vol. 13, no. 8, pp. 414–420, 2012.

[12] R. Wang, X. Sun, Y. S. Deng, and X. W. Qiu, "Effects of MDR1 1236C > T-2677G > T-3435C > T polymorphisms on the intracellular accumulation of tacrolimus, cyclosporine A, sirolimus and everolimus," *Xenobiotica*, vol. 49, no. 11, pp. 1373–1378, 2019.

[13] D. Vivona, L. T. Lima, A. C. Rodrigues et al., "ABCB1 haplotypes are associated with P-gp activity and affect a major molecular response in chronic myeloid leukemia patients treated with a standard dose of imatinib," *Oncology Letters*, vol. 7, no. 4, pp. 1313–1319, 2014.

[14] E. D. Kharasch, C. Hoffer, T. G. Altuntas, and D. Whittington, "Quinidine as a probe for the role of p-glycoprotein in the intestinal absorption and clinical effects of fentanyl," *Journal of Clinical Pharmacology*, vol. 44, no. 3, pp. 224–233, 2004.

[15] C. Yu, M. Yuan, H. Yang, X. Zhuang, and H. Li, "P-Glycoprotein on blood-brain barrier plays a vital role in fentanyl brain exposure and respiratory toxicity in rats," *Toxicological Sciences*, vol. 164, no. 1, pp. 353–362, 2018.

[16] W. Hamabe, T. Maeda, Y. Fukazawa et al., "P-Glycoprotein ATPase activating effect of opioid analgesics and their P-glycoprotein-dependent antinociception in mice," *Pharmacology, Biochemistry, and Behavior*, vol. 85, no. 3, pp. 629–636, 2006.

[17] V. Dzambazovska-Trajkovska, J. Nojkov, A. Kartalov et al., "Association of single-nucleotide polymorhism C3435T in the ABCB1 gene with opioid sensitivity in treatment of postoperative pain," *Prilozi*, vol. 37, no. 2-3, pp. 73–80, 2016.

[18] K. M. Kim, H. S. Kim, S. H. Lim et al., "Effects of genetic polymorphisms of OPRM1, ABCB1, CYP3A4/5 on postoperative fentanyl consumption in Korean gynecologic patients," *International Journal of Clinical Pharmacology and Therapeutics*, vol. 51, no. 5, pp. 383–392, 2013.

[19] X. D. Gong, J. Y. Wang, F. Liu et al., "Gene polymorphisms of OPRM1 A118G and ABCB1 C3435T may influence opioid requirements in Chinese patients with cancer pain," *Asian Pacific Journal of Cancer Prevention*, vol. 14, no. 5, pp. 2937–2943, 2013.

[20] Z. Xiao, G. Yin, Y. Ni et al., "MDR1 polymorphisms affect the outcome of Chinese multiple myeloma patients," *Biomedicine & Pharmacotherapy*, vol. 95, pp. 743–748, 2017.

[21] M. Saiz-Rodríguez, D. Ochoa, C. Herrador et al., "Polymorphisms associated with fentanyl pharmacokinetics, pharmacodynamics and adverse effects," *Basic & Clinical Pharmacology & Toxicology*, vol. 124, no. 3, pp. 321–329, 2019.

[22] I. A. Elkiweri, Y. L. Zhang, U. Christians, K. Y. Ng, M. C. Tissot van Patot, and T. K. Henthorn, "Competitive substrates for P-glycoprotein and organic anion protein transporters differentially reduce blood organ transport of fentanyl and

loperamide: pharmacokinetics and pharmacodynamics in Sprague-Dawley rats," *Anesthesia and Analgesia*, vol. 108, no. 1, pp. 149–159, 2009.

[23] G. Yin, Z. Xiao, Y. Ni et al., "Association of MDR1 single-nucleotide polymorphisms and haplotype variants with multiple myeloma in Chinese Jiangsu Han population," *Tumour Biology*, vol. 37, no. 7, pp. 9549–9554, 2016.

Hindawi
Journal of Nanomaterials
Volume 2021, Article ID 9934539, 5 pages
https://doi.org/10.1155/2021/9934539

Research Article

Application of Rapid Rehabilitation Nursing in Perioperative Period of Laparoscopic Radical Prostatectomy for Prostate Cancer Patients

Huimin Liu, Ke Yang, Fanghua Gong, Yan Wu, and Sanhui Tang

Hunan Provincial People's Hospital, The First Affiliated Hospital of Hunan Normal University, No. 89, Guhan Road, Furong District, Changsha City, 410016 Hunan Province, China

Correspondence should be addressed to Sanhui Tang; 201710310763@uibe.edu.cn

Received 19 March 2021; Revised 23 March 2021; Accepted 26 March 2021; Published 2 April 2021

Academic Editor: Songwen Tan

The purpose of the study is to explore the application of rapid rehabilitation nursing strategy in the perioperative period of laparoscopic radical prostatectomy for patients with prostate cancer. A total of 120 patients with prostate cancer undergoing laparoscopic radical prostatectomy were randomly divided into two groups, with 60 cases per group. The control group was given routine nursing care, and the experimental group received rapid rehabilitation nursing strategies. The stress hormone (cortisol and norepinephrine) levels, patient satisfaction, length of hospitalization, hospitalization costs, and postoperative complication were compared between the two groups before and after nursing. The serum cortisol and norepinephrine levels in the control group before nursing were similar to those in the experimental group ($P > 0.05$). The stress hormone levels in the experimental group were lower than those in the control group ($P < 0.05$). It was found that the experimental group had reduced operation time, less intraoperative blood loss, shortened exhaust time, and hospitalization stay and was earlier to eat and to get out of bed than the control group ($P < 0.05$). The time for the patients in the experimental group to pull out the drainage tube was significantly shorter than that of the control group ($P < 0.05$), and the hospitalization costs were fewer than the control group ($P < 0.05$). The rates of postoperative complications including nausea, vomiting, bleeding, and fever in the experimental group were significantly lower than those in the control group ($P < 0.05$). In conclusion, the study suggests that rapid rehabilitation nursing strategies can reduce the stress hormone levels, shorten the length of hospitalization, reduce hospitalization costs, reduce postoperative complication rates, and improve patient satisfaction for prostate cancer patients undergoing laparoscopic radical prostatectomy, in support of clinical application.

1. Background

Prostate cancer is one of the most common malignant tumors of the urinary system in men, with high incidence [1]. Prostate cancer presents several clinical manifestations including difficulty in urinating, frequent urination, painful urination/ejaculation, or burning sensation [2]. Surgery remains a mainstay in the management of localized prostate cancer [3]. Radical prostatectomy is associated with improvements in cancer-specific mortality and metastasis-free survival, while all aggressive therapy for prostate cancer negatively impacts erectile function and urinary continence [4]. Fast track surgery (FTS) is a new concept that integrates perioperative measures with evidence-based medical evidence and combines the latest evidence in anesthesia, nursing, and surgery disciplines to relieve surgical trauma and stress response and to promote the early recovery of organ function, thereby reducing postoperative complications, shortening the length of hospitalization, and achieving rapid recovery of patients [5]. Its contents are summarized as preoperative patient education, effective anesthesia, pain relief, precise surgical operations, and early postoperative rehabilitation treatment [6]. In recent years, our department has integrated the concept of rapid rehabilitation surgery and clinical pathways into the perioperative nursing of laparoscopic radical prostatectomy and achieved satisfactory

results. Rapid rehabilitation surgery has been involved in urology at home and abroad including laparoscopic adrenalectomy, percutaneous nephrolithotomy, radical cystectomy, urethral diversion, laparoscopic nephrectomy, laparoscopic surgery, radical nephrectomy, and living donor kidney transplantation [7]. A research [8] reported that the implementation of FTS can reduce the incidence of surgical complications and readmission, shorten the hospital stay, and reduce the cost of hospitalization. In this study, the standardized perioperative care plan guided by the FTS concept was applied to prostate cancer patients undergoing laparoscopic radical prostatectomy. In response to this, our hospital has focused on prostate cancer patients undergoing laparoscopic radical prostatectomy in recent years by giving rapid rehabilitation care or conventional care to compare the value of different nursing models.

2. Material and Method

2.1. Study Subjects. A total of 120 patients who were diagnosed with prostate cancer and underwent laparoscopic radical prostatectomy in our hospital were randomly divided into the experimental group and control group, with 60 cases in each group. The inclusion criteria are as follows: diagnosis with prostate cancer by imaging, prostate-specific antigen (PSA) screening, and biopsy; TIM stage T1c-T2c and N0M0; complete data; and signed an informed content. The exclusion criteria are as follows: patients with severe liver and kidney dysfunction, patients with severe inflammation and infection, patients with immune system disease or coagulation dysfunction, and patients with lung metastasis and lymph node metastasis. This study was approved by the Ethics Committee of our hospital.

2.2. Implementation of Rapid Rehabilitation Nursing Care. The control group was given routine nursing care, and the experimental group was given rapid rehabilitation nursing care. Before surgery, the investigator should understand the patient's psychological state, introduce the qualifications of the chief physician and anesthesiologist, and provide psychological counseling to patients. At the same time, he should monitor the patient's various physiological indicators before surgery to ensure that the patient receives good treatment; inform patients of the operation process, time, and cooperation work; improve patient matching; and speed up the operation process. According to the patient's gastrointestinal motility, oral 400-800 mL maltodextrin drink should be taken before 22:00 before surgery and 200-400 mL in the morning, 20 min. Glycerin enema should be taken in the morning. In intraoperative nursing, the patient's general anesthesia combined with epidural anesthesia, temperature, and humidity should be adjusted appropriately during the operation (temperature: 22-25°C, humidity: 40%-60%). Pay attention to intraoperative infusion management, and keep the infusion temperature at about 37°C, and strictly control the infusion volume and infusion speed. The instrument nurse is familiar with the surgical procedure and cooperates well with the attending doctor. Postoperatively, understand the patient's pain degree according to the main complaint of the patient, and carry out related analgesic treatment; drink water for 6 hours after the operation, and drink a small amount: the first time is 10-20 mL; observe the patient's response; if there is no maladjustment, increase the amount of water to ensure. The total amount does not exceed 50 mL, and liquid food is given to the patient on the first postoperative day, and it is gradually changed to semiliquid and ordinary food according to the actual situation of the patient. Six hours after the operation, the patient was in a semirecumbent position, guiding the movement of the lower limbs and guiding the family to assist the patient to turn over. Each exercise time should not be too long but gradually increase the exercise time with the extension of the postoperative time and regularly perform leg massage; 3 days before the operation to the postoperative extubation period, guide the patient to complete the pelvic floor muscle training and improve the pelvic floor muscle—contract the pelvic floor muscles—relax the muscles; each action lasts 10 s; repeat 10 times, and gradually extend the contraction time and number of times; you can exercise anytime, anywhere.

2.3. Observation Indicators. The stress hormone level, satisfaction degree, length of hospitalization, hospitalization costs, and complication rate were compared between the two groups before and after nursing.

2.4. Statistical Processing. SPSS17.0 software was used for data processing. The measurement data conforming to the normal distribution is represented by the mean ± standard deviation, and the comparison was performed by a t-test. A level of $P < 0.05$ is regarded as the presence of significant difference.

3. Results

3.1. Comparison of the Stress Hormone Levels of the Two Groups of Patients. The patients in the experimental group, aged 55-75 years old, had an average age of 63.51 ± 2.38 years, and the control group, aged 58-76 years old, had an average age of 62.21 ± 2.34 years. They were age-matched and comparable ($P > 0.05$). At the beginning of nursing, the stress hormone levels of serum cortisol and norepinephrine in the control group were similar to those in the experimental group ($P > 0.05$). The stress hormone level of the experimental group was lower than that of the control group ($P < 0.05$), as shown in Table 1.

3.2. Comparison of Clinical-Related Indicators between the Two Groups of Patients. The experimental group had reduced operation time, less intraoperative blood loss, shortened exhaust time, and hospitalization stay and was earlier to eat and to get out of bed than the control group ($P < 0.05$) (see Table 2 for details).

3.3. Comparison of the Nursing Effect of the Two Groups of Patients. It was found that the time for the patients in the experimental group to pull out the drainage tube was significantly lower than that of the control group ($P < 0.05$), the hospitalization costs were lower than that of the experimental group ($P < 0.05$), and the patient satisfaction of the

Table 1: Comparison of the stress hormone levels of between the experimental and control groups before and after nursing care.

Group	Phase	Serum cortisol level (nmol/L)	Norepinephrine levels (ng/mL)
Experimental group ($n = 60$)	Before care	125.36 ± 12.65	65.32 ± 5.27
	After care	56.35 ± 3.29*,#	32.65 ± 2.39*,#
Control group ($n = 60$)	Before care	125.69 ± 12.68	65.51 ± 5.23
	After care	85.64 ± 10.36*	45.32 ± 2.58*

*Compared with before care, $P < 0.05$. #Compared with the control group, $P < 0.05$.

Table 2: Comparison of clinical indicators of patients undergoing laparoscopic radical prostatectomy between the experimental and control groups.

Group	Operation time (min)	Intraoperative blood loss (mL)	First exhaust time (h)	Time to start eating (h)	Time of getting out of bed for the first time (h)	Hospitalization time (d)
Experimental group ($n = 60$)	91.2 ± 14.6	73.6 ± 29.8	26.5 ± 11.3	28.9 ± 10.8	24.6 ± 6.9	3.5 ± 2.1
Control group ($n = 60$)	100.3 ± 20.6	87.6 ± 35.6	44.9 ± 13.6	49.8 ± 15.2	41.3 ± 19.6	5.9 ± 3.4
T value	2.65	2.92	6.52	7.51	8.93	3.21
P value	0.02	0.03	0.01	0.01	0.01	0.05

$P < 0.05$ indicates that the difference is statistically significant.

Table 3: Comparison of time to pull out the drainage, hospitalization costs, and patient satisfaction between the experimental and control groups.

Group	Time to pull out the drainage tube (d)	Hospitalization costs (ten thousand yuan)	Patient satisfaction
Experimental group ($n = 60$)	6.5 ± 1.56	1.60 ± 0.46	85.23 ± 2.36
Control group ($n = 60$)	8.2 ± 1.87	1.84 ± 0.58	80.21 ± 2.15
T value	5.46	3.21	4.56
P value	0.01	0.05	0.03

$P < 0.05$ indicates that the difference is statistically significant.

Table 4: Comparison of postoperative complication rates between the experimental and control group.

Group	Feel sick and vomit (n (%))	Bleeding (n (%))	Fever (n (%))	Urinary system infection (n (%))
Experimental group ($n = 60$)	10 (16.7)	5 (8.3)	8 (13.3)	6 (10.0)
Control group ($n = 60$)	18 (30.0)	16 (26.7)	19 (31.7)	9 (15.0)
T value	4.46	5.21	2.56	1.09
P value	0.05	0.03	0.04	0.08

$P < 0.05$ indicates that the difference is statistically significant.

experimental group was significantly better than that of the control group ($P < 0.05$) (see Table 3 for details).

3.4. Comparison of Postoperative Complications between the Two Groups. It was found that the cases of nausea, vomiting, bleeding, and fever in the experimental group were significantly less than those in the control group, and the difference was statistically significant ($P < 0.05$). However, there was no significant statistical difference in urinary system infection between the two groups ($P > 0.05$) (see Table 4 for details).

4. Discussion

Laparoscopic radical prostatectomy is a common type of surgery for patients with prostate cancer. Compared with traditional surgery, laparoscopic radical prostatectomy has the advantages of simple operation, less trauma, fewer complications, and high safety and is easy to be accepted by the majority of patients and medical staff [9]. An effective nursing model can promote the recovery of patients, and accelerated rehabilitation care is a nursing model that implements nursing measures for patients during the perioperative period and

accelerates the recovery of patients [10, 11]. This mode of care can alleviate the patient's stress response. Rapid rehabilitation nursing is to carry out a series of nursing care during the perioperative period of the patient to reduce the patient's stress response, promote the rapid recovery of the body, and reduce the burden on the patient [12]. The concept of rapid recovery is to optimize the perioperative nursing measures to reduce the patient's stress response due to surgical trauma, reduce the risk of complications, shorten the patient's hospital stay, and promote the rapid recovery of the patient [13]. This goal is mainly achieved through anesthesia, minimally invasive surgery and perioperative care. Clinical studies have found that appropriately reducing the amount of infusion under the premise of ensuring the normal vital signs of the patient can not only reduce the occurrence of complications but also shorten the patient's hospital stay and reduce unnecessary hospitalization costs.

In addition, much attention to preoperative psychological care can alleviate patients' anxiety, depression, and stress response, so that patients can maintain a stable emotion during surgery [14]. Intraoperative heat preservation can reduce the risk of complications such as infection and bleeding and improve the safety and feasibility of surgery [15]. The rapid rehabilitation nursing model belongs to the comprehensive treatment model. Comprehensive nursing intervention is performed on patients to achieve psychological health, language, physical health, and overall health. The implementation of the rapid rehabilitation nursing model can effectively shorten the patient's recovery cycle, reduce the patient's economic burden, and reduce the adverse events that occur during the treatment process [16]. Laparoscopic radical prostatectomy is an effective method for the treatment of prostate cancer, but it is easy to be infected and cause complications after the operation. In order to shorten the perioperative period and reduce the complications, FTS nursing program is developed as the situation arises. Through preoperative education, negative emotions can be eliminated, and preoperative evaluation can improve the safety of the patient's surgery. In addition, preoperative preparation can maintain the stability of the patient's intestinal function and avoid problems such as hypoglycemia. Maintaining the stability of his vital signs is conducive to his recovery as soon as possible after the operation. After the operation, it is necessary to carry out nursing interventions in terms of diet, activity training and pipeline care, reasonable intake of water and dietary nutrition, timely training, and removal of drainage pipelines as soon as possible. Finally, nurses need to closely observe the patient's vital signs to prevent complications. In this study, the effect of FTS nursing in the experimental group was better than that in the control group.

In conclusion, the implementation of rapid rehabilitation nursing care during the perioperative period of laparoscopic radical resection of prostate cancer helps to ensure the effect of the operation, promote early recovery of patients after surgery, and effectively improve the quality of life of patients. Further clinical investigations are required due to limitations in the present study, including small sample size and self-reported data.

Data Availability

The data used to support the findings of this study are included within the article.

Conflicts of Interest

The authors declare that they have no conflicts of interest.

References

[1] M. S. Litwin and H. J. Tan, "The diagnosis and treatment of prostate cancer: a review," *JAMA*, vol. 317, no. 24, pp. 2532–2542, 2017.

[2] R. J. Rebello, C. Oing, K. E. Knudsen et al., "Prostate cancer," *Nature Reviews Disease Primers*, vol. 7, no. 1, p. 9, 2021.

[3] J. L. Wright, J. P. Izard, and D. W. Lin, "Surgical management of prostate cancer," *Hematology/Oncology Clinics of North America*, vol. 27, no. 6, pp. 1111–1135, 2013.

[4] E. M. Sebesta and C. B. Anderson, "The surgical management of prostate cancer," *Seminars in Oncology*, vol. 44, no. 5, pp. 347–357, 2017.

[5] C. Y. Ni, Y. Yang, Y. Q. Chang et al., "Fast-track surgery improves postoperative recovery in patients undergoing partial hepatectomy for primary liver cancer: a prospective randomized controlled trial," *European Journal of Surgical Oncology*, vol. 39, no. 6, pp. 542–547, 2013.

[6] H. Kehlet and D. W. Wilmore, "Evidence-based surgical care and the evolution of fast-track surgery," *Annals of Surgery*, vol. 248, no. 2, pp. 189–198, 2008.

[7] L. Bardram, P. Funch-Jensen, and H. Kehlet, "Rapid rehabilitation in elderly patients after laparoscopic colonic resection," *The British Journal of Surgery*, vol. 87, no. 11, pp. 1540–1545, 2000.

[8] N. H. Azawi, T. Christensen, A. L. Petri, and H. Kehlet, "Prolonged length of hospital stay in Denmark after nephrectomy," *Danish Medical Journal*, vol. 59, no. 6, article A4446, 2012.

[9] R. Tooher, P. Swindle, H. Woo, J. Miller, and G. Maddern, "Laparoscopic radical prostatectomy for localized prostate cancer: a systematic review of comparative studies," *The Journal of Urology*, vol. 175, no. 6, pp. 2011–2017, 2006.

[10] K. Larsen, T. B. Hansen, P. B. Thomsen, T. Christiansen, and K. Soballe, "Cost-effectiveness of accelerated perioperative care and rehabilitation after total hip and knee arthroplasty," *The Journal of Bone and Joint Surgery. American Volume*, vol. 91, no. 4, pp. 761–772, 2009.

[11] K. Larsen, T. B. Hansen, and K. Soballe, "Hip arthroplasty patients benefit from accelerated perioperative care and rehabilitation: a quasi-experimental study of 98 patients," *Acta Orthopaedica*, vol. 79, no. 5, pp. 624–630, 2008.

[12] L. Basse, J. E. Thorbol, K. Lossl, and H. Kehlet, "Colonic surgery with accelerated rehabilitation or conventional care," *Diseases of the Colon & Rectum*, vol. 47, no. 3, pp. 271–278, 2004.

[13] B. Leger-St-Jean, Z. Gorica, R. A. Magnussen, W. K. Vasileff, and C. C. Kaeding, "Accelerated rehabilitation results in good outcomes following acute repair of proximal hamstring ruptures," *Knee Surgery, Sports Traumatology, Arthroscopy*, vol. 27, no. 10, pp. 3121–3124, 2019.

[14] I. Tsimopoulou, S. Pasquali, R. Howard et al., "Psychological prehabilitation before cancer surgery: a systematic review,"

Annals of Surgical Oncology, vol. 22, no. 13, pp. 4117–4123, 2015.

[15] A. Lau, N. Lowlaavar, E. M. Cooke et al., "Effect of preoperative warming on intraoperative hypothermia: a randomized-controlled trial," *Canadian Journal of Anaesthesia*, vol. 65, no. 9, pp. 1029–1040, 2018.

[16] G. Zhu, C. Wu, and X. Shen, "Rapid rehabilitation nursing improves clinical outcomes in postoperative patients with colorectal carcinoma: a protocol for randomized controlled trial," *Medicine*, vol. 99, no. 45, article e22857, 2020.

Hindawi
Journal of Nanomaterials
Volume 2021, Article ID 9997939, 6 pages
https://doi.org/10.1155/2021/9997939

Research Article

Identification of Gene Markers for Survival Prediction of Lung Adenocarcinoma Patients Based on Integrated Multibody Data Analysis

Yuwang Bao,[1] **Jianxiong Luo**,[1] **Tianxing Yu**,[1] **Yang Liu**,[1] **Xiaohua Li**,[1] **Qiong Lin**,[1] **and Hao Wang**[2]

[1]*Department of Respiratory Medicine, The Affiliated Fuzhou First Hospital of Fujian Medical University, China*
[2]*Teaching Center of Experimental Medicine, Shanghai Medical College, Fudan University, China*

Correspondence should be addressed to Hao Wang; fdshmuwh@fudan.edu.cn

Received 10 March 2021; Revised 15 March 2021; Accepted 18 March 2021; Published 28 March 2021

Academic Editor: Songwen Tan

We constructed a prognostic-related risk prediction for patients with lung adenocarcinoma by integrating multiple omics information of lung adenocarcinoma clinical information group and genome and transcriptome. Blood samples and cancer and paracancerous lung tissue samples were collected from 480 patients with lung adenocarcinoma. DNA and RNA sequencing was performed on DNA samples and RNA samples. The first follow-up was carried out 3 months after discharge. Clinical information of patients including age, gender, smoking history, and TNM stage was collected. The Cox proportional hazard model evaluated more than 600 potential SNPs related to the prognosis of lung adenocarcinoma. After LASSO analysis, we obtained 4 SNPs related to the prognosis of lung adenocarcinoma (including rs1059292, rs995343, rs2013335, and rs8078328). Through the Cox proportional hazard model, 260 candidate genes related to the prognosis of lung adenocarcinoma were evaluated. After subsequent analysis, 3 genes related to the prognosis of lung adenocarcinoma (LDHA, SDHC, and TYMS) were obtained. All survived patients were spilt into a high-risk group ($n = 170$) and a low-risk group ($n = 170$) according to 4 SNPs and 3 genes related to the prognosis of lung adenocarcinoma. The overall survival rate of patients in the high-risk group was lower than that in the low-risk group. The prognostic risk prediction index constructed by combining clinical information group and genomic and transcriptome characteristics of multiomics information can effectively distinguish the prognosis of patients with lung adenocarcinoma, which will provide effective support for the precise treatment of patients with lung adenocarcinoma.

1. Backgrounds

Despite improvements in knowledge of risk, development, immunologic control, and therapeutic strategies for lung cancer, it still remains the leading cause of cancer death around the world [1]. About 80% of lung cancers are non-small-cell lung cancer (NSCLC) [2]. Due to the lack of lung cancer screening methods in China, it is difficult to achieve early diagnosis and treatment [3]. As a result, about 75% of NSCLC patients are in the middle and advanced stages when they are discovered [4]. The treatment of lung cancer is not standardized and advanced, and only a few patients can benefit from surgery, resulting in a low 5-year survival rate of NSCLC [5]. For this reason, effective molecular markers have been found for early diagnosis and treatment and prognosis evaluation of NSCLC patients, which is of great significance for improving the overall survival of lung cancer patients. The first choice and the main treatment method for NSCLC treatment is surgery. In order to improve the cure rate of lung cancer surgery and the survival rate of patients, it is often necessary to perform adjuvant chemotherapy and radiotherapy before or after surgery [6]. Recently, researchers focus on using metaorganic framework fluorescent nanoparticles as carriers to target drug-resistant cancer cells [7]. Additionally, a review summarized important information on the 3D self-assembly nanostructure, such as peptide hydrogel, graphene,

Table 1: Clinicopathological characteristics of patients with lung adenocarcinoma.

Clinicopathological characteristics	Survival (%) $n = 340$	Death (%) $n = 140$	Median survival time (months)	HR (95% CI)	P value
Age (year)					
≤65	153 (44.92)	49 (35.00)	24.65	1	0.23
>65	187 (55.08)	91 (65.00)	21.36	1.32 (0.85~1.94)	
Gender					
Male	206 (60.58)	64 (45.71)	21.65	1	0.45
Female	134 (39.42)	76 (54.29)	26.35	1.07 (0.72~1.65)	
Smoking status					
Yes	48 (14.12)	18 (12.86)	26.48	1	0.78
No	292 (85.88)	122 (87.14)	23.89	0.91 (0.48~1.76)	
TNM staging					
I-II	294 (86.05)	95 (67.86)	28.94	1	0.01*
III-IV	46 (13.50)	45 (32.14)	12.36	2.83 (1.88~4.25)	

HR: hazard ratio; TNM: tumor node metastasis; CI: confidence interval; *$P < 0.05$.

carbon nanotubes (CNTs), and fullerene, for application in gene delivery and cancer therapy and tissue engineering [8]. However, due to the characteristics of tumor heterogeneity, different patients with the same treatment plan have significant differences in efficacy. In order to solve this problem, the concept of individualized medicine has been proposed, but there is still a lack of effective clinical signs to distinguish individual differences between different patients. It is difficult to effectively distinguish between individual differences in patients and implement individualized treatment.

Although the prognostic analysis of lung adenocarcinoma transcriptome based on TCGA database has been extensively studied, including miRNA, lncRNA, and mRNA, these studies are limited to a single omics data, and the combined use of multiple omics information to predict the prognosis of lung adenocarcinoma still lacks data support [9–11].

At present, the application of molecular targeted therapy that uses the differences between tumor cells and normal cells at the molecular and cellular levels to target cell receptors, genes, and regulatory molecules as drug targets has become a hot spot in the current clinical application research field of lung cancer, but there are still few markers applied to clinical practice. Single nucleotide polymorphism (SNP) is the polymorphism of the DNA sequence in the population caused by a single base variation or short fragment insertion in the genome. The variation reaches a certain frequency in the population (more than 1%) [12]. With the deepening of SNP research, it has been discovered that SNPs in multiple oncogenes or tumor suppressor genes are closely related to the occurrence and development of various diseases, including tumors. In addition, SNPs can also be used to evaluate the efficacy of tumor chemotherapy. Some SNPs that are closely related to the prognosis of patients have been found in NSCLC, but the number is small, and the effect is limited when a single site is used for evaluation. For this reason, we are looking for more SNP sites that can be used for prognostic evaluation of NSCLC and formulating joint analysis strategies, which is of great significance in the individualized treatment of NSCLC.

Table 2: SNPs related to the prognosis of lung adenocarcinoma.

SNP site	MAF (allele)	HR (95% CI)	P value
rs1059292	0.882 (T)	0.65 (0.45~0.89)	0.01*
rs995343	0.470 (G)	1.41 (1.13~1.87)	0.02*
rs2013335	0.475 (A)	1.51 (1.11~1.89)	0.01*
rs8078328	0.456 (A)	1.41 (1.07~1.84)	0.05*

SNP: single nucleotide polymorphism; MAF: minor allele frequency; HR: hazard ratio; *$P < 0.05$.

Table 3: Genes related to the prognosis of lung adenocarcinoma.

Gene	HR (95% CI)	P value
LDHA	1.76 (1.32~2.30)	0.03*
SDHC	1.28 (1.09~1.55)	0.01*
TYMS	1.33 (1.12~1.59)	0.03*

HR: hazard ratio; *$P < 0.05$.

2. Materials and Methods

2.1. Blood Samples. The blood samples and cancer and paracancerous lung tissue samples were surgically resected from patients who were diagnosed as NSCLC and admitted into our hospital from January 2014 to January 2016. The details of blood collection are as follows: before sample acquisition, the patients and their families need to be informed of the plan and significance of this study, and the patients and their families must agree and sign the "Informed Consent"; ensure that the enrolled patients have not undergone blood transfusion or surgery before adjuvant chemotherapy; take a blood sample after 8 hours of fasting before the operation; take 10-20 ml of blood from the vein of the upper extremity, collect it with a special test tube of EDTA anticoagulant, and mark it; collect the sample in a refrigerator at 4°C; keep it for a short time, refrigerate it, and send it to the laboratory as soon as possible to complete the whole genome DNA extraction of the blood sample.

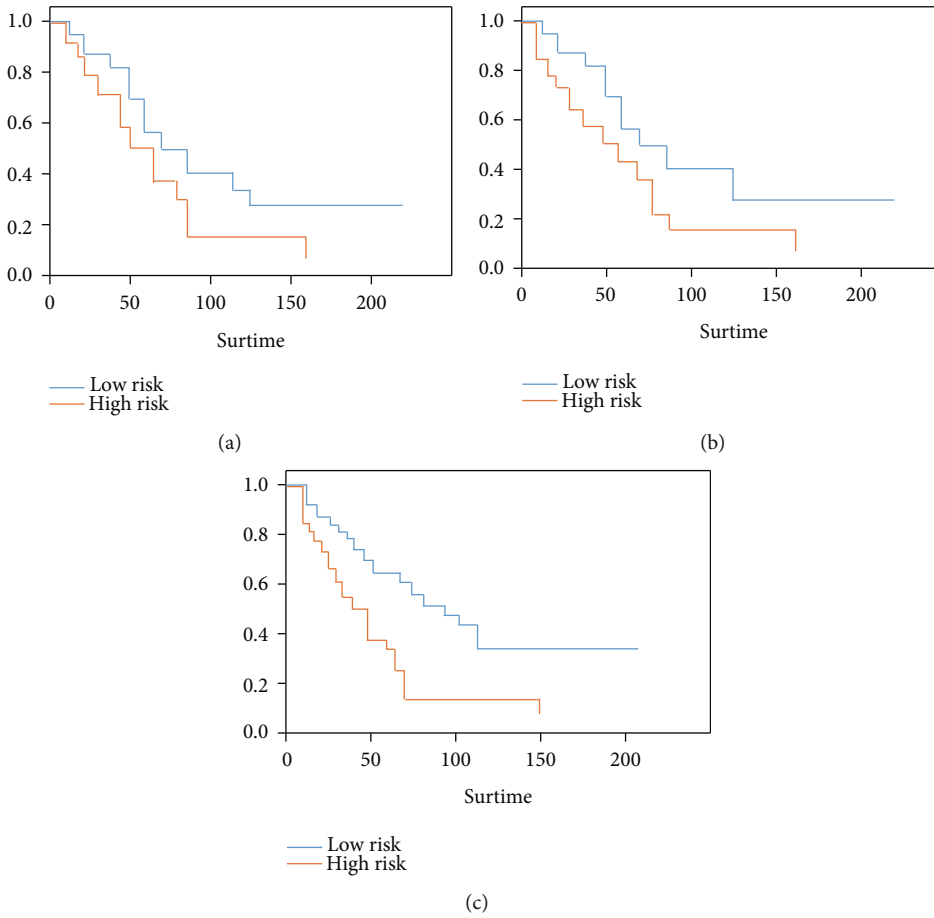

Figure 1: Kaplan-Meier survival curves of patient survival between the high-risk group and the low-risk group. (a) Genetic index alone for analysis; (b) clinical index alone for analysis; (c) combined genetic and clinical index for analysis.

2.2. Plasma Separation. The operation must be completed within 3 hours after blood collection. The specific steps are as follows. Place the anticoagulant test tube with blood sample on the vortexer and shake for 10 seconds, and then, place it in the centrifuge and centrifuge at low speed for 8 minutes (1200 g/min), transfer the plasma to a 1.5 ml centrifuge tube, pay attention to stop at least 0.2 ml supernatant away from the white blood cell layer, so as not to draw the white blood cell layer and affect subsequent use. Place the centrifuge tube containing 1.5 ml supernatant in the centrifuge for 5 minutes (8000 g/min), and then, divide it into 0.5 ml centrifuge tubes, each tube 0.4 ml, mark the sample research number, and place it at -80°C. Store in refrigerator. The separated blood cells were placed in a refrigerator at 4°C for storage, and the whole genome DNA extraction and RNA extraction were performed within 3 days.

2.3. Whole Genome DNA Extraction from Blood Cells. This subject uses the Omega Whole Blood DNA Extraction Kit. The specific steps are as follows. Set the water bath to 65°C before extraction. After the blood sample tube is shaken on the vortexer for 10 seconds, transfer the blood sample to a 15 ml centrifuge tube. Then, add 3 ml CL reagent to the sample tube, shake it slightly, transfer to the centrifuge tube, continue to add 4 ml CL reagent to the centrifuge tube, vortex for 20 seconds to mix, centrifuge for 3 minutes (8000 g/min), and discard the supernatant liquid. Add 5 ml CL reagent to the above centrifuge tube, vortex repeatedly until the precipitate is completely dissolved, centrifuge for 3 minutes (8000 g/min), discard the supernatant, and put the centrifuge tube upside down on absorbent paper for 2 minutes to air dry. Prepare FG&PK working solution (FG reagent: proteinase K = 100 : 1) between centrifugation, and mix it up repeatedly. After air drying, add 2.5 ml FG&PK working solution to the centrifuge tube, vortex to mix. In a 65°C water bath for 30 minutes, shake it horizontally for 3 times during which time it will lyse cells more fully. Add 2.5 ml of precooled isopropanol, shake it horizontally for 20 seconds, and pay attention to precipitation. Centrifuge for 10 minutes (8000 g/min) and discard the supernatant. Add 2.5 ml of 70% ethanol, vortex for 5 seconds, centrifuge for 3 minutes (8000 g/min), and discard the supernatant. Repeat this step once. Let stand at room temperature to dry the DNA precipitation. Add 800 μl of TB elution buffer, vortex at low speed for 5 seconds, and aliquot. NanoDrop 2000 quantitative instrument detects DNA concentration. Store in a refrigerator at -80°C. After the DNA

information of the extracted blood sample is recorded in the "Lung Cancer Sample Registration Form," it is completely entered into the database.

2.4. Sample Preparation before the Experiment. According to the NanoDrop 2000 DNA quantification results, the blood sample DNA was diluted to the experimental concentration (10 ng/μl) one by one, and the diluted samples were loaded into a 96-well plate (10 ng/μl, final) in order. Volume 20 μl, use the random number method to randomly set 4 samples in a 96-well plate as repeated test samples, transfer the prepared 96-well plate to a 384-well plate with a row gun, each well of 10 ng DNA samples, centrifuge 384. Place the well plate in a 37°C oven for 30 minutes. When there is no liquid at the bottom of the well of the 384-well plate, prepare the plate before completing the experiment and store it in a refrigerator at 4°C.

2.5. RNA Extraction. Cells were placed into a 1.5 ml centrifuge tube, add 1 ml Trizol, mix well, and let stand at room temperature for 5 minutes. Add 0.2 ml of chloroform, shake for 15 s, and let stand for 2 min. Centrifuge at 4°C, 12000 g $\times$ 15 min, and take the supernatant. Add 0.5 ml of isopropanol, gently mix the liquid in the tube, and let stand at room temperature for 10 min, followed by centrifugation (4°C, 12000 g $\times$ 10 min). After addition of 75% ethanol, the precipitate was centrifuged at 4°C (7500 g $\times$ 5 min) and added with DEPC H2O to dissolve (65°C for 10-15 min).

2.6. Sequencing. DNA and RNA sequencing was performed on DNA samples and RNA samples.

2.7. Clinical Information Collection. This research group has developed a comprehensive "Individual Basic Information Registration Form." The medical staff in charge of the sample database collects basic patient information, including height, weight, age, gender, ethnicity, and education level, through face-to-face inquiry, and personal information, including family history of tumors, smoking history, long-term medication history, and occupational exposure history. After the patient is discharged from the hospital, the relevant personnel of the sample library will further collect data and fill in the "Medical Record Summary Table," including tumor size, number and location, TNM staging (according to the seventh edition of TNM staging), pathological grade (high, medium, and poorly differentiated), and tumor marker examination results, in addition to collecting the patient's hospital stay, operation time and method, whether to receive neoadjuvant therapy after surgery, and the type of dose.

2.8. Follow-Up. The first follow-up was carried out 3 months after the patient was discharged. The medical staff asked the patient the following information through telephone consultation: whether the patient was rechecked after discharge, including imaging examinations and serological examinations; whether to readmit to the hospital for radiotherapy, chemotherapy, and radiotherapy; whether there is recurrence, reoperation, and the patient's survival and death status, death time, etc. Fill in the "Lung Cancer Patient Follow-up Registration Form" after inquiry. The follow-up interval is 3 months, and the follow-up deadline is January 2018. A total of 40 cases of 480 enrolled cases were lost to follow-up, and the loss to follow-up rate was 8.3%, less than 10%, meeting the research requirements.

2.9. Prognosis Analysis. Organize the collected patient clinical information and prognosis follow-up information. Transform information such as age, gender, smoking history, and TNM stage into the form of categorical variables. For continuous variables, the median will be divided into two points, converted into categorical variables. The survival time is the date of death or the last follow-up date minus the date of diagnosis, and the recurrence time is the date of relapse or the last follow-up date minus the date of diagnosis, all in months. The organized information is saved in SPSS file format for further analysis and use. The chi-square test and Fisher's test were used to analyze whether there were differences in clinical factors such as age, gender, smoking history, and TNM stage. Then, use the Cox proportional hazard regression model to analyze the impact of the above clinical indicators on overall survival (OS) and recurrence-free survival (RFS), and calculate the risk of death and recurrence (hazard ratios (HRs)), 95% confidence intervals (CIs), and P value. In the Cox regression analysis, clinical indicators such as age, gender, smoking history, and TNM stage are used for mutual correction. All tests were considered as significant differences with two-sided $P < 0.05$. The Kaplan-Meier survival curve and log-rank test (log-rank test) are used to assess whether there are differences in overall survival time and recurrence-free survival time in different patient groups.

3. Results

3.1. Clinical Information and Overall Survival Analysis of NSCLC Patients. This study included 480 patients with lung adenocarcinoma with an average age of 65.58 ± 8.98 and a median survival time of 23.65 months. There was no significant difference with regard to age, gender, and smoking status of these patients. See Table 1 for specific details.

3.2. Identification of SNPs Related to Lung Adenocarcinoma Prognosis. The Cox proportional hazard model evaluated more than 600 potential SNPs related to the prognosis of lung adenocarcinoma. After LASSO analysis, 4 SNPs were acquired related to the prognosis of lung adenocarcinoma, including rs1059292 ($P = 0.01$), rs995343 ($P = 0.02$), rs2013335 ($P = 0.01$), and rs8078328 ($P = 0.05$), as shown in Table 2.

3.3. Identification of Prognostic Genes of Lung Adenocarcinoma. The Cox proportional hazard model evaluated 260 candidate genes related to the prognosis of lung adenocarcinoma. After subsequent analysis, three genes related to the prognosis of lung adenocarcinoma (LDHA, SDHC, and TYMS) were obtained, as shown in Table 3.

3.4. Construction and Evaluation of Genetic Prognostic Index. According to the calculation of the SNP loci and genes obtained above, we divided all patients into a high-risk group

($n = 170$) and a low-risk group ($n = 170$). As shown in Figure 1, the overall survival rate of patients in the high-risk group was lower, and the log-rank test indicated that the difference in survival rates between the high-risk and low-risk groups was statistically significant ($P < 0.05$).

4. Discussions

Many phase III clinical trials and meta-analysis have shown that all the studied platinum-based two-line drugs have similar efficacy in the first-line treatment of advanced NSCLC. The remission rate is about 15% to 30%, the progression-free survival period is about 46 months, and the overall survival is about 8-10 months. Compared with platinum-based double glue, the newer combination therapy does not further improve the efficacy [13–15]. Although the efficacy of first-line chemotherapy has reached a plateau, the prognosis of patients with advanced NSCLC is still very poor. With the latest developments in pharmacogenomics research, chemotherapy regimens can be tailored for patients with advanced NSCLC to improve the efficacy and reduce the toxicity of chemotherapy based on the expression level or polymorphism of one or several genes.

As patients with advanced NSCLC cannot or are not suitable for surgery, it is clinically recommended to use radiotherapy or a combination of radiotherapy and chemotherapy. Taking advantage of the molecular and cellular differences between tumor cells and normal cells, molecular targeted therapy targeting cell receptors, genes, and regulatory molecules as drug targets has gradually become a new strategy for the current clinical treatment of lung cancer, such as angiogenesis inhibitors and epidermal growth factor receptor inhibitors which have all been used in clinical applications. In addition, biological treatments including tumor vaccine technology, cytokine technology, monoclonal antibody technology, and gene therapy technology have gradually developed and transformed into clinical applications [16–18].

In this study, the genome and transcriptome data of 480 patients with lung adenocarcinoma were screened, and a total of 4 SNPs and 3 genes that were significantly related to the prognosis of lung adenocarcinoma patients were obtained, which were used to construct prediction models. Using the genetic prognosis index calculated by the model, patients with lung adenocarcinoma were divided into high-risk groups and low-risk groups. The results of survival analysis showed that the survival rate between the groups was significantly different. From previous evidence, the variant-containing genotypes of rs1059292 in 5′-flanking region of CD98 gene were significantly associated with an increased risk of death in lung cancer [19]. Besides, Guo et al. found that rs995343 of the MCT2 gene exhibited an association with poor survival of NSCLC patients [20]. However, due to the lack of previous evidence of rs2013335 and rs8078328 in lung cancer, further investigations are required. As for 3 genes obtained in the present study which were supposed to be associated with prognosis of lung cancer, previous studies reported that knockdown of LDHA, SDHC, or TYMS could impede lung cancer cell migration and invasion [21–23], suggesting three of them were correlated with prognosis of lung cancer.

This study also has some limitations. This study did not consider the relationship between somatic mutations, structural mutations, methylation, and other changes in the levels of lung adenocarcinoma, which will be analyzed in subsequent studies. This study fails to examine the relationship between SNPs and EGFR mutations. After the integration of genetic and clinical indexes, there is no significant increase in HR value compared with the single effect, suggesting that there may be mutual influence between genetic index and clinical index. The prediction model constructed based on the genetic information of the genome and transcriptome can well identify patients with poor prognosis and high risk of lung adenocarcinoma and can predict the prognosis of patients together with clinical prognostic factors, so it can provide basis for evaluating the prognostic risk of patients with lung adenocarcinoma.

Data Availability

The data used to support the findings of this study are included within the article.

Conflicts of Interest

All authors declare that they have no conflict of interest.

Authors' Contributions

Yuwang Bao and Jianxiong Luo contributed equally to this work.

References

[1] B. C. Bade and C. S. Dela Cruz, "Lung cancer 2020: epidemiology, etiology, and prevention," *Clinics in Chest Medicine*, vol. 41, no. 1, pp. 1–24, 2020.

[2] V. M. L. de Sousa and L. Carvalho, "Heterogeneity in lung cancer," *Pathobiology*, vol. 85, no. 1-2, pp. 96–107, 2018.

[3] Q. Y. Hong, G. M. Wu, G. S. Qian et al., "Prevention and management of lung cancer in China," *Cancer*, vol. 121, Supplement 17, pp. 3080–3088, 2015.

[4] C. Genova, G. Rossi, M. Tagliamento et al., "Targeted therapy of oncogenic-driven advanced non-small cell lung cancer: recent advances and new perspectives," *Expert Review of Respiratory Medicine*, vol. 14, no. 4, pp. 367–383, 2020.

[5] N. P. Giustini, A. R. Jeong, J. Buturla, and L. Bazhenova, "Advances in treatment of locally advanced or metastatic non-small cell lung cancer: targeted therapy," *Clinics in Chest Medicine*, vol. 41, no. 2, pp. 223–235, 2020.

[6] S. I. Watanabe, K. Nakagawa, K. Suzuki et al., "Neoadjuvant and adjuvant therapy for stage III non-small cell lung cancer," *Japanese Journal of Clinical Oncology*, vol. 47, no. 12, pp. 1112–1118, 2017.

[7] X. M. Lv, Q. S. Guo, and L. M. Xu, "Study on the chemotherapeutic effect and mechanism of doxorubicin hydrochloride on drug-resistant gastric cancer cell lines using metal-organic framework fluorescent nanoparticles as carriers," *Journal of Nanomaterials*, vol. 2020, Article ID 6681749, 14 pages, 2020.

[8] A. Gholami, S. A. Hashemi, K. Yousefi et al., "3D nanostructures for tissue engineering, cancer therapy, and gene delivery," *Journal of Nanomaterials*, vol. 2020, Article ID 1852946, 24 pages, 2020.

[9] S. X. Ren, A. W. Li, S. W. Zhou et al., "Individualized chemotherapy in advanced NSCLC patients based on mRNA levels of BRCA1 and RRM1," *Chinese Journal of Cancer Research*, vol. 24, no. 3, pp. 226–231, 2012.

[10] L. Xie, W. Chen, R. Dong et al., "Function of macrophage scavenger receptor 1 gene polymorphisms in chronic obstructive pulmonary disease with and without lung cancer in China," *Oncology Letters*, vol. 15, no. 5, pp. 8046–8052, 2018.

[11] L. B. Gansmo, P. Romundstad, E. Birkeland et al., "*MDM4* SNP34091 (rs4245739) and its effect on breast-, colon-, lung-, and prostate cancer risk," *Cancer Medicine*, vol. 4, no. 12, pp. 1901–1907, 2015.

[12] S. Ercan, S. Arinc, S. G. Yilmaz, C. Altunok, F. Yaman, and T. Isbir, "Investigation of caspase 9 gene polymorphism in patients with non-small cell lung cancer," *Anticancer Research*, vol. 39, no. 5, pp. 2437–2441, 2019.

[13] C. Manegold, A. C. Dingemans, J. E. Gray et al., "The potential of combined immunotherapy and antiangiogenesis for the synergistic treatment of advanced NSCLC," *Journal of Thoracic Oncology*, vol. 12, no. 2, pp. 194–207, 2017.

[14] R. Pirker, J. R. Pereira, A. Szczesna et al., "Cetuximab plus chemotherapy in patients with advanced non-small-cell lung cancer (FLEX): an open-label randomised phase III trial," *Lancet*, vol. 373, no. 9674, pp. 1525–1531, 2009.

[15] G. Scagliotti, N. Hanna, F. Fossella et al., "The differential efficacy of pemetrexed according to NSCLC histology: a review of two phase III studies," *The Oncologist*, vol. 14, no. 3, pp. 253–263, 2009.

[16] C. Ling, Y. Xie, D. Zhao, Y. Zhu, J. Xiang, and J. Yang, "Enhanced radiosensitivity of non-small-cell lung cancer (NSCLC) by adenovirus-mediated ING4 gene therapy," *Cancer Gene Therapy*, vol. 19, no. 10, pp. 697–706, 2012.

[17] C. M. Panje, J. E. Lupatsch, M. Barbier et al., "A cost-effectiveness analysis of consolidation immunotherapy with durvalumab in stage III NSCLC responding to definitive radiochemotherapy in Switzerland," *Annals of Oncology*, vol. 31, no. 4, pp. 501–506, 2020.

[18] A. Keegan, B. Ricciuti, P. Garden et al., "Plasma IL-6 changes correlate to PD-1 inhibitor responses in NSCLC," *Journal for immunotherapy of cancer*, vol. 8, no. 2, article e000678, 2020.

[19] X. Guo, H. Li, F. Fei et al., "Genetic variations inSLC3A2/CD98gene as prognosis predictors in non-small cell lung cancer," *Molecular carcinogenesis*, vol. 54, Supplement 1, pp. E52–E60, 2015.

[20] X. Guo, C. Chen, B. Liu et al., "Genetic variations in monocarboxylate transporter genes as predictors of clinical outcomes in non-small cell lung cancer," *Tumour Biology*, vol. 36, no. 5, pp. 3931–3939, 2015.

[21] X. Zhou, R. Chen, W. Xie, Y. Ni, J. Liu, and G. Huang, "Relationship between 18F-FDG accumulation and lactate dehydrogenase A expression in lung adenocarcinomas," *Journal of Nuclear Medicine*, vol. 55, no. 11, pp. 1766–1771, 2014.

[22] X. Guo, D. Li, Y. Wu et al., "Genetic variants in genes of tricarboxylic acid cycle key enzymes are associated with prognosis of patients with non-small cell lung cancer," *Lung Cancer*, vol. 87, no. 2, pp. 162–168, 2015.

[23] S. Sun, W. Shi, Z. Wu, G. Zhang, B. O. Yang, and S. Jiao, "Prognostic significance of the mRNA expression of *ERCC1*, *RRM1*, *TUBB3* and *TYMS* genes in patients with non-small cell lung cancer," *Experimental and Therapeutic Medicine*, vol. 10, no. 3, pp. 937–941, 2015.

Hindawi
Journal of Nanomaterials
Volume 2021, Article ID 5563901, 8 pages
https://doi.org/10.1155/2021/5563901

Research Article

Fentanyl Exerts an Antitumor Effect on Papillary Thyroid Cancer by Regulating the miR-204/KLF5 Axis

Dahao Lu,[1] Lulu Jiang,[2] Chen Dai,[1] Keshi Yan,[1] and Ju Gao[1]

[1]*Department of Anesthesiology, Northern People's Hospital, Medical College of Yangzhou University, China*
[2]*Department of Anesthesiology, The Second Xiangya Hospital of Central South University, China*

Correspondence should be addressed to Ju Gao; subei015047@163.com

Received 24 February 2021; Revised 1 March 2021; Accepted 8 March 2021; Published 26 March 2021

Academic Editor: Tingting Hong

Fentanyl is a strong anesthetic analgesic drug that plays important roles in many types of cancers. However, the role of fentanyl in papillary thyroid cancer (PTC) tumor development remains ambiguous. In this study, we aimed to investigate the potential antitumor effects of fentanyl on PTC cell viability and invasion. Results of cell counting kit-8 and Transwell assays demonstrated that fentanyl treatment (5 ng/ml) reduced the viability and invasion of two PTC cells, TCP-1 and BCPAP. Our data subsequently showed that fentanyl induced antitumor effects by increasing miR-204 expressions. Furthermore, the results of luciferase reporter assays identified that miR-204 directly targets Krüppel-like transcription factor 5 (KLF5), which serves as tumor-promoting genes in many cancers. Further mechanistic analyses revealed that fentanyl performs its tumor-suppressive functions by regulating the miR-204/KLF5 axis in PTC cells. These results contribute to understanding the important role of fentanyl in treating PTC.

1. Introduction

As the most common endocrine-related malignant tumor over the past decades, thyroid cancer has rising incidence with an annual rate of 3% [1, 2]. Papillary thyroid cancer (PTC) is a common histologic type of thyroid cancer that has attained considerable attention in recent years [3]. Although the majority of patients with PTC show relatively good prognosis, some cases still suffer from poor outcomes due to local recurrence and distant metastasis [4]. Thus, determining the underlying mechanism related to PTC tumor metastasis and developing new therapeutic targets against PTC are crucial.

Fentanyl is a strong anesthetic analgesic drug that has been widely applied in clinical anesthesia, especially during cancer surgery [5]. However, fentanyl plays not only important roles in pain management but also exerts its tumor-suppressing functions in many types of cancers [6]. Fentanyl showed an inhibitory effect on cell invasion and migration via the promotion of the miR-302b-ErbB4 axis in esophageal squamous cell carcinoma (ESCC) [7]. Li et al. [8] demonstrated that fentanyl retarded tumor progression in gastric cancer by repressing the expression of matrix metalloproteinase 9 (MMP-9).

MicroRNAs (miRNAs) with a length of nearly 22 nucleotides are a class of noncoding RNAs that perform important regulatory roles in the pathogenesis of many cancers [9–11]. miRNAs regulate their target expressions posttranscriptionally by pairing with 3′-untranslated region (3′UTR) of genes [12]. Recent studies have reported the role of miR-204 in several human cancers, including osteosarcoma, gastric cancer, and acute myeloid leukemia [13–16]. Interestingly, miR-204 was found to be downregulated in papillary thyroid carcinoma tissues [17], while no further mechanistic analysis was performed. Bioinformatics analysis shows Krüppel-like transcription factor 5 (KLF5) as a putative target gene of miR-204. KLF5 has been reported to promoted PTC cell growth, invasion, and migration from previous evidence [18]. In this study, biological functions of fentanyl in PTC cancer progression and its regulatory mechanisms involving

the miR-204/KLF5 axis in reducing cell viability and invasion are explored in this study. The findings of our work can provide new insights into the treatment of PTC.

2. Materials and Methods

2.1. Cells and Tissues. PTC cell lines (TPC-1 and BCPAP) were obtained from the Shanghai Institute for Biological Sciences (http://www.cellbank.org.cn/) and cultured in RPMI-1640 medium (Gibco, USA) containing 10% fetal bovine serum (FBS). Both cells were incubated at 37°C with 5% CO_2. Fentanyl (Sigma-Aldrich, USA) was dissolved in dimethyl sulfoxide (DMSO) and added into the culture medium at different concentrations (0, 0.5, 5, and 50 ng/ml). Addition of only DMSO into the culture medium was performed for the control group.

2.2. Cell Transfection. miR-204 mimic/inhibitor and negative controls (NCs) were purchased from RiboBio (Guangzhou, China). KLF5 expression vector, empty vector, si-KLF5, and scramble siRNA (si-NC) were also designed by RiboBio (Guangzhou, China). TPC-1 and BC-PAP cells were cultured in six-well plates with miR-204 mimic, NC mimic, miR-204 inhibitor, NC inhibitor, KLF5, or NC using Lipofectamine 2000 (Invitrogen, CA) for transfection according to the manufacturer's recommendations.

2.3. RNA Extraction and Quantitative Real-Time PCR Assays. cDNA was reversely transcribed from RNA using a miRNA RT-PCR kit (Takara, China) for miR-204 expression analysis. cDNA was reversely transcribed from RNA using an mRNA RT-PCR kit (Takara, China) for KLF5 expression analysis. Expression levels of miR-204 and KLF5 were quantified using SYBR Green (Applied Biosystems, USA) on an ABI 7500 Fast DX RT-PCR instrument (Applied Biosystems, USA). Primer sequences of miR-204 and U6 were synthesized by RiboBio (Guangzhou, China). Specific primers for KLF5 and β-actin used in the study are presented as follows: KLF5: 5′-CCTGGTCCAGACAAGATGTGA-3′, 5′-GAACTGGTCTACGACTGAGGC-3′ and β-actin: 5′-GGACTTCGAGCAAGAGATGG-3′, 5′-AGCACTGTGTTGGCGTACAG-3′. Fold changes for miR-204 and KLF5 expressions were calculated using the $2^{-\Delta\Delta Ct}$ method.

2.4. Cell Counting Kit-8 (CCK-8) Assays. CCK-8 (KeyGEN) assays were used to evaluate the viability of PTC cells. Transfected PTC cells were planted into 96-well plates at a density of 3×10^3 cells/well. The CCK-8 solution (10 μl) was added to cultured cells in 100 μl of culture medium 24 h after treatment and incubated at 37°C with 5% CO_2 for 1 h. Absorbance values were then determined at 450 nm after 1, 2, 3, and 4 days.

2.5. Transwell Assays. Transwell inserts with Matrigel (BD Biosciences) were used to detect the invasion ability of PTC cells. Then, 200 μl of serum-free media with a density of 2×10^4 cells were transferred to the upper chamber (Corning; NY, USA). A 500 μl medium containing 20% FBS was subsequently added to the lower compartment. Cells that moved to the bottom of the chamber were stained with 0.2% crystal violet after incubation for 24 h. The number of invading cells from five independent visual fields was counted under an inverted microscope with a magnification of ×200.

2.6. Western Blot Analysis. Transfected PTC cells were lysed in RIPA buffer (Beyotime; Shanghai, China) after washing with phosphate buffer solution (PBS). Extracted proteins were subsequently measured using a bicinchoninic acid (BCA) kit (Beyotime; Shanghai, China). Then, 15 μg of protein from each sample was separated on 10% sodium dodecyl sulfate-polyacrylamide gel electrophoresis (SDS-PAGE) gels and transferred onto a polyvinylidene fluoride (PVDF) membrane (Miilp, USA). The membrane was incubated with rabbit polyclonal anti-KLF5 (1 : 1000, Abcam, USA) after blocking with 5% defatted milk at 4°C for 2 h. Anti-β-actin (1 : 2000, CST, USA) was used as the loading control. Immunoreactive bands were visualized using an enhanced chemiluminescence reagent (Beyotime; Shanghai, China).

2.7. Luciferase Reporter Assay. We used a luciferase reporter assay to analyze the binding between miR-204 and KLF5. PTC cells cotransfected with miR-204 or NC mimic and pCDNA3.1 luciferase reporter vector containing KLF5-3′ UTR wild-type (wt) vector or KLF5-3′UTR mutant (mut) fragment using lipofectamine 2000 reagents (Invitrogen; Carlsbad, CA). The Dual-Luciferase Reporter Assay System (Promega) was used to determine luciferase activities after transfection for 48 h.

2.8. Statistical Analysis. Data were statistically analyzed by Student's *t*-test, one-way analysis of variance (ANOVA) with Tukey's test, and repeated measurement ANOVA with Bonferroni corrections using GraphPad 5.0 and SPSS 19.0, respectively. Values were shown as mean ± standard deviation from at least three independent experiments. The P value < 0.05 was considered statistically significant.

3. Results

3.1. Fentanyl Reduced PTC Cell Viability and Invasion. We first used CCK-8 assays to detect the viability of PTC cells under different concentrations of fentanyl stimulation. Figure 1(a) shows that fentanyl reduces TCP-1 and BCPAP cell viability at a dosage- and time-dependent manner. Transwell invasion assays also illustrated that TCP-1 and BCPAP cell invasion was significantly inhibited by fentanyl treatment in a dose-dependent manner (Figures 1(b) and 1(c)). These data demonstrated that the fentanyl treatment repressed the cell viability and invasion of PTC cells.

3.2. Fentanyl Repressed PTC Cell Viability and Invasion via Upregulation of miR-204. A previous study has reported that miR-204 is downregulated in PTC tissues and cells, and its overexpression antagonizes the tumorigenicity of PTC cells [17]. To the best of our knowledge, studies on the relationship between fentanyl and miR-204 in PTC cells are lacking. Results of qRT-PCR demonstrated that miR-204 expression was increased following 5 and 50 ng/ml fentanyl treatment (Figure 2(a)). Concentrations of fentanyl > 5 ng/ml exhibited

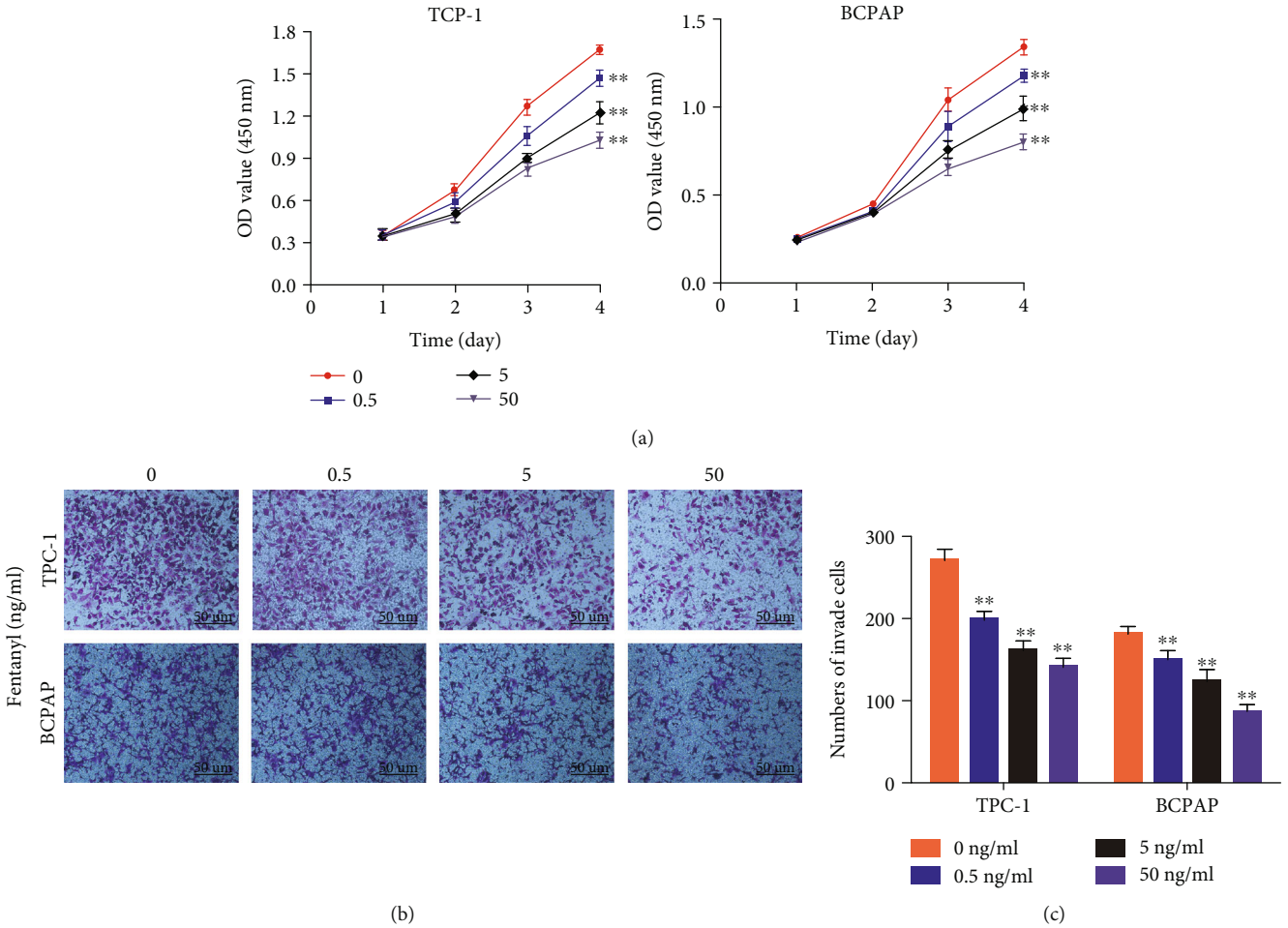

Figure 1: Fentanyl reduced the viability and invasion of PTC cells. (a) The results of CCK-8 assays indicated that fentanyl reduced the cell viability at a dosage- and time-dependent manner. Repeated measurement ANOVA with Bonferroni corrections was used for statistical analysis. (b, c) The results of Transwell invasion assays confirmed that fentanyl significantly inhibited the invasion of PTC cells. One-way ANOVA was used for statistical analysis. Symbol of ** indicates $P < 0.05$ compared with PTC cells without fentanyl stimulation.

a remarkable inhibitory promotion on miR-204-5p expressions in PTC cells, and thus, a concentration of 5 ng/ml of fentanyl was chosen for further investigations. We utilized rescue experiments to understand the role of miR-204 in fentanyl-induced anticancer effects on PTC cells. CCK-8 assays and Transwell invasion assays showed that miR-204 inhibition by its specific inhibitor facilitated TCP-1 and BCPAP cell viability and invasion, which was reversed by following fentanyl treatment (Figures 2(b)–2(d)). These results reveal that miR-204 is involved in fentanyl-induced antitumor effects on PTC.

3.3. KLF5 Was the Target of miR-204. We used miRNA target prediction websites, such as starBase and TargetScan, to ascertain underlying mechanisms of miR-204 functioning in PTC cells and analyze miR-204 candidate targets. On the basis of these bioinformatics analyses, we chose a well-known tumor promoter named KLF5 for further studies. The results of qRT-PCR and western blot analysis revealed a decrease in mRNA and protein levels of KLF5 in PTC cells transfected with miR-204 mimic (Figures 3(a) and 3(b)). Then, we found a complementary match between the seed sequence of miR-204 and the 3′UTR region of KLF5 using the starBase (Figure 3(c)). Further studies were employed to explore whether KLF5 was directly targeted by miR-204. Luciferase reporter assays showed that miR-204 mimics led to inhibitory effects on the luciferase activity of the reporter with the wide-type sequence of KLF5, whereas no significant effect was observed in the mutant group (Figure 3(d)). To further verify the relationship between miR-204 and KLF5, we performed rescue experiments. As the results of CCK-8 assays exhibited, KLF5 knockdown reduced TCP-1 and BCPAP cell viability and reversed the promotion of cell viability induced by the miR-204 inhibitor (Figure 3(e)). As expected, the results of Transwell invasion assays implied that the KLF5 knockdown inhibited TCP-1 and BCPAP cell invasion, which was negated by the miR-204 inhibitor (Figures 3(f) and 3(g)). These findings reveal that miR-204 modulates PTC cell growth by directly targeting KLF5.

3.4. Fentanyl Inhibited PTC Cell Viability and Invasion via the miR-204/KLF5 Axis. In this part, we were interested in the hypothesis that fentanyl may inhibit PTC development via the miR-204/KLF5 axis. For this purpose, more

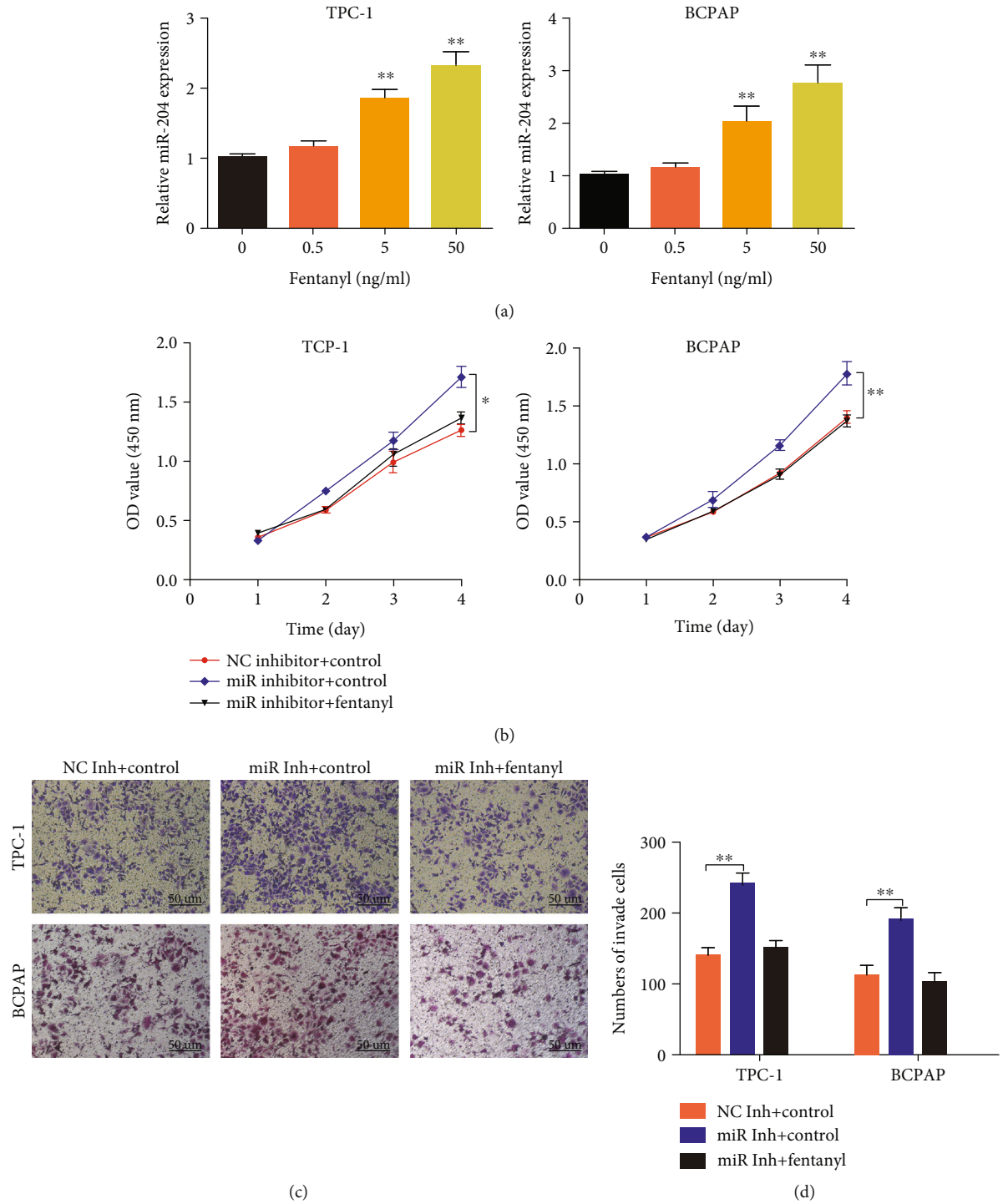

Figure 2: Fentanyl reversed the PTC cell viability and invasion via upregulation of miR-204. (a) The expression of miR-204 was increased by fentanyl treatment in a concentration-dependent manner (>5 ng/ml). (b) CCK-8 assays showed that downregulation of miR-204 reversed the suppression of cell viability caused by fentanyl. (c, d) Transwell assays demonstrated that miR-204 downregulation antagonized the anti-invasion effects induced by fentanyl. Repeated measurement ANOVA with Bonferroni corrections was used for statistical analysis in (b) and one-way ANOVA was used in other panels. $^{**}P < 0.05$.

experiments were used to verify the relationship among fentanyl, miR-204, and KLF5. The CCK-8 analysis of the present study showed that KLF5 overexpression reversed the fentanyl-mediated suppression of PTC viability (Figure 4(a)). The results of Transwell assays demonstrated that the restoration of KLF5 attenuates the enhancement of the cell invasion induced by fentanyl treatment (Figures 4(b) and 4(c)). Furthermore, our data showed that fentanyl inhibited the expression of KLF5, while this inhibition was reversed using the miR-204 inhibitor in PTC cells

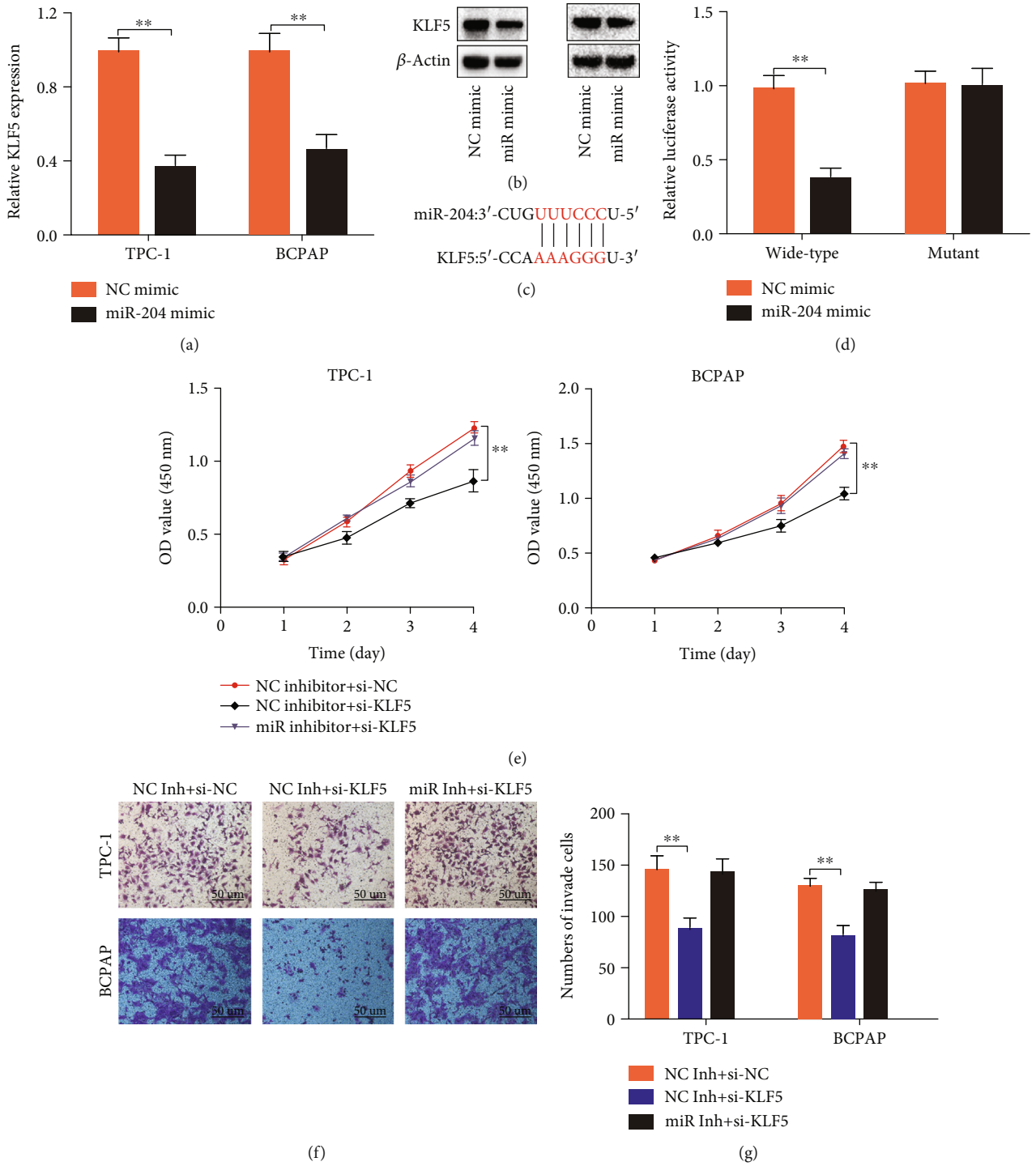

FIGURE 3: KLF5 was the target of miR-204. (a) The results of PCR showed that miR-204 overexpression inhibited the expression of KLF5 at mRNA levels. (b) The results of western blot assays also verified the miR-204 overexpression at protein levels. (c) The sequence of 3′UTR of KLF5 contained the potential binding sites for miR-204. (d) The luciferase reporter assay identified that miR-204 directly targeted KLF5. (e) The results of CCK-8 assays indicated that KLF5 knockdown reversed the positive effects on the proliferation of PTC cells induced by miR-204 inhibitor. (f, g) The results of Transwell showed that miR-204 showed its negative effects on the cell invasion via targeting KLF5. Student's *t*-test was used for statistical analysis in (a, d). Repeated measurement ANOVA with Bonferroni corrections was used in (e). One-way ANOVA was used in (e, g). $^{**}P < 0.05$.

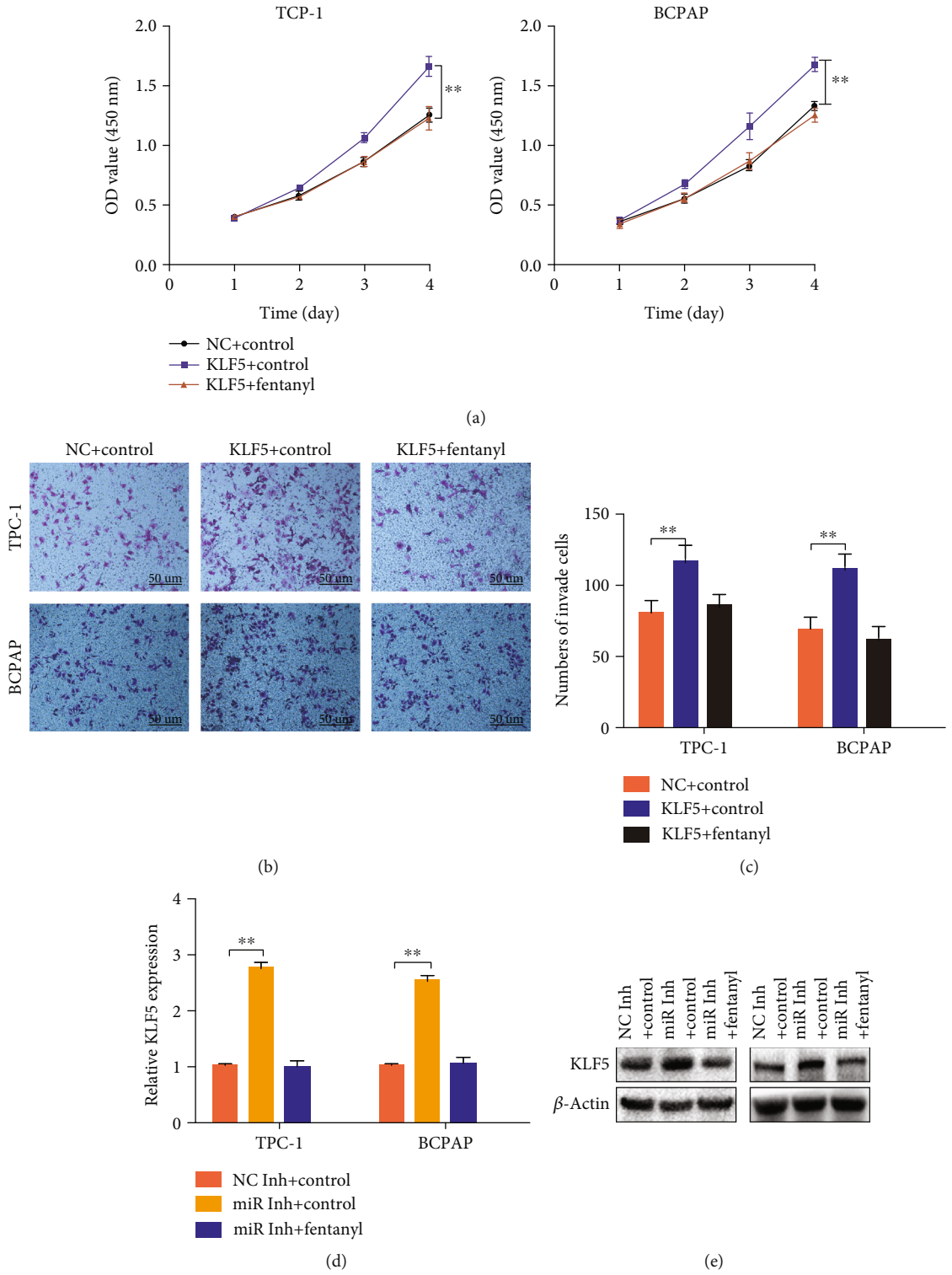

Figure 4: Fentanyl inhibited the cell viability and invasion via miR-204/KLF5 axis. (a) The CCK-8 assays were employed to explore the cell viability of PTC under fentanyl or KLF5 overexpression treatments. (b, c) The Transwell assays were used to test the cell invasion via fentanyl or KLF5 treatment. (d, e) The PCR and western blot assays were implied to detect the expressions of KLF5 under fentanyl or miR-204 inhibitor treatment. Repeated measurement ANOVA with Bonferroni corrections was used for statistical analysis in (a), and one-way ANOVA was used in other panels. $^{**}P < 0.05$.

(Figures 4(d) and 4(e)). Thus, these results indicated that fentanyl exerts its repressive effects on the cell viability and invasion via the miR-204/KLF5 axis.

4. Discussion

To date, surgery remains the predominant treatment for PTC but the distant metastasis is still the challenge of PTC patients [4]. Further investigations on underlying mechanisms of PTC tumorigenesis and metastasis are urgently required. With the advancement of anesthesia techniques, recent studies mainly focus on potential biological roles of anesthetics in tumor development. For instance, propofol showed its antitumor activity in pancreatic cancer cells by affecting miR-34a-mediated LOC285194 and E-cadherin signals [19]. Fentanyl is a commonly used as an anesthesia that exerts its antitumor effects in many human cancers. For example, fentanyl was also demonstrated to inhibit the progression of human gastric cancer [20]. Celik and Duran provided evidence that fentanyl could reduce pancreatic cancer cell proliferation and cancer stem cell differentiation [21]. Zhang et al. [22] reported that fentanyl inhibited cell proliferation and invasion of colorectal cancer cells. A previous study demonstrated that propofol resulted in upregulation of miR-320a concomitant with reduction of HMGB1 and thus suppressed cell malignant behavior in PTC [23]. However, investigations on biological functions of fentanyl in PTC tumor progression are limited.

Wang et al. [7] reported that fentanyl induces the expression of miR-302b and subsequently decreases the cell invasive and proliferative abilities of ESCC. This study suggests that fentanyl partially exerts its functions by affecting miRNA expressions. Accounting studies demonstrated that misregulated miRNAs work as tumor suppressors or promoters participating in the pathogenesis of many cancers [24]. Several researchers focused on the role of miRNAs in tumorigenesis and tumor progression and found that miR-204, an important tumor-suppressive miRNA, repressed the expression of oncogene targets and thus suppressed the growth and metastasis of cancer cells in many tumors, such as colorectal cancer, endometrial carcinoma, and breast cancer [25–27]. A previous study proved that miR-204 is downregulated in PTC cells and tissues. The results of functional experiments indicated that overexpression of miR-204 inhibits the invasion and migration of PTC cells [17]. We identified in this work that miR-204 expression was upregulated under fentanyl treatment in PTC cells and fentanyl weakened the capability of PTC cells to proliferate and invade via repression of miR-204. Therefore, our data revealed that fentanyl inhibited the viability and invasion of PTC cells by enhancing miR-204 expression. Subsequent experiments verified that KLF5 is the target of miR-204 and involved in the mechanism of antitumor role of fentanyl in PTC.

KLF5 is a zinc-finger transcription factor closely correlated with different functions in tumor development, such as cell proliferation, apoptosis, adhesion, and invasion [28]. However, the role of KLF5 in various cancers is conflicting because it serves as a tumor promoter or suppressor. Ma et al. [29] showed that KLF5 reduced STAT3 activity and tumor metastasis in prostate cancer. Sun et al. [30] reported that liver cancer cells with KLF5 knockdown displays a sharp and round shape and promotes mesenchymal-to-epithelial transition. Our experiments demonstrated that KLF5 is the target of miR-204 and functional assays revealed that KLF5 overexpression promoted PTC cell viability and invasion of PTC. Poyil et al. [18] investigated the expression of KLF5 protein in a large cohort of PTC patient samples and explored its functional role and mechanism in PTC cell lines and PTC xenograft in mouse. They found that KLF5 overexpression was observed in 65.1% of all PTC cases, and it was significantly associated with aggressive clinicopathological parameters and poor outcome. However, they failed to perform further discussion concerning the mechanism of KLF5 overexpression in PTC. Fortunately, in our study, mechanistic analyses manifested that fentanyl inhibits the cell viability and invasion via the miR-204/KLF5 axis.

5. Conclusion

In summary, our work verified the antitumor effects of fentanyl in PTC through constant stimulation that reduces cell invasive and proliferative abilities of PTC cells. Further mechanistic analyses revealed that fentanyl performs its tumor-suppressive functions by enhancing miR-204 and reducing KLF5 in PTC cells. However, further investigations are required to strengthen the involvement of miR-204 and KLF5 in the mechanism of antitumor role of fentanyl in PTC. For instance, whether fentanyl inhibited the expression of KLF5 in PTC cells in a dose-dependent manner needs to be explored. Human sample and animal experiment are warranted to support clinical translation of the important role of fentanyl in treating PTC.

Data Availability

The data used to support the findings of this study are included within the article.

Conflicts of Interest

All authors declare that they have no conflict of interest.

Acknowledgments

This work was supported by Jiangsu Province “333” project (BRA2018020).

References

[1] H. Lim, S. S. Devesa, J. A. Sosa, D. Check, and C. M. Kitahara, “Trends in thyroid cancer incidence and mortality in the United States, 1974-2013,” *JAMA*, vol. 317, no. 13, pp. 1338–1348, 2017.

[2] T. Carling and R. Udelsman, “Thyroid cancer,” *Annual Review of Medicine*, vol. 65, no. 1, pp. 125–137, 2014.

[3] H. G. Vuong, N. P. Long, N. H. Anh et al., “Papillary thyroid carcinoma with tall cell features is as aggressive as tall cell variant: a meta-analysis,” *Endocrine Connections*, vol. 7, no. 12, pp. R286–R293, 2018.

[4] R. L. Siegel, K. D. Miller, and A. Jemal, "Cancer statistics, 2020," *CA: a Cancer Journal for Clinicians*, vol. 70, no. 1, pp. 7–30, 2020.

[5] T. K. Nuckols, L. Anderson, I. Popescu et al., "Opioid prescribing: a systematic review and critical appraisal of guidelines for chronic pain," *Annals of Internal Medicine*, vol. 160, no. 1, pp. 38–47, 2014.

[6] S. Mercadante, "Fentanyl buccal tablet for the treatment of cancer-related breakthrough pain," *Expert Review of Clinical Pharmacology*, vol. 8, no. 1, pp. 9–13, 2015.

[7] N. Wang, Z. Zhang, and J. Lv, "Fentanyl inhibits proliferation and invasion via enhancing miR-302b expression in esophageal squamous cell carcinoma," *Oncology Letters*, vol. 16, no. 1, pp. 459–466, 2018.

[8] C. Li, Y. Qin, Y. Zhong et al., "Fentanyl inhibits the progression of gastric cancer through the suppression of MMP-9 via the PI3K/Akt signaling pathway," *Annals of Translational Medicine*, vol. 8, no. 4, p. 118, 2020.

[9] R. C. Lee and V. Ambros, "An extensive class of small RNAs in Caenorhabditis elegans," *Science*, vol. 294, no. 5543, pp. 862–864, 2001.

[10] Z. Wang, Y. Li, A. Ahmad et al., "Targeting miRNAs involved in cancer stem cell and EMT regulation: an emerging concept in overcoming drug resistance," *Drug Resistance Updates*, vol. 13, no. 4-5, pp. 109–118, 2010.

[11] G. Nie, H. Duan, X. Li et al., "MicroRNA205 promotes the tumorigenesis of nasopharyngeal carcinoma through targeting tumor protein p53-inducible nuclear protein 1," *Molecular Medicine Reports*, vol. 12, no. 4, pp. 5715–5722, 2015.

[12] J. Wu, L. Yin, N. Jiang et al., "MiR-145, a microRNA targeting ADAM17, inhibits the invasion and migration of nasopharyngeal carcinoma cells," *Experimental Cell Research*, vol. 338, no. 2, pp. 232–238, 2015.

[13] Y. Zhou, L. Yin, H. Li, L. H. Liu, and T. Xiao, "The LncRNA LINC00963 facilitates osteosarcoma proliferation and invasion by suppressing miR-204-3p/FN1 axis," *Cancer Biology & Therapy*, vol. 20, no. 8, pp. 1141–1148, 2019.

[14] J. Zhang, L. Xing, H. Xu et al., "miR-204-5p suppress lymph node metastasis via regulating CXCL12 and CXCR4 in gastric cancer," *Journal of Cancer*, vol. 11, no. 11, pp. 3199–3206, 2020.

[15] Y. Liang, E. Li, H. Zhang, L. Zhang, Y. Tang, and Y. Wanyan, "Silencing of lncRNA UCA1 curbs proliferation and accelerates apoptosis by repressing SIRT1 signals by targeting miR-204 in pediatric AML," *Journal of biochemical and molecular toxicology*, vol. 34, no. 3, article e22435, 2020.

[16] K. Santiago, Y. Chen Wongworawat, and S. Khan, "Differential microRNA-signatures in thyroid cancer subtypes," *Journal of Oncology*, vol. 2020, Article ID 2052396, 14 pages, 2020.

[17] L. Liu, J. Wang, X. Li et al., "MiR-204-5p suppresses cell proliferation by inhibiting IGFBP5 in papillary thyroid carcinoma," *Biochemical and Biophysical Research Communications*, vol. 457, no. 4, pp. 621–626, 2015.

[18] P. Pratheeshkumar, A. K. Siraj, S. P. Divya et al., "Prognostic value and function of KLF5 in papillary thyroid cancer,," *Cancers (Basel)*, vol. 13, no. 2, p. 185, 2021.

[19] H. Wang, H. Jiao, Z. Jiang, and R. Chen, "Propofol inhibits migration and induces apoptosis of pancreatic cancer PANC-1 cells through miR-34a-mediated E-cadherin and LOC285194 signals," *Bioengineered*, vol. 11, no. 1, pp. 510–521, 2020.

[20] Y. Qin, L. Li, J. Chen et al., "Fentanyl inhibits progression of human gastric cancer MGC-803 cells by NF-κB downregulation and PTEN upregulation in vitro," *Oncology Research*, vol. 20, no. 2, pp. 61–69, 2012.

[21] F. Celik and T. Duran, "Effects of fentanyl on pancreatic cancer cell proliferation and cancer stem cell differentiation," *Cellular and Molecular Biology (Noisy-le-Grand, France)*, vol. 65, no. 7, pp. 21–25, 2019.

[22] X. L. Zhang, M. L. Chen, and S. L. Zhou, "Fentanyl inhibits proliferation and invasion of colorectal cancer via β-catenin," *International Journal of Clinical and Experimental Pathology*, vol. 8, no. 1, pp. 227–235, 2015.

[23] M. Li, L. Qu, F. Chen, and X. Zhu, "Propofol upregulates miR-320a and reduces HMGB1 by downregulating ANRIL to inhibit PTC cell malignant behaviors," *Pathology-Research and Practice*, vol. 216, no. 4, article 152856, 2020.

[24] D. F. Dai, Y. W. Tan, L. F. Guo, A. F. Tang, and Y. S. Zhao, "Identification of exosomal miRNA biomarkers for diagnosis of papillary thyroid cancer by small RNA sequencing," *European Journal of Endocrinology*, vol. 182, no. 1, pp. 111–121, 2020.

[25] C. C. Huang, C. H. Hung, T. W. Hung, Y. C. Lin, C. J. Wang, and S. H. Kao, "Dietary delphinidin inhibits human colorectal cancer metastasis associating with upregulation of miR-204-3p and suppression of the integrin/FAK axis," *Scientific reports*, vol. 9, no. 1, article 18954, 2019.

[26] T. K. Chung, T. S. Lau, T. H. Cheung et al., "Dysregulation of microRNA-204 mediates migration and invasion of endometrial cancer by regulating FOXC1," *International Journal of Cancer*, vol. 130, no. 5, pp. 1036–1045, 2012.

[27] J. Zeng, G. Li, Y. Xia et al., "miR-204/COX5A axis contributes to invasion and chemotherapy resistance in estrogen receptor-positive breast cancers," *Cancer Letters*, vol. 492, pp. 185–196, 2020.

[28] R. Liu, P. G. Shi, Z. M. Zhou et al., "Krüpple-like factor 5 is essential for mammary gland development and tumorigenesis," *The Journal of Pathology*, vol. 246, no. 4, pp. 497–507, 2018.

[29] J. B. Ma, J. Y. Bai, H. B. Zhang et al., "KLF5 inhibits STAT3 activity and tumor metastasis in prostate cancer by suppressing IGF1 transcription cooperatively with HDAC1," *Cell death & disease*, vol. 11, no. 6, p. 466, 2020.

[30] L. Zhang, Y. Wu, J. Wu et al., "KLF5-mediated COX2 upregulation contributes to tumorigenesis driven by PTEN deficiency," *Cellular Signalling*, vol. 75, article 109767, 2020.

Hindawi
Journal of Nanomaterials
Volume 2021, Article ID 5521899, 9 pages
https://doi.org/10.1155/2021/5521899

Research Article

Ginsenoside Compound K Promotes Intestinal Peristalsis and the Pharmacokinetic of Metabolite 20(S)-Protopanaxadiol in Relation to Diarrhea

Lulu Chen,[1,2] Luping Zhou,[2] Xiangchang Zeng,[2] Jianwei Liao,[2] Guoping Yang,[3] Zhirong Tan,[2] Dongsheng Ouyang,[1,2] and Zhenyu Li[4]

[1]*Hunan Key Laboratory for Bioanalysis of Complex Matrix Samples, Changsha 411000, Hunan, China*
[2]*Institute of Clinical Pharmacology, Central South University, Hunan Key Laboratory of Pharmacogenetics, 110 Xiangya Road, Changsha 410078, China*
[3]*Center of Clinical Pharmacology, Third Xiangya Hospital, Central South University, Changsha 410013, China*
[4]*Department of Geriatric Medicine, Xiangya Hospital, Central South University, Changsha 410013, China*

Correspondence should be addressed to Dongsheng Ouyang; 801940@csu.edu.cn and Zhenyu Li; liyu1552@csu.edu.cn

Received 1 February 2021; Revised 14 February 2021; Accepted 3 March 2021; Published 18 March 2021

Academic Editor: Tingting Hong

Ginsenoside compound K (G-CK) is a rare ginsenoside originating from the traditional herbal medicine ginseng. Recently, G-CK has been found to cause diarrhea in preclinical researches as a candidate drug. This study is aimed at the potential mechanism of G-CK-induced diarrhea. In this study, we found that the treatment of G-CK significantly increased the peristaltic index (PI) with the intragastric administration of charcoal meal suspension at 90 minutes (not 30 min) after the administration of G-CK and had a clear role in promoting defecation. The Ach and 5-HT levels in colon tissue were not affected by G-CK. Additionally, the clinical trial revealed that subjects with diarrhea had lower exposure and higher Vz/*F* of 20(S)-protopanaxadiol (PPD) than nondiarrhea subjects, and there were no statistical differences in the pharmacokinetic parameters of G-CK between diarrhea and nondiarrhea subjects. We therefore concluded that the increased intestinal peristalsis and metabolite 20(S)-PPD were involved in G-CK-induced diarrhea.

1. Introduction

Ginsenoside compound K (G-CK) is a product of the degradation of natural protopanaxadiol- (PPD-) type ginsenosides, including Rb1, Rb2, and Rc [1]. It can be further biotransformed into 20(S)-PPD [2]. G-CK has been identified as an active substance in ginseng with multiple beneficial pharmacological properties [3–5] but regrettably has not been utilized as a clinical medication since its discovery in 1972 [6]. In view of the fact that G-CK exhibits satisfactory anti-inflammatory activity [7], Hisun (Hisun Pharmaceutical Co., Ltd., Taizhou, China) has submitted an Investigational New Drug Application (INDA) to the China Food and Drug Administration (CFDA) and aims to develop G-CK as an antirheumatoid arthritis (RA) candidate drug. Ginseng is a traditional herbal medicine, extensively used in Asia for its beneficial effects [8]. But diarrhea is identified as a common side effect of ginseng [9], with the mechanism remaining unclear. In the preclinical safety evaluation and small-scale clinical trial, we found that G-CK treatment leads to soft stool and loose stool. However, the mechanism of G-CK-induced diarrhea has never been reported.

Drug-induced diarrhea (DID) is a common adverse drug reaction, accounting for about 7% of all adverse drug reactions [10]. Diarrhea can affect the normal physiological function of the intestinal tract, thereby reducing the absorption of drugs and nutrients. It can also cause extreme discomfort to patients and greatly reduce their medication

compliance. Therefore, it is necessary to investigate the mechanism behind diarrhea for candidate drugs and to solve it effectively.

Several potentially overlapping mechanisms have been hypothesized to cause DID. The pathophysiology of DID can be described as involving the following mechanisms: osmotic, inflammatory, motility, and secretory [11].

The cystic fibrosis transmembrane regulator (CFTR) has been reported to be closely related to the pathogenesis of diarrhea. The overactivation of CFTR leads to excessive secretion of fluid from the intestinal wall into the enteral cavity, promoting intestinal peristalsis [12]. In addition, the neurotransmitters such as acetylcholine (Ach) and serotonin (5-HT) act on the smooth muscle of the gastrointestinal tract to promote gastrointestinal motility and contribute to diarrhea finally [13]. We observed that G-CK did not make the intestines in a hypertonic state (Figure S1) in our preliminary experiment. Both results from Liu et al. and our early study suggested that G-CK and 20(S)-PPD may interact with CFTR [14, 15]. Additionally, multiple studies have indicated that ginsenoside Rb1 can facilitate the release of acetylcholine (Ach) from nerve terminals [16–18]. Ginsenoside Rb1 can be metabolized to G-CK, and 20(S)-PPD is the metabolite of G-CK [1]. Therefore, we made a hypothesis that the change of CFTR activity and gastrointestinal motility might be causes of diarrhea induced by G-CK.

To summarize, we selected Ach, 5-HT, and CFTR as the research targets to clarify the mechanism of G-CK-induced diarrhea, which is aimed at providing a theoretical basis for follow-up clinical trials and clinical applications of G-CK.

2. Materials and Methods

2.1. Materials. G-CK (98% purity) and Ginsenoside Compound K Tablet were obtained from Hisun Pharmaceutical Co., Ltd. (Taizhou, Zhejiang, China). The following kits were purchased from the cited commercial sources: Acetylcholine Assay Kit (Nanjing Jiancheng Bioengineering Institute, Nanjing, China) and Mouse 5-Hydroxytryptamine (5-HT) ELISA Kit (CusAB, Wuhan, China).

2.2. Clinical Trial. Subjects included in the study were screened from two clinical trials under the approval (CDEL20130379) by the China Food and Drug Administration (CFDA). These trials were approved with No.14050 (single-dose trial) and No.14119 (food-effect trial) by the independent ethics committee of the Third Xiangya Hospital affiliated to Central South University and were in accordance with the Declaration of Helsinki and the International Conference of Harmonization guidelines for Good Clinical Practice. The registration numbers were ChiCTR-TRC-14004824 and ChiCTR-IPR-15005787 (http://www.chictr.org.cn/index.aspx). The design of these clinical trials and participant recruitment were described particularly in previous articles [15, 19, 20]. It is especially necessary to mention that all the enrolled subjects had no history of gastrointestinal diseases or gastrointestinal dysfunction.

Blood samples (5 mL) for pharmacokinetic (PK) analysis were collected from each participant. Plasma concentrations of G-CK and 20(S)-PPD were measured using mass spectrometry and liquid chromatography-tandem mass spectrometry (LC-MS/MS, API 4000, ABI Company), in both trials. The plasma samples were stored and analyzed at the chromatography laboratory, Institute of Clinical Pharmacology, Central South University (Changsha, China). Detailed introduction of the collection method of the blood sample and the detection method of plasma concentration were presented in the earlier articles [15, 19, 20].

All the PK parameters were assessed by the WinNonlin version 6.1 (Pharsight Corporation, Mountain View, CA, USA). The maximum concentrations (C_{max}), minimum plasma concentrations at steady state ($C_{min,ss}$), and time to maximum plasma concentration (t_{max}) could be obtained from the plasma concentration or plasma concentration-time data directly. The area under the plasma concentration-time curve is AUC and from time 0 to the last observation AUC_{last}. The AUC for dosing interval was expressed as AU C_τ, where τ is the dosing interval (24 h). The average steady-state drug concentration (C_{avg}) is calculated as AUC_τ/τ. The elimination rate constant (K) was determined by linear regression analysis of the log-linear part of the plasma concentration-time curve. The half-life ($t_{1/2}$) was calculated based on the elimination rate constant, as equal to $(\ln 2)/K$. The apparent clearance (CL/F) and apparent volume of distribution (Vz/F) were also obtained. Additionally, the dose-normalized (to 1 mg of CK) C_{max} (C_{max}/D), $C_{min,ss}$ ($C_{min,ss}/D$), C_{avg} (C_{avg}/D), AUC_{last} (AUC_{last}/D), and AUC_τ (AUC_τ/D) were calculated by dividing each PK result with the homologous dosage of G-CK.

2.3. Cell Experiment

2.3.1. Cell Line. The cell line used throughout this study consisted of FRT cells stably cotransfected with the EYFP-H148Q fluorescence protein and human wild-type CFTR cDNA. FRT cells were cultured in Nutrient F12 coon's medium (Sigma Chemical Co., St. Louis, MO, USA). The media were supplemented with 10% fetal bovine serum (HyClone company, USA), 500 U/ml penicillin, 500 U/ml streptomycin, and 2 mM L-glutamine. The cells were incubated in a 5% CO_2 incubator maintained at 37°C and 90% humidity for 36 hours.

2.3.2. Iodide Influx Fluorescent Assay. FRT cells transfected with CFTR were plated in a black 96-well plate with a clear bottom (Costar, Corning, NY, USA) at a density of 2×10^4 cells/well and incubated until confluent. The cells were washed three times with 300 μl PBS. After that, 50 μl PBS with 0.1 μM FSK and different concentrations of the test compound, G-CK (3.90 μM-1000 μM) or genistein (0.78 μM-200 μM), were added to each well. Ten minutes later, EYFP fluorescence data were recorded using a FLUOstar Galaxy microplate reader (BMG Lab Technologies, Inc.) equipped with HQ500/20X (500 ± 10 nm) excitation, HQ 535/30M (535 ± 15 nm) emission filters (Chroma Technology Corp.), and syringe pumps. Iodide influx rates ($d[I^-]/dt$) were computed as described by Kristidis et al. [21].

Table 1: Demographics of the study participants.

Sample	N^a	Nondiarrhea				Diarrhea			
		Age (years)	Height (m)	Weight (kg)	BMI ($kg \cdot m^{-2}$)	Age (years)	Height (m)	Weight (kg)	BMI ($kg \cdot m^{-2}$)
Sample 1	30	21 ± 3	1.64 ± 0.08	57.64 ± 9.35	21.08 ± 1.51	21 ± 2	1.62 ± 0.10	59.50 ± 10.10	22.59 ± 1.38
Sample 2	24	23 ± 3	1.65 ± 0.07	58.60 ± 7.22	21.53 ± 1.60	24 ± 4	1.68 ± 0.05	56.88 ± 5.33	20.45 ± 1.66
Sample 3	28	24 ± 3	1.66 ± 0.07	59.25 ± 6.73	21.37 ± 1.40	23 ± 3	1.62 ± 0.09	55.00 ± 7.00	20.94 ± 1.18

Sample 1 was pooled from three dose (100, 200, and 400 mg G-CK) groups of the single-dose trial; sample 2 was pooled from the food-effect trial (200 mg of G-CK under the fed condition); sample 3 was pooled from three dose (100, 200, and 400 mg G-CK) groups of the multiple-dose trial. All values are presented as the mean ± SD. SD: standard deviation; G-CK: ginsenoside compound K; BMI: body mass index. [a]Number of participants. Diarrhea *vs.* nondiarrhea: the independent sample *t*-test.

2.4. Animal Experiment

2.4.1. Animals. Imprinting Control Region strain male mice (weight 18-22 g, 6-8 weeks old) were supplied by the Hunan SJA Laboratory Animal Co. Ltd. (Changsha, China). The mice were housed at a temperature of 20-22°C and humidity of 70-75%, with a 12-hour light-dark cycle, and food and water administered *ad libitum*. All experimental protocols were endorsed by the Ethics Committee of Hunan Research Center for Drug Safety Evaluation and were in strict accordance with the National Institutes of Health *Guide for the Care and Use of Laboratory Animals* (NIH Publications No. 80-23, revised 1996). All possible efforts were done to ensure that the animals were comfortable.

2.4.2. Intestinal Transit. Intestinal transit in mice was measured using the charcoal meal test. The mice were assigned randomly to the following three groups: the vehicle control group received 0.5% CMC-Na suspension at 20 ml/kg body weight orally, while two treatment groups received G-CK at 50 and 250 mg/kg body weight orally, respectively. The test animals were fasted for 16 hours prior to the experiment but were allowed free access to water. These subsequently received a single dose of G-CK or vehicle by intragastric gavage. After 30 minutes or 90 minutes of the administration, 0.2 ml of charcoal meal suspension (5% charcoal in 0.5% CMC-Na) was given to each mouse by intragastric gavage. Thirty minutes later, the animals in each group were sacrificed, and the whole small intestines were isolated immediately. The peristaltic index (PI) was calculated for each mouse as the distance traveled by charcoal as a percentage of the total length of the small intestine (pyloric sphincter to caecum) [22].

2.4.3. Measurement of the Frequency of Defecation. In addition to the charcoal meal transit test, the frequency of defecation was also measured to investigate the impact of G-CK on intestinal peristalsis. The mice were included and randomly allotted to three groups: vehicle control group (0.5% CMC-Na, 20 ml/kg) and LCK (50 mg/kg G-CK) and HCK (250 mg/kg G-CK) treatment groups. After the single-dose administration, all animals were put into different cages (one mouse in each cage) with filter paper. The frequency of defecation was measured every hour until 6 h after the administration.

2.4.4. Single-Dose Treatment of G-CK on Mice. In the single-dose treatment experiment, thirty animals were randomly divided into three groups ($n = 10$): vehicle control (0.5% CMC-Na, 20 ml/kg), LCK, and HCK groups. After 16 hours of fasting, each animal was treated with a corresponding treatment of G-CK or vehicle. Three hours later, the animals were sacrificed for the colon tissues which were washed with ice-cold physiological saline and put into a 2 ml cryogenic vial to be stored in liquid nitrogen until use.

2.4.5. Measurement of Colonic Ach and 5-HT Concentrations. Concentrations of colonic Ach and 5-HT were detected using the Acetylcholine Assay Kit, Mouse CREB ELISA Kit, and Mouse 5-HT ELISA Kit, respectively, according to the manufacturers' manuals.

2.5. Statistical Analysis. Values of PK parameters were also represented as the mean ± standard deviation (SD), except for t_{max} which was expressed as the median (range). The independent sample *t*-test was applied on logarithmic transformed C_{max}/D, AUC_{last}/D, $t_{1/2}$, Vz/F, and CL/F, and nonparametric tests were performed on t_{max}, to determine whether there is a significant difference in the PK parameters between diarrhea and nondiarrhea subjects.

All results of the peristaltic index, defecation frequency, colonic Ach, and 5-HT concentrations in colon tissues were expressed as the mean ± standard deviation (SD), and one-way ANOVA was used to compare group differences, followed by Dunnett *t*-tests for multiple comparisons.

Data were analyzed using SPSS v.22.0 (SPSS Inc., USA). Values of $p < 0.05$ were considered statistically significant.

3. Results

3.1. The Relationship between Pharmacokinetics and Diarrhea. A total of 30 subjects from the single-dose trial (sample 1), 24 subjects from the food-effect trial (sample 2), and 28 subjects from the multiple-dose trial (sample 3) were included in this analysis based on the sample size and the evaluation of the dose proportionality [20]. Five, four, and thirteen subjects had diarrhea from the single-dose trial, food-effect trial, and multiple-dose trial, respectively. The baseline demographics including age, height, weight, and body mass index (BMI) are presented as the mean ± SD and provided in Table 1. There were no statistical differences

Table 2: The relationship between pharmacokinetics and diarrhea.

Parameters	Sample 1		Sample 2		Sample 3	
	Nondiarrhea ($n = 25$)	Diarrhea ($n = 5$)	Nondiarrhea ($n = 20$)	Diarrhea ($n = 4$)	Nondiarrhea ($n = 15$)	Diarrhea ($n = 13$)
G-CK						
C_{max}/D (ng·ml^{-1})	3.57 ± 2.45	3.51 ± 2.21	8.16 ± 3.08	6.30 ± 1.51	24.15 ± 11.71	16.18 ± 7.38
$C_{min,ss}/D$ (ng·ml^{-1})	—	—	—	—	7.79 ± 3.79	5.38 ± 2.10
C_{avg}/D (ng·ml^{-1})	—	—	—	—	1.54 ± 0.68	1.19 ± 0.42
AUC_{last}/D (h·ng·ml^{-1})	29.43 ± 23.40	28.22 ± 17.03	63.33 ± 20.91	61.32 ± 21.12	239.48 ± 116.80	168.36 ± 62.58
AUC_{τ}/D (h·ng·ml^{-1})	—	—	—	—	187.04 ± 90.93	129.19 ± 50.37
Vz/F (l)	1434.96 ± 637.65	1200.00 ± 588.26	650.37 ± 406.46	661.29 ± 262.49	572.59 ± 202.16	510.41 ± 232.53
CL/F (l·h^{-1})	47.82 ± 24.23	43.08 ± 18.34	18.33 ± 10.49	17.49 ± 6.18	11.97 ± 4.15	9.89 ± 2.55
$t_{1/2}$ (h)	22.21 ± 4.54	20.60 ± 6.88	24.51 ± 2.71	26.08 ± 4.58	34.49 ± 9.66	34.86 ± 11.03
t_{max} (h)	3.00 (2.00-6.00)	3.00 (2.50-6.00)	2.25 (1.50-5.00)	2.50 (1.50-3.50)	3.50 (1.50-5.00)	3.50 (1.50-5.00)
20(S)-PPD						
C_{max}/D (ng·ml^{-1})[a]	0.035 ± 0.035	0.008 ± 0.003**	0.021 ± 0.015	0.003 ± 0.002**	0.048 ± 0.030	0.024 ± 0.021*
$C_{min,ss}/D$ (ng·ml^{-1})[a]	—	—	—	—	0.020 ± 0.016	0.009 ± 0.010*
C_{avg}/D (ng·ml^{-1})[a]	—	—	—	—	0.033 ± 0.022	0.014 ± 0.013**
AUC_{last}/D (h·ng·ml^{-1})	0.99 ± 0.97	0.25 ± 0.15	0.63 ± 0.48	0.10 ± 0.05*	1.58 ± 1.04	0.80 ± 0.94*
AUC_{τ}/D (h·ng·ml^{-1})	—	—	—	—	0.79 ± 0.54	0.34 ± 0.30**
Vz/F (l)	79354.83 ± 113809.94	121513.00 ± 9200.87[b]	53043.11 ± 48210.92	—[c]	136169.43 ± 361901.90	373907.03 ± 566133.57**
CL/F (l·h^{-1})	2546.82 ± 3692.48	2509.85 ± 626.72[b]	1558.00 ± 793.29	—[c]	2356.27 ± 2894.14	5736.78 ± 4136.67**
$t_{1/2}$ (h)	37.29 ± 90.42	34.30 ± 6.08	21.24 ± 9.74	—[c]	22.33 ± 17.07	43.38 ± 43.45
t_{max} (h)	24.00 (5.00-48.00)	24.00 (12.00-36.00)	24.00 (24.00-36.00)	24.00 (24.00-24.00)	6.00 (0.25-24.00)	6.00 (0.25-24.00)

C_{max}/D: the maximum plasma concentration normalized to doses of G-CK; $C_{min,ss}/D$: the minimum concentrations normalized to doses of G-CK; C_{avg}/D: the average concentration normalized to doses of G-CK; AUC_{last}/D: the area under the plasma concentration-time curve from zero to the time of the last quantifiable concentration normalized to doses of G-CK; AUC_{τ}/D: the area under the plasma concentration-time curve from zero to 24 h normalized to doses of G-CK; Vz/F: apparent volume of distribution after extravascular administration; CL/F: the apparent plasma clearance of the drug after extravascular administration; $t_{1/2}$: terminal half-life; t_{max}: time to maximum plasma concentration. Sample 1 was pooled from three dose (100, 200, and 400 mg G-CK) groups of the single-dose trial; sample 2.

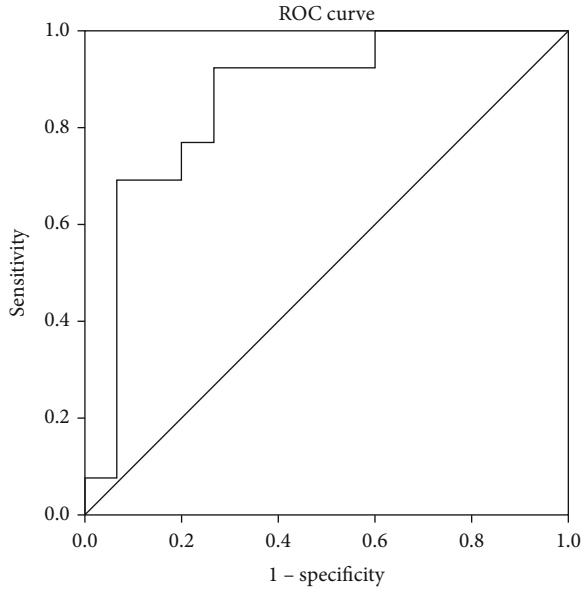

Figure 1: The ROC curve for Vz/F of 20(S)-PPD. The areas under the ROC curve for Vz/F was 0.856 (SE 0.075, 95% C.I. 0.709-1.000, $p = 0.001$). Vz/F: apparent volume of distribution after extravascular administration; 20(S)-PPD: 20(S)-protopanoxadiol; SE: standard error; C.I.: confidence intervals of the areas under the ROC curve.

in age, height, weight, or BMI between diarrhea and nondiarrhea subjects in sample 1, sample 2, or sample 3.

The PK parameters of G-CK and 20(S)-PPD in diarrhea and nondiarrhea subjects are summarized in Table 2. The PK parameters including C_{max}/D, $C_{min,ss}/D$, C_{avg}/D, AUC_{last}/D, AUC_{τ}/D, Vz/F, CL/F, $t_{1/2}$, and t_{max} were used in these comparative analyses. The results showed that there were no statistical differences in all the PK parameters of G-CK analyzed in this study and $t_{1/2}$ and t_{max} of 20(S)-PPD between diarrhea and nondiarrhea subjects (Table 1). Caught by surprise, Vz/F and CL/F in diarrhea subjects were significantly higher than that of nondiarrhea subjects. In diarrhea subjects, the exposure of 20(S)-PPD characterised by the values of C_{max}/D, $C_{min,ss}/D$, C_{avg}/D, AUC_{last}/D, and AUC_{τ}/D were obviously lower than that of nondiarrhea subjects. In a binary logistic regression model, only the Vz/F (beta = 1.120, $p = 0.015$) showed a significant correlation with diarrhea in sample 3. The ROC curves of Vz/F are shown in Figure 1. The areas under the ROC curve for Vz/F in sample 3 were 0.856 (SE 0.075, 95% C.I. 0.709-1.000, $p = 0.001$). The cut-off value was defined as the corresponding value of the parameter, when the value of the sensitivity minus (1-specificity) was maxima. The sensitivity and specificity for the cut-off point of Vz/$F \geq 56980.31$ l were 92.31% and 73.33%, respectively.

3.2. Effects of G-CK on CFTR Chloride Channel Activity. The effect of G-CK on CFTR chloride channel activity was evaluated using a cell-based fluorescence assay. Genistein was used as a positive control and PBS as a negative control. The Fischer rat thyroid epithelial (FRT) cells were incubated with different concentrations of G-CK for 10 min, and I^- was then pumped into each well in the presence of 0.1 μM forskolin (FSK). The EC_{50} of G-CK was 224.7 μM, which suggested that G-CK has a negligible effect on CFTR chloride channel activity (Figure 2).

3.3. Effects of G-CK on Peristaltic Index and Defecation Frequency. To investigate the effects of G-CK on the PI in mice, 0.2 ml of charcoal meal suspension (5% charcoal in 0.5% CMC-Na) was administered to each animal 30 or 90 minutes after treatment with G-CK. The results revealed that 90 minutes after the administration of G-CK, both low dosage (LCK; 50 mg/kg G-CK) and high dosage (HCK; 250 mg/kg G-CK) observably stimulated intestinal transit in mice when compared to the control group (Figure 3). This phenomenon had not been observed under the condition that charcoal meal suspension was given 30 minutes after the administration of G-CK. HCK significantly increased the frequency of defecation compared with the control and LCK groups every hour from 1 h to 4 h after treatment (Figure 3). We also observed that treatment with G-CK caused the mice to produce soft stools and watery stools; the latter was observed only in one mouse from the HCK group.

3.4. Effects of G-CK on Ach and 5-HT Levels in Colon Tissues. For the exact facilitating role of G-CK in gastrointestinal motility, the detection of the neurotransmitter level was preferred. To examine the potential contribution of Ach and 5-HT to G-CK-induced diarrhea, we used the corresponding test kits to evaluate their concentrations in colon tissues. These results indicated that LCK and HCK had no effect on the levels of Ach and 5-HT. All of the above results are presented in Figure 4.

4. Discussion

Ginseng is generally well tolerated in adults and is "generally recognized as safe" by the U.S. Food and Drug Administration. Diarrhea is a common side effect of ginseng and G-CK. In this study, it was proved that G-CK did induce diarrhea both in healthy volunteers and mice, and we first investigated the potential mechanism of diarrhea induced by G-CK. The outline of this study is shown in Figure 5.

Results from clinical trials indicated that G-CK caused diarrhea [19, 20]. It has been reported that some substrates or inhibitors of multidrug resistance-associated protein 4 (MRP4) could activate CFTR-mediated chloride flow by inhibiting MRP4-mediated cAMP efflux [12, 23]. Overactivation of the CFTR channel leads to excessive secretion of fluid from the intestinal wall into the enteral cavity, resulting in secretory diarrhea [12]. In our previous research, we found that G-CK might be the substrate of multidrug resistance protein 4 (MRP4) [15]. In addition, the effect of 20(S)-PPD (the metabolite of G-CK) on CFTR activity has been reported in the literature [14]. Therefore, we analyzed the correlation between diarrhea and pharmacokinetic parameters of G-CK and 20(S)-PPD. Results in the present study indicated that there was no correlation between pharmacokinetic parameters of G-CK and diarrhea, and the diarrhea subjects had a

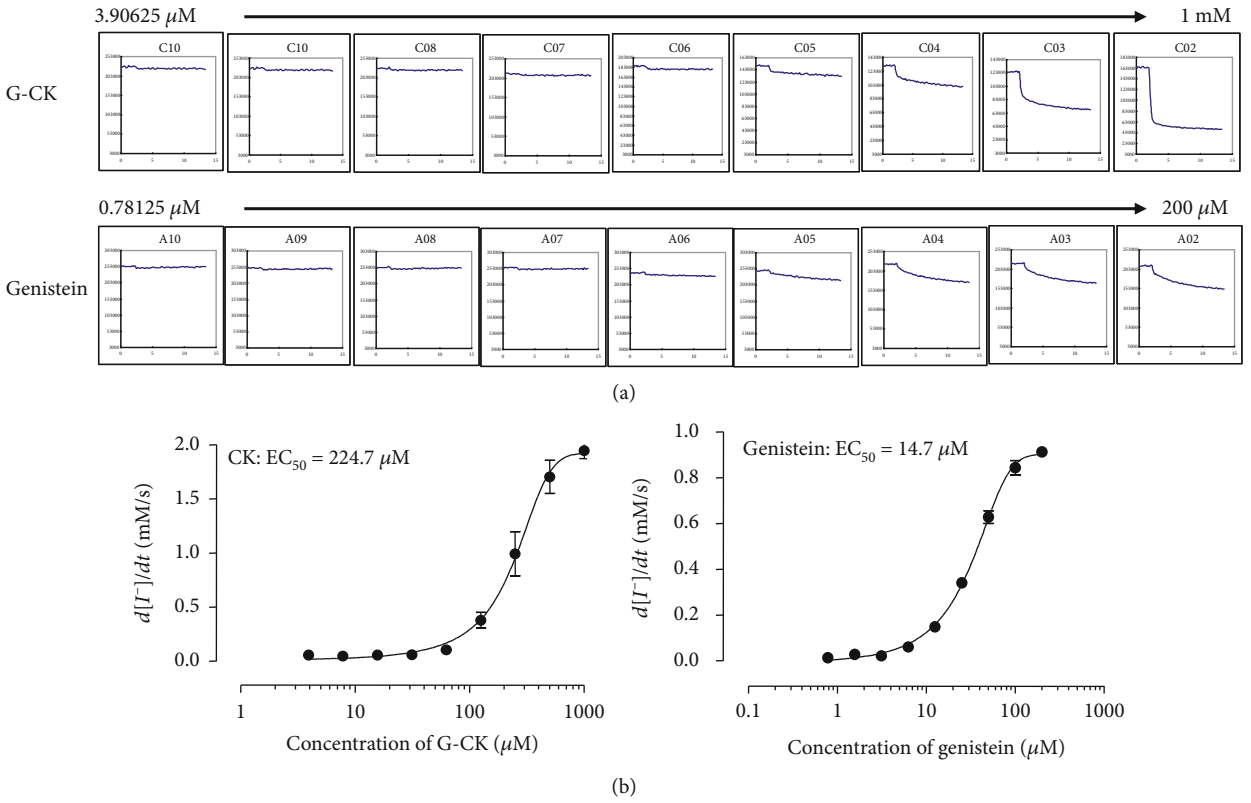

Figure 2: Effects of G-CK on CFTR chloride channel activity: (a) concentration-response curve for G-CK; (b) concentration-response curve for the genistein positive control. G-CK: ginsenoside compound K; CFTR: cystic fibrosis transmembrane conductance regulator.

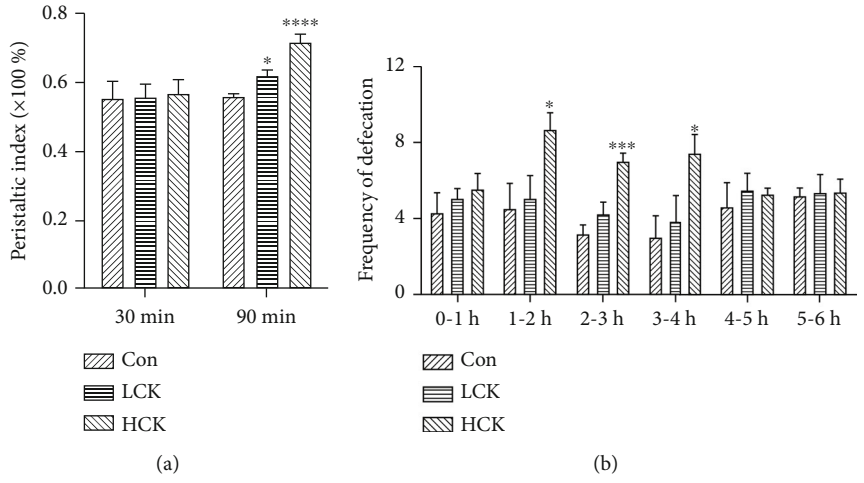

Figure 3: Effects of G-CK on the peristaltic index and frequency of defecation in mice. (a) Effects of G-CK on the peristaltic index when the charcoal meal suspension was given at 30 minutes and 90 minutes after the administration of G-CK; (b) effects of G-CK on the frequency of defecation per hour. Con: 0.5% CMC-Na; LCK: low dose of G-CK (50 mg/kg G-CK); HCK: high dose of G-CK (250 mg/kg G-CK). Values are expressed as the mean ± SD, $n = 10$ per group. SD: standard deviation. $^{*}p < 0.05$, $^{***}p < 0.001$, and $^{****}p < 0.0001$ *vs.* control group (one-way ANOVA followed by Dunnett *t*-tests).

higher Vz/*F* and lower exposure of 20(S)-PPD than nondiarrhea subjects. ROC analysis showed that the high Vz/*F* of 20(S)-protopanaxadiol (PPD) predicted diarrhea in healthy volunteers. Some studies showed that G-CK and 20(S)-PPD in the circulation were mostly excreted into the bile [24, 25]; the higher Vz/*F* in diarrhea subjects suggested a possibility that there were more 20(S)-PPD enriched in the liver and excreted into the bile. Thus, we suspected that G-CK might not affect the activity of CFTR. In order to verify this hypothesis, we explored the impact of G-CK on the CFTR activity *in vitro*. The result indicated that G-CK did not affect the CFTR activity.

Then, we put forward another hypothesis; diarrhea caused by G-CK cannot be separated from absorption; thus,

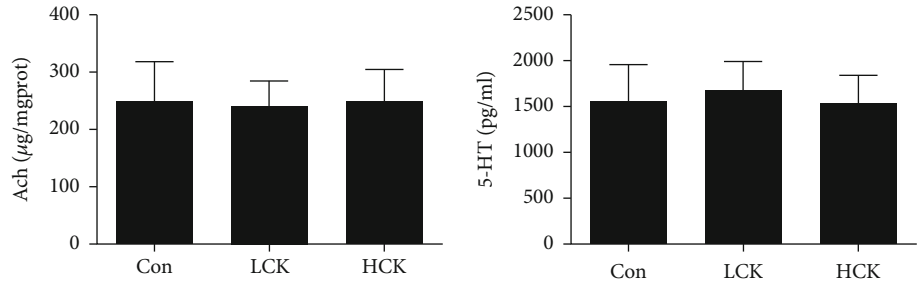

Figure 4: Effects of G-CK on Ach and 5-HT levels in colon tissues. Con: 0.5% CMC-Na; LCK: low dose of G-CK (50 mg/kg G-CK); HCK: high dose of G-CK (250 mg/kg G-CK). Values are expressed as the mean ± SD, $n = 10$ per group. SD: standard deviation (one-way ANOVA followed by Dunnett t-tests).

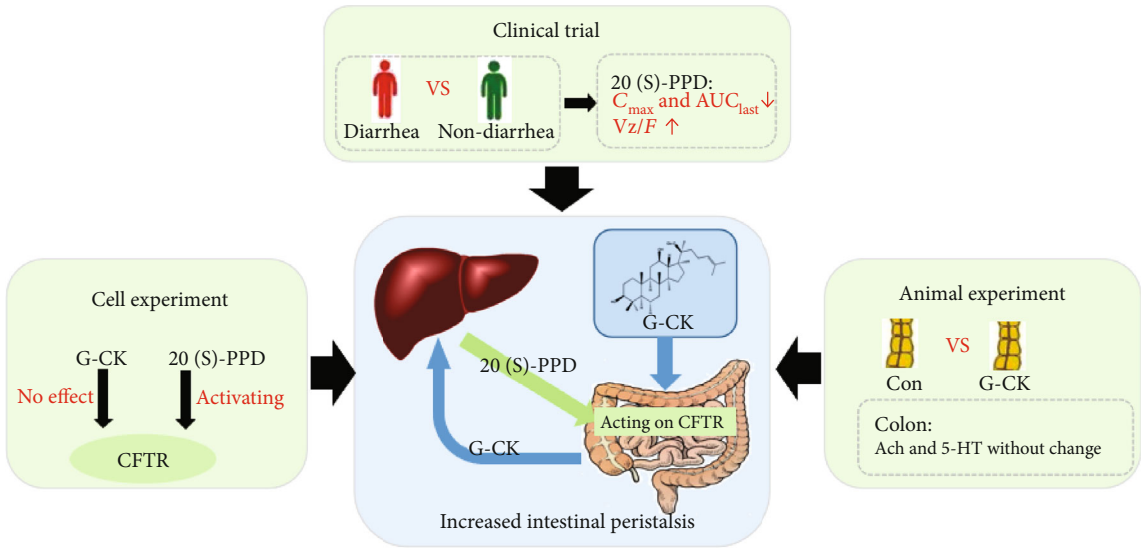

Figure 5: Outline of the present study. G-CK: ginsenoside compound K; 20(S)-PPD: 20(S)-protopanoxadiol; CFTR: cystic fibrosis transmembrane conductance regulator.

the effect of G-CK on the peristaltic index and frequency of defecation were detected. The charcoal meal transit test and the frequency of defecation are classical methods used to assess gastrointestinal motility [26–29]. In this study, the charcoal meal was administered at thirty minutes and 90 minutes (for t_{max} of G-CK is 1.5 h to 3 h in mice) after the G-CK treatment. This test manifested that the charcoal meal forward was urged with the pretreatment of G-CK for 90 min, but not 30 min. In addition, HCK obviously boosted the frequency of defecation in 1-4 h and did not affect that of 0-1 h. This phenomenon further suggested that the absorption was the basis for G-CK to cause diarrhea.

Except CFTR, we also investigated the role of Ach and 5-HT in diarrhea of G-CK. Ach and 5-HT are important neurotransmitters, which play a critical role in the stimulation of the gastrointestinal smooth muscle. Ach is released into the synaptic gap and causes various physiological changes, when the nerve impulse reaches the nerve endings and causes presynaptic membrane depolarization. Once separated from the receptor, Ach is rapidly hydrolyzed by acetylcholinesterase into choline and acetic acid. 90% of 5-HT molecules in the body are synthesized, secreted, and exerted by enterochromaffin cells (EC) in the intestine. In the present study, the G-CK did not disturb the content of Ach and 5-HT in the colon tissues.

5. Conclusions

In this study, it was proved that G-CK did induce diarrhea in the animal model and healthy volunteers, and we first investigated the potential mechanism of diarrhea induced by G-CK. The main results include a clear correlation between higher Vz/F of 20(S)-PPD and diarrhea, no activation of G-CK on CFTR, time-dependent promotional effect of G-CK on PI, and no effect of G-CK on colonic Ach and 5-HT contents, which suggested that the metabolite 20(S)-PPD was the critical factor of diarrhea induced by G-CK. Further studies are needed to elucidate the precise relationship between 20(S)-PPD and diarrhea elicited by G-CK treatment.

Abbreviations

5-HT: Serotonin
Ach: Acetylcholine

AUC: The area under the plasma concentration-time curve
AUC_{last}: The area under the plasma concentration-time curve from time 0 to the last observation
BMI: Body mass index
CFDA: China Food and Drug Administration
CFTR: Cystic fibrosis transmembrane conductance regulator
C_{max}: Maximum concentrations
CL/*F*: The apparent clearance
DID: Drug-induced diarrhea
EC: Enterochromaffin cell
FSK: Forskolin
FRT: Fischer rat thyroid epithelial
G-CK: Ginsenoside compound K
HCK: High dose of G-CK
INDA: Investigational New Drug Application
LCK: Low dose of G-CK
MRP4: Multidrug resistance protein 4
PK: Pharmacokinetic
PPD: Protopanaxadiol
PI: Peristaltic index
PVDF: Polyvinylidene difluoride
RA: Rheumatoid arthritis
t_{max}: Time to maximum plasma concentration
Vz/*F*: The apparent volume of distribution.

Data Availability

As G-CK is a drug candidate, detailed preclinical and clinical data are temporarily classified and not suitable for public disclosure.

Conflicts of Interest

The authors confirm that there are no conflicts of interest.

Authors' Contributions

LC and LZ were responsible for the study design, data collection, statistical analysis, and manuscript writing. XZ helped to carry out animal experiments. DO, GY, and JL were involved in the implementation of trials. ZT participated in the chromatographic analysis. DO and ZL guided the design and implementation of the whole research. All authors reviewed the results and approved the final version of the manuscript.

Acknowledgments

This work was supported by the National Development of Key Novel Drugs for Special Projects of China (grant number 2017ZX09304014), Hunan Key Laboratory for Bioanalysis of Complex Matrix Samples (grant number 2017TP1037), Key R&D Programs of Hunan Province (grant number 2019SK2241), Innovation and Entrepreneurship Investment Project in Hunan Province (grant number 2019GK5020), International Scientific and Technological Innovation Cooperation Base for Bioanalysis of Complex Matrix Samples in Hunan Province (grant number 2019CB1014), and Science and technology project of Changsha (grant number kh1902002). The authors wish to thank all of the investigators, volunteers, and medical, nursing, and laboratory staff who participated in this study. They would also like to thank Hisun Pharmaceutical Co., Ltd. (Taizhou, Zhejiang, China) which produced and provided ginsenoside compound K and Ginsenoside Compound K Tablets, the Hunan Research Center for Drug Safety Evaluation (Liuyang, Hunan, China) which provided help for animal experiments, the Third Xiangya Hospital (Changsha, Hunan, China) which offered the clinical facility, the Institute of Clinical Pharmacology (Changsha, Hunan, China) which was involved in measurement and analysis, and School of Life Science, Liaoning Normal University (Dalian, Liaoning, China), which provided help for the detection of CFTR activity.

Supplementary Materials

Figure S1: effect of G-CK on the intestinal osmotic pressure: A: control (physiologic saline); B: magnesium sulfate; C: 0.5% CMC-Na; D: 400 mg/kg G-CK. G-CK: ginsenoside compound K. Compared with the control group, there was a hypertonic state in the intestinal cavity of the magnesium sulfate group. The intestinal osmotic pressure of the 0.5% CMC-Na and G-CK groups was normal. *(Supplementary Materials)*

References

[1] X. D. Yang, Y. Y. Yang, D. S. Ouyang, and G. P. Yang, "A review of biotransformation and pharmacology of ginsenoside compound K," *Fitoterapia*, vol. 100, pp. 208–220, 2015.

[2] J. Oh and J. S. Kim, "Compound K derived from ginseng: neuroprotection and cognitive improvement," *Food & Function*, vol. 7, no. 11, pp. 4506–4515, 2016.

[3] M. J. Hossen, Y. D. Hong, K. S. Baek et al., "*In vitro* antioxidative and anti-inflammatory effects of the compound K-rich fraction BIOGF1K, prepared from *Panax ginseng*," *Journal of Ginseng Research*, vol. 41, no. 1, pp. 43–51, 2017.

[4] Y. Huang, H. Liu, Y. Zhang et al., "Synthesis and biological evaluation of ginsenoside compound K derivatives as a novel class of LXRα activator," *Molecules*, vol. 22, no. 7, p. 1232, 2017.

[5] Y. C. Hwang, D. H. Oh, M. C. Choi et al., "Compound K attenuates glucose intolerance and hepatic steatosis through AMPK-dependent pathways in type 2 diabetic OLETF rats," *The Korean Journal of Internal Medicine*, vol. 33, no. 2, pp. 347–355, 2018.

[6] I. Yosioka, T. Sugawara, K. Imai, and I. Kitagawa, "Soil bacterial hydrolysis leading to genuine aglycone. V. on ginsenosides-Rb1, Rb2, and Rc of the Ginseng root saponins," *Chemical & Pharmaceutical Bulletin*, vol. 20, no. 11, pp. 2418–2421, 1972.

[7] Y. Wang, J. Chen, X. Luo et al., "Ginsenoside metabolite compound K exerts joint-protective effect by interfering with synoviocyte function mediated by TNF-α and Tumor necrosis factor receptor type 2," *European Journal of Pharmacology*, vol. 771, pp. 48–55, 2016.

[8] T. K. Yun, "Panax ginseng–a non-organ-specific cancer preventive?," *The Lancet Oncology*, vol. 2, no. 1, pp. 49–55, 2001.

[9] H. Jin, J. H. Seo, Y. K. Uhm, C. Y. Jung, S. K. Lee, and S. V. Yim, "Pharmacokinetic comparison of ginsenoside metabolite IH-901 from fermented and non-fermented ginseng in healthy Korean volunteers," *Journal of Ethnopharmacology*, vol. 139, no. 2, pp. 664–667, 2012.

[10] O. Chassany, A. Michaux, and J. F.??. Bergmann, "Drug-induced diarrhoea," *Drug Safety*, vol. 22, no. 1, pp. 53–72, 2000.

[11] N. A. Philip, N. Ahmed, and C. S. Pitchumoni, "Spectrum of drug-induced chronic diarrhea," *Journal of Clinical Gastroenterology*, vol. 51, no. 2, pp. 111–117, 2017.

[12] C. Moon, W. Zhang, N. Sundaram et al., "Drug-induced secretory diarrhea: a role for CFTR," *European Journal of Pharmacology*, vol. 102, pp. 107–112, 2015.

[13] C. M. Surawicz, "Mechanisms of diarrhea," *Current Gastroenterology Reports*, vol. 12, no. 4, pp. 236–241, 2010.

[14] N. X. W. L. Liu Jun, "20 (S) - Protopanaxadiol promotes the opening of chloride channel CFTR," *Journal of Chemistry of Colleges and Universities*, vol. 4, no. 29, p. 731, 2008.

[15] L. Zhou, L. Chen, Y. Wang et al., "Impact of NR1I2, adenosine triphosphate-binding cassette transporters genetic polymorphisms on the pharmacokinetics of ginsenoside compound K in healthy Chinese volunteers," *Journal of Ginseng Research*, vol. 43, no. 3, pp. 460–474, 2019.

[16] Q. Wang, L. H. Sun, W. Jia et al., "Comparison of ginsenosides Rg1 and Rb1 for their effects on improving scopolamine-induced learning and memory impairment in mice," *Phytotherapy Research*, vol. 24, no. 12, pp. 1748–1754, 2010.

[17] C. G. Benishin, "Actions of ginsenoside Rb1 on choline uptake in central cholinergic nerve endings," *Neurochemistry International*, vol. 21, no. 1, pp. 1–5, 1992.

[18] C. G. Benishin, R. Lee, L. C. H. Wang, and H. J. Liu, "Effects of ginsenoside Rbi on central cholinergic metabolism," *Pharmacology*, vol. 42, no. 4, pp. 223–229, 1991.

[19] L. Chen, L. Zhou, Y. Wang et al., "Food and sex-related impacts on the pharmacokinetics of a single-dose of ginsenoside compound K in healthy subjects," *Frontiers in Pharmacology*, vol. 8, p. 636, 2017.

[20] L. Chen, L. Zhou, J. Huang et al., "Single- and multiple-dose trials to determine the pharmacokinetics, safety, tolerability, and sex effect of oral ginsenoside compound K in healthy Chinese volunteers," *Frontiers in Pharmacology*, vol. 8, p. 965, 2018.

[21] P. Kristidis, D. Bozon, M. Corey et al., "Genetic determination of exocrine pancreatic function in cystic fibrosis," *American Journal of Human Genetics*, vol. 50, no. 6, pp. 1178–1184, 1992.

[22] A. Than, H. J. Kulkarni, W. Hmone, and S. J. Tha, "Anti-diarrhoeal efficacy of some Burmese indigenous drug formulations in experimental diarrhoeal test models," *Pharmaceutical Biology*, vol. 27, no. 4, 1989.

[23] C. Li, P. C. Krishnamurthy, H. Penmatsa et al., "Spatiotemporal coupling of cAMP transporter to CFTR chloride channel function in the gut epithelia," *Cell*, vol. 131, no. 5, pp. 940–951, 2007.

[24] L. Li, X. Chen, D. Li, and D. Zhong, "Identification of 20(S)-protopanaxadiol metabolites in human liver microsomes and human hepatocytes," *Drug Metabolism and Disposition*, vol. 39, no. 3, pp. 472–483, 2011.

[25] P. S. Lee, T. Song, J. H. Sung, D. C. Moon, S. Song, and Y. Chung, "Pharmacokinetic characteristics and hepatic distribution of IH-901, a novel intestinal metabolite of ginseng saponin, in rats," *Planta Medica*, vol. 72, no. 3, pp. 204–210, 2006.

[26] A. Degu, E. Engidawork, and W. Shibeshi, "Evaluation of the anti-diarrheal activity of the leaf extract of *Croton macrostachyus* Hocsht. ex Del. (Euphorbiaceae) in mice model," *BMC Complementary and Alternative Medicine*, vol. 16, no. 1, p. 379, 2016.

[27] D. Derebe, M. Abdulwuhab, M. Wubetu, and F. Mohammed, "Investigation of the antidiarrheal and antimicrobial activities of 80% methanolic leaf extract of Discopodium Penninervum (Hochst.)," *Evidence-Based Complementary and Alternative Medicine*, vol. 2018, Article ID 1360486, 7 pages, 2018.

[28] W. Huang, X. Huang, Z. Xing et al., "Meranzin hydrate induces similar effect to Fructus Aurantii on intestinal motility through activation of H1 histamine receptors," *Journal of Gastrointestinal Surgery*, vol. 15, no. 1, pp. 87–96, 2011.

[29] P. D. Williams, W. E. Colbert, T. J. Shetler, and J. A. Turk, "Comparative pharmacological profile of muscarinic agonists in the isolated ileum, the pithed rat, and the mouse charcoal meal transit test," *General Pharmacology*, vol. 23, no. 2, pp. 177–185, 1992.

Hindawi
Journal of Nanomaterials
Volume 2021, Article ID 5596780, 12 pages
https://doi.org/10.1155/2021/5596780

Research Article

Cucurbitacin B as a Chinese Medicine Monomer Inhibits Cell Proliferation, Invasion, and Migration in Nasopharyngeal Carcinoma

Ning Xu,[1] Bei-Bei Zhang,[2] Meng-Zhe Yang,[1] Xian-Yu Bai,[1] Zhen-Qiang Liang,[3] Nan-Nan Cheng,[1] An-Qiao Lv,[1] Jian-Yu Yang,[1] Xing-Zhe Guo,[1] Ai-Jun Jiao,[4] and Yuan-Jiao Huang[5,6]

[1]*Graduate School of Guangxi Medical University, Nanning, China*
[2]*Institute of Biomedical Research, Yunnan University, Kunming, China*
[3]*Department of Otolaryngology-Head and Neck Surgery, The First Affiliated Hospital of Guangxi Medical University, Nanning, China*
[4]*Pharmaceutical College, Guangxi Medical University, Nanning, China*
[5]*Life Science Institute, Guangxi Medical University, Nanning, China*
[6]*School of Basic Medical Sciences, Guangxi Medical University, Nanning, China*

Correspondence should be addressed to Yuan-Jiao Huang; hyjgxmu@126.com

Received 22 January 2021; Revised 19 February 2021; Accepted 23 February 2021; Published 12 March 2021

Academic Editor: Songwen Tan

Nasopharyngeal carcinoma (NPC) is a malignant epithelial tumor in southern China. Cucurbitacin B (CuB) is a tetracyclic triterpene compound isolated from Cucurbitaceae plants which has anti-inflammation and antitumor properties and low toxic side effects. In this study, we use a series of wet experiments and network pharmacology analyses to explore the effects of CuB on cell proliferation, migration, invasion, and apoptosis of highly metastatic 5-8F NPC cells. The findings suggest that CuB inhibits NPC cells in a time- and dose-dependent manner and that cancer migration and invasion abilities decrease significantly after CuB treatments. Mechanistically, CuB could increase the proportion of cells in the G2/M phase and reduce it in the G0/G1 phase, leading to apoptosis. The network pharmacological analyses and wet experiments uncovered that the MAPK pathway is a central target by pathway enrichment analysis, affecting the fate of cancer cells and influencing proliferation and apoptosis. Taken together, our study reveals that CuB could effectively inhibit 5-8F NPC cell proliferation, migration, and invasion via cell cycle blockage and cell apoptosis. Collectively, we have shown that CuB is a promising anti-NPC candidate compound for future preclinical study.

1. Introduction

Nasopharyngeal carcinoma (NPC) is the most common malignant tumor of the nasopharynx. Although global NPC incidence is less than 1/100,000, there are significant regional variations and a much higher incidence rate in North Africa and Southeast Asia, especially in the southern provinces of China. In 2018, there were 129,079 new NPC cases and 72,987 deaths around the world. Of these, more than 45% of the new cases were in China, several times higher than the global average incidence rate, and in some provinces, the rate exceeded 30/100,000 [1, 2]. There are a number of pathological forms including the undifferentiated state [3], the hidden onset, mostly lymph node metastasis, and distant metastasis [4–6]. With the development of intensity-modulated radiotherapy (IMRT) treatment, patients with early stage NPC (stage I) who underwent radiation therapy alone experienced a 5-year survival rate (OS) of over 90% [7, 8]. High survival rates are also seen in patients with stage II cancer who underwent radiotherapy alone, but 10-15% of patients develop recurrence and distant metastasis [9]. Combined chemotherapy can improve patient survival rate and

reduce the rate of recurrence and metastasis, but the toxicity and side effects of chemotherapy drugs seem to do more harm than good [10, 11]. Therefore, there is an urgent need to seek safe and effective radiotherapy adjuvant drugs with low toxicity and side effects which will help to reduce the recurrence and distant metastasis.

A number of studies have shown that many active components in Chinese herbal medicine have antitumor effects and that they are economical and multitarget, have low toxicity and side effects and, as such, are a current focus of antitumor drug research. Cucurbitacin is one of the main bioactive compounds found in Cucurbitaceae, such as cucumber [12]. It has been extracted from a variety of plants, has a wide range of pharmacological activities [13], such as cytotoxic, anti-inflammatory, and anticancer effects [14], and has been used as folk medicine for hundreds of years in countries such as India and China. Among the Cucurbitacin compounds, Cucurbitacin B (CuB) is one of the most widely used active substances for *in vivo* and *in vitro* tumor inhibition studies. With low toxicity and side effects, it is a promising potential antitumor herbal drug [15]; however, no studies have been conducted on its effect on NPC.

In this study, we examined the effect of CuB on the highly metastatic NPC 5-8F cells and reveal its possible mechanism of action using *in vitro* wet experiments and bioinformatics analyses. Our findings suggest that CuB could effectively inhibit 5-8F cell proliferation, migration, and invasion *via* cell cycle blockage and apoptosis. The network pharmacological analyses uncover that the MAPK pathway is a central target. Our findings show that CuB is a promising anti-NPC candidate compound and should be the focus of future research.

2. Material and Methods

2.1. Materials. 5-8F cells were purchased from Shanghai Institute of Cell Research, Chinese Academy of Sciences. CuB was purchased from MCE (United States). 1640 medium and FBS fetal bovine serum were purchased from Gibco (USA), Trypsin solution and DMSO were purchased from Amresco (USA), and BCA Protein Content Assay Kit and AnnexinV-FITC Apoptosis Assay Kit were purchased from Nanjing Kaiji Biotechnology Co., Ltd. CCK-8 reagent was purchased from Dojindo (Japan).

2.2. Cell Culture. NPC 5-8F cells were cultured in RPM-1640 containing 10% fetal bovine serum at 37°C and 5% carbon dioxide. The medium was changed daily, and the cells were isolated with 0.25% trypsin.

2.3. CCK-8 Assay. Cells were seeded into 96-well plates and cultured for 24, 48, and 72 h. Cytotoxicity was detected by the CCK method. Absorbance at 450 nm was measured by an automatic enzyme plate reader (Bio-Tek, VT, USA). Cell mortality was calculated according to the following formula: inhibition rate (%) = (average A450 in the control group − average A450 in the experimental group)/(average A450 in the control group − average A450 in the blank group) × 100%. Each experiment was performed in triplicate.

2.4. Transwell Migration and Invasion Assay. 5-8F cells in each group were resuspended in serum-free medium and a 2×10^5 cells/mL cell suspension was prepared. A Transwell chamber was inoculated with 200 μL cell suspension in the upper chamber and 600 μL serum-free medium in the lower chamber. The cells were incubated at 37°C for 24 h, and after which, sterile cotton swabs were used to remove the upper 5-8F cells and were thoroughly washed in PBS. The cells were fixed in 4% paraformaldehyde for 30 min and stained in 0.1% crystal violet for 10 min. Three fields were randomly selected under the microscope for photography, and the number of stained cells in crystal violet was calculated as the number of migrated cells. For the invasion assay, RPMI 1640 medium was added at a ratio of 1 : 5 to Matrigel, and the upper chamber of Transwell was coated. After drying, the same protocol as the cell migration assay above was performed, and the number of invading cells was counted.

2.5. Flow Cytometry Analysis of Apoptosis. The Annexin V-FITC double-staining method was used to detect the effect of CuB on 5-8F cell apoptosis. 1×10^6 cells were seeded into each well of a six-well plate, and different CuB concentrations (0, 200, 400, and 800 nM) were added after the cells adhered to the wall. Cells were incubated for 48 h, then harvested, resuspended in cold PBS, and stained with the Annexin-FITC apoptosis detection kit according to the manufacturers' instructions. Cell apoptosis was then analyzed by flow cytometry. The experiment was performed in triplicate.

2.6. Flow Cytometry Analysis of Cell Cycle. 5-8F cells in the logarithmic growth stage were seeded into 6-well plates, with a total volume of each well of 2 mL and cell density of 1×10^6 cells/L. After the cells were treated with CuB at final concentrations of 0, 200, 400, and 800 nM for 48 h, they were collected, rinsed twice with 0.01 mol/L PBS (pH = 7.2) for precooling, and fixed overnight with 75% cold ethanol at 4°C. Before detection, the fixation solution was removed and propidium iodide (PI) was added and the samples stained at 4°C for 30 min. 1×10^4 cells from each group were collected for flow cytometry detection. The MFLT SAAINC software was used to analyze the cell cycle phase ratio and early cell apoptosis rate. The experiment was performed in triplicate.

2.7. Bioinformatics Analysis. The PubChem database (https://pubchem.ncbi.nlm.nih.gov) was used to find the 3D compound structure of CuB, the PharmMapper database (http://www.lilab-ecust.cn/pharmmapper) was used to obtain CuB targets, and the GeneCards (http://www.genecards.org) database was used to retrieve target NPC-related diseases. The online tools from (http://bioinformatics.psb.ugent.be/webtools/Venn) were used to make maps of NPC and CuB targets. The PPI analysis of protein interactions was performed using String (https://string-db.org/cgi). The Cytoscape 3.6.1 software was used to construct the CUB-nasopharyngeal carcinoma target network map, and cytoHubba's MCC method was used to search for core genes. The David web site (https://david.ncifcrf.gov/) was used for GO enrichment analysis on the common targets and the Kobas online database (http://kobas.cbi.pku.edu.cn/kobas3) was used for KEGG pathway enrichment analysis.

2.8. Western Blot. Total protein (40 μg) generated by cell lysis was separated on a 12% acrylamide gel (80 V, 30 min; 120 V, 60 min), then transferred to PVDF membrane (270 mA, 65 min), blocked with 5% skim milk for 1 h, washed three times with 0.1% TBST, and incubated in the primary antibody overnight at 4°C. The membrane was then washed three times with TBST, 5 min each, and then incubated with diluted fluorescent secondary goat anti-rabbit antibody for 1 h. The membrane was washed three times in TBST, 5 min each, and the Odyssey infrared fluorescence film scanner was used to sweep the film, adjust the required parameters, and save the picture. The antibodies used in this study were GADPH (Wuhan ProteinTech Company (China)), P-ERK and ERK (ABCAM (USA)), and BCL2 and BAX (Cell Signaling Technology (USA)). All the images were analyzed with ImageJ to calculate the gray value of the relevant target proteins.

2.9. Statistical Analysis. SPSS 25.0 was used for all statistical analysis. Measurement data was expressed as $x \pm s$. A t-test was used for the comparison of two sample means, and one-way analysis of variance was used for comparison of means between groups. A P value < 0.05 indicates statistical significance. For all the data presented in this study, $*$ represents $P < 0.05$, $**$ represents $P < 0.01$, and $***$ represents $P < 0.001$. All experiments were repeated three times.

3. Results

3.1. CuB Inhibits NPC Proliferation. To explore the anticancer effects of CuB, we cultured 5-8F NPC cells (a highly metastatic cell line). The CCK8 assay results showed that CuB had a concentration-time-dependent effect on NPC 5-8F cell proliferation (Figure 1). In detail, the inhibition rate of cell proliferation was $9.25 \pm 2.58\%$, $19.63 \pm 2.14\%$, $27.18 \pm 2.30\%$, $32.30 \pm 3.18\%$, $46.77 \pm 3.08\%$ (IC_{50} 1435.84 ± 272.36 nM) for 24 h CuB treatment at 200 nM, 400 nM, 600 nM, 800 nM, and 1000 nM, respectively. Similarly, the cell proliferation inhibition rate was $27.77 \pm 2.85\%$, $37.72 \pm 4.09\%$, $44.88 \pm 3.63\%$, $54.61 \pm 4.89\%$, and $65.45 \pm 3.57\%$ (IC_{50} 622.94 ± 68.67 nM) for 48 h CuB treatment at 200 nM, 400 nM, 600 nM, 800 nM, and 1000 nM, respectively. Accordingly, the cell proliferation inhibition rate was $41.64 \pm 3.79\%$, $53.14 \pm 2.70\%$, $66.74 \pm 2.70\%$, $74.33 \pm 2.34\%$, and $86.80 \pm 3.44\%$ (IC_{50} was 314.79 ± 30.48 nM) for 72 h CuB treatment at 200 nM, 400 nM, 600 nM, 800 nM, and 1000 nM, respectively. Collectively, CuB could obviously inhibit cell proliferation in the highly metastatic cell line model.

3.2. CuB Suppresses Cell Migration and Invasion in NPC. Since 5-8F is a highly metastatic cell line and metastasis is a clinical concern that needs to be addressed, we examined whether CuB has some effects on cell abilities such as migration and invasion. The results of the scratch experiment (Figure 2) showed that the migration rates of 5-8F cells were $12.84 \pm 2.37\%$, $10.12 \pm 1.75\%$, and $5.56 \pm 0.88\%$ at 24 h and $21.45 \pm 2.13\%$, $12.29 \pm 2.11\%$, and $10.43 \pm 0.93\%$ at 48 h after treatment with CuB at 50, 100, and 200 nM, respectively. Compared to the control group (24 h, $18.98 \pm 0.97\%$; 48 h, $35.15 \pm 5.21\%$), 50 nM CuB could significantly inhibit NPC 5-8F cells migration ($P < 0.05$), and the inhibition of 5-8F migration was positively correlated with concentration.

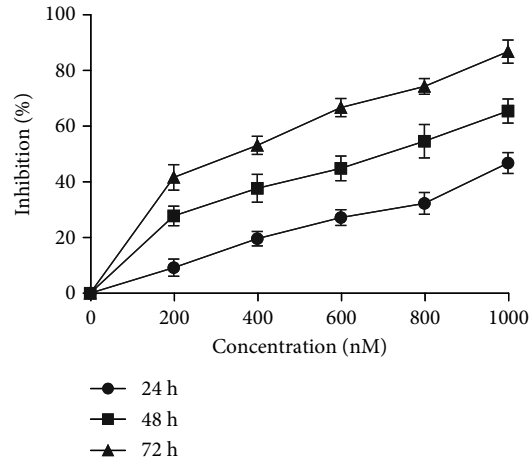

Figure 1: Effect of CuB on NPC cell proliferation.

To further validate these observations, Transwell migration experiments were performed. The results showed that the number of transmembrane cells in control and CuB treatment groups (50 nM, 100 nM, and 200 nM) was 386 ± 7, 187 ± 9, 142 ± 2, and 105 ± 10, respectively. Similarly, the Transwell-invasion experiment showed that the number of transmembrane cells in the control group and the CuB treatment groups (50 nM, 100 nM, and 200 nM) was 305 ± 26, 155 ± 4, 115 ± 9, and 29 ± 14, respectively. These results showed that as the CuB concentration increased, the migration and invasion ability of 5-8F cells decreased significantly ($P < 0.05$) (Figure 3). These results showed that CuB had some effect on metastatic abilities, such as migration and invasion, in NPC.

3.3. CuB Induces Cell Apoptosis in NPC. After seeing that cell proliferation, migration, and invasion were all significantly inhibited, we next explored whether CuB could affect NPC cell fate. Flow cytometry showed that after 48 h treatment with CuB at 200, 400, and 800 nM, the apoptosis rates were $15.58 \pm 3.09\%$, $24.6 \pm 1.83\%$, and $31.76 \pm 5.06\%$, respectively. Compared with the control group ($6.25 \pm 1.42\%$), the apoptosis rate was significantly increased and was correlated with concentration ($P < 0.05$) (Figure 4). These data suggest that CuB could induce cell apoptosis in NPC and that this is closely related to drug concentration.

3.4. CuB Induces G2/M Phase Blockade in the Cell Cycle of NPC. We further examined the cell cycle to uncover the mechanism of action of CuB. Flow cytometry analysis of cell cycle showed that in 5-8F treated with CuB at 200, 400, and 800 nM, the proportion of G2 phase cells increased $17.37 \pm 0.19\%$, $20.44 \pm 1.54\%$, and $24.27 \pm 0.92\%$, respectively, while the proportion of G0/G1 phase cells decreased, $57.58 \pm 1.19\%$, $53.16 \pm 0.42\%$, and $49.63 \pm 2.13\%$, respectively, compared with the control group (G2, $12.42 \pm 0.79\%$, and G0/G1, $60.51 \pm 2.13\%$) (Figure 5). These results indicate that CuB could induce G2/M phase blockade in the NPC cell cycle.

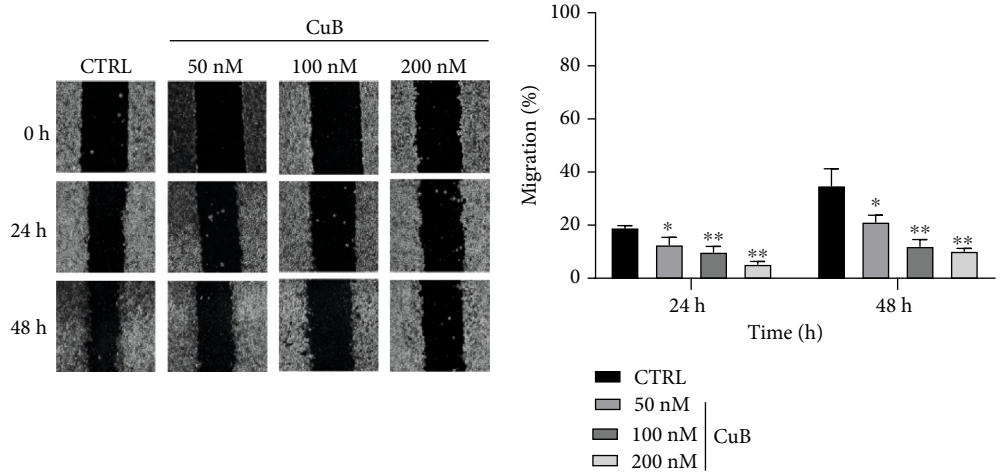

Figure 2: Effect of CuB on 5-8F cell migration.

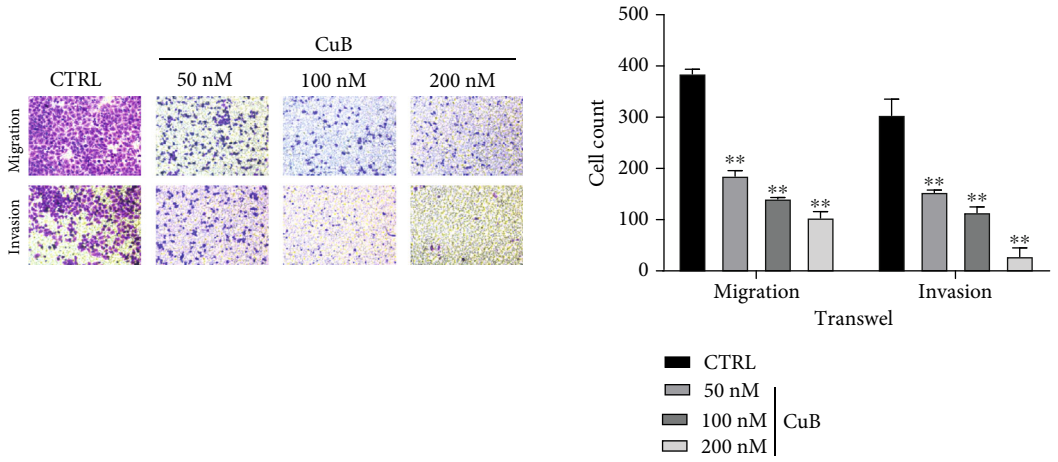

Figure 3: Effect of CuB on 5-8F cell migration and invasion.

3.5. Bioinformatics Analysis Uncovers MAPK as the Main Target of CuB. To explore the overall anticancer effects of CuB against NPC, we performed bioinformatics analysis using a network pharmacology approach. In total, 357 CuB action targets were obtained from the PharmMapper database and 1786 target genes from the GeneCards database. Among them, 116 common targets were validated (Figure 6(a)). The PPI analysis showed that MAPK1 was the most correlated gene among all the target genes, with a total of 30 interrelated genes (Figures 6(b) and 6(c)). MCC analysis of the common target genes with the Cytoscape plug-in showed that MAPK1 had the highest score (Figure 6(d)). Using $P < 0.01$ as the threshold, 119 terms were obtained by GO enrichment analysis, of which, MAPK1 played a role in 28 terms and participated in three functions: BP, CC, and MF (Figure 6(e) shows the three functions of MAPK1 with the top 5 terms). The 28 functions in which MAPK1 is involved are shown in Figure 6(f). Using $P < 0.01$ as the threshold, MAPK1 (ranked by P value) was involved in 101 of the 159 pathways identified by the KEGG enrichment analysis. Figure 6(g) shows the MAPK1 position in the ranking by P value of the top 15 pathways. MAPK1 mainly participates in biological processes through the MAPK pathway, and Figure 6(h) shows all the common target genes enriched in the MAPK pathway. Western blotting showed that the phosphorylation level of ERK (downstream of the MAPK pathway) decreased in a dose-dependent manner after CuB treatment (Figures 7(a) and 7(b)). After CuB treatment, levels of the proapoptotic protein Bax increased and of the apoptosis regulator Bcl-2 decreased (Figures 7(a) and 7(b)). Overall, the bioinformatics analysis and wet experiments show that MAPK is the central target of CuB against NPC.

4. Discussion

Previous studies have shown that there is no obvious toxicity to normal cells at CuB concentrations lower than 5-10 μM [16]. Wakimoto et al. showed that when nude mice transplanted with MD-MB-231 tumor cells were injected with CuB (1 mg/kg) intraperitoneally for 6 weeks, the tumor volume reduced by 55% compared to the control group while body weight did not reduce [17]. At present, no national food and drug administration has included CuB in the list of drugs or harmful substances [18]. The Australian Therapeutic Goods Administration has approved unrestricted use of

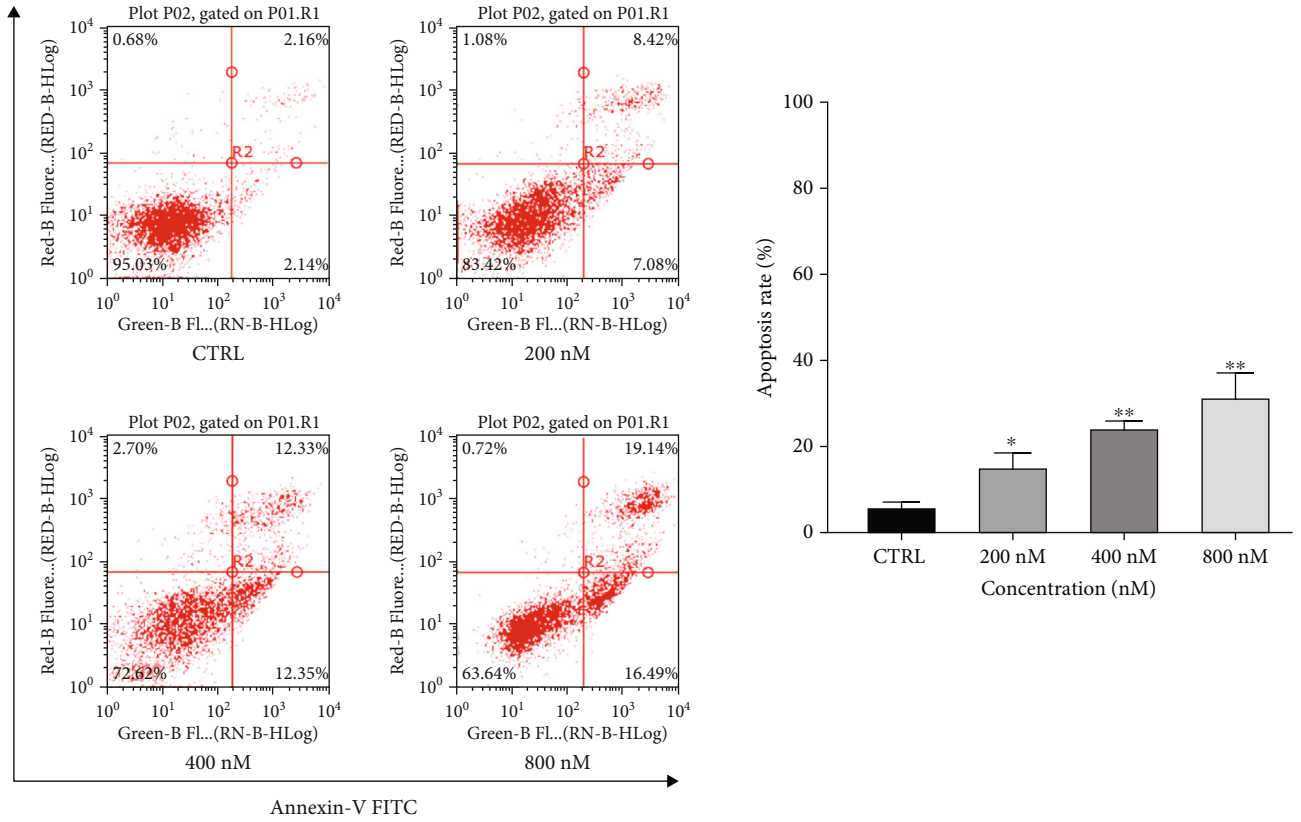

Figure 4: Effect of CuB on 5-8F cell apoptosis.

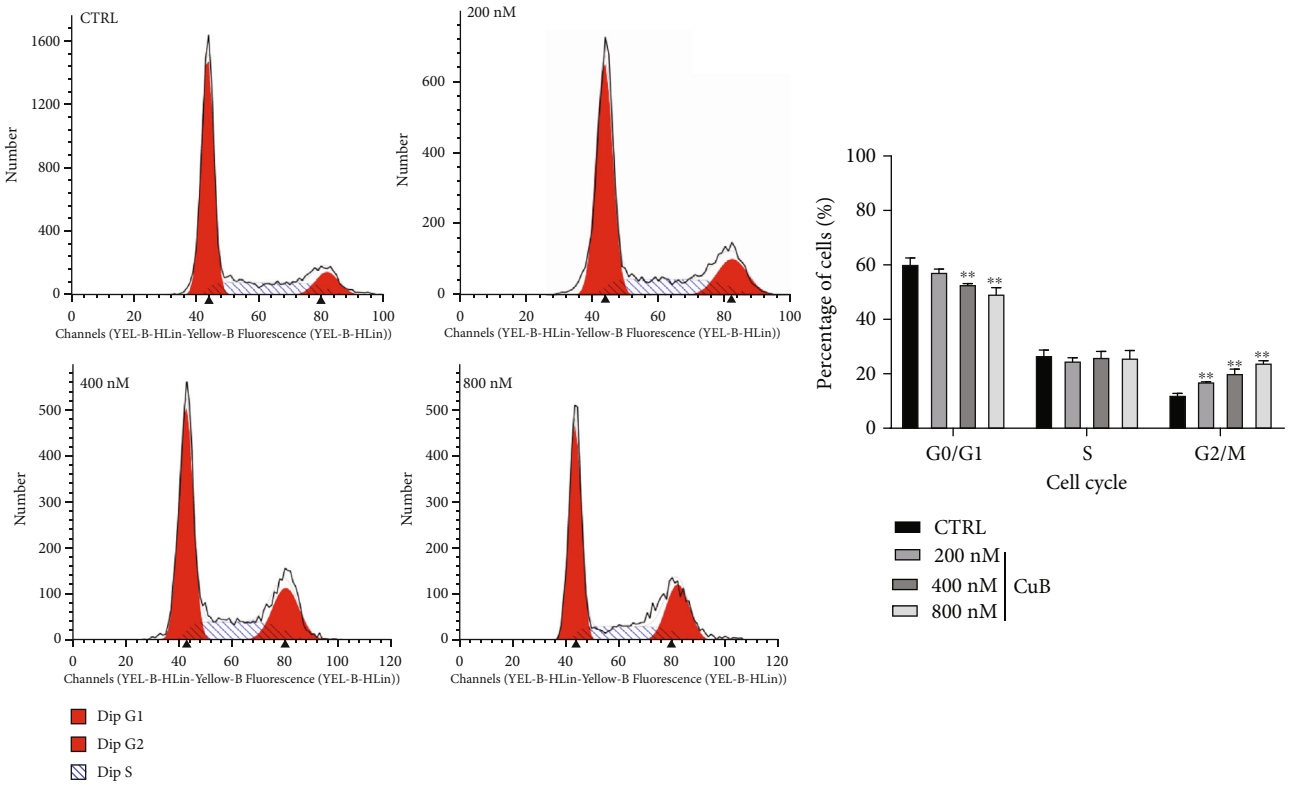

Figure 5: Effect of CuB on 5-8F cell cycle.

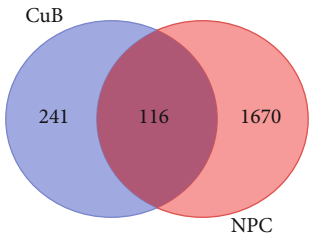

(a)

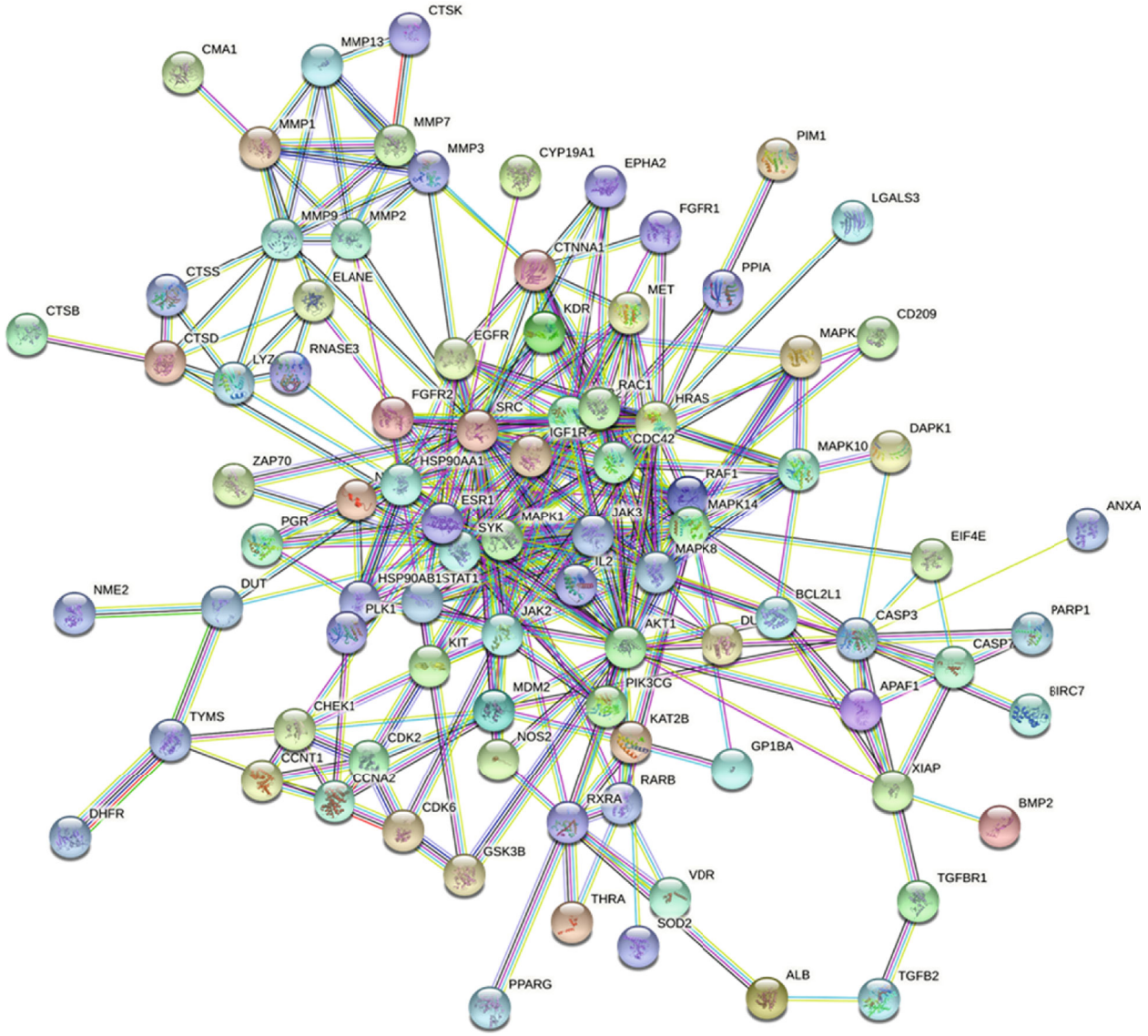

(b)

Figure 6: Continued.

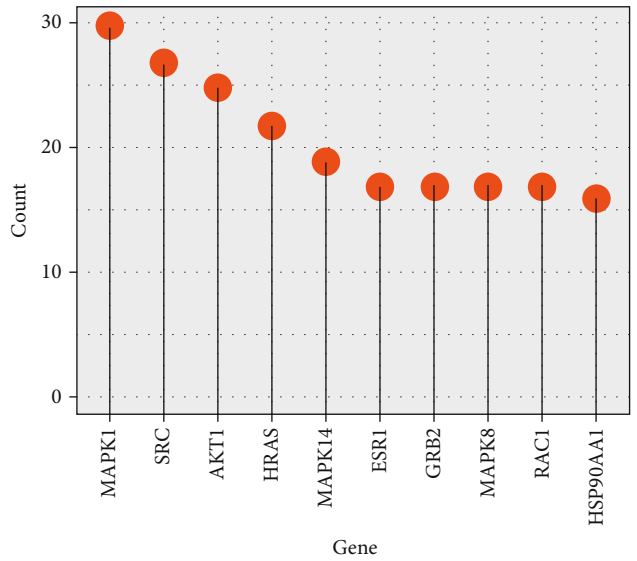

(c)

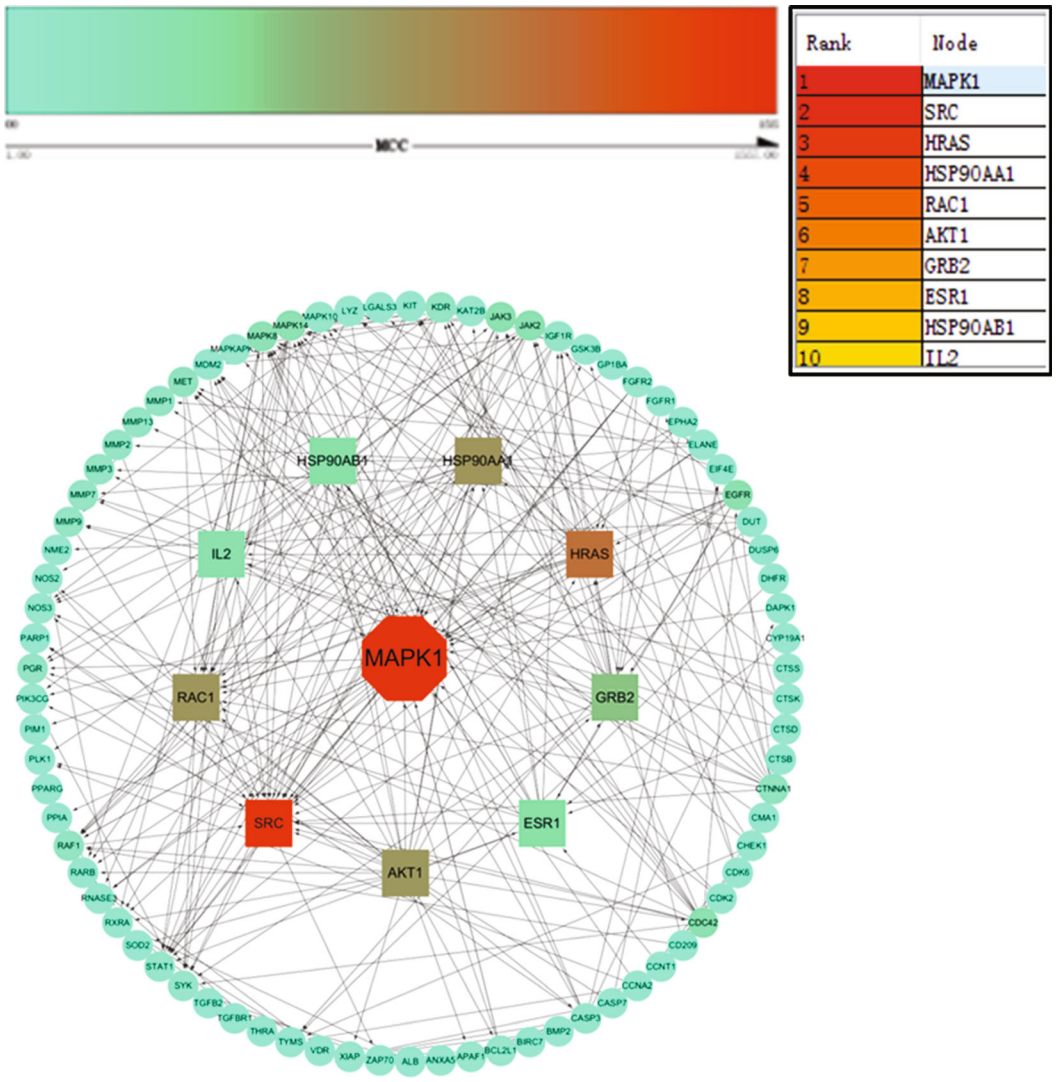

(d)

Figure 6: Continued.

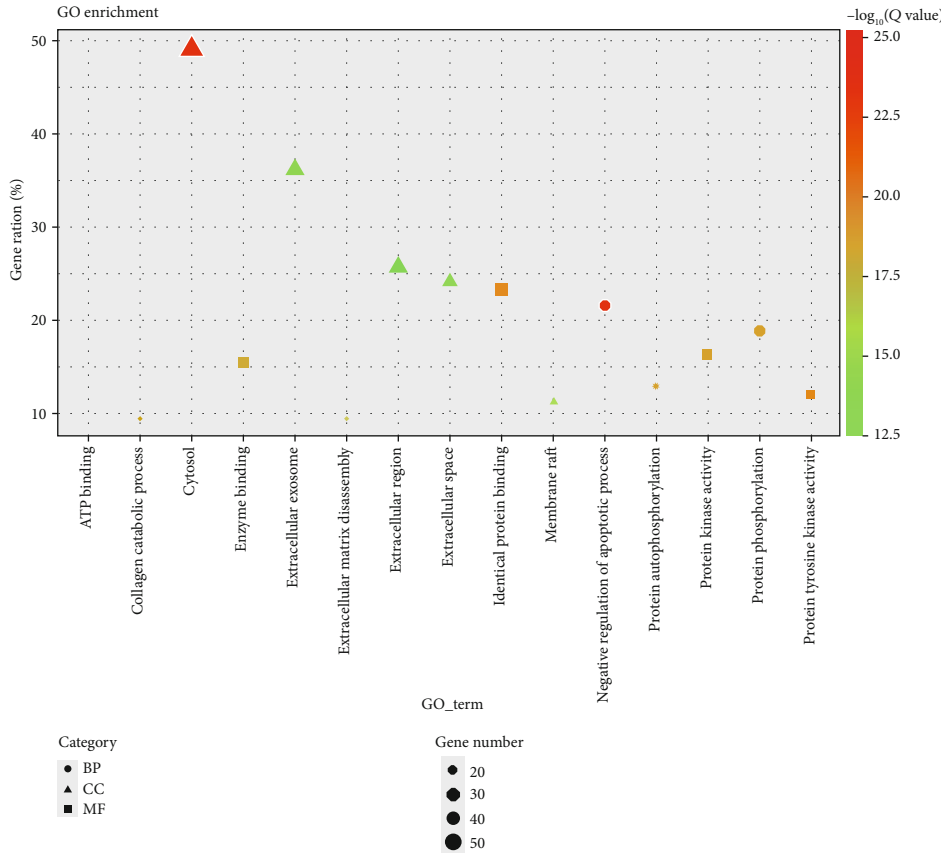

(e)

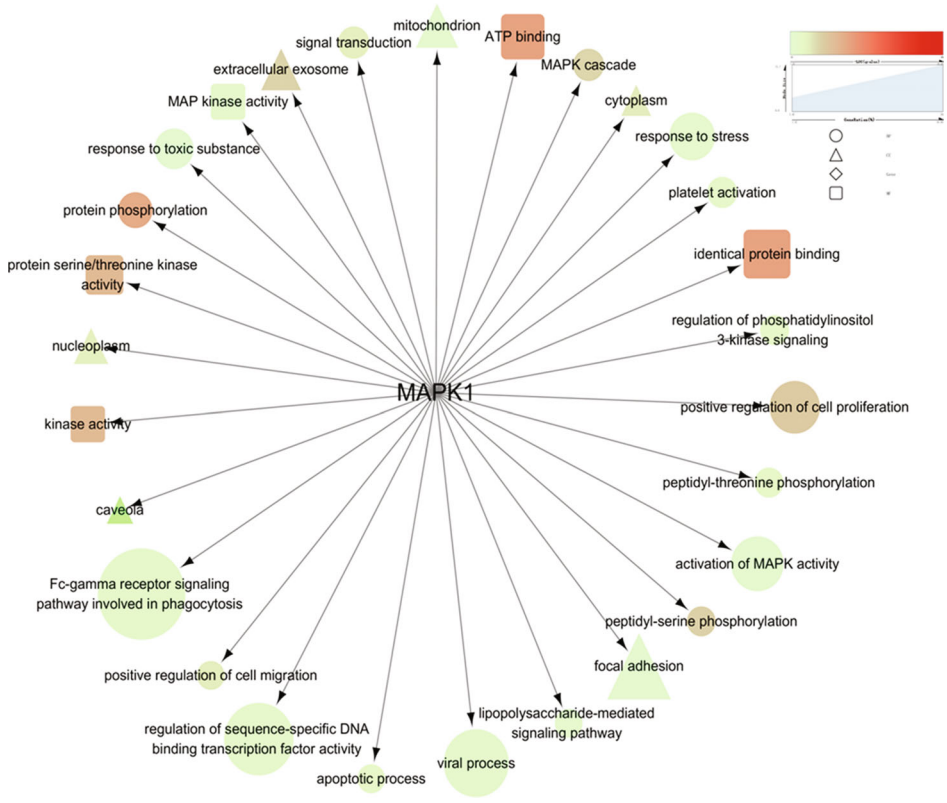

(f)

Figure 6: Continued.

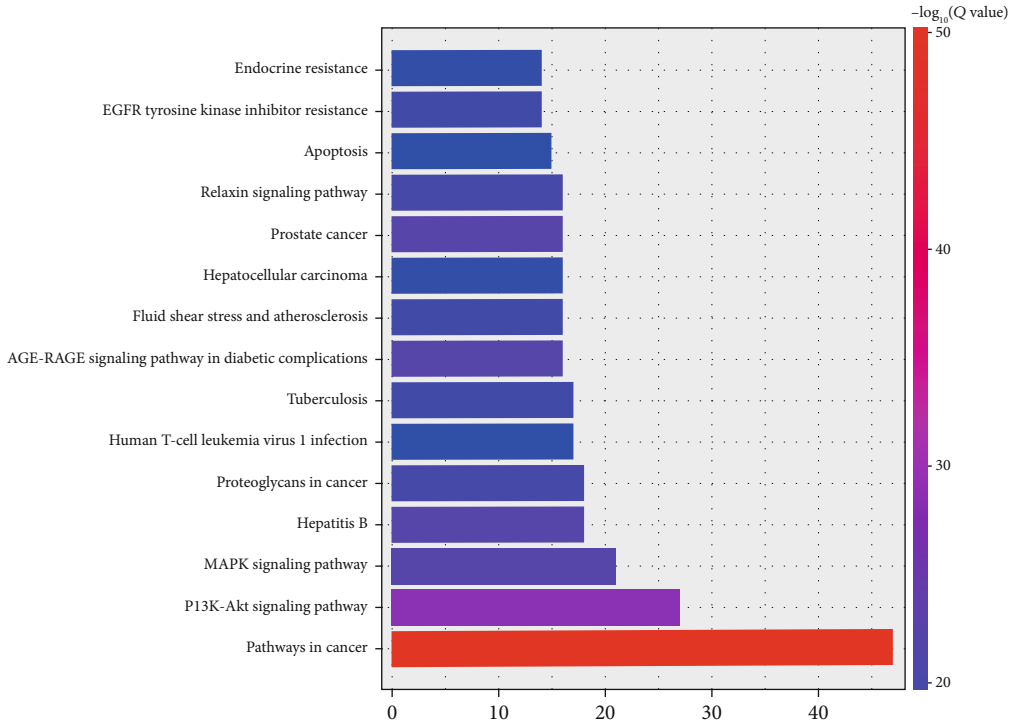

(g)

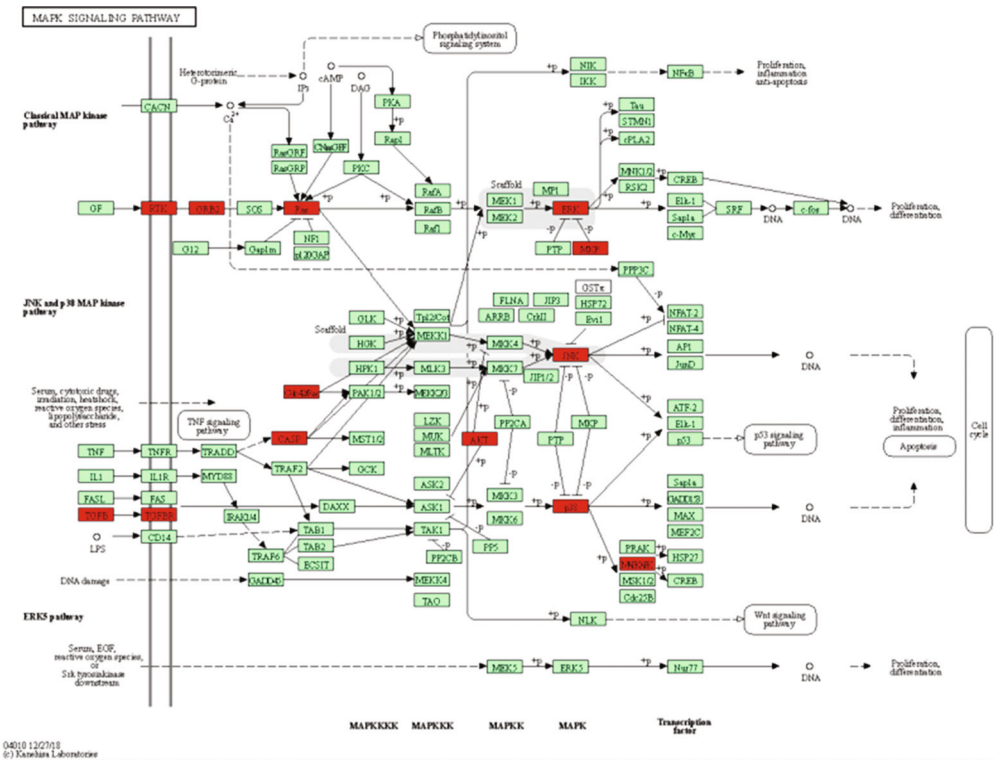

(h)

Figure 6: Bioinformatics analysis uncovers MAPK as the central target of CuB. (a) Venn diagram of NPC therapeutic targets in the GeneCards database and CuB therapeutic targets in the PharmMapper database. (b, c) PPI analysis showing that MAPK1 had the strongest interaction with the other proteins. (d) MCC calculation concluded that MAPK1 has the highest score and is the core gene of the common target genes. (e) GO enrichment analysis of the top 5 functional sets of BF, CC, and MF. (f) The functional set in which MAPK1 was involved as the core. (g) The KEGG analysis of the screened common target genes (top 15 pathway). (h) Genes enriched in the MAPK pathway.

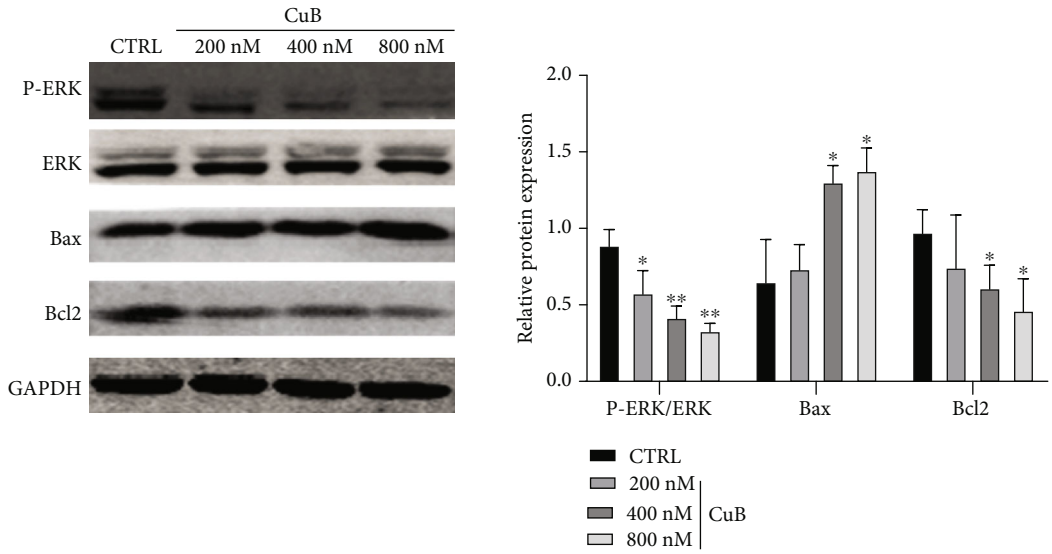

Figure 7: Relevant protein expression levels in 5-8F cells after CuB treatment.

CuB and encourages its use in combination with other drugs [19], and China has developed calabash tablets, 60 percent of the active ingredient is CuB, which are used in the adjuvant treatment of hepatitis and primary liver cancer with the main side effect being mild gastrointestinal reactions. These studies confirm that CuB should be considered safe within therapeutic concentration ranges. In this study, when incubated with 5-8F cells for 24, 48, and 72 h, the IC50 of CuB was 1435.84 $\pm$ 272.36 nM, 622.94 $\pm$ 68.67 nM, and 314.79 $\pm$ 30.48 nM, respectively. Overall, this information suggests that CuB has obvious anti-NPC potential at safe dosage levels.

Studies have shown that CuB can inhibit the invasion and migration of a variety of tumor cells, but the specific mechanism remains unclear. Promkan et al. found that CuB could effectively inhibit the invasion and migration of BRCA1 defective breast cancer cells [20], and Liang et al. showed that it could destroy the cytoskeleton of breast cancer cells, altering their biomechanical properties, and inhibiting their migration and invasion [21]. In non-small cell lung cancer, Garg et al. found that CuB inhibited cell invasion and migration by decreasing mortalin, hnRNP-K, vascular endothelial growth factor, matrix metalloproteinase 2, and fibronectin [22], and Piao et al. found that CuB could inhibit tumor invasion and migration by inhibiting tumor cell angiogenesis [23]. In this study, we showed that CuB could also inhibit invasion and migration of NPC 5-8F cells, which is consistent with the results of previous studies.

Numerous studies have shown that CuB can inhibit the growth of many human cancer cells, including breast [24, 25], prostate [26], lung [27], ovarian [28], liver [29], pancreatic [30], larynx [31], kidney [32], and skin cancer [33]. Although many studies have demonstrated the anticancer activity of CuB, the mechanism of its action is still unclear. It has been reported that CuB inhibits the growth of tumor cells and induces apoptosis by inhibiting the activation of signal transduction and transcriptional activator 3 (STAT3) and regulating its downstream genes such as cyclin D1, cyclin D2, and apoptosis-related genes like Bcl-2 and Bax [34, 35]. In this study, we found that MAPK1 is one of the most important targets of CuB through network pharmacology analysis.

Mitogen-activated protein kinases (MAPK) are the largest subfamily of serine/threonine protein kinases and are involved in many signal transduction pathways and play important roles in protein renewal, cell growth, transcription factor activation, chromatin modification, and gene expression. The MAPK pathway is a well-known stress sensing signal transduction pathway, which can respond to extra- and intracellular stress signals and transmit environmental and self-derived signals into cells. Relevant studies have indicated that CuB is an inhibitor of JAK-STAT3, Wnt, PI3K/Akt, and MAPK signaling pathways, which play an important role in apoptosis and survival of cancer cells [36].

In human chronic myelogenous leukemia studies, CuB inhibited MAPK/ERK pathway activation in various human chronic myelogenous leukemia cells and inhibited STAT3 activation [37]. The analysis in this study showed that there was inhibition of MAPK/ERK activation, which led to the arrest of the G2/M cell cycle and apoptosis. Silva et al. reported that CuB can inhibit PI3 kinase and MAPK pathways, delay cell migration, and reduce cellular invasive potential [38]. It could also induce dose- and time-dependent apoptosis, inhibit MMP release and FAK activation, and downregulate Akt, ERK, and NF-κBp65 phosphorylation. Zhang et al. found CuB had anticancer effects in the SH-SY5Y human neuroblastoma cell line [39]. CuB induced G2/M cell cycle arrest and apoptosis. This was accompanied by downregulation of CDK1 and cyclin B1, essential proteins in the cell cycle process. Another study has also reported that CuB inhibits proliferation and induces apoptosis of human osteosarcoma cells by regulating the JAK2/STAT3 and MAPK pathways [40]. In this study, MTT and Annexin V/propidium iodide staining showed that CuB (20-100 μM dose) significantly reduced cell viability and induced apoptosis and inhibited cell migration. In conclusion, CuB's antitumor effect is mainly attributed to

its induction of cell cycle arrest and apoptosis. The underlying mechanism of action may be attributed to the changes in key proteins involved in the regulation of cell cycle or apoptosis.

In conclusion, our study has shown that the Chinese medicine monomer CuB is a promising anticancer compound which affects cell proliferation, invasion, and migration in NPC cells. Mechanistically, its anticancer effects involve the cell cycle blockade and cell apoptosis, mediated through the MAPK signaling pathway. This shows that CuB is a promising agent for future NPC preclinical research and that this study also provides evidence that it might become part of a useful cancer therapy strategy.

Data Availability

The datasets used and/or analyzed during the current study are available from the corresponding author on the reasonable request.

Conflicts of Interest

The authors declare no conflict of interest.

Authors' Contributions

All authors made a significant contribution to the work reported, either in the conception, study design, execution, acquisition of data, analysis, or interpretation. Ning Xu, Bei-Bei Zhang, and Meng-Zhe Yang contributed equally to this work.

Acknowledgments

This research was funded by the Project for Department of Science and Technology of Guangxi Zhuang Autonomous Region, China (grant number Guike AB19110052), the Natural Science Foundation of Guangxi, China (grant number 2015GXNSFAA139215), and the National Natural Science Foundation of China (grant number 81260405).

References

[1] F. Bray, J. Ferlay, I. Soerjomataram, R. L. Siegel, L. A. Torre, and A. Jemal, "Global cancer statistics 2018: GLOBOCAN estimates of incidence and mortality worldwide for 36 cancers in 185 countries," *CA: a Cancer Journal for Clinicians*, vol. 68, no. 6, pp. 394–424, 2018.

[2] J. Chen, J. Qi, B. Yu et al., "A retrospective study to compare five induction chemotherapy regimens prior to radiotherapy in the reduction of regional lymph node size in patients with nasopharyngeal carcinoma," *Medical Science Monitor*, vol. 24, pp. 2562–2568, 2018.

[3] M. L. K. Chua, J. T. S. Wee, E. P. Hui, and A. T. C. Chan, "Nasopharyngeal carcinoma," *Lancet*, vol. 387, no. 10022, pp. 1012–1024, 2016.

[4] Y. P. Mao, F. Y. Xie, L. Z. Liu et al., "Re-evaluation of 6th edition of AJCC staging system for nasopharyngeal carcinoma and proposed improvement based on magnetic resonance imaging," *International Journal of Radiation Oncology • Biology • Physics*, vol. 73, no. 5, pp. 1326–1334, 2009.

[5] M. Palazzi, E. Orlandi, P. Bossi et al., "Further improvement in outcomes of nasopharyngeal carcinoma with optimized radiotherapy and induction plus concomitant chemotherapy: an update of the Milan experience," *International Journal of Radiation Oncology • Biology • Physics*, vol. 74, no. 3, pp. 774–780, 2009.

[6] G.-Y. Liu, X. Lv, Y.-S. Wu et al., "Effect of induction chemotherapy with cisplatin, fluorouracil, with or without taxane on locoregionally advanced nasopharyngeal carcinoma: a retrospective, propensity score-matched analysis," *Cancer Communications*, vol. 38, no. 1, p. 21, 2018.

[7] A. W. M. Lee, W. M. Sze, J. S. K. Au et al., "Treatment results for nasopharyngeal carcinoma in the modern era: the Hong Kong experience," *International Journal of Radiation Oncology • Biology • Physics*, vol. 61, no. 4, pp. 1107–1116, 2005.

[8] N. Lee, J. Harris, A. S. Garden et al., "Intensity-modulated radiation therapy with or without chemotherapy for nasopharyngeal carcinoma: radiation therapy oncology group phase II trial 0225," *Journal of Clinical Oncology*, vol. 27, no. 22, pp. 3684–3690, 2009.

[9] J. Hu, Q. Huang, J. Gao et al., "Clinical outcomes of carbon-ion radiotherapy for patients with locoregionally recurrent nasopharyngeal carcinoma," *Cancer*, vol. 126, no. 23, pp. 5173–5183, 2020.

[10] F. Zhang, Y. Zhang, W. F. Li et al., "Efficacy of Concurrent Chemotherapy for Intermediate Risk NPC in the Intensity-Modulated Radiotherapy Era: a Propensity-Matched Analysis," *Scientific Reports*, vol. 5, no. 1, p. 17378, 2015.

[11] C. Xu, L. H. Zhang, Y. P. Chen et al., "Chemoradiotherapy versus radiotherapy alone in stage II nasopharyngeal carcinoma: a systemic review and meta-analysis of 2138 patients," *Journal of Cancer*, vol. 8, no. 2, pp. 287–297, 2017.

[12] P. K. Mukherjee, N. K. Nema, N. Maity, and B. K. Sarkar, "Phytochemical and therapeutic potential of cucumber," *Fitoterapia*, vol. 84, pp. 227–236, 2013.

[13] J. C. Chen, M. H. Chiu, R. L. Nie, G. A. Cordell, and S. X. Qiu, "Cucurbitacins and cucurbitane glycosides: structures and biological activities," *Natural Product Reports*, vol. 22, no. 3, pp. 386–399, 2005.

[14] M. A. Blaskovich, J. Sun, A. Cantor, J. Turkson, R. Jove, and S. M. Sebti, "Discovery of JSI-124 (cucurbitacin I), a selective janus kinase/signal transducer and activator of transcription 3 signaling pathway inhibitor with potent antitumor activity against human and murine cancer cells in mice," *Cancer Research*, vol. 63, no. 6, pp. 1270–1279, 2003.

[15] M. Clericuzio, M. Mella, P. Vita-Finzi, M. Zema, and G. Vidari, "Cucurbitane triterpenoids from Leucopaxillus gentianeus," *Journal of Natural Products*, vol. 67, no. 11, pp. 1823–1828, 2004.

[16] S. Garg, S. C. Kaul, and R. Wadhwa, "Anti-stress and glial differentiation effects of a novel combination of Cucurbitacin B and Withanone (CucWi-N): experimental evidence," *Annals of Neurosciences*, vol. 25, no. 4, pp. 201–209, 2019.

[17] N. Wakimoto, D. Yin, J. O'Kelly et al., "Cucurbitacin B has a potent antiproliferative effect on breast cancer cells in vitro and in vivo," *Cancer Science*, vol. 99, no. 9, pp. 1793–1797, 2008.

[18] S. Garg, S. C. Kaul, and R. Wadhwa, "Cucurbitacin B and cancer intervention: chemistry, biology and mechanisms (review)," *International Journal of Oncology*, vol. 52, no. 1, pp. 19–37, 2017.

[19] Therapeutic Goods Association, "Health Safety Regulation-Substances that may be used in listed medicines in Australia," *Government of Australia*, p. 86, 2011.

[20] M. Promkan, S. Dakeng, S. Chakrabarty, O. Bogler, and P. Patmasiriwat, "The effectiveness of cucurbitacin B in BRCA1 defective breast cancer cells," *PLoS One*, vol. 8, no. 2, p. e55732, 2013.

[21] J. Liang, X. L. Zhang, J. W. Yuan et al., "Cucurbitacin B inhibits the migration and invasion of breast cancer cells by altering the biomechanical properties of cells," *Phytotherapy Research*, vol. 33, no. 3, pp. 618–630, 2019.

[22] S. Garg, H. Huifu, A. Kumari, D. Sundar, S. C. Kaul, and R. Wadhwa, "Induction of senescence in cancer cells by a novel combination of Cucurbitacin B and Withanone: molecular mechanism and therapeutic potential," *The Journals of Gerontology. Series A, Biological Sciences and Medical Sciences*, vol. 75, no. 6, pp. 1031–1041, 2020.

[23] X. M. Piao, F. Gao, J. X. Zhu et al., "Cucurbitacin B inhibits tumor angiogenesis by triggering the mitochondrial signaling pathway in endothelial cells," *International Journal of Molecular Medicine*, vol. 42, no. 2, pp. 1018–1025, 2018.

[24] Z. Q. Jin, J. Hao, X. Yang et al., "Higenamine enhances the antitumor effects of cucurbitacin B in breast cancer by inhibiting the interaction of AKT and CDK2," *Oncology Reports*, vol. 40, no. 4, pp. 2127–2136, 2018.

[25] S. Duangmano, P. Sae-lim, A. Suksamrarn, F. E. Domann, and P. Patmasiriwat, "Cucurbitacin B inhibits human breast cancer cell proliferation through disruption of microtubule polymerization and nucleophosmin/B23 translocation," *BMC Complementary and Alternative Medicine*, vol. 12, no. 1, p. 185, 2012.

[26] Y. Gao, M. S. Islam, J. Tian, V. W. Y. Lui, and D. Xiao, "Inactivation of ATP citrate lyase by Cucurbitacin B: a bioactive compound from cucumber, inhibits prostate cancer growth," *Cancer Letters*, vol. 349, no. 1, pp. 15–25, 2014.

[27] P. Lu, B. Yu, and J. Xu, "Cucurbitacin B regulates immature myeloid cell differentiation and enhances antitumor immunity in patients with lung cancer," *Cancer Biotherapy and Radiopharmaceuticals*, vol. 27, no. 8, pp. 495–503, 2012.

[28] Y. Qu, P. Cong, C. Lin, Y. Deng, J. Li-Ling, and M. Zhang, "Inhibition of paclitaxel resistance and apoptosis induction by cucurbitacin B in ovarian carcinoma cells," *Oncology Letters*, vol. 14, no. 1, pp. 145–152, 2017.

[29] K. T. Chan, F. Y. Meng, Q. Li et al., "Cucurbitacin B induces apoptosis and S phase cell cycle arrest in BEL-7402 human hepatocellular carcinoma cells and is effective via oral administration," *Cancer Letters*, vol. 294, no. 1, pp. 118–124, 2010.

[30] N. H. Thoennissen, G. B. Iwanski, N. B. Doan et al., "Cucurbitacin B induces apoptosis by inhibition of theJAK/STATPathway and potentiates antiproliferative effects of gemcitabine on pancreatic cancer cells," *Cancer Research*, vol. 69, no. 14, pp. 5876–5884, 2009.

[31] T. Liu, H. Peng, M. Zhang, Y. Deng, and Z. Wu, "Cucurbitacin B, a small molecule inhibitor of the Stat3 signaling pathway, enhances the chemosensitivity of laryngeal squamous cell carcinoma cells to cisplatin," *European Journal of Pharmacology*, vol. 641, no. 1, pp. 15–22, 2010.

[32] C. J. Henrich, C. L. Thomas, A. D. Brooks et al., "Effects of cucurbitacins on cell morphology are associated with sensitization of renal carcinoma cells to TRAIL-induced apoptosis," *Apoptosis*, vol. 17, no. 1, pp. 79–89, 2012.

[33] T. Zhang, Y. Li, K. A. Park et al., "Cucurbitacin induces autophagy through mitochondrial ROS production which counteracts to limit caspase-dependent apoptosis," *Autophagy*, vol. 8, no. 4, pp. 559–576, 2014.

[34] N. Jing and D. J. Tweardy, "Targeting Stat3 in cancer therapy," *Anti-Cancer Drugs*, vol. 16, no. 6, pp. 601–607, 2005.

[35] J. Sun, M. A. Blaskovich, R. Jove, S. K. Livingston, D. Coppola, and S. M. Sebti, "Cucurbitacin Q: a selective STAT3 activation inhibitor with potent antitumor activity," *Oncogene*, vol. 24, no. 20, pp. 3236–3245, 2005.

[36] Y. Cai, X. Fang, C. He et al., "Cucurbitacins: a systematic review of the phytochemistry and anticancer activity," *The American Journal of Chinese Medicine*, vol. 43, no. 7, pp. 1331–1350, 2015.

[37] K. T. Chan, K. Li, S. L. Liu, K. H. Chu, M. Toh, and W. D. Xie, "Cucurbitacin B inhibits STAT3 and the Raf/MEK/ERK pathway in leukemia cell line K562," *Cancer Letters*, vol. 289, no. 1, pp. 46–52, 2010.

[38] I. T. Silva, F. C. Geller, L. Persich et al., "Cytotoxic effects of natural and semisynthetic cucurbitacins on lung cancer cell line A549," *Investigational New Drugs*, vol. 34, no. 2, pp. 139–148, 2016.

[39] Q. Zheng, Y. Liu, W. Liu et al., "Cucurbitacin B inhibits growth and induces apoptosis through the JAK2/STAT3 and MAPK pathways in SH-SY5Y human neuroblastoma cells," *Molecular Medicine Reports*, vol. 10, no. 1, pp. 89–94, 2014.

[40] Z. R. Zhang, M. X. Gao, and K. Yang, "Cucurbitacin B inhibits cell proliferation and induces apoptosis in human osteosarcoma cells via modulation of the JAK2/STAT3 and MAPK pathways," *Experimental and Therapeutic Medicine*, vol. 14, no. 1, pp. 805–812, 2017.

Hindawi
Journal of Nanomaterials
Volume 2021, Article ID 5566316, 10 pages
https://doi.org/10.1155/2021/5566316

Research Article

Bioinformatics-Based Identification of lncRNA-miRNA-mRNA Network in Dilated Cardiomyopathy and Drug Prediction

Wei Liu,[1] **Jinqiang Cai**,[2] **Mengjie Tang**,[3] **and QinJing Yang**[1]

[1]*Department of Pharmacy, The Third Xiangya Hospital, Central South University, Changsha 410013, China*
[2]*Department of Pharmacy, Xiangya Medical College, Central South University, Changsha 410013, China*
[3]*Hunan Cancer Hospital, The Affiliated Cancer Hospital of Xiangya School of Medicine, Central South University, Changsha 410013, China*

Correspondence should be addressed to QinJing Yang; yangqinjing0624@163.com

Received 27 January 2021; Revised 4 February 2021; Accepted 17 February 2021; Published 4 March 2021

Academic Editor: Tingting Hong

Background. Dilated cardiomyopathy (DCM) is a cardiovascular disease of unknown etiology with progressive aggravation. More and more studies have shown that long noncoding RNAs (lncRNAs) play an essential role in dilated cardiomyopathy formation and development. The mechanism of action of competitive endogenous RNA (ceRNA) networks formed based on the principle that lncRNAs affect mRNAs' expression level by competitively binding microRNAs (miRNAs) in dilated cardiomyopathy has rarely been reported. *Objective*. This study is aimed at constructing a lncRNA-miRNA-mRNA ceRNA network by bioinformatics analysis methods, discovering, and validating potential biomarkers of DCM in the ceRNA network and determining possible therapeutic targets from them for drug prediction. *Methods*. A lncRNA dataset and a mRNA microarray dataset were downloaded from the Gene Expression Omnibus Database (GEO). Gene expression was compared between blood samples from patients with dilated cardiomyopathy and blood samples from normal subjects to identify differential expression of lncRNAs and mRNAs. The lncRNA-miRNA-mRNA network was constructed using bioinformatics tools, and functional and pathway enrichment analysis and protein-protein interactions were performed. The mRNAs in the network and the proteins they encode are then used as targets for predicting drugs. Besides, the expression of lncRNAs in the ceRNA network was validated by real-time quantitative PCR (qRT-PCR) experiments in vitro. *Results*. The differentially expressed lncRNA-miRNA-mRNA ceRNA network in dilated cardiomyopathy was successfully established. Two differentially overexpressed key lncRNAs were found from the network: AC093817 and AC091062, and qRT-PCR experiments further validated the overexpression of AC093817 and AC091062. The mRNAs in the network and the proteins encoded by the mRNAs were used for drug prediction to get related drugs. *Conclusion*. This study supports a possible mechanism and drug development of dilated cardiomyopathy, AC093817 and AC091062 being potential biomarkers of dilated cardiomyopathy.

1. Introduction

Dilated cardiomyopathy is defined as left ventricular dilatation and left ventricular systolic dysfunction in the absence of abnormal load (hypertension, valvular disease) or coronary artery disease sufficient to cause global systolic function impairment [1]. Risk factors for dilated cardiomyopathy include genetic and environmental factors. Dilated cardiomyopathy may present with autosomal dominant, monogenic features with X chromosome, autosomal recessive inheritance, or with the effects of environmental factors such as nutritional deficiency, endocrine dysfunction, and taking cardiotoxic drugs such as Adriamycin [1, 2]. The early symptoms of dilated cardiomyopathy are not obvious, and many patients have progressed to the terminal stage when they are diagnosed with the disease, which can lead to heart failure or even death [3]. Therefore, new biomarkers are essential for the early diagnosis and prognosis of dilated cardiomyopathy. Although previous studies have found that genetic factors play a crucial role in dilated cardiomyopathy, the pathogenesis of dilated cardiomyopathy is still unclear, and new treatment strategies are lacking.

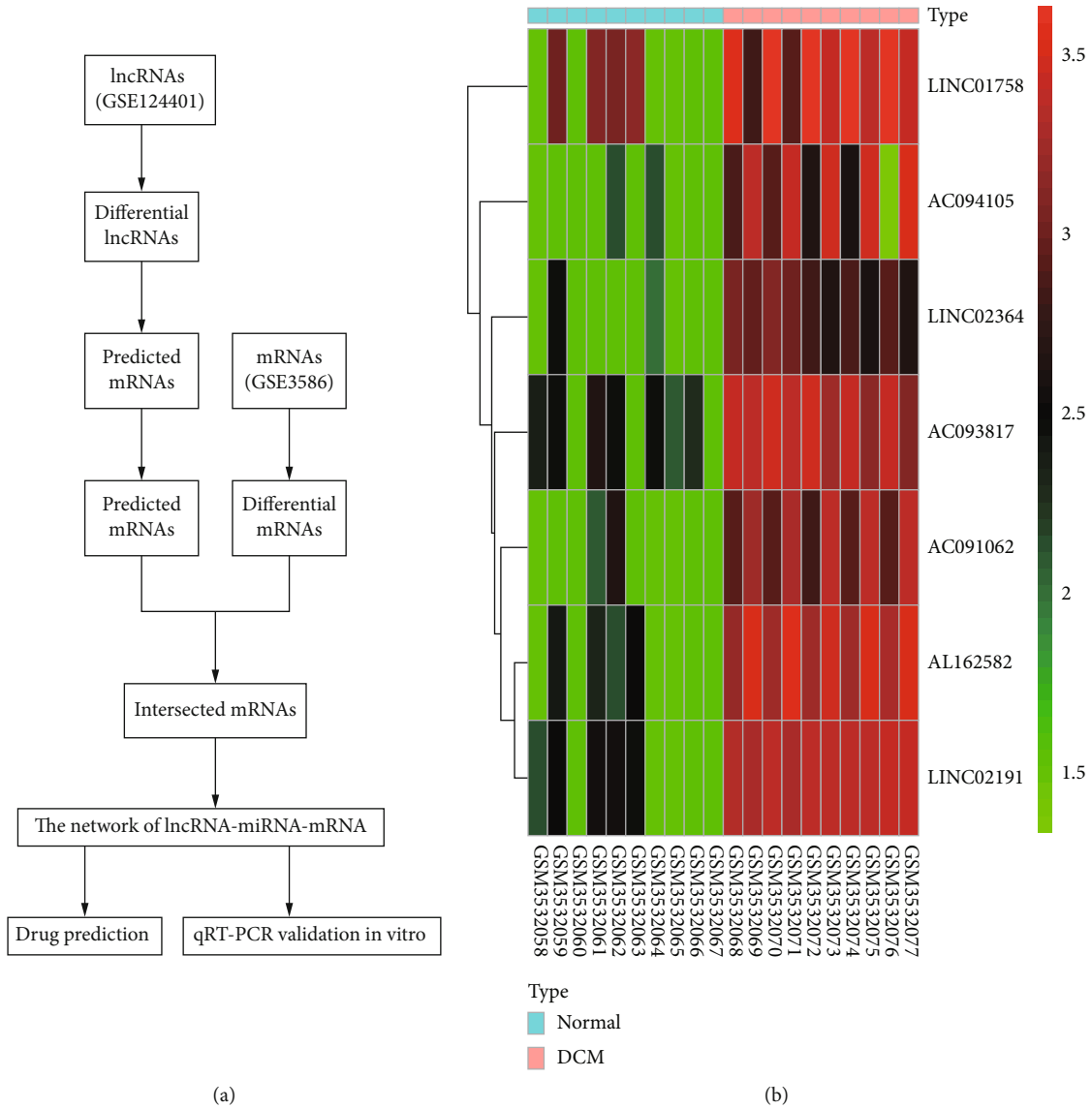

Figure 1: Continued.

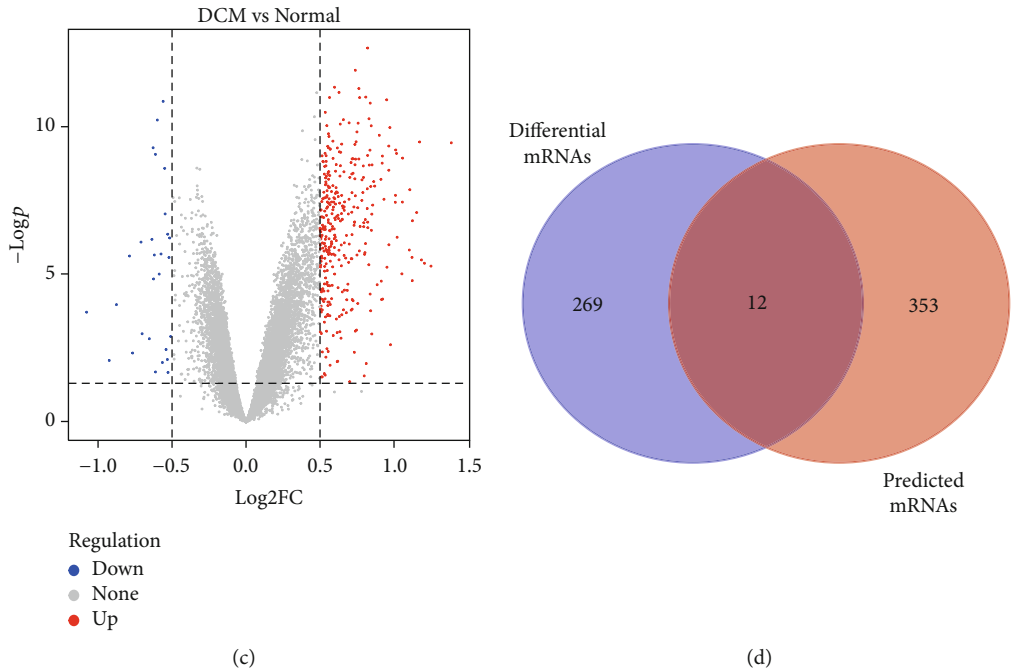

Figure 1: Flow chart of the approach and identification of intersected mRNAs in DCM (dilated cardiomyopathy). (a) Flow chart of the approach utilized in this study. (b) The heatmap of differentially expressed lncRNAs from the GSE124401 dataset. (c) The volcano plot of differentially expressed mRNAs from GSE3586 dataset. (d) The intersection analysis of predicted mRNAs and differential mRNAs.

lncRNAs are a group of RNAs > 200 nucleotides in length, without protein-coding function, regulating gene expression at the epigenetic, transcriptional, and posttranscriptional levels participating actively in various physiological and pathological processes [4, 5]. In recent years, more and more evidence has shown that lncRNAs play a vital role in the occurrence and development of dilated cardiomyopathy and are very critical biomarkers and therapeutic targets. Li et al. found the most upregulated lncRNA RP11-544D21.2 in DCM patients, and this human-specific lncRNA significantly regulated DCM-related genes in cardiomyocytes and affected the ductal formation and cell migration in endothelial cells [6]. Lin et al. found that differentially expressed lncRNAs are involved in some specific biological processes and regulate some signaling pathways in the plasma of heart failure patients with dilated cardiomyopathy and ischemic cardiomyopathy [7]. Wang et al. predicted a novel function of an annotated lncRNA-H19 that may regulate apoptotic signal-regulated kinases through pathway analysis of 39 key lncRNAs that regulate key pathways in myocardial infarction [8]. Cheng and Jiang found that lncRNA HAND2-AS1 may be involved in end-stage dilated cardiomyopathy [3].

Luo et al. identified IDI2-AS1 and XIST two lncRNAs and their associated pathways in the pathogenesis of DCM, providing potential targets for the diagnosis and treatment of DCM [9]. Zhang et al. found that circulating lncRNA ENST00000507296 is a biomarker for the prognosis of DCM patients [10]. Qiu et al. found that AC061961.2, LING01-AS1, and RP11-13E1.5 were downregulated in DCM patients' myocardial tissue, and these lncRNAs could be used as critical diagnostic biomarkers and therapeutic targets for DCM [11]. Zhang et al. found that the H19/miR-675 axis was involved in the promoting effect of cardiomyocyte apoptosis by targeting PA2G4, providing a new therapeutic strategy for treating doxorubicin-induced DCM [5]. Tao et al. identified four lncRNA-miRNA pairs associated with DCM, which can be used as candidate diagnostic biomarkers or potential therapeutic targets for DCM [12]. However, the mechanism of action of lncRNA-associated ceRNA networks in dilated cardiomyopathy is unknown. Therefore, it is necessary to construct a lncRNA-miRNA-mRNA ceRNA network to obtain more information about the treatment and diagnosis of dilated cardiomyopathy from the ceRNA network.

The aim of this study was to identify differentially expressed lncRNAs and mRNAs using the limma package in R software. miRNAs were predicted using the miRcode database by differentially expressed lncRNAs, mRNAs were predicted by the combination of Targetscan, miRTarBase, and miRDB databases, and finally, differentially expressed mRNAs and predicted mRNAs were intersected to construct a lncRNA-miRNA-mRNA ceRNA network by Cytoscape software. mRNAs in the network were subjected to GO enrichment analysis, KEGG enrichment analysis, and construction of protein-protein interaction network. The lncRNAs in the network were validated by qRT-PCR in vitro. The mRNA-encoded proteins in the network were used for drug prediction through the Drugbank database, and mRNA-protein-drug networks were constructed. Drug-Gene interaction database and Connectivity map predicted the mRNAs in the network to find linked chemical drugs. The flow chart is illustrated in Figure 1(a).

2. Materials and Methods

2.1. Microarray Data Sources. From the Gene Expression Omnibus Database (GEO) (https://www.ncbi.nlm.nih.gov/

Table 1: Basic information of the two microarray datasets from GEO.

Data source	Platform	Series	Sample size (N/T)
lncRNA	GPL16956	GSE124401	10/10
mRNA	GPL3050	GSE3586	15/13

N: normal; T: DCM.

geo/), two DCM microarray expression datasets (GSE124401 and GSE3586) were downloaded. The lncRNA dataset included lncRNA expression data in the plasma of 10 normal subjects and ten heart failure (HF) patients diagnosed with dilated cardiomyopathy (DCM). The samples were tested according to GPL16956Agilent-045997 ArraystarhumanlncRNAmicroarrayV3 (ProbeNameVersion) data. The mRNA dataset consisted of mRNA expression data from septal myocardial tissue samples from 13 dilated cardiomyopathy hearts at transplantation and 15 NF donor hearts not transplanted due to visible coronary calcification, tested against data GPL3050HumanUnigene3.1cDNAArray37.5Kv1.0. Table 1 summarizes the necessary information of two DCM microarray expression datasets (GSE124401 and GSE3586).

2.2. Identification of Differentially Expressed Genes. Differential expression analysis was performed on two DCM microarray expression datasets (GSE124401 and GSE3586) using the "limma" package of the R language. The screening criteria for differentially expressed lncRNAs in GSE124401 were $|\log 2FC| > 2$ (p value < 0.05), and the screening criteria for differentially expressed mRNAs in GSE3586 were $|\log 2FC| > 0.5$ (p value < 0.05).

2.3. Acquisition of Predicted miRNAs and Predicted mRNAs. The differentially expressed lncRNAs described above were predicted by the miRcode database to obtain the corresponding predicted miRNAs, and the predicted miRNAs were further predicted by Targetscan (http://www.targetscan.org/vert_72/), miRTarBase (http://mirtarbase.mbc.nctu.edu.tw/index.html), and miRDB (http://www.mirdb.org/), three databases in combination to get the corresponding predicted mRNAs.

2.4. Cross-Analysis of Differentially Expressed mRNA and Predicted mRNA. The intersection of the differentially expressed mRNA with the predicted mRNA described previously was taken to obtain the intersection mRNA, through the Calculate and draw custom Venn diagrams online website (http://bioinformatics.psb.ugent.be/cgibin/liste/Venn/calculate_venn.htpl), for visualization.

2.5. Construction of Network. The intersected mRNAs and the corresponding predicted miRNAs and differentially expressed lncRNAs together were used to construct the lncRNA-miRNA-mRNA ceRNA network by Cytoscape software. The mRNAs in the ceRNA network were then analyzed using the STRING online website (https://string-db.org/), identified the encoded proteins and constructed protein-protein interaction (PPI) networks.

2.6. Functional Enrichment Analysis of Differentially Expressed Genes. Using the DAVID online website (https://david.ncifcrf.gov/home.jsp), GO analysis of differentially expressed mRNAs in the network was performed to assess the cellular component (CC), biological process (BP), and molecular function (MF) of each mRNA. KEGG analysis of differentially expressed mRNAs in the network was performed using the R language clusterProfiler package to enrich the related pathways. The links between differentially expressed mRNAs and corresponding pathways were visualized with Cytoscape software to construct mRNA-pathway networks.

2.7. Acquisition of Drug Molecules. The proteins encoded by the mRNAs in the ceRNA network mentioned above were accessed through the Drugbank online website (https://go.drugbank.com/), for drug prediction, and an mRNA-protein-drug network was constructed by Cytoscape software. The mRNAs in the ceRNA network were analyzed by Drug-Gene interaction database (https://dgidb.genome.wustl.edu/); the drug was predicted directly and visualized with Cytoscape software. The mRNAs in the ceRNA network passed through Connectivity map (https://portals.broadinstitute.org/cmap/), predicted to select drugs with "up score" below -0.645 (i.e., drugs most likely to reverse gene differential expression for DCM), summarized the specific connectivity score of each drug for each mRNA in the specific cell line, and made a heatmap with the R language pack.

2.8. Cell Culture. The establishment of a cellular model of DCM was performed as previously described [13]. H9c2 cardiomyocytes (Type Culture Collection of Chinese Academy of Sciences, Shanghai, China) were cultured in DMEM supplemented with 10% FBS in a humidified atmosphere of 5% CO_2 at 37°C. H9c2 cardiomyocytes were treated as follows: control cells, in which cells were treated with medium only; doxorubicin treatment group, in which cells were treated with 5 μM doxorubicin for 24 hours.

2.9. Real-Time Quantitative PCR. Total RNA was isolated from H9c2 cells using Trizol reagent (TaKaRa, Japan) according to the manufacturer's instructions. One microgram of RNA was reverse transcribed into cDNA using the Revert Aid First Strand cDNA Synthesis Kit (Thermo, USA). Quantitative RT-PCR was then performed with Pro Taq HS Premix Probe qPCR Kit (Accurate, Hunan, China). The amplification program consisted of one cycle of predenaturation at 95°C for 5 min, 37 cycles of denaturation at 95°C for 30 s, annealing at 60°C for 30 s, and extension at 72°C for 10 min. The GAPDH gene was used as an endogenous control gene for normalizing the expression of target genes. Each sample was analyzed in triplicate. Primer sequences are shown in Table 2.

3. Results

3.1. Differential Expression Analysis and Prediction of Genes. Seven differentially expressed lncRNAs were obtained from GSE124401 by the screening criteria of $|\log 2FC| > 2$ (p value < 0.05), and a heatmap was made with the R language pack

Table 2: The sequences of primers used for qRT-PCR.

Gene name	Primer sequences (5′-3′)	Annealing temperature
AC093817	F: GCAGGAGAACGAAATTAAGAGACAAG	60°C
	R: GGCTAGAGGATTATTTGAGACCAGGAT	
AC091062	F: TATTGCCCATGCCCCTAACTC	60°C
	R: CTGAAGCCCCCAGACAGTGA	
Gapdh	F: ACAGCAACAGGGTGGTGGAC	60°C
	R: TTTGAGGGTGCAGCGAACTT	

F: forward primer; R: reverse primer.

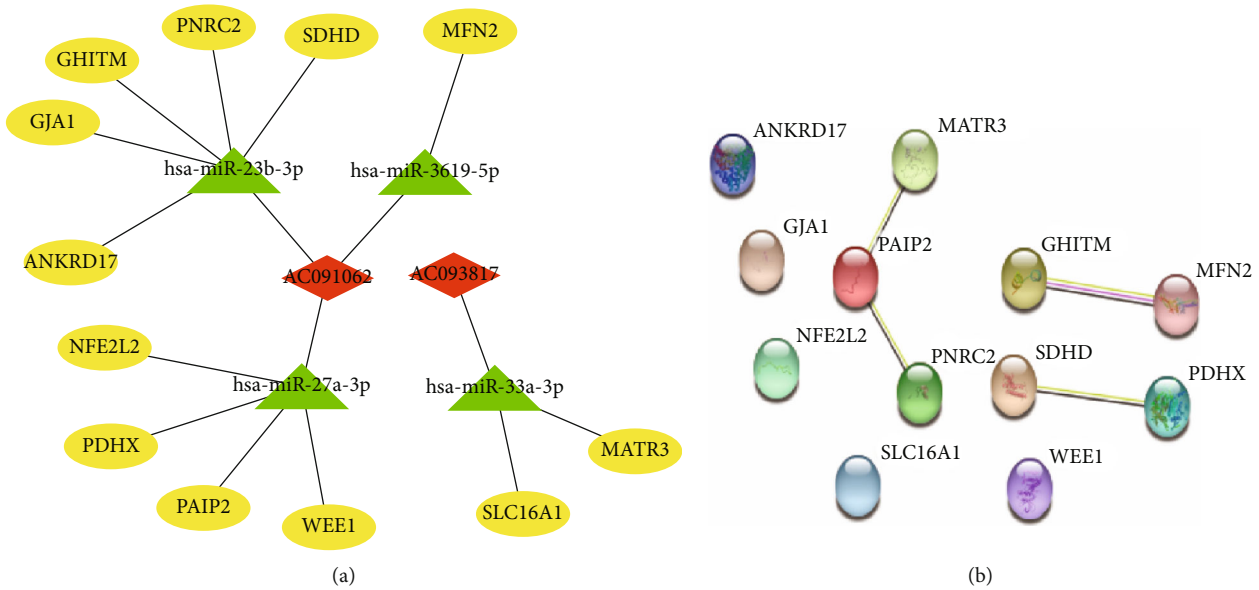

Figure 2: Molecular regulatory interaction network. (a) lncRNA-miRNA-mRNA biomolecular network. Red indicates lncRNA, green indicates miRNA, and yellow indicates mRNA. (b) Protein-protein interaction network of mRNA.

(Figure 1(b)). A screening criterion of $|\log 2FC| > 0.5$ (p value < 0.05) yielded 365 differentially expressed mRNAs from GSE3586, and a volcano map was made with the R language pack (Figure 1(c)). The seven differentially expressed lncRNAs resulted in 47 predicted miRNAs by miRcode prediction, and these 47 predicted miRNAs were further predicted by a combination of three databases: Targetscan, miRTarBase, and miRDB resulting in 281 predicted mRNAs.

3.2. Acquisition of Intersection mRNA and Network Construction. From GSE3586, 365 differentially expressed mRNAs were obtained intersecting with 281 predicted mRNAs to take the intersection resulting in 12 intersection mRNAs, visualized with a Wayne diagram (Figure 1(d)). These 12 intersection mRNAs and the corresponding predicted miRNAs and differentially expressed lncRNAs constructed the lncRNA-miRNA-mRNA ceRNA network by Cytoscape software (Figure 2(a)). Twelve mRNAs in the ceRNA network were identified to encode proteins and create a protein interaction (PPI) network through the STRING online website (Figure 2(b)). In the PPI network, protein PAIP2 was connected to the other two proteins, indicating its central regulatory role.

3.3. Enrichment Analysis of mRNAs in the ceRNA Network. GO and KEGG enrichment analyses were performed on the mRNAs in the ceRNA network (Figure 3). GO enrichment analysis showed that "pyruvate metabolic process," "neuronal projection morphogenesis," and "apoptotic process" were enriched in the biological process (BP) classification and "protein binding" was enriched according to the molecular function (MF) classification. Enrichment of "mitochondria," "chromatin," and "mitochondrial outer membrane" was shown in the cellular component (CC) classification (Figures 3(a) and 3(b)); KEGG enrichment analysis showed that differentially expressed mRNAs in the network were mainly involved in signaling pathways such as "Parkinson's disease," "citric acid cycle (TCA cycle)," "amyotrophic lateral sclerosis," and "neurodegeneration" (Figures 3(c) and 3(d)). The mRNA-pathway network was visualized and constructed with Cytoscape software (Figure 4(a)).

3.4. Drug Prediction of mRNA in the ceRNA Network. Twelve mRNA encoded proteins in the ceRNA network predicted drugs through the online website of Drugbank, and four of them got related drugs and constructed the mRNA-protein-drug network (Figure 4(b)). Twelve mRNAs in the ceRNA network predicted drugs directly through the drug-gene

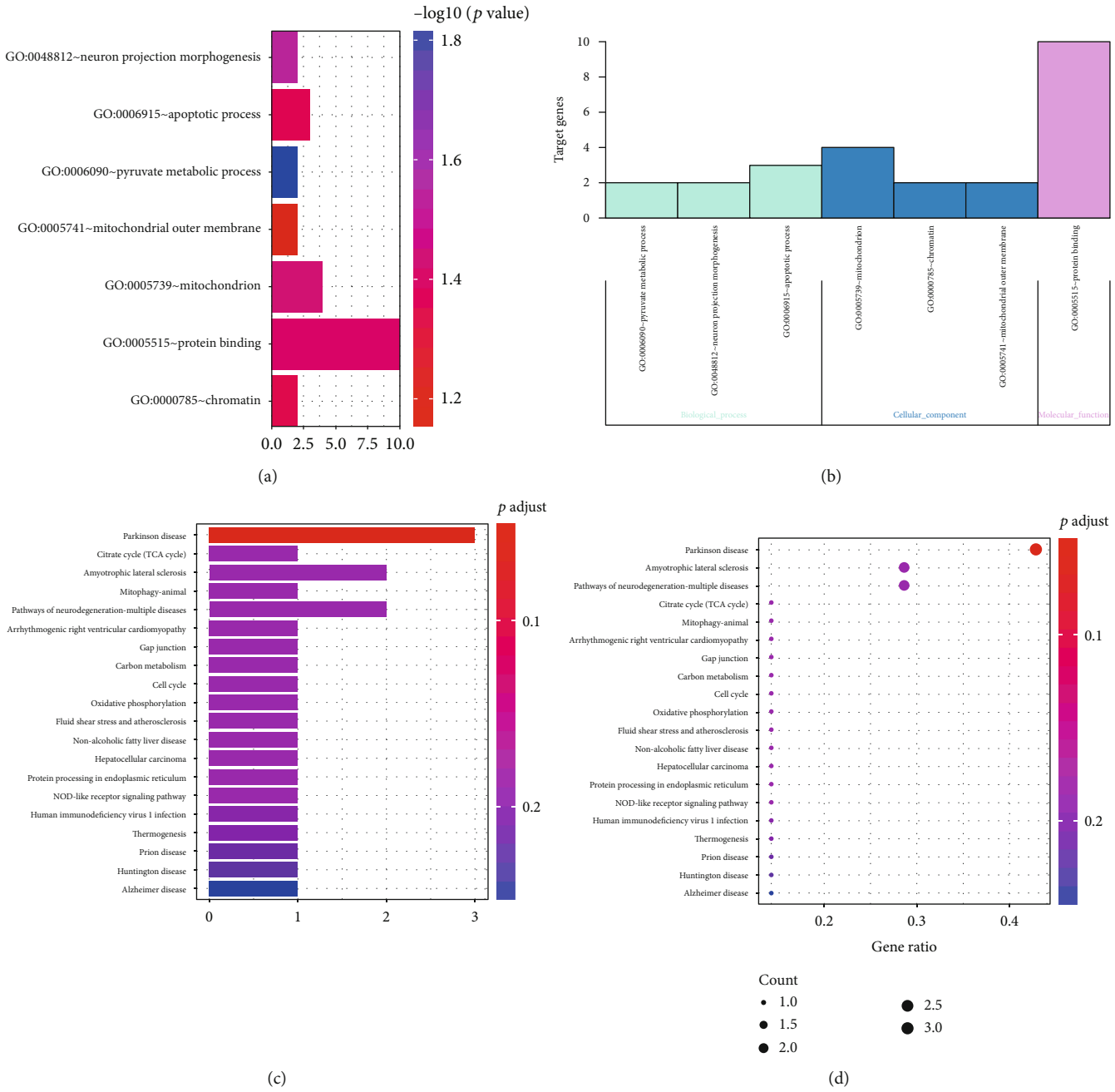

Figure 3: Enrichment analysis of the intersected mRNAs. (a) Bar plot of the GO analysis. (b) Histogram of GO cluster analysis. Target genes are intersected mRNAs. (c) Bar plot of the KEGG analysis. (d) Bubble plot of the KEGG analysis.

interaction database, and five of them got related drugs and constructed the mRNA-drug network (Figure 4(c)). Twelve upregulated mRNAs in the ceRNA network were added to the up tag list. Two downregulated mRNAs were added to the down tag list from GSE3586 differentially expressed mRNAs (setting down downregulated list is only necessary for uploading files, which does not affect drug prediction of the up tag list). The 16 drugs with "up scores" below -0.645 were predicted by the connectivity map. The specific connectivity score of these 16 drugs regarding the expression of 12 upregulated mRNAs was summarized, and the heatmap (Figure 4(d)) was made with the R language package.

3.5. Expression of Two lncRNAs in DCM Cells. To validate the expression levels of these two lncRNAs (AC093817 and AC091062) in DCM cells, we validated them by qRT-PCR. The results showed that both AC093817 and AC091062 were significantly overexpressed in DCM cells compared with the normal group (Figure 5). These results are consistent with the results of bioinformatics analysis.

4. Discussion

Dilated cardiomyopathy (DCM) is a cardiovascular disease of unknown pathogenesis, one of the leading causes of heart

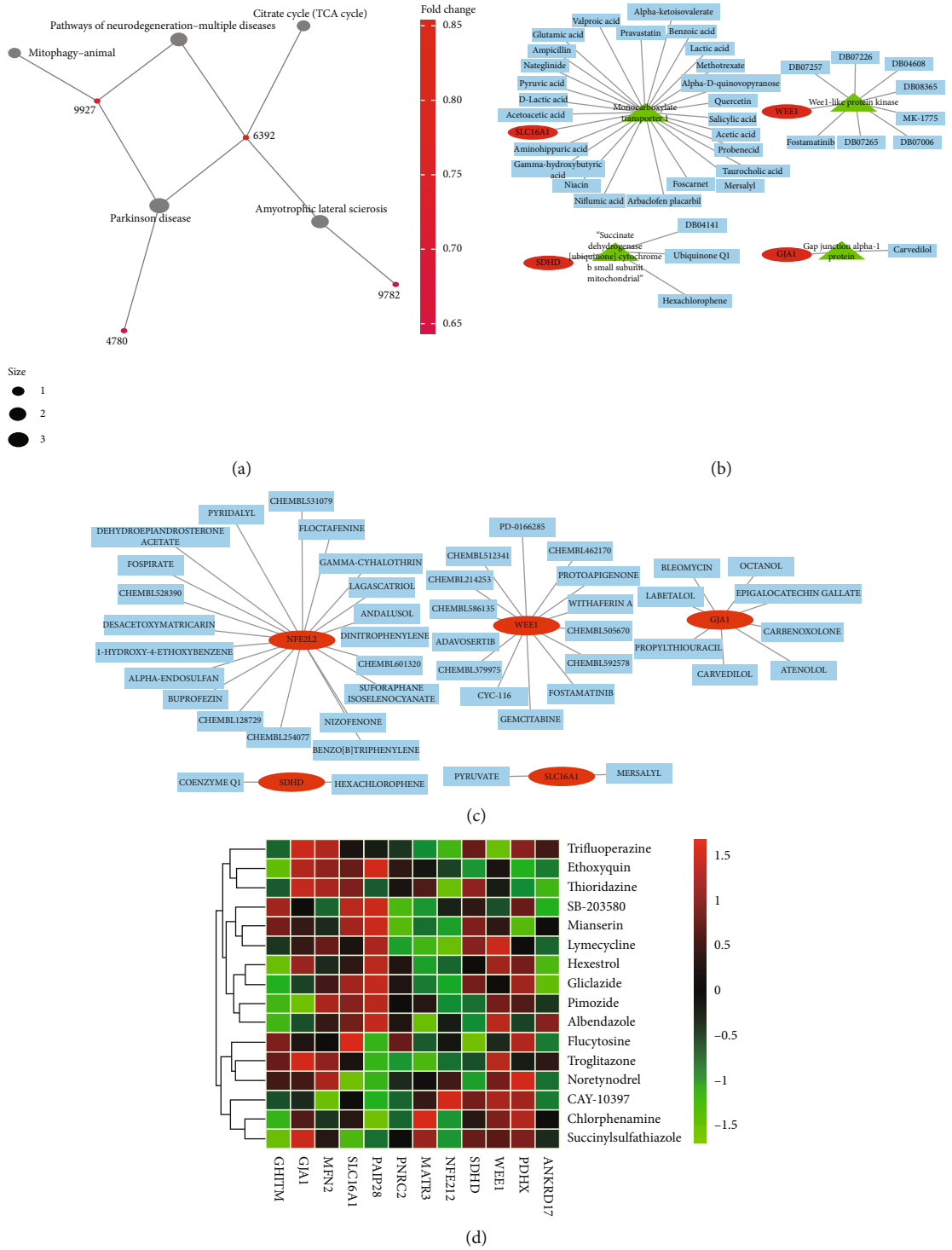

FIGURE 4: mRNA-pathway network and drug prediction. (a) mRNA-pathway network. Red dots indicate entrezID of mRNA, and black dots are pathways. The mRNA's gene name corresponding to entrezID can be obtained from the Supplementary Table S1. (b) mRNA-protein-drug network. Red ovals represent mRNAs, green triangles represent proteins encoded by mRNAs, and blue rectangles are drugs. Seven of these drugs are indicated by Drugbank-ID because the names are too long, and the drug names corresponding to Drugbank-IDs can be obtained from Supplementary Table S2. (c) mRNA-drug network. Red indicates mRNA, and blue indicates drug. Among them, the 821 drugs corresponding to NFE2L2 showed only the top 20, and all 821 drug names can be obtained in Supplementary Table S3. (d) Heatmap of the effect of drugs on gene expression. Green indicates that the drug can downregulate the gene expression, red marks that the drug can upregulate the gene expression, and black means that the drug and gene expression have little correlation.

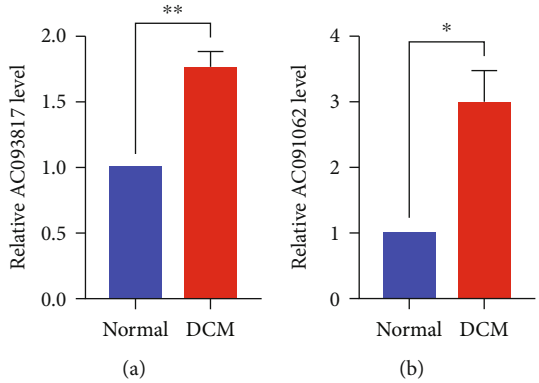

Figure 5: The expression levels of two lncRNAs involved in DCM were measured by qRT-PCR. $n = 3$; $*p < 0.05$ and $**p < 0.01$. (a) AC093817 was upregulated in DCM cells. (b) AC091062 was upregulated in DCM cells.

failure. Patients at any stage of the disease are at risk of sudden death. The etiology of dilated cardiomyopathy is very complex and can be regarded as a complex interaction between environmental factors and genetic background. Dilated cardiomyopathy is more common in men than in women, and its prevalence in the general population is estimated at 36 cases per 100,000 [14]. A large number of patients with dilated cardiomyopathy may have an incubation period, clinical manifestations are asymptomatic, the condition is progressively aggravated, severe myocardial failure has developed at the time of diagnosis, which will lead to heart transplantation or even death, and almost 50% of patients die within five years, which is extremely harmful [14]. Therefore, there is an urgent need to clarify the role of ceRNA networks in the course of DCM and find serum biomarkers and related potential therapeutic agents to provide further support for the diagnosis and treatment of DCM.

Many studies have investigated the mechanism and clinical significance of cardiac lncRNA or even lncRNA-miRNA pairs in DCM in recent years. However, the impact of serum ceRNA networks on DCM in patients with DCM has not been addressed. This study constructed a complete lncRNA-miRNA-mRNA ceRNA network based on lncRNA and mRNA expression profiles for targeted prediction and taking the intersection, providing new ideas for the posttranscriptional level of gene regulation. Drug prediction of mRNAs and their encoded proteins in the ceRNA networks by multiple pharmacogenomics databases may be useful therapeutic molecules in the future. Connectivity map's prediction results showed that all 16 drugs were effective in downregulating the expression of some of these 12 overexpressed mRNAs. However, these 16 drugs also upregulated the expression of some mRNAs to a greater or lesser extent. This may provide support for the active drug structural design of DCM.

The two lncRNAs and 12 mRNAs overexpressed in the network were found for the first time, which are very different from the differentially expressed lncRNAs and mRNAs obtained from previous studies, such as LMNA, FLNC, and TTN, which have been intensely studied in precision medicine for DCM [15]. This may be because previous studies have directly studied differential gene expression from heart samples of DCM patients and controls. Differently, this study newly added the differential gene expression of plasma samples from DCM patients and controls as a starting point on this basis. The new biomarker lncRNAs obtained from the new starting point: AC093817 and AC091062, may provide new ideas for the therapeutic diagnosis of DCM. More importantly, for these two lncRNAs in the ceRNA network, the comparison of qRT-PCR results between doxorubicin-induced derived DCM cells and control further validated that both AC093817 and AC091062 were significantly overexpressed in DCM cells.

The "mitochondria," "pyruvate metabolic process," and "apoptotic process" involved in the overexpressed mRNA in the network may indicate that the cardiac cell metabolism is abnormally active in DCM patients, corresponding to the clinical characteristics of ventricular enlargement in DCM, which is a compensatory mechanism for weakened myocardial contraction and reduced score. The pathway pathways involving overexpressed mRNA not only show cellular metabolic pathways such as citric acid cycle (TCA cycle) and oxidative phosphorylation but also are related to atherosclerosis, viral infection, and even a variety of neurodegenerative diseases (Parkinson's disease, Huntington's disease, Alzheimer's disease, etc.). The diversity of pathways in which it is involved corresponds to its various pathogenic factors such as cardiotoxic compounds, metabolism, rheumatological and endocrine diseases, and cellular infiltration and viral infection [16]. Due to multiple heterogeneous etiologies, dilated cardiomyopathy is an "umbrella" term that describes the final common pathway of different pathogenic processes and gene-environment interactions [17]. A further accurate understanding of the molecular mechanisms and signaling pathways of DCM caused by various etiologies facilitates further subdivision of DCM, which is of great significance for targeted therapy and prognosis of DCM.

In most cases, dilated cardiomyopathy treatment refers to heart failure treatment based on medical treatment with angiotensin-converting enzyme inhibitors (angiotensin receptor blockers or angiotensin receptor/neprilysin inhibitors, if applicable), beta-blockers, and mineralocorticoid receptor antagonists according to current guidelines for heart failure [16]. Different from the previous ideas of symptomatic treatment with drugs to delay disease progression, this study selects the corresponding drugs through multiple

pharmacogenomics databases based on the new thinking of targeted therapy for specific disease mechanisms to reverse the disease process, targeting the 12 mRNAs overexpressed in the network and their encoded proteins, and the mechanistic analysis of the downregulation of mRNA expression and inhibition of proteins by these drugs in the future will further reveal the common pathways of their effects, which can be used as the starting point for subsequent studies.

Validating effective RNA treatment strategies in a number of cancer treatment studies [18–24] can also be used as an adjuvant treatment for DCM. In the future, we can construct a nanotargeted therapeutic system by designing miRNA overexpression vector gene drugs together with chemical drugs through rational encapsulation of nanomaterials such as cationic polymers and liposomes and connecting cardiac-targeting ligands in the outer layer [25–27]. With the rapid development of RNA nanotechnology, we can also construct RNAs with specific folded structures and spatial conformations to achieve downregulation of overexpressed mRNAs, such as miRNAs and siRNAs with specific structures and functions. Of course, this requires a lot of basic analysis and experimental validation [28–30].

5. Conclusion

In conclusion, in this study, we constructed a complete DCM differentially expressed lncRNA-miRNA-mRNA ceRNA network, found that AC093817 and AC091062 are potential biomarkers of dilated cardiomyopathy, and proposed potential therapeutic agents that can be used for this disease by integrating and analyzing microarray gene expression data, providing support for possible mechanisms and drug development of dilated cardiomyopathy.

Data Availability

The data used to support the findings of this study are available in the Gene Expression Omnibus (GEO) repository (https://www.ncbi.nlm.nih.gov/gds).

Conflicts of Interest

The authors declare that there is no conflict of interest regarding the publication of this paper.

Acknowledgments

This study was supported by the Scientific Research Project of Hunan Health Commission (No. 202102041763 and No. 20200985), Natural Science Foundation of Changsha (No. 202045504), and Hunan Cancer Hospital Climb Plan (No. 2020QH001).

Supplementary Materials

Supplementary 1. Table S1: the gene name corresponding to the entrezID of the mRNA on Figure 4(a).

Supplementary 2. Table S2: the drug name corresponding to the Drugbank-ID of the drug on Figure 4(b).

Supplementary 3. Table S3: all 821 drug names corresponding to NFE2L2 on Figure 4(c).

References

[1] P. Elliott, B. Andersson, E. Arbustini et al., "Classification of the cardiomyopathies: a position statement from the European Society of Cardiology Working Group on Myocardial and Pericardial Diseases," *European Heart Journal*, vol. 29, no. 2, pp. 270–276, 2007.

[2] Y. M. Pinto, P. M. Elliott, E. Arbustini et al., "Proposal for a revised definition of dilated cardiomyopathy, hypokinetic non-dilated cardiomyopathy, and its implications for clinical practice: a position statement of the ESC working group on myocardial and pericardial diseases," *European Heart Journal*, vol. 37, no. 23, pp. 1850–1858, 2016.

[3] X. Cheng and H. Jiang, "Long non-coding RNA HAND2-AS1 downregulation predicts poor survival of patients with end-stage dilated cardiomyopathy," *The Journal of International Medical Research*, vol. 47, no. 8, pp. 3690–3698, 2019.

[4] E. K. Robinson, S. Covarrubias, and S. Carpenter, "The how and why of lncRNA function: an innate immune perspective," *Biochimica et Biophysica Acta (BBA) - Gene Regulatory Mechanisms*, vol. 1863, no. 4, article 194419, 2020.

[5] Y. Zhang, M. Zhang, W. Xu, J. Chen, and X. Zhou, "The long non-coding RNA H19 promotes cardiomyocyte apoptosis in dilated cardiomyopathy," *Oncotarget*, vol. 8, no. 17, pp. 28588–28594, 2017.

[6] H. Li, C. Chen, J. Fan et al., "Identification of cardiac long non-coding RNA profile in human dilated cardiomyopathy," *Cardiovascular Research*, vol. 114, no. 5, pp. 747–758, 2018.

[7] F. Lin, X. Gong, P. Yu et al., "Distinct circulating expression profiles of long noncoding RNAs in heart failure patients with ischemic and nonischemic dilated cardiomyopathy," *Frontiers in Genetics*, vol. 10, p. 1116, 2019.

[8] P. Wang, H. Fu, J. Cui, and X. Chen, "Differential lncRNA-mRNA co-expression network analysis revealing the potential regulatory roles of lncRNAs in myocardial infarction," *Molecular Medicine Reports*, vol. 13, no. 2, pp. 1195–1203, 2016.

[9] X. Luo, P. Luo, and Y. Zhang, "Identification of differentially expressed long non-coding RNAs associated with dilated cardiomyopathy using integrated bioinformatics approaches," *Drug Discov Ther*, vol. 14, no. 4, pp. 181–186, 2020.

[10] X. Zhang, X. Nie, S. Yuan et al., "Circulating long non-coding RNA ENST00000507296 is a prognostic indicator in patients with dilated cardiomyopathy," *Mol Ther Nucleic Acids*, vol. 16, pp. 82–90, 2019.

[11] Z. Qiu, B. Ye, L. Yin, W. Chen, Y. Xu, and X. Chen, "Downregulation of AC061961.2, LING01-AS1, and RP11-13E1.5 is associated with dilated cardiomyopathy progression," *Journal of Cellular Physiology*, vol. 234, no. 4, pp. 4460–4471, 2019.

[12] L. Tao, L. Yang, X. Huang, F. Hua, and X. Yang, "Reconstruction and analysis of the lncRNA-miRNA-mRNA network based on competitive endogenous RNA reveal functional lncRNAs in dilated cardiomyopathy," *Frontiers in Genetics*, vol. 10, p. 1149, 2019.

[13] Y. Xia, Z. Chen, A. Chen et al., "LCZ696 improves cardiac function via alleviating Drp1-mediated mitochondrial dysfunction in mice with doxorubicin-induced dilated cardiomyopathy," *Journal of Molecular and Cellular Cardiology*, vol. 108, pp. 138–148, 2017.

[14] H. Mahmaljy, V. S. Yelamanchili, and M. Singhal, "Dilated cardiomyopathy," in *StatPearls*, StatPearls Publishing LLC, Treasure Island (FL), 2020.

[15] A. Morales, D. D. Kinnamon, E. Jordan et al., "Variant interpretation for dilated cardiomyopathy: refinement of the American College of Medical Genetics and Genomics/ClinGen Guidelines for the DCM Precision Medicine Study," *Circulation: Genomic and Precision Medicine*, vol. 13, no. 2, article e002480, 2020.

[16] A. Hänselmann, C. Veltmann, J. Bauersachs, and D. Berliner, "Dilated cardiomyopathies and non-compaction cardiomyopathy," *Herz*, vol. 45, no. 3, pp. 212–220, 2020.

[17] M. Merlo, A. Cannatà, and G. Sinagra, "Dilated cardiomyopathy: a paradigm of revolution in medicine," *Journal of Clinical Medicine*, vol. 9, no. 11, article 3385, 2020.

[18] R. Esteve-Puig, A. Bueno-Costa, and M. Esteller, "Writers, readers and erasers of RNA modifications in cancer," *Cancer Letters*, vol. 474, pp. 127–137, 2020.

[19] J. Desterro, P. Bak-Gordon, and M. Carmo-Fonseca, "Targeting mRNA processing as an anticancer strategy," *Nature Reviews. Drug Discovery*, vol. 19, no. 2, pp. 112–129, 2020.

[20] Y. Xie, Y. Hang, Y. Wang et al., "Stromal modulation and treatment of metastatic pancreatic cancer with local intraperitoneal triple miRNA/siRNA nanotherapy," *ACS Nano*, vol. 14, no. 1, pp. 255–271, 2020.

[21] C. M. Guo, S. Q. Liu, and M. Z. Sun, "miR-429 as biomarker for diagnosis, treatment and prognosis of cancers and its potential action mechanisms: a systematic literature review," *Neoplasma*, vol. 67, no. 2, pp. 215–228, 2020.

[22] R. Li, J. Jiang, H. Shi, H. Qian, X. Zhang, and W. Xu, "CircRNA: a rising star in gastric cancer," *Cellular and Molecular Life Sciences*, vol. 77, no. 9, pp. 1661–1680, 2020.

[23] J. Liu and B. Guo, "RNA-based therapeutics for colorectal cancer: updates and future directions," *Pharmacological Research*, vol. 152, article 104550, 2020.

[24] K. F. Pirollo, A. Rait, Q. Zhou et al., "Materializing the potential of small interfering RNA via a tumor-targeting nanodelivery system," *Cancer Research*, vol. 67, no. 7, pp. 2938–2943, 2007.

[25] L. Li, J. Hou, X. Liu et al., "Nucleolin-targeting liposomes guided by aptamer AS1411 for the delivery of siRNA for the treatment of malignant melanomas," *Biomaterials*, vol. 35, no. 12, pp. 3840–3850, 2014.

[26] S. Guan and J. Rosenecker, "Nanotechnologies in delivery of mRNA therapeutics using nonviral vector- based delivery systems," *Gene Therapy*, vol. 24, no. 3, pp. 133–143, 2017.

[27] E. Keles, Y. Song, D. Du, W. J. Dong, and Y. Lin, "Recent progress in nanomaterials for gene delivery applications," *Biomaterials Science*, vol. 4, no. 9, pp. 1291–1309, 2016.

[28] H. Ohno, S. Akamine, and H. Saito, "RNA nanostructures and scaffolds for biotechnology applications," *Current Opinion in Biotechnology*, vol. 58, pp. 53–61, 2019.

[29] S. Kobori, Y. Nomura, and Y. Yokobayashi, "Self-powered RNA nanomachine driven by metastable structure," *Nucleic Acids Research*, vol. 47, no. 11, pp. 6007–6014, 2019.

[30] D. Jedrzejczyk, E. Gendaszewska-Darmach, R. Pawlowska, and A. Chworos, "Designing synthetic RNA for delivery by nanoparticles," *Journal of Physics: Condensed Matter*, vol. 29, no. 12, article 123001, 2017.

Hindawi
Journal of Nanomaterials
Volume 2021, Article ID 5528347, 14 pages
https://doi.org/10.1155/2021/5528347

Research Article

Immune-Related Genes: Potential Regulators and Drug Therapeutic Targets in Hypertrophic Cardiomyopathy

Wei Liu[1], **Ju Ye**[2], **Jinqiang Cai**[3], **Feng Xie**[4], **Mengjie Tang**[5] and **QinJing Yang**[1]

[1]*Department of Pharmacy, The Third Xiangya Hospital, Central South University, Changsha 410013, China*
[2]*Department of Pharmacy, Zunyi Medical University, Zunyi 563000, China*
[3]*Department of Pharmacy, Xiangya Medical College, Central South University, Changsha 410013, China*
[4]*Department of Pharmacy, The Nanshan District Maternity & Child Healthcare Hospital of Shenzhen, Shenzhen 518052, China*
[5]*Hunan Cancer Hospital, The Affiliated Cancer Hospital of Xiangya School of Medicine, Central South University, Changsha 410013, China*

Correspondence should be addressed to QinJing Yang; yangqinjing0624@163.com

Received 29 January 2021; Revised 5 February 2021; Accepted 9 February 2021; Published 3 March 2021

Academic Editor: Tingting Hong

Background. Accumulating evidence shows that the innate immune system is a key player in cardiovascular repair and regeneration, but little is known about the role of immune-related genes (IRGs) in hypertrophic cardiomyopathy (HCM). *Methods*. The differential mRNA expression profiles of HCM samples were downloaded from the Gene Expression Omnibus (GEO) dataset (GSE89714), and the IRG expression profile was obtained from the ImmPort database. The regulatory pathways of IRGs in HCM were screened out through discrepantly expressive genes (DEGs) analysis, enrichment of gene function/pathway analysis, and protein-protein interaction (PPI) network. Besides, hub IRGs in the PPI network were selected for drug prediction. *Results*. A total of 854 genes were differentially expressed in HCM, of which 88 were IRGs. Functional enrichment analysis revealed that 88 IRGs were mainly involved in the biological processes (BP) of SMAD protein pathway, smooth muscle cell proliferation, protein serine/threonine kinase, and mitogen-activated protein kinase (MAPK) cascade. Cytokine-cytokine receptor interaction, TGFβ signaling pathway, PI3K-Akt signaling pathway, and MAPK signaling pathway were enriched in the pathway enrichment analysis of these 88 IRGs. Furthermore, the PPI regulatory network of IRGs was constructed, and 10 hub IRGs were screened out to construct a regulatory network for HCM. 4 transcription factors (TFs) were the major regulator of 10 hub IRGs. Finally, these 10 hub IRGs were entered into the pharmacogenomics database for prediction, and the relevant drugs were obtained. *Conclusions*. In this study, 10 hub IRGs were coexpressed with 4 TFs to construct a regulatory network for HCM. Drug prediction of these 10 hub IRGs proposed potential therapeutic agents that could be used in HCM. These results indicate that IRGs are potential regulators and drug therapeutic targets in HCM.

1. Introduction

Cardiomyopathy refers to a myocardial disease with cardiac dysfunction, among which hypertrophic cardiomyopathy (HCM) is the most common. HCM is typically characterized by abnormal left and/or right ventricular hypertrophy [1]. HCM is commonly known as hereditary cardiomyopathy [2, 3], which is estimated that more than 16 genes and 900 mutations are responsible for the occurrence of HCM [4–6]. Currently, HCM treatment mainly focuses on gene therapy [7], immune-modulatory therapy [8], and regenerative therapy [9–11].

An abundance of evidence shows that the immune system with the multiple therapeutic targets for HCM plays a pivotal role in cardiac tissue damage and repair [12–15] by blocking the proinflammatory pathway [16, 17] or regulating the circulation of immune cells and the regeneration of resident immune cells [18, 19]. Accumulating evidence indicates that the immune system is also involved in cardiac regeneration and has become a new hotspot in HCM regenerative

therapy [20]. To date, treating MYBPC3 mutations is the only feasible gene therapies of HCM [7]. Nevertheless, the effect of IRGs on the process of HCM remains unclear.

In our study, we performed a systematic investigation of the HCM-related IRGs to identify prognostic biomarkers of HCM. The differentially expressed genes were obtained based on HCM, and the prognostic IRGs were further identified. Besides, functional analysis and the PPI network further revealed that these genes were implicated in the regulation of many biological processes, including SMAD protein pathways, smooth muscle cell proliferation, protein serine/threonine kinase, and MAPK cascade. Mechanistically, these regulatory pathways are involved in cytokine-cytokine receptor interaction, TGFβ signaling pathway, PI3K-Akt signaling pathway, and MAPK signaling pathway. Finally, the abundance of 10 hub IRGs was screened, and these ten hub IRGs were used for drug prediction. Meanwhile, these 10 hub IRGs were coexpressed with 4 TFs to construct a regulatory network for HCM. Altogether, we provided new insights into the regulatory mechanism of the IRGs in HCM, which may be a new direction for the treatment of HCM.

2. Materials and Methods

2.1. Data Acquisition. Transcriptome RNA-sequencing data of HCM (GSE89714, analyzed on Illumina HiSeq 2000) was downloaded from the Gene Expression Omnibus (GEO) database (http://www.ncbi.nlm.nih.gov/geo), which contained data from 5 hypertrophic heart tissue samples and 4 normal samples. The IRGs were obtained from the ImmPort database (http://www.immport.org), including 17 immune categories according to their different molecular function, such as T-cell receptor signaling pathway, B-cell receptor signaling pathway, Natural Killer Cell Cytotoxicity, antimicrobials, cytokine, and TNF family receptors. The list of TFs was getting from the Cistrome database. The function of the IRGs was acquired from Genecards (http://www.genecards.org/).

2.2. Identification of Differentially Expressed Genes (DEGs). The R package "limma" and "voom" functions are used to normalize the data. DEGs between HCM and normal samples were screened using the limma package under the condition of Log fold change (log FC) > 1 and adj. P value < 0.05.

2.3. KEGG Pathway Enrichment Analysis. Kyoto Encyclopedia of Genes and Genomes (KEGG) is a database resource for understanding advanced functions and biological systems from large-scale molecular data generated by high-throughput experimental techniques. KEGG database was used to identify upregulation pathways by DAVID (version 6.8, https://david.ncifcrf.gov/) in the background of Homo sapiens. The pathway with a corrected P value < 0.05 was considered a significant difference.

2.4. GO Enrichment Analysis. Gene ontology (GO) is a major bioinformatics tool for annotating genes and analyzing the biological processes (BPs), cellular components (CCs), and molecular functions (MFs), respectively. GO analysis was performed by DAVID (version 6.8, https://david.ncifcrf.gov/), and P value < 0.05 was considered statistically significant.

2.5. PPI Network Analysis. The PPI regulatory network of IRGs was constructed using the Search Tool for the Retrieval of Interacting Genes/Proteins (STRING; http://string-db.org) database (version 10.0), and interactions with a combined score > 0.4 were considered statistically significant. The PPI network result was displayed using the Cytoscape software version 3.4.0, and the most important modules were identified by Cytoscape's plugin molecular complex detection (MCODE) (version 1.4.2). The selection criteria of differentially expressed IRGs in HCM were as follows: MCODE score > 5, degree cut − off = 2, node score cut − off = 0.2, maximum depth = 100, and k score = 2. P value < 0.01 was considered statistically significant. The top 10 differentially expressed IRGs act as the hub genes by ranking the degree number of genes in the PPI network.

2.6. Drug Prediction. We used three pharmacogenomic databases for drug prediction of 10 hub genes: Drugbank online website (https://go.drugbank.com/), Drug-Gene interaction database (https://dgidb.genome.wustl.edu/), and Connectivity map (https://portals.broadinstitute.org/cmap/).

2.6.1. Drugbank Online Website. The proteins encoded by the 10 hub genes mentioned above were used in Drugbank online website for drug prediction (https://go.drugbank.com/), and the hub gene-protein-drug network was constructed by the Cytoscape software.

2.6.2. Drug-Gene Interaction Database. These 10 hub genes directly predicted drugs through the Drug-Gene interaction database (https://dgidb.genome.wustl.edu/) and visualized with the Cytoscape software.

2.6.3. Connectivity Map. These 10 hub genes were used for drug prediction with Connectivity map (https://portals.broadinstitute.org/cmap/); drugs with connectivity score below -0.879 (i.e., drugs most likely to reverse gene differential expression therapy for DCM) were selected. The connectivity score of each drug for each hub gene in the specific cell line was summarized; a heat map was made with the R software.

3. Results

3.1. Screening Results of Differential Genes and the Enrichment of Gene Function Analysis in HCM. GSE89714 was downloaded from the GEO database, which contained data from 5 hypertrophic heart tissue samples and 4 normal myocardial samples. 854 differentially expressed genes (DEGs) were screened, including 675 upregulated genes and 179 downregulated genes (Figure 1).

After functional enrichment analysis of 854 DEGs in HCM, we found that these 854 DEGs mainly participated in 10 biological processes (BP), including extracellular matrix organization, extracellular structure organization, skeletal system development, ossification, collagen fibril organization, urogenital system development, axon development, bone development, connective tissue development, and renal system development (Figure 2(a)). Additionally, these 854 DEGs were mainly expressed in the extracellular matrix,

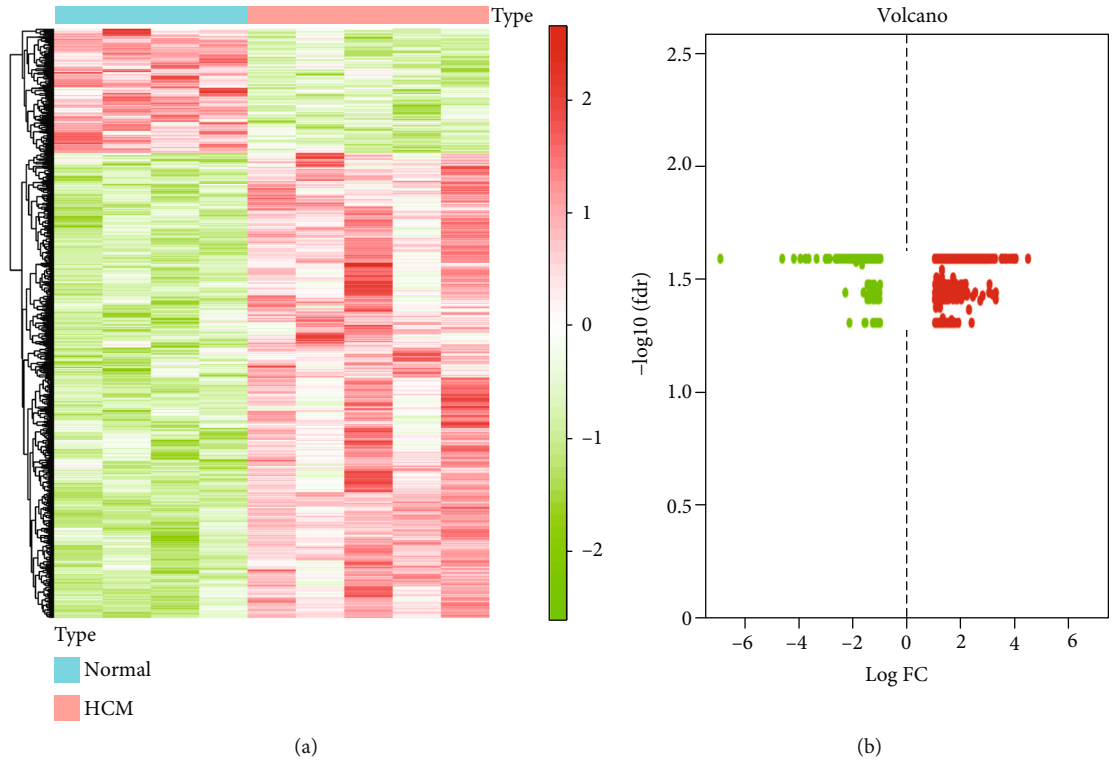

Figure 1: Differentially expressed genes in HCM. (a) The heat map of differentially expressed genes between HCM and normal tissues. Green dots represent lower expressed genes, and red dots represent highly expressed genes. (b) The volcano plot (b) of differentially expressed genes between HCM and normal tissues. Green dots represent lower expressed genes, and red dots represent highly expressed genes.

platelet alpha granule, basement membrane, endoplasmic reticulum lumen, collagen trimer, the complex of collagen trimers, and the cell-substrate junction (Figure 2(b)). Specifically, the molecular function (MF) of these 854 DEGs was mainly related to extracellular matrix structural constituent, collagen binding, glycosaminoglycan binding, extracellular matrix structural constituent conferring tensile strength, extracellular matrix structural constituent conferring compression resistance, heparin-binding, growth factor binding, growth factor activity, sulfur compound binding, and integrin binding (Figure 2(c)).

Subsequently, the results of the KEGG pathway show that there are 11 significantly upregulated pathways, including ECM-receptor interaction, focal adhesion, TGFβ signaling pathway, protein digestion and absorption, proteoglycans in cancer, PI3K-Akt signaling pathway, dilated cardiomyopathy (DCM), AGE-RAGE signaling pathway in diabetic complications, hypertrophic cardiomyopathy (HCM), amoebiasis, and cytokine-cytokine receptor interaction. The upregulated expression of the pathway is shown in Figure 2(d).

3.2. IRG Expression Profile of HCM and the Enrichment of Gene Function Analysis in HCM. The list of IRGs was downloaded through the ImmPort database. Meanwhile, the differentially expressed IRGs were extracted from GSE89714. 88 IRGs were differentially expressed in HCM. The expression levels of these 88 genes are listed in Supplementary Table S1, of which 16 are low expression and 72 are high expression (Figure 3(a)).

Through GO function enrichment analysis of 88 differentially expressed IRGs in HCM, we found that these 88 IRGs are mainly associated with the regulation of 10 biological processes (BP), including 4 processes of SMAD protein, 3 processes of smooth muscle cell proliferation, 2 processes of protein serine/threonine kinase, and MAPK cascade process (Figure 3(b)). Moreover, these 88 IRGs are mainly enriched in 10 Cell Components (CC), especially in platelet, extracellular matrix, vesicle lumen, granule lumen, mast cell, and so on (Figure 3(c)). Furthermore, the MF of these 88 IRGs is mainly correlated with receptor-ligand/regulator activity, growth factor activity/binding, cytokine activity/binding, hormone activity, G protein-coupled peptide receptor activity, and transmembrane receptor protein serine/threonine kinase binding (Figure 3(d)).

Thereafter, KEGG pathway enrichment analysis indicated that there are 30 significantly upregulated pathways in the microarray datasets, including cytokine-cytokine receptor interaction, TGFβ signaling pathway, viral protein interaction with cytokine and cytokine receptor, PI3K-Akt signaling pathway, pluripotency of stem cells regulation, MAPK signaling pathway, Hippo signaling pathway, proteoglycans in cancer, Ras signaling pathway, malaria, chemokine signaling pathway, calcium signaling pathway, hematopoietic cell lineage, amoebiasis, Rap1 signaling pathway, neuroactive ligand-receptor interaction, toxoplasmosis, cGMP-PKG signaling pathway, renal cell carcinoma, melanoma, axon guidance, Leishmaniasis, EGFR tyrosine kinase inhibitor resistance, bladder cancer, focal adhesion, gastric cancer,

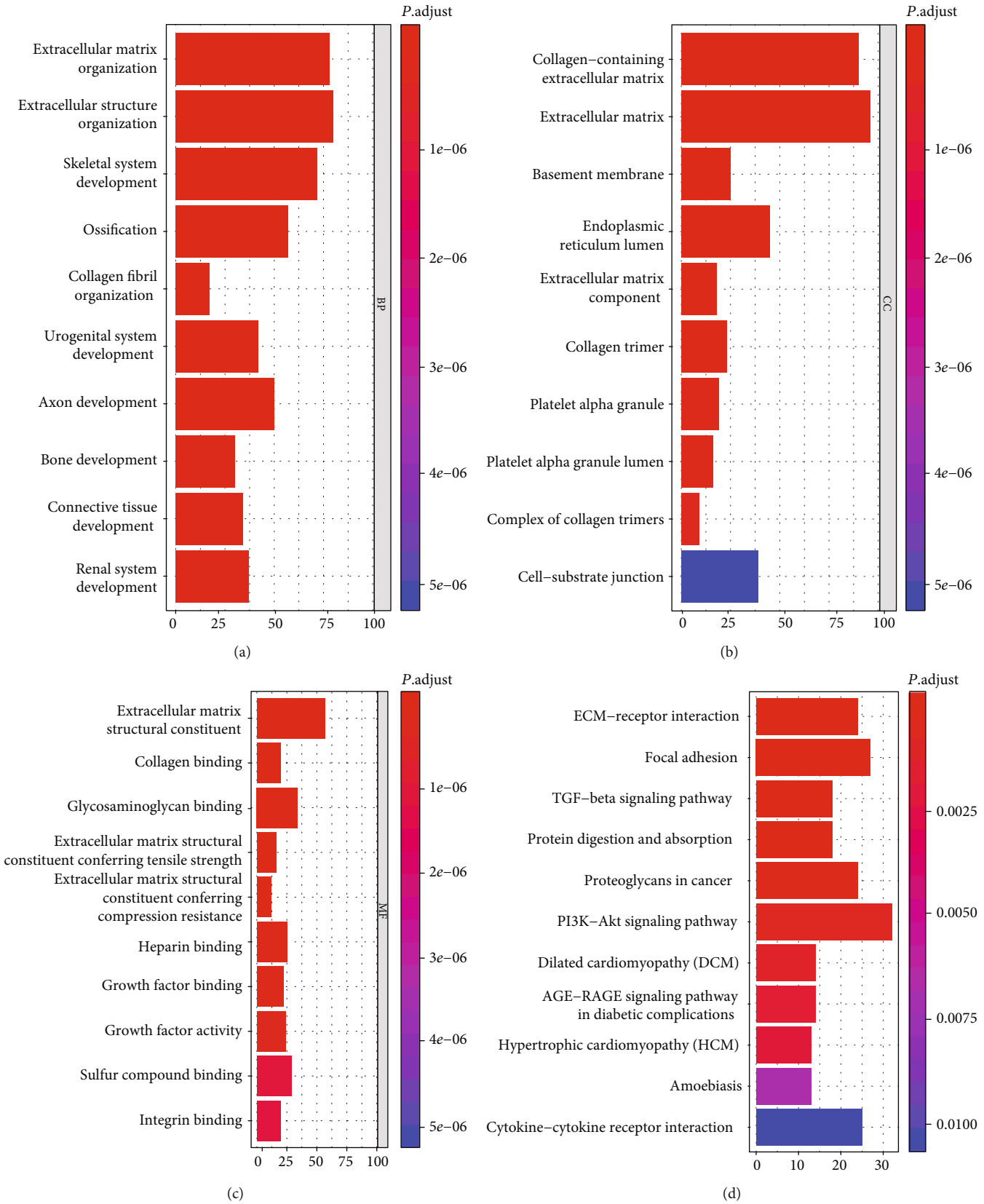

Figure 2: Gene functional enrichment of differentially expressed genes in HCM. (a) Gene ontology analysis: biological process of differentially expressed genes. (b) Gene ontology analysis: cellular component of differentially expressed genes. (c) Gene ontology analysis: molecular function of differentially expressed genes. (d) Encyclopedia of Genes and Genomes analysis: the top 10 significant pathways of differentially expressed genes.

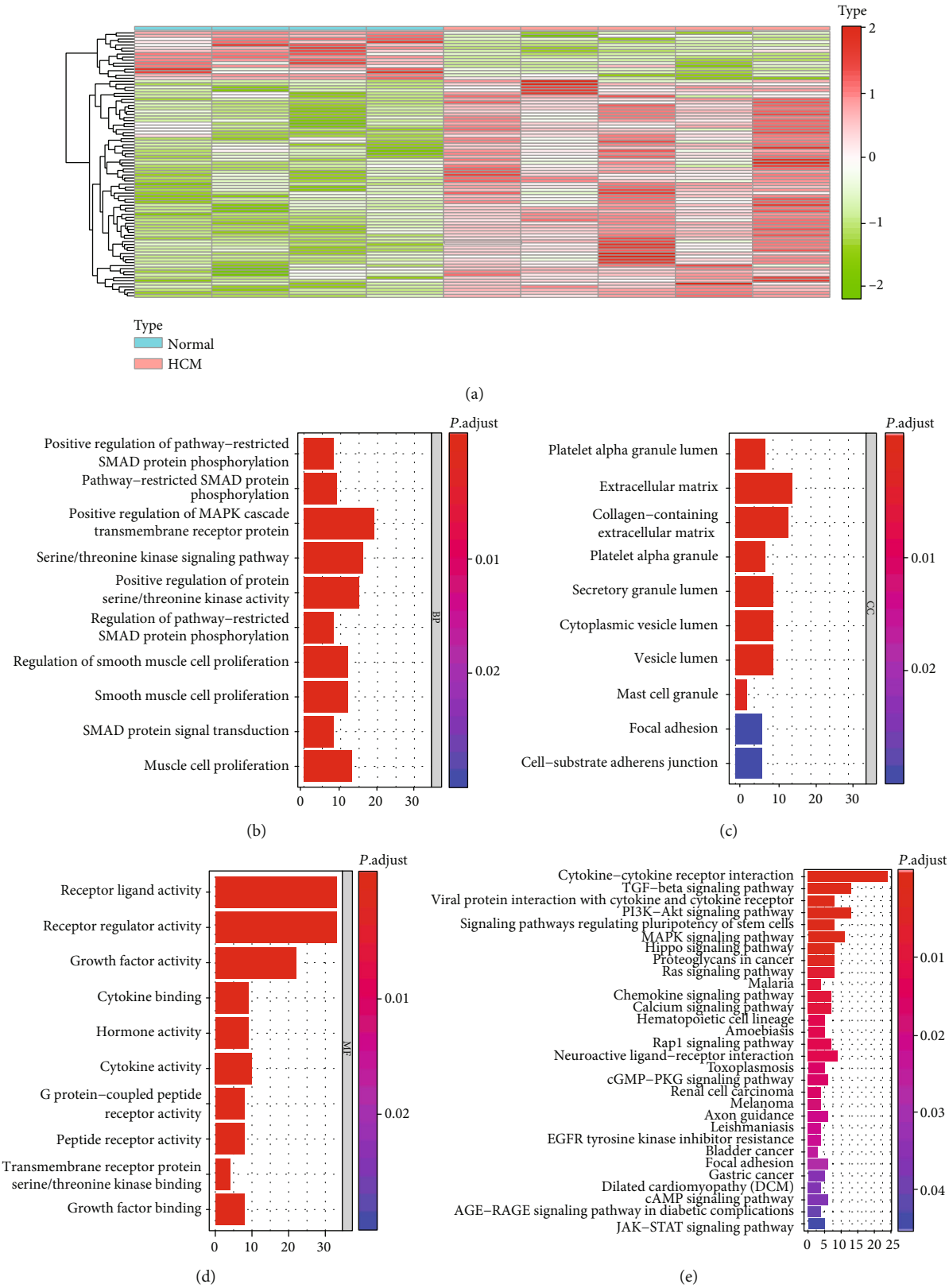

Figure 3: Differentially expressed IRGs in HCM and gene functional enrichment. (a) The differentially expressed IRGs between HCM and normal tissues. Green dots represent lower expressed genes, and red dots represent highly expressed genes. (b) Gene ontology analysis: biological process of differentially expressed IRGs. (c) Gene ontology analysis: cellular component of differentially expressed IRGs. (d) Gene ontology analysis: molecular function of differentially expressed IRGs. (e) Encyclopedia of Genes and Genomes analysis: the top 10 significant pathways of differentially expressed IRGs.

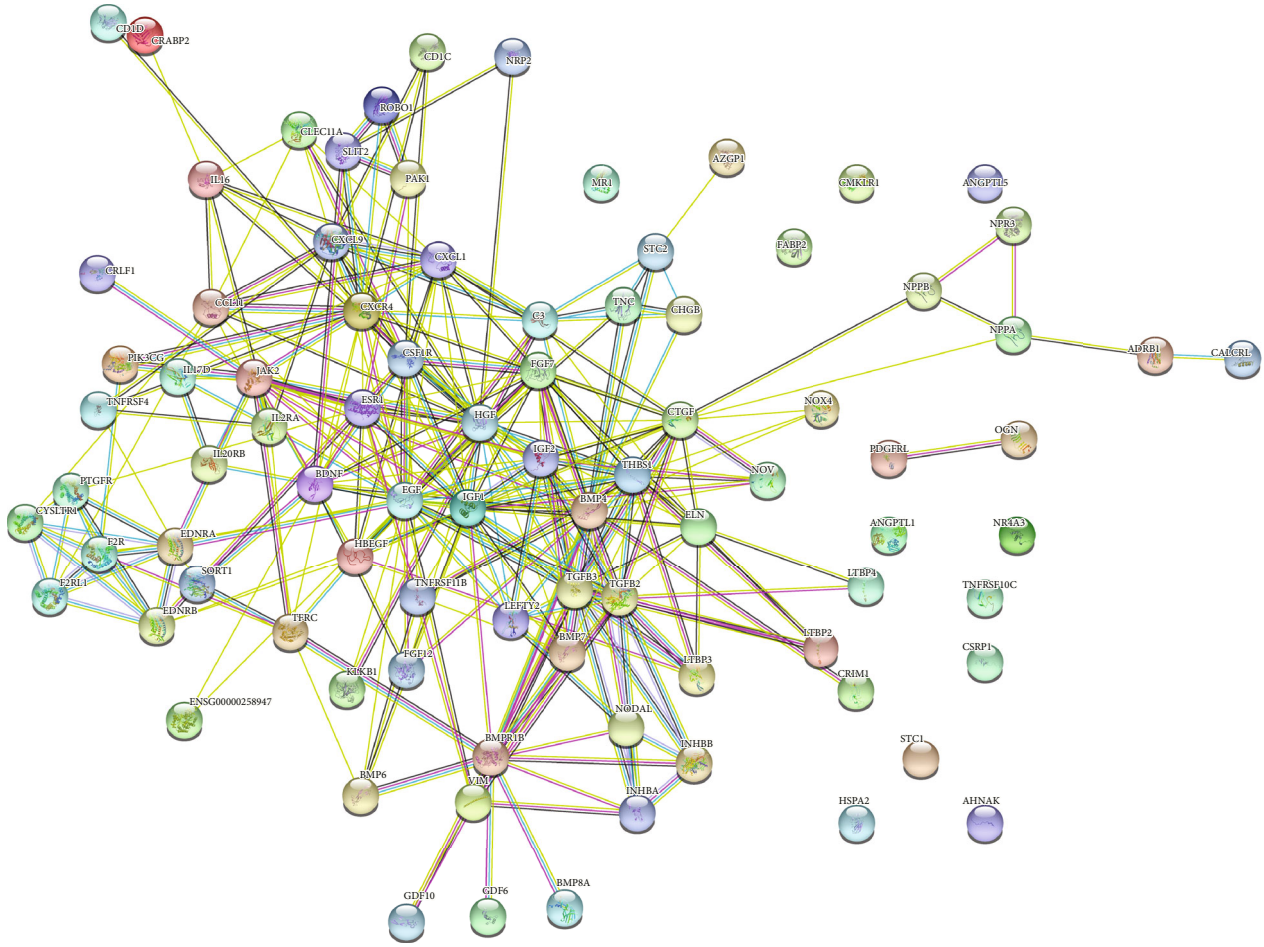

Figure 4: PPI network of IRGs in HCM.

dilated cardiomyopathy (DCM), cAMP signaling pathway, AGE-RAGE signaling pathway in diabetic complications, and JAK-STAT signaling pathway. The results are shown in Figure 3(e). Importantly, cytokine-cytokine receptor interaction, TGFβ signaling pathway, PI3K-Akt signaling pathway, and MAPK signaling pathway are the most obvious upregulation pathways (Figure 3(e)).

3.3. Screening of Differentially Expressed TFs and Coexpression Analysis of TFs and IRGs. The PPI regulatory network of IRGs was based on data collected from the STRING online database (https://string-db.org/). We found that IRGs interacted directly with each other through the analysis of the PPI network (Figure 4). The list of TFs was downloaded through the Cistrome database and screened out 11 differentially expressed TFs in HCM, including POLR3G, EHF, SOX2, TP63, SOX4, KLF5, ESR1, RUNX1, PRDM1, MAFK, and MYH11(Figure 5(a)). Next, coexpression analysis results of TFs and IRGs showed that there were 5 TFs coexpressed with 84 IRGs, including RUNX1, SOX4, KLF5, MAFK, and MYH11(Figure 5(b)). Notably, the 5 TFs are highly expressed in HCM. The expression levels are shown in Table 1. Finally, the regulatory network between 5 TFs and 84 IRGs was constructed by using the software of Cytoscape.

3.4. Identification of Hub IRGs and TF Regulatory Network of IRGs. The top 10 IRGs (EGF, IGF1, HGF, BMP4, CXCR4, CTGF, THBS1, TGFB2, JAK2, TGFB3) were selected as the hub genes. Obviously, they also interacted with each other (Figure 6(a)), especially for IGF1 and HGF, THBS1 and IGF1, THBS1 and HGF, THBS1 and BMP4, CTGF and IGF1, CTGF and HGF, TGFB3 and THBS1, and TGFB3 and CTGF (Figure 6(c)). Except for EGF, the other 9 genes were highly expressed in HCM (Table 1). The functional roles of 10 hub genes were downloaded from the online database (https://www.genecards.org/) and are shown in Table 2. Besides, coexpression analysis results showed that there were 4 TFs with a crucial regulatory role in 10 hub IRGs network, including SOX4, KLF5, MAFK, and MYH11 (Figure 6(b)).

3.5. Drug Prediction of Hub Genes. We used multiple pharmacogenomic databases for drug prediction of 10 hub genes and found that different prediction methods have different results. In Drugbank online website (https://go.drugbank.com/), there are proteins encoded by only 7 hub genes yielded related drugs; proteins encoded by other 3 hub genes have not related drugs (Figure 7(a)). In the Drug-Gene interaction database (https://dgidb.genome.wustl.edu/), all hub genes resulted in the corresponding drugs; only FRESOLIMUMAB and ABT-510 were mainly correspond to two

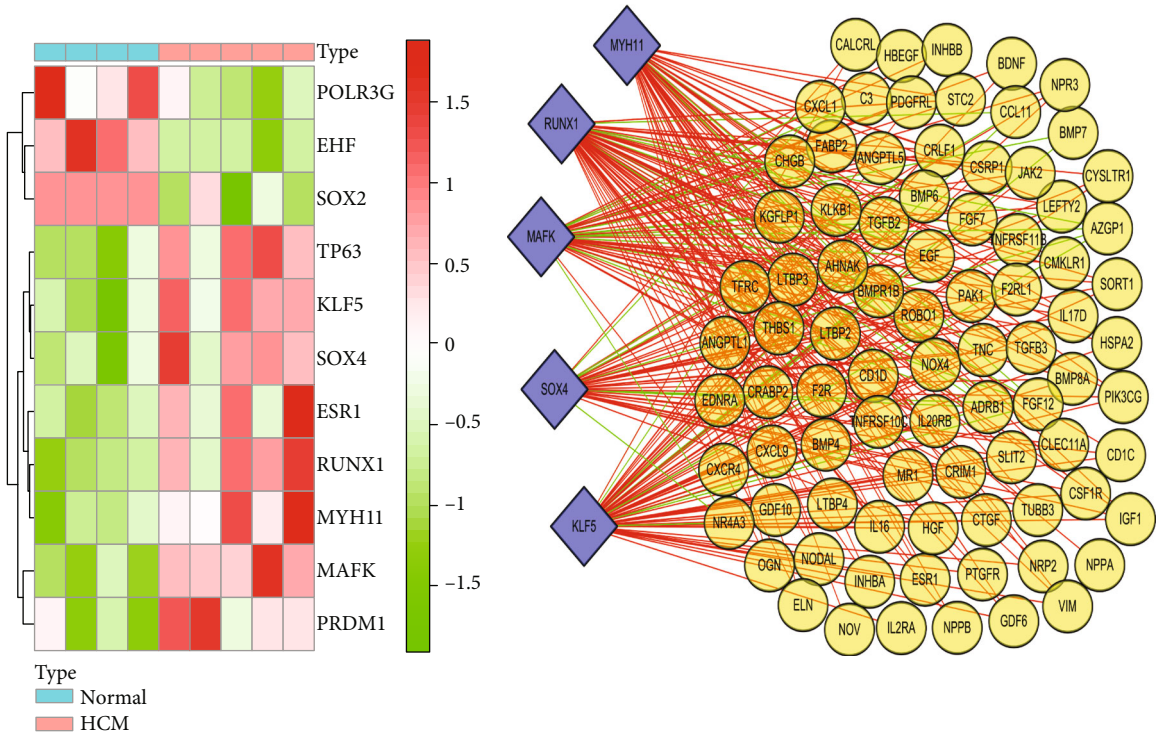

(a) (b)

Figure 5: TF regulatory network. (a) The differentially expressed TFs between HCM and normal tissues. Green dots represent lower expressed TFs, and red dots represent highly expressed TFs. (b) The TF regulatory network of IRGs.

Table 1: Expression levels of 5 TFs that regulate IRGs.

Gene	Normal myocardium	Hypertrophic cardiomyopathy	logFC	*P* value
MAFK	10.2	22.52	1.143	0.016
KLF5	1.35	3.36	1.316	0.019
RUNX1	1.075	4.5	2.067	0.016
SOX4	4.425	10.34	1.224	0.032
MYH11	37.075	88.28	1.252	0.016

genes, while other drugs are all only correspond to one gene (Figure 7(b)). In the Connectivity map (https://portals.broadinstitute.org/cmap/), 13 drugs with connectivity score below -0.879 were predicted, summarizing the connectivity scores of these 13 drugs with 10 hub genes and making a heat map with the R software (Figure 7(c)).

4. Discussion

HCM is an inherited myocardial disease with cardiac dysfunction and genetic disorder [21–23]. Accumulating evidence revealed that the immune system plays a key role in heart injury responses [24–26]. It has been reported that myocardial aging is largely associated with changes in gene expression patterns of immune response [27]. Therefore, it is plausible that the development of HCM is attributed to abnormal IRG expression. In our results, a total of 854 mRNAs were differentially expressed in HCM patients, of which 88 were IRGs, including 16 low-expressed IRGs and 72 high-expressed IRGs. 10 hub IRGs (IGF1, CTGF, TGFB2, TGFB3, HGF, BMP4, CXCR4, THBS1, EGF, JAK2) were selected to construct a regulatory network in HCM, suggesting that these 10 hub IRGs might be the new therapeutic targets for the intervention of HCM.

Insulin-like growth factors 1 (IGF1) is a hormone with pleiotropic effects, which consists of 70 amino acids and is regulated by IGF-binding proteins (IGFBPs) [28–31]. It is generally accepted that IGF1 exhibits a protective effect on myocardium by regulating autophagy, precursor cell differentiation, extracellular matrix activity, and myocardial fibrosis [32, 33]. In our results, insulin-like growth factor 1 (IGF1) and IGF-binding protein (CTGF) are two hub IRGs in HCM. Moreover, CTGF and IGF1 were highly expressed in HCM and significantly interacted with each other($R = 0.92$). Accordingly, IGF1 may provide a novel therapeutic direction for HCM. A plethora of evidence showed that IGF1 could regulate the metabolism of cardiomyocytes through MAPK [34–36] and PI3K-Akt pathway [37]. In the present study, GO function enrichment analysis showed that IRGs participate in the process of MAPK cascade, and the KEGG pathways are enriched in the PI3K-Akt signaling pathway and MAPK signaling pathway. Therefore, PI3K-Akt and MAPK signaling pathway may be the regulatory mechanism of IGF1 on the pathogenesis of HCM.

TGFβs are multifunctional cytokines with three isoforms (TGFβ1, 2, and 3) encoded by three distinct genes, which are essential mediators of cardiac repair [38–42]. Extensive

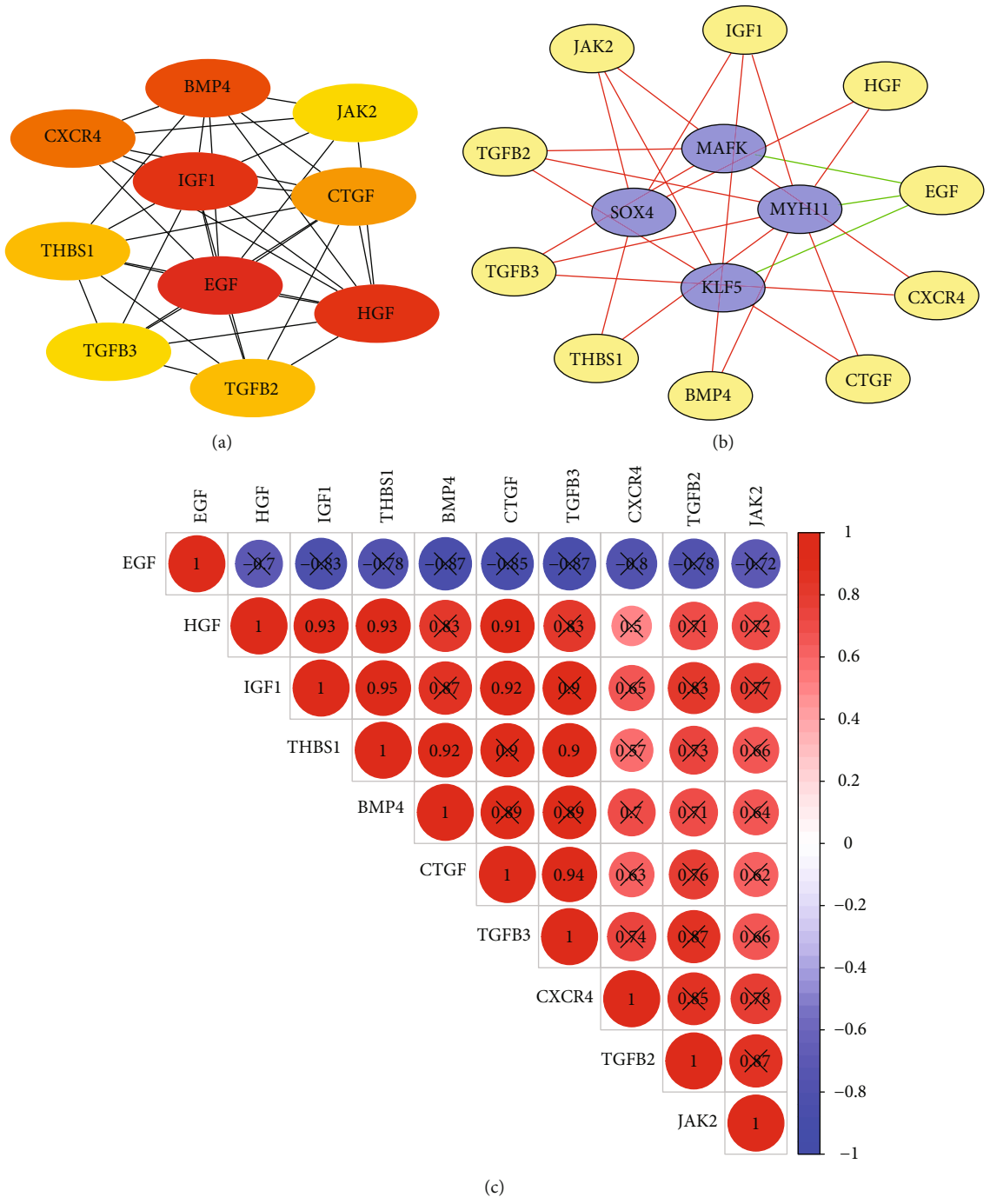

Figure 6: Identification of hub IRGs and the TF regulatory network: (a) the interaction network of hub IRGs; (b) the TF regulatory network of hub IRGs; (c) the correlation coefficient of hub IRGs.

evidence suggests that TGFβ is produced by various cells in response to tissue injury, especially in injured myocardial regions. In general, TGFβ isoforms show different expression patterns in the injured myocardium: TGFβ1 and TGFβ2 are induced in the early stage, whereas TGFβ3 shows a delayed and prolonged upregulation. Importantly, our results reveal that transforming growth factor β2 proprotein (TGFB2) and transforming growth factor β3 (TGFB3) are two hub IRGs in HCM. Moreover, TGFB2 and TGFB3 were highly expressed in HCM, indicating a promising therapeutic target of TGFβ for HCM. TGFβ can be activated by SMAD [43, 44]. Meanwhile, TGFβ-SMAD3 signaling pathway is an important mediator of cardiac fibroblasts and is expected to be an attractive therapeutic target for HCM [45–48]. In our results, these 88 IRGs are involved in the regulation of 4 biological processes of SMAD protein, including positive regulation of pathway-restricted SMAD protein phosphorylation, pathway-restricted SMAD protein phosphorylation, regulation of pathway–restricted SMAD protein phosphorylation, and SMAD protein signal transduction. Furthermore, the

Table 2: Functional roles of the 10 hub genes.

No.	Gene symbol	Full name	Function
1	EGF	Epidermal growth factor	EGF stimulates the growth of various epidermal and epithelial tissues in vivo and in vitro and of some fibroblasts in cell culture.
2	IGF1	Insulin like growth factor 1	The insulin-like growth factors, isolated from plasma, are structurally and functionally related to insulin but have a much higher growth-promoting activity.
3	HGF	Hepatocyte growth factor	Activating ligand for the receptor tyrosine kinase MET by binding to it and promoting its dimerization.
4	BMP4	Bone morphogenetic protein 4	Induces cartilage and bone formation. Also acts in mesoderm induction, tooth development, limb formation, and fracture repair.
5	CXCR4	C-X-C motif chemokine receptor 4	Receptor for the C-X-C chemokine CXCL12/SDF-1 that transduces a signal by increasing intracellular calcium ion levels and enhancing MAPK1/MAPK3 activation.
6	CTGF	IGF-binding protein 8	Major connective tissue mitoattractant secreted by vascular endothelial cells.
7	THBS1	Thrombospondin-1	Adhesive glycoprotein that mediates cell-to-cell and cell-to-matrix interactions.
8	TGFB2	Transforming growth factor beta-2 proprotein	Associates noncovalently with TGF-beta-2 and regulates its activation via interaction with "milieu molecules."
9	JAK2	Janus kinase 2	Nonreceptor tyrosine kinase involved in various processes such as cell growth, development, differentiation, or histone modifications.
10	TGFB3	Transforming growth factor beta 3	Precursor of the latency-associated peptide (LAP) and transforming growth factor beta-3 (TGF-beta-3) chains, which constitute the regulatory and active subunit of TGF-beta-3, respectively.

results of KEGG pathway enrichment analysis showed that the TGFβ signaling pathway is upregulated. Collectively, the above results suggest that two hub IRGs (TGFB2 and TGFB3) regulated the TGFβ-SMAD signaling pathway and participate in the pathological process of HCM.

In the regulatory networks of the 10 hub IRGs, 4 TFs (SOX4, KLF5, MAFK, and MYH11) were coexpressed with these 10 hub IRGs, which suggests that SOX4, KLF5, MAFK, and MYH11 are the major regulators of IRGs during HCM. In detail, SOX4 is a member of the Sox (for Sry-box) family, which is essential for the regulation of embryonic development and cell fate. Also, SOX4 is required for the development of cardiac outflow tract. SOX4 deficiency even causes congenital heart defects in embryonic mice [49–51]. As a member of the Krüppel-like factors (KLFs) family, KLF5 is intimately correlated with cardiovascular remodeling, cardiac energetic, and cardiac fibroblasts [52–55]. Notably, KLF5 has recently been proved as a novel disease gene of familial dilated cardiomyopathy (DCM) and negatively regulates HCM [56, 57]. MAFK, a member of the small Maf family, is an important contributor to hematopoiesis [58]. MAFK is well known for its role in modulating NF-κB activity and controlling immune-inflammatory responses [59, 60]. MYH11 is a smooth muscle myosin belonging to the myosin heavy chain family, which plays a vital role in human disease familial hypertrophic cardiomyopathy (FHC) [61, 62]. In our results, these 4 TFs were not only coexpressed with 10 hub genes but also correlated with each other to form a regulatory network. The network may be a potential therapeutic target for HCM.

Recent studies revealed that the immune system plays a pivotal but complex role in myocardial injury and repair [63, 64]. During the cardiac injury, the immune mechanism is activated, which induces an inflammatory response, and subsequently triggers reparative pathways to promote wound healing [65]. Surprisingly, the overall mobilization of the immune system follows a consistent pattern in response to tissue injury: when an injury occurs, the dying cardiomyocytes trigger an acute inflammatory response and are recognized by resident immune cells, such as macrophages, innate lymphoid cells (ILC), and mast cells (MC) [66]. Subsequently, these resident immune cells also participate in the removal of dying cardiomyocytes, the reconstruction of tissue matrix, the restriction of the spread of inflammatory molecules, and the maintenance of local homeostasis [67, 68]. Besides, macrophages/monocytes secrete various chemokines and cytokines that recruit immune cells to promote wound healing [69]. These processes are highly consistent with the cell constituents (CC) of 88 IRGs, which are differentially expressed in our results. In our results, 88 IRGs are primarily enriched in the collagen-containing extracellular matrix, secretory granule lumen, cytoplasmic vesicle lumen, mast cell granule, and cell-substrate adherens junction.

In this study, we used three pharmacogenomic databases for drug prediction of 10 hub genes and found that different prediction methods have different results. In Drugbank online website (Figure 7(a)), proteins encoded by only 7 hub genes yielded related drugs. In the hub gene-drug network (Figure 7(b)), there are two drugs FRESOLIMUMAB and ABT-510, corresponding to two hub genes at the same time, indicating that these two drugs may be vital therapeutic molecules. Connectivity map prediction results (Figure 7(c)) clearly showed that all 13 drugs could upregulate the differentially underexpressed hub genes, that is, EGF. All these 13 drugs could downregulate most of the differentially highly expressed 9 hub genes. These drugs may be potentially effective therapeutic molecules in the future and may inspire the design of similarly structured active drug molecules.

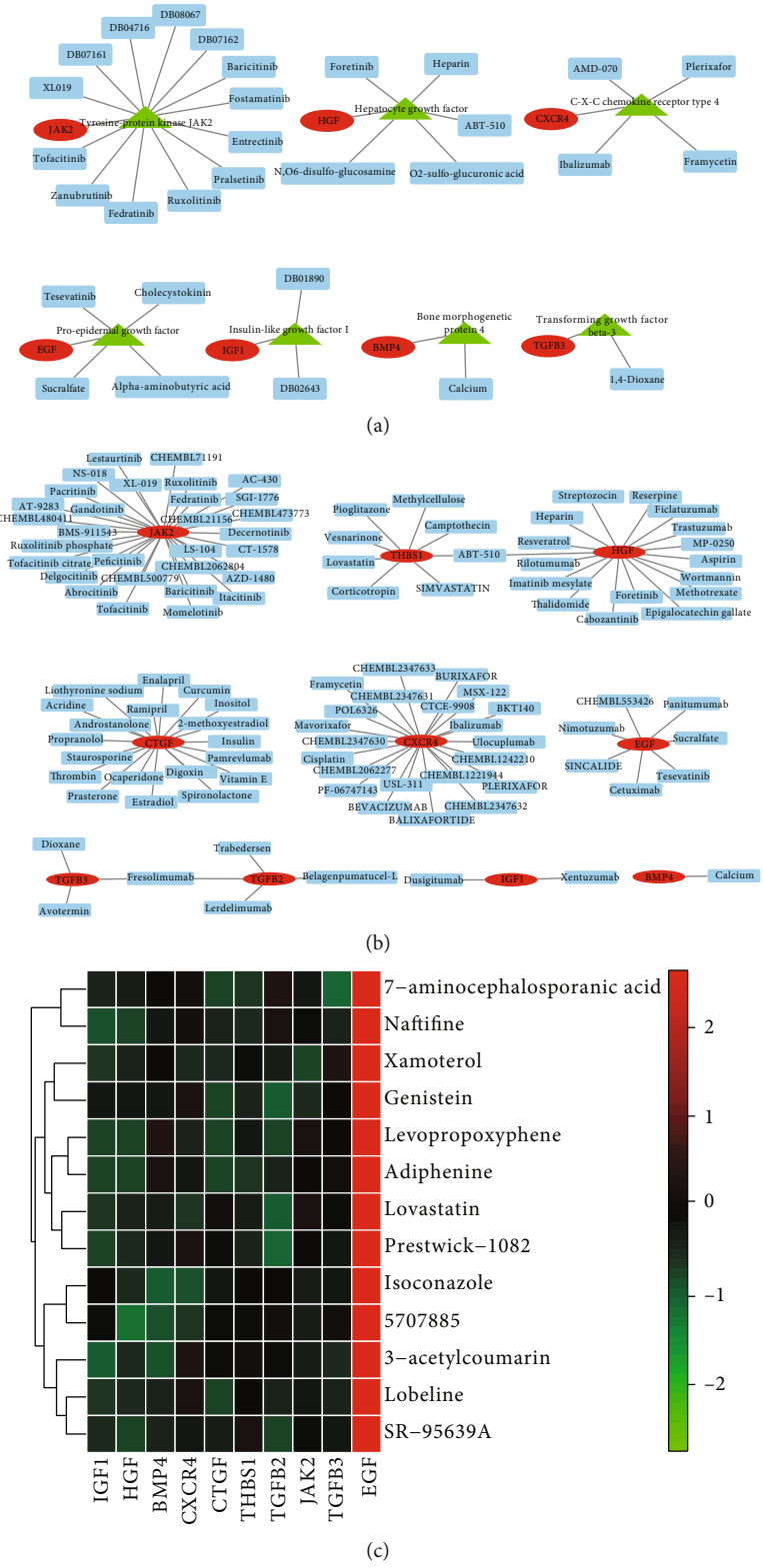

Figure 7: Drug prediction of 10 hub IRGs. (a) Hub gene-protein-drug network. Red ovals represent hub genes, green triangles represent proteins encoded by hub genes, and blue rectangles are drugs. (b) Hub gene-drug network. Red indicates hub genes, and blue indicates drug. Among them, the 78 drugs corresponding to JAK2 showed only the top 30, and all 78 drug names can be obtained in Supplementary Table S2. (c) Heat map of the effect of drugs on hub genes expression. Green indicates that the drug can downregulate the hub gene expression, red marks that the drug can upregulate the hub gene expression, and black means that the drug and the hub gene expression have little correlation.

Generally, cardiac injury activates immune mechanisms, which depend on the close interaction of cells, the regeneration of cardiac resident immune cells, and immune cells [70, 71]. In the process of myocardial injury and repair, immune cells, like $CD4^+$ T cells, $CD8^+$ T cells, B cells, natural killer cells (NK), and macrophages, are the main regulator in wound healing, which includes resident immune cells and circulating immune cells from the blood [72–74]. As mentioned previously, the resident immune cells coordinate the removal of dying cardiomyocytes, the reconstruction of tissue matrix, the restriction of the spread of inflammatory molecules, and the maintenance of local homeostasis. In addition, excessive inflammatory signals can also trigger extramedullary hematopoiesis of the spleen and produce new immune cells that are recruited to the injured site to alleviate tissue injury [75]. Therefore, the balance between self-maintenance of the cardiac resident immune cells and the recruitment of circulating immune cells is crucial for the potential of cardiac regeneration [76]. At present, the replacement of lost cardiomyocytes is the most important strategy for the treatment of cardiomyopathy. In the past, the regenerative therapy of HCM is mainly focused on the "stem cell," especially for pluripotent stem cell-derived cardiomyocytes [77, 78]. However, it seems that "stromal cell types" have got more attention, particularly including resident immune cells and innate immune system. Therefore, the cardiac resident immune cells become a hotspot in cardiac regeneration of HCM [20]. Moreover, macrophages are also implicated in heart regeneration [79, 80]. In our results, the KEGG pathway of 88 differentially expressed IRGs is also mostly enriched in signaling pathways that regulate pluripotency of stem cells and hematopoietic cell lineage, suggesting that IRGs might be another hotspot in cardiac regeneration of HCM by regulating pluripotency of stem cells and hematopoietic cell lineage.

5. Conclusions

IRGs are a key player in the progression of hypertrophic cardiomyopathy, which is mainly involved in immune regulation, cardiac regeneration, and gene therapy. Meanwhile, 10 hub IRGs were coexpressed with 4 TFs to construct a regulatory network for HCM. Mechanistically, PI3K-Akt and MAPK signaling pathway are the main regulatory mechanism of IGF1, and TGFβ-SMAD signaling pathway is another regulatory mechanism in the pathological process of HCM. Drug prediction of these 10 hub IRGs proposed potential therapeutic agents that could be used in HCM. All these data suggest that IRGs may be a new direction for the treatment of HCM.

Data Availability

The data used to support the findings of this study are available in the Gene Expression Omnibus (GEO) repository (https://www.ncbi.nlm.nih.gov/gds).

Conflicts of Interest

The authors declare that they have no competing interests.

Acknowledgments

This study was supported by the Scientific research project of Hunan Health Commission (No. 202102041763, No. 20200985), the Natural Science Foundation of Changsha (No. 202045504), and the Hunan Cancer Hospital Climb Plan.

Supplementary Materials

Supplementary 1. Table S1: the expression levels of 88 IRGs.

Supplementary 2. Table S2: 78 drug names corresponding to JAK2.

References

[1] G. Thiene, D. Corrado, and C. Basso, "Revisiting definition and classification of cardiomyopathies in the era of molecular medicine," *European Heart Journal*, vol. 29, no. 2, pp. 144–146, 2008.

[2] Y. Hata, K. Hirono, Y. Yamaguchi, F. Ichida, Y. Oku, and N. Nishida, "Minimal inflammatory foci of unknown etiology may be a tentative sign of early stage inherited cardiomyopathy," *Modern Pathology*, vol. 32, no. 9, pp. 1281–1290, 2019.

[3] S. Abdullah, M. L. Lynn, M. T. McConnell et al., "FRET-based analysis of the cardiac troponin T linker region reveals the structural basis of the hypertrophic cardiomyopathy-causing Δ160E mutation," *The Journal of Biological Chemistry*, vol. 294, no. 40, pp. 14634–14647, 2019.

[4] C. Lu, W. Wu, F. Liu et al., "Molecular analysis of inherited cardiomyopathy using next generation semiconductor sequencing technologies," *Journal of translational medicine*, vol. 16, no. 1, p. 241, 2018.

[5] N. Adadi, F. Z. Radi, N. Lahrouchi et al., "Inherited dilated cardiomyopathy in a large Moroccan family caused by LMNA mutation," *Anatolian Journal of Cardiology*, vol. 20, no. 1, pp. 65–68, 2018.

[6] C. D. Vera, C. A. Johnson, J. Walklate et al., "Myosin motor domains carrying mutations implicated in early or late onset hypertrophic cardiomyopathy have similar properties," *The Journal of Biological Chemistry*, vol. 294, no. 46, pp. 17451–17462, 2019.

[7] M. Prondzynski, G. Mearini, and L. Carrier, "Gene therapy strategies in the treatment of hypertrophic cardiomyopathy," *Pflügers Archiv*, vol. 471, no. 5, pp. 807–815, 2019.

[8] B. Kardaszewicz, E. Rogala, M. Tendera, P. Kardaszewicz, and J. Jarzab, "Circulating immune complexes in hypertrophic cardiomyopathy and ischemic heart disease," *Kardiologia Polska*, vol. 34, no. 1, pp. 21–24, 1991.

[9] Y. J. Woo, C. M. Panlilio, R. K. Cheng et al., "Myocardial regeneration therapy for ischemic cardiomyopathy with cyclin A2," *The Journal of Thoracic and Cardiovascular Surgery*, vol. 133, no. 4, pp. 927–933, 2007.

[10] G. D. Richardson, S. Laval, and W. A. Owens, "Cardiomyocyte regeneration in the mdx mouse model of nonischemic cardiomyopathy," *Stem Cells and Development*, vol. 24, no. 14, pp. 1672–1679, 2015.

[11] F. Pagano, V. Picchio, I. Chimenti et al., "On the road to regeneration: "tools" and "routes" towards efficient cardiac cell therapy for ischemic cardiomyopathy," *Current cardiology reports*, vol. 21, no. 11, p. 133, 2019.

[12] A. Saparov, V. Ogay, T. Nurgozhin et al., "Role of the immune system in cardiac tissue damage and repair following myocardial infarction," *Inflammation Research*, vol. 66, no. 9, pp. 739–751, 2017.

[13] P. van den Hoogen, S. C. A. de Jager, M. M. H. Huibers et al., "Increased circulating IgG levels, myocardial immune cells and IgG deposits support a role for an immune response in pre- and end-stage heart failure," *Journal of Cellular and Molecular Medicine*, vol. 23, no. 11, pp. 7505–7516, 2019.

[14] S. Sattler and N. Rosenthal, "The neonate versus adult mammalian immune system in cardiac repair and regeneration," *Biochimica et Biophysica Acta (BBA)-Molecular Cell Research*, vol. 1863, no. 7 Part B, pp. 1813–1821, 2016.

[15] N. G. Frangogiannis, "The immune system and cardiac repair," *Pharmacological Research*, vol. 58, no. 2, pp. 88–111, 2008.

[16] S. C. Latet, V. Y. Hoymans, P. L. Van Herck, and C. J. Vrints, "The cellular immune system in the post-myocardial infarction repair process," *International Journal of Cardiology*, vol. 179, pp. 240–247, 2015.

[17] A. Zimmer, A. K. Bagchi, K. Vinayak, A. Bello-Klein, and P. K. Singal, "Innate immune response in the pathogenesis of heart failure in survivors of myocardial infarction," *American Journal of Physiology. Heart and Circulatory Physiology*, vol. 316, no. 3, pp. H435–H445, 2019.

[18] S. Sattler, P. Fairchild, F. M. Watt, N. Rosenthal, and S. E. Harding, "The adaptive immune response to cardiac injury-the true roadblock to effective regenerative therapies?," *NPJ Regenerative medicine*, vol. 2, no. 1, p. 19, 2017.

[19] R. Gentek and G. Hoeffel, "The innate immune response in myocardial infarction, repair, and regeneration," *Advances in Experimental Medicine and Biology*, vol. 1003, pp. 251–272, 2017.

[20] S. J. Forbes and N. Rosenthal, "Preparing the ground for tissue regeneration: from mechanism to therapy," *Nature Medicine*, vol. 20, no. 8, pp. 857–869, 2014.

[21] L. Fang, A. H. Ellims, A. L. Beale, A. J. Taylor, A. Murphy, and A. M. Dart, "Systemic inflammation is associated with myocardial fibrosis, diastolic dysfunction, and cardiac hypertrophy in patients with hypertrophic cardiomyopathy," *American Journal of Translational Research*, vol. 9, no. 11, pp. 5063–5073, 2017.

[22] W. E. Moody, M. Schmitt, and P. Arumugam, "Coronary microvascular dysfunction in hypertrophic cardiomyopathy detected by Rubidium-82 positron emission tomography and cardiac magnetic resonance imaging," *Journal of Nuclear Cardiology*, vol. 26, no. 2, pp. 666–670, 2019.

[23] A. Doolan, L. Nguyen, and C. Semsarian, "Hypertrophic cardiomyopathy: from "heart tumour" to a complex molecular genetic disorder," *Heart, Lung and Circulation*, vol. 13, no. 1, pp. 15–25, 2004.

[24] S. Epelman and D. L. Mann, "Communication in the heart: the role of the innate immune system in coordinating cellular responses to ischemic injury," *Journal of Cardiovascular Translational Research*, vol. 5, no. 6, pp. 827–836, 2012.

[25] G. Baumgarten, S. C. Kim, H. Stapel et al., "Myocardial injury modulates the innate immune system and changes myocardial sensitivity," *Basic Research in Cardiology*, vol. 101, no. 5, pp. 427–435, 2006.

[26] A. A. Knowlton, "Paying for the tolls: the high cost of the innate immune system for the cardiac myocyte," *Advances in Experimental Medicine and Biology*, vol. 1003, pp. 17–34, 2017.

[27] B. Bartling, K. Niemann, R. U. Pliquett, H. Treede, and A. Simm, "Altered gene expression pattern indicates the differential regulation of the immune response system as an important factor in cardiac aging," *Experimental Gerontology*, vol. 117, pp. 13–20, 2019.

[28] T. Halmos and I. Suba, "A növekedési hormon és az inzulinszerű növekedési faktorok élettani szerepe," *Orvosi Hetilap*, vol. 160, no. 45, pp. 1774–1783, 2019.

[29] S. Pouriamehr, H. Barmaki, M. Rastegary, F. Lotfi, and M. Nabi Afjadi, "Investigation of insulin-like growth factors/insulin-like growth factor binding proteins regulation in metabolic syndrome patients," *BMC research notes*, vol. 12, no. 1, p. 653, 2019.

[30] N. R. Bhakta, A. M. Garcia, E. H. Frank, A. J. Grodzinsky, and T. I. Morales, "The insulin-like growth factors (IGFs) I and II bind to articular cartilage via the IGF-binding proteins," *The Journal of Biological Chemistry*, vol. 275, no. 8, pp. 5860–5866, 2000.

[31] J. L. Martin and R. C. Baxter, "Signalling pathways of insulin-like growth factors (IGFs) and IGF binding protein-3," *Growth Factors*, vol. 29, no. 6, pp. 235–244, 2011.

[32] C. Iosef Husted and M. Valencik, "Insulin-like growth factors and their potential role in cardiac epigenetics," *Journal of Cellular and Molecular Medicine*, vol. 20, no. 8, pp. 1589–1602, 2016.

[33] J. Balcells, A. Moreno, L. Audi, J. Roqueta, J. Iglesias, and A. Carrascosa, "Growth hormone/insulin-like growth factors axis in children undergoing cardiac surgery," *Critical Care Medicine*, vol. 29, no. 6, pp. 1234–1238, 2001.

[34] K. J. Pollard and J. M. Daniel, "Nuclear estrogen receptor activation by insulin-like growth factor-1 in Neuro-2A neuroblastoma cells requires endogenous estrogen synthesis and is mediated by mutually repressive MAPK and PI3K cascades," *Molecular and Cellular Endocrinology*, vol. 490, pp. 68–79, 2019.

[35] W. Wang, D. Wen, W. Duan et al., "Systemic administration of scAAV9-IGF1 extends survival in SOD1G93A ALS mice via inhibiting p38 MAPK and the JNK-mediated apoptosis pathway," *Brain Research Bulletin*, vol. 139, pp. 203–210, 2018.

[36] T. L. C. Wolters, M. G. Netea, A. Hermus, J. W. A. Smit, and R. T. Netea-Maier, "IGF1 potentiates the pro-inflammatory response in human peripheral blood mononuclear cells via MAPK," *Journal of Molecular Endocrinology*, vol. 59, no. 2, pp. 129–139, 2017.

[37] P. Massoner, M. Ladurner-Rennau, I. E. Eder, and H. Klocker, "Insulin-like growth factors and insulin control a multifunctional signalling network of significant importance in cancer," *British Journal of Cancer*, vol. 103, no. 10, pp. 1479–1484, 2010.

[38] G. Nicolini, F. Forini, C. Kusmic, L. Pitto, L. Mariani, and G. Iervasi, "Early and short-term triiodothyronine supplementation prevents adverse postischemic cardiac remodeling: role of transforming growth factor-β1 and antifibrotic miRNA signaling," *Molecular Medicine*, vol. 21, no. 1, pp. 900–911, 2016.

[39] M. Dobaczewski, W. Chen, and N. G. Frangogiannis, "Transforming growth factor (TGF)-β signaling in cardiac

remodeling," *Journal of Molecular and Cellular Cardiology*, vol. 51, no. 4, pp. 600–606, 2011.

[40] H. E. Mewhort, B. D. Lipon, D. A. Svystonyuk et al., "Monocytes increase human cardiac myofibroblast-mediated extracellular matrix remodeling through TGF-β1," *American Journal of Physiology. Heart and Circulatory Physiology*, vol. 310, no. 6, pp. H716–H724, 2016.

[41] A. V. Shinde and N. G. Frangogiannis, "Fibroblasts in myocardial infarction: a role in inflammation and repair," *Journal of Molecular and Cellular Cardiology*, vol. 70, pp. 74–82, 2014.

[42] C. Gerarduzzi and J. A. Di Battista, "Myofibroblast repair mechanisms post-inflammatory response: a fibrotic perspective," *Inflammation Research*, vol. 66, no. 6, pp. 451–465, 2017.

[43] C. M. Tinoco-Veras, A. Santos, J. Stipursky et al., "Transforming growth factor beta1/SMAD signaling pathway activation protects the intestinal epithelium from Clostridium difficile toxin A-induced damage," *Infection and immunity*, vol. 85, no. 10, 2017.

[44] H. L. Ma, X. F. Zhao, G. Z. Chen, R. H. Fang, and F. R. Zhang, "Silencing NLRC5 inhibits extracellular matrix expression in keloid fibroblasts via inhibition of transforming growth factor-β1/Smad signaling pathway," *Biomedicine & Pharmacotherapy*, vol. 83, pp. 1016–1021, 2016.

[45] M. Liu, J. Ai, J. Feng et al., "Effect of paeoniflorin on cardiac remodeling in chronic heart failure rats through the transforming growth factor β1/Smad signaling pathway," *Cardiovascular diagnosis and therapy*, vol. 9, no. 3, pp. 272–280, 2019.

[46] C. Y. Zhan, J. H. Tang, D. X. Zhou, and Z. H. Li, "Effects of tanshinone IIA on the transforming growth factor β1/Smad signaling pathway in rat cardiac fibroblasts," *Indian journal of pharmacology*, vol. 46, no. 6, pp. 633–638, 2014.

[47] D. Seo and J. M. Hare, "The transforming growth factor-beta/Smad3 pathway: coming of age as a key participant in cardiac remodeling," *Circulation*, vol. 116, no. 19, pp. 2096–2098, 2007.

[48] F. Yang, A. C. Chung, X. R. Huang, and H. Y. Lan, "Angiotensin II induces connective tissue growth factor and collagen I expression via transforming growth factor-beta-dependent and -independent Smad pathways: the role of Smad3," *Hypertension*, vol. 54, no. 4, pp. 877–884, 2009.

[49] M. H. Paul, R. P. Harvey, M. Wegner, and E. Sock, "Cardiac outflow tract development relies on the complex function of Sox4 and Sox11 in multiple cell types," *Cellular and Molecular Life Sciences*, vol. 71, no. 15, pp. 2931–2945, 2014.

[50] J. Ya, M. W. Schilham, P. A. de Boer, A. F. Moorman, H. Clevers, and W. H. Lamers, "Sox4-deficiency syndrome in mice is an animal model for common trunk," *Circulation Research*, vol. 83, no. 10, pp. 986–994, 1998.

[51] A. Restivo, G. Piacentini, S. Placidi, C. Saffirio, and B. Marino, "Cardiac outflow tract: a review of some embryogenetic aspects of the conotruncal region of the heart," *The Anatomical Record. Part A, Discoveries in Molecular, Cellular, and Evolutionary Biology*, vol. 288, no. 9, pp. 936–943, 2006.

[52] K. Drosatos, N. M. Pollak, C. J. Pol et al., "Cardiac myocyte KLF5 regulates Ppara expression and cardiac function," *Circulation Research*, vol. 118, no. 2, pp. 241–253, 2016.

[53] N. D. Roe, S. W. Standage, and R. Tian, "The relationship between KLF5 and PPARα in the heart," *Circulation Research*, vol. 118, no. 2, pp. 193–195, 2016.

[54] N. Takeda, I. Manabe, Y. Uchino et al., "Cardiac fibroblasts are essential for the adaptive response of the murine heart to pressure overload," *The Journal of Clinical Investigation*, vol. 120, no. 1, pp. 254–265, 2010.

[55] R. Nagai, T. Suzuki, K. Aizawa, T. Shindo, and I. Manabe, "Significance of the transcription factor KLF5 in cardiovascular remodeling," *Journal of Thrombosis and Haemostasis*, vol. 3, no. 8, pp. 1569–1576, 2005.

[56] R. Nagai, T. Shindo, I. Manabe, T. Suzuki, and M. Kurabayashi, "KLF5/BTEB2, a Kruppel-like zinc-finger type transcription factor, mediates both smooth muscle cell activation and cardiac hypertrophy," *Advances in Experimental Medicine and Biology*, vol. 538, pp. 57–65, 2003.

[57] R. M. Di, C. X. Yang, C. M. Zhao et al., "Identification and functional characterization of KLF5 as a novel disease gene responsible for familial dilated cardiomyopathy," *European journal of medical genetics*, vol. 63, article 103827, 2019.

[58] K. Igarashi, K. Itoh, H. Motohashi et al., "Activity and expression of murine small Maf family protein MafK," *The Journal of Biological Chemistry*, vol. 270, no. 13, pp. 7615–7624, 1995.

[59] F. Katsuoka, H. Motohashi, K. Onodera, N. Suwabe, J. D. Engel, and M. Yamamoto, "One enhancer mediates mafK transcriptional activation in both hematopoietic and cardiac muscle cells," *The EMBO Journal*, vol. 19, no. 12, pp. 2980–2991, 2000.

[60] Y. J. Hwang, E. W. Lee, J. Song, H. R. Kim, Y. C. Jun, and K. A. Hwang, "MafK positively regulates NF-κB activity by enhancing CBP-mediated p65 acetylation," *Scientific Reports*, vol. 3, no. 1, p. 3242, 2013.

[61] X. Feng, T. He, J. G. Wang, and P. Zhao, "Asn391Thr mutation of β-myosin heavy chain in a hypertrophic cardiomyopathy family," *International Heart Journal*, vol. 59, no. 3, pp. 596–600, 2018.

[62] D. I. Keller, J. Schwitter, E. R. Valsangiacomo, P. Landolt, and C. H. Attenhofer Jost, "Hypertrophic cardiomyopathy due to beta-myosin heavy chain mutation with extreme phenotypic variability within a family," *International Journal of Cardiology*, vol. 134, no. 3, pp. e87–e93, 2009.

[63] S. Epelman, P. P. Liu, and D. L. Mann, "Role of innate and adaptive immune mechanisms in cardiac injury and repair," *Nature Reviews. Immunology*, vol. 15, no. 2, pp. 117–129, 2015.

[64] T. Kennedy-Lydon, "Immune functions and properties of resident cells in the heart and cardiovascular system: pericytes," *Advances in Experimental Medicine and Biology*, vol. 1003, pp. 93–103, 2017.

[65] E. Turillazzi, C. Pomara, S. Bello, M. Neri, I. Riezzo, and V. Fineschi, "The meaning of different forms of structural myocardial injury, immune response and timing of infarct necrosis and cardiac repair," *Current Vascular Pharmacology*, vol. 13, no. 1, pp. 6–19, 2015.

[66] M. Hulsmans, F. Sam, and M. Nahrendorf, "Monocyte and macrophage contributions to cardiac remodeling," *Journal of Molecular and Cellular Cardiology*, vol. 93, pp. 149–155, 2016.

[67] D. Hashimoto, A. Chow, C. Noizat et al., "Tissue-resident macrophages self-maintain locally throughout adult life with minimal contribution from circulating monocytes," *Immunity*, vol. 38, no. 4, pp. 792–804, 2013.

[68] S. C. Macri, C. C. Bailey, N. M. de Oca et al., "Immunophenotypic alterations in resident immune cells and myocardial fibrosis in the aging rhesus macaque (Macaca mulatta) heart," *Toxicologic Pathology*, vol. 40, no. 4, pp. 637–646, 2012.

[69] F. K. Swirski and M. Nahrendorf, "Cardioimmunology: the immune system in cardiac homeostasis and disease," *Nature Reviews. Immunology*, vol. 18, no. 12, pp. 733–744, 2018.

[70] N. V. Krylova, T. P. Smolina, and G. N. Leonova, "Molecular mechanisms of interaction between human immune cells and far eastern tick-borne encephalitis virus strains," *Viral Immunology*, vol. 28, no. 5, pp. 272–281, 2015.

[71] F. Bonner, N. Borg, S. Burghoff, and J. Schrader, "Resident cardiac immune cells and expression of the ectonucleotidase enzymes CD39 and CD73 after ischemic injury," *PLoS One*, vol. 7, no. 4, article e34730, 2012.

[72] X. Xue and D. M. Falcon, "The role of immune cells and cytokines in intestinal wound healing," *International journal of molecular sciences*, vol. 20, no. 23, 2019.

[73] D. M. Zaiss, C. M. Minutti, and J. A. Knipper, "Immune- and non-immune-mediated roles of regulatory T-cells during wound healing," *Immunology*, vol. 157, no. 3, pp. 190–197, 2019.

[74] M. V. Krasnoselsky, L. I. Simonova, V. Z. Gertman, E. S. Pushkar, and T. S. Zavadskaya, "Tissue immune cells and their role in the healing process of infected radiation ulcers under the impact of photodynamic therapy (experimental study)," *Problemy radiatsiinoi medytsyny ta radiobiolohii*, vol. 24, pp. 250–260, 2019.

[75] F. C. Simoes, T. J. Cahill, A. Kenyon et al., "Macrophages directly contribute collagen to scar formation during zebrafish heart regeneration and mouse heart repair," *Nature communications*, vol. 11, no. 1, p. 600, 2020.

[76] G. Caputa, A. Castoldi, and E. J. Pearce, "Metabolic adaptations of tissue-resident immune cells," *Nature Immunology*, vol. 20, no. 7, pp. 793–801, 2019.

[77] X. Li, W. J. Lu, Y. Li et al., "MLP-deficient human pluripotent stem cell derived cardiomyocytes develop hypertrophic cardiomyopathy and heart failure phenotypes due to abnormal calcium handling," *Cell death & disease*, vol. 10, no. 8, p. 610, 2019.

[78] N. Aoyama, J. Liu, S. Lor, T. K. Feaster, S. Hilcove, and E. Jones, "Assessment of hypertrophic cardiomyopathy using human induced pluripotent stem cell-derived cardiomyocytes reveals abnormal excitation contraction coupling," *Journal of Pharmacological and Toxicological Methods*, vol. 99, p. 106595, 2019.

[79] J. Leor, D. Palevski, U. Amit, and T. Konfino, "Macrophages and regeneration: lessons from the heart," *Seminars in Cell & Developmental Biology*, vol. 58, pp. 26–33, 2016.

[80] A. B. Aurora, E. R. Porrello, W. Tan et al., "Macrophages are required for neonatal heart regeneration," *The Journal of Clinical Investigation*, vol. 124, no. 3, pp. 1382–1392, 2014.

Hindawi
Journal of Nanomaterials
Volume 2021, Article ID 5570596, 7 pages
https://doi.org/10.1155/2021/5570596

Research Article

Perioperative Use of Flurbiprofen Axetil on Renal Function after Transurethral Prostatectomy: A Prospective Randomized Controlled Study

Dong Wang,[1] **Wenxiu Xie**,[1] **Bo Li**,[2] **Yufan Zhao**,[1] **Xing Liu**,[1] **Yufeng Zhang**,[1] **Yongzhong Tang**,[1,3] **and Xinlin Yin**[1,4]

[1]*Department of Anesthesiology, The Third Xiangya Hospital, Central South University, Changsha, 410013 Hunan, China*
[2]*Surgery Center, The Third Xiangya Hospital, Central South University, Changsha, 410013 Hunan, China*
[3]*Hunan Key Laboratory of Brain Homeostasis, China*
[4]*Hunan Key Laboratory of Medical Information Research, China*

Correspondence should be addressed to Xinlin Yin; yxl_email@126.com

Received 30 January 2021; Revised 3 February 2021; Accepted 15 February 2021; Published 27 February 2021

Academic Editor: Tingting Hong

Objective. To explore the role of low-dose flurbiprofen axetil in perioperative renal protection. *Methods.* A total of 83 patients who underwent transurethral resection of the prostate (TURP) between August 2020 and November 2020 at the Third Xiangya Hospital of Central South University were selected, aged 60-85 years old, American Society of Anesthesia (ASA) physical status classes 1-3, BMI 18-30 kg/m^2, randomly divided into the experimental group (group F, $n = 42$) and control group (group C, $n = 41$). 10 minutes before the operation, group F was injected with 100 mg (10 mL) flurbiprofen axetil, and group C was injected with 10 mL 0.9% saline, comparing the incidence of acute kidney injury (AKI) and changes in glomerular filtration rate (eGFR) between the two groups. Cystatin-C, Neutrophil Gelatinase-associated Lipocalin (NGAL), IL-6, and CRP were compared between the two groups at 4 time points (before surgery, 6 hours, 24 hours, and 48 hours after surgery). *Results.* A total of 80 cases were enrolled, 40 in group F and 40 in group C. There was no significant difference in baseline between the two groups ($P > 0.05$). The NGAL of group F was significantly lower than group C at 6 hours after the operation (367.99 ± 311.83 vs. 243.02 ± 151.73, $P = 0.026$), but there was no significant difference in NGAL and Cystatin-C at other time points ($P > 0.05$). And there was no significant difference in the incidence of postoperative AKI between the two groups (0% vs. 2.5%, $P = 0.314$). *Conclusion.* 100 mg flurbiprofen axetil can reduce the NGAL at 6 hours after TURP, and it may have a protective effect on the kidney.

1. Introduction

Acute kidney injury (AKI) is a clinical syndrome characterized by a sharp deterioration in renal function [1]. AKI is one of the serious complications after surgery, and the incidence of perioperative AKI is 6.3%~7.4% [2, 3]. The occurrence of AKI is related to factors such as perioperative hemodynamic changes, systemic inflammatory response, renal ischemia-reperfusion injury, and oxidative stress [4]. Besides, hypovolemia, dehydration, hypoxia, antibiotics, contrast agents, nonsteroidal drugs, antitumor drugs, and antiretroviral drugs are also risk factors for perioperative AKI [5]. Perioperative AKI can develop into chronic kidney disease (CKD) and end-stage renal disease (ESRD) and even lead to death [6]. Therefore, the prevention and treatment of perioperative AKI are particularly important.

KDIGO generally uses serum creatinine (Scr) or urine volume changes as diagnostic criteria for the diagnosis of AKI, but these two indicators have limitations and lag. In recent years, many studies have found that some biomarkers can predict the occurrence of AKI earlier than Scr, including Cystatin-C, NGAL, and N-acetyl-β-D-glucosaminidase (NAG) [7].

Flurbiprofen axetil is a nonselective cyclooxygenase (COX) inhibitor, which can gather at the surgical incision

and inhibit the inflammatory response, thereby reducing postoperative pain, so it is widely used in the perioperative period [8]. However, studies have shown that the use of flurbiprofen may cause renal papillary necrosis and tubulointerstitial inflammation [9, 10]. Studies have shown that nonsteroidal anti-inflammatory drugs (NSAIDs) inhibit the expansion of preglomerular arterioles mediated by prostaglandins by inhibiting COX enzymes, resulting in a decrease in renal blood flow. When renal blood flow is reduced or renal disease is already present, it may cause renal ischemia or acute tubular necrosis (ATN) [11]. Another research has found that NSAIDs can cause hyporeninemia and hyperaldosteronism and can cause ATN, acute tubular interstitial nephritis, glomerulonephritis, renal papillary necrosis, and other nephrotoxicities [12]. Moreover, ATN is an important cause of AKI, and about 40% of AKI is produced by ATN [13]. It has also been found that NSAIDs can cause acute tubulointerstitial nephritis (ATIN), which may be related to immune response [14]. Although the above studies have shown that NSAIDs are toxic to the kidneys, their wide application in the perioperative period is not limited. The retrospective analysis of our team also found that the effect of flurbiprofen axetil on postoperative renal function is dose-dependent in the perioperative period: 50-100 mg flurbiprofen axetil can reduce the incidence of AKI postoperatively, but there is obvious renal damage when it exceeds 250 mg [15]. To this end, we conducted a prospective study to verify whether low-dose flurbiprofen axetil has a protective effect on the kidney by detecting changes in Scr, Cystatin-C, NGAL, and other indicators during the perioperative period.

2. Method

In accordance with the CONSORT statement, the present randomized controlled trial was approved by the appropriate Institutional Review Board (IRB) of the Third Xiangya Hospital of Central South University (IRB: R20255), and written informed consent was provided by all patients.

This is a randomized, double-blind, placebo-controlled clinical study. Between August 2020 and November 2020, male patients undergoing TURP under spinal anesthesia at the Third Xiangya Hospital of Central South University were selected. The researcher collected and recorded basic patient information one day before surgery, including age, body mass index (BMI), comorbid diseases, medication history, and test results. Those who met the following criteria were selected: (1) age 60-85 years; (2) ASA classification 1 to 3; (3) BMI > 18 kg/m^2 and <30 kg/m^2; (4) patients or their family members could provide written informed consent. Patients were excluded if they met one of the following situations: (1) long-term use of NSAIDs before surgery; (2) flurbiprofen axetil contraindication; (3) severe diseases such as sepsis, severe liver insufficiency (Child-Pugh Grade C), CKD stage 3 (eGFR ≤ 60 mL/min/1.73m^2) or higher, NYHA grade 3 to 4, and moderate or higher anemia (Hb < 90 g/L); (4) perioperative use other types of NSAIDs or drugs that affect renal function, including aminoglycoside antibiotics, iodinating agents, contrast agents, antitumor drugs, and antiretroviral drugs; (5) intraoperative hypotension (blood pressure lower than 90/60 mmHg or MAP < 60 mmHg) continued to exceed 20 min; (6) entered ICU after operation; (7) switched to general anesthesia. The included patients were randomly divided into an experimental group (group F) and a control group (group C) at a ratio of 1 : 1.

2.1. Randomization and Masking. The researchers used SAS statistical software to generate 1 : 1 random numbers for the experimental group and the control group on the computer to determine the grouping situation. Surgeons, anesthesiologists, researchers, statistical analysts, and patients did not know the study group. Because the flurbiprofen axetil is milky white, the control group 0.9% normal saline is colorless and transparent. The administer was a nonblind person who was only responsible for the administration and did not participate in information collection, anesthesia, surgery, and statistical analysis.

2.2. Anesthesia and Surgery. After the patient entered the operating room, low-flow oxygen inhalation was performed and vital signs such as blood pressure, electrocardiogram, oxygen saturation, and pulse were monitored. Under the guidance of the anesthesiologist, the patient took the left or right decubitus position, held the knees with both hands, and kept the thighs close to the abdominal wall and the head close to the chest, so that the waist and back were bent back. The anesthesiologist disinfected the towel and used 2% lidocaine 3 mL for local anesthesia. Then, he punctured the subarachnoid space in the L3~4 space, through the skin, subcutaneous tissue, supraspinous ligament, interspinous ligament, ligamentum flavum, dura mater, and arachnoid membrane to subarachnoid space, and injected a mixed solution of 0.5 mL 10% glucose solution, 0.025 mg fentanyl, and 1.5 mL 1% ropivacaine hydrochloride. After successful anesthesia, the same group of surgeons performed TURP on the patient. Closely monitored vital signs after the operation and recorded ASA classification, anesthesia plane, infusion, blood loss, operation time, and blood pressure change. After the operation, the two groups of patients were treated with routine treatment and nursing such as oxygen inhalation, ECG monitoring, continuous bladder irrigation, early enteral nutrition, anti-inflammatory, and stomach protection. Meanwhile, flurbiprofen axetil-related complications and adverse reactions should be taken seriously.

2.3. Intervention. 10 minutes before the operation, the patient in group F received a single injection of 100 mg (10 mL) flurbiprofen axetil through a peripheral vein, and group C received a single intravenous injection of the same volume (10 mL) of 0.9% normal saline by the same administrator.

2.4. Outcome Measurement

2.4.1. Main Outcome. There is an incidence of AKI and eGFR. According to the latest Kidney Disease Improving Global Outcomes (KDIGO) diagnostic criteria for AKI, AKI can be diagnosed if one of the following conditions was met: (1) Scr increased by more than 0.3 mg/dL (≥26.5 μmol/L) 48 hours after surgery compared with the preoperative baseline value; (2) Scr increased by more than

1.5 times 7 days after operation compared with the baseline level before operation; (3) the hourly urine output is less than 0.5 mL/kg and lasts for more than 6 hours [16]. eGFR is calculated by the formula of Chronic Kidney Disease Epidemiology Collaboration (CKD-EPI) [17]: $eGFR = 141 * (Scr/0.9)a * 0.993\,year$ (year represents age. a is a fixed constant, when $Scr > 0.9\,mg/dL$, $a = -1.209$; when $Scr \leq 0.9\,mg/dL$, $a = -0.411$). Scr is determined by the Jaffe detection method.

2.4.2. Secondary Outcome. The changes of serum Cystatin-C, NGAL, IL-6, CRP, and other indicators were compared between the two groups of patients at 4 time points (before operation, 6 hours, 24 hours, and 48 hours after the operation). The immunoturbidimetric method was used to determine the contents of Cystatin-C, NGAL, and CRP. Flow cytometry was used to detect the changes of serum IL-6 over time in 12 patients (6 in group F and 6 in group C).

2.5. Drugs and Experimental Reagents

2.5.1. Flurbiprofen Axetil Injection. The production batch number is H20183054, produced by Wuhan Daan Pharmaceutical Co., Ltd. 0.9% sodium chloride injection: the production batch number is H43020454, produced by Hunan Kelun Pharmaceutical Co., Ltd. 10% glucose injection: the production batch number is H20102904, produced by Hunan Kelun Pharmaceutical Co., Ltd. Fentanyl citrate injection: the production batch number is 91D06021, produced by Yichang Renfu Pharmaceutical Co., Ltd. Ropivacaine hydrochloride: the production batch number is NBEM, produced by AstraZeneca Pharmaceuticals, Sweden. NGAL assay kit: the production batch number is 20152401008, produced by Beijing Danda Biotechnology Co., Ltd. Cystatin-C determination kit: the production batch number is 20162400234, produced by Anhui Iprokang Biotechnology Co., Ltd. CRP determination kit: Zhejiang Quark Biotechnology Co., Ltd., medical device registration number: Zhejiang Machinery Standard Note 20192400387. IL-6 kit: the production batch number is 20180531, produced by Agilent Bio (Hangzhou) Co., Ltd.

2.6. Statistical Analysis. SPSS software version 26.0 was used for analysis. Measurement data were expressed in the form of mean ± standard deviation (mean ± SD) or median (interquartile range). The count data were expressed in percentage (%). The method of kurtosis and skewness coefficient was used to test the normality of measurement data. The measurement data conforming to the normal distribution adopts the t-test, and the measurement data not conforming to the normal distribution adopts the Wilcoxon rank-sum test; the count data adopts the χ^2 test or Fisher's exact test. The changes of serum Cystatin-C and NGAL over time and group were analyzed by two-factor repeated-measures analysis of variance. The significance level for all tests was set at $P < 0.05$.

3. Result

3.1. Subject Recruitment. From August 2020 to November 2020, a total of 88 patients underwent TURP surgery. Among them, 2 patients were younger than 60 years old, 2 patients refused to participate, 2 patients switched to general anesthesia, and 1 patient had a preoperative eGFR less than $60\,mL/min/1.73m^2$; 1 patient used other types of NSAIDs perioperatively. In the end, 80 patients were enrolled, 40 in group F and 40 in group C (Figure 1).

3.2. Baseline of the Two Groups. As shown in Table 1, there were no statistically significant differences in age, BMI, ASA classification, preoperative mean arterial pressure, preoperative comorbidities, level of anesthesia, operation time, and infusion volume between the two groups. From the perspective of preoperative medication, the preoperative dosage of angiotensin-converting enzyme inhibitor (ACEI), angiotensin receptor blockers (ARB), or calcium channel blockers (CCB) was not significantly different between the two groups of patients.

3.3. Comparison of Lab Results between the Two Groups. The Scr, eGFR, and hemoglobin before the operation and 48 hours after operation were no significant difference between the two groups. The CRP in group F was lower than that in group C at 48 hours after surgery ($P = 0.005$), but there was no significant difference preoperatively (Table 2). Table 3 shows the changes in serum IL-6 of 12 patients over time (6 in group C and 6 in group F). The level of serum IL-6 in group C was significantly higher than that in group F at 6 hours after the operation ($P = 0.004$).

3.4. The Incidence of AKI in the Two Groups. A total of 80 patients were included in the analysis. One patient in group C developed AKI, and the incidence was 2.5%. There was no AKI patient in group F, and there was no significant difference in the incidence of AKI between the two groups ($P = 0.314$). Also, there was no significant difference in blood pressure between the two groups of patients from entering the operating room to leaving the operating room ($P > 0.05$).

3.5. Changes in Biomarkers. The effects of group and time on Cystatin-C are as follows:

The interaction between group and time had no significant difference on Cystatin-C ($P = 0.109$). There was no statistical difference in Cystatin-C between group F and group C at the same time point ($P = 0.913$). The Cystatin-C were compared at different time points in the two groups, and it was found that Cystatin-C decreased with time from 0 to 6 hours after surgery ($P < 0.001$), but it began to rise again from 24 hours to 48 hours after surgery ($P < 0.001$). The changes of Cystatin-C in the two groups with time are shown in Figure 2.

The effects of group and time on serum NGAL levels are as follows:

The interaction between group and time had a significant difference on NGAL ($P = 0.002$). At 6 hours after the operation, the NGAL level in group F was significantly lower than that in group C ($P = 0.002$). However, there was no significant difference in NGAL between the two groups before the operation, 24 h after operation, and 48 h after operation ($P > 0.05$). NGAL were compared at different time points in the two groups: in group C, NGAL showed an upward trend

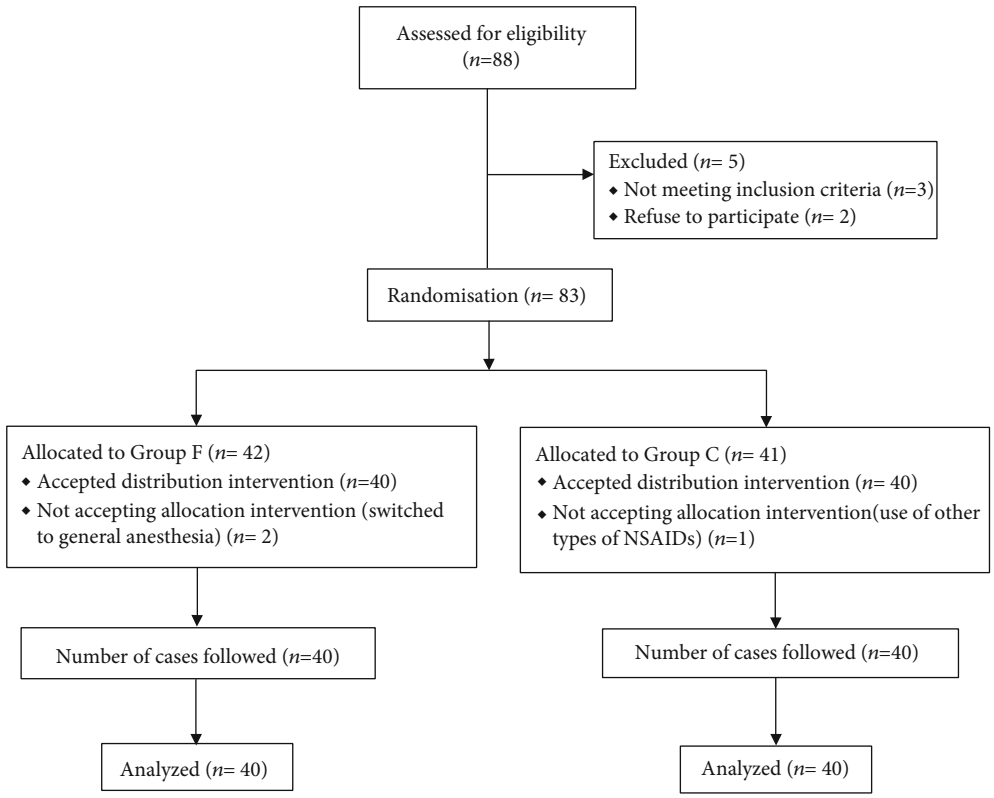

Figure 1: Subject recruitment.

Table 1: Comparison of the basic characteristics of the two groups of patients.

	Group C ($n = 40$)	Group F ($n = 40$)	P value
Mean ± SD age (year)	70.68 ± 7.70	68.40 ± 8.14	0.203
Mean ± SD BMI (kg/m^2)	22.90 ± 3.28	23.02 ± 3.09	0.872
Mean ± SD preoperative MAP (mmHg)	95.56 ± 9.19	98.75 ± 11.42	0.172
Preoperative comorbidities			
High blood pressure	14 (35)	12 (30)	0.633
Diabetes	7 (17.5)	3 (7.5)	0.176
Preoperative medication			
ACEI	2 (2.5)	0 (0)	0.152
ARB	2 (2.5)	1 (2.5)	0.556
CCB	10 (25)	9 (22.5)	0.793
Anesthesia plane			
T6~S5	0 (0)	3 (7.5)	0.246
T8~S5	17 (42.5)	20 (50)	
T10~S5	23 (57.0)	17 (42.5)	
Mean ± SD operation time (min)	69.93 ± 20.87	63.30 ± 21.33	0.445
Mean ± SD infusion volume (mL)	701.50 ± 205.78	736.50 ± 186.64	0.428

Data are number of patients (%) unless otherwise indicated. BMI: body mass index; MAP: mean arterial pressure; ACEI: angiotensin-converting enzyme inhibitor; ARB: angiotensin receptor blockers; CCB: calcium channel blockers.

within 6 hours after surgery ($P = 0.010$), but there was no significant difference from 6 to 48 hours after surgery ($P > 0.05$); in group F, the effect of time on NGAL was no significant difference, that is, there was no significant difference in NGAL with time ($P > 0.05$). The changes of NGAL in the two groups over time are shown in Figure 3.

Table 2: Comparison of lab results between two groups of patients.

	Group C ($n = 40$)	Group F ($n = 40$)	P value
Before surgery			
Scr (μmol/L)	81.40 ± 13.11	80.70 ± 12.67	0.806
eGFR (mL/min/1.73m^2)	84.59 ± 17.81	85.14 ± 15.83	0.883
Hb (g/L)	133.18 ± 13.52	134.91 ± 17.71	0.624
CRP (mg/L)	1.76 ± 1.92	1.93 ± 1.1	0.562
48 hours after surgery			
Scr (μmol/L)	86.63 ± 16.15	87.43 ± 16.73	0.819
eGFR (mL/min/1.73m^2)	79.17 ± 19.13	78.27 ± 16.73	0.824
Hb (g/L)	132.00 ± 12.73	134.20 ± 13.75	0.460
CRP(mg/L)	18.04 ± 17.00	10.33 ± 11.46	0.005*

Data are shown as mean ± SD. Scr: serum creatinine; eGFR: glomerular filtration rate; Hb: hemoglobin; CRP: C reactive protein. *Significant P value.

Table 3: The changes of IL-6 in the two groups over time.

	Preoperative	Postoperative		
		6 hours	24 hours	48 hours
Group C ($n = 6$)	4.10 (2.76-8.31)	11.28 (8.43-36.40)	11.66 (4.97-25.14)	7.94 (4.84-23.00)
Group F ($n = 6$)	3.17 (2.38-4.32)	3.16 (2.38-3.77)	3.92 (2.84-12.66)	3.36 (2.49-16.43)
P value	0.262	0.004*	0.092	0.109

Data are shown as median (IQR). *Significant P value.

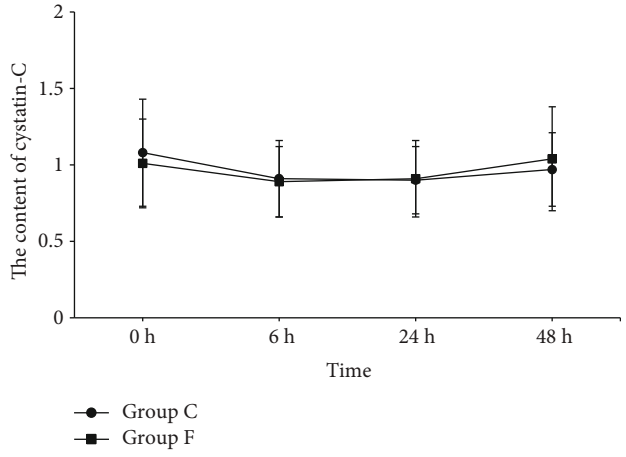

Figure 2: The changes of Cystatin-C in the two groups over time 0 h, 6 h, 24 h, and 48 h represent preoperatively, 6 hours, 24 hours, and 48 hours postoperatively, respectively.

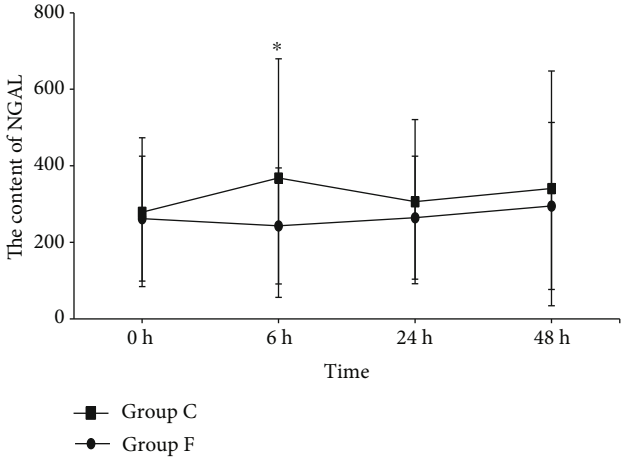

Figure 3: The changes of NGAL in the two groups over time 0 h, 6 h, 24 h, and 48 h represent preoperatively, 6 hours, 24 hours, and 48 hours postoperatively, respectively. *$P < 0.05$.

4. Discussion

In this study, only 1 patient developed AKI (1.3%) after TURP, which was similar to the extremely rare incidence of AKI after TURP showed in previous studies [18]. However, some studies believed that old age, past diseases, and urinary tract obstruction are high-risk factors for postoperative renal injury [19, 20]. For TURP, hemolytic reactions that occur in the bladder and surgical wounds were infused with sterile saline during the operation. The hemoglobin produced by this reaction could also cause renal tubular damage after being absorbed by the bladder and blood [21, 22]. Therefore, our study concluded that in the control group, the NGAL concentration at 6 hours after surgery was significantly higher than that before surgery, indicating that although surgery-related AKI caused by TURP was rare, renal tubular damage caused by surgery can still be observed.

In the experimental group, with a small dose of flurbiprofen axetil, the serum NGAL concentration at 6 hours after surgery did not increase compared with that before the operation, which suggested that flurbiprofen axetil may be related to the protection of renal tubules [7]. As early as 1991, it was

reported that the application of flurbiprofen axetil can cause renal papillary necrosis and renal tubulointerstitial inflammation [9, 10]. As we all know, NSAIDs can inhibit COX enzymes and reduce renal blood flow by blocking prostaglandin-mediated dilation of the glomerular arterioles. The decline of renal blood flow can cause renal ischemia to be further aggravated or renal tubular necrosis in the case of existing renal disease [11]. In a single-center retrospective study, it was found that compared with patients who did not use flurbiprofen axetil, patients who received 100 mg flurbiprofen axetil during the perioperative period had a lower incidence of AKI [15]. These studies have suggested that flurbiprofen axetil may have renal protection.

Although the mechanism of action of flurbiprofen axetil in protecting renal tubules is still unclear, the release of inflammatory mediators is the basis of renal tubular damage [23]. Takaku et al. found that the use of COX-2 enzyme inhibitors can reduce the levels of systemic inflammatory mediators (such as IL-1α, IL-1β, IL-6, and TNF-α) and kidney damage in shock mouse models [24]. In this study, the level of IL-6 in the experimental group was significantly lower than that in the control group at 6 hours after surgery, similar to the results of the former study, suggesting that flurbiprofen axetil can reduce the level of inflammation in the body and reduce renal tubular damage. In addition, the study by Feitoza et al. showed that before renal ischemia and reperfusion, the use of nonselective COX enzyme inhibitors reduces the development of renal fibrosis through its anti-inflammatory effects [25]. In this study, the CRP of the control group was significantly higher than that of the experimental group at 48 hours after the operation due to the inhibitory effect of the COX-2 enzyme ($P = 0.005$). It suggests that compared with the control group, the inflammatory response of the experimental group was significantly lower than that of the control group. It can be seen that flurbiprofen axetil may produce renal tubular protection through its anti-inflammatory mechanism.

In addition, in the case of renal hypoperfusion, the increased expression of COX-2 in the dense macula contributes to the renal vasoconstriction response, and the renal blood flow and glomerular filtration rate decrease through the tubule-glomerular feedback mechanism [26, 27]. It is speculated that, as a nonselective COX enzyme inhibitor, flurbiprofen axetil can also inhibit the COX enzyme in the dense macula of the kidney, thereby improving renal blood flow and protecting renal function. Finally, the COX-2 enzyme can lead to the synthesis and secretion of transforming growth factor (TGF-β), which in turn leads to tubular deposition of collagen and fibrin in the kidney [28]. Cheng and Harris believe that long-term use of selective COX-2 inhibitors shows potential renal protection in cases of glomerular hyperfiltration, such as diabetes and partial nephrectomy, and reduces proteinuria, extracellular matrix deposition, and glomerulosclerosis [29].

Due to various reasons, this research still has some limits. First of all, this was a single-center prospective study. Whether flurbiprofen axetil has a protective effect during the perioperative period requires clinical verification in multiple centers and multiple populations. Second, due to the short hospital stay of patients undergoing transurethral prostate surgery and continuous bladder lavage after the operation, data on postoperative urine output and Scr 7 days after surgery were not available, so only the changes in renal function after 48 hours could be observed. The actual incidence of AKI during the perioperative period might be underestimated. Third, in addition to the detection of IL-6, this study did not observe other perioperative inflammatory mediators (such as IL-1α, IL-1β, and TNF-α). The mechanism of the renal protection of flurbiprofen axetil may need to be verified by animal experiments.

5. Conclusion

100 mg flurbiprofen axetil can reduce the NGAL at 6 hours after TURP and may have a protective effect on the kidneys.

Data Availability

The data used to support the findings of this study may be released upon application to the Department of Anesthesiology, Third Xiangya Hospital, Central South University, which can be contacted at xy3irb@163.com

Conflicts of Interest

The authors declare that they have no competing interests.

Authors' Contributions

Dong Wang and Wenxiu Xie contributed equally to this work.

Acknowledgments

This work was supported by the Project of Health and Health Commission of Hunan Province (20201802), Hunan Province Key Laboratory Project (2018TP1009), Natural Science Foundation of Hunan Province (2020JJ5854), National Natural Science Foundation of China (81901842), China Primary Health Care Foundation (YLGX-WS-2020003), and Research and Innovation Funds from Xiangya Bigdata Foundation of Central South University.

References

[1] R. Bellomo, J. A. Kellum, and C. J. L. Ronco, "Acute kidney injury," *Lancet*, vol. 380, no. 9843, pp. 756–766, 2012.

[2] M. Walsh, P. J. Devereaux, A. X. Garg et al., "Relationship between intraoperative mean arterial pressure and clinical outcomes after noncardiac surgery: toward an empirical definition of hypotension," *Anesthesiology*, vol. 119, no. 3, pp. 507–515, 2013.

[3] L. Y. Sun, D. N. Wijeysundera, G. A. Tait, and W. S. Beattie, "Association of intraoperative hypotension with acute kidney injury after elective noncardiac surgery," *Anesthesiology*, vol. 123, no. 3, pp. 515–523, 2015.

[4] J. Vanmassenhove, J. Kielstein, A. Jörres, and W. V. Biesen, "Management of patients at risk of acute kidney injury," *Lancet*, vol. 389, no. 10084, pp. 2139–2151, 2017.

[5] R. L. Mehta, J. Cerdá, E. A. Burdmann et al., "International Society of Nephrology's 0by25 initiative for acute kidney injury

(zero preventable deaths by 2025): a human rights case for nephrology," *Lancet*, vol. 385, no. 9987, pp. 2616–2643, 2015.

[6] M. E. Grams, Y. Sang, J. Coresh et al., "Acute kidney injury after major surgery: a retrospective analysis of veterans health administration data," *American Journal of Kidney Diseases*, vol. 67, no. 6, pp. 872–880, 2016.

[7] M. Ostermann, "Acute kidney injury 2016: diagnosis and diagnostic workup," *Critical Care*, vol. 20, no. 1, p. 299, 2016.

[8] K. Wang, J. Luo, L. Zheng, and T. Luo, "Preoperative flurbiprofen axetil administration for acute postoperative pain: a meta-analysis of randomized controlled trials," *Journal of Anesthesia*, vol. 31, no. 6, pp. 852–860, 2017.

[9] J. Kaufhold and M. Wilkowski, "Flurbiprofen-associated acute tubulointerstitial nephritis," *American Journal of Nephrology*, vol. 11, no. 2, pp. 144–146, 1991.

[10] H. Berning, K. Orellana, and W. Selberg, "Nierenpapillennekrosen," *DMW - Deutsche Medizinische Wochenschrift*, vol. 99, no. 36, pp. 1749–1754, 1974.

[11] S. Clavé, C. Rousset-Rouvière, L. Daniel, and M. Tsimaratos, "The invisible threat of non-steroidal anti-inflammatory drugs for kidneys," *Frontiers in Pediatric*, vol. 7, 2019.

[12] A. Nessa, "Nonsteroidal anti-inflammatory drugs (NSAIDS) induced acute kidney injury (AKI): patient profile and outcome in Bangladesh armed forces," *JAFMC*, vol. 10, no. 2, pp. 39–43, 2015.

[13] Y. Nechemia-Arbely, D. Barkan, G. Pizov et al., "IL-6/IL-6R axis plays a critical role in acute kidney injury," *Journal of the American Society of Nephrology*, vol. 19, no. 6, pp. 1106–1115, 2008.

[14] J. J. K. I. Rossert, "Drug-induced acute interstitial nephritis," *Kidney International*, vol. 60, no. 2, pp. 804–817, 2005.

[15] D. Wang, S. K. Yang, M. X. Zhao et al., "Low dose of flurbiprofen axetil decrease the rate of acute kidney injury after operation: a retrospective clinical data analysis of 9915 cases," *BMC Nephrology*, vol. 21, no. 1, p. 52, 2020.

[16] P. A. J. N. C. Khwaja, "KDIGO clinical practice guidelines for acute kidney injury," *Nephron. Clinical Practice*, vol. 120, no. 4, pp. c179–c184, 2012.

[17] L. ASJAoim, "A new equation to estimate glomerular filtration rate," *Annals of Internal Medicine*, vol. 150, no. 9, pp. 604–612, 2009.

[18] E. C. Costalonga, "Prostatic surgery associated acute kidney injury," *World Journal of Nephrology*, vol. 3, no. 4, pp. 98–209, 2014.

[19] C. Y. Bilen, A. Şahin, H. Özen, F. T. Aki, Ö. Öge, and S. Kendi, "Nonoliguric renal failure after transurethral resection of prostate," *Journal of Endourology*, vol. 13, no. 10, pp. 751–754, 1999.

[20] D. P. Shipstone, "Irrigating fluids in endoscopic surgery," *BJU International*, vol. 79, no. 5, pp. 669–680, 1997.

[21] G. Orłowska-Kowalik, L. Janicka, and A. J. W. L. Ksiazek, "Acute non-inflammatory renal failure after transurethral electroresection of the prostate combined with irrigation of the bladder with distilled water," *Wiadomości Lekarskie*, vol. 42, no. 9, pp. 608–611, 1989.

[22] R. A. Zager, "Pathogenetic mechanisms in experimental hemoglobinuric acute renal failure," *American Journal of Physiology-Renal Physiology*, vol. 256, no. 3, pp. F446–F455, 1989.

[23] J. V. Bonventre and A. J. K. I. Zuk, "Ischemic acute renal failure: an inflammatory disease?," *Kidney International*, vol. 66, no. 2, pp. 480–485, 2004.

[24] M. Takaku, A. C. da Silva, N. I. Iritsu, P. T. G. Vianna, and Y. M. M. Castiglia, "Effects of a single dose of parecoxib on inflammatory response and ischemic tubular injury caused by hemorrhagic shock in rats," *Pain Research and Treatment*, vol. 2018, Article ID 8375746, 8 pages, 2018.

[25] C. Q. Feitoza, G. M. Gonçalves, P. Semedo et al., "Inhibition of COX 1 and 2 prior to renal ischemia/reperfusion injury decreases the development of fibrosis," *Molecular Medicine*, vol. 14, no. 11-12, pp. 724–730, 2008.

[26] M. Brezis and S. Rosen, "Hypoxia of the renal medulla — its implications for disease," *New England Journal of Medicine*, vol. 332, no. 10, pp. 647–655, 1995.

[27] M. Araujo and W. J. Welch, "Cyclooxygenase 2 inhibition suppresses tubuloglomerular feedback: roles of thromboxane receptors and nitric oxide," *American Journal of Physiology-Renal Physiology*, vol. 296, no. 4, pp. F790–F794, 2009.

[28] A. Miyajima, K. Ito, T. Asano, K. Seta, A. Ueda, and M. Hayakawa, "Does cyclooxygenase-2 inhibitor prevent renal tissue damage in unilateral ureteral obstruction?," *Journal of Urology*, vol. 166, no. 3, pp. 1124–1129, 2001.

[29] H. F. Cheng and R. C. J. H. Harris, "Cyclooxygenases, the kidney, and hypertension," *Hypertension*, vol. 43, no. 3, pp. 525–530, 2004.

Hindawi
Journal of Nanomaterials
Volume 2021, Article ID 6679515, 9 pages
https://doi.org/10.1155/2021/6679515

Research Article

Simultaneous Determination of Methamphetamine and Its Isomer N-Isopropylbenzylamine in Forensic Samples by Using a Modified LC-ESI-MS/MS Method

Yangxu Luo,[1] Juan Du,[1,2] Huadi Xiao,[1] Ling Zheng,[1] Xuncai Chen,[2,3] Ande Ma,[1,2] and Qizhi Luo[2,3]

[1]*Hygiene Detection Center, School of Public Health, Southern Medical University, Guangzhou, China*
[2]*Forensic Science Center, Southern Medical University, Guangzhou, China*
[3]*Department of Forensic Toxicology, School of Forensic Medicine, Southern Medical University, Guangzhou, China*

Correspondence should be addressed to Xuncai Chen; xche3815@smu.edu.cn, Ande Ma; mandmy@126.com, and Qizhi Luo; luoqizhi12@126.com

Received 17 December 2020; Revised 23 December 2020; Accepted 12 January 2021; Published 3 February 2021

Academic Editor: Hassan Karimi-Maleh

Accurate identification and quantification of methamphetamine (MA) and its related substances are essential for the investigation and fair trial of drug offenses. In this study, a modified LC-ESI-MS/MS method for the simultaneous determination of MA and its isomer N-isopropylbenzylamine (N-IBA) in forensic samples was developed and validated. Optimum chromatographic separation of the target analytes was achieved on an Agilent Poroshell 120 SB-C18 column (4.6 × 100 mm, 2.7 μm) at 40°C with isocratic elution at the flow rate of 0.40 mL/min. The mobile phase was acetonitrile and 20 mM ammonium acetate solution containing 0.1% formic acid (80 : 20, *v*/*v*). Positive ESI-MS/MS detection was performed in multiple reaction monitoring (MRM) mode to identify and quantify the target analytes. Method validation showed excellent linearity in the range of 0.51 ng/mL~51 ng/mL for MA and N-IBA. The low limit of detection (LLOD) and low limit of quantification (LLOQ) reached 0.1 ng/mL and 0.3 ng/mL for both analytes. The method showed a satisfactory accuracy with an inter- and intraday-relative error (RE) <20%, and a precision of inter- and intraday relative standard deviation (RSD) less than 15%. The validated method was successfully applied in real forensic samples and resulted in the detection of MA and N-IBA in 8 suspected samples in drug cases that only deemed MA positive using our previous routine screening procedure, which avoided the misidentification of N-IBA as MA.

1. Introduction

Drug abuse has been increasingly becoming one of the most severe social problems all over the world. Among drugs of abuse, methamphetamine (MA) is the second most popular illicit drug worldwide which has been listed as a category I psychotropic substance under strict state control in most countries [1]. According to the United Nations Office on Drugs and Crime (UNODC), MA is one of the most dangerous drugs due to its central nervous excitatory effect, highly addictive, and numerous related disorders [2–4]. MA causes toxicity such as liver, brain neurological, cardiovascular, immune system injury, physical, and mental problems (violence, anxiety, and paranoia) [5–11]. Thus, accurate identification and quantification of MA in the forensic samples is particularly important for investigations and fair trials of drug crimes [12]. However, an isomer of MA, called N-isopropylbenzylamine (N-IBA), has often been used as the adulterant of MA in drug crimes due to their high similarity in structure (Figure 1), which easily resulted in the misidentification of N-IBA as MA in suspected samples [13]. For example, the forensic science laboratory of the United States Drug Enforcement Administration (DEA) reported several cases of counterfeiting MA hydrochloride with N-IBA hydrochloride from 2007 to 2008 [14]. Since 2011, the material identification center of the Ministry of State Security of the People's Republic of China has also reported several drug cases that N-IBA hydrochloride was mixed with MA

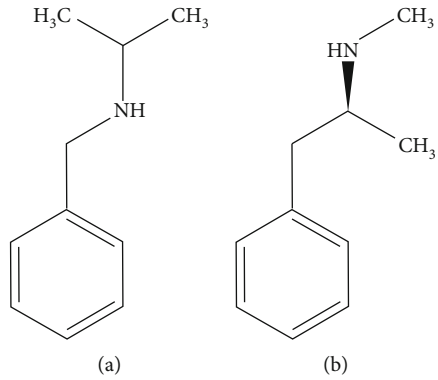

Figure 1: Chemical structure of (a) N-IBA and (b) MA.

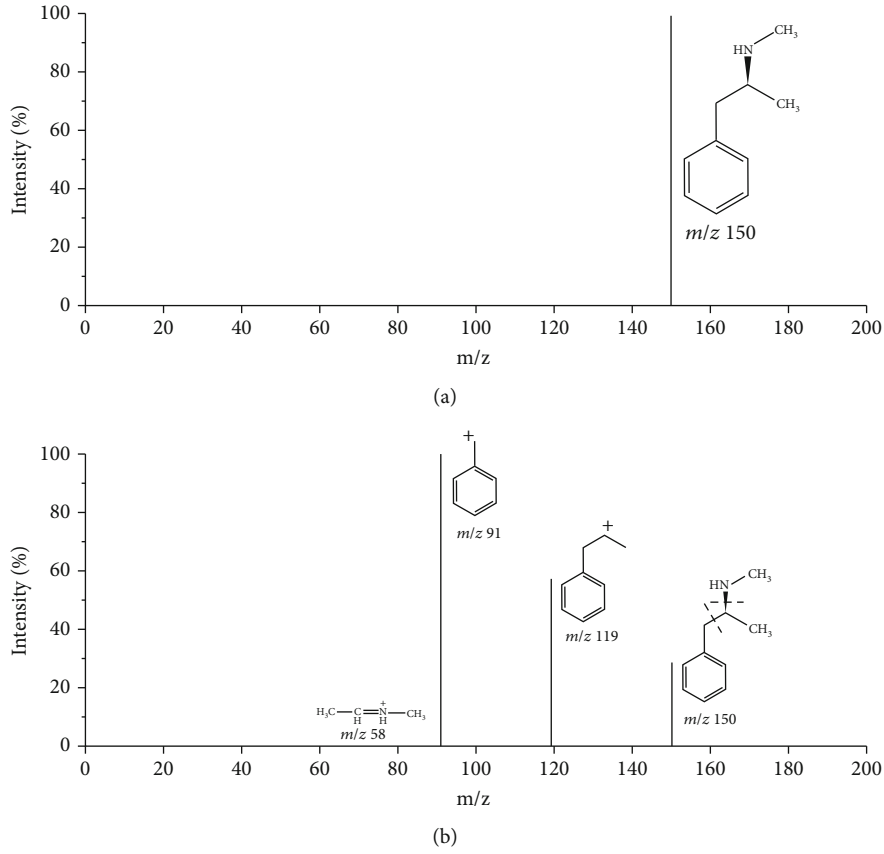

Figure 2: Mass spectra of methamphetamine (MA). (a) Molecular ion spectrum by (a) mass spectrum by ESI-MS (molecular ion $[M + H]^+ = 150$). (b) Product ion spectrum by ESI-MS/MS (precursor ion $[M + H]^+ = 150$, fragment ions = 119/91/58).

hydrochloride in China [14]. It is worth to mention that N-IBA with unknown toxicity is an important organic synthetic raw material commonly used in industrial productions [13, 15], which is not included in the illicit drug category. The misidentification of N-IBA in MA forensic samples may result in false-positive results, which would cause the misleading legal sentence to the suspects [14]. Therefore, it is necessary to establish an effective detection method for the discrimination of MA and I-NBA in suspected drugs.

At present, many researches have mainly focused on the detection of MA [16–23], while the simultaneous determination of MA and its isomer N-IBA in suspected drugs is rarely studied. The commonly used methods including infrared spectroscopy, colloidal gold-based immunoassays, and color tests are not suitable for the discrimination between MA and N-IBA since their poor specificity [24–28]. GC/MS analysis in full scan mode has been used to simultaneously quantify MA and N-IBA in suspected drugs [25, 27, 28]. However, the two compounds were hard to be effectively discriminated by GC/MS when there was a large concentration difference between them. Because the retention times for MA and N-IBA chromatographic separation were very close due to their high similar chemical structure, the compound with high concentration would

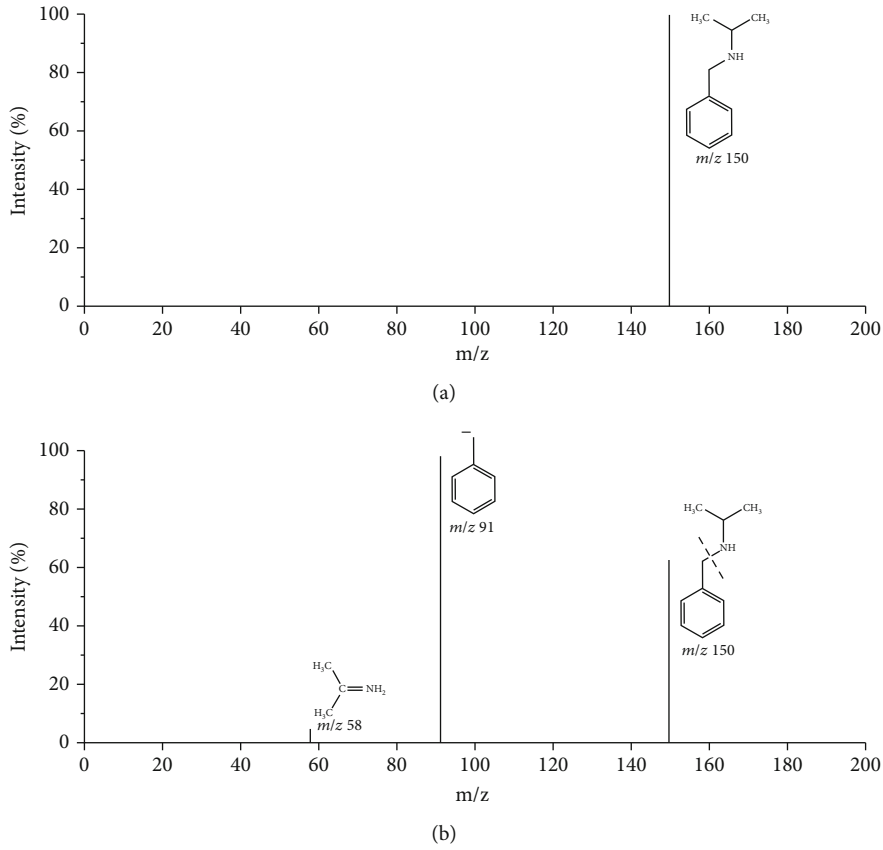

Figure 3: Mass spectra of N-isopropylbenzylamine (N-IBA). (a) Molecular ion spectrum by (a) mass spectrum by ESI-MS (molecular ion $[M + H]^+ = 150$). (b) Product ion spectrum by ESI-MS/MS (precursor ion $[M + H]^+ = 150$, fragment ions = 91/58).

interfere with another one with low concentration as the two compounds yield similar ion fragments for detection [25]. Liquid chromatography-mass spectrometry (LC-MS/MS) has fully proved itself as a powerful tool for detecting and confirming the presence of drugs in complex matrices [29, 30]. In consideration of the highly similar ion fragments between MA and N-IBA, the commonly used LC-MS/MS is insufficient to separate the MA from N-IBA. Hence, to develop a high efficient chromatographic separation technique in LC-MS/MS is highly desirable for the simultaneous determination of MA and its isomer N-IBA.

In this work, a modified LC-ESI-MS/MS method conducted with positive electrospray ionization (ESI) in multiple reaction monitoring (MRM) mode was subsequently developed and validated to discriminate MA and N-IBA in forensic science [24]. Optimum chromatographic separation of the target analytes was achieved on an Agilent Poroshell 120 SB-C_{18} column (4.6 × 100 mm, 2.7 μm) at 40°C with isocratic elution at the flow rate of 0.40 mL/min. The method was successfully applied to determine the MA and N-IBA with satisfactory selectivity, sensitivity, accuracy, and repeatability. In addition, 8 suspected samples in drug cases deemed MA positive were screened by using this new method, and the N-IBA was seized in all samples, illustrating the ubiquity of adulteration of N-IBA to MA.

2. Materials and Methods

2.1. Chemicals and Reagents. MA (purity 98%) was purchased from Merck Sigma-Aldrich (Darmstadt, Germany). N-IBA (purity 98%) was purchased from Energy Chemical (Shanghai, China). Methanol and acetonitrile of HPLC grade were purchased from Merck Millipore (Darmstadt, Germany). Ammonium acetate (purity 99.0%) was purchased from Aladdin Bio-Chem Technology Co., Ltd. (Shanghai, China). Formic acid of HPLC grade was from Tianjin Kemiou Chemical Reagent Co., Ltd. (Tianjin, China). Ultrapure water ($R > 18$ MΩ/cm) was obtained from a Millipore Milli-Q system (Merck Millipore, Darmstadt, Germany).

2.2. Solutions. Individual stock solutions of MA and N-IBA were prepared in methanol at the concentration of 1 mg/mL and stored at −20°C for up to 6 months. Appropriate concentrations of calibrator and QC working solutions were prepared by diluting the stock solutions with methanol. The mixed calibrator solutions were prepared with concentrations of 0.1, 0.2, 0.5, 1.0, 5.0, 10.0, 20.0, and 50.0 ng/mL. The QC samples were prepared in methanol at the low, medium, and high concentrations of 2.0 ng/mL, 10.0 ng/mL, and 20.0 ng/mL. The calibrator solutions, QC solutions were stored at 4°C prior to analysis.

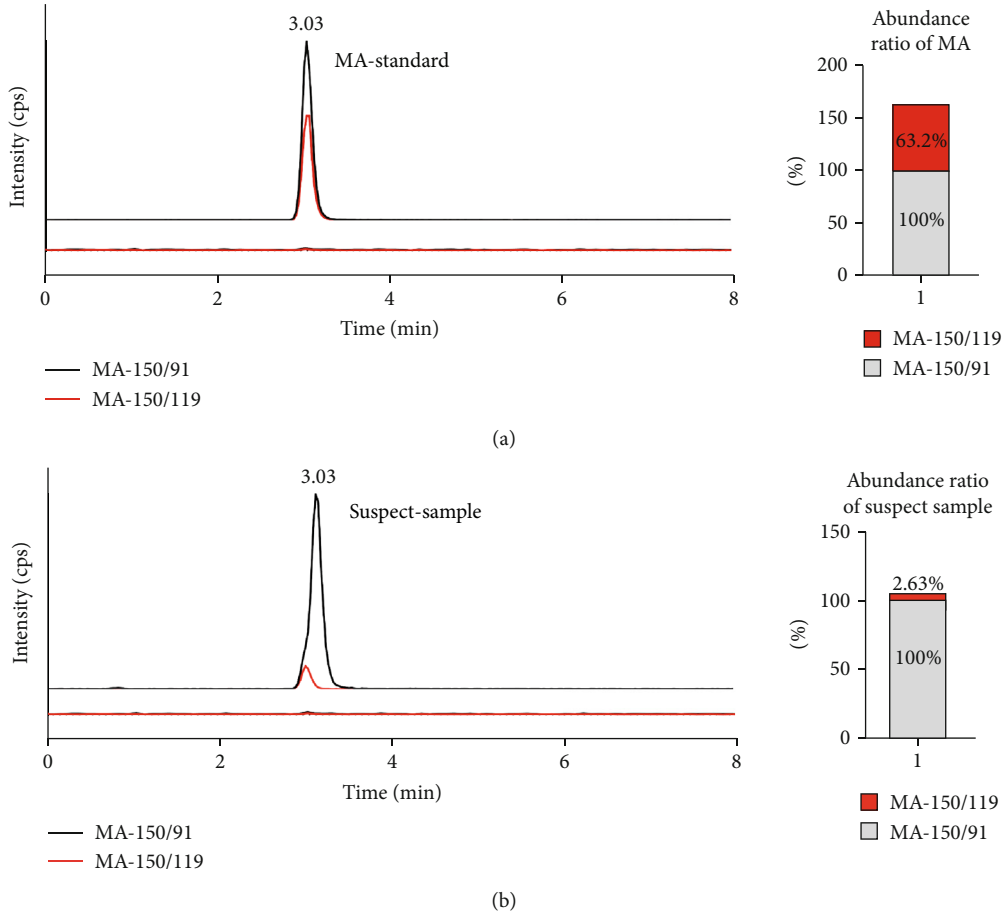

Figure 4: MRM chromatograms for the detection of MA and N-IBA by our routine screening procedures. (a) Upper: detected MA-Standard and the abundance ratio of MA-Standard between *m/z* 150/91and *m/z* 150/119, lower: blank. (b) Upper: detected suspect sample and the abundance ratio of suspect sample between *m/z* 150/91 and *m/z* 150/119, lower: blank.

2.3. Specimen Preparation. The specimens (white crystalline substances) were obtained from suspected cases of drug production and drug trafficking from 2017 to 2018 in Guangdong province, China. After homogenization, 50 mg of forensic crystal samples was accurately weighed, dissolved in methanol, and gradually diluted to a constant concentration of 1 mg/mL, 100 μg/mL, and 20 ng/mL. The sample solutions were then filtered by a 0.22 μm filter before further analysis.

2.4. Instrumentation. Experiments were performed on a Shimadzu HPLC system (Tokyo, Japan) consisting of two LC-20ADvp pumps, a CTO-20ACvp column heater, a SIL-20A autosampler, and a CBM-20A/20Alite controller. The HPLC was interfaced with an AB Sciex API 4000 QTRAP mass spectrometer (Foster City, USA) equipped with an ESI&Turb spray ionization source. All data were acquired and analyzed using the Analyst software (Version 1.5.2, AB Sciex, Foster City, USA).

2.5. LC-ESI-MS/MS Conditions

2.5.1. Routine Screening Procedures. The separation was performed on an RESREK Allure PFPP C_{18} column (2.1 × 100 mm, 5 μm) protected by RESREK Allure PFPP C_{18} column (2.1 × 10 mm, 5 μm) with isocratic elution at 0.40 mL/min, giving a total run time of 13.5 min. The column temperature is the same as the room temperature. The mobile phase consisted of methyl alcohol (eluent A) and 20 mM ammonium acetate solution containing 0.1% formic acid (eluent B) in a volume ratio of 70/30. The autosampler tray temperature was maintained at 15°C, and the injection volume was 20 μL.

The MS conditions were as follows: the ion polarity was positive, the ionspray voltage applied was 5500 V, the source temperature was set at 600°C, and the ion source gas1 (N_2), ion source gas2 (N_2), and curtain gas (N_2) were set at 65 psi, 65 psi, and 15 psi, respectively. The ion pairs of MA are 150/119 and 150/91.

2.5.2. Modified Detection Method. The separation was performed on an Agilent Poroshell 120 SB-C_{18} column (4.6 × 100 mm, 2.7 μm) protected by an Idec Health and Science precolumn (filter assay size: 2 μm) with isocratic elution at 0.40 mL/min, giving a total run time of 6.5 min. The column temperature was 40°C. The mobile phase consisted of acetonitrile (eluent A) and 20 mM ammonium acetate solution containing 0.1% formic acid (eluent B) in a volume ratio of 20/80 [14, 19]. The

autosampler tray temperature was maintained at 15°C, and the injection volume was 10 μL.

MS/MS parameters were optimized with standard solutions of each analyte infused into the ESI source at 10 μL/min via a syringe infusion pump. The MS conditions were as follows: the ion polarity was positive, the ionspray voltage applied was 5500 V, the source temperature was set at 600°C, and the ion source gas1 (N_2), ion source gas2 (N_2), and curtain gas (N_2) were set at 55 psi, 65 psi, and 15 psi, respectively. MRM scans were performed with each analyte utilizing one molecular ion and two most predominant fragments; of the two, the most sensitive transition was used as quantifier ions and the other transition as qualifier ions, the ratios of which are indicative of the analyte of interest. The selected MRM transitions, declustering potentials and collision energies for each analyte are given in Supplementary material Table 1.

2.6. Method Validation. This method was validated according to the CFDA drug analytical method validation guidelines with minor modifications [31]. The validation items include selectivity, the calibration curves and their linearity, LLOD and LLOQ, accuracy, precision, and stability.

2.6.1. Selectivity and Discrimination Capability. Method selectivity was tested by comparing the chromatograms obtained from six blank samples free of MA and N-IBA with those from standard solutions. The extracted ion chromatograms at the retention times of the target analytes were examined for interfering peaks.

The discrimination capability of the method was evaluated by analyzing low, medium, and high concentrations of mixed standard solutions of MA and N-IBA. The extracted ion chromatograms were then inspected for unequivocal identification of the two isomers.

2.6.2. Calibration Curves. The calibration curves were constructed by running six concentration levels of standard solutions ranging from 0.5 ng/mL to 50 ng/mL in three replicates. Determination coefficients (R^2) were determined by applying a weighted ($1/x^2$) least-squares linear regression. Calibrators and triplicate of QC samples at low, medium, and high concentrations were analyzed daily in each set of specimens.

2.6.3. LLOD and LLOQ. LLOD and LLOQ were evaluated using a triplicate of standard solutions at the lowest calibration concentrations of the target analytes. LLOD was defined as the concentration producing a Gaussian-shaped peak eluting within ±2% of mean calibration retention time, a minimum signal to noise (S/N) ratio of 3 : 1; LLOQ was defined as the concentration that met LLOQ criteria and quality control precision and accuracy within ±20% and had a minimum S/N ratio of 10 : 1.

2.6.4. Accuracy and Precision. Intraday precision was evaluated using five replicated of QC solutions at low, medium, and high concentrations (2.0, 10.0, and 20.0 ng/mL, respectively) on a single day, while interday precision was assessed on three separate days. The precision expressed as RSD,

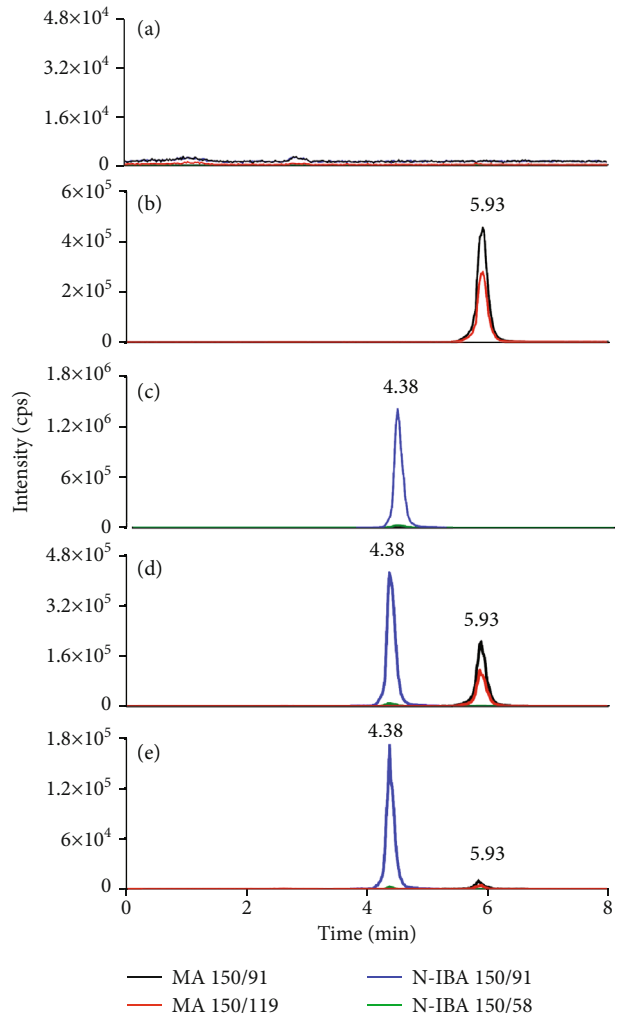

Figure 5: MRM chromatograms by LC-ESI-MS for detection of MA and N-IBA. (a) Blank. (b) Standard of MA. (c) Standard of N-IBA. (d) Mix-standard of MA and N-IBA (N-IBA standard at concentration of 9.14 ng/mL was mixed with MA standard at concentration of 10.27 ng/mL at equal volume ratio). (e) Actual forensic sample, SUM-1.

which was calculated as follows:

$$\text{RSD} = [\text{standard deviation (SD)}/C_{\text{mea}}] \times 100\%. \quad (1)$$

The accuracy was evaluated using triplicate of QC samples solutions at low, medium, and high concentrations; the relative error (RE) was calculated by the mean value of the measured concentrations (C_{mea}) from the theoretical concentration (C_{theo}).

$$\text{RE} = C_{\text{mea}}/C_{\text{theo}} \times 100\%. \quad (2)$$

2.6.5. Stability. Stability of suspected samples, calibrators, and QC samples was tested by reanalyzing them when these samples were kept for three days in an autosampler at 15°C, one week in room temperature at 20°C as well as one month in the freezer at 4°C. Stability was expressed as the relative

Table 1: Linearity, LLOD, and LLOQ for determining MA and N-IBA.

Compounds	LLOD (ng/mL)	LLOQ (ng/mL)	Linear range (ng/mL)	Equation	R^2
MA	0.1	0.3	0.51~51.30	$y = 3.24e^4x + 9.39e^4$	0.9959
N-IBA	0.1	0.3	0.51~51.20	$y = 8.49e^4x + 1.25e^4$	0.9973

Table 2: The accuracy and precision for quantification of N-IBA and MA.

Compounds	Nominal concentration (ng/mL)	Intraday ($n = 5$)		Interday ($n = 15$)	
		Accuracy (RE, %)	Precision (RSD, %)	Accuracy (RE, %)	Precision (RSD, %)
MA	2.05	110.1	5.4	121.9	10.0
	10.27	101.8	3.5	101.0	3.6
	20.53	101.1	4.0	110.0	9.9
N-IBA	1.83	96.2	5.1	110.7	11.6
	9.14	98.5	1.7	100.1	4.3
	18.28	97.2	2.7	103.6	6.4

average deviation (RAD) of the measured concentrations in different time.

3. Results

3.1. Development of Confirmatory Method. According to the structural data, N-IBA is an isomer of MA, normally exhibiting similar patterns of collision-induced dissociation (CID) and retention times with MA. Thus, the simultaneous identification for N-IBA and MA was easily confused.

The mass spectra for MA and N-IBA were obtained in full-scan MS and MS/MS mode. The predominant fragments of MA (Figure 2) were *m/z* 119 $[M\text{-}CH_4N]^+$, *m/z* 91 $[M\text{-}C_3H_8N]^+$, and *m/z* 58 $[M\text{-}C_7H_7]^+$, while the predominant fragments of N-IBA (Figure 3) were *m/z* 91 $[M\text{-}C_3H_8N]^+$ and *m/z* 58 $[M\text{-}C_7H_7]^+$. There are two overlapped fragments (*m/z* 91 $[M\text{-}C_3H_8N]^+$ and *m/z* 58 $[M\text{-}C_7H_7]^+$) between MA and N-IBA, besides the specific fragments at *m/z* 119 $[M\text{-}CH_4N]^+$ for MA. Thus, it is difficult to discriminate whether the N-IBA is adulterated in the MA forensic samples by mass spectra directly, especially when the quantity of the adulterated N-IBA is low. Based on our initial analysis of several suspected samples following our routine screening procedures for drug cases, three predominant fragments of MA were observed in the chromatogram of MA, but the unobservable difference was found in the abundance ratio between *m/z* 150/91 and *m/z* 150/119, comparing with the MA standard solution. As the analysis result of MA standard solution shown, the predominant fragments of MA were *m/z* 91, *m/z* 119, and *m/z* 58, and the abundance ratio between *m/z* 150/91and *m/z* 150/119 was approximately 1 : 0.63 (Show as Figure 4(a), supplementary material Table 2). The suspected samples showed the same fragments but the higher abundance ratio (1 : 0.026) (show as Figure 4(b)). To see this, we speculate that the existence of N-IBA in the suspected samples interfered the determination of MA. In order to simultaneously determine the N-IBA and MA in the forensic samples, a chromatographical separation was needed to well separate them, before testing them by mass spectra. Several different columns, mobile phases, and gradients were studied, and the isocratic separation using acetonitrile and 20 mM ammonium acetate solution containing 0.1% formic acid (20 : 80, *v/v*) as mobile phase on an Agilent Poroshell 120 SB-C_{18} column (4.6 × 100 mm, 2.7 μm) showed the best separation effect. Then, the MRM transition *m/z* 150/91 was selected as the quantitative ion pair for MA and N-IBA, and the predominant fragment *m/z* 119 of MA and *m/z* 58 of N-IBA was also utilized for the discrimination between MA and N-IBA. Compared to the reported GC/MS method, the excellent chromatographical separation and a minimum of two transitions in the MS/MS spectra for each analyte provide direct evidence to identify MA and N-IBA. The method was subsequently evaluated in compliance with the CFDA drug analytical method validation guidelines with minor modifications.

Table 3: Recoveries and RSDs of MA and N-IBA spiked in a suspected drug sample.

Compound	Background (ng/mL)	Sample Add (ng/mL)	Recovery (%)	RSD (%)
MA	0.48	2.05	87.8	2.8
		20.50	112.6	2.1
		51.30	112.1	1.9
N-IBA	5.28	1.83	96.7	0.5
		18.30	105.1	3.4
		51.20	108.1	0.9

3.2. Method Validation

3.2.1. Selectivity and Discrimination Capability. Selectivity of the method was examined by comparing chromatograms of individual standard solutions with blank sample. As Figure 5(a) showed that no interfering peaks were observed in the chromatogram of blank sample at the retention times of the target analytes.

The capability of the method to discriminate between MA and N-IBA was evaluated by analyzing individual standard

Table 4: The stability of MA and N-IBA under different conditions ($n = 3$).

Conditions	Samples	Compounds	Day 0 concentration (mean ± SD, ng/mL)	Measured concentration (mean ± SD, ng/mL)	RAD (%)
Autosampler for three days (15°C)	Suspect sample	MA	1.08 ± 0.05	1.15 ± 0.01	3.0
		N-IBA	15.27 ± 0.12	15.13 ± 0.15	0.4
	Mixed standard solution	MA	10.43 ± 0.23	10.23 ± 0.06	1.0
		N-IBA	9.39 ± 0.18	9.26 ± 0.20	0.7
Room temperature for one week (20°C)	Suspect sample	MA	1.45 ± 0.08	1.45 ± 0.05	0.1
		N-IBA	15.33 ± 0.12	15.00 ± 0.10	1.1
	Mixed standard solution	MA	10.53 ± 0.32	10.21 ± 0.24	1.5
		N-IBA	10.2 ± 0.20	9.38 ± 0.18	4.2
Freezer for 30 days (4°C)	Suspect sample	MA	1.16 ± 0.04	1.10 ± 0.10	2.4
		N-IBA	15.93 + 0.21	15.33 ± 0.15	1.9
	Mixed standard solution	MA	11.23 ± 0.125	10.43 ± 0.31	3.7
		N-IBA	9.91 ± 0.14	9.15 ± 0.06	4.0

solutions and mixed standard solutions at low (0.2 ng/mL), medium (20 ng/mL), and high (100 ng/mL). This range was chosen based on the LLODs and LLOQs. As Figures 5(b) and 5(c) shown, the retention times of MA and N-IBA were approximate 5.86 and 4.36 min, respectively. We also observed single peaks for each target analyte in the chromatograms of mixed standard solutions and suspected samples (Figures 5(d) and 5(e)), indicating the method with highly satisfactory capability of discrimination. Deserved to be mentioned, the routine screening procedure we had performed for psychotropics and narcotics screening more than a few thousands of samples cannot chromatographically separate MA and N-IBA; both compounds have the same retention time, which may result in misidentification. The routine screening samples that had been deemed MA positive were additionally tested, and some samples were ultimately confirmed as N-IBA or mixture of MA and N-IBA.

3.2.2. Linearity, LLOD, and LLOQ. Linearity was investigated by calculating the coefficient of determination (R^2) of calibration curve, and along with calibration curve equations, linear ranges, LLOD, and LLOQ of each target analyte are listed in Table 1. The calibration curves are in good linearity in the concentrations of 0.51~51.30 ng/mL for MA and 0.51~51.20 ng/mL for N-IBA with an R^2 above 0.99. The LLODs and LLOQs were 0.1 ng/mL and 0.3 ng/mL for MA and N-IBA.

3.2.3. Accuracy and Precision. Accuracy and precision were evaluated with five replicates of QC samples at low, medium, and high concentrations for each target analyte. The results of accuracy and precision of intraday ($n = 5$) and interday ($n = 5$) are shown in Table 2. The intra- and interday accuracy ranged from 96.2% to 110.1% and 100.1% to 121.9%. The intra- and interday precision ranged from 1.7% to 5.4% and from 3.6% to 11.6%. These results demonstrated that the modified LC-ESI-MS/MS method was reproducible and reliable for simultaneous determination of MA and N-IBA in forensic samples.

Table 5: Contents of MA and N-IBA in the suspected samples.

Sample ID	Quantity weighed (mg)	Contents of N-IBA (%)	Contents of MA (%)
SMU-1	54.7	80.4	7.31
SMU-2	54.0	74.5	0.21
SMU-3	54.7	75.4	Not detected
SMU-4	54.6	80.4	Not detected
SMU-5	55.0	0.5	Not detected
SMU-6	62.0	87.2	1.45
SMU-7	70.1	77.3	1.80
SMU-8	55.0	5.2	0.55

3.2.4. Recovery. Recovery was evaluated by adding low, medium, and high concentration levels of mixed standard solutions into known concentration samples. As shown in Table 3, the recovery value was in the range of 87.8-112.6%, and the RSD value was less than 10%.

3.2.5. Stability. Suspected samples and mixed standard samples were used to evaluate the stability of MA and N-IBA under different conditions. As shown in Table 4, the deviation values between two measured concentrations were less than 5% of RAD, indicating that MA and N-IBA were stable for three days in an autosampler at 15°C, for one week in room temperature at 20°C and one month in the freezer at 4°C. Matrix effect, recovery, and stability were within the acceptable range, indicating that the LC-MS/MS method was reliable.

3.3. Application to Real Forensic Drug Samples. During 2017-2018, 8 suspected samples were screened using our routine screening procedure and deemed MA positive, but the 8

suspected samples showed a quite unusual abundance ratio between m/z 150/91 and m/z 150/119 (show as Figure 4). Subsequently, the suspected samples were tested with the modified LC-ESI-MS/MS method, and the adulteration of N-IBA in MA forensic samples was confirmed (Table 5). The main components of these samples were N-IBA and a small amount of MA was found in some samples. Afterwards, all suspected samples in drug cases deemed MA positive were routinely analyzed by the modified LC-ESI-MS/MS method to prevent misidentification of MA and N-IBA.

4. Conclusions

According to the 2018 China drug report [32], MA is the most popular and easily accessible substances for drug addicts in China. In China, those suspected of producing, manufacturing, transporting, and possessing MA will face tough sentences. As we know, N-IBA is the positional isomer of MA, and both isomers have the same retention times using the previous routine screening procedure, which means that the identification of both isomers was easily confused. Since N-IBA is legal to use, misidentification of N-IBA for MA may result in serious consequences.

In the present work, a highly efficient modified LC-ESI-MS/MS method was developed and validated for the simultaneous determination of MA and N-IBA in forensic samples. The method exhibited excellent selectivity, linearity, accuracy, precision, and stability with a significantly lower LLOD and LLOQ than those in previous studies. When the method was applied to identify MA and N-IBA in several suspected samples in forensic cases, the MA and N-IBA were well separated and quantified. This work could offer new improvements for the forensic routine analysis of MA and N-IBA in suspected drug samples for clinical and forensic laboratories.

Data Availability

All data generated or analyzed during this study are included within the article.

Conflicts of Interest

The authors declare that they have no conflicts of interest.

Authors' Contributions

Yangxu Luo performed the conceptualization; Yangxu Luo, Juan Du, and Xuncai Chen performed the data curation; Yangxu Luo and Qizhi Luo performed the formal analysis; Juan Du and Ande Ma performed the investigation; Juan Du, Huadi Xiao, and Ling Zheng performed the methodology; Ande Ma and Qizhi Luo gather the resources; Ande Ma performed the validation; Yangxu Luo performed the visualization; Yangxu Luo wrote the original draft; Xuncai Chen and Qizhi Luo wrote, reviewed, and edited the manuscript. Yangxu Luo and Juan Du contributed equally to this work.

Acknowledgments

This work was supported by the Southern Medical University (grant no: G620522046)

Supplementary Materials

The following are available online at http://www.mdpi.com/xxx/s1. Table S1: modified detection method of multiple reaction monitoring parameters for determining MA and N-IBA. Table S2: abundance ratio of MA-Standard and suspect sample. *(Supplementary Materials)*

References

[1] P. Boshears, M. Boeri, and L. Harbry, "Addiction and sociality: perspectives from methamphetamine users in suburban USA," *Addiction Research & Theory*, vol. 19, no. 4, pp. 289–301, 2011.

[2] J. Ma, X. J. Sun, R. J. Wang et al., "Profile of psychiatric symptoms in methamphetamine users in China: greater risk of psychiatric symptoms with a longer duration of use," *Psychiatry Research*, vol. 262, pp. 184–192, 2018.

[3] C. McGregor, M. Srisurapanont, J. Jittiwutikarn, S. Laobhripatr, T. Wongtan, and J. M. White, "The nature, time course and severity of methamphetamine withdrawal," *Addiction*, vol. 100, no. 9, pp. 1320–1329, 2005.

[4] S. R. Radfar and R. A. Rawson, "Current research on methamphetamine: epidemiology, medical and psychiatric effects, treatment, and harm reduction efforts," *Addiction and Health*, vol. 6, no. 3-4, pp. 146–154, 2014.

[5] Y. Cheng, C. K. Tung, A. K. K. Chung et al., "Screening of pulmonary hypertension in methamphetamine abusers (SOPHMA): rationale and design of a multicentre, cross-sectional study," *BMJ Open*, vol. 9, no. 8, article e027193, 2019.

[6] L. S. Seiden and K. E. Sabol, "Methamphetamine and methylenedioxymethamphetamine neurotoxicity: possible mechanisms of cell destruction," *NIDA Research Monograph*, vol. 163, pp. 251–276, 1996.

[7] L. Sun, Y. Lian, J. Ding et al., "The role of chaperone-mediated autophagy in neurotoxicity induced by alpha-synuclein after methamphetamine exposure," *Brain and Behavior: A Cognitive Neuroscience Perspective*, vol. 9, article e01352, 2019.

[8] A. Urbina and K. Jones, "Crystal methamphetamine, its analogues, and HIV infection: medical and psychiatric aspects of a new epidemic," *Clinical Infectious Diseases*, vol. 38, no. 6, pp. 890–894, 2004.

[9] R. McKetin, A. Voce, R. Burns, and M. Shanahan, "Health-related quality of life among people who use methamphetamine," *Drug and Alcohol Review*, vol. 38, no. 5, pp. 503–509, 2019.

[10] D. C. Vidot, J. A. Manuzak, N. R. Klatt et al., "Brief report: hazardous cannabis use and monocyte activation among methamphetamine users with treated HIV infection," *JAIDS Journal of Acquired Immune Deficiency Syndromes*, vol. 81, no. 3, pp. 361–364, 2019.

[11] K. Merchant, C. Schammel, and J. Fulcher, "Acute methamphetamine-induced hepatic and pancreatic ischemia," *The American Journal of Forensic Medicine and Pathology*, vol. 40, no. 3, pp. 285–288, 2019.

[12] C. Dobkin and N. Nicosia, "The war on drugs: methamphetamine, public health, and crime," *The American Economic Review*, vol. 99, no. 1, pp. 324–349, 2009.

[13] D. Poppendieck, G. Morrison, and R. Corsi, "Desorption of a methamphetamine surrogate from wallboard under remediation conditions," *Atmospheric Environment*, vol. 106, pp. 477–484, 2015.

[14] J. Li and H. Liao, "Identification of N-isopropyl-benzylamine in vitro and urine," *Forensic Science and Technology*, vol. 44, pp. 30–33, 2019.

[15] W. L. Xiong, S. Q. Zhang, C. M. Ji, L. Li, Z. H. Sun, and C. Song, "Temperature-induced reversible isostructural phase transition in _N-isopropylbenzylammonium trifluoromethanesulfonate," *Inorganic Chemistry Communications*, vol. 41, pp. 79–83, 2014.

[16] S. B. Sachs and F. Woo, "A detailed mechanistic fragmentation analysis of methamphetamine and select regioisomers by GC/MS," *Journal of Forensic Sciences*, vol. 52, no. 2, pp. 308–319, 2007.

[17] A. Oztunc, A. Onal, and S. E. Toker, "Detection of methamphetamine, methylenedioxymethamphetamine, and 3,4-methylenedioxy-N-ethylamphetamine in spiked plasma by HPLC and TLC," *Journal of AOAC International*, vol. 93, pp. 556–561, 2007.

[18] H. T. Andas, A. Enger, A. M. Oiestad et al., "Extended detection of amphetamine and methamphetamine in oral fluid," *Therapeutic Drug Monitoring*, vol. 38, no. 1, pp. 114–119, 2016.

[19] Y. Zhang, L. Li, Q. Wang et al., "Simultaneous determination of metabolic and elemental markers in methamphetamine-induced hepatic injury to rats using LC-MS/MS and ICP-MS," *Analytical and Bioanalytical Chemistry*, vol. 411, no. 15, pp. 3361–3372, 2019.

[20] M. Di Rago, M. Chu, L. N. Rodda, E. Jenkins, A. Kotsos, and D. Gerostamoulos, "Ultra-rapid targeted analysis of 40 drugs of abuse in oral fluid by LC-MS/MS using carbon-13 isotopes of methamphetamine and MDMA to reduce detector saturation," *Analytical and Bioanalytical Chemistry*, vol. 48, pp. 3737–3749, 2016.

[21] T. Wang, B. Shen, Y. Shi, P. Xiang, and Z. Yu, "Chiral separation and determination of R/S-methamphetamine and its metabolite R/S-amphetamine in urine using LC-MS/MS," *Forensic Science International*, vol. 246, pp. 72–78, 2015.

[22] N. Nuntawong, P. Eiamchai, W. Somrang et al., "Detection of methamphetamine ∗∗/∗∗ amphetamine in human urine based on surface ∗∗ − ∗∗ enhanced Raman spectroscopy and acidulation treatments," *Sensors and Actuators B: Chemical*, vol. 239, pp. 139–146, 2017.

[23] H. Segawa, Y. T. Iwata, T. Yamamuro et al., "Simultaneous chiral impurity analysis of methamphetamine and its precursors by supercritical fluid chromatography–tandem mass spectrometry," *Forensic Toxicology*, vol. 37, no. 1, pp. 145–153, 2019.

[24] Q. Tan, Z. Zhang, and H. Bai, "Determination of N-isopropylaniline in workplace air by high-performance liquid chromatography," *Zhonghua lao dong wei sheng zhi ye bing za zhi = Zhonghua laodong weisheng zhiyebing zazhi = Chinese journal of industrial hygiene and occupational diseases*, vol. 33, no. 4, pp. 294–296, 2015.

[25] J. Xuan, X. Pan, X. Liu, H. Yan, and Y. Zhang, "Gas chromatography for determination of N-isopropylaniline in workplace atmosphere," *Zhonghua Lao Dong Wei Sheng Zhi Ye Bing Za Zhi*, vol. 33, no. 2, pp. 143–145, 2015.

[26] R. M. Correia, E. Domingos, F. Tosato et al., "Portable near infrared spectroscopy applied to abuse drugs and medicine analyses," *Analytical Methods*, vol. 10, no. 6, pp. 593–603, 2018.

[27] K. Sugie, D. Kurakami, M. Akutsu, and K. Saito, "Rapid detection of tert-butoxycarbonyl-methamphetamine by direct analysis in real time time-of-flight mass spectrometry," *Forensic Toxicology*, vol. 36, no. 2, pp. 261–269, 2018.

[28] J. Welter, M. R. Meyer, E. Wolf, W. Weinmann, P. Kavanagh, and H. H. Maurer, "2-methiopropamine, a thiophene analogue of methamphetamine: studies on its metabolism and detectability in the rat and human using GC-MS and LC-(HR)-MS techniques," *Analytical and Bioanalytical Chemistry*, vol. 405, no. 10, pp. 3125–3135, 2013.

[29] A. Ptak, A. El Tahchy, F. Dupire et al., "LCMS and GCMS for the screening of alkaloids in natural and in vitro extracts of Leucojum aestivum," *Journal of Natural Products*, vol. 72, no. 1, pp. 142–147, 2009.

[30] T. K. Sinha, R. Maiti, B. Adhikari, and S. K. Ray, "Volatile aroma sensing performance of high quality pristine graphene, obtained via a facile exfoliation technique," *Materials Today: Proceedings*, vol. 5, no. 3, pp. 9888–9891, 2018.

[31] China Food and Drug Administration (CFDA), "Drug analytical method validation guidelines," 2015, http://samr.cfda.gov.cn/directory/web/WS01/images/u6Rp9KpzuWysGv9jWxrfWzva3vbeo0enWpLy8yvXWuLW81K3U8i5wZGY=.pdf.

[32] The Ministry of Public Security of the People's Republic of China, "Report on China's drug situation 2018," 2018, http://www.mps.gov.cn/n6557558/c6535096/content.html.

Hindawi
Journal of Nanomaterials
Volume 2021, Article ID 6685355, 9 pages
https://doi.org/10.1155/2021/6685355

Research Article

Controllable Architecture of Mesoporous Double-Nanoshell SiO_2/TiO_2 Hollow Tube Based on Layer by Layer Method

Zhenzhong Chen,[1] Jia Li,[2] Zheng Zhang,[2] Jun-fa Liang,[3] Qizhi Luo,[2] and Xuncai Chen[2]

[1]*School of Mechanical Engineering, Sungkyunkwan University, Suwon 16419, Republic of Korea*
[2]*School of Forensic Medicine, Southern Medical University, Guangzhou, Guangdong 510515, China*
[3]*Guangzhou Institute of Food Inspection, Guangzhou, Guangdong 511405, China*

Correspondence should be addressed to Qizhi Luo; luoqizhi12@126.com and Xuncai Chen; xche3815@smu.edu.cn

Received 16 December 2020; Revised 24 December 2020; Accepted 13 January 2021; Published 29 January 2021

Academic Editor: Wenjie Liu

Double-shell tubular on-dimensional structure can be fabricated through a layer by layer method, in which the core template was removed to create the tubular shape. In this paper, we report, for the first time, the double nanoshell SiO_2/TiO_2 hollow tubes prepared through a layer-by-layer deposition method involving the sol-gel process for the SiO_2 and TiO_2 generation. During TEOS and TEOT hydrolysis/condensation for the SiO_2 and TiO_2 shell layer formation, cetyltrimethylammonium bromide (CTAB) is adopted both as the structure-directing template and as the mesopore-channel template distributing around the shell. The obtained double-nanoshell hollow tubes illustrate a large surface area and high pore volume. Also, mesoporous double-nanoshell SiO_2/TiO_2 hollow tubes have the inner and outer shell thickness of about 80 nm and 120 nm, respectively. Plus, the shell thickness of SiO_2 and TiO_2 is controllable depending on the used concentration of TEOS and TEOT during their sol-gel process. Therefore, the technique for the preparation of SiO_2/TiO_2 mesoporous double-nanoshell hollow tubes could provide new insights into the construction of mesoporous double-shell and hollow structure for other multicomponent and hierarchical hybrid systems.

1. Introduction

Hollow-structured mesoporous materials with unique features of high surface area, high permeability, low density, confined inner cavity, and optical properties have been of great interest and received much research, which makes them a promising application in drug delivery systems [1–3], chemical and catalysts [4–10], biological sensors [11–17], and solar cells [18–20]. For example, the inner cavity of the hollow structure is very essential for drug delivery by offering a large volume transportation for DNA, drugs, and cosmetics [21, 22]. In addition, the inner- and outer-shell surface provides more active sites; when contacting with reactant molecules, the hollow-structured materials would display high sensor and catalytic activities [23–26]. Also, the hollow-structured materials enable to enhance the light-scattering effect through adjusting the refractive indices of the empty inner cavity and solid shell [19, 27]. Even with these advantages of hollow-structured material, the design of an optimized structure based on the hollow-structure to further enhance their performance for specific application fields remains a challenge.

To improve the advantages of the hollow structure, multishell hollow-structured materials have recently been considered to be a promising structure owning to their unique properties, such as large surface area, multiple components, and outstanding light-scattering effect [28–31]. The light scattering was enhanced through repeated reflection and scattering events between the inner and outer shells in the multishell structure. Furthermore, the multishell structure has a larger active surface area when comparing with a single shell one, which is because of the increasing surface area by the additional inner shells. As a result, the fabrication of multishell hollow-structured materials with enhanced performance in various applications has been widely studied. For example, a double-shell $LiMn_2O_4$ hollow sphere was

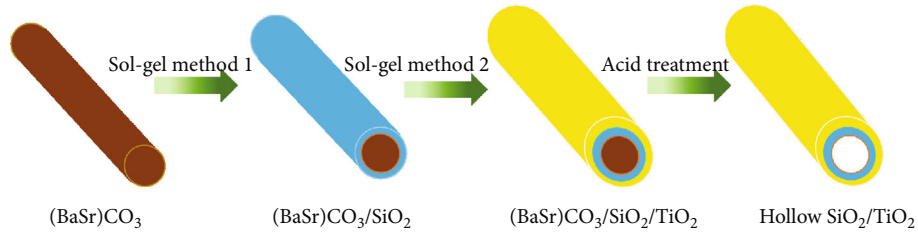

Scheme 1: Schematic representation of the synthesis of mesoporous double-nanoshell SiO_2/TiO_2 hollow tube.

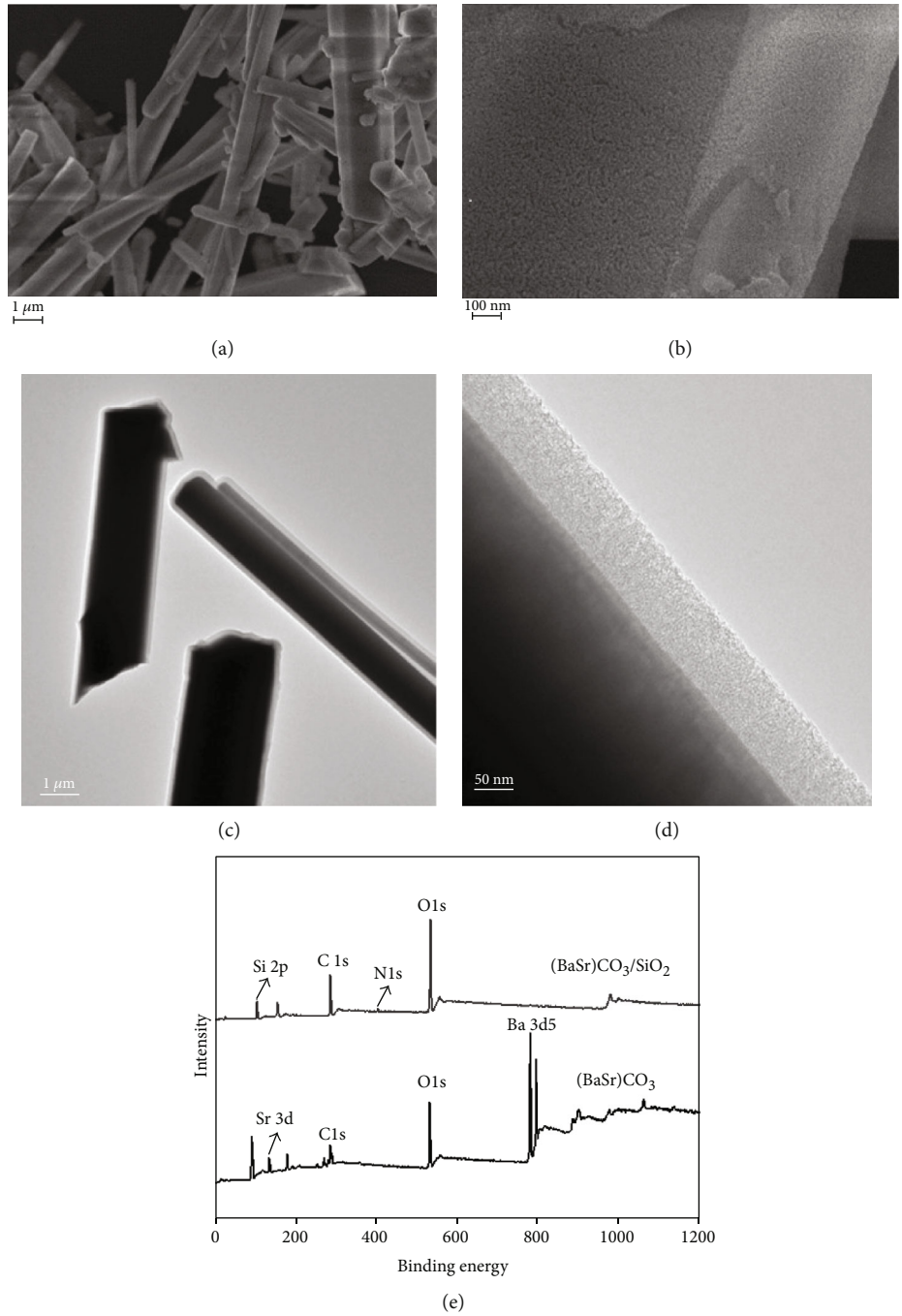

Figure 1: (a) FE-SEM images of $(BaSr)CO_3/SiO_2$ core@shell rods and (b) high resolution of $(BaSr)CO_3/SiO_2$ core@shell rod surface. (c) FE-TEM image of $(BaSr)CO_3/SiO_2$ core@shell rods, and (d) FE-TEM image of the interface of $(BaSr)CO_3/SiO_2$ core@shell rod. (e) XPS spectra of $(BaSr)CO_3$ and $(BaSr)CO_3/SiO_2$ core@shell rods.

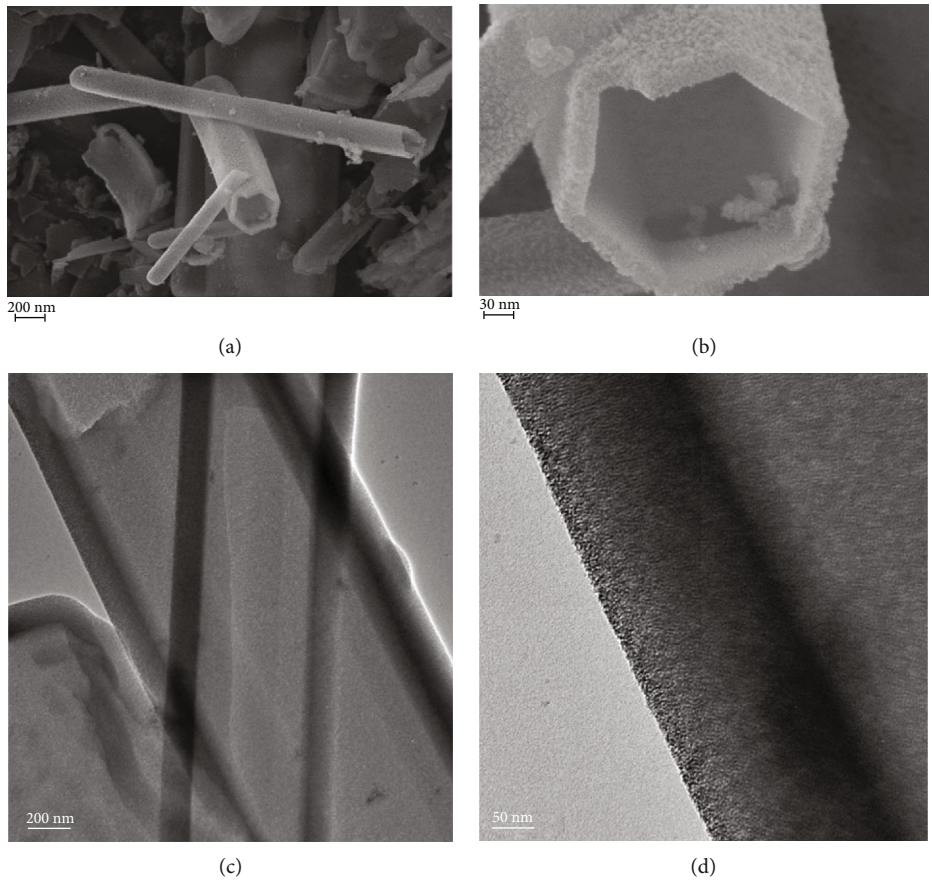

Figure 2: (a) FE-SEM images of SiO_2 hollow tube and (b) high resolution of hollow tube. (c) FE-TEM image of the hollow tube, and (d) FE-TEM image of the interface of hollow tube.

fabricated by using a hydrothermal synthesis method to optimize the performance of lithium-ion batteries [32]. With the double-shell configuration, the battery showed improved performance, which was ascribed to the larger contact area between the electrolyte and electrode generated by the gap and hollow interior between the shells. In addition, multishell hollow spheres of microscale ZnO were prepared via the hydrothermal method by Zhang et al., which presented extraordinary sensitivity for the detection of toluene [33]. Furthermore, the double-shell TiO_2 hollow spheres were prepared via the hydrothermal method by Wu et al., exhibiting a reinforced light-scattering ability in the application of dye-sensitized solar cell (DSSC) [34]. However, hydrothermal reactions using an autoclave were mainly adopted to fabricate multishell hollow structures in the previous approach, which easily resulted in the size uncontrollable and particle aggregation inevitable because of high reaction temperature and high pressure involved. Therefore, methods for synthesizing particles with multishell hollow structure at the nanoscale were in growing demand.

Recently, layer-by-layer (LBL) assembly has already been proved to be a simple, convenient, and controllable method for the design and fabrication of core-shell/core-double-shell particles with tailored chemical composition and controllable architecture on varied substrate surfaces [35–41]. Xing et al. synthesized stable colloidal gold-collagen core-shell nanoconjugates with improved mechanical properties by using the LBL assembly method [42]. In addition, Liao and coworkers the unique TiO_2-C/MnO_2 core-double-shell nanowires using as anode materials for lithium-ion batteries was prepared by layer-by-layer deposition approach [43]. It is not hard to imagine that the core-double-shell particle could be converted to a double-shell hollow particle, when its core was removed. Thus, the layer-by-layer assembly method was supposed to be an applicative approach to fabricate multishell hollow particles.

Herein, we report the synthesis of SiO_2/TiO_2 mesoporous double-shell hollow tubes from $(BaSr)CO_3/SiO_2/TiO_2$ core-double-nanoshell rods based on the layer-by-layer method. It should be mentioned that the hybrid SiO_2/TiO_2 particles have been proved to be a versatile material for various application, such as self-cleaning and antireflective coatings, electrorheological fluids, and photocatalysts [44–54]. In this work, the SiO_2/TiO_2 double-shell hollow tubes was prepared via selectively removing the core material from the $(BaSr)CO_3/SiO_2/TiO_2$ core-double-shell rods. In addition, the thickness of SiO_2 and TiO_2 shell can be easily controlled by regulating the concentration of tetraethyl orthosilicate (TEOS) and tetraethyl titanate (TEOT). Lastly, the formation mechanism for the double-shell SiO_2/TiO_2 hollow tubes was also studied.

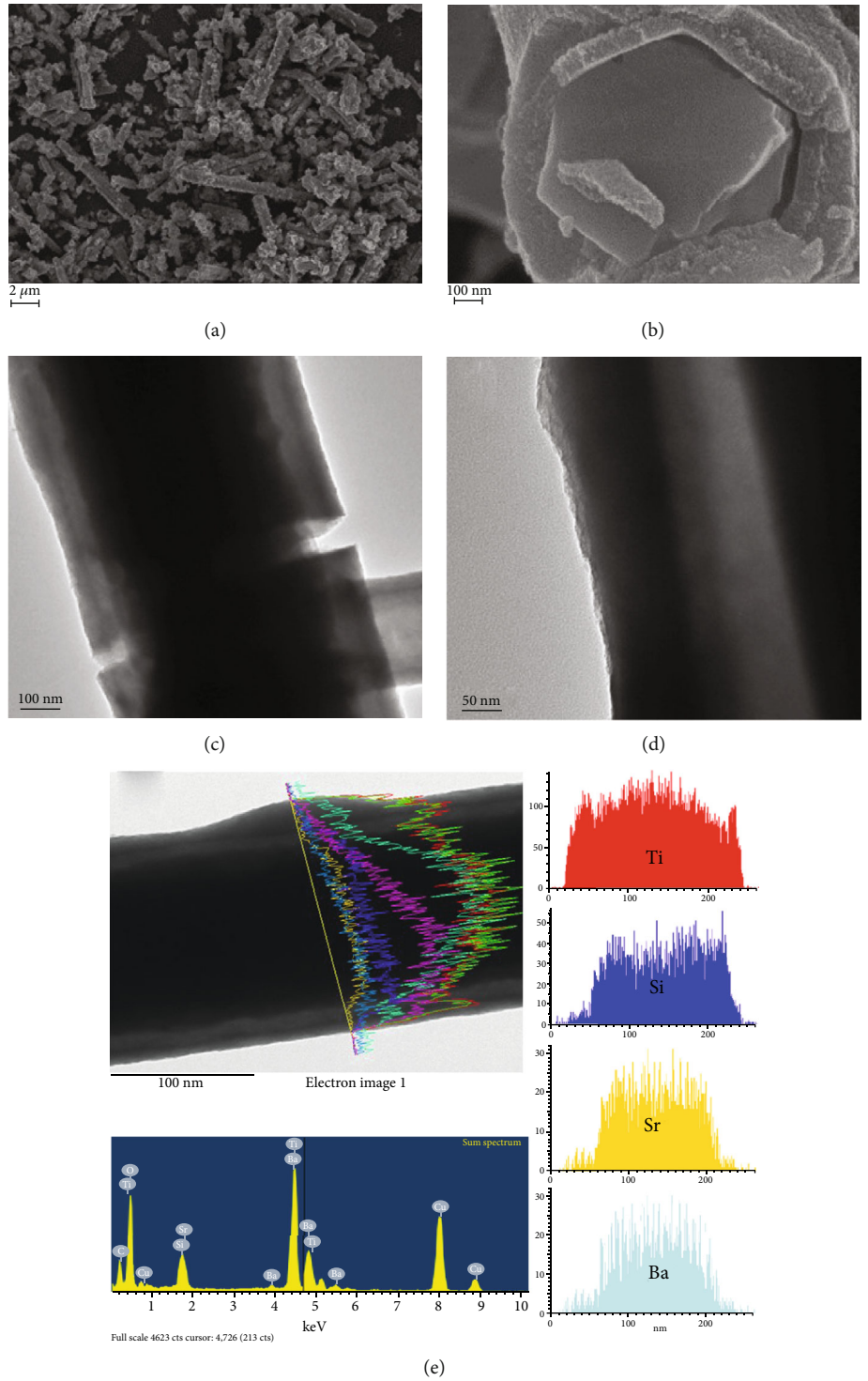

FIGURE 3: (a) FE-SEM images of $(BaSr)CO_3/SiO_2/TiO_2$ core@ double-shell rods and (b) high resolution of cross-section view of $(BaSr)CO_3/SiO_2/TiO_2$ core@ double-shell rods. (c) FE-TEM image of $(BaSr)CO_3/SiO_2/TiO_2$ core@ double-shell rods, and (d) FE-TEM image of interface of $(BaSr)CO_3/SiO_2/TiO_2$ core@ double-shell rods. (e) EDS line scanning analysis of Ba, Sr, Si, and Ti in $(BaSr)CO_3/SiO_2/TiO_2$ core@ double-shell rod.

2. Experimental Section

2.1. Synthesis of SiO_2 Hollow Tubes. Firstly, $(BaSr)CO_3$ was prepared by our previously reported coprecipitation method; the details can be seen in literatures [52–54]. Subsequently, 1.0 g $(BaSr)CO_3$ white powders were dispersed in 40 ml of water and then added 2 ml of aqueous ammonia solution (25~28 wt%), 60 ml of ethanol, and 1.0 g of CTAB. Then,

100 ml of TEOS solution (6×10^{-3} ml-TEOS/ml-H_2O) was slowly fed into the above suspension at a flow rate of 0.2 ml/min under rigorous agitation at 30°C. After complete feeding, the product suspension was continuously stirred for 2 h. The final product suspension was filtered out using a filter paper and washed with water and ethanol several times to attain the (BaSr)CO_3/SiO_2 core@shell rods. Next, the core@shell rods were added into the 10% HCl solution to generate the SiO_2 hollow tubes.

2.2. Synthesis of (BaSr)CO_3/SiO_2/TiO_2 Core@ Double-Nanoshell Rods and SiO_2/TiO_2 Double-Nanoshell Hollow Tubes. The above (BaSr)CO_3/SiO_2 core@shell rods were dispersed in 100 ml of ethanol and then mixed 0.25 g of CTAB and 0.2 ml of pure TEOT reagent, followed by slow feeding 2 ml of H_2O into the above (BaSr)CO_3/SiO_2 core@shell rod suspension with a pump at a flow rate of 0.1 ml/min under rigorous agitation at 30°C. After complete feeding, the product suspension was continuously stirred for 20 h. The final product suspension was filtered out using a filter paper and washed several times with water and ethanol. Next, the attained (BaSr)CO_3/SiO_2/TiO_2 core@ double-nanoshell rods were calcinated at 350°C to remove CTAB and then was added into the 1 M HCl to dissolve (BaSr)CO3 core materials. Finally, the resulting sample was filtered out using a filter paper and washed several times with water and ethanol.

2.3. Characterizations. The size and shape of (BaSr)CO_3/SiO_2 core@shell rods, SiO_2 hollow tubes, (BaSr)CO_3/SiO_2/TiO_2 core@ double-shell rods, and SiO_2/TiO_2 double-shell hollow tubes were measured by using an FE-SEM (LEO SUPRA 55 microscope, Carl Zeiss, Germany) and FE-TEM (using a JEM-2100F microscope operated at 200 kV). Their structure was also analyzed by powder X-ray diffraction (M18XHF-SRA, Mac Science, Japan) with Cu Kα radiation ($\lambda = 1.54056$ Å). The X-ray photoelectron spectroscopy (XPS) spectra were observed using a Quantum 2000 XPS system (Physical Electronics, Inc.). The atomic composition of the rods was analyzed by using EDS element mapping (Oxford INCA Resolution 30 mm^2 136 eV at Mn Kα 5 B to 92 U). Finally, the surface areas were calculated using the Brunauer-Emmett-Teller (BET) method, and the pore sizes were calculated using the Barrett-Joyner-Hatenda (BJH) model (BELSORP-max(MP), Japan).

3. Results and Discussion

3.1. Synthesis of (BaSr)CO_3/SiO_2 Core@Shell Rods and SiO_2 Hollow Tubes. First, the core@shell structure of (BaSr)CO_3/SiO_2 was prepared based on the sol-gel method, as shown in Scheme 1. The structure and composition of (BaSr)CO_3 core have been discussed in the published paper by current authors [54, 55]. As shown in Figures 1(b) and 1(d), the rod-shaped (BaSr)CO_3/SiO_2 core@shell with a uniform thickness of around 80 nm was attained. Particularly, from XPS spectra (Figure 1(e)), the peaks for Sr 3d and Ba 3d5 in (BaSr)CO_3/SiO_2 core-shell rods disappeared, while new peaks appeared for Si 2p assigned to SiO_2. Therefore, this result also indicated that the (BaSr)CO_3 core was fully covered with SiO_2 shell. In addition, the thickness of SiO_2 shell layer could be controlled by tuning the concentration of TEOS, as shown in Supplementary Figure 1. As a result, the thickness of SiO_2 shell layer increased from 40 nm to 180 nm when increasing the TEOS concentration from 0.2% to 0.8%. After that, the (BaSr)CO_3 core was removed by dissolving in the acid solution. Then, the SiO_2 hexagonal tubes with a rough surface were produced as shown in Figure 2. In this tubular structure of SiO_2, the outer diameters were around 600 nm~800 nm and the wall thickness was 80 nm. The CTAB was used as the template for the structure-directing polymerization during the SiO_2 and TiO_2 formation. Thus, before dissolving the (BaSr)CO_3 into an acid solution, the CTAB was calcinated at 350°C to remove the CTAB; the mesopores were created on the SiO_2 shell, which was confirmed by the high-resolution TEM analysis (Figure 2(d)). The TEM images showed perpendicularly directed pore channels in the SiO_2 shell.

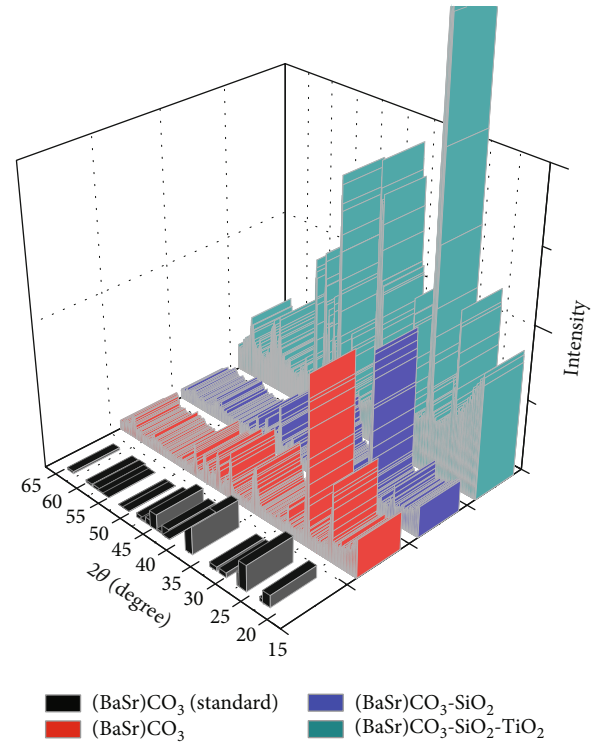

FIGURE 4: XRD patterns of (BaSr)CO_3, (BaSr)CO_3/SiO_2 core@shell rods, (BaSr)CO_3/SiO_2/TiO_2 core@ double-shell rods, and the (BaSr)CO_3 reference: JCPDS no. 47-0223.

3.2. Synthesis of (BaSr)CO_3/SiO_2/TiO_2 Core@ Double-Shell Rods and SiO_2/TiO_2 Double-Nanoshell Hollow Tubes. According to the layer-by-layer method, the TiO_2 outer layer was successfully coated on the surface of the (BaSr)CO_3/SiO_2 core@shell rods by a sol-gel method to form the (BaSr)CO_3/SiO_2/TiO_2 core@ double-shell rods. From the cross-section view (Figure 3(b)), the first boundary between the core and SiO_2 inner layer, and the second boundary between SiO_2 inner layer and TiO_2 outer layer were clearly presented. In

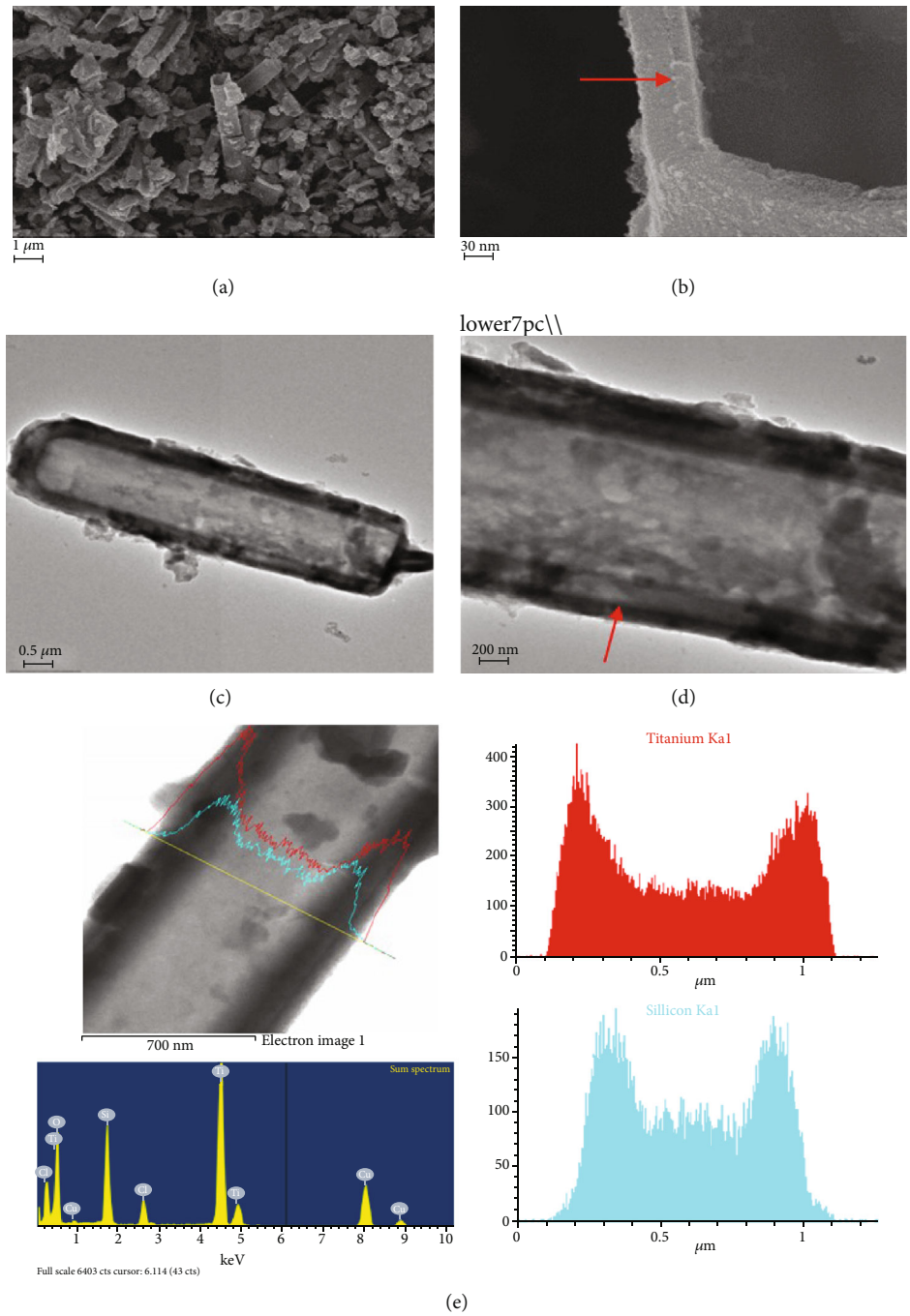

FIGURE 5: (a) FE-SEM images of SiO_2/TiO_2 double-nanoshell hollow tubes and (b) high resolution of SiO_2/TiO_2 double-nanoshell hollow tube edge. (c) FE-TEM image of SiO_2/TiO_2 double-nanoshell hollow tubes, and (d) FE-TEM image of the interface of SiO_2/TiO_2 double-nanoshell hollow tubes. (e) EDS line scanning analysis of Si and Ti in SiO_2/TiO_2 double-nanoshell hollow tubes.

particular, the inner shell with a thickness of around 80 nm uniformly wrapped the core, and the 120 nm thick outer shell homogenously wrapped the inner shell. In addition, the TEM images confirmed the core@double-nanoshell structure of $(BaSr)CO_3/SiO_2/TiO_2$ (Figures 3(c) and 3(d)). The EDS line detection showed that the metal ions were only found in the core region, and the Si covered the diameter of the core and inner shell, whereas Ti overridden the total diameter of the $(BaSr)CO_3/SiO_2/TiO_2$ core@double-nanoshell rods, strongly suggesting a core@double-nanoshell structure of $(BaSr)CO_3/SiO_2/TiO_2$. In addition, the XRD pattern (Figure 4) shows there is no difference among the $(BaSr)CO_3$ core, $(BaSr)CO_3/SiO_2$, and $(BaSr)CO_3/SiO_2/TiO_2$, that is because of the amorphous form of the SiO_2 and TiO_2. Similar to the silica formation, the thickness of the TiO_2 shell also could be adjusted by controlling the concentration of TEOT. The thickness of TiO_2 varies from 20 nm to 160 nm, when increasing the concentration of TEOT from 0.05 ml to

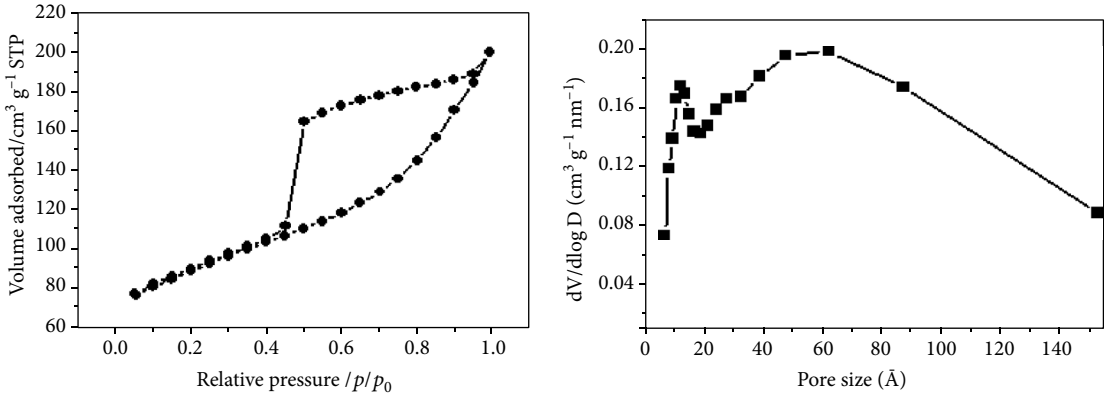

FIGURE 6: Structural characterization of SiO_2/TiO_2 double-nanoshell hollow tubes: (a) nitrogen adsorption-desorption isotherms and (b) pore size distribution calculated from the adsorption branch of isotherms.

0.25 ml, as shown in Supplementary Figure 2. Next, the SiO_2/TiO_2 double-shell hollow tubes were prepared by removing the core template. The boundary between the double-shell was obviously seen in the hollow tube structure (Figures 5(b) and 5(d)). Besides, the TEM analysis also confirms the tubular structure and presented the double shell. The EDS line presented a valley-like intensity profile of Si concentrating on the inner shell and Ti centralized on the outer shell, which further proved the formation of SiO_2/TiO_2 double-shell hollow tubes. Similarly, during the formation of TiO_2, the CTAB was continually employed as the template for the structure-directing polymerization of TiO_2 uniform formation, which suggests that the pores would be created in the double-shell of SiO_2/TiO_2 when removing the CTAB by calcinating at 350°C. Then, nitrogen physisorption characterization was used to confirm the porosity of the SiO_2/TiO_2 double-shell hollow tubes, which illustrated that the tubes were mesoporous based on the nitrogen adsorption-desorption isotherms (Figure 6(a)), as identified by the increase of the adsorption amount in the relative pressure (P/P_0) range of 0.2-0.4. In addition, the pore size distribution curve calculated from the adsorption branch of the isotherms (Figure 6(b)) was around 1 nm to 14 nm, and the surface area of the SiO_2 tubes was calculated to be 304 m^2g^{-1}, demonstrating a highly mesoporous double-nanoshell and high surface area of the tube.

The SiO_2/TiO_2 double-nanoshell hollow tubes not only could be applied as light scattering material for highly efficient dye-sensitized solar cells but also enable to be used as camptothecin (CPT) delivery agents for cancer treatment. Details of their potential application will be reported in due course.

4. Conclusion

In conclusion, the SiO_2 hollow tubes and SiO_2/TiO_2 double-nanoshell hollow tubes were successfully prepared based on a layer-by-layer method. The as-prepared SiO_2/TiO_2 double-nanoshelll layer is highly porous and has large surface area, allowing direct interaction between the inner surface of the tube and its surrounding environment. In addition, the layer thickness both of SiO_2 and TiO_2 is adjustable by controlling their used concentration. Therefore, the technique for the preparation of SiO_2/TiO_2 double-nanoshell hollow tubes can clearly be extended to other mesoporous double-shell architectures and hollow structure of other dimensions and also could be used as a platform for multicomponent, hierarchical hybrid systems. Finally, the proposed method represents a relevant and directed approach to the design of new and novel hollow particles specialized for various applications at the discretion of the end-users.

Data Availability

All data generated or analyzed during this study are included within the article.

Conflicts of Interest

The authors declare that they have no conflicts of interest.

Acknowledgments

This work was supported by the Southern Medical University (grant no: G620522046).

Supplementary Materials

Results: influence of TEOS and TEOT concentration on double shell thickness. *(Supplementary Materials)*

References

[1] F. P. Dong, I. Firkowska-Boden, M. M. L. Arras, and K. D. Jandt, "Responsive copolymer–graphene oxide hybrid microspheres with enhanced drug release properties," *RSC Advances*, vol. 7, no. 7, pp. 3720–3726, 2017.

[2] Y. H. Li, N. Li, W. Pan, Z. Z. Yu, L. M. Yang, and B. Tang, "Hollow mesoporous silica nanoparticles with tunable

structures for controlled drug delivery," *ACS Applied Materials & Interfaces*, vol. 9, no. 3, pp. 2123–2129, 2017.

[3] Y. J. Zhu, X. X. Guo, and T. K. Sham, "Calcium silicate-based drug delivery systems," *Expert Opinion on Drug Delivery*, vol. 14, no. 2, pp. 215–228, 2017.

[4] J. F. Chang, Q. Lv, G. Q. Li, J. J. Ge, C. P. Liu, and W. Xing, "Core-shell structured $Ni_{12}P_5/Ni_3(PO_4)_2$ hollow spheres as difunctional and efficient electrocatalysts for overall water electrolysis," *Applied Catalysis B: Environmental*, vol. 204, pp. 486–496, 2017.

[5] F. A. La Porta, A. E. Nogueira, L. Gracia et al., "An experimental and theoretical investigation on the optical and photocatalytic properties of ZnS nanoparticles," *Journal of Physics and Chemistry of Solids*, vol. 103, pp. 179–189, 2017.

[6] C. Liu, J. Wang, J. S. Li et al., "Fe/N decorated mulberry-like hollow mesoporous carbon fibers as efficient electrocatalysts for oxygen reduction reaction," *Carbon*, vol. 114, pp. 706–716, 2017.

[7] Y. Peng, K. K. Wang, T. Liu, J. Xu, and B. Xu, "Synthesis of one-dimensional Bi_2O_3-$Bi_2O_{2.33}$ heterojunctions with high interface quality for enhanced visible light photocatalysis in degradation of high-concentration phenol and MO dyes," *Applied Catalysis B: Environmental*, vol. 203, pp. 946–954, 2017.

[8] T. Tesfu-Zeru, M. Sakthivel, and J. F. Drillet, "Investigation of mesoporous carbon hollow spheres as catalyst support in DMFC cathode," *Applied Catalysis B: Environmental*, vol. 204, pp. 173–184, 2017.

[9] J. S. Zhang, T. J. Yao, C. C. Guan et al., "One-step preparation of magnetic recyclable quinary graphene hydrogels with high catalytic activity," *Journal of Colloid and Interface Science*, vol. 491, pp. 72–79, 2017.

[10] T. S. Zhou, Y. Zhou, R. G. Ma et al., "Nitrogen-doped hollow mesoporous carbon spheres as a highly active and stable metal-free electrocatalyst for oxygen reduction," *Carbon*, vol. 114, pp. 177–186, 2017.

[11] J. J. Jiang, K. Zhang, X. D. Chen et al., "Porous Ce-doped ZnO hollow sphere with enhanced photodegradation activity for artificial waste water," *Journal of Alloys and Compounds*, vol. 699, pp. 907–913, 2017.

[12] L. Qiao, Y. F. Bing, Y. Z. Wang, S. S. Yu, Z. Z. Liang, and Y. Zeng, "Enhanced toluene sensing performances of Pd-loaded SnO_2 cubic nanocages with porous nanoparticle-assembled shells," *Sensors & Actuators, B: Chemical*, vol. 241, pp. 1121–1129, 2017.

[13] Q. Y. Yang, Y. L. Wang, J. Liu et al., "Enhanced sensing response towards NO_2 based on ordered mesoporous Zr-doped In_2O_3 with low operating temperature," *Sensors & Actuators, B: Chemical*, vol. 241, pp. 806–813, 2017.

[14] T. Y. Yang, H. Yu, B. X. Xiao, Z. F. Li, and M. Z. Zhang, "Enhanced 1-butylamine gas sensing characteristics of flower-like V_2O_5 hierarchical architectures," *Journal of Alloys and Compounds*, vol. 699, pp. 921–927, 2017.

[15] S. Zhang, P. Song, J. Li, J. Zhang, Z. X. Yang, and Q. Wang, "Facile approach to prepare hierarchical Au-loaded In_2O_3 porous nanocubes and their enhanced sensing performance towards formaldehyde," *Sensors & Actuators, B: Chemical*, vol. 241, pp. 1130–1138, 2017.

[16] S. Zhang, P. Song, J. Zhang et al., "Highly sensitive detection of acetone using mesoporous In_2O_3 nanospheres decorated with Au nanoparticles," *Sensors & Actuators, B: Chemical*, vol. 242, pp. 983–993, 2017.

[17] T. T. Zhou, T. Zhang, R. Zhang et al., "Highly sensitive sensing platform based on $ZnSnO_3$ hollow cubes for detection of ethanol," *Applied Surface Science*, vol. 400, pp. 262–268, 2017.

[18] R. Ahmad, J. K. Kim, J. H. Kim, and J. Kim, "Well-organized, mesoporous nanocrystalline TiO2 on alumina membranes with hierarchical architecture: antifouling and photocatalytic activities," *Catalysis Today*, vol. 282, pp. 2–12, 2017.

[19] R. K. Chava, W. M. Lee, S. Y. Oh, K. U. Jeong, and Y. T. Yu, "Improvement in light harvesting and device performance of dye sensitized solar cells using electrophoretic deposited hollow TiO_2 NPs scattering layer," *Solar Energy Materials & Solar Cells*, vol. 161, pp. 255–262, 2017.

[20] J. Li, H. Z. Cui, X. J. Song, N. Wei, and J. Tian, "The high surface energy of NiO {110} facets incorporated into TiO_2 hollow microspheres by etching Ti plate for enhanced photocatalytic and photoelectrochemical activity," *Applied Surface Science*, vol. 396, pp. 1539–1545, 2017.

[21] J. P. Shi, M. Sun, X. Sun, and H. W. Zhang, "Near-infrared persistent luminescence hollow mesoporous nanospheres for drug delivery and in vivo renewable imaging," *Journal of Materials Chemistry B*, vol. 4, no. 48, pp. 7845–7851, 2016.

[22] H. S. Varol, O. Alvarez-Berrmudez, P. Dolcet et al., "Crystallization at nanodroplet interfaces in emulsion systems: a soft-template strategy for preparing porous and hollow nanoparticles," *Langmuir*, vol. 32, no. 49, pp. 13116–13123, 2016.

[23] X. Y. Li, H. Liu, S. Liu et al., "Effect of Pt-Pd hybrid nanoparticle on CdS's activity for water splitting under visible light," *International Journal of Hydrogen Energy*, vol. 41, no. 48, pp. 23015–23021, 2016.

[24] M. Tian, X. L. Cui, C. X. Dong, and Z. P. Dong, "Palladium nanoparticles dispersed on the hollow aluminosilicate γ-AlOOH as an excellent catalyst for the hydrogenation of nitroarenes under ambient conditions," *Applied Surface Science*, vol. 390, pp. 100–106, 2016.

[25] Q. Wang, R. G. Zhang, L. T. Jia, B. Hou, D. B. Li, and B. J. Wang, "Insight into the effect of surface coverage and structure over different Co surfaces on the behaviors of H_2 adsorption and activation," *International Journal of Hydrogen Energy*, vol. 41, no. 48, pp. 23022–23032, 2016.

[26] Q. M. Wang, S. G. Chen, F. Shi et al., "Structural Evolution of Solid Pt Nanoparticles to a Hollow PtFe Alloy with a Pt-Skin Surface via Space-Confined Pyrolysis and the Nanoscale Kirkendall Effect," *Advanced Materials*, vol. 28, pp. 10673–10678, 2016.

[27] S. Q. Xu, X. J. Xu, M. Xu, T. R. O'Leary, and L. N. Zhang, "Heat-induced conformation transition of the comb-branched β-glucan in dimethyl sulfoxide/water mixture," *Carbohydrate Polymer*, vol. 157, pp. 1404–1412, 2017.

[28] Z. G. An and J. J. Zhang, "Glass–NiP–CoFeP triplex-shell particles with hollow cores and tunable magnetic properties," *ACS Applied Materials & Interfaces*, vol. 5, no. 3, pp. 989–996, 2013.

[29] M. Y. Gao, Y. H. Zhao, S. H. Zeng, and H. Q. Su, "Multishell hollow CeO2/CuO microbox catalysts for preferential CO oxidation in H2-rich stream," *Catalysis Communications*, vol. 72, pp. 105–110, 2015.

[30] S. Hong, J. A. I. Acapulco, H. Y. Jang, and S. Park, "Au nanodisk-core multishell nanoparticles: synthetic method for controlling number of shells and intershell distance," *Chemistry of Materials*, vol. 26, no. 12, pp. 3618–3623, 2014.

[31] X. C. Li, L. Wang, J. H. Shi, N. X. Du, and G. H. He, "Multi-shelled nickel–cobalt oxide hollow microspheres with

optimized compositions and shell porosity for high-performance pseudocapacitors," *ACS Applied Materials & Interfaces*, vol. 8, no. 27, pp. 17276–17283, 2016.

[32] S. Q. Liang, J. Yi, and A. Q. Pan, "Synthesis of Double-Shelled LiMn2O4 Hollow Microspheres with Enhanced Electrochemical Performance for Lithium Ion Batteries," *International Journal of Electrochemical Science*, vol. 8, pp. 6535–6543, 2013.

[33] L. L. Wang, Z. Lou, T. Fei, and T. Zhang, "Zinc oxide core–shell hollow microspheres with multi-shelled architecture for gas sensor applications," *Journal of Materials Chemistry*, vol. 21, no. 48, pp. 19331–19336, 2011.

[34] X. Wu, G. Q. Lu, and L. Z. Wang, "Shell-in-shell TiO2 hollow spheres synthesized by one-pot hydrothermal method for dye-sensitized solar cell application," *Energy & Environmental Science*, vol. 4, no. 9, pp. 3565–3572, 2011.

[35] H. N. Cao, J. He, L. Deng, and X. Q. Gao, "Fabrication of cyclodextrin-functionalized superparamagnetic Fe_3O_4/amino-silane core-shell nanoparticles via layer-by-layer method," *Applied Surface Science*, vol. 255, no. 18, pp. 7974–7980, 2009.

[36] J. Y. Chen, D. M. Chao, X. F. Lu, and W. J. Zhang, "Preparation of PS-Cores/Au nanoparticles and polyaniline-shells submicrospheres via layer-by-layer method," *Solid State Phenomen*, vol. 121-123, pp. 263–266, 2007.

[37] Y. P. Chen, Y. M. Xu, D. G. Cheng et al., "Synthesis of CuO–ZnO–Al2O3 @ SAPO-34 core@shell structured catalyst by intermediate layer method," *Pure and Applied Chemistry*, vol. 86, no. 5, pp. 775–783, 2014.

[38] B. Hwang, S. H. Jang, H. H. Ahn, J. Yoon, S. Y. Kim, and Y. K. Kwon, "Preparation of magnetite core-titania shell and hollow titania nanoparticles via layer-by-layer (LbL) assembly method," *Macromolecular Research*, vol. 22, no. 2, pp. 223–226, 2014.

[39] H. Y. Liu, Y. J. Song, S. S. Li et al., "Synthesis of core/shell structured Pd3Au@Pt/C with enhanced electrocatalytic activity by regioselective atomic layer deposition combined with a wet chemical method," *RSC Advances*, vol. 6, no. 71, pp. 66712–66720, 2016.

[40] F. P. Ramanery, A. A. P. Mansur, and H. S. Mansur, "Synthesis and characterization of water-dispersed CdSe/CdS core-shell quantum dots prepared via layer-by-layer method capped with carboxylic-functionalized poly(vinyl alcohol)," *Materials Research - Ibero-American Journal*, vol. 17, suppl 1, pp. 133–140, 2014.

[41] X. M. Wang, J. D. Song, and H. L. Chen, "Preparation of ZnO@void@SiO2Rattle Type Core–Shell Nanoparticles via Layer-by-Layer Method," *Nano*, vol. 11, no. 9, article 1650103, 2016.

[42] R. R. Xing, T. F. Jiao, K. Ma, G. H. Ma, H. Mohwald, and X. H. Yan, "Regulating Cell Apoptosis on Layer-by-Layer Assembled Multilayers of Photosensitizer-Coupled Polypeptides and Gold Nanoparticles," *Scientific Reports*, vol. 6, no. 1, 2016.

[43] J. Y. Liao, D. Higgins, G. Lui, V. Chabot, X. C. Xiao, and Z. W. Chen, "Multifunctional TiO2–C/MnO2 core–double-shell nanowire arrays as high-performance 3D electrodes for lithium ion batteries," *Nano Letters*, vol. 13, no. 11, pp. 5467–5473, 2013.

[44] Z. G. Cheng, K. Cheng, and W. J. Weng, "SiO2/TiO2 nanocomposite films on polystyrene for light-induced cell detachment application," *ACS Applied Materials & Interfaces*, vol. 9, no. 3, pp. 2130–2137, 2017.

[45] F. Huang, A. T. Rad, W. Zheng, M. P. Nieh, and C. J. Cornelius, "Hybrid organic-inorganic 6FDA-6pFDA and multiblock 6FDA-DABA polyimide SiO2–TiO2 nanocomposites: synthesis, FFV, FTIR, swelling, stability, and X-ray scattering," *Polymer*, vol. 108, pp. 105–120, 2017.

[46] M. Momeni, H. Saghafian, F. Golestani-Fard, N. Barati, and A. Khanahmadi, "Effect of SiO2 addition on photocatalytic activity, water contact angle and mechanical stability of visible light activated TiO2 thin films applied on stainless steel by a sol gel method," *Applied Surface Science*, vol. 392, pp. 80–87, 2017.

[47] N. Saxena, T. Naik, and S. Paria, "Organization of SiO2and TiO2 nanoparticles into fractal patterns on glass surface for the generation of superhydrophilicity," *Journal of Physical Chemistry C*, vol. 121, no. 4, pp. 2428–2436, 2017.

[48] L. Shen, Y. F. Shen, and F. Li, "Corrigendum to 'Optimized utilization of NIR spectrum with interfacial $TiO_2/SiO_2/TiO_2$ trilayer in hybrid-integrated multijunction architecture' [Sol. Energy Mater. Sol. Cells 160 (2017) 425-429]," *Solar Energy Materials & Solar Cells*, vol. 161, pp. 460–460, 2017.

[49] L. Shen, Y. F. Shen, and F. Li, "Optimized utilization of NIR spectrum with interfacial $TiO_2/SiO_2/TiO_2$ trilayer in hybrid-integrated multijunction architecture," *Solar Energy Materials & Solar Cells*, vol. 160, pp. 425–429, 2017.

[50] W. Urbanski, K. Marycz, J. Krzak, C. Pezowicz, and S. F. Dragan, "Cytokine induction of sol-gel-derived TiO2 and SiO2 coatings on metallic substrates after implantation to rat femur," *International Journal of Nanomedicine*, vol. 12, pp. 1639–1645, 2017.

[51] Z. W. Yang, Y. Y. Shi, and B. Wang, "Photocatalytic activity of magnetically anatase TiO2 with high crystallinity and stability for dyes degradation: Insights into the dual roles of SiO2 interlayer between TiO2 and $CoFe2O_4$," *Applied Surface Science*, vol. 399, pp. 192–199, 2017.

[52] X. Chen and W. S. Kim, "Template-engaged solid-state synthesis of barium magnesium silicate Yolk@Shell particles and their high photoluminescence efficiency," *Chem-Eur J*, vol. 22, no. 21, pp. 7190–7197, 2016.

[53] X. C. Chen, J. Kim, T. Jung, J. Park, and W. S. Kim, "Architecture of directed-channel mesoporous silica/titania shell on bi-alkaline-earth carbonate particles for core-shell structure," *ChemistrySelect*, vol. 1, no. 13, pp. 3520–3526, 2016.

[54] X. C. Chen and W. S. Kim, "Template-engaged solid-state synthesis of barium-strontium silicate hexagonal tubes," *Journal of Alloys and Compounds*, vol. 647, pp. 1128–1135, 2015.

[55] X. Chen, T. Jung, J. Park, and W. S. Kim, "Preparation of single-phase three-component alkaline earth oxide of (BaSrMg)O: a high capacity and thermally stable chemisorbent for oxygen separation," *Journal of Materials Chemistry A*, vol. 3, no. 1, pp. 258–265, 2015.